The Coalinga, California, Earthquake of May 2, 1983

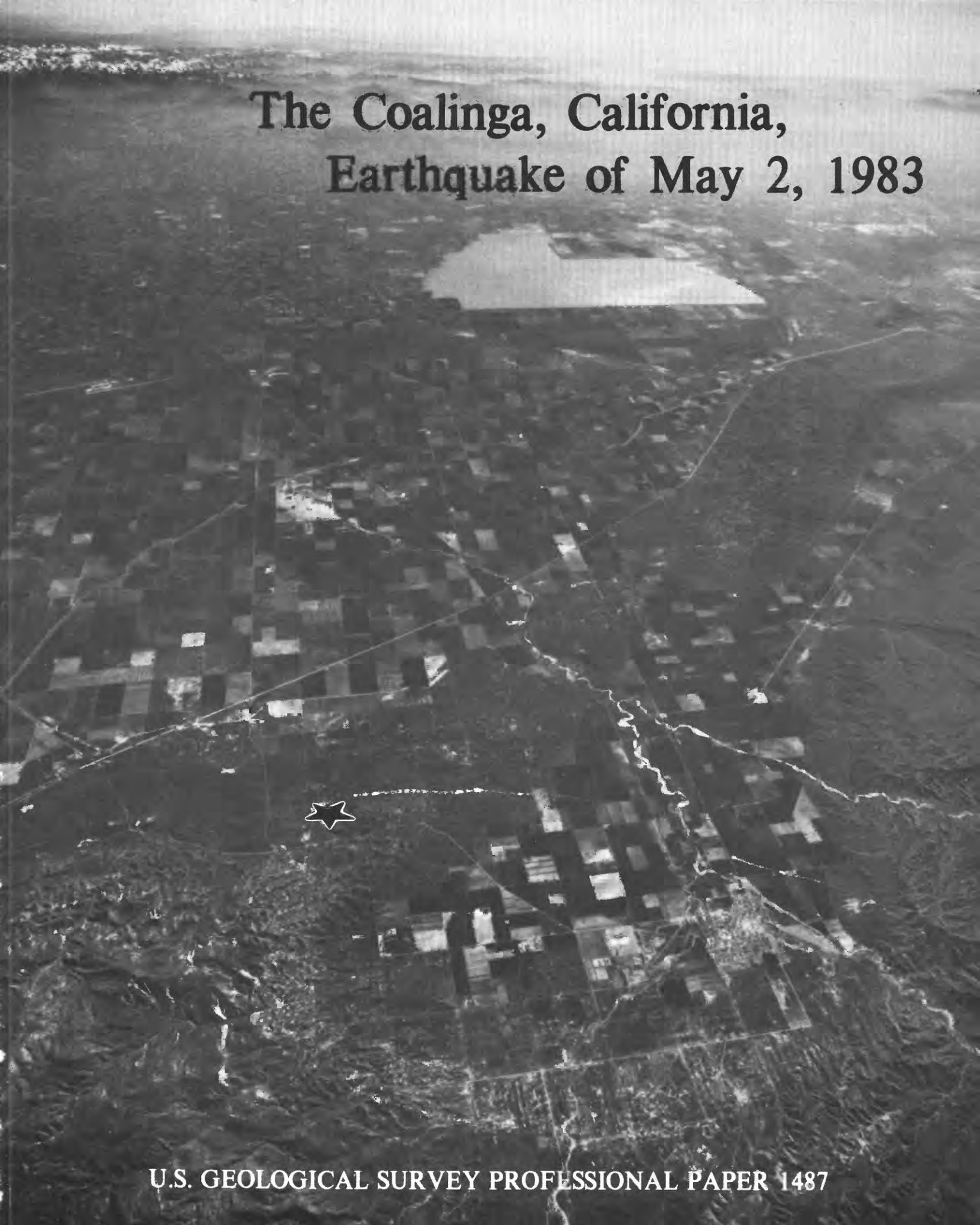

U.S. GEOLOGICAL SURVEY PROFESSIONAL PAPER 1487

COVER

Coalinga area and central San Joaquin Valley, Calif. Epicenter of May 2, 1983, earthquake (star) is above buried fault about 12 km northeast of Coalinga. Fault-related anticlines, the Coalinga anticline and the Kettleman Hills, extend from lower left to upper right and represent compression along east side of the Coast Ranges. The chapters in this volume are focused on area in foreground, except for studies of surface displacement along the Nuñez fault (outside area of photograph at bottom) and of slip-rate changes along the San Andreas fault (outside area of photograph at right). View east-southeastward; U.S. Air Force aerial photograph, taken April 2, 1970.

The Coalinga, California, Earthquake of May 2, 1983

MICHAEL J. RYMER *and* WILLIAM L. ELLSWORTH, *Editors*

U.S. GEOLOGICAL SURVEY PROFESSIONAL PAPER 1487

Contributions from:
ARCO Exploration Co.
ARCO Oil and Gas Co.
Chevron U.S.A., Inc.
Department of the Interior, U.S. Geological Survey
EQE Engineering
San Jose State University
Stanford University
University of Arizona, Tuscon
University of California, Berkeley
University of California, Riverside
West Hills College, Coalinga

UNITED STATES GOVERNMENT PRINTING OFFICE, WASHINGTON : 1990

DEPARTMENT OF THE INTERIOR

MANUEL LUJAN, JR., *Secretary*

U.S. GEOLOGICAL SURVEY

Dallas L. Peck, *Director*

Library of Congress Cataloging-in-Publication Data

The Coalinga, California earthquake of May 2, 1983 / Michael J. Rymer and William L. Ellsworth, editors.
p. cm.—(U.S. Geological Survey professional paper ; 1487)
Includes bibliographical references.
Supt. of Docs. no.: I 19.16:1487
1. Earthquakes—California—Coalinga. 2. Geology—California—Coalinga Region. I. Rymer, Michael J. II. Ellsworth, William L. III. Series.
QE535.2.U6C62 1989 551.2'2'0979483—dc20 89-600394
CIP

For sale by the Books and Open-File Reports Section, U.S. Geological Survey,
Federal Center, Box 25425, Denver, CO 80225

CONTENTS

[Numbers designate chapters]

ILLUSTRATIONS

[Plates are in pocket]

THE COALINGA, CALIFORNIA, EARTHQUAKE OF MAY 2, 1983

INTRODUCTION

By MICHAEL J. RYMER and WILLIAM L. ELLSWORTH,
U.S. GEOLOGICAL SURVEY

At 2342 G.m.t. May 2, 1983, a magnitude (M_L) 6.7 earthquake occurred about 12 km northeast of the town of Coalinga, approximately halfway between Los Angeles and San Francisco. The shock was felt from Los Angeles to 200 km north of Sacramento and as far east as Las Vegas. Unlike other well-documented, major earthquakes in California in the 20th century, this event was not associated with any previously known or suspected active fault. Comprehensive geologic and geophysical investigations begun soon after the event have demonstrated the absence of a near-surface fault responsible for the earthquake. Instead, the earthquake was closely associated with a fault zone concealed beneath folds developed along the structural boundary between the Coast (Diablo) Ranges and the San Joaquin Valley.

The May 2 earthquake occurred 35 km northeast of the San Andreas fault, in a region that has produced only scattered seismicity in historical time. Although there is abundant evidence of active folding along the boundary between the Coast Ranges and the San Joaquin Valley, little attention had been paid to Quaternary tectonics and potential earthquake sources in this region. Thus, this earthquake has provided a unique opportunity to examine the structural setting and the mechanisms of earthquake generation near Coalinga and, by analogy, along the entire boundary between the Coast Ranges and the San Joaquin and Sacramento Valleys.

This volume contains 23 chapters on the following topics related to the May 2 earthquake: geologic and seismologic setting, seismologic and geophysical studies, surface deformation and landslides, and engineering studies. The chapters range in scope from detailed to broad and from theoretical to descriptive. Earlier compilations of preliminary reports on the earthquake have been published by the U.S. Geological Survey (Borcherdt, 1983; Rymer and Ellsworth, 1985), the California Division of Mines and Geology (Bennett and Sherburne, 1983), and the Earthquake Engineering Research Institute (Scholl and Stratta, 1984). The chapters in this volume largely supersede these earlier reports and generally represent the culmination of research on the particular topics. Strong-motion studies of the earthquake and its aftershocks are currently under way.

Seismologic and geophysical studies indicate that the 1983 Coalinga earthquake sequence was complex, involving both primary and secondary slip along several faults. This earthquake sequence defines a zone 20 by 35 km long and 14 km deep, located in the vicinity of the Coalinga anticline. Clusters of instrumentally recorded earthquakes observed during 1973–83 were broadly distributed throughout this region; these earthquakes occurred within a relatively quiescent zone framed by three of these previous clusters.

New advances in instrumentation and event processing provided hypocentral and magnitude determinations for more than 6,000 aftershocks in the first 5 months after the May 2 earthquake. Hypocentral locations of aftershocks indicate a complex pattern of faulting on several seismically active fault surfaces, including a horstlike structure above the main shock. Focal mechanisms of the larger events show predominantly crustal shortening in a northeast-southwest direction, accommodated by thrusting and reverse faulting in a direction normal to the San Andreas fault. Broadband teleseismic recordings of the main shock indicate that it, too, was a complex event, involving ruptures on approximately parallel surfaces.

The May 2 earthquake occurred on the periphery of a region being actively studied in the U.S. Geological Survey's Earthquake Prediction Program. Although a seismic station was located near the epicenter, the nearest instrumental strain sensors or geodetic-survey

Manuscript approved for publication, April 26, 1988.

lines were located nearly 40 km to the southwest, near the town of Parkfield, along the San Andreas fault. Careful examination of all available data failed to reveal any clear precursory changes in the Parkfield region within the minutes to days before the May 2 earthquake. Some unusual accelerations in creep rate were observed along the San Andreas fault adjacent to the Coalinga region about 6 months before the event; however, they may have been caused by unusually heavy rainfall rather than by tectonic activity.

Special studies carried out to improve our knowledge of the geologic structure and Quaternary tectonics of the Coalinga region are reported in this volume, including detailed seismic-refraction, seismic-reflection, and gravity and magnetic surveys. These studies, together with the wealth of seismologic data, provide invaluable insight into the geologic history and faulting processes in the Coalinga region. Together, they suggest a buried wedge of Mesozoic oceanic crust being forced eastward beneath a thick section of Cretaceous and younger sedimentary rocks. Within the sedimentary rocks an anticlinal fold has developed subparallel to the San Andreas fault. Similar anticlinal features have been noted elsewhere along the east flank of the Coast Ranges.

Documentation of surface geologic effects of the main shock, and of surface faulting associated with another earthquake 40 days after the main shock, provide new perspectives on faulting processes in the Coalinga region. For example, although no surface faulting was associated with the main shock, surface displacement on the Nuñez fault, 14 km west of the main shock, did accompany a shallow-focus aftershock. Displacement on the Nuñez fault during the 1983 earthquake sequence was large relative to that during some major earthquakes in California in the 20th century, even though the Nuñez fault is only a minor structure. Moreover, a second coseismic-slip event occurred on the Nuñez fault. This later event was associated with the second largest event in the Coalinga earthquake sequence (M_L=6.0), 80 days after the main shock; the later slip was also associated with postseismic slip. This is the first well-documented example of postseismic slip associated with reverse faulting.

The timing of major earthquakes similar to those of 1983 beneath the Coalinga anticline and on the Nuñez fault were studied by detailed stratigraphic analyses. Careful analysis of alluvial deposits laid down by a stream cut through the Coalinga anticline indicates that major earthquakes with the same amount of uplift as in 1983 have minimum average repeat rates in the range 200–1,000 years during past 2,000 years. In contrast, movements on the Nuñez fault have not occurred in the past 1,700 to 1,900 years.

Two chapters in this volume deal with pore-fluid pressure in the Coalinga region. Chapter 13 documents abnormally high fluid pressures that might have reduced stress across the causative fault and thus led to the May 2 earthquake. This study also shows that the zone of abnormally high fluid pressure extends along the southwestern margin of the San Joaquin Valley. Chapter 14 analyzes whether oil-field operations, such as oil withdrawal and steam injection, near Coalinga might have induced the May 2 earthquake. Techniques of this analysis may be applicable to other oil fields in tectonically active regions.

Four chapters in this volume describe damage to manmade structures due to strong earthquake shaking in the Coalinga area: residences and commercial structures (chaps. 19, 20), industrial facilities (chap. 21), and oil-field structures (chap. 22). A common observation is that construction meeting modern building-code requirements performed very well, whereas older structures were more prone to failure.

The observations gained from the studies reported in this volume have helped clarify the faulting processes, regional tectonics, and earthquake potential of a previously enigmatic part of California. This information will be useful to scientists and engineers studying earthquake problems elsewhere in California and in other regions of the world with similar tectonic settings.

REFERENCES CITED

Bennett, J.H., and Sherburne, R.W., eds., 1983, The 1983 Coalinga, California earthquakes: California Division of Mines and Geology Special Publication 66, 335 p.

Borcherdt, R.D., compiler, 1983, The Coalinga earthquake sequence commencing May 2, 1983: U.S. Geological Survey Open-File Report 83-511, 79 p.

Rymer, M.J., and Ellsworth, W.L., eds., 1985, Proceedings of Workshop XXVII: Mechanics of the May 2, 1983 Coalinga earthquake: U.S. Geological Survey Open-File Report 85-44, 438 p.

Scholl, R.E., and Stratta, J.L., eds., 1984, Coalinga, California, earthquake of May 2, 1983: Reconnaissance report: Berkeley, Calif., Earthquake Engineering Research Institute Report 84-03, 300 p.

1. A SUMMARY OF THE CENOZOIC STRATIGRAPHY AND GEOLOGIC HISTORY OF THE COALINGA REGION, CENTRAL CALIFORNIA

By J. Alan Bartow,
U.S. Geological Survey

CONTENTS

INTRODUCTION

Cenozoic strata along the southwest side of the San Joaquin Valley (fig. 1.1) provide a nearly complete record of the depositional history and structural evolution of this large sedimentary basin. The diverse sedimentary facies represented are evidence of repeated cycles of transgression and regression that are due to relative changes in sea level. These changes, in turn, can be interpreted in terms of either tectonic activity—that is, uplift or subsidence—or eustatic sea-level change. This chapter briefly describes the stratigraphy and outlines the geologic history of the region surrounding Coalinga and the epicenter of the May 2, 1983, earthquake, concentrating on Cenozoic time, during which tectonic relations most relevant to the existing stress field were established. A more comprehensive and up to date review of the Cenozoic geologic evolution of the San Joaquin Valley is provided by Bartow (in press).

The Coalinga region includes the southern Diablo Range, bounded on the southwest by the San Andreas fault, and the central San Joaquin Valley, bounded on the east by the Sierra Nevada. The stratigraphy of the area is summarized in table 1.1 and figure 1.2, and the interrelations of stratigraphic units are illustrated in figures 1.3 through 1.5. The stratigraphic names used here are, with minor exceptions, formally defined and widely recognized; the exceptions (for example, "Gatchell and McAdams sands") are those of subsurface units for which the local oil-field terminology is used.

GEOLOGIC SETTING

The town of Coalinga is located in Pleasant Valley, a reentrant in the southern Diablo Range at the west side of the San Joaquin Valley. Pleasant Valley is separated from the San Joaquin Valley proper by Anticline Ridge (the epicenter of the May 2 earthquake), the Guijarral Hills, and the north end of the Kettleman Hills (fig. 1.1). The folds forming these aligned topographic highs mark the local east limit of the Cenozoic fold belt that bounds the San Joaquin Valley on the west and includes the southern Diablo Range and the Temblor Range. The San Joaquin Valley itself is an asymmetric structural trough (fig. 1.3), with an axis well west of the geographic midline of the valley and with a broad and relatively undeformed east flank.

During the late Mesozoic and earliest Tertiary, the area of the San Joaquin Valley and southern Diablo Range was part of a forearc basin (Dickinson and Seely, 1979) between the Sierran magmatic arc to the east and a trench and associated subduction complex (the Franciscan assemblage) to the west. A westward-thickening wedge of sediment (the Great Valley sequence) deposited in this basin reaches a thickness of more than 8 km (Mansfield, 1979) in the Coalinga area and, together with slivers of the underlying ophiolite, has been tectonically juxtaposed with structurally lower Franciscan in the Diablo Range (Page, 1981). The Upper Cretaceous part of this sequence overlaps gently west sloping Sierra Nevada crystalline basement rocks under the eastern part of the valley (fig. 1.2).

The sedimentary deposits composing the Great Valley sequence were derived from the Sierran magmatic arc to the east and northeast and deposited in submarine-fan environments. These deposits in the Diablo Range are characterized by a retrograding sequence of fan facies—that is, slope/inner fan/midfan (Panoche Formation)—followed by prograding slope deposits (Moreno Shale) (Ingersoll, 1979; Mansfield, 1979).

The Cenozoic strata filling the asymmetric San Joaquin Valley trough reach a thickness of more than 4.5 km

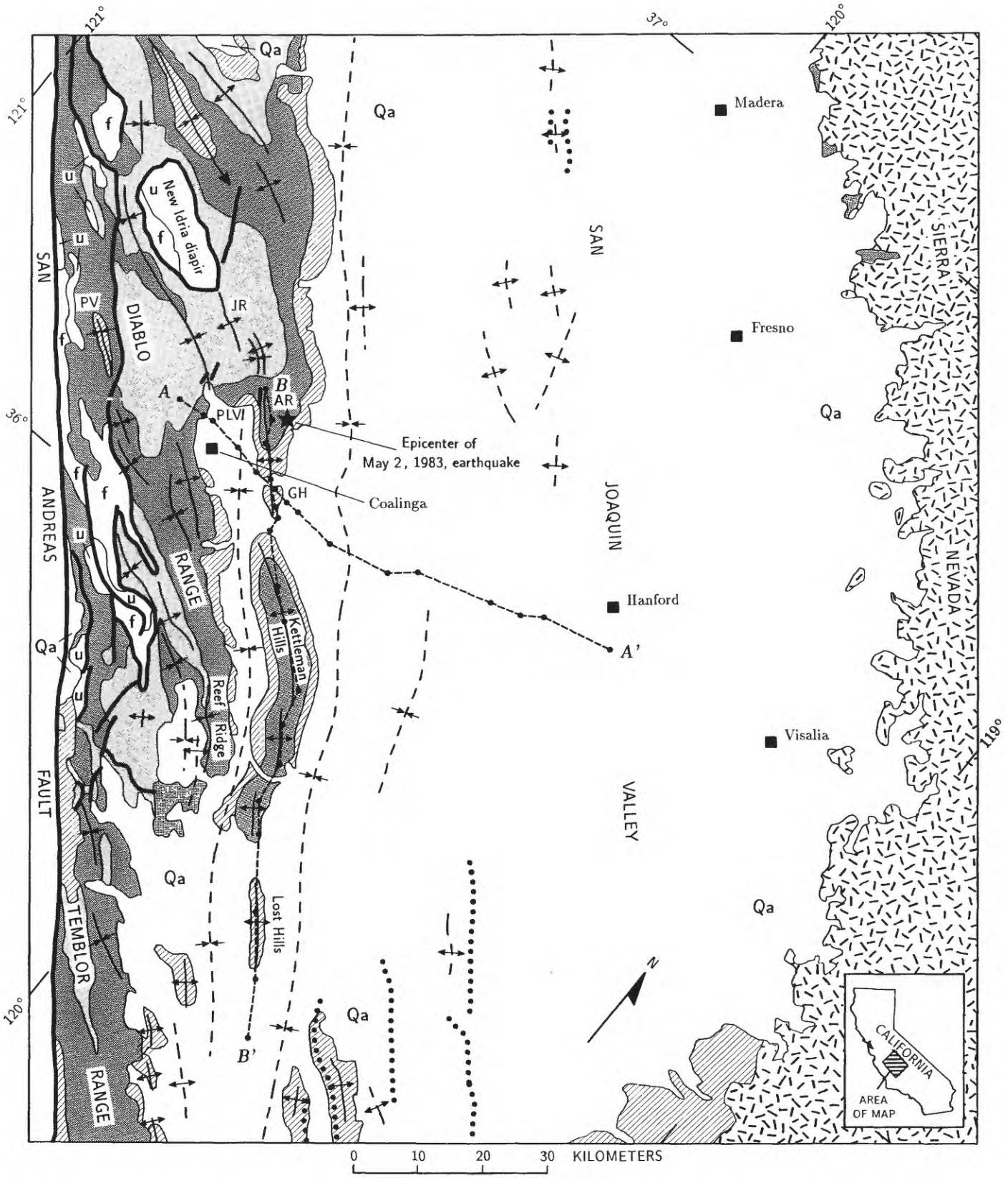

FIGURE 1.1.—Geologic index map of the Coalinga-Kettleman Hills region, Calif., showing locations of cross sections (see figs. 1.3–1.5). Geology modified from Jennings (1977). AR, Anticline Ridge; GH, Guijarral Hills; JR, Joaquin Ridge; PLV, Pleasant Valley; PV, Priest Valley.

under the west side of the valley near Coalinga and thin eastward toward the Sierra Nevada and westward, partly by erosion, toward the Diablo Range (figs. 1.3, 1.4). Along strike to the southeast, the Cenozoic section shows a consistent thickening from Anticline Ridge through the Lost Hills, except for local thinning of upper Cenozoic units in the area of Kettleman Hills South Dome and the Lost Hills (fig. 1.4).

PALEOGENE HISTORY

The principal paleogeographic elements that existed in the Coalinga region during the Paleogene were: (1) a marine basin with an eastern shelf occupying the area of the present San Joaquin Valley; (2) the ancestral Sierra Nevada bounding the basin on the east; and (3) a continental borderland of basins and highs, probably formed during Late Cretaceous and Paleocene wrench faulting along the proto-San Andreas fault, on the west (Clarke and others, 1975; Nilsen and Clarke, 1975). Paleogene strata (Lodo Formation or equivalent) unconformably overlie the Great Valley sequence (figs. 1.2–1.5), although the angular discordance is generally small or nonexistent. The absence of evidence for strong deformation suggests that this unconformity may be due at least in part to a eustatic lowering of sea level at about 62 Ma (Vail and Hardenbol, 1979).[1]

The lower Paleogene in the San Joaquin Valley consists of two depositional sequences, the lower ranging in age from Paleocene through lower Eocene, and the upper from middle through upper Eocene. The lower, transgressive-regressive sequence includes deep-marine sedimentation in the basin trough (Lodo Formation), followed by westward- or southwestward-prograding, nearshore marine and deltaic sedimentation (Gatchell sand of Coalinga anticline and McAdams sand of Kettleman Hills). The upper sequence consists of a locally transgressive sandstone (Domengine or Avenal Sandstone), followed by a widespread hemipelagic shale (Kreyenhagen Shale). Sedimentation in the deeper part of the basin to the southeast, which included a deep-sea-fan deposit (Point of Rocks Sandstone Member of the Kreyenhagen), may have been partly contemporaneous with the shallow-marine sedimentation (Avenal Sandstone) in the Kettleman Hills and southern Diablo Range area (Nilsen and Clarke, 1975). The two sequences are separated by an unconformity in the northern and eastern parts of this area, as well as in the Diablo and northern Temblor Ranges, but appear to be conformable in the Kettleman Hills area and in the deeper part of the basin to the south. Truncation of older units at the base of the upper sequence in the Diablo and Temblor Ranges, together with local evidence of Franciscan provenance in the basal sandstone (Regan, 1943), indicates uplift in those areas. Elsewhere, such as in the eastern shelf area, the unconformity may be due as much to the lowered sea level at about 52 Ma (Vail and Hardenbol, 1979) as to the uplift.

There was continuous sedimentation from the Eocene into the Oligocene in the deep southeast end of the San Joaquin Basin, and an overall regressive trend with only minor and relatively brief intervals of shoaling in the Oligocene deposits of the Kettleman Hills area (lower part of the Temblor Formation)[2], leading to an unconformity near the Oligocene-Miocene boundary (figs. 1.2–1.5). The Oligocene record in many parts of California, however, shows widespread nonmarine deposits and unconformities indicating a major regression (Nilsen, 1984). In the San Joaquin Basin north of Coalinga,

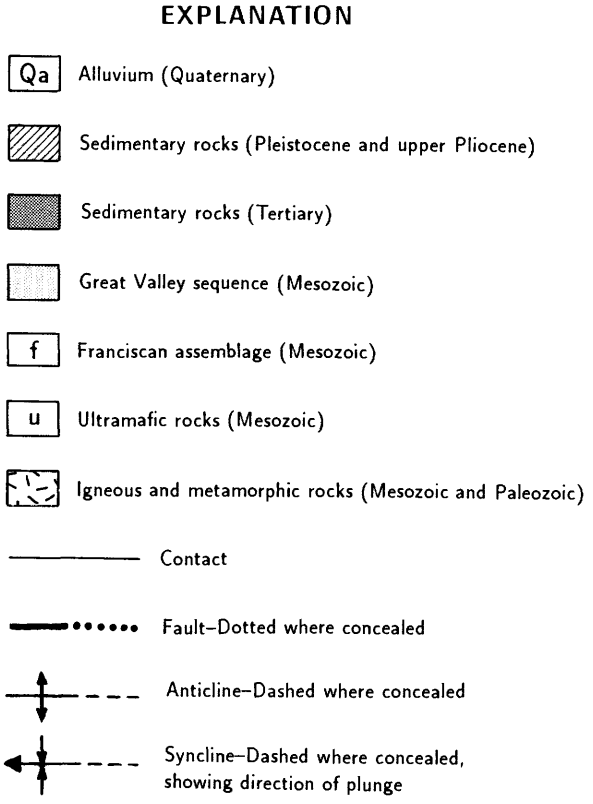

FIGURE 1.1.—Continued

[1]The marine onlap curve of Vail and Hardenbol (1979) was modified to fit the Cenozoic chronology of Berggren and others (1985).

[2]The use of the name "Temblor Formation" here is consistent with past USGS usage (Woodring and others, 1940; Dibblee 1973), but is at variance with local oil-field usage. The Temblor Formation is bounded by the Kreyenhagen Shale below and the Monterey Formation above, and in the Coalinga-Kettleman Hills area contains an angular unconformity that progressively truncates the lower part of the Temblor northward and westward (figs. 1.2–1.5). Oil-field usage, on the other hand, restricts the name "Temblor Formation" to strata above the unconformity and applies local informal names, such as "Felix siltstone," "Burbank sand," "Whepley shale," "Allison sand," "Vaqueros sand," and "Leda sand," to the various subunits below the unconformity.

TABLE 1.1.—*Stratigraphic units of the Coalinga-Kettleman Hills region, California*

[Data compiled from Woodring and others (1940), Adegoke (1969), Stanton and Dodd (1972), Dibblee (1973), Dibblee and Nilsen (1974), Nilsen and Clarke (1975), Casey and Dickinson (1976), Ingersoll (1979), Mansfield (1979), Cooley (1982), Graham and others (1982), Kuespert (1983), and Bates (1984)]

Formation	Age	Thickness (m)	Lithology	Environment of deposition
Tulare Formation	Late Pleistocene and Pliocene.	300->800	Conglomerate, sandstone, siltstone, and claystone; coarsens westward toward the Diablo Range.	Alluvial fan, fluvial, and lacustrine.
San Joaquin Formation	Pliocene	350->750	Mostly silty sandstone, siltstone, and claystone; coarsens westward and includes much coarser grained sandstone and conglomerate.	Fluvial and nearshore marine.
Etchegoin Formation	Pliocene and late Miocene.	200->1,600	Silty sandstone, silstone, mudstone, blue adestic sandstone, buff to gray sandstone, and conglomerate; coarsens southward and westward.	Shallow marine, lagoonal, and fluvial.
Kern River Formation	Pleistocene(?) to late Miocene.	800±-1,600±	Sandstone, conglomerate, and siltstone; coarsens eastward.	Alluvial fan and fluvial.
Santa Margarita Formation.	Late Miocene	0-250±	Silty arkosic sandstone, conglomerate, siltstone, and mudstone, locally calcareous.	Nearshore marine.
Reef Ridge Shale	do	0->650	Silty shale, siltstone, and minor silty sandstone.	Marine shelf (neritic to upper bathyal).
Monterey Formation	Late and middle Miocene.	---	---	Mostly deep marine (bathyal), locally near-shore marine.
McLure Shale Member		<60->650	Porcelaneous mudstone and siliceous shale; local conglomerate at base.	
Devilwater Shale Member.		0->250	Shale, calcareous shale, and siltstone	
Gould Shale Member		0->60	Siliceous shale and calcareous shale	
Big Blue Formation	Miocene	0-50	Breccia, conglomerate, conglomeratic mudstone, sandstone and mudstone, all composed of serpentinite debris.	Mass flow, fluvial, and shallow marine.
Temblor Formation[1]	Middle Miocene to Oligocene.	0->1,200	Calcareous sandstone, sandy siltstone, silty shale, conglomerate, and shale--mostly sandstone, with thin siltstone beds in the north and west, decreasing sand/shale ratio southeastward, and mostly shale in the Temblor Range.	Complex of shallow-marine, nearshore-marine, and deltaic and tidal deposits to north and west, deeper marine-slope, basinal, and submarine-fan deposits in central basin to west, grading into nonmarine deposits to north and northwest.
Kreyenhagen Shale	Eocene	<60->900	Porcelaneous or diatomaceous shale, porcelaneous mudstone, and shale.	Deep marine (bathyal).
Point of Rocks Sandstone Member.	do	0->300	Arkosic sandstone and interbedded shale	Deep-sea fan.
Domengine Sandstone, Avenal Sandstone.[2]	Middle Eocene	0-125	Arkosic sandstone and conglomerate, locally glauconitic.	Shallow marine (nearshore shelf) and deltaic.
Gatchell sand of Coalinga anticline, McAdams sand of Kettleman Hills.	Eocene	0-430	Quartzose sandstone and silty sandstone, kaolinitic in part; includes widespread unit of carbonaceous shale and sandstone.	Nearshore marine (barrier island?) and (or) deltaic.
Lodo Formation	Early Eocene and late Paleocene.	50->300	Silty shale or mudstone, and claystone	Deep marine (lower neritic to bathyal).
Great Valley sequence				
Moreno Shale	Paleocene and Late Cretaceous.	0->600	Claystone or shale, and siltstone	Deep marine (slope).
Panoche Formation	Late Cretaceous	1,000-6,000	Arkosic sandstone, siltstone, shale, and conglomerate.	Deep marine (lower slope and submarine fan).
Gravelly Flat Formation.	Early Cretaceous and Late Jurassic.	0->700	Shale with graywacke interbeds	Deep marine (slope?).
Franciscan assemblage	Cretaceous and Jurassic.	Unknown	Graywacke, claystone, greenstone, and chert, commonly intensely sheared.	Trench and slope deposits, tectonically mixed with oceanic sediment and volcanic material in subduction complex.

[1]Formally named members, the Buttonbed Sandstone, Media Shale, Carneros Sandstone, Santos Shale, Agua Sandstone, Wygal Sandstone, and Cymric Shale, are not recognized in the Kettleman Hills and Coalinga area.
[2]Domengine Sandstone equivalent in the Reef Ridge area.

Miocene deposits (upper part of the Temblor and nonmarine correlatives) unconformably overlie marine Eocene deposits (Kreyenhagen Shale) (fig. 1.2). Eustatic lowering of sea level, particularly at mid-Oligocene time (Vail and Hardenbol, 1979), probably contributed to the Oligocene regression; but tectonic activity, possibly associated with the approach of the Pacific-Farallon spreading ridge, was the dominant influence (Nilsen, 1984) and effectively masked eustatic sea-level effects for most of the San Joaquin Basin.

NEOGENE AND QUATERNARY HISTORY

The Neogene history of the San Joaquin Basin is closely tied to the evolution of the San Andreas fault system. The south-to-north progression of local volcanism through central and northern California during the Miocene, and the rapid subsidence of the southern San Joaquin Basin during middle to late Miocene time (although that deepening was augmented by a global highstand of sea level;

Vail and Hardenbol, 1979), closely correspond in time and space to northwestward migration of the Mendocino triple junction and consequent northwestward propagation of the San Andreas transform fault (Dickinson and Snyder, 1979).

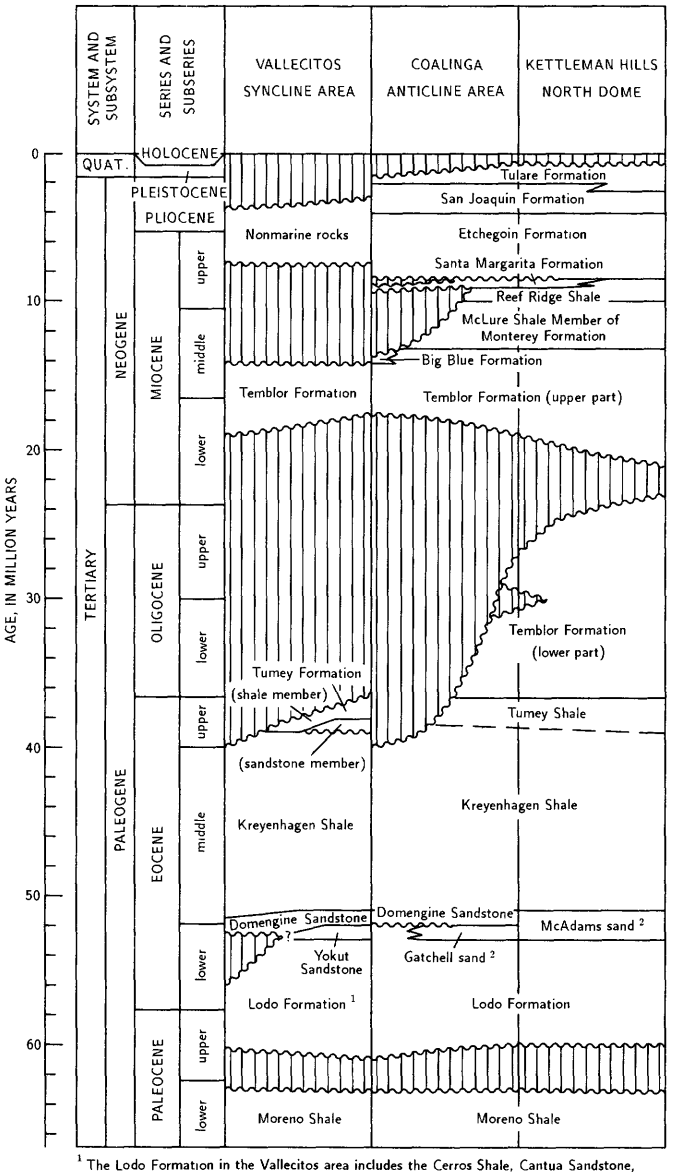

[1] The Lodo Formation in the Vallecitos area includes the Cerros Shale, Cantua Sandstone, and Arroyo Hondo Shale Members.
[2] Informal names of local usage.

FIGURE 1.2.—Correlation of Cenozoic stratigraphic units of the Coalinga region. Sources of stratigraphic information: Vallecitos syncline area—Phillips and others (1974), Dibblee (1979), Nilsen (1979), and Rentschler (1985); Coalinga anticline area—Woodring and others (1940), Church and Krammes (1959), and Bate (1985); Kettleman Hills North Dome—Woodring and others (1940), Church and Krammes (1959), Sullivan (1966), and Kuespert (1985). Series and subseries boundaries from Berggren and others (1985).

1. In the simplest view, the Neogene history of the west-central part of the San Joaquin Basin can be thought of as a single depositional sequence, although that history is complicated by several discrete episodes of tectonic activity that produced results ranging from slight shoaling to major unconformities. Miocene sedimentation began in the Coalinga area with a transgression and the deposition of shallow-marine sandstone (upper part of the Temblor Formation) over truncated Oligocene (lower part of the Temblor Formation) and Eocene (Kreyenhagen Shale) strata (figs. 1.2, 1.3, 1.5). This overall transgressive trend was interrupted by two pulses of uplift. The first uplift, near the end of the early Miocene, was centered to the southeast in the southernmost Diablo Range and Temblor Range area, resulting in an unconformity there and producing eastward-prograding deltaic and nonmarine deposits in the Coalinga-Kettleman Hills area (Kuespert, 1983). With renewed subsidence, shallow-marine sand onlapped westward over these deltaic deposits and the formerly emergent areas (upper part of the Temblor Formation in the Coalinga-Kettleman Hills area, Buttonbed Sandstone Member of the Temblor in areas to the southeast), and were followed in the Kettleman Hills area and to the southeast by deep-marine slope and submarine-fan deposits (Kuespert, 1983). The second uplift, during middle Miocene time, was centered to the north of Coalinga in the New Idria-Joaquin Ridge area of the Diablo Range (fig. 1.1) and produced southeastward-prograding deltaic and nonmarine deposits (uppermost part of the Temblor Formation) in the Coalinga anticline area (Kuespert, 1983; Bate, 1985). A subsequent serpentinite mass flow and associated deposits in the areas adjacent to Joaquin Ridge (Big Blue Formation) indicate exposure of the New Idria serpentinite (Bate, 1985).
2. The San Joaquin Basin deepened rapidly during late middle Miocene time as shelf deposits, followed by deep-water hemipelagic shale (Monterey Formation), were deposited over formerly emergent areas. The Neogene marine basin reached its maximum extent in early late Miocene time, approximately coincident with a middle to late Miocene global highstand of sea level (Graham and others, 1982). The Kettleman and Lost Hills anticlines are not expressed in isopachs of the lower parts of the Monterey Formation; however, the presence of banktop-type pure diatomite in the upper parts of the Monterey on the Lost Hills anticline suggests syndepositional growth of this structure (Graham and others, 1982).
3. A basinwide regression began in late Miocene time with shallowing of the basin to shelf depths and a transition from hemipelagic shale to shale and

siltstone richer in terrigenous material (Reef Ridge Shale). Concurrently, nearshore coarse clastic deposits (Santa Margarita Formation) prograded basinward from the north and east. Much of the basin-margin area, including the uplifted Diablo and Temblor Ranges, became fully emergent before the final marine transgression deposited shallow-marine sediment (Etchegoin Formation) over truncated older strata in the uplifted areas (figs. 1.3, 1.4). The San Joaquin Basin had been open to the ocean at its deep southwest end through middle Miocene time (Bandy and Arnal, 1969), but beginning in late Miocene time the basin was progressively closed off on the west by northwestward movement of the Salinian block highs west of the San Andreas fault and by folding and uplift in the Temblor and Diablo Ranges (Harding, 1976). By latest Miocene time, the basin had become a semienclosed shallow-marine embayment, with an opening to the northwest through the Warthan Creek-Priest Valley area near Coalinga, and with high areas to the north at Joaquin Ridge and to the southeast in the southern Diablo and Temblor Ranges.

4. The basin gradually became shallower through Pliocene time as it filled with sediment (upper part of the Etchegoin and San Joaquin Formations). Nonmarine deposits prograded into the basin from all sides (nonmarine facies of the Etchegoin and San Joaquin Formations on the west side, and the Kern River Formation on the east side), leading to the final transition to nonmarine sedimentation during latest Pliocene time (lower part of the Tulare Formation). Folding along the west side of the San Joaquin Valley

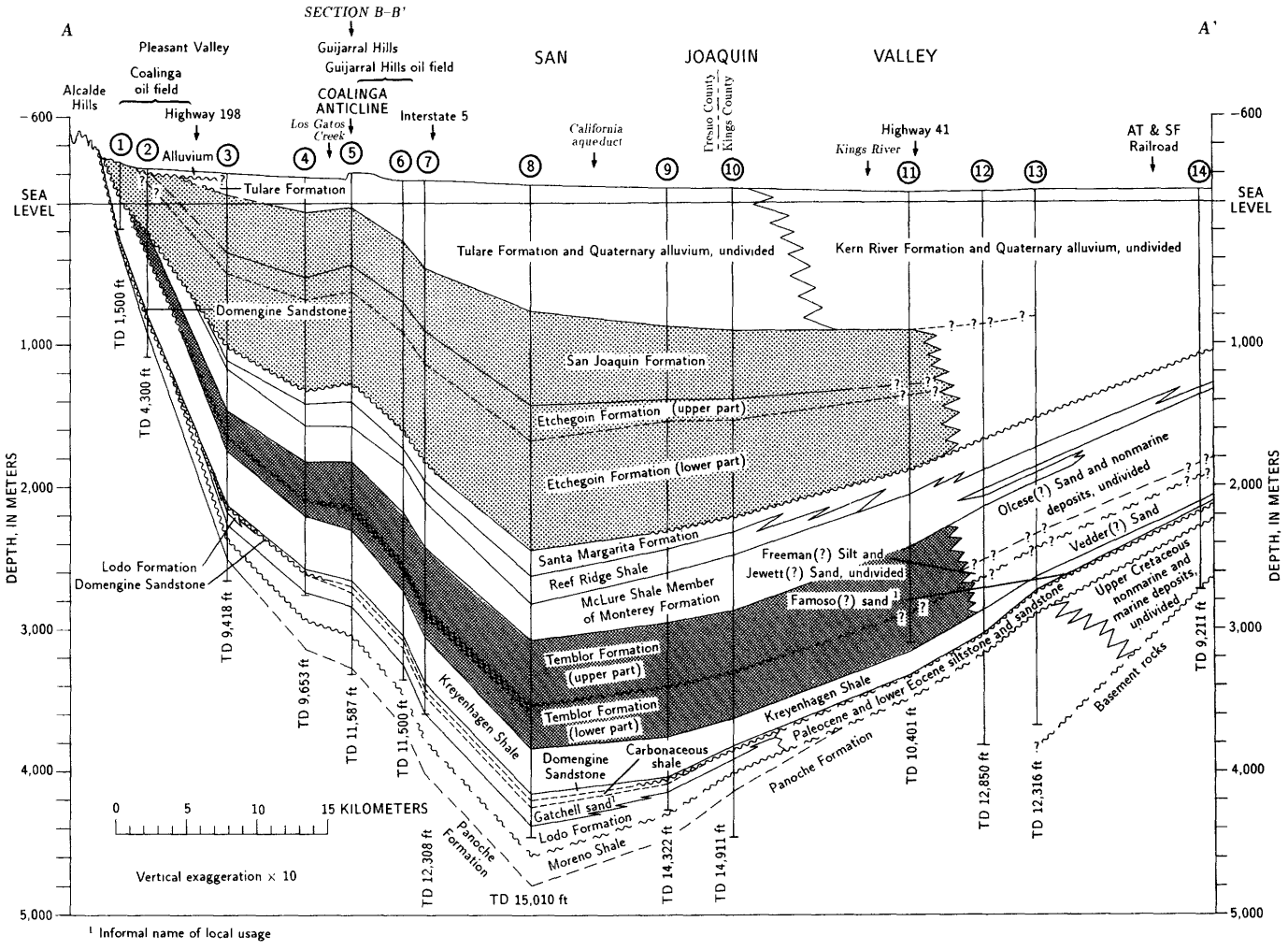

FIGURE 1.3.—East-west cross section of western San Joaquin Valley from near Coalinga to near Hanford. Numbered vertical lines denote wells listed in table 1.2. Datum is sea level. Solid line, known formational contact; long-dashed line, inferred formational contact, queried where uncertain; short-dashed line, electric-log marker; wavy line, unconformity; dashed wavy line, inferred unconformity; TD, total depth.

grew progressively basinward through Miocene and Pliocene time (Harding, 1976), and by late Pliocene time there was evidence, provided by the slight thinning of upper Pliocene strata (San Joaquin Formation) over the structure (figs. 1.3, 1.4), of growth of the Coalinga anticline. Growth of the Kettleman Hills structure must have been initiated at about this time or later because late Pliocene facies trends (Stanton and Dodd, 1972) are apparently unaffected by the presence of a growing structure at that locality.

The final transition to nonmarine conditions was augmented by continued deformation in the Temblor and Diablo Ranges during late Pliocene and Pleistocene time (Page, 1981), and it was probably at about that time that the western outlet of the basin through Priest Valley was finally closed off by Coast Range deformation. Latest Pliocene and Pleistocene alluvial-fan deposits (Tulare Formation) overlie truncated older strata along the west side of the San Joaquin Valley, although only a short distance basinward more distal facies are apparently conformable with underlying Pliocene deposits (fig. 1.3). Dominantly fluvial sedimentation has continued to the present, with intermittent lacustrine deposits concentrated in the central part of the basin. Episodic alluvial sedimentation in the San Joaquin Valley throughout the Quaternary probably has been controlled more by climatic fluctuations than by tectonic activity (Marchand, 1977; Lettis, 1982); however, the Quaternary growth of such structures as the Coalinga anticline and the Kettleman Hills, as well as Quaternary folding and faulting elsewhere in the Diablo Range (Lettis, 1982), demonstrates continued tectonic activity in that period. Furthermore, the occurrence of such earthquake sequences as that beginning in May 1983 indicates ongoing deformation in the Coalinga region.

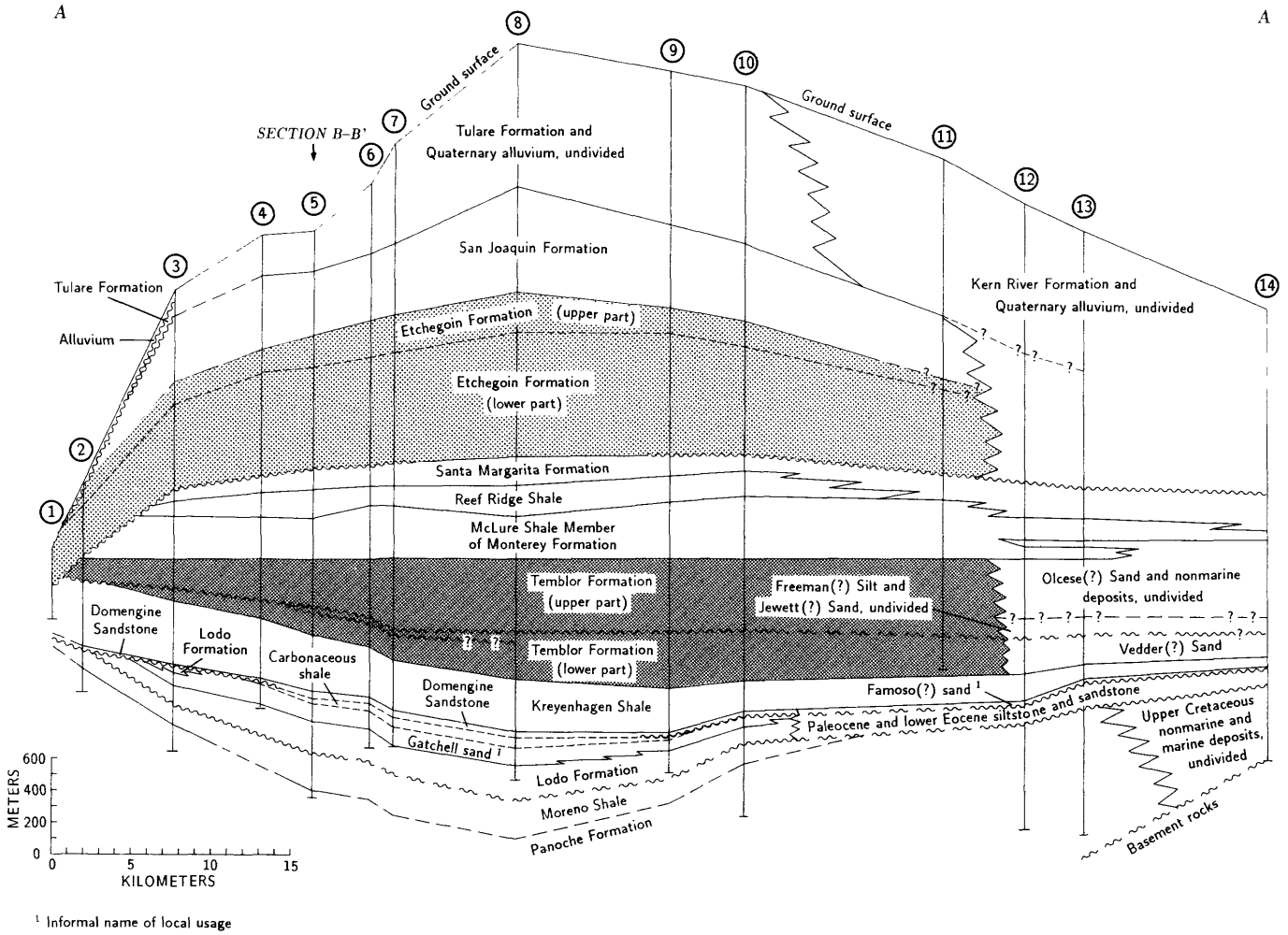

[1] Informal name of local usage

FIGURE 1.4.—East-west stratigraphic cross section of western San Joaquin Valley. Datum is top of the Temblor Formation. Same location and symbols as in figure 1.3.

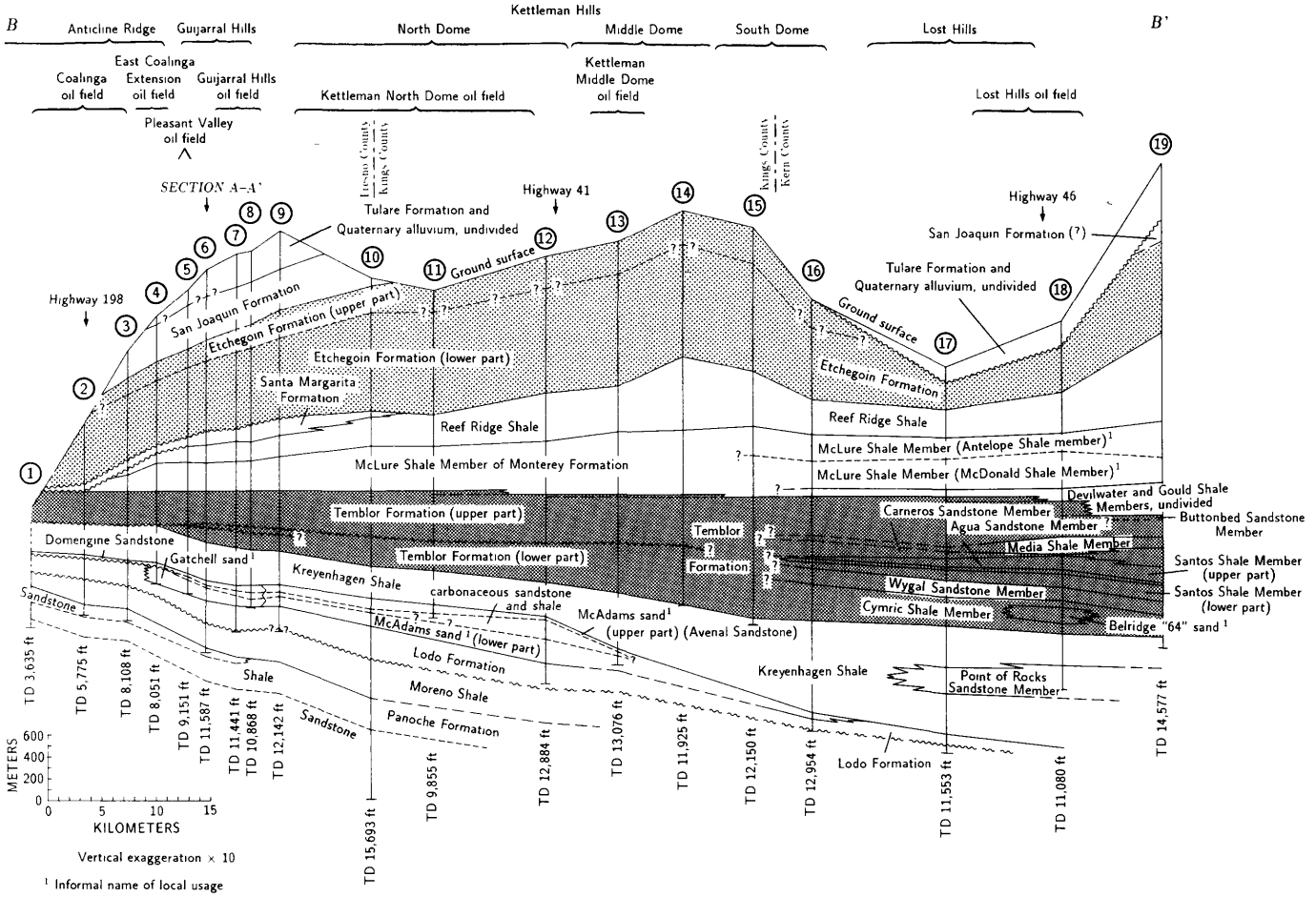

FIGURE 1.5.—Northwest-southeast stratigraphic cross section from Anticline Ridge to Lost Hills. Numbered vertical lines denote wells listed in table 1.2. Datum is top of the Temblor Formation. Same symbols as in figure 1.3.

REFERENCES CITED

Adegoke, O.S., 1969, Stratigraphy and paleontology of the marine Neogene formations of the Coalinga region, California: University of California Publications in Geological Sciences, v. 80, 269 p.

Bandy, O.L., and Arnal, R.E., 1969, Middle Tertiary basin development, San Joaquin Valley, California: Geological Society of America Bulletin, v. 80, no. 5, p. 783–819.

Bartow, J.A., in press, The Cenozoic evolution of the San Joaquin Valley, California: U.S. Geological Survey Professional Paper 1501.

Bate, M.A., 1985, Depositional sequence of Temblor and Big Blue Formations, Coalinga anticline, California, *in* Graham, S.A., ed., Geology of the Temblor Formation, western San Joaquin Basin, California: Society of Economic Paleontologists and Mineralogists, Pacific Section Volume and Guidebook, p. 69–86.

Berggren, W.A., Kent, D.V., Flynn, J.J., and Van Couvering, J.A., 1985, Cenozoic geochronology: Geological Society of America Bulletin, v. 96, p. 1407–1418.

Casey, T.A.L., and Dickinson, W.R., 1976, Sedimentary serpentinite of the Miocene Big Blue Formation near Cantua Creek, California, *in* Fritsche, A.E., TerBest, Harry, and Wornardt, W.W., eds., The Neogene symposium: Society of Economic Paleontologists and Mineralogists, Pacific Section Annual Meeting, San Francisco, 1976, Papers, p. 65–74.

Church, H.V., Jr., and Krammes, Kenneth, cochairmen, 1959, Correlation section longitudinally north-south thru westside San Joaquin Valley from Coalinga to Midway Sunset and across San Andreas fault into southeast Cuyama Valley: American Association of Petroleum Geologists, Pacific Section.

Clarke, S H., Jr., Howell, D.G., and Nilsen, T.H., 1975, Paleogene geography of California, *in* Weaver, D.W., Hornaday, G.R., and Tipton, Ann, eds., Paleogene symposium & selected technical papers: American Association of Petroleum Geologists-Society of Economic Paleontologists and Mineralogists-Society of Exploration Geophysicists, Pacific Sections Annual Meeting, Long Beach, Calif., 1975, Papers, p. 121–154.

Cooley, S.A., 1982, Depositional environments of the lower and middle Miocene Temblor Formation of Reef Ridge, Fresno and Kings Counties, California, *in* Williams, L.A., and Graham, S.A., eds., Monterey Formation and associated coarse clastic rocks, central San Joaquin Basin, California: Society of Economic Paleontologists and Mineralogists, Pacific Section Annual Fall Field Trip, 1982, Volume and Guidebook, p. 55–72.

Dibblee, T.W., Jr., 1973, Stratigraphy of the southern Coast Ranges near the San Andreas fault from Cholame to Maricopa, California: U.S. Geological Survey Professional Paper 764, 45 p.

Dibblee, T.W., Jr., 1979, Middle and late Cenozoic deposition and

TABLE 1.2.—*Wells shown on cross sections* A–A' *(fig. 1.3) and* B–B' *(fig. 1.4)*

No.	Well	Location		
		Sec.	T.	R.
	Cross section A-A'			
1	Producers Oil "Zier" 18----------	23	20 S.	14 E.
2	Chevron USA 302----------	19	20 S.	15 E.
3	Superior Oil "Pleasant Valley" 1.	22	20 S.	15 E.
4	Lloyd A. Harnish "Guijarral Service" 65-30F.	30	20 S.	16 E.
5	Union Oil "Gatchell" 65-28-------	28	20 S.	16 E.
6	Texaco "Spieler" 1----------	26	20 S.	16 E.
7	C.W. Colgrove "Bordagaray" 18-30.	30	20 S.	17 E.
8	Great Basins Petroleum 1-35------	35	20 S.	17 E.
9	Chevron USA "Haven-Boston" 313---	23	20 S.	18 E.
10	Mobil Oil "B.L.C." 48-7----------	7	20 S.	19 E.
11	Scope Industries "SoCal-Bergan" 88-32.	32	19 S.	20 E.
12	Terra Resources "Piexoto" 1------	26	19 S.	20 E.
13	Canus Petroleum "Hansen Farms" 1.	19	19 S.	21 E.
14	Chevron USA "Mills" 58-8---------	8	19 S.	22 E.
	Cross section B-B'			
1	Fresno Oil Investment "Phelps-Gov't." 2.	20	19 S.	15 E.
2	Chevron USA 213----------	35	19 S.	15 E.
3	Gulf Oil "Leavitt-Hintze" 1------	12	20 S.	15 E.
4	Union Oil "USL" 68----------	18	20 S.	16 E.
5	Chevron USA "P.V.F." 82-29F------	29	20 S.	16 E.
6	Union Oil "Gatchell" 65-28-------	28	20 S.	16 E.
7	Sun Oil "Dessel" 41-2----------	2	21 S.	16 E.
8	Chevron USA "Bourdieu" 1-A-------	1	21 S.	16 E.
9	Artnell Co. "Helm-Sumpf-SOCO Fee" 42-13.	13	21 S.	16 E.
10	Kettleman North Dome Unit 423-34J.	34	21 S.	17 E.
11	Kettleman North Dome Unit E27-7Q.	7	22 S.	18 E.
12	Kettleman North Dome Unit E1-1U.	1	23 S.	18 E.
13	Middle Dome Corp. 38-19V---------	19	23 S.	19 E.
14	Chevron USA "SF & FL" 68---------	4	24 S.	19 E.
15	Occidental Petroleum "USL" 27-27.	27	24 S.	19 E.
16	Chevron USA "SF & FL" 4-2--------	12	25 S.	19 E.
17	Mobil Oil "Williamson" 33-11-----	11	26 S.	20 E.
18	Chevron USA "Cahn" 58-4----------	4	27 S.	21 E.
19	Chevron USA "Van Sicklin" 45-----	36	27 S.	21 E.

tectonics of the central Diablo Range between Hollister and New Idria, *in* Nilsen, T.H., and Dibblee, T.W., Jr., eds., Geology of the central Diablo Range between Hollister and New Idria, California: Geological Society of America, Cordilleran Section Field Trip, 1979, Guidebook, p. 56–63.

Dibblee, T.W., Jr., and Nilsen, T.H., 1974, Lower Tertiary stratigraphy from Panoche Creek area to Domengine Creek area and Vallecitos area, California, *in* Hornaday, G.R., ed., The Paleogene of the Panoche Creek-Cantua Creek area, central California: Society of Economic Paleontologists and Mineralogists, Pacific Section Annual Fall Field Trip, 1974, Guidebook, p. 28–37.

Dickinson, W.R., and Seely, D.R., 1979, Structure and stratigraphy of forearc regions: American Association of Petroleum Geologists Bulletin, v. 63, no. 1, p. 2–31.

Dickinson, W.R., and Snyder, W.S., 1979, Geometry of triple junctions related to San Andreas transform: Journal of Geophysical Research, v. 84, no. B2, p. 561–572.

Graham, S.A., Williams, L.A., Bate, M., and Weber, L.S., 1982, Stratigraphic and depositional framework of the Monterey Formation and associated coarse clastics of the central San Joaquin Basin, *in* Williams, L.A., and Graham, S.A., eds., Monterey Formation and associated coarse clastic rocks, central San Joaquin Basin, California: Society of Economic Paleontologists and Mineralogists, Pacific Section Annual Fall Field Trip, 1982, Volume and Guidebook, p. 3–16.

Harding, T.P., 1976, Tectonic significance and hydrocarbon trapping consequences of sequential folding synchronous with San Andreas faulting, San Joaquin Valley, California: American Association of Petroleum Geologists Bulletin, v. 60, no. 3, p. 356–378.

Ingersoll, R.V., 1979, Evolution of the Late Cretaceous forearc basin, northern and central California: Geological Society of America Bulletin, pt. 1, v. 90, no. 9, p. 813–826.

Jennings, C.W., compiler, 1977, Geologic map of California: California Division of Mines and Geology Geologic Data Map 2, scale 1:750,000.

Kuespert, Jon, 1985, Depositional environments and sedimentary history of the Miocene Temblor Formation and associated Oligo-Miocene units in the vicinity of Kettleman North Dome, San Joaquin Valley, California, *in* Graham, S.A., ed., Geology of the Temblor Formation, western San Joaquin Basin, California: Society of Economic Paleontologists and Mineralogists, Pacific Section Volume and Guidebook, p. 53–67.

Lettis, W.R:, 1982, Late Cenozoic stratigraphy and structure of the western margin of the central San Joaquin Valley, California: U.S. Geological Survey Open-File Report 82-526, 203 p.

Mansfield, C.F., 1979, Upper Mesozoic subsea fan deposits in the southern Diablo Range, California: Record of the Sierra Nevada magmatic arc: Geological Society of America Bulletin, pt. 1, v. 90, no. 11, p. 1025–1046.

Marchand, D.E., 1977, The Cenozoic history of the San Joaquin Valley and adjacent Sierra Nevada as inferred from the geology and soils of the eastern San Joaquin Valley, *in* Singer, M.J., ed., Soil development, geomorphology and Cenozoic history of the northeastern San Joaquin Valley and adjacent areas, California: American Society of Agronomy-Geological Society of America-Soil Science Society of America Joint Field Section, 1977, Guidebook, p. 39–50.

Nilsen, T.H., 1979, Early Cenozoic stratigraphy, tectonics and sedimentation of the central Diablo Range between Hollister and New Idria, *in* Nilsen, T.H., and Dibblee, T.W., Jr., eds., Geology of the central Diablo Range between Hollister and New Idria, California: Geological Society of America, Cordilleran Section Field Trip, 1979, Guidebook, p. 31–55.

Nilsen, T.H., 1984, Oligocene tectonics and sedimentation, California, *in* Nilsen, T.H., ed., Fluvial sedimentation and related tectonic framework, western North America: Sedimentary Geology, v. 38, no. 1–4 (special issue), p. 305–336.

Nilsen, T.H., and Clarke, S.H., Jr., 1975, Sedimentation and tectonics in the early Tertiary continental borderland of central California: U.S. Geological Survey Professional Paper 925, 64 p.

Page, B.M., 1981, The southern Coast Ranges, *in* Ernst, W.G., ed., The geotectonic development of California (Rubey volume 1): Englewood Cliffs, N.J., Prentice-Hall, p. 329–417.

Phillips, F.J., Tipton, Ann, and Watkins, Rodney, 1974, Outcrop studies of the Eo-Oligocene Tumey Formation, Monocline Ridge, Fresno County, California, *in* Hornaday, G.R., ed., The Paleo-

gene of the Panoche Creek-Cantua Creek area, Society of Economic Paleontologists and Mineralogists, Pacific Section Annual Fall Field Trip, 1974, Guidebook, p. 38–68.

Regan, L.J., Jr., 1943, Origin of the Eocene sands of the Coalinga District, California: Pasadena, California Institute of Technology, Ph.D. thesis, 73 p.

Rentschler, M.S., 1985, Structurally controlled Neogene sedimentation in the Vallecitos syncline, *in* Graham, S.A., ed., Geology of the Temblor Formation, western San Joaquin Basin, California: Society of Economic Paleontologists and Mineralogists, Pacific Section Volume and Guidebook, p. 87–96.

Stanton, R.J., Jr., and Dodd, J.R., 1972, Pliocene cyclic sedimentation in the Kettleman Hills, California, *in* Geology and oil fields—west side central San Joaquin Valley: American Association of Petroleum Geologists-Society of Exploration Geophysicists-Society of Economic Paleontologists and Mineralogists, Pacific Sections Annual Meeting, 1972, Field Trip Guidebook, p. 50–58.

Sullivan, J.C., 1966, Kettleman North Dome oil field: California Division of Oil and Gas Summary of Operations—California Oil Fields, v. 52, no. 1, p. 5–21.

Vail, P.R., and Hardenbol, Jan, 1979, Sea-level changes during the Tertiary: Oceanus, v. 22, no. 3, p. 71–79.

Woodring, W.P., Stewart, Ralph, and Richards, R.W., 1940, Geology of the Kettleman Hills oil field, California: Stratigraphy, paleontology, and structure: U.S. Geological Survey Professional Paper 195, 170 p.

2. TECTONIC SETTING

By R.F. YERKES,
U.S. GEOLOGICAL SURVEY

CONTENTS

ABSTRACT

The 1983 Coalinga main shock occurred about 45 km east of the San Andreas fault and about 10 km below the Coalinga anticline on the east edge of the southern Diablo Range, central Coast Ranges of California. The aftershock pattern broadly outlined the southeast-plunging Coalinga anticline of late Cenozoic strata but generally excluded Joaquin Ridge, an east-plunging anticline of Tertiary and older strata contiguous on the north. The Coalinga anticline plunges southeast toward Kettleman North Dome, the northern of four narrow, elongate uplifts of late Cenozoic strata along the Diablo Range-San Joaquin Valley margin. These uplifts are notable for their near-lithostatic pore-fluid pressures at depth.

The San Joaquin Valley, the large southern part of the Great Valley of California, is a broad asymmetric trough. Its sedimentary sequence, locally more than 9 km thick, ranges in age from Late Jurassic through Holocene and is chiefly marine upward into the Pliocene sequence. The fill conceals the eastern margin of Franciscan rocks, which underlie the Diablo Range, and the western margin of Sierran basement, as well as intervening rocks and structures. A 20- to 30-km-wide band of narrow elongate folds, many containing oil fields, extends along the west side of the valley for at least 115 km southeast of Joaquin Ridge. Fold axes generally trend subparallel to the San Andreas fault, and many are cut by reverse faults of similar trend. The eastern margin of this fold belt is 15 to 20 km east of the mapped Franciscan substrate but essentially coincides with the eastern margin of an extensive subsurface field of abnormally high pore pressures.

The Coast Range-Great Valley boundary is marked by an abrupt westward thickening and upturning of late Mesozoic and overlying strata along most of its length. The buried eastern margin of Franciscan rocks beneath the Coalinga anticline forms the east tip of a tectonic wedge that peels up late Mesozoic and younger strata to form anticlines, such as the Coalinga anticline, as the wedge is thrust eastward during 1983-type earthquakes. Structure contours on young basin deposits and geophysical profiles suggest that the western margin of the San Joaquin Basin is controlled by this wedging process and that the original axis of the ancestral basin lay far west of the present margin.

The western and eastern margins of the central Coast Ranges and all of the western Transverse Ranges are characterized by isolated clusters of thrust/reverse earthquakes. Examples of $M_L \geq 5$ thrust reverse earthquakes include the 1980 Point Sal and 1983 Coalinga earthquakes in the central Coast Ranges, and the 1971 San Fernando, 1973 Point Mugu, and 1978 Santa Barbara earthquakes in the western Transverse Ranges. A broad section of California, from Monterey Bay to the Los Angeles Basin and from the Continental Shelf to the San Joaquin Valley, is characterized by northeast-southwest compression, as shown by the *P*-axes of numerous such earthquakes and the maximum-compressive-stress axis compatible with the 1971 San Fernando and 1983 Coalinga earthquake sequences. Fold axes throughout this region are oriented generally normal to this compression, rather than as wrench folds in the San Andreas system. Shortening normal to the San Andreas fault—such as during the 1983 Coalinga main shock—is generally attributed to divergence between the fault and Pacific-North American plate motion, and to northwestward extension of the Basin and Range province. Unusual aspects of the resulting deformation include sole thrusts or regional decollements beneath the central Coast and western Transverse Ranges, probably permitted or aided by abnormally high pore pressures at depth.

INTRODUCTION

The 1983 Coalinga main shock occurred beneath the Coalinga anticline, about 45 km east of the San Andreas near the boundary between the San Joaquin Valley and the southeastern Diablo Range of the central California Coast Ranges (fig. 2.1). The main shock and most aftershocks occurred 6 to 14 km beneath the Coalinga anticline-Pleasant Valley syncline area. The main-shock epicenter was about 10 km northeast of the town of Coalinga, near the axis of the Coalinga anticline. The aftershock epicenters form an elliptical pattern, about 35 km long from Nuñez Canyon on the northwest to the Guijarral Hills on the southeast, and about 15 km wide from Coalinga on the southwest to the main-shock epicenter (fig. 2.2). This pattern includes most of the southeast-plunging Coalinga anticline but lies south of contiguous, east-southeast-plunging Joaquin Ridge. This chapter outlines aspects of the structural history, seismicity, and inferred stress regime of the Diablo Range-San Joaquin Valley region.

GEOLOGY AND STRUCTURE

The Diablo Range extends about 325 km from the Sacramento River near lat 38° N. on the northwest to

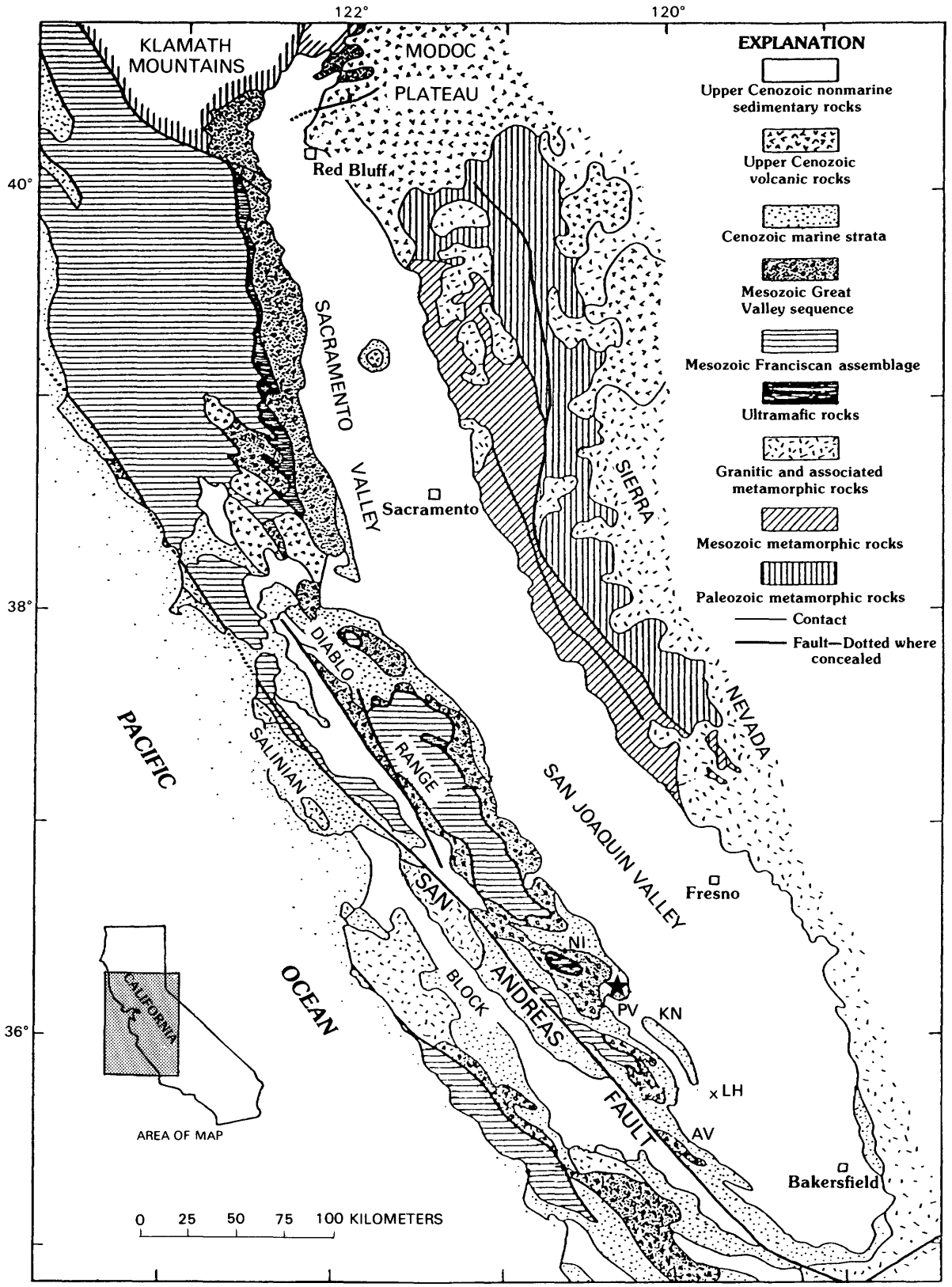

FIGURE 2.1.—Sketch map of the Sacramento and San Joaquin Valleys and Diablo Range, showing major geographic and geologic features: AV, Antelope Valley; KN, Kettleman Hills, North Dome; LH, Lost Hills; NI, New Idria ultramafic body; PV, Pleasant Valley. Star denotes location of 1983 main shock below the Coalinga anticline.

Antelope Valley on the southeast (fig. 2.1); it averages about 40 km in width from the San Andreas-Calaveras-Hayward faults on the southwest to the San Joaquin Valley on the northeast. The main mass of the range, centered about 125 km northwest of the Coalinga anticline, is about 120 km long and generally antiformal in style. The core of the mass is a tectonic assemblage of Franciscan rocks, chiefly late Mesozoic melange, mudstone, sandstone, graywacke, greenstone, and blueschist. The core is flanked by generally coeval strata of

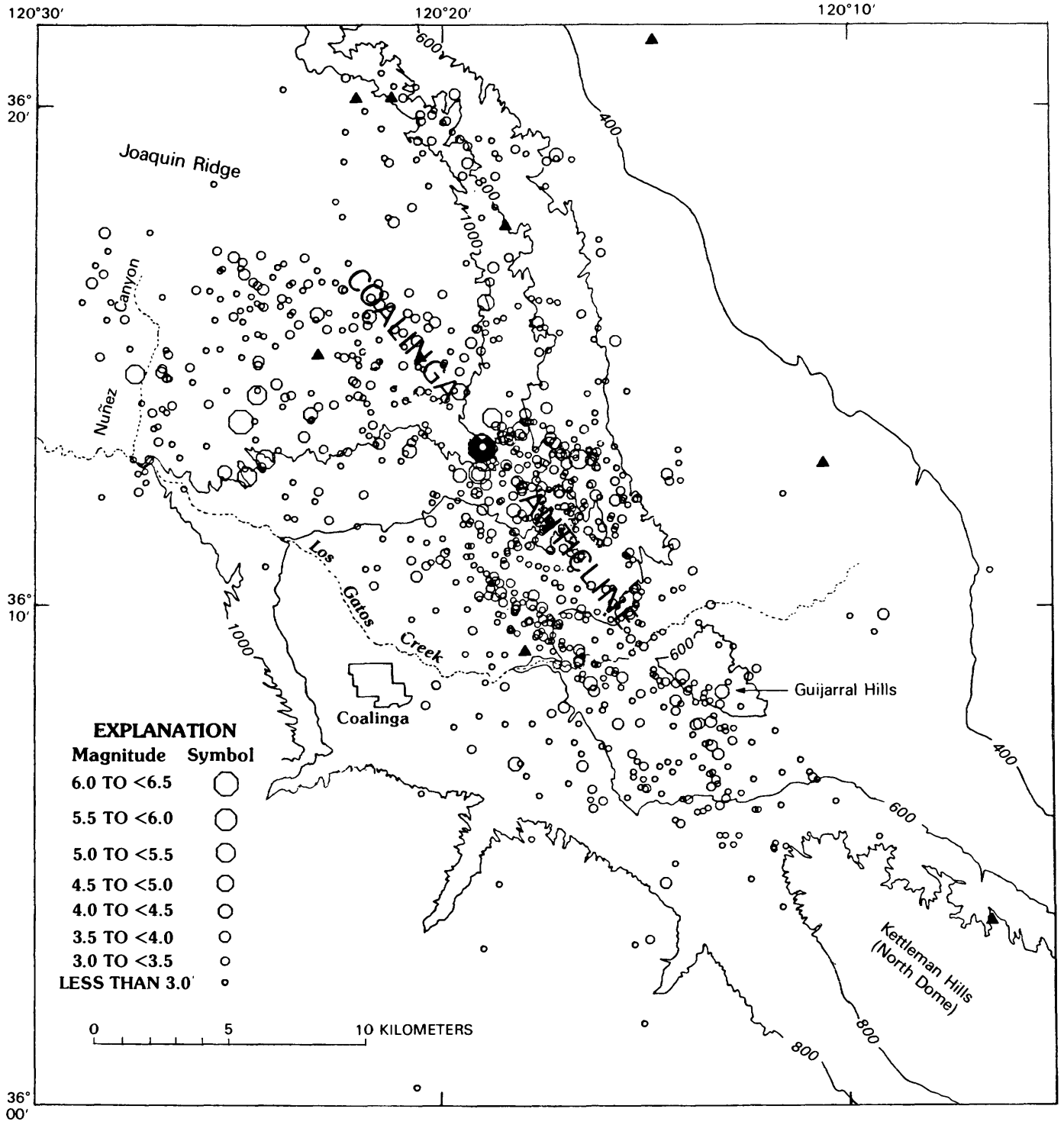

FIGURE 2.2.—Locations of epicenters of the 1983 Coalinga earthquake sequence, including aftershocks of M_L = 2.5 through September 30, 1983. Solid symbol, main-shock epicenter (M_L = 6.7); triangle, recording station. Contour interval, 200 ft. Modified from Eaton (1985b, fig. 2).

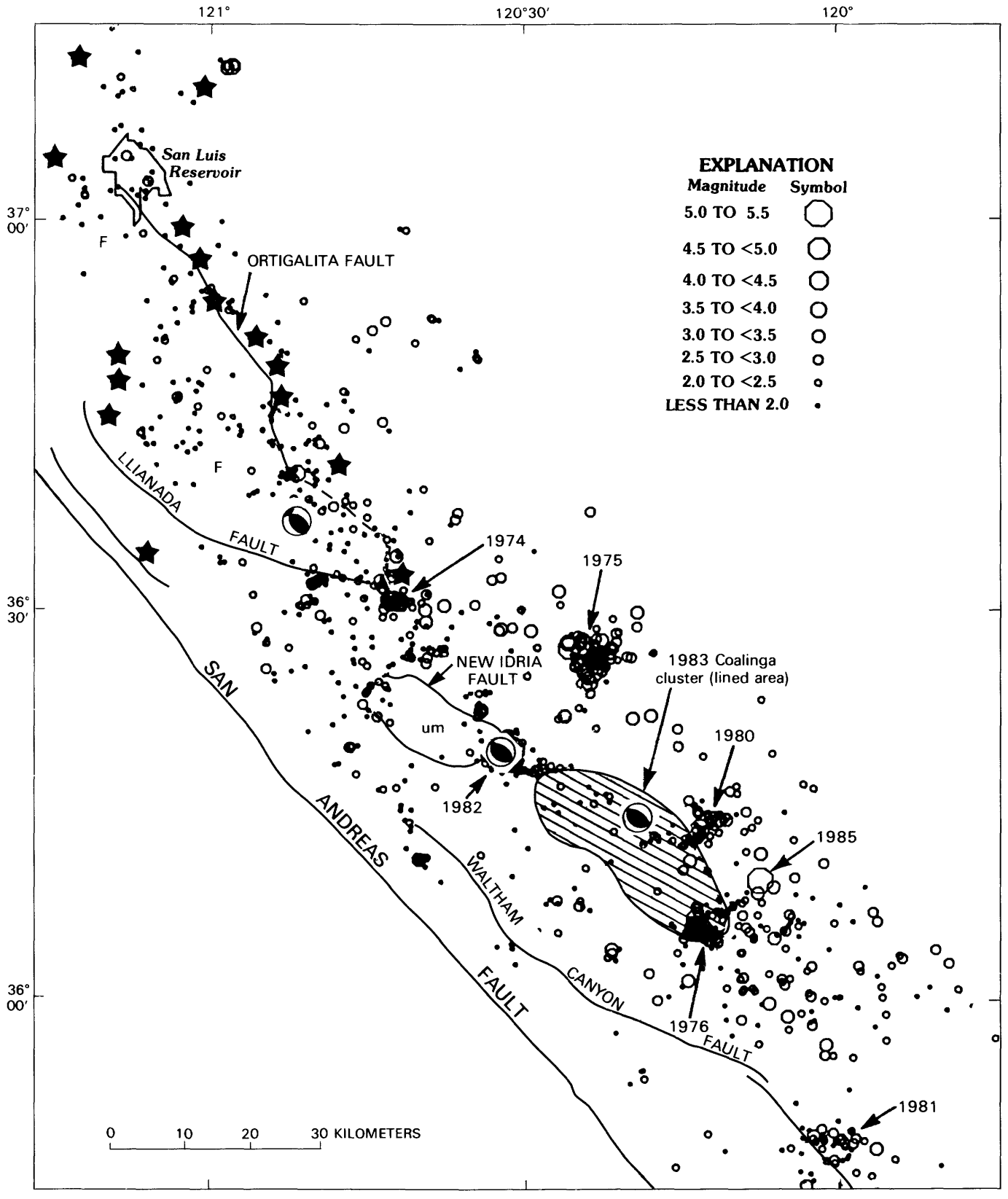

FIGURE 2.3.—Seismicity in the eastern Diablo Range, January 1969 to August 1985, showing dates of conspicuous clusters and fault-plane solutions for selected events. Earthquakes along San Andreas fault are not shown. Stars denote strike-slip events (from LaForge and Lee, 1982, figs. 2, 3); northwest-trending focal planes (shaded circles) indicate right-lateral displacement. F, Franciscan rocks; um, ultramafic rocks, chiefly serpentinite. Partly modified from Eaton and others (1983; fig. 1; J.P. Eaton, 1985, written commun.).

the Great Valley sequence, chiefly marine turbidites, which form the structural cover of the Franciscan assemblage. Locally it can be shown that basal Great Valley strata were deposited on ophiolite (Bailey and others, 1970), but the contact with the Franciscan is everywhere faulted. Great Valley strata are overlain unconformably by late Cenozoic deposits.

The structure of the south half of the range consists of numerous closely spaced folds. The axes generally are subparallel to the San Andreas fault near the fault zone but may diverge eastward away from the fault. The anticlines near the San Andreas fault are cored by Franciscan or ultramafic rocks, flanked by Great Valley and Cenozoic strata, and commonly cut by reverse or thrust faults.

One of the largest anticlinal features in the south half of the range, San Benito Mountain-Joaquin Ridge, is cored by a 10- by 20-km-long elliptical body of ultramafic rocks, chiefly serpentinite (New Idria serpentinite), with Franciscan sedimentary rocks along the southwestern and northern margins. Great Valley strata dip away from the core on all sides, and the contact is faulted and locally overturned (Eckel and Myers, 1946). Whether this ultramafic body represents ophiolite on which the Great Valley sequence was deposited or a diapir from beneath Franciscan rocks is questionable (Page, 1981, p. 371). On the basis of its magnetic anomaly, the body appears to have a restricted lateral extent in the subsurface (see chap. 5).

From the San Benito Mountain (New Idria) structural high, Great Valley and Cenozoic strata plunge easterly toward the San Joaquin Valley and form the east-southeast-trending axis of Joaquin Ridge. The Coalinga anticline (Anticline Ridge) is a relatively small, sharply defined, narrow fold in chiefly Tertiary and Quaternary strata, whose axis extends more than 20 km southeastward from Joaquin Ridge and plunges gently southeast toward Kettleman North Dome. The Coalinga anticline has a gently dipping northeastern limb, but its southwestern limb is much narrower and has a straight, locally steep to overturned southwestern margin.

The Kettleman Hills-Lost Hills trend is a chain of narrow anticlinal hills, subparallel to the San Andreas fault, that extends for about 65 km along the west side of the San Joaquin Valley southeast of the Coalinga anticline (fig. 2.1). This chain is separated from the Diablo Range by synclinal Pleasant Valley. Three separate anticlines, with exposed cores of marine Pliocene strata, are called North, Middle, and South Domes, although none is domal and South Dome is not doubly plunging. The axis of each anticline is offset right laterally from the next, as is the axis of the Coalinga anticline from that of North Dome. North dome is cut by several reverse faults subparallel to the anticlinal axis, and by numerous crossfaults (Woodring and others, 1940). Dip separation on exposed faults is as much as 100 m (Woodring and others, 1940). A north-south-trending, west-dipping reverse fault with at least 100 m of slip separates North and Middle Domes (Woodring and others, 1940). The Lost Hills is a fold in nonmarine Pliocene and Pleistocene strata, aligned with, but about 10 km southeast of, South Dome. Each of these anticlinal structures contains an oil field. The Kettleman Hills-Lost Hills structure trend is notable for its near-lithostatic pore-fluid pressures at depth (Berry, 1973). The distribution of such abnormally high pressures in this trend and adjoining parts of the region, and their significance to the Coalinga earthquake sequence, are described in chapter 13.

Along the Kettleman Hills trend, the cores of the folds, as marked by the Cretaceous-Tertiary boundary, crest at about 3,350 m below sea level (see fig. 13.3). Northwestward on the Coalinga anticline, however, this boundary rises to exposures at about 610 m above sea level. Because the base of the Pliocene and Pleistocene Tulare Formation on the Coalinga anticline is folded to the same degree as the base of the Tertiary sequence, most uplift and tilting of the anticline have probably occurred since deposition of the Tulare began about 2 m.y. ago. If this age estimate is correct, the long-term average rate of uplift is at least 2 mm/yr.

The Cenozoic structural history of the Coalinga region includes at least three major deformational events, each of which is marked by a conspicuous hiatus and (or) unconformity (see chap. 1). The earliest of these events, which resulted in a disconformity at the base of the Tertiary sequence, may represent emplacement of the Coast Range thrust. The second, a middle Tertiary event, caused an extensive angular unconformity at the base of the middle Miocene sequence, which is discordant on Eocene strata. A structure-contour map of this unconformity shows that, northeast of the Coalinga anticline, the structure of the rocks above the unconformity generally accords with that of the older rocks below (see fig. 4.4). The axis of Joaquin Ridge, however, which is northwest of the Coalinga anticline, plunges about S. 80° E., whereas the axis of the much sharper and asymmetric Coalinga anticline, as expressed in younger rocks, plunges about S. 45° E. Southwest of the Coalinga anticline, the structure of exposed pre-Tertiary strata is truncated by the unconformity, and the axes of Kettleman North Dome and the Pleasant Valley syncline generally parallel that of the Coalinga anticline. Serpentinite clasts in the upper part of the middle Miocene sequence probably represent unroofing of the New Idria serpentinite during the middle Tertiary event. The third major deformational event is marked by an angular unconformity, as great as 30°, at the base of the lower Pliocene sequence, which locally rests on Upper

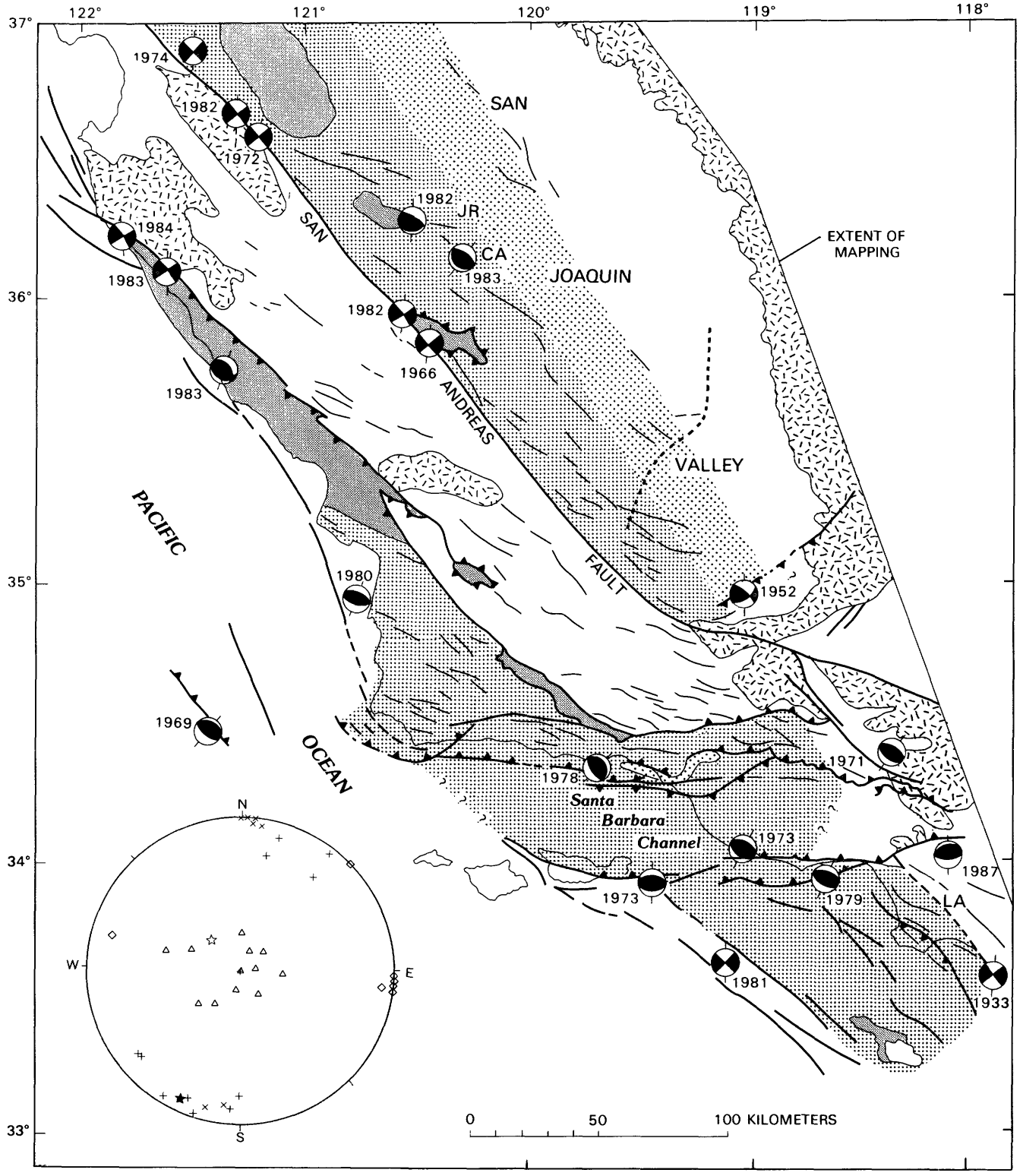

FIGURE 2.4.—Faults, fault-plane solutions for $M_L \geq 5$ earthquakes since 1933, and fold axes in central California. CA, Coalinga anticline; JR, Joaquin Ridge; LA, Los Angeles. East edge of the Franciscan assemblage in the San Joaquin Valley from Walter (see chap. 3) and Wentworth and Zoback (see chap. 4). Inset shows distribution of pressure (P) and tension (T) axes for mapped events. Solid star, orientation of maximum-compressive-stress axis (S_1); open star, orientation of minimum-compressive-stress axis (S_3), derived from 1983 Coalinga earthquake sequence by method of P and T dihedra (Angelier, 1984). Tickmarks on diameter of circle indicate trend of the San Andreas fault in central California (N. 41° W.). All thrust/reverse-fault solutions are compatible with indicated S_1 and S_3 axes. Sources listed in table 2.1.

Cretaceous strata southwest of the Coalinga anticline (Jennings and Strand, 1958). Subsequent—and continuing—deformation produced a local angular discordance at the base of the Pleistocene sequence. Each of these deformational events is associated with uplift and folding in the Coalinga anticline area and may be attributable to thrust wedging, as described below.

The Coast Range-Great Valley boundary is marked by an abrupt westward thickening and upturning of the Great Valley sequence along most of its 355-km length (Wentworth and others, 1984). Franciscan and coeval Great Valley rocks are juxtaposed at the surface along the Coast Range thrust (Bailey and others, 1970), a regional-scale feature that, in the context of plate tectonics, has been considered to dip east into the crust and represent a subduction-zone suture. The buried eastern margin of Franciscan rocks beneath the Coalinga anticline is the tip of a tectonic wedge that peels up Great Valley and overlying strata as the wedge is thrust eastward during Coalinga-type earthquakes. The Coast Range thrust may thus form the roof thrust of this wedge (Wentworth and others, 1984). Franciscan wedges, which underlie the Coalinga anticline and the South Dome-Lost Hills area, presumably are associated with such intervening structures as North and Middle Domes. The east tips of the wedges mapped near the Coalinga anticline and the Lost Hills coincide with the west flank of the San Joaquin Valley as defined by structure contours on the top of the lower Pliocene sequence (Hoots and others, 1954). This relation suggests that the west edge of the basin is controlled by advance of the wedges and that the original axis of the basin lay far west of the present western margin.

The history of folding in a 20- to 30-km-wide belt that extends along the western margin of the San Joaquin Valley for at least 115 km southeast of Joaquin Ridge has been described by Harding (1976). More than 125 separate structures were mapped by Harding (1976), including numerous exposed, but chiefly buried, folds, many containing oil fields. Individual axes are as long as 25 km, generally trend as much as 20° more westerly than the San Andreas fault, and are arranged generally in echelon, deflected 1 to 5 km right laterally. In the belt as a whole, folding has been essentially continuous since early Miocene time. Both the area involved and individual folds were inferred by Harding (1976) to have developed progressively eastward, away from the San Andreas fault. Oil-producing anticlines nearest the fault are folded more tightly and commonly are disrupted by reverse faults. Harding (1976) associated the fold belt with the

TABLE 2.1.—*Data on fault-plane solutions*

[References: 1, Hanks (1979); 2, Gawthrop (1978b); 3, Smith and Hamilton (1978); 4, Savage and Prescott (1978); 5, Stein and Thatcher (1981); 6, Gawthrop (1978a); 7, Whitcomb and others (1973); 8, Woodward-Clyde Consultants (1979); 9, Lee and others (1979); 10, R.S. Cockerham (written commun., 1981); 11, Lee and others (1978); 12, Eaton (1985a); 13, Eaton (1985b); 14, Corbett and Piper (1981)]

Date	Location Lat (°N.)	Long (°W.)	M_L	Fault	Reference
Nov. 4, 1927	34.6	120.9	7.3 (M)	?----------	1
	34.9	120.7	7.3 (M_S)	?----------	2
	34.65	120.9	7.5 (M_S)	Offshore Lompoc.	3
	34.88	120.78	7.3	?----------	4
Mar. 11, 1933	33.62	117.97	6.3	Newport-Inglewood.	8
July 21, 1952	35.00	119.02	7.2	White Wolf-----	5
June 22, 1966	35.795	120.34	5.5	San Andreas----	12
Nov. 5, 1969	34.61	121.44	5.6	Santa Lucia Banks.	6
Feb. 9, 1971	34.41	118.40	6.4	San Fernando---	7
Feb. 24, 1972	36.59	121.20	5.1	San Andreas----	10
Feb. 21, 1973	34.08	119.04	5.9	Anacapa--------	9
Aug. 6, 1973	33.97	119.45	5.0	do----------	9
Nov. 28, 1974	36.92	121.48	5.2	San Andreas----	10
Aug. 13, 1978	34.37	119.72	5.1-5.9	Santa Barbara Channel.	11, 12
Jan. 1, 1979	33.95	118.7	5	Anacapa(?)-----	10
May 29, 1980	34.98	120.71	5.1	Hosgri---------	12
Sept. 4, 1981	33.68	119.12	5.2-5.6	Near Santa Barbara Island.	10, 14
Aug. 11, 1982	36.63	121.30	4.8	San Andreas----	12
Oct. 25, 1982	36.32	120.52	5.2	New Idria(?)---	12
May 2, 1983	36.22	120.32	6.7	Coalinga (buried).	13
Aug. 29, 1983	35.84	121.35	5.4	Hosgri---------	12
Jan. 23, 1984	36.37	121.36	5.2	Hosgri-San Gregorio.	12

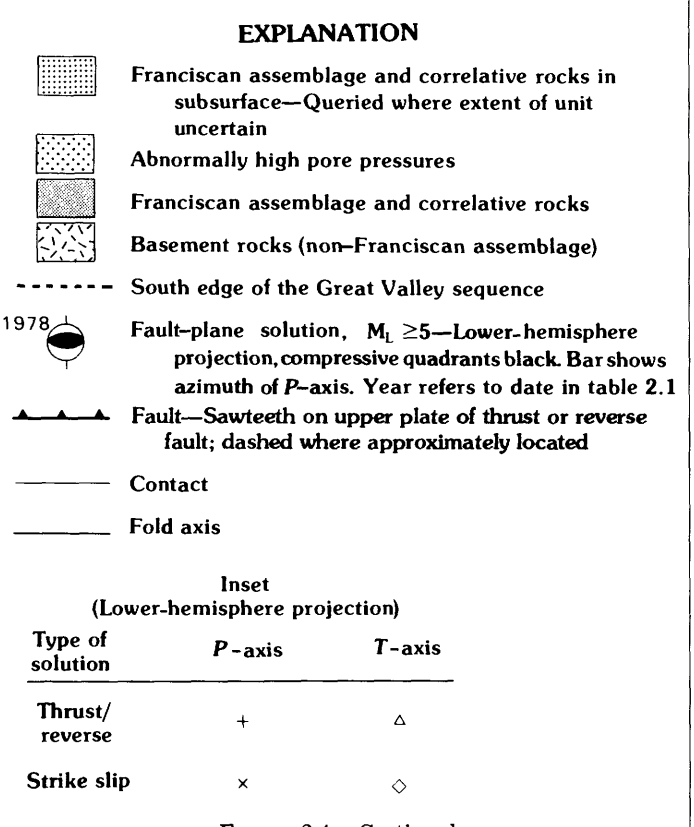

FIGURE 2.4.—Continued

presence of buried Franciscan rocks, but it extends as much as 30 km east of the Franciscan wedges mapped from seismic profiles by Wentworth and others (1984; see chaps. 3, 4). The east edge of the fold belt, however, essentially coincides with that of a subsurface field of abnormally high pore pressures (fig. 2.4; see chap. 13).

SEISMICITY

The 1983 Coalinga thrust/reverse-displacement main shock, which occurred below the young Coalinga anticline, may be attributable to eastward thrusting of a buried east-facing wedge of Franciscan rocks (see fig. 13.9). On August 4, 1985, an M_L=6 thrust/reverse earthquake occurred about 17 km due east of Coalinga and about 17 km southeast of the 1983 main-shock epicenter at a depth of about 13 km. The fault-plane solution and aftershock pattern of this event suggest that it may be associated with eastward thrusting of a buried wedge of Franciscan rocks, similar to the 1983 sequence (fig. 2.3).

A 50-km-wide band of seismicity for 1972–83 along the eastern margin of the Diablo Range north of the Kettleman Hills is characterized by several small clusters (see fig. 8.3). This rather diffuse seismic pattern is interrupted by Franciscan-bounding faults, such as the Ortigalita, New Idria, and Waltham Canyon faults. The clusters extend northwestward and southeastward, generally along the eastern margin of the range; the 1983 seismic rupture filled the gap between the clusters of 1976, 1980, and 1982. A fault-plane solution for a large earthquake in the 1982 cluster at the southeast tip of the New Idria serpentinite is similar to that for the 1983 Coalinga main shock: reverse-thrust displacement on faults trending about N. 55° W. (Eaton, 1985). The Llanada and Ortigalita faults, which bound the Franciscan core of the central Diablo Range, have (at least since 1969) been characterized by small earthquakes with chiefly strike-slip solutions, compatible with right-lateral displacement on these faults (fig. 2.3; La Forge and Lee, 1982). However, fault-plane solutions for one event near the junction of the two faults, as well as for the 1982 New Idria and 1983 Coalinga earthquakes to the southeast, indicate reverse-thrust displacement on northwest-trending faults.

STRESS REGIME

A broad region of California, from San Francisco to the Transverse Ranges and from the San Joaquin Valley to the Continental Shelf, is characterized by late Cenozoic deformation under generally northeast-southwest compression. As recognized by Reed (1933) more than 50 years ago and by many other workers since, the central and southern Coast Ranges, both west and east of the San Andreas fault, are dominated by compressive structures aligned subparallel to the fault—for example, the Kettleman Hills-Lost Hills trend. Seismic data support the geologic evidence (fig. 2.4): The orientation of the maximum compressive stress axis S_1 of the 1983 Coalinga earthquake sequence, the concentration of gently plunging P-axes in the northeast and southwest quadrants of the solutions, and the distribution of reverse/thrust-fault solutions on both sides of the San Andreas fault all indicate an appreciable component of northeast-southwest shortening normal to the trend of the fault and at variance with pure transform motion.

The shortening orthogonal to the San Andreas fault is attributable to (1) approximately 6° divergence in trend between the fault and Pacific-North American plate motion; and (2) northwestward extension of the Basin and Range province, thus shortening the distance between the Sierra Nevada and the San Andreas fault and causing left-lateral displacement on the Garlock and White Wolf faults. Estimates of the rate of shortening during the past 5.5 m.y. range from 4 to 13 mm/yr (Carter, 1982; Crouch and others, 1984; Minster and Jordan, 1984) but involve many tenuous assumptions. All the deformation in the region (fig. 2.4), including that of 1983 in the Coalinga area, is compatible with and attributable to shear between the Pacific and North American plates (Wise, 1963; Atwater, 1970; Scholz and others, 1971; Sbar, 1982).

This deformation has some unusual aspects only now being perceived. The concept of a regional decollement beneath the Coast Ranges dates at least from Dixon and Farrar (1980), and beneath the Transverse Ranges from Hadley and Kanamori (1978); such a feature was described by Yeats (1981). Crouch and others (1984) described post-Miocene thrust faults, as indicated by offshore reflection profiles, and suggested the presence of a sole thrust beneath the southern Coast and western Transverse Ranges. Wentworth and others (1984; see chaps. 3, 4), using reflection and refraction profiles that cross the Coast Range-Great Valley boundary at several localities, present specific documented models of buried east-thrusting tectonic wedges of Franciscan rocks along the boundary, including one for the Coalinga anticline that explains the 1983 earthquake sequence. Webb and Kanamori (1985) summarized data for about 20 fault-plane solutions in the Transverse Ranges that suggest a regional decollement.

Chapter 8 emphasizes the change in pattern of seismicity and style of faulting in the Coast Ranges (fig. 2.4): linear bands of small strike-slip earthquakes along faults of the San Andreas system northwest of the 1857 rupture, but isolated clusters of thrust-reverse events in the Coast Ranges and Transverse Ranges opposite that

rupture (now locked). Chapter 8 notes that this change may be related to the long-recognized change in behavior of the San Andreas fault from creep accompanied by many small earthquakes (unlocked) northwest of the 1857 rupture to no creep and virtually no small earthquakes (locked) along that segment. Much or all of the terrain characterized by thrust/reverse-fault earthquakes is underlain by Franciscan rocks, and at least parts are underlain by abnormally high pore pressures. The distribution of these abnormally high pressures in the southwestern San Joaquin Valley and western Transverse Ranges, and how they permit or aid thrusting, has been mapped (fig. 2.4) and is described in chapter 13. The clusters of thrust earthquakes are inferred to occur on subhorizontal faults rooted in detachment zones below seismogenic depths, which may extend some distance back toward the San Andreas. In this model, the locked (1857 rupture) segment of the San Andreas fault, including the "Fort Tejon" segment along the northern margin of the Transverse Ranges, is characterized by unusually strong crustal rocks that are clamped by an abnormally large component of compressive stress due to convergence across the transform (see chap. 8). The association of the creeping segments with Franciscan rocks, which are known sources of diagenetic/metamorphic fluids and abnormally high fluid pressures, has long been recognized (Berry, 1973; Irwin and Barnes, 1975).

REFERENCES CITED

Angelier, Jacques, 1984, Tectonic analysis of fault slip data: Journal of Geophysical Research, v. 89, no. B7, p. 5835–5848.

Atwater, Tanya, 1970, Implications of plate tectonics for the Cenozoic tectonic evolution of western North America: Geological Society of America Bulletin, v. 81, no. 12, p. 3513–3535.

Bailey, E.H., Blake, M.C., Jr., and Jones, D.L., 1970, On-land Mesozoic oceanic crust in California Coast Ranges, *in* Geological Survey research, 1970: U.S. Geological Survey Professional Paper 700–C, p. C70–C81.

Berry, F.A.F., 1973, High fluid potentials in California Coast Ranges and their tectonic significance: American Association of Petroleum Geologists Bulletin, v. 57, no. 7, p. 1219–1249.

Carter, B., 1982, Neogene displacement on the Garlock fault, California [abs.]: Eos (American Geophysical Union Transactions), v. 63, no. 45, p. 1124.

Corbett, E.J., and Piper, K.A., 1981, Santa Barbara Island, California earthquake, September 4, 1981 [abs.]: Eos (American Geophysical Union Transactions), v. 62, no. 45, p. 958.

Crouch, J.K., Bachman, S.B., and Shay, J.T., 1984, Post-Miocene compressional tectonics along the central California margin, *in* Crouch, J.K., and Bachman, S.B., eds., Tectonics and sedimentation along the California margin (volume 38): Society of Economic Paleontologists and Mineralogists, Pacific Section Annual Convention, San Diego, 1984, Papers, p. 37–54.

Dixon, J.M., and Farrar, Edward, 1980, Ridge subduction, eduction, and the Neogene tectonics of southwestern North America: Tectonophysics, v. 67, no. 1–2, p. 81–99.

Eaton, J.P., 1985a, Regional seismic background of the May 2, 1983 Coalinga earthquake, *in* Rymer, M.J., and Ellsworth, W.L., eds., Proceedings of Workshop XXVII: Mechanics of the May 2, 1983 Coalinga earthquake: U.S. Geological Survey Open-File Report 85-44, p. 44–60.

—— 1985b, The May 2, 1983, Coalinga earthquake and its aftershocks: A detailed study of the hypocenter distribution and of the focal mechanisms of the larger aftershocks, *in* Rymer, M.J., and Ellsworth, W.L., eds., Proceedings of Workshop XXVII: Mechanics of the May 2, 1983 Coalinga earthquake: U.S. Geological Survey Open-File Report 85-44, p. 132–201.

Eaton, J.P., Cockerham, R.S., and Lester, F.W., 1983, Study of the May 2, 1983 Coalinga earthquake and its aftershocks, based on the USGS seismic network in northern California, *in* Bennett, J.H., and Sherburne, R.W., eds., The 1983 Coalinga, California earthquakes: California Division of Mines and Geology Special Publication 66, p. 261–273.

Eckel, E.B., and Myers, W.B., 1946, Quicksilver deposits of the New Idria district, San Benito and Fresno Counties, California: California Journal of Mines and Geology, v. 42, no. 2, p. 81–122.

Gawthrop, W.H., 1978a, Seismicity and tectonics of the central California coastal region, *in* Silver, E.A., and Normark, W.R., eds., San Gregorio-Hosgri fault zone, California: California Division of Mines and Geology Special Report 137, p. 45–56.

—— 1978b, The 1927 Lompoc, California earthquake: Seismological Society of America Bulletin, v. 68, no. 6, p. 1705–1716.

Hadley, David, and Kanamori, Hiroo, 1978, Recent seismicity in the San Fernando region and tectonics in the west-central Transverse Ranges, California: Seismological Society of America Bulletin, v. 68, no. 5, p. 1449–1457.

Hanks, T.C., 1979, The Lompoc, California earthquake (November 4, 1927; M=7.3) and its aftershocks: Seismological Society of America Bulletin, v. 69, no. 2, p. 451–462.

Harding, T.P., 1976, Tectonic significance and hydrocarbon trapping consequences of sequential folding synchronous with San Andreas faulting, San Joaquin Valley, California: American Association of Petroleum Geologists Bulletin, v. 60, no. 3, p. 356–378.

Hauksson, Egill, and Saldivar, G.V., 1986, The 1980 Santa Monica and the 1979 Malibu, California, earthquakes: Seismological Society of America Bulletin, v. 76, no. 6, p. 1542–1559.

Hauksson, Egill, Jones, L.M., Davis, T.L., Hutton, L.K., Brady, A.G., Reasenberg, P.A., Michael, A.J., Yerkes, R.F., Etheridge, E.C., Porcella, R.L., Johnston, M.J.S., Reagor, B.G., Stover, C.W., Bufe, C.G., Cranswick, Edward, and Shakal, A.K., 1988, The 1987 Whittier Narrows earthquakes in the Los Angeles metropolitan area, California: Science, v. 239, p. 1409–1412.

Hoots, H.W., Bear, T.L., and Kleinpell, W.D., 1954, Geological summary of the San Joaquin Valley, California, [pt.] 8 *of* Geology of the natural provinces, chap. 2 *of* Geology of southern California: California Division of Mines and Geology Bulletin 170, p. 113–129.

Irwin, W.P., and Barnes, Ivan, 1975, Effect of geologic structure and metamorphic fluids on seismic behavior of the San Andreas fault in central and northern California: Geology, v. 3, no. 12, p. 713–716.

Jennings, C.W., and Strand, R.G., compilers, 1958, Santa Cruz sheet *of* Geologic map of California: Sacramento, California Division of Mines, scale 1:250,000.

LaForge, R., and Lee, W.H.K., 1982, Seismicity and tectonics of the Ortigalita fault and southeast Diablo Range, California, *in* Hart, E.W., Hirschfeld, S.E., and Schulz, S.S., eds., Conference on Earthquake Hazards in the Eastern San Francisco Bay Area, Hayward, Calif., 1982, Proceedings: California Division of Mines and Geology Special Publication 62, p. 93–101.

Lee, W.H.K., Johnson, C.E., Henyey, T.L., and Yerkes, R.F., 1978, A preliminary study of the Santa Barbara, California, earthquake of August 13, 1978 and its major aftershocks: U.S. Geological Survey Circular 797, 11 p.

Lee, W.H.K., Yerkes, R.F., and Simirenko, M.J., 1979, Recent

earthquake activity and focal mechanisms in the western Transverse Ranges, California: U.S. Geological Survey Circular 799–A, p. 1–26.

Minster, J.B., and Jordan, T.H., 1984, Vector constraints on Quaternary deformation of the western United States east and west of the San Andreas fault, *in* Crouch, J.K., and Bachman, S.B., eds., Tectonics and sedimentation along the California margin (volume 38): Society of Economic Paleontologists and Mineralogists, Pacific Section Annual Convention, San Diego, 1984, Papers, p. 1–16.

Page, B.M., 1981, The southern Coast Ranges, chap. 13 *of* Ernst, W.G., ed., The geotectonic development of California (Rubey volume 1): Englewood Cliffs, N.J., Prentice-Hall, p. 329–417.

Reed, R.D., 1933, Geology of California: Tulsa, Okla., American Association of Petroleum Geologists, 355 p.

Savage, J.C., and Prescott, W.H., 1978, Geodetic control and the 1927 Lompoc, California earthquake: Seismological Society of America Bulletin, v. 68, no. 6, p. 1699–1704.

Sbar, M.L., 1982, Delineation and interpretation of seismotectonic domains in western North America: Journal of Geophysical Research, v. 87, no. B5, p. 3919–3928.

Scholz, C.H., Barazangi, Muawia, and Sbar, M.L., 1971, Late Cenozoic evolution of the Great Basin, western United States, as an ensialic interarc basin: Geological Society of America Bulletin, v. 82, no. 11, p. 2979–2990.

Smith, S.W., and Hamilton, D.H., 1978, Sea floor expression of the 1927 Lompoc earthquake [abs.]: Eos (American Geophysical Union Transactions), v. 59, no. 12, p. 1128.

Stein, R.S., and Thatcher, Wayne, 1981, Seismic and aseismic deformation associated with the 1952 Kern County, California earthquake and relationship to the Quaternary history of the White Wolf fault: Journal of Geophysical Research, v. 86, no. B6, p. 4913.

Webb, T.H., and Kanamori, Hiroo, 1985, Earthquake focal mechanisms in the western Transverse Ranges and San Emigdio Mountains, southern California and evidence for a regional decollement: Seismological Society of America Bulletin, v. 75, no. 3, p. 737–757.

Wentworth, C.M., Blake, M.C., Jr., Jones, D.L., Walter, A.W., and Zoback, M.D., 1984, Tectonic wedging associated with emplacement of the Franciscan assemblage, California Coast Range, *in* Blake, M.C., Jr., ed., Franciscan geology of northern California (book 43): Los Angeles, Society of Economic Paleontologists and Mineralogists, Pacific Section, p. 163–173.

Whitcomb, J.H., Allen, C.R., Garmany, J.D., and Hileman, J.A., 1973, San Fernando earthquake series, 1971: Focal mechanisms and tectonics: Reviews of Geophysics and Space Physics, v. 11, no. 3, p. 693–730.

Wise, D.U., 1963, An outrageous hypothesis for the tectonic pattern of the North American Cordillera: Geological Society of America, v. 74, no. 3, p. 357–362.

Woodring, W.P., Stewart, Ralph, and Richards, R.W., 1940, Geology of the Kettleman Hills oil field, California: Stratigraphy, paleontology, and structure: U.S. Geological Survey Professional Paper 195, 170 p.

Woodward-Clyde Consultants, 1979, Analysis of teleseismic data for the 1933 Long Beach earthquake, app. E *of* Report of the evaluation of maximum earthquake and site ground motion parameters associated with the offshore zone of deformation San Onofre Nuclear Generating Station: Los Angeles, 28 p.

3. UPPER-CRUSTAL VELOCITY STRUCTURE NEAR COALINGA, AS DETERMINED FROM SEISMIC-REFRACTION DATA

By ALLAN W. WALTER,
U.S. GEOLOGICAL SURVEY

CONTENTS

ABSTRACT

Interpretation of seismic-refraction data collected along two profiles intersecting in the hypocentral region of the May 2 earthquake provides a velocity structure for the Coalinga region. An 83-km-long east-west profile extended from the San Joaquin Valley to the Diablo Range across Anticline Ridge, 1 km south of the M_L=6.7 main-shock epicenter. A 102-km-long northwest-southeast profile extended subparallel to the Diablo Range front along the syncline west of Anticline Ridge. Traveltime data from four shotpoints along the east-west profile and five shotpoints along the northwest-southeast profile have been modeled by two-dimensional ray-tracing techniques. In the San Joaquin Valley, the velocity of Cenozoic strata increases from 1.6 km/s near the surface to about 3.6 km/s at 3.6-km depth. Near the top of the Cretaceous Great Valley sequence, the velocity increases abruptly to 4.0–4.3 km/s. With increasing depth of burial, the velocity of Great Valley sequence in the valley increases to 5.0 km/s. On the west flank of the valley, velocity inversions within the Great Valley sequence indicate high formation pore pressures. These velocity inversions do not extend under the Diablo Range. At equivalent depths of burial, the velocities of the lower Great Valley units in the Diablo Range (4.8–4.9 km/s) are higher than those found for the Great Valley sequence farther east in the San Joaquin Valley (4.0–4.3 km/s).

In the San Joaquin Valley, the Great Valley sequence overlies a basement with a velocity of 6.3 to 6.4 km/s, indicative of a mafic composition. The dip of the basement increases westward of the valley axis from less than 5° to about 10°–12°. The basement plunges to an estimated 14- to 15-km depth at the front of the Diablo Range where an east-pointing wedge of Franciscan assemblage (5.7–6.1 km/s) lies between Great Valley sequence exposed at the surface and the mafic basement. Depth of the boundary separating the Great Valley sequence and Franciscan wedge increases eastward to a junction with the mafic basement under the upturned west flank of the San Joaquin Valley. East of the Franciscan wedge, the San Joaquin Valley is underlain by a basin containing several additional kilometers of sedimentary strata associated with the Great Valley sequence. Unreversed refraction data support a deeper layer within the mafic basement with velocities exceeding 7 km/s, and a Moho depth of 28 to 30 km near the front of the Diablo Range. Comparison of the refraction velocity models with the hypocentral locations of the 1983 earthquake sequence reveals that the source region for the M_L=6.7 main shock and larger aftershocks is within the Franciscan wedge and that the seismicity extends upward into the Great Valley sequence.

INTRODUCTION

The May 2 earthquake (M_L=6.7) was unexpected in that it occurred at the structural transition between the southern Diablo Range and the San Joaquin Valley, part of the 500-km-long Coast Ranges-Great Valley boundary. Since 1981, the U.S. Geological Survey (USGS) has been acquiring both seismic reflection and refraction data along profiles that cross this boundary. The occurrence of the May 2 earthquake provided motivation to acquire additional seismic reflection and refraction data in the hypocentral region with the goal of understanding the structural relations responsible for the unexpected seismicity. This understanding is needed to assess the probability of large earthquakes occurring elsewhere along the Coast Ranges-Great Valley boundary.

The locations of the acquired seismic profiles relevant to interpreting the regional structure near Coalinga are

shown in figure 3.1. Three east-west reflection profiles, SJ–3, SJ–6, and SJ–19, were purchased from Western Geophysical, and a shorter east-west reflection profile, C1, was acquired from the Consortium for Continental Reflection Profiling (COCORP). Three refraction profiles were recorded by the USGS: an east-west profile more or less coincident with the southernmost reflection profile (SJ–6); an east-west profile through the Coalinga epicentral region; and a northwest-southeast profile just east of the Diablo Range front, connecting the two east-west refraction profiles.

The reflection and refraction data along profile SJ–6 were acquired before the May 2 earthquake; a preliminary interpretation of this profile was presented by Wentworth and others (1984b). An interpretation of the reflection data along profiles SJ–3 and SJ–19 is presented in chapter 4. This chapter presents an interpretation of the two seismic-refraction profiles crossing the hypocentral region of the 1983 Coalinga earthquake sequence.

GEOLOGIC SETTING

The study area crossed by the profiles, the southern San Joaquin Valley and the Diablo Range, is bounded on the east by the Sierra Nevada and on the west by the San Andreas fault. The San Joaquin Valley is an asymmetric sedimentary trough lying west of the Sierra Nevada, with its axis near its western margin with the Diablo Range. Data from wildcat oil wells and the seismic-reflection profiles show that sediment has been deposited above a gently west dipping basement surface since Cretaceous time. Well cores and aeromagnetic data are interpreted to indicate that the composition of the valley basement changes westward from continental to oceanic; the suture is east of the center of the valley.

The Cretaceous sedimentary units are collectively referred to as the Great Valley sequence. Both the Cretaceous and overlying Tertiary sections consist of alternating shale and sandstone with local conglomerate. Unconformities occur throughout the sedimentary section, indicating alternating cycles of marine transgression and regression. The facies of the entire section changes from marine to continental eastward of the valley axis, and the Quaternary units are nonmarine (see chap. 1).

Few wells west of the center of the valley penetrate the basement, and the seismic-reflection profiles are ambiguous as to the depth of basement under the west edge of the valley and the adjacent folds. Data from oil wells in the valley show that the thickness of the sedimentary section increases westward to at least 7 km at the valley axis and increases southward along the valley axis. Pliocene and younger strata represent more than half the Cenozoic section.

Along the front of the Diablo Range, the San Joaquin Valley strata are folded upward; and northwest-trending anticlines, such as the Coalinga anticline and the Kettleman Hills (fig. 3.1), are superimposed on the west flank of the San Joaquin Valley syncline. Unconformities revealed by well data indicate that major uplift of the Diablo Range occurred during post-Eocene time (Page, 1981). The Eocene and older sedimentary formations thicken westward to an erosional unconformity exposed on the upturned west flank of the San Joaquin Valley, whereas the Miocene and younger formations thicken eastward from this unconformity to the axis of the valley trough. A decrease in the thickness of Pliocene and Quaternary strata over the crest of the Coalinga and the Kettleman Hills anticlines indicates that the secondary folding commenced in early Pliocene time (see chap. 1).

Folding and faulting associated with uplift of the Diablo Range created local structural highs and lows with the major folds internal to the range trending west-northwest. Most of the west-northwest/east-southeast deformation is associated with the development of the proto-San Andreas fault zone starting in Eocene time (Harding, 1976). Continuing uplift and shortening of the Diablo Range from subsequent east-west compression has resulted in the Pliocene growth of the Coalinga anticline and the Kettleman Hills on the flank of the San Joaquin Valley syncline. The May 2 main shock occurred near the intersection of the west-northwest-trending Joaquin Ridge anticline with the northernmost projection of the northwestward Kettleman Hills trend—the Coalinga anticline (fig. 3.1).

Within the Diablo Range, folded and faulted Great Valley units overlie Jurassic and Cretaceous Franciscan assemblage. The Franciscan assemblage consists of deformed, fault-bounded blocks of graywacke, greenstone, chert, their metamorphic equivalents, and serpentinite, believed to be part of an accretionary wedge formed above a subduction zone on the continental margin and coeval with the Great Valley sequence (Bailey and others, 1964). The Great Valley-Franciscan contact, exposed 6 to 9 km east of the San Andreas fault and in the cores of the larger northwest-trending anticlines, is inferred to be a thrust fault (Bailey and others, 1970).

FIGURE 3.1.—Generalized geologic map of southern Diablo Range-San Joaquin Valley, showing locations of seismic profiles. Reflection profiles: SJ–3, SJ–6, SJ–19 (Western Geophysical) and C–1 (COCORP). Refraction profiles: east-west profile (shotpoint 9 to shotpoint 12) and northwest-southeast profile (shotpoint 13 to shotpoint 17). CA, Coalinga anticline; JR, Joaquin Ridge; KP, Kettleman Plain syncline; PV, Pleasant Valley; WC, White Creek syncline. Geology adapted from Jennings (1977); no contacts shown southwest of the San Andreas fault.

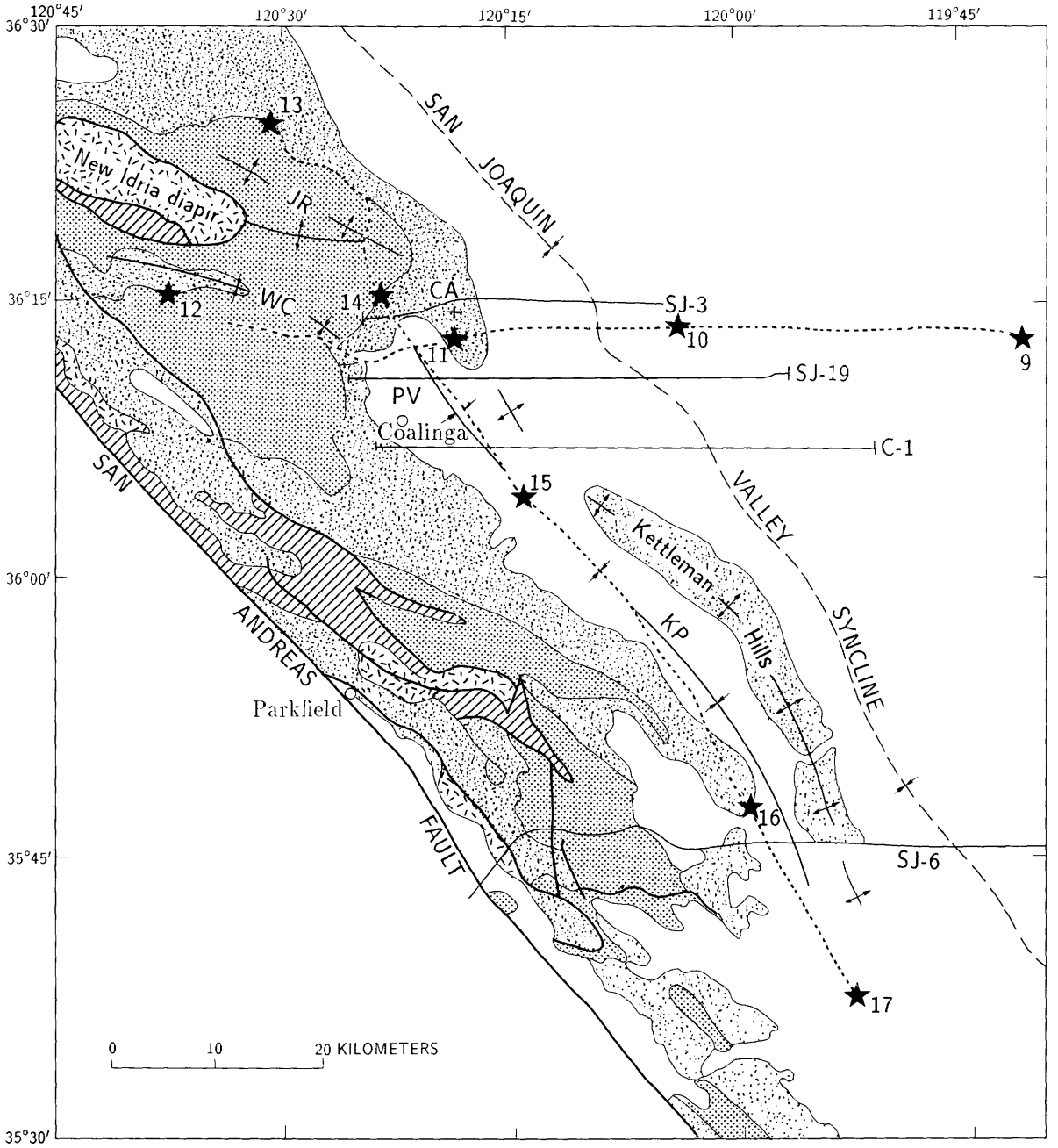

EXPLANATION

- Sedimentary rocks (Pliocene and younger)
- Sedimentary rocks (Tertiary)
- Great Valley sequence (Cretaceous)
- Franciscan assemblage (Cretaceous and Jurassic)
- Serpentinite (Mesozoic)
- Contact
- Fault

- Major folds—Dashed where approximately located
- Syncline
- Anticline
- ★12 Shotpoint—Numbered
- Seismic-refraction line
- Shot pre-May 2, 1983
- Shot post-May 2, 1983
- \+ Main shock, M_L=6.7

Serpentinite blocks included within the Franciscan, such as the New Idria diapir, are inferred to be derived from underlying oceanic basement (Page, 1985). In the core of the Diablo Range, 100 km north of Coalinga, 14 to 18 km of Franciscan assemblage is estimated to lie above a lower crust composed of oceanic basement (Walter and Mooney, 1982).

SEISMIC-REFRACTION EXPERIMENT

Two intersecting seismic-refraction profiles, one striking east-west and the other northwest-southeast, were recorded across the epicentral region of the Coalinga earthquake sequence in summer 1983. The east-west profile extends 83 km from the center of the San Joaquin Valley, across Anticline Ridge and Pleasant Valley, into the Diablo Range. The northwest-southeast profile extends 103 km from Joaquin Ridge southeastward along the Pleasant Valley-Kettleman Plain syncline (fig. 3.1). A total of 120 vertical-component seismographs (Healy and others, 1982) were deployed along each profile. Four shotpoints were located along the east-west profile, and five along the northwest-southeast profile; shot sizes ranged from 900 to 1,400 kg. The quality of the shot records varies greatly along both profiles, owing to differences in shot coupling and background-noise levels. Tables of the shot and station data, location maps, and record sections of the explosion seismograms were presented by Colburn and Walter (1984).

EAST-WEST PROFILE

The east-west profile crosses from the San Joaquin Valley to Anticline Ridge along a straight line and continues along a crooked line westward across Pleasant Valley into the Diablo Range, where it lies near the axis of the west-northwest-trending White Creek syncline (fig. 3.1). The four shotpoints on the east-west profile are labeled, from east to west, 9 through 12 (fig. 3.1). Shotpoint 9 is located near the center of the San Joaquin Valley, about 60 km east of the epicenter of the Coalinga main shock; shotpoint 10 is located about 5 km east of the axis of the San Joaquin Valley trough; shotpoint 11 is located on Anticline Ridge near the main-shock epicenter; and shotpoint 12 is located in the Diablo Range just south of Joaquin Ridge and about 30 km west of Anticline Ridge.

NORTHWEST-SOUTHEAST PROFILE

The northwest-southeast profile is subparallel to the strike of the Coalinga anticline and Kettleman Hills folds, except where it crosses over the axis of the Joaquin Ridge anticline. Shotpoints 13 and 14 are located, respectively, on the northeastern and southwestern limbs of the west-northwest-trending Joaquin Ridge anticline near the Tertiary-Cretaceous contact (fig. 3.1). Limited road access between these two shotpoints resulted in deployment of the seismographs along a crooked line across the crest of the ridge. South of shotpoint 14 the profile follows the southeast-plunging axis of the Pleasant Valley syncline to shotpoint 15. From shotpoint 15, the profile line strikes southward away from the synclinal axis onto the western limb of the syncline. The profile reaches its highest structural level on the western limb just north of shotpoint 16, where Pliocene rocks are exposed at the surface (fig. 3.1). South of shotpoint 16, the fold structure is buried under a mantle of recent alluvium, and the profile strikes downsection toward the projected synclinal axis.

QUALITY OF SEISMIC DATA

Representative normalized record sections of the seismic data are shown in figure 3.2. From both shotpoints 9 and 10, arrivals were clearly recorded out to the west end of the east-west profile. The signals from shotpoints 11 and 12, however, were overwhelmed by high noise levels in the San Joaquin Valley. No traveltime data were recorded within the first 6 km of shotpoint 12. The signals from shotpoints 13 and 14 were recorded to the south end of the northwest-southeast profile, but the signals from shotpoints 15, 16, and 17 were so weak that very few northward-reversing velocity data were recorded. On the record section of shotpoint 16, clear first arrivals were observed only out to 40 km north; and from shotpoint 17, no arrivals whatsoever were observed at distances beyond 30 km north. Poor signals were due principally to firing the shots in unconsolidated sediment above the water table.

VELOCITY MODELING

The observed traveltimes were modeled by two-dimensional ray-tracing techniques (Červený and others, 1977). Beginning with a starting-velocity model, the calculated traveltimes from each shotpoint were compared with the observed traveltime plots, and then the velocity structure was iteratively modified to reduce discrepancies. Seismic amplitudes were not modeled.

In constructing the velocity models, surface geology, well logs, and the nearby reflection profiles provided constraints on the configuration of the sedimentary section in the model. Published velocity measurements of clastic sedimentary rocks (Schock and others, 1974), Franciscan metasedimentary rocks (Stewart and Peselnick, 1978), and mafic basement rocks (Christensen, 1982) were compared with the modeled refraction velocities to identify four basic stratigraphic-structural units in the models: Cenozoic strata (1.6–4.2 km/s), Great

Valley sequence (3.0–5.3 km/s), Franciscan assemblage (5.5–6.2 km/s), and mafic basement (6.3 km/s).

Predictability of the velocities within the sedimentary units was assumed, in that for a given stratigraphic unit, the velocity is a simple function of age and depth of burial, increasing with increasing age and depth (Gardner and others, 1974). Under this assumption, the velocity contours parallel the stratigraphy rather than cut across stratigraphic boundaries. This assumption, however, was not found to be correct everywhere along the profiles because of unpredictable changes in formation pore pressure.

From examination of the drilling histories of selected wells in the Coalinga region (see chap. 23), zones of abnormally high pore pressure are inferred to exist in the sedimentary section at various depths and locations. The locations of these zones shown in chapter 23 do not reveal any predictable pattern, except that shale provides the confinement for the pore pressures. Most of the inferred zones are thin relative to the seismic wavelengths, but in a few places the abnormally high pressure zones extend over intervals large enough to be resolved with the refraction data as velocity inversions or low-velocity zones.

EAST-WEST VELOCITY MODEL

The velocity model and the corresponding geologic correlations derived for the east-west profile are shown in figure 3.3. The depth of the Tertiary-Cretaceous boundary in the model is tightly constrained by oil wells along the two east-west seismic-reflection profiles SJ–3 and SJ–19, respectively located 3 km north and 5 km south of the east-west refraction line (fig. 3.1). Few wells penetrated far into the Great Valley sequence, and so the configuration of the stratigraphic boundaries below the top of the Great Valley sequence was inferred solely from the two east-west seismic-reflection profiles and surface geology. These reflection profiles, however, are ambiguous as to the location of the base of the Great Valley sequence. One constraint on the depth of the Great Valley-basement interface is provided by two oil wells, one 8 km north and the other 22 km south of shotpoint 9, both of which penetrated basement. The interpolated depth at the intersection of the line connecting these two wells and the refraction profile, 4 km, is the depth of Great Valley-basement interface assigned in the velocity model 1.3 km west of shotpoint 9.

From shotpoint 9 to about 7 km east of shotpoint 10, the sedimentary units dip less than 3° W., and the mafic basement dips 4°–5° W.. The modeled depth of the basement in this section increases from 3.9 to 5.8 km. Westward to shotpoint 10, the overlying sedimentary units flatten, and the basement plunges at an even steeper dip of 10°–12°, reaching a depth of 14 to 15 km under the Pleasant Valley syncline. The steepening of the basement dip west of shotpoint 10 is supported not only by traveltime delays of the basement arrivals but also by gravity data along the east-west profile (see chap. 5). West of Pleasant Valley, the seismic and gravity data only poorly constrain the depth of mafic basement in the Diablo Range, and so for the purposes of ray-trace modeling, the basement was projected westward under the Diablo Range at a constant depth of 15 km.

West of Anticline Ridge (shotpoint 11) and into the Diablo Range (shotpoint 12), the sedimentary section is uplifted by a wedge of Franciscan rocks lying below the Great Valley sequence and above the mafic basement. The top of this wedge is assumed to intersect the basement at the east limit of uplift, the toe of the eastern limb of the Coalinga anticline (fig. 3.3). The location of this toe in the refraction model was constrained by its respective locations on the adjacent reflection profiles.

The Cenozoic strata thin across the Coalinga anticline and pinch out on the west side of Pleasant Valley, where the Cenozoic-Cretaceous (Great Valley sequence) contact dips 30°–40° E. (Dibblee, 1971). In the Diablo Range, the structural geometry within the Great Valley sequence is not constrained by reflection data or wells, and so the internal geometry was assumed to be conformable with surficial bedding attitudes down to the base of the Great Valley sequence. The Great Valley units are horizontal in the cross section because the profile strikes subparallel to the White Creek synclinal axis; the true dip at the surface is from 25° to 35° into the plane of the cross section.

The calculated thickness of Great Valley sequence west of the toe of the Coalinga anticline depends on the depth of the Great Valley-Franciscan contact and the amount of section eroded in the Diablo Range. The modeled thickness decreases from about 7 km at the toe of the Coalinga anticline to about 5 km under Pleasant Valley. Near shotpoint 12, the thickness is from 5.5 to 6.5 km, but the Great Valley sequence units exposed at shotpoint 12 are not at the top of the Great Valley sequence. About 10 km southeast of shotpoint 12, the calculated thickness of Great Valley sequence exposed between the Tertiary-Cretaceous contact and the Great Valley-Franciscan contact to the west is 7 to 8 km (Mansfield, 1979). One possible explanation for the decrease in thickness under Pleasant Valley is that the Franciscan wedge actually overrode the lowermost Great Valley units.

In the model presented here, the thickness of the Franciscan wedge increases westward from 0 km at the toe of the Coalinga anticline to about 9 km under shotpoint 12. Assuming both that the Franciscan rocks exposed in the Diablo Range west of shotpoint 12 represent the top of this wedge and that the depth of mafic basement does not decrease west of Pleasant

Valley, then the wedge is at least 15 km thick near the San Andreas fault.

VELOCITIES WITHIN THE CENOZOIC AND GREAT VALLEY SECTIONS

Not all reflection events evident in the reflection records were associated with velocity boundaries in the refraction model, because the resolution of the refraction data is much coarser and because reflection events represent impedance contrasts that may be unrelated to velocity contrasts. Where the thickness of a stratigraphic unit is less than one seismic wavelength, the modeled refraction velocity represents an average velocity through a group of formations.

In the San Joaquin Valley near shotpoint 9, the velocity of the Cenozoic strata increases from 1.6 km/s near the surface to about 3.6 km/s at 3.6-km depth. Near the base of the Cenozoic section or the top of the Great Valley sequence, the modeled velocity increases abruptly by 0.5 to 0.7 km/s. West of shotpoint 10, the modeled velocities

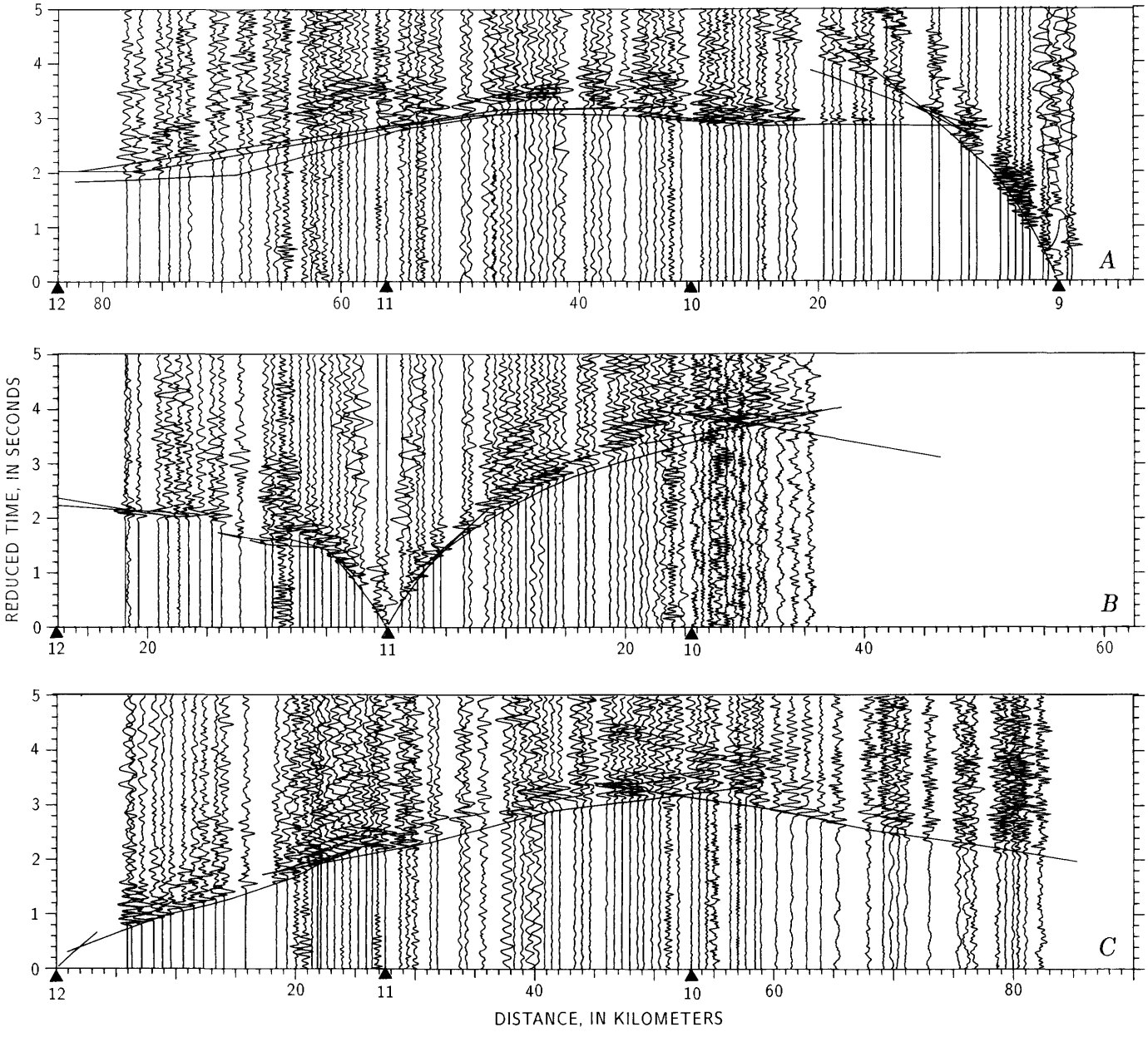

FIGURE 3.2.—Record section of seismic-refractions data from shotpoints 9 (*A*), 11 (*B*), 12 (*C*), 13 (*D*), 14 (*E*), and 16 (*F*). Trace widths are normalized. Traveltimes are reduced by distance/(6.0 km/s). Lines connect traveltimes calculated for rays traced through the velocity models shown in figures 3.3 and 3.4. Triangles, shotpoints.

of the Cenozoic and Great Valley rocks below 3-km depth exceed those found at equivalent depths between shotpoints 9 and 10. A reported facies change from continental to marine between shotpoints 9 and 10 (see chap. 1) may explain the observed westward increase in velocity, particularly if there is an accompanying decrease in formation pore pressure.

West of the San Joaquin Valley axis and continuing into the Diablo Range, the uplift of the older, more compacted rocks to shallow depths results in higher velocities than those observed at equivalent depths of burial in the San Joaquin Valley. The velocity of the Great Valley sequence modeled at 3-km depth under shotpoint 12 (4.8–4.9 km/s) is higher than that modeled at 5 km depth under shotpoints 9, 10, and 11 (4.0–4.3 km/s). One possible explanation for this difference is that higher pore pressures exist in the Great Valley sequence east of Pleasant Valley, whereas in the Diablo Range, erosional truncation or increased fracturing of the Great Valley sequence units has lowered the pore pressures. Because lateral variations in pore pressure are unpredictable, the velocities in the lowermost Great Valley sequence cannot

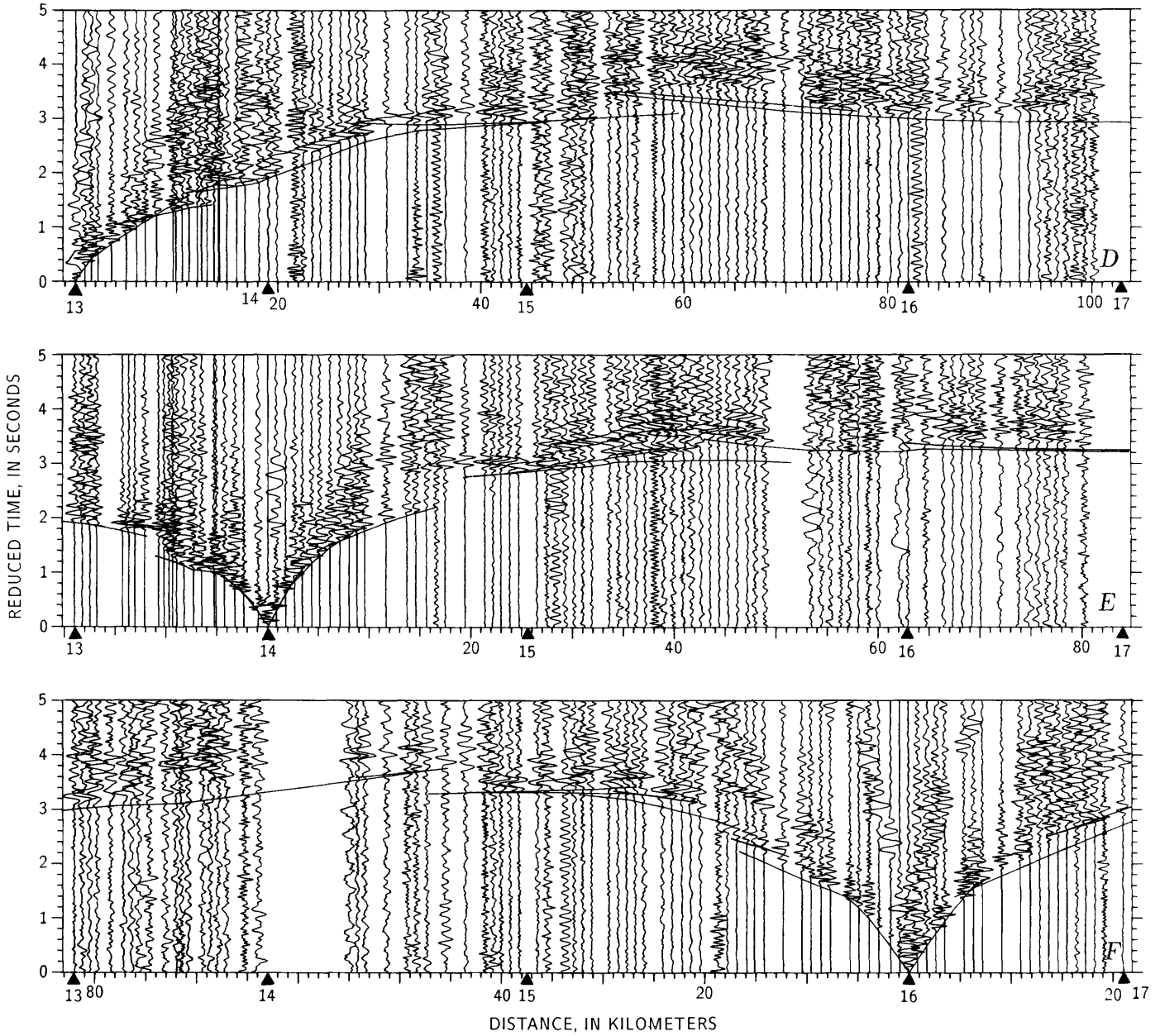

FIGURE 3.2.—Continued

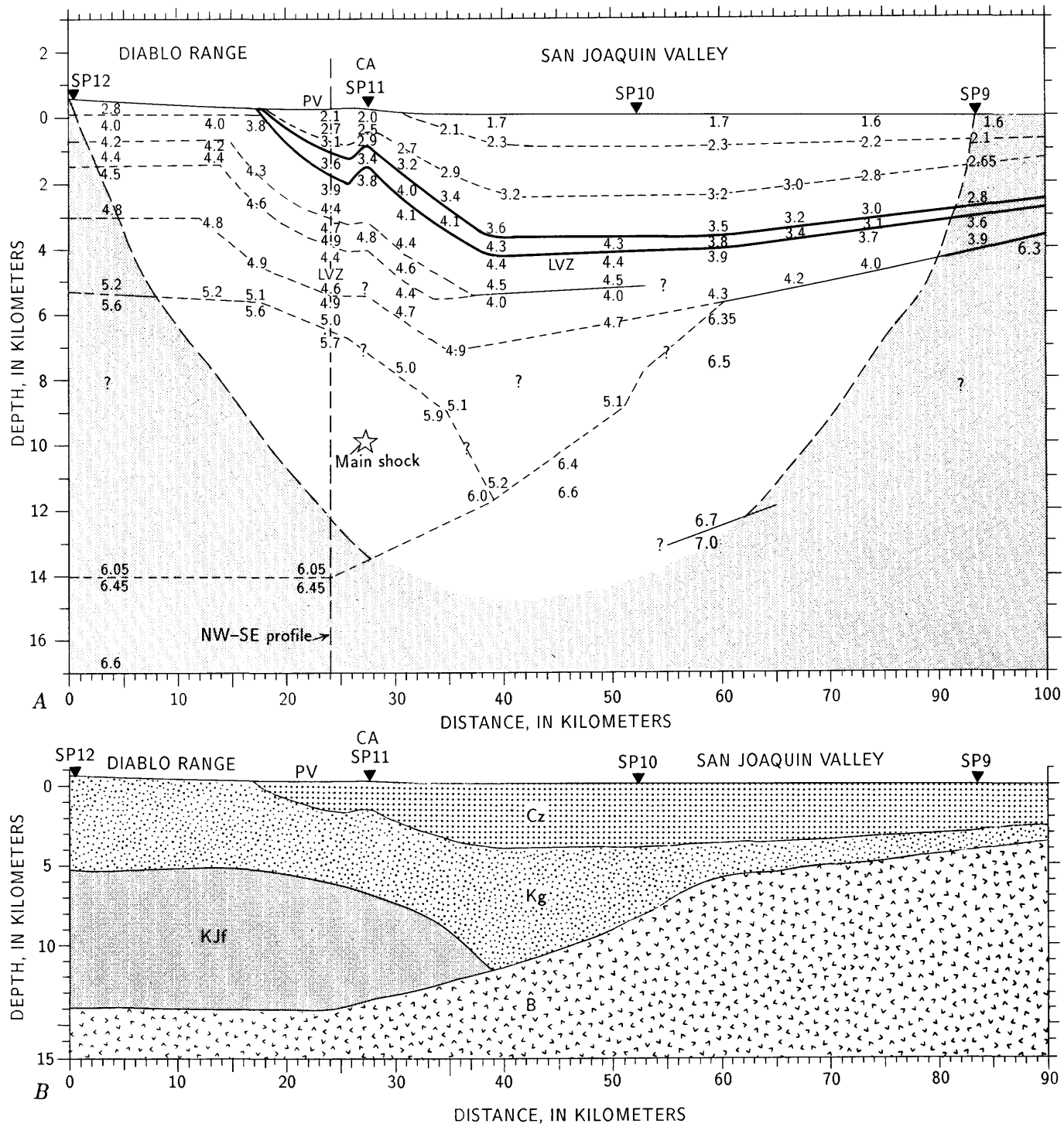

FIGURE 3.3.—East-west refraction profile. *A*, Velocity model derived for east-west refraction profile (shotpoint 9 to shotpoint 12), showing velocities in kilometers per second. Solid triangles, shotpoint locations. CA, Coalinga anticline; LVZ, low-velocity (velocity inversion) zone; PV, Pleasant Valley syncline. Heavy solid line, geologic contact constrained by well data; light solid line, velocity boundary constrained by reversing refraction data; dashed line, velocity boundary inferred from unreversed refraction data; question marks, extrapolated velocities. Shaded area is outside reciprocal ray path for two outermost shotpoints. Vertical dashed line shows intersection with northwest-southeast profile. Location of main shock is projected into cross section. *B*, Model cross section showing geologic-stratigraphic interpretation of velocity structure. B, basement, Cz, Cenozoic strata; Kg, Cretaceous Great Valley sequence; KJf, Jurassic and Cretaceous Franciscan assemblage.

be interpolated with certainty between shotpoints 9 and 12.

On the record sections (fig. 3.2), the arrivals from lowermost Great Valley units are behind the basement arrivals. In the absence of abnormally high pore pressure, the maximum velocity obtainable in Great Valley rocks at 10-km depth is constrained by the laboratory velocity measurements reported for sandstone and shale to be less than 5.3 km/s (Schock and others, 1974). In some localities, the high pore pressure causes a velocity inversion. The low-velocity zone (LVZ) modeled below 5-km depth under the eastern limb of the Coalinga anticline is inferred from the record section of shotpoint 11 (fig. 3.2*B*); at distances greater than 20 km east of this shotpoint, the cutoff of first arrivals together with a delay of subsequent arrivals indicates an LVZ. This velocity inversion shallows beneath the Pleasant Valley syncline, as inferred from the refraction data recorded from shotpoint 14 on the axial profile (fig. 3.2*D*). The record sections of shotpoints 11 and 12 (figs. 3.2*B*, 3.2*C*) show no evidence of the LVZ extending westward into the Diablo Range.

VELOCITIES WITHIN THE FRANCISCAN ASSEMBLAGE

The velocities modeled within the Franciscan wedge are similar to those reported for Franciscan rocks in the core of the Diablo Range, 100 km farther northwest (Walter and Mooney, 1982). The Franciscan wedge was modeled as a homogeneous unit because refracted arrivals from within the wedge were recorded only from shotpoint 12. (The northwest-southeast model does show stratification within the Franciscan, but it is not evident how to integrate the structure into the east-west model.) On the record section of shotpoint 12, between 25- and 50-km distance, arrivals from the Franciscan wedge define three subparallel branches offset by time delays (fig. 3.2*C*). Such delays could be caused by downward steps in the top of the Franciscan wedge between the Diablo Range and Anticline Ridge, by alternating higher and lower velocity units, or by both. Although the velocity was assumed to increase abruptly across the Great Valley-Franciscan contact, it could just as well increase over a narrow transition zone.

Interpretation of the velocities within the Franciscan wedge in terms of lithology is ambiguous for distinguishing between metasedimentary rocks and serpentinite because laboratory velocities of both rock suites overlap (Stewart and Peselnick, 1978). Modeled aeromagnetic data, however, provide some discrimination. Chapter 5 presents aeromagnetic data that show evidence of a serpentinite body west of or directly below shotpoint 12, but no evidence of the magnetic body extending eastward under Pleasant Valley or Anticline Ridge. The aeromagnetic data do not preclude the existence of small lenses of serpentinite farther east.

VELOCITIES WITHIN THE BASEMENT

Limited refraction data from the basement make it difficult to distinguish whether changes in basement velocity are due to compositional variation or to structural geometry. Therefore, to reduce the number of variables in the modeling, the composition of the basement was assumed to be laterally homogeneous and its velocity to depend only on the depth of burial. If the composition does vary laterally, however, such a change would be reflected in the model as a change in the basement geometry.

The 6.3- to 6.4-km/s velocity modeled for the top of the basement, together with the observed aeromagnetic anomaly (see chap. 5), suggests that the upper basement is probably a serpentinized peridotite. The velocity transition from Great Valley strata to basement is assumed to be an abrupt step increase, but because the seismic amplitudes were not modeled, the traveltime data alone do not preclude that the velocity at the top of basement may actually increase from less than 6.0 to 6.3 km/s across a thin zone. Realistically, the basement probably has some lateral heterogeneity due to differing degrees of serpentinization.

The modeled basement velocity increases with depth to 6.5 to 6.6 km/s 3 km below the top of basement (fig. 3.3). On the record section of shotpoint 9 (fig. 3.2*A*), secondary arrivals recorded at a distance of 35 to 50 km west suggest a velocity boundary at about 12-km depth beneath shotpoint 10. At this boundary, the modeled velocity increases from 6.7 to 7.0 km/s; however, the velocity-depth function in the basement is poorly constrained because of uncertainties in the overlying velocity structure. The east-west profile was not long enough to record the *Pn* arrivals needed to constrain the velocity structure at the Moho.

NORTHWEST-SOUTHEAST VELOCITY MODEL

The velocity model for the northwest-southeast profile and the corresponding geologic correlations are shown in figure 3.4. Unlike for the east-west profile, no parallel reflection profile is available to constrain the geometry of the sedimentary section along this profile. From shotpoint 14 southeastward to shotpoint 15, surface dips and oil well data define the depth of the Cenozoic-Cretaceous contact. The modeled thickness of the Cenozoic section increases southward from 0 near shotpoint 14 to about 4 km under shotpoint 17. The structural high apparent in the model near shotpoint 16 is due to the profile crossing

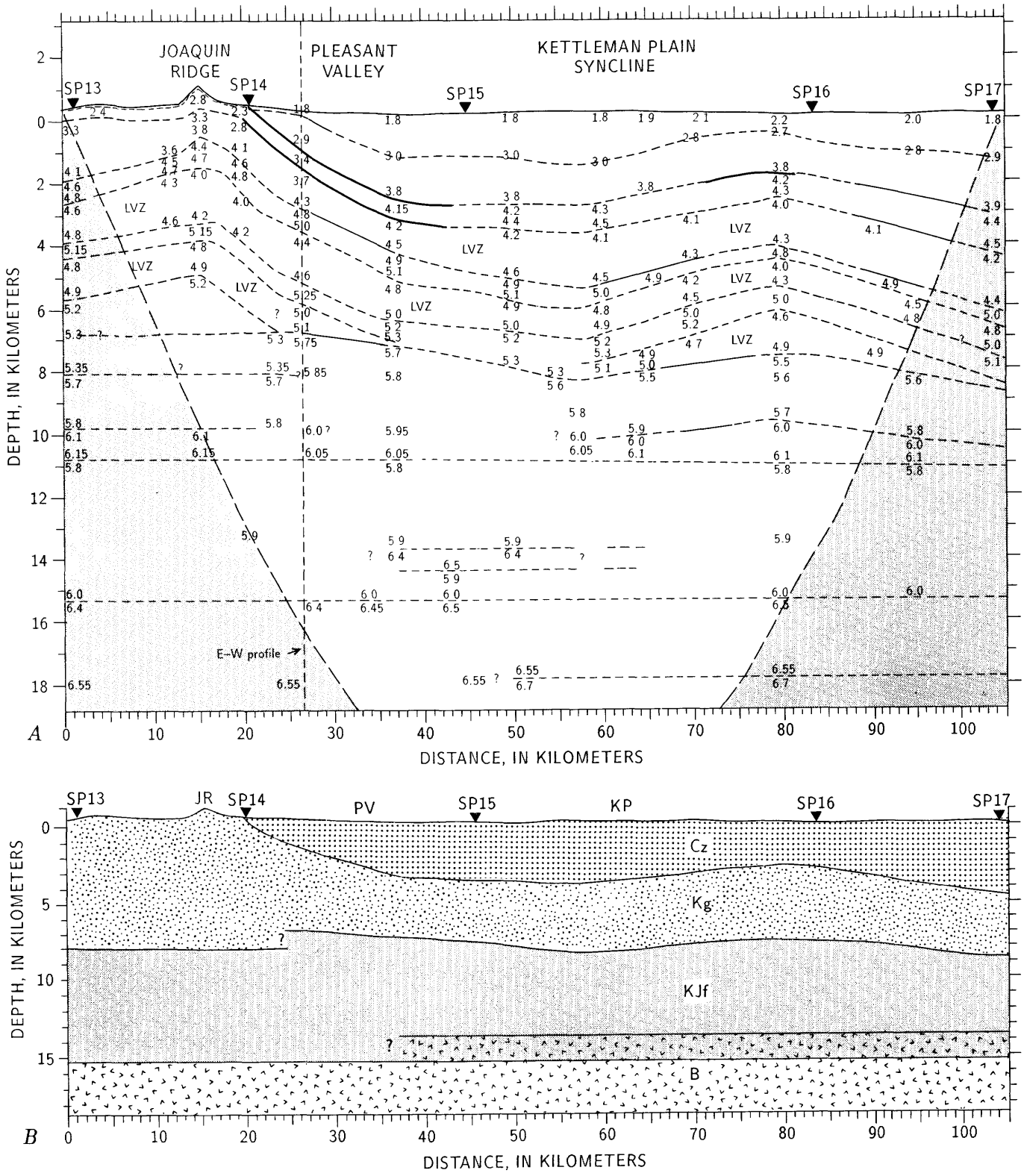

FIGURE 3.4.—Northwest-southeast profile. *A*, Velocity model derived for northwest-southeast refraction profile (shotpoint 13 to shotpoint 17), showing velocities in kilometers per second. Same symbols as in figures 3.1 and 3.3. *B*, Model cross section showing geologic-stratigraphic interpretation of velocity structure. Same symbols as in figure 3.3*B*.

onto the western limb of the Kettleman Plain syncline. The true dip of the strata is into the plane of the cross section.

Along the length of the model, the Great Valley-Franciscan contact lies between 7- and 9-km depth. The refraction data do not constrain the depth of the boundary south of shotpoint 16. Note that the Great Valley-Franciscan contact is modeled deeper beneath the axis of Joaquin Ridge (greater than 8 km depth) than under the syncline south of shotpoint 14 (approx 7 km depth). Thus, the thickness of the Great Valley sequence decreases from 8 km under the axis of Joaquin Ridge to about 5 km under the Pleasant Valley syncline. The implication of this sudden thinning south of Joaquin Ridge is that the lower part of the Great Valley sequence was truncated by faulting.

The estimated thickness of Franciscan assemblage along the axial northwest-southeast profile ranges from 6 to 7 km. The change in depth of the Franciscan-basement contact along this profile is not well constrained because the traveltime data from shotpoint 13 support a 15.5-km depth, those from shotpoint 14 support a 14-km depth, and the reversing data from shotpoint 16 are obscured by noise. Because a similar sense of structural offset between Joaquin Ridge and Pleasant Valley was modeled for the overlying Great Valley-Franciscan contact, the basement under Pleasant Valley may have been uplifted with respect to the basement beneath Joaquin Ridge by a fault crossing the profile at the north end of Pleasant Valley near shotpoint 14. The existence of these breaks in the model could be artifacts either of modeling assumptions, such as that units are flat layers with constant velocities, or of a poor correlation of respective phases between shotpoints.

VELOCITIES WITHIN THE CENOZOIC AND GREAT VALLEY SECTIONS

The velocities modeled within the Cenozoic section are comparable to those found along the east-west profile. However, the velocities within the upper 2 km of Great Valley sequence across Joaquin Ridge are lower than those modeled for the Great Valley sequence near shotpoint 12. This difference is probably due to the increasing age and greater compaction of the rocks west of shotpoint 12. The velocities within the Great Valley sequence increase with depth and age except where zones of abnormally high pore pressure result in velocity inversions.

The record sections of shotpoints 13 and 14 (figs. 3.2*D*, 3.2*E*) show evidence of a major LVZ within the Great Valley sequence under Joaquin Ridge: an abrupt truncation of first arrivals, accompanied by a time delay of the arrivals from deeper units. This LVZ correlates with a zone of abnormally high pore pressure encountered in a wildcat oil well drilled 3 km west of the northwest-southeast profile (see chap. 23). At the ridge axis, the top of the LVZ is at 2.4-km depth, and the LVZ is less than 2 km thick; but the plunge of the LVZ into the Pleasant Valley syncline suggests that the velocity inversion is stratigraphically controlled. The pattern of traveltime delays between 20 and 30 km east of shotpoint 13 requires that between the Joaquin Ridge axis and shotpoint 14 the average velocity in the LVZ decreases or the thickness of the zone increases, or, possibly, both. The velocity within the zone increases southward of shotpoint 14, and between shotpoints 14 and 15 the lowermost Great Valley strata associated with the LVZ are truncated by fault contact with the Franciscan assemblage. The LVZ must be confined to the Pleasant Valley syncline because the data recorded between shotpoints 11 and 12 on the east-west profile (figs. 3.2*B*, 3.2*C*) show no evidence of the LVZ extending into the Diablo Range. Farther south, the refraction data from shotpoint 16 (fig. 3.2*F*) show evidence for velocity inversions under the western limb of the Kettleman Plain syncline both near the top of the Great Valley sequence and lower in the sequence.

Although the presence of velocity inversions increases the uncertainty in interpreting the arrivals from underlying units, modeled velocities of 5.2 to 5.3 km/s at depths of 6 to 8 km are assigned to the Great Valley sequence because the reported velocities of Franciscan metasedimentary rocks are greater than 5.5 km/s below 6-km depth of burial (Stewart and Peselnick, 1978; Lin and Wang, 1980; Walter and Mooney, 1982). The velocities modeled for the lower part of the Great Valley sequence under Joaquin Ridge may be slightly high, however, because the reversing ray paths from shotpoints 13 and 14 are initially updip. If the average velocity in the lower part of the Great Valley sequence is reduced to 4.9 km/s, the depth to the Great Valley-Franciscan contact under Joaquin Ridge is about 7.5 km. A 7.5-km thickness for the Great Valley sequence under Joaquin Ridge is comparable to the measured thickness of Great Valley rocks exposed at the surface south of shotpoint 12.

VELOCITIES WITHIN THE FRANCISCAN ASSEMBLAGE

The Franciscan assemblage is divided into three units: an upper unit below the Great Valley contact, with velocities of 5.5 to 6.0 km/s; a discontinuous middle unit between 10- and 11-km depth, with velocities of 6.0 to 6.15 km/s; and a lower unit, with velocities of 5.8 to 6.0 km/s, extending down to the basement contact.

Traveltime data from shotpoint 13 (fig. 3.2*D*) place the top of the upper Franciscan unit from 7.5- to 8.5-km depth under Joaquin Ridge, depending on the velocities assumed in the lower part of the Great Valley sequence, whereas the data from shotpoint 14 (fig. 3.2*E*) place the top of this unit at 7-km depth under Pleasant Valley. The

velocities within the upper unit vary laterally along profile, ranging from 5.5 to 5.8 km/s along its contact with the Great Valley sequence and from 5.8 to 6.0 km/s along its bottom. The variation is attributable to changes in the apparent velocities between the shotpoints, but it is difficult to determine how much of it is actually due to changes in composition and how much is an artifact of the modeling assumptions.

Secondary arrivals observed between 30 and 40 km from shotpoints 13 and 16 (figs. 3.2*D*, 3.2*F*) support the existence of a higher velocity Franciscan unit between 10- and 11-km depth, whereas the data from shotpoint 14 (fig. 3.2*E*) support a higher average velocity in the upper unit, with no abrupt increase in velocity at the top of the middle unit. The record sections of all three shotpoints show a truncation of arrivals from this middle unit and a delay of the basement arrivals, supporting the existence of a continuous velocity inversion near 11-km depth. One possible explanation for this velocity layering within the Franciscan assemblage is that the units represent different metamorphic-rock types, such as graywacke and metagraywacke or melange units, juxtaposed by thrust faults; another possibility is that the lowermost Franciscan unit has higher fluid pressures than the overlying Franciscan unit.

VELOCITIES WITHIN THE BASEMENT

Because of the absence of reversing traveltime data from the basement, the flat-lying velocity boundaries shown in the model (fig. 3.4*A*) are highly speculative. Different patterns of basement arrivals recorded from shotpoints 13 and 14 suggest a laterally varying basement structure. Alternative velocity-depth functions derived for the basement, using the traveltime data from shotpoints 13 and 14, are shown in figure 3.5.

Note that the function derived from the shotpoint 13 data shows a somewhat simpler velocity structure than that derived from the shotpoint 14 data. The overall increase in modeled velocities from 6.4 km/s at the top of the basement to more than 7.1 km/s below 24-km depth indicates an increasingly mafic composition with increasing depth. Although the data show no evidence for a continuous LVZ in the basement, they do not exclude the possibility of localized velocity inversions. At equivalent depths, the velocities modeled using the data of shotpoint 13 average 0.3 km/s lower than those modeled using the data of shotpoint 14. If this lateral change is real and not an artifact of the modeling assumptions, it could have resulted from mineralogic differentiation during petrogenesis or from juxtaposition of different rock types by faulting.

The depth of the base of the crust (Moho) along the northwest-southeast profile is uncertain because the profile was not long enough to record the *Pn* phase. One constraint on the depth of the Moho, however, is provided by the record section of shotpoint 13 (fig. 3.2*D*). At distances from 80 km to the end of the profile at 100 km, the record section shows secondary arrivals that could be the *PmP* phase, the reflection from the Moho. Assuming that the velocity across the Moho increases from 7.4 to 7.9 km/s, the observed arrival times are approximately fitted by placing the Moho at a depth of 28 km in the model. Oppenheimer and Eaton (1984) reported a similar depth estimate from regional earthquake *Pn* traveltimes recorded at nearby earthquake-network stations. If the Moho under Pleasant Valley is no deeper than the 30 km reported for the central Diablo Range (Walter and Mooney, 1982), the overlying mafic basement is 13 to 15 km thick.

COMPARISON OF THE VELOCITY MODELS AT THEIR POINT OF INTERSECTION

The velocity-depth functions for the two crossing profiles at their point of intersection in Pleasant Valley are shown in figure 3.6. The depth of the Cenozoic-Cretaceous contact is constrained by wells to be 2 km in both models. The respective depths modeled for the Great Valley-Franciscan and Franciscan-basement contacts are 6 and 14 km in the east-west model and 7 km and 15.5 km in the northwest-southeast model. Thus, the section above the basement comprises 4 to 5 km of Great Valley sequence and 7 to 8 km of Franciscan assemblage. The two models show a similar range of velocities for the

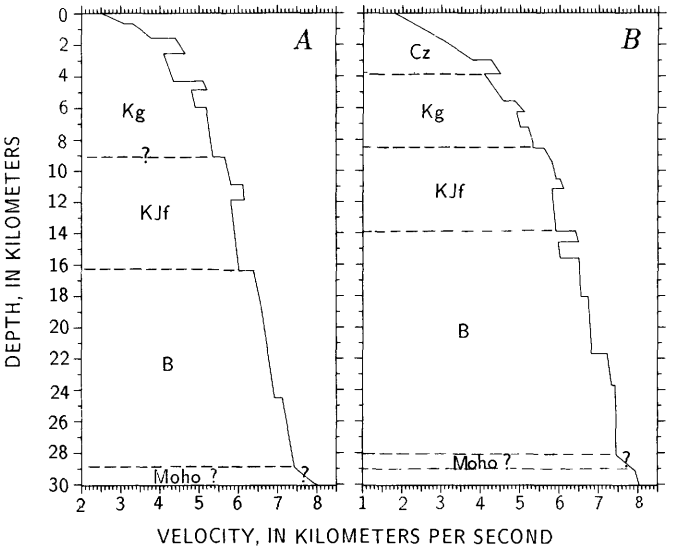

FIGURE 3.5.—Velocity-depth functions interpreted for northwest-southeast profile. *A*, Joaquin Ridge at model location 16 km SE. (fig. 3.4), using unreversed data from shotpoint 13 south. *B*, Kettleman Plain syncline at model location 55 km SE. (fig. 3.4), using unreversed data from shotpoint 14 south. Same symbols as in figure 3.3*B*.

four defined stratigraphic units but disagree on the internal details within each unit. The estimated depth range to the top of the mafic basement under Pleasant Valley, 14 to 15.5 km, is comparable to the 16±3-km depth range estimated for the central Diablo Range (Walter and Mooney, 1982).

COMPARISON BETWEEN THE COALINGA VELOCITY MODELS AND THE VELOCITY MODEL DERIVED FOR PROFILE SJ–6

Before the May 2 earthquake, the USGS recorded an east-west refraction profile across the San Joaquin Valley, the Kettleman Hills, and the Diablo Range, about 60 km south of the east-west Coalinga profile (fig. 3.1) and coincident with seismic-reflection profile SJ–6. Overall, preliminary interpretation of the profile SJ–6 refraction data shows the same basic structural transition between the San Joaquin Valley into the Diablo Range: West of the valley axis, an eastward-thinning wedge of 5.6- to 6.0-km/s rocks lies between a 6.3-km/s basement and overlying folded sedimentary rocks. The profile SJ–6 data support a 14- to 15-km depth for the Franciscan-basement contact under the western limb of the valley syncline, comparable to the depth modeled for the intersecting northwest-southeast Coalinga profile. In addition, the profile SJ–6 data support the Great Valley-Franciscan contact rising to a shallow depth west of the San Joaquin Valley synclinal axis. East of the Kettleman Hills, the major difference between these profiles is that the sedimentary section is thicker along profile SJ–6 and an LVZ exists in the Cenozoic section near the valley axis on profile SJ–6.

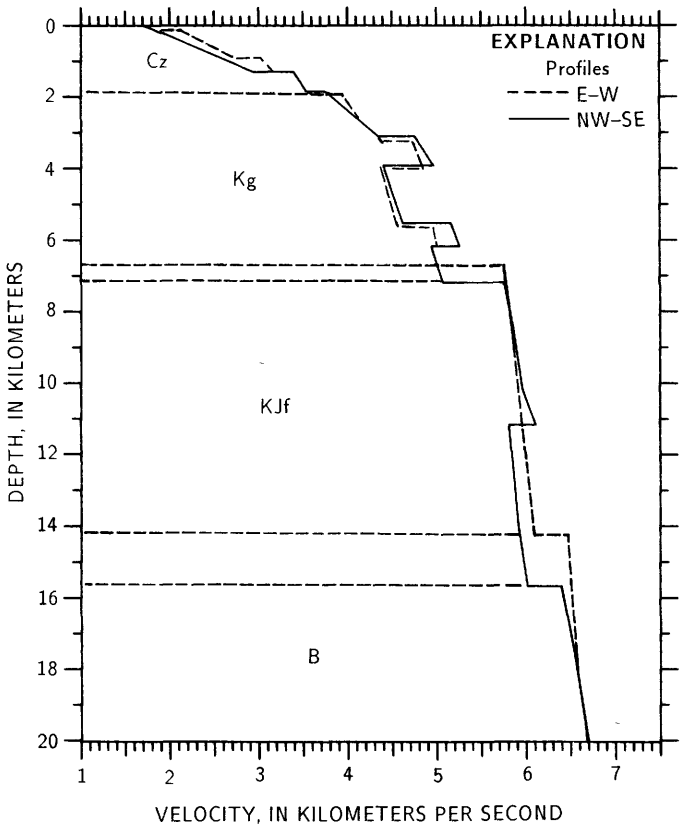

FIGURE 3.6.—Velocity-depth functions from the two refraction models at their point of intersection (see fig. 3.1); dashed line, 24.1 km E. of shotpoint 12 (fig. 3.3); solid line, 26.2 km SE. of shotpoint 13 (fig. 3.4). Same symbols as in figure 3.3*B*.

COMPARISON BETWEEN THE REFRACTION VELOCITY STRUCTURE AND NEARBY SEISMIC-REFLECTION PROFILES

A COCORP east-west reflection profile collected 12 km south of the Coalinga east-west refraction profile shows a west-dipping band of reflections near the axis of the San Joaquin Valley that correlates with the thick section of Great Valley sequence modeled with the refraction data. Fielding and others (1984) interpreted these reflection as evidence that downdropping of the basement surface west of the present valley axis along normal faults during Cretaceous time resulted in a much thicker section of Great Valley sequence. They concluded that normal faults in the basement were reactivated as reverse faults by Cenozoic compression and now determine the locus of folding on the west side of the valley; that is, the Cenozoic strata and Great Valley sequence strata are draped over the fault and buckling.

Reflection records collected along profile SJ–19 show evidence of a wedge-shaped structure below the top of the Great Valley sequence under Anticline Ridge and Pleasant Valley (see chap. 4). This structure is outlined by both offsets and a divergence of reflection events, which can be interpreted as the locations of reverse and thrust faults. Several west-dipping reverse faults disrupt the Great Valley sequence, and one east-dipping reverse fault penetrates upward into the lower Cenozoic section. The similarity in internal stratification of the wedge between the faults to the overlying Great Valley sequence implies that the wedge consists of either Great Valley units or stratified Franciscan units which have a seismic signature similar to that of the overlying Great Valley sequence. At Pleasant Valley, the depth to the top of this reflection wedge is estimated to be about 5.5 km, which results in a thickness of about 3 km of Great Valley sequence overlying the reflection wedge. Because this thickness is about 2 km less than that suggested by refraction modeling, the uppermost reflections in the wedge are probably from units assigned to the Great Valley sequence, rather than from the Franciscan

assemblage. Surprisingly, no large-amplitude reflection event is evident in the reflection records to support the abrupt step increase in velocity across the Great Valley-Franciscan contact shown in the refraction models.

The profile SJ–6 reflection data, collected farther south, also show evidence of high-angle reverse faults in the sedimentary section beneath the Kettleman Hills anticline, as well as of a subhorizontal thrust fault at the base of the syncline west of this anticline (Wentworth and others, 1984b). Thus, it is reasonable to assume that reverse faults underlie the entire length of the Kettleman Hills fold trend south of Joaquin Ridge.

RELATION BETWEEN COALINGA SEISMICITY AND THE VELOCITY STRUCTURE

The locations of epicenters in the Coalinga region for the period May 2, 1983, to September 30, 1983, are shown on the map in figure 3.7, on which is superimposed the generalized geology and the locations of the two refraction profiles. The May 2 main shock occurred at 10-km depth under Anticline Ridge near shotpoint 11. The aftershock zone extended from Anticline Ridge westward to the Diablo Range, northward to Joaquin Ridge, and southward to the Kettleman Hills. Most aftershocks

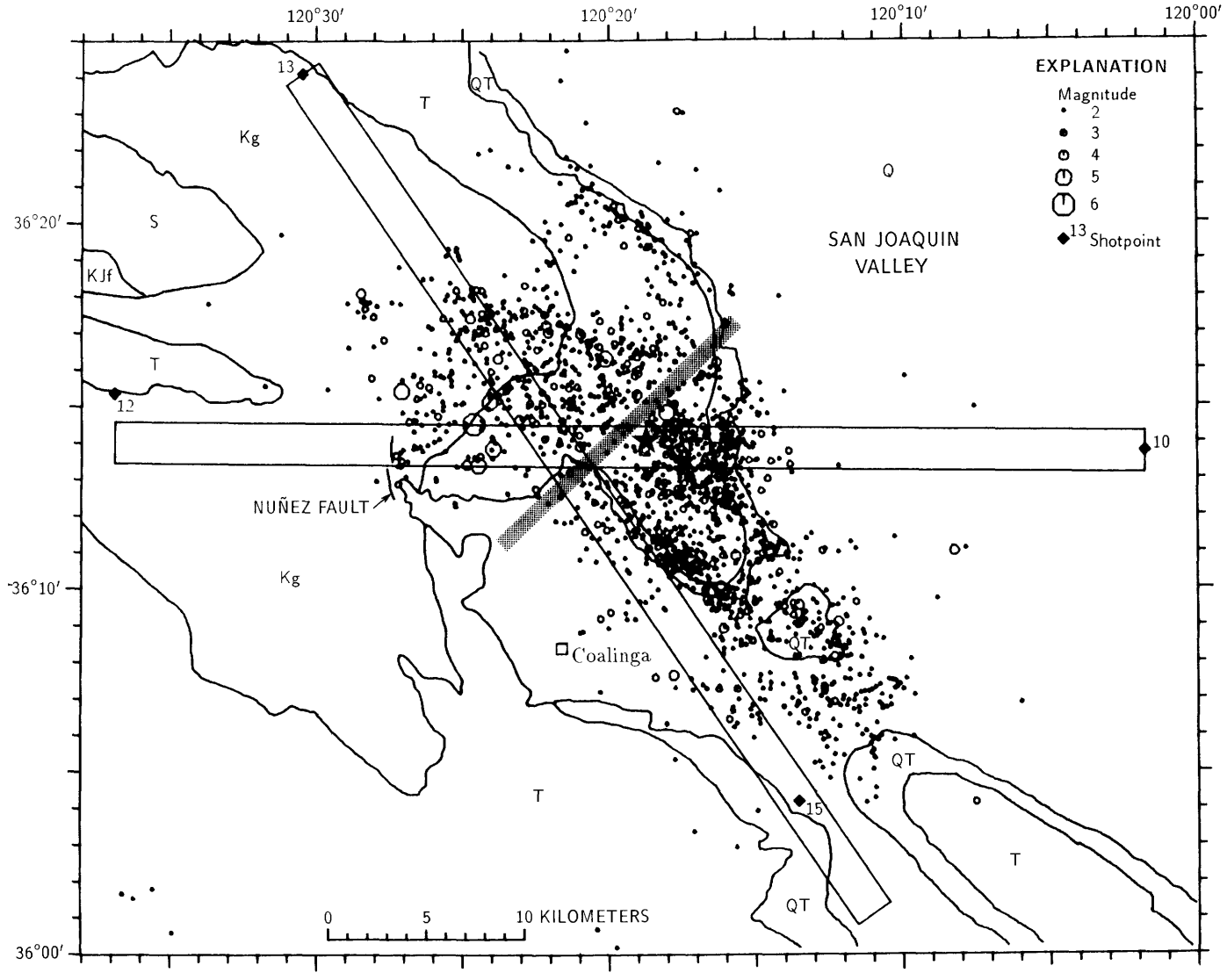

FIGURE 3.7.—Seismicity in the Coalinga region from May 2 to September 9, 1983, showing locations of epicenters (see chap. 8) with respect to general geology and refraction profiles. Star, epicenter of May 2 main shock (M_L = 6.7). Hypocenters of events located within outlined 2-km-wide strips are plotted on the respective velocity model cross sections in figure 3.9. Stippled band is "quiet zone" marking break in structure discussed in text. Kg, Great Valley sequence (Cretaceous); KJf, Franciscan assemblage (Cretaceous and Jurassic); QT, sedimentary rocks (Pliocene and younger); S, serpentinite (Mesozoic); T, sedimentary rocks (Tertiary). Q, Quaternary deposits.

occurred below 5-km depth, with an abrupt cutoff near 13-km depth (see chaps. 8, 9). The temporal-spatial pattern of hypocenters with respect to the fault-plane solutions favors a subhorizontal thrust on a southwest-dipping plane for the main shock, and this thrusting was subsequently accompanied by reverse faulting on steeply northeast and southwest dipping planes under Anticline Ridge. Both the postseismic elevation changes measured across Anticline Ridge (see chap. 13) and the fault offsets observed in the seismic-reflection records (see chap. 4) support this style of deformation.

The map view of the located hypocenters (see chap. 8) shows a narrow aseismic band or "quiet zone" (fig. 3.7), striking northeast-southwest across the north end of Pleasant Valley, that is bordered on the northwest by a line of aftershocks with right-lateral strike-slip solutions. From a comparison of the focal mechanisms and temporal-spatial patterns of seismicity on either side of this strike-slip zone, the thrust plate is inferred to be more rigid north of the zone, under Joaquin Ridge, than south of the zone, under Pleasant Valley. Fortuitously or not, the strike-slip zone intersects the northwest-southeast profile near the "break" in velocity structure modeled on the southern limb of Joaquin Ridge near shotpoint 14 (fig. 3.4).

The velocity-depth function used in chapter 8 to solve for the hypocentral locations is shown in figure 3.8, along with the velocity-depth functions taken from the refraction models at their point of intersection. This velocity function was derived by iteratively adjusting a flat-layer model so as to minimize the rms traveltime residuals for the events, as well as to comply with the requirement that the first-motion plots correspond to double-couple focal mechanisms. Note that below 3-km depth, the model used to locate the earthquakes closely approximates the velocity structure found at the intersection of the two profiles: The Great Valley-Franciscan contact is at 7 km, and the Franciscan-basement contact at 14 to 16 km.

Hypocenters of the 1983 Coalinga earthquake sequence that are located within 1 km of the refraction profiles (fig. 3.6) are shown projected into the respective velocity-model cross sections in figure 3.9. Note that the hypocenters of the main shock and most of the larger aftershocks are located within the Franciscan wedge; however, the seismicity extends into the Great Valley sequence both under the Coalinga anticline and along the projection of the Nuñez fault west of Pleasant Valley. The zones of abnormally high pore pressure and low velocity in the Great Valley sequence under Pleasant Valley and the Coalinga anticline could have aided the extension of faulting into the Great Valley sequence by reducing the effective confining pressure (see chap. 23). The abrupt cutoff of seismicity below 13-km depth in the Franciscan assemblage may indicate a change in rock strength, allowing aseismic deformation (Sibson, 1984).

SUMMARY OF MODELING RESULTS

1. The velocity in upper Cenozoic strata along both profiles increases with increasing depth. The velocity gradient in the uppermost kilometer is about 1 s^{-1}. Near the base of the Cenozoic or the top of the Cretaceous section, the velocity abruptly increases by about 0.5 km/s, and the velocity gradient decreases to less than 0.5 s^{-1}. The velocity of the lower Cenozoic and Cretaceous strata is less predictable. East of the Diablo Range, the Great Valley sequence is characterized by alternating sections of higher- and lower-velocity rock units, probably indicating large variations in formation pore pressure. These velocity inversions increase the uncertainty in the underlying structure, particularly the velocities of the lowermost sedimentary units, as well as the depth to the underlying basement.

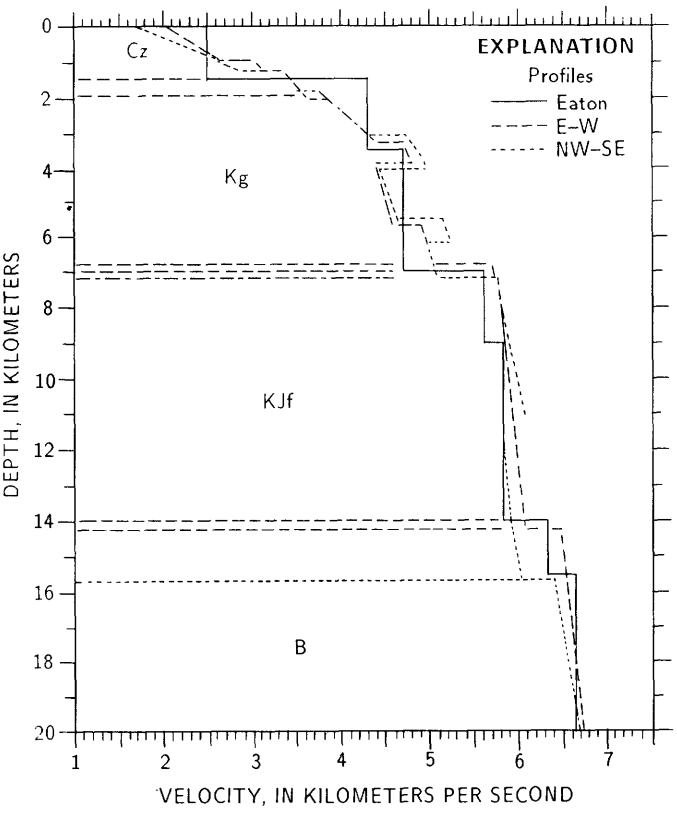

FIGURE 3.8.—Velocity-depth functions at point of intersection of the two refraction models, in comparison with velocity-depth function derived in chapter 8 and used to locate earthquake epicenters shown in figure 3.7. Same symbols as in figure 3.3*B*.

2. From Anticline Ridge westward into the Diablo Range, a wedge of intermediate-velocity Franciscan rocks lies between the Great Valley sequence and the underlying basement. The velocity structure within this Franciscan wedge is not laterally uniform. Along the northwest-southeast profile, the refraction data show evidence of a velocity inversion in the wedge, supporting a change in either composition or pore pressure within the lowermost units of the wedge.
3. East of the toe of the Franciscan wedge, the steeper dip or offset of the basement between the valley axis and the Coalinga anticline results in a basin containing several additional kilometers of Great Valley sequence. The velocity at the top of the basement suggests a composition such as serpentinized peridotite, but owing to the absence of reversed refraction data, the velocity structure of the underlying basement is not well constrained. Both profiles show evidence of deeper layering in the basement, and along the northwest-southeast profile the data suggest a Moho depth of 28 to 30 km.
4. The source region of the M_L=6.7 main shock and the larger aftershocks is within the Franciscan wedge, but the refraction data have insufficient resolution to

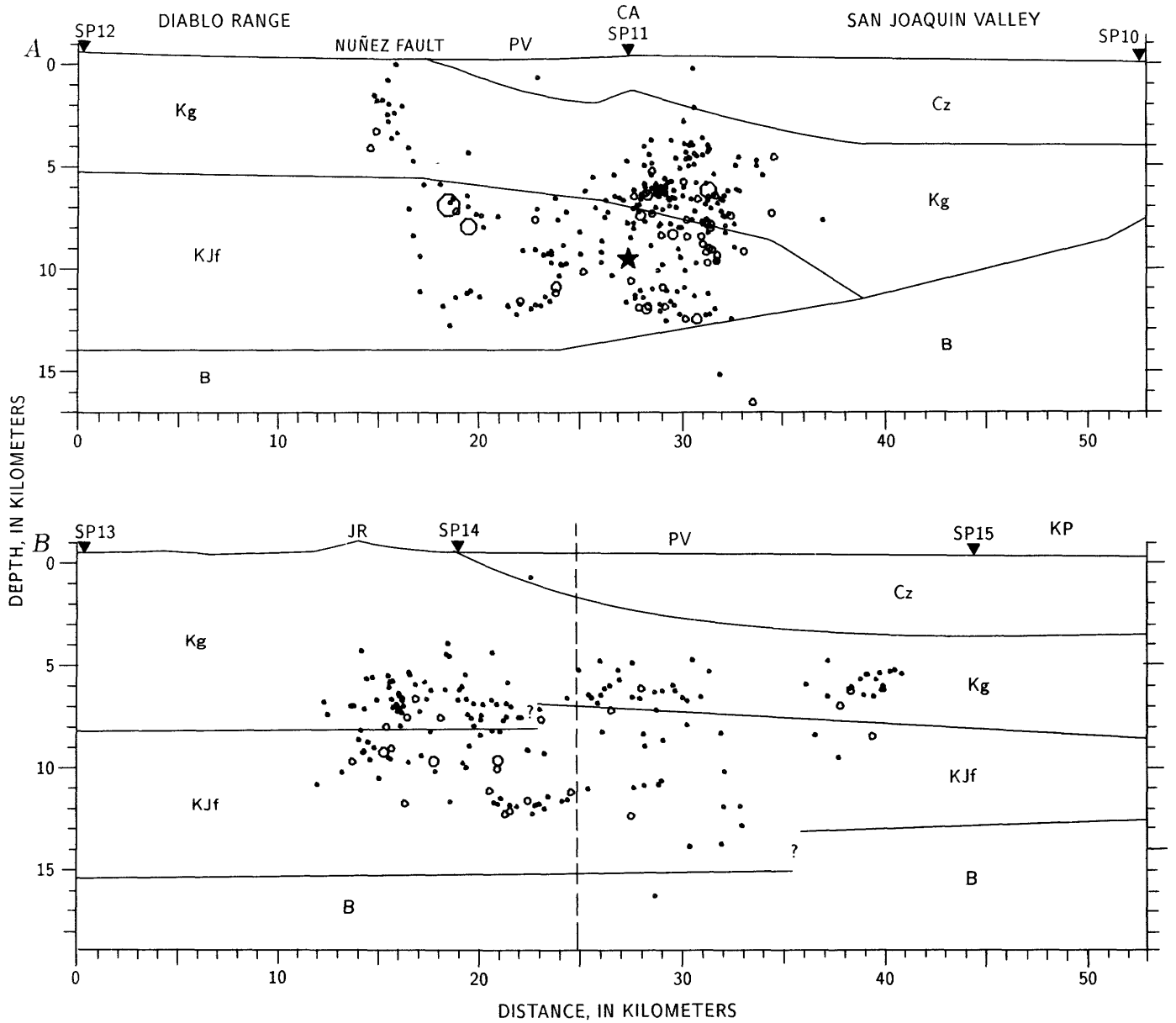

FIGURE 3.9.—Velocity-model cross sections showing superimposed seismicity. Cross-section end points correspond to those of strips outlined on figure 3.7. Seismicity located within strips was projected into plane of respective cross sections: east-west (*A*) and northwest-southeast (*B*). Vertical dashed line in northwest-southeast cross section indicates intersection with "quiet zone" shown in figure 3.7. Star, location of main shock. Same symbols as in figures 3.1 and 3.3*B*.

determine fault offsets. The observed folding and faulting within the sedimentary section are probably promoted by elevated pore pressures in the lower part of the Great Valley sequence under Pleasant Valley and the Coalinga anticline. The cutoff in seismicity near 13-km depth may result from a change in the strength of the Franciscan assemblage.

5. Before acquisition of the seismic reflection and refraction profiles across the Diablo Range-San Joaquin Valley margin, the Great Valley-Franciscan contact was interpreted as the suture of a fossil subduction zone in which the Franciscan assemblage underthrust the San Joaquin Valley basement. The seismic-refraction interpretation, however, supports obduction of the Franciscan assemblage onto the same basement that underlies the Great Valley sequence in the San Joaquin Valley (Wentworth and others, 1984a). That is, wedges of Franciscan assemblage were thrust eastward, underplating and deforming the Cretaceous and Cenozoic strata while flexing the mafic basement downward. The Coalinga anticline has grown above the easternmost tip of a Franciscan wedge. East-west compression along the San Andreas fault continues to uplift the San Joaquin Valley margin, as evidenced by focal mechanisms of the 1983 Coalinga earthquake sequence.

ACKNOWLEDGMENTS

E. Criley and G. Fuis played crucial roles in the acquisition of the refraction data. J. Murphy, V. Sutton, P. Meador, L. Hwang, A. Bloomfield, S. Gallantine, A. Loqcquiao, G. Molina, C. Criley, and L. Pace provided field support. R. Colburn processed the seismic data.

REFERENCES CITED

Bailey, E.H., Blake, M.C., Jr., and Jones, D.L., 1970, On-land Mesozoic oceanic crust in California Coast Ranges, *in* Geological Survey research, 1970: U.S. Geological Survey Professional Paper 700–C, p. C70–C81.

Bailey, E.H., Irwin, W.P., and Jones, D.L., 1964, Franciscan and related rocks and their significance in the geology of western California: California Division of Mines and Geology Bulletin 183, 177 p.

Červený, Vlastislav, Molotkov, I.A., and Pšenčik, Ivan, 1977, Ray method in seismology: Prague, Karlova University, 214 p. Christensen, N.I., 1982, Seismic velocities, chap. 1 *of* Carmichael, R.S., ed., Handbook of physical properties of rocks: Boca Raton, Fla., CRC Press, v. 2, p. 2–228.

Colburn, R.H. and Walter, A.W., 1984, Data report for two seismic-refraction profiles crossing the epicentral region of the 1983 Coalinga, California earthquakes: U.S. Geological Survey Open-File Report 84-643, 57 p.

Dibblee, T.W., Jr., 1971, Geological maps of the Coalinga, Joaquin Rocks, New Idria, and Priest Valley 15-minute quadrangles, California: U.S. Geological Survey open-file maps, scale 1:62,500.

Fielding, Eric, Barazangi, Muawia, Brown, Larry, Oliver, Jack, and Kaufman, Sidney, 1984, COCORP seismic profiles near Coalinga, California: Subsurface structure of the western Great Valley: Geology, v. 12, no. 5, p. 268–273.

Gardner, G.H.F., Gardner, L.W., and Gregory, A.R., 1974, Formation velocity and density—the diagnostic basics for stratigraphic traps: Geophysics, v. 39, no. 6, p. 770–780.

Harding, T.P., 1976, Tectonic significance and hydrocarbon trapping consequences of sequential folding synchronous with the San Andreas faulting, San Joaquin Valley, California: American Association of Petroleum Geologists Bulletin, v. 60, no. 3, p. 356–378.

Healy J.H., Mooney, W.D., Blank, H.R., Gettings, M.E., Kohler, W.M., Lamson, R.J., and Leone, L.E., 1982, Saudi Arabian deep seismic refraction profile: Final project report: Jiddah, Saudi Arabia, U.S. Geological Survey, Saudi Arabian Mission Report OF–02–37, 429 p.

Jennings, C.W., compiler, 1977, Geologic map of California: California Division of Mines and Geology Geologic Data Map 2, scale 1:750,000.

Lin, Wunan, and Wang, C.Y., 1980, *P*-wave velocities in rocks at high pressure and temperature and the constitution of the central California crust: Royal Astronomical Society Geophysical Journal, v. 61, no. 2, p. 379–400.

Mansfield, C.F., 1979, Upper Mesozoic subsea fan deposits in the southern Diablo Range, California: Record of the Sierra Nevada magmatic arc: Geological Society of America Bulletin, v. 90, pt. 1, no. 11, p. 1025–1046.

Oppenheimer, D.H., and Eaton, J.P., 1984, Moho orientation beneath central California from regional earthquake travel times: Journal of Geophysical Research, v. 89, no. B12, p. 10267–10282.

Page, B.M., 1981, The southern Coast Ranges, *in* Ernst, W.G, ed., The geotectonic development of California (Rubey volume 1): Englewood Cliffs, N.J., Prentice Hall, p. 329–417.

—— 1985, Geologic background of the Coalinga earthquake of May 2, 1983, *in* Rymer, M.J., and Ellsworth, W.L., eds., Proceedings of workshop XXVII: Mechanics of the May 2, 1983 Coalinga earthquake: U.S. Geological Survey Open-File Report 85-44, p. 4–9.

Schock, R.N., Bonner B.P., and Louis, H., 1974, Collection of ultrasonic velocity data as a function of pressure for polycrystalline solids: Livermore, Calif., Lawrence Livermore Laboratory Technical Report UCRL–51508, 123 p.

Sibson, R.H., 1984, Roughness at the base of the seismogenic zone: Contributing factors: Journal of Geophysical Research, v. 89, no. B7, p. 5791–5799.

Stewart, R.M., and Peselnick, Louis, 1978, Systematic behavior of compressional velocity in Franciscan rocks at high pressure and temperature: Journal of Geophysical Research, v. 83, no. B2, p. 831–839.

Walter, A.W. and Mooney, W.D., 1982, Crustal structure of the Diablo and Gabilan Ranges, central California: A reinterpretation of existing data: Seismological Society of America Bulletin, v. 72, no. 5, p. 1567–1590.

Wentworth, C.M., Blake, M.C., Jr., Jones, D.L., Walter, A.W., and Zoback, M.D., 1984a, Tectonic wedging associated with emplacement of the Franciscan assemblage, California Coast Ranges, *in* Blake, M.C., Jr., ed., Franciscan geology of northern California (book 43): Los Angeles, Society of Economic Paleontologists and Mineralogists, Pacific Section, p. 163–173.

Wentworth, C.M., Walter, A.W., Bartow, J.A., and Zoback, M.D., 1984b, Evidence on the tectonic setting of the 1983 Coalinga earthquakes from deep reflection and refraction profiles across the southeastern end of Kettleman Hills, *in* Bennett, J.H., and Sherburne, R.W., eds., The 1983 Coalinga, California earthquakes: California Division of Mines and Geology Special Publication 66, p. 113–126.

4. STRUCTURE OF THE COALINGA AREA AND THRUST ORIGIN OF THE EARTHQUAKE

By CARL M. WENTWORTH,
U.S. GEOLOGICAL SURVEY

and

MARK D. ZOBACK,
STANFORD UNIVERSITY

CONTENTS

ABSTRACT

The 1983 Coalinga main shock occurred at the eastern margin of the Coast Ranges beneath Coalinga anticline, which forms the northwest segment in a 100-km-long zone of young anticlines about 35 km northeast of the San Andreas fault. Northeast-directed thrusts (here named the "Coalinga thrust zone") terminate beneath the anticline at a depth of about 10 km in a series of upward-splaying reverse faults, above which the anticline has grown in the past 2 Ma. A distinct flattening near the center of the northeastern limb of the fold separates it into upper and lower tiers, which are related to separate reverse-fault splays below.

The main shock appears to have occurred at the base of a reverse-fault splay beneath the upper tier of the fold and produced a focal mechanism with a gently southwest-dipping focal plane that strikes parallel to the fold axis. Rupture propagated bilaterally back down the thrust and up the reverse fault. Dislocation modeling that reasonably fits the observed surface uplift across the anticline indicates about 2 m of slip on a 4-km-wide thrust rupture dipping 10° SW. and about 1.2 m of slip on a reverse rupture, which dips 55° SW. and extends 7 km updip to a depth of about 3.4 km beneath the center of the eastern limb of the fold. Aftershocks delineated both rupture zones, as well as various other zones along which complex readjustment to the main-shock deformation occurred.

Thrusting of the type responsible for the growth of Coalinga anticline probably extends the length of the Coalinga-Kettleman Hills-Lost Hills anticlinal trend, with tear faults at the echelon steps in the trend. The earthquake occurred east of the north-trending Pleasant Valley cross-structure, a large tear structure against which Coalinga anticline and other folds terminate. Aftershocks with strike-slip mechanisms aligned with the cross-structure indicate right-lateral movement, which is consistent with the 20-km right step in the eastern front of the Diablo Range that occurs there. Although the main-shock rupture surface probably terminated northwestward at the cross-structure, aftershock mechanisms suggest that related thrusts extend farther northwest beneath Joaquin Ridge anticline in the southern Diablo Range. Such thrusting may be characteristic of the eastern margin of the Coast Ranges throughout its length.

The structural setting for this recent thrusting east of the San Andreas fault was established in the Mesozoic under a different tectonic regime. Structure at the Coast Ranges boundary indicates eastward thrusting of a tectonic wedge of Mesozoic Franciscan assemblage onto west-dipping basement and concurrent peeling up of the coeval Great Valley sequence, which unconformably overlies that basement farther east. The basement shallows northeastward from its 15-km depth beneath the Diablo Range, first at 15°–20° beneath the west side of the San Joaquin Valley and then more gently. This shallowing of basement probably limited northeastward penetration of the Franciscan wedge and seems to be limiting the more recent thrusting as well.

INTRODUCTION

The Coalinga main shock of May 2, 1983, occurred 35 km northeast of the San Andreas fault at the eastern margin of the southern Coast Ranges (fig. 4.1). Although it was a large earthquake (M=6.7) and occurred near the San Andreas system, it was not a typical San Andreas event. Initial analysis (Eaton, 1983) indicated that the earthquake resulted from thrust or reverse movement at a depth of about 10 km on a fault striking parallel to the San Andreas fault. No ready explanation existed for a large earthquake at the Coast Ranges boundary that involved compression normal to the San Andreas fault.

The earthquake occurred beneath Coalinga anticline, which forms the northwestern segment of a 100-km-long zone of Quaternary anticlines that is parallel to the San Andreas fault and is aligned with the main eastern front of the Coast Ranges on strike to the northwest. No surface or subsurface faults appropriate to generate the earthquake were known, although early results of our study of the Coast Ranges boundary suggested that eastward-directed thrusting beneath the young folds might be involved (Wentworth and others, 1983). The occurrence of a large earthquake in this setting raises the possibility that similar earthquakes could occur elsewhere along the young-fold trend, or perhaps anywhere along the 600-km length of the Coast Ranges boundary.

The Coast Range thrust, a major tectonic feature near the Coast Ranges boundary, has been viewed as a fossil subduction zone for nearly 25 years. Our recent work (Wentworth and others, 1984a; Wentworth and Zoback, 1985), in contrast, suggests that the Coast Range thrust does not extend eastward to depth through the crust and emphasizes the need to improve our understanding of subsurface structural relations across this boundary. Deep structure in the vicinity of Coalinga anticline embodies several fundamental issues of the Coast Ranges boundary: the eastward, downdip extent of the Coast Range thrust; the abrupt westward thickening of the Great Valley sequence (Upper Mesozoic sandstone and shale that connect Coast Range and Great Valley geology); and the relation of the contrasting basements on which the Great Valley sequence was deposited (Coast Range ophiolite in the Coast Ranges and presumed Sierran crystalline rock beneath the Great Valley).

We first explore the origin of the earthquake and its regional implications by setting the general context of the earthquake at the Coast Ranges boundary and developing the structural anatomy and inferred tectonic history of the Coalinga area itself. The primary basis for our analysis of the Coalinga area is two seismic-reflection profiles across Coalinga anticline. These not only show details of the shallow folding but contain reflections at hypocentral depth that we conclude represent eastward-directed thrusts that have created Coalinga anticline.

We then apply our structural interpretation to the generation of the Coalinga earthquake sequence, which is described in other chapters of this volume. Eaton (chap. 8) determined the locations and focal mechanisms of the main shock and principal aftershocks. The main-shock focal mechanism yields both a steep (reverse fault) and a low-angle (thrust) focal plane, although Eaton considers it unlikely that the steeply dipping plane broke during the main shock. He concludes that the main shock occurred as a result of thrusting on a fault that dips 23° SW. and strikes N. 53° W. beneath Coalinga anticline. Eberhart-Phillips and Reasenberg (chap. 9), through an analysis of several thousand aftershocks and several hundred well-determined focal mechanisms, conclude that main-shock rupture probably occurred on a steeply southwest dipping plane beneath Coalinga anticline that appears to flatten southwestward at a depth of 10 km and (or) on a steeply northeast dipping plane. Dislocation modeling of observed coseismic elevation changes over Coalinga anticline (Stein and King, 1984; Stein, 1985) suggests that the earthquake occurred on the steeply northeast dipping focal plane of the main-shock focal mechanism. We use similar modeling of this surface deformation to test our conclusion that main-shock rupture occurred, instead, on a gently west dipping thrust and steeper reverse-fault splay.

REGIONAL SETTING

In its broadest context, the Coalinga main shock occurred at the 600-km-long boundary (the Coast Ranges boundary) between the uplifted mountains of the Coast Ranges and the alluvial lowland of the Great Valley. West of this boundary, in the Coast Ranges, late Cenozoic structures were formed in the right-lateral strike-slip regime of the San Andreas fault system. East of it, the vast Sierran block is tilted gently down toward the Coast Ranges and is covered by sediment along its depressed southwestern margin, but is otherwise largely intact.

FIGURE 4.1.—Geologic map of the San Joaquin Valley and adjacent Coast Ranges, showing regional setting of May 2 main shock and locations of seismic-reflection lines (solid lines with dots). Geology modified from Jennings (1977). L (east of junction of Calaveras and San Andreas faults), Lanada ophiolite at base of Great Valley sequence; PVCS, Pleasant Valley cross-structure; Qa, Quaternary alluvium; Ts, Tertiary sedimentary rocks; Tv, Tertiary volcanic rocks; Mzg, Mesozoic Great Valley sequence; Mzm, Mesozoic metamorphic rocks; f, Franciscan assemblage; u, ultramafic rocks; gr, granitic rocks; Pzm, Paleozoic metamorphic rocks.

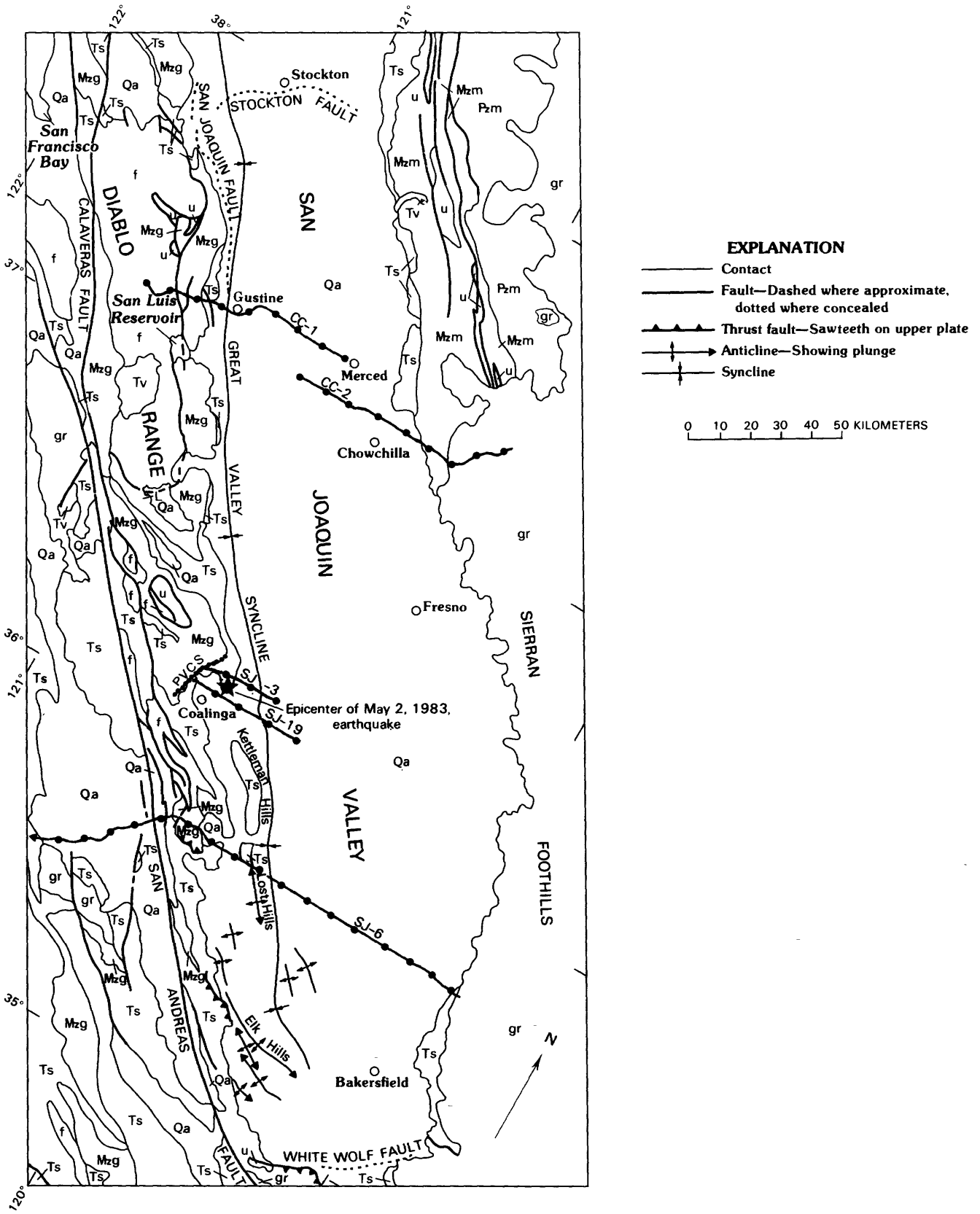
122°
38°
121°
37°
36°
35°
120°
Stockton
STOCKTON FAULT
SAN JOAQUIN FAULT
San Francisco Bay
DIABLO RANGE
CALAVERAS FAULT
San Luis Reservoir
Gustine
CC-1
CC-2
Merced
Chowchilla
GREAT VALLEY
SAN JOAQUIN VALLEY
SYNCLINE
Fresno
SIERRAN FOOTHILLS
PVC-5
SJ-3
SJ-19
Coalinga
Epicenter of May 2, 1983, earthquake
Kettleman Hills
SAN ANDREAS FAULT
Lost Hills
SJ-6
Elk Hills
Bakersfield
WHITE WOLF FAULT
Qa
Ts
Mzg
Mzm
Pzm
Tv
gr
u
f
EXPLANATION
Contact
Fault—Dashed where approximate, dotted where concealed
Thrust fault—Sawteeth on upper plate
Anticline—Showing plunge
Syncline
0 10 20 30 40 50 KILOMETERS

GREAT VALLEY SEQUENCE

A thick, east-dipping sequence of marine sandstone and shale, the Great Valley sequence, is exposed along the eastern margin of the Coast Ranges. Where complete, this section ranges in age from Late Jurassic to Late Cretaceous and depositionally overlies mafic and ultramafic rocks of the Coast Range ophiolite (Bailey and others, 1970; Hopson and others, 1981). In the southern Coast Ranges, however, the base of the section is generally cut out by faulting at the contact with the Franciscan assemblage (Jennings, 1977).

Only the upper part of the Great Valley sequence is present to the east beneath the Great Valley, where it overlies and thins eastward across crystalline basement. Correlation of the Upper Cretaceous strata beneath the valley with the Upper Cretaceous part of the Great Valley sequence exposed in the Coast Ranges yields a vast asymmetric synclinorium, 600 km long, with its axial trough near the western margin of the Great Valley (fig. 4.1; see Page and others, 1979).

The westward transition from the Upper Cretaceous section beneath the Great Valley to the Jurassic and Cretaceous section in the Coast Ranges occurs abruptly. For most of the length of the Great Valley, the thickness of the nearly flat-lying section beneath its western side ranges from about 1.5 to 4 km. Minimum stratigraphic thicknesses in the steeply dipping Great Valley sequence exposed to the west, in contrast, range from 3 to 8 km in the Diablo Range to as much as 15 km farther north. Some interpretations account for this change by eastward onlap of the sequence during sedimentation (for example, Schilling, 1962), although the transition is so abrupt that gradual onlap alone seems insufficient. Other interpretations suggest westward deepening of the late Mesozoic sedimentary basin across dip-slip faults (for example, Brown and Rich, 1967).

FRANCISCAN ASSEMBLAGE

The main mass of the Coast Ranges west of the Great Valley sequence is composed of the Franciscan assemblage, also of Late Jurassic to Late Cretaceous age, which is an accretionary prism that consists principally of oceanic sedimentary and lesser volcanic rocks. Some tectonostratigraphic units in the Franciscan consist of well-bedded, albeit variously folded, rocks, whereas others are a melange of various kinds and sizes of blocks in a matrix of sheared mudstone (Blake and others, 1984). Most of the rocks have varyingly undergone high-pressure, low-temperature metamorphism to blueschist grade. The structural base of the Franciscan is nowhere exposed at the surface.

CRYSTALLINE BASEMENT

In the Great Valley, crystalline basement rock of the tilted Sierran block extends southwestward from exposure in the Sierran foothills beneath unconformably overlying Cretaceous and Cenozoic sedimentary rocks (fig. 4.2). The surface of this basement rock dips 3°–5° SW. across the San Joaquin Valley for about three-fourths of its width. Drill holes to basement define this surface down to a depth of about 4.5 km.

The shape of the basement surface beneath the valley seems extraordinarily simple. In the southern part of figure 4.2, however, the surface is cut by several northwest-trending faults that have vertical separations as large as 1.2 km. Identification of the strike extension of one of these faults (associated with the Semitropic anticline) as a reverse fault on reflection profile SJ–6 (Wentworth and others, 1983a) implies that other basement faults beneath the western San Joaquin Valley may also be reverse.

West of the area of well control, reflection and refraction profiles indicate that this same surface (the top of rock with a seismic velocity of 6.2–6.5 km/s) extends westward beneath the leading edge of the Coast Ranges (Wentworth and others, 1984a; Wentworth and Zoback, 1985). The gentle southwestward dip increases to 10°–15° near the western margin of the San Joaquin Valley and then flattens at a depth of about 15 km beneath the eastern Diablo Range. This continuity of crystalline basement at depth across the boundary between the Great Valley and the eastern Coast Ranges is supported at Coalinga by the gravity and magnetic modeling of Griscom and Jachens (chap. 5), who confirm the basement configuration determined from refraction profiling (see chap. 3) and find that a major break in the basement surface is not tenable.

Granitic and metamorphic rocks of the Sierran foothills form the uppermost crystalline basement as far west as the deepest basement wells northeast of Coalinga (fig. 4.2; see table 4.2). Farther west, however, the refraction velocities and gravity and magnetic modeling indicate the presence of higher velocity (6.3–6.5 km/s), denser (2.90 g/cm^3), magnetic basement rock that Griscom (1982) infers to be a slab of ophiolite that was obducted onto the continental margin during Jurassic time.

COAST RANGE THRUST AND FRANCISCAN WEDGE

The Franciscan assemblage and Great Valley sequence are juxtaposed across the Coast Range thrust, which is a major northeast-dipping fault that extends the length of the Coast Ranges near their eastern margin. This thrust was conceived (Bailey and others, 1964, p. 163–165; Irwin, 1964) to account for the structural juxtaposition of these two different masses of Mesozoic rock. In the

context of plate tectonics, the Coast Range thrust has since been viewed as a subduction-zone suture that extends eastward to depth in the mantle (for example, Dickinson, 1981).

From its exposure in the eastern Coast Ranges (fig. 4.1), the Coast Range thrust projects downward to the east beneath the Coast Ranges boundary. Because the surface of the crystalline basement under the Great Valley extends westward beneath this boundary without major offset, however, the Coast Range thrust cannot extend eastward to depth through the crust as a subduction zone suture. On the contrary, it must terminate at or above the continuous basement surface. These relations, both at Coalinga and elsewhere near the Coast Ranges boundary, led to the proposal that the Coast Range thrust is the roof thrust of a wedge of obducted Franciscan rock that was thrust northeastward onto the continental margin, where it concurrently peeled up the overlying Great Valley sequence (Wentworth and others, 1984a). The gross structure at the Coast Ranges boundary thus involves a deep basement surface overlain by an eastward thinning wedge of Franciscan rock that is

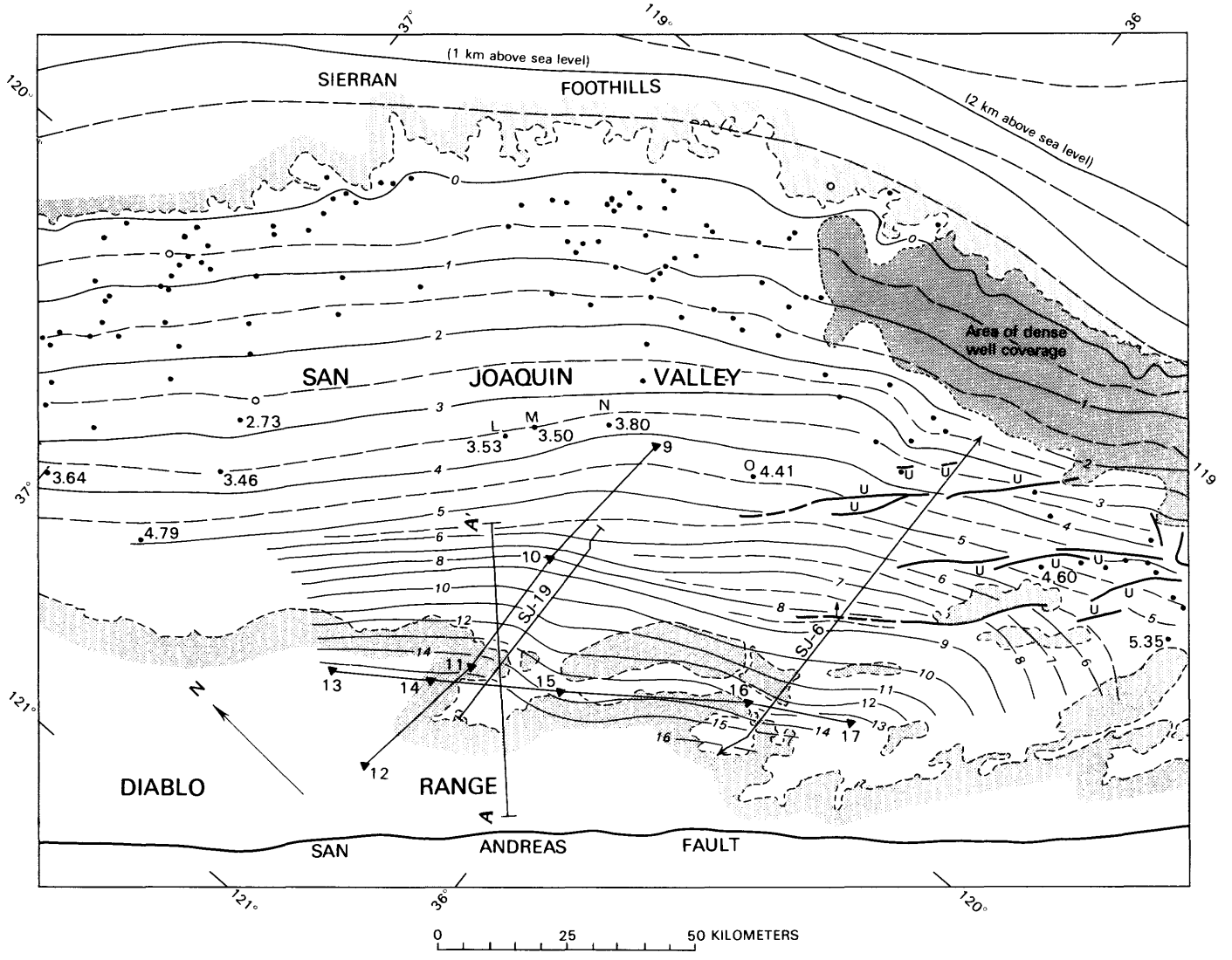

FIGURE 4.2.—Surface configuration of Great Valley basement. Contours (in kilometers below sea level; long-dashed line, 500 m) drawn from depth to crystalline rock in wells (solid dots; depth shown in kilometers for westernmost wells) in east two-thirds of valley (circles mark wells with inconsistent basement depths) and from seismic-reflection and refraction profiles in the west (SJ–6, Wentworth and others, 1983a; SJ–19, this chapter; refraction lines, chap. 3; triangles mark shotpoints). Basement faults (bold solid line, dashed where approximate; U on upthrown side; arrow indicates direction of dip) and their vertical separations largely from Western Geophysical Co. (1975). Lettered wells provide westernmost control east of Coalinga on thickness of Great Valley sequence (see table 4.2). Surface of exposed basement (above sea level) is a topographic envelope on ridge crests. Short-dashed line marks alluvial boundary. *A–A'*, location of figure 4.6. Light shading, rock exposures.

bounded above and below by thrusts and is structurally overlain by Great Valley sequence.

SHALLOW STRUCTURE

Structure above the basement surface within the San Joaquin Valley is relatively simple: a homocline that dips very gently southwestward and is interrupted locally by slight anticlinal warps. Some of these anticlines overlie basement faults (fig. 4.2), but it has also been suggested that some lie above foreland thrust ramps (such as the Turk anticline; see chap. 6).

The Coast Ranges boundary is marked by abrupt upturning of the gently west dipping strata beneath the San Joaquin Valley to form a nearly linear, northeast-facing flank to the San Joaquin Valley syncline (fig. 4.1). In the Coast Ranges southwest of this simple fold flank, however, structure varies considerably.

From the main-shock epicenter southeastward, the abrupt upturning marks the northeast flank of the Coalinga-Kettleman Hills-Lost Hills anticlinal zone, which strikes nearly parallel to the San Andreas fault for 100 km along the southwestern margin of the San Joaquin Valley. West of this zone, structure generally strikes more westerly. Northwest of the epicenter for about 50 km, similar oblique-trending structures extend right up to the range front.

At the junction between these two reaches of the Coast Ranges boundary, the main structural uplift of the Coast Ranges—represented by exposure of the Great Valley sequence—steps to the right about 20 km (fig. 4.3) along an obscure, north-northeast-trending structure that we here term the "Pleasant Valley cross-structure" (see figs. 4.1, 4.4, 4.8). This feature is situated near the exposed Cretaceous-Tertiary contact at the northwest end of Pleasant Valley. Its northern end is defined by the termination of Coalinga anticline against the south flank of Joaquin Ridge anticline, and its south end by the abutment of Jacalitos anticline against the south flank of White Creek syncline. That large syncline dies out toward the cross-structure, as does the Pleasant Valley syncline from the opposite side. No faults that might accommodate differential movements along the cross-structure have been recognized at the surface.

QUATERNARY DEFORMATION

The southern part of the Coast Ranges boundary is marked by differential Quaternary movement between the mountains and the valley. The evident structure at the boundary is a homocline of Cretaceous and Cenozoic strata that dips northeast toward the valley. Southeast of the main-shock epicenter, this homocline forms the northeast flanks of the anticlines of the Coalinga-Kettleman Hills-Lost Hills zone, which have grown in Pliocene and Quaternary time. The folds stand as hills above the surrounding alluvial plain and involve strata at least as young as about 0.6 Ma.

Northwest of the epicenter, the homocline fronts the main mass of the Diablo Range, where it also involves strata as young as about 0.6 Ma. These young strata (represented by the Corcoran Clay Member of the Tulare Formation) are consistently tilted up at the valley margin as steeply as about 3° (Page, 1986). In the foothills southeast of San Luis Reservoir (fig. 4.1), Lettis (1982) found a similar amount of northeastward tilting of old stream terraces west of the valley margin. This observation suggests that late Quaternary uplift of the Coast Ranges here has been accommodated by folding across the Coast Ranges boundary.

Range-front faulting has also occurred along the east side of the northern Diablo Range (San Joaquin Valley fault, fig. 4.1; Herd, 1979a; Lettis, 1982). This faulting involves as much as about 200 m of down-to-the-east separation on Quaternary terraces. Herd (1979b) considered this faulting to be normal, and Lettis (1982) suggested lateral movement, but our work indicates that the basic style of faulting beneath the range front should be west-dipping reverse or thrust faulting. In the same foothills area southeast of San Luis Reservoir, Quaternary terraces are broken by a series of small, northeast-dipping reverse faults (O'Neill fault system of Herd, 1979b; Lettis, 1982). These faults seem to represent bedding-plane slip that occurred as the northeast-dipping Great Valley sequence was tilted another increment.

STRUCTURE AND TECTONICS OF THE COALINGA AREA

The 1982 main shock occurred beneath Coalinga anticline near the junction of the Pleasant Valley cross-structure with the west flank of San Joaquin Valley syncline. Structure and timing of deformation in this area are well defined by a thick Cretaceous and Cenozoic stratigraphic section that includes more than a kilometer of Pliocene and Quaternary marine and alluvial sediment (see chap. 1). These strata are exposed in the mountains

FIGURE 4.3.—Geologic map of the Coalinga area, showing locations of seismic-reflection lines (every fifth kilometer mark numbered), refraction shotpoints (labeled triangles), and wells (lettered dots) used in interpretation. f, Franciscan assemblage; Kg, Gravelly Flat Formation; Kp, Panoche Formation; Kps, sandstone unit in Panoche Formation; Ks, Cretaceous sedimentary rocks, undivided; Qa, Quaternary alluvium; Qs, Quaternary sediment; Qt, Tulare Formation; sp, serpentinite; Te, Etchegoin Formation; Tk, Kreyenhagen Formation; TKm, Moreno Formation undivided; Ts, Tertiary sedimentary rocks; Tsj, San Joaquin Formation. Geology modified from Dibblee (1971) and Mansfield (1972).

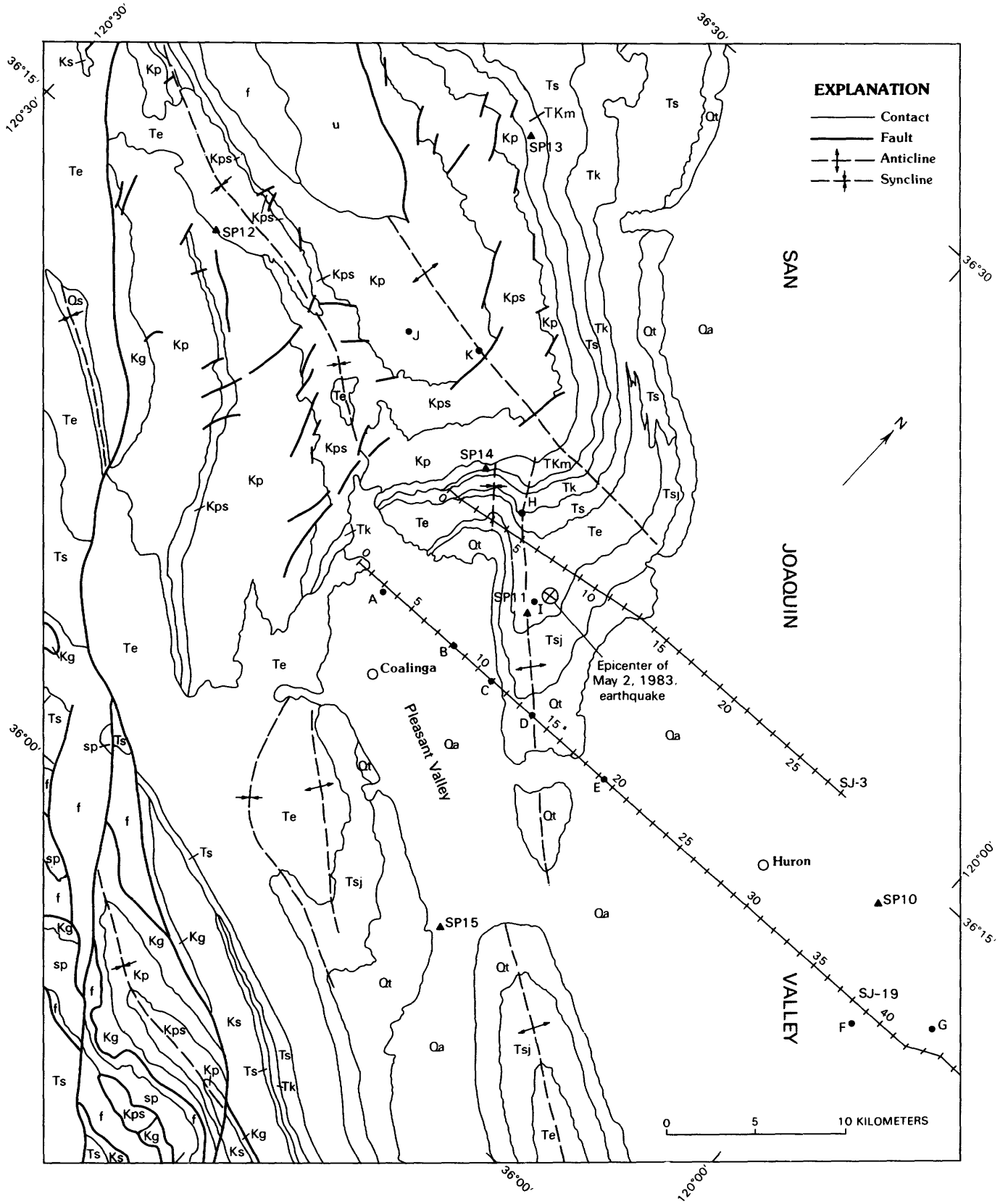
EXPLANATION
Contact
Fault
Anticline
Syncline
SAN JOAQUIN VALLEY
Coalinga
Huron
Pleasant Valley
Epicenter of May 2, 1983, earthquake
SP10
SP11
SP12
SP13
SP14
SP15
SJ-3
SJ-19
A
B
C
D
E
F
G
H
I
J
K
0 5 10 KILOMETERS
120°30'
36°30'
36°15'
36°00'
120°00'

in the western part of the area (fig. 4.3) and are evident in drill holes and reflection profiles downdip to the east in the subsurface.

1. The folds of principal interest (fig. 4.4) are (1) Joaquin Ridge anticline, which raises the reconstructed top of the Cretaceous section about 9 km relative to the trough of the San Joaquin Valley syncline; (2) flanking White Creek syncline, whose 4.5 km of structural relief dies out abruptly eastward toward the Pleasant Valley cross-structure; (3) Coalinga anticline, which plunges southeastward off the south flank of Joaquin Ridge anticline but nowhere exceeds about 1.5 km in amplitude; and (4) flanking Pleasant Valley syncline, which plunges and tightens southeastward from the Pleasant Valley cross-structure toward the deep, poorly defined trough southwest of Kettleman North Dome. Coalinga anticline gives way southeastward across a series of right steps to North Dome and the other folds in the Coalinga-Kettleman Hills-Lost Hills zone of anticlines.
2. Some of the folds in the Coalinga area had an earlier history of growth through the Tertiary, but all have undergone major growth during the past several million years. Joaquin Ridge anticline and its flanking synclines were influencing sedimentation in early to middle Tertiary time (Harding, 1976), although about half of the limb rotation (Dibblee, 1971) recorded in Cretaceous strata along the White Creek syncline (dips of 40°–60°) is shared by the unconformably overlying Etchegoin Formation (dips of 15°–30°) of largely Pliocene age. Uplift of the western limb of Pleasant Valley syncline influenced sedimentation in the early and middle Tertiary (see chap. 1, figs. 1.2, 1.3). Although Harding (1976) presented evidence suggesting that Coalinga anticline had enough structural relief in the early Tertiary to influence the distribution of the nearshore Gatchell and "Leda" sands (of local usage), this relief may have been associated, instead, with Joaquin Ridge anticline and, in any case, need not have been large.
3. Beginning in Pliocene time, Coalinga anticline began to grow fast enough to cause distinct thinning of the San Joaquin Formation being deposited across its crest (see chap. 1), although principal folding is younger, postdating the beginning of Tulare deposition. Dips in exposed Tulare strata are at least as steep as 15°, similar to those in older strata in the core of the fold (Dibblee, 1971).
4. The age of volcanic tuff in Kettleman North Dome makes the age of the Tulare-San Joaquin boundary about 2 Ma (Sarna-Wojcicki and others, 1985), indicating that this principal folding began later than 2 Ma. The top of the Tulare Formation (horizon C) is also folded. This horizon is equivalent to the Corcoran Clay Member of the Tulare Formation (see chap. 1; J.A. Bartow, oral commun., 1984) and correlates approximately with the 0.6-Ma-old Friant Ash Member of the Turlock Lake Formation (Marchand and Allwardt, 1981). Modern growth of the fold is documented by leveling surveys after the Coalinga main shock (Stein, 1985, fig. 2). Page (1984) pointed out that the cutting and subsequent arching of an erosional surface on Kettleman North Dome indicates that this young folding was not continuous over time.

SEISMIC-REFLECTION PROFILES

The seismic-reflection profiles studied here (pls. 4.1, 4.2; fig. 4.5), which cross Coalinga anticline north and south of the main-shock epicenter (figs. 4.3, 4.4), provide detailed structural information in the subsurface down to the hypocentral depth of the main shock. In concert with the refraction work of Walter (chap. 3), these profiles provide the basis for a structural cross section through the source region of the Coalinga main shock (fig. 4.6).

Reflection profiles SJ–19 and SJ–3 were collected and processed by the Western Geophysical Co. in 1981–83. Rights to these profiles were purchased by the U.S. Geological Survey in 1983. The profiles are conventional 24-fold Vibroseis profiles collected using an upsweep and a maximum receiver offset of 3.5 km (profile SJ–19). They were originally processed to a two-way traveltime of 6 s and were subsequently recorrelated to a record length of 12 s and reprocessed for the U.S. Geological Survey (table 4.1; see Okaya, 1986, for recorrelation technique). Our emphasis is on profile SJ–19 (pl. 4.1), which contains much more information than profile SJ–3 (pl. 4.2) and best defines deep structure.

A third east-west reflection line (COCORP line 1), located 6.4 km south of profile SJ–19, was collected in 1977 to image deep structure by the Consortium for Continental Reflection Profiling (COCORP). Recent interpretation of this profile (Fielding and others, 1983, 1984; Fielding and Barazangi, 1985) yielded a different structural model than we propose here.

FIGURE 4.4.—Structure-contour map of the Coalinga area. Top of Eocene Kreyenhagen Formation mapped (from well control) downdip from its surface exposure (dotted line) near sea level (0.0 contour; dashed where approximate); top of Cretaceous strata (largely top of Moreno Formation) approximately reconstructed (from exposed structure) updip to the northwest from its surface exposure (shaded line) near sea level (0 contour; dashed where approximate). Cretaceous surface lies about 1 km vertically below the Kreyenhagen surface near their surface exposures. Dots, drill holes to Kreyenhagen Formation; circles, drill holes to Temblor Formation. Bold hachured line, top of lower tier of Coalinga anticline; bold line marked N, Nuñez fault trace; circled x, main-shock epicenter; cross-hatched lines, reflection lines showing kilometer marks; triangles, refraction shotpoints.

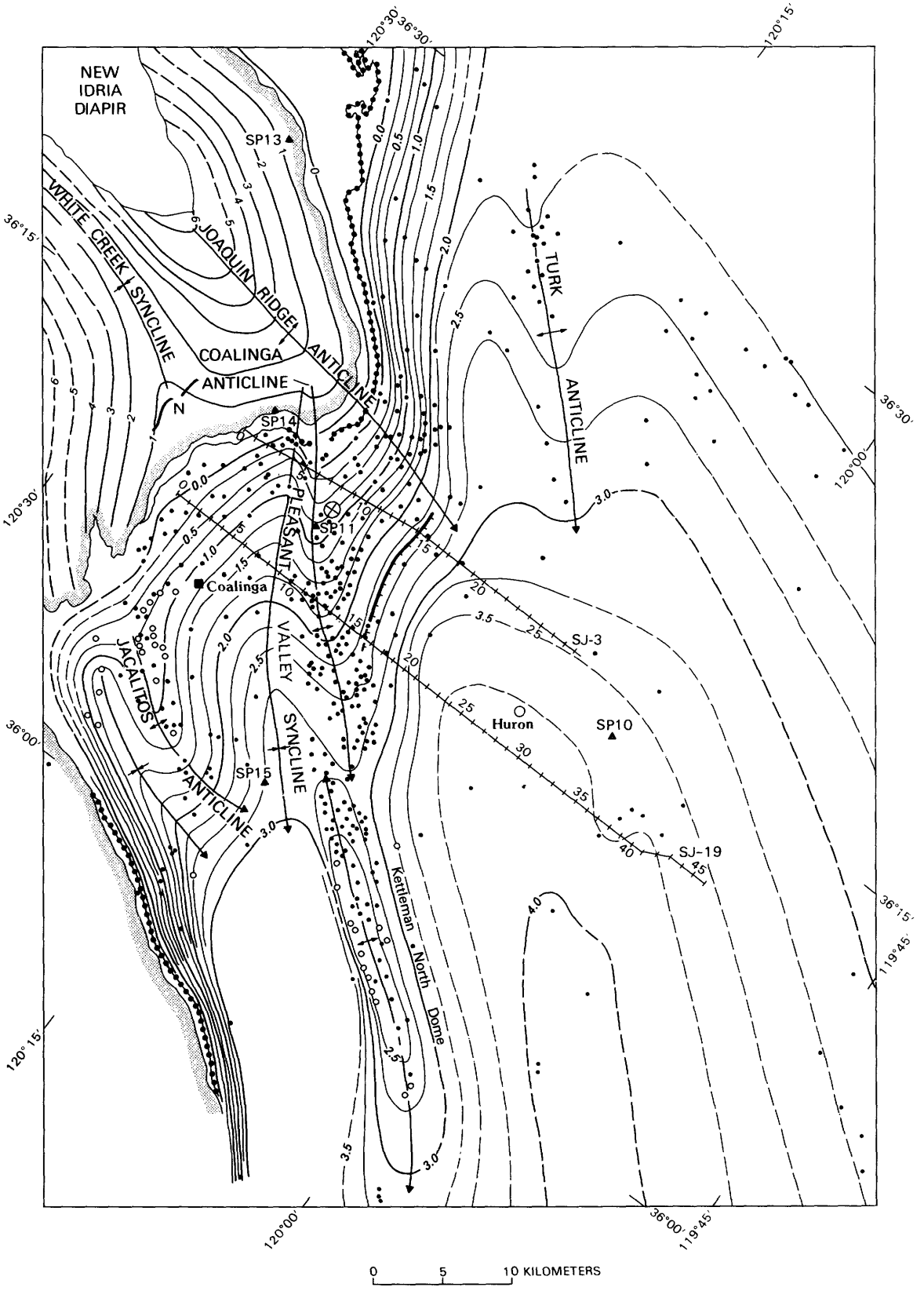
NEW IDRIA DIAPIR
SP13
WHITE CREEK SYNCLINE
JOAQUIN RIDGE ANTICLINE
COALINGA ANTICLINE
N
SP14
SP11
PLEASANT VALLEY SYNCLINE
Coalinga
JACALITOS ANTICLINE
SP15
TURK ANTICLINE
SJ-3
Huron
SP10
SJ-19
Kettleman North Dome
120°30'
36°30'
120°15'
36°15'
120°00'
36°00'
119°45'
0 5 10 KILOMETERS

COCORP line 1 is similar to profile SJ–19 but lacks the clarity and detail beneath Coalinga anticline that are evident in profile SJ–19.

Interpretation of the reflection profiles is straightforward in the Cenozoic and uppermost Cretaceous section, where the reflections are regularly layered and the section is penetrated by nearby wells. Below the top of the Panoche Formation (horizon P), however, the rocks have not been sampled by the drill. Lateral constraints on the identity of these deep rocks from wells to the east of the profile and outcrops to the west require complex structure across the Coast Ranges boundary. Beneath the San Joaquin Valley to the east, about a kilometer of Cretaceous strata overlying crystalline basement (penetrated in wells L–O, table 4.2) dips gently west toward the reflection profile. In the Diablo Range to the west, in contrast, an exposed section of uppermost Jurassic and largely Cretaceous Great Valley sequence, about 8 km thick (fig. 4.3) and locally attached to a basement of Coast Range ophiolite (L, fig. 4.1), structurally overlies Franciscan assemblage and dips east toward the profile.

SHALLOW STRATIGRAPHY

Reflections in the upper part of profile SJ–19 (pl. 4.1) show a regular stratigraphy and define a more detailed version of the same fold structure that is determined from the top of the Kreyenhagen Formation (horizon K) penetrated in wells (fig. 4.4). The stratigraphic units and their tops shown in plate 4.1B were identified from geophysical logs of seven wells that lie within 1 km of profile SJ–19 and approach or penetrate the base of the Cenozoic section (fig. 4.3; table 4.2). We use the stratigraphy and well-log picks of Bartow (chap. 1).

Interval velocities were calculated from stacking-velocity analyses of the reflection data spaced every 1 to 2

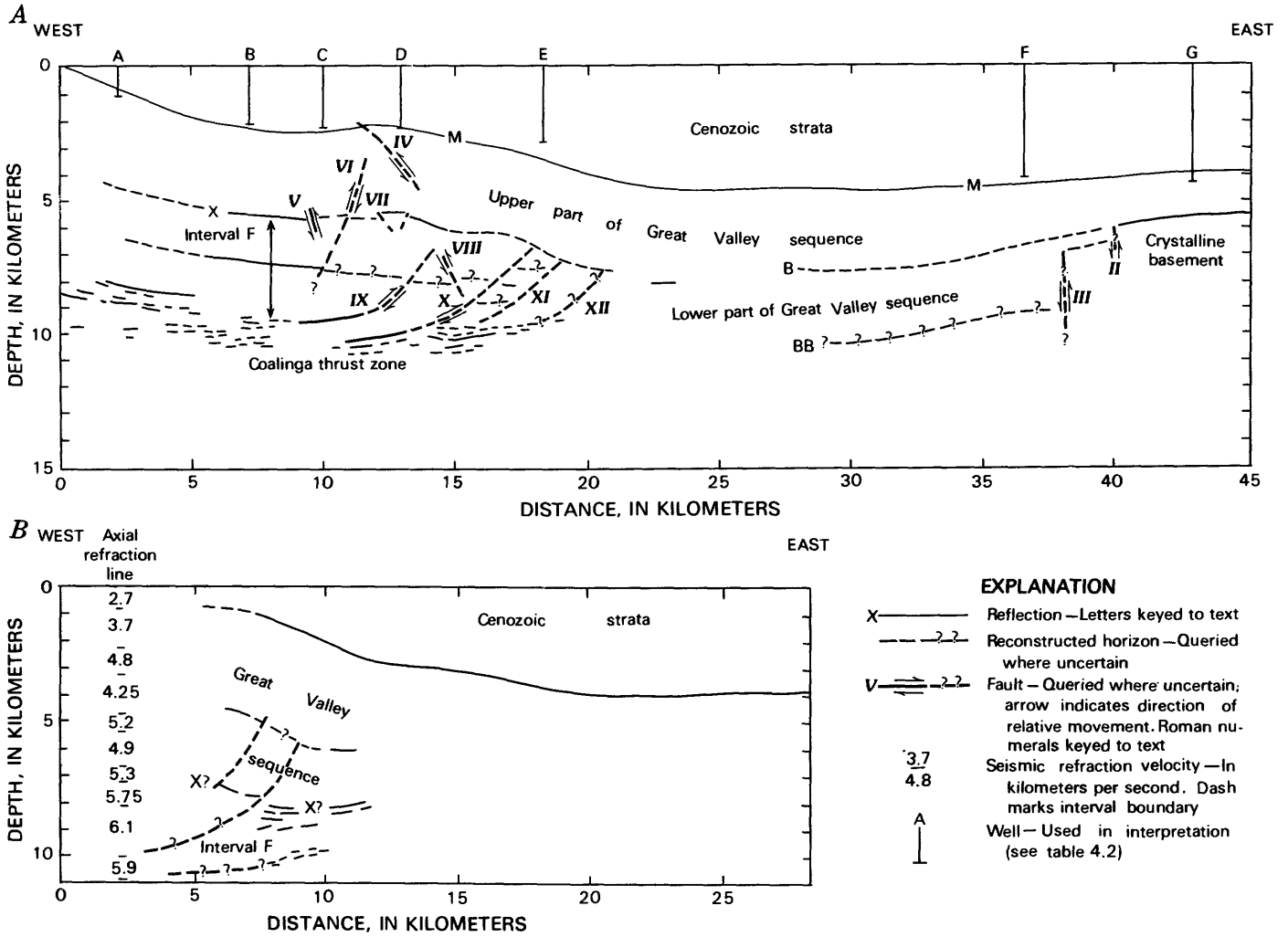

FIGURE 4.5.—Cross sections through Coalinga anticline, showing structure evident along reflection lines SJ–19 (*A*) and SJ–3 (*B*). Structure converted to depth from plates 4.1B and 4.1C.

km along the profile. Velocity control is reasonably good where reflections are clear and close to horizontal, because maximum source-receiver offsets of 3.5 km on profile SJ-19 yield about 0.25 s of normal moveout at a two-way traveltime of 3.0 s east of the anticline. The interval velocities were generalized for portrayal on plate 4.1B under the assumption that lateral variations are regular. The calculated velocities in the upper part of the

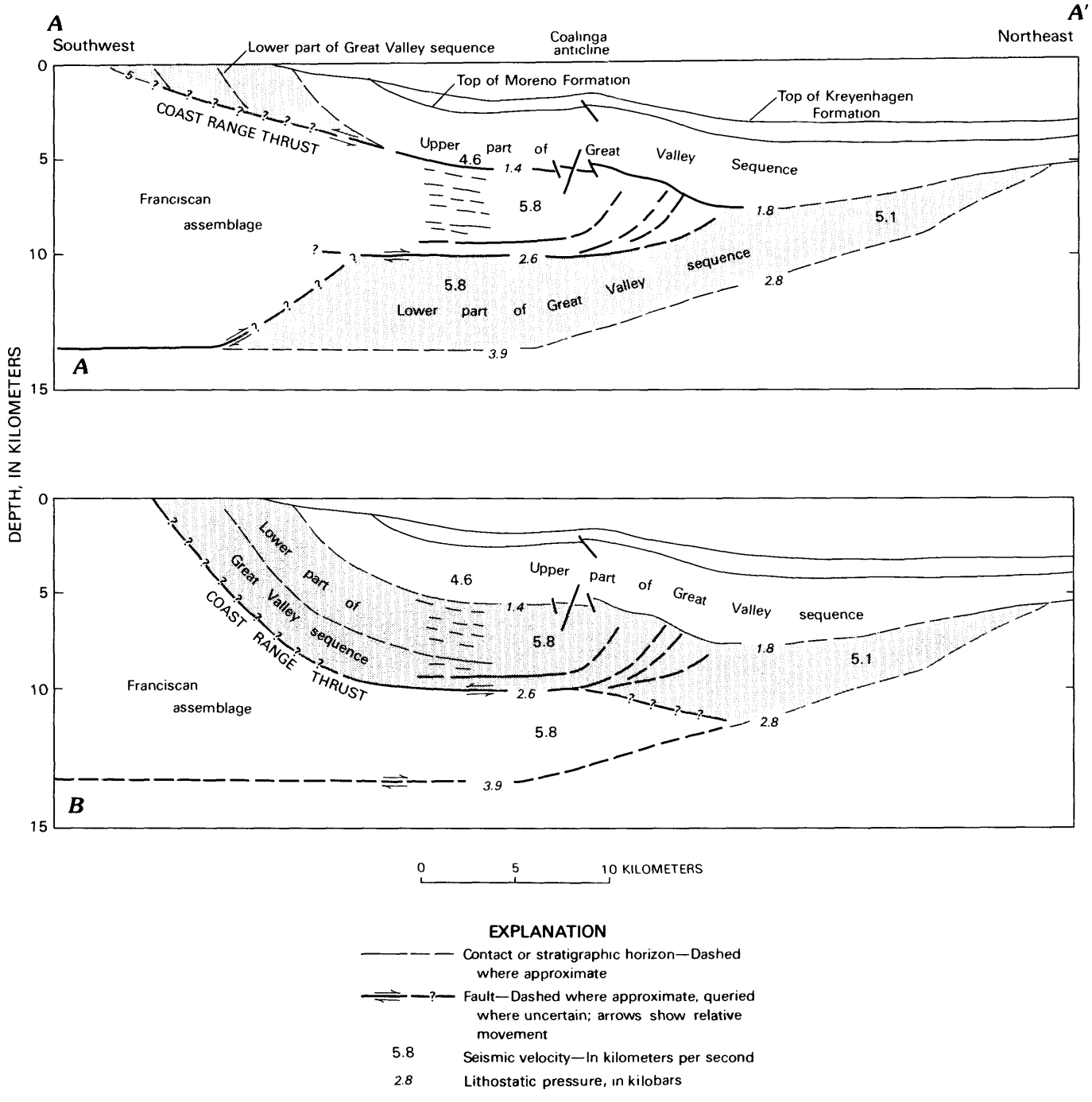

FIGURE 4.6.—Structural cross sections across Coalinga anticline along line *A–A'* (fig. 2), projected from profile SJ-19 (fig. 4.5*A*), showing alternative positions of the Franciscan wedge. All features are common to both alternatives except rock identities and bounding faults associated with the wedge. Upturning of reflections at west end of profile SJ-19 modified to accommodate breadth of syncline along section (see fig. 4.4). Surface of crystalline basement from figure 4.2. *A*, Shallow-wedge alternative, in which interval F is the Franciscan wedge that has ramped up into the Great Valley sequence and raised its upper part farther east. *B*, Deep-wedge alternative, in which interval F is Great Valley sequence and the Franciscan wedge intrudes along the basement surface and raises the entire Great Valley sequence.

TABLE 4.1.—*Recording and processing parameters for reflection profiles SJ–3 and SJ–19*

Recording parameters
Parameters for reflection profile SJ-3 shown in parentheses where different than those of profile SJ-19:
Group interval, 110 (220) ft, 24 geophones per group
Sample interval, 4 ms
Vibrator interval, 220 ft
Spread, 0-880-11,330 (5,940) ft
Pilot, 10-58 Hz, 20-s duration
5 (4) vibrators, 10 (12) sweeps
24-fold composite data
Processing parameters
Trace edit
Crosscorrelation
Deconvolution
Statics--datum is mean sea level
Velocity analysis
Normal moveout
Stack
Time-variant filter
Finite-diference migration

record are generally uniform along each stratigraphic interval and are probably accurate to within ±0.1 km/s. They are more erratic, however, between horizons T (top of the Temblor Formation) and P (top of the Panoche Formation), presumably owing to the high sensitivity of calculated interval velocities to small variations in stacking velocity. Here, we generalized the velocity structure from a running average of three adjacent values of interval velocity along each stratigraphic interval, and estimate the resultant uncertainty to be about ±0.3 km/s.

The Tulare Formation (interval C–J) thins westward against Coalinga anticline. Its uppermost part, the lateral equivalent of the Corcoran Clay Member (identified in well G by J.A. Bartow, oral commun., 1984), is folded, but to a lesser degree than its base, a difference that indicates progressive growth of the anticline during and through the end of Tulare time (approx 2–0.6 Ma). No similar thinning is evident lower in the section. At the west side of Pleasant Valley syncline, in contrast, there is evidence of westward thinning lower in the Cenozoic section and of angular discordance at its base. This difference indicates that uplift there began much earlier, near the beginning of the Cenozoic.

The base of the Cenozoic section is marked essentially by the unconformable contact between two deep-water shales, the lower Tertiary Lodo Formation over the largely Cretaceous Moreno Formation (see chap. 1). The simplest correlation of this contact westward across the reflection record from its position in well G (pl. 4.1B) carries it across the updip ends of several reflections, beneath well F, and onto reflection M, which extends westward discontinuously across the balance of the record.

The top of the underlying sandstone units of the Upper Cretaceous Panoche Formation (horizon P) is penetrated in well G, where it is marked by a strong, continuous reflection. This reflection can be traced westward to km 29, where it is lost in noise. The equivalent reflection beyond the noisy area continues from km 20 westward to km 1.5. The Moreno interval thus defined (M–P) thins both eastward and westward from a maximum east of Coalinga anticline.

The eastward thinning is at least partly due to onlap of the Moreno onto the gentle Panoche high that overlies the basement high between faults I and II. The westward thinning, however, culminates in an unconformity at the west end of the record. There, clear angular relations occur beneath a reflection that seems best correlated eastward with horizon M in Coalinga anticline. At the surface, the Moreno is cut out southward from refraction shotpoint 14 beneath converging lower Cenozoic unconformities (fig. 4.3; see chap. 1). There is an unresolved mismatch of about 75 m (0.6 wavelength) between this identification of horizon M and its position in well A. The interval velocity required to achieve a match (2.0 km/s below horizon K) seems too low in comparison with the reflection interval velocity of 2.4 km/s and the even higher velocities indicated by the sonic log of a nearby well (Superior West Coalinga Fee 31, sec. 31, T. 20 S., R. 15 E.).

The shallow stratigraphy in profile SJ–3 (pl. 4.1D) is essentially the same as that in profile SJ–19. The sequence of reflections down to horizon P is very similar in the two records, and identification of horizons at the east end of profile SJ–3 is based on correlation of reflections with profile SJ–19. No deep wells lie close to the SJ–3 profile line, but interpolation between two wells that straddle this line at the crest of Coalinga anticline (wells H and I, fig. 4.3; table 4.2) allows approximate identification of the labeled horizons at 5.5 km on plate 4.1D.

LOW-VELOCITY ZONES

The reflection interval velocities on profile SJ–19 (pl. 4.1B) define three low-velocity zones above horizon P that are probably the result of high fluid pressure (see chap. 23). Opposed lateral gradients in velocity in the intervals between horizons t and G (largely Kreyenhagen Formation) and G and P (largely Moreno Formation) in the eastern part of profile SJ–19 produce a stepped pair of low-velocity zones. Although associated high fluid pressure was not found by Yerkes and others in well G, which penetrates interval t–G near the reflection profile, they did recognize it in a well about 10 km to the northwest along strike (North Central Boston Ranch 1,

TABLE 4.2.—*Well control*

[Wells A through G lie along reflection line SJ-19, wells H and I straddle reflection line SJ-3 at the crest of Coalinga anticline, and wells J and K lie on the crest of the Joaquin Ridge anticline (see fig. 4.3 for locations). Wells L through O reach crystalline basement off the east end of reflection line SJ-19. Wells also used by Bartow in chapter 1 are indicated in parentheses by cross section (A or B) and well number]

Well	Name	Year	Location			Total depth (ft)	Elevation (ft)	Thickness of Cretaceous strata (m)
			Sec.	T. S.	R. E.			
A	Standard 302 (A2)----------	1955	19	20	15	4,302	776	---
B	Rheem Standard 28----------	1954	15	20	15	7,753	743	---
C	Zwang 2-14----------	1954	14	20	15	8,110	693	---
D	Union (R.S. Lyttle) USL 68 (B4)--	1940	18	20	16	8,051	749	---
E	Union Helm, Sumpf and Sumpf, Pleasant Valley 8-14.	1955	14	20	16	9,578	513	---
F	Standard Haven Boston 313 (A9)---	1959	23	20	18	14,322	289	---
G	Mobil BLC 48-7 (A 10)----------	1951	7	20	19	14,911	269	---
H	Fresno Exploration-Phelps Government 2.	1947	20	19	15	4,582	1,594	---
I	Standard 213----------	1947	35	19	15	5,775	930	---
J	Arco Bravo 1----------	1969	7	19	14	6,502	2,100	---
K	Arco Joaquin Ridge 1----------	1975	39	19	14	14,409	3,786	---
N	Amerada Lawton 58----------	1942	26	17	19	11,990	228	1,111
M	Sunray A.J. Borba 1----------	1962	6	18	20	11,724	222	922
N	Exxon Capital Co. G-1----------	1961	7	19	21	12,816	231	1,069
O	Occidental Hansen 1----------	1966	14	22	22	14,680	191	945

sec. 21, T. 19 S., R. 18 E.; top of high-pressure zone at 11,485 ft, top of Kreyenhagen at 11,500 ft).

Low velocities also occur in interval G–P near its intersection with the east-dipping reverse fault (fault IV) in the core of Coalinga anticline. Here, the interval velocities have not been smoothed as severely for presentation on plate 4.1B as elsewhere because of their regular decrease inward toward the fault from each side. The coincident local increase in transit time across interval G–P (0.26, 0.4, and 0.35 s at km 8, 11.8, and 13 km, respectively) may be caused by this velocity anomaly, although westward thinning of the Gatchell sand (of local usage, top at horizon G) is also involved (Harding, 1976). Yerkes and others (chap. 23) did not detect high fluid pressures associated with this low-velocity zone in such wells as C and D (pl. 4.1B), which bottom within interval G–P.

DEEP UNITS

Identification of the rocks below the top of the Panoche Formation (horizon P) depends largely on extrapolation from the geologic relations known east and west of profile SJ–19 and on inference from the velocity structure along the cross and axial refraction profiles determined by Walter (chap. 3, figs. 3.2*A*, 3.3*A*; see fig. 4.2 for profile locations).

EASTERN BASEMENT AND UPPER PART OF THE GREAT VALLEY SEQUENCE

About 20 km northeast of the east end of profile SJ–19, several wells penetrate 0.9 to 1.1 km of Upper Cretaceous strata and the underlying crystalline basement (wells L–O, fig. 4.2; table 4.2). Walter's interpretation of the cross refraction profile (see chap. 3), which is fitted to this westernmost basement well control near shotpoint 9, yields basement rock with a velocity of about 6.3 km/s and a basement surface that dips gently west from shotpoint 9 for about 25 km and then abruptly steepens. Near the east end of profile SJ–19, this refraction boundary lies at a depth of 5.6 km. Because the strong reflection at 3.7 to 3.9 s in the reflection record (B, pl. 4.1B) coincides in time with this basement depth, this reflection must represent the basement surface.

The less continuous subhorizontal events below this basement reflection have stacking velocities that yield an interval velocity of 4.5 km/s, characteristic of the Great Valley sequence, and thus are probably multiples. Similar layered events and interval velocities occur at the east end of COCORP line 1. Fielding and others (1983, 1984) placed the basement surface below those events at about 5 s (8.5 km).

East of km 44.5, apparent downfaulting of the basement reflection (B) by about 200 m to the strong reflection at 3.8 s (B?, pl. 4.1B) leads to our inference of fault I. Similar relations are evident at the east end of COCORP line 1 (Fielding and others, 1984). The inferred fault is presumably steep, either normal or reverse, and, if correlative between the two reflection lines, strikes slightly west of north. On plate 4.1A, reflection B breaks up as it approaches fault I from the west. A stacking velocity only 3 percent higher, however, yields a nearly continuous reflection across the inferred fault, a result suggesting that principal fault offset ceased during the Late Cretaceous, prior to deposition of the overlying Cretaceous strata.

Stratigraphy encountered in well G, together with the basement surface identified beneath the well, defines a Cretaceous section (interval M–B, Moreno and Panoche

Formations, 1.6 km thick at 4.5 km/s) that represents a slight westward thickening from the Cretaceous section drilled farther east. This upper interval of Great Valley sequence (GVSa, pl.4.1B) thickens more rapidly westward from well G above an extension of horizon B that is drawn below the well-layered reflections. It reaches a thickness of 3.1 km at km 27, where it becomes obscured by noise in the record.

The same interval reappears west of the area of noise (km 20 and beyond), where it is also about 3 km thick. It projects updip beyond the end of the record section to the west into surface exposures of the upper part of the Great Valley sequence (figs. 4.3, 4.6). In contrast to interval GVSa farther east, the base of GVSa beneath Coalinga anticline is defined in the reflection record by a series of two or three strong reflections (horizon X). The approximate concordance of this lower horizon with overlying structure is achieved partly by folding and partly by faulting.

Interval velocities within GVSa east of km 30 vary somewhat but range predominantly from 4.3 to 4.6 km/s and are here generalized as 4.5 km/s. This velocity is consistent with that determined for Great Valley sequence at similar depth elsewhere (table 4.3). West of km 20, interval velocities within GVSa are poorly constrained by the data and range from about 3.6 to 5.4 km/s. Refraction velocities range from 4.6 to at least 4.9 km/s and include a velocity inversion. For our present purposes, we generalize the velocity of this part of interval GVSa as a uniform 4.6 km/s.

The upper section of Great Valley sequence (interval GVSa) thus defined extends eastward from outcrop in the Coast Ranges, through Coalinga anticline, and on beneath the San Joaquin Valley, where it thins onto identifiable crystalline basement (km 40). Layering within this interval is concordant with that in the overlying Cenozoic section.

LOWER PART OF THE GREAT VALLEY SEQUENCE

West of the prominent basement reflection (horizon B) at the east end of the profile between km 29 and 39, interval GVSa is underlain by a zone of short, variably west dipping reflections (pl. 4.1B). These reflections coincide with a westward-thickening prism of 5.1-km/s material that is evident on the cross refraction profile of Walter (chap. 3). Because this zone appears to be layered, occurs beneath the upper part of the Great Valley sequence, and has a refraction velocity appropriate for Great Valley sequence (table 4.3), we infer it to be a lower interval of Great Valley sequence (GVSb). A similar zone of crude, west-dipping events in about the equivalent position on the COCORP reflection line is also interpreted to represent sedimentary strata (Fielding and others, 1984). Horizon BB represents an approximate envelope at the base of the zone on profile SJ–19. The termination of interval GVSb on the east is unclear in the seismic record. To avoid carrying this interval eastward beneath the basement reflection (horizon B east of km 40), where the cross refraction model places higher velocity rock, we terminate the interval somewhat arbitrarily at a pair of dip-slip faults (II and III) where the reflections are no longer apparent.

We thus identify an older interval of Great Valley sequence (GVSb), at least 2.5 km thick at km 30, which is bounded on the east by presumably steep faults that are truncated by the base of interval GVSa. Horizon B west of km 39 could thus be an unconformity within the Great Valley sequence. West of km 29 in the seismic section, the evidence for interval GVSb is lost in noise. Basement beneath the interval may lie at or below horizon BB. The cross refraction profile indicates that basement deepens westward, possibly across a series of dip-slip faults.

INTERVALS F AND D

The interval between the base of interval GVSa and crystalline basement thickens westward to about 10 km beneath Coalinga anticline (fig. 4.6). There, in contrast to interval GVSb farther east, the interval is characterized by seismic velocities of 5.6 to 6.1 km/s. These velocities are distinctly higher than in interval GVSa above or in interval GVSb to the east and considerably exceed those known in Great Valley sequence elsewhere (table 4.3).

A natural division of this 10-km-thick interval into two parts, interval F above and interval D below, is provided by the central T reflections and a coincident 6.1-km/s layer in the axial refraction profile (see chap. 3). These T reflections are strong and form a discordant base to overlying layered reflections. No distinct reflections are observed below the T reflections.

The interval velocity across interval F (between horizons X and T), picked from constant-velocity panels, is 5.8 km/s. The cross and axial refraction profiles similarly indicate velocities that range from 5.6 to 6.1 km/s, not only throughout most of interval F but throughout the underlying interval D as well (fig. 4.6, pl. 4.1B; see chap. 3, figs. 3.2*A*, 3.3*A*).

We assign the top of the upper, 5.8-km/s interval to reflection horizon X, despite a discrepancy of about 1 km in depth between that horizon and the top of 5.7-km/s rock in the axial refraction profile (pl. 4.1B). The X reflections are particularly strong, and, more importantly, this correlation places structural discordance in both the reflection and refraction profiles at the same horizon, as described below. This discrepancy in depth is similar to the half-kilometer discrepancy in the depth of the same top of 5.7-km/s rock at the crossing of the two refraction profiles (see chap. 3, fig. 3.5).

TABLE 4.3.—*Compressional seismic velocities*

Source	Method	Location	Velocity (km/s)	Depth (km)
		Great Valley sequence		
Walter and Mooney (1982).	Refraction----	Central Diablo Range.	3.5-4.8	0.5-3.5
Mooney and Walter (1981).	do----------	Central Coast Ranges.	3.8	0-4
Zoback and Wentworth (1985).	Reflection----	Central Diablo Range and Great Valley.	2.9-4.6	0-5
Blumling and others (1985).	Refraction----	Southern Calaveras fault zone.	3.1-4.7	0-5
Wentworth and others (1983).	Reflection----	Southeastern Kettleman Hills.	3.9-5.1	0-10
Bailey and others (1964).	Inferred from rock density[1]	Coast Ranges:		0
		Upper Cretaceous strata.	4.6	---
		Lower Cretaceous strata.	4.8	---
		Upper Jurassic strata.	4.9	---
		Franciscan assemblage		
Denlinger and Kovach (1981).	Reflection----	Castle Rock Springs, Geysers geothermal area.	2.4-5.0	0-1
Warren (1981)	Refraction----	Mendocino-Geysers area.	5.0-5.2	1.5
Mooney and Walter (1981).	do----------	Central Coast Ranges.	4.8-5.2	0-4
Blumling and Prodehl (1983).	do----------	Central Diablo Range.	3.6-5.75	0-12
Stewart and Peselnick (1978).	Laboratory----	Central and northern California.	5.2-6.5	[1]-122
Zoback and Wentworth (1985).	Reflection----	Central Diablo Range.	5.2-5.8	0-14
Walter and Mooney (1982).	Refraction----	do----------	4.8-5.9	1-15
Wentworth and others (1983).	do----------	Southeastern Kettleman Hills.	5.6-5.9	3-15
Blumling and others (1985).	do----------	Southern Calaveras fault zone.	5.7-6.3	4-13.5
		Serpentinite		
Christensen (1982).	Laboratory----	Coast Ranges---------	[3]0.5-5.7	2-15
Do----------	do----------	do----------	[4].9-7.4	2-15

[1]Velocities calculated from median densities reported for each stratigraphic interval, using relation of Gardiner and others (1974). Densities are bulk densities of surface samples of sandstone soaked briefly in water (Irwin, oral commun., 1986).
[2]Inclusion of temperature increase with depth yields little change in velocity with increasing pressure for individual samples.
[3]Five serpentinite samples: velocity of individual samples varies by 0.1 to 5 km/s with depth.
[4]Eleven samples of serpentinized peridotite: velocity of individual samples varies by 0.1 to 0.3 km/s with depth.

The upper and western parts of interval F contain layered reflections that are largely concordant with those of interval GVSa above. Except for the high seismic velocity (5.8 km/s), this 5-km-thick interval could be viewed simply as a continuation of the lower part of the Great Valley sequence, equivalent to interval GVSb east of Coalinga anticline (fig. 4.6*B*). The resulting 7-km-thick layered section beneath horizon M (3.1 s at 4.6 km/s) would correlate nicely with the 8-km-thick section of Great Valley sequence that dips toward the reflection profile from exposures farther west (figs. 4.3, 4.6*B*).

We thus define two intervals below the upper interval of Great Valley sequence (GVSa) along the western part of SJ–19: an upper interval (F), 5 km thick, that contains layered reflections concordant with interval GVSa above and has a seismic velocity of about 5.8 km/s; and a lower interval (D), also about 5 km thick, that has a seismic velocity of about 5.9 km/s. The identity of these intervals is uncertain because of conflicting evidence and is discussed further below.

DEEP UNITS IN PROFILE SJ–3

Reflection profile SJ–3 (pls. 4.1C, 4.1D) is much less informative below horizon P than is profile SJ–19, although both similarities and differences with profile SJ–19 are evident. No conspicuous basement reflection is present at the east end of the record. As in profile SJ–19, however, a boundary (horizon B) can be drawn between the regularly layered reflections of interval GVSa above and the cruder reflections of interval GVSb below, which defines a GVSa interval that is about 2.6 km thick at the east end of the record.

Comparison of profile SJ–3 with the velocity structure of the axial refraction profile where the two profiles cross (pl. 4.1D) suggests that the top of interval F in profile SJ–19 (horizon X) best corresponds with horizon E. This correlation defines an overlying interval of Great Valley sequence (interval M–E) that is about 6.5 km thick (3.85 s at 4.6 km/s), or twice the thickness of the Great Valley sequence above horizon X on profile SJ–19. Within interval M–E, horizon D may be equivalent to horizon B farther east and thus define an interval of GVSa that is 4 km thick. The northwestward rise of velocity intervals in the axial refraction model represents a northwestward rise in the top of the Great Valley sequence above a flat to probably depressed top of the 5.8-km/s layer below (see chap. 3, fig. 3.3*B*).

Structural discordance below horizon E, marked by eastward convergence of reflections between km 7.5 and 9, is consistent with horizon E being a structural boundary at the top of the 5.8-km/s layer. A clear set of reflections similar to the T events in profile SJ–19 is absent in SJ–3, although the few aligned events at about 4.6 s (horizon F) may represent them. If so, the equivalent of interval F here is only about 2 km thick, as is the equivalent 5.8-km/s layer in the axial refraction line.

FOLDS AND FAULTS

The gross uplift of the Cenozoic strata and upper Great Valley sequence west of the San Joaquin Valley, and their folding in Coalinga anticline, are well defined in the reflection records. Offsets and terminations of reflections also define several small faults, all but one restricted to the pre-Cenozoic rocks, which have dip separations of tens to hundreds of meters. The major faults, in contrast, are indicated principally by structural anatomy and, within interval F, by their relation to folding. In the western part of the record, the relation we infer between the faults and the overlying Coalinga anticline denies a

large strike-slip component to the faulting. East of the anticline there is no such constraint, but the faults there predate the upper part of the Great Valley sequence. Because the reflection lines cross structure obliquely, structural relations are somewhat distorted in the records.

Coalinga anticline rises westward out of the San Joaquin Valley trough in two distinct steps, or tiers, that are separated by a flattening near the center of the eastern limb of the anticline (conspicuous on profile SJ–3 at km 12–13 and subtle on profile SJ–19 at km 15–16). The lower tier rises 1.7 km to a depth of 2.25 km at horizon K on both profiles (fig. 4.4), whereas the upper tier has a greater amplitude on the northern profile.

The core of the anticline in profile SJ–19 is broken by an east-dipping reverse fault (fault IV) that, at this latitude, has about 30 m of offset at horizon M (pl. 4.1B). The fault can be carried downdip from the offset in horizon M along a series of reflection terminations well into interval GVSa, where net offset is similar to that above. Although the detailed shape of fault IV is uncertain, the fault must steepen downdip unless velocities at least as low as 3 km/s apply to the whole prism of GVSa above the fault.

Throw on the reverse fault decreases upward from horizon M and seems to be converted into folding to produce the abrupt kink at the base of the western limb of Coalinga anticline. This relation is complicated, however, by the sharp westward thinning of interval G–M by 0.06 s at about the same position, due in part to lateral change in velocity and in part to thinning of the Gatchell sand (Harding, 1976, fig. 10). This westward thinning of interval G–M accounts for half of the 0.12 s of structural relief on horizon T above.

Although there is no direct evidence for a similar fault beneath Coalinga anticline on profile SJ–3, the absence of reflections west of km 6 permits one. If present there, such a fault probably ends downdip within interval M–D, for horizon D shows no east-side-up reverse movement.

The horizons bounding interval F above and below are marked by structural discordance from which we infer faults subparallel to layering. East of about km 16, the otherwise-concordant layered reflections in intervals GVSa and F become discordant across horizon X. The east-dipping interval GVSa cuts obliquely downward across subhorizontal layering in F and then flattens farther east. Structural discordance beneath the upper part of the Great Valley sequence is also suggested by relations in the axial refraction profile (see chap. 3), where a low-velocity zone (4.9–5.1 km/s) bounded by 5.1-km/s layers butts downward against the top of the 5.8-km/s interval. We have assigned these two discordant features and the top of the 5.8-km/s interval to a common horizon, X. At the base of interval F, the Z reflections, which are concordant with those above, butt obliquely downward to the east against the flatter T zone (pl. 4.1B).

Horizon X at the top of interval F participates in the folding of Coalinga anticline, whereas the T reflections at the base of that interval do not. This difference requires deformation within interval F that is associated with the base of the fold. Reflections L and N diverge upward to the east from the T reflections. Smoothly curved projections beyond their ends lead upward to aligned terminations of reflections that mark faulting or abrupt folding in the upper part of the interval. East-facing fold steps in horizon X and associated reflections overlie the updip parts of each of these projections.

We interpret these relations together to indicate eastward-directed thrusting along the T zone that splays upward into reverse faults (faults IX, X, pl. 4.1B). These splay faults dip 40°–50° W. in the plane of the section (fig. 4.5). This reverse faulting, in turn, gives way upward to folding that coincides with the two tiers of Coalinga anticline above. Reflection terminations imply at least two more reverse faults forward of fault X (faults XI and XII). Structure is not well imaged in the eastern tip of interval F here, probably because structure is complex, and even the identity of horizon X becomes uncertain. If the location of horizon X shown on plate 4.1B east of fault X is correct, that fault has about 700 m of vertical separation, although interval GVSa above shows no such faulting.

The T zone has thus undergone northeastward-directed thrusting that was absorbed updip within interval F by reverse faulting and the folding that created Coalinga anticline. We name these faults the "Coalinga thrust zone" for their spatial and causal relation to Coalinga anticline. Several kilometers of offset along the Coalinga thrust zone is required to accomplish the updip folding. This estimate is obtained by summing the horizontal movements required to generate the monoclinal uplifts above each fault incline.

Several minor reverse faults are evident beneath fault IV within interval F and the overlying Great Valley sequence. The most conspicuous of these, the west-dipping fault VI, offsets horizon X only 100 to 150 m, yet it extends updip and downdip along a series of reflection terminations for a vertical distance of 4.5 km. The other minor faults (V, VII, and VIII), which are also drawn as reverse faults to conform to the structural style established by faults IV, VI, and the Coalinga thrusts, seem to have more limited vertical extents.

The deep reflections on profile SJ–3 (pls. 4.1C, 4.1D) are too sparse to provide much control on faulting. Beneath Coalinga anticline, the two correlated segments of horizon D may be connected across the intervening gap by a steeper fold limb, in a fashion similar to the

monoclinal steps in horizon X on profile SJ–19, although some faulting may be involved as well.

At horizon E, if correlation of the two offset segments is correct, a fault is required. The reflection terminations imply a steep westward dip of about 50°–55°. Because the relation of this fault to the overlying folding is the same as that of fault IX on profile SJ–19, we conclude that it is the same fault. Both these faults presumably root westward in the 6.1-km/s refraction layer in a fashion similar to the thrusts on profile SJ–19.

FRANCISCAN WEDGE AND LOWER PART OF THE GREAT VALLEY SEQUENCE

The identity of the rock composing the interval between the upper part of the Great Valley sequence and crystalline basement along profile SJ–19 is uncertain. East of Coalinga anticline, seismic velocity and apparent layering, together with position beneath interval GVSa, lead us to conclude that there the interval represents a lower part of the Great Valley sequence that we call GVSb. Farther west, however, the higher seismic velocities of intervals F and D pose an obstacle to simple continuation of interval GVSb westward beneath Coalinga anticline, despite the concordant layered reflections of interval F and the compatibility of such a continuation with the 8-km thick section of Great Valley sequence exposed west of the reflection profile.

These high velocities are characteristic of Franciscan rock (table 4.3) and raise the possibility that the whole 10-km interval consists of Franciscan rock, emplaced as a tectonic wedge that has been thrust eastward between crystalline basement and overlying Great Valley sequence (interval GVSa). The only other exposed rock in the region that can have such velocities is Coast Range ophiolite (table 4.3). Although little ophiolite is exposed in the region (Jennings, 1977), it is known to underlie Great Valley sequence locally and could be more extensive in the subsurface. Any significant thickness of ophiolite seems excluded, however, by the absence of a high in the magnetic field, which is typical of such rocks in central California (see chap. 5).

The whole 10-km interval cannot be Franciscan, however, because a wedge that thick should have raised the overlying interval GVSa considerably more than the existing 2.5-km difference in the altitude of interval GVSa west and east of Coalinga anticline. Such a thick wedge would also deny westward continuation of the lower interval of Great Valley sequence (GVSb), and yet there is no satisfactory way to account for such a westward termination of interval GVSb beneath the east flank of the anticline. Neither an unconformity nor an east-facing basement fault are reasonable, and there is no room for interval GVSb to have been driven eastward in front of an advancing Franciscan wedge.

It is equally unreasonable, even disregarding seismic velocity, that the whole 10-km-thick interval between GVSa and crystalline basement is Great Valley sequence. The presence of such an undisturbed sedimentary sequence would require awkward changes in the thickness of interval GVSb, from about 4.5 km east of Coalinga anticline, through 10 km beneath the anticline, to about 5 km farther west (to match the 8-km-thick section exposed to the west). Thrust repetition of interval GVSb might account for local thickening of the Great Valley sequence beneath the anticline, but this thickening is inconsistent with the structure or the 8-km-thick surface section to the west.

In the face of conflicting evidence, then, we consider the remaining alternative, that the 10-km-thick interval between GVSa and crystalline basement is partly Great Valley sequence and partly Franciscan rock. Reflection zone T and the coincident 6.1-km/s layer divide this interval into two 5-km-thick intervals (F and D), and we conclude that either interval F or D is Franciscan and the other, despite its high velocity, must be Great Valley sequence. This leads to the two alternative interpretations portrayed in figure 4.6—a shallow Franciscan wedge that has overridden part of the Great Valley sequence (fig. 4.6*A*) or a deep Franciscan wedge that has lifted the whole 8-km-thick section of Great Valley sequence (fig. 4.6*B*).

The concordance of layered reflections from within interval GVSa down through interval F makes simple downward continuation of the layered sedimentary sequence (fig. 4.6*B*) attractive. Such regular, concordant layering seems less likely in an independent mass of Franciscan rock that has been structurally juxtaposed beneath Great Valley sequence (fig. 4.6*A*). Much of the Franciscan actually is quite regularly layered, however, despite the common view that it is a vast melange. In particular, the Yolla Bolly and Burnt Hills terranes (Blake and others, 1984), which form much of the exposed Franciscan in the Diablo antiform 75 km to the northwest (fig. 4.1), retain the gross well-bedded aspect of their protolith sandstone and shale sequences. Thus, although regular, concordant layering would be expected of an interval F composed of Great Valley sequence, it could exist in Franciscan rock as well.

These layered reflections within interval F define structural discordance at the east tip of the interval that resembles a thrust ramp, formed as interval GVSa was thrust westward over its lateral equivalent, interval F. This discordance, and that present elsewhere at the top of 5.8-km/s rock, probably represents thrusting, but not between a repeated GVSa section. The seismic velocities deny correlation of the two adjacent units, and such gross repetition of section is unknown in the exposed Great Valley sequence. Available fossil control in the Juniper

Ridge-Joaquin Ridge area west and northwest of the reflection profile also makes such repetition there unlikely (J.A. Bartow, written commun., 1985).

The bounding of interval F above and below by faults is consistent with the thrust boundaries required for a shallowly emplaced Franciscan wedge, as is a thrust ramp at the east tip of the wedge. Thrusting along the top of the interval and, especially, the degree of discordance indicated in the axial refraction line make that shallow-wedge interpretation particularly attractive. The steep secondary faults that offset horizon X require this X-horizon thrusting to predate Coalinga thrusting, a timing inherent in the shallow-wedge interpretation. With a deep wedge, it may be that, once the wedge was emplaced, eastward thrusting shifted upward to move the lower part of the Great Valley sequence (interval F) forward far enough to create the bounding faults, although creation of the upper thrust and its relative timing remain problems. In this case, the thrust ramp must be only apparent, the result of folding and thrusting within the tip of the thrust mass.

Seismic velocity in Great Valley sequence ranges as high as 4.6 to 5.1 km/s elsewhere in the region (table 4.3) and reaches 5.2 km/s at the base of interval GVSb east of Coalinga anticline (see chap. 3). Sandstone densities determined throughout the Great Valley sequence farther north in the Coast Ranges reach a mean of 2.59 g/cm^3 in the lowest, Upper Jurassic part (Bailey and others, 1964, fig. 27). This density represents a bulk seismic velocity of about 4.9 km/s (table 4.3). Such a velocity implies a rock porosity of about 4.5 to 10 percent, according to the velocity-porosity relations for silicic clastic rocks summarized by Dobrin (1976, fig. 2–23). For these same rocks to have a velocity of 5.8 km/s, porosity must be reduced to about 0.5 percent. Cementation to cause this reduction in porosity seems unlikely, given the general absence of pore-filling cement in exposed Great Valley sequence and the lower velocity of interval GVSb east of the anticline. Compaction under increased lithostatic pressure is a more likely cause, especially if some recrystallization is involved. Such compaction cannot account for the high velocity of interval F because both it and interval GVSb to the east are under similar lithostatic pressures (fig. 4.6); but it could affect interval D. The pressure in interval D is not strikingly higher than in interval F, however, especially in its upper part; and it seems doubtful that simple load compaction of interval GVSb there, relative to GVSb to the east, is a sufficient source of the difference in velocities.

The two alternative levels of emplacement of the Franciscan wedge have markedly different implications for structure west of profile SJ–19 (fig. 4.6). With a deep wedge, the overlying Great Valley sequence is continuous from the exposed surface section eastward through Coalinga anticline. The shallow wedge, in contrast, requires the full surface section to have been obliquely truncated and raised above a thrust ramp in the lower part of the Great Valley sequence. That ramp lifted the tip of the intruding Franciscan wedge up into the center of the Great Valley sequence, trapping interval GVSb below. Such a geometry is quite plausible, as illustrated in figure 4.7. It can account for the abrupt upfolding of Great Valley sequence west of profile SJ–19, and it provides a reasonable explanation for the presence in the gravity model (see chap. 5) of higher density rock underlying exposed Great Valley sequence at shallow depth, despite the contrary implications of surface structure.

From the data now available, we cannot confidently select one of the two alternative interpretations illustrated in figure 4.6. In either case, it is difficult to explain the high velocities associated with interval GVSb beneath Coalinga anticline, although this dilemma is more serious in the deep-wedge interpretation, where the GVSb interval is at shallower depth. The deep-wedge interpretation does provide a more satisfactory explanation of the concordant layered reflections in interval F. Structural relations are simpler in the deep-wedge interpretation, but structural history is more straightforward in the shallow-wedge interpretation. Elements of the gravity model are satisfied by the truncation of the Great Valley sequence inherent in the shallow-wedge interpretation.

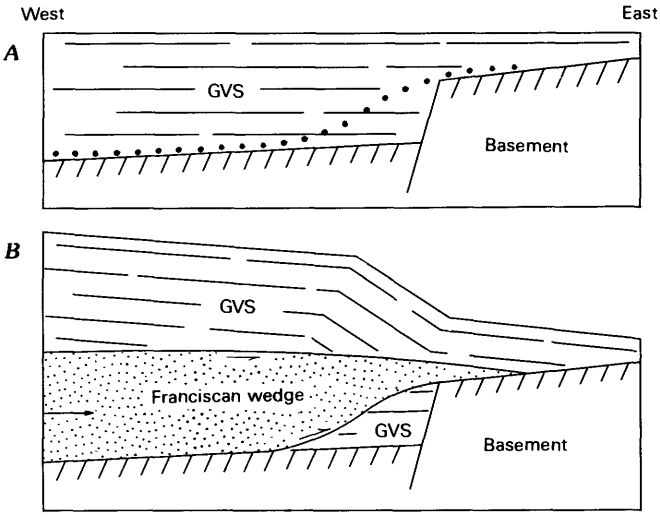

FIGURE 4.7.—Schematic cross section showing buckle in uplifted Great Valley sequence (GVS) caused by eastward shallowing of tectonic wedge of Franciscan rock above a thrust ramp. *A*, Westward-thickening Great Valley sequence before emplacement of wedge along dotted line. *B*, Great Valley sequence uplifted above Franciscan wedge and folded above thrust ramp. Half-arrows, direction of relative movement; full arrow, general direction of wedge emplacement.

TECTONIC HISTORY

The Coalinga main shock occurred at the major structural boundary in central California where folds and thrusts of the uplifted Coast Ranges abut the depressed, gently west dipping basement and overlying sedimentary rocks of the Sierran block. Coincident with this prominent structural demarcation are three underlying features: (1) a marked southwestward deepening of crystalline basement that extends beneath the boundary, (2) an abrupt southwestward thickening of the overlying Great Valley sequence, and (3) the buried east edge of the Franciscan terrane, which composes much of the Coast Ranges. These features are interrelated and represent a predominant and persistent tectonic boundary about 600 km long near the western margin of North America.

The Mesozoic sedimentary basin in which the Great Valley sequence was deposited must have deepened southwestward to provide room for the thick Coast Range section to accumulate. The refraction and reflection profiles at Coalinga support such southwestward deepening, probably across dip-slip faults that were active during deposition of all but the uppermost part of the sequence, which overlaps the inferred faults I and II at the east end of profile SJ–19. The result was an Upper Jurassic and Cretaceous sedimentary section that thinned and onlapped eastward from an 8-km-thick section on the southwest to a 1.5-km-thick section some 25 km farther northeast.

Structural relations at Coalinga, and to the northwest and southeast at reflection profiles CC–1 and SJ–6 (fig. 4.1), indicate that, after initial accretion at the continental margin, the late Mesozoic Franciscan assemblage was thrust northeastward onto that margin and beneath the coeval Great Valley sequence (Wentworth and others, 1984a; Zoback and Wentworth, 1986). The earlier view that the east margin of the Franciscan assemblage marks an east-dipping crustal suture is made untenable by these relations. Once this landward-directed thrusting was established, it seems to have persisted, at least sporadically, through later changes in tectonic regime. Although its timing is not well constrained, the thrusting probably began by the end of Cretaceous time, when strong convergence was underway at the continental margin (Page and Engebretsen, 1984). It has probably continued intermittently throughout the Cenozoic, including important movement during the San Andreas regime.

Uplift in the Coast Ranges must have occurred during initial emplacement of the Franciscan wedge onto the continental margin, possibly leading to unroofing of the Franciscan and shedding of Franciscan detritus into the local sedimentary basin in Eocene time (see chap. 1). Later uplift accompanied folding and faulting that, at least at the eastern margin of the Coast Ranges, we infer to have been underlain by northeastward-directed thrusting. Northeastward termination of that deformation near the shallowing of basement led to the sharp upturning of Great Valley sequence and younger strata at the valley margin. The Pleasant Valley cross-structure represents a subsurface tear in those underlying thrusts across which folding was independent and the main Coast Range uplift stepped to the right about 20 km.

The uplift must have been underway by earliest Cenozoic time to create the unconformities in the lower Tertiary section around the northwest end of Pleasant Valley. Joaquin Ridge anticline and associated folds were probably established then above underlying thrusts, and by Miocene time the New Idria serpentinite core of Joaquin Ridge anticline (fig. 4.3) was exposed and shedding subaerial debris flows (Big Blue Formation of Casey and Dickenson, 1976). The strikes of these folds and of the Pleasant Valley cross-structure suggest that a principal direction of thrusting was north-northeastward.

The growth of Coalinga anticline must have occurred in two related stages. Initial eastward movement of the Franciscan wedge raised the overlying strata to form the beginning of the lower tier of the fold. Continued thrusting developed the Coalinga thrusts, then backed up into interval F, thickening its tip beneath the growing lower fold tier and breaking upward to raise the upper tier of the fold.

The principal thrusting at Coalinga anticline began in Pliocene time, as indicated particularly by the thinning of the Tulare Formation westward against the fold. This thrusting, which occurred well after establishment of the San Andreas fault system, may have resulted from compression across the San Andreas system caused by a shift in relative motion between the Pacific and North American plates that occurred about 5 Ma (Cox and Engebretsen, 1985).

A thrust origin for Coalinga anticline suggests that the whole Coalinga-Kettleman Hills-Lost Hills anticlinal trend has been created by northeastward-directed thrusting. The thin, 6.0-km/s layer in the axial refraction model, with which the Coalinga thrusts are associated, extends along the length of the syncline west of the anticlinal trend at a depth of 10 to 11 km. If this association is causal, then thrusts are implied along the whole length of the syncline and associated fold trend. Details of these inferred thrusts probably vary along the length of the fold trend because the depth of the syncline changes and the steep limb of the anticline shifts from the west side on Kettleman North and Middle Domes to the east side on Kettleman South Dome and the Lost Hills anticline (Zigler and others, 1986 and 1987). The right steps between individual anticlines in the trend should

represent crossfault tears in the thrusts. Wentworth and others (1983a) proposed that Kettleman South Dome grew during Pliocene and Quaternary time above the blind tip of a west-dipping thrust. If that thrust lies at a depth of 10 km beneath the syncline, however, some details of that interpretation must be changed.

This recent thrusting may also extend northwestward from Coalinga anticline. The lower tier of folding on reflection line SJ–3 is part of the nose of the Joaquin Ridge anticline, a relation implying that lower-tier thrusting extends northwestward at least that far. The Quaternary folding and faulting along the range front farther northwest may also result from continuing movement on underlying thrusts.

SOURCE OF THE COALINGA EARTHQUAKE SEQUENCE

The 1983 Coalinga earthquake sequence occurred at depths of 2 to 14 km beneath Coalinga anticline and the adjacent south flank of Joaquin Ridge anticline, and involved subhorizontal compression largely perpendicular to the axis of Coalinga anticline (fig. 4.8; see chap. 8). The main shock occurred at a depth of about 10 km, which coincides with the Coalinga thrust zone (fig. 4.9). Its focal-mechanism solution yields a subhorizontal pressure axis that trends northeast and focal planes that strike N. 53° W., essentially parallel to the N. 43° W. strike of Coalinga anticline. The planes dip 23° SW. and 67° NE., representing either thrust or reverse faulting, respectively.

The numerous aftershocks occupy a large volume surrounding the main shock. Their distribution and focal-plane orientations, though complex, define several different zones in three dimensions (fig. 4.8), as described by Eaton (chap. 8) and Eberhart-Phillips and Reasenberg (chap. 9).

The dominant style of Quaternary deformation in the vicinity of the main shock has been thrusting and associated reverse faulting directed northeastward beneath Coalinga anticline. The occurrence of the main shock in the Coalinga thrust zone and the near-parallelism of the thrust focal plane with that zone lead us to conclude that the earthquake resulted from continued thrusting beneath the anticline. The coseismic uplift at the ground surface (Stein, 1985) that occurred over the upper tier of Coalinga anticline (see fig. 4.11) indicates that the main-shock thrusting splayed upward along fault IX, rather than continuing farther forward beneath the lower tier of the fold.

The aftershock pattern contains elements consistent with this faulting configuration. Both of the aftershock analyses represented in figure 4.8 contain events with steeply southwest dipping focal planes that occur near fault IX beneath the upper northeastern limb of the anticline, and both contain events with flatter, southwest-dipping focal planes that occur at a depth of 8 to 10 km beneath the crest of the anticline where fault IX joins the Coalinga thrust zone (B and C, respectively, in fig. 4.8*D* and equivalents in fig. 4.8*C*).

The hypocenter of the main shock is determined by Eaton (chap. 8) to lie 1 km northeast of the axis of Coalinga anticline (fig. 4.4) at a depth of 10 km, which places it near the base of fault IX. The 23° dip of the thrust focal plane, intermediate between the 10° dip of the thrust zone and the 55° dip of reverse fault IX, places the initial rupture of the main-shock event on a fault segment of intermediate dip in the region where the two faults join. Simple projection of the hypocenter 7.5 km along the trend of the fold axis to profile SJ–19 places it beneath fault X in the gently dipping Coalinga thrust zone (fig. 4.6). This projection leads to a misfit in main-shock location of about 2 km horizontal and 1 km vertical, which is probably within the combined uncertainties of the projection, the absolute location of the hypocenter, and the positions of faults in our cross section. Location of the main shock at the junction between the thrust and reverse faults requires, if seismogenic rupture occurred on both faults, that fault rupture propagated both downdip along the thrust and updip along the reverse fault.

MODEL FOR MAIN-SHOCK RUPTURE

We construct a specific fault model for the Coalinga main shock (figs. 4.10, 4.11) that consists of two connected, southwest-dipping fault planes: a gently dipping (10°) thrust that is equivalent to part of the Coalinga thrust zone and, farther updip, a steeper (55°) reverse-fault splay that is equivalent to fault IX. The two planes strike N. 43° W., parallel to the fold axis of Coalinga anticline, and join at a depth of 9.1 km. This configuration was

FIGURE 4.8.—Stereograms of structure and earthquakes in the Coalinga area. Box is 15 km from top (at sea level) to bottom; 2.5-km depth increments shown at right. All views along a common azimuth from 40 km away, first from 10 km above sea level (*A*) to see the folds, and then from 5 km below sea level (*B* through *E*) to see relation of faults and earthquakes beneath the folds. Letters keyed to text. *A*, Fold configuration represented by structural contours of figure 4.4. Coalinga anticline plunges gently toward viewer in center and away from Joaquin ridge anticline in background. Beneath Coalinga anticline, traces of principal faults are shown that are evident in reflection lines SJ-19 and SJ-3 (fig. 4.5). *B*, Same as figure 4.8*A*, except viewpoint is 5 km below sea level. *C*, Selected focal planes of larger aftershocks, from Eaton (chap. 8). *D*, Southwest-dipping focal planes of aftershocks near May 2 main shock, from Eberhart-Phillips and Reasenberg (chap. 9). *E*, Northeast-dipping focal planes of aftershocks shown in figure 4.8*D*.

determined from the faults on profile SJ–19 and the gross trend of the fold axis. Despite the 9-km distance from profile SJ–19 to SJ–3 along the fold axis and the northwestward broadening of the upper tier of the fold (fig. 4.4), the fault model also fits the structure along profile SJ–3 reasonably well.

The model faults are 16 km long and approximately centered on the main-shock hypocenter. Their northwest end was constrained by the location of the Pleasant Valley cross-structure and by the suggestion in the uplift contours that coseismic uplift dies off there as well. The southeast end of the model faults was similarly controlled

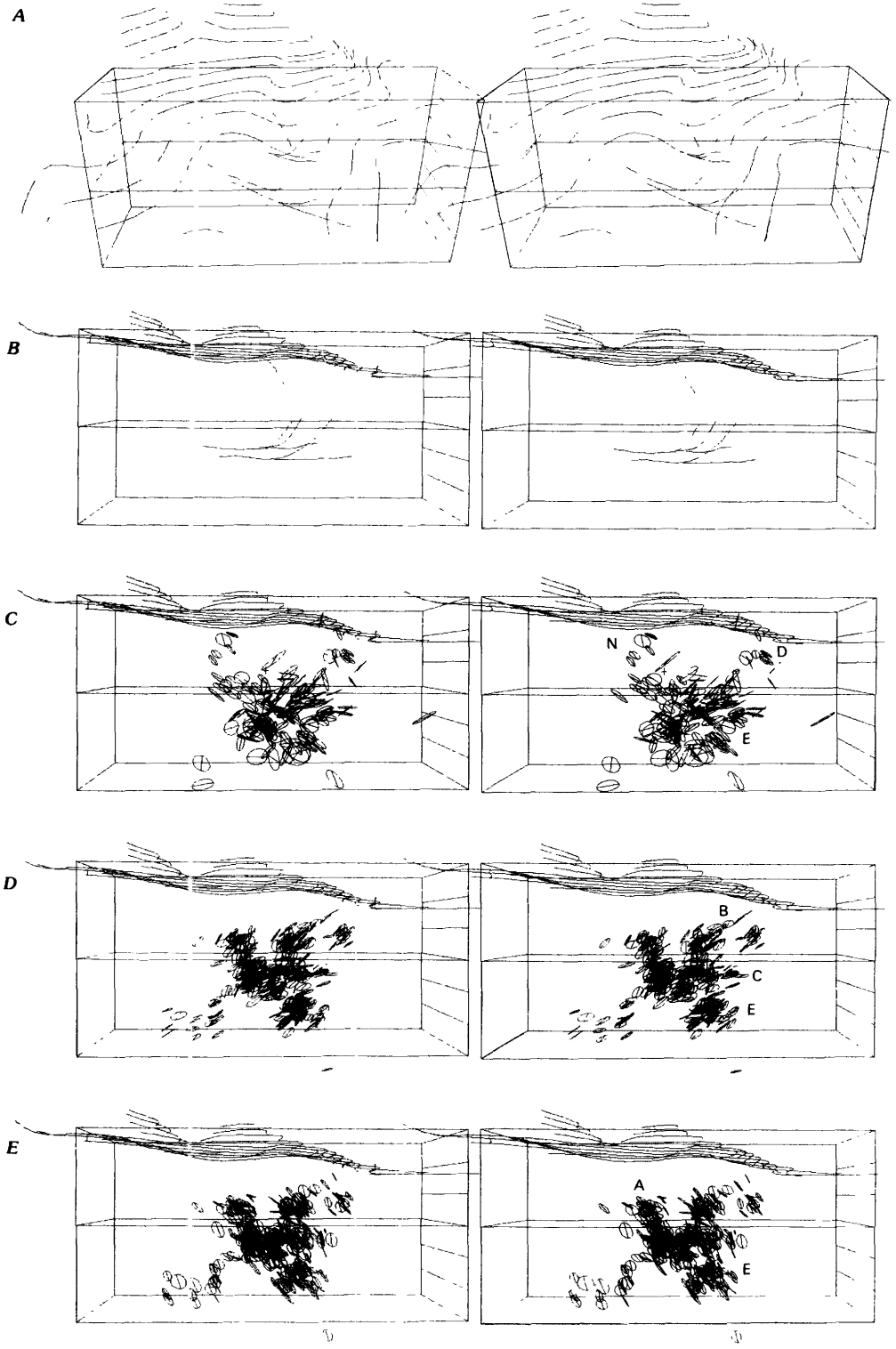

by the uplift closure there, as well as by the southeast limit of aftershocks with focal mechanisms similar to that of the main shock (see chap. 8).

Widths and slips for the two fault planes were selected through dislocation modeling to fit the surface uplift defined by Stein (1985; see next subsection): a width of 4 km and slip of 2 m for the thrust plane, and a width of 7 km and a slip of 1.2 m for the reverse plane. These parameters, together with the 16-km fault length, yield nearly equivalent seismic moments of about 4.3×10^{25} dyne-cm on each fault segment.

A 7-km width for the reverse fault carries the rupture updip almost to the base of the Cenozoic section, which is farther than we would infer from the reflection records alone (fig. 4.5). Occurrence of aftershocks beneath the northeastern limb of the fold as high as the top of the Kreyenhagen Formation (fig. 4.8) indicates, however, that the reverse faulting can have reached 7 km updip. This contrast between inferred rupture in the 1983 event and detectable offsets in the reflection record implies that, as deformation is proceeding, the reverse faults are extending upward into the anticline.

CONSISTENCY WITH SURFACE DEFORMATION

The surface deformation documented by leveling surveys across the epicentral area before and after the earthquake (fig. 4.10; Stein, 1985) can be used to test our interpretation that the 1983 main shock resulted from eastward-directed thrusting and reverse faulting. We calculate vertical deformation at the surface through dislocation modeling applied to the fault model just described, and compare the results with the observed surface deformation. Examination of the calculated uplift patterns for various widths and slips on the thrust and reverse planes leads to selection of the model values that best reproduce the observed uplift.

We consider the results along three profiles (figs. 4.10, 4.11): two that cross the anticline obliquely along the two seismic profiles, and one almost normal to strike that follows the greatest cross-strike extent of the uplift data. Because of the irregular distribution of resurveyed bench marks, we compare the calculated model results both with uplift at bench marks located within 1 km of the profiles and with curves defined by the uplift contours. In drawing those contours, we sought to honor the data points directly, to place the axis of uplift northeast of the fold axis where the data require it along profile *A–A'*, and otherwise to conform to the shape of the underlying fold (fig. 4.4).

The calculated surface uplifts fit the observed uplifts quite well, without recourse to varying the fault slip or fault geometry along strike (fig. 4.11). The best fit occurs along profile *B–B'*, where both the maximum amount of uplift and the decay of uplift eastward is well matched. The fit is nearly as good along profile *A–A'*. Two bench

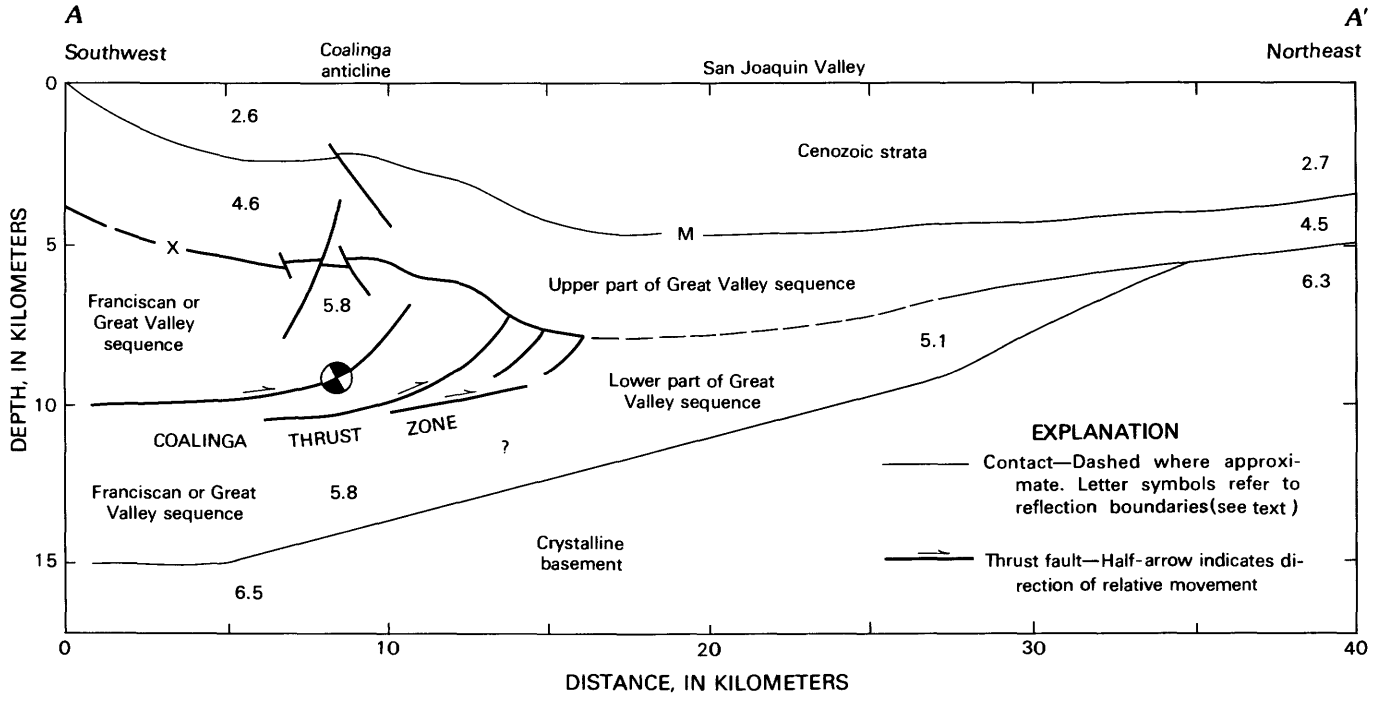

FIGURE 4.9.—Structural cross section across Coalinga anticline along part of line *A–A'* (fig. 4.2), showing Coalinga thrust zone and related structure (from fig. 4.6). Generalized seismic velocities shown in kilometers per second. Vertical section of main-shock focal mechanism (shaded circle; see chap. 8) located as described in text.

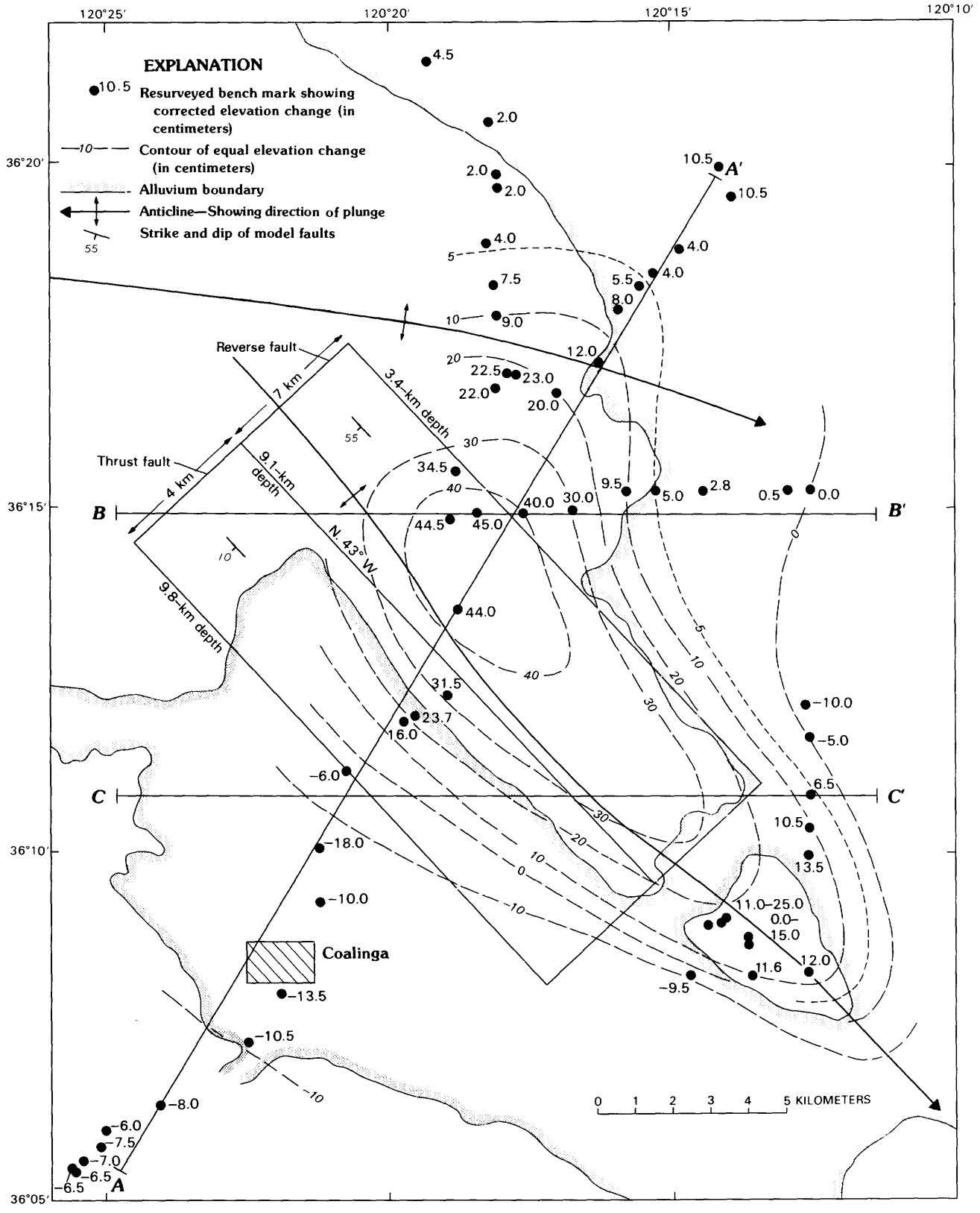

FIGURE 4.10.—Model of Coalinga thrust and reverse fault IX beneath Coalinga anticline and its relation to coseismic surface deformation. Locations of resurveyed bench marks and corrected elevation changes from Stein (1985). Profiles *A–A′*, *B–B′*, and *C–C′* are shown in figure 4.11; profile *B–B′* approximately coincides with reflection line SJ-3; and profile *C–C′* coincides with western part of reflection line SJ-19. Fold axes from figure 4.4. Uplift values all contain an adjustment of –7.0 cm applied by Stein (1985) in matching his best-fit model, under the assumption that deformation extended beyond the limit of resurveyed bench marks southwest of Coalinga.

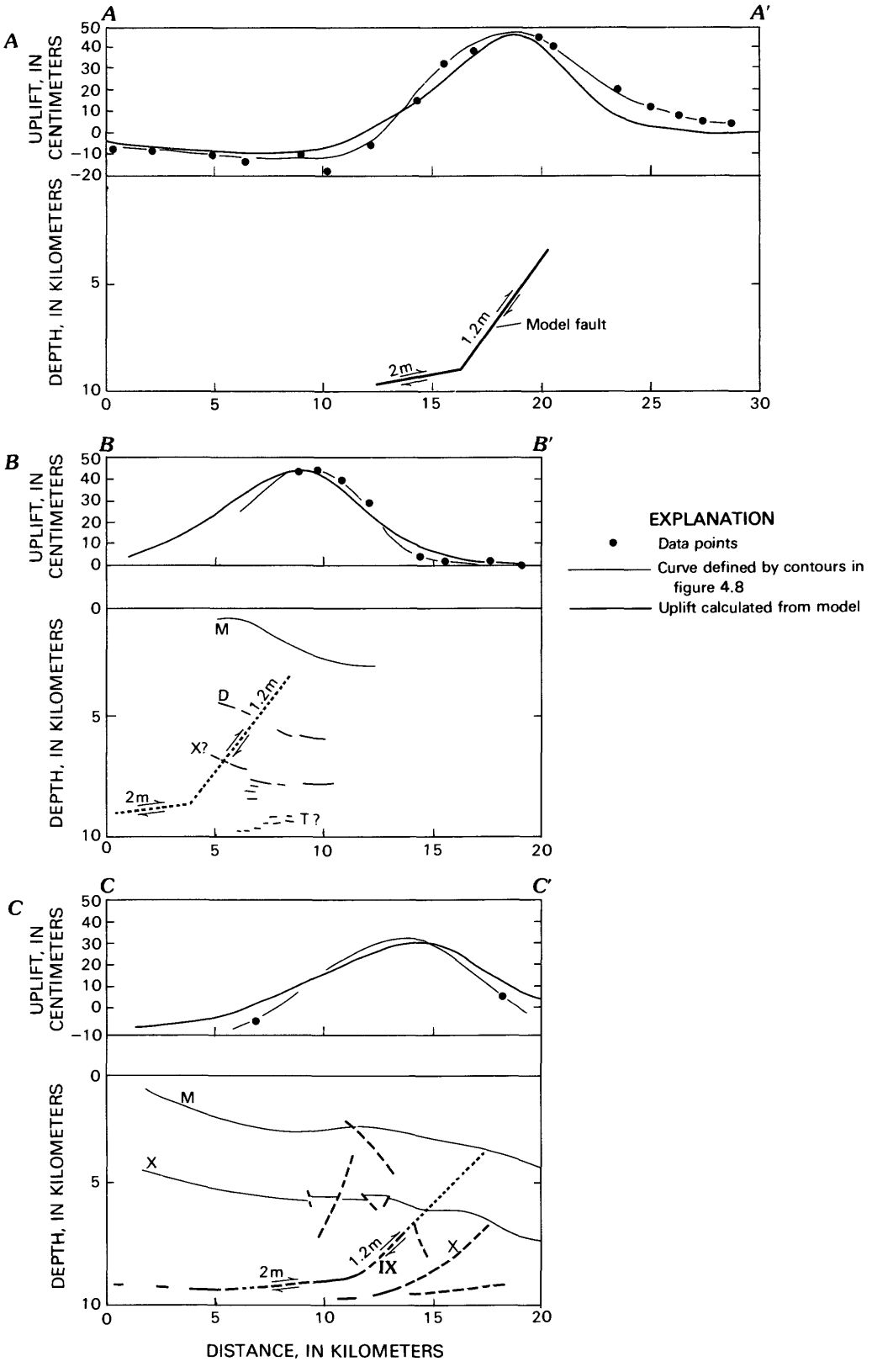

Figure 4.11.—Comparison of observed and calculated elevation changes along profiles *A–A'* (*A*), *B–B'* (*B*), and *C–C'* (*C*) for fault model of figure 4.8. Model faults in profiles *B–B'* and *C–C'* dotted across cross sections from figure 4.5. Letters, selected reflection horizons; Roman numerals, selected faults, keyed to text.

marks in the center of Pleasant Valley show a significantly greater decrease in elevation than is predicted by the model; however, the subsidence correction is more poorly known there than elsewhere along the profile (R.S. Stein, written commun., 1985). Along the northeastern part of this profile, the calculated elevation change drops more rapidly than does the observed change. In this part of the profile, however, the plan pattern of uplift departs considerably from a two-dimensional pattern; the northeastward bulge in the uplift contours suggests a more complex pattern of faulting here than our simple model can represent. A reasonably good fit is also obtained along profile *C–C'*, although little direct control exists on the uplift here, and the model results along this profile should be particularly sensitive to the exact position of the southeast end of the model faults.

Stein examined dislocation models of the elevation changes in terms of slip on various faults at depth. His preferred result (Stein, 1985, fig. 3*A*) consists of a steeply northeast dipping reverse fault that is oriented parallel to the steep focal plane of the main-shock focal mechanism and is pinned at the downdip end by the hypocenter reported by Eaton and others (1983). Although this result is the best fit that he considers and is consistent with the main shock, there is no evidence in the aftershock pattern that this fault moved in 1983, nor is it consistent with the structure evident in the reflection records. This northeast-dipping fault would have to cross the southwest-dipping fault VI evident on profile SJ–19 (pl. 4.1B). Stein found that to obtain a reasonably good fit for faulting on a west-dipping thrust at hypocentral depth, he had to include a steeper updip fault segment (Stein, 1985, fig. 3*D*). This alternative interpretation is nearly identical to our fault model.

RECURRENCE

The progressive construction of Coalinga anticline through late Pliocene and Quaternary time has required many individual movements on the Coalinga thrusts, each presumably similar to the 1983 event. It is difficult to estimate the recurrence rate for such events because of the complex deformation pattern at the northeast end of the Coalinga thrusts and the absence of direct information on the amount or rate of fault offset. The most straightforward method of estimation is to relate the 1983 increment of fold growth (0.45 m) to the whole amplitude of the upper tier of the fold at the main-shock epicenter (1.5 km), and to assume a constant rate of deformation. For a 2-Ma history of folding, this relation yields 3,300 events, or a recurrence interval of 600 years. The similar amplitude of the lower fold tier implies a separate series of earthquakes on the thrusts responsible for its growth. The resulting estimate of the recurrence interval of large earthquakes beneath Coalinga anticline, about 300 years, is similar to the 200- to 600-year estimate determined by Stein and King (1984) for the reverse-fault model.

SUBORDINATE DEFORMATION

The occurrence of aftershocks throughout a large volume of suprabasement rock represents extensive minor deformation around the main-shock rupture. Such distributed deformation seems reasonable in this boundary region where the northeastward-thrusting Coast Ranges abut relatively undeformed Great Valley basement and overlying sedimentary rocks.

A group of aftershocks with southeast-dipping focal planes (A, fig. 4.8*E*) define a steeply southeast dipping zone beneath the western limb of Coalinga anticline that approximately coincides with fault V on profile SJ–19. This zone has an orientation similar to that of Stein's preferred fault but lies 2 to 3 km farther southwest. Principal main-shock rupture on this zone is denied by the pattern of surface uplift, which peaks too far to the northeast.

Another, deeper group of aftershocks underlies the Coalinga thrust zone beneath the crest of the anticline (E, figs. 4.8*C*–4.8*E*). Some of these events could represent a downdip extension of the southeast-dipping zone just described, but in aggregate they seem better interpreted to represent southwest-dipping reverse faulting.

The Nuñez group of aftershocks (N, fig. 4.8*C*) defines a north-south-striking zone that dips east beneath the surface expression of the Pleasant Valley cross-structure and reaches the depth of the Coalinga thrust zone. The reverse motion on the Nuñez zone, which led to surface faulting across the axis of the White Creek syncline during the aftershock sequence (fig. 4.4; see chap. 15), represents shortening across the Pleasant Valley cross-structure.

At and below the level of the Coalinga thrust zone, in contrast, the cross-structure is marked by several strike-slip events in the aftershock sequence (see chap. 8). The right-lateral focal planes of these events are consistent with the right-lateral style of that structure inferred from the right step in the main range front.

Numerous aftershocks with thrust mechanisms extend for 10 km northwest of the cross-structure at a depth of 8 to 12 km beneath the south flank of Joaquin Ridge anticline (see chap. 8). These aftershocks suggest that thrusts similar to the Coalinga thrusts extend northwestward beyond the end of Coalinga anticline, although the more easterly trend of their pressure axes suggests some independence of the Coalinga thrusts. The west-northwest trends of Joaquin Ridge anticline and its flanking synclines must be due to more northerly trending com-

pression than is indicated by these earthquakes, possibly involving shallower thrusting.

The Domengine cluster of aftershocks (D, fig. 4.8*C*) occurred on the northeast flank of Joaquin Ridge anticline. The northeast-dipping focal planes of these aftershocks seem to lie in the bedding and represent bedding-plane slip, like the slip on faults of the O'Neill zone farther northwest.

CONCLUSIONS

Seismic-reflection profiles across Coalinga anticline have proved important in understanding the 1983 Coalinga main shock. They indicate the presence of previously unknown thrust faults that extend northeastward from beneath Pleasant Valley at hypocentral depth and splay upward as reverse faults beneath the anticline. This upward splaying at the buried northeast termination of the thrusts has raised the anticline, principally during the past 2 Ma. Because of their relation with the anticline, we name these faults the "Coalinga thrust zone." The main shock occurred at the thrust-splay junction 9 km beneath the crest of the anticline and involved northeastward-directed movement on both the thrust and reverse fault. We estimate the recurrence interval of a characteristic M=6.7 earthquake beneath Coalinga anticline to be about 300 years.

Our structural interpretation of the epicentral region is founded on the seismic-reflection profiles, associated refraction profiles (see chap. 3), drill-hole information, surface geology, and the distribution and focal mechanisms of earthquakes. Together, they provide a coherent picture of structural relations and implied tectonic history at Coalinga. The magnetic and gravity modeling of Griscom and Jachens (chap. 5) provides an important test of the structural anatomy on which our interpretation is based. The dominant style of deformation we infer at Coalinga, and the specific faults evident in the reflection records, nicely match deformation represented by the thrust focal plane of the main-shock mechanism (see chap. 8). The aftershock patterns described by Eaton (chap. 8) and Eberhart-Phillips and Reasenberg (chap. 9) also are compatible with our interpretation. Furthermore, dislocation modeling of a simple fault model demonstrates that our interpretation satisfies the coseismic surface deformation above the main shock described by Stein (chap. 13), and leads to selection of specific fault dimensions and slip. The resulting bilateral fault rupture involves equivalent seismic moment on the thrust and reverse-fault planes of 4.3×10^{25} dyne-cm, the sum of which satisfies the moment of the earthquake.

The Coalinga thrusts, the overlying anticline, and the focal plane of the main-shock mechanism all strike northwestward, parallel to the San Andreas fault 35 km to the southwest. The thrusting and this most recent earthquake thus result from compression at the northeastern margin of the Coast Ranges that is oriented perpendicular to the San Andreas fault. Folds like Coalinga anticline extend southeastward along the Coast Ranges boundary for 100 km and probably represent similar compression and thrusting. Structure northwest of Coalinga along the range front differs, but also involves Quaternary folding and faulting that may be related to underlying thrusts. We thus expect that large earthquakes like the 1983 Coalinga event may be possible elsewhere along the Coast Ranges boundary. Northeast-southwest compression seems characteristic of this boundary between the strongly deformed Coast Ranges and the gently tilted Sierran block to the east.

The examination of structure across the Coast Ranges boundary at Coalinga supports conclusions about the history of that boundary derived from our more general study. The southwest-dipping crystalline basement beneath the Great Valley extends westward beneath the leading edge of the Coast Ranges and is overlain by a wedge of rock that, from its position and seismic velocity, we infer includes Franciscan rock. This relation requires that a wedge of Franciscan rock has been thrust northeastward onto Great Valley basement while it concurrently peeled up the overlying Great Valley sequence. A southwestward steepening of the basement surface beneath the southwest side of the valley seems to have controlled southwestward thickening in the Great Valley sequence and, later, the northeastward extent of thrusting. That termination of thrusting, in turn, probably controls the position of the northeast front of the Coast Ranges. The thrusting now underway at Coalinga and, by inference, elsewhere along the Coast Ranges boundary is thus a continuing expression of a long-established pattern of deformation.

ACKNOWLEDGMENTS

Our work has benefited from the generous help of our colleagues and assistants. J.A. Bartow shared his expertise in the stratigraphy of the region. A.W. Walter patiently tolerated our questions and challenges as he worked on refraction models. R.S. Stein shared his data on coseismic uplift. R.K. Mark helped J.L. Zigler apply a computer program provided by P.A. Reasenberg to prepare the stereograms of figure 4.8. R.E. von Huene and J.I. Ziony provided stimulating reviews. Discussions with M.C. Blake, Jr., J.P. Eaton, D. Eberhart-Phillips, A. Griscom, R.C. Jachens, D.L. Jones, and R.F. Yerkes have been particularly helpful. R.A. Williams and J.L. Zigler compiled maps, gathered data from well logs and the literature, and provided much other support. P. Levine gathered and compiled data on basement well depths.

REFERENCES CITED

Bailey, E.H., Blake, M.C., Jr., and Jones, D.L., 1970, On-land Mesozoic oceanic crust in California Coast Ranges, *in* Geological Survey research, 1970: U.S. Geological Survey Professional Paper 700–C, p. C70–C81.

Bailey, E.H., Irwin, W.P., and Jones, D.L., 1964, Franciscan and related rocks and their significance in the geology of western California: California Division of Mines and Geology Bulletin 183, 177 p.

Blake, M.C., Jr., Howell, D.J., and Jayko, A.S., 1984, Tectonostratigraphic terranes of the San Francisco Bay Region, *in* Blake, M.C., Jr., ed., Franciscan geology of northern California (book 43): Los Angeles, Society of Economic Paleontologists and Mineralogists, Pacific Section, v. 43, p. 5–22.

Blumling, Peter, Mooney, W.D., and Lee, W.H.K., 1985, Crustal structure of the southern Calaveras fault zone, central California, from seismic refraction investigations: Seismological Society of America Bulletin, v. 75, no. 1, p. 193–209.

Blumling, Peter, and Prodehl, Claus, 1983, Crustal structure beneath the eastern part of the Coast Ranges (Diablo Range) of central California from explosion seismic and near earthquake data: Physics of the Earth and Planetary Interiors, v. 31, no. 4, p. 313–326.

Brown, R.D., Jr., and Rich, E.I., 1967, Implications of two Cretaceous mass transport deposits, Sacramento Valley, California: Comment on a paper by Gary L. Peterson: Journal of Sedimentary Petrology, v. 37, p. 240–248.

Casey, T.A.L., and Dickinson, W.R., 1976, Sedimentary serpentinite of the Miocene Big Blue Formation near Cantua Creek, California, *in* Fritsche, A.E., TerBest, Harry, Jr., and Wornardt, W.W., eds., The Neogene symposium: Los Angeles, Society of Economic Paleontologists and Mineralogists, Pacific Section, p. 65–74.

Christensen, N.I., 1982, Seismic velocities, chap. 1 *of* Carmichael, R.S., ed., Handbook of physical properties of rocks: Boca Raton, Fla., CRC Press, v. 2, p. 2–228.

Cox, Allan, and Engebretsen, David, 1985, Change in motion of Pacific plate at 5 Myr BP: Nature, v. 313, no. 6002, p. 472–474.

Denlinger, R.P., and Kovach, R.L., 1981, Seismic-reflection investigations at Castle Rock Springs in the Geysers geothermal area, *in* McLaughlin, R.J., and Donnelly, J.M., eds., Research in the Geysers-Clear Lake geothermal area, northern California: U.S. Geological Survey Professional Paper 1141, p. 117–128.

Dibblee, T.W., Jr., 1971, Geologic maps of the Coalinga, Joaquin Rocks, New Idria, and Priest Valley 15-minute quadrangles, California: U.S. Geological Survey Open-File Report 71-87, scale 1:62,500.

Dickinson, W.R., 1981, Plate tectonics and the continental margin of California, *in* Ernst, W.G., ed., The geotectonic development of California (Rubey volume 1): Englewood Cliffs, N.J., Prentice Hall, p. 1–25.

Dix, C.H., 1955, Seismic velocities from surface measurements: Geophysics, v. 20, no. 1, p. 68–86. Dobrin, M.B., 1976, Introduction to geophysical prospecting (3d ed.): New York, McGraw-Hill, 630 p.

Eaton, J.P., 1983, Seismic setting, location and focal mechanism of the May 2, 1983, Coalinga earthquake, *in* Borcherdt, R.D., compiler, The Coalinga earthquake sequence commencing May 2, 1983: U.S. Geological Survey Open-File Report 83-511, p. 20–26.

Eaton, J.P., Cockerham, R.S., and Lester, F.W., 1983, Study of the May 2, 1983 Coalinga earthquake and its aftershocks, based on the USGS seismic network in northern California, *in* Bennett, J.H., and Sherburne, R.W., eds., The 1983 Coalinga, California earthquakes: California Division of Mines and Geology Special Publication 66, p. 261–274.

Fielding, Eric, and Barazangi, Muawia, 1985, Basement faults beneath the western Great Valley of California based on COCORP seismic reflection profiles near Coalinga, *in* Rymer, M.J., and Ellsworth, W.L., eds., Proceedings of Workshop XXVII: Mechanics of the May 2, 1983 Coalinga, California earthquake: U.S. Geological Survey Open-File Report 85-44, p. 31–37.

Fielding, Eric, Barazangi, Muawia, Brown, Larry, Oliver, Jack, and Kaufman, Sidney, 1983, COCORP seismic reflection profiles near the 1983 Coalinga earthquake sequence: Deep structures, *in* Bennett, J.H., and Sherburne, R.W., eds., The 1983, Coalinga, California earthquakes: California Division of Mines and Geology Special Publication 66, p. 113–126.

—— 1984, COCORP seismic profiles near Coalinga, California: Subsurface structure of the western Great Valley: Geology, v. 12, no. 5, p. 268–273.

Gardiner, G.H.F., Gardiner, L.W., and Gregory, A.R., 1974, Formation velocity and density: The diagnostic basis for stratigraphic traps: Geophysics, v. 39, p. 770–778.

Griscom, Andrew, 1982, Magnetic interpretation of ophiolites and batholiths in California [abs.]: Geological Society of America Abstracts with Programs, v. 9, no. 4, p. 426–427.

Harding, T.P., 1976, Tectonic significance and hydrocarbon trapping consequences of sequential folding synchronous with San Andreas faulting, San Joaquin Valley, California: American Association of Petroleum Geologists Bulletin, v. 60, no. 3, p. 356–378.

Herd, D.G., 1979a, Neotectonics of the San Francisco Bay region, California, *in* Seiders, W.H., compiler, Summaries of technical reports: Menlo Park, Calif., U.S. Geological Survey, Office of Earthquake Studies, v. 8, p. 29–31.

—— 1979b, The San Joaquin fault zone—evidence for late Quaternary faulting along the west side of the northern San Joaquin Valley, California [abs.]: Geological Society of America Abstracts with Programs, v. 11, no. 3, p. 83.

Hopson, C.A., Mattinson, J.M., and Pessagno, E.A., Jr., 1981, Coast Range ophiolite, western California, *in* Ernst, W.G., ed., The geotectonic development of California (Rubey Volume 1): Englewood Cliffs, N.J., Prentice-Hall, p. 418–510.

Irwin, W.P., 1964, Late Mesozoic orogenies in the ultramafic belts of northwestern California and southwestern Oregon, *in* Geological Survey research, 1964: U.S. Geological Survey Professional Paper 501–C, p. C1–C9.

Jennings, C.W., 1977, compiler, Geologic map of California: California Division of Mines and Geology Geologic Data Map 2, scale 1:750,000.

Lettis, W.R., 1982, Late Cenozoic stratigraphy and structure of the western margin of the central San Joaquin Valley, California: Berkeley, University of California, Ph.D. thesis, 587 p. [also published as U.S. Geological Survey Open-File Report 82-526].

Mansfield, C.F., III, 1972, Petrology and sedimentology of the late Mesozoic Great Valley sequence, near Coalinga, California: Stanford, Calif., Stanford University, Ph.D. thesis, 102 p.

Mooney, W.D., and Walter, A.W., 1981, Seismic refraction studies in the Coast Ranges, central California [abs.]: Eos (American Geophysical Union Transactions), v. 62, no. 17, p. 328.

Okāya, D.A., 1986, Seismic profiling of the lower crust: Dixie Valley, Nevada, *in* Barazangi, Muawia, and Brown, Larry, eds., Reflection seismology: The continental crust (Geodynamics Series, v. 14): Washington, American Geophysical Union, p. 269–280.

Page, B.M., 1981, The southern Coast Range, *in* Ernst, W.G., ed., The geotectonic development of California: Englewood Cliffs, N.J., Prentice-Hall, p. 329–417.

—— 1984, Geologic background of the Coalinga earthquake of May 2, 1983, *in* Rymer, M.J., and Ellsworth, W.L., eds., Proceedings of Workshop XXVII: Mechanics of the May 2, 1983 Coalinga, California earthquake: U.S. Geological Survey Open-File Report 85-44, p. 4–9.

Page, B.M., and Engebretsen, D.C., 1984, Correlation between the

geologic record and computed plate motions for central California: Tectonics, v. 3, no. 2 p. 133–155.

Page, B.M., Wagner, H.C., McCulloch, D.S., Silver, E.A., and Spotts, J.H., 1979, Geologic cross section of the continental margin off San Luis Obispo, the southern Coast Ranges, and the San Joaquin Valley, California: Geological Society of America Map and Chart Series MC–28G.

Sarna-Wojcicki, A.M., Meyer, C.E., Bowman, H.R., Hall, N.T., Russell, P.C., Woodward, M.J., and Slate, J.L., 1985, Correlation of the Rockland ash bed, a 400,000-year-old stratigraphic marker in northern California and western Nevada, and implications for middle Pleistocene paleogeography of central California: Quaternary Research, v. 23, no. 2 p. 236–257.

Schilling, F.A., Jr., 1962, Generalized geologic section of the central San Joaquin Valley, California, pl. 12 *of* Bowen, O.E., Jr., ed., Geologic guide to the gas and oil fields of northern California: California Division of Mines and Geology Bulletin 181.

Stein, R.S., 1985, Evidence for surface folding and subsurface fault slip from geodetic elevation changes associated with the 1983 Coalinga, California, earthquake, *in* Rymer, M.J., and Ellsworth, W.L., eds., Mechanics of the May 2, 1983 Coalinga earthquake: U.S. Geological Survey Open-File Report 85–44, p. 225–253.

Stein, R.S., and King, G.C.P., 1984, Seismic potential revealed by surface folding: 1983 Coalinga, California, earthquake: Science, v. 224, no. 4651, p. 869–872.

Stewart, R.M., and Peselnick, Louis, 1978, Systematic behavior of compressional velocity in Franciscan rocks at high pressure and temperature: Journal of Geophysical Research, v. 83, no. B2, p. 831–839.

Vedder, J.G., 1970, Geologic map of the Wells Ranch and Elkhorn Hills quadrangles, San Luis Obispo and Kern Counties, California: U.S. Geological Survey Miscellaneous Geologic Investigations Map I–585, scale 1:24,000.

Walter, A.W., and Mooney, W.D., 1982, Crustal structure of the Diablo and Gabilan Ranges, central California: A reinterpretation of existing data: Seismological Society of America Bulletin, v. 72, no. 5, p. 1567–1590.

Warren, D.H., 1981, Seismic-refraction measurements of crustal structure near Santa Rosa and Ukiah, California, *in* McLaughlin, R.J., and Donnelly, J.M., eds., Research in the Geysers-Clear Lake geothermal areas, northern California: U.S. Geological Survey Professional Paper 1141, p. 167–181.

Waters, K.H., 1981, Reflection seismology: New York, John Wiley & Sons, 453 p.

Wentworth, C.M., Blake, M.C. Jr., Jones, D.L., Walter, A.W., and Zoback, M.D., 1984a, Tectonic wedging associated with emplacement of the Franciscan assemblage, California Coast Ranges, *in* Blake, M.C., Jr., ed., Franciscan geology of northern California (book 43): Los Angeles, Society of Economic Paleontologists and Mineralogists, Pacific Section, v. 43, p. 163–173.

Wentworth, C.M., Walter, A.W., Bartow, J.A., and Zoback, M.D., 1983a, Evidence on the tectonic setting of the 1983 Coalinga earthquakes from deep reflection and refraction profiles across the southeastern end of Kettleman Hills, *in* Bennett, J.H., and Sherburne, R.W., eds., The 1983 Coalinga, California earthquakes: California Division of Mines and Geology Special Publication 66, p. 113–126.

Wentworth, C.M., Walter, A.W., Zoback, M.D., Blake, M.C., Jr., Griscom, Andrew, Lindh, A.G., and Mooney, W.D., 1983b, Deep seismic reflection profile across the southern Diablo Range and western San Joaquin Valley near Kettleman Hills, California: Evidence for possible west over east thrusting [abs.]: American Association of Petroleum Geologists, Pacific Section Annual Meeting, 58th, Sacramento, Calif., 1983, Program and Abstracts, p. 57.

Wentworth, C.M., Zoback, M.D., and Bartow, J.A., 1984b, Tectonic setting of the 1983 Coalinga earthquakes from seismic reflection profiles: A progress report, *in* Rymer, M.J., and Ellsworth, W.L., eds., Proceedings of Workshop XXVII: Mechanics of the May 2, 1983 Coalinga, California earthquake: U.S. Geological Survey Open-File Report 85-44, p. 19–30.

Western Geophysical Co., 1975, Acoustic basement, pl. 1 *of* Los Angeles Department of Water and Power, San Joaquin Nuclear Project, Early Site Review Report: Los Angeles Department of Water and Power report to U.S. Nuclear Regulatory Commission, v. 2A, scale 1:126,720.

Woodring, W.P., Stewart, Ralph, and Richards, R.W., 1940, Geology of the Kettleman Hills oil field, California: Stratigraphy, paleontology, and structure: U.S. Geological Survey Professional Paper 195, 170 p.

Zigler, J.L., Frei, L.S., Wentworth, C.M., and Bartow, J.A., 1987, Structure contour map of the top of the Oligocene to middle Miocene Temblor Formation in the Kettleman Hills and Lost Hills areas, Fresno, Kings, and Kern Counties, California: U.S. Geological Survey Miscellaneous Field Studies Map MF–1896, scale 1:100,000.

Zigler, J.L., Wentworth, C.M., and Bartow, J.A., 1986, Structure contour map of the tops of the Kreyenhagen Formation and Cretaceous strata in the Coalinga area, Fresno and Kings Counties, California: U.S. Geological Survey Miscellaneous Field Studies Map MF–1843, scale 1:100,000.

Zoback, M.D., and Wentworth, C.M., 1986, Crustal studies in central California using an 800-channel seismic reflection recording system, *in* Barazangi, Muawia, and Brown, Larry, eds., Reflection seismology: A global perspective (Geodynamics Series, v. 13): Washington, American Geophysical Union, p. 183–196.

5. TECTONIC IMPLICATIONS OF GRAVITY AND MAGNETIC MODELS ALONG EAST-WEST SEISMIC PROFILES ACROSS THE GREAT VALLEY NEAR COALINGA

By ANDREW GRISCOM and ROBERT C. JACHENS,
U.S. GEOLOGICAL SURVEY

CONTENTS

ABSTRACT

We have used gravity and magnetic data to compute east-west crustal models along a profile extending eastward from the San Andreas fault in the eastern Coast Ranges, through the town of Coalinga, and across the Great Valley of California. These models agree well with seismic refraction and reflection models, support the idea that the Franciscan assemblage near its contact with the Great Valley sequence was emplaced by tectonic wedging, and do not indicate the presence of a fossil subduction zone. The west half of the Great Valley is underlain by a thick, west-dipping slab of magnetic high-density rock that may be an ophiolite obducted from the west onto the continental margin during Jurassic time. Warping and faulting of this slab during deposition of the overlying Great Valley sequence created structures parallel to the basin's east side that later may have acted as barriers limiting the eastward intrusion of Franciscan wedges. Multiple wedging is implied by a mostly concealed magnetic slab, presumed to be Coast Range ophiolite, that is consistently present for a strike distance of 600 km along the contact of the Franciscan assemblage and the Great Valley sequence, and that has its west edge emplaced within the Franciscan assemblage.

INTRODUCTION

We use gravity and magnetic data to compute crustal models based initially on geologic and seismic interpretations across the boundary between the Great Valley and the Coast Ranges in California, as part of a multidisciplinary investigation of the Earth's crust. Potential-field data, such as gravity and magnetic surveys, are especially sensitive to steeply dipping boundaries and thus provide powerful additional constraints to seismic reflection and refraction techniques, which work best for relatively flat lying boundaries. The models described here are constructed along or near seismic-reflection profile SJ–19 (see chap. 4), which extends in an east-west direction along a parallel located 5 km north of Coalinga (fig. 5.1). The models continue beyond the ends of profile SJ–19, extending westward to the San Andreas fault and eastward to the Sierra Nevada foothills. The models computed from the potential-field data agree well with both the seismic-reflection interpretation (see chap. 4) and the seismic-refraction velocity model (see chap. 3), and provide considerable new information concerning subsurface geologic structures and inferred lithology in the Coalinga region and the Great Valley.

GEOLOGIC SETTING

The geology and tectonic setting of the Coalinga area along profile SJ–19 are described in chapter 4. In the Great Valley (here, the San Joaquin Valley) east of Coalinga, sedimentary rocks of Cretaceous and Cenozoic age rest on an unconformity that dips gently west to depths of 5 to 10 km on the west side of the valley. According to drill-hole data, crystalline rocks of the Sierra Nevada foothills, composed of weakly to moderately metamorphosed Paleozoic and Mesozoic sedimentary and volcanic rocks, all intruded by Mesozoic granitic rocks of the Sierra Nevada batholith (Matthews and Burnett, 1965), lie below the same unconformity on the east side of the valley. A 20-km-wide belt of rocks forming the Kings-Kaweah ophiolite (Saleeby, 1978) trends north-south along the east border of the valley; this ophiolite is intruded by younger gabbroic rocks associated with the Sierra Nevada batholith. Basement rocks of the central and western Great Valley are also

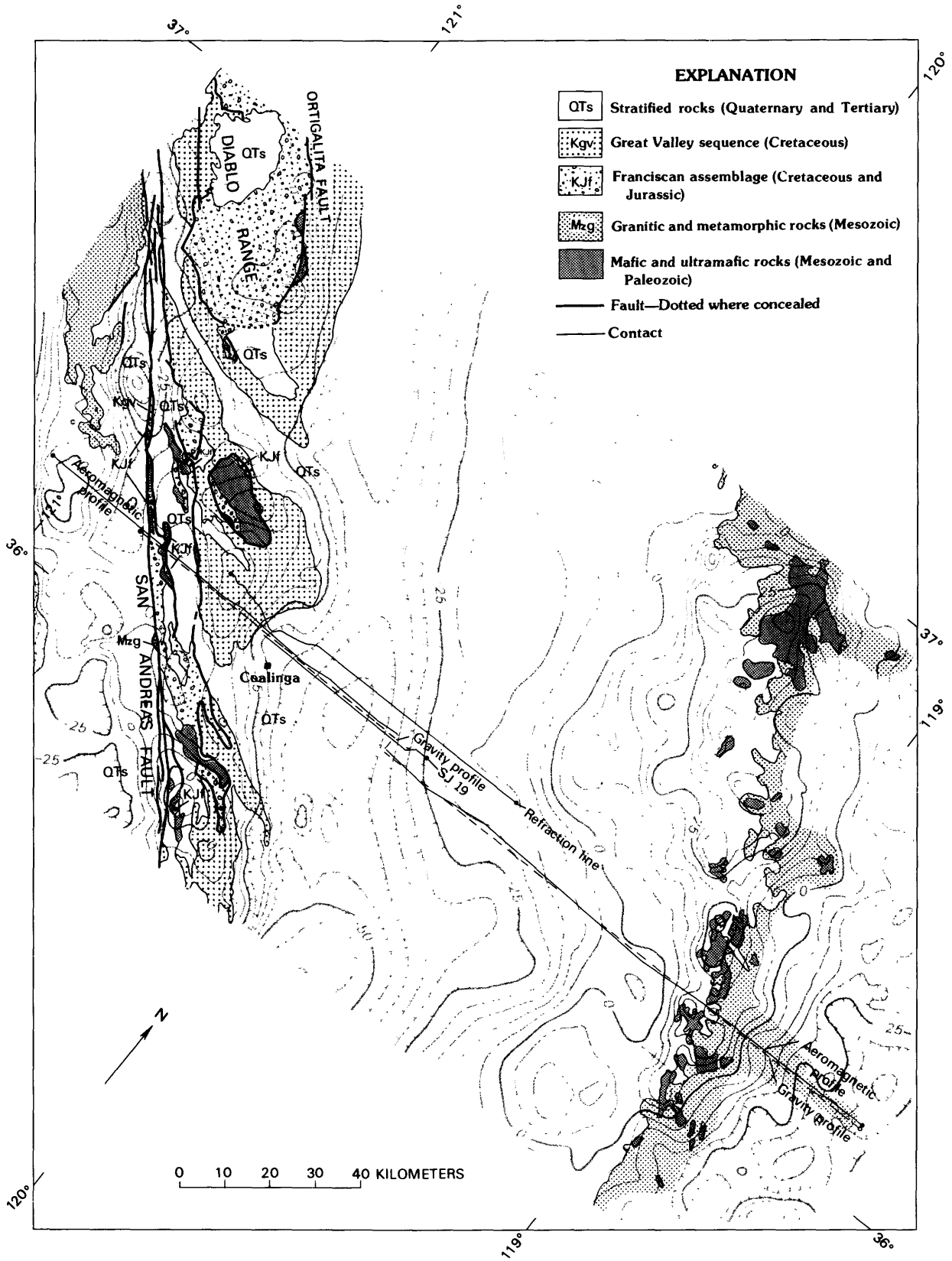

FIGURE 5.1.—Isostatic-residual-gravity-anomaly map (Roberts and others, 1981) and generalized geologic map (from Jennings, 1977) of the Coalinga, Calif., area, showing locations of seismic-refraction profile (see chap. 3), seismic-reflection profile (SJ–19; see chap. 4), gravity profile, and aeromagnetic profile. Contour interval, 5 mGal. Hachures indicate closed minimums.

considered to be an ophiolite assemblage, on the basis of lithologic data from a few drill cores and an association with large magnetic and gravity anomalies (Blake and others, 1978; Oliver and Griscom, 1980, p. 28–29). The basement rocks lying between the two ophiolites have been sampled by numerous drill holes and are probably equivalent to the igneous and metamorphic rocks of the Sierra Nevada foothills (May and Hewitt, 1948; Thompson and Talwani, 1964; M.C. Blake, Jr., oral commun., 1984).

Melange and imbricate layered rocks of a Late Jurassic to Cretaceous subduction complex occur west of Coalinga along the east side of the San Andreas fault. These rocks are the Franciscan assemblage (Bailey and others, 1964; Hamilton, 1978), which consists predominantly of turbiditic graywacke, siltstone, shale, and lesser amounts of chert and volcanic rocks. Additional rocks characteristically found in melange of the complex are serpentinite, gabbro, diabase, limestone, and high-pressure metamorphic rocks, including jadeitic metagraywacke. In the antiformal core of the Diablo Range 90 km northwest of Coalinga, regional high-pressure metamorphism of Franciscan rocks tends to reach a maximum along the east border of the Franciscan (Bailey and others, 1964); this regional observation is supported by the higher densities of the more easterly Franciscan sandstone units in the Diablo Range (Bailey and others, 1964), as well as by the distribution of Franciscan metamorphic facies along the east side of the Coast Ranges north of San Francisco (Blake and others, 1967).

Throughout northern California, the Franciscan assemblage is juxtaposed with the coeval Great Valley sequence, a thick section of marine clastic rocks ranging in age from Late Jurassic to Late Cretaceous, by a major low-angle fault, the Coast Range fault, which is locally interrupted by younger steeply dipping faults. This fault is believed by many workers to be the position of a former subduction zone (Hamilton, 1969); these relations were summarized by Wentworth and others (1984). A belt of serpentinite and less abundant mafic rocks, the Coast Range ophiolite, that lies between these two predominantly sedimentary rock assemblages is believed to be Jurassic oceanic crust and upper mantle (Bailey and others, 1970; Lanphere, 1971), commonly in fault contact but locally in depositional contact beneath the overlying Great Valley sequence. The parallel association for nearly 400 km of the Coast Range ophiolite and Coast Range fault with the inferred ophiolite beneath the west half of the Great Valley suggests to some investigators that the two ophiolites may be correlative (Bailey and others, 1964; Griscom, 1966; Blake and others, 1978). Overlying all these Mesozoic units in the Coast Ranges are Tertiary marine sedimentary rocks, as well as Pliocene and Quaternary continental deposits.

GRAVITY AND MAGNETIC DATA

Gravity data for this study are presented as isostatic-residual-gravity anomalies (Jachens and Griscom, 1983). The large components of the Bouguer gravity anomalies, which are caused by isostatic compensation of the topography, both local mountain ranges and the continental margin, are eliminated from the gravity data; remaining anomalies are caused principally by intracrustal and near-surface density inhomogeneities. These data were part of the set used to compile the isostatic-residual-gravity map of California (Roberts and others, 1981). The gravity data are displayed in map form in figure 5.1 and in profile form in figure 5.2. In the western section of the profile in the Coast Ranges, gravity values are near 0, whereas a major low is associated with the western Great Valley; a major gravity high is located at the east border of the Great Valley. This general pattern to the isostatic gravity field extends well to the north and south of the analyzed profile, and so the assumption of two-dimensionality in the gravity analysis is reasonably well met for these large features.

Although detailed aeromagnetic contour maps of the study area are unavailable, a generalized compilation at a scale of 1:1,000,000 has been published by Blake and others (1978). In addition, east-west magnetic profiles flown by helicopter at a height of 120 m above ground and at a spacing of about 5 km (High Life Helicopters, Inc., and QEB, Inc., 1980, 1981) are also available. The published profile data have been previously corrected by removal of diurnal variation, by tying to a common magnetic datum, and by removal of the International Geomagnetic Reference Field of 1975, updated to the time of the survey (1979). Magnetic profile 5 from High Life Helicopters, Inc., and QEB, Inc., (1981), on the west and approximately colinear profile 4 from High Life Helicopters, Inc., and QEB, Inc., (1980) on the east were selected as being closest to seismic-reflection profile SJ–19. Before analysis, the large magnetic anomalies at each end of the combined profiles (fig. 5.3) were smoothed by visual approximation to remove the very high frequency anomalies caused by exposed mafic and ultramafic rocks within 120 m of the helicopter. This smoothing was done only after careful inspection of profiles from several adjacent flightlines, so that the form of the broad, more deeply seated anomalies could be retained. The features removed had maximum wavelengths of about 10 km. Examination of adjacent flightlines and of the regional magnetic map of Blake and others (1978) indicates that the general configuration of the analyzed magnetic profile (fig. 5.3) extends well to the north and south of the profile; therefore, the assumption of two-dimensionality in the magnetic analysis is reasonably well met.

PHYSICAL PROPERTIES

Rock densities used for the gravity model were obtained from various sources. The densities of the Franciscan assemblage, the Great Valley sequence, and the basement of the Great Valley were generally derived from the preliminary seismic-refraction velocity model (Wentworth and others, 1984; Walter, 1985), using published velocity-density relations (J.P. Eaton, in Bateman and Eaton, 1967, p. 1412; Gardner and others, 1974). Other density information on Franciscan rocks is from Irwin (1961) and Stewart and Peselnick (1978). Basement beneath the west half of the Great Valley has relatively high compressional-wave velocities (6.3–6.6 km/s) and is assigned a density of 2.90 g/cm^3. The Franciscan assemblage in the refraction profile paralleling SJ–19 appears to display a range of compressional-wave velocities, increasing downward, from 4.8 to 6.0 km/s, and is assigned a relatively low density of 2.59 g/cm^3 for the near-surface material down to the 5-km-deep interface and of 2.71 g/cm^3 for the material at depths of 5 to 14 km. The Great Valley sequence is assigned a density of 2.49 to 2.61 g/cm^3 (velocities, 4.0–5.1 km/s); the highest densities are in the deepest part of the trough. Assigned densities for the Tertiary strata range from 2.07 to 2.37 g/cm^3 (velocities, 1.7–3.4 km/s), following the velocity-density curves for sandstone and shale (Gardner and others, 1974).

1. If the Coast Range ophiolite (serpentinite, mafic rocks, and partially serpentinized ultramafic rocks) is present in the subsurface along the cross section as a layer between the Great Valley sequence and the Franciscan assemblage, it is not evident in either the reflection or refraction data (see chaps. 3, 4). However, gravity surveys elsewhere across the exposed Coast Range ophiolite show that in most places it displays little or no clear gravity expression relative to the Franciscan assemblage and thus commonly has approximately the same density. Nevertheless, in the areas of Coast Range ophiolite known to contain significant amounts of mafic rocks (which are uncommon), the mafic rocks are denser than the surrounding rocks and cause a local gravity high. Therefore, the Coast Range ophiolite, if solely composed of low-density serpentinite, may have a density as low as 2.5 g/cm^3, whereas the ophiolite generally has a density of 2.60 to 2.70 g/cm^3 and, if significant amounts of mafic rocks are present, locally as great as 2.90 g/cm^3.
2. Rocks of the Sierra Nevada foothills are subdivided for the purposes of this chapter into two general groups, following the density data tabulated by Oliver and Robbins (1982). (1) The Kings-Kaweah ophiolite

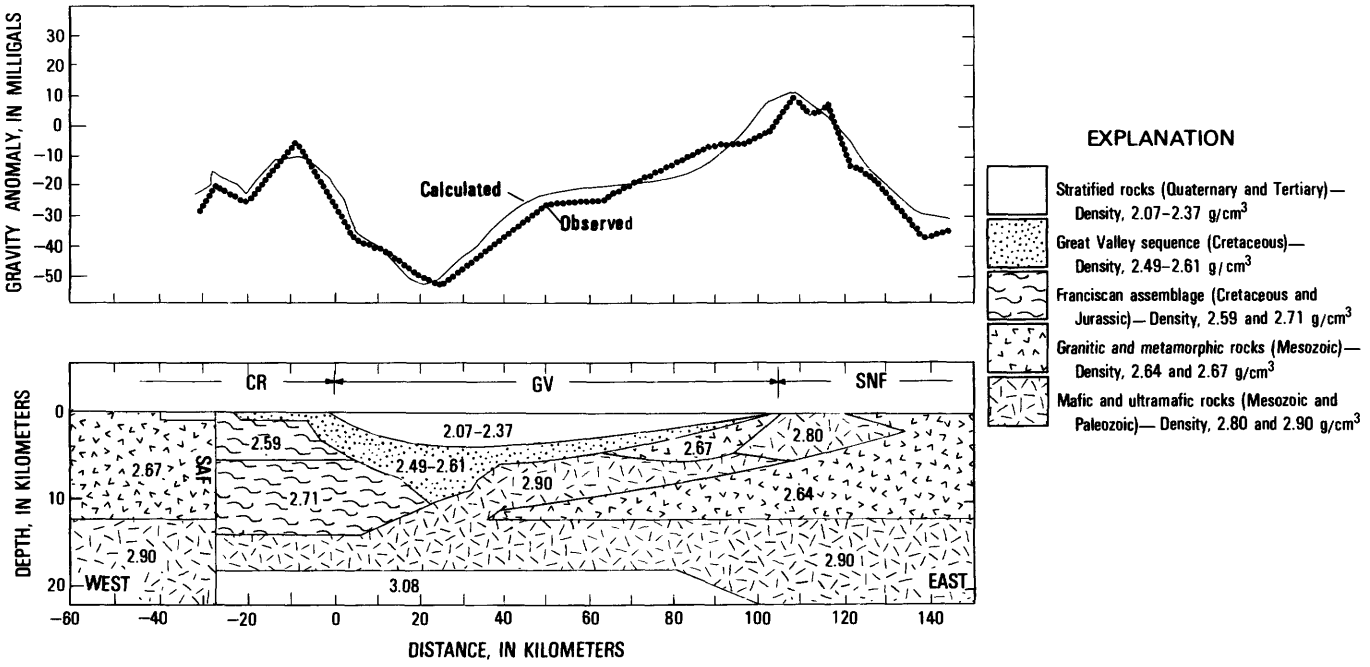

FIGURE 5.2.—Isostatic-residual-gravity profile and calculated density model extending from the San Andreas fault, across the Coalinga area and Great Valley, to the Sierra Nevada foothills. See figure 5.1 for locations. Circles, observed; X's, calculated. CR, Coast Ranges; GV, Great Valley; SAF, San Andreas fault; SNF, Sierra Nevada foothills. Thin, small masses exposed at the surface on each side of the San Andreas fault (SAF) are Tertiary sedimentary basins, with an assumed density of 2.2 g/cm^3. Note thin layer of Great Valley sequence overlying Franciscan assemblage in the Coast Ranges but continuous with similar strata in the Great Valley. Vertical exaggeration, ×2.

belt, including later intrusive gabbros of the Sierra Nevada batholith, contains much serpentinite (as well as higher density mafic and ultramafic rocks) and is assigned, somewhat arbitrarily, a density of 2.80 g/cm^3. (2) Granitic rocks of the Sierra Nevada batholith and small amounts of older metasedimentary and metavolcanic rocks are assigned a density of 2.64 g/cm^3, which may appear to be somewhat low but is supported by measurements on samples collected near the east end of the profile.

3. Magnetic properties assigned to the segments of the magnetic model have been chosen to match the amplitudes of the calculated anomalies with the observed anomalies. Because the upper surfaces of the magnetic model are mostly constrained by other data and because the model is already rather thick, the magnetic properties, though large, are essentially minimum values. Assigned magnetizations range from 3.3 to 5.5 A/m and are aligned in the direction of the present Earth's field. These values represent the vector sum of the induced and remanent magnetizations, which are both unknown for these rocks. Because the rocks of the magnetic units beneath the Great Valley are believed to have average densities of about 2.90 g/cm^3, as described above, substantial amounts of highly magnetic mafic and, possibly, partially serpentinized ultramafic rocks, in addition to relatively minor associated magnetic serpentinites, must be present. Lithologic data from a few deep drill holes penetrating basement in the central Great Valley (summarized by Thompson and Talwani, 1964) include gabbro, diabase, serpentinite, and mafic metaigneous rocks—all suitable components for the postulated ophiolite. Magnetic properties, however, have not been measured for these drill cores. The magnetic properties of rocks from the Kings-Kaweah ophiolite belt were measured by Saleeby (1975), who established that the younger Cretaceous gabbroic rocks are by far the most magnetic. The darker gabbros have an average remanent magnetization of 10 A/m and an average induced magnetization of about 1.8 A/m; the equivalent values of Saleeby for the less mafic gabbros are 5 and 1.8 A/m, respectively. The remanent-magnetization directions are scattered but lie approximately near that of the present Earth's field and thus may be primary—that is, may represent thermoremanent magnetization acquired at the time the intrusions cooled. Therefore, the major component for the highly magnetic mafic rocks in figure 5.3 may well be remanent magnetization, although the basement rocks under the west half of the Great Valley may be Jurassic and not necessarily similar in their properties to those of the Cretaceous gabbros. Rocks cropping out in the Coast Range ophiolite generally are pre-

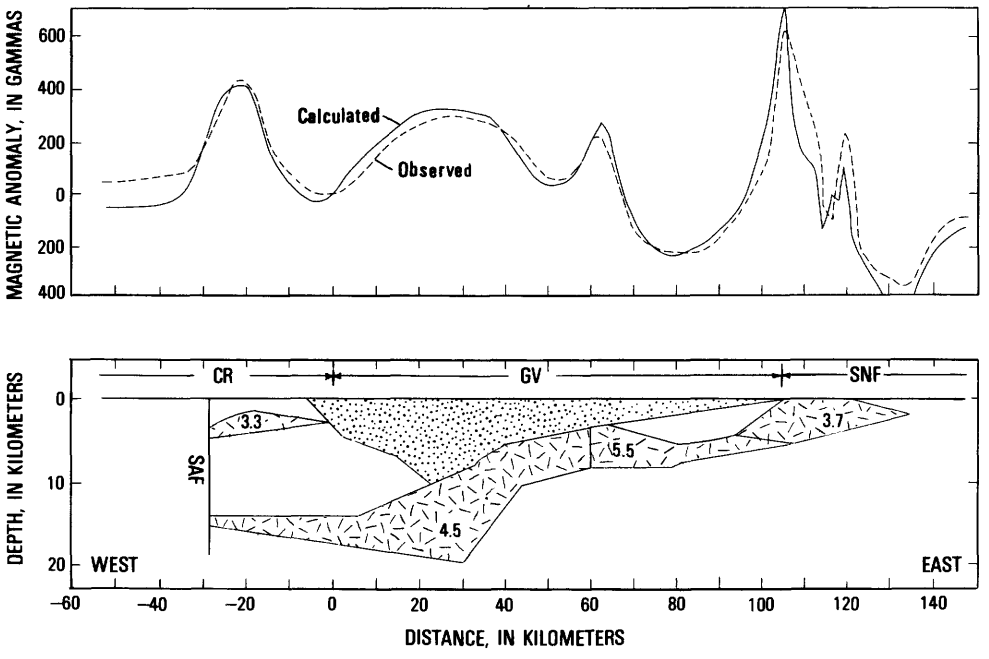

FIGURE 5.3.—Aeromagnetic profile and calculated magnetic model extending from the San Andreas fault, across the Coalinga area and Great Valley, to the Sierra Nevada foothills. Magnetic objects are labeled with magnetization values in amperes per meter and are mafic or ultramafic rocks. Stippled area is sedimentary rocks of Great Valley for easy comparison with figure 5.2. See figure 5.1 for locations. Same symbols as in figure 5.2. Vertical exaggeration, ×2.

dominantly serpentinite, for which measured magnetizations rarely are as large as the value of 3.3 A/m shown in figure 5.3 for the concealed magnetic mass at the west end of the profile. Mafic constituents of the Coast Range ophiolite have even weaker magnetizations than the serpentinites, on the basis of ground magnetic profiles and physical-property measurements by Griscom. Nevertheless, the result in figure 5.3 is plausible, and the magnetic data of Griscom (1977) for the extensive Trinity ophiolite in northern California show that enormous volumes of serpentinite there have total magnetizations higher than 8 A/m, although the associated gabbros are only weakly magnetic.

4. The high-density (2.90 g/cm^3) rocks underlying exposed crystalline rocks of the Sierra Nevada, and those of the area west of the San Andreas fault below depths of 15 km, are believed to differ significantly from the other magnetic rocks described above: They are probably nonmagnetic or, at most, very weakly magnetic because they do not appear to produce magnetic anomalies. These rocks may be metamorphosed mafic and ultramafic rocks, in part former oceanic crust or island-arc lower crust.

GRAVITY PROFILE

To test the seismic reflection and refraction models, we constructed an east-west isostatic residual-gravity profile (figs. 5.1, 5.2) approximately along and beyond seismic-reflection profile SJ–19, extending from the Sierra Nevada foothills on the east to the San Andreas fault on the west. This profile was then projected onto a line striking N. 60° E., approximately normal to the strike of the gravity contours and the geologic structure. Thus, the analysis could be conducted with a computer program that assumed two-dimensionality, and subsequently the profile was restored to its original east-west configuration.

The density model was initially constructed from an interpretation of the seismic-refraction profile paralleling SJ–19 (Wentworth and others, 1984; see chap. 4). This model was supplemented in the Sierra Nevada foothills by the seismic-refraction model of Eaton (1966), a longitudinal seismic cross section through the Sierra Nevada that indicates a depth of 12 km to the bottom of the 2.64-g/cm^3 layer. In addition, the deeper, 3.08-g/cm^3 layer is derived from the seismic-refraction profile of A.W. Walter (oral commun., 1985; see chap. 3), which is located transverse to the cross section and intersects it at approximately the 8-km point. The configurations of the various density units in the basement between 50 and 130 km in the profile are from the magnetic interpretation of figure 5.3.

The density units west of the San Andreas fault are not exactly based on the available refraction data but are somewhat arbitrarily set to match the crustal structure on the east end of the profile, so that there will be no significant gravity anomaly across the San Andreas fault, as is the case. The several seismic models, however, are not in mutual isostatic balance. In general, seismic-refraction data should be used in a gravity model only after determining that the total mass of each column of the seismic model is in balance with all the others, because gravity calculations are exceedingly sensitive to slight discrepancies in balance between adjacent seismic crustal models. (The densities of the various parts of the gravity model are discussed in the previous section.) We note that the density units of Tertiary deposits in the Great Valley follow the seismic-refraction velocity model and do not necessarily represent stratigraphic units. The bottom of the model at a depth of 23 km is arbitrary and represents the depth to which the model must be extended to explain the gravity features in terms of the various seismic data. All isostatic effects relating to topography have already been removed from the data, and such other factors as variations in crustal thickness are presumably accounted for by isostasy. The low-density materials in the sedimentary basin of the Great Valley are substantially compensated themselves by the deepest layer of density 3.08 g/cm^3. This layer is not well controlled and may partly include the effects of other, still deeper density distributions. Any additional, deeper density distributions needed to compensate these low-density sedimentary deposits will produce broad gravity anomalies of no more than 5 mGal, which are below the general precision level of the calculations.

GRAVITY INTERPRETATION

1. The gravity model is entirely consistent with the seismic-refraction model of Walter (see chap. 3) between the 0- and 50-km points on the horizontal scale.
2. The gravity model confirms the refraction-model interpretation, in that the top of basement in the Great Valley appears to extend westward as a relatively smooth, west-dipping surface from the deepest part of the basin (25-km point) all the way west to the 0-km point.
3. The gravity model shows that the steep basement slope or inflection between 35 and 40 km is the probable cause of a steep gravity gradient between 35 and 45 km. This gradient is a major feature of the Great Valley gravity field that extends on strike for 650 km along the length of the valley (Roberts and others, 1981) and suggests a similar extent for the causative structural feature. In addition, this feature occupies a consistent position some 40 to 50 km east of

the exposed Franciscan-Great Valley contact along its entire length.

4. The gravity model predicts a relatively low density mass (for convenience, 2.64 g/cm^3) at about 5-km depth below the basement surface and beneath the postulated Great Valley ophiolite (density, 2.90 g/cm^3) between 35 and 60 km. This interpreted density inversion should appear as a velocity inversion on the seismic-refraction data, but cannot be seen in the refraction model (see chap. 3) because the data do not extend below the basement surface in this location.
5. West of the seismic section between –8 and –16 km, the gravity data require that material with a density higher than 2.50 g/cm^3 be very close to the surface, and the model is satisfied by the chosen density of 2.59 g/cm^3. This result suggests that the Franciscan assemblage may be at very shallow depths here, even though a stratigraphic section of Great Valley strata at least 6 km thick is exposed at the surface (see chap. 4). The model in figure 5.2 between –8 and –16 km shows a thin (0.5 km thick) layer of Great Valley strata overlying the Franciscan assemblage; these two rock units are separated by a horizontal surface that is presumed to be a flat-lying thrust fault (the Coast Range fault?) cutting disconformably across the overlying Great Valley strata. We note that Franciscan rocks are, in fact, exposed between the San Andreas fault and –20 km where gravity values are unexpectedly somewhat lower than those between –8 and –16 km. The problem (of lower gravity over exposed Franciscan rocks to the west) can be partly resolved by assuming metamorphism of the near-surface Franciscan rocks between –8 and –16 km to high-pressure-mineral assemblages similar to those exposed in the serpentinite-cored antiform 20 km northwest of this part of the gravity profile (fig. 5.1), and so the upper portion of these concealed rocks may be denser than 2.59 g/cm^3. If the Franciscan assemblage here is denser, then the Great Valley sequence in the area could be somewhat thicker than shown in figure 5.2, but it must still be substantially thinner than the 6 km of strata exposed at the surface.
6. The configuration of density units in the basement between 60 and 130 km follows the magnetic interpretation of figure 5.3, and so the gravity model supports the magnetic interpretation. Because of the absence of seismic data, other gravity models and interpretations are also possible for this area, but the agreement with the magnetic model adds strength to the interpretation illustrated here. The exposed mafic and ultramafic rocks of the Kings-Kaweah belt from 105 to 125 km are modeled to be about 5.5 km thick, somewhat thinner than the 9-km layer modeled at a higher point on the anomaly by Saleeby (1975) and Oliver and Robbins (1982). The gravity and magnetic models both display a patch of low-density (2.67 g/cm^3) nonmagnetic rocks similar to those of the Sierra Nevada foothills at the basement surface between 65 and 105 km on the profile. We have left slight differences remaining between the models (figs. 5.2, 5.3) to emphasize that these details are not necessarily meaningful for either model.
7. The isolated shallow magnetic mass at the west end of the magnetic profile (fig. 5.3; see next section) is not evident in the seismic data and fails to cause a gravity anomaly (fig. 5.2). It is interpreted to be Coast Range ophiolite, which, as mentioned above, generally fails to cause a gravity anomaly where exposed because the ultramafic rocks are serpentinized to lower densities, comparable to those of the adjacent sedimentary rocks, and because mafic rocks are scarce.

MAGNETIC PROFILE AND INTERPRETATION

The magnetic data in figure 5.3 were projected onto a line striking N. 60° E., normal to the strike of the data, and the model was then calculated from the observed aeromagnetic profile, using a computer program which assumes that the data are two dimensional, an approximately correct assumption here (see magnetic-contour map of Blake and others, 1978). The final model and data were then projected back to the original east-west configuration and illustrated as figure 5.3. Constraints for this model include: (1) the form of the basement surface of the Great Valley, as determined from the seismic and gravity models between the San Andreas fault (at –28 km) and 50 km; (2) drill-hole data defining the basement surface of the Great Valley east of 50 km; and (3) mapped exposures of the Kings-Kaweah ophiolite belt in the Sierra Nevada foothills at the east edge of the Great Valley. The magnetic properties of the rocks are discussed above; the direction of magnetization is assumed to be that of the present Earth's field. An additional constraint is available for the isolated body of magnetic rock in the upper left (west) corner of the model; the west end of this rock mass is believed to be terminated by the San Andreas fault on the basis of the pattern of contours for this anomaly (Blake and others, 1978). These constraints place substantial limitations on the ordinary ambiguities of any potential-field interpretation.

The anomaly bounded by –28 and 0 km on the magnetic profile is caused by a relatively shallow magnetic object; the source of this anomaly, a slab of magnetic material shown in the upper left (west) corner of the model, is terminated by the San Andreas fault, and so the causative object cannot be more than a few kilometers deep and is relatively tabular, with a convex top. A few local

magnetic highs caused by exposed serpentinite were removed from the west half of the anomaly in figure 5.3 by hand-smoothing, as previously mentioned; these small serpentinite bodies may be surface exposures of the Coast Range ophiolite. The existence of several small exposed masses of serpentinite in the Franciscan assemblage at the surface above this magnetic object (fig. 5.3) offers additional evidence that the object is probably at shallow depth. This magnetic anomaly and its source are major regional features, extending nearly continuously for 600 km along strike at the Great Valley-Franciscan contact (Blake and others, 1978; Griscom, 1983). Over much of this distance, the anomaly is partly concealed by a superimposed magnetic anomaly caused by exposed rocks of the Coast Range ophiolite, but the problem is not serious here because the serpentinite masses are relatively minor along our profile (fig. 5.1). The western part of the source generally lies beneath rocks of the Franciscan assemblage (fig. 5.3), whereas the eastern part is generally situated at or near the inferred contact between the Great Valley sequence and the Franciscan assemblage (fig. 5.3; Griscom, 1983). These observations, together with the common association of the central part of the mass vertically beneath the exposed Coast Range fault and Coast Range ophiolite, strongly suggest that the rocks causing the concealed magnetic feature are also themselves Coast Range ophiolite.

The magnetic anomaly between 0 and 50 km on the profile is the Great Valley magnetic anomaly (Griscom, 1966; Cady, 1975), which extends north-southward along the entire Great Valley for a distance of 700 km. Here, in the southern Great Valley, the anomaly is relatively smooth and wide, with a lower amplitude than farther north; but it is relatively uniform in both shape and amplitude (Blake and others, 1978). These observations suggest that the shape and position of the anomaly are due predominantly to the geometric form (or structure) of the causative rock mass. The same observations also require a great thickness (approx 10 km) of magnetic material in the model. To generate such an anomaly, this maximum thickness of the magnetic mass must be under the approximate center of the anomaly, and so an east-dipping bottom is necessary between the San Andreas fault and 30 km on the profile (the upper surface is constrained by seismic and drill-hole data). Because heat flow here decreases eastward from the Coast Ranges toward the Great Valley (Lachenbruch and Sass, 1980), this east-dipping boundary may approximately represent an isothermal surface below which the remanent magnetization of the rocks has been destroyed.

The magnetic model additionally supports the refraction-model interpretation, in that the top of Great Valley basement appears to extend westward as a relatively smooth, west-dipping surface from 40 to at least 0 km on the profile. There is no evidence on the magnetic profile for any significant vertical offset in this basement surface, such as might be the expected expression of a possible former subduction zone on the downdip extension of the inferred east-dipping Coast Range fault (presumably situated along the Great Valley-Franciscan contact). The position of the vertical boundary at the east border (60 km) of the magnetic rock mass causing the Great Valley magnetic anomaly approximately agrees with that of the boundary between crystalline rocks of the Sierra Nevada and ophiolitic rocks shown on a preliminary basement map of the Great Valley based on drill-hole data (C.W. Wentworth, written commun., 1985). The general form of the mass causing the Great Valley magnetic anomaly is that of a thick west-dipping slab; this structure was interpreted to represent a slab of ophiolite obducted from the west onto the continent during Jurassic time (Griscom, 1982).

Between 60 and 70 km on the profile is a high that represents an elliptical magnetic anomaly, one member of a belt of three such anomalies between here and Bakersfield, 100 km to the southeast (Blake and others, 1978), which are probably caused by mafic intrusions, possibly related to the Sierra Nevada batholith (fig. 5.3). The intrusion according to our model appears to be connected (by means of magnetic rocks in the basement subsurface) with the magnetic rocks in the Kings-Kaweah ophiolite belt (at 105–125 km) and their associated, highly magnetic gabbroic intrusions related to the Sierra Nevada batholith (fig. 5.3). An area of nonmagnetic basement rocks, about 5 km thick, similar to those of the Sierra Nevada foothills, lies at the top of Great Valley basement between 65 and 105 km on the profile.

CONCLUSIONS

1. Our gravity and magnetic models provide strong support for, and agree well with, the seismic refraction and reflection models in chapters 3 and 4.
2. The magnetic data identify a concealed subhorizontal, sheetlike magnetic mass (magnetization, 3.3 A/m; depth, 2–4 km below the surface), the west end of which lies beneath the Franciscan assemblage at the west end of the profile and the east end of which may lie structurally between Franciscan rocks and overlying Great Valley strata. This magnetic mass, which probably consists mostly of serpentinite, may be equivalent to the Coast Range ophiolite. The feature is of major regional importance, extending nearly continuously for 600 km along strike at the Great Valley-Franciscan contact. The feature has no gravity expression, just as the exposed Coast Range ophiolite generally has no gravity expression elsewhere, because its density is similar to that of the adjacent Franciscan assemblage.

3. The gravity and magnetic models do not identify a major basement step or discontinuity at the projected downdip intersection of the east-dipping Coast Range fault with the basement surface of the Great Valley, and so they do not support the existence of an east-dipping fossil subduction zone at this point. We believe that the Coast Range fault is the expression of a refaulted former subduction zone from which the downdip extension has been removed by later thrust faulting in the opposite direction (west-rooted rather than east-rooted).
4. The magnetic mass causing the Great Valley magnetic anomaly is a thick west-dipping slab of ophiolite obducted from the west onto the continental margin during Jurassic time, on the basis of correlation with the Coast Range ophiolite of Jurassic age. The magnetic and gravity models predict a low-velocity zone beneath the ophiolite between 35 and 60 km in figures 5.2 and 5.3. If the inferred ophiolite underlying the Great Valley does, indeed, correlate with the exposed Coast Range ophiolite, then the ultramafic rocks of the Coast Range ophiolite were metamorphosed to low-density serpentinite (approx 2.60–2.70 g/cm^3) after being tectonically separated from the ophiolite of the Great Valley, because the Great Valley ophiolite has a relatively high compressional-wave velocity and, accordingly, a density of about 2.90 g/cm^3, too high for a well-serpentinized rock unit.
5. Conclusions 2, 3, and 4 support the idea that the Franciscan assemblage was here emplaced by tectonic wedging (Wentworth and others, 1984) and that two separate wedges of the Franciscan assemblage may be consistently present on top of each other. These two wedges are separated by the slab of presumed Coast Range ophiolite identified on the magnetic model (conclusion 2). The Coast Range ophiolite may have been ripped off the ophiolite basement of the Great Valley by the advancing wedges.
6. The steep gravity gradient between 30 and 45 km on the gravity profile is caused by an abrupt westward deepening or downwarping of Great Valley basement and a consequent rapid westward thickening of the overlying Mesozoic sedimentary section. This gravity gradient is a consistent linear feature along the entire 700-km length of the Great Valley, and so its structural cause is equally consistent. The linear basement downwarp may have operated as a resistant barrier or dam to the Franciscan tectonic wedges intruding eastward along the basement surface of the Jurassic ophiolite from the west; its presence may explain the parallel relation of the downwarp to the exposed Great Valley-Franciscan contact and associated structures.
7. East of the area defined by the seismic results, the gravity and magnetic models agree closely and indicate that the dense, magnetic gabbro plutons intruding the Kings-Kaweah ophiolite at the boundary between the Great Valley and the Sierra Nevada foothills may be connected by similar rocks at depth with a belt of inferred mafic intrusions near 65 km on the profile.

REFERENCES CITED

Bailey, E.H., Blake, M.C., Jr., and Jones, D.L., 1970, On-land Mesozoic oceanic crust in California, *in* Geological Survey research, 1970: U.S. Geological Survey Professional Paper 700–C, p. C70–C81.

Bailey, E.H., Irwin, W.P., and Jones, D.L., 1964, Franciscan and related rocks, and their significance in the geology of western California: California Division of Mines and Geology Bulletin 183, 177 p.

Bateman, P.C., and Eaton, J.P., 1967, Sierra Nevada batholith: Science, v. 158, no. 3807, p. 1407–1417.

Blake, M.C., Jr., Irwin, W.P., and Coleman, R.G., 1967, Upside down metamorphic zonation, blueschist facies, along a regional thrust in California and Oregon, *in* Geological Survey research, 1967: U.S. Geological Survey Professional Paper 575–C, p. C1–C9.

Blake, M.C., Jr., Zietz, Isidore, and Daniels, D.L., 1978, Aeromagnetic and generalized geologic map of parts of central California: U.S. Geological Survey Geophysical Investigations Map GP–918, scale 1:1,000,000.

Cady, J.W., 1975, Magnetic and gravity anomalies in the Great Valley and western Sierra Nevada metamorphic belt, California: Geological Society of America Special Paper 168, 56 p.

Eaton, J.P., 1966, Crustal structure in northern and central California from seismic evidence, *in* Subcrustal structure, chap. 9 *of* Bailey, E.H., ed., Geology of northern California: California Division of Mines and Geology Bulletin 190, p. 419–426.

Gardner, G.H.F., Gardner, L.W., and Gregory, A.R., 1974, Formation velocity and density-the diagnostic basics for stratigraphic traps: Geophysics, v. 39, no. 6, p. 770–780.

Griscom, Andrew, 1966, Magnetic data and regional structure in northern California, *in* Subcrustal structure, chap. 9 *of* Bailey, E.H., ed., Geology of northern California: California Division of Mines and Geology Bulletin 190, p. 407–417.

—— 1977, Aeromagnetic and gravity interpretation of the Trinity ophiolite complex, northern California [abs.]: Geological Society of America Abstracts with Programs, v. 9, no. 4, p. 426–427.

—— 1982, Magnetic interpretation of ophiolites and batholiths in California [abs.]: Geological Society of America Abstracts with Programs, 1982, v. 14, no. 7, p. 503.

—— 1983, The contact between the Great Valley Sequence and the Franciscan Assemblage, California, from magnetic data [abs.]: Eos (American Geophysical Union Transactions), v. 64, no. 45, p. 867–868.

Hamilton, Warren, 1969, Mesozoic California and the underflow of Pacific mantle: Geological Society of America Bulletin, v. 80, no. 12, p. 2409–2430.

—— 1978, Mesozoic tectonics of the western United States, *in* Howell, D.G., and McDougall, K.A., eds., Mesozoic paleogeography of the western United States: Pacific Coast Paleogeography Symposium 2: Los Angeles, Society of Economic Paleontologists and Mineralogists, Pacific Section, p. 33–70.

High Life Helicopters, Inc., and QEB, Inc., 1980, Airborne gamma-ray spectrometer and magnetometer survey, Fresno quadrangle, California [1° by 2° sheet; National Uranium Resource Evaluation program, GJBX–231 (80)]: Grand Junction, Colo., U.S. Department of Energy.

—— 1981, Airborne gamma-ray spectrometer and magnetometer survey, Santa Cruz quadrangle, California [1° by 2° sheet; National Uranium Resource Evaluation program, GJBX-050 (81)]: Grand Junction, Colo., U.S. Department of Energy.

Holbrook, W.S., Mooney, W.D., Walter, A.W., and Catchings, R.D., 1985, Crustal structure of the Great Valley, California, from seismic refraction data [abs.]: Geological Society of America Abstracts with Programs, v. 17, no. 6, p. 362.

Irwin, W.P., 1961, Specific gravity of sandstones in the Franciscan and related upper Mesozoic formations of California, art. 78 *of* Short papers in the geologic and hydrologic sciences: U.S. Geological Survey Professional Paper 424-B, p. B189-B191.

Jachens, R.C., and Griscom, Andrew, 1983, Three-dimensional geometry of the Gorda Plate beneath North America: Journal of Geophysical Research, v. 88, no. B11, p. 9375-9392.

Jennings, C.W., compiler, 1977, Geologic map of California: California Division of Mines and Geology Geologic Data Map Series 2, scale 1:750,000.

Lachenbruch, A.H., and Sass, J.H., 1980, Heat flow and energetics of the San Andreas fault zone: Journal of Geophysical Research, v. 85, no. B11, p. 6185-6222.

Lanphere, M.A., 1971, Age of the Mesozoic oceanic crust in the California Coast Ranges: Geological Society of America Bulletin, v. 82, no. B11, p. 3209-3211.

Matthews, R.A., and Burnett, J.L., compilers, 1965, Fresno sheet *of* Geologic map of California: Sacramento, California Division of Mines and Geology, scale 1:250,000.

May, J.C., and Hewitt, R.L., 1948, The basement complex in well samples from the Sacramento and San Joaquin Valleys: California Journal of Mines and Geology, v. 44, no. 2, p. 129-158.

Oliver, H.W., and Griscom, Andrew, 1980, Great Valley, *in* Oliver, H.W., ed., Interpretation of the preliminary gravity map of California and its continental margin: California Division of Mines and Geology Bulletin 205, p. 27-30.

Oliver, H.W., and Robbins, S.L., 1982, Fresno sheet *of* Bouguer gravity map of California: Sacramento, California Division of Mines and Geology, 23 p., scale 1:250,000.

Roberts, C.W., Jachens, R.C., and Oliver, H.W., 1981, Preliminary isostatic residual gravity map of California: U.S. Geological Survey Open-File Report 81-573, scale 1:750,000, 5 sheets.

Saleeby, J.B., 1975, Structure, petrology, and geochronology of the Kings-Kaweah mafic-ultramafic belt, southwestern Sierra Nevada foothills, California: Santa Barbara, University of California, Ph.D. thesis, 200 p.

—— 1978, Kings River ophiolite, southwest Sierra Nevada foothills, California: Geological Society of America Bulletin, v. 89, no. 4, p. 617-636.

Stewart, R.M., and Peselnick, Louis, 1978, Systematic behavior of compressional velocity in Franciscan rocks at high pressure and temperature: Journal of Geophysical Research, v. 83, no. B2, p. 831-839.

Thompson, G.A., and Talwani, Manik, 1964, Crustal structure from Pacific Basin to central Nevada: Journal of Geophysical Research, v. 69, no. 22, p. 4813-4837.

Walter, A.W., 1985, Velocity structure near Coalinga, California, *in* Rymer, M.J., and Ellsworth, W.L., eds., Mechanics of the May 2, 1983 Coalinga, California, earthquake: U.S. Geological Survey Open-File Report 85-44, p. 10-18.

Wentworth, C.M., Blake, M.C., Jr., Jones, D.L., Walter, A.W., and Zoback, M.D., 1984, Tectonic wedging associated with emplacement of the Franciscan assemblage, California Coast Ranges, *in* Blake, M.C., Jr., ed., Franciscan geology of northern California (book 43): Los Angeles, Society of Economic Paleontologists and Mineralogists, Pacific Section, p. 163-173.

6. TECTONIC HISTORY AND THRUST-FOLD DEFORMATION STYLE OF SEISMICALLY ACTIVE STRUCTURES NEAR COALINGA

By J.S. NAMSON,[1]
ARCO OIL AND GAS CO.;

and

T.L. DAVIS[1] and M.B. LAGOE,[2]
ARCO EXPLORATION CO.

CONTENTS

ABSTRACT

The stratigraphy of the Coalinga region can be divided into tectostratigraphic facies whose boundaries delineate two major tectonic events—one in the mid-Cenozoic (38–17 Ma) and one in the late Cenozoic (less than 3 Ma). The succession of these tectostratigraphic facies, and an integration of geology, subsurface well data, a seismic-reflection profile, and earthquake seismicity on a retrodeformable cross section, yield a model for the tectonic evolution of the Coalinga region. This model suggests that the structural style of both deformational events is characteristic of fold and thrust belts. Our model also indicates that the causative fault of the May 2 earthquake is a ramped thrust. The results of this study, in combination with regional geologic relations, suggest that the Coalinga region is part of an active fold and thrust belt which borders the west and south sides of the San Joaquin Valley. The potential for future earthquakes due to movement of other "blind" thrust faults within this belt should be evaluated.

INTRODUCTION

The Coalinga main shock (M=6.7) of May 2, 1983, and subsequent aftershocks have resulted in new attempts to understand the origin of structural deformation in the central California Coast Ranges. Surface geologic maps (Dibblee, 1971) and subsurface geologic studies (Kaplow, 1945) show that the region consists of northwest-trending folds which plunge mostly south (fig. 6.1). The causative structure for the earthquake has remained somewhat of a mystery because no major faults are recognized on the surface or in the shallow subsurface, and only minor tectonic ground breakage was associated with an aftershock of the May 2 event (see chap. 16; Clark and others, 1983). It is apparent, however, from these observations and the 7- to 11-km depth of the main-shock hypocenter (Sherburne and others, 1983) that the causative fault is active at depth; and tight oil-well control indicates that this fault does not extend to within 1 to 3 km of the surface. Any explanatory structural model must accommodate these features.

Several structural models have been proposed to explain the origin of late Cenozoic deformation and associated seismicity in the Coalinga region (Oakeshott, 1968; Harding, 1976; Stein, 1983). In this study, we use geologic mapping, subsurface well correlations, the stratigraphic and biostratigraphic record, seismic-reflection profiles, and earthquake seismicity data to develop an internally consistent model that explains the tectonic, geologic, and structural history of the region. The main results of this analysis are construction of a kinematically restorable cross section and a model for the tectonic

[1]Current affiliation: Davis & Namson, Glendale, CA 91208.
[2]Current affiliation: Department of Geological Sciences, University of Texas, Austin, TX 78713.

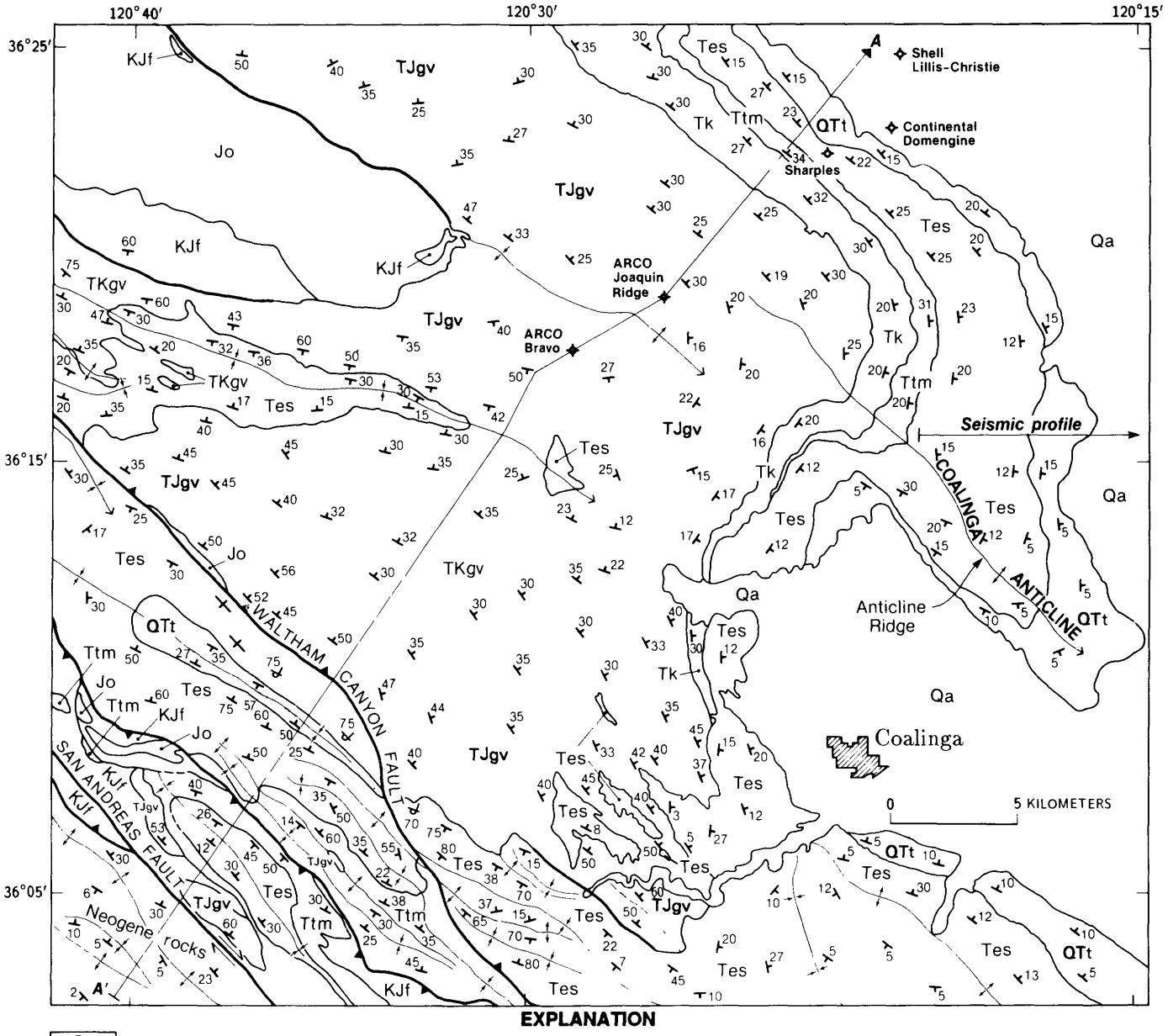

EXPLANATION

- Qa — Alluvium (Quaternary)
- QTt — Tulare Formation (Pleistocene and Pliocene)
- Tes — Etchegoin and San Joaquin Formations, undivided (Pliocene and Miocene)—represents late Miocene-Pliocene facies
- Ttm — Temblor, Monterey, Big Blue, Santa Margarita and Reef Ridge Formations, undivided (Miocene)—represents Miocene facies
- Tk — Kreyenhagen Formation and lower Eocene and Paleocene rocks, undivided (Eocene and Paleocene)—represents Paleocene-Eocene facies
- TJgv — Great Valley sequence (Paleocene to Jurassic)
- KJf — Franciscan assemblage (Cretaceous and Jurassic)
- Jo — Coast Range ophiolite (Jurassic)

- Contact — Dashed where approximately located
- Fault — Arrows indicate direction of relative movement
- Thrust fault — Sawteeth on upper plate
- Strike and dip of beds
  - Inclined
  - Vertical
  - Overturned
- Syncline — Arrow indicates direction of plunge
- Anticline — Arrow indicates direction of plunge

FIGURE 6.1.—Geologic map of the Coalinga, California, area (modified from Dibblee, 1971), showing locations of structural cross section *A–A′* in figure 6.3 and seismic-reflection profile in figure 6.4.

history across the Coalinga region. Our structural interpretation also suggests that the main shock was caused by movement on a low-angle thrust.

This chapter begins with a review of the local stratigraphy and the principal structural and stratigraphic relations of the Coalinga region. Next, we describe the details of our structural interpretation for the Coalinga region and the sequence of tectonic events that this interpretation indicates, as well as alternative structural models proposed for the region and our reservations about these models. Finally, we discuss the effects of the thrust-fold mechanism on surface deformation and the seismic and tectonic implications of thrust-fold structural style with respect to the western and southern margins of the San Joaquin Valley.

STRATIGRAPHY OF THE COALINGA REGION

Stratigraphic relations in the Coalinga region reflect a complex depositional and tectonic history. We use these relations to divide the section into tectostratigraphic facies that bracket the major geologic events and provide both relative and numerical timing for these events (fig. 6.2). The numerical time scale is derived from a calibration of various biozonations with the paleomagnetic time scale and radiometric ages (for example, Keller and Barron, 1981; Barron, 1986). This time scale is principally derived by using data from the study area (for example, Repenning, 1976; Obradovich and others, 1978; Obradovich and Naeser, 1981; J.A. Barron, oral commun., 1984; S.A. Graham, oral commun., 1984), augmented by some regional data (for example, Keller and Barron, 1981; Lindberg, 1984; Barron, 1986).

First, we briefly summarize the relevant characteristics of each tectostratigraphic facies used in reconstructing the tectonic history of the region.

FRANCISCAN ASSEMBLAGE AND COAST RANGE OPHIOLITE

The structurally and, probably, stratigraphically lowest rocks in the Coalinga region belong to the Franciscan assemblage. These rocks are composed of melange and coherent units of sandstone, shale, and chert that yield both Jurassic and Cretaceous fossils (Page, 1981). The Franciscan assemblage is exposed in the core of the Diablo Range, where it is tectonically overlain by the Coast Range ophiolite along the Coast Range thrust (Page, 1981). The Coast Range ophiolite is generally composed of ultramafic plutonic rock, basalt, serpentinite, volcanic breccia, and chert. The plutonic rocks yield radiometric ages of 163±2 to 165±2 Ma (Hopson and others, 1981).

We note that the Coast Range ophiolite in the core of the Coalinga anticline consists mostly of serpentinite (Dibblee, 1971); it was omitted from the regional study by Hopson and others (1981). This serpentinite body has generally been considered to be one of many ultramafic bodies that are common within the Franciscan assemblage (Page, 1981). We include the serpentinite body within the Coast Range ophiolite because it occurs in a typical structural position, at the top of the Franciscan assemblage and at the base of the Great Valley sequence (fig. 6.1). Furthermore, the serpentinite is far larger than any known ultramafic inclusion within the Franciscan assemblage (C.A. Hopson, oral commun., 1984), but similar in size to known exposures of the Coast Range ophiolite throughout the Coast Ranges.

Under the San Joaquin Valley, the Coast Range ophiolite and, presumably, the Coast Range thrust dip gently west (see chap. 4; Wentworth and others, 1983). Thus, the relative depth of the Coast Range ophiolite in the deformed Coalinga region versus its depth in the San Joaquin Valley can be used to determine the total structural relief between the Coalinga anticline and the valley.

GREAT VALLEY SEQUENCE

The Great Valley sequence, which depositionally overlies the Coast Range ophiolite, consists of as much as 8 km of Cretaceous to Paleocene rocks in the Coalinga area (J.Q. Anderson, unpub. data, 1941; Payne, 1962). The sequence is principally composed of marine conglomerate, sandstone, and shale; siliceous shale and diatomite are common near the top (Payne, 1962; J.C. Ingle, oral commun., 1984). In many areas along the western and southern margins of the San Joaquin Valley, part or all of the Great Valley sequence has been removed by erosion beneath the basal Paleocene-Eocene facies or basal Miocene facies. The provenance for the Great Valley sequence was the Mesozoic Sierra Nevada (Payne, 1962).

PALEOCENE-EOCENE TECTOSTRATIGRAPHIC FACIES

A major regional unconformity (disconformity or very low angle unconformity in the Coalinga region) separates the Great Valley sequence from lower Tertiary marine strata of the Paleocene-Eocene facies (Nilsen and McKee, 1979). This facies is composed of marine Paleocene to early Eocene rocks of the Lodo Formation, Domengine Sandstone, Avenal Sandstone, and Kreyenhagen Formation (Mallory, 1959; Foss and Blaisdell, 1968; Addicott, 1972). The absence or near-absence of angular discordance between this facies and the Great Valley sequence on the Coalinga anticline suggests that this part of the Coast Ranges was not a tectonic high from Late Cretaceous through early Tertiary time. Previous work suggests that the dominant sediment source was from the

east (Graham and Berry, 1979; Nilsen and McKee, 1979). The time gap between the Great Valley sequence and the Paleocene-Eocene facies coincides with, and may reflect, emplacement of the Coast Range thrust. However, the absence of an angular discordance between these two tectostratigraphic facies (Dibblee, 1971) suggests that the geometry of the thrust must have been a decollement (parallel to bedding) in the Coalinga region.

MIOCENE TECTOSTRATIGRAPHIC FACIES

The Paleocene-Eocene facies is overlain unconformably by the Miocene tectostratigraphic facies, which is

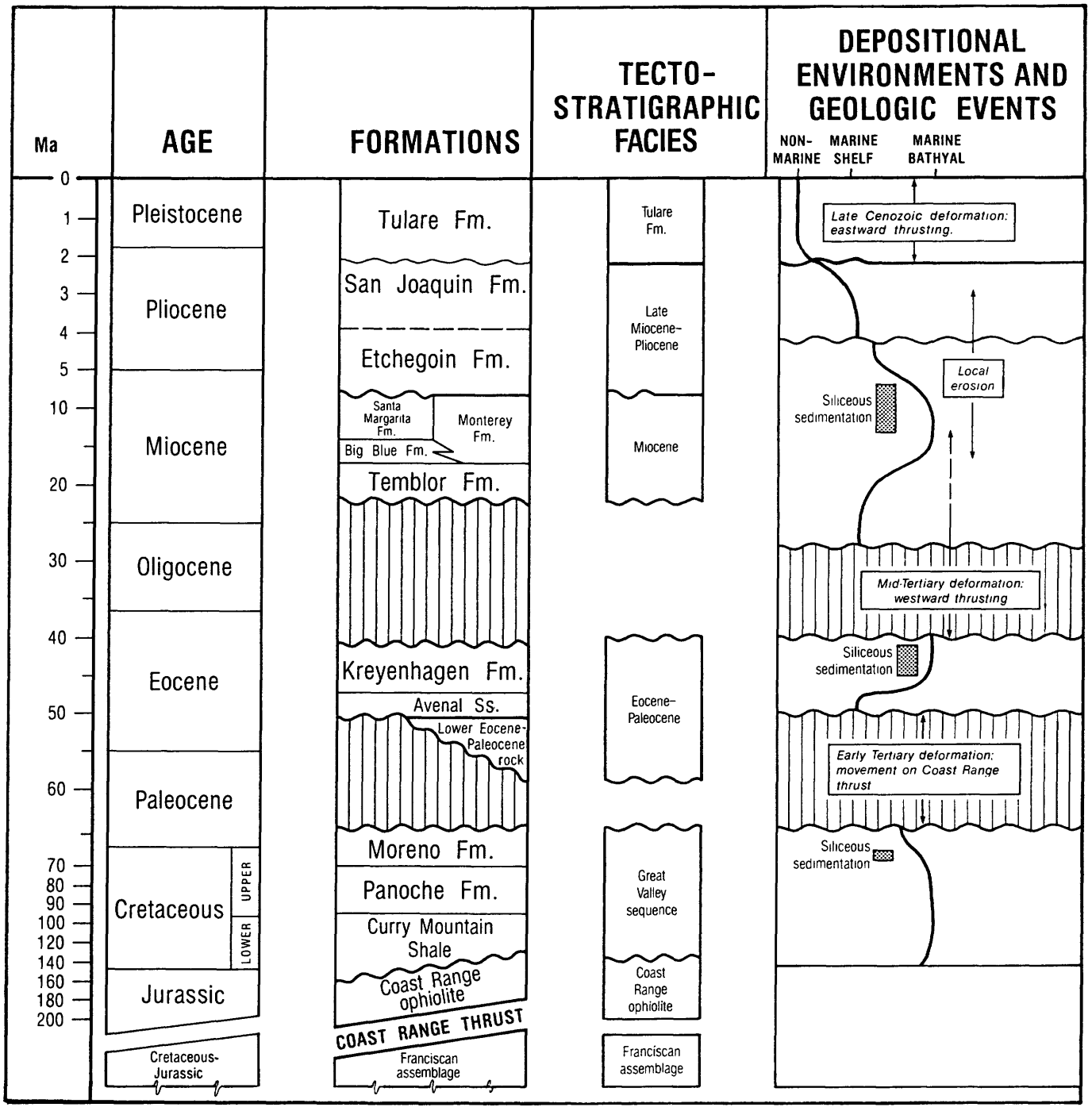

FIGURE 6.2.—Stratigraphy in the Coalinga, California, area. Stratigraphic correlation with the numerical time scale is derived from intercalibration of biozonations, radiometric ages, and the paleomagnetic time scale. Formations are grouped into tectostratigraphic facies that bracket major tectonic events in the Coalinga region.

composed of various units, including the upper part of the Temblor, Big Blue, Santa Margarita, Monterey (McClure Shale Member), and Reef Ridge Formations. The basal unconformity of this facies coincides with a striking change in the paleogeography of the San Joaquin Basin from a west-facing continental slope (Nilsen and McKee, 1979) to an asymmetric semiclosed basin.

In the area of the Coalinga anticline (for example, the Coalinga Nose) the lower part of the Miocene facies (upper part of the Temblor Formation) is composed of shallow-marine sandstone and conglomerate, commonly containing metamorphic-rock fragments and chert clasts (Adegoke, 1969). These basal rocks contain "Temblor"-stage mollusks, indicating an age no older than late Saucesian or early Relizian (late early Miocene; Adegoke, 1969; Bate, 1985; Coolery, 1985). Serpentinite clasts become more abundant near the top of the Temblor Formation, which is overlain by a chaotic sequence of serpentinite boulders of the Big Blue Formation (Adegoke, 1969). The Big Blue Formation, in turn, is overlain by shallow-marine sandstone and conglomerate of the Santa Margarita Formation that contain abundant clasts of Franciscan assemblage. The coarseness and provenance of these deposits probably reflect unroofing of the Coalinga anticline and exposure of the Coast Range ophiolite and Franciscan assemblage (Bate, 1984). South and east of the Coalinga anticline, the Big Blue and Santa Margarita Formations grade laterally into shale, siliceous shale, and sandstone of the Monterey Formation and the Reef Ridge Shale (Woodring and others, 1940; Stewart, 1946; Adegoke, 1969).

The basal unconformity, lithologies, coarse deposits, and rapid facies changes reflect development of a topographic high in the Coalinga region (Bate, 1984), in response to mid-Cenozoic tectonism before and during deposition of the Miocene tectostratigraphic facies. This high was situated near the present-day Coalinga anticline. The age of basal Temblor sedimentary deposits becomes older (as old as Zemorrian; Oligocene), and deeper marine environments occur both to the east and southeast of this high (Woodring and others, 1940; Bate, 1984, 1985; Kuespert, 1985). The magnitude of this basal unconformity was evidently accentuated by the Coalinga anticline.

In addition, we emphasize that the Miocene basal unconformity is not restricted to the Coalinga region but is widespread in the San Joaquin Basin (Bandy and Arnal, 1969; Nilsen and others, 1973), including the central and southern Diablo Range (Dibblee, 1973), the Temblor Range (Dibblee, 1973), and the San Emigdio Mountains (Davis and Lagoe, 1984). Thus, the mid-Cenozoic tectonism responsible for this unconformity (angular in many places) was also expressed regionally along the western and southern margins of the San Joaquin Basin and not just within the Coalinga region (Namson and Davis, 1984).

LATE MIOCENE-PLIOCENE TECTOSTRATIGRAPHIC FACIES

The late Miocene-Pliocene facies is composed of the Etchegoin and San Joaquin Formations. In the vicinity of the Coalinga anticline, the basal part of the Etchegoin Formation onlaps and overlies older facies with an angular discordance of as much as 30° (fig. 6.1). In other places, however, such as Reef Ridge (approx 30 km south of Coalinga), the late Miocene-Pliocene facies is conformable on the Miocene facies. The Etchegoin Formation, which is late Miocene and Pliocene in age (Repenning, 1976; J.A. Barron, oral commun., 1984), is composed of about 1,000 m of nonmarine and marine sandstone and mudstone (Adegoke, 1969). It is overlain by the Pliocene San Joaquin Formation, which is 500 to 1,000 m thick and, within the Coalinga region, is composed of complexly interbedded marine and nonmarine sandstone and mudstone becoming more marine to the east and south.

The angular unconformity at the base of the late Miocene-Pliocene facies is also present throughout the central California Coast Ranges (summarized by Christensen, 1965). We believe that these shallow-marine to nonmarine sedimentary rocks were deposited on erosional remnants of the structures which formed during mid-Cenozoic tectonism. Thus, deposition of the late Miocene-Pliocene facies postdates the mid-Cenozoic tectonic event and represents a period during which little structural relief existed in the Coalinga region.

TULARE FORMATION

The Tulare Formation, which is late Pliocene and Pleistocene in age, forms the youngest tectostratigraphic facies. It was deposited within a basin that covered the present San Joaquin Valley and extended farther to the west (Foss, 1972). Along the Coalinga anticline, it consists of about 100 m of nonmarine sandstone, conglomerate, and mudstone, deposited in fluvial and lacustrine environments. In the Coalinga region, the Tulare Formation/late Miocene-Pliocene facies contact ranges from a conformity to an angular unconformity; the area of conformable contact occupied part of the depositional axis of the Tulare-age basin. In contrast, the Tulare Formation along much of the west edge of the San Joaquin Valley rests with angular discordance on older rocks (Foss, 1972). Along the Coast Range mountain front and within the Diablo Range, the Tulare Formation is overlain unconformably by alluvial terraces. The Tulare Formation represents synorogenic deposits formed during the late Cenozoic deformational event in response to

uplift of the Coalinga anticline and nearby Coast Ranges (Christensen, 1965).

STRUCTURAL AND STRATIGRAPHIC RELATIONS

Several structural relations indicating multiple phases of deformation must be accounted for in any structural interpretation of the Coalinga region. For example, the structural relief varies for different stratigraphic units. The maximum structural relief on the Coalinga anticline along cross section *A–A'* (fig. 6.3) is 6 to 7 km, calculated by comparing the depth of the base of the Great Valley sequence along the fold axis with its depth in the undeformed San Joaquin Valley to the east. However, the structural relief at the base of the late Miocene-Pliocene facies is only 2.5 km, calculated by measuring the change in elevation of the base of this facies from the anticlinal axis (by projection to the line of section, fig. 6.1) to its position in the San Joaquin Valley to the east. The 30° angular discordance of the folded late Miocene-Pliocene facies on the Great Valley sequence and Paleocene-Eocene facies observed in the southern, central, and eastern parts of the map area (fig. 6.1) also indicates at least two phases of deformation.

Furthermore, geologic relations along the Waltham Canyon fault indicate multiple deformations. This fault separates a thick, east-dipping homoclinal section of Great Valley sequence on the east from an overturned syncline of the Miocene facies, late Miocene-Pliocene facies, and Tulare Formation on the west. The Miocene facies west of the fault unconformably overlies the Franciscan assemblage or a thin section of Great Valley sequence. This relation is observed at the surface (fig. 6.1) and in shallow drill holes in the area. Thus, 6 to 7 km of Great Valley sequence is missing beneath the Miocene facies unconformity. The absence of this section is due to uplift and erosion, before Miocene facies deposition, during the mid-Cenozoic deformation phase. The steep dips within upper Cenozoic rocks (late Miocene-Pliocene facies and Tulare Formation) in the syncline west of the Waltham Canyon fault suggests that this area was also deformed during the late Cenozoic deformation phase.

Another explanation for the juxtaposition of thick and thin Great Valley units along the Waltham Canyon fault is lateral transport as a result of strike-slip motion. However, the sinuous trace, the associated overturned syncline to the west, and the homoclinal sequence to the east of this fault suggest that it is an east-side-up thrust (note barbs on fault trace, fig. 6.1). These relations reflect a common structural geometry observed in fold and thrust belts (Dahlstrom, 1970).

Geologic relations along the east flank of the Coalinga anticline and the relatively small folds farther east in the San Joaquin Valley (for example, the Turk anticline, fig. 6.3) must be included in models of the tectonic history of the region. Thinning and shallowing of the Miocene facies from the valley onto the east flank of the Coalinga anticline suggest that the anticline was a paleogeographic high during Miocene facies deposition (Bate, 1984, 1985). The angular discordance between the Miocene and late Miocene-Pliocene facies west and south of the Coalinga anticline is absent along the eastern limb (fig. 6.1). This relation suggests that although the anticline was a positive feature during Miocene facies deposition, the mid-Cenozoic deformation did not extend so far eastward as the present-day structure. More recent deformation (late Cenozoic) has extended eastward, as evidence by the angular discordance between the Tulare Formation and late Miocene-Pliocene facies, and the present limits of the active Coalinga anticline. This angular discordance is generally small (approx 5°) but present regionally to the north and south of the study area (Dibblee, 1971). The Turk anticline, one of many small Pliocene to Quaternary folds along the west side of the San Joaquin Valley (fig. 6.3), probably resulted from eastward migration of the late Cenozoic deformation. This deformation has caused about 200 m of structural relief at the Turk anticline, as revealed by subsurface well correlations of paleontologic and electric-log marker horizons.

STRUCTURAL INTERPRETATION

The structural interpretation presented here is primarily based on construction of a kinematically restorable cross section (fig. 6.3). Our interpretation accounts for the stratigraphic relations, depositional history, major unconformities, geometry of folds and faults, and structural relief in the Coalinga region. In constructing the cross section, we employed the "balanced cross section" techniques that have been developed and are commonly used in fold and thrust belts (Dahlstrom, 1969; Bally and others, 1966; Suppe, 1983; Cooper and others, 1983). Although these techniques do not assure a unique solution, they give one that is kinematically possible (Elliot, 1983).

The general structural style of map-scale folds and faults in the Coalinga region suggests a thrust-belt geometry, as is also indicated by a seismic-reflection profile and earthquake seismicity, as discussed below. In addition, a thrust-belt deformational style has been suggested previously for parts of the northern Coast Ranges (Suppe and Foland, 1978; Suppe, 1978; Phipps, 1984a) and the western Transverse Ranges (Davis, 1983, 1986; Yeats, 1983; Namson, 1987). Thus, the general deformational style of our solution (fig. 6.3) is characteristic of fold and thrust belts where bedding-plane thrusts step upsection to higher levels, resulting in folds of the

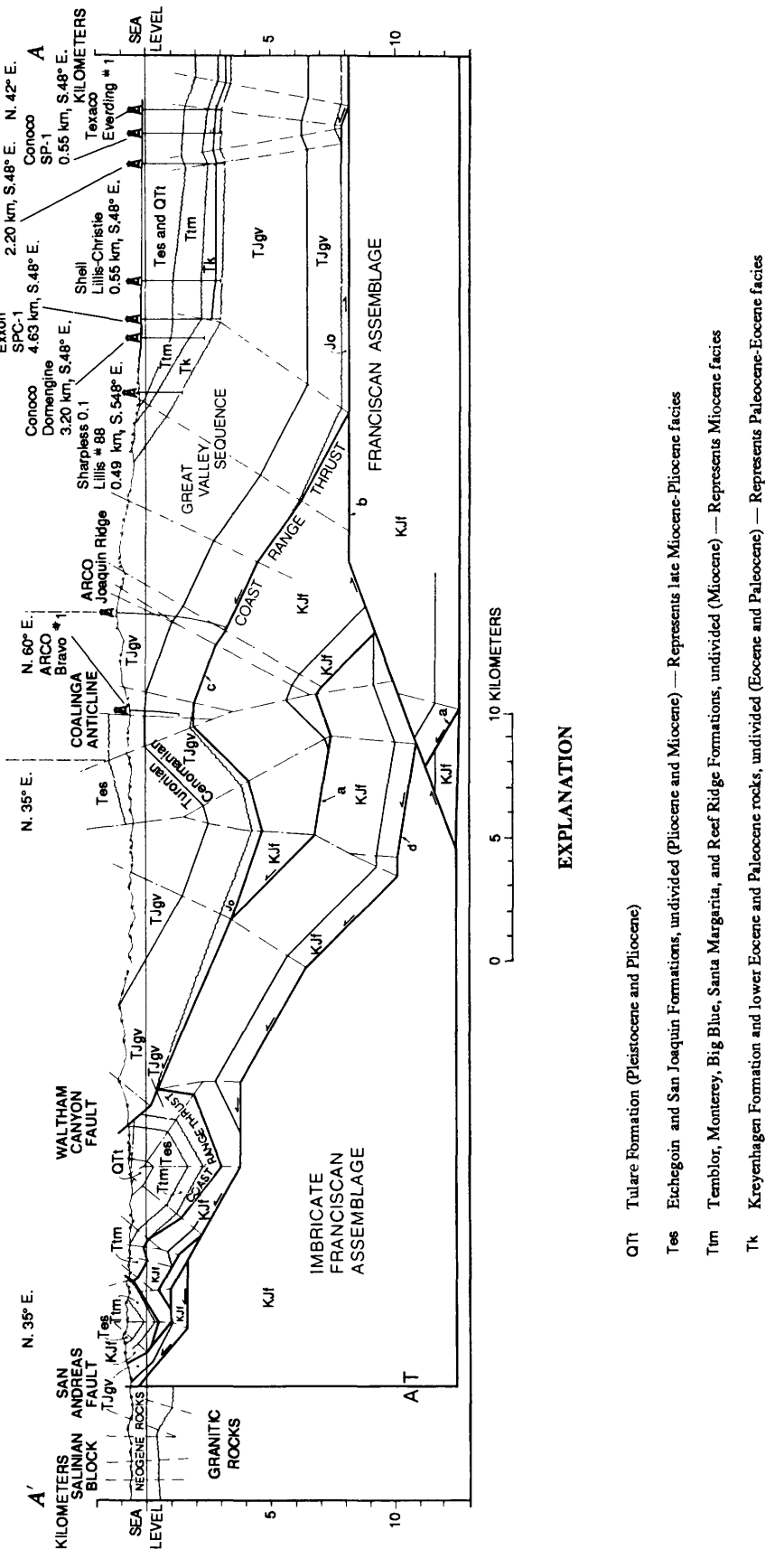

FIGURE 6.3.—Geologic cross section *A–A'* (see fig. 6.1 for location), illustrating general low-angle thrust geometry and multiphase deformations in the Coalinga region. Surface dips are from the geologic map, and dipmeter data (dashed lines on wells) are from well logs. Dot-dashed lines, construction lines; a–d, faults explained in text.

hanging-wall sheet (Rich, 1934; Dahlstrom, 1970; Boyer and Elliot, 1982; Suppe, 1983). The following explanation shows that this deformational style can satisfactorily account for the observed complex geologic relations in the Coalinga region.

The total structural relief on the Coalinga anticline is 6.7 km, as determined from fold geometry, biostratigraphy, and unit thicknesses in the ARCO Joaquin Ridge No. 1 well, and from stratigraphic thicknesses in the undeformed section east of the fold (fig. 6.3). The angular unconformity and lower structural relief at the base of the late Miocene-Pliocene facies show that the structural development must have occurred in at least two phases: a mid-Cenozoic phase (before late Miocene-Pliocene facies deposition) and a late Cenozoic phase (during Tulare Formation deposition, less than 3 Ma).

The Etchegoin Formation of the late Miocene-Pliocene facies is a widespread deposit over much of the central Coast Ranges (Hoots and others, 1954; Christensen, 1965; Dibblee, 1971). Thus, the geometry of the mid-Cenozoic deformation can be partly determined by restoring the basal late Miocene-Pliocene facies angular unconformity (approx 30°) to horizontal. This restoration shows that the pre-late Miocene-Pliocene facies Coalinga anticline had a western-limb dip of 20°–30° and a total structural relief of approximately 4.2 km. The absence of a basal late Miocene-Pliocene facies angular unconformity on the east flank of the Coalinga anticline marks an east boundary to the mid-Cenozoic deformation. In our solution, we hypothesize that the mid-Cenozoic structural relief of the Coalinga anticline resulted from a thrust (fault a, fig. 6.3) that ramps up to the west, forming an upper-plate fold. The exact position of this fault beneath the Coalinga anticline is not well constrained; nonetheless, its presence is required to explain the origin of structural relief at that time, as well as the fold geometry. No other faults are known near the surface or from subsurface drilling that can account for this structural deformation.

The mid-Cenozoic deformation was more intense and resulted in greater structural relief west of the Coalinga anticline. Subsequent erosion caused the removal of 6 to 7 km of Great Valley sequence west of the Waltham Canyon fault before Miocene facies and late Miocene-Pliocene facies deposition. This structural relief is shown to result from a westward-directed imbricate stack of Franciscan assemblage (fig. 6.3). Although little control exists on the internal geometry of this stack, large structural relief is required to explain the missing Great Valley sequence.

Westward motion of the mid-Cenozoic thrust system is assumed for several reasons. (1) The structural relief requires a minimum of several tens of kilometers of slip on the faults. If the thrusts are eastward directed, then we must explain their rapid termination into coeval, but undeformed, strata of the San Joaquin Valley; westward-directed thrusts are not so constrained by a similar undeformed section. (2) As indicated by the Paleocene-Eocene facies/Miocene facies unconformity (38–17 Ma), the thrust belt was partly active in the Coalinga region simultaneously with the Farallon/North American subduction zone. This subduction zone is presumed to have North America as the overriding plate, a relation consistent with westward-directed thrusting (Atwater, 1970). (3) The thrust-belt-style structural interpretation based on regional mapping in the northern Coast Ranges also indicates westward-directed thrusting (Suppe, 1978; Phipps, 1984a).

Initiation of late Cenozoic deformation is documented by the late Miocene-Pliocene facies/Tulare Formation angular unconformity. The lithology and age of the Tulare Formation indicate that it is a synorogenic deposit, and so its deformation generally diminishes upsection and eastward into the San Joaquin Valley. Because the late Miocene-Pliocene facies predates late Cenozoic deformation, its geometry can be used to determine the amount of folding and structural relief during this deformation phase.

The late Cenozoic structural relief on the Coalinga anticline is interpreted to have resulted from a major thrust that ramps up to the east from about 12.5- to 8-km depth (fault b, fig. 6.3). Several lines of evidence support the position and geometry of this fault: (1) It can satisfy the geometry of the fold observed in the surface and subsurface, (2) it is consistent with seismic-reflection data (fig. 6.4), and (3) it is supported by earthquake data.

Our geometric analysis suggests that the structural relief on fault b is about 2.5 km and that the slip along the higher decollement is nearly 6 km. As this thrust sheet is translated eastward up the ramp, the resulting fold increases in structural relief, refolding the western limb (Great Valley sequence/late Miocene-Pliocene facies unconformity in the Coalinga anticline). Eastward translation of the hanging-wall cutoff onto the higher decollement generates the eastern limb of the anticline. The eastern limb of the preexisting fold that formed during mid-Cenozoic deformation is translated up the ramp but not onto the higher decollement (see fig. 6.5). Thus, the structural relief increases with no refolding of the eastern limb.

A seismic-reflection profile over the eastern limb of the Coalinga anticline (fig. 6.4), located several kilometers south of cross section *A–A′* (see fig. 6.1), also supports the presence of fault b in figure 6.3. At a depth of about 4.3 s, east-dipping reflectors terminate downward into flat reflectors. This discordance is interpreted as the flat

thrust (higher decollement of fault b, fig. 6.3) that is overlain by a hanging-wall-cutoff section of the Franciscan assemblage.

Initial seismologic studies of the Coalinga earthquake sequence also support the presence of a low-angle thrust beneath the Coalinga anticline (Eaton and others, 1983; O'Connell and Murtha, 1983). In a more detailed analysis of the earthquake sequence, Eaton (see chap. 8) argues that seismicity on several faults may be necessary to explain the distribution and orientation of focal mechanisms

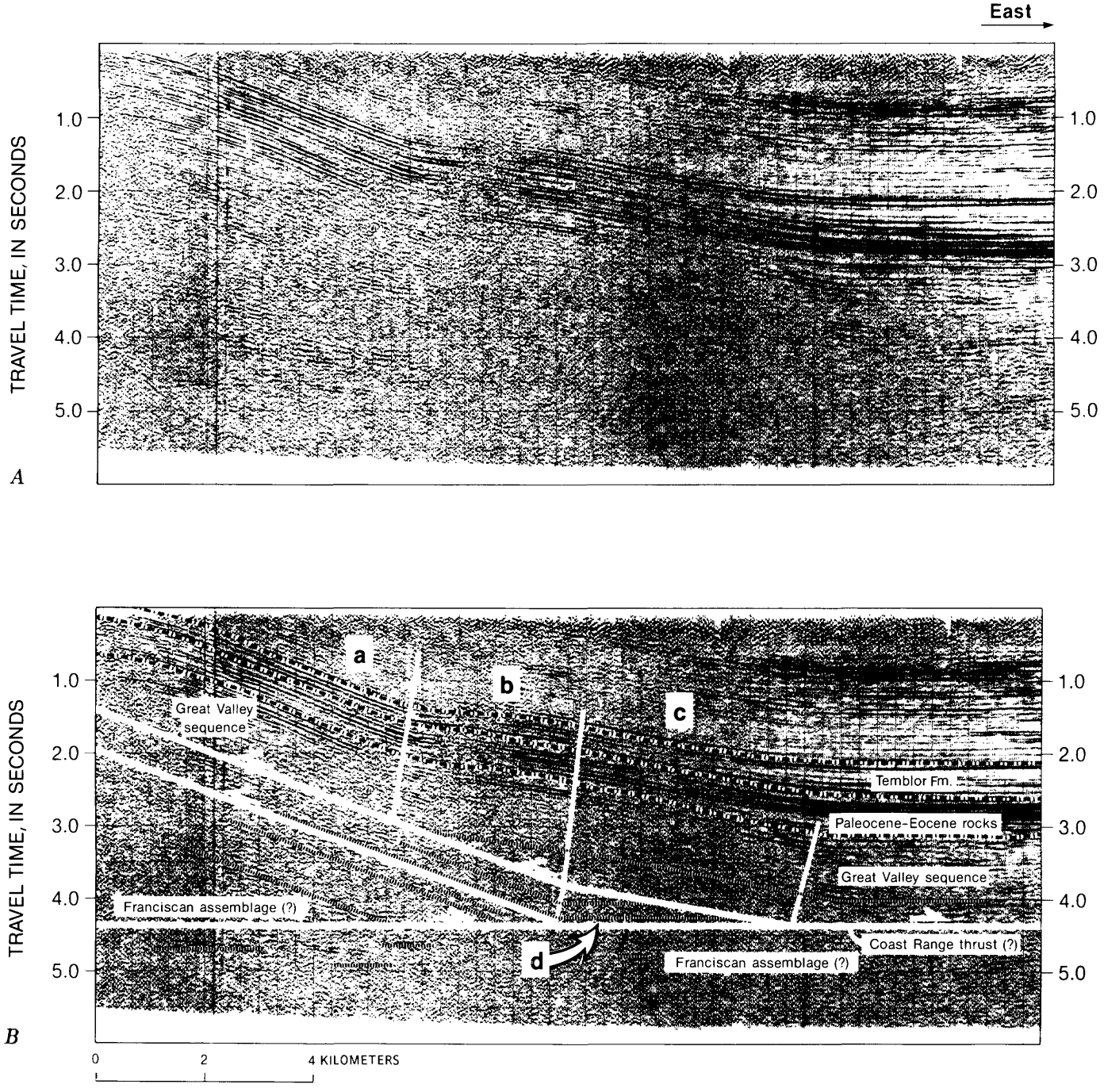

FIGURE 6.4.—Seismic-reflection profile SJ–3 through eastern limb of the Coalinga anticline (see fig. 6.1 for location). *A*, data; *B*, interpretation. Low-angle thrust geometry is illustrated by downward termination of east-dipping reflectors into flat reflectors at about 4.3 s. Structural complexity of eastern limb is due to a backthrust. Origin of fold panels a, b, and c is discussed in text. Fault d is upper detachment for the Coalinga ramp anticline.

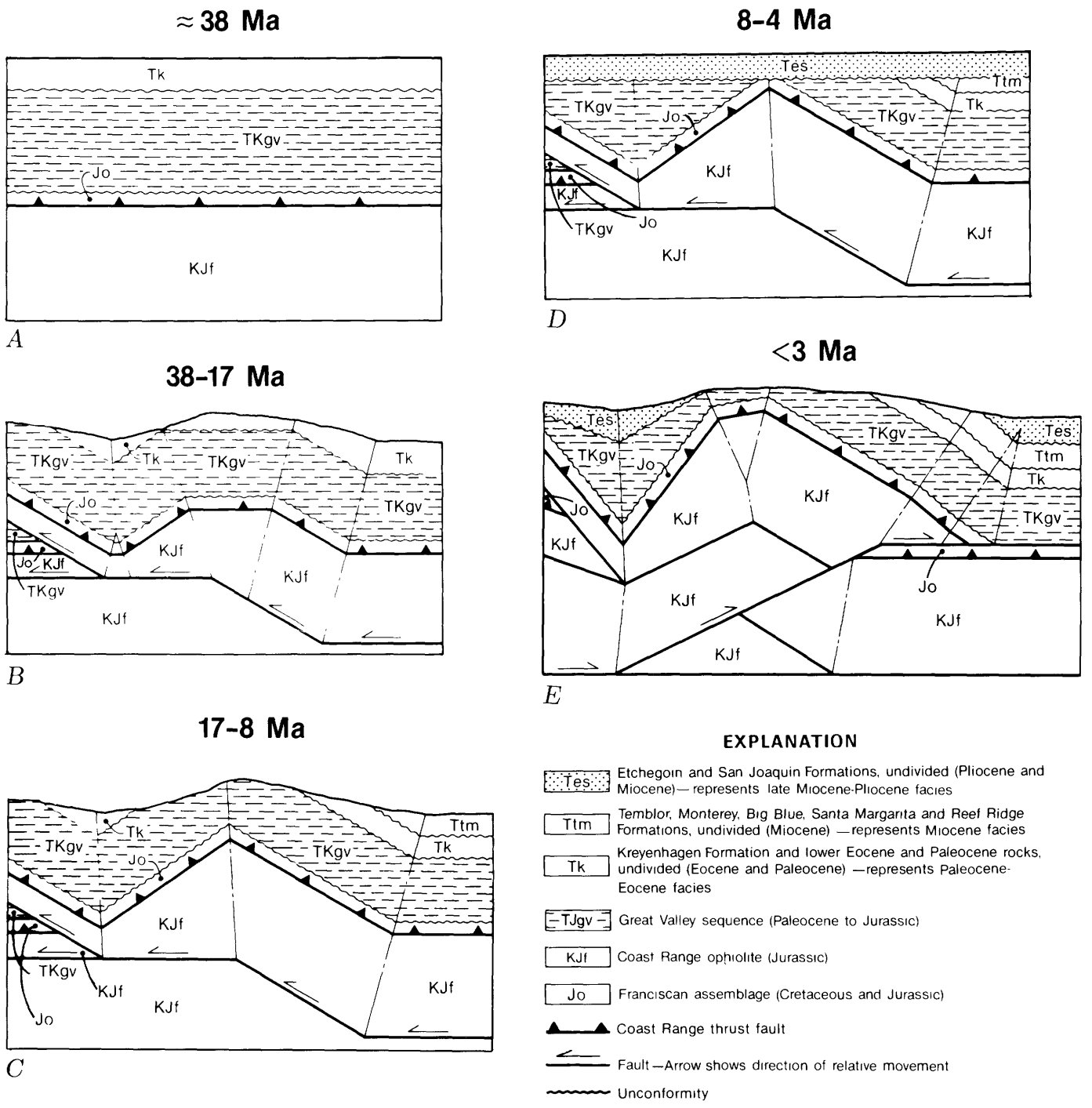

FIGURE 6.5.—Structural evolution of the Coalinga region. *A*, End of Paleocene-Eocene facies deposition, about 38 Ma. The Coast Range thrust is already emplaced, and no angular discordance exists between the Franciscan assemblage, Coast Range ophiolite, Great Valley sequence, and Paleocene-Eocene facies. Dominant sediment source is the Sierran arc to the east. *B*, Mid-Cenozoic deformation, beginning 38–17 Ma. Structural style is movement on westward-directed, low-angle thrusts. Basal Temblor Formation deposition occurs near the end of this interval. *C*, Erosion of the Coalinga anticline is dominant during 17–8 Ma, with decreasing deformation. The Miocene facies is deposited, derived locally from structures in the Coalinga area. *D*, The Coalinga anticline is eroded to base level by 8 Ma, and the late Miocene-Pliocene facies is deposited during 8–4 Ma. *E*, Before Tulare Formation deposition, later than 3 Ma, late Cenozoic deformation occurs on eastward-directed, low-angle thrusts. Dot-dashed lines, construction lines.

of the more than 100 events studied. He concludes, however, that the sum of the evidence strongly favors a thrust-fault solution for the main shock. Thus, thrust movement on fault b may have been the source of the May 2 earthquake.

Our solution shows nearly 6 km of slip continuing eastward on the higher decollement. This slip must be accounted for by shortening of the overlying thrust sheet. Some slip can be absorbed by westward-directed faults in forming the small folds, like the Turk anticline, that border the western margin of the San Joaquin Valley. Our structural interpretation for the Turk anticline shows a reversal of slip direction to the west and formation of a ramp-related fold; this structure accounts for about 1 km of slip on the main decollement. Some slip may also be taken up in smaller scale structures that are not expressed at the surface; however, there is not enough observed deformation within the San Joaquin Valley to account for the remaining 5 km of slip.

We hypothesize that much of the excess eastward-directed slip indicated for fault b reverses to westward-directed slip along the decollement at the base of the Great Valley sequence (fault c, fig. 6.3). Fault c breaks the surface as the Waltham Canyon fault, which juxtaposes the Great Valley sequence with small slivers of serpentinite (Coast Range ophiolite) over the late Miocene-Pliocene facies (figs. 6.1, 6.3). Deformation of the late Miocene-Pliocene facies and the Tulare Formation in the footwall of the Waltham Canyon fault probably results from late Cenozoic backthrusting along a structurally lower thrust (possibly reactivation of part of the mid-Cenozoic deformation thrust plane) or deeper thrust splays of the Waltham Canyon fault. This solution links deformation of the Waltham Canyon fault with growth of the thrust-related Coalinga anticline. Therefore, we might expect the May 2 earthquake to have caused surface rupture along the Waltham Canyon fault, although such surface breakage has not been reported.

Slip reversal on backthrusts can be documented for the Coalinga area on the seismic-reflection profile (fig. 6.4), which is located south of cross section *A–A′* (fig. 6.1). The main feature of this profile is the angular discordance at 4.3 s that separates near-horizontal reflectors below from east-dipping reflectors above; this discordance is interpreted as a deep detachment surface. However, some complexities in the fold limb above the detachment surface suggest the presence of a backthrust. The fold limb can be separated into three dip panels: steep dips on the west (a, fig. 6.4), gentle dips in the middle (b, fig. 6.4), and steep dips on the east (c, fig. 6.4). The east panel of steep dips is caused by a backthrust ramping upsection to the west, with flat reflectors beneath it (d, fig. 6.4). The fault follows a bedding plane, where it intersects the fold axis bounding the major hanging-wall cutoff. The gently dipping panel results from translation of the hanging-wall cutoff (b, fig. 6.4) of the backthrust from the ramp position onto a higher bedding-plane position (c, fig. 6.4).

Several folds and faults are exposed at the surface between the Waltham Canyon fault and the San Andreas fault (figs. 6.1, 6.3). Although most structural relief in this area is associated with mid-Cenozoic deformation, the late Miocene-Pliocene facies and the Tulare Formation have also been deformed here during the late Cenozoic event. We interpret these structures to have a thrust origin. Slip on the various faults shown in the cross section (fig. 6.3) roots into the same lower decollement (fault d, fig. 6.3) of the Coalinga anticline. The total late Cenozoic slip on this section of the fault system is about 2.5 km. As the thrust climbs to the surface, it ramps upsection in several places, causing folding of the hanging-wall sheet. Some of the slip reverses direction, forming eastward-directed thrust faults at the surface; all of the slip probably reaches the surface east of the San Andreas fault.

TECTONIC EVOLUTION OF THE COALINGA ANTICLINE

We constructed a sequential diagrammatic model for the evolution of the Coalinga anticline by combining the stratigraphic relations with our structural interpretation (fig. 6.5). This model, which begins at about 38 Ma (all numeric age estimates are derived from calibration of local biostratigraphic and chronostratigraphic information to regional time scales; see Lindberg, 1984; Barron, 1986), shows a stratigraphic sequence of Franciscan assemblage, Coast Range ophiolite, Great Valley sequence, and Paleocene-Eocene facies at the surface (fig. 6.5*A*). At 38 Ma, the Coast Range thrust was already emplaced, and the overlying units were undeformed. Below the Coast Range thrust, the Franciscan assemblage had a complex internal deformational fabric that developed before emplacement of the thrust (Page, 1981). Our sequential model does not attempt to explain the nature of these older deformational events. The absence of angular discordance between the Great Valley sequence and the Paleocene-Eocene facies indicates that the Coast Range thrust was a decollement over the Coalinga anticline and thus did not create any upper-plate structural relief.

The mid-Cenozoic deformation, between about 38 to 17 Ma, is represented by the angular discordance separating the Paleocene-Eocene facies and Miocene facies (fig. 6.5*B*). We believe that mid-Cenozoic thrusting explains the major shift in provenance and the change in paleogeography during this hiatus. The structural style was westward-directed low-angle thrusting.

From 17 to 8 Ma, the Coalinga anticline was being eroded, and the Miocene facies was being deposited on its flanks (fig. 6.5*C*); however, diminishing deformation associated with the westward-directed thrust system may have continued into the Miocene. Late-stage deformation is suggested by such coarse-grained deposits as the Big Blue Formation, and significant erosion of the Franciscan assemblage and Coast Range ophiolite in the core of the Coalinga anticline.

By 8 Ma, the Coalinga anticline was substantially eroded and unconformably covered by the late Miocene-Pliocene facies (fig. 6.5*D*). The fine-grained texture of this facies, which is as young as 4 Ma, is due to tectonic quiescence in the Coalinga region. The late Cenozoic deformation, which began before Tulare Formation deposition (later than 3 Ma), created the angular discordance between the late Miocene-Pliocene facies and the Tulare Formation in parts of the Coalinga region. This deformation is characterized by movement on eastward-directed, low-angle thrusts that continue to be seismically active, as evidenced by the May 2 earthquake (fig. 6.5*E*).

ALTERNATIVE STRUCTURAL MODELS FOR THE COALINGA REGION

Several other structural models for the Coalinga region have been proposed to explain the origin of the May 2, 1983, main shock and the development of the Coalinga anticline during the late Cenozoic (fig. 6.6). Stein (1983), using geodetic-elevation changes subsequent to the main shock, postulated a reverse fault, dipping 67° NE., beneath the nose of the Coalinga anticline (Anticline Ridge) (figs. 6.6*A*, 6.6*B*). This fault would extend from a depth of 10–13 km up to 3–5 km below the surface before dying out. Stein estimated that the cumulative dip slip required on this buried fault to create the fold at Anticline Ridge is from 2 to 5 km.

There are several problems with Stein's interpretation. First, this model requires the Coalinga anticline to be a large drape fold above a buried fault. Drape folds are characterized by an asymmetric profile, and so the fold limb above the fault should show evidence of extension (Stearns, 1978; Weinberg, 1978). If the total structural relief on the Coalinga anticline resulted from buried high-angle faults, then the deformation mechanism would require extensive thinning on the fold limbs. However, there is no evidence for bed thinning on fold limbs from surface geology (Dibblee, 1971) and subsurface data (Kaplow, 1945); instead, these data indicate parallel folding and bedding-plane slip as the deformational style. Fuller and Real (1983) took issue with Kaplow's mapping of the top of the Kreyenhagen Formation and postulated the presence of a high-angle reverse fault that cuts the top of the formation along the west side of Anticline Ridge. Kaplow's mapping, however, is based on extremely tight well control, which would have documented even a very small displacement fault if it existed. Furthermore, Stein's model is inconsistent with the seismic-reflection data (fig. 6.4), and studies of the Coalinga earthquake sequence also indicate a low-angle fault plane (see chap. 8; O'Connel and Murtha, 1983). Harding (1976) proposed that the Coalinga anticline lies within a set of northwest-trending, echelon wrench folds that developed along the west side of the San Joaquin Valley in response to right-lateral shear on the San Andreas fault system (fig. 6.6*C*). Fuller and Real (1983, p. 180), using this wrench-fault model, proposed that the May 2 earthquake was "* * * a manifestation of strain accumulation related to the San Andreas fault zone which has relieved compressive stresses." Page (1981), with considerable reservation, extended the wrench-fault deformational style to include most late Cenozoic folds, thrusts, and mountain building of the Coast Ranges. Christensen (1965) and Davis (1983), however, questioned the validity of the wrench-fault deformational model in explaining late Cenozoic uplift, thrust faulting, and folding in the Coast Ranges and north-central Transverse Ranges. They pointed out several problems in applying the wrench-fold model to explain late Cenozoic deformation in these areas.

The structural geometry of the Coalinga region is incompatible with the structural style of wrench faulting. The previously presented surface and subsurface data indicate that the Coalinga anticline is not associated with oblique-slip faults that steepen with depth, as is considered characteristic of wrench faulting (Lowell, 1972). Furthermore, the seismic-reflection line shows that the Coalinga anticline is underlain by relatively flat reflectors, which indicate a structural style inconsistent with models of wrench-fault folding. No significant strike-slip faults are present within the Coalinga area east of the San Andreas fault, and the low-angle thrust that we have documented probably has little or no lateral component of slip, as evidenced by the absence of transverse folds in the area and by the compressive mode of the Coalinga main shock.

If the San Andreas fault or associated structures were the cause of the Coalinga anticline, then the structural histories of these two features should be closely related. The San Andreas fault started in late middle Miocene time and accumulated about 60 km of offset by the end of the Miocene (Crowell, 1979). Most of the structural relief associated with mid-Cenozoic thrusting predates activity along the modern San Andreas fault trace and cannot be considered part of its effects. According to wrench-fault principles (Wilcox and others, 1973), folding should have developed during the early stages of strike-slip displace-

ment—certainly by the end of Miocene time—and terminated as the principal strand of the San Andreas fault developed. As discussed earlier, however, the late Cenozoic structural relief on the Coalinga anticline has developed during the past 3 Ma and is still developing, as evidenced by the May 2 earthquake and subsequent uplift (Stein, 1983).

Oakeshott (1968) proposed a diapiric model to explain the large exposure of serpentinite (Coast Range ophiolite) in the core of the Coalinga anticline (figs. 6.6*A*, 6.6*D*), but there are several problems with his model, also. Diapirs have steep boundaries that extend to great depth (Braunstein and O'Brien, 1968). The subsurface geometry of the Coast Range ophiolite/Great Valley sequence contact has a low to moderate dip concordant with the surface dips, as revealed by biostratigraphic evidence in the ARCO Bravo No. 1 and ARCO Joaquin Ridge wells which indicate that this contact is no more than 1,000 m below the total depths of the wells (cross section *A*–*A*′, fig. 6.3). Steepening of this contact near the surface, as indicated by surface mapping, is probably due to downhill creep and landsliding (Cowan and Mansfield, 1970). The cover rocks surrounding the serpentinite core lack the extensional-fault pattern and rim syncline that are characteristic of cover rocks surrounding diapirs (Braunstein and O'Brien, 1968). The density contrasts between the serpentinite reported at New Idria and throughout the Diablo Range (Byerly, 1966; Oakeshott,

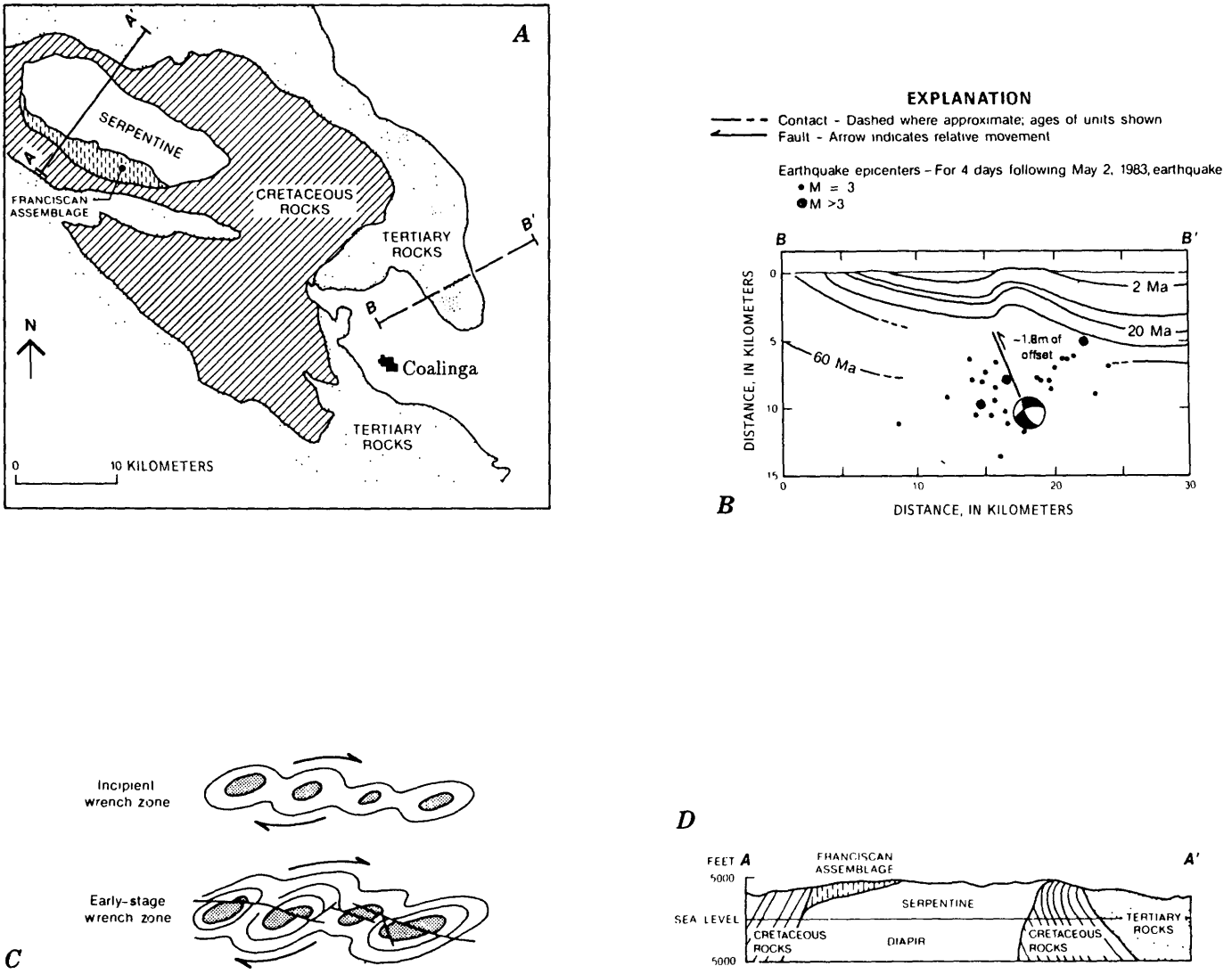

FIGURE 6.6.—Alternate structural models of the Coalinga region. *A*, Coalinga anticline, showing locations of schematic cross sections. *B*, High-angle-fault solution for the Coalinga anticline and May 2 earthquake (after Stein, 1983). *C*, Plan view of wrench-fault model showing development of folds above a strike-slip fault, arrows indicate direction of relative movement (after Wilcox and others, 1973, and Harding, 1976). *D*, Serpentinite diapir model for the Coalinga anticline (after Oakeshott, 1968).

1968) and these cover rocks are insufficient to induce diapiric processes (Phipps, 1984b). Finally, a diapiric model is inconsistent with the regional geology because several other exposures of ultramafic rock that Oakeshott proposed as diapirs are now known to be ophiolitic crust in the hanging wall of the Coast Range thrust (for example, Del Puerto Canyon; Hopson and others, 1981).

SURFACE DEFORMATION RESULTING FROM THE THRUST-FOLD STYLE

Surface deformation associated with the May 2 earthquake was studied intensely in the months following the main shock (see chaps. 15, 16; Hart and McJunkin, 1983; King and Stein, 1983; Stein, 1983), including surface-rupture and landslide mapping, as well as detailed analyses of elevation changes in the Coalinga area. These observations, though useful in gaining insight into the deformational process, probably are complexly related to the earthquake source.

A detailed analysis of the October 10, 1980, El Asnam, Algeria, earthquake illustrates the complexity of surface deformation associated with a large thrust-related earthquake (Philip and Meghraoui, 1983). This analysis showed that the surface-deformational style for a seismic event may vary with the superficial stress field; such variation makes it difficult to relate surface breaks or elevation changes directly to earthquake mechanisms at depth. Similar surface-deformation complexities may have existed during the Coalinga earthquake sequence.

A block model of a fold forming over a blind thrust, similar to the one in our structural interpretation of the Coalinga anticline, illustrates several types of possible surface deformation (fig. 6.7). Flexural-slip faults, shown as shear couples, form in parallel folding, and the magnitude of slip is directly related to the dip angle and thickness of the slip packages (Ramsay, 1974). Backthrusts may also form as slip of reverse vergence is transferred across the anticline along the decollement horizon. Change in horizon on these thrusts along the strike of the structure may result in the formation of transverse tear faults. Although this model presents a hypothetical situation, it illustrates the types of surface deformation that can result from movement on a blind thrust.

REGIONAL IMPLICATIONS

Our interpretation of the low-angle thrust source of the May 2 earthquake has important regional implications for the structural style on the western and southern margins of the San Joaquin Valley. The thrust-fold style of deformation is probably responsible for most late Cenozoic structural relief, much of which is expressed as topographic relief (Christensen, 1965; Stein, 1983). Preliminary evaluation of surface maps and well data along the margins of the San Joaquin Valley reveal many folds that deform Pliocene and Quaternary deposits, delineating a deformed belt more than 200 km long (fig. 6.8). If the thrust-belt style of deformation is occurring at Coalinga, this style is probably consistent along the entire length of the deformed belt.

This fold and thrust-belt model of the Coalinga region, and extension of this model to explain late Cenozoic deformation along the western and southern margins of the San Joaquin Valley, have important implications for the direction of future seismic-hazard studies, as well as for our understanding of the tectonic development of California. If the fault responsible for the May 2 earthquake is a blind thrust, as we propose, traditional seismic-hazard investigations, such as trench studies or detailed mapping of surface breaks, probably will not reveal the overall seismic potential or history of these areas. Instead, restorable cross sections across the deformed margins of the San Joaquin Valley will need to be constructed with the aid of seismic-reflection profiling and stratigraphic studies if we are to determine the active structural geometry and timing of recent deformation.

Much late Cenozoic deformation along the western and southern margins of the San Joaquin Valley, Coast Ranges, and Transverse Ranges has been explained in terms of wrench-fault deformation. We believe that this deformation model is inappropriate for the region and that individual ranges will have to be reexamined in light of the recent findings at Coalinga and elsewhere in the San Joaquin Valley.

CONCLUSIONS

Structural and stratigraphic analyses of surface and subsurface data document a two-phase deformational history for the growth of structures in the Coalinga region during the Cenozoic. The mid-Cenozoic phase occurred between 38 and 17 Ma, and the late Cenozoic phase began later than 3 Ma.

Both deformational phases are characterized by thrust-belt structural styles. The mid-Cenozoic phase was a westward-directed thrust system, and the late Cenozoic phase is eastward-directed, with westward-directed backthrusts. The May 2 earthquake is probably related to an eastward-verging, low-angle thrust that steps up from a decollement within the Franciscan assemblage to the base of the Great Valley sequence.

The active-thrust deformation style observed at Coalinga is probably representative of many young structures along the western and southern margins of the San Joaquin Valley. We believe that the topographic and

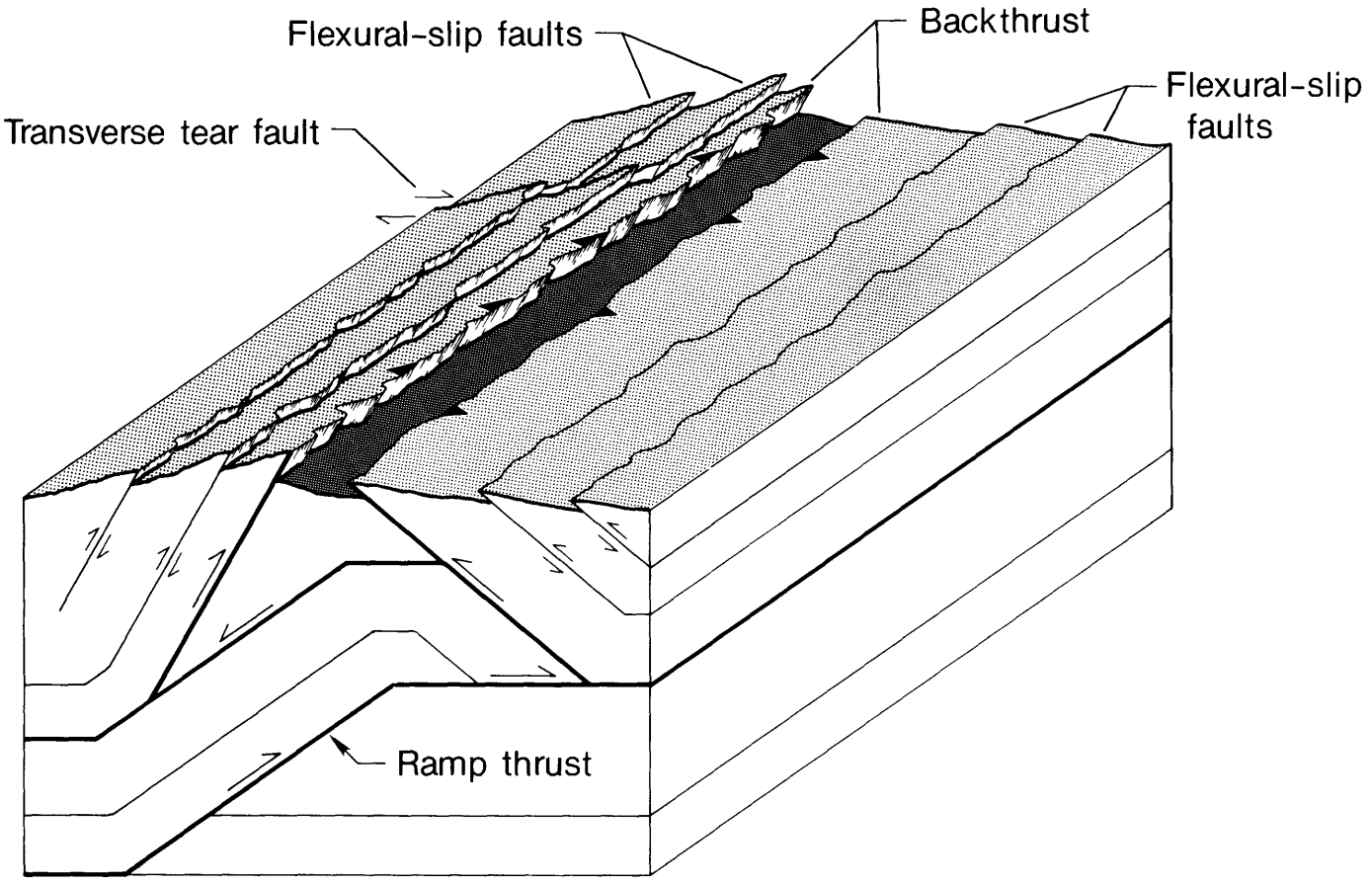

FIGURE 6.7.—Hypothetical surface deformation associated with ramp-related folds like the Coalinga anticline. These deformation mechanisms may explain the surface deformation associated with the Coalinga earthquake sequence. Half-arrows indicate relative direction of movement.

structural relief of the central Coast Ranges and north-central Transverse Ranges, with their high seismicity, is partly attributable to an actively deforming thrust belt along the western and southern margins of the San Joaquin Valley.

REFERENCES CITED

Addicott, W.O., 1972, Biostratigraphy and correlation of Tertiary sandstones at Big Tar Canyon, Reef Ridge, California, *in* Rennie, E.W., Jr., ed., Geology and oilfields, west side central San Joaquin Valley: American Association of Petroleum Geologists-Society of Exploration Geophysicists-Society of Economic Paleontologists and Mineralogists Guidebook, 1972, p. 65–69.

Adegoke, O.S., 1969, Stratigraphy and paleontology of the marine Neogene formations of the Coalinga region, California: University of California Publications in Geological Sciences, v. 80, 269 p.

Atwater, Tanya, 1970, Implications of plate tectonics for the Cenozoic tectonic evolution of western north America: Geological Society of America Bulletin, v. 81, no. 12, p. 3513–3535.

Bally, A.W., Gordy, P.L., and Stewart, G.A., 1966, Structure, seismic data, and orogenic evolution of the southern Canadian Rocky Mountains: Bulletin of Canadian Petroleum Geology, v. 14, no. 3, p. 337–381.

Bandy, O.L., and Arnal, R.E., 1969, Middle Tertiary basin development, San Joaquin Valley, California: Geological Society of America Bulletin, v. 80, no. 5, p. 783–819.

Barron, J.A., 1986, Updated diatom biostratigraphy for the Monterey Formation of California, *in* Casey, R.E., and Barron, J.A., eds., Siliceous microfossil and microplankton studies of the Monterey Formation and modern analogs: Society of Economic Paleontologists and Mineralogists, Pacific Section annual field trip guidebook, p. 105–120.

Bate, M.A., 1984, Temblor and Big Blue Formations: Interpretation of depositional environment sequence on Coalinga anticline, Fresno County, California: Stanford, Calif., Stanford University, M.S. thesis, 123 p.

—— 1985, Depositional sequence of Temblor and Big Blue Formations, Coalinga anticline, California, *in* Graham, S.A., ed., Geology of the Temblor Formation, western San Joaquin Basin, California: Society of Economic Paleontologists and Mineralogists, Pacific Section annual field trip guidebook, p. 69–86.

Boyer, S.E., and Elliott, David, 1982, Thrust systems: American Association of Petroleum Geologists Bulletin, v. 66, no. 9, p. 1196–1230.

Braunstein, Jules, and O'Brien, G.D., eds., 1968, Diapirism and diapirs: A symposium: American Association of Petroleum Geologists Memoir 8, 444 p.

Byerly, P.E., 1966, Interpretations of gravity data from the central Coast Ranges and San Joaquin Valley, California: Geological Society of America Bulletin, v. 77, no. 1, p. 83–94.

Christensen, M.N., 1965, Late Cenozoic deformation in the central

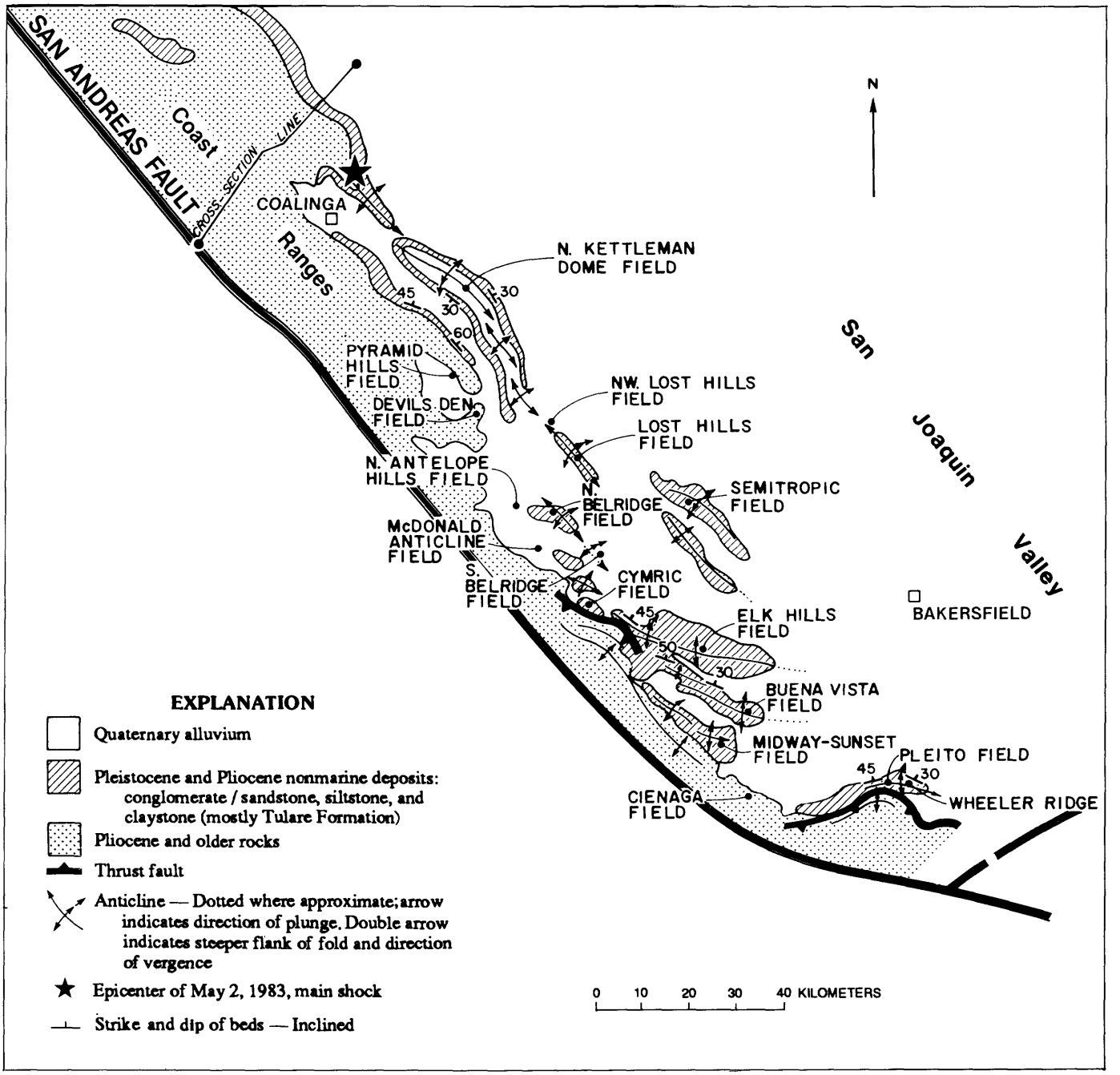

FIGURE 6.8.—Quaternary structures of the southwestern San Joaquin Valley. Deformation of Pliocene and Pleistocene deposits at Coalinga and throughout the southern San Joaquin Valley is interpreted to be due to an actively deforming thrust belt. Major oil fields are labeled.

Coast Ranges of California: Geological Society of America Bulletin, v. 76, no. 10, p. 1105–1124.

Clark, M.M., Harms, K.K., Lienkaemper, J.J., Perkins, J.A., Rymer, M.J., and Sharp, R.V., 1983, The May 2, 1983 earthquake at Coalinga, California: The search for surface faulting, *in* Borcherdt, R.D., ed., The Coalinga earthquake sequence commencing May 2, 1983: U.S. Geological Survey Open-File Report 83-511, p. 8–11.

Cooley, S.A., 1985, Depositional environments of the lower and middle Miocene Temblor Formation of Reef Ridge, Fresno and Kings Counties, California, *in* Graham, S.A., ed., Geology of the Temblor Formation, western San Joaquin Basin, California: Society of Economic Paleontologists and Mineralogists, Pacific Section annual field trip guidebook, p. 35–52.

Cooper, M.A., Gorton, M.R., and Hossack, J.R., 1983, The origin of the Basse Normandie duplex, Boulonnais, France: Journal of Structural Geology, v. 5, no. 2, p. 139–152.

Cowan, D.S., and Mansfield, C.F., 1970, Serpentinite flows on Joaquin Ridge, southern Coast Ranges, California: Geological Society of America Bulletin, v. 81, no. 9, p. 2615–2628.

Crowell, J.C., 1979, The San Andreas fault system through time:

Geological Society of London Journal, v. 136, pt. 3, p. 293–302.

Dahlstrom, C.D.A., 1969, Balanced cross sections: Canadian Journal of Earth Sciences, v. 6, no. 4, p. 743–757.

—— 1970, Structural geology in the eastern margin of the Canadian Rocky Mountains: Bulletin of Canadian Petroleum Geology, v. 18, no. 3, p. 332–406.

Davis, T.L., 1983, Late Cenozoic structure and tectonic history of the western "big bend" of the San Andreas fault and adjacent San Emigdio Mountains: Santa Barbara, University of California, Ph.D. thesis, 579 p.

Davis, T.L., 1986, A structural outline of the San Emigdio Mountains, *in* Davis, T.L., and Namson, J.S., eds., Geologic transect across the western Transverse Ranges: Society of Economic Mineralogists and Paleontologists, Pacific Section guidebook, p. 23–32.

Davis, T.L., and Lagoe, M.B., 1984, Cenozoic structural development of the north-central Transverse Ranges and southern margin of the San Joaquin Valley [abs.]: Geological Society of America Abstracts with Programs, v. 16, no. 6, p. 484.

Dibblee, T.W., 1971, Geologic maps of the Coalinga, Joaquin Rocks, New Idria, and Priest Valley 15-minute quadrangles, California: U.S. Geological Survey open-file maps, scale 1:62,500.

Eaton, J.P., Cockerham, R.S., and Lester, F.W., 1983, Study of the May 2, 1983 Coalinga earthquake and its aftershocks, based on the USGS seismic network in northern California, *in* Bennett, J.H., and Sherburne, R.W., eds., The 1983 Coalinga, California earthquakes: California Division of Mines and Geology Special Publication 66, p. 261–273.

Elliot, David, 1983, The construction of balanced cross-sections: Journal of Structural Geology, v. 5, no. 2, p. 101.

Foss, C.D., 1972, A preliminary sketch of the San Joaquin Valley stratigraphic framework, *in* Rennie, E.W., Jr., ed., Geology and oilfields, west side central San Joaquin Valley: American Association of Petroleum Geologists-Society of Exploration Geophysicists-Society of Economic Paleontologists and Mineralogists, Pacific Section Annual Meeting, 1972, Guidebook, p. 40–49.

Foss, C.D., and Blaisdell, Robert, 1968, Stratigraphy of the west side southern San Joaquin Valley, *in* Karp, S.E., ed., Geology and oilfields, west side southern San Joaquin Valley: American Association of Petroleum Geologists-Society of Exploration Geophysicists-Society of Economic Paleontologists and Mineralogists, Pacific Section Annual Meeting, 1968, Guidebook, p. 33–43.

Fuller, D.R., and Real, C.R., 1983, High-angle reverse faulting, a model for the 2 May 1983 Coalinga earthquake, *in* Bennett, J.H., and Sherburne, R.W., eds., The 1983 Coalinga, California earthquakes: California Division of Mines and Geology Special Publication 66, p. 177–184.

Graham, S.A., and Berry, K.D., 1979, Early Eocene paleogeography of the central San Joaquin Valley: Origin of the Cantua Sandstone, *in* Armentrout, J.M., Cole, M.R., and TerBest, Harry, Jr., eds., Cenozoic paleogeography of the western United States: Pacific Coast Paleogeography Symposium 3: Los Angeles, Society of Economic Paleontologists and Mineralogists, Pacific Section, p. 119–128.

Harding, T.P., 1976, Tectonic significance and hydrocarbon trapping consequences of sequential folding synchronous with San Andreas faulting, San Joaquin Valley, California: American Association of Petroleum Geology Bulletin, v. 60, no. 3, p. 356–378.

Hart, W.W., and McJunkin, R.D., 1983, Surface faulting northwest of Coalinga, California, June and July 1983, *in* Bennett, J.H., and Sherburne, R.W., eds., The 1983 Coalinga, California earthquakes: California Division of Mines and Geology Special Publication 66, p. 201–219.

Hoots, H.W., Bear, T.L., and Kleinpell, W.D., 1954, Geological summary of the San Joaquin Valley, California, [pt. 8] *of* Geology of the natural provinces, chap. 2 *of* Jahns, R.H., ed., Geology of southern California: California Division of Mines Bulletin 170, p. 113–129.

Hopson, C.A., Mattinson, J.M., and Pessagno, E.A., Jr., 1981, Coast Range ophiolite, western California, *in* Ernst, W.G., ed., The geotectonic development of California: Englewood Cliffs, N.J., Prentice-Hall, p. 418–510.

Kaplow, E.J., 1945, Coalinga oil field: California State Oil and Gas Supervisor Annual Report 31 (California Division of Oil and Gas Summary of Operations, California Oil Fields), no. 2, p. 5–22.

Keller, Gerta, and Barron, J.A., 1981, Integrated planktic foraminiferal and diatom biochronology for the northeast Pacific and the Monterey Formation, *in* Garrison, R.E., and Douglas, R.G., eds., The Monterey Formation and related siliceous rocks of California: Society of Economic Paleontologists and Mineralogists, Pacific Section special publication, p. 43–54.

King, Geoffrey, and Stein, R.S., 1983, Surface folding, river terrace deformation rate and earthquake repeat time in a reverse faulting environment: The Coalinga, California, earthquake of May 1983, *in* Bennett, J.H., and Sherburne, R.W., eds., The 1983 Coalinga, California earthquakes: California Division of Mines and Geology Special Publication 66, p. 165–176.

Kuespert, J.G., 1985, Depositional environments and sedimentary history of the Miocene Temblor Formation and associated Oligo-Miocene units in the vicinity of Kettlèman North Dome, San Joaquin Valley, California, *in* Graham, S.A., ed., Geology of the Temblor Formation, western San Joaquin Basin, California: Society of Economic Paleontologists and Mineralogists, Pacific Section annual field trip guidebook, p. 53–68.

Lindberg, F.A., ed., 1984, Correlation of stratigraphic units in North America (COSUNA) project—central California region: Tulsa, Okla., American Association of Petroleum Geologists.

Lowell, J.D., 1972, Spitsbergen Tertiary orogenic belt and the Spitsbergen fracture zone: Geological Society of America Bulletin, v. 83, no. 10, p. 3091–3102.

Mallory, V.S., 1959, Lower Tertiary biostratigraphy of the California Coast Ranges: Tulsa, Okla., American Association of Petroleum Geologists, 416 p. Namson, J.S., 1987, Structural transect through the Ventura basin and western Transverse Ranges, *in* Davis, T.L., and Namson, J.S., eds., Structural evolution of the western Transverse Ranges: Society of Economic Mineralogists and Paleontologists, Pacific Section Guidebook 48A, p. 29–41.

Namson, J.S., and Davis, T.L., 1984, Deformational history, thrust-belt structural styles and plate tectonic origin of Coast Range structures along the San Joaquin Valley, California [abs.]: Geological Society of America Abstracts with Programs, v. 16, no. 6, p. 607.

Nilsen, T.H., Dibblee, T.W., Jr., and Addicott, W.O., 1973, Lower and middle Tertiary stratigraphic units of the San Emigdio and western Tehachapi Mountains, California: U.S. Geological Survey Bulletin 1372–H, p. H1–H23.

Nilsen, T.H., and McKee, E.H., 1979, Paleogene paleogeography of the western United States, *in* Armentrout, J.M., Cole, M.R., and TerBest, Harry, Jr., eds., Cenozoic paleogeography of the western United States: Pacific Coast Paleogeography Symposium 3: Los Angeles, Society of Economic Paleontologists and Mineralogists, Pacific Section, p. 257–276.

Oakeshott, G.B., 1968, Diapiric structures in Diablo Range, California, *in* Braunstein, Jules, and O'Brien, G.D., Diapirism and diapirs: A symposium: American Association of Petroleum Geologists Memoir 8, p. 228–243.

Obradovich, J.D., and Naeser, C.W., 1981, Geochronology bearing on the age of the Monterey Formation and siliceous rocks in California, *in* Garrison, R.E., and Douglas, R.G., eds., The Monterey Formation and related siliceous rocks of California: Society of Economic Paleontologists and Mineralogists, Pacific Section spe-

cial publication, p. 87–96.

Obradovich, J.D., Naeser, C.W., and Izett, G.A., 1978, Geochronology of late Neogene marine strata in California [abs.], *in* Correlation of tropical through high latitude marine Neogene deposits of the Pacific Basin: Stanford, Calif., Stanford University Publications in the Geological Sciences, v. 14, p. 40–41.

O'Connell, D.R., and Murtha, P.E., 1983, Source parameters of Coalinga aftershocks from the U.C. Berkeley portable digital array, *in* Bennett, J.H., and Sherburne, R.W., eds., The 1983 Coalinga, California earthquakes: California Division of Mines and Geology Special Publication 66, p. 293–306.

Page, B.M., 1981, The southern Coast Ranges, *in* Ernst, W.G., ed., The geotectonic development of California: Englewood Cliffs, N.J., Prentice-Hall, p. 329–417.

Payne, M.B., 1962, Type Panoche Group (Upper Cretaceous) and overlying Moreno and Tertiary strata on the west side of the San Joaquin Valley, *in* Bowen, O.E., Jr., ed., Geologic guide to the gas and oil fields of northern California: California Division of Mines and Geology Bulletin 181, p. 165–175.

Philip, H., and Meghraoui, M., 1983, Structural analysis and interpretation of the surface deformations of the El Asnam earthquake of October 10, 1980: Tectonics, v. 2, no. 1, p. 17–50.

Phipps, S.P., 1984a, Mesozoic ophiolitic olistostromes and Cenozoic imbricate thrust faulting in the northern California Coast Ranges: Geology of the Mysterious Valley area, Napa County: Princeton, N.J., Princeton University, Ph.D. thesis, 669 p.

—— 1984b, Ophiolitic olistostromes in the basal Great Valley sequence, Napa County, northern California Coast Ranges, *in* Raymond, L.A., ed., Melanges: Their nature, origin and significance: Geological Society of America Special Paper 198, p. 103–125.

Ramsay, J.G., 1974, Development of chevron folds: Geological Society of America Bulletin, v. 85, no. 11, p. 1741–1753.

Repenning, C.A., 1976, *Enhydra* and *Enhydriodon* from the Pacific coast of North America: U.S. Geological Survey Journal of Research, v. 4, no. 3, p. 305–315.

Rich, J.L., 1934, Mechanics of low-angle overthrust faulting as illustrated by Cumberland thrust block, Virginia, Kentucky, and Tennessee: American Association of Petroleum Geologists Bulletin, v. 18, no. 12, p. 1584–1596.

Sherburne, R.W., McNally, Karen, Brown, Ethan, and Aburto, Arturo, 1983, The mainshock-aftershock sequence of 2 May, 1983: Coalinga, California, *in* Bennett, J.H., and Sherburne, R.W., eds., The 1983 Coalinga, California earthquakes: California Division of Mines and Geology Special Publication 66, p. 275–292.

Stearns, D.W., 1978, Faulting and forced folding in the Rocky Mountains foreland, *in* Matthews, Vincent, III, ed., Laramide folding associated with basement block faulting in the western United States: Geological Society of America Memoir 151, p. 1–37.

Stein, R.S., 1983, Reverse slip on a buried fault during the 2 May 1983 Coalinga earthquake: Evidence from geodetic elevation changes, *in* Bennett, J.H., and Sherburne, R.W., eds., The 1983 Coalinga, California earthquakes: California Division of Mines and Geology Special Publication 66, p. 151–163.

Stewart, R.B., 1946, Geology of Reef Ridge, Coalinga district, California: U.S. Geological Survey Professional Paper 205–C, p. 81–115.

Suppe, John, 1978, Geological map and cross section of the southern part of the northern Coast Ranges and Sacramento Valley, California: Geological Society of America map and Chart Series, no. MC–28B, scale 1:250,000.

—— 1983, Geometry and kinematics of fault-bend folding: American Journal of Science, v. 283, no. 7, p. 684–721.

Suppe, John, and Foland, K.A., 1978, The Goat Mountain schists and Pacific Ridge complex: A redeformed but still-intact late Mesozoic Franciscan schuppen complex, *in* Howell, D.G., and McDougall, K.A., eds., Mesozoic paleogeography of the western United States: Pacific Coast Paleogeography Symposium 2: Los Angeles, Society of Economic Paleontologists and Mineralogists, Pacific Section, p. 431–452.

Weinberg, D.M., 1978, Some two-dimensional kinematic analyses of the drape-fold concept, *in* Matthews, Vincent, III, ed., Laramide folding associated with basement block faulting in the western United States: Geological Society of America Memoir 151, p. 51–78.

Wentworth, C.M., Walter, A.W., Bartow, J.A., and Zoback, M.D., 1983, Evidence on the tectonic setting of the 1983 Coalinga earthquakes from deep reflection and refraction profiles across the southeastern end of Kettleman Hills, *in* Bennett, J.H., and Sherburne, R.W., eds., The 1983 Coalinga, California earthquakes: California Division of Mines and Geology Special Publication 66, p. 113–126.

Wilcox, R.E., Harding, T.P., and Seely, D.R., 1973, Basic wrench tectonics: American Association of Petroleum Geology Bulletin, v. 57, no. 1, p. 74–96.

Woodring, W.P., Stewart, R.B., and Richards, R.W., 1940, Geology of the Kettleman Hills oil field, California: Stratigraphy, paleontology, and structure: U.S. Geological Survey Professional Paper 195, 170 p.

Yeats, R.S., 1983, Large-scale Quaternary detachments in Ventura Basin, southern California: Journal of Geophysical Research, v. 88, no. B1, p. 569–583.

7. REGIONAL SEISMOTECTONIC MODEL FOR THE SOUTHERN COAST RANGES

By J.P. EATON and MICHAEL J. RYMER,
U.S. GEOLOGICAL SURVEY

CONTENTS

ABSTRACT

On the basis of seismicity in the southern Coast Ranges for the 11 years before the May 2 earthquake and on focal mechanisms of selected moderate recent earthquakes in the region, we propose a model for the generation of reverse- and thrust-fault earthquakes, such as the May 2 earthquake, along both the east and west flanks of the Coast Ranges. These earthquakes appear to result from a component of apparent convergent displacement across the San Andreas transform system in the southern Coast Ranges.

Earthquakes with reverse and thrust focal mechanisms occur in regions with a distinctive pattern of seismicity characterized by detached clusters of epicenters. These regions lie along the flanks of the southern Coast Ranges and are separated from the San Andreas fault by other regions of relative quiescence. In our model, the reverse- and thrust-fault earthquakes occur where detachment zones within a ductile lower crust beneath the center of the transform system pass upward into the brittle upper crust along its margins. Convergence across the transform system, together with regions of unusually strong materials in the brittle upper crust flanking the San Andreas fault southeast of Cholame, may also play an important role in producing great earthquakes in that region.

INTRODUCTION

The occurrence of the May 2 earthquake was a surprise for three reasons: (1) No potentially active fault capable of producing an M=6.7 event had been mapped in the Coalinga region, (2) the historical record does not place such a large earthquake near Coalinga, and (3) the pattern of recent seismicity in the region had not been interpreted to indicate the presence of an active, concealed fault capable of causing such an event. We shall pursue the last point by examining the seismicity in the southern Coast Ranges during the 11 years before the earthquake to determine whether the seismicity data might have revealed the potential for a large earthquake.

The primary data set we examine is the catalog of earthquakes located by the U.S. Geological Survey telemetered seismic network from January 1972 through April 1983. Because this network was reinforced and extended during these years, the catalog is not uniform in either spatial or temporal coverage. The numbers of stations in the northern subregion (Carquinez to San Benito) and the southern subregion (San Benito to Santa Margarita) were, respectively, 54 and 24 in 1972, 73 and 52 in 1975, and 87 and 68 in 1982. Critical stations near Coalinga, including Anticline Ridge, were installed in 1975; and critical stations near San Luis Obispo, including Santa Margarita, were installed in 1978. Because the network was initially designed to study the San Andreas, Hayward, and Calaveras faults, station density was high near these faults and low elsewhere, particularly along the west edge of the Great Valley and along the coast. Thus, the ability of the network to detect and locate small events in these last two regions, particularly in their southern parts, lagged seriously behind the capability of the network elsewhere in the southern Coast Ranges during the entire period 1972–83. Moreover, the persistent concentration of small earthquakes along slipping segments of the major faults noted above permits these segments to be delineated by seismicity within a relatively short recording interval, whereas the intermittent, sparse earthquakes in other parts of the region must be recorded over a much longer interval of time to accumulate a sufficient number of earthquakes to delineate the active structures from which they emanate.

We here examine three seismicity maps of the southern Coast Ranges and two maps portraying focal mechanisms of selected recent moderate earthquakes in the southern Coast Ranges and western Transverse Ranges. The first seismicity map (fig. 7.1), which covers the period January 1982–April 1983, shows the regional distribution of earthquakes, relatively unbiased by the

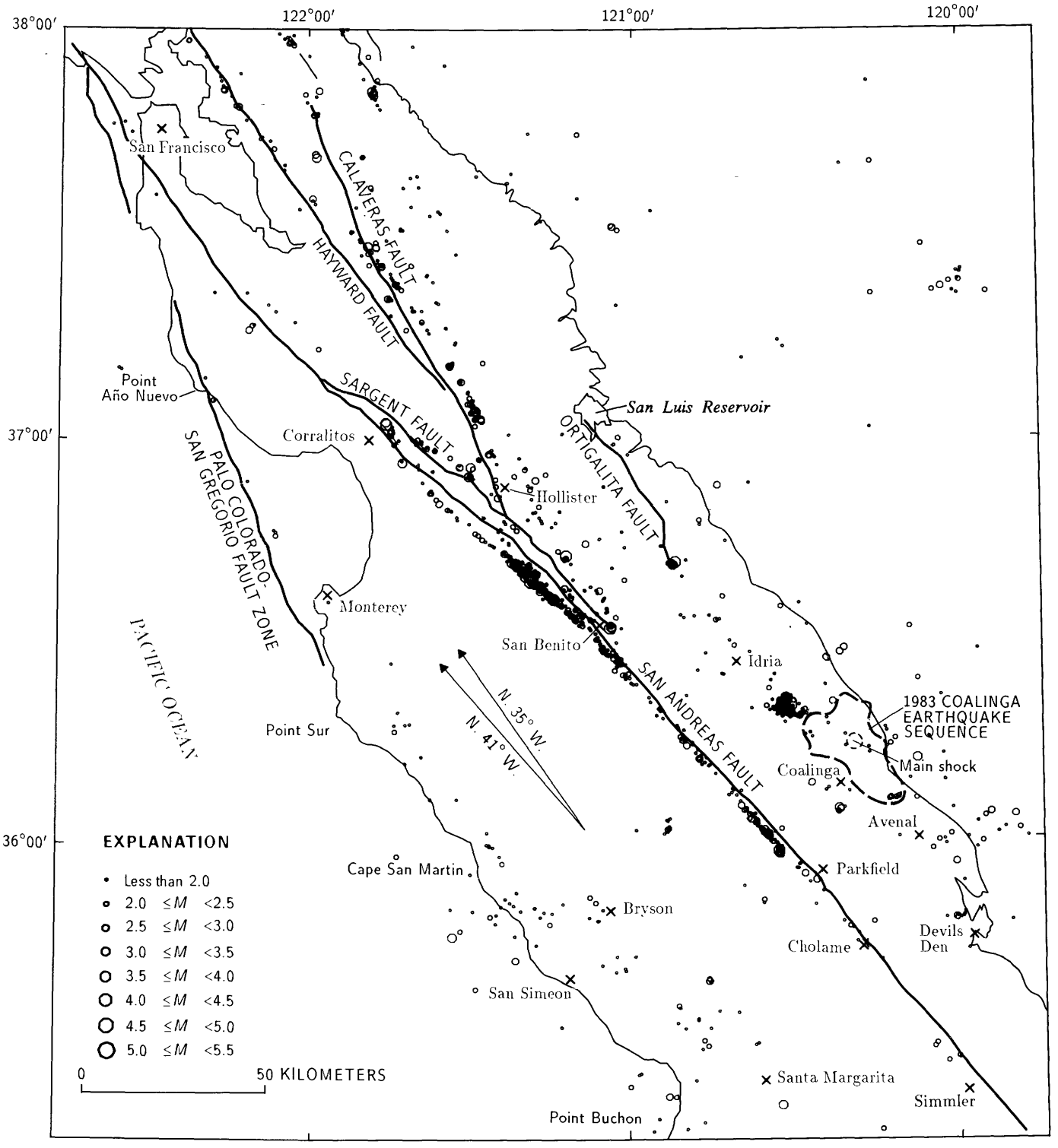

FIGURE 7.1.—Central Coast Ranges, Calif., showing locations of $M>1.5$ earthquakes from January 1982 through April 1983. 500-ft contour (shown only along west side of the Great Valley) marks approximate boundary between the Coast Ranges and the Great Valley. Average strike of the San Andreas fault between Cholame and Hollister is N. 41° W., and direction of relative motion of the Pacific plate to the North American plate in the same region is N. 35° W.

evolution of the network. The second and third seismicity maps, which cover the period January 1972–April 1983, show the cumulative distribution of earthquakes in the southern Coast Ranges (fig. 7.2) and in the southern Coast Ranges east of the San Andreas fault (fig. 7.3), respectively. These two maps are biased by the loss of

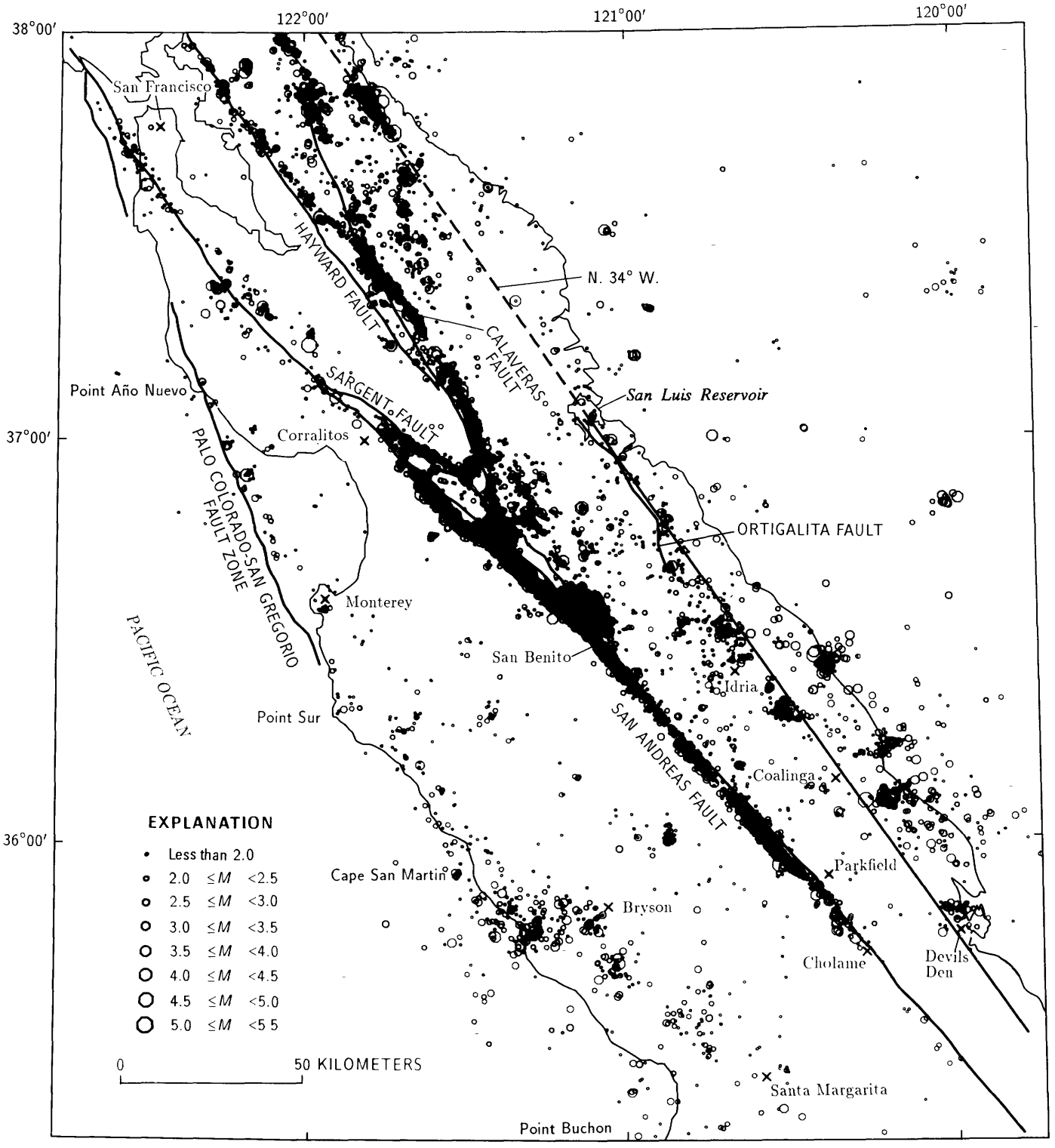

FIGURE 7.2.—Central Coast Ranges, Calif., showing locations of $M>1.5$ earthquakes from January 1972 through April 1983. 500-ft contour marks approximate boundary between the Coast Ranges and the Great Valley.

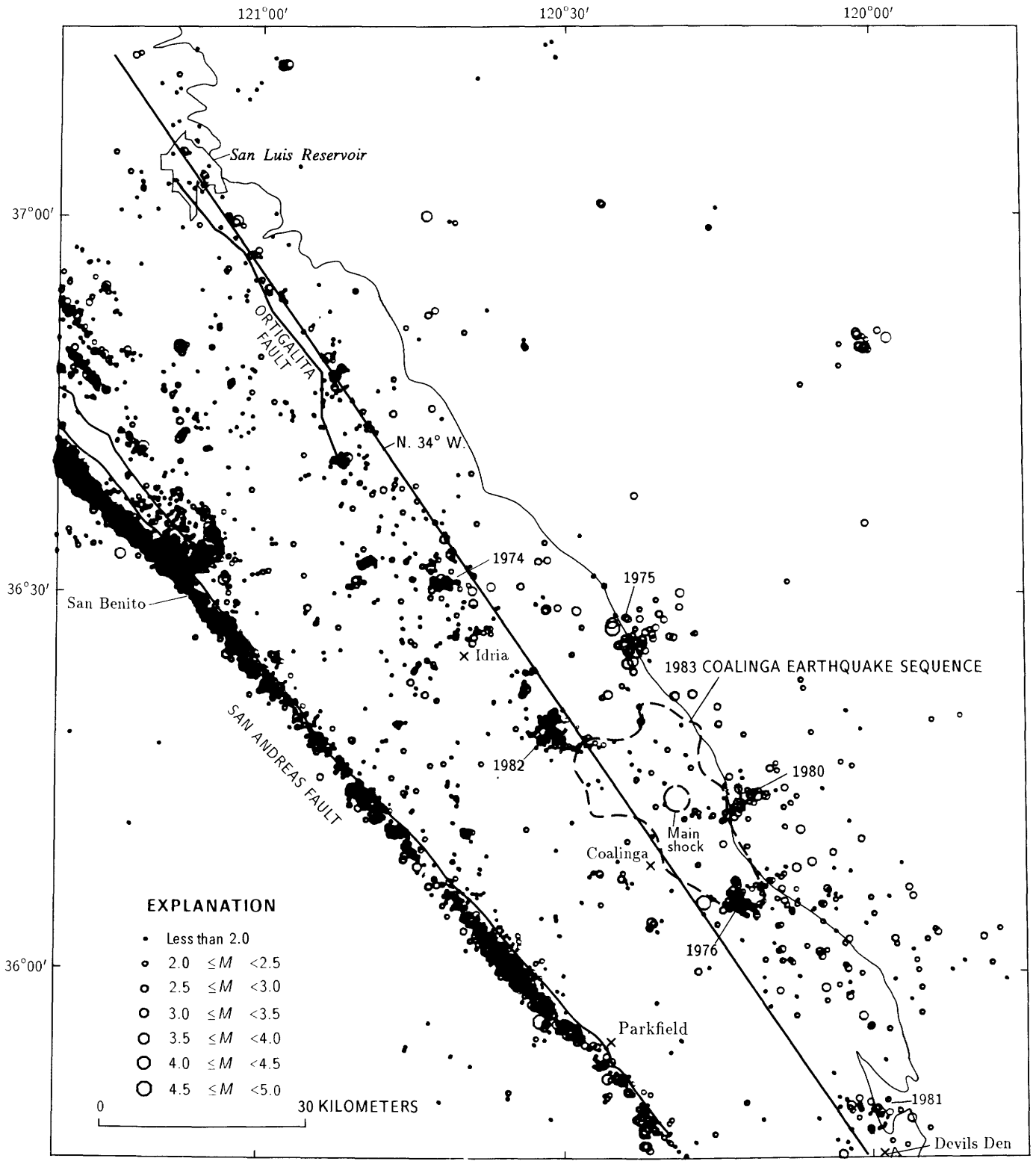

FIGURE 7.3.—Central Coast Ranges, Calif., showing locations of $M>1.5$ earthquakes and earthquake clusters east of the San Andreas fault from January 1972 through April 1983. 500-ft contour marks approximate boundary between the Coast Ranges and the Great Valley.

smaller earthquakes along the coast and along the west edge of the Great Valley. The first focal-mechanism map (fig. 7.4) shows first-motion solutions and *P*-axis orientations; the second map (fig. 7.5) shows the orientation and dip of the focal planes believed to correspond to the fault planes, as well as the corresponding relative displacements on the faults. Using these data, together with other geologic and geophysical information, we then develop a regional seismotectonic model that accounts for the May 2 earthquake.

SHORT-TERM SEISMICITY PATTERN

Southern Coast Range earthquakes for the 16 months preceding the May 2 earthquake are plotted in figure 7.1. The 500-ft elevation contour is the approximate boundary between the Coast Ranges and the Great Valley. The directions N. 41° W. and N. 35° W. correspond, respectively, to the average strike of the San Andreas fault between Cholame and Hollister and to the relative motion between the Pacific and North American plates in the same region, derived by Minster and Jordan (1978) from a global inversion of plate motions from which data on the San Andreas fault were excluded.

The short-term pattern of seismicity shown in figure 7.1 is generally similar to that for any comparable time interval from 1970 onward. Such maps for earlier times, however, show fewer events in the southern parts of the coastal and Great Valley margin regions because of the inadequacy of the network in those regions in earlier years. The pattern of seismicity revealed by comparison, in 1978, of yearly plots from 1970 through 1977 suggested (Eaton, 1985) that they were composed of several types of epicenter distributions: (1) linear concentrations of epicenters of rather uniform density, along sections of the principal faults of the region, which are repeated with little variation from year to year; (2) episodes of seismicity that spring up suddenly and then die out slowly over a period of a year or more—these episodes are moderate, isolated earthquakes and their aftershocks, and they occur both on and off well recognized faults; and (3) scattered epicenters throughout seismically active parts of the Coast Ranges from the Pacific shoreline to the west edge of the Great Valley.

In figure 7.1, the principal linear concentrations of epicenters along mapped faults are: (1) along the San Andreas fault from Parkfield to Corralitos, (2) along the Hayward fault east of the San Francisco Bay, (3) along the Calaveras fault from Hollister to the south end of the San Francisco Bay, and (4) along the Sargent fault. The cluster of events southeast of Idria in figure 7.1 represents the aftershock zone of the October 25, 1982, Idria earthquake (M=5.5). The scattered epicenters away from the principal faults mapped in figure 7.1 show more clearly defined trends and clusters than were evident on earlier maps. Such trends include one that lies east of Hollister and extends from San Benito on the south to the junction of the Calaveras and Hayward faults north of Hollister, another that parallels the coast from east of Point Sur to west of Bryson, and another that extends from the southeast end of the Ortigalita fault to the Idria aftershock cluster. Broader trends of activity, composed of diffuse patches of epicenters, lie along the coast from Bryson to Santa Margarita, along the west edge of the Great Valley from Idria to Devils Den, and east of the Calaveras fault.

LONG-TERM SEISMICITY PATTERN

Southern Coast Range earthquakes for the 11-year period January 1972–April 1983 are mapped on figure 7.2, where nearly 13,000 events are plotted. The short-term features that were evident in figure 7.1 are reinforced and extended in the long-term pattern. Additional features well expressed in the long-term pattern were not visible in figure 7.1; such new features include the linear zones of epicenters along the San Andreas fault between Corralitos and San Francisco and between Parkfield and Cholame, along the Palo Colorado-San Gregorio fault between Point Año Nuevo and Point Sur, along other faults that are parallel to and east of the Hayward fault in the region east of the San Francisco Bay, and (probably) along a zone that runs diagonally across the quiet region west of the San Andreas fault from Monterey to Cholame.

Another striking feature of the overall pattern is the virtual absence of activity along the San Andreas fault southeast of Cholame and along the edge of the Great Valley southeast of Devils Den. Other regions of very low seismicity include the San Francisco Bay block between the San Andreas and Hayward faults, a large quiet region east of the southern section of the Calaveras fault, and most of the broad region between the San Andreas fault and the zone of epicenters along the coast from Point Año Nuevo to Santa Margarita.

For a more detailed look at the long-term pattern of seismicity in the Coalinga region, an enlarged version of the southeast quarter of figure 7.2. is shown in figure 7.3. Here, we are interested primarily in the region east of the San Andreas fault. As in the earlier figures, the 500-ft contour marks the approximate boundary between the Coast Ranges and the Great Valley. Seismicity drops off abruptly north of Idria and east of the medial line striking N. 34° W. that lies parallel to and just east of the Ortigalita fault. West of this medial line and northwest of Idria, epicenters are broadly scattered, without conspicuous clusters. Southeast of Idria, clusters of events are evident, and most of the epicenters lie east of the medial

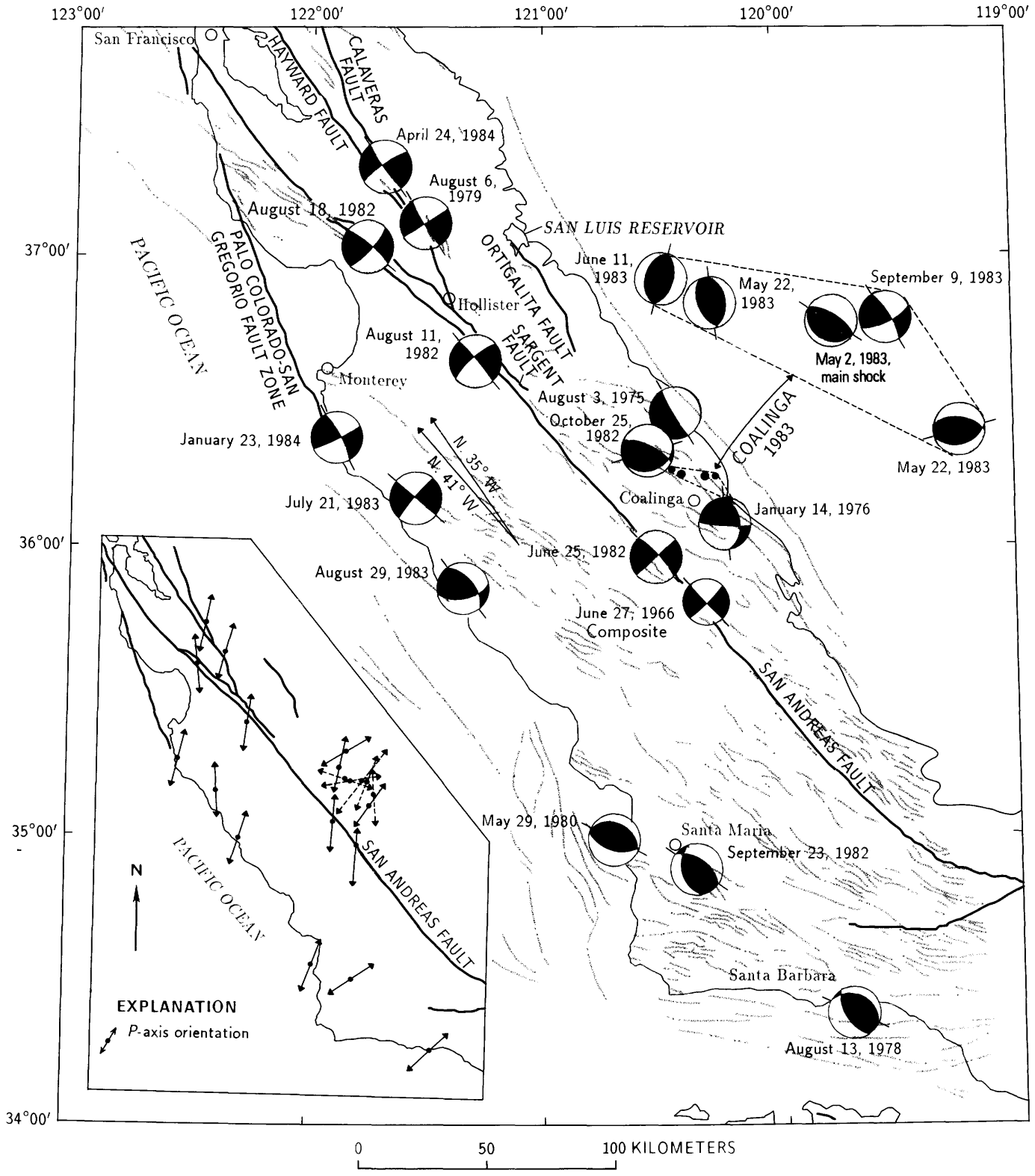

FIGURE 7.4.—First-motion diagrams and *P*-axis orientations for selected earthquakes in the southern Coast Ranges and western Transverse Ranges. Individual earthquakes are identified by their date of occurrence. First-motion diagrams of events in the 1983 Coalinga earthquake sequence are shown at an expanded scale. Inset shows *P*-axis orientations, with events of the Coalinga earthquake sequence plotted with dashed lines. Hypocentral and focal-mechanism data are summarized in table 7.1. Fold axes (light lines) after Hoskins and Griffiths (1971) and Jennings (1977).

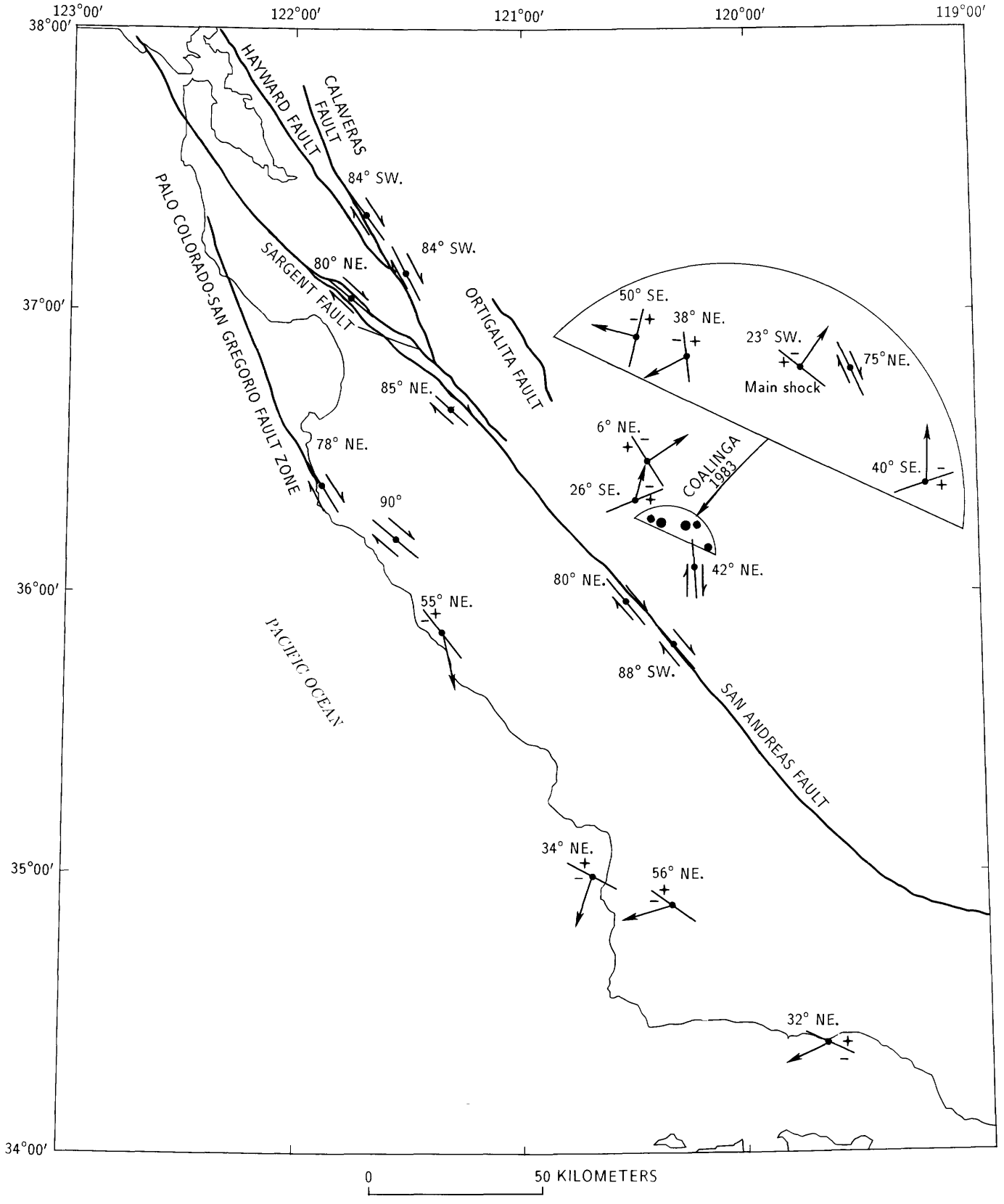

FIGURE 7.5.—Fault-plane orientations and slip directions for selected earthquakes in the Coast Ranges and Transverse Ranges. Strike directions are indicated by line segment drawn through epicenter symbol; dip angles and directions are shown by each solution. Slip sense and direction for strike-slip solutions are indicated by half-barbed pairs of arrows. For events with appreciable dip-slip displacement, an arrow indicates direction of slip of upper plate relative to lower plate, and plus and minus signs indicate relative vertical displacement of the two plates. Events in the 1983 Coalinga earthquake sequence are shown at an expanded scale.

line. The Coalinga earthquake sequence was located almost entirely between this medial line and the 500-ft contour; the aftershocks filled in a region of relative quiescence that was framed by the clusters of 1976, 1980, and 1982. Another quiet zone of comparable size lies just east of Idria; it is framed by the 1983 aftershock region and the clusters of 1975, 1974, and 1982. An even larger quiet zone lies between the 1983 aftershock zone and the San Andreas fault (fig. 7.3). The significance of these quiet zones is discussed below.

If the medial line suggested by the distribution of epicenters east of the San Andreas fault in figure 7.3 is extended to the northwest (dashed line, fig. 7.2), it passes through the easternmost linear concentration of epicenters (near Livermore) east of the San Francisco Bay. So extended, the medial line parallels the direction of relative plate motion (approx N. 35° W., fig. 7.1) and is defined by various abrupt transitions in the pattern of seismicity for 300 km along the east edge of the southern Coast Ranges. We suggest that this line marks a zone of transition between a ductile lower crust overlying a transform zone beneath the center of the Coast Ranges and a more brittle lower crust beneath the Great Valley. Also, the progressive change from northwest to southeast in the overall pattern of seismicity across the breadth of the Coast Ranges appears to correlate with changes in behavior of the San Andreas itself. From San Benito southeastward to Cholame, earthquakes are concentrated in a narrow band along the main trace of the San Andreas fault and in bands of earthquake clusters along the two flanks of the Coast Ranges. The main trace is flanked by broad regions of low seismicity. The strike of the fault, N. 41° W., is misaligned by 6° from the direction of relative plate motion (Minster and Jordan, 1978). If the transform zone in the upper mantle (and lower crust?) is, indeed, aligned with the direction of relative plate motion, then slip within the brittle crust along the San Andreas fault results in a widening of the crust above the transform zone and tends to drive the crust outward over the edges of the transform zone in a direction approximately perpendicular to the fault. For such a process to produce the observed seismicity pattern, however, the brittle upper crust would have to be largely decoupled from the lower crust and mantle beneath the quiet zones that flank the San Andreas fault.

In the northern part of figure 7.2, the San Andreas fault and its principal branch, the Hayward fault, strike nearly parallel to the direction of relative plate motion. The concentration of earthquakes on the San Andreas fault, which is locked in this region, is much lower than on the Hayward fault, which creeps intermittently. Most of the earthquakes not on these two major fault traces are concentrated in two other bands with similar trends farther east; the easternmost of these bands lies along the projection of the medial line described above. Scattered earthquakes east of this line are far less abundant than along the edge of the Great Valley east of the medial line between Idria and Devils Den farther south.

The pattern of seismicity in the central part of figure 7.2 is dominated by branching of the Calaveras and other faults off the San Andreas fault between San Benito and Corralitos, and by the end of the dense band of earthquakes along the San Andreas fault at Corralitos. Concentrations of earthquakes in a large cluster just east of the San Andreas fault at San Benito, and in northwest-trending bands east of the San Andreas fault between San Benito and the main trace of the Calaveras fault north of Hollister, indicate the length and eastward extent of the zone of auxiliary faulting related to the branching. The principal seismicity along the flanks of the Coast Ranges in the central part of figure 7.2 is in relatively sparse linear zones between Point Año Nuevo and Cape San Martin on the west and between the San Luis Reservoir and Idria on the east.

FOCAL MECHANISMS IN THE SOUTHERN COAST RANGES AND WESTERN TRANSVERSE RANGES

To search further for an explanation of the changes in seismicity pattern from northwest to southeast in the central Coast Ranges, we turn to data on the focal mechanisms of 20, mostly recent, earthquakes in the southern Coast Ranges and western Transverse Ranges. Except for the composite solution for the 1966 Parkfield aftershocks, the first-motion solutions are for individual events of M=3.9–6.7, the records for which were played back from magnetic tape for analysis. The earthquakes were sufficiently well recorded at distances greater than 100 km that many *Pn* arrivals at a broad range of azimuths, as well as refractions from shallower crustal boundaries and direct arrivals, were used in the solutions. Most of these solutions are very well constrained, although some events along the San Andreas had many systematically discordant arrivals due to a horizontal contrast in velocity across the fault. Details of the seven new solutions worked out for this chapter are shown in figure 7.6; details of the remaining solutions are given in the references cited in table 7.1.

Four of the events studied were on the San Andreas fault between Parkfield and Corralitos, two on the Calaveras fault north of Hollister, and six along the coast between Santa Barbara and Monterey. In the Coalinga region, three were events along the edge of the Great Valley near Coalinga that preceded the May 2 earthquake, and five were from the Coalinga earthquake sequence itself. First-motion diagrams and *P*-axis orientations are shown in figure 7.4, and the corresponding (inferred) fault-plane orientations and slip directions in figure 7.5.

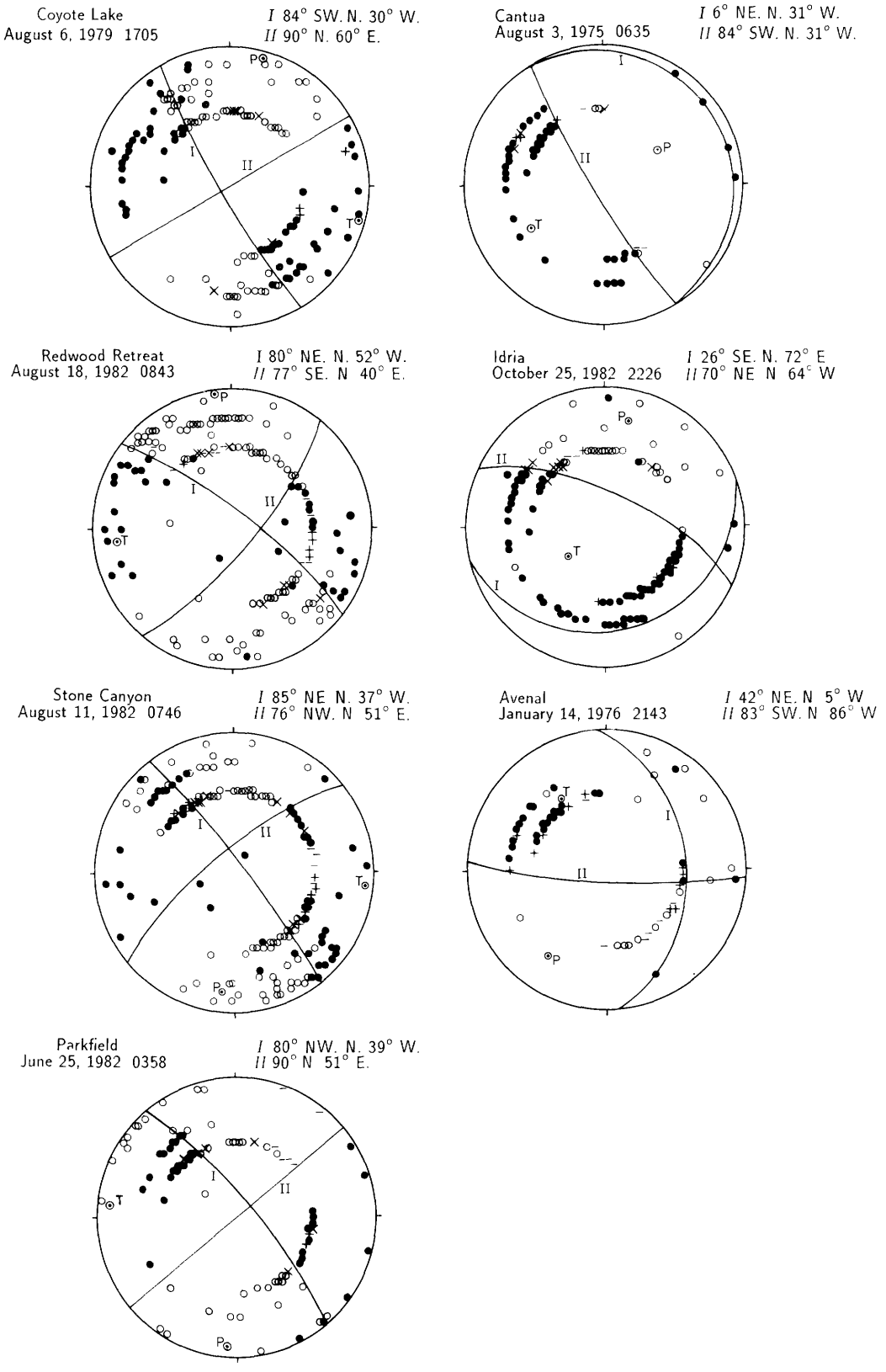

FIGURE 7.6.—First-motion plots and focal plane solutions for selected events shown in figures 7.4 and 7.5. Dots and circles denote unambiguous compressional and dilatational first wave onsets, respectively; ×'s, conflicting arrivals. Plus and minus signs indicate less certain compressional and dilatational first-wave onsets, respectively. P and T, inferred axes of maximum and minimum compressional stress (pressure axis and tension axis), respectively.

TABLE 7.1.—*Summary of hypocentral and focal-mechanism data for the earthquakes shown in figures 7.4 and 7.5*

[Gap, maximum azimuth of stations used in hypocentral solution. References: 1, this chapter; 2, Eaton (1984a); 3, Eaton (1984b); 4, Cockerham and Eaton (1984); 5, Eaton and others (1970)]

Date	Time (G.m.t.)	Lat N.	Long W.	Depth (km)	M_L	P-axis orientation		Fault-Plane orientation		Auxiliary-plane orientation		Reference showing first-motion plot
						Azimuth	Dip (plunge)	Strike	Dip	Strike	Dip	
8/3/75	0635:17.32	36°27'.03	120°26'.43	10.33	4.9	050°	51°	N. 31° W.	6° NE.	N. 31° W.	84° SW.	1
1/14/76	2143:59.15	36°04'.48	120°14'.62	11.94	4.7	215°	26°	N. 5° W.	42° NE.	N. 86° W.	83° SW.	1
8/13/78	2254:51.80	34°23'.18	119°42'.60	11.34	5.9	228°	15°	N. 64° W.	32° NE.	N. 30° W.	62° SW.	2
8/6/79	1705:22.28	37°06'.15	121°30'.80	7.79	5.9	015°	4°	N. 30° W.	84° SW.	N. 60° E.	90°	1
5/29/80	0338:47.51	34°58'.65	120°42'.37	9.17	5.1	202°	11°	N. 62° W.	34° NE.	N. 72° W.	57° SW.	2
6/25/82	0358:22.97	35°57'.43	120°33'.11	9.06	4.2	184°	7°	N. 39° W.	80° NE.	N. 51° E.	90°	1
8/11/82	0746:43.04	36°37'.64	121°18'.16	11.62	4.8	187°	13°	N. 37° W.	85° NE.	N. 51° W.	76° NW.	1
8/18/82	0843:49.50	37°01'.49	121°44'.63	12.21	4.3	353°	2°	N. 52° W.	80° NE.	N. 40° E.	77° SE.	1
9/23/82	2042:50.60	34°52'.19	120°21'.76	4.77	4.0	055°	8°	N. 54° W.	56° NE.	N. 12° W.	42° SW.	2
10/25/82	2226:03.67	36°19'.31	120°30'.44	10.95	5.5	012°	24°	N. 72° E.	26° SE.	N. 64° W.	70° NE.	1
5/2/83	2342:38.14	36°13'.96	120°18'.57	10.01	6.7	037°	23°	N. 53° W.	23° SW.	N. 53° W.	67° NE.	3
5/22/83	0839:21.74	36°09'.03	120°12'.09	10.48	4.2	356°	6°	N. 74° E.	40° SE.	N. 85° W.	52° NE.	3
6/11/83	0309:52.21	36°15'.33	120°27'.01	2.40	5.2	107°	5°	N. 17° E.	50° SE.	N. 17° E.	40° NW.	3
7/21/83	0123:32.97	36°09'.17	121°32'.64	5.24	3.9	176°	4°	N. 49° W.	90°	N. 41° E.	84° NW.	2
7/22/83	0239:54.07	36°14'.44	120°24'.53	7.37	6.0	260°	7°	N. 5° W.	38° NE.	N. 21° W.	53° SW.	3
8/29/83	1010:30.90	35°50'.17	121°21'.70	6.57	5.4	198°	2°	N. 39° W.	55° NE.	N. 77° E.	58° SE.	2
9/9/83	0916:13.47	36°13'.91	120°15'.90	6.69	5.3	022°	1°	N. 26° W.	75° NE.	N. 68° E.	72° SE.	3
1/23/84	0540:19.88	36°22'.13	121°52'.74	7.74	5.2	194°	9°	N. 30° W.	78° NE.	N. 62° E.	84° SE.	2
4/24/84	2115:18.78	37°18'.56	121°40'.68	8.42	6.2	191°	3°	N. 34° W.	84° SW.	N. 57° E.	80° NW.	4
6/27/66	---	35°47'.70	120°20'.50	7.0	5.5	004°	3°	N. 41° W.	88° SW.	N. 49° E.	84° SE.	5

The six solutions along the San Andreas and Calaveras faults indicate right-lateral strike slip on near-vertical fault surfaces, with strike and slip directions that parallel the sections of the faults on which the earthquakes occurred. The six solutions along the coast show a progressive change from predominantly strike slip in the northwest to predominantly reverse slip in the southeast: Point Sur (1/23/84), right-lateral strike-slip displacement on a near-vertical fault, with a location and orientation corresponding to the Palo Colorado-San Gregorio fault; San Simeon (8/29/83), right-oblique reverse slip on a fault parallel to the coast (and the nearby offshore Hosgri fault) and dipping 55° NE.; Point Sal (5/29/80), thrust displacement on a fault striking N. 62° W. and dipping 34° NE.; and Santa Barbara (8/13/78), left oblique reverse slip on a fault striking N. 64° W. and dipping 32° NE. The solutions for the Coalinga region indicate a preponderance of reverse faulting, but with diverse orientations. Inferred *P*-axis azimuths of the main shock and of two of the three pre-May 2 earthquakes are nearly perpendicular to the San Andreas fault. The inferred *P*-axis orientations of the Coalinga aftershocks vary systematically across the aftershock zone, from nearly east-west in the northwestern part to nearly north-south in the southeastern part of the region.

The focal mechanisms shown in figures 7.4 and 7.5 suggest that the fault planes and slip directions of large earthquakes along the major strike-slip faults are controlled by preexisting fault surfaces. Maximum-stress azimuths cannot be inferred reliably from such solutions. Focal mechanisms of the larger earthquakes along the flanks of the Coast Ranges indicate a predominance of thrust or reverse-slip faulting, with considerable variation in fault-plane orientations and slip directions, but with inferred *P*-axis orientations that are nearly perpendicular to the strike of the contiguous section of the San Andreas fault.

Focal-mechanism studies of smaller earthquakes in the western Transverse Ranges and Santa Barbara Channel confirm the dominance of contemporary left-oblique reverse slip throughout these regions (Yerkes and Lee, 1979; Yerkes and others, 1981; Yerkes, 1985). Moreover, the inferred near-horizontal *P*-axes are normal to, and change direction with, the San Andreas fault in the "big bend" region.

DISCUSSION

Effective use of seismicity data to predict earthquakes requires that such data be interpreted within the context of a specific seismotectonic model which organizes and explains existing data and provides a vehicle for extrapolating from the historical record and current trends to predict future events in the modeled system. The global plate-tectonic model and seismic-gap approach to predicting earthquakes provide a general framework for the model we need, but they are not sufficiently specific to be of practical use, except on a very large scale. On a global scale, the San Andreas fault is a simple transform fault along which the Pacific and North American plates move past one another parallel to the fault. On a regional scale, that transform is a broad, rather complex zone of

interaction between the plates. It has a width that is a significant fraction of its length, a complex internal structure that varies with position within it, poorly understood transitions to other global structures at its ends, and a poorly known variation in elastic properties with depth. Moreover, the northern and southern sections of the zone are dissimilar, and there is a large left-stepping offset ("big bend") in its longitudinal axis where it crosses the Transverse Ranges.

To fill the need for a more specific seismotectonic model of the southern Coast Ranges, we outline a model based on (1) the seismicity and focal-mechanism data presented above, (2) the gross geologic features of the region, and (3) the general results of detailed studies of earthquakes and crustal structures in the region (fig. 7.7).

The zone of interaction between the Pacific and North American plates appears to extend entirely across the Coast Ranges. The occurrence of earthquakes at depths of a few kilometers to about 12 km throughout this zone implies that the crust is being deformed and is both brittle and elastic in that depth range. Studies of the distribution of earthquakes with depth on the major strike-slip faults, using both large earthquakes and their aftershocks and the long-term background of smaller earthquakes, show that the transition from the seismic to the aseismic zone is abrupt (Eaton and others, 1970; Reasenberg and Ellsworth, 1982; Cockerham and Eaton, 1984; Sibson, 1984). A similar abrupt cutoff in seismicity below about 12 km was observed for the Coalinga earthquake sequence, which occurred near the edge of the Great Valley more than 30 km northeast of the San Andreas fault and consisted almost entirely of reverse-faulting events (see chap. 8).

P-wave velocities also appear to increase abruptly from near 6.0 to about 6.5 km/s at depths of 12 to 15 km beneath the region (see chap. 3; Walter and Mooney, 1982). The depth to the mantle and the velocity of *P* waves in the upper mantle appear to range across the southern Coast Ranges from less than 25 km and about 8.1 km/s, respectively, along the coast to nearly 30 km and 7.9–8.0 km/s, respectively, along the edge of the Great Valley (Oppenheimer and Eaton, 1984).

We interpret these observations as indicating an abrupt transition from brittle elastic behavior to ductile behavior at a depth of 12 to 15 km, at or near the transition from upper- to lower-crustal velocities (materials?), throughout the southern Coast Ranges (see Sibson, 1982, 1984). This ductile lower crust provides sufficient decoupling between the deforming transform zone in the mantle beneath the Coast Ranges and the brittle upper crust that the pattern of deformation in the heterogeneous upper crust is strongly influenced by local physical properties of this upper crust and by the characteristics of structures within it (see Lachenbruch and Sass, 1973).

Particularly strong sections of the crust resist internal deformation, and earthquakes are concentrated along their boundaries. Weaker sections of the crust can undergo deformation and generate earthquakes internally as well as along their boundaries. Once established as zones of relative weakness, major throughgoing faults remain active even when the pattern of intracrustal stresses no longer favors their initiation (see Hill, 1982). Large sections of the brittle upper crust may, indeed, be rotated or pushed laterally along subhorizontal zones of detachment in the lower crust without symptomatic earthquakes, except where a detachment surface passes upward into the brittle crust.

Features of the seismicity and focal-mechanism maps that suggest the presence of a detachment zone include: (1) the complex branching of major strike-slip faults northwest of San Benito, (2) the mismatch between the strike of the San Andreas fault and the direction of relative plate motion (N. 41° W. versus N. 35° W.) between San Benito and Cholame, and (3) the evidence for reverse and thrust faulting along the flanks of the Coast Ranges southeast of Cape San Martin (Crouch and others, 1984) and southeast of Idria (see chaps. 4, 8).

In the upper part of figure 7.2, the heavy concentration of seismicity on strike-slip faults spaced at subequal intervals across the entire width of the Coast Ranges suggests that a thin, brittle upper crust is being cut into strips by shear deformation across a transform zone which spans the whole region. A degree of decoupling in the lower crust permits distributed shear deformation at depth to be concentrated along just a few faults in the upper crust. The preponderance of strike-slip to reverse-slip earthquakes in this region suggests that the current rate of convergence (perpendicular to the N. 35°± strike of the faults) across this zone is low (see Minster and Jordan, 1984).

Along both flanks of the Coast Ranges in the lower part of figure 7.2, the seismicity maps show scattered large clusters of epicenters, rather than the linear concentrations of epicenters commonly associated with strike-slip faults. Focal mechanisms of moderate and large recent earthquakes in these regions show predominantly thrust or reverse faults. We suggest that the distinctive pattern of seismicity in these regions indicates a predominance of reverse-slip and thrust faulting. Large earthquakes and their aftershocks scattered over one or more subhorizontal reverse or thrust faults cutting upward through the crust would appear as clusters of epicenters rather than as the linear concentrations characteristic of vertical faults. Because the underlying deformation of the transform zone is predominantly shear, however, the crust in

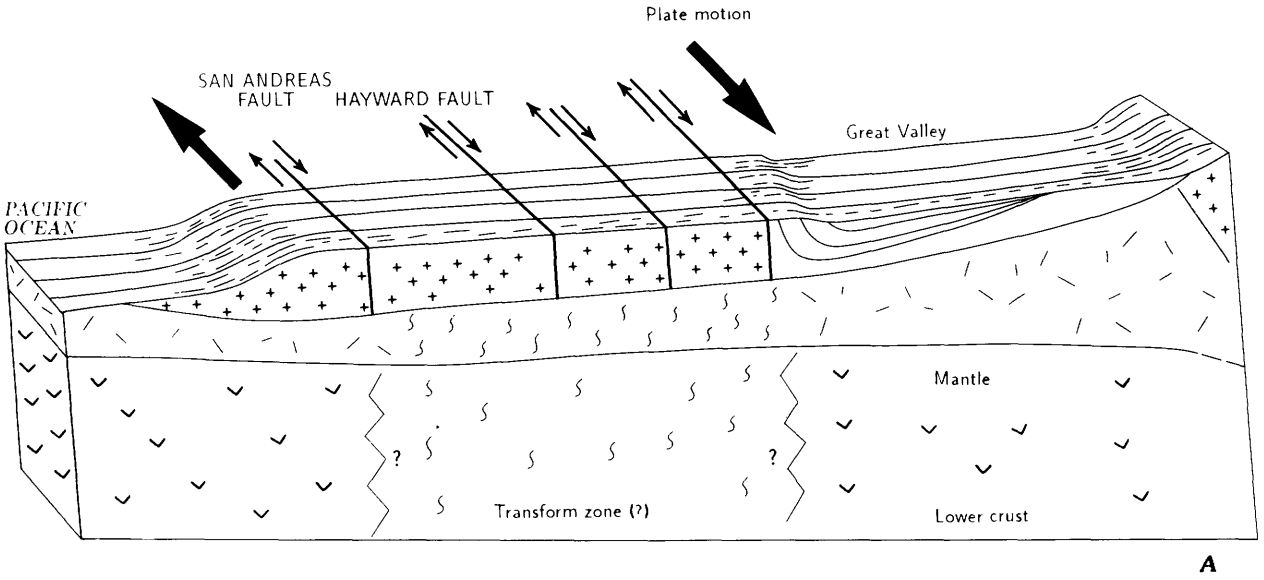

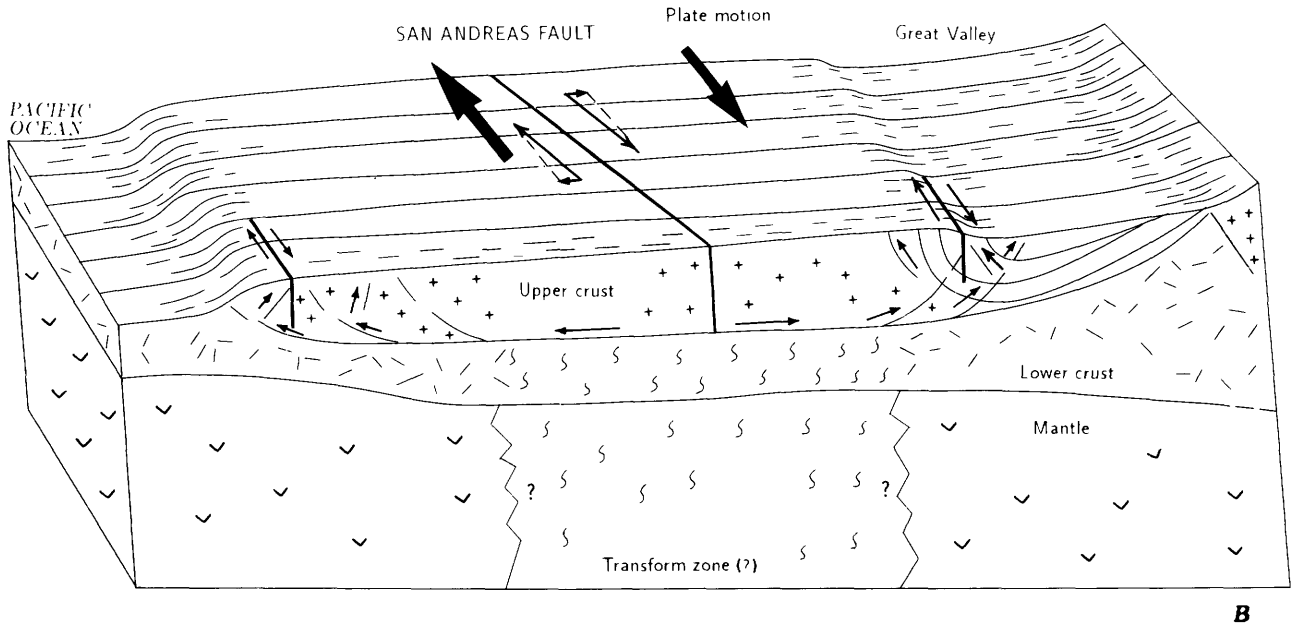

FIGURE 7.7.—Schematic cross sections at latitudes of San Francisco (*A*) and Coalinga (*B*), illustrating the seismotectonic model proposed for the southern Coast Ranges. In both regions, a brittle upper crust (crosses) overlies a lower crust (short slashes) that lies on the mantle (checks). Beneath the central part of the ranges, ductility of the lower crust and upper mantle (vertical "squiggles") accommodates relative motion of the plates and provides for decoupling of the upper crust from the lower crust. In figure 7*A*, major (strike slip) faults parallel the direction of relative plate motion, and almost all relative movement between the plates is accommodated by those faults. In figure 7*B*, slip along the misaligned San Andreas fault accommodates most motion between the plates but also widens the upper crust over the transform and drives the outer edges of the Coast Range crust out beyond the ductile part of the lower crust over the transform. Earthquakes occur on thrust and high-angle reverse faults along the edges of the range where the detachment zone beneath the center of the range encounters less ductile lower crust and passes up into brittle upper crust.

these regions is subjected to a component of shear stress that can be expressed as strike-slip faulting subparallel to the San Andreas fault if the normal stresses across such fault surfaces are not too large. Such a fault slipped to cause an M=5.3 strike-slip event along the east edge of the Coalinga aftershock zone on September 9, 1983.

The reverse faults along the flanks of the southern Coast Ranges may be rooted in detachment zones below 12-km depth (see chap. 4; Crouch and others, 1984), which may extend for some distance back toward the San Andreas fault in the middle of the ranges. The paucity of earthquakes between the San Andreas fault and the flanking zones of reverse faulting indicates that the crust above the transform zone is sufficiently strong and sufficiently decoupled from the crust below that it can resist internal deformation while sustaining the compressive forces required to push its outer margins out over the edges of the transform zone. The evidence presented here does not indicate whether such compressive forces result from a real convergence of the transform zone (see Minster and Jordan, 1984) or from an apparent convergence caused by a widening of the crust above the transform zone, due to movement on the misaligned section of the San Andreas fault between San Benito and the Transverse Ranges.

Looking farther south toward the Carrizo Plain and the locked section of the San Andreas fault between Cholame and San Bernardino, we speculate whether the same process is responsible for the great earthquakes that occur on that section of the fault: abnormally strong crustal rocks pinned together along the fault by an abnormally large normal component of stress resulting from real or apparent convergence of the plates along that section of the transform.

We return briefly to the question of the significance of the "seismic gaps" (fig. 7.3) contiguous to the Coalinga aftershock zone. We have argued that the broad zone of low seismicity between the San Andreas fault and the Coalinga aftershock zone represents a block of strong crust that is underlain by a detachment zone in the lower crust, over which the block is being driven northeast toward the Great Valley. According to this hypothesis, the low seismicity in this region does not portend a future earthquake. The zones of low seismicity just southeast and just northwest of the Coalinga aftershock zone, however, are in a different situation. The zone of thrust and reverse faulting along the northeast edge of the detachment zone at Coalinga can reasonably be supposed to continue toward both the southeast and northwest from Coalinga. Relative quiescence in those regions can be fairly interpreted as "seismic gaps" and possible precursors of earthquakes. In fact, a 20-km-long region immediately southeast of the Coalinga aftershock zone generated the M=5.7 North Kettleman Hills earthquake on August 4, 1985. The quiet region shown in figure 7.3 just northwest of the Coalinga aftershock zone remains a good candidate for an $M=6\pm1/2$ earthquake during the next few years.

Our model is only one of many that include a detachment zone or decollement within the crust of the San Andreas fault system. Lachenbruch and Sass (1973, 1980) explained heat-flow patterns in the Coast Ranges by a model in which the crust is formed directly on top of a window of freshly emplaced mantle near the Mendocino triple junction. The presence of a detachment zone beneath the Transverse Ranges has been proposed by many authors (for example, Anderson, 1971; Hadley and Kanamori, 1978; Yeats, 1981; Davis, 1983; Sibson, 1983; Webb and Kanamori, 1985). Crouch and others (1984) suggested a detachment zone below about 12- to 15-km depth on the basis of seismic-reflection profiles across faults offshore, between Point San Luis and Santa Barbara.

The time of initiation and the extent of the inferred detachment zone are not known but would, presumably, be related to the development of the San Andreas system. Page and Engebretson (1984) addressed these problems, without citing a specific model, when they suggested that the rise of individual parts of the Coast Ranges, starting 1–3 Ma, as well as the development of folds and reverse faults parallel to the plate boundary, may be related to slight convergence superposed on the San Andreas system within the past 5 Ma. The presence of zones of thrusting along both flanks of the southern Coast Ranges suggests a component of convergent movement between the Pacific and North American plates across this part of the transform. Minster and Jordan (1984) concluded that between 4- and 13-mm/yr of compression normal to the San Andreas fault is occurring across the fault system. Such compression might account for fold axes subparallel to parallel to the San Andreas fault in central California (fig. 7.4). In the San Francisco Bay region, farther north, Aydin and Page (1984) concluded that most folds and reverse faults are due to interaction between major strike-slip faults; but they also noted a peculiar geometry of folds and reverse faults parallel to the major faults. These latter folds and faults may have been due to compression normal to the San Andreas fault like that inferred near Coalinga (see chaps. 4, 8, 13).

CONCLUSIONS

The model of the earthquake-generating process most commonly considered for California earthquakes is applicable to the major strike-slip faults of the San Andreas system. Relatively little attention, however, has been paid to potential earthquake sources along the flanks of

the Coast Ranges. The moderate level of background seismicity and the occurrence of several $M \geq 5$ earthquakes along the edge of the Great Valley between Idria and Devils Den from 1975 through 1982 did cause some concern, but the seismicity data for this region was incomplete and had not been organized so as to support its thoughtful interpretation. The monitoring and evaluation of earthquakes along the flanks of the Coast Ranges were lagging behind such work on the nearby San Andreas fault because of limited resources and the higher priority assigned to the San Andreas itself. Moreover, a plausible model to explain the occurrence of earthquakes in such regions and to place them in the context of broader processes at work in the transform zone was unavailable.

The occurrence of the May 2 earthquake has increased concern over future large earthquakes elsewhere along the flanks of the Coast Ranges (see chap. 4), and postearthquake analysis of the instrumental record of seismicity in the southern Coast Ranges during the 11 years before this earthquake has led to the formulation of a seismotectonic model for the generation of similar events.

Nevertheless, a seismotectonic model like that sketched above for the southern Coast Ranges (fig. 7) will not lead directly to reliable earthquake predictions. It must be tested against additional data and modified and improved by new observations and insights. The model that will evolve through this process can be expected to enhance the usefulness of the historical seismic record, as well as the stream of current seismic observations, for predicting earthquakes. Both further development of such models and their effective application to evaluating earthquake potential and predicting specific events will require improved monitoring and analysis of earthquakes along the flanks of the Coast Ranges. The same effort should lead to a better understanding of the process that generates great earthquakes along the section of the San Andreas fault southeast of Cholame.

REFERENCES CITED

Anderson, D.L., 1971, The San Andreas fault: Scientific American, v. 225, no. 5, p. 52–66.

Aydin, Atilla, and Page, B.M., 1984, Diverse Pliocene-Quaternary tectonics in a transform environment, San Francisco Bay region, California: Geological Society of America Bulletin, v. 95, no. 11, p. 1303–1317.

Cockerham, R.S., and Eaton, J.P., 1984, The April 24, 1984, Morgan Hill earthquake and its aftershocks: April 24 through September 30, 1984, *in* Bennett, J.H., and Sherburne, R.W., eds., The 1984 Morgan Hill, California earthquake: California Division of Mines and Geology Special Publication 66, p. 215–236.

Crouch, J.K., Bachman, S.B., and Shay, J.T., 1984, Post-Miocene compressional tectonics along the central California margin, *in* Crouch, J.K., and Bachman, S.B., eds., 1984, Tectonics and sedimentation along the California margin (volume 38): Society of Economic Paleontologists and Mineralogists, Pacific Section Annual Convention, San Diego, 1984, Papers, p. 37–54.

Davis, T. L., 1983, Late Cenozoic structure and tectonic history of the western "Big Bend" of the San Andreas fault and adjacent San Emigdio Mountains: Santa Barbara, University of California, Ph.D. thesis.

Eaton, J.P., 1984, Focal mechanisms of near-shore earthquakes between Santa Barbara and Monterey, California: U.S. Geological Survey Open-File Report 84-477.

—— 1985, Temporal variation in the pattern of seismicity in central California, *in* Earthquake prediction: Tokyo, Terra Scientific, p. 425–437.

Eaton, J.P., O'Neill, M.E., and Murdock, J.N., 1970, Aftershocks of the 1966 Parkfield-Cholame, California, earthquake: A detailed study: Seismological Society of America Bulletin, v. 60, no. 4, p. 1151–1197.

Hadley, D.M., and Kanamori, Hiroo, 1978, Recent seismicity in the San Fernando region and tectonics in the west-central Transverse Ranges, California: Seismological Society of America Bulletin, v. 68, no. 5, p. 1449–1457.

Hill, D.P., 1982, Contemporary block tectonics: California and Nevada: Journal of Geophysical Research, v. 87, no. B7, p. 5433–5450.

Hoskins, E.G., and Griffiths, J.R., 1971, Hydrocarbon potential of northern California offshore, *in* Cram, I.H., ed., Future petroleum provinces of the United States—their geology and potential: American Association of Petroleum Geologists Memoir 15, p. 212–228.

Jennings, C.W., compiler, 1977, Geologic map of California: Sacramento, California Division of Mines and Geology, scale 1:750,000.

Lachenbruch, A.H., and Sass, J.H., 1973, Thermo-mechanical aspects of the San Andreas fault system, *in* Proceedings of the conference on tectonic problems of the San Andreas fault system: Stanford, Calif., Stanford University Press, p. 192–205.

—— 1980, Heat flow and energetics of the San Andreas fault zone: Journal of Geophysical Research, v. 85, no. B11, p. 6185–6222.

Minster, J.B., and Jordan, T.H., 1978, Present-day plate motions: Journal of Geophysical Research, v. 83, no. B11, p. 5331–5354.

—— 1984, Vector constraints on Quaternary deformation of the western United States east and west of the San Andreas fault, *in* Crouch, J.K., and Bachman, S.B., eds., Tectonics and sedimentation along the California margin (volume 38): Society of Economic Paleontologists and Mineralogists, Pacific Section Annual Convention, San Diego, 1984, Papers, p. 1–16.

Oppenheimer, D.H., and Eaton, J.P., 1984, Moho orientation beneath central California from regional earthquake travel times: Journal of Geophysical Research, v. 89, no. B12, p. 10267–10282.

Page, B.M., and Engebretson, D.C., 1984, Correlation between the geologic record and computed plate motions for central California: Tectonics, v. 3, no. 2, p. 133–155.

Reasenberg, Paul, and Ellsworth, W.L., 1982, Aftershocks of the Coyote Lake, California earthquake of August 6, 1979: A detailed study: Journal of Geophysical Research, v. 87, p. 10637–10655.

Sibson, R.H., 1982, Fault zone models, heat flow, and the depth distribution of earthquakes in the continental crust of the United States: Seismological Society of America Bulletin, v. 72, no. 1, p. 151–163.

—— 1983, Continental fault structure and the shallow earthquake source: Geological Society of London Journal, v. 140, pt. 5, p. 741–767.

—— 1984, Roughness at the base of the seismogenic zone: Contributing factors: Journal of Geophysical Research, v. 89, no. B7, p. 5791–5799.

Walter, A.W., and Mooney, W.D., 1982, Crustal structure of the Diablo and Gabilan Ranges, central California: A reinterpretation of existing data: Seismological Society of America Bulletin, v. 72, no.

5, p. 1567–1590.

Webb, T.H., and Kanamori, Hiroo, 1985, Earthquake focal mechanisms in the eastern Transverse Ranges and San Emigdio Mountains, southern California and evidence for a regional decollement: Seismological Society of America Bulletin, v. 75, no. 3, p. 737–757.

Yeats, R.S., 1981, Quaternary flake tectonics of the California Transverse Ranges: Geology, v. 9, no. 1, p. 16–20.

Yerkes, R.F., 1985, Geologic and seismologic setting, *in* Ziony, J.I., ed., Evaluating earthquake hazards in the Los Angeles region—an earth-science perspective: U.S. Geological Survey Professional Paper 1360, p. 25–41.

Yerkes, R.F., Greene, H.G., Tinsley, J.C., and Lajoie, K.R., 1981, Seismotectonic setting of Santa Barbara Channel area, southern California: U.S. Geological Survey Miscellaneous Field Studies Map MF–1169, 25 p., scale 1:250,000.

Yerkes, R.F., and Lee, W.H.K., 1979, Faults, fault activity, epicenters, focal depths, focal mechanisms, 1970–75 earthquakes, western Transverse Ranges, California: U.S. Geological Survey Miscellaneous Field Studies Map MF-1032, scale 1:250,000, 2 sheets.

8. THE EARTHQUAKE AND ITS AFTERSHOCKS FROM MAY 2 THROUGH SEPTEMBER 30, 1983

By J.P. Eaton,
U.S. Geological Survey

CONTENTS

ABSTRACT

Analysis of the Coalinga earthquake sequence, based on the Allen/Ellis real-time-processor (RTP) automatic *P*-phase-onset time and duration measurements, provides hypocentral and magnitude determinations for more than 6,000 events from May 2 through September 30, 1983. Focal mechanisms and local magnitudes of more than 140 of the larger aftershocks were calculated from more detailed observations obtained from magnetic-tape playbacks from both the temporary Coalinga seismic network and the permanent telemetered central California seismic network (Calnet).

The combined catalog appears to be substantially complete for events of $M \geq 3$ within about 3 hours, and for events of $M \geq 1.7$ within about 1 day, after the main shock. The rate of occurrence of aftershocks of $M \geq 1.7$ diminishes approximately as $(t+1.0)^{-1}$, where t is the time (in hours) after the main shock. Cumulative number of aftershocks versus magnitude is described by $\log N(M) = 5.05 - 0.87M$, where $N(M)$ is the number of events in the sequence of magnitude greater than or equal to M. The most prevalent focal depth increases markedly with increasing magnitude, but events of all magnitudes die out abruptly below about 13 km.

The first-motion plot of the main shock offers two choices for the main-shock fault: a thrust fault striking N. 53° W. and dipping 23° SW. (the preferred fault plane), or a high-angle reverse fault striking N. 53° W. and dipping 67° NE. Focal mechanisms of the larger aftershocks also indicate predominantly thrust or reverse faulting. *P*-axis orientations of the aftershocks vary systematically across the aftershock region: Along Anticline Ridge in the center of the aftershock zone they are parallel to the *P* axis of the main shock (southwest-northeast); however, farther northwest they are rotated clockwise, and farther southeast they are rotated counterclockwise, relative to the *P* axis of the main shock.

The long axis of the aftershock zone, which is 35 km long and 15 to 20 km wide, coincides with the axis of the Anticline Ridge-Guijarral Hills structure at the Coast Ranges-Great Valley boundary northeast of Coalinga. A transverse (southwest to northeast) quiet band with very few events crosses the aftershock zone where northwest-trending Anticline Ridge joins broader, east-west-trending Joaquin Ridge just northwest of the main shock. Southeast of this quiet band, the principal concentrations of aftershocks lie along the flanks of Anticline Ridge; farther southeast, they lie beneath and west of the Guijarral Hills. Northwest of the quiet band, aftershocks are more evenly dispersed and appear to be cut off along the axis of Joaquin Ridge.

Stereoplots of fault-plane solutions for the larger aftershocks outline several probable fault surfaces. The most pervasive surface coincides with the southwest-dipping thrust-fault solution for the main shock and underlies most of the aftershock region. The most conspicuous northeast-dipping reverse fault crops out near Nuñez Canyon at the west edge of the aftershock zone northwest of the quiet band; its strike is almost due north, and it extends downward to the principal thrust surface. The most conspicuous northeast-dipping reverse fault southeast of the quiet zone is along the west edge of the concentration of aftershocks beneath the west flank of Anticline Ridge; it is best developed at depths of 5 to 10 km and appears to terminate against the principal thrust surface at depth. Another northeast-dipping reverse fault lies along the northeast edge of the aftershock region; it penetrates to a depth of only about 5 km, where it appears to terminate against the principal thrust surface. The smaller aftershocks occur mostly in the hanging-wall blocks above the faults outlined by the larger aftershocks.

INTRODUCTION

The Coalinga earthquake sequence presents a rare opportunity to study a large non-San Andreas earthquake in the central Coast Ranges. An understanding of the faulting that caused it may provide insight into the relation of Coast Range structures to the San Andreas

fault and to the underlying tectonic processes that generate earthquakes on the San Andreas fault, as well as elsewhere in the Coast Ranges. The large size of the main shock and its location adjacent to the Parkfield section of the San Andreas fault, at the transition from the creeping section (northwest of Parkfield) to the locked section (in the Carrizo Plains and beyond toward the southeast) of the fault, raise the question whether such earthquakes may play a role in locking or unlocking the Fort Tejon section of the fault.

Excellent records of the main shock were obtained on 29 telemetered seismographs within 80 km of its epicenter, including one station (PAR) on Anticline Ridge near the center of the aftershock region. Nonetheless, azimuthal station coverage for the main shock was poor because it occurred east of the dense network around Parkfield and west of the seismically noisy Great Valley, which had no nearby stations on May 2. Beginning about 24 hours after the main shock, coverage was augmented by a portable network of 12 stations, and within the first week 4 permanent stations were installed along the west edge of the Great Valley to close the gap in coverage northeast of the main shock.

The complex geology at the Coast Ranges-Great Valley boundary where the sequence occurred, and our poor knowledge of the velocity structure of the crust in that region, were serious impediments to determining reliable, accurate hypocenters for events in the Coalinga earthquake sequence. Determination of a suitable structure from the earthquake data was, therefore, undertaken in conjunction with determination of the earthquake hypocenters. In this process, possible structures were constrained by the requirement that they yield first-motion plots corresponding to double-couple focal mechanisms, as well as that they result in hypocentral solutions with suitably small traveltime residuals. To suppress the systematic bias in hypocenter location that is introduced by the rapid lateral variation of velocity in the upper crust at the Coast Ranges-Great Valley boundary, station delays derived by an interactive procedure, beginning with *Pn* time-term differences, were used with the crustal-velocity model that met the requirements stated above.

This chapter completes the second phase of the analysis of the Coalinga data. The first phase, reported by Eaton and others (1983), was based primarily on an analysis of arrival times for several thousand earthquakes that were detected and timed by the Allen/Ellis real-time processor (RTP) in Menlo Park, Calif. (Allen, 1982), and on detailed studies of the main shock and nine aftershocks played back from magnetic tape. For the present study, the RTP data from the telemetered network were augmented by RTP data picked from magnetic tape playbacks of the portable network (see chap. 18), and the number of large aftershocks played back from both the telemetered and portable networks for focal-plane determinations was increased to 148. The goals of this study are (1) to refine the crustal model and station delays to permit more reliable hypocentral determinations; (2) to resolve major features of the faulting that caused the earthquakes in the sequence, through a joint study of the focal mechanisms and hypocentral distribution of the largest aftershocks; and (3) to examine the relation between the distribution of the several thousand well-recorded smaller aftershocks, the pattern of faulting suggested by the larger aftershocks, and the principal geologic features of the Coalinga region.

SEISMIC DATA AVAILABLE FOR STUDY OF THE COALINGA EARTHQUAKE SEQUENCE

The May 2 earthquake occurred about 5 km west of the Coast Ranges-Great Valley boundary and about 3 km southeast of station PAR, the nearest station of the telemetered central California seismic network (Calnet; fig. 8.1). Although 17 network stations were located

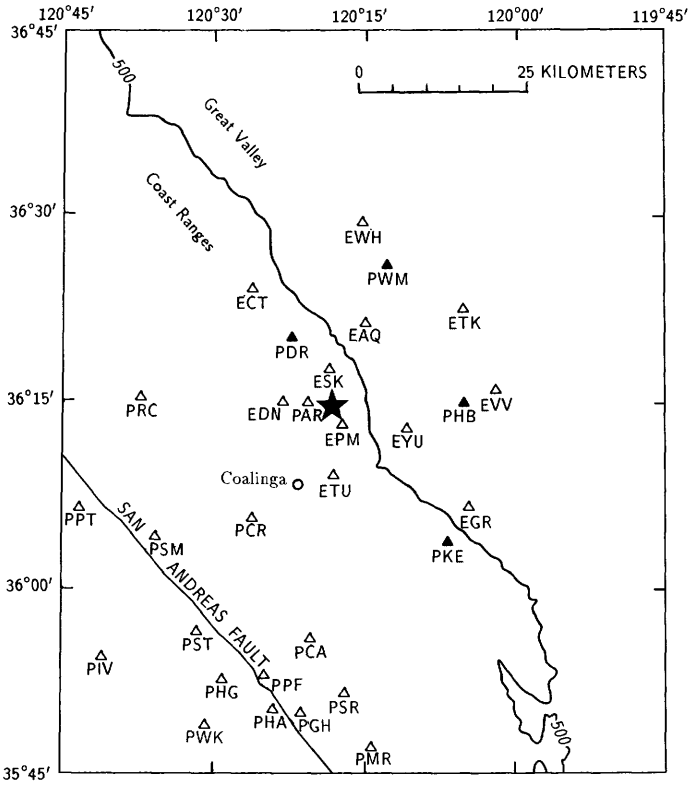

FIGURE 8.1.—Schematic map of Coalinga, Calif., area, showing locations of May 2 earthquake (star), San Andreas fault, Coast Ranges-Great Valley boundary (500-ft-elevation contour), seismograph stations in portable network (open triangles labeled "E"), pre-May 2 telemetered network (open triangles labeled "P"), and post-May 2 additions to permanent network (solid triangles).

within 50 km of the epicenter, they were all in the Coast Ranges, entirely on one side of the epicenter. The records used here for the first 24 hours of the aftershock sequence came exclusively from stations in the original (May 2) telemetered network, which were recorded on magnetic tape and film, as well as processed automatically by the RTP in Menlo Park. Beginning about 24 hours after the main shock, 12 portable three-component, 5-day-tape-recorder stations recording at two gain levels for each component were installed rapidly around the main-shock epicenter to provide improved near-in and azimuthal station coverage of the aftershock region (fig. 8.1). Four new permanent stations of the telemetered network, at locations chosen to complement the original telemetered network in the Coalinga region, began recording on May 6 (fig. 8.1). The original 5-day-tape-recorder network was operated until the end of May; the number of stations was then reduced to 8, and it was operated in its diminished form until the end of June.

Though under development and evaluation at the time of the Coalinga earthquake sequence, the RTP performed remarkably well throughout the aftershock sequence. In spite of hardware problems requiring occasional dependence on hand analysis of the film records, it provided an ongoing overview of activity in the aftershock region. In addition to rapid location and magnitude determinations for tracking the progress of the aftershock sequence, the RTP provided a vast record of onset-time and duration data on individual events in the sequence. These data, reprocessed to eliminate spurious readings and relocated using an improved model and improved station corrections, composed the primary catalog of Coalinga aftershocks (Eaton and others, 1983). The most serious deficiency in the original RTP data set was that it included only stations in the telemetered network. Tapes from the portable stations were subsequently processed by an offline version of the RTP, and the data read from them have been added to the original RTP data file.

The RTP data are also inadequate for the detailed studies carried out on the large aftershocks: Stations beyond 150 km from Coalinga generally were not picked, first-motion directions were unreliable, and maximum amplitudes recorded at unclipped stations for determining the magnitudes of large events were not read. Accordingly, nearly 150 aftershocks of $M \geq 3.2$ in the original RTP catalog were played back from magnetic tape for both the telemetered and the portable networks. Although only stations at distances of 80 km or less were used for hypocentral calculations, more distant stations were used for determining magnitudes and focal mechanisms. The low-gain, multicomponent, telemetered network stations were particularly useful for magnitude determinations, and telemetered stations at distances of 80 to 300 km and at a wide range of azimuths were indispensable for the focal-mechanism determinations.

CRUSTAL MODELS, STATION DELAYS, AND MAGNITUDE CORRECTIONS

The region of the Coalinga earthquake sequence lies at the east edge of a dense part of Calnet and just west of the Coast Ranges-Great Valley boundary; the velocity model routinely used for central California earthquakes gives poor results there. Crustal structure varies abruptly from east to west across the region, particularly with respect to the thickness of low-velocity material in the upper crust. Although recent refraction profiles provide better information along selected lines (see chap. 3; Wentworth and others, 1983), coverage is not yet sufficiently broad to provide an adequate model for earthquake-hypocenter determinations.

I have employed data from well-recorded, well-distributed Coalinga "calibration" events to develop a more appropriate model and set of station delays. An initial (standard Calnet) model and set of station delays were varied systematically in a succession of relocations of the calibration events to minimize rms traveltime residuals and to comply with the requirement that first-motion plots be separable into distinct fields of compressions and dilatations by the two orthogonal nodal planes of a double-couple earthquake source. This requirement imposes constraints on the ratios of the velocity at the focus to velocities at the refractors from which first motions are recorded.

Arrival-time residuals of individual events were analyzed with respect to size and variation with distance along each boundary returning first arrivals in the tested model. Model corrections to layer depths and velocities suggested by this analysis were then made, and the process was repeated until a satisfactory fit was obtained. The somewhat different models obtained from separate calibration events were then compared, and a "consensus" model was drawn up and checked with the individual calibration events. The entire set of calibration events was then located by using the consensus model and the initial station delays. Average station traveltime residuals from this run were added to the initial set of station delays to obtain an improved set of station delays. This procedure was repeated once more to get the final set of station delays.

The delays so determined embody traveltime variations due to purely local (near-surface) structural anomalies at the individual stations, as well as possible systematic errors due to a mismatch of the crustal model to the Earth. It can be argued that the use of station delays thus obtained improves the relative locations of hypocenters, particularly for events that were not well recorded by the entire set of stations used for location of

the calibration events; however, absolute location errors resulting from gross regional variations in structure, such as the transition from the Coast Ranges to the Great Valley, are not removed. This deficiency can be partly offset by using an initial set of station delays that reflects the gross regional variation in traveltimes due to the anomalous structure. I have used a set of initial station delays based on *Pn* time-term differences determined from well-recorded events at appropriate distances and azimuths from the network stations around Coalinga (J.P. Eaton, unpub. data, 1979). This procedure is valid to the extent that the relative delays at these stations are due primarily to variations in the shallow structure beneath the stations that is traversed both by *Pn* waves from regional earthquakes and by direct or refracted waves from the local Coalinga earthquakes that we wish to locate. However, these delays are only first-order estimates of the delays undergone by waves traversing the anomalous structures at angles of incidence different from that of the *Pn* waves.

In an earlier study of the May 2 earthquake (Eaton and others, 1983), I used *Pn* time-term-difference data that were rather weak in the Coalinga region; they were determined before the installation of telemetered network stations in the Great Valley east of Coalinga. Values for the new Great Valley stations were estimated from very meager data at stations along the west edge of the Sacramento Valley, far to the north. Since that earlier study, however, four additional well-recorded, well-located earthquakes in central California have provided good *Pn* data in the part of the network used to locate the Coalinga events. These new data have been used, together with data from the earlier *Pn* travel time-term-difference study, to establish an improved set of initial station delays for the Coalinga region.

Beginning with the final crustal model (CM4) from my previous study and the improved set of initial station delays discussed above, I have repeated the procedure described above to obtain a new crustal model (CM5) and station-delay set that should more adequately suppress the bias in hypocenter locations resulting from the east-to-west variation in crustal structure across the Coalinga region.

Model 4 is as follows:

Velocity (km/s)	*Depth to layer (km)*
2.50	0.00
4.30	2.00
5.60	7.00
5.70	10.00
6.40	14.00
7.90	28.00

and for comparison, model 5 is:

Velocity (km/s)	*Depth to layer (km)*
2.50	0.00
4.30	1.50
4.70	3.50
5.60	7.00
5.80	9.00
6.30	14.00
6.60	15.00
7.95	28.00

This model and station-delay set have been used for hypocentral determinations of the main shock and 148 larger aftershocks analyzed in this study, as well as for relocation of the several thousand smaller aftershocks on the basis of the augmented RTP onset times.

Maximum amplitudes and associated periods were read from unclipped records of both Calnet and the portable network to provide a basis for computing local magnitudes of the larger aftershocks. To reduce the dependence of computed magnitudes of individual events on the subset of stations used to determine them, we have computed average station-magnitude residuals from a set of 100 of the best recorded aftershocks. These average residuals were then applied as corrections in the calculation of the magnitudes of individual events. The station delays used with crustal models CM4 and CM5, as well as the station-magnitude corrections applied in this study, are listed in table 8.1.

DETERMINATION OF THE HYPOCENTERS OF AFTERSHOCKS

The detection threshold and record quality, as well as the areal coverage provided by the network, changed over time during the Coalinga earthquake sequence. During the first 24 hours or so (from the main shock at 2342 g.m.t. May 2 through May 3), only stations in the original telemetered network were in operation, and the high rate of occurrence of aftershocks and resulting high level of background noise in the epicentral region made detection of small events and accurate timing of wave onsets difficult. For many small to moderate events, the only nearby station (PAR, near the center of the aftershock region) was too noisy to read. As portable stations were installed in the aftershock region, beginning in the early hours of May 4, network coverage improved significantly, and the number of small events escaping detection decreased sharply. Background noise also had diminished considerably by that time, although small events continued to be lost because they were masked by larger aftershocks. The frequency of aftershocks and the level of background noise continued to decrease, and from about May 6 onward the detection capability of the network was limited primarily by the number and location of stations.

Reduction of the portable network from 11 to 8 stations at the end of May had little effect on the adequacy of the network, but removal of the 8 other portable stations at the end of June impaired the precision of focal-depth determinations. This reduced network was still substantially better than the pre-May 2 network, however, because of the four new telemetered network stations just east of the aftershock region.

ANALYSIS OF RTP DATA FOR THE COMPLETE AFTERSHOCK SEQUENCE

The RTP in Menlo Park continuously monitors signals from the south two-thirds (about 250 stations) of Calnet. The signal from each station is sampled 100 times per second and processed by a microcomputer running an algorithm that (1) detects a sudden increase in signal level, (2) determines the onset time and polarity of the signal-level increase, and (3) measures the time that the signal remains above a level equivalent to 1 cm on the standard Develocorder film. The microcomputer also monitors the occurrence of such onsets at all processed stations to detect the presence of an earthquake on the basis of the spatial and temporal pattern of onsets detected by the individual stations. Groups of onsets that satisfy the conditions for an earthquake are written to a file which is passed on to a minicomputer, a DEC 11/70, that determines its location and records it in an earthquake-summary file for the day. The hypocenter is determined by the program HYPO71 (Lee and Lahr, 1975), using a regional crustal model, and the magnitude is calculated from the recorded duration times. Duration times longer than 140 s are truncated by the RTP, and so magnitudes larger than about 3.7 are underestimated.

The RTP does not save the seismic traces, only the onset times, onset directions, and event durations; thus, the validity of a recorded event must be judged indirectly on the basis of the recorded data. The primary criteria that we have applied are (1) redundancy (the greater the number of recorded onsets beyond the minimum four required for a solution, the more certain that the event is real) and (2) quality of the hypocentral solution (a large rms residual argues against the reality of an event recorded by only a few stations).

The processing of the RTP data employed in this study was experimental, and so it is outlined in detail here. (1) The daily RTP hypocenter-summary list produced in routine processing was screened to select all events with usable onsets from seven or more stations that occurred within 1° of latitude and longitude of the Coalinga main-shock epicenter. The corresponding phase data were then extracted from the daily RTP phase files. (2) The extracted events were relocated with the program HYPO71, using crustal model CM4 and associated station corrections. (3) The detailed hypocenter solutions (location summary plus station residuals, and so on) were examined to eliminate stations with residuals larger than 3 times the total rms residual, and a revised phase list was generated. The events were then relocated on the basis of this list. (4) I examined solutions with an rms residual larger than 0.25 s. Many substandard solutions resulted from one or more obviously spurious readings, which were removed. Many other poor solutions resulted from mixed readings from a small preliminary event and a slightly larger later event; most of these solutions were improved by judicious elimination of the very early or very late readings. Fewer than 1 event in 10 required this step of analysis; good solutions were ultimately obtained for almost all the events selected for reprocessing. (5) When the offline RTP picks from the portable network became available, they were added to the reprocessed phase lists from the telemetered networks. (6) The augmented phase lists were then relocated with the program HYPO71, using model CM5 and associated station corrections. (7) The few events with an rms residual greater than 0.25 s were examined, corrected, and relocated to complete the list of RTP locations. (8) During episodes of very frequent aftershocks, when signals failed to drop to the equivalent of 1 cm on the standard Develocorder film, the RTP was unable to determine valid event-duration times for the computation of magnitudes. At such times, duration magnitudes were calculated from estimated duration times read from Develocorder monitor records or, for the first 6 hours of the Coalinga earthquake sequence, from continuous low-gain playbacks of selected stations at various epicentral distances.

ANALYSIS OF THE LARGER AFTERSHOCKS

The 148 larger aftershocks were selected from the RTP summary list at stage 4 (above) before the portable-network phase data were available. The selection threshold was set at M=3.4 to ensure selection of M=3.5 events; however, some smaller events were also selected on the basis of the number of phases used in the hypocenter determination, which depends on the size and onset clarity of the events. The records of these aftershocks were read "by hand" on paper playbacks from magnetic tape. All available portable-network records were used. Records from Calnet stations at critical azimuths out to several hundred kilometers were read. P-wave-onset times and first motions were read from high-gain vertical components, and S-wave-onset times were read when available, generally from low-gain horizontal components. Maximum trace amplitudes and associated periods were read from unclipped traces, which were generally from low-gain recording channels.

For hypocenter determinations, model CM5 and associated station corrections were used with the program

TABLE 8.1.—*Station list with station delays for models CM4 and CM5, magnitude station corrections, and calibration factors showing relative magnification of stations*

[Asterisks denote stations farther than 120 km from the main shock, which were not used in hypocenter calculations]

Station	Location		Elevation (m)	Station delay		Magnitude correction	Calibration factor
	Lat N.	Long W.		Model CM4	Model CM5		
ADW*	38°26.35'	120°50.89'	251	0	.58	-.02	11.152
ALA*	38°34.00'	120°57.37'	293	0	.56	.13	23.300
AOD*	38°36.89'	120°43.71'	520	0	1.38	.21	11.152
ARJ*	38°41.19'	120°57.38'	460	0	.77	.14	11.152
BAV	36°38.75'	121° 1.79'	604	-.43	-.47	.82	23.300
BAVE	36°38.75'	121° 1.79'	604	0	-.47	.34	.353
BAVN	36°38.75'	121° 1.79'	604	0	-.47	.33	.353
BAVZ	36°38.75'	121° 1.79'	604	0	-.47	.46	.353
BBG	36°35.48'	121° 1.52'	1,216	.09	.02	.37	11.152
BBN	36°30.60'	121° 4.53'	448	-.09	-.26	.25	23.300
BCG	36°42.55'	121°20.60'	305	-.05	-.01	.34	5.590
BEH	36°39.88'	121°10.45'	342	-.13	-.26	.29	5.590
BEM	36°39.68'	121° 5.76'	488	-.09	-.28	.36	11.152
BHR*	36°43.67'	121°15.83'	213	-.09	-.25	-.19	5.590
BHS	36°21.35'	121°32.39'	646	-.34	-.25	2.04	5.590
BJC	36°32.82'	121°23.53'	207	-.60	-.62	.84	23.300
BJO	36°36.65'	121°18.81'	1,052	-.49	-.58	.52	11.152
BLR	36°39.96'	121°16.36'	232	.12	.07	.25	11.152
BMS	36°39.78'	120°47.51'	811	-.08	-.05	.36	5.590
BPC	36°34.32'	121°37.56'	183	-.32	-.25	.13	11.152
BPCN	36°34.32'	121°37.56'	183	0	-.25	-.49	.353
BPF	36°13.80'	121°46.30'	349	-.49	-.61	.26	5.590
BPFN	36°13.80'	121°46.30'	349	0	-.61	-.25	.353
BPI	36°29.40'	121°10.41'	329	-.66	-.75	.58	23.300
BPP	36°10.12'	121°22.68'	1,591	-.45	-.59	.17	11.152
BRM	36°50.70'	120°49.42'	372	.01	.16	.11	5.590
BRV	36°25.49'	121° 1.10'	541	-.01	-.32	.30	5.590
BSC	36°38.50'	121°15.59'	323	-.22	-.37	.37	11.152
BSCE	36°38.50'	121°15.59'	323	-.22	-.37	.11	.353
BSCN	36°38.50'	121°15.59'	323	-.22	-.37	.19	.353
BSCZ	36°38.50'	121°15.59'	323	-.22	-.37	.28	.353
BSG	36°24.83'	121°15.22'	192	-.65	-.78	.47	5.590
BSGE	36°24.83'	121°15.22'	192	-.65	-.78	.08	.353
BSGN	36°24.83'	121°15.22'	192	-.65	-.78	-.02	.353
BSGZ	36°24.83'	121°15.22'	192	-.65	-.78	.30	.353
BSR	36°39.99'	121°31.12'	395	-.37	-.38	.52	11.152
BSRE	36°39.99'	121°31.12'	395	0	-.38	-.23	.353
BSRN	36°39.99'	121°31.12'	395	0	-.38	-.18	.353
BVL	36°34.51'	121°11.34'	510	-.29	-.39	.57	23.300
BVY	36°44.96'	121°24.80'	585	-.27	-.26	.63	23.300
CAL*	37°27.07'	121°47.95'	265	0	-.25	.57	23.300
CALE*	37°27.07'	121°47.95'	265	0	-.25	.27	.353
CALN*	37°27.07'	121°47.95'	265	0	-.25	.38	.353
CALZ*	37°27.07'	121°47.95'	265	0	-.25	.37	.353
CAO	37°20.96'	121°31.96'	628	-.42	-.17	.40	23.300
CAOE*	37°20.96'	121°31.96'	628	0	-.17	.22	.353
CAON*	37°20.96'	121°31.96'	628	0	-.17	.19	.353
CAOZ*	37°20.96'	121°31.96'	628	0	-.17	.29	.353
CDV*	37°33.98'	121°40.81'	250	0	-.11	.73	11.152
CDVE*	37°33.98'	121°40.81'	250	0	-.11	.26	.353
CDVN*	37°33.98'	121°40.81'	250	0	-.11	.17	.353
CDVZ*	37°33.98'	121°40.81'	250	0	-.11	.24	.353
CLK*	37°35.44'	118°49.45'	2,576	0	1.58	0	0
CMP	37°21.46'	121°18.51'	799	-.60	-.44	.45	5.590
DOE*	37°38.25'	118°50.00'	1,700	0	1.96	0	0
EAQ	36°21.31'	120°14.80'	97	.20	.65	.16	4.504
EAQE	36°21.31'	120°14.80'	97	.20	.65	-.11	4.504
EAQN	36°21.31'	120°14.80'	97	.20	.65	-.14	4.504
ECT	36°24.09'	120°26.14'	232	.35	.38	.78	17.930
ECTE	36°24.09'	120°26.14'	232	.35	.38	.66	17.930
ECTN	36°24.09'	120°26.14'	232	.35	.38	.41	17.930
EDG	36°20.15'	120°21.25'	296	.35	.28	.54	17.930
EDGE	36°20.15'	120°21.25'	296	.35	.28	.55	17.930
EDGN	36°20.15'	120°21.25'	296	.35	.28	.35	17.930
EDN	36°15.00'	120°23.04'	415	.30	.08	.46	17.930
EDNE	36°15.00'	120°23.04'	415	.30	.08	.33	17.930
EDNN	36°15.00'	120°23.04'	415	.30	.08	.24	17.930
EGR	36° 6.53'	120° 4.47'	101	.26	.32	-.16	4.504
EGRE	36° 6.53'	120° 4.47'	101	.26	.32	-.25	4.504
EGRN	36° 6.53'	120° 4.47'	101	.26	.32	-.37	4.504
EMH*	37°40.00'	118°56.35'	2,451	0	1.86	0	0
EPM	36°13.12'	120°17.07'	250	.35	.05	.31	4.504
EPME	36°13.12'	120°17.07'	250	.35	.05	.02	4.504
EPMN	36°13.12'	120°17.07'	250	.35	.05	-.04	4.504
ESK	36°17.58'	120°18.41'	256	.35	.15	.41	8.990
ESKE	36°17.58'	120°18.41'	256	.35	.15	.28	8.990
ESKN	36°17.58'	120°18.41'	256	.35	.15	.16	8.990
ETK	36°22.42'	120° 5.04'	77	.04	.38	.18	4.504
ETKE	36°22.42'	120° 5.04'	77	.04	.38	-.16	4.504
ETKN	36°22.42'	120° 5.04'	77	.04	.38	-.29	4.504
ETM	36°24.06'	120° 5.04'	72	.04	.25	-.17	2.256
ETME	36°24.06'	120° 5.04'	72	.04	.25	-.48	2.256
ETMN	36°24.06'	120° 5.04'	72	.04	.25	-.59	2.256
ETU	36° 9.09'	120°17.95'	186	.30	.07	.10	4.504
ETUE	36° 9.09'	120°17.95'	186	.30	.07	-.05	4.504
ETUN	36° 9.09'	120°17.95'	186	.30	.07	-.16	4.504
EVV	36°15.89'	120° 1.78'	88	.07	.44	-.08	8.880
EVVE	36°15.89'	120° 1.78'	88	.07	.44	-.34	8.880
EVVN	36°15.89'	120° 1.78'	88	.07	.44	-.35	8.880
EWH	36°29.44'	120°15.11'	76	.10	.61	-.06	2.256
EWHE	36°29.44'	120°15.11'	76	.10	.61	-.20	2.256
EWHN	36°29.44'	120°15.11'	76	.10	.61	-.38	2.256
EYU	36°12.83'	120°10.63'	128	.27	.23	-.04	8.990
EYUE	36°12.83'	120°10.63'	128	.27	.23	-.22	8.990
EYUN	36°12.83'	120°10.63'	128	.27	.23	0	8.990
HFE	36°59.00'	121°24.09'	323	-.13	-.09	.19	5.590
HFP	36°45.22'	121°29.43'	705	-.51	-.48	.60	23.300
HGS	37° 5.75'	121°26.83'	778	-.35	.01	.25	11.152
HJG	36°47.88'	121°34.43'	171	-.41	-.36	.47	11.152
HJS	36°48.99'	121°17.92'	215	-.45	-.24	.35	11.152
HLT	36°53.07'	121°18.49'	183	-.13	-.05	.41	11.152
HMO	36°36.03'	121°55.06'	192	-.52	-.42	.31	5.590
HPL	37° 3.13'	121°17.40'	152	-.31	-.16	.25	5.590
HPLE*	37° 3.13'	121°17.40'	152	0	-.16	-.04	.353
HPLN*	37° 3.13'	121°17.40'	152	0	-.16	.24	.353
HPLZ*	37° 3.13'	121°17.40'	152	0	-.16	.38	.353
HQR	36°50.02'	121°12.76'	536	-.15	-.06	.44	11.152
HQRE	36°50.02'	121°12.76'	536	-.15	-.06	-.05	.353
HQRN	36°50.02'	121°12.76'	536	-.15	-.06	-.03	.353
HQRZ	36°50.02'	121°12.76'	536	-.15	-.06	.24	.353
HSL	37° 1.16'	121° 5.13'	520	-.58	-.44	.14	5.590
HSP	37° 6.91'	121°30.94'	850	-.30	-.34	.30	11.152
JSF*	37°24.31'	122°10.55'	143	0	-.11	.07	2.800
JSFE*	37°24.31'	122°10.55'	143	0	-.11	-.12	.353
JSFN*	37°24.31'	122°10.55'	143	0	-.11	.01	.353
JSFZ*	37°24.31'	122°10.55'	143	0	-.11	.18	.353
KMPE	40°25.04'	124° 7.21'	957	0	-.20	-.15	.353
KMPN	40°25.04'	124° 7.21'	957	0	-.20	-.19	.353
LCC*	37°36.65'	118°54.92'	2,511	.14	1.52	0	0
LMC*	37°43.70'	118°56.71'	2,530	0	2.16	0	0
LTCN	40°12.50'	122° 7.45'	257	0	-.20	-.62	.353
MAT	37°52.40'	119°52.00'	1,353	-.50	.87	-.02	5.590
MCH*	38° 1.12'	120°30.57'	475	0	.47	.16	11.152
MGN*	37°48.80'	118°41.73'	2,472	0	2.37	0	0
MHD	37° 7.18'	119°54.97'	146	-1.46	-1.22	.71	11.152
MLK*	37°39.88'	118°58.53'	2,671	0	1.83	0	0
MMC*	38°21.65'	119° 7.70'	2,548	0	2.25	0	0
MNH*	38° 8.75'	120°48.82'	219	0	.03	.32	23.300
MNP	37°24.88'	119°43.68'	1,000	-.59	-.20	.39	11.152
MNPN*	37°24.82'	119°43.51'	975	0	.87	-.31	.353
MOY*	37°54.00'	120°34.04'	176	0	.09	.24	11.152
MRF*	38°14.72'	120°31.24'	799	0	.94	.03	11.152
MST*	37°54.27'	120°24.29'	366	0	.35	.10	11.152
NMHN	38°40.17'	122°37.93'	1,311	0	.20	-.22	.353
NVE*	38°22.36'	122°26.17'	707	0	-.22	.26	2.800
NVEN	38°22.36'	122°26.17'	707	0	-.22	-.27	.353
ORC*	37°38.12'	118°39.36'	2,301	0	2.02	0	0
PAD	35°38.36'	120°51.86'	471	-.12	-.44	.26	5.590
PAG	35°43.92'	120°14.96'	482	- 26	-.68	07	5.590
PAN	35°46.78'	120°54.44'	451	-.11	-.48	.25	11.152
PAP	35°54.77'	121°21.70'	1,015	-.21	-.43	.54	11.152
PAR	36°14.95'	120°20.52'	485	.24	.10	.25	5.590
PAV	35°10.55'	120°37.95'	133	-.13	-.07	-.08	2.800
PBI	35° 9.68'	120°28.42'	561	.11	.02	.25	11.152
PBR	35°32.91'	121° .54'	85	.03	-.31	-.03	5.590
PB'	36°18.90'	120°55.75'	381	-.16	-.41	.52	5.590
PBY	35°48.90'	121° 4.89'	335	-.29	-.56	.25	5.590
PCA	35°55.90'	120°20.22'	1,189	.17	-.26	1.36	11.152
PCG	35°25.52'	120°44.34'	314	-.08	-.45	.60	11.152
PCR	36° 5.63'	120°26.08'	296	-.14	-.58	.25	11.152
PDR	36°20.14'	120°22.12'	488	.15	.22	.25	0
PGH	35°49.86'	120°21.17'	433	-.08	-.52	.76	11.152
PGHE*	35°49.86'	120°21.17'	433	0	0	.25	5.590
PHA	35°50.16'	120°23.91'	455	.20	-.26	.25	11.152
PHB	36°14.93'	120° 4.96'	100	.47	.55	.25	0
PHC	35°40.93'	121° 9.15'	514	-.12	-.34	.67	11.152
PHG	35°52.56'	120°29.01'	792	.25	-.19	1.52	11.152
PHGE	35°52.56'	120°29.01'	792	0	-.19	-.19	.353
PHGN	35°52.56'	120°29.01'	792	0	-.19	-.26	.353
PHGZ	35°52.56'	120°29.01'	792	0	-.19	.01	.353
PHR	36°22.38'	120°49.10'	732	-.23	-.40	.25	11.152
PHRN	36°22.38'	120°49.10'	732	0	-.40	.16	.353
PIV	35°54.39'	120°40.94'	497	.20	-.26	.25	2.800
PJL	36° 5.39'	121° 9.33'	290	-.24	-.45	.94	11.152
PJLE	36° 5.39'	121° 9.33'	290	0	-.45	-.14	.353
PJLN	36° 5.39'	121° 9.33'	290	0	-.45	-.11	.353
PKE	36° 3.69'	120° 6.54'	288	.26	.06	.25	0
PLO	36°14.79'	121° 2.55'	308	-.40	-.70	.07	5.590
PMC	35°43.48'	120°22.23'	488	0	-.39	.25	11.152
PMCE	35°43.48'	120°22.23'	488	0	-.39	.02	.353
PMCN	35°43.48'	120°22.23'	488	0	-.39	-.06	.353
PMCZ	35°43.48'	120°22.23'	488	0	-.39	.11	.353
PMG	35°25.79'	120°31.22'	529	-.54	-.81	.43	11.152
PMP	36°12.91'	120°47.69'	784	.05	-.24	.25	11.152
PMPN	36°12.91'	120°47.69'	784	0	-.24	.02	.353
PMR	35°47.09'	120°14.14'	512	-.03	-.44	.25	11.152
PPF	35°52.91'	120°24.81'	469	.25	-.20	.25	11.152
PPR	35°38.86'	120°42.04'	279	-.19	-.63	.22	2.800
PPT	36° 6.50'	120°43.27'	506	-.04	-.33	.25	5.590
PRC	36°15.37'	120°37.20'	623	-.12	-.28	.25	11.152
PRCN	36°15.37'	120°37.20'	623	0	-.28	.08	.353
PSE	35°14.71'	120°45.88'	201	-.30	-.45	.17	11.152
PSH	35°35.45'	120°24.92'	390	-.05	-.41	.83	11.152
PSM	36° 4.18'	120°35.68'	988	.34	.01	.25	11.152
PSR	35°51.47'	120°16.81'	552	.22	-.18	.25	11.152
PTR	35°39.28'	120°12.67'	643	-.13	-.53	.45	5.590
PWK	35°48.87'	120°30.67'	503	.16	-.25	.25	11.152
PWM	36°25.97'	120°12.66'	72	.61	.75	.25	0
SCC	34°56.38'	120°1.32'	610	-.26	.05	.59	11.152
SCH*	37°21.95'	118°41.22'	2,365	.68	1.49	0	0
SHL*	37°37.05'	118°57.25'	2,499	0	1.50	0	0
SLP*	34°33.57'	120°24.02'	134	0	-.35	.18	5.590
TAC*	37°37.93'	118°57.91'	2,398	0	1.67	0	0
TBH	35°11.10'	120° 5.05'	1,140	-.54	-.56	.80	23.300
TBM*	35° 8.15'	118°35.81'	1,237	0	-.66	.63	23.300
TCG	35°14.53'	119°43.40'	1,204	.20	-.51	.25	5.590
TTR	35° 5.24'	119°32.08'	1,021	.30	-.67	-.21	2.800
TYG	35°26.18'	119°57.56'	939	-.46	-.82	.55	11.152
WAS	35°44.29'	118°33.42'	1,871	-.59	-.29	.49	11.152
WBR*	35°36.48'	117°53.40'	925	0	1.03	-.18	11.152
WBS*	35°32.22'	118° 8.37'	1,932	0	1.76	-.05	11.152
WCH*	35°52.98'	118° 4.48'	2,475	0	1.04	.20	11.152

TABLE 8.1.—*Station list with station delays for models CM4 and CM5, magnitude station corrections, and calibration factors showing relative magnification of stations*—Continued

Station	Location		Elevation (m)	Station delay		Magnitude correction	Calibration factor
	Lat N.	Long W.		Model CM4	Model CM5		
WCO*	35°37.35'	118°26.25'	1,609	0	-.07	.67	23.300
WCS*	36° 1.58'	117°46.01'	1,143	0	.93	.32	23.300
WCX*	35°42.63'	117°35.98'	671	0	.28	.31	23.300
WHF*	35°41.77'	118°20.91'	902	0	.18	.11	11.152
WHS*	36° 6.30'	117°45.67'	1,448	0	.94	-.01	23.300
WHV*	35°30.60'	118°31.07'	1,006	0	-.50	.15	11.152
WKI*	35°47.64'	118°26.55'	890	0	-.17	.01	11.152
WNM*	35°50.57'	117°54.29'	951	0	1.11	-.03	11.152
WOF	35°32.14'	118°42.75'	1,341	-1.10	-.95	.10	11.152
WOR*	35°41.79'	118°14.52'	837	0	.38	.09	11.152
WRC*	35°57.04'	117°38.89'	945	0	1.13	-.02	23.300
WSH*	35°37.96'	117°29.50'	780	0	.41	-.37	11.152
WSN*	35°41.51'	117°44.96'	698	0	1.04	-.45	5.590
WTO*	35°48.50'	117°45.90'	314	0	1.22	-.62	5.590
WWP*	35°44.13'	118° 5.22'	1,151	0	.81	.45	23.300

HYPO71, the same as for the RTP data at step 6 (above). Magnitudes were computed from maximum-amplitude and associated-period data, with the station-magnitude corrections described above, by the program HYPO71. For this calculation, HYPO71 reduces the recorded maximum amplitude to the corresponding Wood-Anderson amplitude and uses the Richter log-amplitude-versus-distance, zero-magnitude-earthquake reference curve. Focal mechanisms were determined by hand-fitting nodal lines to a lower-hemisphere, equal-area projection of the first-motion data prepared on a printer plot.

Data from the May 2 earthquake and its larger aftershocks, including origin times, locations, focal depths, magnitudes, and the focal planes deduced from first-motion plots, are summarized in table 8.2. First-motion plots of the main shock and 143 of its aftershocks are shown in the section below entitled "Supplementary Data."

COMBINED CATALOG OF COALINGA EVENTS

The hypocenter solutions for the larger aftershocks (table 8.2) were substituted for their counterparts in the final RTP event-summary list (step 8, above) to produce a complete Coalinga event list. Magnitudes reported in the list are local magnitudes (M_L) for $M \geq 3.4$ events, and duration magnitudes (M_D) for $M \leq 3.0$ events. For $3.0 \leq M \leq 3.4$ events, most of the reported magnitudes are duration magnitudes, although a few (in table 8.2) are local magnitudes.

A total of 6,155 events were located by the process described above for May 2 through September 30, 1983. Many of these events were very small and poorly located. To obtain a more reliable and homogeneous set of earthquakes for further analysis, the subset of events that satisfies the following conditions was selected: mag≥1.5, nst≥8, rms≤40, dmin≤40 km, gap≤270°, and erh≤20 km, where mag is the magnitude, nst is the number of stations used to determine the hypocenter, rms is the root-mean-square traveltime residual, dmin is the distance to the nearest station, gap is the largest azimuthal gap between stations used in the hypocenter determination, and erh is the estimated error in epicenter location. A total of 3,820 such events satisfied these conditions.

To indicate the quality of hypocenter solutions and to show how that quality changed over time, median values of the variables noted above are listed in table 8.3 for the periods May 2–3, May 4–5, May 6–June 10, and June 11–September 30, as well as median values of the estimated error in focal depth (erz), the percentage of solutions for which gap≤180°, and the percentage of solutions for which dmin≤5, 10, and 20 km.

The largest changes in table 8.3 contrast the detection threshold and solution quality for the interval May 2–3 with those for the rest of the recording interval. The most important parameters for this comparison are median magnitude, median distance to the nearest station, median gap, percentage of events with gap≤180°, and percentage of stations with distance to the nearest station less than 5 or 10 km. The other parameters (median rms, median erh, median erz, and median nst) show surprisingly little variation.

ANALYSIS OF THE COALINGA EARTHQUAKE CATALOG

SPATIAL DISTRIBUTION AND EVOLUTION OF AFTERSHOCKS

To reduce clouding of plots of the Coalinga earthquake sequence, the only events included are those that meet the conditions: mag≥1.7, rms≤0.20 s, nst≥10, dmin≤30 km, and erh≤3 km. A total of 2,897 events satisfied these conditions. For some plots, that number of events obscures other features that might be compared with the aftershock distribution. For these plots, the magnitude cutoff was increased to $M=2.0$, reducing the number of events to 1,957. The 2,897 events of $M \geq 1.7$ are plotted in figure 8.2. From the location of the main shock and the location and orientation of the aftershock region, the May 2 earthquake appears to be closely related to the Anticline Ridge-Guijarral Hills structure.

Details of the aftershock pattern and its evolution are more clearly shown in figure 8.3, which plots earthquakes of $M \geq 1.7$ for the time intervals May 2–3, May 4–5, May 6–June 10, and June 11–September 30. Nearly the entire aftershock region, as well as most of its principal features, was marked out during the first day of the sequence (fig. 8.3*A*). Those features were less clearly defined by the first day's activity than during later

TABLE 8.2.—*Data for larger aftershocks in the Coalinga earthquake sequence*

[Asterisks denote restrained depth. mag, magnitude; nst, number of stations used to determine hypocenter; gap, largest azimuthal gap between stations used to determine hypocenter; rms, root-mean-square traveltime residual; d_{min}, distance to nearest station; erh, estimated error in epicenter location; erz, estimated error in focal depth; dd, fault-plane dip azimuth; da, fault-plane dip angle; rake, motion of hanging wall relative to footwall: 0°, left lateral, 90°, reverse, ±180°, right lateral, -90°, normal]

Date (1983)	Time (G.m.t)	Location		Depth (km)	mag	nst	gap (°)	rms	d_{min}	erh	erz	Focal mechanism		
		Lat. N.	Long W.									dd(°)	da(°)	rake(°)
May 2	2342:38.14	36°13.96'	120°18.58'	9.98	6.22	30	214	3.0	.05	.3	.2	217	23	90
May 2	2355:29.16	36° 9.22'	120°13.97'	9.03	4.24	13	220	37.0	.09	.8	1.5	242	36	107
May 3	0009:22.55	36°10.11'	120°16.29'	7.37	4.31	16	242	27.0	.08	.7	.7	023	82	129
May 3	0014:48.17	36°13.99'	120°22.16'	12.02	3.73	29	235	17.0	.12	.7	.4	226	30	40
May 3	0015:36.17	36° 6.34'	120°11.43'	5.13	4.45	22	244	23.0	.17	1.3	2.2	215	40	147
May 3	0022:12.73	36°15.97'	120°21.60'	8.23	3.61	32	209	23.0	.13	.6	.9	161	26	112
May 3	0039:46.01	36°13.80'	120°20.92'	11.24	4.52	31	153	2.0	.06	.3	.2	294	70	156
May 3	0047:31.20	36°12.60'	120°16.17'	9.06	3.92	28	218	8.0	.11	.6	.7	200	6	90
May 3	0050:33.33	36°13.27'	120°20.32'	11.00	4.07	14	209	32.1	.19	2.4	1.7	---	---	---
May 3	0057:44.26	36°16.21'	120°20.12'	8.13	5.08	31	214	2.0	.07	.4	.3	256	56	90
May 3	0116:40.23	36°14.66'	120°15.62'	7.90	3.38	28	222	7.0	.15	.8	.9	239	22	117
May 3	0136:19.30	36°13.92'	120°19.38'	.07	3.81	29	212	27.0	.26	1.4	.8	---	---	---
May 3	0141:46.04	36° 8.63'	120°13.08'	8.70	4.54	27	221	16.0	.11	.7	.8	223	44	130
May 3	0155:46.39	36°14.00'	120°17.68'	6.87	4.01	32	216	5.0	.20	1.0	.7	231	44	134
May 3	0215:14.89	36°14.32'	120°17.03'	8.82	4.08	30	218	5.0	.07	.4	.3	195	10	-90
May 3	0217:40.45	36°17.20'	120°15.95'	5.55	3.79	28	224	8.0	.16	.8	.9	235	46	90
May 3	0226:08.84	36°17.41'	120°22.20'	9.84	3.30	36	193	5.0	.13	.5	.4	246	32	90
May 3	0322:02.04	36°14.13'	120°20.96'	11.63	3.98	34	145	2.0	.07	.3	.2	299	74	180
May 3	0328:40.73	36°17.40'	120°18.67'	4.50	3.47	32	219	5.0	.15	.7	.5	118	80	149
May 3	0340:35.19	36°12.61'	120°13.88'	11.01	3.79	25	223	11.0	.28	1.5	1.0	192	0	90
May 3	0431:11.58	36°18.10'	120°24.29'	11.10	3.78	35	177	8.0	.08	.3	.2	221	74	-96
May 3	0432:32.04	36°16.95'	120°22.02'	11.10	4.42	30	191	4.0	.07	.3	.2	245	40	125
May 3	0455:17.64	36°13.52'	120°15.96'	10.22	3.33	29	220	7.0	.08	.4	.3	090	10	113
May 3	0458:12.93	36°13.90'	120°15.64'	10.14	3.48	30	221	8.0	.11	.7	.4	343	30	-161
May 3	0501:52.00	36°12.65'	120°17.60'	11.99	3.48	32	215	6.0	.11	.5	.3	---	---	---
May 3	0558:29.14	36°13.82'	120°15.83'	9.56	3.50	31	220	7.0	.09	.5	.4	270	30	90
May 3	0604:46.18	36°16.22'	120°23.73'	10.08	4.51	34	155	5.0	.09	.3	.3	074	31	103
May 3	0612:50.38	36°15.25'	120°22.55'	8.40*	3.77	36	140	3.0	.22	.8	.8	208	10	-90
May 3	0635:03.22	36°13.05'	120°17.12'	12.89	4.25	32	216	6.0	.07	.4	.2	261	44	138
May 3	0728:34.62	36° 8.20'	120°12.64'	6.15	3.60	25	222	17.0	.14	.9	1.5	253	48	137
May 3	0735:25.06	36° 9.25'	120°12.27'	8.84	3.87	28	224	16.0	.11	.7	1.2	190	30	110
May 3	0855:01.99	36° 8.84'	120°15.98'	10.32	4.70	27	206	13.0	.08	.4	.4	144	34	36
May 3	0939:45.71	36°16.12'	120°16.38'	9.91	4.11	34	222	7.0	.20	.9	.7	241	38	64
May 3	1035:20.24	36°11.21'	120°15.90'	6.34	3.83	28	217	18.0	.10	.6	1.0	043	8	-90
May 3	1257:05.19	36° 7.95'	120°12.60'	11.17	3.92	29	222	18.0	.10	.6	.4	248	66	90
May 3	1309:14.62	36°10.82'	120°15.62'	12.46	4.04	29	217	11.0	.11	.6	.3	229	40	95
May 3	1347:28.95	36°16.92'	120°22.80'	10.85	3.40	36	178	5.0	.07	.3	.2	236	46	90
May 3	1348:52.45	36°14.29'	120°16.00'	9.70	3.52	30	221	7.0	.10	.6	.4	267	10	90
May 3	1420:22.44	36°18.20'	120°22.89'	9.96	3.48	37	192	7.0	.07	.3	.3	177	26	50
May 3	1426:54.23	36°16.81'	120°18.84'	.60	3.94	32	218	4.0	.09	.3	.2	228	76	90
May 3	1450:46.87	36°10.80'	120°17.35'	10.60	3.99	34	205	9.0	.08	.4	.3	200	18	90
May 3	1504:02.54	36°14.45'	120°17.28'	8.60	3.61	32	218	5.0	.07	.4	.3	233	46	90
May 3	1510:35.73	36°17.25'	120°20.25'	8.17	3.95	33	215	4.0	.08	.4	.3	259	52	131
May 3	1541:41.56	36°14.13'	120°18.15'	7.89	4.78	30	215	4.0	.10	.5	.4	208	42	74
May 3	1617:01.27	36° 9.55'	120°14.85'	10.36	2.94	27	217	13.0	.15	.9	.7	009	10	51
May 3	1617:02.61	36° 9.60'	120°15.39'	10.49	3.87	27	214	13.0	.19	1.1	.8	041	32	126
May 3	1622:37.64	36°13.61'	120°16.27'	7.03	3.39	26	219	7.0	.07	.5	.5	020	8	90
May 3	1701:29.51	36°13.39'	120°17.48'	8.87	3.60	30	216	5.0	.06	.3	.3	027	6	90
May 3	1841:53.93	36° 7.01'	120°12.73'	5.43	3.27	25	218	19.0	.27	1.6	1.2	---	---	---
May 3	1850:18.96	36°10.74'	120°18.27'	9.93	3.21	27	195	8.0	.08	.4	.4	233	44	106
May 3	2136:57.88	36° 9.64'	120°16.55'	10.89	3.70	29	205	11.0	.09	.5	.4	234	66	-105
May 3	2229:44.60	36°12.24'	120°20.44'	7.59	3.77	33	170	5.0	.11	.4	.5	243	46	90
May 3	2346:04.40	36° 8.87'	120°20.35'	13.55	3.96	38	147	10.0	.15	.4	.4	090	46	59
May 4	0818:08.61	36°13.97'	120°16.32'	8.60	2.93	42	94	2.0	.15	.3	.3	239	30	75
May 4	0848:53.12	36°13.50'	120°16.80'	12.89	3.48	45	96	1.0	.12	.3	.2	246	70	92
May 4	1329:15.91	36° 6.46'	120°13.17'	10.00*	3.39	37	135	9.0	.17	.5	.7	030	45	126
May 4	1559:13.99	36°14.64'	120°17.44'	7.22	3.78	42	84	3.0	.11	.2	.3	242	48	90
May 4	1611:19.63	36°16.89'	120°20.93'	11.69	4.39	47	53	4.0	.07	.2	.1	234	48	113
May 4	1945:02.87	36° 7.14'	120°16.09'	7.44	3.44	39	121	5.0	.20	.5	.9	183	60	62
May 5	0027:50.85	36°13.71'	120°16.20'	8.85	3.48	43	48	2.0	.11	.2	.3	212	19	50
May 5	0156:42.40	36°13.19'	120°17.10'	8.04	3.36	45	45	0	.15	.3	.3	230	18	76
May 5	0437:48.59	36° 8.37'	120°12.05'	11.22*	4.01	44	74	9.0	.33	.7	.8	134	34	57

TABLE 8.2.—*Data for larger aftershocks in the Coalinga earthquake sequence*—Continued

Date (1983)	Time (G.m.t)	Location		Depth (km)	mag	nst	gap (°)	rms	d_{min}	erh	erz	Focal mechanism		
		Lat. N.	Long W.									dd(°)	da(°)	rake(°)
May 5	0806:26.69	36° 9.03'	120°13.37'	8.69	3.73	40	70	7.0	.13	.3	.4	207	40	113
May 5	1020:44.09	36°17.12'	120°22.11'	11.48	4.61	43	46	5.0	.05	.1	.1	239	46	114
May 5	1133:40.67	36°15.48'	120°21.80'	10.44	3.69	50	39	2.0	.10	.2	.2	057	8	-104
May 5	1150:49.98	36°10.87'	120°17.11'	10.52	3.47	44	61	4.0	.09	.2	.2	172	27	67
May 5	1242:15.72	36°15.34'	120°23.92'	11.85	3.89	52	54	5.0	.08	.2	.2	143	52	61
May 5	2246:12.38	36°18.04'	120°25.14'	9.93	3.35	54	64	6.0	.12	.2	.3	226	50	107
May 6	0457:09.46	36°12.07'	120°17.58'	10.76	3.38	52	56	2.0	.11	.2	.2	205	28	105
May 6	0943:38.98	36°11.81'	120°20.27'	13.01	3.71	49	56	6.0	.12	.3	.3	199	76	-89
May 6	1151:44.39	36°16.46'	120°22.45'	10.68	3.33	51	37	3.0	.09	.2	.2	093	48	109
May 7	0017:15.91	36°16.08'	120°19.44'	8.88	3.88	49	49	3.0	.08	.2	.2	318	58	-171
May 7	0543:57.34	36°14.11'	120°16.76'	8.90*	3.46	47	47	2.0	.10	.2	.2	231	28	78
May 7	1242:30.37	36°18.10'	120°24.46'	10.60	3.62	51	65	6.0	.07	.2	.2	052	10	-99
May 8	0120:14.74	36°12.76'	120°18.04'	8.69	3.46	52	47	2.0	.11	.2	.2	232	50	65
May 8	0147:25.90	36°12.32'	120°16.68'	8.07	3.03	53	38	2.0	.14	.2	.3	232	46	71
May 8	0345:33.89	36°15.43'	120°26.17'	1.80*	3.37	52	32	5.0	.15	.2	.3	081	28	80
May 8	0738:11.61	36°15.67'	120°16.87'	5.09	3.31	55	40	4.0	.17	.3	.2	246	27	101
May 8	1037:21.12	36°13.15'	120°21.27'	11.62	3.27	59	30	4.0	.11	.2	.2	300	82	173
May 8	1523:32.93	36°11.52'	120°19.99'	6.61	3.34	55	31	5.0	.13	.2	.2	246	60	49
May 8	1918:24.21	36°17.59'	120°28.27'	11.61	3.72	57	42	9.0	.09	.2	.2	222	30	68
May 8	2025:40.03	36°12.78'	120°18.23'	7.96	3.60	49	39	2.0	.12	.2	.3	235	64	86
May 9	0249:11.55	36°14.74'	120°17.97'	12.04	5.30	46	32	3.0	.05	.1	.1	226	44	106
May 9	0319:11.25	36°14.30'	120°17.89'	12.33	3.63	56	32	3.0	.10	.2	.2	237	50	108
May 9	0326:37.42	36°14.42'	120°18.00'	12.48	4.60	47	39	3.0	.09	.2	.2	209	40	106
May 9	1324:33.76	36°12.06'	120°16.44'	9.59	3.29	49	55	2.0	.09	.2	.2	167	74	33
May 10	1326:29.44	36°19.78'	120°18.97'	4.79	3.85	50	56	3.0	.10	.2	.2	084	37	141
May 10	1522:43.36	36°20.12'	120°19.53'	4.13	2.85	44	59	3.0	.17	.3	.3	041	46	74
May 10	1522:45.53	36°19.45'	120°18.76'	4.08	3.37	43	55	4.0	.13	.3	.3	034	35	65
May 11	0814:47.28	36° 9.19'	120°15.45'	11.67	3.48	53	48	4.0	.15	.3	.3	255	54	121
May 12	1341:06.82	36° 9.99'	120°16.10'	10.99	4.50	48	66	3.0	.09	.2	.2	210	26	67
May 13	1422:15.90	36° 7.29'	120°12.54'	11.36	3.29	51	51	9.0	.16	.3	.5	170	62	15
May 14	0502:03.11	36°16.51'	120°18.46'	11.16	3.90	49	50	4.0	.08	.2	.2	230	48	125
May 14	1715:17.02	36°11.10'	120°17.37'	11.35	2.60	47	44	4.0	.11	.2	.2	248	18	126
May 14	1715:35.69	36°10.44'	120°16.97'	8.74	3.49	44	45	3.0	.19	.4	.4	338	24	131
May 16	0131:37.66	36° 8.54'	120°15.20'	12.22	3.61	42	51	4.0	.10	.2	.3	302	60	2
May 16	1217:43.00	36° 7.03'	120°12.47'	9.70*	3.15	45	50	9.0	.20	.4	.8	192	75	48
May 16	1421:48.38	36° 9.58'	120°16.48'	9.17	3.90	42	104	2.0	.09	.2	.4	214	70	97
May 17	2222:13.18	36°13.89'	120°21.62'	8.07	3.49	49	37	3.0	.08	.2	.2	242	60	78
May 19	1105:30.15	36°13.75'	120°16.26'	12.81	4.16	50	58	2.0	.14	.3	.2	233	50	90
May 19	2326:06.56	36°15.45'	120°26.05'	1.93	3.48	45	35	5.0	.12	.2	.3	060	30	60
May 21	1005:41.06	36°11.13'	120°14.58'	11.07	3.21	48	54	5.0	.11	.2	.2	119	32	-36
May 22	0839:21.74	36° 8.98'	120°11.93'	10.50*	4.25	49	62	9.0	.16	.3	.5	164	40	73
May 24	0902:17.70	36°15.25'	120°18.99'	8.87	4.70	45	39	2.0	.05	.1	.1	256	18	111
May 24	0903:56.56	36°15.82'	120°18.96'	8.01	3.44	15	83	3.4	.09	.3	.5	---	---	---
May 24	1226:07.74	36°11.37'	120°18.02'	10.84	3.24	56	59	4.0	.12	.2	.2	217	46	99
May 26	0854:55.06	36°14.16'	120°16.61'	8.12	3.16	44	57	2.0	.13	.3	.3	234	19	59
May 27	2040:49.21	36°14.58'	120°22.58'	12.63	3.81	51	30	1.0	.10	.2	.2	250	50	119
May 29	0124:03.43	36°14.45'	120°22.53'	12.48	3.49	46	42	1.0	.10	.2	.2	250	49	117
May 30	0321:52.45	36°15.00'	120°22.66'	11.52	3.33	45	39	1.0	.07	.2	.1	212	15	41
Jun 7	0518:37.78	36° 9.50'	120°13.51'	11.56	4.13	41	84	7.0	.11	.3	.3	110	42	14
Jun 11	0309:52.21	36°15.34'	120°27.00'	2.43	5.20	45	66	6.0	.12	.2	.4	107	50	90
Jun 11	1427:05.58	36°14.66'	120°26.96'	4.10*	3.22	55	62	6.0	.25	.4	.6	125	25	100
Jun 11	2302:19.84	36°15.51'	120°26.44'	3.56	3.37	50	65	5.0	.17	.3	.5	066	52	90
Jun 12	0131:27.55	36° 7.50'	120°17.71'	14.32	4.03	44	59	3.0	.15	.4	.5	296	44	168
Jun 16	1737:23.61	36°14.55'	120°21.57'	10.58	3.54	53	37	2.0	.10	.2	.2	264	20	93
Jun 29	0641:07.80	36° 9.59'	120°11.50'	13.13	3.54	46	73	6.0	.16	.4	.3	176	32	74
Jul 5	2210:14.39	36°20.39'	120°19.76'	4.66	3.26	37	84	4.0	.15	.4	.4	092	52	128
Jul 7	0030:33.59	36°13.39'	120°16.31'	12.50*	3.65	31	219	7.0	.18	.9	.5	256	56	129
Jul 9	0740:51.30	36°15.04'	120°24.01'	9.02	5.39	39	50	5.0	.11	.3	.4	108	41	116
Jul 14	1525:35.65	36°13.13'	120°18.50'	9.76	2.52	27	60	5.0	.07	.2	.3	232	48	74
Jul 14	1525:41.48	36°13.21'	120°18.40'	6.72	3.69	26	115	18.0	.11	.4	1.1	212	0	-91
Jul 17	2158:08.20	36°16.93'	120°19.77'	12.00*	3.66	35	67	4.0	.15	.2	.2	336	80	-166
Jul 18	1928:05.45	36°10.82'	120°16.79'	10.91	4.16	31	64	9.0	.07	.2	.3	158	28	51
Jul 22	0239:54.07	36°14.44'	120°24.53'	7.43	6.04	36	48	6.0	.09	.2	.4	085	38	102
Jul 22	0249:09.98	36°13.31'	120°24.77'	6.79	4.14	37	45	7.0	.11	.2	.4	012	40	38
Jul 22	0303:41.56	36°13.48'	120°24.20'	7.80	3.19	33	43	6.0	.07	.2	.3	327	84	-158
Jul 22	0311:42.69	36°20.64'	120°20.90'	3.98	2.34	26	89	2.0	.14	.4	.4	360	67	90
Jul 22	0311:47.62	36°19.93'	120°19.96'	1.80*	3.31	30	82	16.0	.14	.4	.8	072	70	173
Jul 22	0343:01.01	36°13.30'	120°24.39'	7.91	5.02	35	43	7.0	.09	.2	.4	072	30	85

TABLE 8.2.—*Data for larger aftershocks in the Coalinga earthquake sequence*—Continued

Date (1983)	Time (G.m.t)	Location		Depth (km)	mag	nst	gap (°)	rms	d_{min}	erh	erz	Focal mechanism		
		Lat. N.	Long W.									dd(°)	da(°)	rake(°)
Jul 22	0430:27.23	36°21.06'	120°19.73'	7.50*	3.61	39	88	4.0	.24	.5	.8	235	36	95
Jul 22	0712:10.86	36°16.58'	120°24.20'	7.01	3.35	39	56	6.0	.12	.3	.6	078	44	92
Jul 22	2152:32.68	36°15.77'	120°23.83'	7.72	3.32	36	52	5.0	.12	.3	.5	088	44	106
Jul 25	2231:39.57	36°13.73'	120°23.87'	8.38	5.33	35	42	6.0	.09	.2	.3	078	38	90
Jul 31	1643:52.54	36°13.84'	120°15.88'	9.50	3.54	34	71	7.0	.08	.2	.4	197	28	33
Jul 31	1724:10.15	36° 9.41'	120°13.93'	11.11	3.54	28	220	14.0	.11	.5	.4	163	16	22
Jul 31	1754:20.30	36°13.86'	120°15.62'	9.70	3.36	33	72	8.0	.09	.2	.4	230	24	56
Aug 5	1006:01.10	36°14.13'	120°26.51'	5.00*	3.26	44	57	9.0	.13	.2	.3	066	54	108
Aug 12	0114:41.14	36°17.42'	120°23.85'	9.80*	4.04	46	59	6.0	.13	.3	.4	280	75	160
Aug 12	2202:34.73	36°11.02'	120° 8.42'	8.70*	4.10	31	151	9.0	.13	.5	.8	244	32	67
Aug 14	1243:35.73	36°17.29'	120°24.67'	9.60*	4.30	41	67	7.0	.13	.3	.4	251	44	105
Aug 26	0321:17.24	36°18.05'	120°28.30'	12.00	4.04	48	85	10.0	.12	.3	.3	228	42	98
Aug 26	1957:40.64	36°12.65'	120°22.42'	11.78	3.83	43	47	5.0	.07	.2	.2	287	80	169
Sep 7	2307:26.19	36°16.73'	120°27.62'	11.97	3.81	47	80	10.0	.10	.2	.2	246	40	117
Sep 9	0916:13.47	36°13.92'	120°15.89'	6.73	5.30	34	71	7.0	.06	.2	.2	064	75	161
Sep 9	0921:31.81	36°14.35'	120°16.71'	6.23	3.89	37	71	6.0	.10	.3	.3	116	50	173
Sep 11	1148:06.61	36°14.52'	120°23.00'	10.05	4.48	41	42	4.0	.07	.2	.2	080	32	81
Sep 18	1434:32.05	36°16.66'	120°20.66'	9.00	3.45	39	63	3.0	.10	.2	.3	238	32	125

TABLE 8.3.—*Quality and change in quality over time of hypocenter solutions for events in the Coalinga earthquake sequence*

[rms, root-mean-square traveltime residual; erh, estimated error in epicenter determination; erz, estimated error in focal depth; nst, number of stations used to determine hypocenter; mag, magnitude; d_{min}, distance to nearest station; gap, largest azimuthal gap between stations used in hypocenter determination]

Period	May 2-3	May 4-5	May 6-June 10	June 11-Sept. 30
Total number of events--	534	612	1,711	963
Median rms (s)----------	.12	.13	.12	.11
Median erh (km)---------	1.0	.6	.5	.5
Median erz (km)---------	.8	.7	.6	.7
Median nst--------------	18	17	17	16
Median mag--------------	2.39	2.08	1.99	2.01
Median dmin (km)--------	8.1	3.5	4.4	7.0
Median gap (°)----------	216	107	85	104
Gap ≤180°---------------	16	87	97	82
d_{min} ≤5 km---------------	27	67	58	31
d_{min} ≤10 km--------------	61	90	90	77
d_{min} ≤20 km--------------	93	100	100	100

intervals, however, because of the relative weakness of the network and the high noise levels during the first day of the sequence. On the first day, the aftershock zone was about 30 km long from northwest to southeast and 10 to 12 km wide from northeast to southwest, and the main shock was 3 to 4 km north of its center. Improvements in the network and reduced background-noise levels after the first day led to improved hypocenter determinations and sharper definition of internal features in the aftershock pattern, as shown in figure 8.3*B*.

The aftershock pattern shown in figures 8.3*A* and 8.3*B* was repeated, but intensified, during the next 36 days of the sequence (May 6–June 10, fig. 8.3*C*). From north to south, the persistent features in the aftershock pattern were:

1. Domengine cluster—a nearly detached cluster of small quakes near the Domengine Ranch, about 5 km north of the main aftershock zone.
2. North bridge—a small cluster of quakes linking the northwest end of the Domengine cluster to the main aftershock zone.
3. Northwest triangle—a triangular pattern, 10 to 15 km on a side, of rather evenly spaced aftershocks at the northwest end of the aftershock region.
4. Quiet band—a narrow band with almost no aftershocks that cuts across the aftershock zone from southwest to northeast just northwest of the main shock.
5. Northeast cluster—a small cluster of aftershocks just north of the main shock cluster.
6. Main shock cluster—an elliptical patch of dense aftershocks, about 10 km long by 5 km wide, extending southeastward from the main shock.
7. Southwest band—a narrow band of dense aftershocks, about 10 km long, lying southwest of and parallel to the main-shock cluster.
8. Southeast cluster—an equidimensional patch of aftershocks, about 10 km across, at the southeast end of the aftershock region. This cluster could be further subdivided into a northern part that lies beneath the Guijarral Hills and a southern part that lies northwest of the Kettleman Hills.
9. Nuñez extension—beginning with an M=5.2 aftershock near Nuñez Canyon on June 11 and culminating with an M=6.0 earthquake about 4 km to the southeast on July 22, a conspicuous 8- by 10-km aftershock cluster that overlapped the northwest triangle and extended it toward the southwest developed between

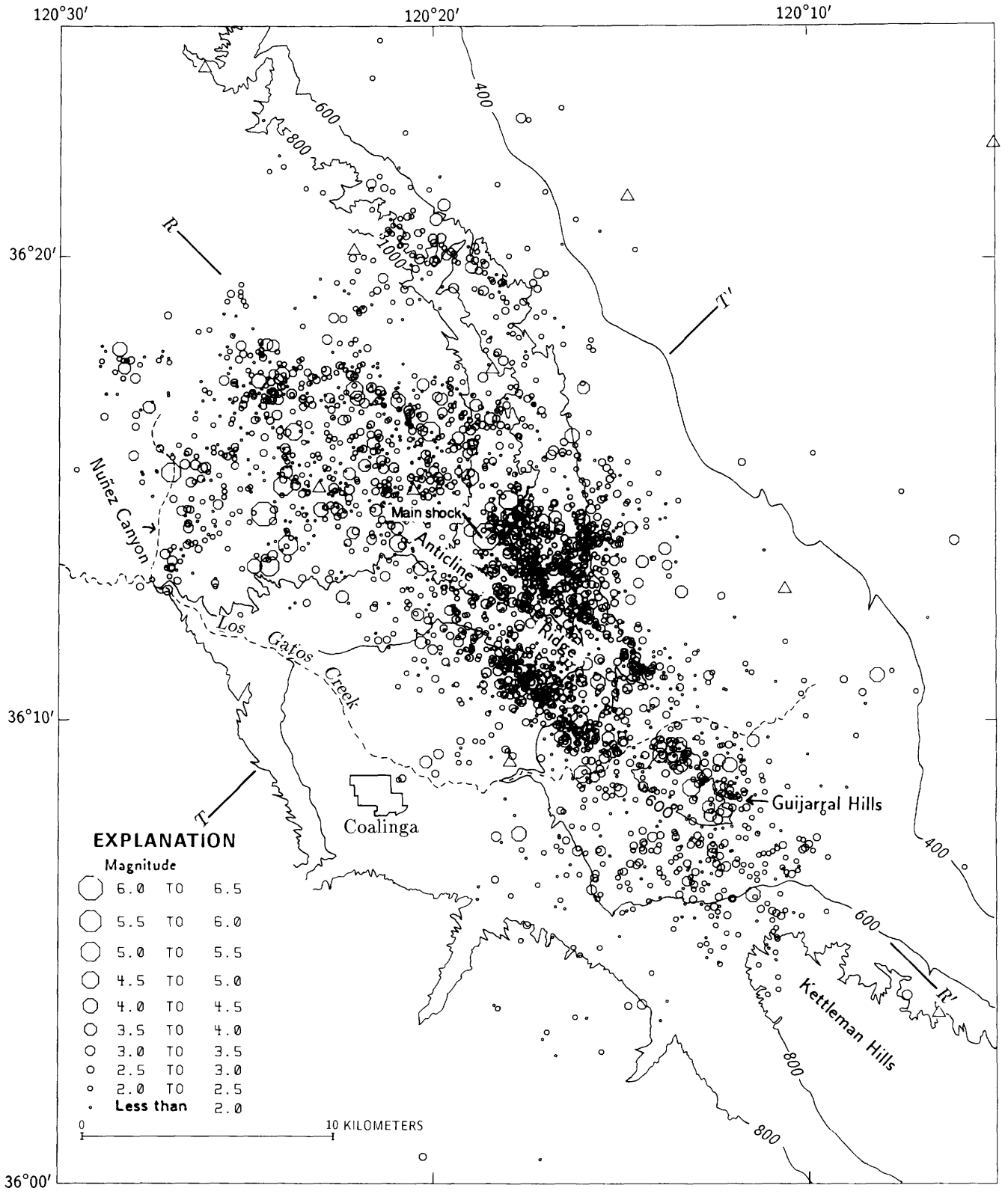

FIGURE 8.2.—Coalinga, Calif., area, showing locations of May 2 earthquake and aftershocks from May 2 through September 30. Contours below 400 and above 1,000 ft are omitted for simplicity. Aftershock-screening parameters: magnitude, ≥1.7; rms traveltime residual, ≤0.20 s; number of stations used in solution, ≥10; distance to nearest station, ≤3 km; estimated epicentral error, ≤3 km. *R–R′* and *T–T′*, orientations of longitudinal and transverse cross sections, respectively, in figures 8.14 and 8.15. Triangles, seismograph stations.

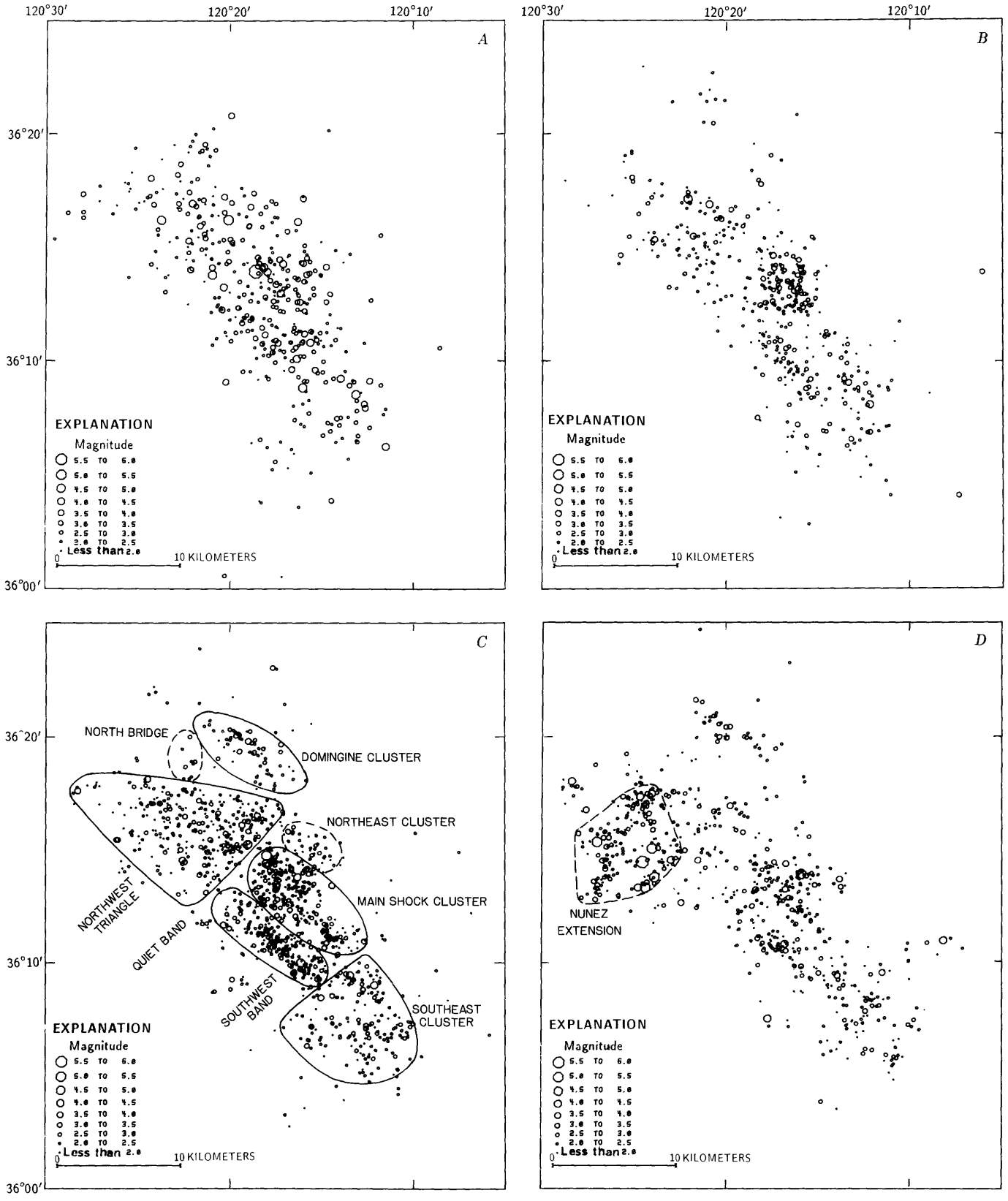

FIGURE 8.3.—Coalinga, Calif., area, showing locations of May 2 earthquake and aftershocks for four periods: May 2–3 (*A*), May 4–5 (*B*), May 6–June 10 (*C*), and June 11–September 30 (*D*). Aftershock-screening parameters same as in figure 8.2.

June 11 and September 30 (fig. 8.3*D*). The clusters identified in figure 8.3*C* also continued to be active during this period.

PATTERN OF AFTERSHOCKS IN SPACE AND TIME AS A FUNCTION OF MAGNITUDE

In an analysis of the aftershock sequences of shallow (less than 80 km deep) Japanese earthquakes of $M \geq 6$ that occurred from 1926 through 1959, Utsu (1961) found that the rate of occurrence of aftershocks decreases according to the modified Omori formula $n(t)=A/(t+c)^p$, where $n(t)$ is the frequency of occurrence of aftershocks at time t measured from the origin time of the main shock, and A, c, and p are constants: A is related to the intensity of the aftershock sequence, c is a small positive offset of the time base (approx 1 h to 1 d), and p is a value (normally a little greater than 1.0) that describes the falloff of the sequence over time. Omori's hyperbolic law corresponds to $p=1.0$. Curves for the cumulative frequency of aftershocks, $N(t)$, can be obtained by integration of $n(t)$ (Utsu, 1961):

$$N(t) = \frac{A}{p-1}\left[\frac{1}{C^{(p-1)}} - \frac{1}{(t+C)^{(p-1)}}\right], \text{ for } p>1$$

and $$N(t) = A \log[(t/C)+1], \text{ for } p=1.$$

For $p=1$, a plot of $N(t)$ versus log t approaches a straight line with slope A as time increases. This result underlies the usefulness of using a log-time abscissa in plots of the frequency of aftershocks versus time: For $p \simeq 1$, the number of events per unit of log t does not change over time, and so the attenuated later part of the sequence is visually equivalent to the early part. Also, if the number (or log number) of events per unit log t (for example, 0.1 unit) is plotted versus log t, that number is nearly independent of time and determines a horizontal line on the plot. This feature provides a means of testing the completeness of the aftershock catalog with respect to events larger than a prescribed magnitude during the early part of an aftershock sequence.

The location of Coalinga aftershocks relative to their projection onto the northwest-southeast long axis (az 315°) of the aftershock zone is plotted versus time for $M \geq 3.0$ in figure 8.4*A* and for $M \geq 1.7$ in figure 8.4*B*. In both of these plots, the abscissa is log [t (in hours)+1]. The occurrence of aftershocks of $M \geq 4.7$ is noted along the tops of the plots. If the catalog were complete and the occurrence of aftershocks followed Omori's law with $p=1$, then the distribution of plotted points versus the log-time axis should be constant over time. Overall, such appears to be the case except for the first few hours of the plot for $M \geq 3$ and the first day of the plot for $M \geq 1.7$. In both of these plots, the quiet band just northwest of the main shock is a persistent feature. In figure 8.4*B*, the larger aftershocks are marked by concentrated bands of their own aftershocks that suggest the linear extent of the faulting that caused them. The largest aftershock ($M=6.0$, July 22) is marked by the longest zone of secondary aftershocks, which is about 7 km long in this projection.

The log number of events per 0.1 unit log t is plotted versus log t (in hours) for $M \geq 1.7$, $M \geq 2.5$, and $M \geq 3.0$ in figure 8.5. All three curves become nearly horizontal after an initial buildup at the beginning of the sequence. The times required for the different curves to reach their final average levels are about 2½ h for $M \geq 3$, 8 h for $M \geq 2.5$, and 20 h for $M \geq 1.7$. These differences reflect the gradual increase in network performance as the initial high levels of background noise diminished and new stations were installed in the aftershock region. The difference between the actual curve and its final average level is a measure of the "loss" of earthquakes early in the sequence. All three curves are nearly horizontal from the end of the initial buildup to the end of the interval plotted (165 d), corresponding to $p=1.0$. The curves for the larger events, however, particularly that for $M \geq 3$, decline slowly from the end of the initial buildup until July, when the curves rise abruptly owing to the group of large aftershocks in the Nuñez extension during July. From the 1st to the 66th day (before the July increase), a line through the $M \geq 3.0$ curve has a slope corresponding to $p=1.10$. A longer period of recording will be required to determine a more reliable value of p for the sequence.

All three curves show fairly regular fluctuations through a range of 0.3 to 0.4 log units (factor of 2.0–2.5 in frequency), and successive troughs follow one another after about 0.4 log units (each interval about 2½ times the preceding one).

FREQUENCY OF AFTERSHOCKS VERSUS MAGNITUDE

In evaluating the frequency of Coalinga aftershocks as a function of magnitude, two characteristics of the data set should be noted: (1) During the first day of the sequence, there appears to have been a severe loss of small ($M<2$) events but only a modest loss of larger ($M>3$) ones; and (2) magnitudes for aftershocks of $M \geq 3.4$ were determined by one method (maximum amplitudes), whereas smaller ones were determined by another (duration). Examination of these magnitude-frequency data should help to quantify the effects introduced by these characteristics.

Cumulative magnitude versus frequency plots for the first day of the aftershock sequence (May 2–3) and the first 5 months of the aftershock sequence (May 2–September 30) are shown in figure 8.6. The main shock ($M=6.7$) and the largest shock in the Nuñez extension

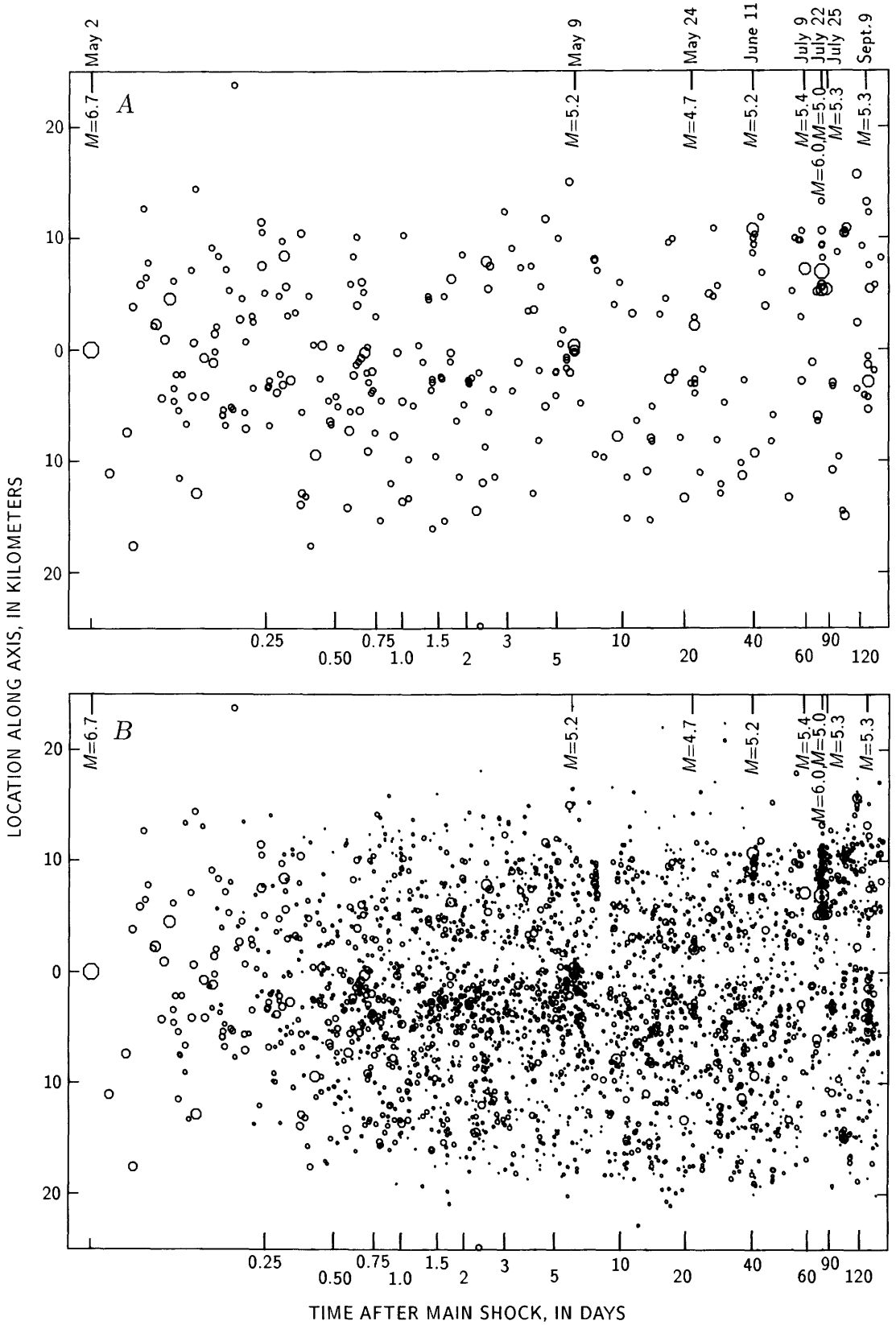

FIGURE 8.4.—Aftershock locations along northwest-southeast axis of aftershock region versus occurrence time (days after main shock + 1) for events of $M \geq 3.0$ (*A*) and $M \geq 1.7$ (*B*). Dates and magnitudes of events of $M \geq 4.7$ are labeled at top.

(M=6.0) were excluded. The plotted points represent the log number of events in each ¼-magnitude unit from M=1.5 to 7.0. The line fitted by inspection to the May 2–September 30 data has a slope of –0.87. The slope of the curve fitted to the same data (but including the M=6.7 main shock and M=6.0 aftershock) by the formula

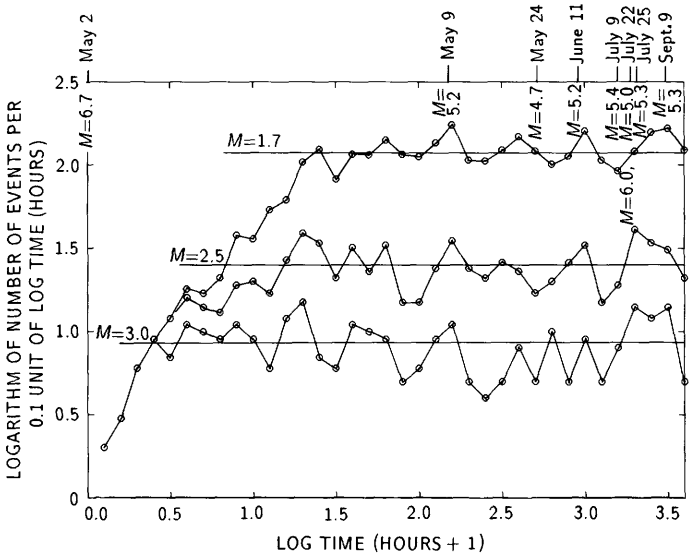

FIGURE 8.5.—Frequency versus time for Coalinga aftershocks of $M \geq 1.7$, $M \geq 2.5$, and $M \geq 3.0$. Dates and magnitudes of events of $M \geq 4.7$ are labeled at top.

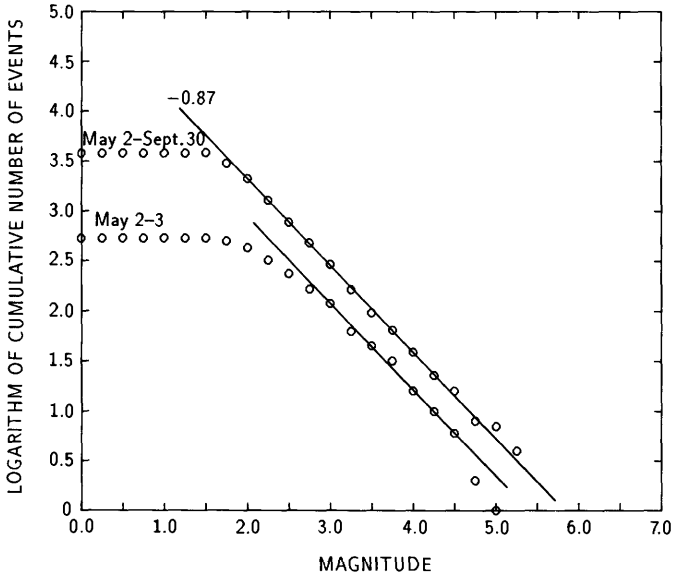

FIGURE 8.6.—Frequency versus magnitude for Coalinga aftershocks during first day (May 2–3) and first 5 months (May 2–Sept. 30) of the earthquake sequence. M = 6.7 main shock and M = 6.0 July 22 aftershock are omitted. Application of Utsu's (1961) formula gives b = –0.88 for longer data interval and for $M \geq 2.0$.

$$b = \frac{s \log e}{M_i - sM_c}$$

(Utsu, 1966) for various magnitude-cutoff levels (M_c) is:

M_c	b
1.5	– 0.66
1.75	– .79
2.0	– .88
2.5	– .89
3.0	– .88

These b values have been corrected (by –0.02) for the effect of magnitude-sampling-window size (0.25 unit) (Utsu, 1966). The small values of b for M_c=1.5 and 1.75 reflect a loss of earthquakes of M<2.0. The plot shows a similar effect, in that the points for M=1.75 and 1.5 fall below the line through the rest of the data. It is gratifying that there is no offset or change in slope of the plotted data at the transition from duration to amplitude magnitudes (M=3.0–3.5). I judge that the best estimate of the slope is b=–0.87. A line of slope –0.87 drawn through the data for the first day of the sequence shows a loss of earthquakes of M<3.0. From M=3.0 to M=4.50, the line fits the data closely.

MAGNITUDE VERSUS DEPTH

The distribution of aftershocks with depth as a function of magnitude is plotted in figure 8.7, which shows the number of events in each 1-km depth interval versus

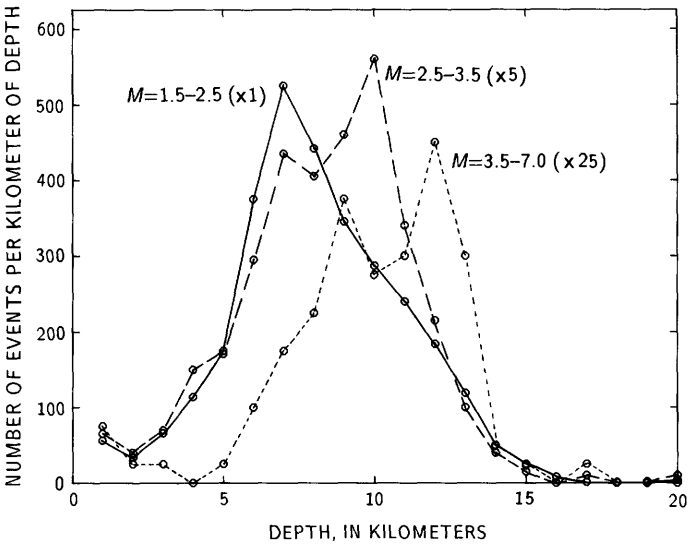

FIGURE 8.7.—Depth versus frequency for three ranges of earthquake magnitude. Ordinates of curves for M = 1.5–2.5, M = 2.5–3.5, and M = 3.5–7.0 have been multiplied by 1.0, 5.0, and 25.0, respectively, to facilitate comparison. Points are plotted at upper end of depth range—for example, at 5 km for depth interval 4–5 km.

depth for the magnitude intervals M=1.5–2.5, M=2.5–3.5, and M=3.5–7.0. Depth increases systematically with increasing magnitude. The frequency-versus-depth curves for the three magnitude ranges shown peak at 6 to 7 km for M=1.5–2.5, at 9 to 10 km for M=2.5–3.5, and at 11 to 12 km for M=3.5–7.0. From their peaks, all three curves drop off steadily with depth to about 1/10 of their maximum values over the range 13–14 km. This decrease in the numbers of events with increasing depth below the peaks is progressively more abrupt with increasing magnitude; for the largest events (M=3.5–7.0), it occurs within only 2 km: 11–12 to 13–14 km.

LOCATIONS AND FOCAL MECHANISMS OF THE MAIN SHOCK AND LARGER AFTERSHOCKS

The epicenters of the main shock and larger aftershocks (table 8.2) are plotted in figure 8.8. The focal mechanism of the main shock, based on first-motion directions at stations within 500 km of the epicenter (fig. 8.9), defines two nodal planes, the first striking N. 53° W. and dipping 23° SW., and the second striking N. 53° W. and dipping 67° NE. Both the strike and dip of the second focal plane are well determined, but only the dip of the first focal plane is well determined; its strike is constrained only to lie between about N. 20° W. and N. 80° W. Thus, the solution drawn in figure 8.9 with pure dip-slip motion could contain a significant component of either right- or left-lateral slip. As discussed below, the first, more shallowly dipping focal plane is identified as the fault. According to this solution, the main shock occurred on a thrust fault dipping 23° SW.; the other choice would correspond to a reverse fault dipping 67° NE.

Changes in elevation of the Earth's surface that accompanied the earthquake, measured along a road that crosses Anticline Ridge near the main shock, provide important constraints on the style and extent of causative faulting. Stein (1983) concluded that the simplest fault which can explain the leveling changes would correspond closely to a high-angle reverse fault indicated by the second focal plane described above. Somewhat more complex faulting, however, based on a thrust fault similar to that indicated by the first focal plane described above, can explain the leveling changes almost as well.

First-motion fault-plane solutions for the main shock and 143 aftershocks are shown in the section below entitled "Supplementary Data," and the corresponding focal mechanisms are plotted in figure 8.10. The larger aftershocks show the same clustering as the $M \leq 1.7$ shocks plotted in figure 8.3. The most notable feature of the focal-mechanism map is the preponderance of thrust and reverse-fault solutions over strike-slip solutions.

Though few in number, the strike-slip solutions are highly interesting in their distribution: Their greatest concentration is along the southeast edge of the northwest triangle, near the 1,000-ft contour, just northwest of the quiet band. These solutions, which are interpreted as right-slip events, appear to align along a zone cutting from southwest to northeast across Anticline Ridge northwest of the quiet band. The largest event with a strike-slip solution is the M=5.3 earthquake at 0916 G.m.t. September 9, which is interpreted as involving right-slip faulting and lies along the east edge of the main-shock cluster. One strike-slip solution is located south of the main shock in the main-shock cluster, one strike-slip solution is located in the Domengine cluster, and several strike-slip solutions are located in the southeast cluster near the Guijarral Hills.

Although the preponderant strike direction of the reverse-fault solutions is northwest, in the Nuñez extension the average strike direction is a few degrees west of north, and in the Guijarral Hills most solutions have strike directions of nearly due west.

The regional variation in orientation of the focal mechanisms is shown more clearly on a map of inferred maximum-pressure (P)-axis orientations (fig. 8.11). Line segments indicating P-axis orientations are scaled according to magnitude, and most P-axes are nearly horizontal. P-axis orientations in the main-shock cluster, in the southwest band, in the Domengine cluster, and along the north edge of the northwest triangle are predominantly northeast-southwest, approximately perpendicular to the axis of the Coalinga anticline. West of the main shock in the Nuñez extension, the most prevalent P-axis orientation is nearly due east-west. South of the main shock in the southeast cluster the most common P-axis orientation is nearly north-south. Individual solutions with northeast-southwest P-axis orientations are scattered through both the southeast cluster and the Nuñez extension. In the Nuñez extension, the northeast-southwest orientations characterize the deeper events. The widespread systematic variation in P-axis orientations suggests that stresses in the aftershock area reflect regional variations in stress related to the main shock. The deflections of P-axis orientations are symmetrical relative to a vertical plane through the main-shock epicenter and parallel to its P-axis direction (which is also its slip direction). Northwest of this plane, P-axes are rotated clockwise relative to the P-axis of the main shock, whereas southeast of that plane they are rotated counterclockwise.

Epicenters of the main shock and aftershocks of $M \geq 2.0$ are superposed on simplified geologic and structural maps in figures 8.12 and 8.13, respectively. Both map bases, which are from chapter 4, bear a strong resemblance to topography. The aftershocks coincide with the

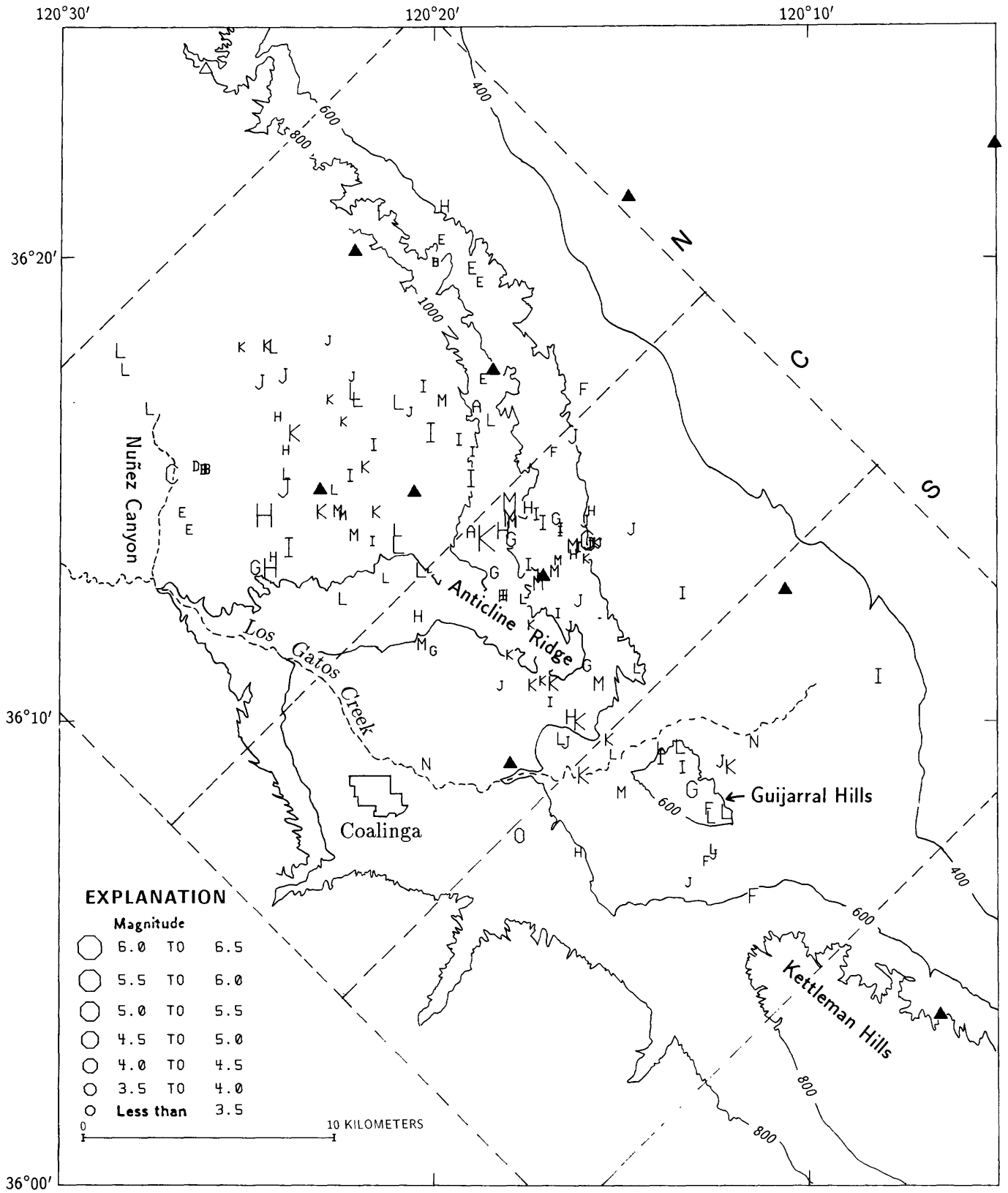

FIGURE 8.8.—Coalinga, Calif., area, showing locations of May 2 earthquake and larger aftershocks for May 2 to September 30. Contours below 400 and above 1,000 ft are omitted for simplicity. Symbols are scaled according to magnitude and coded for depth according to the following scheme: A, 0–1 km; B, 1–2 km; C, 2–3 km; and so on. Large letter K denotes main shock, 11 km N. 20° E. of Coalinga. Boundaries of rectangular regions N, C, and S outline frames used in figures 8.18 through 8.37. Triangles, seismograph stations.

two principal geologic structures north and east of Coalinga, the Joaquin Ridge anticline and the Coalinga anticline, which intersect near the epicenter of the main shock. The quiet band and its bordering alignment of right-lateral strike-slip aftershocks mark the zone where the narrow, northwest-trending Coalinga anticline laps onto the much broader, east-west-trending Joaquin Ridge anticline. The main-shock cluster and southwest band of aftershocks lie along the steep northeast and southwest flanks of the central section of the Coalinga anticline, respectively, and their *P*-axis orientations suggest compression perpendicular to the axis of the anticline. The northern and southern parts of the southeast cluster lie on the plunging noses of the Coalinga anticline and the Kettleman Hills anticline, respectively. The entire southeast cluster may be offset right laterally along a northeast-trending zone across Anticline Ridge just northwest of Los Gatos Creek (fig. 8.2).

North of the main shock, the north edge of the northwest triangle lies along the axis of the Joaquin Ridge anticline. *P*-axis orientations beneath the crest of this anticline are mostly northeast-southwest, approximately perpendicular to the axis of the Coalinga anticline. Beneath the south flank of the Joaquin Ridge anticline between the onlapping Coalinga anticline on the east and Nuñez Canyon on the west, *P*-axis orientations are nearly east-west, approximately parallel to the axis of the Joaquin Ridge anticline and perpendicular to a set of north-south-trending faults, including the Nuñez fault, in the Cretaceous section on and south of Joaquin Ridge. The Domengine cluster of aftershocks lies beneath and parallels the northeast-dipping upper Tertiary strata just west of the Great Valley.

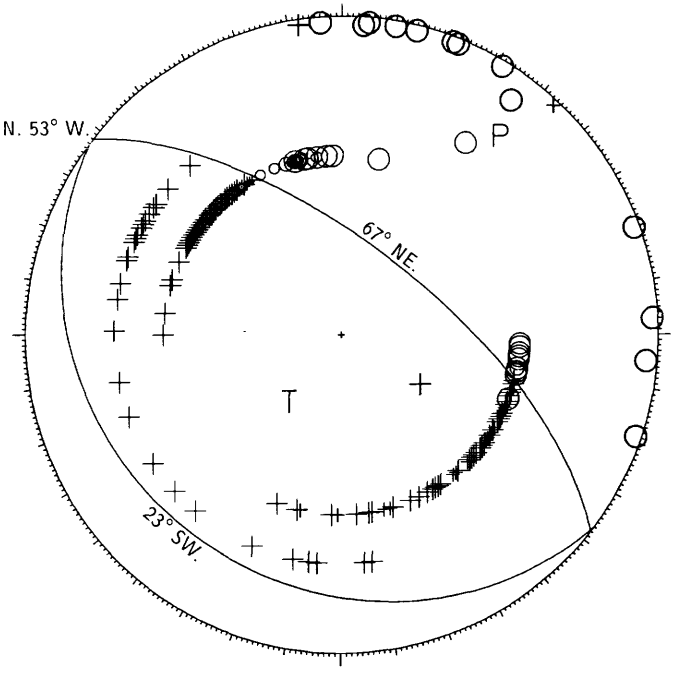

FIGURE 8.9.—First-motion focal-mechanism solution for Coalinga main shock (2342 G.m.t. May 2, 1983). Crosses, compressional first arrivals; circles, dilatational first arrivals; P, direction of maximum compressive stress (*P*-axis); T, direction of minimum compressive stress (*T*-axis). Less certain first arrivals are shown by smaller symbols. Figure drawn by FPPLOT (Reasenberg and Oppenheimer, 1985).

CROSS SECTIONS OF THE AFTERSHOCK ZONE

Cross sections of the aftershock zone for events of $M \geq 2.0$ are shown in figures 8.14 and 8.15 for the time intervals May 2–June 10 and June 11–September 30, respectively. The longitudinal section (figs. 8.14*A*, 8.15*A*) is parallel to the Coalinga anticline (az 135°). The transverse sections, B and C, are perpendicular to Coalinga anticline (az 315°) and cover the subregions northwest and southeast of the quiet zone, respectively. On the longitudinal sections, these subregions correspond to distance ranges of –0.8 km to –22.0 (northwestern subregion) and +22.0 to –0.8 km (southeastern subregion). The interval May 2–June 10 (fig. 8.14) covers the Coalinga aftershock sequence before the first large event in the Nuñez extension, and the interval June 11–September 30 (fig. 8.15) covers the period of the Nuñez extension (principally, June 11–July 31), as well as that of the declining Coalinga earthquake sequence.

The longitudinal sections (figs. 8.14*A*, 8.15*A*) appear similar. Aftershocks are concentrated in the depth range 5–13 km except at the northwest end of the section, where they rise virtually to the Earth's surface. The region around, just north of, and above the main shock (0-km distance, 10-km depth), particularly in figure 8.14*A*, is practically devoid of aftershocks. The region of the main-shock cluster and the southwest band stands out as a dense patch of aftershocks on both plots. Southeast of this patch, aftershocks are concentrated into horizontal bands between 5-7 km and 8-11 km in both figure 8.14*A* and 8.15*A*. A plane dipping 32° SW. and passing through the main shock separates a region of denser concentration above from one of sparser concentration below in both figure 8.14*C* and 8.15*C*. A second plane, dipping about 35° NE. and passing about 2 km beneath the main shock, forms an approximate lower boundary for a zone of aftershocks beneath and northeast of the main shock. Three-dimensional analysis of the aftershock distribution suggests that the alignment of events on the cross sections in this region is not significant. A third plane, dipping 72° NE. and passing about 3 km southwest of the main shock, forms an approximate southwest boundary of a dense zone of aftershocks corresponding to the southwest band of aftershocks in figure 8.12.

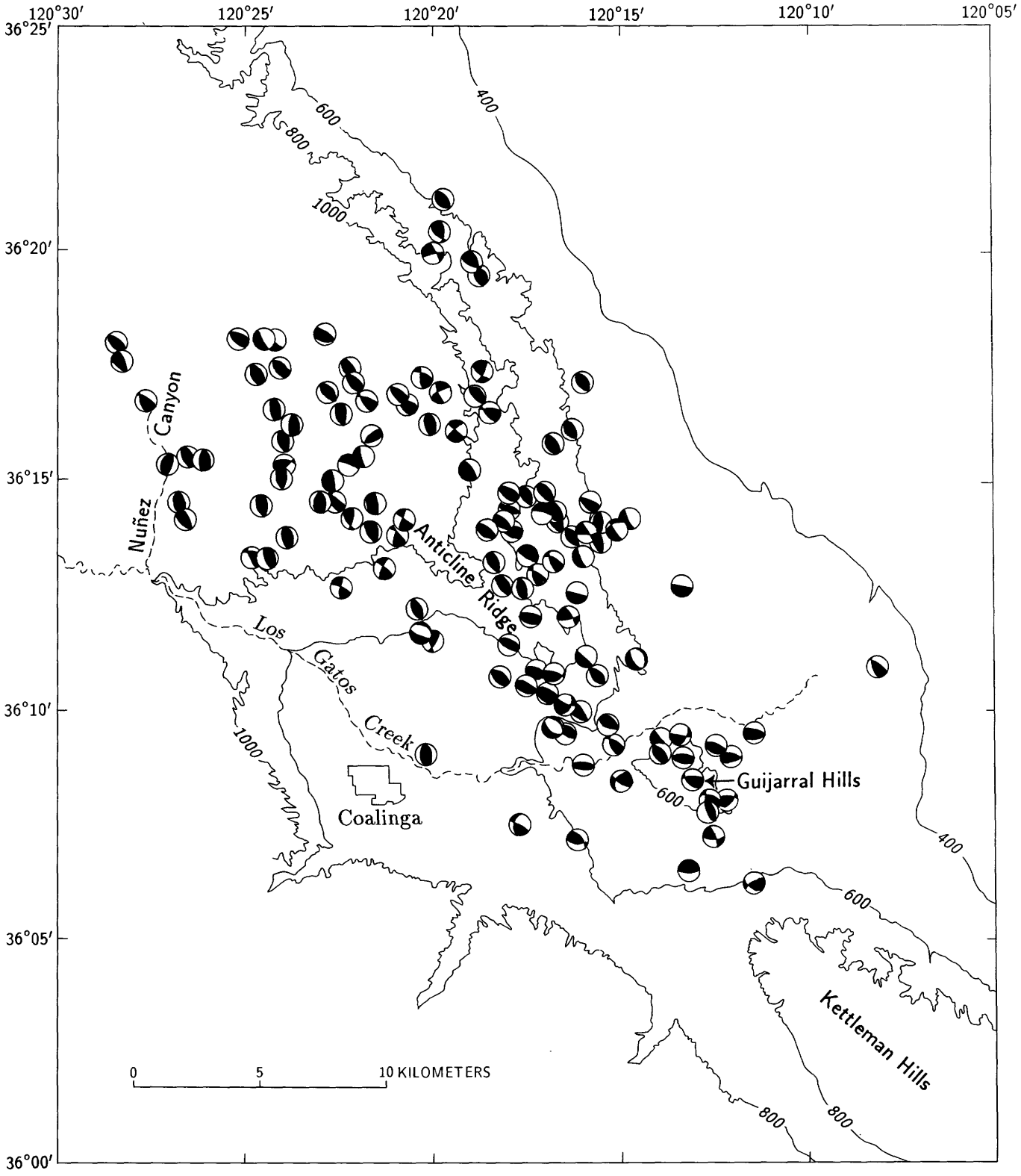

FIGURE 8.10.—Focal mechanisms of May 2 earthquake and larger aftershocks. On focal-mechanism symbols, dark areas represent compressional first arrivals, and white areas dilatational first arrivals. Symbols are not scaled according to magnitude. Some small events were omitted because they coincided with larger events, and others were shifted slightly to avoid excessive overlap with their neighbors.

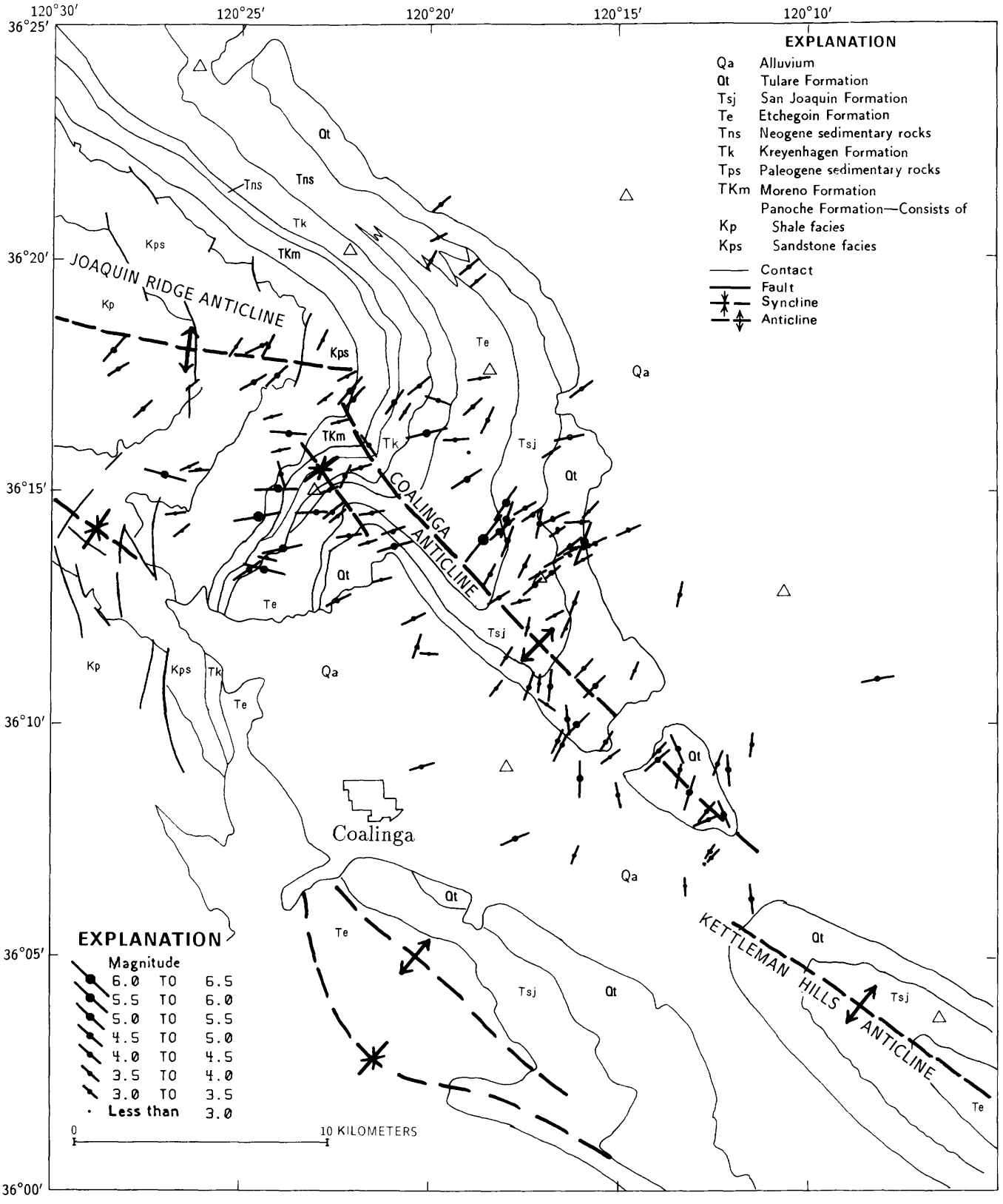

FIGURE 8.11.—Inferred *P*-axis directions of May 2 earthquake and larger aftershocks. Line segments indicating orientations of *P*-axes are scaled according to magnitude. Base is a simplified geologic map of the Coalinga region (see fig. 4.3) showing principal formation-boundaries, axes of major fold structures, and selected faults. Formation boundaries, which are nearly identical in shape to the topographic contours (fig. 8.8), appear to model such features as Anticline Ridge, the Guijarral Hills, and the Kettleman Hills. Triangles, seismograph stations.

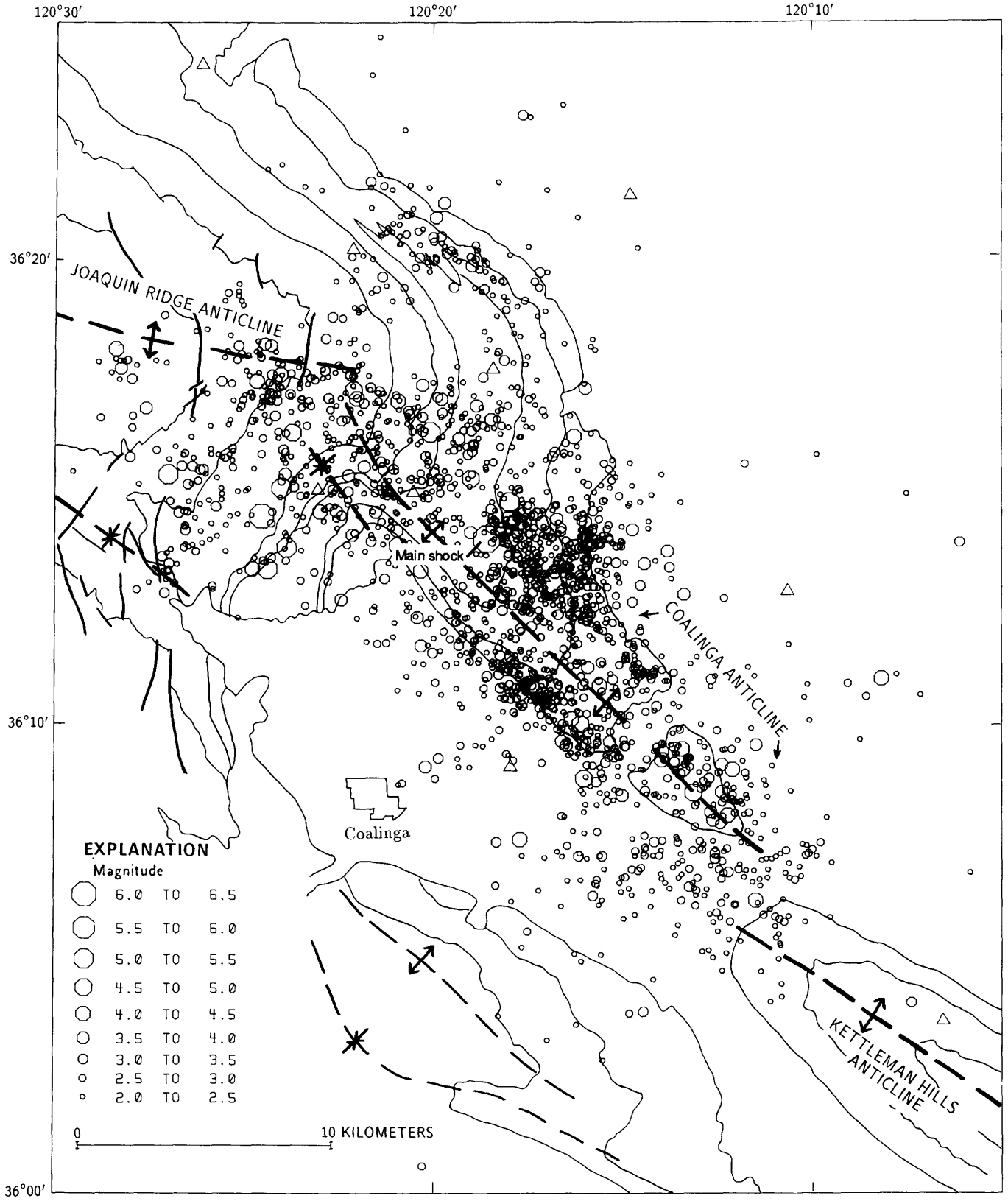

FIGURE 8.12.—Coalinga, Calif., area, showing locations of May 2 earthquake and aftershocks of $M \geq 2.0$. Map base same as in figure 8.11.

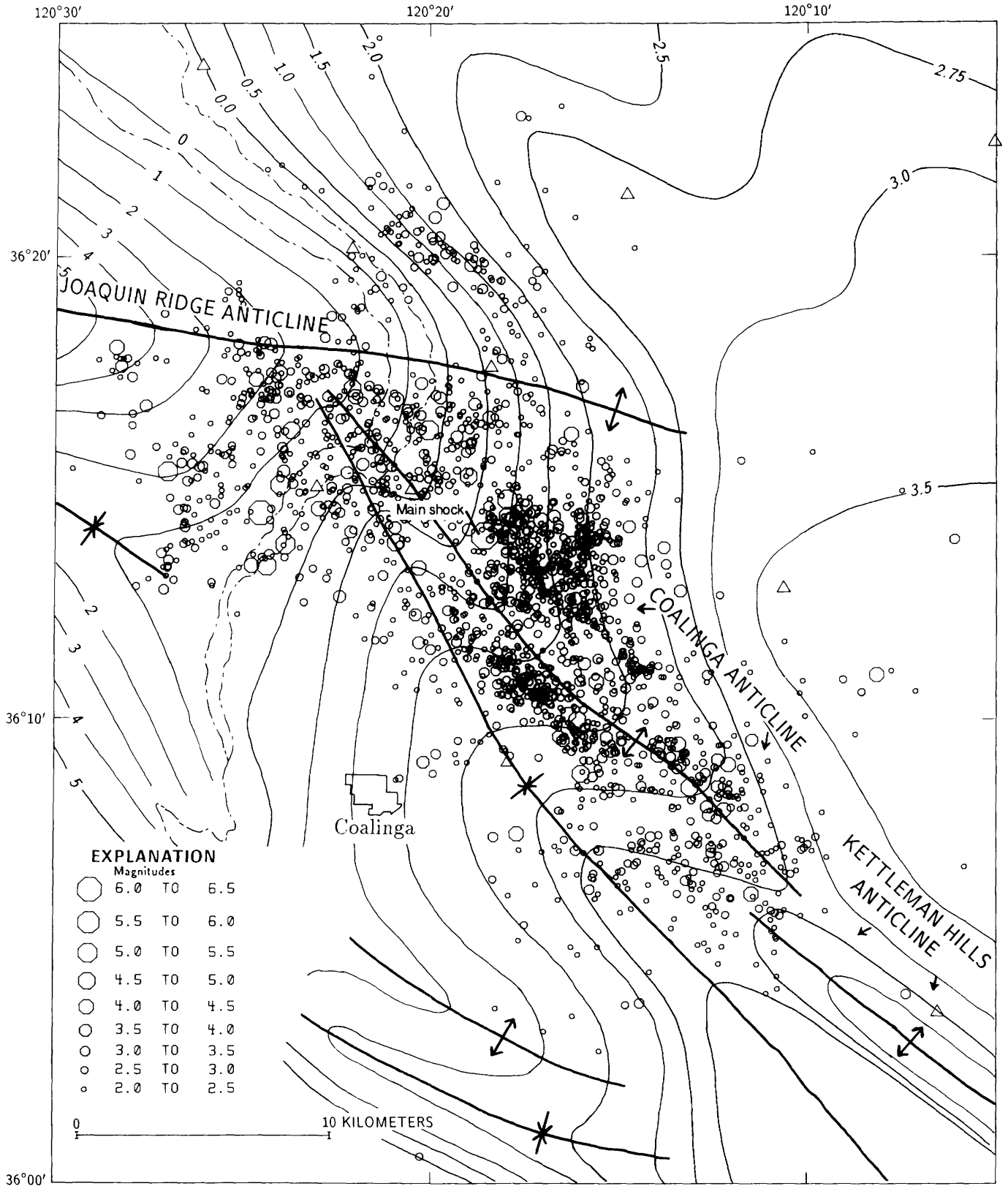

FIGURE 8.13.—Coalinga, Calif., area, showing locations of May 2 earthquake and aftershocks of $M \geq 2.0$ (see fig. 4.4). Contours on right show depth (in kilometers) to top of the Tertiary Kreyenhagen Formation; contours on left show height (in kilometers) to top of the Cretaceous section (unconformity). Dot dashed line, limit of surface exposure of the Kreyenhagen Formation (see fig. 4.4). Triangles, seismograph stations.

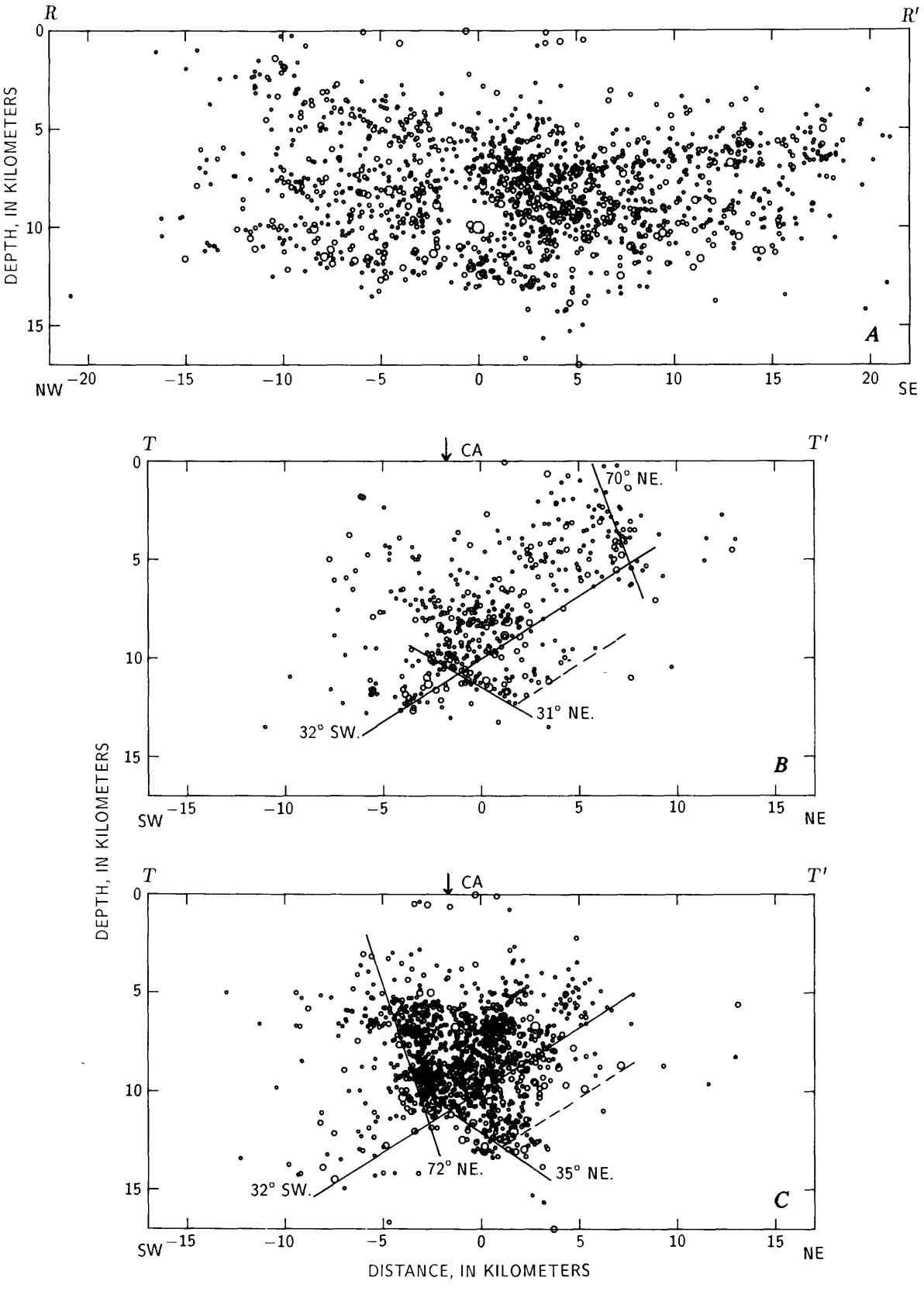

FIGURE 8.14.—Longitudinal (*A*) and transverse (*B*, *C*) cross sections of hypocentral distribution of May 2 earthquake and aftershocks of $M \geq 2.0$ for May 2–June 10. Orientation of cross sections is shown in figure 8.2: *R*–*R'*, longitudinal section (az 135°); *T*–*T'*, transverse section (az 315°). CA, location of axis of Coalinga anticline. Transverse section in figure 8.14*B* shows events northwest of quiet band (–0.8 to –22.0 km on longitudinal profile), and transverse section in figure 8.14*C* shows events southeast of quiet band (–0.8 to +22.0 km on longitudinal profile). Solid and dashed lines are reference lines discussed in text.

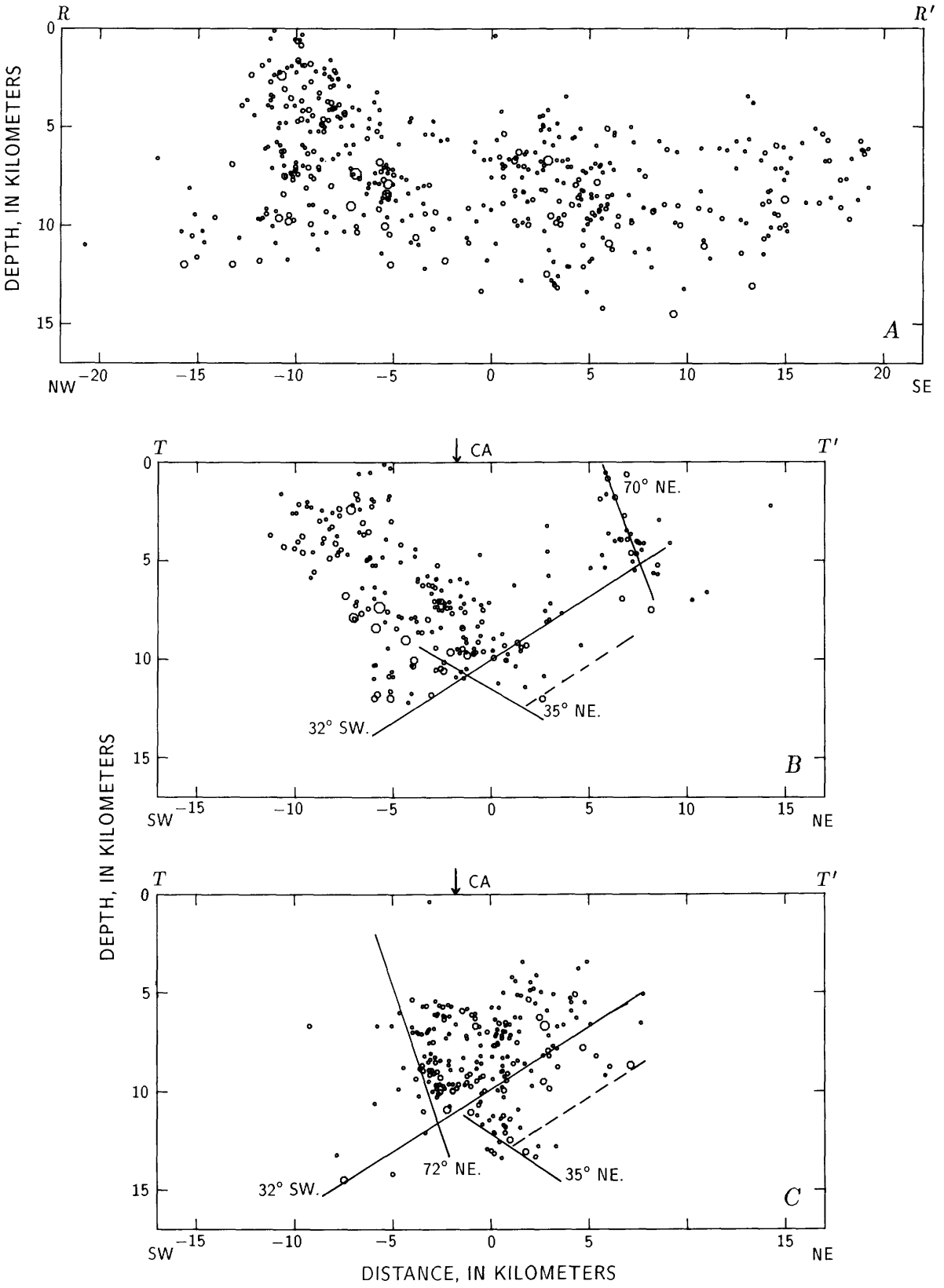

FIGURE 8.15.—Longitudinal (*A*) and transverse (*B*, *C*) cross sections of hypocentral distribution of Coalinga aftershocks of $M \geq 2.0$ for June 11–September 30. Same symbols as in figure 8.14. Solid and dashed lines are reference lines discussed in text.

On the transverse sections for the northwestern subregion (figs. 8.14*B*, 8.15*B*), a plane dipping 32° SW. and passing through the main shock separates a region with abundant aftershocks above from one with far fewer aftershocks below. A plane dipping about 70° NE. that matches the apparent dip of the Domengine cluster in Figure 8.15*B* passes through a concentrated, but less clearly defined, patch of aftershocks in the same region in figure 8.14*B*. Also in figure 8.14*B*, a narrow band of aftershocks dipping about 31° NE. and passing about 1 km below the main shock extends to a depth of about 12 km.

The largest concentration of events on figure 8.15*B* defines a broad northeast-dipping band that extends from the surface to a depth of 10 to 12 km, where it is cut off by the southwest-dipping plane through the main shock. The part of this band above about 9 km represents events of the Nuñez extension, but the orientation of this cross section is not perpendicular to the average *P*-axis orientation of Nuñez events, and so they are spread out artificially in figure 8.15*B*. In figure 8.14*B*, there is no counterpart of the conspicuous northeast-dipping band above and southwest of the main shock in figure 8.15*B*. At most, the southwest edge of the dense cluster of events above the main shock in figure 8.14*B* corresponds to the cluster of small events that define the lower northeast edge of the Nuñez extension in figure 8.15*B*.

The transverse sections for the southeastern subsection (figs. 8.14*C*, 8.15*C*) are nearly identical; aftershocks are densely packed in the region around and above the main shock. A plane dipping the main-shock cluster and the southwest band stands out as a dense patch of aftershocks on both plots. Southeast of this patch, aftershocks are concentrated into horizontal bands between 5–7 km and 8–11 km in both figure 8.14*A* and 8.15*A*. On the transverse sections for the northwestern subregion (figs. 8.14*B*, 8.15*B*), a plane dipping 32° SW. and passing through the main shock separates a region with abundant aftershocks above from one with far fewer aftershocks below. A plane dipping about 70° NE. that matches the apparent dip of the Domengine cluster in Figure 8.15*B* passes through a concentrated, but less clearly defined, patch of aftershocks in the same region in figure 8.14*B*. Also in figure 8.14*B*, a narrow band of aftershocks dipping about 31° NE. and passing about 1 km below the main shock extends to a depth of about 12 km. The largest concentration of events on figure 8.15*B* defines a broad northeast-dipping band that extends from the surface to a depth of 10 to 12 km, where it is cut off by the southwest-dipping plane through the main shock. The part of this band above about 9 km represents events of the Nuñez extension, but the orientation of this cross section is not perpendicular to the average *P*-axis orientation of Nuñez events, and so they are spread out artificially in figure 8.15*B*. In figure 8.14*B*, there is no counterpart of the conspicuous northeast-dipping band above and southwest of the main shock in figure 8.15*B*. At most, the southwest edge of the dense cluster of events above the main shock in figure 8.14*B* corresponds to the cluster of small events that define the lower northeast edge of the Nuñez extension in figure 8.15*B*. The transverse sections for the southeastern subsection (figs. 8.14*C*, 8.15*C*) are nearly identical; aftershocks are densely packed in the region around and above the main shock. A plane dipping 32° SW. and passing through the main shock separates a region of denser concentration above from one of sparser concentration below in both figure 8.14*C* and 8.15*C*. A second plane, dipping about 35° NE. and passing about 2 km beneath the main shock, forms an approximate lower boundary for a zone of aftershocks beneath and northeast of the main shock. Three-dimensional analysis of the aftershock distribution suggests that the alignment of events on the cross sections in this region is not significant. A third plane, dipping 72° NE. and passing about 3 km southwest of the main shock, forms an approximate southwest boundary of a dense zone of aftershocks corresponding to the southwest band of aftershocks in figure 8.12.

Two additional pairs of transverse cross sections for the northwestern region (fig. 8.16) explore the distribution of hypocenters in that region. From a series of transverse cross sections for the period June 11–September 30, perpendicular to azimuths 340°–020°, it was found that the one perpendicular to an azimuth of 005° showed the tightest concentration of hypocenters for events in the Nuñez extension. The same events, plotted on a section perpendicular to Anticline Ridge in figure 8.15*B* (az 315°), are replotted in figure 8.16*B* (az 005°). A plane through the larger events in the Nuñez extension in figure 8.16*B* dips about 52° E. However, a plane through these events that is also constrained to pass through the surface rupture dips about 61° E. (see chaps. 15, 16). A similar cross section for the period May 2–June 10 (fig. 8.16*A*) shows no concentration of events corresponding to the Nuñez extension (fig. 8.16*B*).

Transverse cross sections perpendicular to the axis of the Joaquin Ridge anticline (az 280°) are shown in figures 8.16*C* and 8.16*D* for the periods May 2–June 10 and June 11–September 30, respectively. These sections were chosen to examine the north edge of the northwest triangle, which lies along the axis of the anticline. In both figure 8.16*C* and 8.16*D*, a vertical plane through the axis of the anticline separates a region of dense hypocenters on the south from one with few hypocenters on the north, particularly at depths between 6 and 12 km. A few hypocenters extend across this boundary below about 10

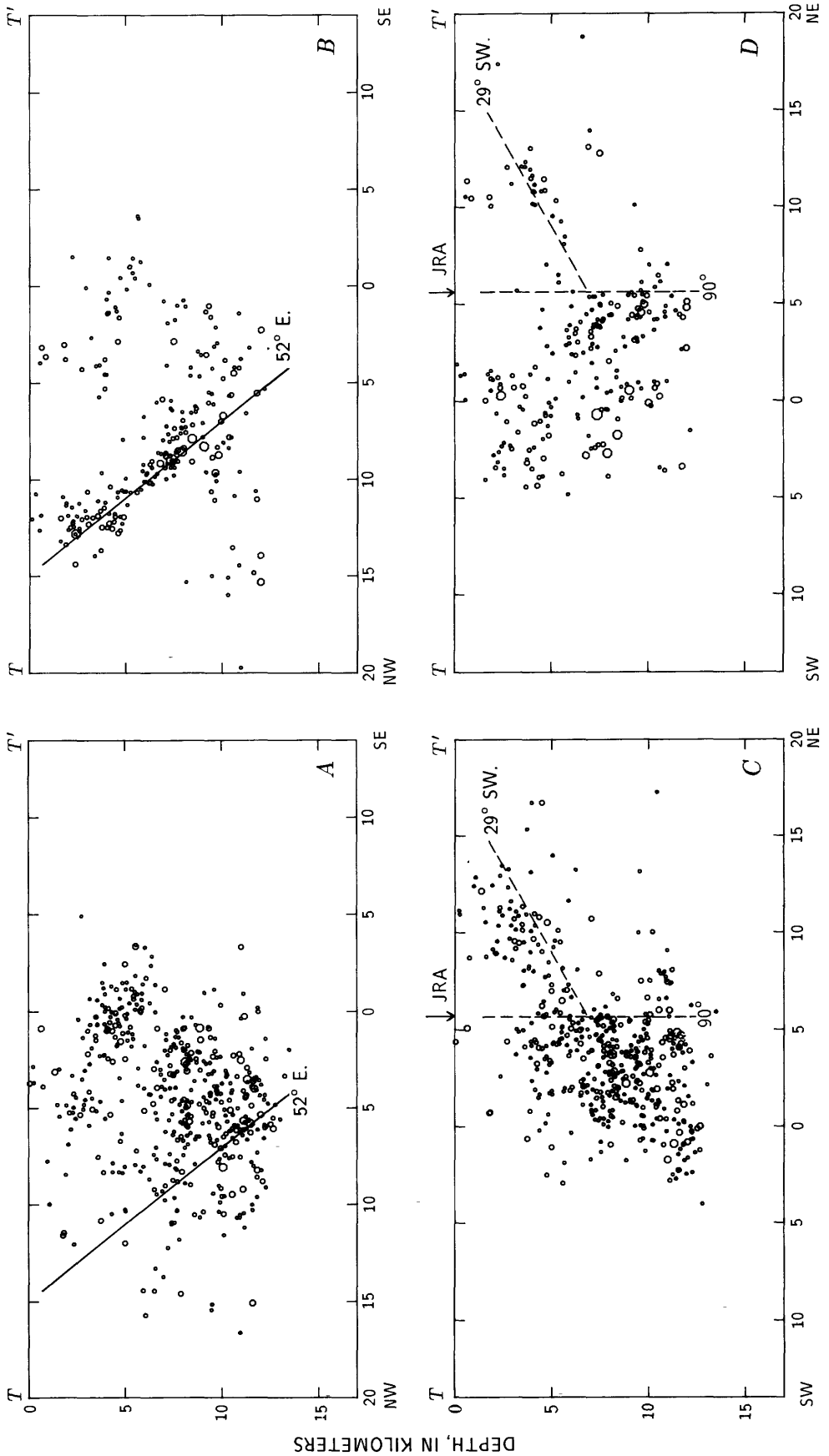

FIGURE 8.16.—Transverse cross sections of hypocentral distribution of Coalinga aftershocks of $M \geq 2.0$ for May 2–June 10 and June 11–September 30. Events plotted are all northwest of quiet zone (–0.8 to –22.0 km on longitudinal profile) in figures 8.14 and 8.15. Sections in figures 8.16*A* (May 2–June 10) and 8.16*B* (June 11–Sept. 30) are perpendicular to an azimuth of 005°, apparent strike direction of the Nuñez fault at depth. Sections in figures 8.16*C* (May 2–June 10) and 8.16*D* (June 11–Sept. 30) are perpendicular to an azimuth of 280°, approximate orientation of axis of the Joaquin Ridge anticline (JRA). Solid and dashed lines are reference lines discussed in text.

km; and above 6 km, scattered hypocenters join the northwest triangle to the Domengine cluster north of Joaquin Ridge.

SPATIAL DISTRIBUTION OF AFTERSHOCKS AS A FUNCTION OF MAGNITUDE

The spatial distribution of Coalinga aftershocks as a function of magnitude is illustrated in figure 8.17, which maps events of $M \geq 3$ (fig. 8.17*A*), $M \geq 4$ (fig. 8.17*B*), $M \geq 4.5$ (fig. 8.17*C*), and $M \geq 5$ (fig. 8.17*D*). For $M \geq 3$, the major clusters of aftershocks are well represented. For $M \geq 4$, the distribution is much reduced. A northern group, consisting primarily of events of the Nuñez extension, the northeast triangle, and the main-shock cluster, as well as a southern group, consisting primarily of the south end of the southwest band and the north end of the southeast cluster, remains. For $M \geq 4.5$, the southern group is reduced to 3 events, and the northern group to 15 events. For $M \geq 5$, the southern group is entirely eliminated, and the northern group is reduced to nine events that lie in an east-west-trending zone, 17 km long by 6 km wide. These nine events form two clusters at the ends of the zone: three plus the $M = 6.7$ main shock on the east, and four plus the $M = 6.0$ July 22 event on the west. The zone of strike-slip faulting that cuts across Anticline Ridge just northwest of the main shock and the quiet zone runs diagonally across the middle of the zone of $M \geq 5$ events.

THREE-DIMENSIONAL ANALYSIS OF THE HYPOCENTERS AND FOCAL PLANES OF COALINGA AFTERSHOCKS

Maps and cross sections appear to be inadequate to unravel the complex geometry of the hypocentral distribution and focal-plane orientations of the Coalinga aftershocks. To pursue this problem further, I consider a three-dimensional analysis, employing stereopair plots of the Coalinga hypocenter and focal-mechanism results.

For preparation of the stereoplots, the aftershock area was divided into three regions (northern, central, and southern) based on groupings of events on the epicenter map. These three regions have a common central axis parallel to the axis of Anticline Ridge and are separated by lines, perpendicular to the central axis, through the quiet band and between the combined southwest band/main-shock cluster and the southeast cluster. The three regions are outlined in figure 8.8.

To show the temporal evolution of the aftershock pattern and to separate the relatively poor data of the first 2 days of the sequence from the rest of the data, plots were prepared for several time intervals.

May 2–May 4.—During this period, before significant augmentation of the network and while background noise was unusually high, hypocenter and focal-mechanism determinations were substandard.

May 5–June 10.—After augmentation of the network and after the background noise subsided, high-quality hypocenter and focal-mechanism determinations were obtained for events in the Coalinga earthquake sequence that preceded the June 11 Nuñez Canyon earthquake.

June 11–September 30.—From the June 11 earthquake to the end of our study period on September 30, high-quality hypocenter and focal-mechanism solutions were obtained for the ongoing Coalinga earthquake sequence, as well as for the Nuñez extension, which had its largest events in June and July.

The stereoplot program is from Paul Reasenberg (written commun., 1984), who augmented an earlier program written by German and Johnson (1981). Reasenberg's program permits plotting of surface features (contours, and so on) and a three-dimensional reference framework, as well as depiction of earthquake focal mechanisms and hypocenter locations with different symbols that are scaled separately according to magnitude. The position of the viewpoint can be adjusted to obtain clear views of the data being plotted. The three reference frames used here correspond to the three regions outlined in figure 8.8. The central axis that runs through all three frames has an azimuth of 315°. In separate plots of the data in the northern, central, and southern regions, the corresponding frames are used. In plots of data for the entire epicentral region, the central frame only is used for reference, and the data extend out both ends of the frame.

To facilitate comparison of the plotted focal mechanisms with that of the main shock, a reference plane is depicted by a gridwork of points projected vertically downward onto the reference plane from a 1- by 1-km gridwork of points on the Earth's surface. The rectangular surface region chosen to represent the thrust-fault solution for the main shock has a long axis trending N. 53° W. and a length and width corresponding approximately to the distribution of epicenters shown in figure 8.8. This region is probably larger than the rupture surface of the main shock, particularly in its width.

Because the focal-mechanism solution does not distinguish between the fault plane and the auxiliary plane, identification of the fault plane must be based on other considerations. In figures 8.18 through 8.37, the selection was made so that the focal-mechanism fault plane corresponds, where possible, to the fault plane suggested by the spatial distribution of hypocenters of other larger aftershocks near the event in question. The number of events for which focal-mechanism solutions are available is relatively small, considering the size of the region

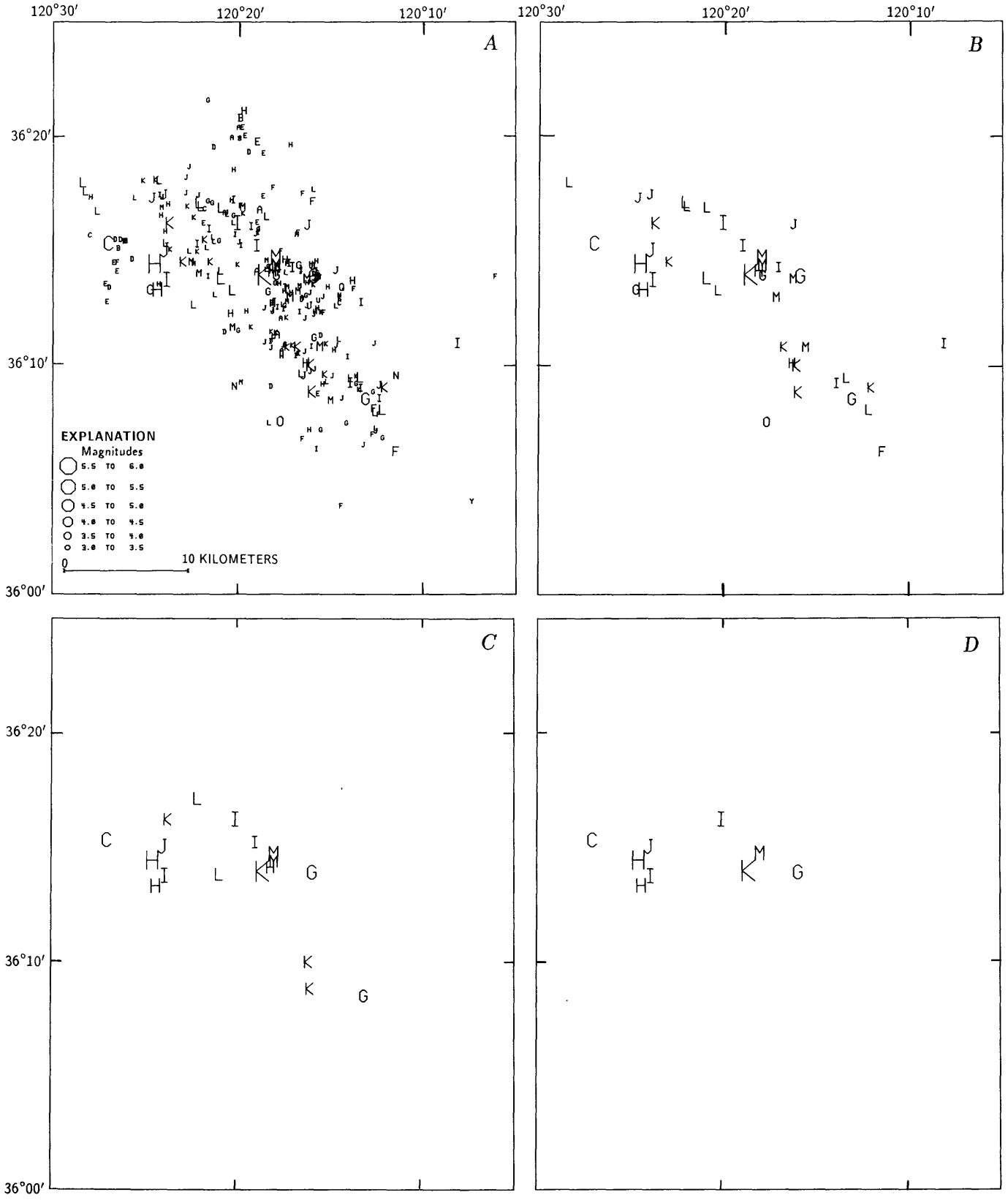

FIGURE 8.17.—Schematic maps of Coalinga, Calif., area, showing locations of May 2 earthquake and aftershocks for May 2–September 30 of $M \geq 3.0$ (*A*), $M \geq 4.0$ (*B*), $M \geq 4.5$ (*C*), and $M \geq 5.0$ (*D*). Symbols are scaled by magnitude and coded for depth according to the following scheme: A, 0–1 km; B, 1–2 km; C, 2–3 km; and so on. Large letter K denotes main shock.

through which they are distributed and the apparent complexity of the faulting associated with the Coalinga earthquake sequence; thus, the evidence for choosing the fault plane is not compelling for many events.

For practical considerations, focal planes with southwestward dips were chosen as fault planes for the first stereoplots. Upon examination of the stereoplots, choices for individual events were altered to fulfill the criterion stated above. In the final plots presented here, the evidence for choice of a fault plane is judged to be strong where the data points are relatively dense and describe parts of structures that are somewhat isolated from intersecting structures. For isolated events or for events in regions of greater complexity, the evidence for choice of a fault plane is weak.

Two series of stereoplots are presented. In the first series, the fault planes of larger aftershocks are examined to determine whether they reveal the location and orientation of faults associated with the Coalinga earthquake sequence, particularly with the main shock. In the second series, the hypocenters of smaller aftershocks are plotted together with the fault planes of larger after-

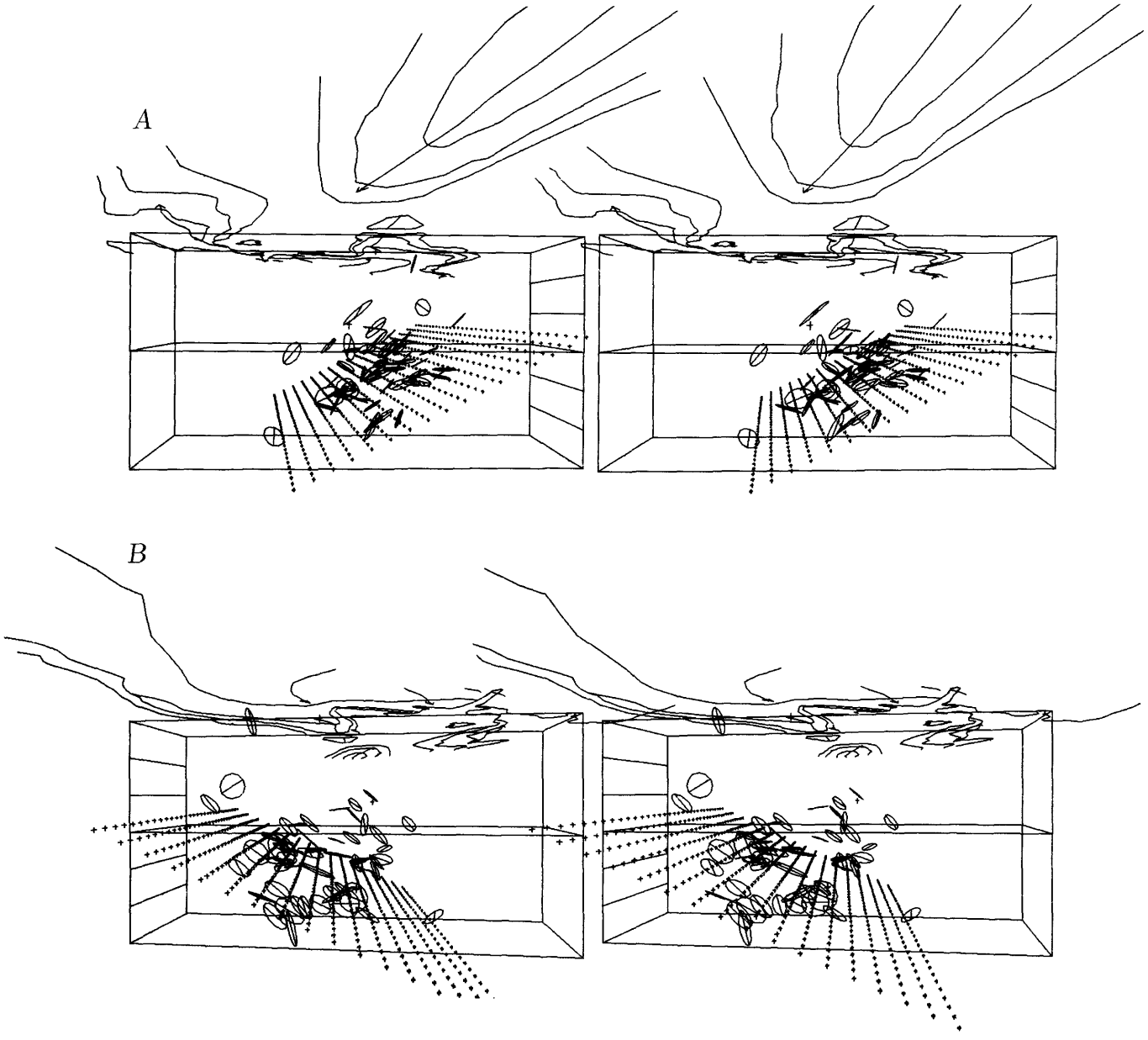

FIGURE 8.18.—Stereopairs showing fault planes of May 2 earthquake and aftershocks for May 2–4, viewed from southeast (*A*) and northwest (*B*) (fig. 8.8). Thrust reference plane strikes N. 53° W. and dips 25° SW. Horizontal spacing of points on the reference plane is 1 by 1 km.

shocks to explore the relation between these two classes of events, as well as between smaller aftershocks and the faults suggested by the fault planes of larger aftershocks.

We begin with a sequence of plots (figs. 8.18–8.22) that show the development of the aftershock pattern in space and time and permit an evaluation of the early, substandard data separately from the higher quality data obtained during most of the later sequence. The reference plane strikes N. 53° W. and dips 25° SW. (in comparison with N. 53° W. and 23° SW. for the thrust solution for the main shock). Each figure contains two stereopairs, one viewing the data from the northwest, and the other from the southeast. The whole aftershock zone is included, but only the central-zone stereoframe is used for reference. The viewpoint is at a depth of 5 km, above the reference plane. Lines depicting formation boundaries (fig. 8.10) at the Earth's surface appear to float overhead. In the view from the southeast (upper pair), the viewpoint is beneath the Kettleman Hills, and the line of sight is northwestward along the axis of Anticline Ridge, which is visible in the surface geology just to the right of center of the reference frame. The town of Coalinga lies on the near

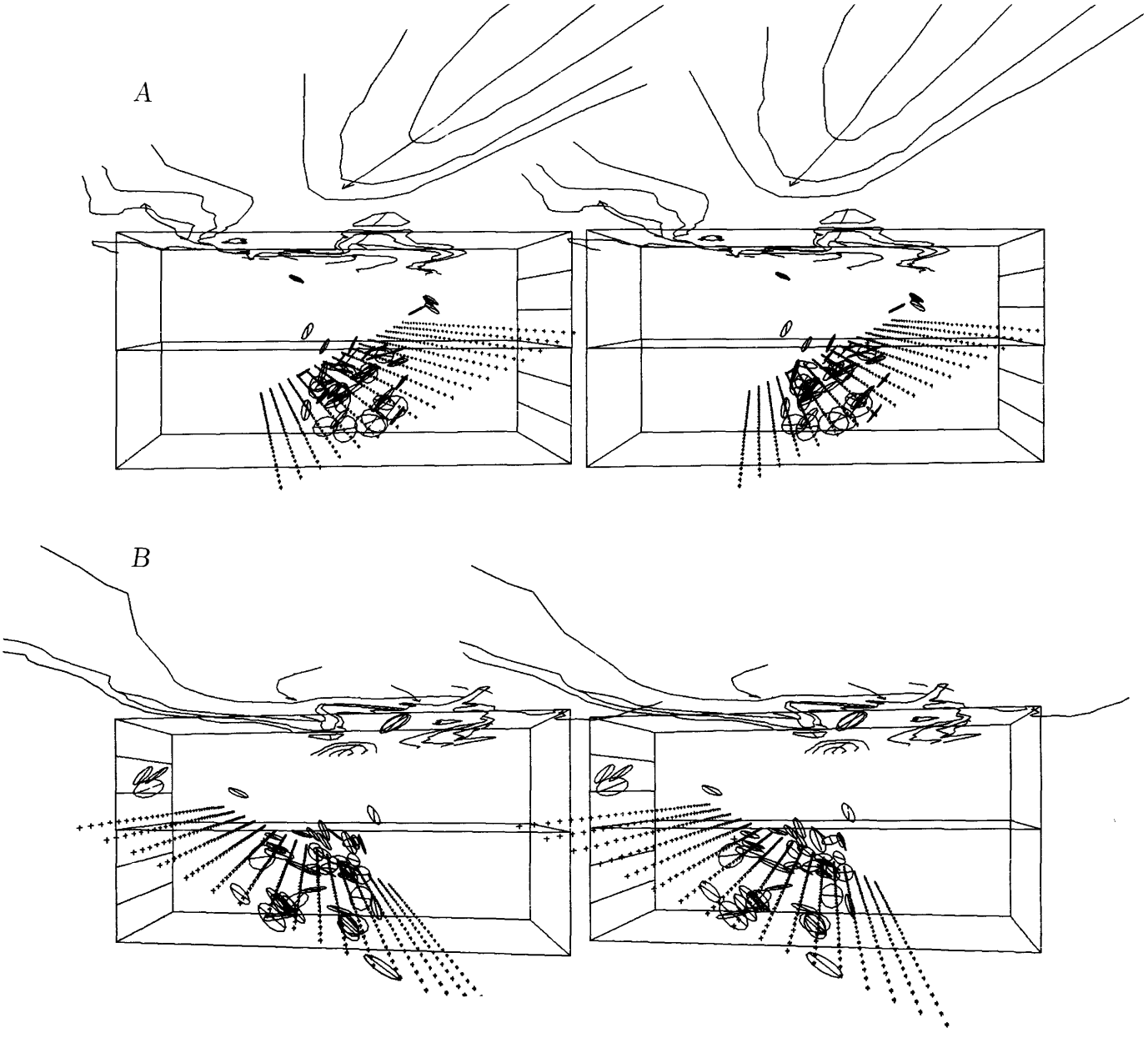

FIGURE 8.19.—Stereopairs showing fault planes of May 2 earthquake and aftershocks for May 5–June 10, viewed from southeast (*A*) and northwest (*B*). Thrust reference plane strikes N. 53° W. and dips 25° SW. Horizontal spacing of points on reference plane is 1 by 1 km.

edge of the reference frame just to the right of the left-hand side of the frame. The frame is 15 km high and has horizontal lines marking 2½-km depth internals along its right-hand side. The spacing of the gridpoints, referred to a horizontal surface, on the reference plane is 1 km in each direction. In the view from the northwest (lower pair), the viewpoint is northwest of Anticline Ridge, and the line of sight is southeastward along the axis of Anticline Ridge. The northwest end of the Kettleman hills is in the distance at the center of the frame, Coalinga appears on the far boundary of the reference frame just to the left of the right-hand side of the frame. In all plots containing the central section of the aftershock zone, the main shock is shown for reference, whether or not it occurred within the time interval shown in the figure; it lies near the northwest edge of the central reference frame, between the 8th and 10th highest horizontal rows of points on the reference plane.

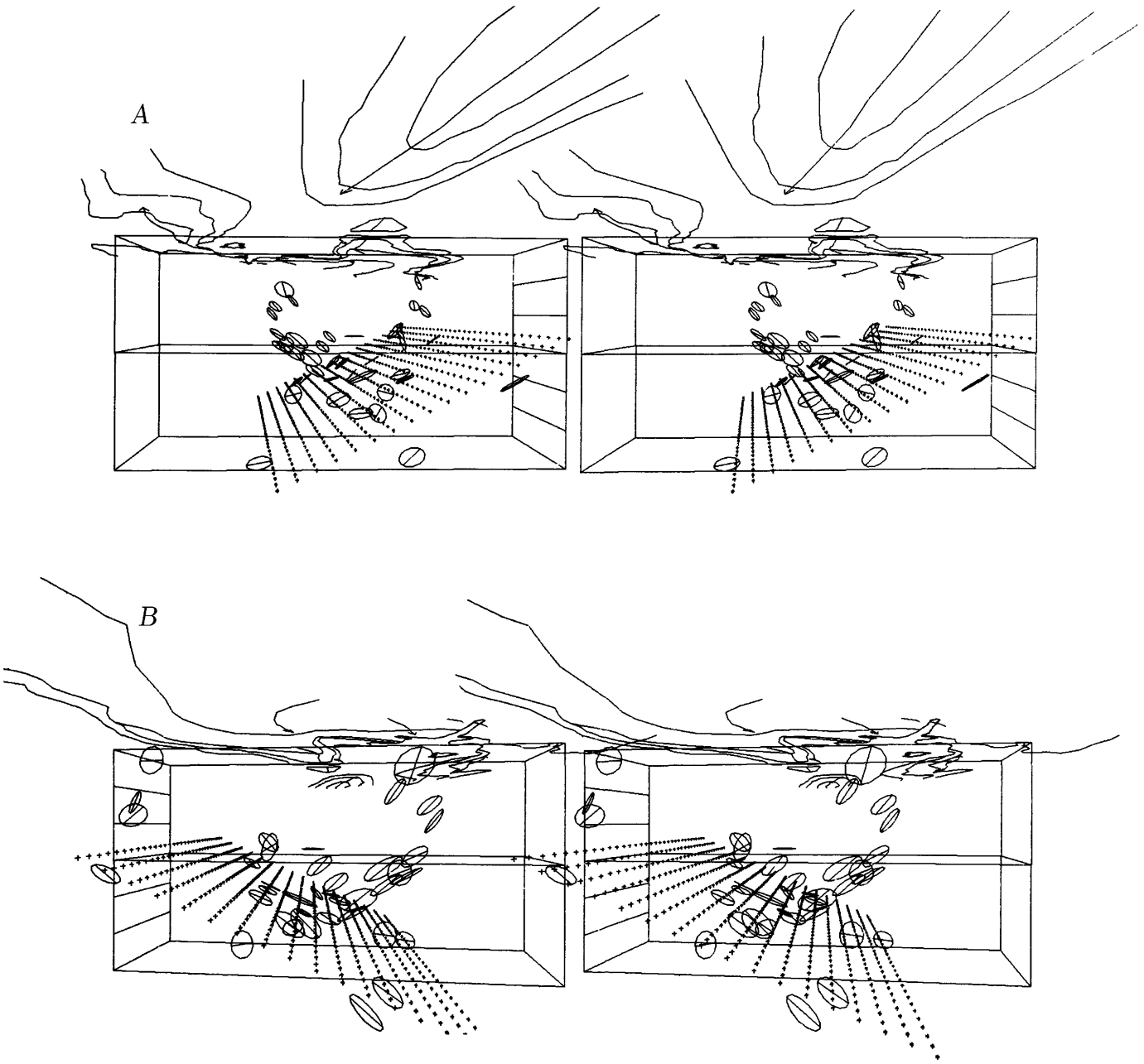

FIGURE 8.20.—Stereopairs showing fault planes of May 2 earthquake and aftershocks for June 11–September 30, viewed from southeast (*A*) and northwest (*B*). Thrust reference plane strikes N. 53° W. and dips 25° SW. Horizontal spacing of points on reference plane is 1 km by 1 km.

While viewing figures 8.18 through 8.22, the reader should recall that the circle depicting an event lies in the fault plane deduced from its focal mechanism and that the diameter-line shows the direction of slip.

May 2–4 (fig. 8.18).—Aftershocks are spread widely across the aftershock region, but in the southern part they are not close to the reference plane. Station coverage was particularly poor for the southern part of the aftershock zone during this interval.

May 5–June 10 (fig. 8.19).—Many events throughout the aftershock region cluster around the reference plane and have fault planes that parallel it. A northwest-southeast alignment of events beneath the central part of the reference plane can be interpreted as a southwest-dipping thrust parallel to the reference plane or as a northeast-dipping reverse fault extending from the reference plane to a depth of about 12 km. In the main-shock cluster southeast of the main shock and in the southern

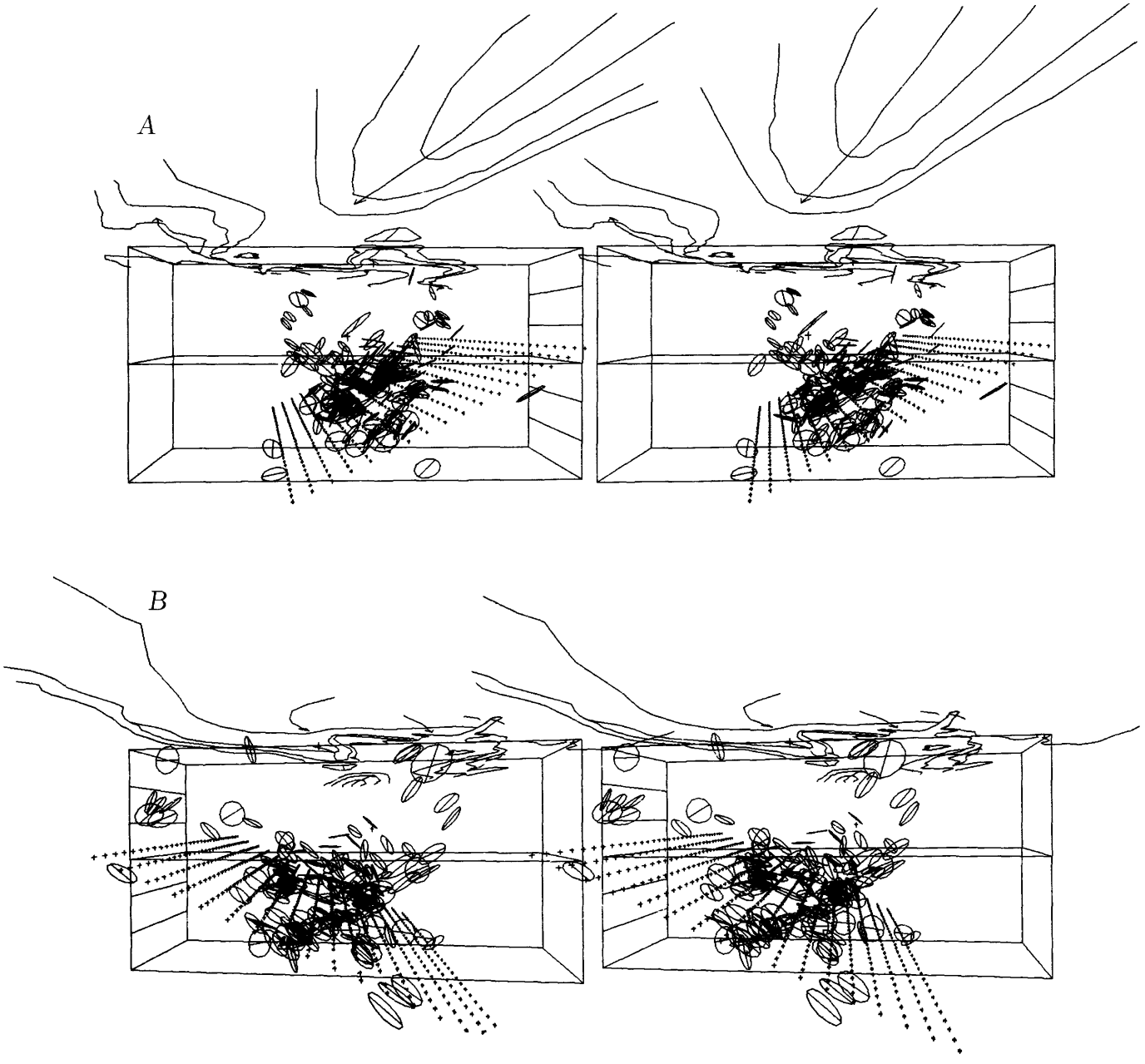

FIGURE 8.21.—Stereopairs showing fault planes of May 2 earthquake and aftershocks for May 2–September 30, viewed from southeast (*A*) and northwest (*B*). Thrust reference plane strikes N. 53° W. and dips 25° SW. Horizontal spacing of points on reference plane is 1 km by 1 km.

cluster farther south events are several kilometers above the reference plane, as well as on it.

June 11–September 30 (fig. 8.20).—This interval covers the development of the Nuñez extension and the continuation of activity throughout the Coalinga aftershock region. Its principal features are (1) a north-south-trending fault surface extending from the reference plane upward to the June 11 Nuñez Canyon earthquake beneath the zone of surface breakage that accompanied it, (2) the wide distribution of aftershocks that practically coincide with the reference plane, and (3) an M=5.3 right-slip earthquake that occurred at the east edge of the main-shock cluster on September 9. Several additional aftershocks occurred in the Domengine cluster, and several more beneath the reference plane.

May 2–September 30 (fig. 8.21).—These plots show the entire sequence in all its complexity. Many aftershocks lie on or near the reference plane and have fault planes that parallel it. Note, also, that the Nuñez fault surface appears to be truncated by the reference plane.

May 2–September 30 (fig. 8.22).—In these plots, the line of sight is shifted from parallel to perpendicular to the aftershock zone. In the lower plot, where the aftershock region is viewed from the northeast, the solutions that lie below the reference plane are shown. These events lie near a line that descends from the reference plane, at about 10-km depth, on its north end to a depth of about 12 km beneath the main shock. They have been interpreted as southwest-dipping reverse-fault earthquakes lying along the downdip edge of a fault that is below and subparallel to the reference plane. In an alternative interpretation (northeast-dipping reverse-fault earthquakes), they would define a zone of faulting that extends from the reference plane to a depth of 12 to 13 km. In figure 8.22*A*, where the aftershock region is viewed from the southwest, the solutions that are above or near the reference plane are shown. This is the best overall view of the entire set of larger aftershocks.

In figures 8.23 through 8.25, the aftershock sequence is examined section by section in more detail. The reference plane corresponds to the thrust solution for the main shock, and the line of sight parallels the long axis of the aftershock region.

May 2–September 30 (northern region, fig. 8.23).—Aftershocks in the northern region are separated into well-defined, distinct groups that appear to trace out the faults that caused them. The clearest groups of events are: (1) aftershocks in the Nuñez extension that trace out

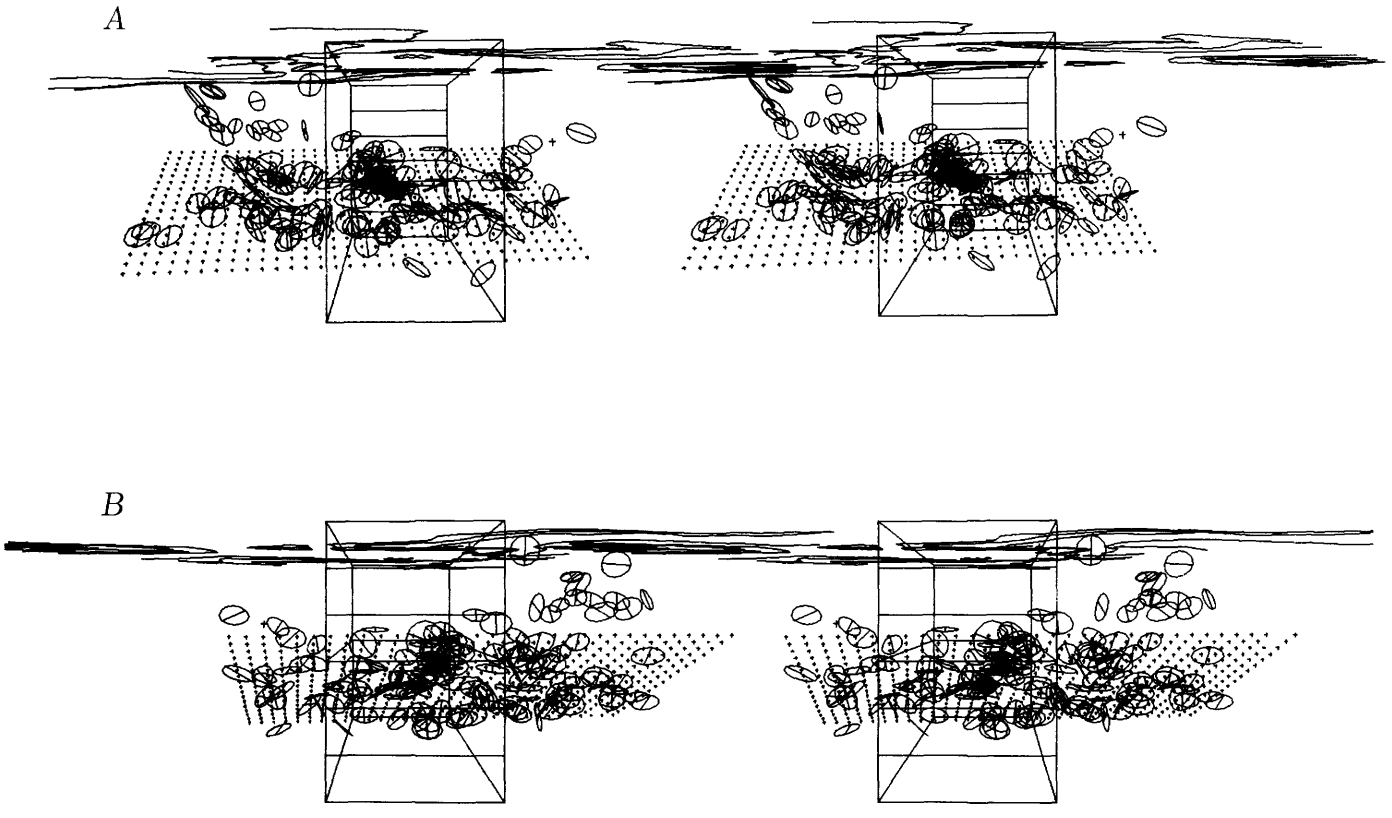

FIGURE 8.22.—Stereopairs showing fault planes of May 2 earthquake and aftershocks for May 2–September 30, viewed from southwest (*A*) and northeast (*B*). Thrust reference plane strikes N. 53° W. and dips 25° SW. Horizontal spacing of points on the reference plane is 1 km by 1 km.

an east-dipping reverse fault which extends upward from the reference plane to the June 11 Nuñez Canyon earthquake that occurred beneath the zone of surface cracking associated with it; (2) aftershocks of the Domengine cluster that appear to trace out a northeast-dipping reverse fault beneath the Coast Ranges-Great Valley boundary; (3) a line of aftershocks with right-lateral strike-slip solutions that trace out the southeast boundary of the northern region along the northeast-trending quiet band (most of these solutions lie near the reference plane, although their fault planes are nearly perpendicular to the reference plane); (4) aftershocks beneath the reference plane that trace out the downdip edge of a reverse fault which is subparallel to the reference plane; and (5) several widely scattered aftershocks, including most of those with strike-slip solutions, that lie near the reference plane.

May 2–September 30 (central region, fig. 8.24).—The central region contains the main shock and several concentrations of events around it. Some of these concentrations are on or near the reference plane, but others are off it. The most conspicuous clusters are: (1) aftershocks in the southwest cluster that have locations and fault-plane orientations suggesting a reverse fault dipping steeply northeast (these events lie above the reference plane and appear to be truncated by it; the fault they

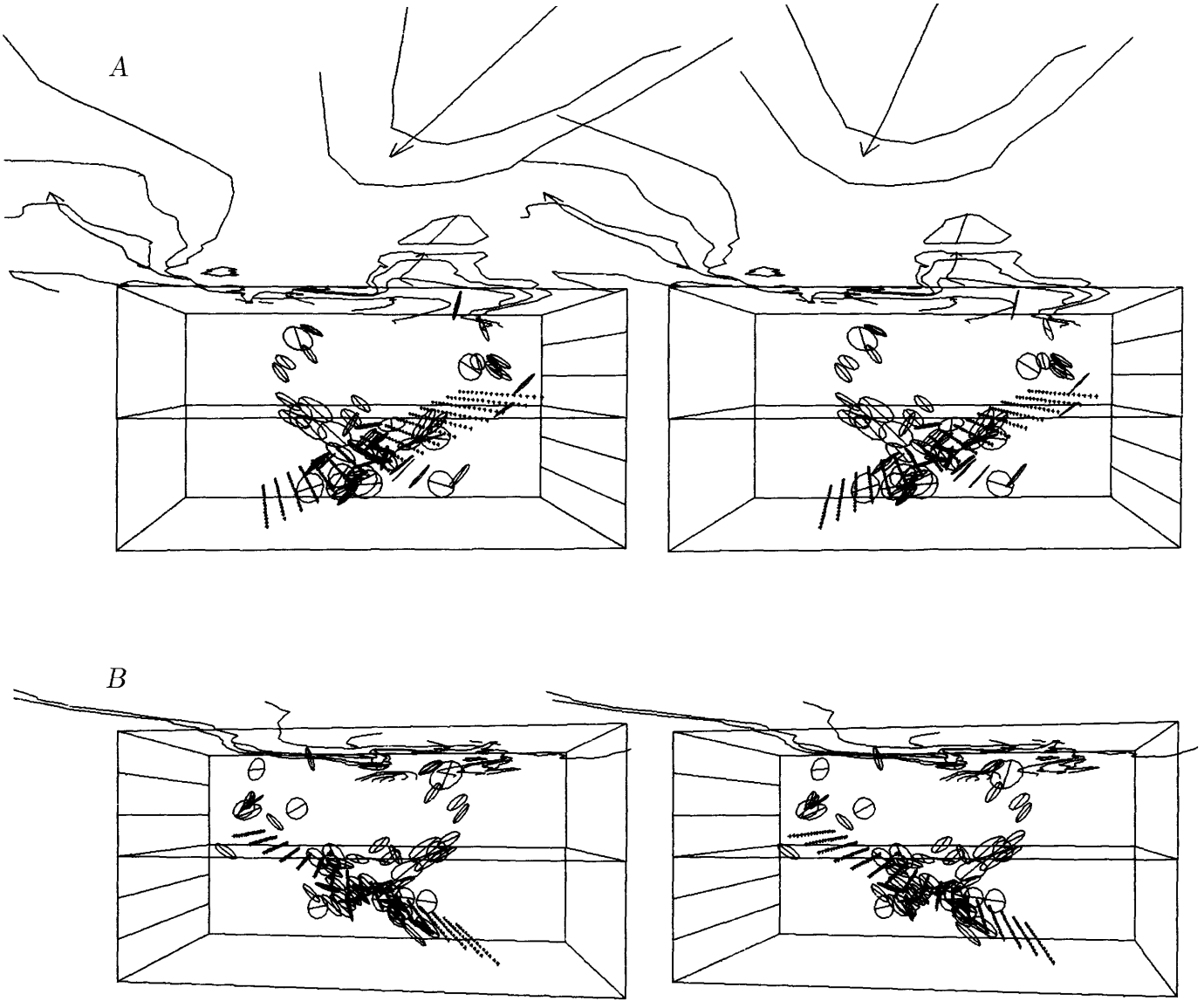

FIGURE 8.23.—Stereopairs showing fault planes of Coalinga aftershocks for May 2–September 30 in reference frame N (fig. 8.8), viewed from southeast (*A*) and northwest (*B*). Thrust reference plane strikes N. 53° W. and dips 25° SW. Horizontal spacing of points on reference plane is 1 km by 1 km.

suggest would pass about 3 km southwest of the main shock); (2) aftershocks beneath the reference plane in a group extending southeastward from beneath the main shock to the southeast end of the southwest band, (these events appear to lie on a southwest-dipping reverse fault that is a continuation of the one described under item 4 in the northern region; the May 9 M=5.3 event is the largest earthquake in the group, and its hypocenter is about 2 km below and 2 km northeast of that of the main shock); (3) a group of aftershocks above the reference plane that appears to define a 5- by 5-km thrust parallel to and several kilometers above the reference plane in the region of the main shock; and (4) scattered events near the reference plane, including two clusters several kilometers east of the main shock and two isolated events 5 and 8 km southwest of the main shock.

May 2–September 30 (southern region, fig. 8.25).—The principal features outlined by focal planes of the larger aftershocks in the southern region are (1) a 4-km-wide band of aftershocks very near the reference plane, at depths between 10 and 12 km; and (2) scattered aftershocks in a tabular zone extending upward, to a depth of about 5 km, from the band of aftershocks noted in item 1.

From study of these stereo-plots and the focal-mechanism map (for sense of motion on the faults), I believe that the data support the following conclusions.

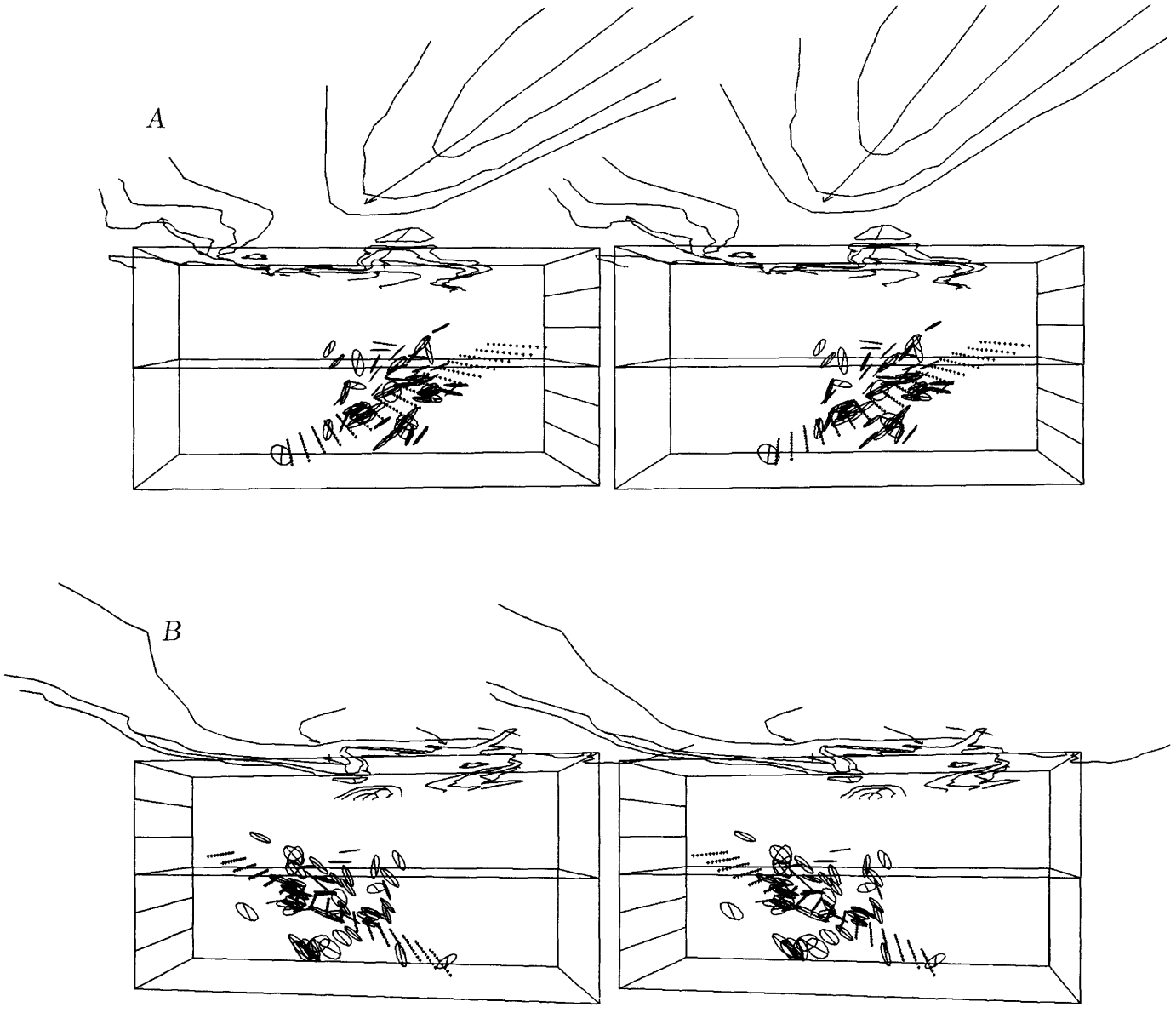

FIGURE 8.24.—Stereopairs showing fault planes of Coalinga aftershocks for May 2–September 30 in reference frame C (fig. 8.8), viewed from southeast (*A*) and northwest (*B*). Thrust reference plane strikes N. 53° W. and dips 25° SW. Horizontal spacing of points on reference plane is 1 km by 1 km.

1. The distribution and focal mechanisms of the aftershocks studied are more compatible with an interpretation of the main-shock mechanism as a thrust striking N. 53° W. and dipping 23° SW. than as a high-angle reverse fault striking N. 53° W. and dipping 67° NW. because (a) aftershock focal planes lie on or near the thrust plane over much of the early aftershock region (fig. 8.3*A*) in what may be called the axial concordant zone, (b) conspicuous secondary structures that rise above the thrust surface appear to root in or terminate against it, and (c) most out-of-plane events lie in the (weaker) upper plate above the concordant zone.
2. The sequence developed in two phases: (a) May 2–June 10—the spatial pattern of events established on the first day was filled in and intensified by events with the same basic distribution; and (b) June 11–September 30—the Nuñez fault break developed over a period of 6 to 8 weeks, while activity in the first-phase aftershock region continued.
3. The axial concordant zone is cut by northeast-trending right-slip faulting along the northwest edge of the quiet zone northwest of the main shock.
4. The detached cluster of events north of the main epicentral region (Domengine cluster) appears to define a northeast-dipping reverse fault.
5. Except for the events in the Nuñez extension and the Domengine cluster, few larger aftershocks lie between the thrust surface and the Earth's surface in the northern region, northwest of the quiet zone.
6. South of the quiet zone, in the central and southern regions, aftershocks between the concordant zone on the thrust and the Earth's surface are plentiful, but the style of faulting above the thrust in the southern region is not well established by the present data.
7. An abrupt cutoff in activity apparently occurs at about

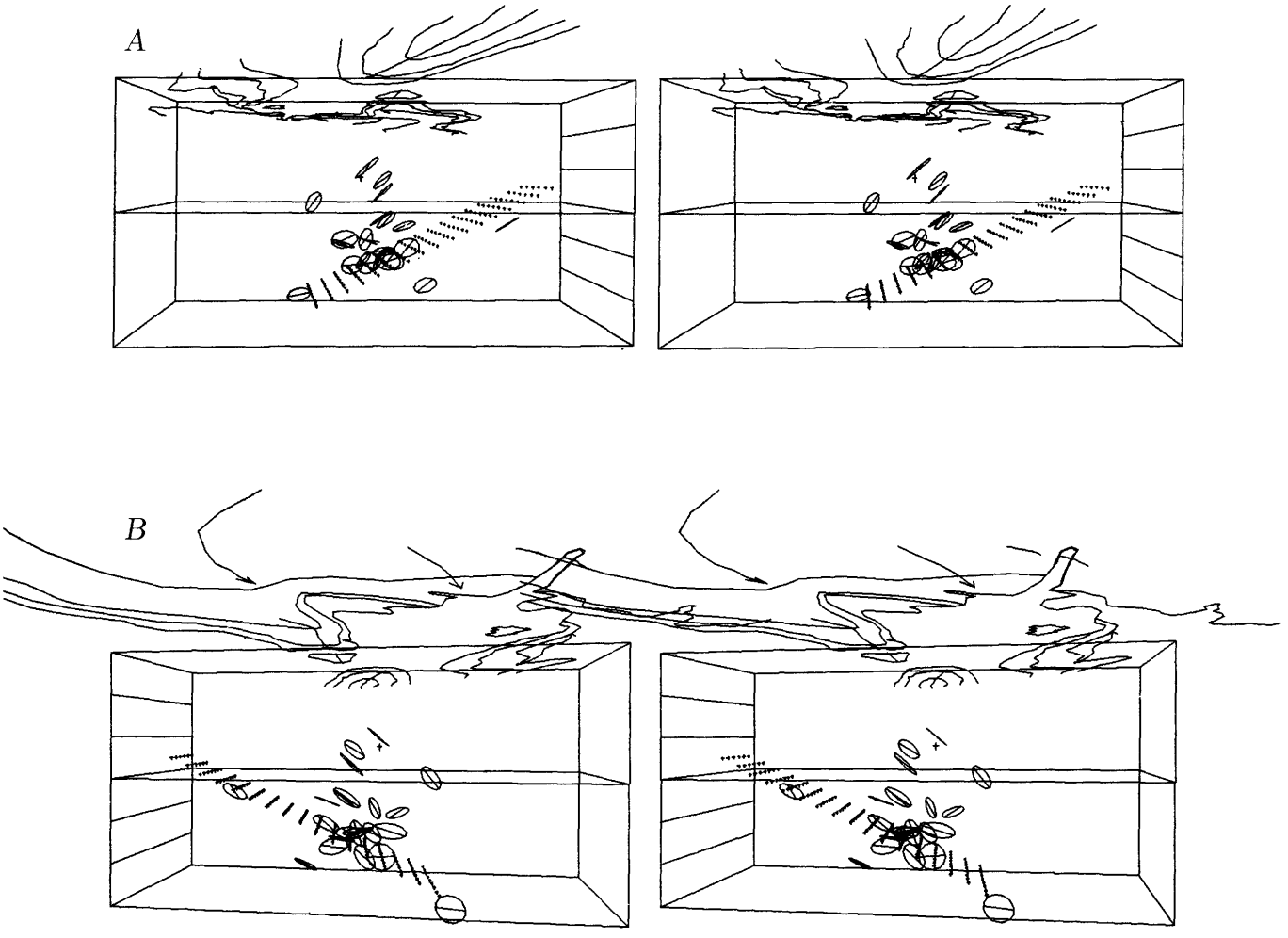

FIGURE 8.25.—Stereopairs showing fault planes of Coalinga aftershocks for May 2–September 30 in reference frame S (fig. 8.8), viewed from southeast (*A*) and northwest (*B*). Thrust reference plane strikes N. 53° W. and dips 25° SW. Horizontal spacing of points on the reference plane is 1 km by 1 km.

13-km depth in the Coalinga region. This depth is essentially the same as the cutoff depth of earthquakes on the San Andreas fault in the Parkfield region, 30 km to the southwest.

8. In figures 8.26 through 8.28, the hypocenters of smaller ($M \geq 2.0$) aftershocks for the entire period of May 2–September 30 are superposed for comparison on stereoplots of the larger aftershocks shown in figures 8.23 through 8.25. Hypocenters of $M \geq 1.7$ events are plotted with the focal planes of larger aftershocks for each of three periods: May 2–4 in figures 8.29 through 8.31, May 5–June 10 in figures 8.32 through 8.34, and June 11– September 30 in figures 8.35 through 8.37.
9. *May 2–September 30, M≥2 (northern region, fig. 8.26).*—Hypocenters of smaller aftershocks appear to extend several kilometers into the hanging-wall block along fault zones that are marked out by the focal planes of larger aftershocks, as is evident near the Nuñez fault surface. Alignment of the hypocenters of smaller aftershocks in the Domengine cluster supports the conclusion from focal-plane data that those events occurred on a northeast-dipping reverse fault parallel to the edge of the Great Valley. Smaller aftershocks in the Domengine cluster extend southeastward to the zone of right-slip faulting north of the quiet zone, where they appear to step to the right several kilometers. In the northern region as a whole, smaller

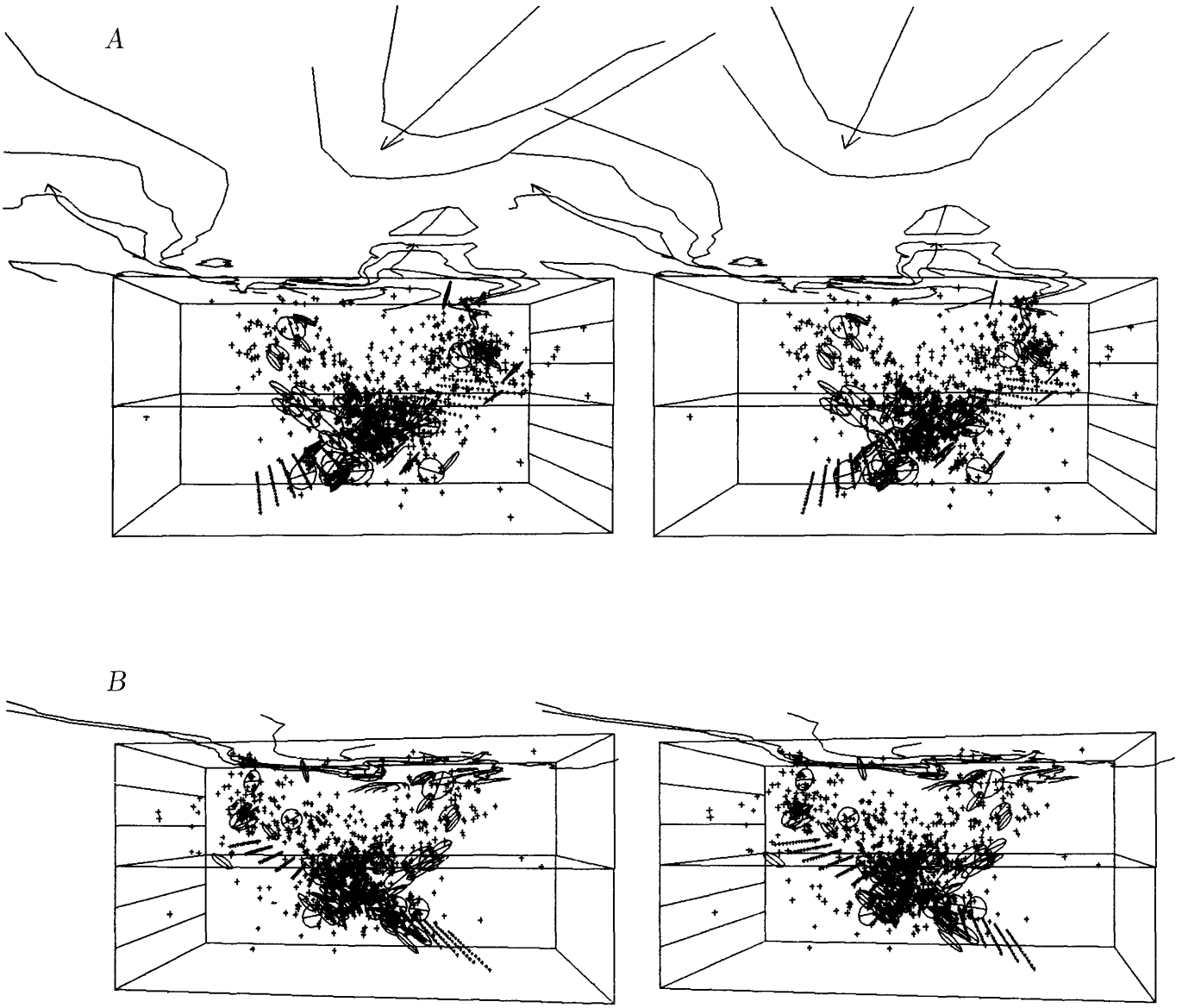

FIGURE 8.26.—Stereopairs showing aftershocks of $M \geq 2.0$ and focal planes of larger Coalinga aftershocks for May 2–September 30 in reference frame N (fig. 8.8), viewed from southeast (*A*) and northwest (*B*). Thrust reference plane strikes N. 53° W. and dips 25° SW. Horizontal spacing of points on reference plane is 1 km by 1 km.

aftershocks are generally concentrated in the trough between the reference plane and the Nuñez fault surface.

10. *May 2–September 30, M≥2 (central region, fig. 8.27).*—Smaller aftershocks are much more abundant here than in the northern region. The southwest cluster is well defined by a dense zone of smaller aftershocks that essentially coincides with the surface suggested by the fault planes of larger aftershocks. Many smaller aftershocks extend into the hanging-wall block above the zone of southwest-dipping reverse faulting beneath the reference plane from the May 9 $M=5.3$ earthquake to the southeast end of the southwest band. Concentrations of smaller aftershocks in the main-shock cluster overlap the faults suggested by the focal planes of larger aftershocks, but these smaller events are too scattered to confirm those individual structures. The northeast cluster appears to mark a southeastward continuation of the reverse faulting along the edge of the Great Valley, similar to that in the Domengine cluster.
11. *May 2–September 30, M≥2.0 (southern region, fig. 8.28).*—The distribution of smaller aftershocks over-

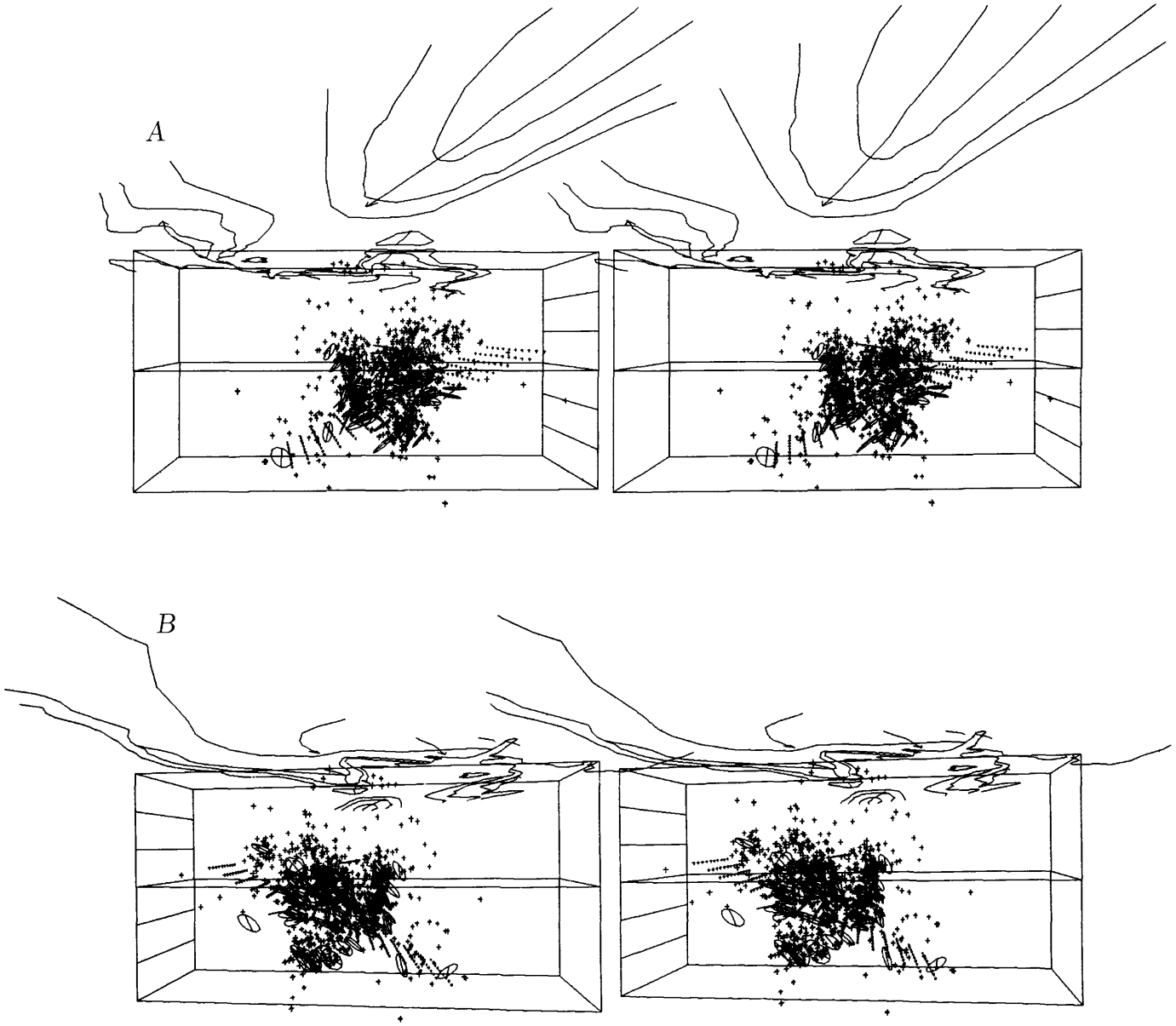

FIGURE 8.27.—Stereopairs showing aftershocks of $M\geq 2.0$ and focal planes of larger Coalinga aftershocks for May 2–September 30 in reference frame C (fig. 8.8), viewed from southeast (*A*) and northwest (*B*). Thrust reference plane strikes N. 53° W. and dips 25° SW. Horizontal spacing of points on the reference plane is 1 km by 1 km.

laps that of larger ones, but the smaller events are more numerous and broadly spread out than the larger ones. Concentrations of hypocenters are not conspicuous. There appears to be one modest concentration in a vertical zone beneath the Guijarral Hills that extends from the reference surface up to about 8 km, and a second, somewhat clearer concentration in a subhorizontal zone between 5- and 7-km depth that lies southwest of the Guijarral Hills on the trend of the Kettleman Hills.

12. *May 2–May 4*, M≥*1.7 (figs. 8.29–8.31).*—During this period, virtually all features of the aftershock sequence, except the Nuñez fault surface, were well established during the first 24 hours of the sequence. The smaller aftershocks emphasize the northeast-dipping zone of reverse faulting through the southwest band more strongly than do the larger aftershocks. Moreover, in the northern region, where the larger aftershocks did not show such a fault in the upper plate, the smaller aftershocks appear to be cut off southwest of an invisible northeast-dipping surface that would correspond approximately to the zone of northeast-dipping faulting along the southwest band in the southern region.

13. *May 5–June 10*, M≥*1.7 (figs. 8.32–8.34).*—Events during this period give the clearest view of the Coalinga earthquake sequence before the onset of activity on the Nuñez fault. The features noted for the previous period are even more clearly exhibited here. In the northern region, the northeast-dipping zone of small aftershocks above the reference plane has moved a little farther northeast. In the northern

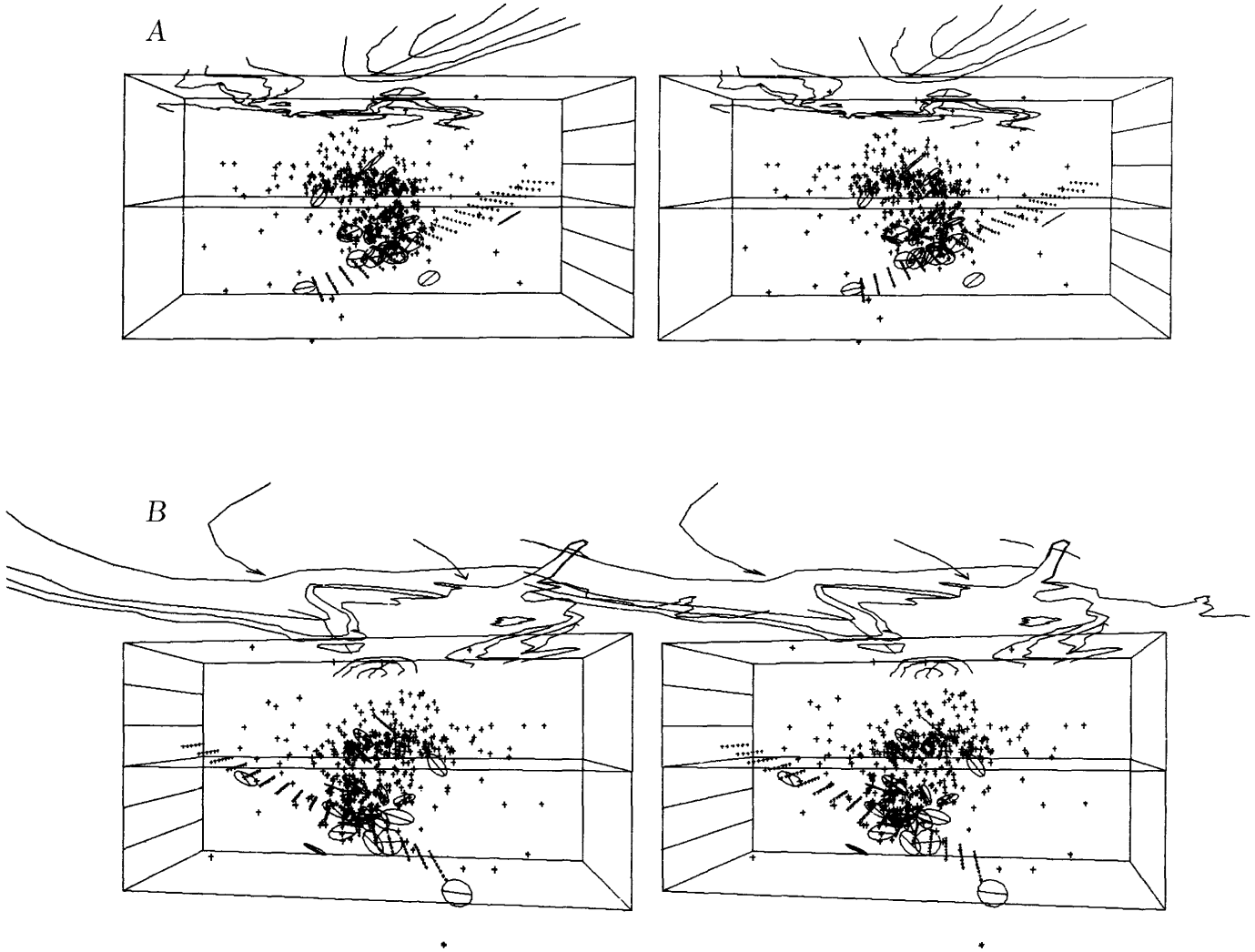

FIGURE 8.28.—Stereopairs showing aftershocks of $M \geq 2.0$ and focal planes of larger Coalinga aftershocks for May 2–September 30 in reference frame S (fig. 8.8), viewed from southeast (*A*) and northwest(*B*). Thrust reference plane strikes N. 53° W. and dips 25° SW. Horizontal spacing of points on the reference plane is 1 km by 1 km.

and central regions, the concentration of smaller aftershocks in a northwest-southeast band several kilometers beneath the central part of the reference plane appears to lie near and just above the southwest-dipping reverse fault suggested by larger aftershocks in the same region. In the northern region, a few scattered small aftershocks suggest the updip continuation of this fault into the Domengine area.

14. *June 11–September 30*, M≥*1.7 (figs. 8.35– 8.37).*— The principal feature during this period is evident in the northern region (fig. 8.35), where aftershocks of the Nuñez extension are shown with minimal overwriting by the rest of the Coalinga earthquake sequence. The larger aftershocks appear to define the fault surface, and the smaller ones appear to lie near, but almost entirely above, the fault in the hanging-wall block.

DISCUSSION

We propose the following explanation for the cause and development of the Coalinga sequence. The Coalinga earthquake was generated by movement on a southwest-dipping thrust underlying the epicentral zone of aftershocks on the first day of the sequence. The upper plate was driven northeastward against resisting rocks beneath the west edge of the Great Valley and was abruptly shortened in the northeast-southwest direction, by an amount equal to the slip on the thrust. Initial rupture on several closely related faults occurred during the main

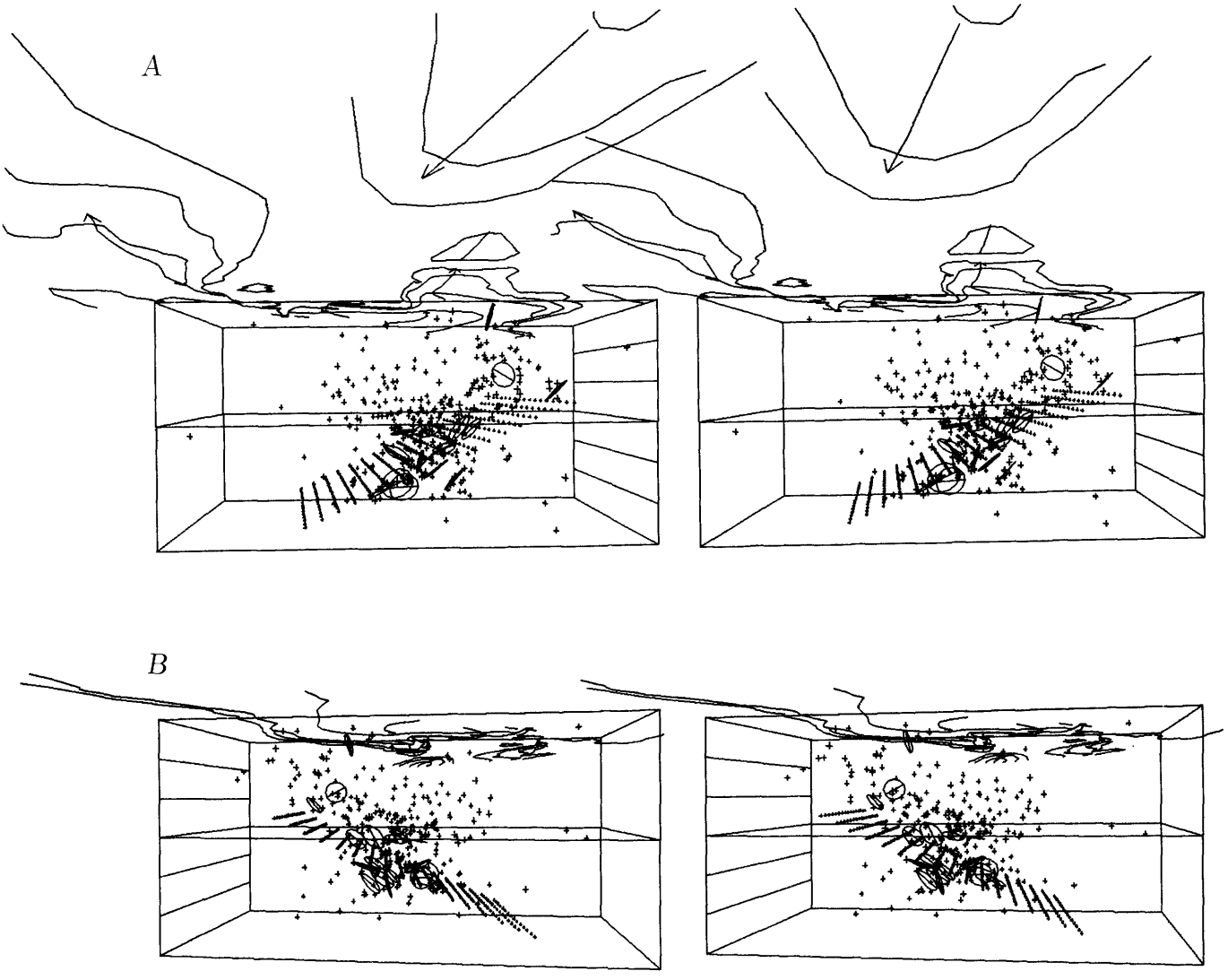

FIGURE 8.29.—Stereopairs showing aftershocks of $M \geq 1.7$ and focal planes of larger Coalinga aftershocks for May 2–4 in reference frame N (fig. 8.8), viewed from southeast (*A*) and northwest (*B*). Thrust reference plane strikes N. 53° W. and dips 25° SW. Horizontal spacing of points on reference plane is 1 by 1 km.

shock or within a few fours thereafter. Such faults included the southwest-dipping reverse faults beneath the main thrust both northwest and southeast of the quiet zone, the northeast-dipping reverse faults above the main thrust along the southwest flank of Anticline Ridge and along the edge of the Great Valley in the Domengine area, and the southwest-dipping thrust fault above the main shock.

The upper plate appears to have been stronger northwest of the quiet zone than southeast of it. Southeast of this zone, the upper plate yielded to the sudden application of northeast-southwest compression, caused by motion on the thrust, by faulting and folding in a narrow zone beneath Anticline Ridge and the Guijarral Hills. Northwest of the quiet zone, the stiff upper plate above the slipped zone on the thrust resisted internal deformation elastically and distributed the resulting northeast-southwest stress over a broad region, causing shallow earthquakes beneath the Domengine area and near Nuñez Canyon. For the next 5 weeks, continuing forward creep

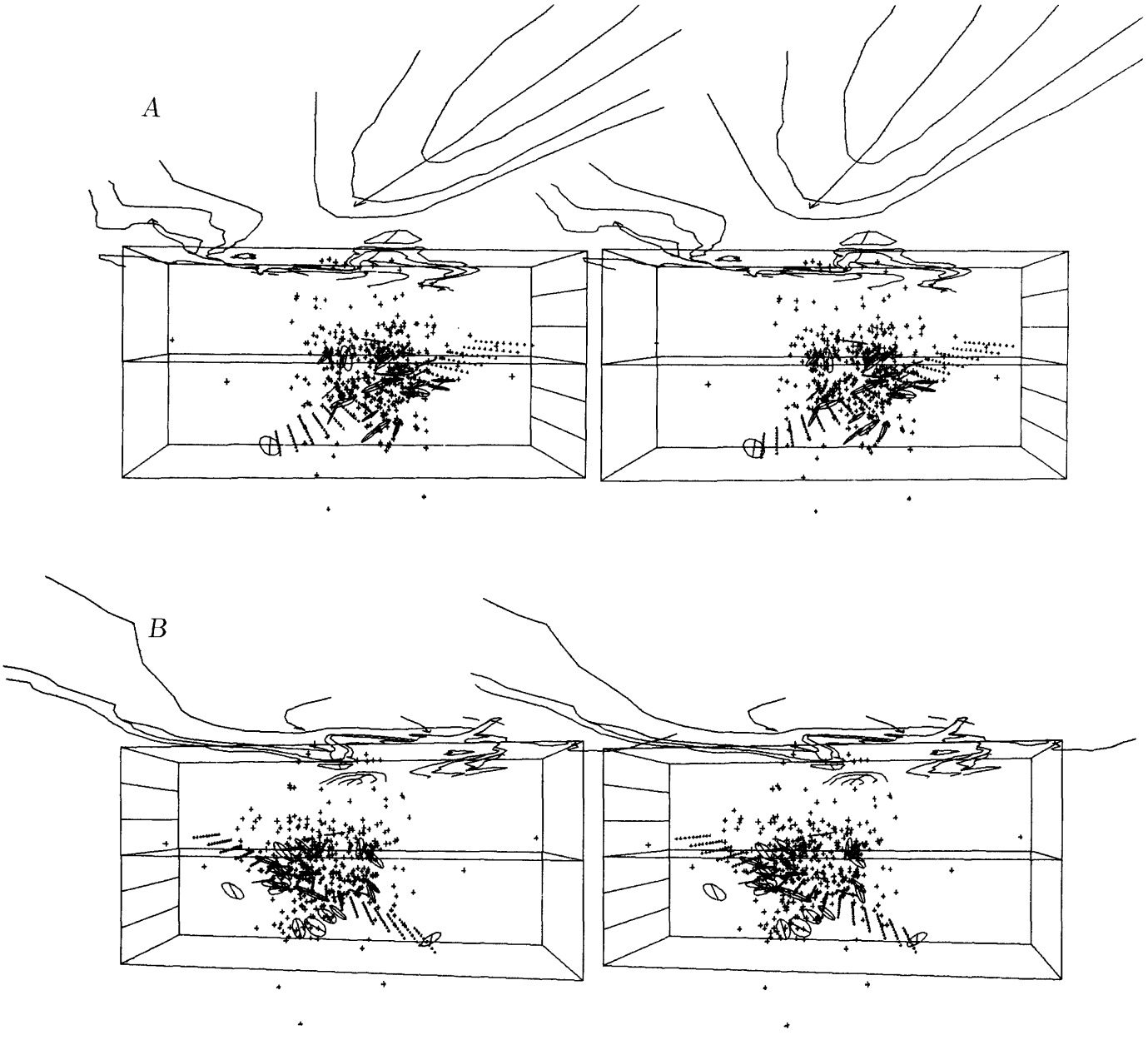

FIGURE 8.30.—Stereopairs showing aftershocks of $M \geq 1.7$ and focal planes of larger Coalinga aftershocks for May 2–4 in reference frame C (fig. 8.8), viewed from southeast (*A*) and northwest (*B*). Thrust reference plane strikes N. 53° W. and dips 25° SW. Horizontal spacing of points on reference plane is 1 by 1 km.

on the thrust, in response to the changes induced by the main shock, generated aftershocks along the initial slip surfaces and extended their areas; it continued to load the upper plate, which responded with additional aftershocks in the regions brought to life by the main shock. Northeastward movement of the upper plate in the region northwest of the quiet zone relative to that to the southeast was accompanied by right-lateral strike-slip faulting in the upper plate along a northeast-trending zone along the northwest edge of the quiet zone.

Beginning on June 11 and accelerating in mid-July, the additional stored elastic strain in the upper plate northwest of the quiet zone was relieved by reverse faulting on the east-dipping fault that extended from near Nuñez Canyon downward to the main thrust surface. From June 11 through the end of September, continuing forward creep on the thrust and relaxation of stored strain in the upper plate continued to cause aftershocks in the regions that were active before June 11, as well as on the Nuñez fault.

By September 9, deformation of the upper plate in the main-shock cluster had sufficiently reduced compressive forces perpendicular to Anticline Ridge that a north-northwest-trending strike-slip fault at the northeast edge of this cluster came unpinned by reduction of the normal component of stress across it, and movement (right slip) on it caused the last $M=5+$ earthquake of the sequence.

The foregoing scenario is based partly on the evidence from the earthquake sequence presented above and partly on broader regional conclusions from regional seismicity and plate tectonics. Examination of seismicity in the southern Coast Ranges from 1972 through 1983 suggests that the San Andreas fault is only one element of the Pacific-North American plate boundary in central California. The Coast Ranges are undergoing deformation throughout their width from offshore to the Great Valley, and earthquakes are concentrated along the edges of that zone, as well as along the San Andreas fault, which cuts diagonally across it (see chap. 7). Thus, the transform zone at depth appears to underlie the entire

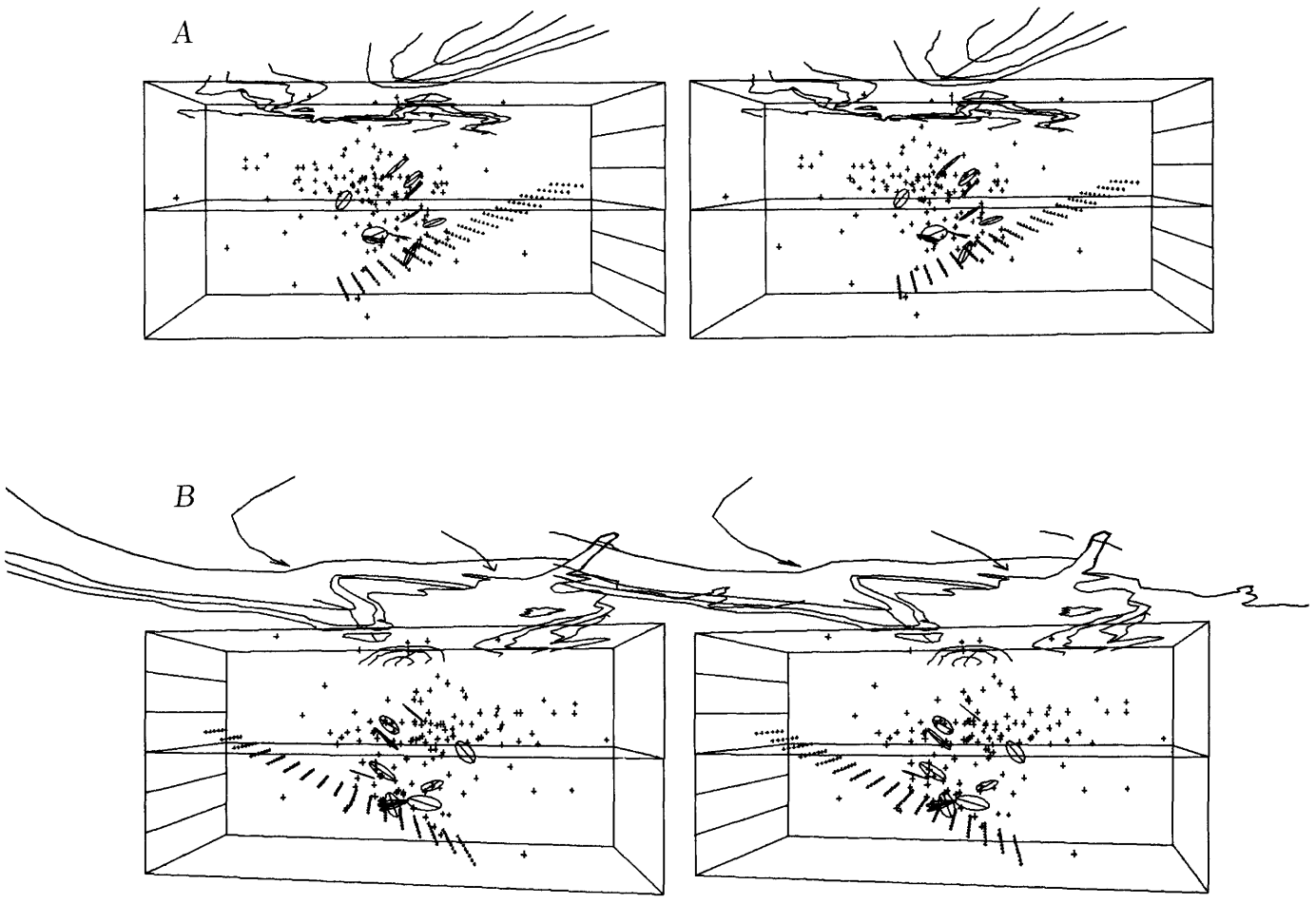

FIGURE 8.31.—Stereopairs showing aftershocks of $M \geq 1.7$ and focal planes of larger Coalinga aftershocks for May 2–4 in reference frame S (fig. 8.8), viewed from southeast (*A*) and northwest (*B*). Thrust reference plane strikes N. 53° W. and dips 25° SW. Horizontal spacing of points on reference plane is 1 by 1 km.

Coast Ranges and is not confined to a narrow region beneath the San Andreas fault. From global analysis of the relative motion of lithospheric plates, Minster and Jordan (1978) concluded that the direction of relative movement between the Pacific and North American plates in the southern Coast Ranges (N. 35° W.) disagrees with the average strike of the San Andreas fault (N. 41° W.). This discrepancy requires a contraction of the transform zone perpendicular to the San Andreas fault of 4 to 13 mm/yr (Minster and Jordan, 1984).

The focal mechanisms of larger ($M \geq 4.5$) earthquakes in the central and southern Coast Ranges and in the western Transverse Ranges provide additional information on earthquake-generating processes in different parts of this region (see chap. 7). Along major strike-slip faults, the focal mechanisms agree in strike and slip directions with those predicted from geologic evidence. Such is the case for the San Andreas fault between Cholame and San Juan Bautista, for the Calaveras fault between Hollister and San Jose, and for the San Gregorio-Palo Colorado fault near Monterey. Along the coast southeast of Cape San Martin and along the edge of the Great Valley southeast of Idria, focal mechanisms show that reverse faulting is predominant. In both these regions, the pattern of seismicity is characterized by equidimensional clusters of events 10 to 20 km across and not by linear zones of events like those along the major strike-slip faults.

A further important result from detailed studies of aftershocks and local earthquakes is that earthquakes are concentrated at depths of 5 to 10 km and are cut off abruptly below 12 or 13 km throughout the southern

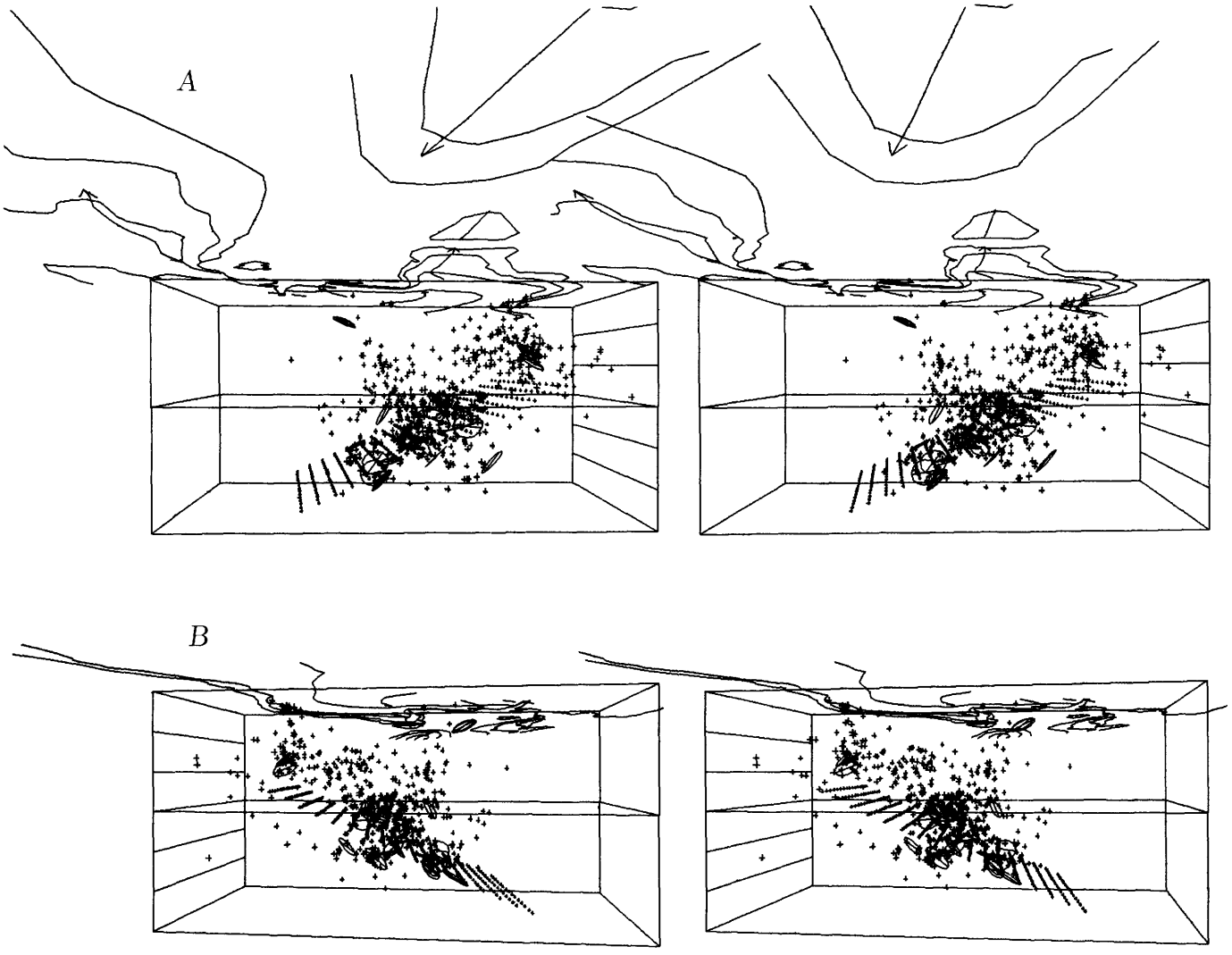

FIGURE 8.32.—Stereopairs showing aftershocks of $M \geq 1.7$ and focal planes of larger Coalinga aftershocks for May 5–June 10 in reference frame N (fig. 8.8), viewed from southeast (*A*) and northwest (*B*). Thrust reference plane strikes N. 53° W. and dips 25° SW. Horizontal spacing of points on reference plane is 1 by 1 km.

Coast Ranges. This cutoff depth corresponds approximately to the depth of an increase in P-wave velocities from about 6 to 6.5 km/s.

The foregoing results suggest that a zone of horizontal decoupling between a brittle upper crust and a ductile lower crust underlies the southern Coast Ranges at a depth of 12 to 15 km. Apparent contraction of the transform zone has led to a compression of the southern Coast Ranges and a thickening of the crust, expressed partly as an increase in surface elevation and partly as a depression of the base of the crust. At the outer edges of the thickened region along the boundaries of the transform zone, the detachment surface cuts upward through the crust into a region of brittle deformation. Continued apparent contraction of the transform zone drives the upper crust within the zone out over its edges, causing reverse-fault earthquakes along its borders (fig. 8.7; see chap. 7). In this process, the activating structure is the detachment surface, which dips, at a shallow angle, back toward the center of the transform zone and over which the upper crust is thrust out over the edges of the transform zone. The advancing edge of the upper plate is thickened by the development of folds and by movement on high-angle reverse faults in the upper plate.

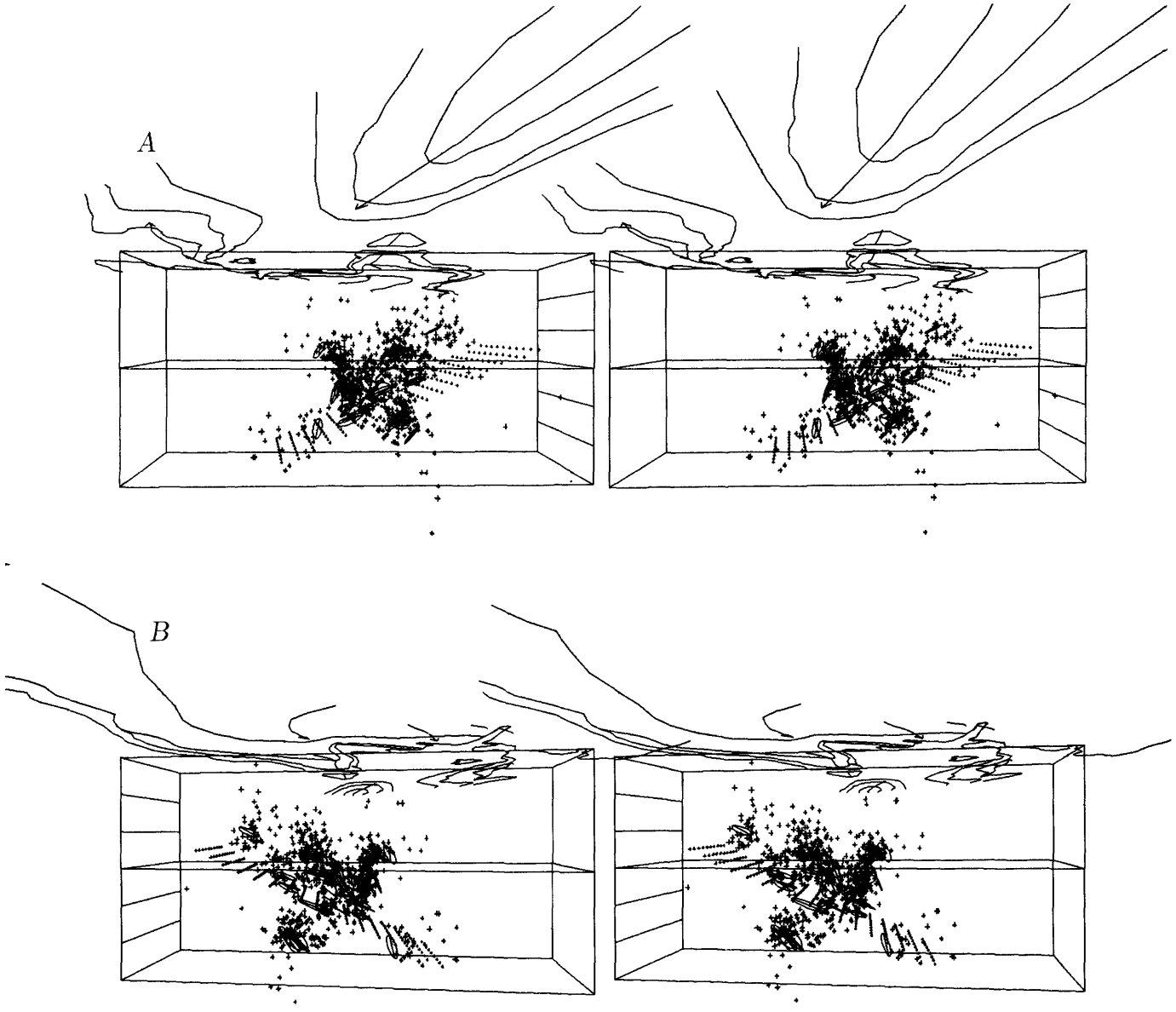

FIGURE 8.33.—Stereopairs showing aftershocks of $M \geq 1.7$ and focal planes of larger Coalinga aftershocks for May 5–June 10 in reference frame C (fig. 8.8), viewed from southeast (*A*) and northwest (*B*).Thrust reference plane strikes N. 53° W. and dips 25° SW. Horizontal spacing of points on reference plane is 1 by 1 km.

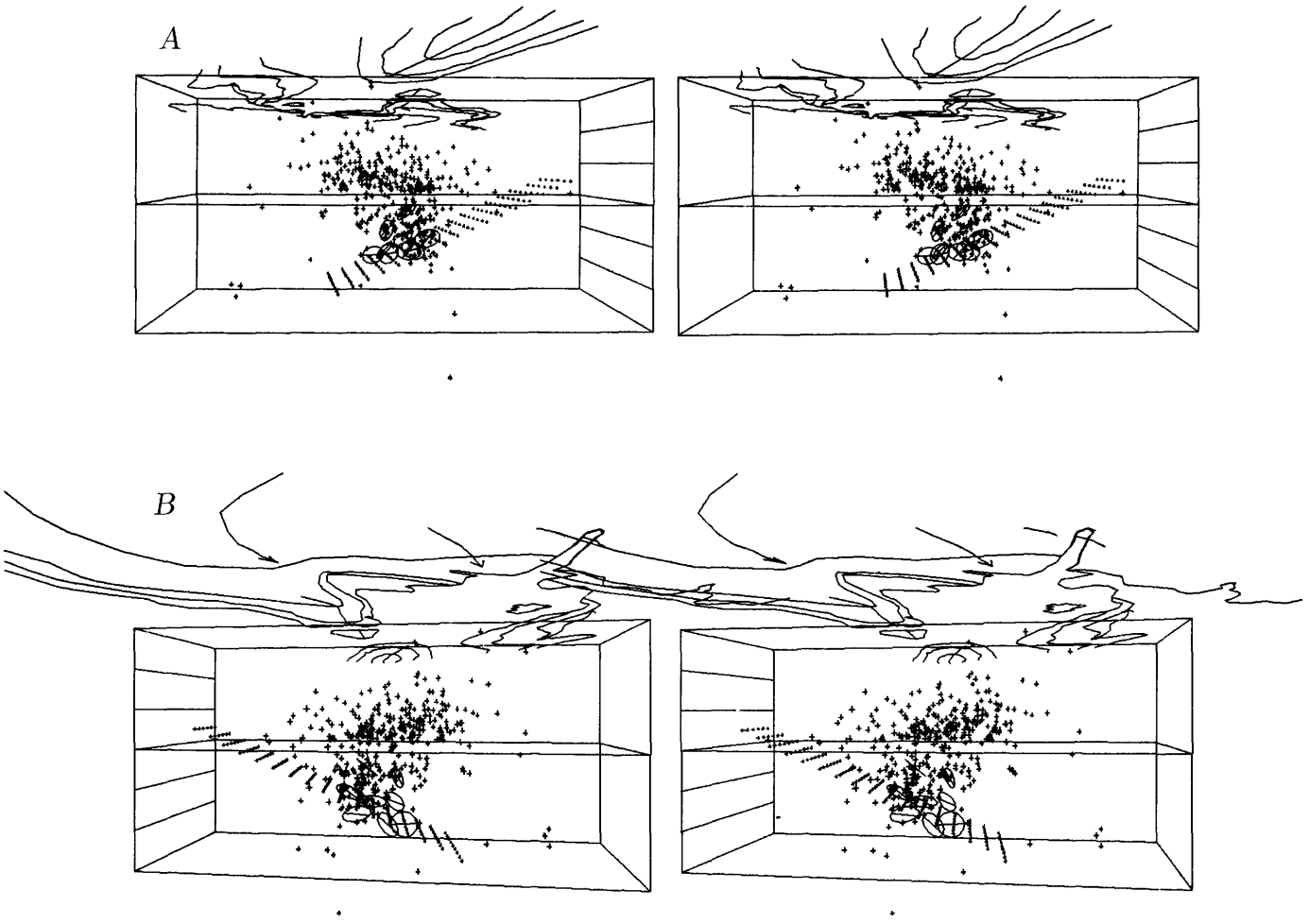

FIGURE 8.34.—Stereopairs showing aftershocks of $M \geq 1.7$ and focal planes of larger aftershocks for May 5–June 10 in reference frame S (fig. 8.8), viewed from southeast (*A*) and northwest (*B*). Thrust reference plane strikes N. 53° W. and dips 25° W. Horizontal spacing of points on reference plane is 1 by 1 km.

REFERENCES CITED

Allen, Rex, 1982, Automatic phase pickers: Their present use and future prospects: Seismological Society of America Bulletin, v. 72, no. 6, p. S225–S242.

Eaton, J.P., Cockerham, R.S., and Lester, F.W., 1983, Study of the May 2, 1983 Coalinga earthquake and its aftershocks, based on the USGS seismic network in northern California, *in* Bennett, J.H., and Sherburne, R.W., eds., The 1983 Coalinga, California earthquakes: California Division of Mines and Geology Special Publication 66, p. 261–273.

German, Peter, and Johnson, Carl, 1981, *STEREO*, a computer program for projecting and plotting stereograms: U.S. Geological Survey Open-File Report 82–726, 56 p.

Lee, W.H.K., and Lahr, J.C., 1975, HYPO71 (revised): A computer program for determining hypocenter, magnitude, and first motion pattern of local earthquakes: U.S. Geological Survey Open-File Report 75-311, 113 p.

Minster, J.B., and Jordan, T.H., 1978, Present-day plate motions: Journal of Geophysical Research, v. 83, no. B11, p. 5331–5354.

—— 1984, Vector constraints on Quaternary deformation of the western United States east and west of the San Andreas fault, *in* Crouch, J.K., and Bachman, S.B., eds., Tectonics and sedimentation along the California margin (volume 38): Society of Economic paleontologists and Mineralogists, Pacific Section Annual Convention, San Diego, 1984, Papers, p. 1–16.

Reasenberg, P.A., and Oppenheimer, David, 1985, FPFIT, FPPLOT, and FPPAGE: Fortran computer programs for calculating and displaying earthquake fault-plane solutions: U.S. Geological Survey Open-File Report 85-739, 108 p.

Stein, R.S., 1983, Reverse slip on a buried fault during the May 2, 1983 Coalinga earthquake: Evidence from geodetic elevation changes, *in* Bennett, J.H., and Sherburne, R.W., eds., The 1983 Coalinga, California earthquakes: California Division of Mines and Geology Special Publication 66, p. 151–163.

Utsu, Tokuji, 1961, A statistical study of the occurrence of aftershocks: Geophysical Magazine, v. 30, no. 4, p. 521–605.

—— 1966, A statistical significance test of the difference in *b*-value between two earthquake groups: Journal of Physics of the Earth, v. 14, no. 2, p. 37–40.

Wentworth, C.M., Walter, A.W., Bartow, J.A., and Zoback, M.D., 1983, The tectonic setting of the 1983 Coalinga earthquakes: Evidence from deep reflection and refraction profiles across the southeastern end of the Kettleman Hills, *in* Bennett, J.H., and Sherburne, R.W., eds., The 1983 Coalinga, California earthquakes: California Division of Mines and Geology Special Publication 66, p. 113–126.

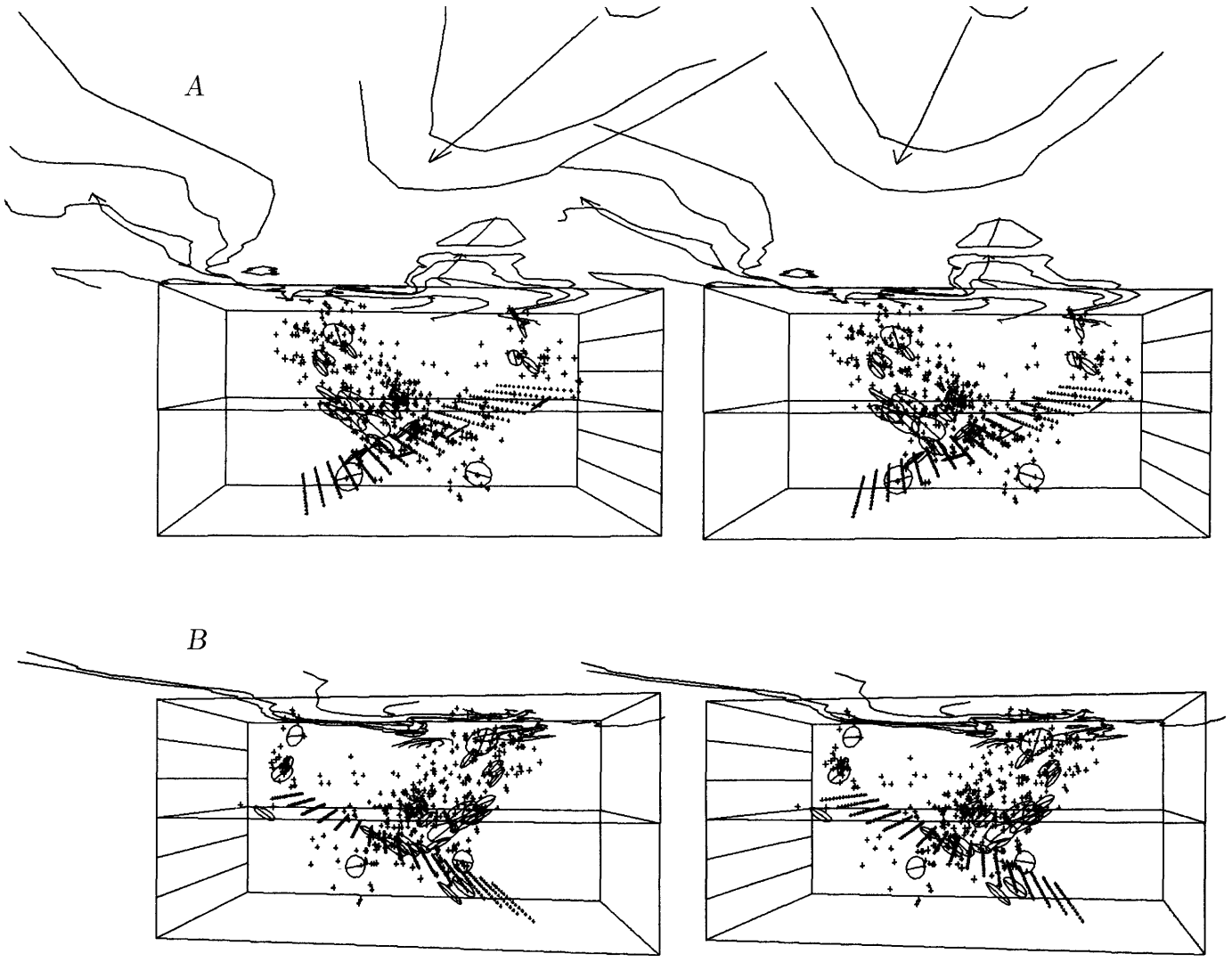

FIGURE 8.35.—Stereopairs showing aftershocks with $M \geq 1.7$ and focal planes of larger Coalinga aftershocks for June 11–September 30 in reference frame N (fig. 8.8), viewed from southeast (*A*) and northwest (*B*). Thrust reference plane strikes N. 53° W. and dips 25° SW. Horizontal spacing of points on reference plane is 1 by 1 km.

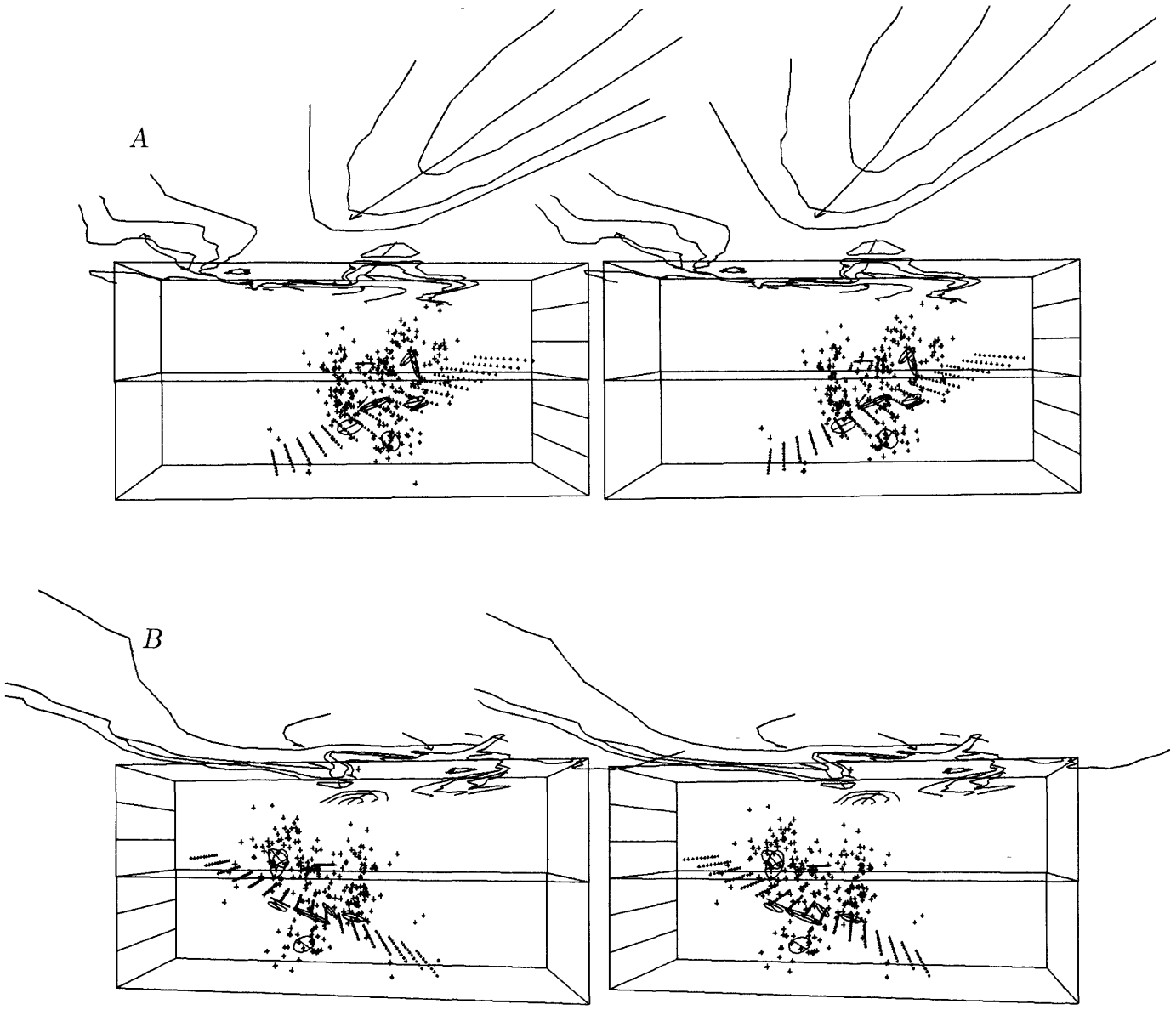

FIGURE 8.36.—Stereopairs showing aftershocks with $M \geq 1.7$ and focal planes of larger Coalinga aftershocks for June 11–September 30 in reference frame C (fig. 8.8), viewed from southeast (*A*) and northwest (*B*). Thrust reference plane strikes N. 53° W. and dips 25° SW. Horizontal spacing of points on reference plane is 1 by 1 km.

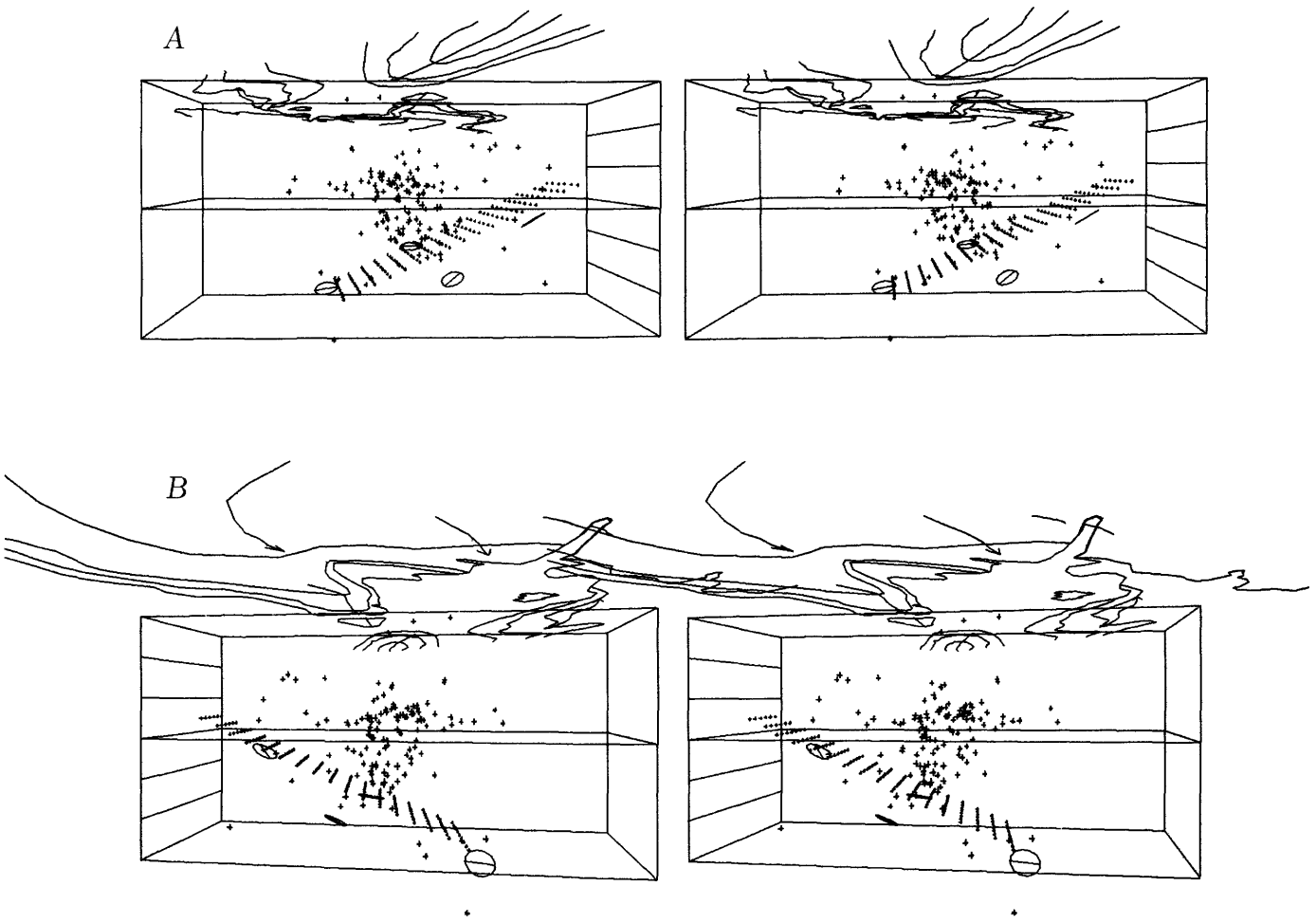

FIGURE 8.37.—Stereopairs showing aftershocks with $M \geq 1.7$ and focal planes of larger Coalinga aftershocks for June 11–September 30 in reference frame S (fig. 8.8), viewed from southeast (*A*) and northwest(*B*). Thrust reference plane strikes N. 53° W. and dips 25° SW. Horizontal spacing of points on reference plane is 1 by 1 km.

SUPPLEMENTARY DATA

First-motion focal-mechanism solutions for the May 2 earthquake and 143 of the largest aftershocks. Crosses, compressional first arrivals; circles, dilatational first arrivals; P, direction of maximum compressive stress (P-axis); T, direction of minimum compressive stress (T-axis); M, magnitude; Z, hypocentral depth. Less certain first arrivals are shown by smaller symbols. Fault-plane parameters (dip azimuth and dip angle) and rake (direction of motion of hanging wall relative to footwall) are listed in table 8.3. Figures drawn by FPPAGE (Reasenberg and Oppenheimer, 1985).

May 2, 1983 2342
Z=10.01 *M*=6.70

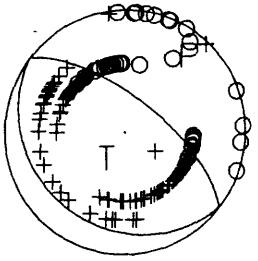

May 3, 1983 0014
Z=12.02 *M*=3.73

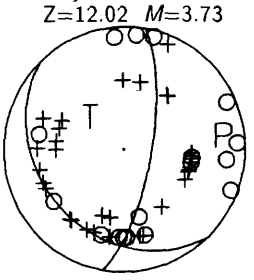

May 3, 1983 0039
Z=11.24 *M*=4.52

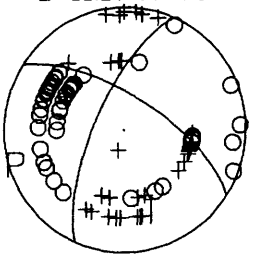

May 3, 1983 0116
Z=7.90 *M*=3.38

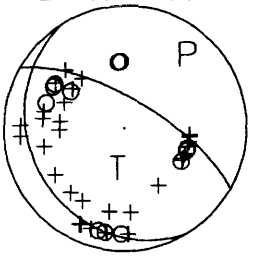

May 2, 1983 2355
Z=9.03 *M*=4.24

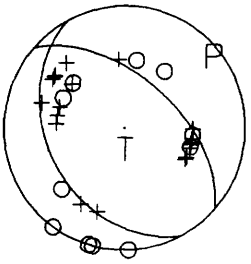

May 3, 1983 0015
Z=5.13 *M*=4.45

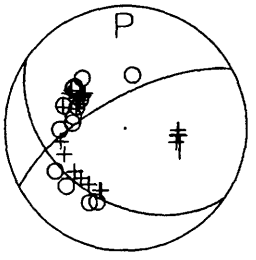

May 3, 1983 0047
Z=9.06 *M*=3.92

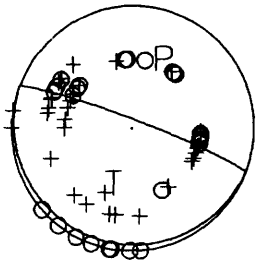

May 3, 1983 0141
Z=8.70 *M*=4.54

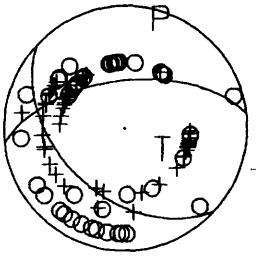

May 3, 1983 0009
Z=7.37 *M*=4.31

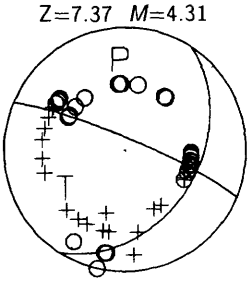

May 3, 1983 0022
Z=8.23 *M*=3.61

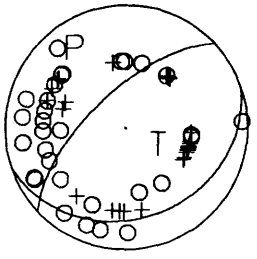

May 3, 1983 0057
Z=8.13 *M*=5.08

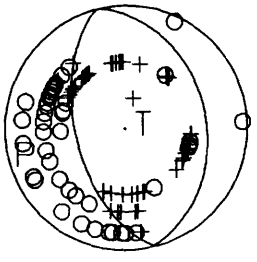

May 3, 1983 0155
Z=6.87 *M*=4.01

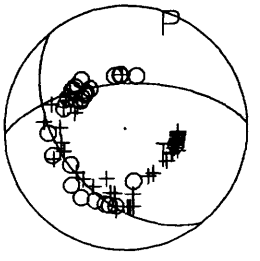

May 3, 1983 0215
Z=8.82 *M*=4.08

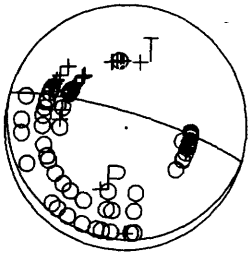

May 3, 1983 0322
Z=11.63 *M*=3.98

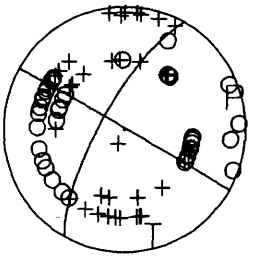

May 3, 1983 0431
Z=11.10 *M*=3.78

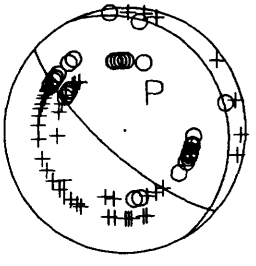

May 3, 1983 0458
Z=10.14 *M*=3.48

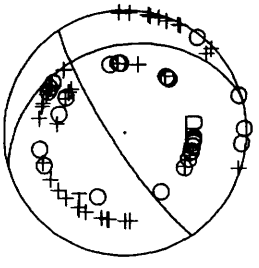

May 3, 1983 0217
Z=5.55 *M*=3.79

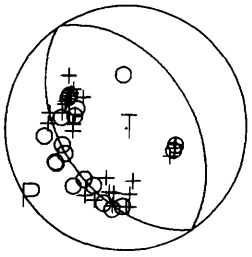

May 3, 1983 0328
Z=4.50 *M*=3.47

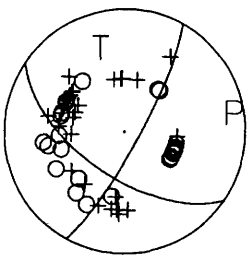

May 3, 1983 0432
Z=11.10 *M*=4.42

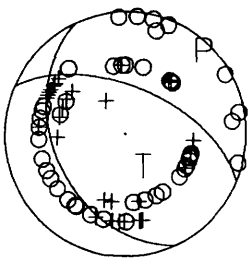

May 3, 1983 0501
Z=11.99 *M*=3.48

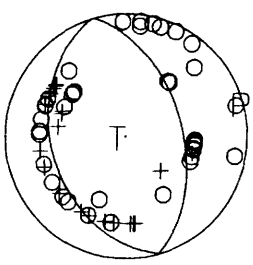

May 3, 1983 0226
Z=9.84 *M*=3.30

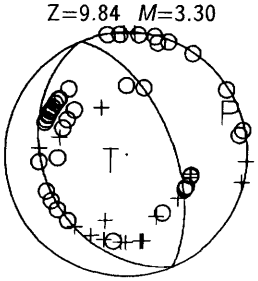

May 3, 1983 0340
Z=11.01 *M*=3.79

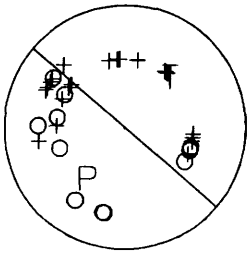

May 3, 1983 0455
Z=10.22 *M*=3.33

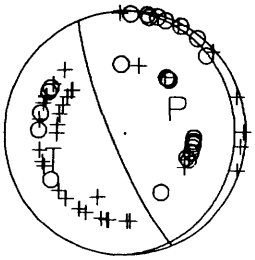

May 3, 1983 0533
Z=9.67 *M*=3.63

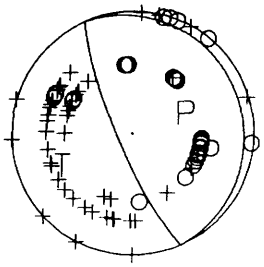

May 3, 1983 0558
Z=9.56 *M*=3.50

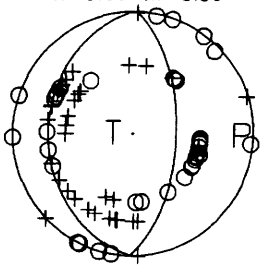

May 3, 1983 0635
Z=12.89 *M*=4.25

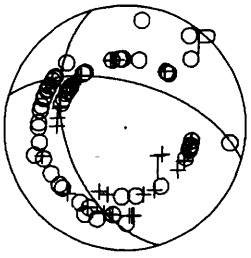

May 3, 1983 0855
Z=10.32 *M*=4.70

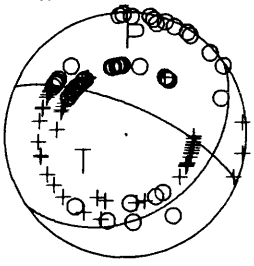

May 3, 1983 1257
Z=11.17 *M*=3.92

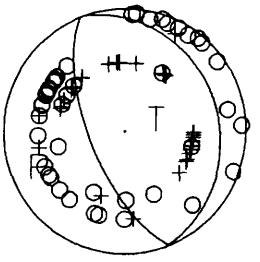

May 3, 1983 0604
Z=10.08 *M*=4.51

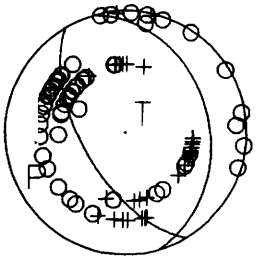

May 3, 1983 0728
Z=6.15 *M*=3.60

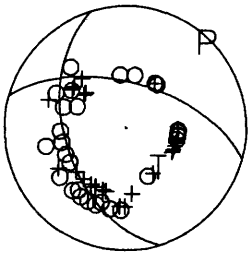

May 3, 1983 0939
Z=9.91 *M*=4.11

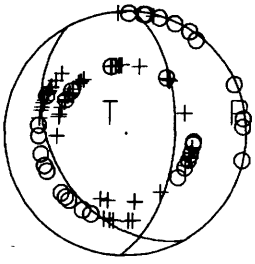

May 3, 1983 1309
Z=12.46 *M*=4.04

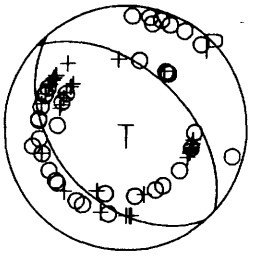

May 3, 1983 0612
Z=8.40 *M*=3.77

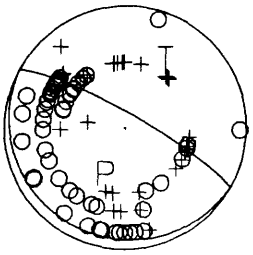

May 3, 1983 0735
Z=8.84 *M*=3.87

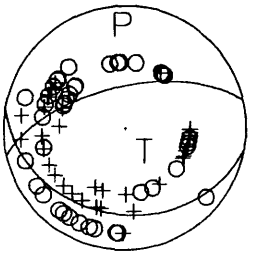

May 3, 1983 1035
Z=6.34 *M*=3.83

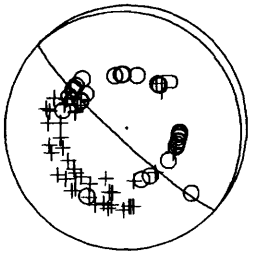

May 3, 1983 1347
Z=10.85 *M*=3.40

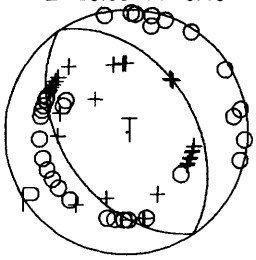

May 3, 1983 1348
Z=9.70 *M*=3.52

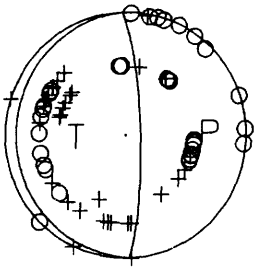

May 3, 1983 1450
Z=10.60 *M*=3.99

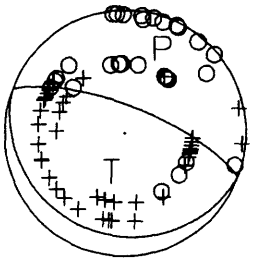

May 3, 1983 1541
Z=7.89 *M*=4.78

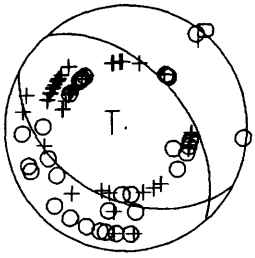

May 3, 1983 1622
Z=7.03 *M*=3.39

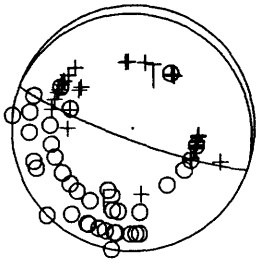

May 3, 1983 1420
Z=9.96 *M*=3.48

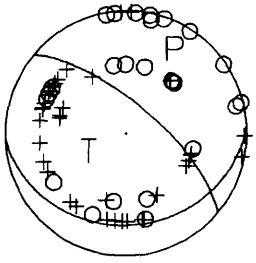

May 3, 1983 1504
Z=8.60 *M*=3.61

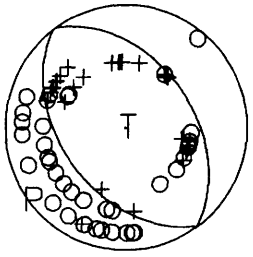

May 3, 1983 1617
Z=10.36 *M*=2.94

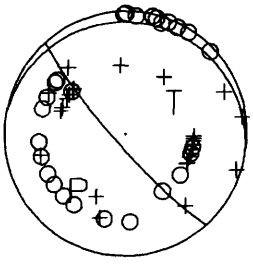

May 3, 1983 1701
Z=8.87 *M*=3.60

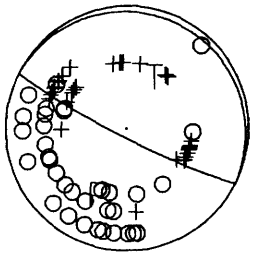

May 3, 1983 1426
Z=0.60 *M*=3.94

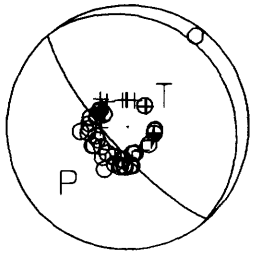

May 3, 1983 1510
Z=8.17 *M*=3.95

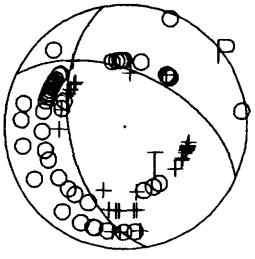

May 3, 1983 1617
Z=10.49 *M*=3.87

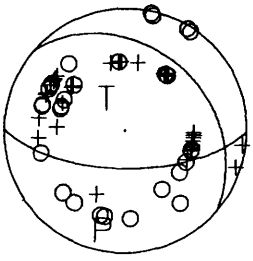

May 3, 1983 1850
Z=9.93 *M*=3.21

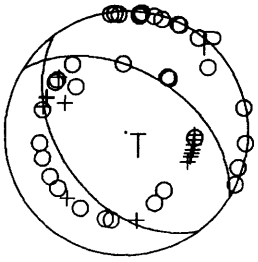

May 3, 1983 2136
Z=10.89 *M*=3.70

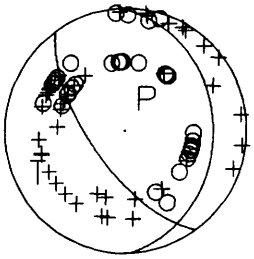

May 4, 1983 0818
Z=8.60 *M*=2.93

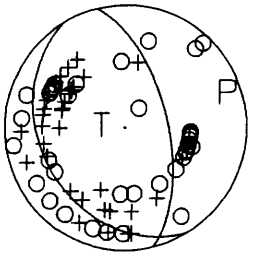

May 4, 1983 1559
Z=7.22 *M*=3.78

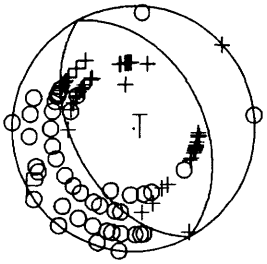

May 5, 1983 0027
Z=8.85 *M*=3.48

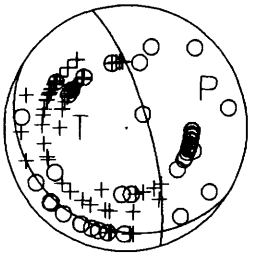

May 3, 1983 2229
Z=7.59 *M*=3.77

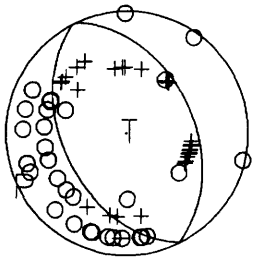

May 4, 1983 0848
Z=12.89 *M*=3.48

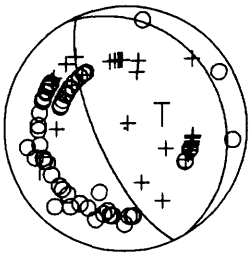

May 4, 1983 1611
Z=11.69 *M*=4.39

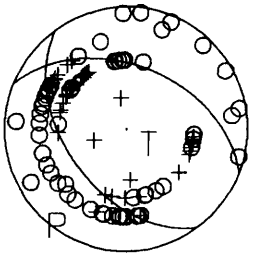

May 5, 1983 0156
Z=8.04 *M*=3.36

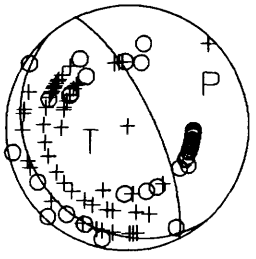

May 3, 1983 2346
Z=13.55 *M*=3.96

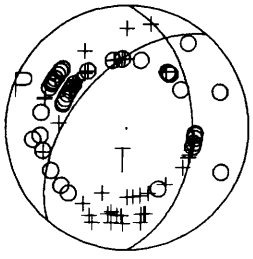

May 4, 1983 1329
Z=10.00 *M*=3.39

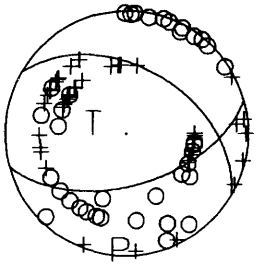

May 4, 1983 1945
Z=7.44 *M*=3.44

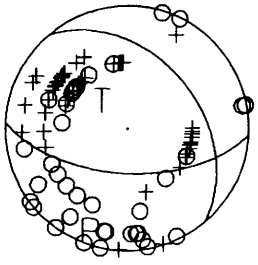

May 5, 1983 0437
Z=11.22 *M*=4.01

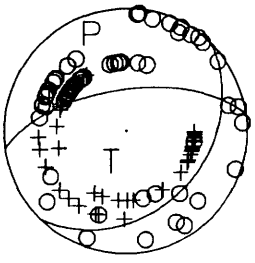

May 5, 1983 0806
Z=8.69 *M*=3.73

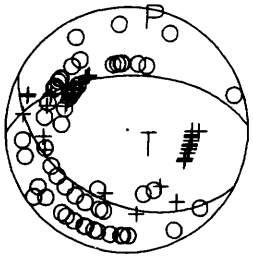

May 5, 1983 1150
Z=10.52 *M*=3.47

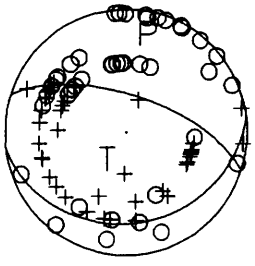

May 6, 1983 0457
Z=10.76 *M*=3.38

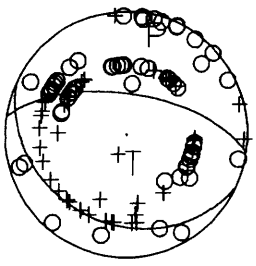

May 7, 1983 0017
Z=8.88 *M*=3.88

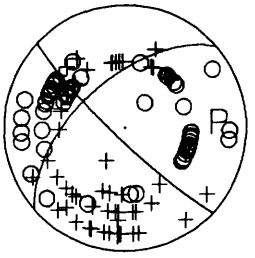

May 5, 1983 1020
Z=11.48 *M*=4.61

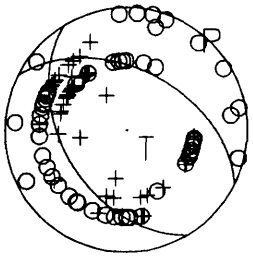

May 5, 1983 1242
Z=11.85 *M*=3.89

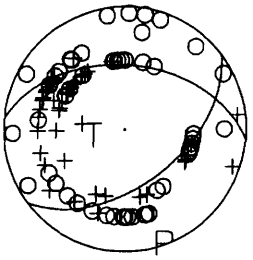

May 6, 1983 0943
Z=13.01 *M*=3.71

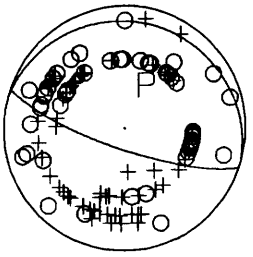

May 7, 1983 0543
Z=8.90 *M*=3.46

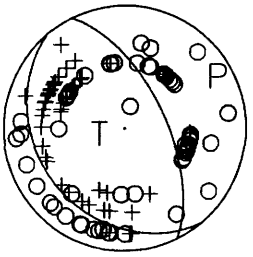

May 5, 1983 1133
Z=10.44 *M*=3.69

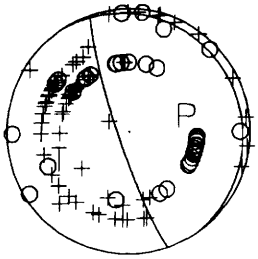

May 5, 1983 2246
Z=9.93 *M*=3.35

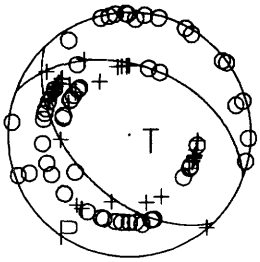

May 6, 1983 1151
Z=10.68 *M*=3.33

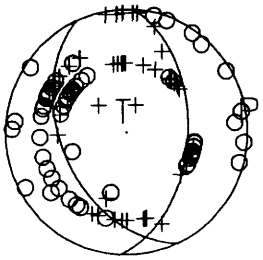

May 7, 1983 1242
Z=10.60 *M*=3.62

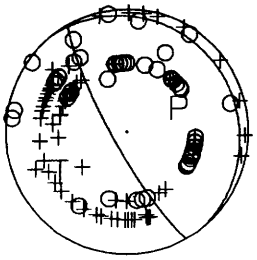

May 8, 1983 0120
Z=8.69 *M*=3.46

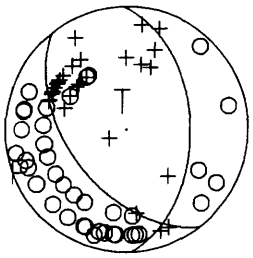

May 8, 1983 0738
Z=5.09 *M*=3.31

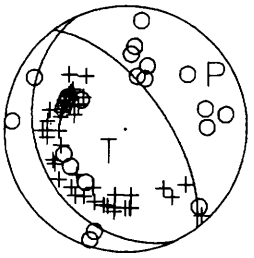

May 8, 1983 1918
Z=11.61 *M*=3.72

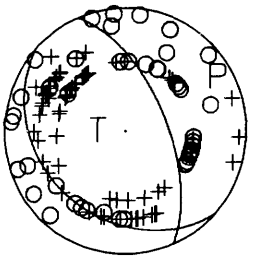

May 9, 1983 0319
Z=12.33 *M*=3.63

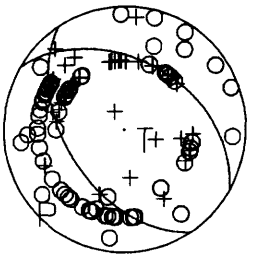

May 8, 1983 0147
Z=8.07 *M*=3.03

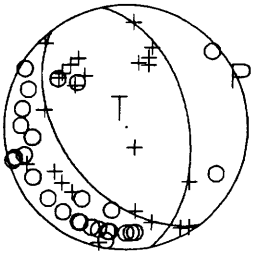

May 8, 1983 1037
Z=11.62 *M*=3.27

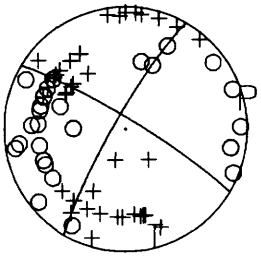

May 8, 1983 2025
Z=7.96 *M*=3.60

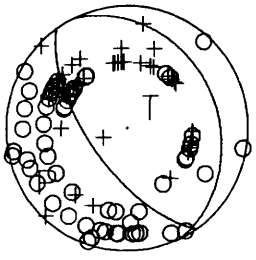

May 9, 1983 0326
Z=12.48 *M*=4.60

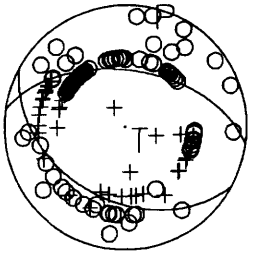

May 8, 1983 0345
Z=1.80 M=3.37

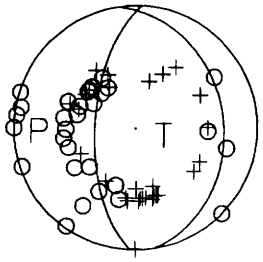

May 8, 1983 1523
Z=6.61 M=3.34

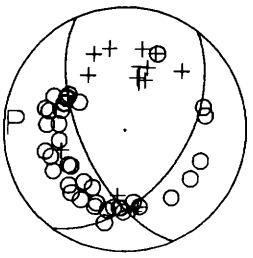

May 9, 1983 0249
Z=12.04 M=5.30

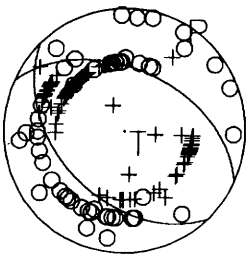

May 9, 1983 1324
Z=9.59 M=3.29

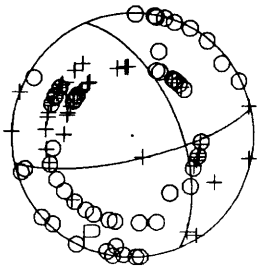

May 10, 1983 1326
Z=4.79 M=3.85

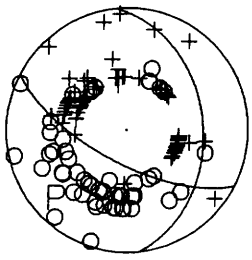

May 11, 1983 0814
Z=11.67 M=3.48

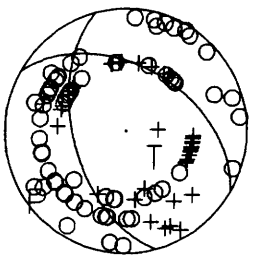

May 14, 1983 0502
Z=11.16 M=3.90

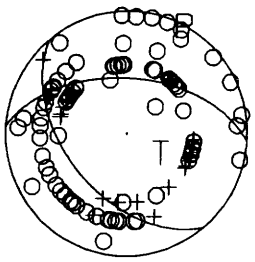

May 16, 1983 0131
Z=12.22 M=3.61

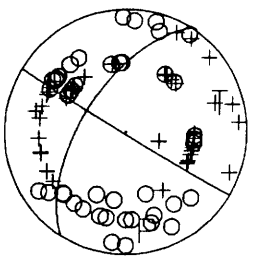

May 10, 1983 1522
Z=4.13 M=2.85

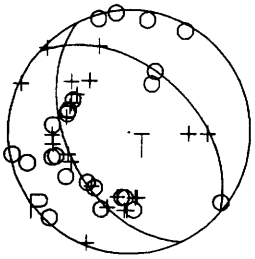

May 12, 1983 1341
Z=10.99 M=4.50

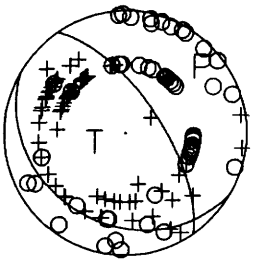

May 14, 1983 1715
Z=11.35 M=2.60

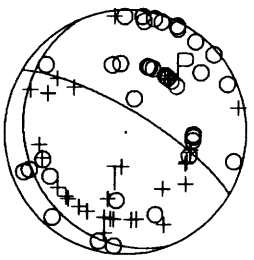

May 16, 1983 1217
Z=9.70 M=3.15

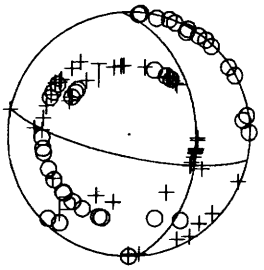

May 10, 1983 1522
Z=4.08 M=3.37

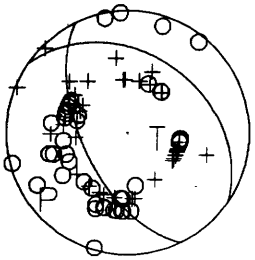

May 13, 1983 1422
Z=11.36 M=3.29

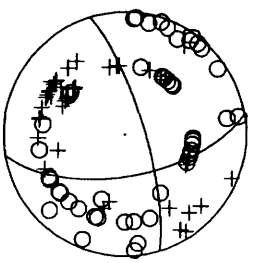

May 14, 1983 1715
Z=8.74 M=3.49

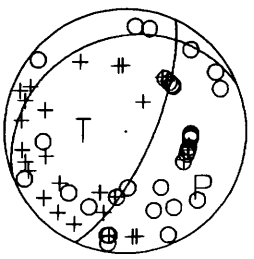

May 16, 1983 1421
Z=9.17 M=3.90

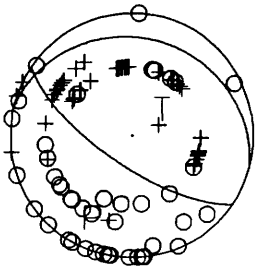

May 17, 1983 2222
Z=8.07 *M*=3.49

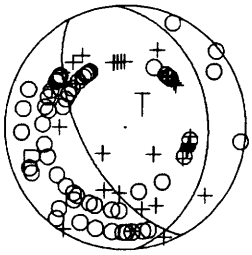

May 21, 1983 1005
Z=11.07 *M*=3.21

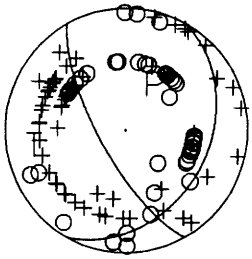

May 24, 1983 1226
Z=10.84 *M*=3.24

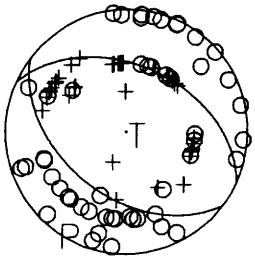

May 29, 1983 0124
Z=12.48 *M*=3.49

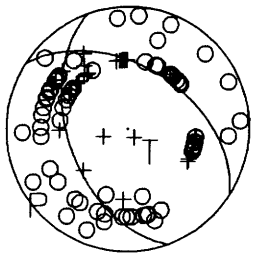

May 19, 1983 1105
Z=12.81 *M*=4.16

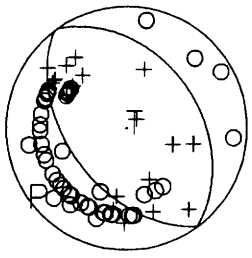

May 22, 1983 0839
Z=10.50 *M*=4.25

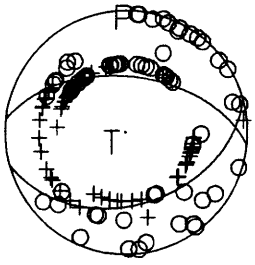

May 26, 1983 0854
Z=8.12 *M*=3.16

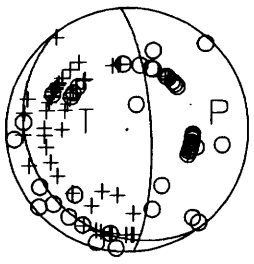

May 30, 1983 0321
Z=11.52 *M*=3.33

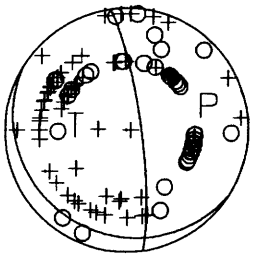

May 19, 1983 2326
Z=1.93 *M*=3.48

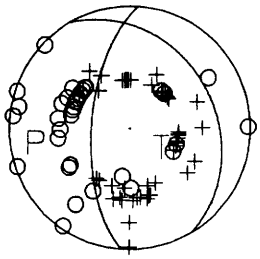

May 24, 1983 0902
Z=8.87 *M*=4.70

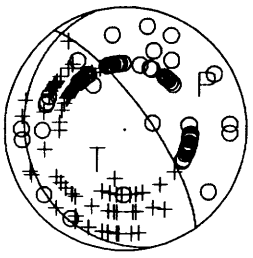

May 27, 1983 2040
Z=12.63 *M*=3.81

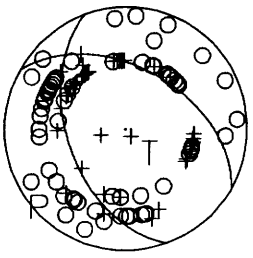

June 7, 1983 0518
Z=11.56 *M*=4.13

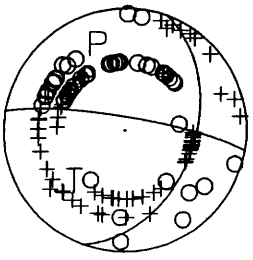

June 11, 1983 0309
Z=2.43 *M*=5.20

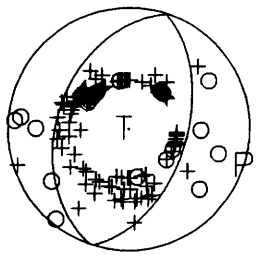

June 12, 1983 0131
Z=14.32 *M*=4.03

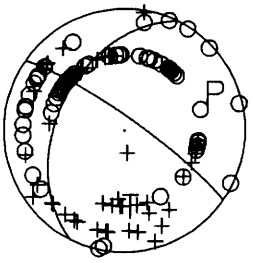

July 5, 1983 2210
Z=4.66 *M*=3.26

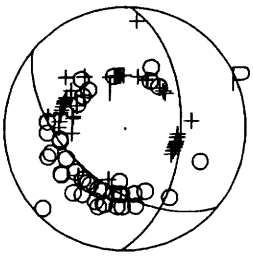

July 14, 1983 1525
Z=9.76 *M*=2.52

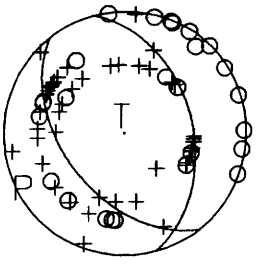

June 11, 1983 1427
Z=4.10 *M*=3.22

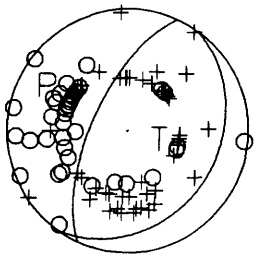

June 16, 1983 1737
Z=10.58 *M*=3.54

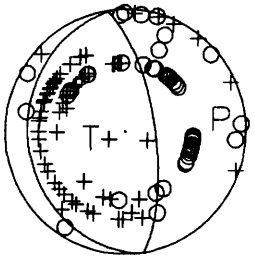

July 7, 1983 0030
Z=12.50 *M*=3.65

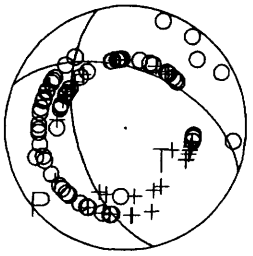

July 14, 1983 1525
Z=6.72 *M*=3.69

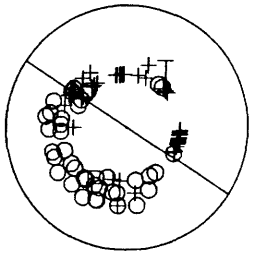

June 11, 1983 2302
Z=3.56 *M*=3.37

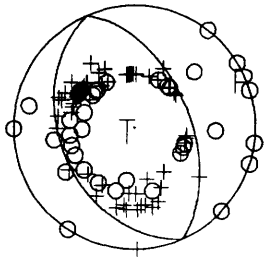

June 29, 1983 0641
Z=13.13 *M*=3.54

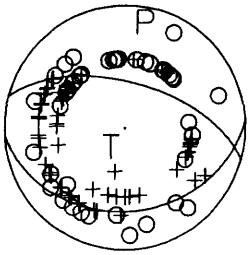

July 9, 1983 0740
Z=9.02 *M*=5.39

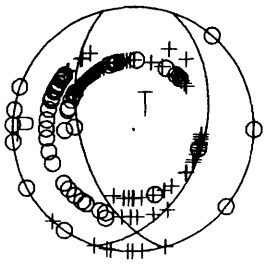

July 17, 1983 2158
Z=12.00 *M*=3.66

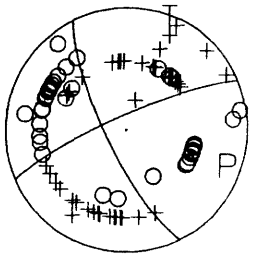

July 18, 1983 1928
Z=10.91 *M*=4.16

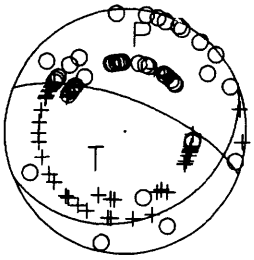

July 22, 1983 0303
Z=7.80 *M*=3.19

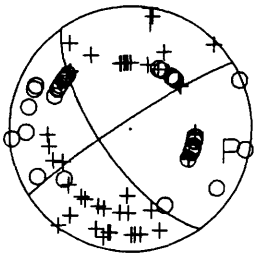

July 22, 1983 0430
Z=7.50 *M*=3.61

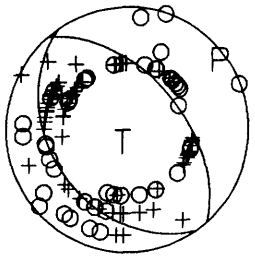

July 25, 1983 2231
Z=8.38 *M*=5.33

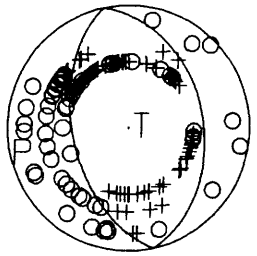

July 22, 1983 0239
Z=7.43 *M*=6.04

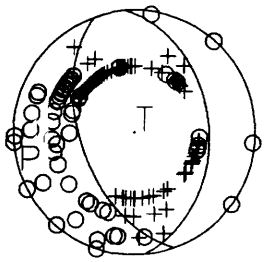

July 22, 1983 0311
Z=1.80 *M*=3.31

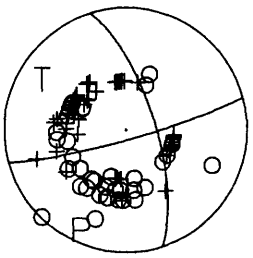

July 22, 1983 0712
Z=7.01 *M*=3.35

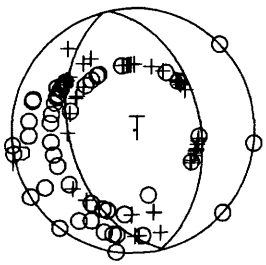

July 31, 1983 1643
Z=9.50 *M*=3.54

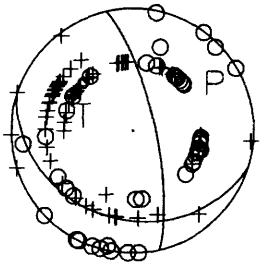

July 22, 1983 0249
Z=6.79 M=4.14

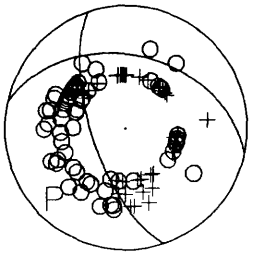

July 22, 1983 0343
Z=7.91 M=5.02

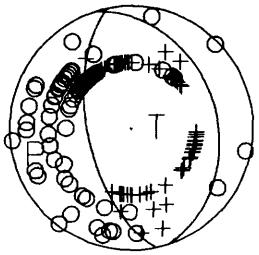

July 22, 1983 2152
Z=7.72 M=3.32

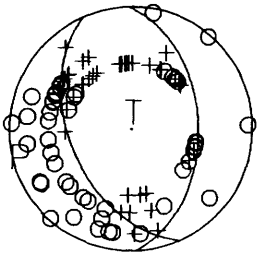

July 31, 1983 1724
Z=11.11 M=3.54

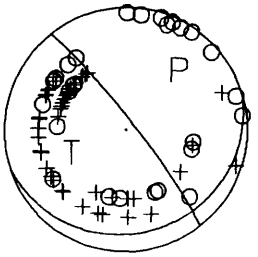

July 31, 1983 1754
Z=9.70 M=3.36

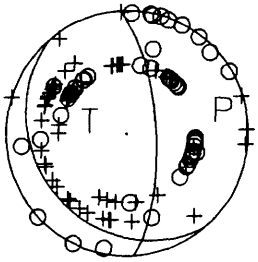

August 12, 1983 2202
Z=8.70 M=4.10

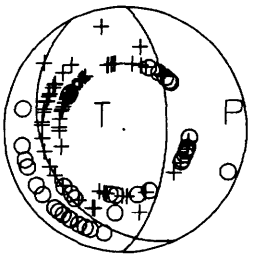

August 26, 1983 1957
Z=11.78 M=3.83

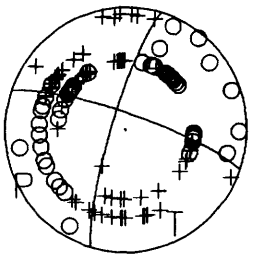

September 9, 1983 0921
Z=6.23 M=3.89

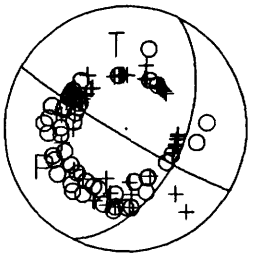

August 5, 1983 1006
Z=5.00 M=3.26

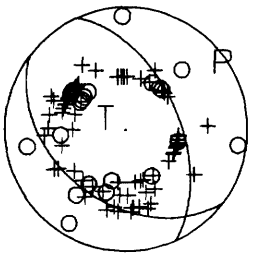

August 14, 1983 1243
Z=9.60 M=4.30

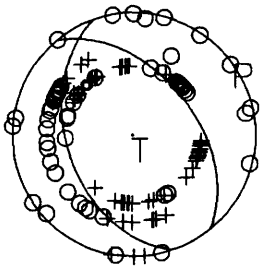

September 7, 1983 2307
Z=11.97 M=3.81

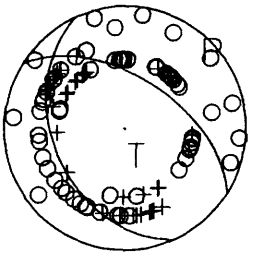

September 11, 1983 1148
Z=10.05 M=4.48

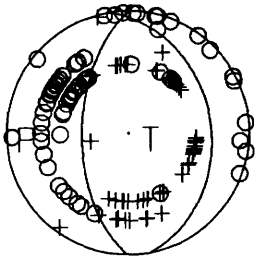

August 12, 1983 0114
Z=9.80 M=4.04

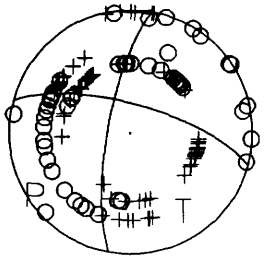

August 26, 1983 0321
Z=12.00 M=4.04

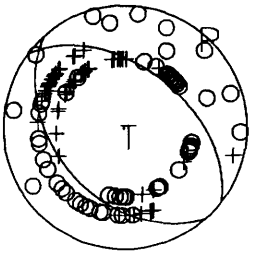

September 9, 1983 0916
Z=6.73 M=5.30

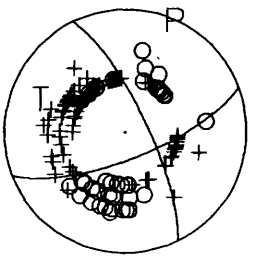

September 18, 1983 1434
Z=9.00 M=3.45

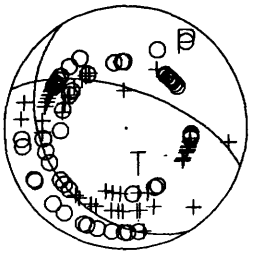

9. COMPLEX FAULTING STRUCTURE INFERRED FROM LOCAL SEISMIC OBSERVATIONS OF $M \geq 1.0$ AFTERSHOCKS, MAY 2–JUNE 30, 1983

By DONNA EBERHART-PHILLIPS and PAUL A. REASENBERG,
U.S. GEOLOGICAL SURVEY

CONTENTS

ABSTRACT

The geometric structure of aftershocks of the May 2 earthquake supports a complex model of faulting for the Coalinga earthquake sequence. Local seismic observations after the M_L=6.5 main shock were used to determine 4,412 hypocenters and 3,108 fault-plane solutions for aftershocks during the first 2 months of the sequence. The resulting distribution and orientation of a subset of 2,618 well-determined hypocenters and 677 well-determined fault-plane solutions were analyzed for evidence of faulting structure.

The model consists of two principal planes between 5- and 12.5-km depth, striking approximately parallel to the axis of the Coalinga anticline, dipping 75°±5° NE. and 50°±5° SW. The planes join at the depth of the main-shock hypocenter (10 km), defining a wedge-shaped horst beneath the Coalinga anticline and the east side of Pleasant Valley. This horst may have been uplifted during the earthquake sequence by displacement on one or both planes. The distribution of aftershocks during the first 3 to 6 hours after the main shock suggests that the first and largest displacement was probably on the southwest-dipping plane.

Analysis of the aftershock distribution allows the introduction of further complexity into this model. The southwest-dipping surface appears to dip less steeply below 10-km depth and may represent a listric main-shock fault. Extension of the aftershock distribution to shallow depths on the northeast-dipping plane defines the Nuñez fault rupture on a plane consistent with surface observations of the Nuñez fault scarp. Shallow to moderately deep aftershocks beneath the northeast flank of the Coalinga anticline suggest secondary fault slip parallel to bedding.

INTRODUCTION

The May 2 earthquake occurred beneath the Coalinga anticline on the east flank of the central California Coast Ranges. Fault-plane solutions for the main shock from teleseismic observations (see chap. 10) and from local and regional observations (see chap. 8) are double couples consistent with horizontal crustal shortening approximately perpendicular to the strikes of the Coast Ranges and the Coalinga anticline. These solutions are consistent with either a shallowly southwest dipping thrust or a steeply northeast dipping reverse fault. Unambiguous identification of the main fault surface remains an unresolved question, however, because of several factors. First, the absence of surface faulting associated with the main shock precludes any direct observation of the fault. Second, although analysis of the permanent vertical surface deformation favors a simple planar rupture on a fault dipping steeply northeast over one on a southwest-dipping thrust, it does not rule out a thrust model (Stein, 1985). Third, the diffuse distribution of aftershocks strongly favors neither a simple southwest-dipping thrust nor a simple northeast-dipping reverse fault and, in fact, suggests that the main-shock deformation may be complex, occurring on multiple surfaces within the volume defined by the distribution.

The absence of a satisfactory simple planar model for the main shock, as well as the complexity of the aftershock distribution, provides the basis for consideration of more complex faulting models for this earthquake. In this study, we used seismic observations of numerous small aftershocks to resolve their structure. In inferring a faulting model, we made a crucial assumption that the aftershock structure indicates continuous fault surfaces which may have been activated by slip during the main shock. In this chapter, we present a complex faulting model for the May 2 earthquake consistent with the resolved structure.

Augmentation of the U.S. Geological Survey's permanent telemetered seismic network in central California

(Calnet) with portable and supplementary telemetered seismographs during the first few days of the Coalinga earthquake sequence resulted in a large suite of local observations capable of resolving considerable detail in the aftershock structure. Eaton (1985) used these local data and regional seismic observations to obtain a picture of the structure suggested by the distribution and orientation of 771 $M \geq 2.5$ aftershocks. In this study, we extended the magnitude range down to about $M=1.0$ and increased the number of events included to 2,618.

We performed an automated analysis, using data from Calnet and the portable stations, timed by the Allen-Ellis real-time processor (RTP) (Allen, 1982). Automated data processing, producing results from which detailed structural inferences can be drawn, has for some time been commonplace in reflection seismology. Only in the past few years, however, have advances in microprocessor-based pickers for earthquake phases, and their application to the dense U.S. Geological Survey microearthquake network, provided the basis for automated earthquake-data analysis. In this study, we used an automated procedure to analyze 2,618 hypocenters and 677 fault-plane solutions. The results reveal a spatially complex distribution of aftershocks, and form the basis for the complex faulting model proposed here. Some advantages of a completely automated analysis suitable for the interpretation of earthquake data are an increase in the number of earthquakes that can be included, with a concomitant decrease in the minimum event magnitude, and the ability to make rapid changes during the analysis, such as to include previously unused data or to modify the velocity model.

The following data were used in this study (fig. 9.1): (1) *P*-wave arrival times and first-motion polarities at 24 Calnet telemetered seismograph stations located within an 80-km radius of the main shock; (2) *P*-wave arrival times and first-motion polarities of vertical-component signals from 12 portable (5-day recorder) seismographs installed within 4 days after the main shock, within a 30-km radius; and (3) *S–P* intervals observed at 11 portable wideband digital General Earthquake Observation System (GEOS) seismographs located directly above the aftershock zone.

METHOD OF ANALYSIS

HYPOCENTER LOCATIONS

P-wave-arrival times, first-motion polarities, and coda lengths for the Calnet stations were identified and picked by the RTP (Allen, 1982). For the 5-day recorder stations, a similar system was developed to read and pick the vertical-component seismic signal from the tapes played back at a speed 20 times real time. For the GEOS stations, *S–P* intervals were hand-timed from three-component traces. The raw set of arrival times picked by the RTP from the 5-day tapes was contaminated with bogus picks caused by noise in the field recorder and playback systems. Most of these bogus picks were identified by applying the method of Eaton and others (1983), in which observations with extremely large residuals in the hypocenter determination are systematically reduced in weight.

A one-dimensional velocity model with station corrections for the Calnet and 5-day stations was obtained by inverting 2,000 observations from a spatially distributed set of 83 well-recorded aftershocks. The starting model was Eaton and others' (1983; see chapter 8) six-layer crustal model (CM4); velocities in the final model are within 2 percent of those for this model. A total of 69 events for which GEOS station data are available were then located with the model. The average residuals for these stations were taken as the station corrections for subsequent locations. These station corrections, and those for the Calnet and 5-day stations, contour smoothly, in general agreement with the shape of the Coalinga anticline—a result suggesting that they primarily reflect local lateral crustal structure (fig. 9.2). The largest positive corrections correspond to stations located in the

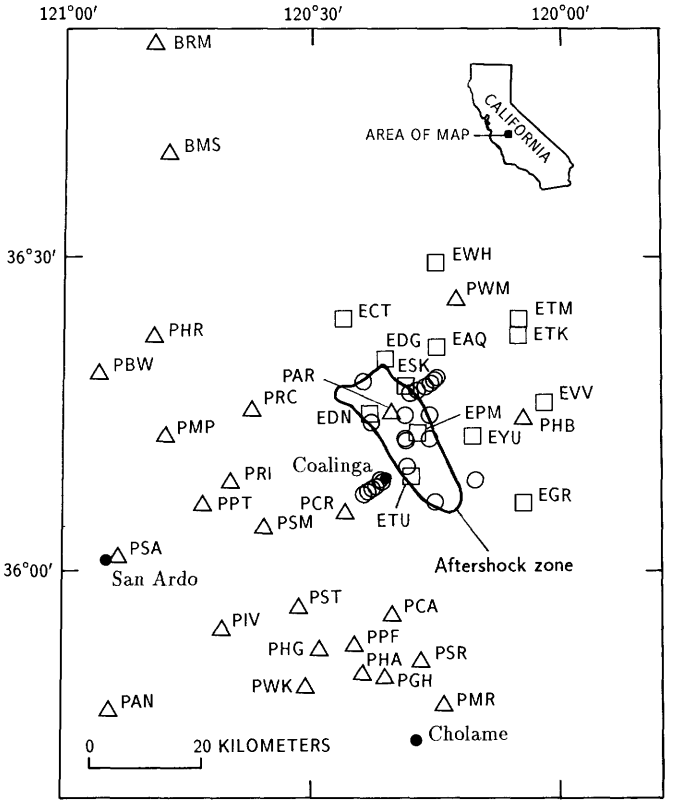

FIGURE 9.1.—Study area near Coalinga, Calif., showing locations of seismograph stations used in this investigation: triangles, Calnet; squares, 5-day recorder; circles, GEOS.

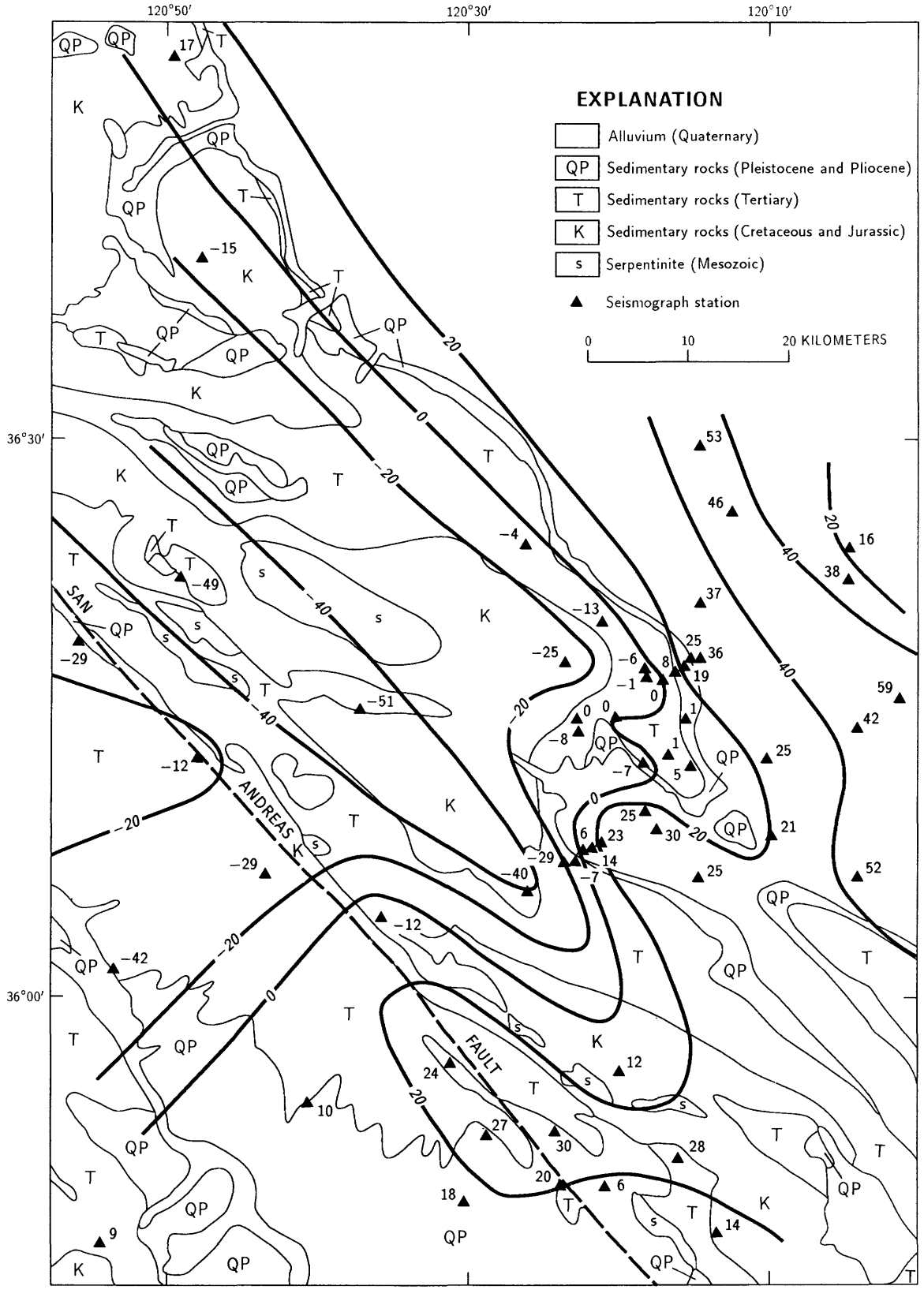

FIGURE 9.2.—Generalized geologic map of Coalinga, Calif., area, showing station corrections (in hundredths of a second) obtained in simultaneous inversion and used in aftershock locations. Positive corrections correspond to average relative delays, and negative corrections to relatively early arrivals.

San Joaquin Valley. Other positive station corrections are associated with Quaternary alluvium in Pleasant Valley near Coalinga and in Cholame Valley along the San Andreas fault. The largest negative station corrections are associated with the Jurassic and Cretaceous Franciscan assemblage in the Diablo Range.

For the set of hypocenter solutions, the relative uncertainty in epicenter is approximately 1 km, and in depth approximately 2 km. Near the periphery of the aftershock zone (especially under Nuñez Canyon and near Kettleman North Dome), the depths of some events may be in error by as much as 3 km. These errors are believed to be a result of the method used to eliminate noise picks. In the peripheral regions, where the model is relatively poor, this method can erroneously discard good data. For some events in these regions, the pattern of unresolved residuals suggests that data from the nearest stations were incorrectly weighted, and so the hypocenters are thought to be artificially deep by 2 to 3 km. We estimate that fewer than 2 percent of the events used here are so affected.

Absolute location errors, affecting the entire hypocenter set and resulting from large-scale discrepancies

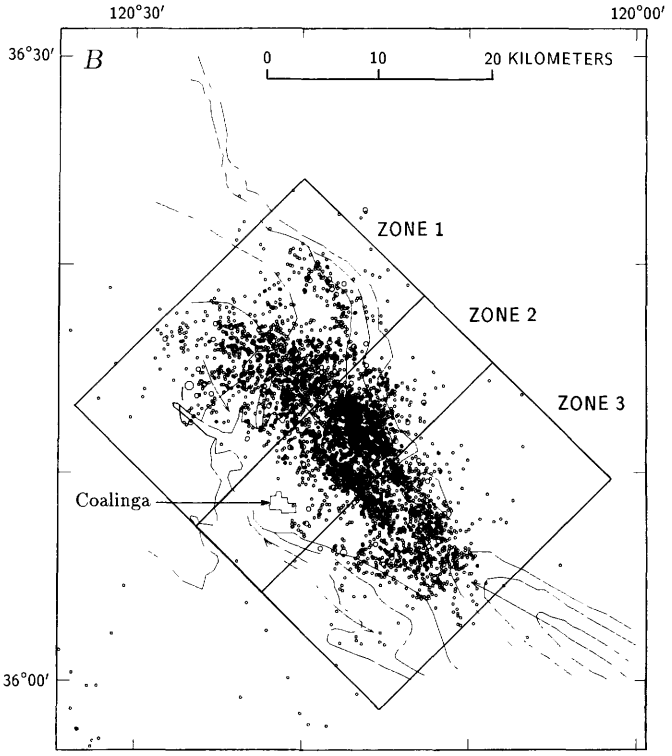

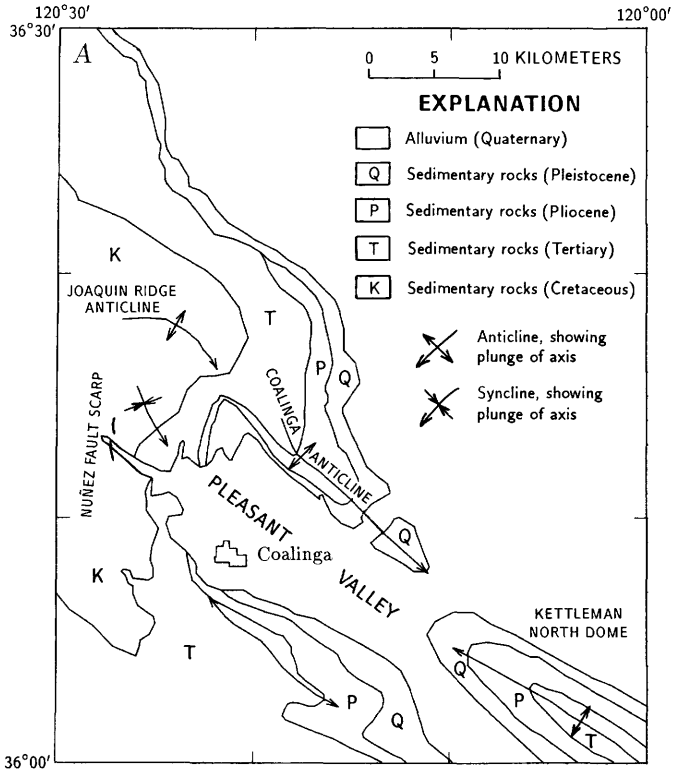

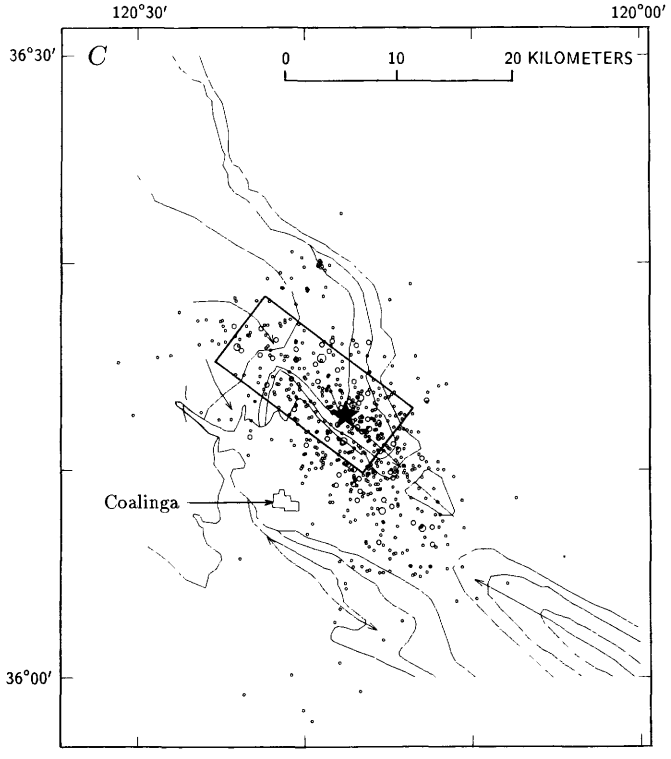

FIGURE 9.3.—Relocated epicenters for the Coalinga earthquake sequence. All solutions are from six or more observations and of HYPO71 quality A, B, or C. *A*, Simplified geologic map of Coalinga, Calif., area (from Stein, 1985), used as base map in some of the following figures. *B*, May 2 through June 30. Outlined areas indicate zones 1, 2, and 3, which are shown separately in figures 9.7, 9.8, and 9.9, respectively. *C*, First 24 hours (May 2–3). Star, main-shock epicenter. Box outlines surface projection of a modeled thrust fault for the main shock (Stein, 1983, fig. 3D).

between the actual and modeled crustal structure, have not been removed. The epicenters plotted in figure 9.3 are shifted by an average of 2 km SSE. from those obtained by Eaton and others (1983) with their crustal model CM4, and 3 km SE. from those obtained by Eaton (1985; see chap. 8) with his crustal model CM5.

In all, 2,618 aftershocks were relocated with the computer program HYPO71 to A- or B-quality solutions, and 3,850 to A-, B-, or C-quality solutions (fig. 9.3):

Magnitude	*Number*
0.00–0.99	64
1.00–1.99	2,165
2.00–2.99	1,428
3.00–3.99	171
4.00–4.99	18
5.00–5.99	3
6.00–6.99	1
Total	3,850

The main-shock hypocenter obtained with our final model is located at lat 36°12.73° N., long 120°17.61° W., at 10.0-km depth. The magnitudes adopted in this study are those calculated by the RTP, based on coda duration, for events of $M<3.7$, and on local and regional amplitudes for larger events (J.P. Eaton, written commun., 1984).

FAULT-PLANE SOLUTIONS

Fault-plane solutions were obtained from RTP arrival times and first-motion polarities for the Calnet and 5-day recorder data, and from hand-read Calnet and GEOS station data, using an automated grid-search (model and fit) procedure. Although the accuracy of RTP *P*-wave arrival times has been shown to equal or exceed that of routine network handpicks (Reasenberg, 1980; Allen, 1982), no comparable assessment of the RTP first-motion polarities has yet been made. To assess their fidelity, we compared the polarities for *P* phases from 10 events handpicked by J.P. Eaton (written commun., 1984) with those reported by the RTP. By assuming the handpicked polarities to be correct, the rate of error in polarity for 152 zero-weight RTP picks was found to be 20 percent. The first-motion data used in the following analysis were similarly selected and are presumed to be of comparable quality. The quality of the first-motion data thus obtained is lower than that normally used for focal-mechanism studies by current Calnet standards, and so our ability to constrain the fault planes is diminished. This adversity is partly compensated by the high density of station coverage, which provides redundancy in the observations.

A fault-plane solution was determined for each event by repeatedly fitting the observed first-motion polarities to the radiation pattern calculated for a suite of double-couple source models that uniformly span a selected range of orientations. On the basis of the preliminary modeling of fault-plane solutions by Eaton and others (1983) for some of the larger aftershocks, the source models were constrained to be pure reverse dip slip, striking west to north-northeast. Dip and strike (within az 270°–020°) of the nodal planes are free parameters.

This fitting scheme compares the observed polarity at each observed point on the focal sphere with that calculated for a given source model. A fit function, F, is defined as

$$F = \frac{\Sigma \mid P_o - P_t \mid w_o w_t}{N_W}, \quad (1)$$

where

$$N_W = \Sigma w_o w_t \quad (2)$$

and P_o and P_t are terms representing the observed and theoretical first-motion polarities (0.5 for compressions and –0.5 for dilatations), respectively. The observation weight, w_o, is set equal to the HYPO71 (Lee and Lahr, 1975) parameter PWT, and the theoretical weight, w_t, to the square root of the theoretical P-wave-radiation amplitude for a given source model and ray. This weighting scheme downweights observations near nodal planes and thus minimizes the effect of inconsistencies near the nodal planes, such as those caused by unmodeled refractions.

The fit function, F, is calculated for each source model in the suite, and the model that minimizes F is adopted as the fault-plane solution. An assessment of quality is made for each adopted solution, on the basis of the degree to which the observations fit the model, the weighted number of observations used in the solution (N_W), and the uncertainty in the parameters of the adopted solution. The uncertainties in strike and dip are the ranges corresponding to an increase in F of 0.05 above its minimum value. Using the algorithm in table 9.1, a quality A, B, C, or D is assigned to each solution. The ranges in parameter uncertainties typical of the A- and B-quality solutions obtained in this study are illustrated in figure 9.4. In general, dip is better determined than strike, a result reflecting the favorable position of rays on the focal sphere for resolving the dip of northwest-striking thrust- and reverse-faulting mechanisms.

To investigate the ability of the grid-search procedure to find correct fault-plane solutions, we applied it to a set of aftershocks for which fault-plane solutions had been independently obtained by Eaton (see chap. 8; J.P. Eaton, written commun., 1984), whose hand-read data were used in place of the relatively low grade RTP data. Assuming Eaton's solutions to be correct, we estimated the error in the automatically determined solutions from the differences between these two sets, as illustrated in

TABLE 9.1.—*Quality parameters for constrained fault-plane solutions*

[Solutions of a given quality satisfy all four of the inequalities listed for that quality]

	F	N_W	WS	WD	Number of solutions
A	≤.2	≥6	≤20	≤20	210
B	≤.3	≥5	≤35	≤30	472
C	≤.4	≥4	≤45	≤40	680
D	>.4	<4	>45	>40	1,689

figure 9.5 and summarized in table 9.2. The strong coupling between errors in strike and slip (fig. 9.5) suggests that the principle difference in these solution sets results from the constraint that the automatically determined solutions be pure dip slip.

Fault-plane-solution uncertainty also includes errors arising from the 20-percent polarity errors randomly present in the RTP first-motion data. The quality of the RTP fault-plane solutions may be directly assessed by inspection of some typical solutions obtained with the RTP data (fig. 9.6); these solutions include a total of 256 observations, 85 percent of which are consistent with the adopted fault-plane solutions. This percentage is somewhat higher than the overall accuracy rate of 80 percent estimated for the RTP polarity data, a result indicating that A- and B-quality solutions are obtained for earthquakes with better than average observational accuracy. From inspection of figures 9.5 and 9.6, we conclude that conservative estimates of the maximum uncertainties in strike and dip for the fault-plane solutions presented in the rest of this report are those listed in table 9.1 for B-quality solutions. Most errors, however, are probably closer to the standard deviations listed in table 9.2.

In addition to uncertainty in the modeled fault-plane solutions, the constraints imposed on the range of solutions considered limit our ability to resolve the complete faulting structure. The requirement that solutions be pure dip slip within the allowed range of strike produces a faulting model that includes only north-northeast- to northwest-striking thrust or reverse-slip elements. Because fault-plane solutions with a strike or slip angle outside the allowed range cannot be obtained, strike-slip and northeast-striking elements are unresolvable. For example, the procedure is unable to resolve the northeast-trending right-slip feature approximately 3 km northwest of the main-shock epicenter apparent in the structure of the larger aftershocks (see chap. 8).

RESULTS

EPICENTER DISTRIBUTION

The relocated epicenters for the period May 2–June 30 are shown in figure 9.3. The distribution is divided into three epicentral zones perpendicular to the longitudinal trend of the aftershock zone and approximately perpendicular to the Coalinga anticline. Zones 1 and 2 include Stein's (1983, fig. 3*D*) modeled main-shock fault, zone 2 includes the main-shock epicenter, and zone 3 extends from the southeast end of the modeled main-shock fault to Kettleman North Dome. The dense, elongate concentration of epicenters surrounding and southeast of the main shock (zone 2, fig. 9.3*B*) has a major axis striking 320°±5° and includes Eaton's "main-shock cluster" (see chap. 8, fig. 8.3*C*). To the north-northwest (zone 1), a band relatively devoid of aftershocks separates the main bulk of the distribution from an arm of shallow seismicity, corresponding to Eaton's "Domengine cluster" (see chap. 8, fig. 8.3*C*), that wraps around the northeast flank of the

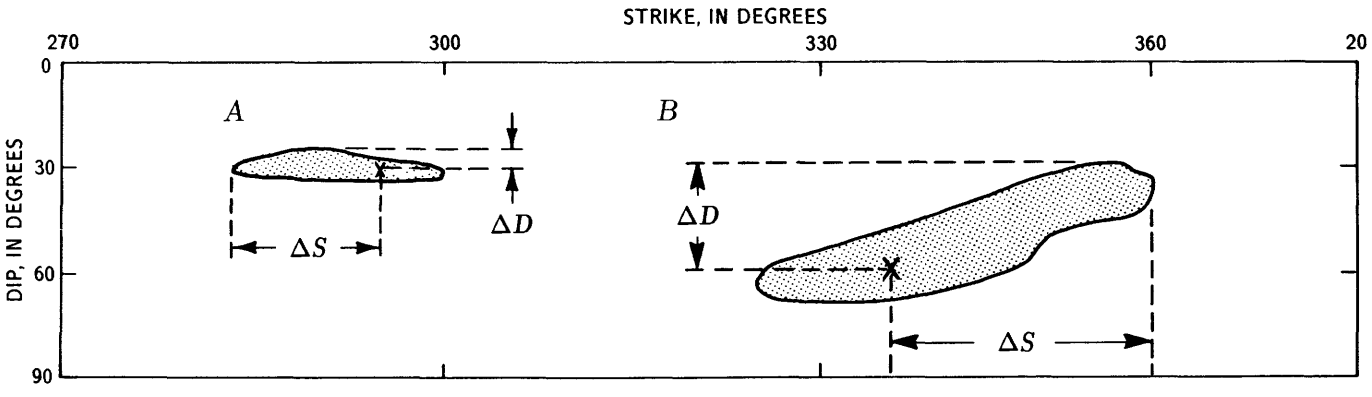

FIGURE 9.4.—Fit of fault-plane solutions for two earthquakes, showing range of solution orientations considered in the grid search. *A*, Typical A-quality solution. *B*, Typical B-quality solution. "x" denotes dip and strike of adopted solution ($F=F_{min}$); shaded area contains all solutions with a slightly worse fit ($F=F_{min}+0.05$). For each earthquake, ΔS and ΔD are uncertainty in strike and dip, respectively, of adopted solution.

TABLE 9.2.—*Comparison of manually and automatically determined fault-plane solutions*

	Mean difference (°)	Standard deviation (°)
Strike-------	-6	29
Dip----------	5	10
Slip---------	-5	29

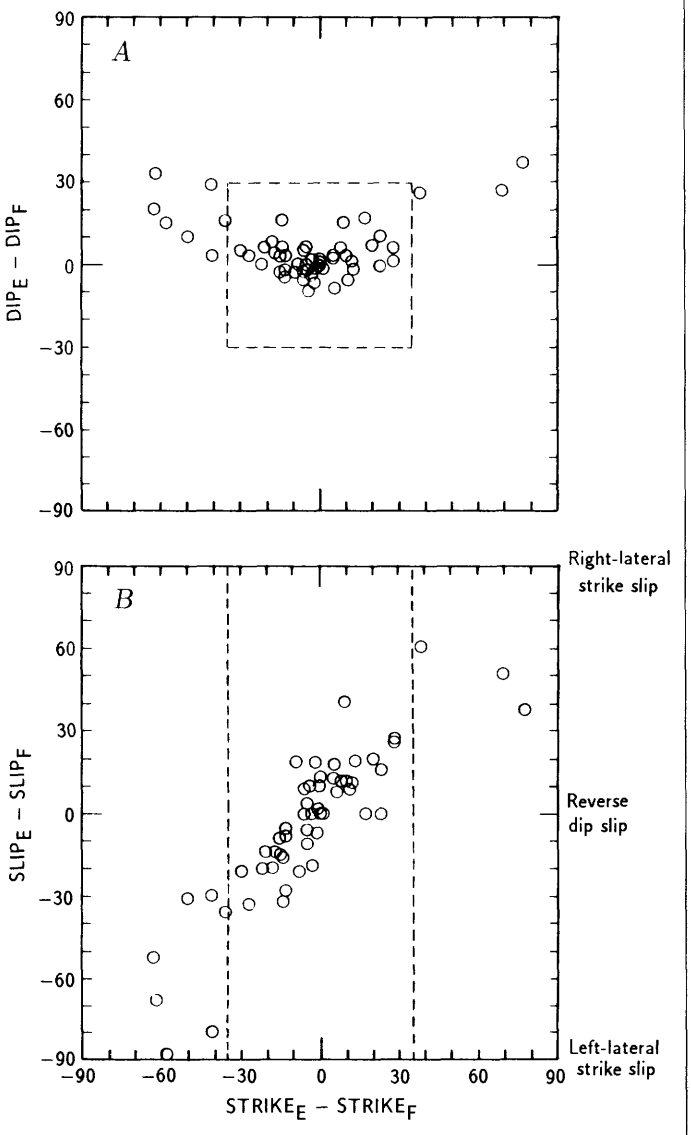

FIGURE 9.5.—Comparison of Eaton's (1985) hand-fitted fault-plane solutions (subscript E) with our A- and B-quality fault-plane solutions (subscript F) obtained with grid-search procedure from the same hand-timed data, showing differences in dip angle (*A*) and slip angle (*B*) as a function of difference in strike. Broken lines represent uncertainty limits in dip and strike estimated for B-quality solutions (table 9.1).

Joaquin Ridge anticline and approximately follows the trace of mapped stratigraphic contacts on this flank.

In general, the structure apparent in the epicentral distribution of $M \geq 1.0$ aftershocks for the first 60 days (fig. 9.3*B*) resembles that apparent for the first 150 days of $M > 2.5$ events (Eaton, 1985). Essentially the entire extent of the aftershock zone is evident in the first day's activity (fig. 9.3*C*).

HYPOCENTER DISTRIBUTION AND FAULT-PLANE SOLUTIONS

The hypocenter distribution and the orientations of nodal planes obtained for aftershocks within zones 1, 2, and 3 (fig. 9.3*B*) are shown in figures 9.7, 9.8 and 9.9, respectively. A total of 677 A- or B-quality fault-plane solutions were selected for analysis:

Magnitude	*Number*
0.00–0.99	1
1.00–1.99	229
2.00–2.99	372
3.00–3.99	70
4.00–4.99	5
Total	677

Each fault-plane solution is represented by a circle oriented in either the southwest- or northeast-dipping nodal plane; circle radius is proportional to event magnitude. Most of these circles are considerably larger than the inferred rupture areas associated with them. For example, assuming a 3-MPa stress drop, $M=2$ and $M=4$ events are approximately 6 and 1.5 times smaller, respectively, than their corresponding symbols. The diameter drawn in each circle represents the slip vector, and because these solutions are constrained to be pure reverse dip slip, the slip is necessarily updip and normal to strike. In each stereoview, the box surrounding the hypocentral zone corresponds to one of the zones in figure 9.3*B* and extends from the surface to 15-km depth, with a middepth line at 7.5 km drawn for reference. Views are toward the northwest from a point located 7.5 km below the surface. The surface features, which appear to be floating above, are the town of Coalinga and generalized contacts between mapped stratigraphic units, as shown in figure 9.3*A*. A 1-km cube, with horizontal edges aligned north-south and east-west, is shown for scale.

The hypocenters within zone 2 extend from approximately 3–4- to 13–14-km depth (fig. 9.8*A*). Their spatial distribution suggests a V-shaped pattern formed by two conjoint planes striking approximately parallel to the axis of the Coalinga anticline. The main-shock hypocenter is located in this zone at 10-km depth, approximately 3 km east of the intersection of these planes. Northeast-dipping fault-plane solutions align with the 70°–80°-

NE.-dipping plane (A, fig. 9.8*B*) but generally crosscut the 45°–55°-SW.-dipping plane (B, in fig. 9.8*A*). Southwest-dipping fault-plane solutions (fig. 9.8*C*) align with plane B. An alignment of shallowly (10°–15°) southwest dipping fault-plane solutions at 9- to 11-km depth (C, fig. 9.8*C*) approximately bisects planes A and B near the main-shock hypocenter and dips approximately 5°–10° SW. A peak in the distribution of dip for the events considered indicates a distinct group of solutions in the depth range 7–11 km, with dips of 10°–15° SW. or 75°–80° NE. (fig. 9.10). The fact that the distribution of these events in a diffuse, shallowly southwest dipping zone (fig. 9.11) aligns with the general orientation of the fault planes suggests the presence of a diffuse zone of subhorizontal thrusting surrounding the main shock. A corresponding structure or style of faulting is not apparent in the distribution of larger aftershocks (Eaton, 1985). Below 10 km and northeast of the main shock is a group of events with fault planes generally subparallel to plane A. Seismicity at 4- to 7-km depth on the northeast side of zone 2 appears as a separate cluster (D, fig. 9.8). Northeast-dipping fault-plane solutions (fig. 9.8*B*) are better aligned with this cluster's hypocenter distribution than are southwest-dipping solutions (fig. 9.8*C*), which tend to crosscut it.

Aftershock hypocenters extend from approximately 3–4- to 14–15-km depth in zone 1 (fig. 9.7*A*); the greatest concentration occurs at 9- to 11-km depth in the center of the distribution. The distribution of hypocenters and fault planes (figs. 9.7*A*, 9.7*B*) suggests a continuation of the northeast-dipping plane A from zone 2, extending it to the northwest and to a depth of 3 to 5 km. Also in zone 1, an extension of plane C from zone 2 is suggested by the presence of shallow-angle (15°) thrust planes at 9- to 11-km depth (fig. 9.7*C*). Seismic expression of plane B in zone 1 is relatively weak or absent. A separate cluster of hypocenters to the north, at 3- to 8-km depth, extending cluster D in zone 2 northwestward and deeper, corresponds to the Domengine cluster of epicenters on the northeast flank of the Coalinga anticline (fig. 9.3*B*).

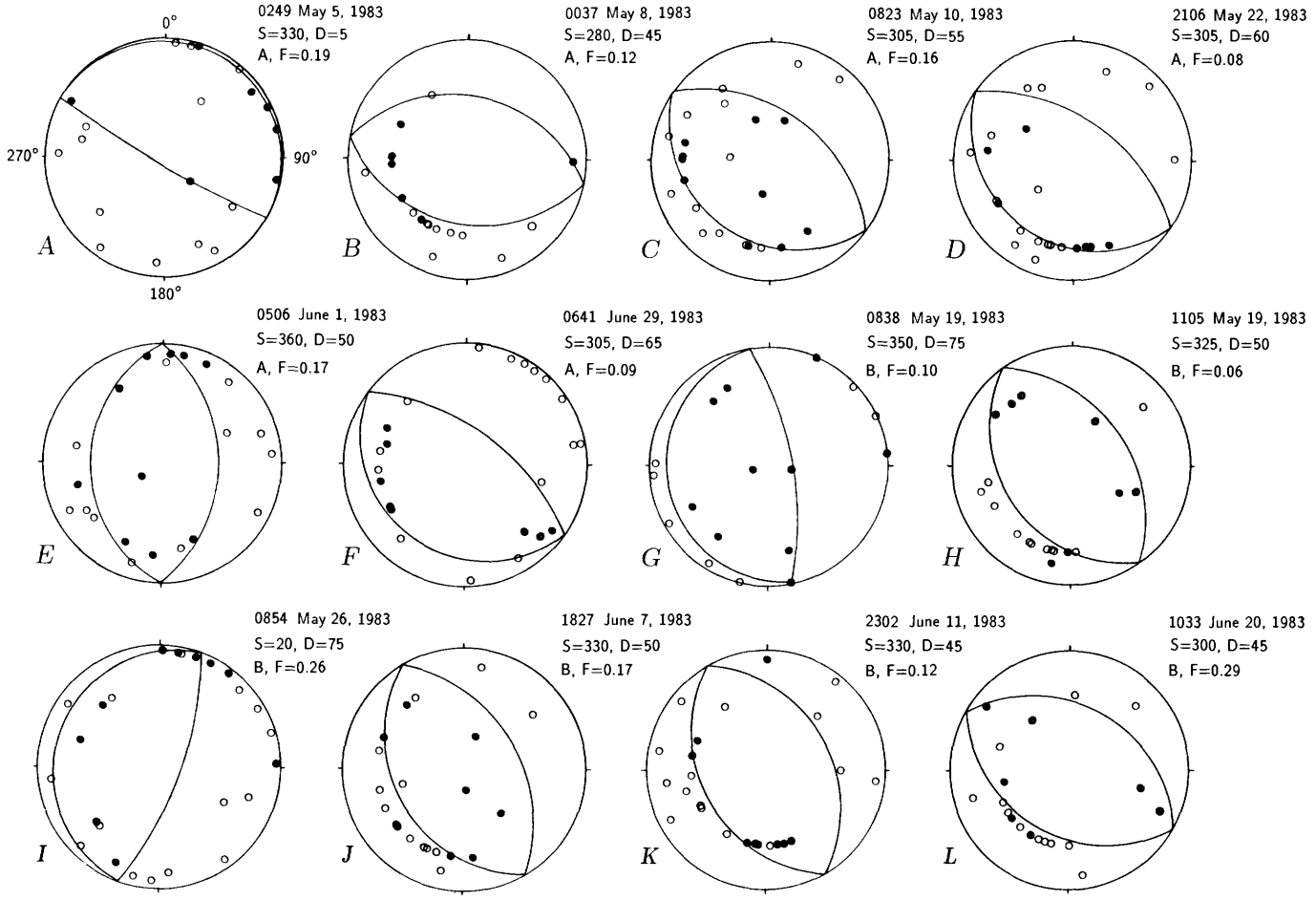

FIGURE 9.6.—Lower-hemisphere stereographic projections of fault-plane solutions obtained in this study. Dots, compressions; circles, dilatations. A or B, quality; D, dip; F, fit parameter; S, strike. *A–G*, Typical A-quality solutions. *H–L*, Typical B-quality solutions. Solutions are constrained to be pure reverse dip slip. Strike and dip of northeast-dipping nodal plane is given, but not necessarily preferred.

Northeast-dipping fault-plane solutions align with the hypocenter distribution in this cluster better than do southwest-dipping solutions (figs. 9.7*B*, 9.7*C*). The westernmost group of hypocenters in zone 1, between 3- and 7-km depth, is associated with rupture on the Nuñez fault, where activity intensified a month after the main

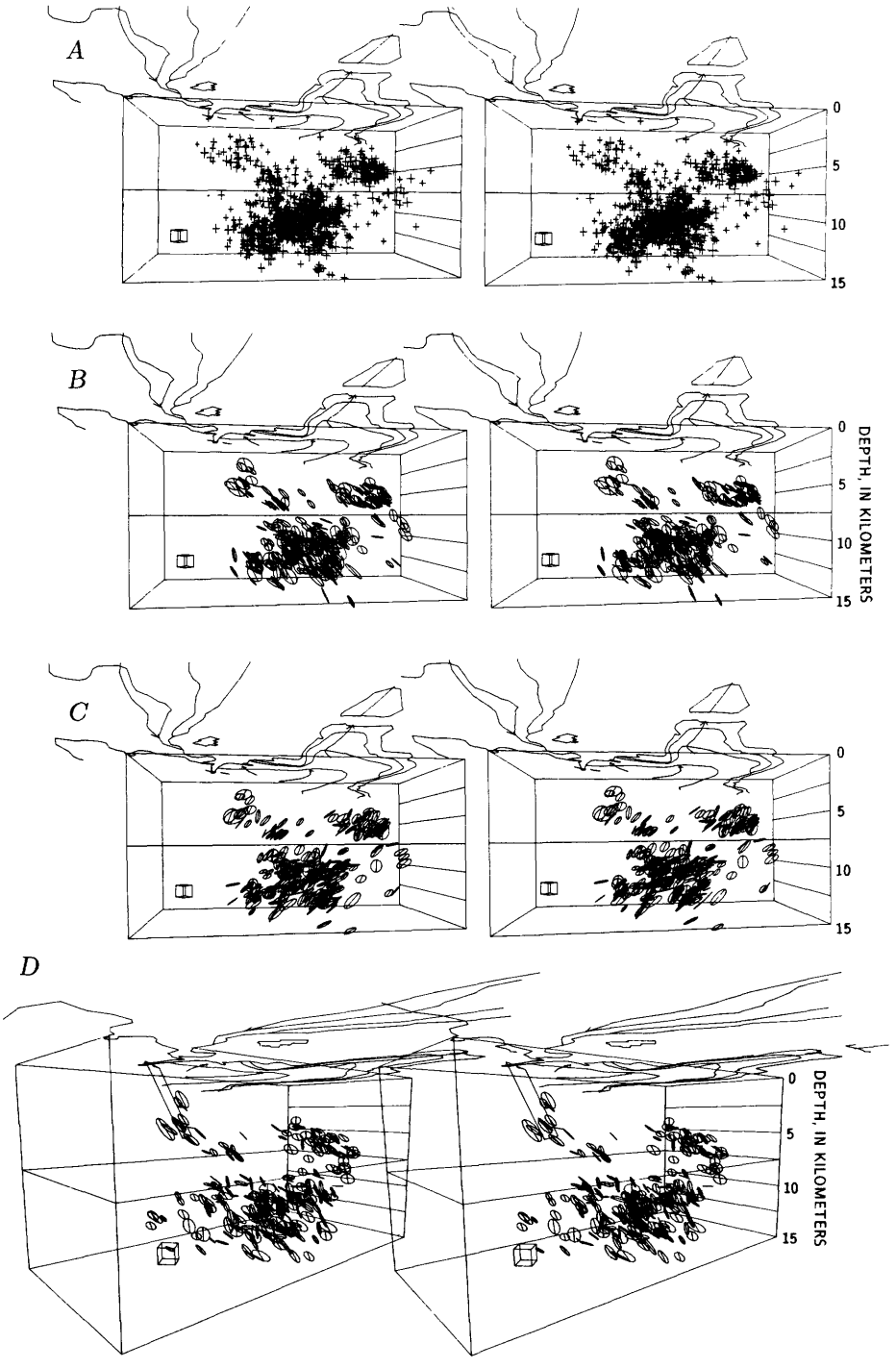

FIGURE 9.7.—Stereoscopic views of aftershocks occurring May 2–June 30, 1983, within zone 1 of figure 9.3*B*. Box extends from surface to 15-km depth. Simplified geology from figure 9.3*A* is drawn on the surface. View in figures 9.7*A* through 9.7*C* is from the southeast toward azimuth 315°, from a point located 7.5 km below the surface. A 1-km cube with horizontal edges aligned north-south and east-west is shown for scale. *A*, Relocated hypocenters with A- or B-quality solutions. *B*, Fault-plane solutions with A- or B-quality solutions, represented by circles oriented in northeast-dipping nodal planes. *C*, Same as in figure 9.7*B* but with southwest-dipping nodal planes represented. *D*, Northeast-dipping fault-plane solutions (fig. 9.7*B*), viewed from a point 4 km beneath the surface at lat 36°00′ N., long 120°35′ W.

shock. Although the hypocenter distribution of this group (fig. 9.7*A*) suggests a continuation of plane A, the average strike of slip planes is rotated 30°–40° clockwise relative to plane A (figs. 9.7*B*, 9.7*D*). The positions and orientation of these aftershocks are consistent with a plane dipping 65° E. and passing through the 4.5-km

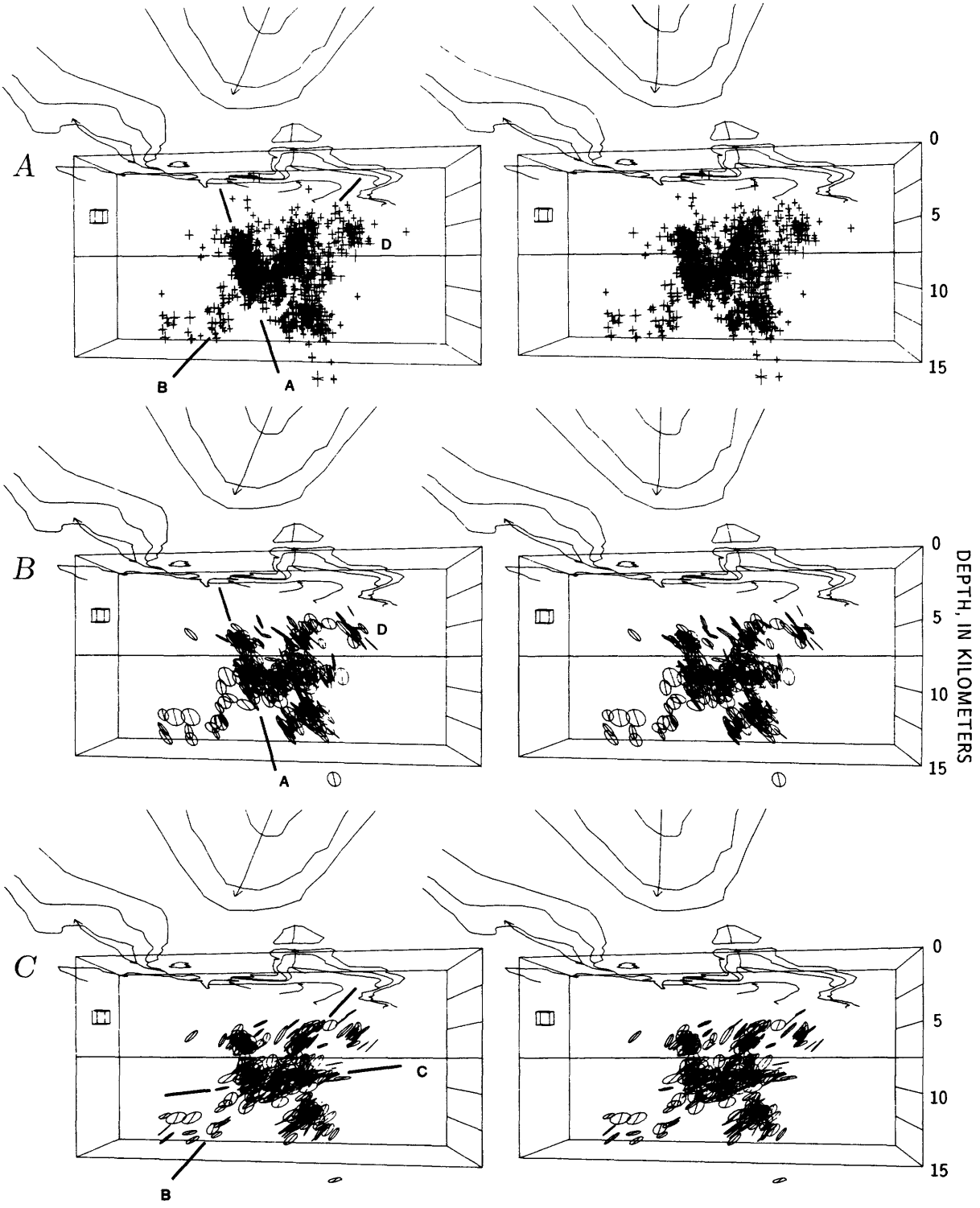

FIGURE 9.8.—Stereoscopic views of aftershocks during period May 2–June 30, 1983, within zone 2 of figure 9.3*B*. Same conventions as in figures 9.7*A* through 9.7*C*.

segment of the north-south-striking Nuñez fault that sustained reverse displacement after the $M=5.2$ event on June 11 (fig. 9.7*D*; see chap. 15).

The hypocenters in zone 3 extend from approximately 3- to 12–13-km depth (fig. 9.9*A*). A spatial concentration of hypocenters suggests a steeply northeast-dipping planar structure between 4- and 10-km depth as an extension of plane A from zone 2; this structure can also be seen in the downdip view of fig. 9.12*A*. Northeast-dipping fault-plane solutions align better with this structure than do southwest-dipping fault planes (figs. 9.9*B*, 9.9*C*). In both map view (fig. 9.3*B*) and downdip view

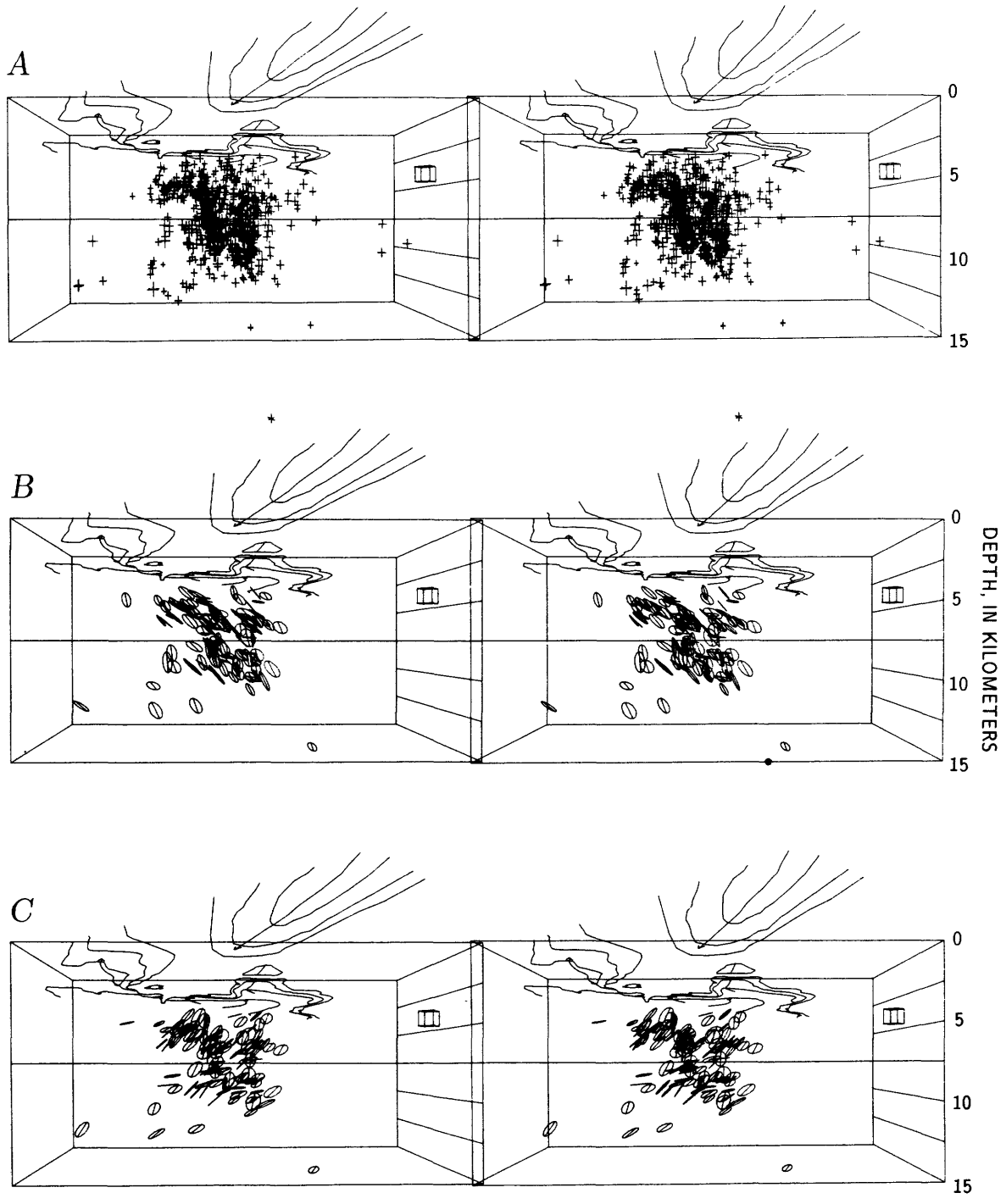

FIGURE 9.9.—Stereoscopic views of aftershocks during period May 2–June 30, 1983, within zone 3 of figure 9.3*B*. Same conventions as in figures 9.7*A* through 9.7*C*.

(fig. 9.12*A*), this northeast-dipping planar feature appears to terminate approximately 3 km southeast of the southeast edge of zone 2. At that point, the seismicity becomes relatively diffuse, and the aftershock zone widens approximately 4 km to the southwest. Similarly, the fault-plane solutions in zone 3, rather than suggesting planar features, vary widely in strike and dip.

Stereoscopic views of the entire aftershock distribution, looking downdip along planes A and B, are shown in figures 9.12*A* and 9.12*B*, respectively. Clustering of hypocenters in planes A and B as defined above is apparent, although in each view one plane forms a confusing background partly obscuring the other. Using these views, we estimate the horizontal dimensions of planes A and B to be 8±3 and 10±3 km, respectively.

The principal fault elements suggested by the aftershock structure, as discussed above, are illustrated in

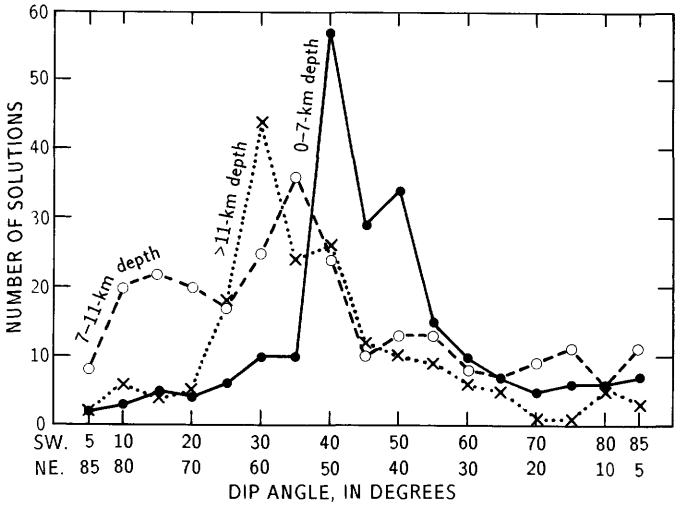

FIGURE 9.10.—Distribution of dip angle for A- and B-quality fault-plane solutions, shown separately for hypocentral depth ranges 0–7 km, 7–11 km, and greater than 11 km. A total of 677 solutions for events between May 2 and June 30, 1983, are represented. All three depth ranges have a preferred dip-angle range of 30°–40° SW. (50°–60° NE.); however, only the middepth group includes a significant population of 10°–15° SW. (75°–80° NE.)-dipping solutions.

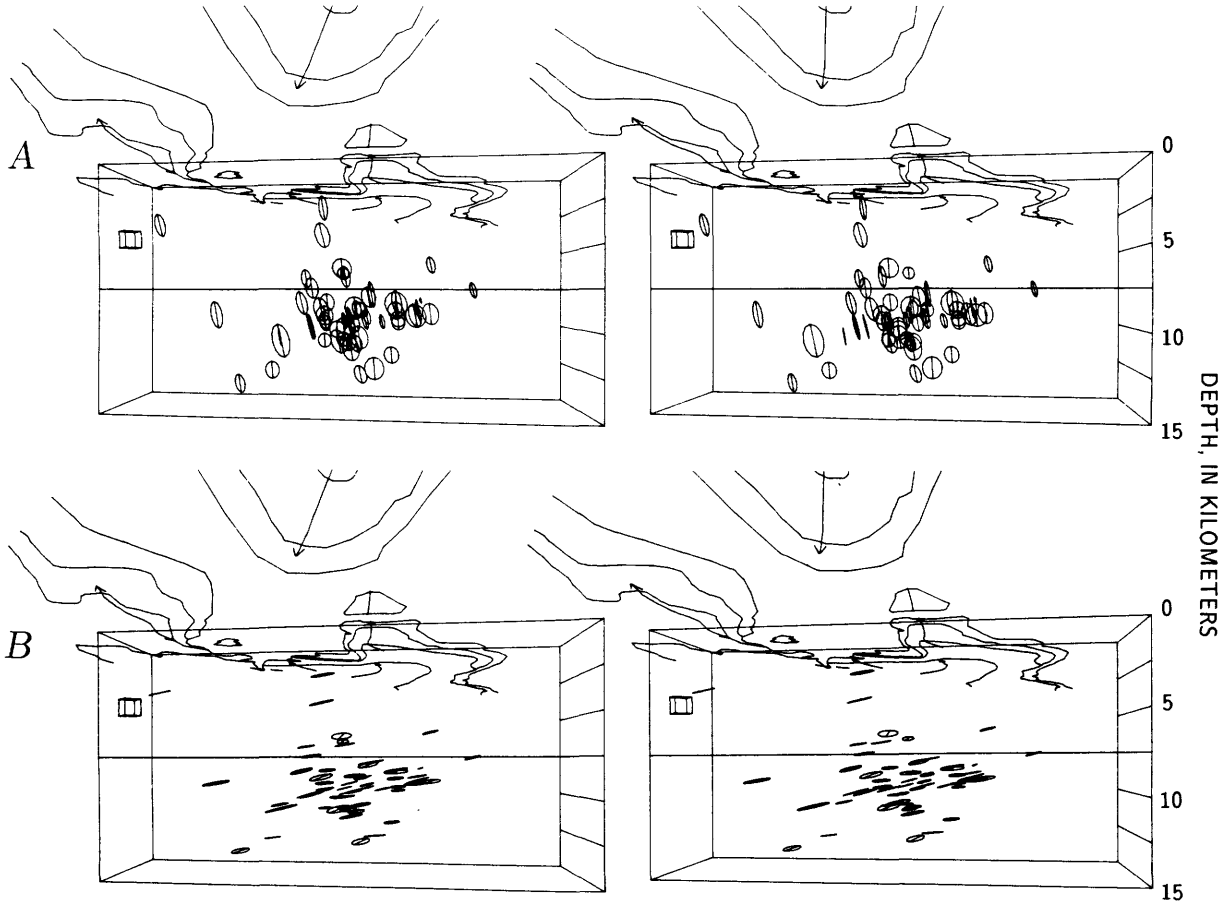

FIGURE 9.11.—Stereoscopic views of subset of aftershocks with 10°–15° SW. (75°–80° NE.)-dipping fault-plane solutions. Box outlines zone 2, although events in all zones are included. *A*, Northeast-dipping nodal planes. *B*, Southwest-dipping nodal planes.

cartoon form in figure 9.13. The spatial relations among planes A and B, the main-shock hypocenter and fault-plane solution, and the Coalinga anticline are apparent, as well as those between the Nuñez fault plane and the surface trace of the Nuñez fault, and between the Domengine cluster and the Coalinga anticline (table 9.3). The aftershock hypocenters are shown together with the suggested fault model in figure 9.14.

EARLY DEVELOPMENT OF THE AFTERSHOCK ZONE

The locations of hypocenters in zones 1 and 2 during the first 12 hours of the earthquake sequence are shown together with the thrust and reverse-fault nodal planes obtained for the main shock by Eaton (see chap. 8) in figures 9.15*A* and 9.15*B*, respectively. This period precedes the installation of the 5-day and GEOS portable seismographs, as well as the augmentation of the Calnet telemetered network with two key stations (PHB and PWM) to the north and east of the aftershock zone (fig. 9.1). Thus, azimuthal coverage is relatively poor for this period, and the resulting locations (including that for the main shock) are somewhat degraded. All solutions for events during the first 12 hours are of C quality, owing to the large azimuthal gap to the northeast, whereas figures 9.7*A*, 9.8*A*, and 9.9*A* include only A- and B-quality solutions. Eaton's (see chap. 8) main-shock fault plane is drawn centered on the hypocenter, with a 6-km radius corresponding to the source dimension obtained from teleseismic body waves by Choy (see chap. 10). The distribution of hypocenters during the first 12 hours is better aligned with the main-shock thrust plane than with the reverse-fault plane. Similarly, southwest-dipping nodal planes for aftershocks during this period (fig. 9.15*D*) align with the hypocentral distribution, whereas the northeast-dipping nodal planes (fig. 9.15*C*) crosscut the distribution.

The locations of hypocenters in zones 1 and 2, together with Eaton's (see chap. 8) fault-plane solution for the main shock, during the first 3 and 6 hours of the sequence

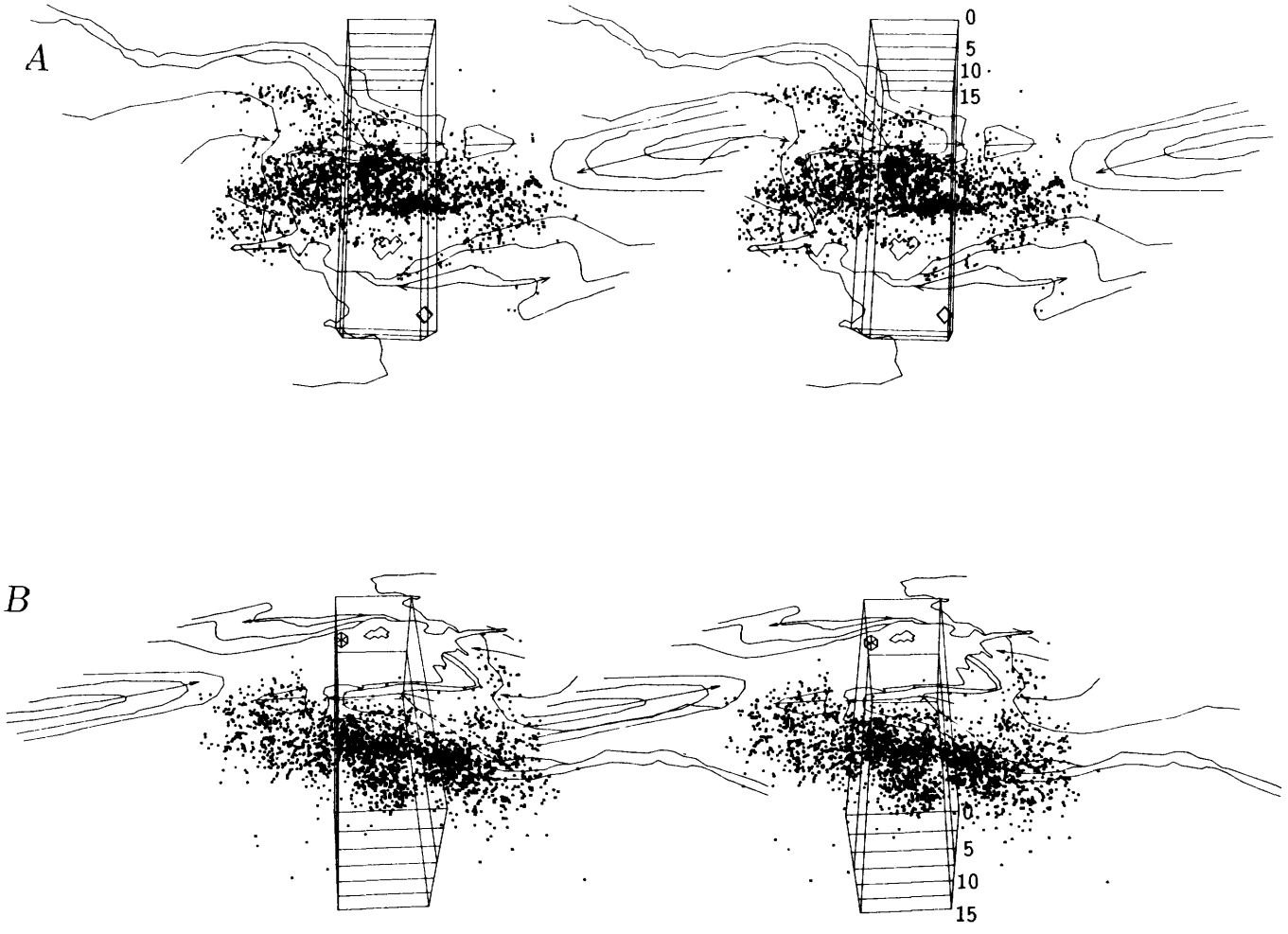

FIGURE 9.12.—Stereoscopic projections of all A- and B-quality hypocenter solutions. *A*, View downdip along plane A (see fig. 9.8). *B*, View downdip along plane B.

TABLE 9.3.—*Specification of the planes suggested for faulting structure as shown in figures 9.13 and 9.14*

Plane	Associated feature	Strike (°)	Dip	Minimum depth (km)	Maximum depth (km)	Length of plane along strike (km)	Centerpoint of upper edge of plane	
							Lat° N.	Long° W.
1	Plane A ------	319	75° NE.	5	10	10	36.153	120.302
2	Plane B ------	319	50° SW.	5	12.5	10	36.215	120.270
3	Nuñez fault---	357	65° E.	0	5	4.5	36.220	120.450
4	Domingine cluster (D).	307	45° NE.	3	6	6	36.295	120.300

are shown in figures 9.16 and 9.17, respectively. Identification of the distribution of hypocenters during the early hours of the aftershock sequence with the main-shock rupture favors a southwest- over a northeast-dipping nodal plane. Location of these earliest aftershocks mainly in zone 1, northwest of the main-shock hypocenter, suggests that the main-shock rupture propagated northwestward.

DISCUSSION

Our interpretation of the observations presented here rests on assumptions about what the structure of the aftershock distribution may represent. Studies of aftershock sequences suggest that hypocenters and fault-plane solutions in some cases define the geometry of the main-shock rupture surfaces (Eaton and others, 1970;

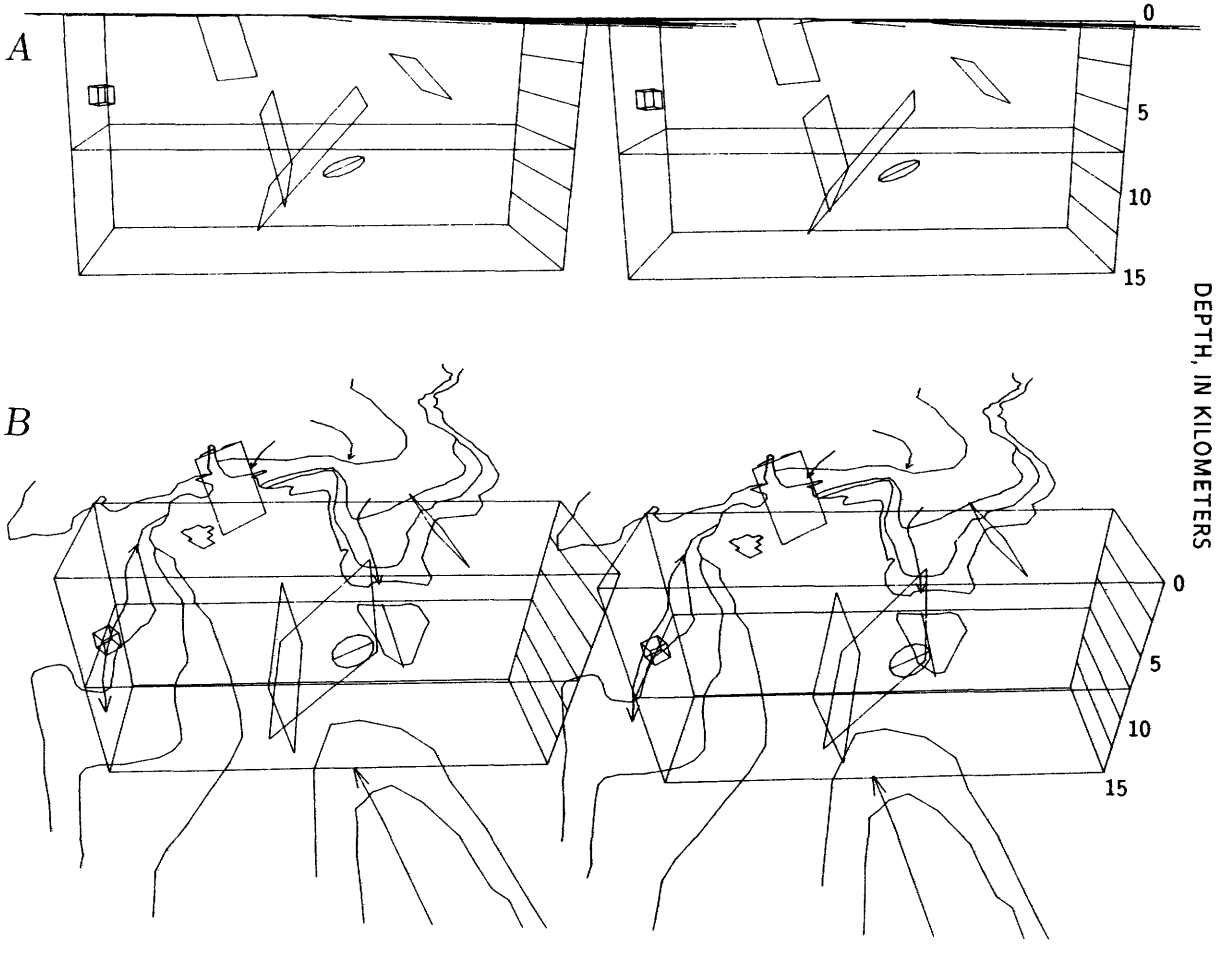

FIGURE 9.13.—Cartoon depicting planar fault model suggested by aftershock structure, and southwest-dipping-thrust fault-plane solution for the main shock (see chap. 8). See table 9.3 for specification of planes in model. *A*, View from 2 km below Kettleman North Dome. *B*, View from 15 km above Kettleman North Dome.

Reasenberg and Ellsworth, 1982; Wetmiller and others, 1984); in other cases they indicate secondary faulting off the main rupture (Hamilton, 1972; Brown and others, 1973; Das and Scholz, 1981; Stein and Lisowski, 1983). In

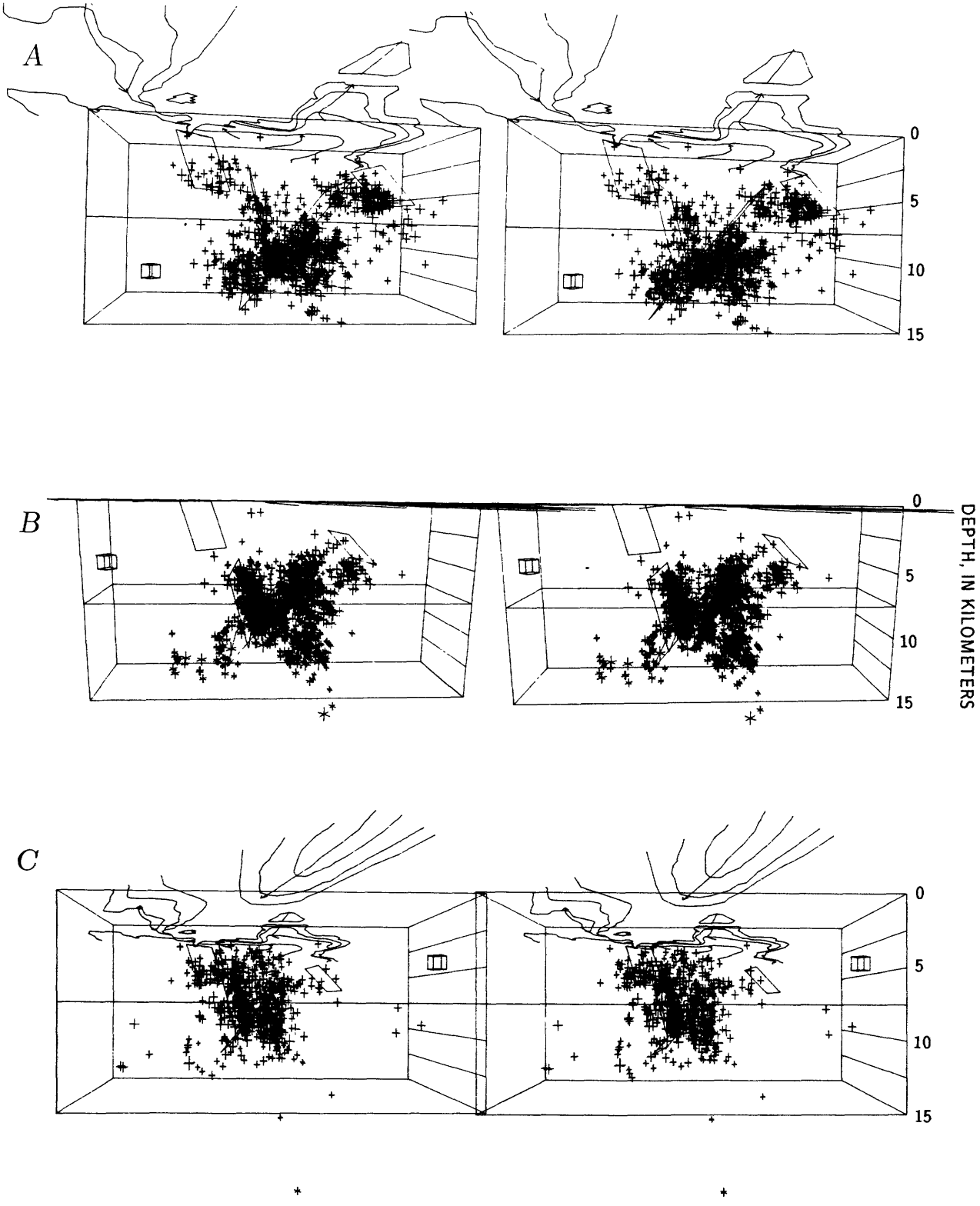

FIGURE 9.14.—Aftershock hypocenter locations with A- or B-quality solutions, and suggested fault model from figure 9.13. *A*, Zone 1. *B*, Zone 2. *C*, Zone 3.

the following discussion, we interpret the observed structure in the Coalinga aftershock distribution as evidence for a complex main-shock rupture surface and for secondary faulting. Quasi-planar structures in the aftershock distribution are associated with fault surfaces. Although the faulting model suggested by such an interpretation is not unique, after-the-fact justification for our interpretation lies in the consistency of the resulting model with the other independent geophysical and geologic observations of this earthquake sequence reported in this volume and discussed below.

The distribution of hypocenters and alignments in the orientation of nodal planes suggest that the main shock was a complex event, involving as many as three principal planes of failure, all striking approximately parallel to the Coalinga anticline but differing widely in dip. The distribution of aftershocks in zones 1 and 2 during the first 12 hours of the earthquake sequence, particularly during the first 6 hours, favors the southwest-dipping plane B and suggests that this plane was the principal faulting surface in the main-shock rupture. However, the complexity in the distribution of aftershocks presented in figures 9.7 through 9.9 suggests that the rupture may have been complex, with slip distributed on planes A and B and, possibly, in zone C. The relatively simple distribution of early aftershocks does not preclude a complex model but suggests that if the main rupture was complex, the greatest displacement was on plane B. Indeed, a simple, southwest-dipping planar dislocation at the depth of the main-shock hypocenter is inconsistent with observed coseismic surface-elevation changes (Stein, 1985).

Evidence also exists for secondary faulting in the earthquake sequence, in a cluster of relatively shallow aftershocks (D, figs. 9.7, 9.8). Both the development of this cluster largely after the first 24 hours of the sequence and its location just outside the upper crack tip in the

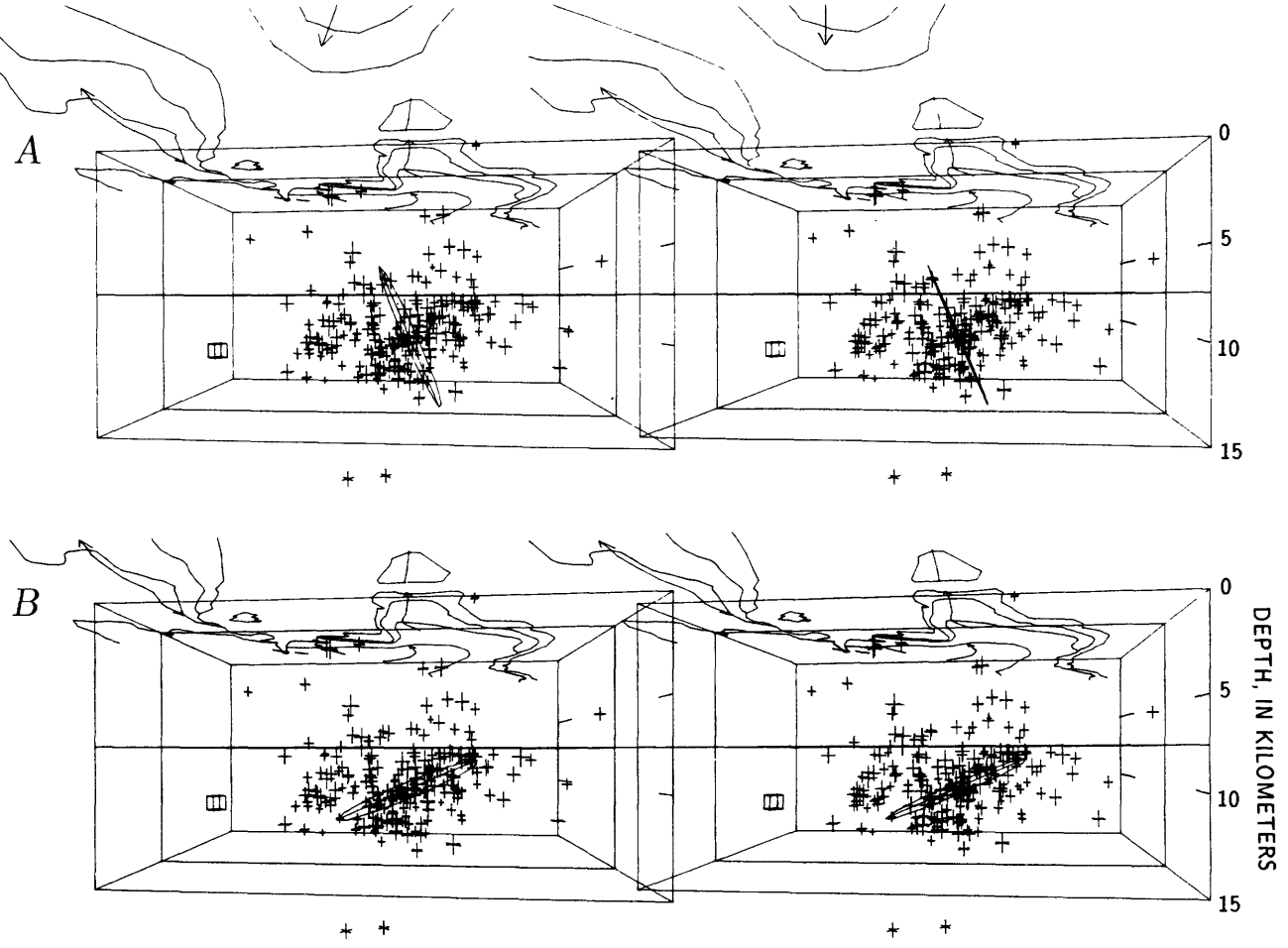

FIGURE 9.15.—Distribution of hypocenters and orientation of nodal planes for aftershocks in zones 1 and 2 during the first 12 hours of the Coalinga earthquake sequence. *A*, A- to C-quality hypocenter locations, shown with Eaton's (see chap. 8) northeast-dipping nodal plane for the main shock (circle). Main shock is shown centered on its hypocenter and is plotted with a 6-km radius. *B*, Same hypocenters, shown with southwest-dipping main-shock nodal plane. *C*, Northeast-dipping nodal planes for aftershocks. *D*, Southwest-dipping nodal planes for aftershocks.

extended plane inferred for the main rupture suggest that these events represent secondary faulting. Discontinuity between this cluster and most events in the aftershock zone also suggests that the events in this cluster are located off the main-shock fault structure. Although the surface defined by these events dips more steeply than the mapped stratigraphic contacts above them, correspondence of these events in location and strike to the buried northeast flank of the Coalinga anticline suggests that they may be associated with slip on northeast-dipping bedding planes. Their depths place them within the layered Great Valley sequence (see chaps. 3, 4), which, owing to its relatively undisturbed, layered structure, may provide a favorable environment for bedding-plane slip.

A multiple-slip-plane hypothesis is consistent with other observations of the Coalinga earthquake sequence. First, slip distributed on planes A, B, and C (with most of the displacement on B) could be well fitted to surface-leveling data (R.S. Stein, oral commun., 1984). Reverse or thrust movement on planes A and B would result in uplift of the wedge of rock between and above them and create a buried horst beneath the Coalinga anticline and the east side of Pleasant Valley. The measured coseismic surface uplift is a maximum at a point directly above the main shock, approximately 3 km east of the intersection of planes A and B. Greater displacement on plane B than on plane A results in an asymmetric distribution of surface-elevation change similar to that observed by Stein (see chap. 13), with greater uplift to the northeast than depression to the southwest. Namson and others (see chap. 6) have constructed balanced cross sections to argue that several fault planes (a southwest-dipping thrust, with west-verging backthrusts in the hanging wall) are required to account for the Pliocene to Holocene Coalinga uplift.

Second, the main-shock rupture process has been modeled from teleseismic body waves as two events, occurring approximately 3.2 s apart, on separate rupture planes striking northwest and dipping either steeply northeast or shallowly southwest (see chap. 10). If the first event is associated with our plane B, then this source model is in first-order agreement with the structure revealed by the aftershock distribution (compare fig. 10.10 with figs. 9.8 and 9.14). The smaller, shallower second event, located a few kilometers southwest of the first, may correspond to plane A, dipping northeast.

Third, the main-shock fault-plane solution obtained by Eaton (see chap. 8) agrees with our interpretation of aftershock locations if his southwest-dipping nodal plane

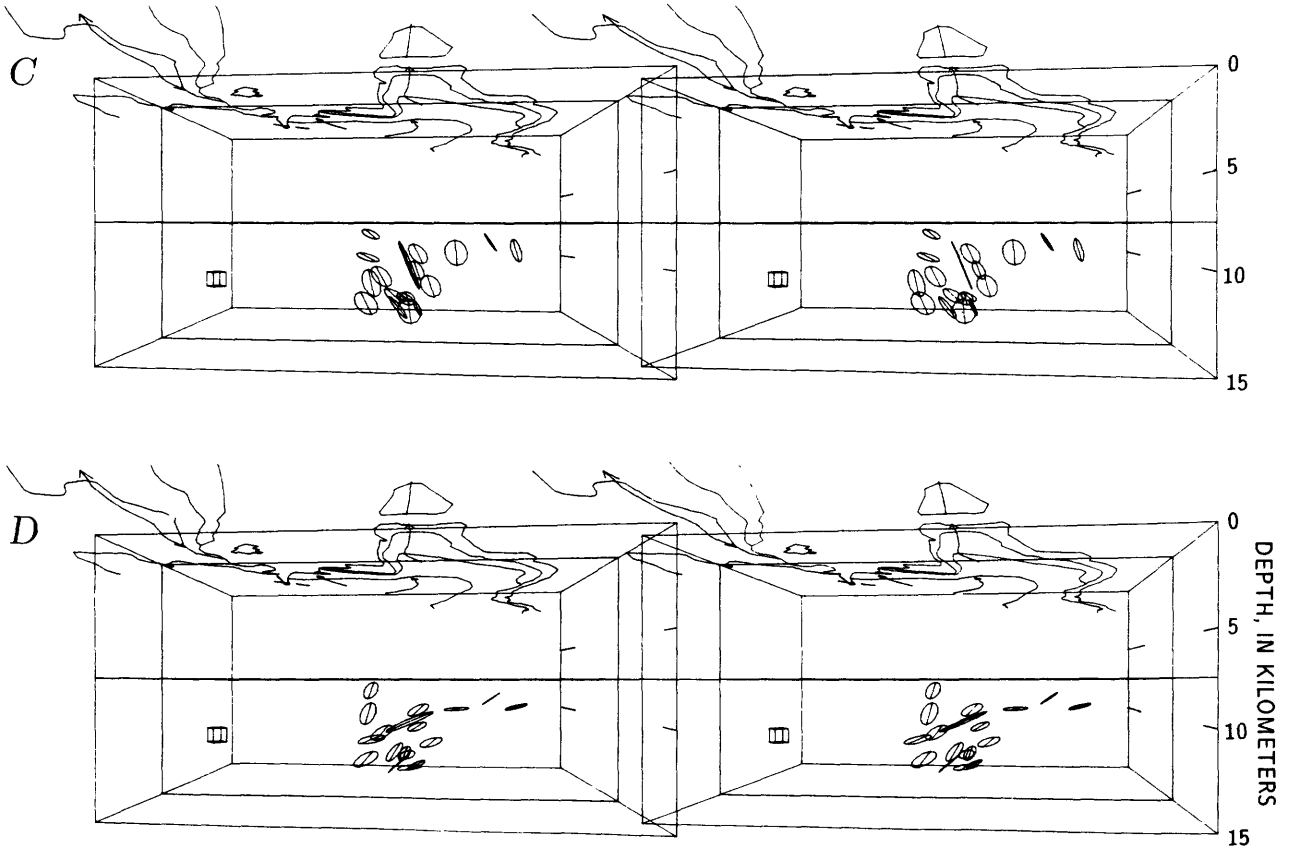

FIGURE 9.15.—Continued

is identified as the main-shock fault. Assuming that the distribution of aftershock hypocenters and the orientation of aftershock nodal planes during the first 12 hours and, especially, during the first 3 to 6 hours of the sequence map the main-shock rupture plane, we infer that the main shock's first motions resulted from slip on a southwest-dipping thrust plane. The location of the main-shock hypocenter approximately 3 km northeast of plane B (fig. 9.11*A*) may indicate a mislocation of the main shock. Earthquakes during the first 24 hours were located without data from the portable seismographs and without the key stations (PWM and PHB) later added to the telemetered network northeast of the aftershock zone. Thus, a 216° azimuthal gap exists in the distribution of stations used to locate the main shock. Because this gap is centered northeast of the main shock, degradation in epicentral control along a northeast-southwest direction is expected.

The approximately 20° discrepancy in dip angle between Eaton's (see chap. 8) main-shock thrust plane and plane B may be due to listric curvature in the main rupture. The aftershock distribution in figure 9.8*C* suggests that plane B dips less steeply below 8- to 10-km depth. If so, then faulting may be represented by a curved or dihedral surface dipping 23° SW. below 10-km depth, in accord with the main-shock first motions, and dipping approximately 45° SW. above 10-km depth. Slip on a fault model with this geometry was shown by Stein (1985) to provide an acceptable (but inferior, relative to a northeast-dipping plane) fit to the coseismic elevation changes, and is consistent with the faulting model inferred by Wentworth and Zoback (see chap. 3) from seismic-reflection profile SJ–19 through the Coalinga anticline some 5 to 8 km to the southeast.

The case of a simply bent or dihedral fault was considered by King (1984), who, by assuming a fractal model for faulting geometry, showed that much of the total deformation in such a system must occur on secondary faults separate from the main fault, in the vicinity of the bend. In his model, the orientations of

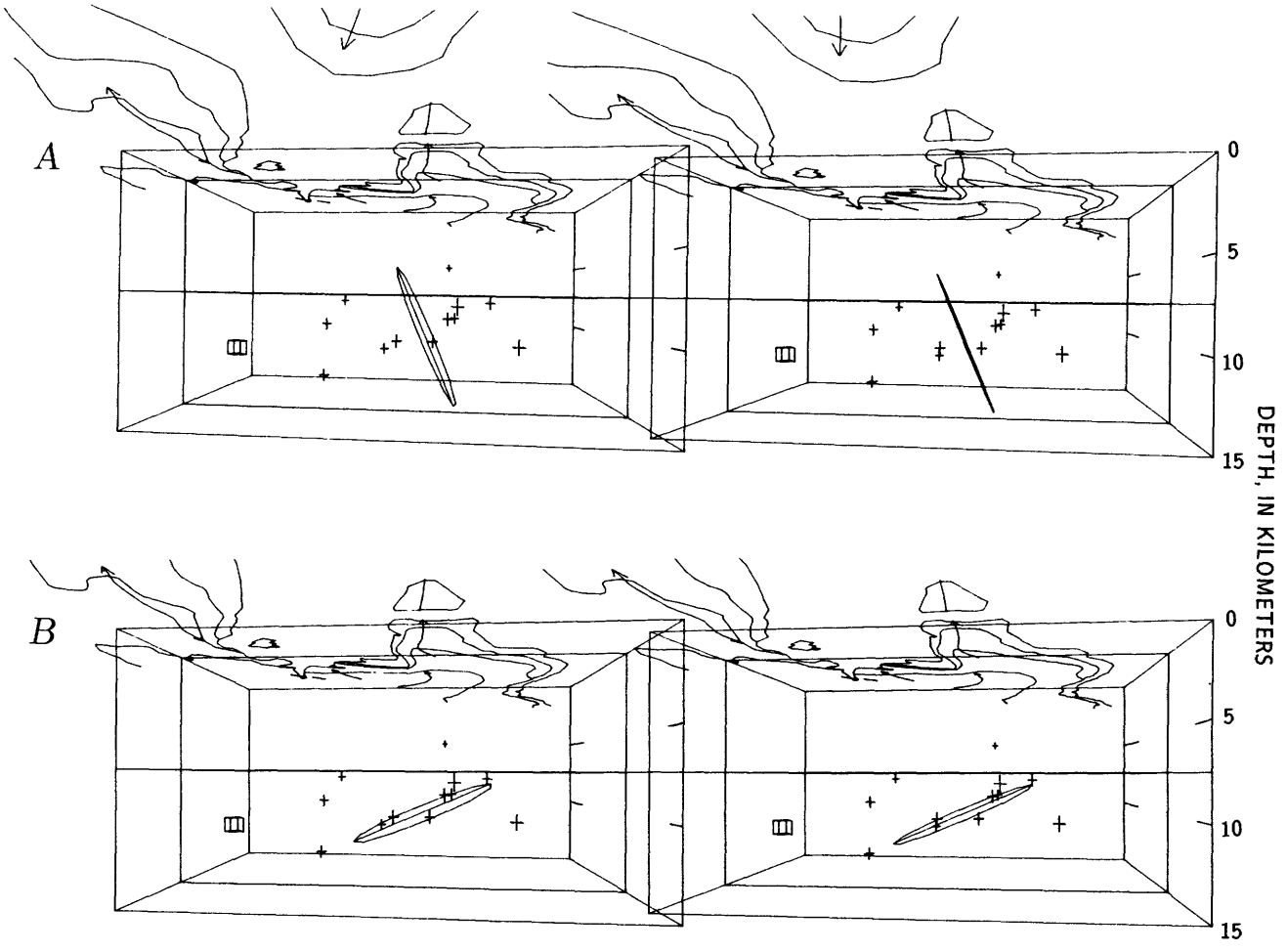

FIGURE 9.16.—Distribution of hypocenters for aftershocks in zones 1 and 2 during first 3 hours of the sequence. *A*, A- to C-quality hypocenters shown with Eaton's (see chap. 8) northeast-dipping nodal plane for the main shock. *B*, Same hypocenters shown with corresponding southwest-dipping nodal plane. See figure 9.15 for explanation.

secondary faults may differ substantially from those on either side of the bend in the main fault and may be controlled by preexisting conditions in the surrounding region, such as bedding structure or a system of fossil faults. The location of secondary faulting necessary to accommodate displacement across the fault bend or dihedral may be either inside or outside the bend (King, 1984; King and Nábělek, 1985). For example, in the case of the Corinth, Greece, earthquake of 1981, whose inferred fault geometry closely resembles the one proposed here for the May 2 earthquake, most aftershocks locate inside an inferred bend in the fault, in the hanging wall (fig. 9.18; King and others, 1985). In the case of the El Asnam, Algeria, earthquake of 1980, most aftershocks are confined to the footwall, outside the bend (Ouyed and others, 1983). In our interpretation of the Coalinga earthquake sequence, most off-fault aftershocks are located in the hanging wall (inside the suggested bend in surface B). These aftershocks include the events constituting plane A and the Nuñez fault plane. In this context, the fact that the diffuse, shallow-angle thrusting in zone C clusters in the vicinity of the bend in plane B suggests that it, too, is a candidate for the secondary faulting required in King's (1984) model to transmit displacement through the bend.

Finally, we briefly compare the Coalinga earthquake sequence with the 1982 New Brunswick, Canada (M=5.7), earthquake (Wetmiller and others, 1984). Both are thrust or reverse-fault earthquake sequences without significant surface rupture. Well-located aftershocks and composite fault-plane solutions for the New Brunswick earthquake sequence display a V-shaped distribution that flattens with depth. Wetmiller and others concluded that faulting occurred on conjugate fault planes. They

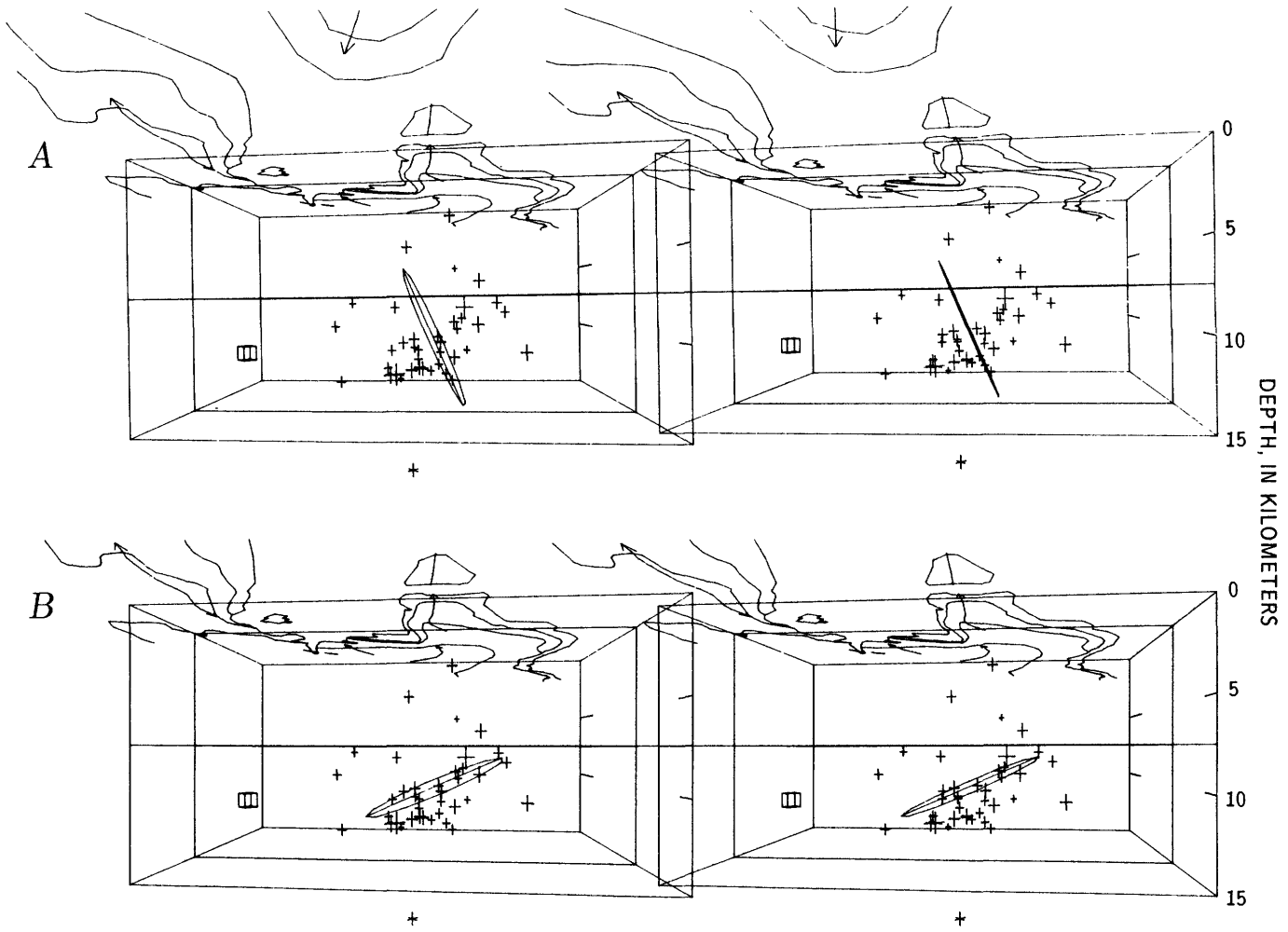

FIGURE 9.17.—Distribution of hypocenters and orientation of nodal planes for aftershocks in zones 1 and 2 during first 6 hours of the Coalinga earthquake sequence. *A*, A- to C-quality hypocenters shown with Eaton's (see chap. 8) northeast-dipping nodal plane for the main shock (circle). Main shock is shown centered on its hypocenter and is plotted with a 6-km radius. *B*, Same hypocenters, shown with southwest-dipping main-shock nodal plane.

inferred that the main shock ruptured only one of these planes and the largest (M=5.4) aftershock, 2 days later, ruptured the other. Teleseismic observation of the New Brunswick main shock is consistent with a single event source (Choy and others, 1983), in contrast to the Coalinga earthquake sequence, where we resolve a similar complex, V-shaped pattern of aftershocks but where local seismic and teleseismic observations favor multiple slip planes and a complex main-shock time function.

The similarities among the faulting models proposed for these earthquake sequences are illustrated in figure 9.18. The proposed mechanisms of graben formation at Corinth and of horst formation at Coalinga are geometrically identical. The dominance of diffuse seismicity in all four earthquakes is an expected consequence of the presence of nonconservative bends in the proposed main faults (King and Yielding, 1984).

CONCLUSIONS

Application of automated analysis to local earthquake data from the Coalinga earthquake sequence has produced a large suite of well-determined hypocenter locations and fault-plane solutions. These results have been interpreted as evidence for a complex faulting geometry for this earthquake sequence (fig. 9.11). The distribution of hypocenters and fault-plane orientations can be described by a set of planar or quasi-planar structures that we interpret as main-shock and secondary faulting surfaces. The rupture during the main shock was probably complex, with slip distributed on two (possibly, three) surfaces, each parallel to the axis of the Coalinga anticline but widely differing in dip. The first and greatest slip probably took place on a southwest-dipping plane, dihedral, or listric surface, with rupture propagating northwestward. Slip on a second, steeply northeast dipping plane is suggested by the aftershock pattern in zones 2 and 3. Delayed rupture toward the northwest on the north-south-striking Nuñez fault resulted in surface rupture on June 11. Complexities in the aftershock

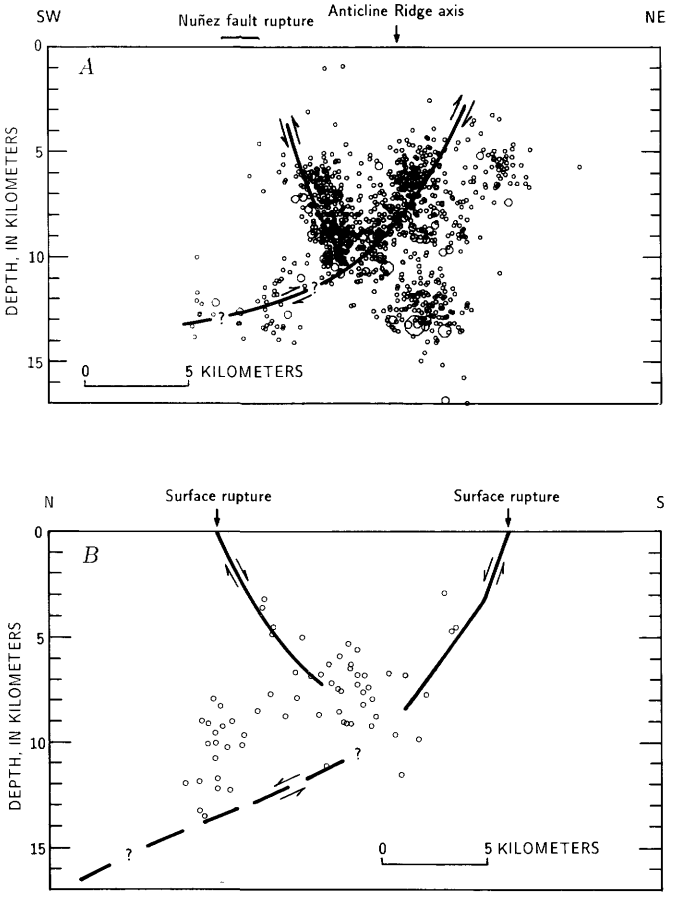

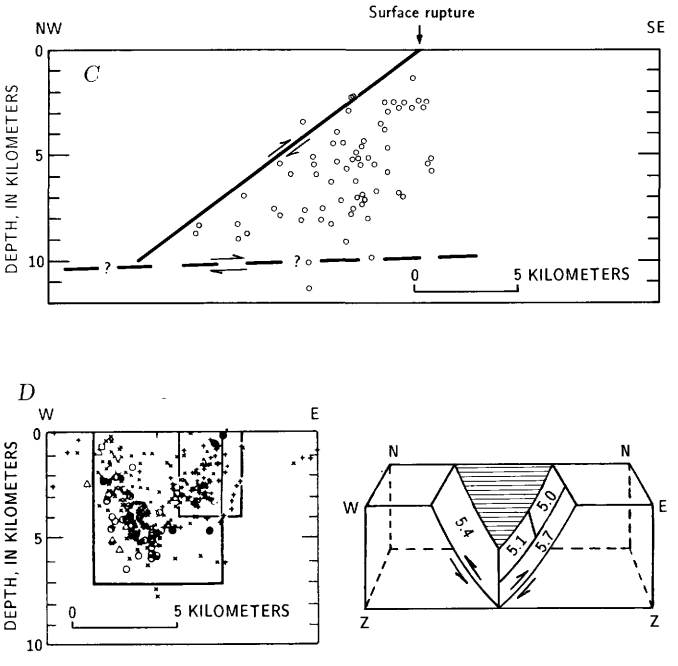

FIGURE 9.18.—Comparison of earthquake sequences for which listric or dihedral faulting surfaces are inferred. Arrows indicate inferred direction of motion. Question marks indicate planes of uncertain position or orientation. *A*, Vertical cross section showing well-located aftershocks in zone 2 (fig. 9.3*B*) for the Coalinga earthquake sequence. Solid line represents generalization of the faulting model shown in figure 9.13, in which plane B is represented by a listric surface. *B*, Well-located aftershocks and an inferred faulting model for the Corinth, Greece, earthquake sequence of February–March 1981 (after King and others, 1985). *C*, Aftershocks and inferred dihedral thrust fault for the El Asnam, Algeria, earthquake of October 1980 (adapted from Ouyed and others, 1983). *D*, Well-located aftershocks and proposed conjugate fault model for the 1982 Miramichi, New Brunswick, Canada, earthquakes (after Wetmiller and others, 1984). Boxes in plot indicate different time periods (large, January; small, April). E, east; W, west; Z, depth; numbers, magnitudes of earthquakes.

structure are qualitatively consistent with those predicted by a fractal model of faulting for the earthquake in which displacement on a simply bent or dihedral thrust is accompanied by antithetic reverse faulting adjoining the main thrust in the vicinity of the bend, and by diffuse shallow-angle thrusting surrounding the bend.

The two principal planes in the model may form a buried horst under the Coalinga anticline that is being uplifted by thrust and reverse-fault displacements on them. Coseismic elevation changes across the Coalinga anticline are qualitatively consistent with this model (R.S. Stein, oral commun., 1984). In general, inferred seismic deformation occurred primarily at depths below approximately 4 to 5 km, and folding was inferred to be largely confined to the upper 4 to 5 km of the crust. An exception is the upward extension of the northeast-dipping plane under Nuñez Canyon that resulted in surface rupture on June 11. Inferred secondary faulting on the northeastern limb of the anticline (Domengine cluster) is associated with bedding-plane slip there, as the newly disturbed Great Valley sequence folds in response to the faulting below. This change in style of deformation occurs at approximately 4- to 7-km depth, under the Coalinga anticline, with complex faulting below and passive folding above.

ACKNOWLEDGMENTS

This work would not have been possible without the careful and diligent effort of Mari Gunn Kauffmann, who processed and organized the voluminous data sets. We thank Mary Andrews for providing S–P intervals from the GEOS instruments. We also gratefully acknowledge many stimulating discussions with Jerry Eaton, Geoffrey King, Alan Lindh, Dave Oppenheimer, Paul Segall, Ross Stein, and Carl Wentworth. We benefited greatly from our participation in the 1984 Asilomar, Calif., conference on the Coalinga earthquake sequence, convened by Bill Ellsworth.

REFERENCES CITED

Allen, R.V., 1982, Automatic phase pickers: Their present use and future prospects: Seismological Society of America Bulletin, v. 72, no. 6, p. S225–S242.

Brown, R.D., Jr., Ward, P.L., and Plafker, George, 1973, Geologic and seismologic aspects of the Managua, Nicaragua, earthquakes of December 23, 1972: U.S. Geological Survey Professional Paper 838, 34 p.

Choy, G.L., Boatwright, John, Dewey, D.W., and Sipkin, S.A., 1983, A teleseismic analysis of the New Brunswick earthquake of January 9, 1982: Journal of Geophysical Research, v. 88, no. B3, p. 2199–2212.

Das, Shamita, and Scholz, C.H., 1981, Off-fault aftershock clusters caused by shear stress increase?: Seismological Society of America Bulletin, v. 71, no. 5, p. 1669–1675.

Eaton, J.P., 1985, The May 2, 1983 Coalinga earthquake and its aftershocks: A detailed study of the hypocenter distribution and of the focal mechanisms of the larger aftershocks, *in* Rymer, M.J., and Ellsworth, W.L., eds., Mechanics of the May 2, 1983 Coalinga earthquake: U.S. Geological Survey Open-File Report 85-44, p. 132–201.

Eaton, J.P., Cockerham, R.S., and Lester, F.W., 1983, Study of the May 2, 1983 Coalinga earthquake and its aftershocks, based on the USGS seismic network in northern California, *in* Bennett, J.H., and Sherburne, R.W., eds., The 1983 Coalinga, California earthquakes: California Division of Mines and Geology Special Publication 66, p. 261–273.

Eaton, J.P., O'Neill, M.E., and Murdock, J.N., 1970, aftershocks of the 1966 Parkfield-Cholame, California earthquake: A detailed study: Seismological Society of America Bulletin, v. 60, no. 4, p. 1151–1197.

Hamilton, R.M., 1972, Aftershocks of the Borrego Mountain earthquake from April 12 to June 12, 1968, *in* The Borrego Mountain earthquake of April 9, 1968: U.S. Geological Survey Professional Paper 787, p. 31–54.

King, Geoffrey, 1984, The accommodation of large strains in the upper lithosphere of the Earth and other solids by self-similar fault systems: The geometrical origin of *b*-value: Pure and Applied Geophysics, v. 121, no. 5–6, p. 761–815.

King, Geoffrey, and Nábělek, John, 1985, Role of fault bends in the initiation and termination of earthquake rupture: Science, v. 228, no. 4702, p. 984–987.

King, Geoffrey, and Yielding, Graham, 1984, The evolution of a thrust fault system: Processes of rupture initiation, propagation and termination in the 1980 El Asnam (Algeria) earthquake: Royal Astronomical Society Geophysical Journal, v. 77, no. 3, p. 915–933.

King, G.C.P., Ouyang, Z.X., Papadimitriou, P., Deschamps, A., Gagnepain, J., Houseman, G., Jackson, J.A., Soufleris, C., and Virieux, Jean, 1985, The evolution of the Gulf of Corinth (Greece): An aftershock study of the 1981 earthquakes: Royal Astronomical Society Geophysical Journal, v. 80, no. 3, p. 677–693.

Lee, W.H.K., and Lahr, J.C., 1975, HYPO71 (revised): A computer program for determining hypocenter, magnitude, and first motion pattern of local earthquakes: U.S. Geological Survey Open-File Report 75-311, 113 p.

Ouyed, M., Yielding, Graham, Hatzfeld, D., and King, G.C.P., 1983, An aftershock study of the El Asnam (Algeria) earthquake of 1980 October 10: Royal Astronomical Society Geophysical Journal, v. 73, no. 3, p. 605–639.

Reasenberg, Paul, 1980, Comparison of performance of automatic and human p-picking systems using a common data set [abs.]: Eos (American Geophysical Union Transactions), v. 61, no. 46, p. 1030.

Reasenberg, Paul, Eberhart-Phillips, Donna, and Segall, Paul, 1983, Preliminary views of the aftershock distribution of the May 2, 1983, Coalinga earthquake, *in* Borcherdt, R.D., ed., The Coalinga earthquake sequence commencing May 2, 1983: U.S. Geological Survey Open-File Report 83-511, p. 27–37.

Reasenberg, Paul, and Ellsworth, W.L., 1982, Aftershocks of the Coyote Lake, California, earthquake of August 6, 1979: A detailed study: Journal of Geophysical Research, v. 87, no. B13, p. 10637–10655.

Stein, R.S., 1983, Reverse slip on a buried fault during the 2 May 1983 Coalinga earthquake: Evidence from geodetic elevation changes, *in* Bennett, J.H., and Sherburne, R.W., eds., The 1983 Coalinga, California earthquakes: California Division of Mines and Geology Special Publication 66, p. 151–163.

Stein, R.S., 1985, Evidence for surface folding and subsurface fault slip from geodetic elevation changes associated with the 1983 Coalinga, California earthquake, *in* Rymer, M.J., and Ellsworth, W.L., eds., Mechanics of the May 2, 1983 Coalinga earthquake: U.S. Geological Survey Open-File Report 85–44, p. 225–253.

Stein, R.S., and Lisowski, Michael, 1983, The 1979 Homestead Valley earthquake sequence, California: Control of aftershocks and postseismic deformation: Journal of Geophysical Research, v. 88, no. B8, p. 6477–6490.

Wetmiller, R.J., Adams, J., Anglin, F.M., Hasegawa, H.S., and Stevens, A.E., 1984, Aftershock sequences of the 1982 Miramichi, New Brunswick, earthquakes: Seismological Society of America Bulletin, v. 74, no. 2, p. 621–653.

10. SOURCE PARAMETERS OF THE EARTHQUAKE, AS INFERRED FROM BROADBAND BODY WAVES

By GEORGE L. CHOY,
U.S. GEOLOGICAL SURVEY

CONTENTS

ABSTRACT

Source characteristics of the May 2 earthquake (m_b=6.2, M_s=6.7) have been determined from an analysis of teleseismic data that were digitally recorded by the Global Digital Seismograph Network. Broadband displacement and velocity records of *P* waves have sufficient frequency content to determine that the main shock was a complex rupture, consisting of two events that occurred about 3.2 s apart. By fitting the broadband-pulse shapes with synthetics, we find that the first event had a depth of 9.5 km and a predominantly thrust focal mechanism, with a strike of azimuth 300°, a dip of 65°,and a rake of 85°. The hypocenter of the second event had a depth of 5.6 km; the fault-plane solution, with a strike of azimuth 300°, a dip of 80°, and a rake of 80°, is similar to that of the first event. The moments of these two events are 1.9×10^{25} and 0.8×10^{25} dyne-cm, respectively. By inverting *P*-wave arrival-time differences at each station, the second hypocenter was located on a separate echelon fault southwest of the first hypocenter.

The surface projections of these faults bracket a substantial part of the aftershock zone. From an inversion of *P*-wave-pulse durations, the rupture geometries of each event could be estimated. The rupture geometries are nearly circular, with a radius of about 6.0 km for the first event and of 4.7 km for the second event. For an assumed circular rupture geometry, the static-stress drop of the first event is about 34 bars, and of the second event about 19 bars. An estimate of the dynamic-stress drop could be obtained only for the first event because of the waveform complexity. A lower bound for this parameter is 24 or 31 bars, depending on whether the steeply or shallowly dipping nodal plane is chosen as the fault plane. From inverting the energy flux in the velocity waveforms, the energy radiated by the earthquake is found to be 1.6×10^{21} dyne-cm, implying an average apparent stress of 18 bars.

The complexity of the main shock and aftershock sequence indicate that strain could have accumulated on a system of strongly interdependent faults. As the region became critically loaded, the effect of a major rupture was to critically stress faults adjacent to the initial nucleation. The ensuing stress release, which reflects the complexity of the fault system, occurred in both a rapid mode (the second event of the main shock) and a slow mode (the aftershock sequence).

INTRODUCTION

The use of theoretical seismograms to model teleseismically recorded body waves has significantly enhanced the ability of seismologists to describe the dynamics of the rupture process in earthquakes. Recent reports (for example, Choy and Boatwright, 1981; Choy and others, 1983) have demonstrated that broad-bandwidth data—with spectral information from several hertz to tens of seconds—can provide greater resolution of the rupture process. These reports demonstrated that variations in pulse shape about the focal sphere could be readily quantified and related to both dynamic and static properties of the source, including estimates of associated stress drops and the rupture geometry. The variations in pulse shape were relatively easy to quantify for the earthquakes studied in these reports because the direct phases of the events were well separated from depth phases. However, body waves generated by shallow earthquakes generally are not well separated. In the *P* waves from such earthquakes, the direct phase, surface-reflected phases, and phases arising from a complex source may all interfere with one another. The purpose of this chapter is to demonstrate that even for a shallow earthquake, broadband data can be used to great advantage in interpreting the dynamics of the rupture process.

As one example of such an analysis, this chapter describes the modeling of broadband body waves from the 2342:37.85 G.m.t. May 2, 1983, Coalinga earthquake (m_b=6.2, M_s=6.7). The teleseismically inferred source parameters are derived entirely from properties of the body waves. The resulting rupture history provides an independent complement to aftershock and strong-motion data for understanding this earthquake.

DATA PROCESSING

To study the rupture complexity of teleseismically recorded earthquakes, phase and amplitude information about and above the corner frequency is needed. For moderate-size earthquakes (that is, events of $5.5 \leqq m_b \leqq 6.5$), the frequency band of interest ranges from 0.1 to 5 Hz. Although such broadband data were not yet routinely recorded by any global network, they are obtainable by data-processing techniques in which seismograms from band-limited instruments at a single station are combined to give a record with an overall broadband response. Because of the difficulty in accurately preserving information at intermediate and high frequencies by hand digitization of analog records, data from the Global Digital Seismograph Network (GDSN) (fig. 10.1) are used. The high quality and digital format of these data permit easy and accurate retrieval of original broadband ground displacements and velocities by the recombination of long- and short-period seismograms. The method for the retrieval using GDSN data was described by Harvey and Choy (1982). A comparison of typical broadband data with conventional band-limited data is shown in figure 10.2. As seen in figure 10.2*A*, in comparison with the broadband displacement pulse (solid curve), the original long-period record (dashed curve) is significantly spread out in time, and the waveform is devoid of high-frequency details. Likewise, the original short-period record is compared with the broadband velocity record in figure 10.2*B*. By emphasizing energy in a narrow bandwidth near 1 Hz, short-period instruments commonly introduce a ringing appearance in seismograms that makes arrivals from a complex source or from depth phases very difficult to discern. The velocity records are generally better than the displacement records for identifying the onsets of arrivals. All the broadband P waves used in this study have a flat response to displacement or velocity between 0.02 and 5 Hz.

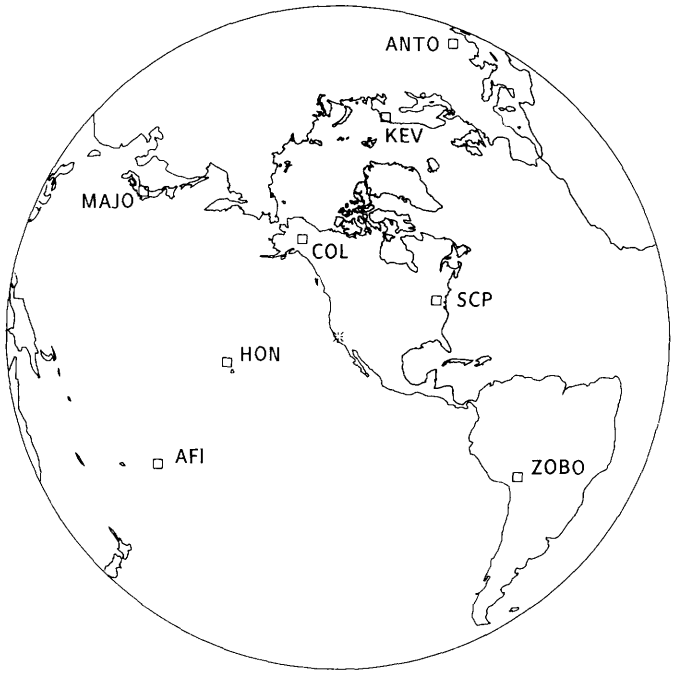

FIGURE 10.1.—Stations of the Global Digital Seismograph Network used in this study, plotted on an azimuthal equidistant projection centered on epicenter of the May 2 earthquake.

This analysis of the May 2 earthquake emphasizes the simultaneous use of broadband displacement and velocity to quantify source parameters. The P-wave data for the main shock (figs. 10.3–10.10) are shown in three ways: The top trace shows the original short-period recording, the next trace shows the broadband ground displacement, and the bottom trace shows the corresponding broadband ground velocity.

COMPUTATION OF BODY-WAVE SYNTHETICS

The basic procedure in inverting seismograms for details of the rupture is to compare the observed records of displacement with synthetics generated by a source model. This comparison is repeated until by trial and error the best possible fit to the suite of waveforms about the focal sphere is obtained. Observed body waves from a complex source are synthesized by a summation of simple sources. For a single shallow source, the far-field P wave may be written as the sum of the direct P wave and the depth phases:

$$u(x,t) = \frac{g_P(\Delta,t) * \Omega_P(x,t)}{R(\vartheta_P, \varphi_P)} + \frac{g_{pP}(\Delta,t-t_{pP}) * \Omega_{pP}(x,t)}{R(\vartheta_{pP}, \varphi_{pP})} + \frac{g_{sP}(\Delta,t-t_{sP}) * \Omega_{sP}(x,t)}{R(\vartheta_{sP}, \varphi_{sP})} \quad (1)$$

where $g_P(\Delta,t)$ is the propagation operator for a point source at a distance Δ for the direct P wave; $\Omega_P(x,t)$ is the undistorted body-wave-pulse shape radiated by the source toward a receiver at x; $R(\vartheta_P, \varphi_P)$ is the radiation-pattern coefficient for the body wave with takeoff angle ϑ_p relative to the fault normal and azimuth φ_p relative to the slip direction; g_{pP}, g_{sP} and Ω_{pP}, Ω_{sP} are the propagation and source operators, respectively, for pP and sP phases; and t_{pP} and t_{sP} are the delays of the depth phases. Note that equation 1 implies that the direct and surface-reflected pulses are expected to be sufficient to describe the rays radiated by the source to the receiver. The various crustal models that have been proposed for the Coalinga region (for example, Eaton and others, 1983; Fielding and others, 1983; Sherburne and others, 1983;

Walter and Mooney, 1983; Wentworth and others, 1983) indicate that the refractors which are present are either weak or inconsistent. Although most of these models use flat layers to represent the crust, the velocity-depth functions for Coalinga can be represented equally well by velocity gradients, as can be seen in the detailed model of Fielding and others (1983), which uses high-angle reflections from a Consortium for Continental Reflection Profiling (COCORP) signal source. These COCORP data indicate that the crust can consist of fine laminations, too small to be resolved by refraction data, rather than of thick layers with homogeneous velocities. Although the discretization of velocity gradients into layers is justified and useful for simplifying the inversion of traveltime data, it may be less appropriate for modeling waveforms. For teleseismic body waves propagating through the gradient at relatively steep angles of incidence, no significant secondary arrivals would be generated. For body waves propagating through discretized velocity models, synthetic broadband seismograms computed by the reflectivity method (R. Kind, oral commun., 1985) show that our analysis remains unaffected. Significant reverberations would not arrive until after the time window in which the broadband body waves have already radiated most of their energy. (The duration of this window, as discussed in the next section, is about 12 s.)

For body waves recorded between approximately $30° < \Delta < 90°$, the effects of propagation consist primarily of geometric spreading and attenuation. The propagation operator here is computed by using the full-wave method (Richards, 1973; Choy, 1977; Cormier and Richards, 1977). For Earth structure, the Jeffreys-Bullen (JB) Earth model is used except near the source. Near the source, the velocity profile at the intersection of lines 1 and 3 in the COCORP study by Fielding and others (1983) is used. The COCORP model, derived from high-angle-reflection data, is probably more applicable to modeling teleseismic waveforms than are models derived from refraction data. The attenuation operator must be both frequency-dependent and dispersive to remain valid over the broad bandwidth of frequencies to be modeled. The t^* operator used here, from Choy and Cormier (1986), ranges from 1.0 s at 0.1 Hz to 0.4 s at 2.0 Hz.

The crustal response at the receiver can easily be calculated by using the matrix method of Haskell (1962), but it is unnecessary in this analysis. At teleseismic distances (more than 30°), the angles of incidence are very steep. For most commonly used Earth models (where there are no high-impedance velocity contrasts other than the crust-mantle interface), crustal reverberations on the vertical-component seismograms are unimportant. Models with intracrustal low-velocity layers, which have been suggested for some anomalous stations (Rial and Brown, 1983), predict a significant arrival about 15 s after the first P-wave arrival. This late arrival may have to be considered in long-period and moment-tensor inversions because, owing to the phase response of typical long-period seismographs, rather long time windows must be processed, even for a simple impulse response. The broadband body waves of the May 2 earthquake, however, have a typical duration of about 12 s (figs. 10.2–10.10).

The source pulse is a triangular function. The depth phases are not constrained to have the same time function as the direct body wave because for any given station, P, pP, and sP phases generally have different takeoff angles with respect to the fault plane. Any significant variation in the pulse durations can be used to constrain the source geometry (Boatwright, 1984).

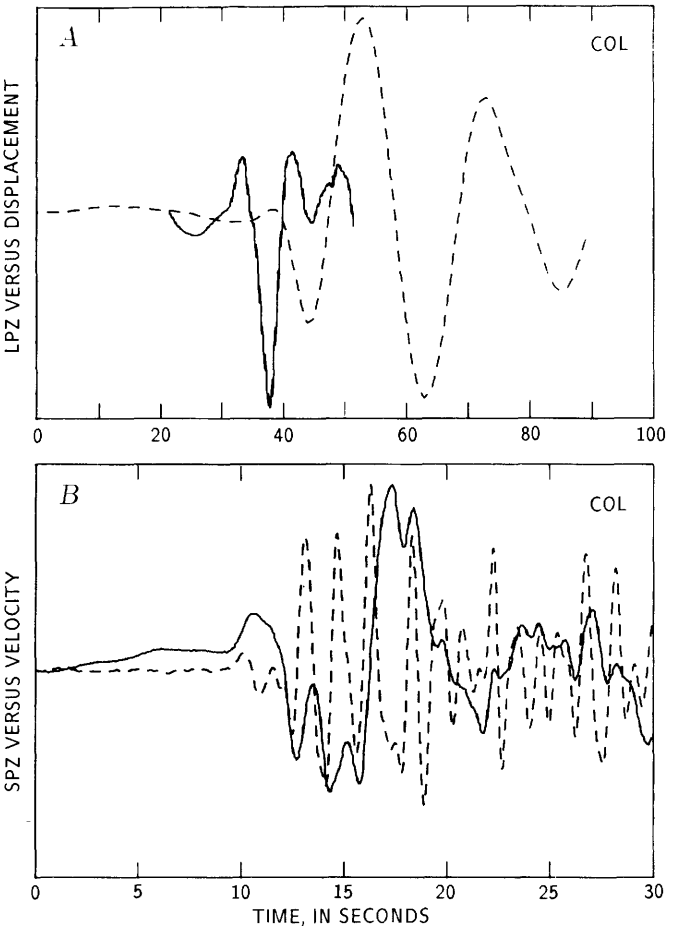

FIGURE 10.2.—Station COL of the earthquake. *A*, Digitally recorded long-period, vertical-component P-wave (LPZ) record (dashed line); broadband-displacement record (solid line) is shown for comparison. Apparently later arrival of long-period P wave is due to strong phase delay in long-period instrument response. Nyquist frequency of broadband record is 10 Hz. *B*, Short-period P-wave (SPZ) record (dashed line); broadband velocity record (solid line) is shown for comparison. Note different time scale from figure 10.2.*A*.

For a complex earthquake, the synthetics are obtained by summing several simple sources, lagged in time to account for the different traveltimes of spatially separated foci. Although this strategy is similar to that used in other analyses of earthquakes (for example, Langston and Helmberger, 1975; Rial, 1978), the major difference here is the emphasis on analyzing *broadband* displacements rather than long-period records.

DATA ANALYSIS

SEISMOGRAM SYNTHESIS

First, the broadband waveforms are modeled with a single source. If the best synthetic waveforms still disagree systematically with the data, waveforms from additional events are superimposed on the data until it is clear that the fit between observed and synthetic records can no longer be improved. For the May 2 earthquake, two rupture events are required to satisfy the complexity in the observed waveforms. The focal mechanisms of the two events are shown in figure 10.4, along with the velocity waveforms used to derive the rupture histories. To illustrate the procedure used to model the earthquake, the construction of the synthetic for the displacement at station COL is detailed below. The same procedure is followed for the construction of the synthetic displacements at the other stations.

The first step is to model the observed displacement with the best fitting single source, using a focal mechanism consistent with observed P-wave first motions. As shown in figure 10.5*A*, the first-motion data are sufficient to clearly define one nodal plane. Resolution of the rake requires additional information that can be provided by seismogram synthesis of the observed interference pattern of P, pP, and sP phases at the GDSN stations. This synthesis requires some knowledge of the depth of the event and the time function of each body wave. These constraints are detailed here for the displacement pulse at station COL; the analysis is similar for the data at the other stations.

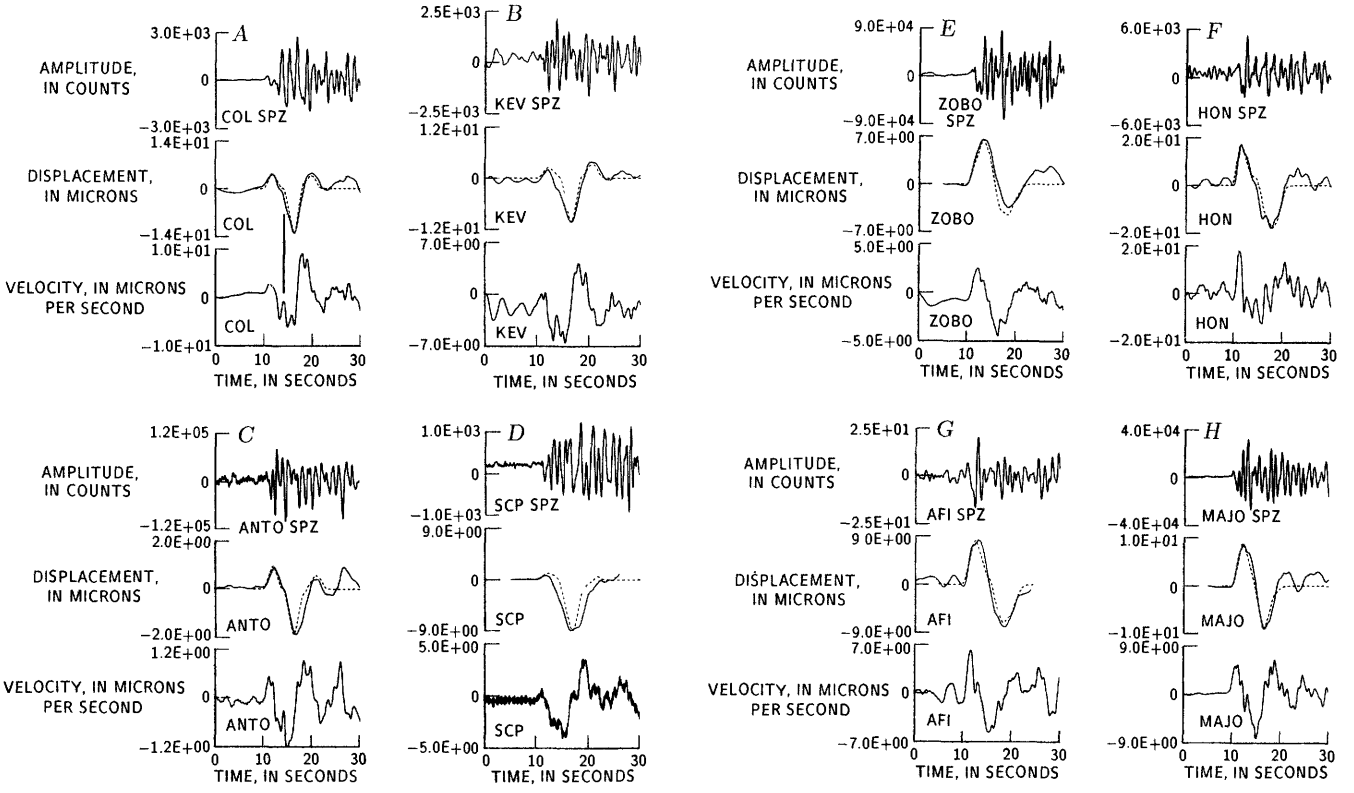

FIGURE 10.3.—Broadband data of the earthquake. *A*, Station COL. Upper record, original short-period P-wave record (Δ= 33.1°, θ= 338.9°). Middle records, broadband ground displacement (solid line); response is flat to displacement from 0.02 to 5 Hz. Dashed line is a synthetic, shown in greater detail in figure 10.6. Bottom record, broadband ground velocity. Inflection in displacement record is a strong pulse in velocity (vertical line), interpreted as onset of pP phase. *B*, Station KEV (Δ=71.7°, θ=11.4°). *C*, Station ANTO (Δ=100.3°, θ=20.7°). *D*, Station SCP (Δ=33.3°, θ=69.0°). *E*, Station ZOBO (Δ=71.8, θ=127.0). *F*, Station HON (Δ=36.0°, θ=256.0°). *G*, Station AFI (Δ= 69.6°, θ=234.1°). *H*, Station MAJO (Δ=77.3°, θ=306.0°).

The first positive pulse of the station COL displacement (fig. 10.3*A*) is interpreted as the direct *P* wave from the first event; this pulse corresponds to the first cycle in the velocity record. Because the velocity pulse is nearly complete, the triangular function approximating the *P* wave is well constrained. Before the *P*-wave-velocity pulse completely returns to the zero baseline, it is reversed by a sharp negative pulse (vertical line, fig. 10.3*A*). This sharp pulse can be seen at about 4.0 to 4.2 s behind the initial *P*-wave arrival across the entire suite of velocity records, except possibly at stations HON and AFI, where microseism levels are rather high. Identifying this arrival as a *pP* phase yields a depth of 9.5±9.6 km. The corresponding *sP* phase should arrive 5.8 s after the *P* wave. Although we expect this phase to be masked by the *pP* waveform, some energy is visible on the velocity records at the appropriate time at several stations (COL, KEV, SCP, MAJO, AFI).

At this point, we have the following information. Knowing the depth, we know the arrival time of *sP*, as well as of *pP*; knowing the strike, dip and, to a lesser extent, the rake of the focal mechanism, we know fairly well the relative amplitudes of the body waves; and we know the time function of *P* very well. To proceed with the modeling, we impose an a priori constraint on the duration of the *pP* and *sP* displacement pulses: Their durations must be less than or nearly equal to the duration of the *P* wave. This constraint corresponds to the physical condition that the direction of rupture is upward rather than downward. Note that the depth of the main shock is near the bottom of the zone defined by the aftershocks (see chap. 8).

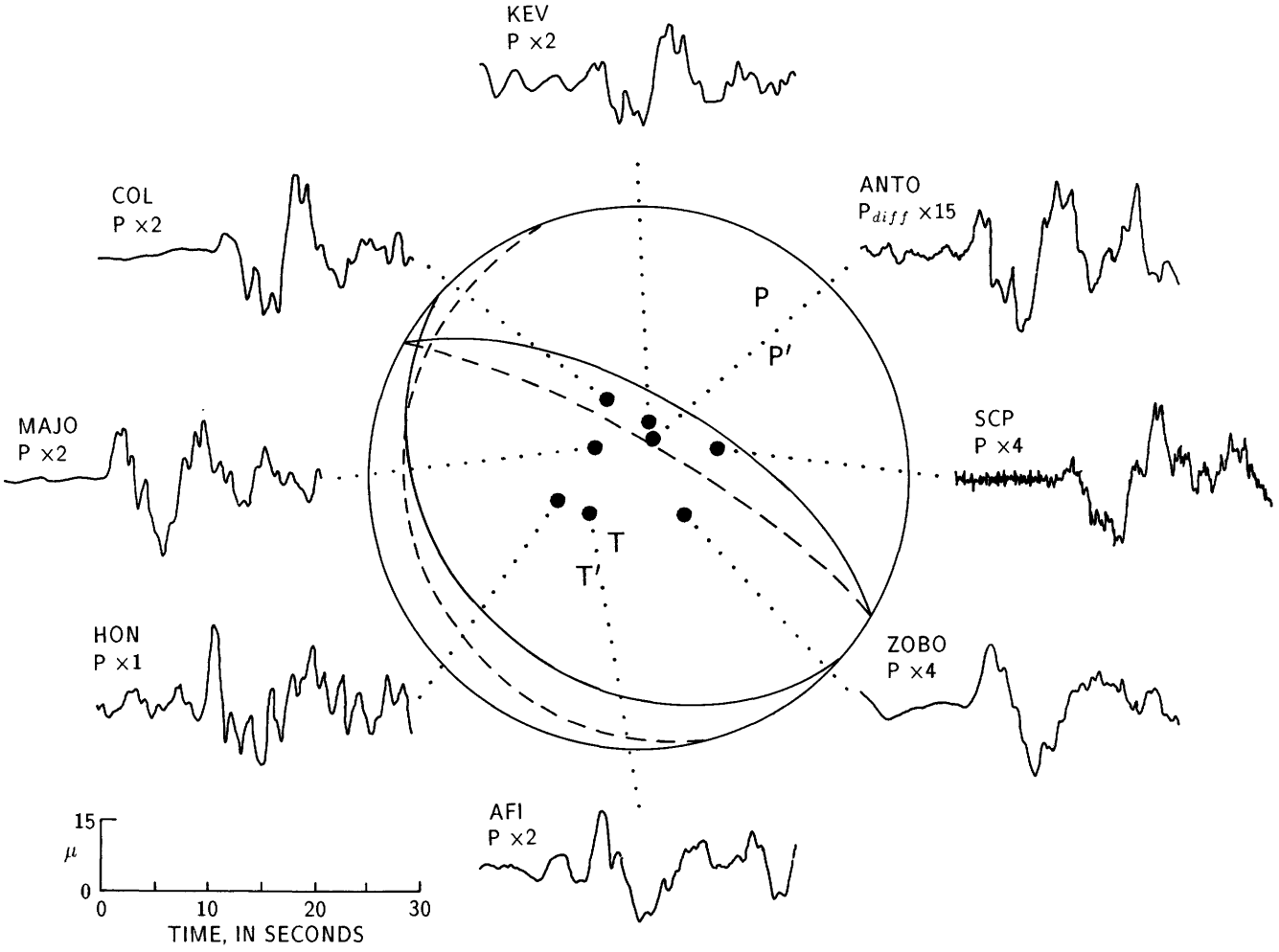

FIGURE 10.4.—Lower-hemisphere projection of focal mechanisms of the two rupture events composing the main shock. Strike, dip, and rake of first event (solid lines) are 300°, 80°, and 80°, respectively. Distributed about the focal sphere are the velocity waveforms used in the analysis. Takeoff angles of four stations (COL, KEV, ANTO, SCP) are well located to provide constraints on change in dip of steeply dipping nodal planes.

The best fit to the displacements that can be obtained by using a single rupture event has a focal mechanism with a strike of azimuth 300°, a dip of 65°, and a rake of 85°. The uncertainties in strike and dip are constrained to better than ±5° by the relative amplitudes and polarities of the *P* and *pP* waveforms, with takeoff angles in the proximity of the steeply dipping nodal plane. The uncertainty in rake is ±10°. Rake is constrained by the amplitudes and polarities of the *sP* phases, which have takeoff angles near a nodal line of the *SV*-radiation pattern (fig. 10.5*B*); the rake is also constrained by the first motions of the digitally recorded long-period *SH*

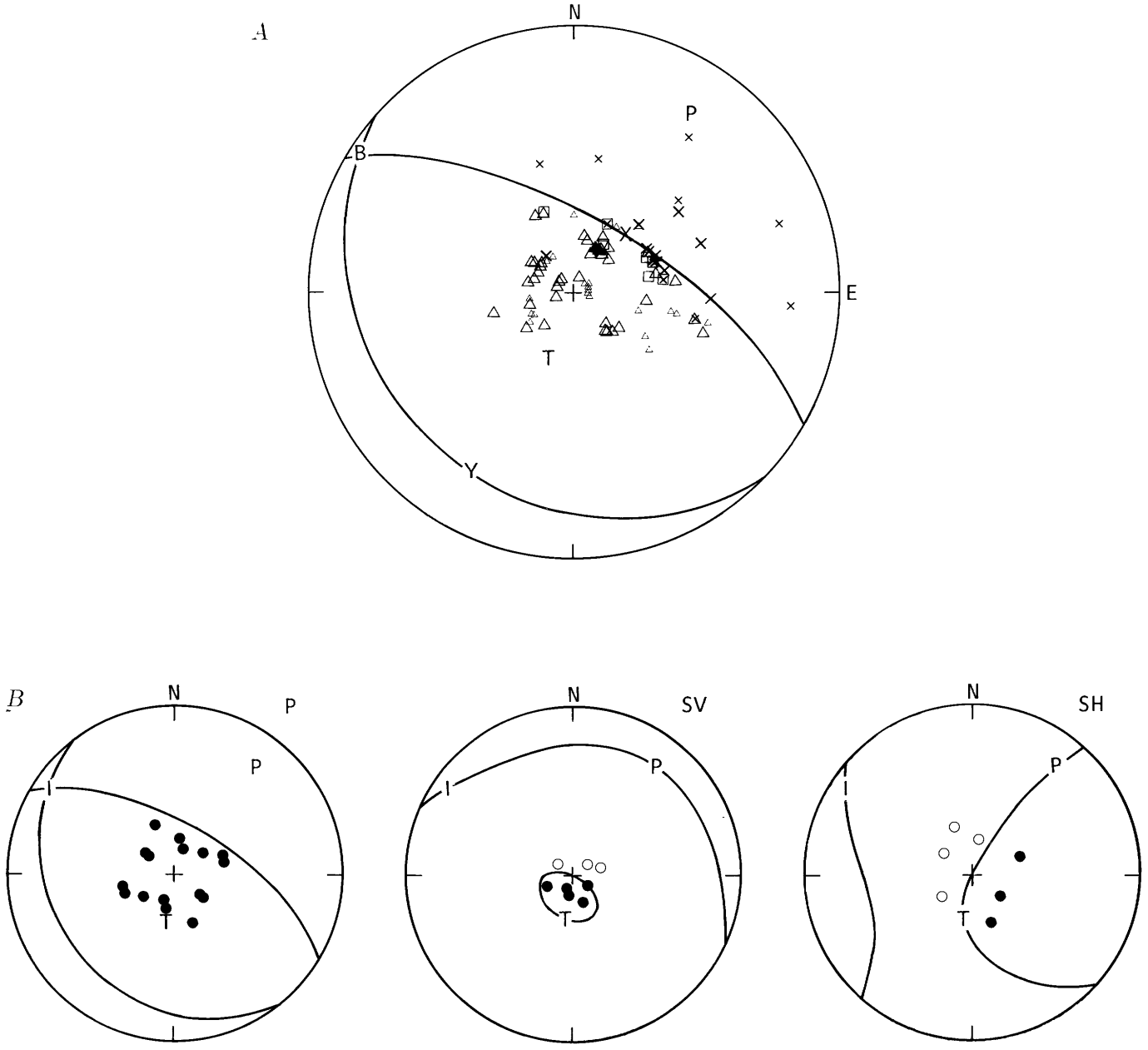

FIGURE 10.5.—May 2 earthquake. *A*, Lower-hemisphere projection with first motions of teleseismically recorded *P*-wave data (R.E. Needham, written commun., 1983) for the May 2 earthquake. Triangles, compressions; X's, dilatations; squares, nodal readings. First-motion data are insufficient to constrain shallowly dipping fault plane. Nodal planes are those of first rupture event. *B*, *P*, *SV*, and *SH* radiation patterns for focal mechanism of the first rupture event of the May 2 earthquake. Polarities are indicated by solid circles (compression) or open circles (dilatation). Both *P*- and *pP*-phase takeoff angles used in the analysis are plotted on focal sphere for *P*-wave-radiation pattern. *sP*-phase takeoff angles are plotted in *SV* projection. Polarities of first-motion *SH* body waves read from rotated long-period GDSN records are indicated in *SH* pattern.

body waves. The moments and time functions derived from the body waves for each station are listed in table 10.1. The average weighted moment for the source is 1.9×10^{25} dyne-cm. Before we describe the extent to which we can derive other source parameters, such as stress drop and rupture geometry, we must complete our analysis of the waveforms.

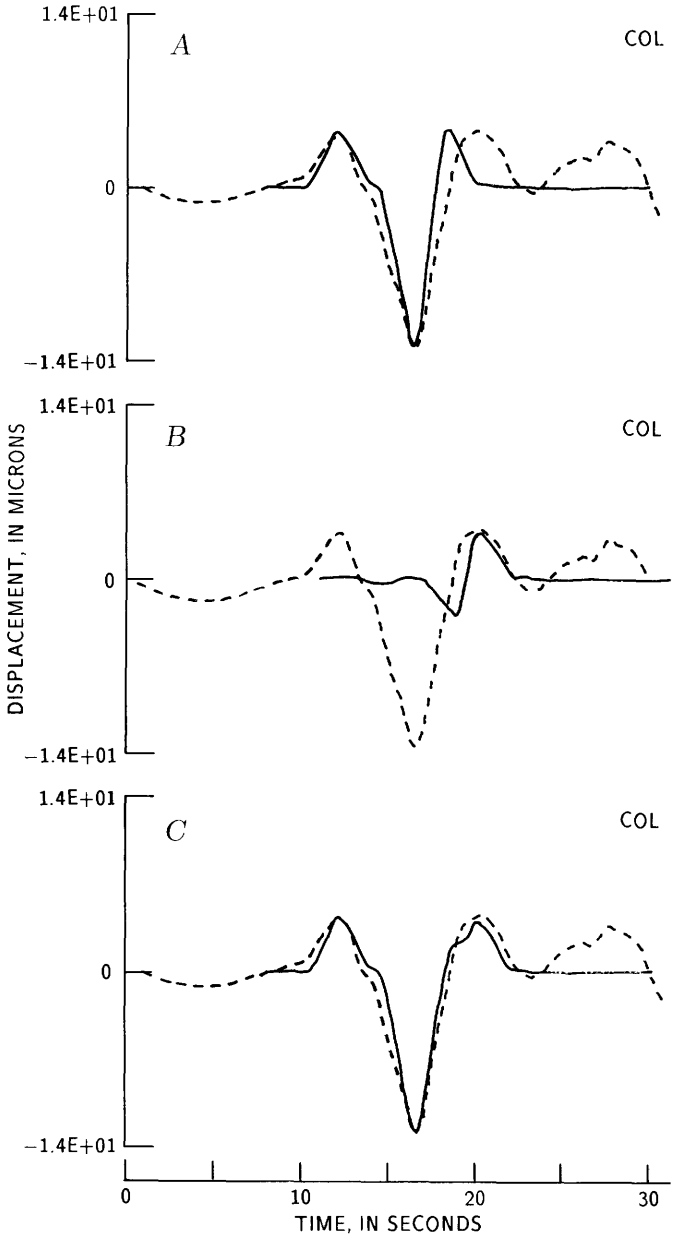

FIGURE 10.6.—Example of construction of synthetic displacement records, using P wave at station COL. Dashed line, observed displacement; solid lines, synthetic waveforms. A, Best fit for a single rupture that satisfies initial part of waveform. It does not, however, match last (positive) backswing. B, Synthetic pulse shape of best fitting second event, obtained through forward modeling. C, Sum of synthetic waveforms compared with actual displacement waveform.

A typical fit, using the single-rupture-event model, is shown in figure 10.6A for station COL. The first cycle of displacement, consisting predominantly of P and pP phases, is fitted rather well. However, there is a large discrepancy in the match of the last (positive) backswing of the synthetic and observed waveforms, which is dominated by the sP-phase contribution. The peak in the last backswing of the synthetic arrives earlier than the corresponding peak on the actual record. The total duration of the synthetic displacement is also much shorter than that of the observed waveform. As previously discussed, neither receiver structure nor source structure is likely to account for such a discrepancy. Association of this feature of the waveform with the rupture process is further corroborated by an examination of body waves from the largest aftershock of the May 2 earthquake (0239:53.7 G.m.t. July 22, 1983; m_b=6.0). Its location is very well constrained by data from the

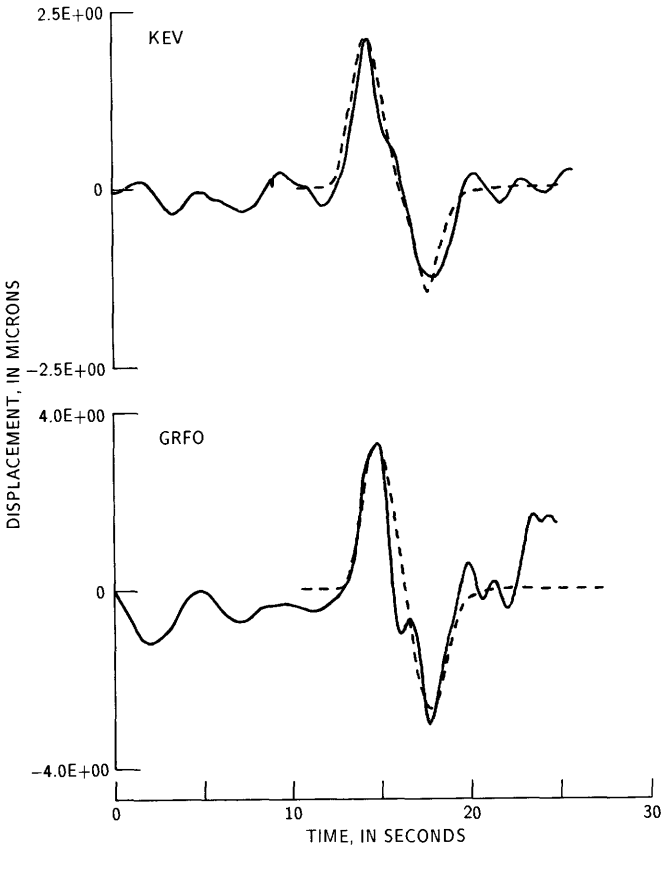

FIGURE 10.7.—Broadband P-wave displacements (solid lines) from aftershock of July 22, 1983, at stations KEV and GRFO. The data are easily matched by synthetics (dashed lines) employing one rupture event. Focal mechanism used in the synthetics has a strike of azimuth 340°, a dip of 45°, and a rake of 90°; best fitting depth is 9.5 km.

northern California network to be within 9 km of the main-shock epicenter (see chap. 8). In contrast to the main shock, the two displacement waveforms available for this event can easily be modeled by using a single source (fig. 10.7) with a focal mechanism that agrees with the *P*-wave first-motion data from local and teleseismic data (see chap. 8; R.E. Needham, written commun., 1984). One of the stations, KEV, recorded both the main shock and the aftershock. The *P* waves of these two earthquakes would have traversed nearly identical propagation paths to that station. Thus, the large difference in the *P* waves generated by the two earthquakes must arise from different properties of the rupture processes. We also note that long-period waveform inversions require significant complexity for the main shock. The moment tensor solution has a 28-percent non-double-couple component (see chap. 11).

In describing how the second rupture event is modeled, refer again to figure 10.6. The synthetic seismogram in figure 10.6*A* is the waveform predicted by the best fitting single-rupture event. We cannot merely double the duration of the synthetic *sP* phase just to match the duration of the observed wavetrain. As noted previously, an *sP*-phase duration twice that of the *P*-phase duration implies a rupture that proceeds in the unlikely downdip direction. Furthermore, to conserve moment, stretching the duration would require halving the amplitude of the displacement pulse. The resulting synthetic fits the data very poorly. Instead, we strip the synthetic displacement from the observed record; then, we proceed to fit a second rupture event to the rest of the waveform. The synthetic waveform that best fits the data at station COL is shown in figure 10.6*B*. The sum of the synthetics from the two rupture events is the final synthetic (fig. 10.6*C*). The second event has a strike of azimuth 300°, a dip of 80°, and a rake of 80°; the depth of nucleation is 5.6 km. The moments, time functions, and delay times with respect to the initial *P*-wave arrival at each station for the second event are listed in table 10.1. The average weighted moment of the second event is 0.8×10^{25} dyne-cm.

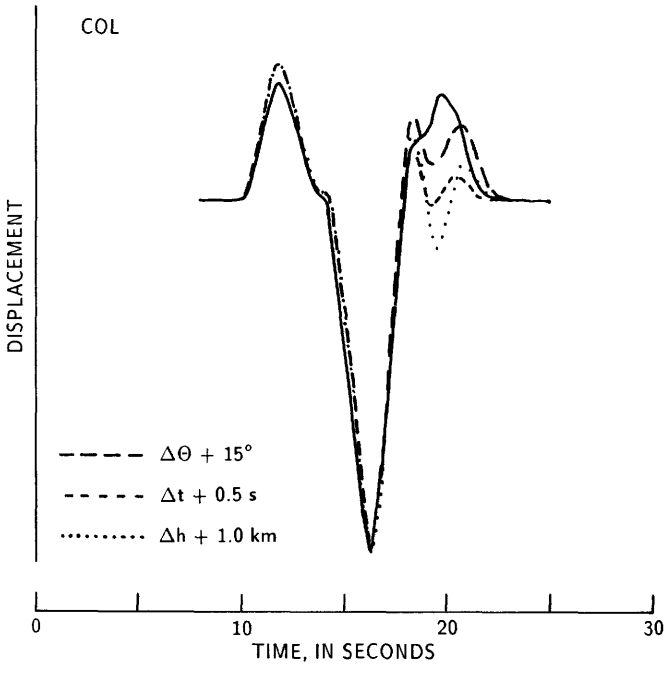

FIGURE 10.8.—Sensitivity of waveforms to perturbations of source parameters of second event. Synthetic displacements for station COL are computed by using the source parameters of the first event but perturbing the source parameters of the second event. Solid line, synthetic that best fits the data. The other synthetics are computed by using the parameters of the best fitting second event but in each case changing one parameter. Lines shown are for a change in depth of +1 km (dotted), in delay time of +0.5 (short dashed), and in strike of +15° (long dashed).

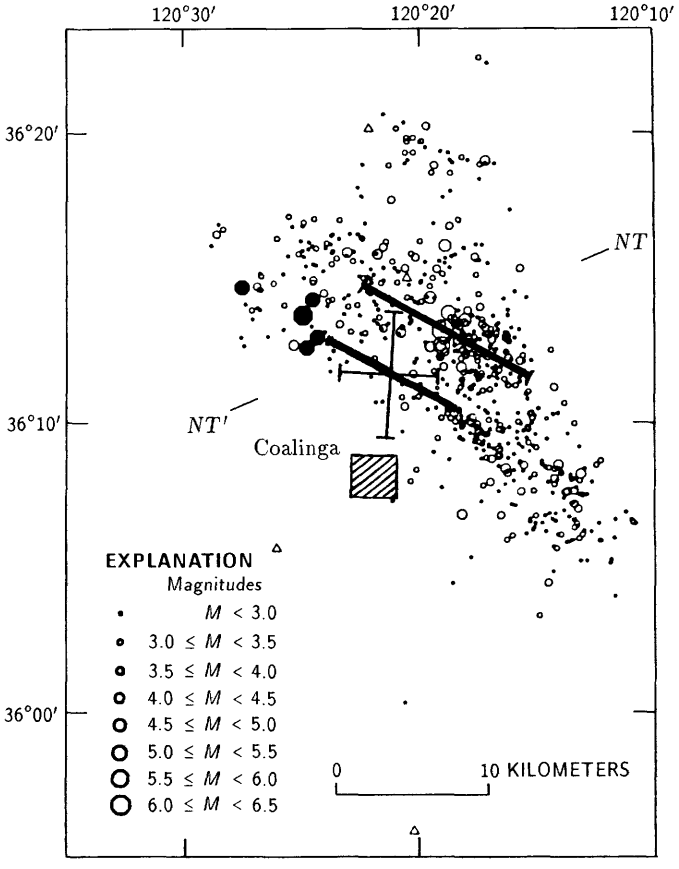

FIGURE 10.9.—Sketch map of Coalinga area, showing locations of epicenters of the May 2 earthquake and aftershocks of m_b>2.5 from May 2 through July 31 (from Eaton and others, 1983). Fault lengths of the two events of the main shock (heavy lines) are projected to the surface. Location-error ellipse of second event is indicated by error bars. Large solid circles, epicenters of some large aftershocks associated with the Nuñez fault. Triangles, seismograph stations. See figure 10.10 for cross section *NT*′–*NT*′.

TABLE 10.1.—*Time functions of P, pP, and sP phases at each station for each event of the main shock*

[The first value is the rise time; the second value (in parentheses) is the total duration. Delay times given for event 2 are differences in arrival time between the onsets of the second P wave with respect to the first P wave]

Station	Time function (s)			Moment (10^{25} dyne-cm)	Delay time (s)
	P	pP	sP		
			Event 1		
COL	1.6 (3.6)	1.8 (3.6)	1.8 (3.6)	1.6	---
KEV	1.6 (3.8)	1.9 (3.8)	1.9 (3.8)	1.9	---
ANTO	1.8 (3.8)	1.9 (3.8)	1.9 (3.8)	1.1	---
SCP	2.0 (4.5)	2.5 (4.5)	2.5 (4.5)	.8	---
ZOBO	3.0 (4.5)	3.0 (4.0)	3.0 (4.0)	1.6	---
HON	1.2 (3.7)	1.8 (3.7)	1.8 (3.7)	1.8	---
AFI	2.1 (4.2)	2.1 (4.2)	2.1 (4.2)	2.4	---
MAJO	2.0 (4.3)	2.0 (4.3)	2.0 (4.3)	2.3	---
			Event 2		
COL	1.7 (3.4)	1.7 (3.4)	1.7 (3.4)	0.8	4.2
KEV	2.0 (2.2)	2.0 (4.0)	2.3 (4.0)	4.0	4.1
ANTO	2.0 (4.0)	2.0 (4.0)	2.0 (4.0)	.5	4.2
SCP	2.5 (4.0)	2.5 (5.0)	2.5 (5.0)	2.0	4.0
ZOBO	2.0 (4.0)	2.0 (4.0)	2.0 (4.0)	.6	4.0
HON	1.5 (3.0)	1.5 (3.0)	1.5 (3.0)	.6	3.5
AFI	2.0 (4.0)	2.0 (4.0)	2.0 (4.0)	1.1	3.6
MAJO	1.8 (3.6)	1.8 (3.6)	1.8 (3.6)	.9	3.6

Although the uniqueness of the parameters describing the second event is not easy to quantify, one measure is the difficulty in finding other solutions that match the waveform. Figure 10.8 compares the best fitting waveform for station COL with synthetics computed by using slight perturbations in the source parameters of the second event. These perturbations are for a change in depth of 1 km, a change in delay time relative to the first event of 0.5 s, and a change in strike of 15°. The sensitivity of the synthetics to these perturbations is evident. In addition, the final solution must satisfy all of the waveforms distributed about the focal sphere (fig. 10.4) with takeoff angles and azimuths that straddle both sides of a *P*-nodal plane and an *SV*-nodal line. On the basis of synthetics computed for perturbations of this solution, we estimate uncertainties in depth at ±0.8 km, in strike and dip at ±5°, in rake at ±15°, and in delay time at ±0.3 s.

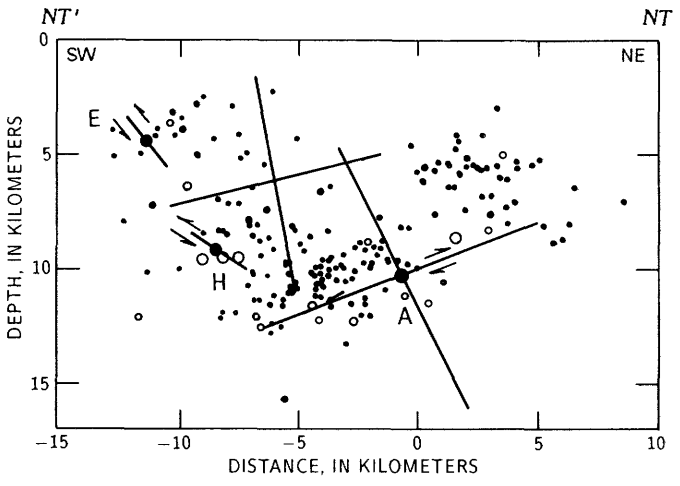

FIGURE 10.10.—Vertical cross section of seismicity data for May 2 to July 31, 1983, in northern part of figure 10.9 (modified from Eaton and others, 1983). Solid lines, fault lengths of steep and shallow nodal planes for the two events; arrows, directions of relative movement. Location of first event is hypocenter of the main shock (dot A) from Eaton and others. Events E and H are relatively large aftershocks related to the Nuñez fault. Note that there is some distortion because the azimuth of the cross section (line *NT–NT'*, fig. 10.9) is not quite perpendicular to the strike of fault planes of the main shock.

The location of the hypocenter of the second event relative to that of the first event can be computed by inverting the *P*-wave arrival-time differences at each station. Typical inversion techniques were discussed by Spence (1980). The location and axes of the error ellipse are shown in figure 10.9. The hypocenter is significantly to the southwest of the first event. The analysis here has also shown that the second hypocenter was shallower. The second event occurred 3.2 s after the first event. (Note that the *P*-wave delays listed in table 10.1 are between 3.5 and 4.2 s; the variation is due to both the azimuth of a particular station and the difference in depth between the events.) The extent of the vertical and lateral separation in hypocenters indicates that the events occurred on separate fault planes, regardless of whether rupture occurred on the steep or shallow set of nodal planes. In the next section, the computation of some source parameters (namely, dynamic-stress drop and rupture geometry) requires that a fault plane be chosen. Where this choice is necessary, the parameters are computed for both possibilities.

CHARACTERISTICS OF THE RUPTURE PROCESS

ASSOCIATED STRESSES AND RADIATED ENERGY

Assuming that an event grows as a self-similar crack, the dynamic-stress drop can be measured from the initial slope of the velocity waveforms, using the relation given by Boatwright (1980):

$$\tau_e = \frac{[\rho(\xi_0)\rho(x)c(x)]^{1/2}c(\xi_0)^{5/2}}{C(v/\beta)v^2\beta(\xi_0)}\left[\frac{R(\xi_0,x)}{F(\vartheta,\varphi)}\right](1-\zeta^2)^2\left[\frac{\dot{u}(x,t)}{t}\right] \quad (2)$$

where ρ and c are the density and wave velocity at coordinates ξ_0 and x, the source and receiver coordinates, respectively; $C(v/\beta)$ is the Kostrov function; v is the rupture velocity; β is the shear-wave velocity; $\xi = v \sin \vartheta / c(\xi_0)$, where ϑ is the takeoff angle relative to the fault normal; $R(\xi_0,x)$ is the ray-theory coefficient describing the geometric spreading between source and receiver, including appropriate free-surface corrections; and F is the radiation-pattern coefficient for the body wave, with a takeoff angle relative to the fault normal and an azimuth relative to the slip direction. The last term in brackets is the average initial slope after correcting for attenuation.

Because of the complexity of the rupture, only the slope of the P wave of the first event can be measured. The dynamic-stress drop of the second event cannot be estimated. Using the direct P waves, we obtain a dynamic-stress drop of 24±16 or 31±16 bars, depending on whether the steeply or shallowly dipping nodal plane is chosen as the fault plane, respectively. However, because the takeoff angles of the direct P waves sample only a small solid angle of the focal sphere in a downdip direction, these values of dynamic-stress drop should be considered minimum estimates. The effect of sampling a rupture in the direction away from the direction of rupture is to bias the estimate of stress drop to a smaller value.

Where the velocity pulses of P, pP, and sP phases are not well separated, the expression relating radiated energy to the energy flux of the P-wave group is given by Boatwright and Choy (1986) as

$$E_s = \frac{8\pi}{5}(1+q)\left(\frac{R^P}{F^{gP}}\right)I^* , \qquad (3)$$

where I^* is the integral of the velocity squared of the P-wave group, corrected for attenuation; R^P is the P-wave geometric spreading factor; q is the ratio of S-wave to P-wave energy, taken to be 13.5 (Boatwright and Fletcher, 1984); and F^{gP} is the generalized radiation-pattern term, defined as

$$F^{gP} = (F^P)^2 + (F^{pP})^2 + \frac{2q}{3}\left(\frac{\alpha}{\beta}\right)(F^{sP})^2 , \qquad (4)$$

where the F^i are the radiation-pattern coefficients, corrected for free-surface reflection if necessary, for $i = P$, pP, and sP. For dip-slip motion on a 65°-dipping fault plane, F^{gP} varies only weakly with changes in the mechanism. The energy radiated by the earthquake is $1.6\pm0.3\times10^{21}$ dyne-cm.

The apparent stress can be computed by using $\tau_a = \mu E_s/M_0$ (Wyss and Brune, 1968), where μ is the average rigidity at the hypocenter. The average apparent stress for the earthquake, computed from the total radiated energy and total moment, is 18 bars.

RUPTURE GEOMETRY

Displacement pulses about the focal sphere can be used to invert for the rupture geometry of each event. If the fault plane and rupture direction for each event are known, we can employ a simplification of the method used by Boatwright (1984). The rise time [or rupture phase of Boatwright's (1980) rupture model] is first corrected for attenuation. We then minimize the χ^2 error

$$\chi^2 = \sum_{i=1}^{N} \frac{[\tau_i - (1-e)\tau_c(a/v) - e\tau_u(a/v, \varphi_r)]^2}{\sigma_i^2} , \qquad (5)$$

where τ_i and σ_i are the durations of the rupture phase and its standard deviation, respectively, measured from N body-wave arrivals; e is the percentage of unilateral rupture; $\tau_c(a/v)$ is the pulse duration expected from a circular rupture of radius a and rupture velocity v; and $\tau_u(a/v, \varphi_r)$ is the pulse duration expected from a unilateral rupture of length a in the direction φ_r. Formulas for τ_c and τ_u are derived in the appendix to the report by Boatwright (1984). We assume a rupture velocity of 0.75β. For a particular rupture direction, the best fitting rupture length and percentage of unilateral rupture can be computed from equation 5. The rupture half-width is estimated from the rupture length and percentage of unilateral rupture as

$$w = \frac{a[1 + (1-e^2)^{1/2}]}{2(1+e)} . \qquad (6)$$

The static-stress drop is then estimated as

$$\Delta\sigma = \frac{1+e}{2aw^2} M_0 . \qquad (7)$$

Any directivity in the waveforms that may have enabled us to favor one nodal plane over another as the fault plane for either event is masked by interference of the waveforms. Thus, we estimate the source dimensions by carrying out the inversion for both the steeply and shallowly dipping nodal planes of the mechanism for each event. We also do not know a priori the direction of rupture. However, the main shock is located in the midst of the aftershocks laterally, though deeper than most of the aftershocks (see chap. 8). For each possible fault plane, we compute the best fitting source geometries for a suite of directions ±60° from the updip direction.

For the first event, the rupture geometry is independent of the choice of fault plane and the direction of rupture. The best fitting rupture geometries for either plane for directions ±60° about the updip direction are all approximately circular, with a rupture radius of 6.0±2.0 km. The corresponding static-stress drop, assuming either nodal plane as the fault plane, is 34 bars. Seismic slip can be estimated at 52 cm from $d = M_0/\mu A$, where μ is the rigidity (3.2×10^{11} dyne-cm) and A is the rupture area.

The inversion for the rupture geometry of the second event is significantly less certain than for that of the first event because the durations of the P waves are inferred and not directly measured. We can only obtain an idea, albeit crude, of the rupture length by making an arbi-

trary assumption about the rupture geometry. Assuming, for example, that the geometry is circular, we obtain a radius of 4.7±2.0 km, a static-stress drop of 19 bars, and a slip of 36 cm. As for the first event, the source radius is basically unchanged whether the steeply or shallowly dipping nodal plane is used as the fault plane. Because no surface faulting was found for the main shock (Clark and others, 1983), the source radius is probably smaller. Note that the uncertainty in fault length is about 40 percent. The source radius can also be reduced if a smaller rupture velocity is assumed, as is possible for secondary or triggered events, which may have released stress less coherently than the initial event.

In plan view, the aftershock zone (see chap. 8) covers a complex and broad zone (fig. 10.9). In figure 10.9, the fault lengths of the two events are drawn by using the strikes of the steep nodal planes of the focal mechanisms and projecting them to the surface. (For the shallowly dipping planes, the trace of the first event would be nearly the same as that shown in fig. 10.9, and the strike of the second event would be rotated clockwise 35° with respect the strike of the steep plane.) For the first event, we use the location determined by Eaton (chap. 8) for the main shock. Although the location of the second event is somewhat uncertain, figure 10.9 shows that the echelon fault traces bracket a substantial part of the aftershock area. Figure 10.10 shows that this is true whether we choose as the fault planes for each event the set of steeply dipping nodal planes, the set of shallowly dipping nodal planes, or one shallowly dipping and one steeply dipping plane. The aftershock activity of the northern subarea in a vertical cross section, as obtained by Eaton (chap. 8), is shown in figure 10.10. The traces, representing the steep and shallow nodal planes for each event, are slightly distorted because the cross section (line *NT–NT'*, fig. 10.9) is not exactly perpendicular to the strike of the focal-mechanism solutions for these two events. If the azimuth of the cross section were perpendicular to the strike of the first event, then most of the seismicity would be bounded by the shallow plane of the first event and the steep plane of the second event.

Although the waveform data do not favor one configuration of fault planes over another, the choice of a shallow fault plane for the first event is somewhat supported by aftershock studies (see chaps. 8, 9) that show the predominant clustering of earlier and larger aftershocks on a shallowly southwest dipping surface. A choice of the steeply dipping nodal plane for the fault plane of the second event would indicate conjugate faulting. Such an explanation was suggested, for example, by Wetmiller and others (1984) for the New Brunswick, Canada, earthquake of January 9, 1982, and its aftershocks. The existence of steeply dipping faults in the epicentral region is known from reflection data (for example, Fielding and others, 1983; see chap. 4). This configuration of fault planes is also consistent with the geologic arguments of Fuller and Real (1983) for a steeply dipping fault plane.

DISCUSSION

The May 2 earthquake occurred in an area of the California Coast Ranges characterized by various geologic structures, including numerous folds that are punctuated by several high-angle reverse faults (Fielding and others, 1983; see chap. 4). The complexity of the main shock and the aftershock sequence may reflect this geologic complexity. The process of strain accumulation in the Coalinga region could have occurred so as to critically load the entire region; that is, in the presence of a system of faults of nearly equal strength, strain accumulates on all the faults. The state of stress on each fault segment comes to depend on the state of stress of adjacent faults. The effect of a major rupture on any fault may result in the rupture of any critically stressed adjacent faults. Applied to our source model of the main shock, this interpretation implies that the first rupture event activated the second fault, and the subsequent aftershock activity represents a slower response to the stress release.

The complexity of the rupture history explains many characteristics of the aftershock distribution, despite the uncertainty in the choice of fault planes. There is, as expected, a concentration of activity in the vicinity of the fault plane of the first event, as well as at the southeast end of the second fault. These events define a diffuse lineation with the same strike as the second event. The fault-plane solution of a large aftershock in this region (event F of Eaton and others, 1983) indicates high-angle reverse faulting similar to the second event. The second event of the main shock and these aftershocks may lie on the same fault plane.

The epicenters of several moderate ($5.4<m_b<6.0$) aftershocks that occurred on June 11 and July 9, 22, and 25, 1983 (large dots, fig. 10.9), are located within a couple of kilometers of the north end of the second event of the main shock. Hart and McJunkin (1983) found surface faulting associated with some of these aftershocks. As inferred from the surface faulting and observed displacements, these events could be related to steeply east dipping reverse faults possibly associated with the Nuñez fault (see chap. 16). However, fault-plane solutions of these events (see chap. 8) have different strikes and dips than the mechanism of the second event; thus, the second event is probably not associated with the Nuñez fault. Nonetheless, the proximity of the Nuñez fault to the rupture plane of the second event suggests that this fault could have been critically loaded by the occurrence of the second event.

Our source model might also explain why damage was so severe in the town of Coalinga (about 10 km southwest of the epicenter) but relatively light near the epicenter. As seen in figure 10.9, the fault trace of the second rupture event obviously falls much closer to the town of Coalinga (hachured zone) than does any part of the first fault. Furthermore, accelerograms at the Pleasant Valley Pumping Plant, the station nearest to the epicenter, exhibit complexity. As processed by Maley and others (1983), both the corrected acceleration and velocity records from the 45° horizontal component (fig. 3*C*) shows two relatively distinct arrivals. The time separation of these two arrivals—slightly less than 4 s—is about what would be expected from the two-event rupture model. Note also that the peak acceleration identified by Maley and others is associated with the second event of the main shock.

TABLE 10.2.—*Summary of rupture characteristics inferred from broad-band analysis of the earthquake*

[For dynamic-stress drop and rupture radius, a rupture velocity of 0.75 was used]

Parameter	Event 1	Event 2
Depth (km)	9.5±0.6	5.5±0.8
Strike (az)	300°±5°	300°±5°
Dip	65°±5°	80°±5°
Rake	85°±10°	80°±15°
Rupture radius (km)	6.0±2.0	4.7±2.0
Moment (10^{25} dyne-cm)	.9±0.3	.8±0.4
Dynamic-stress drop:		
Steep plane (bars)	24±16	---
Shallow plane (bars)	31±16	---
Static-stress drop (bars)	34±18	19±10
Seismic slip (cm)	52±40	36±36
Total moment (10^{25} dyne-cm).	2.7±0.7	---
Radiated energy (10^{21} dyne-cm).	1.6	---
Apparent stress (bars)	18	---

CONCLUSIONS

Commonly, as was the case with the May 2 earthquake, both the main shock and the ensuing aftershock sequence are complex. A detailed rupture history of the main shock is critical to understanding the mechanics of rupture and the tectonic activity of a given region. Using high-quality digital data with broadband content, I have shown that body waves can be used to obtain details of the rupture process of moderate shallow earthquakes. Except for the choice of fault plane, these details have been derived entirely from characteristics of the waveforms. Thus, they provide an independent but complementary source of information from which to obtain an overall picture of the earthquake process. The source parameters obtained for the May 2 earthquake are summarized in table 10.2.

This description of the May 2 earthquake has important implications for estimating seismic hazards in California. I have shown that the Coalinga main shock consisted of two events: The second event had about half the moment of the first and was located to the southwest of the first event. The complexity of the rupture suggests that strain may be accumulating on many faults in this geologically complex region. Once critically loaded, the state of stress on each fault comes to depend on the state of stress of adjacent faults. A major rupture of one fault would result in rupture of any critically stressed adjacent faults. Thus, damage can arise from faults other than the one that initially failed.

ACKNOWLEDGMENTS

I thank Jack Boatwright for rousing and beneficial discussions. Madeleine Zirbes provided valuable help in the data processing.

REFERENCES CITED

Boatwright, John, 1980, A spectral theory for circular seismic sources: Simple estimates of source dimensions, dynamic stress drop, and radiated seismic energy: Seismological Society of America Bulletin, v. 70, no. 1, p. 1–27.

Boatwright, John, and Choy, G.L., 1986, Teleseismic estimates of the energy radiated by shallow earthquakes: Journal of Geophysical Research, v. 91, no. B2, p. 2095–2112.

Boatwright, John, and Fletcher, J.B., 1984, The partition of radiated energy between *P* and *S* waves: Seismological Society of America Bulletin, v. 74, no. 2, p. 361–376.

Choy, G.L., 1977, Theoretical seismograms of core phases calculated by a frequency-dependent full wave theory, and their interpretation: Royal Astronomical Society Geophysical Journal, v. 51, no. 2, p. 275–312.

Choy, G.L., and Boatwright, John, 1981, The rupture characteristics of two deep earthquakes inferred from broadband GDSN data: Seismological Society of America Bulletin, v. 71, no. 3, p. 691–711.

Choy, G.L., Boatwright, John, Dewey, J.W., and Sipkin, S.A., 1983, A teleseismic analysis of the New Brunswick earthquake of January 9, 1982: Journal of Geophysical Research, v. 88, no. B3, p. 2199–2212.

Choy, G.L., and Cormier, V.F., 1986, Direct measurement of the mantle attenuation operator from broadband *P* and *S* waveforms: Journal of Geophysical Research, v. 91, no. B7, p. 7326–7342.

Clark, M.M., Harms, K.K., Lienkaemper, J.J., Perkins, J.A., Rymer, M.J., and Sharp, R.V., 1983, The search for surface faulting, *in* Borcherdt, R.D., ed., The Coalinga, California earthquake sequence commencing May 2, 1983: U.S. Geological Survey Open-File Report 83-511, p. 8–11.

Cormier, V.F., and Richards, P.G., 1977, Full wave theory applied to a discontinuous velocity increase: Journal of Geophysics, v. 43, no. 1–2, p. 3–31.

Eaton, J.P., Cockerham, R.S., and Lester, F.W., 1983, Study of the May 2, 1983 Coalinga earthquake and its aftershocks, based on the USGS seismic network in northern California, *in* Bennett, J.H.,

and Sherburne, R.W., eds., The 1983 Coalinga, California earthquakes: California Division of Mines and Geology Special Publication 66, p. 261–273.

Fielding, Eric, Barazangi, Muawia, Brown, Larry, Oliver, Jack, and Kaufman, Sidney, 1983, COCORP seismic reflection profiles near the 1983 Coalinga earthquake sequence: Deep structures, *in* Bennett, J.H., and Sherburne, R.W., eds., The 1983 Coalinga, California earthquakes: California Division of Mines and Geology Special Publication 66, p. 137–149.

Fuller, D.R., and Real, C.R., 1983, High-angle reverse faulting, a model for the 2 May 1983 Coalinga earthquake, *in* Bennett, J.H., and Sherburne, R.W., eds., The 1983 Coalinga, California earthquakes: California Division of Mines and Geology Special Publication 66, p. 177–184.

Hart, E.W., and McJunkin, R.D., 1983, Surface faulting northwest of Coalinga, California June and July 1983, *in* Bennett, J.H., and Sherburne, R.W., eds., The 1983 Coalinga, California earthquakes: California Division of Mines and Geology Special Publication 66, p. 201–219.

Harvey, D., and Choy, G.L., 1982, Broad-band deconvolution of GDSN data: Royal Astronomical Society Geophysical Journal, v.69, no. 3, 659–668.

Haskell, N.A., 1962, Crustal reflection of P and SV waves: Journal of Geophysical Research, v. 67, no. 12, p. 4751–4767.

Langston, C.A., and Helmberger, D.V., 1975, A procedure for modelling shallow dislocation sources: Royal Astronomical Society Geophysical Journal, v. 42, no. 1, p. 117–130.

Maley, R.P., Brady, A.G., Etheredge, E.C., Johnson, D.A., Mork, P.N., and Switzer, J.C., 1983, Analog strong motion data and processed main event records, *in* Borcherdt, R.D., ed., The Coalinga, California earthquake sequence commencing May 2, 1983: U.S. Geological Survey Open-File Report 83-511, p. 38–60.

Rial, J.A., 1978, The Caracas, Venezuela, earthquake of July 1967: A multiple-source event: Journal of Geophysical Research, v. 83, no. B11, p. 5405–5414.

Rial, J.A., and Brown, E.D., 1983, Waveform modeling of long-period P waves from the Coalinga earthquake of May 2, 1983, *in* Bennett, J.H., and Sherburne, R.W., eds., The 1983 Coalinga, California earthquakes: California Division of Mines and Geology Special Publication 66, p. 247–259.

Richards, P.G., 1973, Calculation of body waves, for caustics and tunnelling in core phases: Royal Astronomical Society Geophysical Journal, v. 35, no. 1–3, p. 243–264.

Sherburne, R.W., McNally, K.C., Brown, E.D., and Aburto, Arturo, 1983, The mainshock-aftershock sequence of 2 May 1983: Coalinga, California, in Bennett, J.H., and Sherburne, R.W., eds., The 1983 Coalinga, California earthquakes: California Division of Mines and Geology Special Publication 66, p. 275–292.

Spence, W.J., 1980, Relative epicenter determination using P wave arrival-time differences: Seismological Society of America Bulletin, v. 70, no. 1, p. 171–183.

Walter, A.W., and Mooney, W.D., 1983, Preliminary report on the crustal velocity structure near Coalinga, California, as determined from seismic refraction survey in the region, *in* Bennett, J.H., and Sherburne, R.W., eds., The 1983 Coalinga, California earthquakes: California Division of Mines and Geology Special Publication 66, p. 127–135.

Wentworth, C.M., Walter, A.W., Bartow, J.A., and Zoback, M.D., 1983, Evidence on the tectonic setting of the 1983 Coalinga earthquakes from deep reflection and refraction profiles across the southeastern end of Kettleman Hills, *in* Bennett, J.H., and Sherburne, R.W., eds., The 1983 Coalinga, California earthquakes: California Division of Mines and Geology Special Publication 66, p. 113–126.

Wetmiller, R.J., Adams, J., Anglin, F.M., Hasegawa, H.S., and Stevens, A.E., 1984, Aftershock sequences of the 1982 Miramichi, New Brunswick, earthquakes: Seismological Society of America Bulletin, v. 74, no. 2, p. 621–653.

Wyss, Max, and Brune, J.N., 1968, Seismic moment, stress, and source dimensions for earthquakes in the California-Nevada region: Journal of Geophysical Research, v. 73, no. 14, p. 4681–4694.

11. KINEMATIC SOURCE PARAMETERS DETERMINED BY TIME-DEPENDENT MOMENT-TENSOR INVERSION AND AN ANALYSIS OF TELESEISMIC FIRST MOTIONS

By STUART A. SIPKIN and RUSSELL E. NEEDHAM,
U.S. GEOLOGICAL SURVEY

CONTENTS

ABSTRACT

A waveform-inversion technique was applied to the digitally recorded long-period *P*-waveform data from the Global Digital Seismograph Network for the May 2 earthquake. The solution was constrained to be purely deviatoric but not to be a double couple. The source depth was determined by finding a trial depth that minimized the misfit to the data. By allowing the elements of the moment tensor to be independent, arbitrary functions of time, a gross estimate of the source-time history of the rupture process was obtained. A moderately well constrained fault-plane solution was also obtained by fitting the available long- and short-period teleseismic first-motion data. The strike, dip, and rake of the first-motion solution are 307°, 70°, and 90°, respectively. This solution is very close to the best double-couple of the step-function moment-tensor solution of 303°, 72°, and 97°. The best fitting depth is 11 km and the scalar moment is 4.7×10^{25} dyne-cm. The non-double-couple part of the moment tensor is 28 percent. This substantial non-double-couple component is apparently due to source complexity in which the strike of the fault plane rotated clockwise during rupture, from a strike of approximately 292° to a strike of 302°.

INTRODUCTION

Most seismic source studies in which long-period body waves are analyzed use a trial-and-error procedure to estimate various source parameters. In these studies, a lengthy modeling procedure is usually followed in which every apparent arrival is identified as an effect of either near-source or near-receiver structure or source multiplicity. This procedure both is time consuming and requires a certain amount of subjective judgment. The technique used in the analysis here is an inversion procedure based on multichannel signal-enhancement (MSE) theory (Robinson, 1967). In this algorithm, the far-field Green's functions are the multichannel input, the observed seismograms are the desired output, and the moment-rate tensor is the convolution filter operating on the input. Because the convolution filter found is not only a signal-enhancement filter but also a noise-rejection filter, arrivals in the waveform that are not specifically accounted for in the Green's functions (such as those generated by near-receiver or near-source structure, other than *pP* and *sP* phases), and that are not coherent across the suite of seismograms to be inverted will be regarded as noise and will not affect the solution. Although the resolution of broadband data is clearly superior to that of long-period data, an inversion procedure is more objective than trial-and-error modeling; and, indeed, some of the gross features of the rupture process for this event using broadband data (see chap. 10) are resolvable with the long-period data. It is clear from this exercise that more information is contained in long-period data than is commonly utilized.

The MSE algorithm for estimating seismic source parameters developed by Sipkin (1982) has now been in routine use at the U.S. Geological Survey since July 1982. This algorithm was later expanded to include source depth as a variable parameter. However, the research capabilities of this algorithm go beyond this routine application. In routine use, the best parameters are estimated for a point source with a step-function source-time history (delta function in the far field); however, the algorithm can also be used to determine a moment tensor in which each element is an independent function of time. This time-dependent moment tensor may then be used to estimate the time history of the rupture process.

The first step is to estimate the best depth by approximating the source as a pure step-function point source and then varying the depth until a best fit to the data is obtained. Next, using this depth, we perform the inversion, approximating the source as a quasi-point source, that is, as a point in space but not in time. The moment tensor is then decomposed into the principal axis

system for each point in time. This procedure has already been applied to several earthquakes (Julian and Sipkin, 1985; Sipkin, 1986). The advantages of using the MSE waveform-inversion algorithm include (1) more objectivity (and much shorter analysis time) than trial-and-error methods and (2) insensitivity to lateral heterogeneity in seismic velocity, unlike inversion techniques using long sections of the wave train. In addition to moment-tensor solutions, first-motion fault-plane solutions determined by one of us (R.E.N.) have been reported by the U.S. National Earthquake Information Center (NEIC) on a routine basis since January 1981.

STEP-FUNCTION SOLUTIONS

Available long- and short-period teleseismic first-motion data were used to determine a moderately well controlled fault-plane solution for the May 2 earthquake. This analysis, using 163 first motions, yields a reverse mechanism with a strike, dip, and rake of 307°, 70°, and 90°, respectively (fig. 11.1; tables 11.1, 11.2). Although the shallowly dipping nodal plane is not well constrained, the strike and dip of the steeply dipping nodal plane are tightly constrained by the first-motion data, especially by nodal readings from many of the North American stations; however, the rake this nodal plane is not well constrained. In this case, the teleseismic first-motion data were inadequate to determine the magnitude of the strike-slip component (if any), and the rake was held at 90°. However, the data do not preclude rakes as much as 30° on either side of this value.

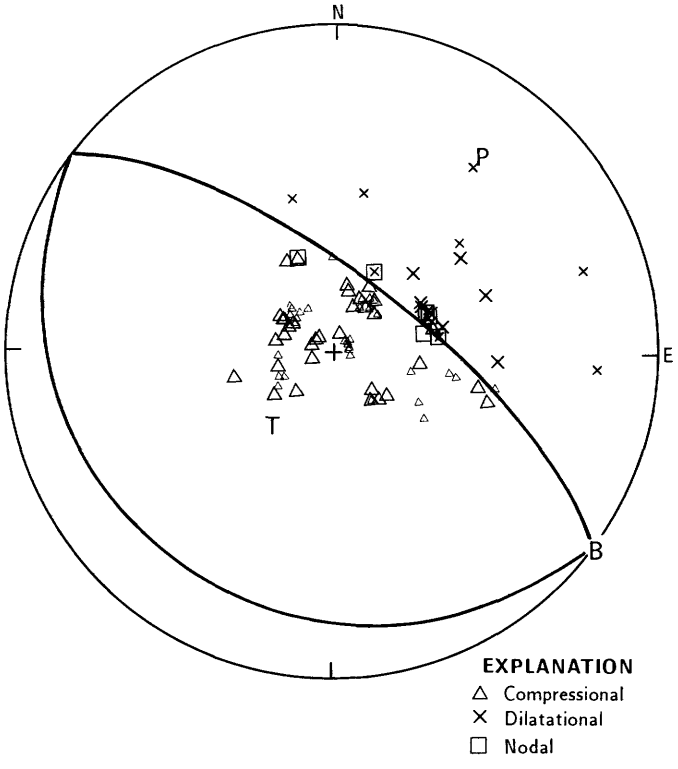

FIGURE 11.1.—First-motion fault-plane solution showing first motions used. Small symbols, short-period first-motions; large symbols, long-period first motions.

TABLE 11.1.—*Source parameters*

	Moment tensor			First motions	
No. of stations	9			163	
Depth (km)	11±5			10(assumed)	
Principal axes (scale, 10^{25} dyne-cm)					
	Length	Plunge	Azimuth	Plunge	Azimuth
T	4.35	63°	224°	65°	217°
I	.71	7°	121°	0°	127°
P	5.07	26°	028°	25°	037°
Best double couple					
M_0 (10^{25} dyne-cm)	4.7			---	
M_w (10^{25} dyne-cm)	6.4			---	
	Strike	Dip	Rake	Strike	Dip	Rake
NP1	303°	72°	97°	307°	70°	90°
NP2	102°	20°	70°	127°	20°	90°

The MSE waveform-inversion technique was applied to the digitally recorded long-period *P*-waveform data from the Global Digital Seismograph Network (GDSN) stations that were between 36° and 98° in epicentral distance (fig. 11.2). The solution was constrained to be purely deviatoric, but not to be a double couple. The source depth was determined by varying the trial depth at 1-km intervals to find a focal depth that minimized the misfit to the data. Because the *P* waveforms contain both *pP* and *sP* phases, as well as direct *P*-wave arrivals, this procedure generally is highly sensitive to source depth. The depth found depends somewhat on the velocity model used in the inversion. The model used in this experiment was 1066B (Gilbert and Dziewonski, 1975). Although this model is quite adequate for describing the effects of mantle structure, its crustal structure may be too simple. This deficiency will not affect the mechanism found but may bias the depth estimate. The effect of introducing more realistic lower-velocity crustal layers is to move the focus to a shallower depth.

The step-function inversion procedure yields a source depth of 11 km (fig. 11.3); the mechanism is illustrated in figure 11.4 and described in table 11.1. The best double couple is a thrust mechanism with a strike, dip, and rake of 303°, 72°, and 97°, respectively, and a scalar moment of 4.7×10^{25} dyne-cm. This moment corresponds to a moment magnitude (M_w) of 6.4. There is a substantial non-double-couple component, however, in this solution of approximately 28 percent. The interpretation of this non-double-couple component is discussed below. The fits of the resulting synthetics to the data are shown in figure

TABLE 11.2.—*First-motion parameters*

[Quality: E, emergent; I, impulsive. Polarity: C, compressional; D, dilatational; N, nodal. Channel: LPZ, long-period vertical; SPZ, short-period vertical]

Station code	Distance (°)	Azimuth (°)	$\frac{dT}{d\Delta}$ (s/°)	Takeoff angle (°)	Quality	Polarity	Channel	Phase
BDW	10.57	048.47	13.67	43.30	I	D	SPZ	P
ALQ	11.36	092.37	13.54	42.79	I	D	LPZ	P
ANMO	11.36	092.35	13.54	42.79	I	D	LPZ	P
NEW	12.26	010.10	13.40	42.24	I	D	SPZ	P
EPT	12.29	107.18	13.40	42.24	I	C	LPZ	P
GOL	12.30	069.10	13.40	42.24	I	D	LPZ	P
OZB	13.29	345.01	13.25	41.66	I	D	SPZ	P
RSSD	14.72	052.62	13.08	41.01	I	D	LPZ	P
RSSD	14.72	052.62	13.08	41.01	I	D	SPZ	P
JCT	18.06	102.58	12.42	38.54	I	C	LPZ	P
ATX	19.66	100.97	12.10	37.38	I	C	SPZ	P
HKT	21.42	099.93	10.08	30.38	I	C	SPZ	P
FVM	23.86	076.77	9.62	28.86	I	D	LPZ	P
RSON	24.04	044.18	9.62	28.86	I	D	LPZ	P
IIC	24.70	125.92	9.55	28.63	E	C	SPZ	P
RSCP	28.05	080.87	9.20	27.49	I	D	SPZ	P
RSCP	28.05	080.87	9.20	27.49	E	N	LPZ	P
AAM	28.87	066.56	9.05	27.00	I	D	LPZ	P
PMR	31.19	333.57	8.83	26.30	I	C	LPZ	P
BLA	31.84	076.11	8.76	26.07	I	C	LPZ	P
MRG	31.84	071.48	8.76	26.07	I	C	SPZ	P
COL	33.06	338.85	8.69	25.85	E	N	LPZ	P
SCP	33.30	069.00	8.66	25.75	E	N	LPZ	P
INY	34.18	065.87	8.63	25.66	I	D	LPZ	P
GAC	34.77	060.07	8.56	25.43	I	D	LPZ	P
LPS	35.39	120.01	8.53	25.34	I	C	SPZ	P
RSNY	35.47	062.04	8.53	25.34	I	D	LPZ	P
HON	35.98	256.04	8.51	25.27	I	C	LPZ	P
MNT	36.07	060.37	8.51	25.27	I	D	SPZ	P
PAL	36.25	068.00	8.51	25.27	E	C	SPZ	P
WES	37.98	065.30	8.39	24.89	E	N	LPZ	P
MBC	40.12	000.36	8.27	24.51	I	C	SPZ	P
BEC	45.60	077.88	7.97	23.57	E	N	LPZ	P
GDH	48.46	025.96	7.79	23.01	E	N	LPZ	P
SJG	50.80	095.75	7.59	22.38	I	C	LPZ	P
GUV	59.12	103.92	6.97	20.47	I	C	SPZ	P
AKU	62.32	027.20	6.69	19.61	I	C	LPZ	P
AFI	69.59	234.14	6.11	17.85	I	C	LPZ	P
KEV	71.67	011.42	5.96	17.40	E	C	LPZ	P
ZOBO	71.80	126.98	5.93	17.31	I	C	LPZ	P
LPB	72.01	127.15	5.93	17.31	E	C	LPZ	P
VAL	73.14	037.42	5.86	17.10	E	C	LPZ	P
EAB	73.16	031.68	5.86	17.10	I	C	SPZ	P
ELO	73.24	031.22	5.86	17.10	I	C	SPZ	P
DMU	73.50	034.51	5.82	16.98	I	C	SPZ	P
DCN	73.68	035.10	5.82	16.98	I	C	SPZ	P
EAU	73.77	031.61	5.79	16.89	I	C	SPZ	P
DLE	74.06	034.85	5.79	16.89	I	C	SPZ	P
ESK	74.22	031.92	5.79	16.89	I	C	SPZ	P
ESK	74.22	031.92	5.79	16.89	E	N	LPZ	P
ECB	74.54	035.69	5.75	16.77	I	C	SPZ	P
ETA	74.60	035.19	5.75	16.77	I	C	SPZ	P
ECP	74.85	035.67	5.72	16.68	I	C	SPZ	P
ANT	75.97	133.72	5.65	16.47	E	C	LPZ	P
KJF	76.78	013.77	5.59	16.29	I	C	LPZ	P
MAJO	77.34	306.01	5.56	16.20	I	C	LPZ	P
MAT	77.34	306.01	5.56	16.20	I	C	SPZ	P
MDJ	77.69	316.64	5.56	16.20	I	C	SPZ	P
UPP	78.19	020.21	5.52	16.08	I	C	SPZ	P
VUN	79.06	238.16	5.45	15.87	I	C	SPZ	P
FLN	79.94	035.66	5.37	15.63	I	C	SPZ	P
COP	79.99	024.98	5.37	15.63	I	C	SPZ	P
COP	79.99	024.98	5.37	15.63	I	C	LPZ	P
DBN	80.02	030.66	5.37	15.63	I	C	LPZ	P
GRR	80.02	036.11	5.37	15.63	I	C	SPZ	P
LPF	80.18	036.46	5.37	15.63	I	C	SPZ	P
LDF	80.22	035.61	5.37	15.63	I	C	SPZ	P
CN2	80.48	317.97	5.31	15.45	I	C	SPZ	P
UCC	80.64	031.94	5.31	15.45	E	D	LPZ	P
WTS	80.77	029.97	5.27	15.33	I	C	SPZ	P
HAM	80.85	027.54	5.27	15.33	I	C	SPZ	P
DOU	81.27	032.30	5.22	15.18	E	C	LPZ	P
ENN	81.33	031.21	5.22	15.18	I	C	SPZ	P
MFF	81.62	037.05	5.22	15.18	I	C	SPZ	P
LIS	82.07	047.44	5.18	15.06	I	C	SPZ	P
SHK	82.15	307.16	5.18	15.06	I	C	SPZ	P
LSF	82.68	036.47	5.15	14.97	I	C	SPZ	P
JACH	82.83	139.57	5.12	14.88	I	C	SPZ	P
BRN	82.89	026.59	5.12	14.88	I	C	SPZ	P
TCF	82.98	036.10	5.12	14.88	I	C	SPZ	P
SSF	83.02	034.91	5.12	14.88	I	C	SPZ	P
LOR	83.03	034.59	5.12	14.88	I	C	LPZ	P
LOR	83.03	034.59	5.12	14.88	I	C	SPZ	P
BGF	83.08	035.59	5.12	14.88	I	C	SPZ	P
PEL	83.14	139.92	5.12	14.88	I	C	LPZ	P
AVF	83.15	035.17	5.12	14.88	I	C	SPZ	P
MZF	83.21	035.96	5.12	14.88	I	C	SPZ	P
LFF	83.24	037.79	5.12	14.88	I	C	SPZ	P
LGR	83.32	041.23	5.09	14.80	I	C	SPZ	P
RJF	83.36	037.13	5.09	14.80	I	C	SPZ	P
LNV	83.40	140.90	5.09	14.80	I	C	SPZ	P
GWF	83.41	031.54	5.09	14.80	I	C	SPZ	P
SMF	83.49	035.02	5.09	14.80	I	C	SPZ	P
FCH	83.49	139.77	5.09	14.80	I	C	SPZ	P
HAU	83.60	032.83	5.09	14.80	I	C	SPZ	P
LPO	83.64	037.74	5.09	14.80	I	C	SPZ	P
CDF	83.69	032.09	5.09	14.80	I	C	SPZ	P
CLL	83.71	027.35	5.09	14.80	I	C	SPZ	P
MOX	83.72	028.46	5.09	14.80	I	C	LPZ	P
ECH	83.79	032.27	5.06	14.71	I	C	SPZ	P
CAF	83.90	037.11	5.06	14.71	I	C	SPZ	P
BSF	83.92	032.71	5.06	14.71	I	C	SPZ	P
BAF	84.01	032.61	5.06	14.71	I	C	SPZ	P
HOF	84.08	028.53	5.06	14.71	I	C	SPZ	P
STU	84.22	030.87	5.06	14.71	I	C	LPZ	P
TOL	84.25	043.91	5.06	14.71	I	C	LPZ	P
EPF	84.40	039.34	5.03	14.62	I	C	SPZ	P
BRG	84.41	027.13	5.03	14.62	I	C	SPZ	P
SLE	84.71	031.87	5.03	14.62	E	C	LPZ	P
ZUL	84.89	032.11	4.99	14.50	E	C	LPZ	P
SFS	85.32	047.59	4.96	14.41	I	C	SPZ	P
PRU	85.35	027.33	4.96	14.41	I	C	SPZ	P
DIX	85.54	033.52	4.96	14.41	E	C	LPZ	P
LLS	85.62	032.17	4.96	14.41	E	C	LPZ	P
MMK	85.81	033.24	4.91	14.26	E	C	LPZ	P
GUA	85.91	283.67	4.91	14.26	I	C	LPZ	P
PVC	86.10	244.85	4.91	14.26	I	C	SPZ	P
TMA	86.16	032.72	4.91	14.26	E	C	LPZ	P
MAL	86.20	046.41	4.91	14.26	I	C	SPZ	P
KMR	86.78	028.67	4.83	14.02	E	C	LPZ	P
F F	87.11	035.57	4.83	14.02	I	C	SPZ	P
LMR	87.22	035.79	4.83	14.02	I	C	SPZ	P
ALI	87.30	043.07	4.80	13.93	I	D	LPZ	P
HNR	87.34	256.39	4.80	13.93	I	C	SPZ	P
CTI	87.40	031.23	4.80	13.93	I	D	SPZ	P
ZST	87.78	026.94	4.78	13.88	I	D	SPZ	P
SRO	88.55	026.47	4.75	13.79	I	C	SPZ	P
JOS	88.74	024.84	4.75	13.79	I	C	SPZ	P
CVF	88.92	034.94	4.73	13.73	I	C	SPZ	P
NOU	90.34	242.46	4.70	13.64	I	C	SPZ	P
RAB	90.44	265.17	4.70	13.64	I	C	SPZ	P
TIM	91.36	025.83	4.69	13.61	I	D	SPZ	P
LPA	91.54	133.24	4.69	13.61	I	C	SPZ	P
SSE	91.65	311.04	4.69	13.61	E	C	LPZ	P
NJ2	92.37	313.13	4.66	13.52	I	C	SPZ	P
COZ	92.79	024.12	4.65	13.49	I	D	SPZ	P
SGO	93.41	032.26	4.63	13.43	I	D	SPZ	P
VTS	94.79	026.14	4.58	13.28	I	D	SPZ	P
PVL	94.99	024.60	4.58	13.28	I	D	SPZ	P
VAY	95.68	027.18	4.56	13.23	I	C	SPZ	P
TATO	95.73	306.49	4.56	13.23	I	C	LPZ	P
GTA	96.15	329.85	4.55	13.20	I	C	SPZ	P
XAN	96.36	320.74	4.54	13.17	I	C	SPZ	P
SNZO	97.42	223.51	4.52	13.11	I	C	LPZ	P
QZH	97.61	308.34	4.52	13.11	I	C	SPZ	P
ANTO	100.35	020.72	4.45	12.90	I	C	LPZ	P_{diff}
BAG	102.26	300.89	4.45	12.90	I	C	LPZ	P_{diff}
DAV	104.82	290.44	4.45	12.90	I	C	LPZ	P_{diff}
CHG	113.87	319.04	1.88	5.42	E	C	LPZ	PKP
SNG	122.22	309.78	1.87	5.39	I	C	LPZ	PKP
BNG	124.20	052.47	1.87	5.38	I	C	SPZ	PKP
PSI	126.74	307.95	1.86	5.36	I	C	SPZ	PKP
LEM	127.41	291.87	1.86	5.36	I	C	LPZ	PKP
ARO	129.93	021.73	1.85	5.33	I	C	LPZ	PKP
MUN	133.56	258.02	1.83	5.26	E	C	LPZ	PKP
SUR	147.80	094.68	1.62	4.65	I	C	SPZ	PKP
MTD	148.44	059.57	1.62	4.65	I	C	SPZ	PKP
BUL	148.45	067.93	1.62	4.65	I	C	SPZ	PKP
SWZ	149.54	082.61	1.56	4.49	I	C	SPZ	PKP
KSR	150.20	079.01	1.56	4.49	I	C	SPZ	PKP
SLR	151.23	077.56	1.53	4.40	I	C	SPZ	PKP
SEK	151.87	082.95	1.50	4.31	I	C	SPZ	PKP
NPA	152.15	046.20	1.50	4.31	I	C	SPZ	PKP

11.5. This solution differs slightly from that published in the NEIC *Monthly Listing* because more stations were used in this inversion than in the previously published result. In particular, the addition of several nodal stations to the data set resulted in a lower estimate of the scalar moment. The solution is very close to both the solution determined from first-motion data and the centroid-moment tensor (CMT) solution reported in the NEIC *Monthly Listing* by the group at Harvard University (depth, 12 km; strike, 304°; dip, 67°; rake, 77°; $M_0=5.7\times10^{25}$ dyne-cm; 60 percent double couple). For most earthquakes with a magnitude near that of the Coalinga event, a sharp minimum in the normalized mean-squared error versus depth can be identified as the average source depth (Sipkin, 1986). Here, however, the minimum is relatively broad, flat, and symmetrical, spanning the depth range 5–16 km. The approximate center of this range is 11 km; the uncertainty, determined

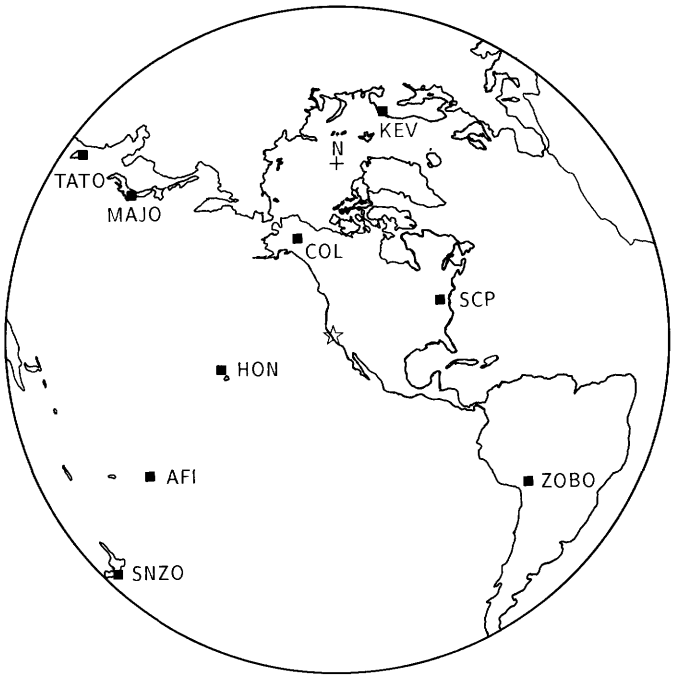

FIGURE 11.2.—Azimuthal equidistant projection, centered on epicenter of the May 2 earthquake, showing locations of GDSN stations (squares) used in waveform inversions. Edge of circle is at an epicentral distance of 100°.

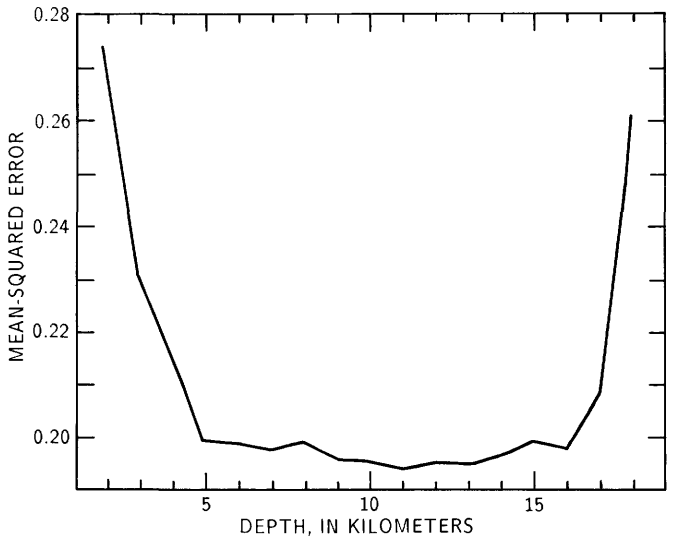

FIGURE 11.3.—Mean-squared error versus source depth, using multichannel signal-enhancement inversion procedure.

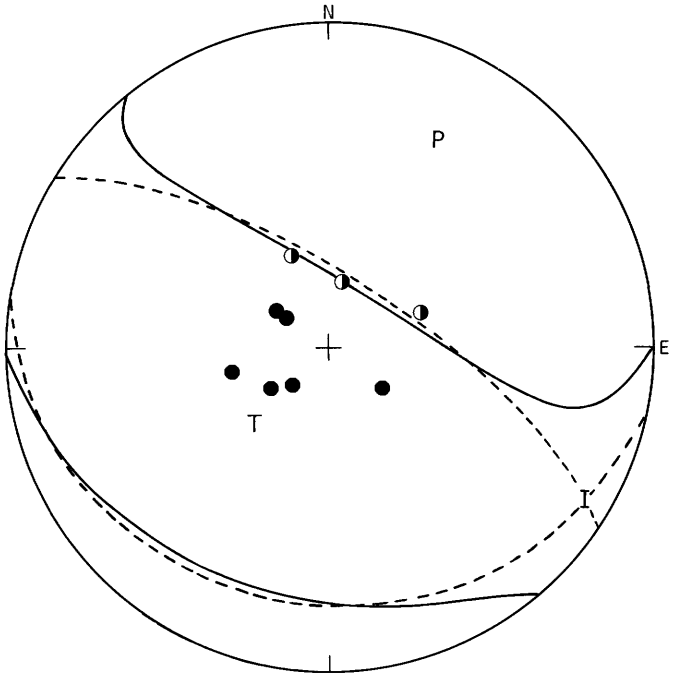

FIGURE 11.4.—Step-function inversion results for a source depth of 11 km. Solid lines, nodal lines of moment tensor; dashed lines, nodal planes of best double-couple source. Solid and half-filled circles indicate compressional and nodal first motions, respectively.

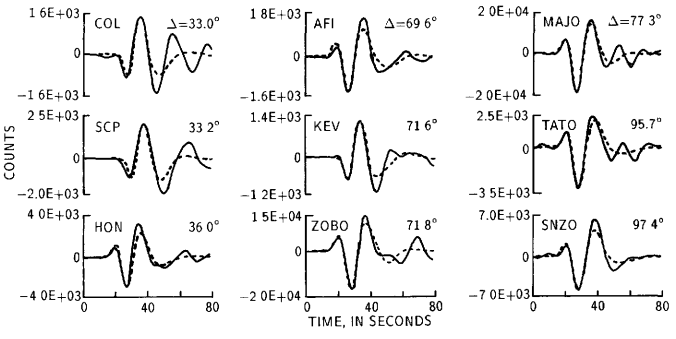

FIGURE 11.5.—Fits of real (solid) and synthetic (dashed) *P*-wave data from GDSN stations. Synthetic seismograms are computed for source shown in figure 11.4.

by the width of the minimum, is approximately 5 km. The best double-couple mechanism, however, is a very robust parameter with respect to source depth. Figure 11.6 shows that the differences in the mechanisms obtained in the depth range 5–16 km are very small.

Using a different inversion technique, Sipkin (1986) also performed a simultaneous inversion of the *P* and *SH* waveforms. The inversion yielded very similar results to those given above (depth, 11 km; strike, 294°; dip, 67°; rake, 71°; $M_0=4.2\times10^{25}$ dyne-cm; 60 percent double couple). The 90-percent-confidence interval for the double-couple component of the moment tensor was 49.5 to 71.2 percent. This estimate was computed under the assumption that all errors are noise induced. Because of the presence of unmodeled errors, this confidence interval is only approximate. It does, however, indicate that, under the assumptions used, the hypothesis that this earthquake had a pure double-couple mechanism can be rejected at the 90-percent-confidence level. In the following section, we show that this result is due to the assumption that the source had a step-function time history.

TIME-DEPENDENT SOLUTION

The time-dependent mechanism obtained when the moment tensor is allowed to be an arbitrary function of time is shown in the principal-axis system in figure 11.7.

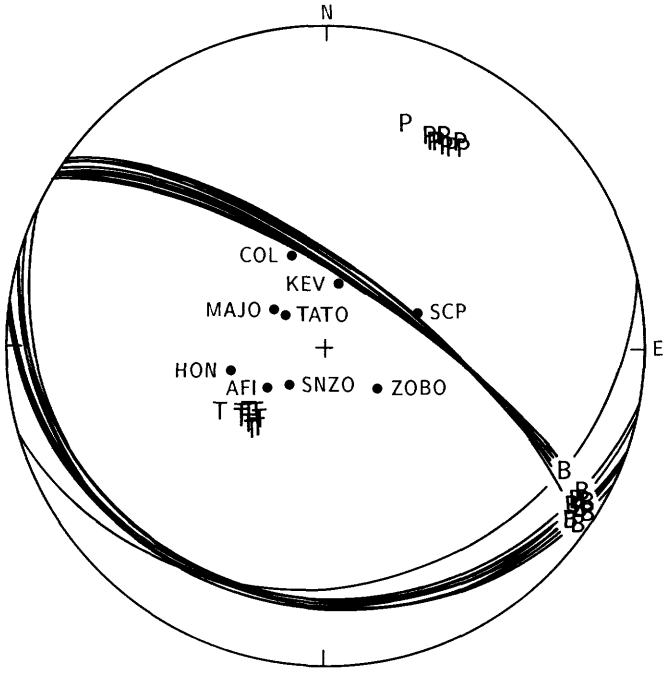

FIGURE 11.6.—Fault-plane solutions determined for source depths of 5 to 16 km at 1-km intervals. Solutions shown are best double-couples of moment-tensor solutions.

The source orientation changes somewhat, and the principal axes undergo a small, but coherent, clockwise rotation corresponding to a rotation of the nodal planes of approximately 10°, from a strike of 292° to 302° for the steeply dipping nodal plane. The final strike of 302° agrees very closely with that obtained in the step-function inversion. The scalar moment is plotted as a function of time in figure 11.8. The long-period origin time is shifted to approximately 6 s later than the short-period origin time given by the NEIC. The source duration, over which the change in geometry occurred, is approximately 15 s. The waveforms are band-pass filtered by the GDSN long-period response, which peaks at

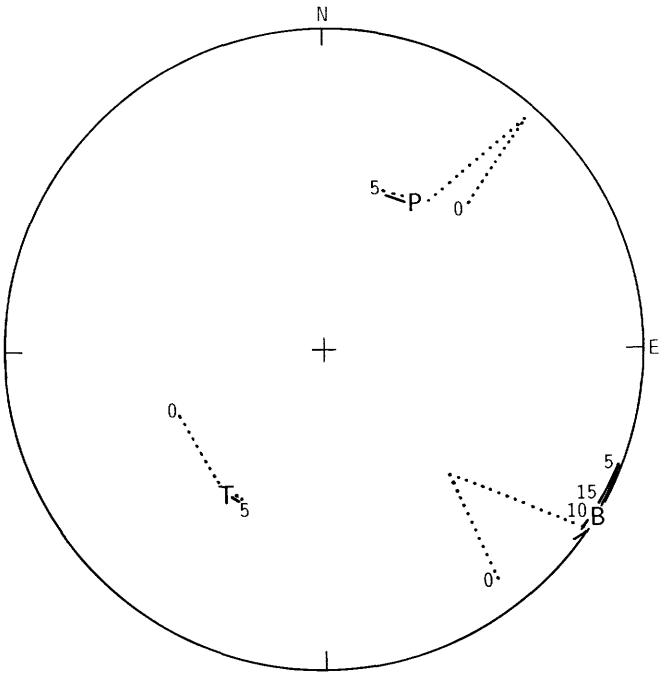

FIGURE 11.7.—Principal axes as a function of time. Dashed lines indicate orientations for times at which scalar moment is less than $0.1M_{max}$. Orientations at 0, 5, 10, and 15 s after the origin time are indicated. P, T, and B denote orientations at 21 s. The 10- and 15-s markers for P and T axes overlap with P and T labels and have been omitted for clarity.

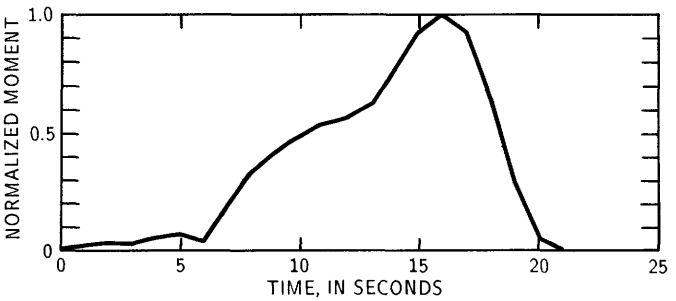

FIGURE 11.8.—Normalized scalar moment as a function of time.

a period of 25 s, and so these times should be considered upper bounds on the actual source-process times. For example, the short-period teleseismic data appear to have a 2-s low-amplitude initiation phase, suggesting that less energetic faulting occurred at the beginning of rupture (Hartzell and Heaton, 1983); the time-dependent inversion of the long-period data shows a delay of 6 s before any substantial release of moment. Although the asymmetry of the time function suggests source multiplicity, individual subevents cannot be resolved by the long-period GDSN data. Although discontinuous rupture cannot be ruled out by this data set, the shape of the time function could also be due to a continuous, but nonuniform, rupture.

The resolution permitted by the data depends on the station distribution, as well as the character of the noise and the bandwidth of the instrument. Given the seismograms to be fitted, a noise sample from each seismogram, and the inversion kernal functions, we can compute a set of averaging functions appropriate for the given data set, according to the procedure of Oldenburg (1982). The resolution can then be inferred from these averaging functions. Figure 11.9 shows one of the averaging functions computed for this data set. The width is about 6 s; thus, two subevents less than 6 s apart would be unresolvable. This estimate is computed under the assumption that all errors are noise induced; because unmodeled errors are present, the resolving length is probably somewhat greater than 6 s. Given this absence of resolution in the long-period data, it is impossible to choose between a continuous rupture or a discontinuous rupture with a delay time of 6 s or less as the preferred mechanism. However, in a study of the strong-motion data, Cramer and Shakall (1983) found no compelling evidence for source multiplicity. This result, though seeming to rule out this possibility, is consistent with a continuous rupture with a change in geometry. Such a change would explain the relatively large non-double-couple part of the moment tensor because it was computed under the assumption that the source had a step-function time history. Furthermore, when the time-dependent moment-tensor solution is decomposed for each point in time, the non-double-couple part of the source is less than 5 percent at all times during which there is any significant release of moment.

DISCUSSION

The solutions determined in this study are consistent with results from a wide variety of investigations. The strike, dip, and rake found using both teleseismic first motions and step-function moment-tensor waveform inversion are very close to the solutions found by waveform modeling of teleseismic P waves (Hartzell and Heaton, 1983; Rial and Brown; 1983) and by first-motion studies using local data (see chap. 8). In fact, the results from the teleseismic and local first-motion studies are virtually identical; the only difference is a steeper dip of 3° in the teleseismic solution. The focal depth found using waveform inversion is also very close to that found by waveform modeling (12 km; Hartzell and Heaton, 1983) and by an analysis of the local data (10 km; see chap. 8). Furthermore, the deepest aftershocks located by various investigators range in depth from 12 to 14 km (see chaps. 8, 9; Sherburne and others, 1983; Urhammer and others, 1983).

The source-process time of 21 s (including the 6-s "initiation phase") is comparable to the 8-s "half-duration" determined for the CMT solution and the 20-s source-process time found by Kanamori (1983) using long-period surface waves. The latter two techniques, however, lacked the resolution to detect any change in source orientation. The source-process time is an estimate of the long-period duration of the source, which consists of three terms: a delay of the main faulting from the initial break, a rise time, and a propagation time of the main rupture (Furumoto, 1979). The source durations of 4 and 5 s determined for this event by Rial and Brown (1983) and Hartzell and Heaton (1983) correspond to the time associated with the main rupture and are much smaller than the source-process times, a difference indicating a significant long-period component to the entire rupture process.

The diffuse pattern of aftershock activity (see chaps. 8, 9; Sherburne and others, 1983) is consistent with either a

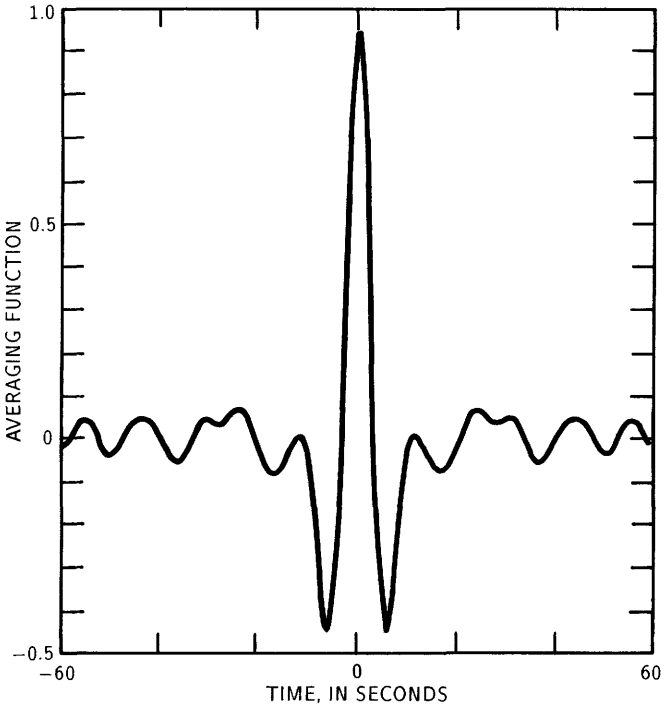

FIGURE 11.9.—Averaging function for $M_{\theta\phi}$ component of moment tensor.

continuous or discontinuous change in source orientation during rupture. Although any source multiplicity is unresolvable from the long-period data, the change in source geometry during the rupture process obtained by using the time-dependent moment-tensor inversion algorithm is remarkably consistent with the results from an analysis of the broadband data (see chap. 10) in which the source is found to consist of two subevents, 3.2 s apart, with differences in source geometry similar to those reported here.

For the May 2 earthquake, the non-double-couple component of the step-function moment tensor appears to be due to a change in the source geometry, with no source multiplicity detected in the long-period data. This solution contrasts with that obtained for the December 13, 1982, Yemen earthquake, which also had a substantial non-double-couple component but in which the source orientation appeared to remain constant and two distinct subevents were resolved (Sipkin, 1986).

CONCLUSIONS

The mechanism of the May 2 earthquake was determined from both an analysis of the teleseismic long- and short-period first motions and a moment-tensor inversion of the teleseismic long-period P waveforms. The 163 first motions yielded a solution with a strike, dip, and rake of 307°, 70°, and 90°, respectively. The step-function moment-tensor inversion yielded a best double-couple with a strike, dip, and rake of 303°, 72°, and 97°, respectively, at a depth of 11 km, with a scalar moment of 4.7×10^{25} dyne-cm. This source, however, had a non-double-couple component of 28 percent. A time-dependent point-source inversion indicates that this non-double-couple part is due to source complexity. This analysis yielded a source duration of 15 s, during which the nodal plane rotated from a strike of 292° to one of 302°.

ACKNOWLEDGMENTS

We thank George Choy for many discussions of the preliminary results, and Jack Boatwright for his improvements to the manuscript.

REFERENCES CITED

Cramer, C.H., and Shakall, A.F., 1983, Discrepancies in strong motion and sensitive arrival time data for the M6.7 Coalinga earthquake of 2 May 1983, *in* Bennett, J.H., and Sherburne, R.W., eds., The 1983 Coalinga, California earthquakes: California Division of Mines and Geology Special Publication 66, p. 307–319.

Furumoto, Muneyoshi, 1979, Initial phase analysis of R waves from great earthquakes: Journal of Geophysical Research, v. 84, no. B12, p. 6867–6974.

Gilbert, Freeman, and Dziewonski, A.M., 1975, An application of normal mode theory to the retrieval of structural parameters and source mechanisms from seismic spectra: Royal Society of London Philosophical Transactions, ser. A, v. 278, no. 1280, p. 187–269.

Hartzell, S.H., and Heaton, T.H., 1983, Teleseismic mechanism of the May 2, 1983, Coalinga, California, earthquake from teleseismic long-period P waves, *in* Bennett, J.H., and Sherburne, R.W., eds., The 1983 Coalinga, California earthquakes: California Division of Mines and Geology Special Publication 66, p. 241–246.

Julian, B.R., and Sipkin, S.A., 1985, Earthquake processes in the Long Valley caldera area, California: Journal of Geophysical Research, v. 90, no. B13, p. 11155–11169.

Kanamori, Hiroo, 1983, Mechanism of the Coalinga earthquake determined from long-period surface waves, *in* Bennett, J.H., and Sherburne, R.W., eds., The 1983 Coalinga, California earthquakes: California Division of Mines and Geology Special Publication 66, p. 233–240.

Oldenburg, D.W., 1982, Multichannel appraisal deconvolution: Royal Astronomical Society Geophysical Journal, v. 69, no. 2, p. 405–414.

Rial, J.A., and Brown, Ethan, 1983, Waveform modeling of long period P waves from the Coalinga earthquake of May 2, 1983, *in* Bennett, J.H., and Sherburne, R.W., eds., The 1983 Coalinga, California earthquakes: California Division of Mines and Geology Special Publication 66, p. 247–259.

Robinson, E.A., 1967, Multichannel time series analysis with digital computer programs: San Francisco, Holden-Day, 298 p.

Sherburne, R.W., McNally, Karen, Brown, Ethan, and Aburto, Arturo, 1983, The mainshock-aftershock sequence of 2 May 1983: Coalinga, California, *in* Bennett, J.H., and Sherburne, R.W., eds., The 1983 Coalinga, California earthquakes: California Division of Mines and Geology Special Publication 66, p. 275–292.

Sipkin, S.A., 1982, Estimation of earthquake source parameters by the inversion of waveform data: Synthetic waveforms: Physics of the Earth and Planetary Interiors, v. 30, no. 2–3, p. 242–259.

—— 1986, Interpretation of non-double–couple earthquake source mechanisms derived from moment tensor inversion: Journal of Geophysical Research, v. 91, no. B1, p. 531–547.

Urhammer, R.A., Darragh, R.B., and Bolt, B.A., 1983, The 1983 Coalinga earthquake sequence: May 2 through August 1, *in* Bennett, J.H., and Sherburne, R.W., eds., The 1983 Coalinga, California earthquakes: California Division of Mines and Geology Special Publication 66, p. 221–231.

12. GROUND-MOTION AND SOURCE PARAMETERS OF THE COALINGA EARTHQUAKE SEQUENCE

By A. McGarr, C. Mueller, J.B. Fletcher, and M. Andrews,
U.S. Geological Survey

CONTENTS

ABSTRACT

Ground-motion and seismic-source parameters, determined from acceleration measured in the epicentral region of the May 2 earthquake, were analyzed with regard to the scaling of source processes responsible for the seismic radiation, as well as the effect of the crustal environment at the hypocenter on these processes. The 30 events, including the M_L=6.7 main shock, studied here were especially well suited to an investigation of how the various parameters scale with earthquake size, in that nearly six orders of magnitude in seismic moment M_0 were represented, extending over a range from about 4×10^{18} down to 7×10^{12}.

In contrast to the results of another study in which the analysis of a large suite of earthquakes indicated that ground-motion parameters could be predicted on the basis of constant-stress-drop scaling in conjunction with the state of crustal stress or strength at the hypocenter, the observations at Coalinga have revealed substantial complexities in the earthquake scaling that appear to be general features of individual earthquake sequences. Specifically, at Coalinga the ground-motion parameters for *S* waves were found to accord with previous expectations only for two events of $M_0>10^{17}$ N·m, with peak velocity v scaling as $Rv \propto M_0^{1/3}$, where R is the hypocentral distance, and with peak acceleration a scaling as ρRa independent of M_0, where ρ is the density. For $M_0<10^{17}$ N·m, however, the ground-motion parameters exhibit a remarkably well defined and strong dependence on seismic moment, with $Rv \propto M_0^{0.73}$ and $\rho Ra \propto M_0^{0.67}$; the transition in scaling appears to be quite abrupt at about 10^{17} N·m. The seismic-stress drop $\Delta\tau$, surprisingly, also shows clear moment-dependent scaling, in that $\Delta\tau \propto M_0^{0.60}$. These unexpected scaling results are attributed at least partly to source processes, rather than wave-propagation or recording effects. Analysis of the *P*-wave ground motion provided confirmation of the *S*-wave results and, furthermore, indicated a highly consistent "corner-frequency shift" for which $f_0(P)/f_0(S)=1.52$, where f_0 is the frequency at which the high- and low-frequency asymptotes of the displacement spectra intersect.

A comparison of the total seismic moment of the Coalinga earthquake sequence of about 5.36×10^{18} N·m to the long-term regional tectonic-strain rate, estimated from plate-tectonic results, suggested a repeat time for "Coalinga" events, considered as characteristic earthquakes, of about 1,000 years. The earthquakes are assumed to be accommodating northeast-southwest-oriented compressional strain at a rate of approximately 4×10^{-8} to 6×10^{-8}/yr, with corresponding expansion vertically.

INTRODUCTION

Ground-motion data recorded in the epicentral regions of major aftershock sequences during the past 10 years have provided a wealth of information bearing both on prediction of ground-motion parameters for the purposes of seismic-hazards assessment and on the source processes responsible for high-frequency seismic radiation. The ground-motion-data set acquired for the Coalinga earthquake sequence has been particularly valuable in terms of providing new insights, partly because the well-recorded events represent an exceptionally broad range of magnitudes, with many shocks of M_L=5–6, but also because of substantial improvements in portable digital recording systems in recent years.

Shortly after the May 2 main shock, two types of instrumentation for recording ground motion were installed in the vicinity of the epicenter (fig. 12.1): General Earthquake Observation System (GEOS) digital recorders (Borcherdt and others, 1983, 1985; Mueller and others, 1984) and SMA–1 accelerometers (Maley and others, 1983). The aftershock data recorded at these stations were then processed to obtain corrected acceleration, velocity, and spectra of the ground displacement.

This chapter reports the analysis of ground-motion and seismic-source parameters for 30 of the Coalinga events, including the main shock. The emphasis here is on near-source recordings of acceleration, so as to gain as

much information as possible about seismic-source processes by keeping the complexities due to wave-propagation effects to a minimum. Thus, nearly all the recordings used here are at epicentral distances that are less than the focal depth, resulting in typical hypocentral distances in the range 10–17 km.

In the context of the results presented by McGarr (1984), the Coalinga data set represented an unusually good opportunity to determine how ground-motion parameters are linked to the crustal environment at the hypocenter and how they scale with earthquake size. In his previous study, which reported the analysis of 66 events from various tectonic situations, McGarr (1984) showed not only that ground-motion parameters scale according to generally accepted principles but also, more interestingly, that these parameters appear to be well-defined functions of the focal depth and state of stress. The ground-motion parameters for peak acceleration ρRa and peak velocity Rv, where ρ is the density, R is the hypocentral distance, a is the peak acceleration, and v is the peak velocity, were shown to vary approximately linearly with focal depth for a given stress state. The parameters for events in compressional environments, and with thrust or reverse-faulting mechanisms, were several times larger, at fixed focal depth, than the corresponding parameters in extensional, or normal-faulting, tectonic settings. Specifically, those data served to define regression lines for peak acceleration

$$\rho Ra \text{ (extensional)} = -1.08 \text{ MPa} + 3.06 \text{ (MPa/km)}z \quad (1a)$$

$$\rho Ra \text{ (compressional)} = 5.65 \text{ MPa} + 8.76 \text{ (MPa/km)}z \quad (1b)$$

and for peak velocity

$$Rv/M_0^{1/3} \text{ (extensional)} = 10^{-4}(\text{m}^2/\text{s})(\text{N}\cdot\text{m})^{-1/3}[3.00 + 0.69(\text{km}^{-1})z] \quad (2a)$$

$$Rv/M_0^{1/3} \text{ (compressional)} = 10^{-4}(\text{m}^2/\text{s})(\text{N}\cdot\text{m})^{-1/3}[4.63 + 1.82(\text{km}^{-1})z] \quad (2b)$$

In short, McGarr (1984) indicated that both the focal depth and the state of stress, as defined according to the directions of the three principal stresses within the crust, are important factors controlling the level of ground motion at small hypocentral distance.

Because equations 1b and 2b are based on many fewer data than equations 1a and 2a, owing to the paucity of appropriate ground-motion data available when McGarr (1984) developed these relations, the data acquired for the Coalinga earthquake sequence, which occurred in a compressional tectonic environment (see chap. 8), provided an opportunity to augment substantially the observational basis for the corresponding regression lines. As described below, the new data provided some confirmation but, more importantly, indicated certain important qualifications regarding the limits of applicability for these equations. In brief, it appears that earthquake ground-motion parameters cannot be predicted solely on the basis of such equations as 1 and 2, which assume that the scaling of the seismic source is independent of earthquake size, as measured by the seismic moment M_0. Analysis of the new data suggests a transition in scaling below which (near $M_0 = 10^{17}$ N·m for the Coalinga earthquake sequence) the ground-motion parameters depend much more strongly on M_0 than above, where equations 1 and 2 still seem appropriate. Thus, the Coalinga ground-motion-data set provides some important insights into earthquake-source processes but makes the prediction of ground-motion parameters less straightforward than indicated by McGarr (1984).

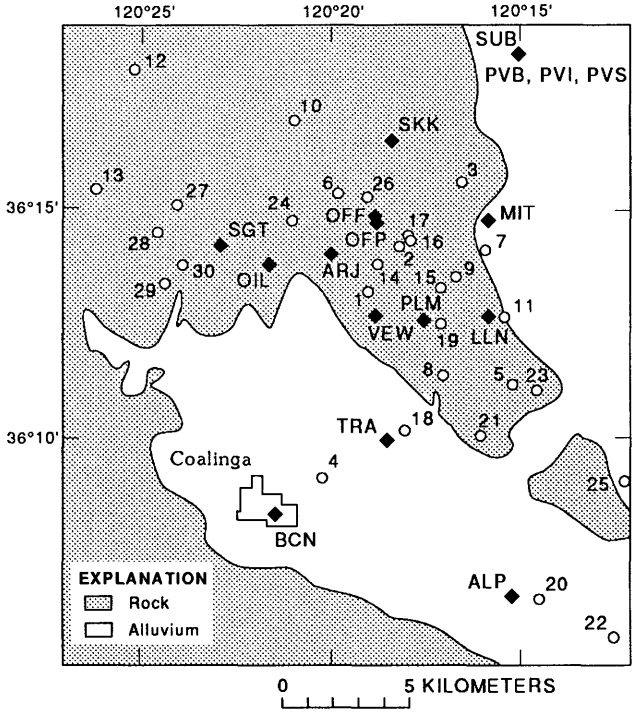

FIGURE 12.1.—Geologic sketch map of Coalinga, Calif., area, showing locations of earthquake epicenters (circles) and recording stations (diamonds) used in this study. Numbers denote events listed in table 12.1. GEOS recorders were used at stations MIT, LLN, VEW, ALP, TRA, SGT, and SUB, and SMA-1 accelerographs at the others. Colocated stations ARP and ARF (table 12.2) are denoted "ARJ".

GROUND-MOTION-DATA PROCESSING

Most of the data analyzed here were recorded on a network of GEOS digital recorders with force-balance accelerometers during a period of about 3 weeks after the

main shock (Borcherdt and others, 1983; Mueller and others, 1984). The remaining data, including those of the main shock and all events after May 25, 1983, were obtained from SMA–1 accelerographs at temporary and permanent sites (Maley and others, 1983). Recording of the 0249 G.m.t. May 9 aftershock at many sites in both networks permitted a detailed comparison of the two recording systems, as discussed below.

Figure 12.1 provides a plan view of the locations of the main shock and the 29 aftershocks investigated here (table 12.1), as well as of the recording stations. The main shock, which was recorded only at several SMA–1 stations colocated at the Pleasant Valley Pumping Plant (PVB), was analyzed by McGarr (1984); those results are included here for comparison with the aftershock data. Most of the aftershocks analyzed here were recorded at multiple sites within the epicentral region.

The events studied here are listed in table 12.1, along with the essential results. These events include all the largest shocks (M_L>4) for which high-quality ground-motion data were available, as well as a sampling of smaller events that was sufficient to acquire scaling information. Most of the results listed in table 12.1 are based on far-field S waves, which were responsible for all the major ground motion at small hypocentral distances; in addition, many of the events recorded at the GEOS stations yielded useful P-wave data that provided both confirmatory and novel information regarding source and ground-motion parameters.

Processing of the ground-motion data is illustrated in figure 12.2, where the acceleration trace of the north-south horizontal component has been integrated to yield a record of ground velocity. Displacement-amplitude spectra are then calculated for the purposes of determining the source parameters, seismic moment M_0 and source radius r_0 (Brune, 1970, 1971); the methodologies involved in estimating the seismic-source parameters from ground-motion records were discussed extensively by Fletcher and others (1980, 1984). In brief, for each recording site a seismic moment is estimated from

$$M_0 = \frac{4\pi\rho\beta^3 R\Omega(0)}{0.57}, \tag{3}$$

where ρ is the density, β is the shear-wave velocity, R is the hypocentral distance, and $\Omega(0)$ is the vector sum of the long-period asymptotes of the spectra of S-wave ground displacement, with the free-surface correction taken into account; 0.57 represents the median value of the radiation factor for S waves (Spottiswoode and McGarr, 1975; Boore and Boatwright, 1984). For all the events analyzed here, ρ is taken as 2,700 kg/m^3, and β is assumed to be 3.3 km/s (see chap. 8). The source radius r_0 is determined from (Brune, 1970, 1971)

$$r_0 = \frac{2.34\beta}{2\pi f_0}, \tag{4}$$

where f_0 is the "corner frequency" at which the low- and high-frequency asymptotes intersect (fig. 12.2). Above f_0, the displacement spectra diminish with frequency f according to f^{-2} or f^{-3} out to a frequency termed f_{max} (Hanks, 1982), beyond which they diminish at a much higher rate, as seen in figure 12.2. f_{max} was estimated from all the spectra analyzed in this study primarily for the purposes of ensuring that f_{max} was not influencing the estimates of either source or ground-motion parameters. For all the events listed in table 12.1, f_{max} was at least 3 or 4 times greater than f_0 and was readily identifiable.

The seismic moments listed in table 12.1 are arithmetic averages of the moments determined at individual sites, and the source radii are the result of applying equation 2 to the geometric average of all the measured corner frequencies f_0 for a particular event. After determining these two source parameters, the stress drop is estimated from (Brune, 1970)

$$\Delta\tau = \frac{7}{16}\frac{M_0}{r_0^3}. \tag{5}$$

The ground-motion parameters measured at each station are ρRa, for peak acceleration, and Rv, for peak velocity. The term "R" appears in each of these parameters to account for the expected effect of geometric spreading according to $1/R$. The density is included in the peak-acceleration parameter, according to Hanks and Johnson (1976), to make its units those of stress, for the purpose of facilitating comparisons with stress drops or crustal strengths (see McGarr, 1984).

As in some previous studies involving these ground-motion parameters (for example, McGarr, 1984), the peaks on the traces are chosen so as to maximize Rv, where v is the peak vector sum of the three components of ground velocity, as would be recorded in a whole space; the correction for the free surface generally entails division of the horizontal components by a factor of 2. It is thus important to measure the ground motion at corresponding times from component to component and from station to station, so that the resulting averaged ground-motion parameters are measures of the single most important impulse radiated from the source. As shown in figure 12.2, the impulsive, simple shape of the signals generally allows consistent peaks to be chosen with little uncertainty.

For a particular impulse, the peak in acceleration generally must either lead or lag the corresponding velocity peak. For nearly all the Coalinga data, the acceleration peak lagged the velocity peak, including the sample illustrated in figure 12.2. This observation

TABLE 12.1.—*Source and ground-motion parameters*

[Event locations from chapters 8 and 9]

No. (fig. 12.1)	Event Time (G.m.t.)	Event Date (1983)	Lat. (°)	Long. (°)	Depth (km)	M_0^S (10^{15} N·m)	r_0 (km)	$\Delta\tau$ (MPa)	Rv (m²/s)	ρRa (MPa)	M_L	$\frac{Rv}{\beta r_0}$ (×10^{-4})	$\frac{Rv}{M_0^{1/3}}$ (10^{-4} m²/s(N·m)$^{-1/3}$)	$f_0(S)$ (Hz)	$f_0(P)$ (Hz)	M_0P (10^{15} N·m)	$Rv(P)$ (m²/s)	$\rho Ra(P)$ (MPa)
1	2342	May 2	36.219	120.317	10.2	3,950	- - -	- - -	3,860	96.2	6.7	- - -	24.4	- - -	- - -	- - -	- - -	- - -
2	1541	May 3	36.236	120.303	7.89	39.7	.897	24.1	690	36.5	4.78	2.33	20.2	1.37	2.13	21.2	117	7.92
3	1842	May 3	36.260	120.275	7.3	.050	.241	1.6	6.5	.84	- - -	.082	1.76	5.11	8.0	.049	1.8	.28
4	2346	May 3	36.152	120.337	13.88	2.52	.600	5.1	65.4	5.58	3.96	.33	1.81	2.05	3.11	1.18	9.8	1.20
5	0246	May 4	36.186	120.253	8.9	.103	.452	.49	5.03	.40	- - -	.034	1.07	2.72	- - -	- - -	.97	.09
6	0728	May 4	36.255	120.330	13.0	25	.814	20.6	396	24.7	- - -	1.474	13.54	1.51	2.33	18.5	46.2	3.60
7	0818	May 4	36.235	120.265	8.76	.054	.386	.41	2.16	.19	2.93	.017	.57	3.18	- - -	- - -	1.86	.25
8	0848	May 4	36.189	120.283	5.7	.0072	.433	.04	.54	.06	- - -	.004	.28	2.84	- - -	- - -	- - -	- - -
9	0848	May 4	36.225	120.278	12.94	.577	.532	1.68	15.2	1.16	3.48	.087	1.83	2.31	3.65	.544	5.03	.57
10	1611	May 4	36.282	120.349	11.69	3.5	.945	1.8	44.5	4.3	4.39	.143	2.93	1.30	- - -	- - -	7.13	.94
11	0032	May 5	36.211	120.257	9.77	.80	.597	1.64	29.5	4.60	- - -	.150	3.18	2.06	- - -	- - -	4.99	.92
12	2246	May 5	36.301	120.419	10.10	.097	.369	.84	6.56	.62	3.36	.054	1.43	3.33	- - -	- - -	1.68	.30
13	0345	May 8	36.257	120.436	1.8	.306	.605	.6	6.07	.45	3.37	.030	.90	2.03	- - -	- - -	2.47	.25
14	0249	May 9	36.229	120.312	12.04	42	.842	30.8	619	36.8	5.30	2.228	17.81	1.46	2.41	45.9	194	15.1
15	0312	May 9	36.221	120.285	13.02	.13	.556	.33	4.28	.32	- - -	.023	.84	2.21	3.48	.26	3.73	1.10
16	0319	May 9	36.239	120.298	12.31	.339	.312	4.9	29.9	2.83	3.62	.290	4.29	3.94	4.69	.72	14.7	2.03
17	0326	May 9	36.240	120.299	12.43	21.2	1.241	4.85	186	11.2	4.60	.454	6.72	.99	1.57	22.7	57.8	5.80
18	1815	May 9	36.169	120.301	10.00	.131	.410	.83	9.70	.92	- - -	.072	1.91	3.0	- - -	- - -	4.26	.77
19	2014	May 9	36.208	120.285	8.12	.076	.324	.98	7.02	.65	- - -	.066	1.66	3.79	- - -	- - -	5.41	.75
20	0157	May 12	36.108	120.241	9.54	.111	.494	.40	4.20	.25	- - -	.026	.87	2.49	- - -	- - -	- - -	.25
21	1341	May 12	36.167	120.268	10.98	8.08	.732	9.0	168	9.7	4.50	.695	8.37	1.68	- - -	- - -	24.9	2.32
22	1501	May 13	36.094	120.209	10.5	.21	.437	1.1	7.4	.58	- - -	.051	1.24	2.81	4.39	.213	3.49	.46
23	0246	May 18	36.184	120.242	8.88	2.06	.527	6.2	109.0	11.1	- - -	.627	8.57	2.33	- - -	- - -	14.6	3.37
24	2039	May 18	36.245	120.350	8.5	.41	.508	1.4	18.6	1.2	- - -	.111	2.50	2.42	3.70	.444	3.77	.54
25	0839	May 22	36.151	120.202	10.48	1.28	.561	3.2	39.1	2.95	4.24	.211	3.60	2.19	3.0	.429	3.47	.36
26	0902	May 24	36.254	120.317	8.86	21.2	.740	22.9	256	15.7	4.70	1.048	9.25	1.66	2.70	12.6	37.5	7.5
27	0740	July 9	36.251	120.400	9.02	63.2	1.107	20.4	409	27.5	5.39	1.120	10.27	1.11	- - -	- - -	- - -	- - -
28	0239	July 22	36.241	120.409	7.37	450	1.781	34.9	1,480	74.3	6.04	2.518	19.30	.69	- - -	- - -	- - -	- - -
29	0343	July 22	36.222	120.406	7.89	42.3	.727	48.2	525	34.9	5.02	2.188	15.07	1.69	- - -	- - -	- - -	- - -
30	2231	July 25	36.229	120.398	8.42	78.3	.672	112.9	976	52.9	5.33	4.401	22.81	1.83	- - -	- - -	- - -	- - -

suggests that the peak acceleration is not generally associated with the initiation of the rupture event which gives rise to the most important pulse of ground motion.

An important emphasis in this study involves the scaling of the ground motion, some features of which are illustrated in figure 12.3, where traces of horizontal ground velocity are shown for a representative suite of seven events, each separated in seismic moment by about an order of magnitude, with M_0 ranging from about 4×10^{18} N·m for the main shock down to 7×10^{12} N·m. Although the amplitudes of the velocity pulses increase markedly with M_0, the pulse shapes vary surprisingly little. Although the velocity traces of the largest events are generally composed of multiple pulses, in contrast to

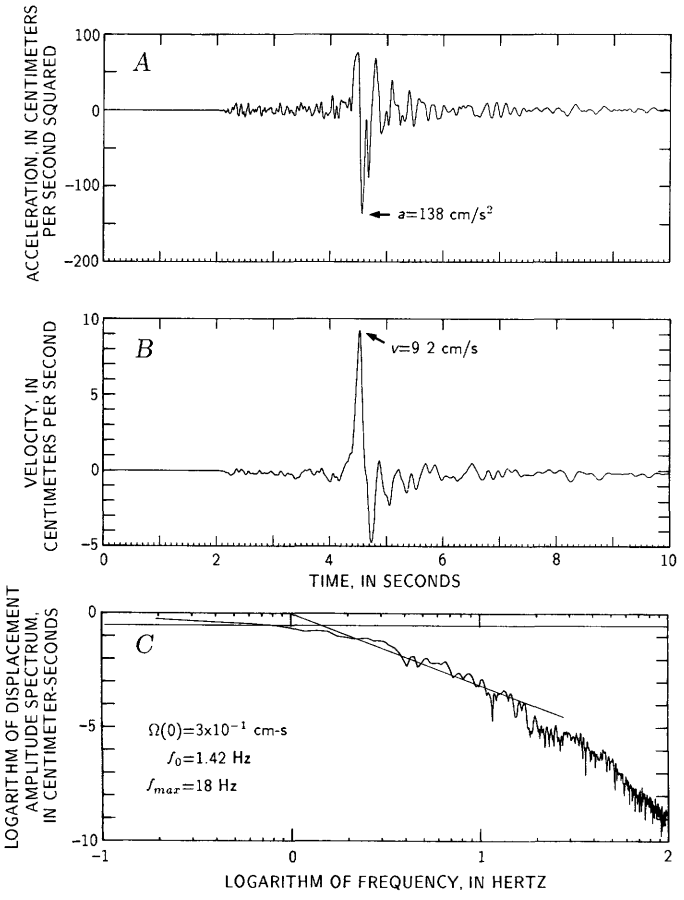

FIGURE 12.2.—Records of 0249 G.m.t. May 9 event on north-south component at GEOS station VEW. *A*, Ground acceleration. *B*, Velocity. *C*, Displacement.

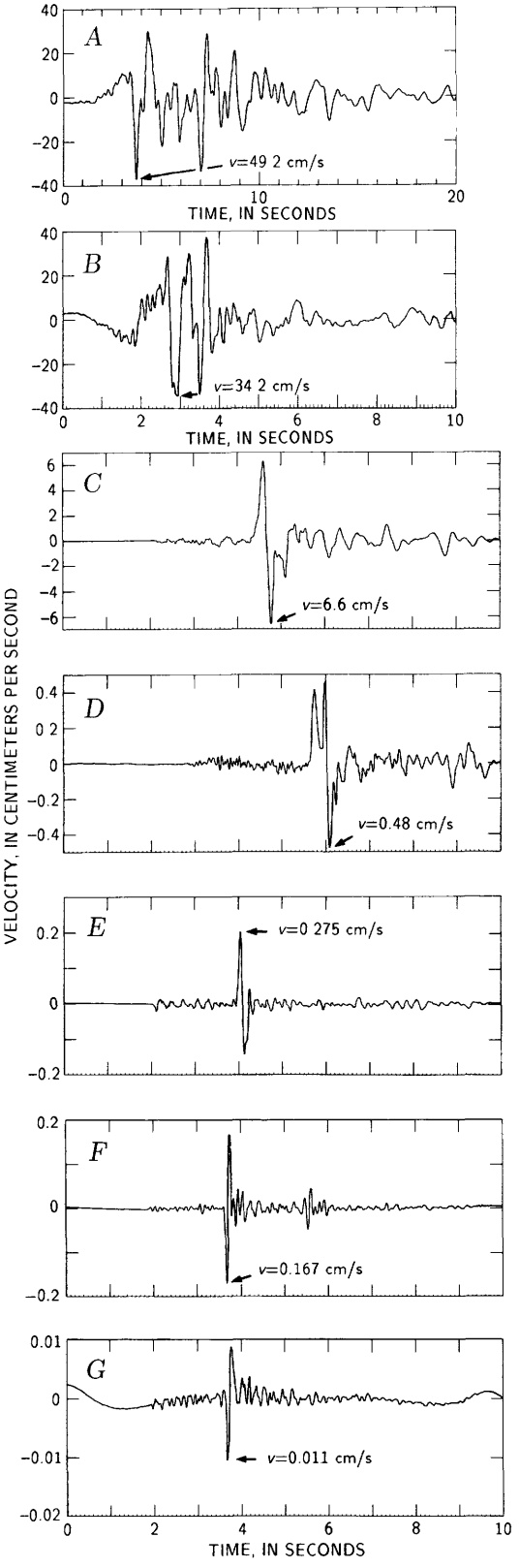

FIGURE 12.3.—Horizontal components of ground velocity for seven events spanning nearly six orders of magnitude. *A*, 2342 G.m.t. May 2 event on northeast-southwest component at station PVB. *B*, 0239 G.m.t. July 22 event on east-west component at station OIL. *C*, 0249 G.m.t. May 9 event on north-south component at station LLN. *D*, 1611 G.m.t. May 4 event on north-south component at station LLN. *E*, 2039 G.m.t May 18 event on N. 5° E. component at station VEW. *F*, 1842 G.m.t. May 3 event on S. 80° E. component at station MIT. *G*, 0848 G.m.t. May 4 event on N. 5° E. component at station VEW.

the single-pulse shape of those for the smaller shocks, the shapes of all the pulses are quite similar. Possibly the most important point illustrated by figure 12.3 is the excellent clarity of recording for the entire suite of events from largest to smallest. This wide dynamic range provided a means of addressing some difficult scaling issues, as shown below.

Although P waves are not generally significant in terms of damaging ground motion, in comparison with S waves, their analysis can nonetheless provide important information regarding the source processes that give rise to S-wave seismic radiation. Accordingly, as shown in figure 12.4, P-wave pulses of events recorded at the GEOS stations were processed and analyzed much the same as the S waves, to the extent permitted by the signal-to-noise ratios. As recorded at station MIT, the P-wave pulse of the 1842 G.m.t. May 3 event was exceptionally clear, as was the corresponding S-wave pulse illustrated in figure 12.3F. The parameters measured from the P waves (table 12.1) included the seismic moment, denoted M_0^P to distinguish it from that estimated from the S waves, as well as $f_0(P)$, $Rv(P)$, and $\rho Ra(P)$. M_0^P is estimated from (for example, Hanks and Wyss, 1972)

$$M_0^P = \frac{4\pi\rho\alpha^3 4R\Omega(0)^P}{0.39}, \qquad (6)$$

where α is the P-wave velocity, here taken as 5.7 km/s (see chap. 8), and $\Omega(0)^P$ is the long-period level of the corresponding displacement spectrum, corrected for the effect of the free surface (see Gutenberg, 1944). The factor 0.39 represents the median value of the P-wave-radiation factor (Spottiswoode and McGarr, 1975; Boore and Boatwright, 1984). Note that the moments calculated from P waves (table 12.1) with equation 6 are used here only for the purposes of comparison with the S-wave moments, partly because M_0^P could not be estimated for all the events but also because of the lower signal-to-noise ratios of the P-wave spectra. Thus, in this study the size of the event is defined exclusively on the basis of M_0^S or, simply, M_0 (eq. 3).

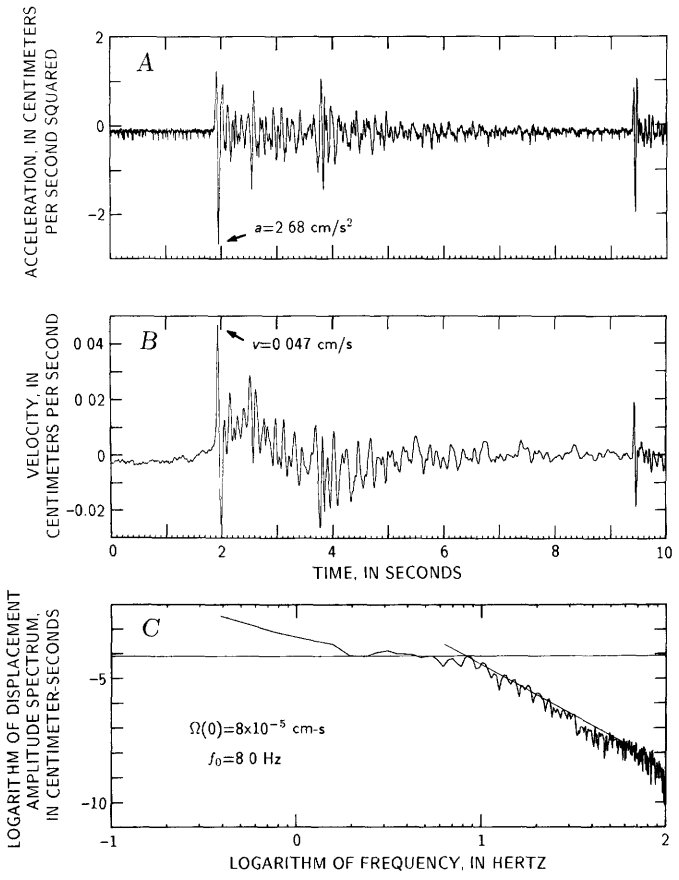

FIGURE 12.4.—Vertical component of ground acceleration (A), velocity (B), station, and P-wave displacement (C) for 1842 G.m.t. May 3 event recorded at station MIT (table 12.1). Note similarity of P-wave-velocity pulse to its S-wave counterpart (fig. 12.3F).

As illustrated in figure 12.4, the measurements of the "corner frequency" $f_0(P)$ and the ground-motion parameters $Rv(P)$ and $Ra(P)$ are performed exactly the same as for their S-wave counterparts. $f_0(P)$ is measured only for comparison with $f_0(S)$ or f_0. Similarly, $Rv(P)$ and $\rho Ra(P)$ were measured primarily to obtain independent evidence regarding the scaling of the S-wave ground-motion parameters, as described below.

Because the emphasis of this study is on source processes rather than wave-propagation or recording-site effects, it is important to know the extent to which the recorded body waves are influenced, or contaminated, by phenomena extraneous to the seismic source, other than those that can be easily incorporated into the analysis, such as geometric spreading and the effect of the free surface. Similarly, it is essential to know whether or not the ground-motion data are influenced in some unpredictable way by the recording system. The data obtained for the 0249 G.m.t. May 9 event provided the means of investigating both of these issues because, as mentioned above, this event was well recorded by both the GEOS and SMA–1 networks.

The seismic moments, corner frequencies, and ground-motion parameters as estimated at 14 sites for the 0249 G.m.t. May 9 event are listed in table 12.2. Only the data from SMA–1 stations ARP and ARF appear to show a clear-cut site effect, in that both ρRa and Rv at these two stations, which are colocated (Maley and others, 1983), are many times larger than typical values measured elsewhere. The traces of ground motion, as well as the spectra, at stations ARP and ARF indicate a resonance at about 4 Hz, which is almost certainly associated with marked amplification of the ground-motion parameters.

TABLE 12.2.—*Source and ground-motion parameters for the 0249 G.m.t. May 9 event, as measured at 14 stations*

Station	Recorder	R (km)	ρRa (MPa)	Rv (m^2/s)	f_0 (N-S) (Hz)	f_0 (E-W) (Hz)	M_0 (10^{15} N·m)	$\rho Ra(P)$ (MPa)	$Rv(P)$ (m^2/s)	$f_0(P)$ (Hz)	M_0^P (10^{15} N·m)
VEW	GEOS	12.66	30.7	768	1.42	1.15	48.7	---	---	---	---
SUB	GEOS	16.26	47.8	907	1.23	1.32	87.0	7.3	90.3	2.69	43.7
LLN	GEOS	13.40	21.9	483	1.33	1.46	31.0	10.4	161	1.74	86
MIT	GEOS	13.40	30.2	398	1.15	---	40.1	27.5	330	---	---
SGT	GEOS	13.98	59.3	633	1.40	1.15	53.8	---	---	3.00	7.9
TRA	GEOS	14.33	31.1	749	1.54	1.47	65.0	---	---	---	---
OIL	SMA-1	13.20	63.7	593	1.51	1.57	39.8	---	---	---	---
ARP	SMA-1	12.65	156.2	1,750	1.37	1.89	44.4	---	---	---	---
ARF	SMA-1	12.65	168.0	1,710	1.39	1.73	42.2	---	---	---	---
PVI	SMA-1	16.30	29.3	658	2.00	1.28	38.4	---	---	---	---
OFF	SMA-1	12.66	24.5	367	1.56	1.76	18.1	---	---	---	---
PRA	SMA-1	12.82	50.7	858	1.62	1.84	31.8	---	---	---	---
SKK	SMA-1	13.52	31.5	548	1.42	1.65	22.8	---	---	---	---
BCN	SMA-1	16.60	20.8	464	1.39	1.35	32.3	---	---	---	---

Interestingly, however, the seismic moments estimated for these two Anticline Ridge stations fall near the middle of the distribution of moments measured elsewhere (table 12.2).

Except for stations ARP and ARF (table 12.2), there seem to be no obvious site effects, although the disagreements in the results for stations SUB and PVI, which are nearly colocated at the Pleasant Valley Pumping Plant (fig. 12.1), are somewhat worrisome. M_0, ρRa, and Rv are all larger at station SUB than at station PVI; this discrepancy may be related to the fact that station SUB is a free-field site, whereas station PVI is on the first floor of the pumping plant. In view of the ground-motion data for numerous other events, however, for which the values of the source and ground-motion parameters at station SUB are not exceptional, it seems unlikely that this station has any substantial site effects.

With regard to possibly systematic effects of recording instrumentation on the results of interest here, we consider comparisons between ground-motion parameters and seismic moments based on the GEOS and SMA-1 data, excluding the station ARP and ARF data (table 12.2). First, the average value of ρRa for the GEOS stations is 36.8±13.9 MPa, whereas that obtained for the SMA-1 sites is 36.8±16.8 MPa; that is, the agreement is embarrassingly good for peak acceleration. The same comparison for Rv yields 656±190 m^2/s for the GEOS records and 581±169 m^2/s for the SMA-1 data, which, again, represents respectable agreement. For the seismic moments, the GEOS sites give an average of $5.43\pm1.98\times10^{16}$ N·m; and the six SMA-1 stations, excluding stations ARP and ARF, $3.05\pm0.86\times10^{16}$ N·m. In summary, there appear to be no systematic and substantial differences between the results measured using the two different types of instrumentation. Thus, for the purpose of analyzing S waves, the GEOS and SMA-1 data available for this study appear to provide consistent results, within their respective recording bandwidths.

SOURCE PARAMETERS

The seismic moments listed in table 12.1 are of interest for at least two reasons. First, they are the most robust and model-independent measure of earthquake size, being the product of the modulus of rigidity, the fault area, and the average slip, and so M_0 serves as the independent variable of scaling. Second, the seismic moments can be used in estimating seismic deformation from, for example (Brune, 1968), the relation

$$\bar{u} = \frac{\Sigma M_0}{\mu S}, \tag{7}$$

where $\bar{u}$ represents the average seismic slip over a fault of area S and modulus of rigidity μ due to a series of earthquakes of total moment ΣM_0.

For either purpose, it is useful to know the uncertainties in the estimates of M_0, which, though largely independent of source model, are subject to uncertainties associated with velocity and density structure, the radiation factor, and errors in measuring the long-period level of the displacement spectra. Multiple, independent measurements of M_0, preferably using different techniques, yield the most realistic estimates of its uncertainty. In table 12.1, the moment of the main shock, as explained by McGarr (1984), was the result of arithmetically averaging four independent estimates, using the procedures of Hartzell and Heaton (1983), Kanamori (1983), Rial and Brown (1983), and Urhammer and others (1983), who obtained the following respective values: 3.8×10^{18}, 5.4×10^{18}, 4.3×10^{18}, and 2.3×10^{18} N·m, yielding a standard deviation of 1.29×10^{18}, which is about 33

percent of the average value listed in table 12.1. For the 0249 G.m.t. May 9 event, the 14 S-wave estimates of M_0 listed in table 12.2 have a standard deviation of 1.76×10^{16}, or 41 percent of the average value in table 12.1. For the other multiple-site estimates of M_0 used here, nearly all the standard deviations indicate uncertainties between 25 and 50 percent of the average value.

In addition to the main shock, teleseismic estimates of M_0 for the events of 0740 G.m.t. July 9, 0343 and 2239 G.m.t. July 22, and 2231 G.m.t. July 25 are, respectively, 6.3×10^{16}, 2.5×10^{16}, 5.3×10^{17}, and 9.3×10^{16} N·m (centroid moment-tensor solutions; U.S. National Earthquake Information Service monthly listing). A comparison of these values with the corresponding near-source estimates listed in table 12.1 indicates good agreement. The moment estimates by Urhammer and others (1983) of 13 of the events listed in table 12.1 provide yet another independent check on the estimates used here. The geometric average of the ratio of the moments listed in table 1 of Urhammer and others to the corresponding moments listed in table 12.1 is $0.73^{+0.49}_{-0.29}$, a result indicating that systematic differences associated with procedure and data are almost insignificant. Finally, we note that the moments estimated using P waves generally agree well with the S-wave estimates, as shown in figure 12.5 and listed in table 12.1, where we observe that nearly all the P- and S-wave estimates of M_0 are within a factor of 2 of each other. In summary, it appears, from all the independent information bearing on the estimates of M_0 used here, that typical uncertainties range from 30 to 40 percent of the listed value; no significant systematic bias is evident.

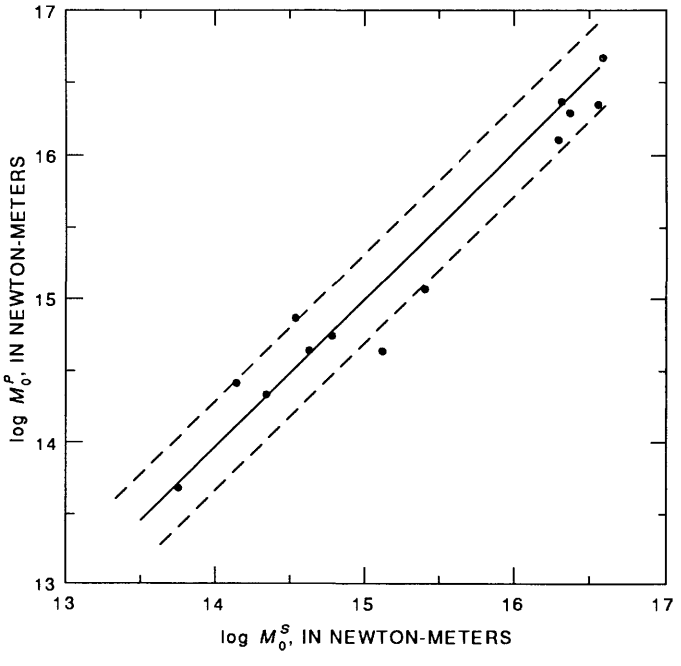

FIGURE 12.5.—Seismic moments estimated using P and S waves. Solid line, perfect agreement; dashed lines, disagreement by a factor of 2.

MAGNITUDE-MOMENT RELATION

Because it has not been feasible to calculate seismic moments rigorously (equations 3, 6) for all the events in the Coalinga earthquake sequence, it is useful to determine an approximate relation between M_0 and local magnitude M_L for the purpose of a reasonably complete assessment of the seismic deformation. Local magnitudes (see chap. 8, table 8.3) are plotted in figure 12.6 and listed in table 12.1, where we see that the relation between magnitudes and log M_0 is very well defined. A least-squares fit through these data yields

$$\log M_0 = 10.06(\pm0.34) + 1.28(\pm0.07)M_L\,, \qquad (8)$$

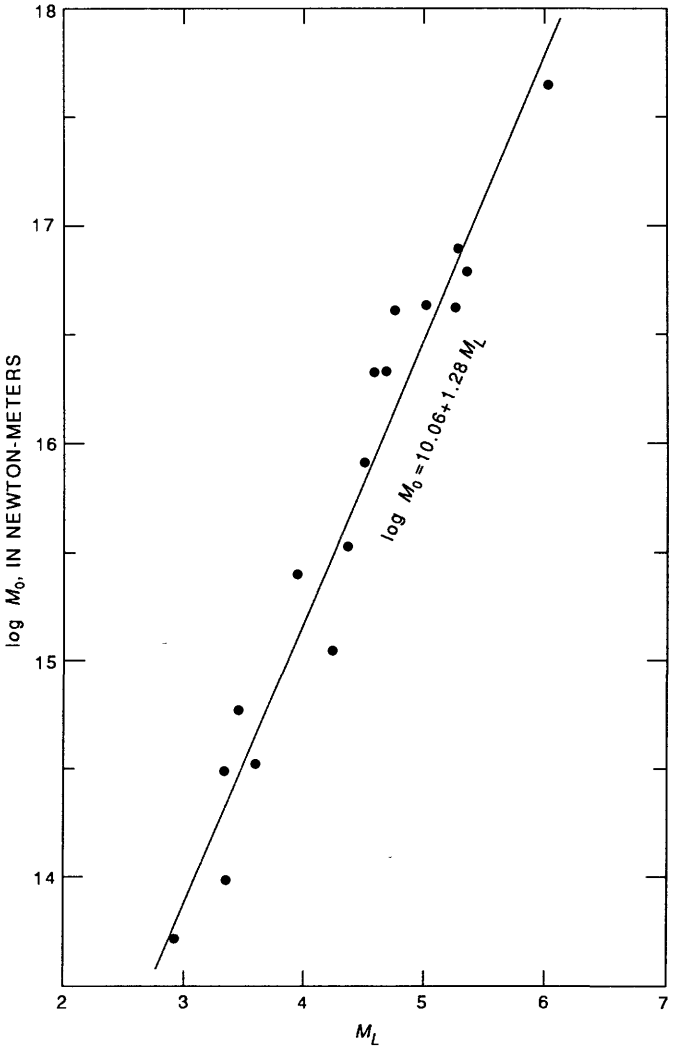

FIGURE 12.6.—Seismic moment as a function of local magnitude M_L, as estimated by Eaton (chap. 8).

where M_0 is in newton-meters. From the tight fit of the 17 data to equation 8, it is clear that M_L, as assigned by Eaton (chap. 8), is quite a reliable predictor of M_0.

SEISMIC DEFORMATION

We have attempted to assess the overall seismic deformation, as measured by M_0, by combining the moments derived from table 1 of Urhammer and others (1983) and table 8.3 of Eaton (chap. 8) with those listed in table 12.1 here. Equation 8 permits estimates of M_0 from the M_L assignments by Eaton, whereas Urhammer and others listed estimates of M_0 in their table 1. Thus, table 12.3 is intended as a reasonably complete compilation of Coalinga events of $M_0 \geq 2\times10^{15}$ N·m for the period May 2 through September 30, 1983.

There are several points of interest to the data listed in table 12.3. First, the very largest events clearly account for nearly all the deformation. The total of the listed moments is 5.20×10^{18} N·m, of which 76 percent is accounted for by the main shock; another 13 percent of the total is attributable to the two events of $10^{17} < M_0 < 10^{18}$ N·m. Thus, all the remaining smaller events account for only about 11 percent of the total M_0 listed in table 12.3.

The distribution of seismic deformation can be investigated more comprehensively by forming a moment-frequency distribution from the data listed in table 12.3, as shown in figure 12.7, where N represents the number of events of moment $\geq M_0$ during the 5-month period from May 2 through September 30. The fit to the data

$$\log N = 9.98 - 0.55 \log M_0 \qquad (9)$$

was made by using the maximum-likelihood technique (Aki, 1965); the standard deviation of the slope in equation 9 is about 0.18.

In view of other studies for which moment or magnitude distributions have been determined, the slope of 0.55 (equation 9) is slightly lower than normal, though not significantly so. In a study of the worldwide distribution of moments, Chinnery and North (1975) found that a slope of 0.61 represented their data well over a broad range of M_0 extending from 2×10^{18} to 2×10^{23} N·m. Wesnousky and others (1983), on the basis of studies in Japan and California, concluded that a slope of about 0.67 is typical.

We note that from the data listed in table 12.3, the slope of the moment-frequency distribution appears to be invariant over time. To demonstrate this relation, we calculate maximum-likelihood slopes for the first and second halves of the data, considered separately. This slope is given by (Aki, 1965; Page, 1968):

TABLE 12.3.—*Moments and magnitudes for events of $M_0 > 2\times10^{15}$ N·m between May 2 and October 2, 1983*

[Data sources: B, Urhammer and others (1983); E, Eaton (chap. 8); M, this chapter]

Event		M_L	M_0 (10^{15} N·m)
Time (G.m.t.)	Date (1983)		
2342	May 2	6.7 (E,B)	3,950
2346	May 2	5.6 (B)	209
0009	May 3	4.0 (B)	2.0
0015	May 3	4.1 (B)	2.6
0018	May 3	4.4 (B)	9.4
0039	May 3	4.52 (E)	7.08
0057	May 3	5.08 (E)	36.5
0141	May 3	4.54 (E)	7.43
0432	May 3	4.2 (B)	3.9
0604	May 3	4.51 (E)	6.80
0635	May 3	4.25 (E)	3.16
0855	May 3	4.70 (E)	11.9
0939	May 3	4.11 (E)	2.09
1541	May 3	4.78 (E)	39.7
2346	May 3	3.96 (E)	2.52
0728	May 4	4.8 (B)	25
1611	May 4	4.39 (E)	3.5
1020	May 5	4.61 (E)	9.14
0249	May 9	5.30 (E)	42
0326	May 9	4.60 (E)	21.2
1341	May 12	4.50 (E)	8.08
0246	May 18	- - -	2.06
1105	May 19	4.16 (E)	2.42
0902	May 24	4.70 (E)	21.2
0518	June 7	4.13 (E)	2.22
0309	June 11	5.20 (E)	52.0
0740	July 9	5.39 (E)	63.2
1928	July 18	4.16 (E)	2.42
0239	July 22	6.04 (E)	451
0249	July 22	4.14 (E)	2.29
0343	July 22	5.02 (E)	42.3
2231	July 25	5.33 (E)	78.3
2202	Aug. 12	4.10 (E)	2.03
1243	Aug. 14	4.30 (E)	3.66
0916	Sept. 9	5.30 (E)	69.8
1148	Sept. 11	4.48 (E)	6.23

$$\text{slope} = \frac{0.4343}{\overline{\log M_0} - \log M_0(\text{min})} \pm \frac{1.96 \text{ slope}}{\sqrt{n}},$$

where $\overline{\log M_0}$ is the average value of $\log M_0$ for the set of events under consideration, $\log M_0(\text{min})$ is the threshold value (15.30 in this case), and n is the number of data used. For the first 18 data listed in table 12.3, $\overline{\log M_0}=16.06$; and for the second 18, $\overline{\log M_0}=16.12$, yielding respective slopes of 0.57 ± 0.26 and 0.53 ± 0.24. This apparent time independence of the slope in the moment-frequency distribution is equivalent to the phenomenon termed "magnitude stability," recognized by Lomnitz (1966).

To obtain a slightly more complete accounting of the seismic deformation at Coalinga, we use equation 9 to estimate the contribution due to events of $M_0 < 2\times10^{15}$ N·m, the threshold for table 12.3. Specifically (for example, Molnar, 1979), the total moment implied by equation 9 is given by

$$M_0(\text{tot}) = \int_0^\infty M_0\left(-\frac{dN}{dM_0}\right)dM_0$$

where $N(M_0)$ is truncated at a given maximum M_0, termed $M_0(\max)$. If $M_0(\max)=2\times10^{15}$ N·m, which when added to what is accounted for in table 12.3 yields a total overall moment of 5.36×10^{18} N·m. Thus, the events omitted from table 12.3 contributed only 3 percent to the total deformation, whereas the main shock contributed about 74 percent to the recomputed total.

SOURCE RADIUS AND STRESS DROP

The normally assumed scaling of seismic-source and ground-motion parameters (for example, Hanks and McGuire, 1981; Boore, 1983; Joyner, 1984; McGarr, 1984) is based partly on the observation by Hanks (1977) that the seismic-stress drop does not vary systematically with seismic moment. If so, then from equation 5 the source radius should scale as $M_0^{1/3}$.

As plotted in figure 12.8, the source radii listed in table 12.1 show a fairly well defined dependence on moment; but the exponent of 0.13 determined from the regression fit is lower than expected, from constant-stress-drop scaling, by a factor of more than 2. Thus, we sense that the common scaling assumptions may not be applicable to the Coalinga earthquake sequence.

The plot of seismic-stress drops (fig. 12.9), calculated from equation 5 and listed in table 12.1, as a function of seismic moment provides the most straightforward indication that $\Delta\tau$ depends critically on M_0. The stress drops show a remarkably unambiguous moment dependence, consistent with the weak dependence shown by the source radii. Specifically,

$$r_0 \propto M_0^{0.13} \tag{10a}$$

and

$$\Delta\tau \propto M_0^{0.60} . \tag{10b}$$

Analysis of a more comprehensive data set, reported by Andrews and others (1984), indicated a similarly strong moment dependence for stress drops of the Coalinga aftershocks. Several reports on other earthquake sequences (for example, Tucker and Brune, 1973; Johnson and McEvilly, 1974; Archuleta and others, 1982; Fletcher and others, 1984) have noted a tendency for stress drops to increase with seismic moment. What is remarkable about the Coalinga earthquake sequence, however, is the superb definition of this moment dependence (figs. 12.8, 12.9).

The exceptionally broad range in the stress drops listed in table 12.1 has several interesting aspects. First, the value of about 113 MPa estimated for the 2231 G.m.t. July 25 shock is one of the highest ever estimated, although in the context of figure 12.9 it is not outside the range of expectations. This particular stress drop was estimated from ground-motion data recorded at four sites, with hypocentral distances ranging from 9.1 to 13.7 km. Eight estimates of corner frequency yielded a

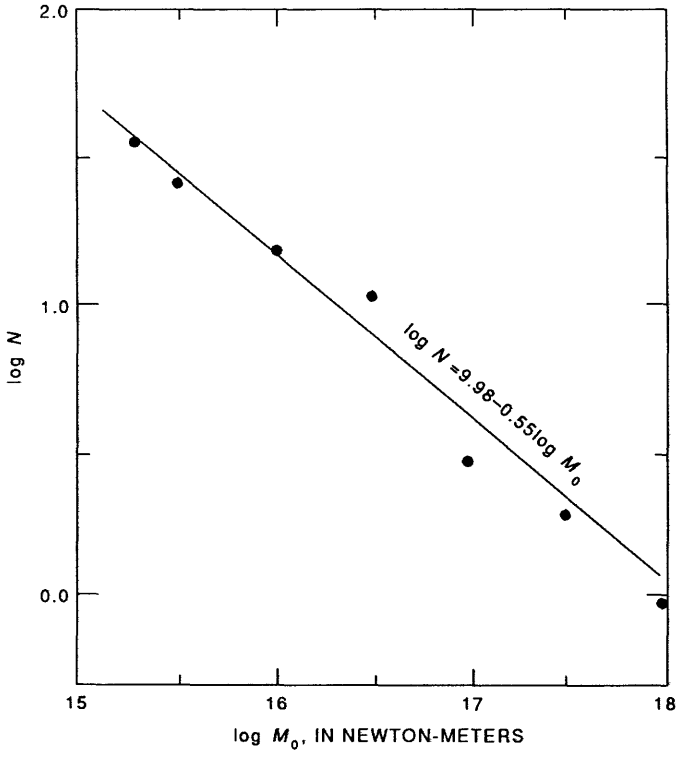

FIGURE 12.7.—Seismic-moment/frequency distribution for events of $M_0>2\times10^{15}$ N·m in the Coalinga earthquake sequence. N, number of events of moment $\geq M_0$, between May 2 and October 1, 1983. Main shock is included in this distribution.

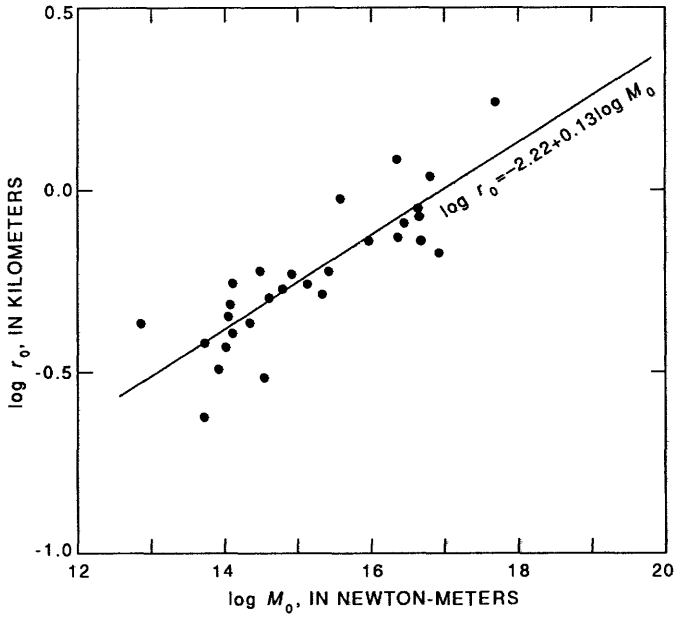

FIGURE 12.8.—Source radius as a function of seismic moment for 29 events listed in table 12.1.

geometric average of $1.83^{+0.34}_{-0.38}$, and the uncertainty in the four estimates of seismic moment is 5.71×10^{16} N·m, or 73 percent of the listed value. As mentioned above, the teleseismic estimate of M_0 for this event is 9.3×10^{16} N·m, which suggests a value at least as high as that listed in table 12.1. If the corner frequency were reduced by one standard deviation, then the resulting stress drop would be (equation 5) about 69 MPa, still well above the normally expected range of 0.1 to 10 MPa (see Hanks, 1977; McGarr and others, 1981).

The lowest stress drops are also of interest in that, from the pattern shown in figure 12.9, there is no apparent lower bound. By analyzing smaller events than those listed in table 12.1, stress drops significantly lower than the minimum of 0.04 MPa would probably have been estimated. In short, the normally expected upper and lower bounds for stress drops of 10 and 0.1 MPa, respectively, do not seem to apply to the Coalinga events.

P- AND *S*-WAVE CORNER FREQUENCIES

Because there is no generally accepted relation between *P*-wave corner frequency $f_0(P)$ and source radius (see Hanks and Wyss, 1972; Trifunac, 1972) corresponding to equation 4 for *S* waves, we have not attempted to use measurements of $f_0(P)$ to obtain independent estimates of r_0. In view of the current state of the art, it is useful simply to know the relation, if any, between $f_0(P)$ and $f_0(S)$. As recently reviewed by Hanks (1981), the available observations generally indicate that $f_0(P)>f_0(S)$ and, moreover, are largely consistent with $1.2\leq f_0(P)/f_0(S)\leq1.7$, with some exceptions.

As shown in figure 12.10, the corner-frequency measurements for the Coalinga events (table 12.1) indicate quite an unambiguous relation between $f_0(P)$ and $f_0(S)$, in contrast to other studies (for example, Molnar and others, 1973), in which impressive scatter is the rule. The line in figure 12.10 was drawn on the basis of the geometric average of $f_0(P)/f_0(S)$ of $1.52^{+0.14}_{-0.13}$ for the 13 data points. Thus, for Coalinga, values of $f_0(P)/f_0(S)$ are all near the middle of the range 1.2–1.7 suggested by Hanks (1981). The corresponding result for the 14 Oroville, Calif., events analyzed by Fletcher (1980) is $1.75^{+0.48}_{-0.38}$, which does not differ significantly from the Coalinga average, although the scatter in the ratios is about 2.5 times as great. Because, however, other observational studies for which $f_0(P)$ and $f_0(S)$ are each well determined indicate much broader distributions in

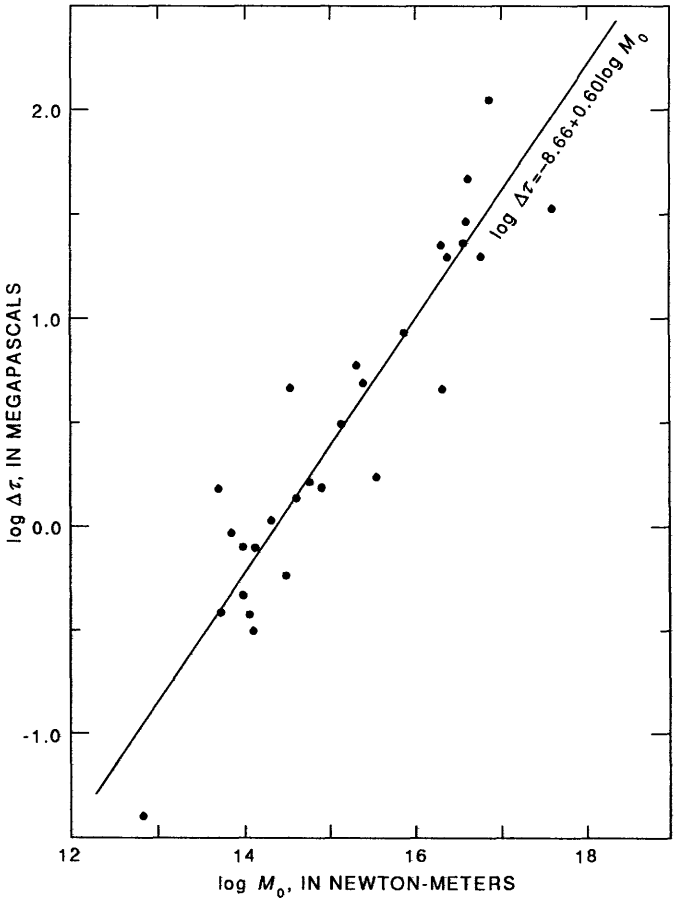

FIGURE 12.9.—Stress drop as a function of seismic moment for 29 events listed in table 12.1.

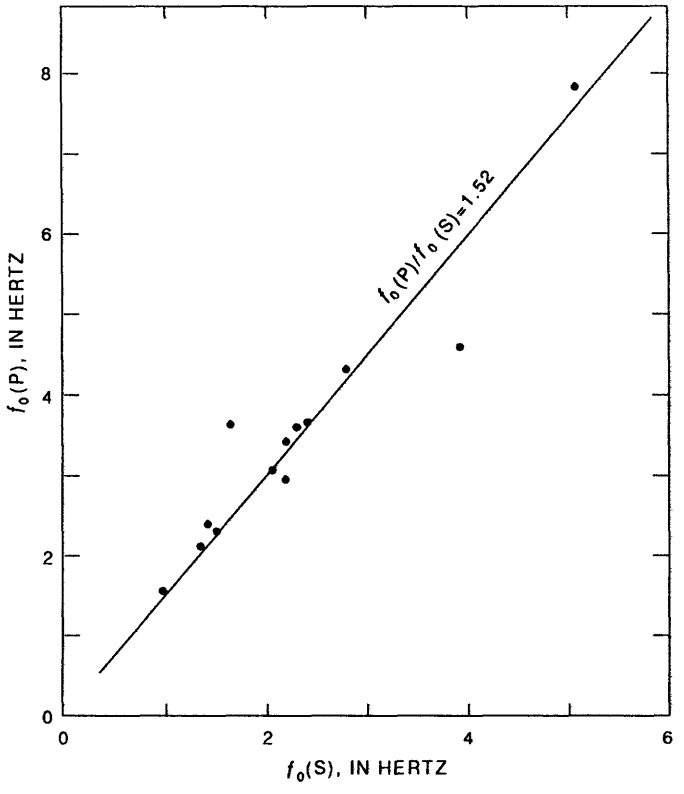

FIGURE 12.10.—*P*-wave corner frequency as a function of *S*-wave corner frequency for 13 events (table 12.1) for which both could be estimated. Solid line represents the relation $f_0(P) = 1.52f_0(S)$, determined from geometric average of $f_0(P)/f_0(S)$.

corner-frequency ratios (for example, Molnar and others, 1973), we do not suggest that the result in figure 12.10 necessarily is generally applicable.

GROUND-MOTION PARAMETERS

As noted above in the section entitled "Introduction," the Coalinga ground-motion data were originally viewed as an opportunity to refine and confirm our knowledge regarding the depth dependence of ground-motion parameters due to earthquakes in a compressive tectonic environment, for which few data were available at the time of McGarr's (1984) report. A glance at figures 12.11 and 12.12 is sufficient to realize that such confirmation is not forthcoming. For the peak-acceleration parameter ρRa (fig. 12.11), which in the previous study had shown quite a well-defined depth dependence, as described by equation 1b, the Coalinga data indicate singularly little systematic depth dependence, although the regression line from the previous study appears to be an upper-bounding envelope to the data. The main shock and the largest aftershock (table 12.1) provided the only acceleration data in good agreement with previous expectations.

For the peak-velocity parameter (fig. 12.12), the regression line (eq. 2b) from McGarr (1984), as for peak acceleration, appears to be, at best, an upper bound to the data, rather than a fit to the points. Here, however, possibly 5 or 6 of the 30 data points are acceptably close to the regression line, including the main-shock data point. Another representation of the depth dependence of peak velocity, using a different normalization for earthquake size, is illustrated in figure 12.13, which shows that the regression line from the previous study does not serve even as an upper bound.

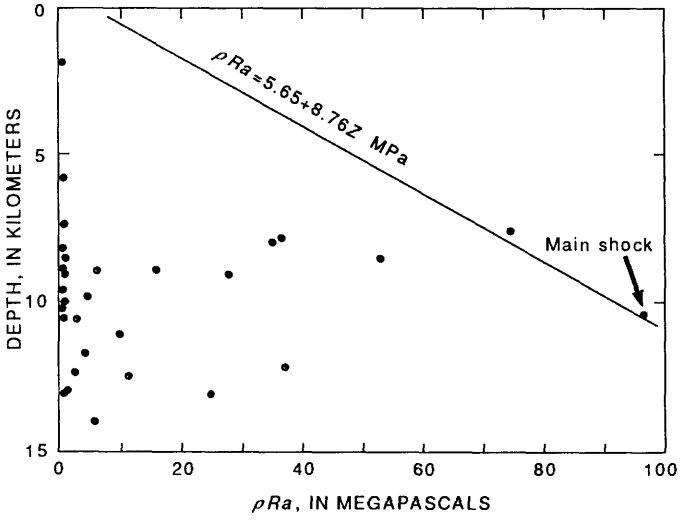

FIGURE 12.11.—Ground-motion parameter for peak acceleration as a function of hypocentral depth. Solid line represents regression fitted to data of McGarr (1984).

To recapitulate, the ground-motion parameters for peak acceleration and peak velocity of the Coalinga earthquake sequence show no obvious depth dependence, although for ρRa and $Rv/M_0^{1/3}$ the regression lines for

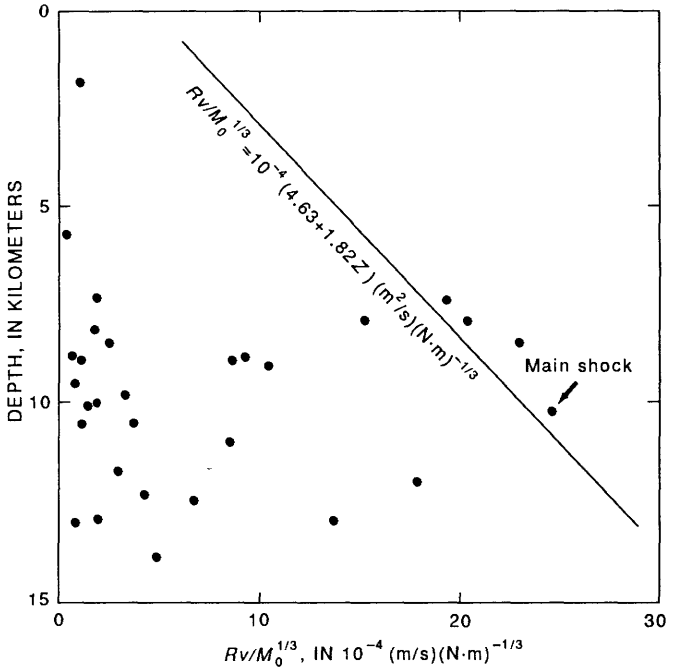

FIGURE 12.12.—Peak-ground-velocity parameter, normalized according to seismic moment, as a function of focal depth. Regression line from McGarr (1984).

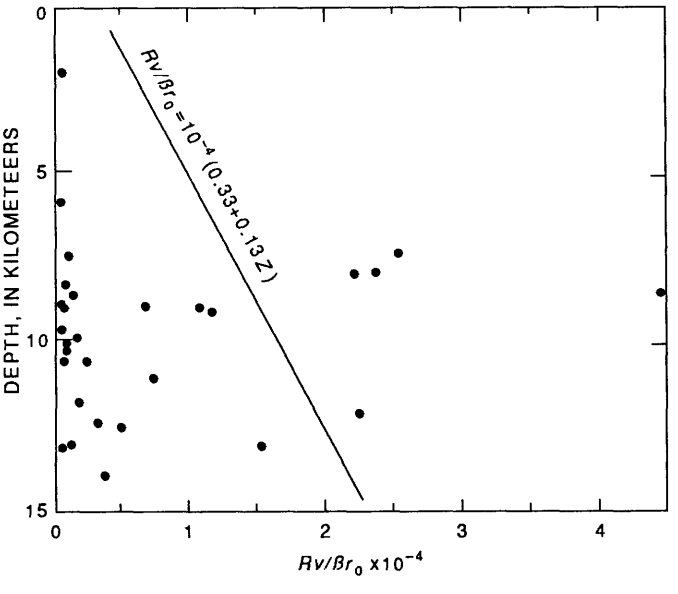

FIGURE 12.13.—Peak-ground-velocity parameter, normalized by source radius, as a function of focal depth. Regression line from McGarr (1984).

depth behavior, developed previously, appear to be upper bounds to the data. Therefore, the Coalinga ground-motion data could not have served as a basis for defining any sort of systematic depth behavior corresponding to what was found previously (McGarr, 1984).

SCALING OF GROUND-MOTION PARAMETERS

As reviewed by McGarr (1984), to the extent that the seismic-stress drop does not depend on seismic moment, we expect, from basic scaling considerations, the ground-motion parameter ρRa to be independent of M_0 and Rv to scale according to $M_0^{1/3}$. Although these scaling expectations seem to have been largely realized in the previous study, we show here that, in common with the source parameter $\Delta\tau$, they do not apply to many of the Coalinga data. Indeed, the Coalinga ground-motion parameters, as plotted in figures 12.14 and 12.15, each show an unexpectedly strong and well-defined dependence on seismic moment. In figure 12.4, the peak-acceleration data, excluding the main-shock datum, define a regression line for which

$$\rho Ra \propto M_0^{0.67}, \tag{11}$$

in contrast to the expectation (eq. 1b), represented by the dashed line, of no moment dependence. Similarly, the peak-velocity data (fig. 12.15) yield a well-determined regression fit for which

$$Rv \propto M_0^{0.73}, \tag{12}$$

which has more than double the expected dependence of $M_0^{1/3}$ (dashed line, fig. 12.15). Both the acceleration and velocity data (figs. 12.14, 12.15) are consistent with a transition from strong M_0 scaling to the previously expected scaling (dashed lines) at a moment of about 10^{17} N·m, with strong scaling obtaining below this transition point.

The unexpected scaling found for the Coalinga ground-motion data, as well as the source parameters (figs. 12.8, 12.9), raises some important questions. First, is the scaling found for Coalinga unique to this earthquake sequence, possibly because of some unusual tectonic feature (see chap. 23)? Results from a study (McGarr,

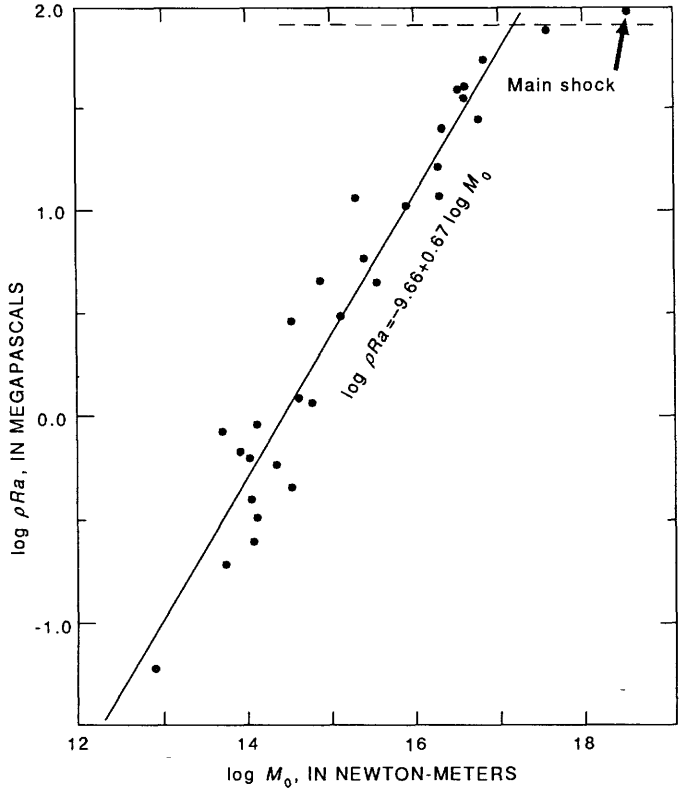

FIGURE 12.14.—Peak-acceleration parameter as a function of seismic moment for events listed in table 12.1. Regression line was fitted to all these data points except that for the main shock; dashed line represents previously expected scaling.

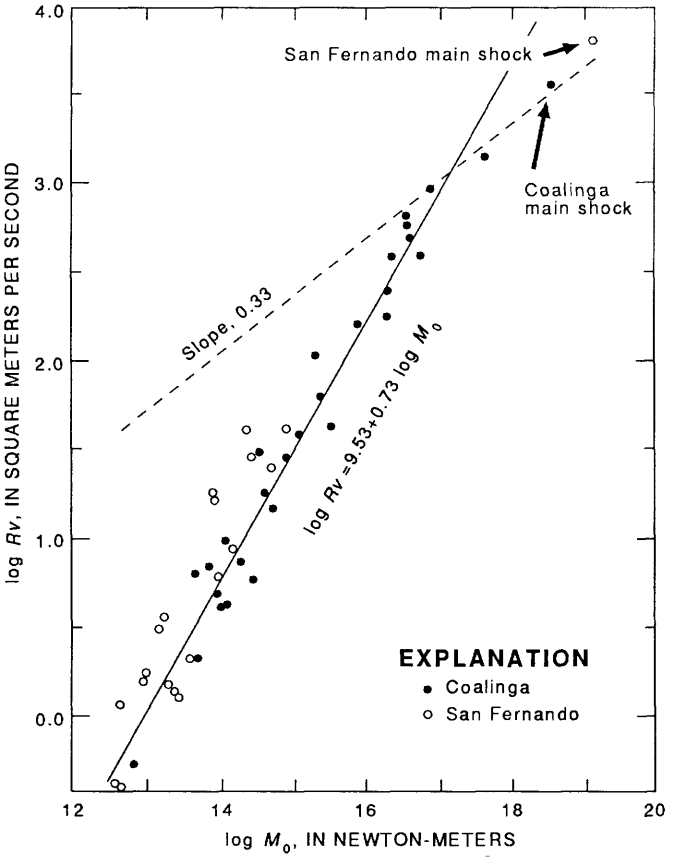

FIGURE 12.15.—Peak-velocity ground-motion parameter as a function of seismic moment for both Coalinga (table 12.1) and 1971 San Fernando (Tucker, 1975) data. Dashed line represents previously expected scaling; solid line was fitted to Coalinga data points except that for the main shock.

1986) of other earthquake sequences indicate that the Coalinga scaling is not so unusual. In particular, peak-velocity data for the 1971 San Fernando, Calif., earthquake sequence, which also occurred in a compressive tectonic regime (Tucker, 1975; McGarr, 1984), are reasonably consistent in terms of M_0 dependence with those measured at Coalinga, as shown in figure 12.15. For $M_0<10^{17}$ N·m, the San Fernando data, derived from information presented by Tucker (1975), coincide very closely with the corresponding Coalinga data; the San Fernando points (fig. 12.15) suggest, if anything, a somewhat stronger dependence of Rv on M_0 than for the Coalinga data. At $M_0>10^{17}$ N·m, the data point for the San Fernando main shock is situated slightly above the line corresponding to $M_0^{1/3}$ scaling that was fitted to the Coalinga main-shock and largest-aftershock data. This somewhat elevated position for the San Fernando main-shock data point is presumably due to the hypocentral depth of 13 km, in contrast to 10 km for the Coalinga main shock (eq. 2b). In short, the unexpected scaling found for the Coalinga events at $M_0<10^{17}$ N·m appears to apply also to San Fernando. For $M_0<10^{17}$ N·m, the previously expected scaling (for example, McGarr, 1984) agrees well with the data for both sequences. Thus, the Coalinga earthquake sequence seems not to be unique with regard to the scaling of ground-motion parameters.

In addition, analysis of four other earthquake sequences by McGarr (1986)—the 1975 Oroville, Calif., 1980 Mammoth Lakes, Calif., and 1982 New Brunswick, Canada, and a sequence of tremors within two South African gold mines—showed that in all cases, the peak-velocity parameters of the smaller events, in particular sequences,scale similarly with moment as the data at small M_0 plotted in figure 12.15. The moment at which a transition in scaling occurs, however, varies considerably from sequence to sequence. For example, whereas the transition occurs near $M_0=10^{17}$ N·m in figures 12.14 and 12.15, this same transition was found at $M_0=3\times10^{14}$ N·m for the 1975 Oroville, Calif., earthquake sequence.

Having concluded that the seismic ground-motion data of the Coalinga earthquake sequence are not unique in their scaling, we now address the question whether this unexpected scaling is the result of anelastic attenuation and (or) band-limited recording effects, or to seismic-source processes. We present three different arguments indicating that the ground-motion scaling described here reflects more the rupture processes, rather than effects exterior to the source region. First, the unusual scaling found for the ground-motion parameter Rv is entirely consistent with that determined for the source radius r_0 and the stress drop $\Delta\tau$. Specifically, for most models of the seismic source, $Rv \propto \Delta\tau r_0$. For example, McGarr and others (1981) showed that

$$Rv^B = \frac{0.57\beta\Delta\tau r_0}{\mu}, \tag{13}$$

where v^B is the peak velocity of the far-field S wave, calculated using the model of Brune (1970, 1971). Thus, if $\Delta\tau \propto M_0^{0.60}$ (fig. 12.9) and $r_0 \propto M_0^{0.13}$ (fig. 12.8), then the predicted scaling for peak velocity is $Rv \propto M_0^{0.73}$, which is exactly what is observed (fig. 12.15) for $M<10^{17}$ N.m. The next question is whether or not the unexpected source-parameter scaling is simply a consequence of anelastic attenuation and (or) band-limited recording. Because most of the corner frequencies (see figs. 12.2, 12.4) were reasonably well defined and substantially separated from the spectral frequency used to characterize anelastic attenuation, termed f_{max} by Hanks (1982), it is unlikely that either anelastic attenuation or band-limited recording was a factor in the estimates of f_0. f_{max} is typically 15 Hz for S-wave spectra and 30 Hz for P waves (figs. 12.2, 12.4), whereas f_0 ranges as high as about 6 Hz (table 12.1). Moreover, as shown in figure 12.10, the ratio $f_0(P)/f_0(S)$ does not appear to depend on earthquake size.

Ground-motion parameters determined for P waves (table 12.1) provide the basis of a second argument to the effect that the unexpected scaling is not a result of wave propagation or recording effects. In figures 12.16 and 12.17, the parameters $Rv(P)$ and $\rho Ra(P)$ show scaling that is entirely consistent with that of their S-wave counterparts (figs. 12.14, 12.15). To demonstrate this consistency, lines with their slopes determined from the S-wave data were drawn through the centroids of the P-wave parameters in figures 12.16 and 12.17. These lines describe the P-wave ground-motion scaling essentially as well as that for the S waves. Because f_{max}, characterizing anelastic attenuation (Hanks, 1982), is typically twice as large for P waves as for S waves, the virtually identical scaling of the P- and S-wave parameters (figs. 12.14–12.17) suggests that anelastic attenuation was not the primary factor in any of the scaling outlined here.

The third, and least direct, argument tending to discount the importance of wave-propagation effects in the scaling observations emphasized here involves the predictions of models incorporating the effects of anelastic attenuation and band-limited recording. Stochastic simulations of the scaling of ground-motion parameters by Boore (1983) for various assumed values of f_{max} indicate a continual, progressive steepening of the slopes of ground-motion curves, corresponding to those shown in figures 12.14 and 12.15, as moment or magnitude is reduced. This theoretical expectation contrasts with observations showing quite an abrupt transition in scaling at about $M_0=10^{17}$ N·m.

In summary, the available evidence suggests that the scaling presented here for ground-motion, as well as source, parameters results more from source processes than wave-propagation or recording effects. This conclusion is important because it highlights essential differences between the sources of small and large earthquakes.

DISCUSSION AND CONCLUSIONS

The conclusions of this study fall into two groups: the first of results of general interest with regard to our understanding of the seismic-source processes that give rise to high-frequency ground motion within the epicentral regions of earthquakes, and the second of results of more specific application to the tectonic and earthquake-hazard situation at Coalinga itself. The first group of conclusions involves the scaling of source and ground-motion parameters. The Coalinga ground-motion data set seems to have been much better suited than any other for elucidating various features of this scaling, and the resulting insights have indicated serious limitations in the applicability of previous conclusions regarding the prediction of ground motion. In particular, the notion that small earthquakes scale similarly to large ones no longer seems tenable (see figs. 12.14, 12.15). McGarr (1984), for example, demonstrated a link between the crustal environment (stress state, focal depth) at the hypocenter and the corresponding ground-motion parameters, which also were observed to depend on seismic moment according to scaling principles for which variables with dimensions of stress do not change systematically. The similarity, in his previous study, of the observed dependence of the ground-motion parameter ρRa on focal depth and stress state (compressional or extensional) to corresponding predictions of crustal strength (for example, Sibson, 1974; Brace and Kohlstedt, 1980) led to the conclusion that the material

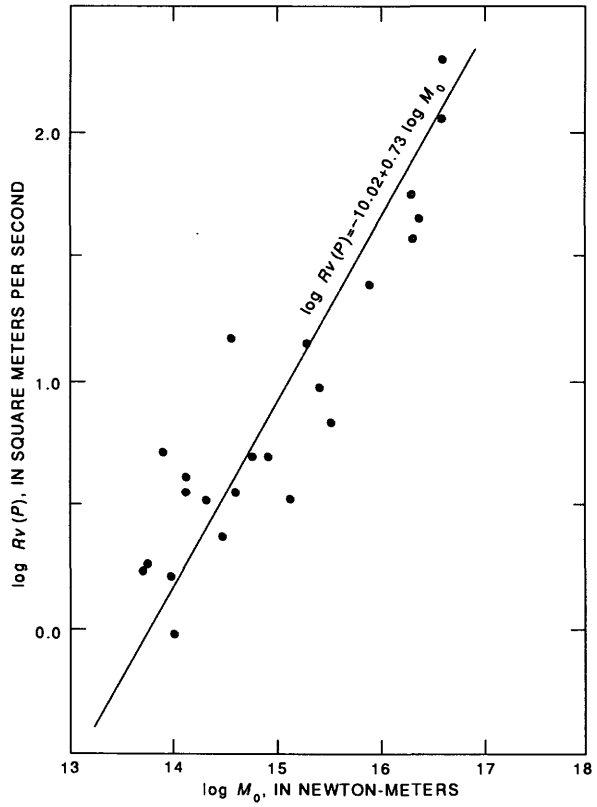

FIGURE 12.16.—Peak-ground-velocity parameters for P waves as a function of seismic moment. Slope of solid line is same as for S-wave data in figure 12.15.

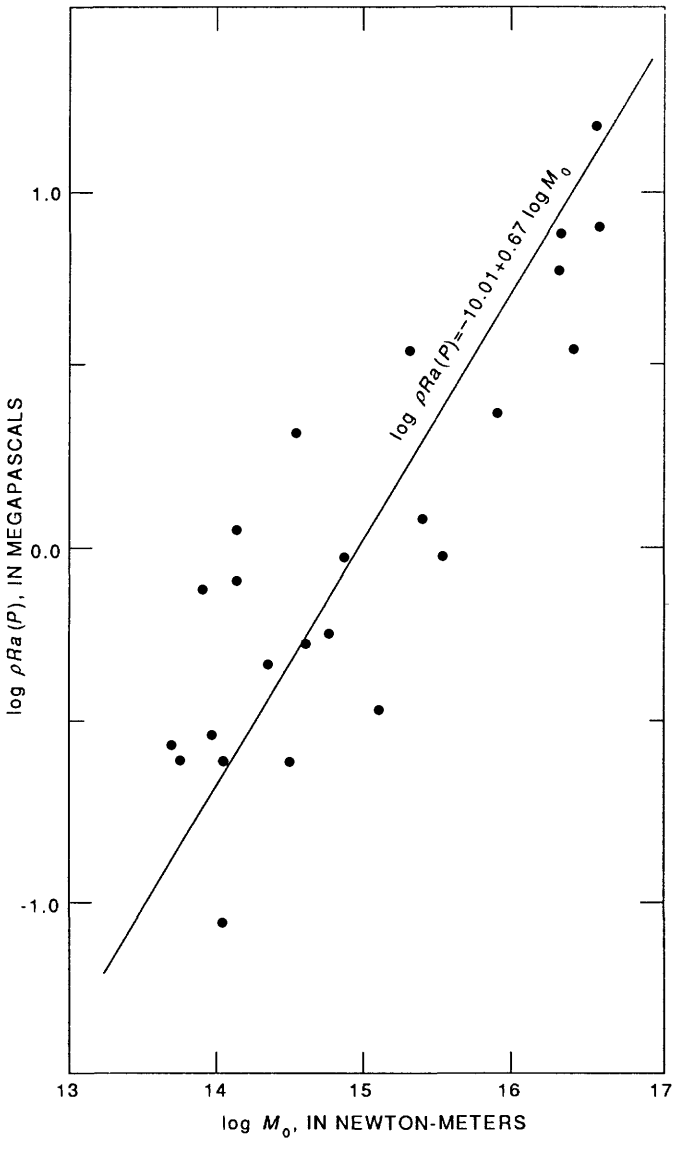

FIGURE 12.17.—Peak-ground-acceleration parameter for P waves as a function of seismic moment. Slope of solid line is same as for S-wave data in figure 12.14.

strength at the hypocenter was probably the factor controlling the parameters ρRa and Rv. In a preliminary report on the Coalinga ground-motion analysis, McGarr and others (1985) extended this notion further by proposing specific relations between the ground-motion parameters and crustal strength, based on earlier observations by McGarr (1984), and then applied these relations to try to map crustal strength within the aftershock zone. In view of the more comprehensive results presented here, especially those indicating the limited applicability of constant-stress-drop scaling (see figs. 12.14, 12.15), this attempt to estimate the crustal-strength distribution from the aftershock data was inappropriate. We now see that the tremendous variation in inferred crustal strength (McGarr and others, 1985), in fact, results from the unexpectedly strong scaling with seismic moment of peak velocity, peak acceleration, and, most surprisingly, stress drop for moments less than about 10^{17} N·m.

It seems that for the two largest events in the Coalinga earthquake sequence, the constant-stress-drop scaling still applies for which $Rv \propto M_0^{1/3}$ and ρRa does not depend on M_0 (figs. 12.14, 12.15). Moreover, these largest events (table 12.1) show an expected link with crustal environment, in that the corresponding ground-motion data are quite consistent with McGarr's (1984) regression lines describing the depth dependence of ground-motion parameters in compressional tectonic environments (figs. 12.11, 12.12).

Thus, the Coalinga ground-motion data, in conjunction with similar observations of other earthquake sequences (McGarr, 1985), indicate that only those earthquakes with moments greater than some threshold value, which varies from sequence to sequence and is approximately 10^{17} N·m for the Coalinga events, have ground-motion parameters Rv and ρRa which are controlled presumably by the crustal strength in the vicinity of the hypocenter and exhibit constant-stress-drop scaling. For earthquakes smaller than this threshold value, the stress drop and the ground-motion parameters scale much more strongly with seismic moment, and there is no apparent link with the crustal environment.

These scaling results have important implications regarding the prediction of ground-motion parameters in the context of earthquake-hazards assessment. Specifically, the use of observations based on small earthquakes to estimate near-source ground motion due to large events appears to be much less straightforward, now that substantial differences have been recognized between small- and large-earthquake scaling. Similar remarks apply regarding the downward extrapolation from large to small events. The observations described here serve to discount the appropriateness of ground-motion or source-parameter analyses based on the idea that a single type of source scaling is applicable to earthquakes in general or even within a particular region. For example, observations reviewed by Nuttli (1983) suggesting that midplate earthquakes scale differently from those near plate margins—for example, in California—should be reassessed in terms of the scaling complexities described here; in view of the strong moment dependence of the stress drop found for the Coalinga events, the moment dependence found for stress drops of midplate earthquakes probably is not a distinguishing feature of those events, as proposed by Nuttli. Although the ground-motion parameters estimated for P waves (figs. 12.16, 12.17) were used here primarily as independent confirmation of the scaling attributed to the corresponding S-wave parameters, these P-wave results are also of interest with regard to the information they provide about the source processes responsible for high-frequency ground motion. Although damaging ground motion has rarely been associated with P waves, their ground-motion parameters $Rv(P)$ and $\rho Ra(P)$ (table 12.1) are nonetheless related to the seismic source as closely as are the S-wave parameters. Where P waves were better recorded than S waves, the P-wave ground-motion parameters could be used to characterize the source and, thus, could serve to estimate the S-wave parameters. At the very least, as demonstrated here, the P-wave data provide valuable independent information regarding the seismic source.

Accordingly, it is of interest to know how the P- and S-wave parameters are related. The most straightforward assumption is that the respective ground-motion parameters differ by a constant multiplicative factor. A comparison of the results plotted in figures 12.16 and 12.17 with those in figures 12.14 and 12.15 indicates that for the Coalinga earthquake sequence, $Rv(S)/Rv(P) \approx 3.1$ and $\rho Ra(S)/\rho Ra(P) \approx 2.2$. Similar studies of other earthquake sequences are required to assess the generality of these results.

Regarding the second group of conclusions, more relevant to Coalinga in particular, we first discuss several aspects of the ground-motion parameters of the largest events in terms of corresponding damage or felt effects. Although the connection between various ground-motion parameters and attendant damage has been the subject of much debate, it is becoming clearer that peak velocity is much more closely linked to damage than is peak acceleration (see McGarr and others,1981). A comparison of the ground-motion parameters of the main shock, which caused a remarkable amount of damage, especially in the town of Coalinga, with those of the large 0239 G.m.t. July 22 aftershock, which apparently did not cause appreciable damage, corroborates that peak velocity is a much more useful predictor of damage. Whereas the peak-acceleration parameters Ra

for these two shocks are of comparable magnitude (table 12.1), the peak velocity parameters Rv differ by a factor of 2.6 (see fig. 12.3).

One of the most damaging aftershocks, according to local reports (M.J. Rymer, oral commun., 1983), was that of 2231 G.m.t. July 25, for which significant damage was reported in Coalinga, in contrast to the other large aftershocks. At first, these observations seem anomalous in view of the ground-motion parameters for this event (table 12.1), neither of which is as large as those for the 0239 G.m.t. July 22 event. The damage reports are consistent, however, if we consider ground-motion parameters measured specifically at the only station within Coalinga, BCN (fig. 12.1), where the Rv values for the events of July 22 and 25 were found to be 1,330 and 2,510 m^2/s, respectively, and the corresponding ρRa values are 54.0 and 119.8 MPa. Thus, at station BCN, either measure of ground motion was a factor of about 2 higher for the July 25 event. This difference is clearly not a recording-site effect because out of four events for which ground motion was measured at station BCN, only that of the July 25 event was at all exceptional, relative to the ground motion at the other stations. Somehow, for this event, the seismic radiation appears to have been especially focused in the direction of Coalinga.

Finally, we discuss the relation between the seismic deformation estimated for the Coalinga earthquake sequence and the regional tectonic strains. First, we note that to a good approximation the seismic focal mechanisms (see chap. 8) are consistent with the recent geology in the central Coast Ranges (for example, Page and Engebretson, 1984), including Coalinga, inasmuch as northeast-southwest compression, in conjunction with uplift, is indicated. In view of the findings that multiple faults were apparently involved in the Coalinga earthquake sequence (see chap. 8), it seems most realistic to try to relate the seismic deformation, estimated from the moments, to the regional tectonic-strain-rate field, rather than attempting to analyze the deformation as slip on a single fault (eq. 7). If such a field can somehow be assessed, or guessed, then it can be compared to a strain change corresponding to the earthquakes, given by (Kostrov, 1974; Molnar, 1983)

$$\Delta\varepsilon_{ij} = \frac{1}{2\mu V}\sum M_{ij}\,, \tag{14}$$

where M_{ij} represents the moment tensor of an individual earthquake in a sequence and V is the volume of the seismogenic region under consideration. In the present analysis, the summation is over all the events in the Coalinga earthquake sequence between May 1 and October 1, 1983.

Previously, we showed that the sum of the scalar moments for the entire sequence is given by

$$\Sigma M_0 \simeq 5.36\times10^{18}\ \text{N·m}. \tag{15}$$

If we consider a coordinate system whose axes are aligned with the principal moment tensor

$$\begin{Bmatrix} M_{11} & 0 & 0 \\ 0 & 0 & 0 \\ 0 & 0 & M_{33} \end{Bmatrix}$$

then to a reasonable approximation (see chap. 8), most of the seismic deformation can be represented by principal moment tensors whose 1-axes are aligned in a northeast-southwest direction, with vertical 3-axes. In terms of the scalar moments, the principal components are thus given by

$$\Sigma M_{11} = -\Sigma M_0$$

and

$$\Sigma M_{33} = +\Sigma M_0\,,$$

where negative moments correspond to contractional deformation. To estimate the appropriate volume V in equation 14, we note from the seismic locations of Eaton (chap. 8) (see figs. 12.1, 12.11, 12.12) that the important seismic deformation occurred within an area about 14 km wide and extending from 5- to 14-km depth. Thus, V is taken as $9\times14\times14=1{,}764$ km^3. For $\mu=3\times10^4$ MPa, equation 14 finally yields

$$\Delta\varepsilon_{11} = -\Delta\varepsilon_{33} = -5.06\times10^{-5}. \tag{16}$$

Therefore, our best estimate of the seismic deformation corresponds to a contraction of about 51 ppm in a northeast-southwest direction and the same amount of vertical expansion.

To estimate the tectonic deformation that presumably gives rise to the seismicity, we refer to the plate-tectonic analysis by Minster and Jordan (1984), who found that the vector representing motion between the Pacific and North American plates has not only a component parallel to the San Andreas fault in central California but also a significant component normal to the San Andreas fault, at N. 49° E., corresponding to interplate compression. The magnitude of this vector is 5.85 mm/yr. If the zone of compressional tectonics and associated seismicity in central California is due to this interplate compression, then the most straightforward assumption is that this component of deformation is accommodated evenly over the belt of seismicity about 150 km wide and straddling the San Andreas fault (Urhammer, 1985). Thus, dividing the

compressional vector by the width of the zone yields a compressional strain rate of

$$\dot{\varepsilon}_{11} = -3.9\times10^{-8}/\text{yr}. \quad (17)$$

Assuming conservation of material volume, we expect the same amount of regional vertical expansion. A comparison of equations 16 and 17, then, leads to the conclusion that the seismic deformation during the 5 months beginning just before the Coalinga main shock accounted for about 1,300 years of strain accumulation. Because it seems unlikely that post-September 1983 seismicity near Coalinga is likely to contribute materially to the moment sum, the seismically inferred strain change given by equation 16 is probably a good total estimate for the sequence. Therefore, to the extent that all of our assumptions are appropriate, 1,300 years may be a good estimate of the interval between "Coalinga" events, within the crustal volume considered here.

Since this analysis was first done, independent evidence regarding the regional strain rate (equation 17) has become available from the study by Harris and Segall (1987), who analyzed data from a trilateration network extending southwestward from the San Andreas fault at Parkfield to the Pacific coast. Their inversion indicates a strain rate for the component normal to the San Andreas fault (northeast) of -6×10^{-8}/yr. Thus, if the strain field accommodating the interplate compression is symmetrical about the San Andreas fault, then the strain rate estimate of Harris and Segall (1987) can be considered as surprisingly good confirmation of the estimate given in equation 17. If Harris and Segall's result were used instead of equation 17, then the strain release of the Coalinga sequence (eq. 16) accounts for about 840 years of strain accumulation, in comparison with the 1,300-yr interval estimated above.

One of the implications of this analysis is that vertical expansion ε_{33}, mostly manifested as uplift, is an ongoing process at the same rate as for $\dot{\varepsilon}_{11}$ in equation 17. Assuming that the thickness of the brittle seismic layer undergoing this expansion is 9 km, then the uplift rate is about 0.4 mm/yr, and from equation 16 the earthquake sequence was associated with about 0.46 m of this uplift.

An indication that this consequence is reasonable is provided by two leveling studies of coseismic vertical deformation. Leveling surveys before and after the main shock revealed that Anticline Ridge, near the northeast edge of the zone of major seismicity, was uplifted by about 0.5 m at the time of the earthquake (see chap. 13). Near the west boundary of this zone, Rymer and others (chap. 15) found that the total vertical deformation across the Nuñez fault, which began slipping only in June 1983 after a large nearby aftershock, was 0.5 to 0.6 m. Each of these measurements, which presumably indicate the release of strain built up since the previous major sequence, agrees well with the uplift of about 0.46 m attributed to seismic deformation.

ACKNOWLEDGMENTS

We thank A.G. Brady, B. Silverstein, and R. Maley for providing SMA–1 data in advance of publication. Conversations with J. Boatwright and M. Rymer helped to constrain some of the conclusions of this report.

REFERENCES CITED

Aki, Keiiti, 1965, Maximum likelihood estimate of *b* in the formula log $N=a-bM$ and its confidence limits: University of Tokyo, Earthquake Research Institute Bulletin, v. 43, no. 2, p. 237–239.

Andrews, M.C., Mueller, C.S., and McGarr, Arthur, 1984, Moment-dependent source and peak ground motion parameters of the Coalinga, California, aftershock sequence [abs.]: Eos (American Geophysical Union Transactions), v. 65, no. 45, p. 1005.

Archuleta, R.J., Cranswick, Edward, Mueller, C.S., and Spudich, Paul, 1982, Source parameters of the 1980 Mammoth Lakes, California, earthquake sequence: Journal of Geophysical Research, v. 87, no. B6, p. 4595–4607.

Boore, D.M., 1983, Stochastic simulation of high-frequency ground motions based on seismological models of the radiated spectra: Seismological Society of America Bulletin, v. 73, no. 6, p. 1865–1894.

Boore, D.M., and Boatwright, John, 1984, Average body-wave radiation coefficients: Seismological Society of America Bulletin, v. 74, no. 5, p. 1615–1621.

Borcherdt, R.D., Cranswick, Edward, Maxwell, G.L., Mueller, C.S., McClearn, R., Sembera, E.D., and Wennerberg, L.G., 1983, Digital strong motion data recorded by the U.S. Geological Survey near Coalinga, California, *in* Borcherdt, R.D., compiler, The Coalinga earthquake sequence commencing May 2, 1983: U.S. Geological Survey Open-File Report 83-511, p. 61–76.

Borcherdt, R.D., Fletcher, J.B., Jensen, E.G., Maxwell, G.L., VanSchaack, J.R., Warrick, R.E., Cranswick, E., Johnston, M.J.S., and McClearn, R., 1985, A general earthquake-observation system (GEOS): Seismological Society of America Bulletin, v. 75, no. 6, p. 1783–1825.

Brace, W.F., and Kohlstedt, D.L., 1980, Limits on lithospheric stress imposed by laboratory experiments: Journal of Geophysical Research, v. 85, no. B11, p. 6248–6252.

Brune, J.N., 1968, Seismic moment, seismicity, and rate of slip along major fault zones: Journal of Geophysical Research, v. 73, no. 2, p. 777–784.

—— 1970, Tectonic stress and the spectra of seismic shear waves: Journal of Geophysical Research, v. 75, no. 26, p. 4997–5009.

—— 1971, Correction: Journal of Geophysical Research, v. 76, no. 20, p. 5002.

Chinnery, M.A., and North, R.G., 1975, The frequency of very large earthquakes: Science, v. 190, no. 4220, p. 1197–1198.

Eaton, J.P., 1985, The May 2, 1983 Coalinga earthquake and its aftershocks: A detailed study of the hypocenter distribution and of the focal mechanisms of the larger aftershocks, *in* Jacobson, Muriel, compiler, Proceedings of Workshop XXVI—Mechanics of the May 2, 1983 Coalinga earthquake: U.S. Geological Survey Open-File Report 85-44, p. 132–201.

Eberhart-Phillips, Donna, and Reasenberg, Paul, 1985, Hypocenter locations and constrained fault-plane solutions for Coalinga aftershocks, May 2–24, 1983: Evidence for a complex rupture geome-

try, *in* Jacobson, Muriel, compiler, Proceedings of Workshop XXVII—Mechanics of the May 2, 1983 Coalinga earthquake: U.S. Geological Survey Open-File Report 85-44, p. 202–224.

Fletcher, J.B., 1980, Spectra from high-dynamic range digital recordings of Oroville, California aftershocks and their source parameters: Seismological Society of America Bulletin, v. 70, no. 3, p. 735–755.

Fletcher, J.B., Brady, A.T., and Hanks, T.C., 1980, Strong-motion accelerograms of the Oroville, California, aftershocks: Data processing and the aftershock of 0350 August 6, 1975: Seismological Society of America Bulletin, v. 70, no. 1, p. 243–267.

Fletcher, J.B., Boatwright, John, Haar, Linda, Hanks, T.C., and McGarr, Arthur, 1984, Source parameters for aftershocks of the Oroville, California, earthquake: Seismological Society of America Bulletin, v. 74, no. 4, p. 1101–1123.

Gutenberg, Beno, 1944, Energy ratio of reflected and refracted seismic waves: Seismological Society of America Bulletin, v. 34, no. 2, p. 85–102.

Hanks, T.C., 1977, Earthquake stress drops, ambient tectonic stresses and stresses that drive plate motions: Pure and Applied Geophysics, v. 115, no. 1–2, p. 441–458.

—— 1981, The corner frequency shift, earthquake source models, and Q: Seismological Society of America Bulletin, v. 71, no. 3, p. 597–612.

—— 1982, f_{max}: Seismological Society of America Bulletin, v. 72, no. 6, p. 1867–1879.

Hanks, T.C., and Johnson, D.A., 1976, Geophysical assessment of peak accelerations: Seismological Society of America Bulletin, v. 66, no. 3, p. 959–968.

Hanks, T.C., and McGuire, R.K., 1981, The character of high-frequency ground motion: Seismological Society of America Bulletin, v. 71, no. 6, p. 2071–2095.

Hanks, T.C., and Wyss, Max, 1972, The use of body-wave spectra in the determination of seismic source parameters: Seismological Society of America Bulletin, v. 62, no. 2, p. 561–589.

Harris, R.A., and Segall, Paul, 1987, Detection of a locked zone at depth on the Parkfield, California, segment of the San Andreas fault: Journal of Geophysical Research, v. 92, no. B8, p. 7945–7962.

Hartzell, S.H., and Heaton, T.H., 1983, Teleseismic mechanism of the May 2, 1983 Coalinga, California, earthquake from long-period P waves, *in* Bennett, J.H., and Sherburne, R.W., eds., The 1983 Coalinga, California earthquakes: California Division of Mines and Geology Special Publication 66, p. 241–246.

Johnson, L.R., and McEvilly, T.V., 1974, Near-field observations and source parameters of central California earthquakes: Seismological Society of America Bulletin, v. 64, no. 6, p. 1855–1886.

Joyner, W.B., 1984, A scaling law for the spectra of large earthquakes: Seismological Society of America Bulletin, v. 74, no. 4, p. 1167–1188.

Kanamori, Hiroo, 1983, Mechanism of the 1983 Coalinga earthquake determined from long-period surface waves, *in* Bennett, J.H., and Sherburne, R.W., eds., The 1983 Coalinga, California earthquakes: California Division of Mines and Geology Special Publication 66, p. 233–240.

Kostrov, B.V., 1974, Seismic moment and energy of earthquakes, and seismic flow of rock: U.S.S.R. Academy of Sciences Izvestiya, Physics of the Solid Earth, v. 1, p. 23–44.

Lomnitz, Cinna, 1966, Magnitude stability in earthquake sequences: Seismological Society of America Bulletin, v. 56, no. 1, p. 247–249.

Maley, R.P., Brady, G.A., Etheridge, E.C., Johnson, D., Mork, P.N., and Switzer, J.C., 1983, Analog strong motion data and the processed main event records obtained by the U.S. Geological Survey near Coalinga, California, *in* Borcherdt, R.D., ed., The Coalinga earthquake sequence commencing May 2, 1983: U.S. Geological Survey Open-File Report 83-511, p. 38–60.

McGarr, Arthur, 1984, Scaling of ground motion parameters, state of stress, and focal depth: Journal of Geophysical Research, v. 89, no. 8, p. 6969–6979.

—— 1986, Some observations indicating complications in the nature of earthquake scaling, *in* Earthquake source mechanics: American Geophysical Union Geophysical Monograph 37 (Ewing volume 6), p. 217–225.

McGarr, Arthur, Green, R.W.E., and Spottiswoode, S.M., 1981, Strong ground motion of mine tremors: Some implications for near-source ground motion parameters: Seismological Society of America Bulletin, v. 71, no. 1, p. 295–319.

McGarr, Arthur, Mueller, C.S., Fletcher, J.B., and Andrews, M.C., 1985, Ground motion parameters of the 1983 Coalinga, California earthquakes: Implications for crustal strength, *in* Jacobson, Muriel, compiler, Proceedings of Workshop XXVII—Mechanics of the May 2, 1983 Coalinga earthquake: U.S. Geological Survey Open-File Report 85-44, p. 254–275.

Minster, J.B., and Jordan, T.H., 1984, Vector constraints on Quaternary deformation of the western United States east and west of the San Andreas fault, *in* Crouch, J.K., and Bachman, S.B., eds., Tectonics and sedimentation along the California margin: Society of Economic Paleontologists and Mineralogists, Pacific Section annual field trip guidebook, v. 38, p. 1–16.

Molnar, Peter, 1979, Earthquake recurrence intervals and plate tectonics: Seismological Society of America Bulletin, v. 69, no. 1, p. 115–133.

—— 1983, Average regional strain due to slip on numerous faults of different orientations: Journal of Geophysical Research, v. 88, no. B8, p. 6430–6432.

Molnar, Peter, Tucker, B.E., and Brune, J.N., 1973, Corner frequencies of P and S waves and models of the earthquake source: Seismological Society of America Bulletin, v. 63, no. 6, p. 2091–2104.

Mueller, C.S., Sembera, E.D., and Wennerberg, L.G., 1984, Digital recordings of aftershocks of the May 2, 1983 Coalinga, California earthquake: U.S. Geological Survey Open-File Report 84-697, 57 p.

Nuttli, O.W., 1983, Average seismic source-parameter relations for mid-plate earthquakes: Seismological Society of America Bulletin, v. 73, no. 2, p. 519–535.

Page, B.M., and Engebretson, D.C., 1984, Correlation between the geologic record and computed plate motions for central California: Tectonophysics, v. 3, no. 2, p. 133–156.

Page, R.A., 1968, Aftershocks and microaftershocks of the great Alaska earthquake of 1964: Seismological Society of America Bulletin, v. 58, no. 3, p. 1131–1168.

Rial, J.A., and Brown, E.D., 1983, Waveform modeling of the long period P-waves from the Coalinga earthquake of May 2, 1983, *in* Bennett, J.H., and Sherburne, R.W., eds., The 1983 Coalinga, California earthquakes: California Division of Mines and Geology Special Publication 66, p. 247–259.

Rymer, M.J., Harms, K.K., Lienkaemper, J.J., and Clark, M.M., 1985, Rupture of the Nuñez fault during the Coalinga earthquake sequence, *in* Jacobson, Muriel, compiler, Proceedings of Workshop XXVII—Mechanics of the May 2, 1983 Coalinga earthquake: U.S. Geological Survey Open-File Report 85-44, p. 294–312.

Sibson, R.H., 1974, Frictional constraints on thrust, wrench and normal faults: Nature, v. 249, no. 5457, p. 542–544.

Spottiswoode, S.M., and McGarr, Arthur, 1975, Source parameters of tremors in a deep-level gold mine: Seismological Society of America Bulletin, v. 65, no. 1, p. 93–112.

Stein, R.S., 1985, Evidence for surface folding and subsurface fault slip from geodetic elevation changes associated with the 1983 Coalinga, California, earthquake, *in* Jacobson, Muriel, compiler, Proceedings of Workshop XXVII—Mechanics of the May 2, 1983

Coalinga earthquake: U.S. Geological Survey Open-File Report 85-44, p. 225–253.

Trifunac, M.D., 1972, Stress estimates for the San Fernando, California, earthquake of February 9, 1971: Main event and thirteen aftershocks: Seismological Society of America Bulletin, v. 62, no. 3, p. 721–750.

Tucker, B.E., 1975, Source mechanisms of aftershocks of the 1971 San Fernando, California earthquake: San Diego, University of California, Ph.D. thesis, 230 p.

Tucker, B.E., and Brune, J.N., 1973, Seismograms, *S*-wave spectra, and source parameters for aftershocks of the San Fernando earthquake, *in* Benfer, N.A., Coffman, J.L., and Bernick, J.R., eds., San Fernando, California, earthquake of February 9, 1971: Washington, U.S. Department of Commerce, v. 3, p. 69–121.

Urhammer, R.A., Darragh, R.B., and Bolt, B.A., 1983, The 1983 Coalinga earthquake sequence: May 2 through August 1, *in* Bennett, J.H., and Sherburne, R.W., eds., The 1983 Coalinga, California earthquakes: California Division of Mines and Geology Special Publication 66, p. 221–231.

Urhammer, R.A., 1985, The May 2, 1983 Coalinga earthquake and seismicity rates and strain energy in the central Coast Ranges, *in* Jacobson, Muriel, compiler, Proceedings of Workshop XXVII—Mechanics of the May 2, 1983 Coalinga earthquake: U.S. Geological Open-File Report 85-44, p. 61–82.

Wesnousky, S.G., Scholz, C.H., Shimazaki, K., and Matsuda, T., 1983, Earthquake frequency distribution and the mechanics of faulting: Journal of Geophysical Research, v. 88, no. B11, p. 9331–9340.

13. ABNORMALLY HIGH FLUID PRESSURES IN THE REGION OF THE COALINGA EARTHQUAKE SEQUENCE AND THEIR SIGNIFICANCE

By R.F. YERKES, PAIA LEVINE, and C.M. WENTWORTH,
U.S. GEOLOGICAL SURVEY

CONTENTS

ABSTRACT

Abnormally high fluid pressures permitted or aided thrusting of buried tectonic wedges of Franciscan assemblage eastward beneath coeval Great Valley sequence onto mafic basement and thus contributed to the 1983 Coalinga earthquake sequence. Much of the southwestern San Joaquin Valley and adjoining parts of the Diablo Range are underlain by rocks with pressure/depth (P/D) ratios near or greater than 0.5 psi/ft (the hydrostatic gradient for oil-field waters is about 0.47 psi/ft). Plots of P/D ratio versus depth for more than 300 wells show an average ratio of about 0.6 psi/ft above 14,000-ft depth, a lower bound of 0.47 psi/ft, and an upper bound greater than 0.9 psi/ft; ratios greater than 0.60 psi/ft are interpreted to be abnormally high. P/D ratios are relatively high in the uplifted Tertiary strata and Great Valley sequence along the Lost Hills-Kettleman Hills trend, and are inferred to extend northwestward beneath the Coalinga anticline (site of the 1983 earthquake sequence) to Joaquin Ridge, where they are present in the Great Valley sequence. Below about 14,800 ft, the average P/D ratio increases with depth at a rate greater than 1.00 psi/ft—greater than the rate of increase in vertical stress—indicating an inverse relation between crustal strength and depth.

The abnormally high pressures (AHP's) extend to the limit of drilling (approx 23,000 ft) and locally into non-Franciscan basement rocks. All high-pressure wells are located southwest of the valley axis, where Great Valley sequence and (or) Franciscan rocks are present. AHP's are also present in the southeast end of the valley, however, where neither Great Valley sequence nor Franciscan rocks are present. Several likely sources of AHP's are recognized, but their relative contributions cannot be determined. Chief of these sources are diagenetic-metamorphic generation of fluids in the Great Valley sequence and Franciscan rocks, compaction disequilibrium and aquathermal pressuring in Tertiary strata, and horizontal tectonic compression. Sonic logs for numerous wells show abrupt reversals in the velocity/depth gradient at the top of the AHP field; and where well data coincide with seismic reflection and refraction profiles, the top of the AHP field marks the top of a seismic low-velocity zone.

We infer the presence of near-lithostatic fluid pressures in the Great Valley sequence and Franciscan rocks below the Coalinga anticline on the basis of (1) a mapped seismic low-velocity zone; (2) active generation of metamorphic fluids in the Great Valley sequence and Franciscan rocks, which pond below relatively impermeable layers and thus increase fluid pressure; and (3) apparent southward and westward propagation of the 1983 main-shock rupture, which indicates rupture on a gently southwest dipping surface and implies an inverse relation between depth and crustal strength.

INTRODUCTION

We postulate that abnormally high pore-fluid pressures at seismogenic depths (20,000–46,000 ft below the Coalinga anticline) greatly reduced normal stress across a gently southwest dipping thrust fault and led to much-reduced shear strength of the rocks and, thus, to the 1983 Coalinga earthquake sequence. A tectonic model of the buried thrust wedge of Franciscan assemblage that underlies the eastern margin of the Diablo Range was presented by Wentworth and others (1984; see chap. 4). Abnormally high pressures (AHP's) are those that depart from the normal hydrostatic gradient, which for fluids in the southwestern San Joaquin Valley averages about 0.47 psi/ft. AHP's significantly exceed those attributable to the hydrostatic gradient. AHP plays a critical role in thrust faulting of porous rocks. As shown by Hubbert and Rubey (1959), it counteracts the vertical and normal stress and greatly reduces shear stress at failure. By the Coulomb failure criterion,

$$T = C_0 + \mu(S_n - p)\,, \qquad (1)$$

normal stress (S_n) and shear stress (T) are offset by fluid pressure, and effective stress approaches zero as fluid pressure (p) approaches the lithostatic stress. Cohesion (C_0) is small at depths of a few kilometers, and the coefficient of friction (μ) is generally known from empirical and laboratory studies to be less than 1.

The Coulomb failure criterion explains two well-known examples of earthquakes induced by an increase in fluid pressure. The strike-slip earthquakes of the early 1960's near Denver, Colo., are attributed to a release of tectonic stress triggered by an increase in pore pressure due to injection of waste fluid (Healy and others, 1968). At the Rangely oil field, western Colorado, a detailed experiment on the relation between fluid pressure and earthquakes along an active strike-slip fault involved controlled injection of fluid and determination of principal stresses from hydraulic-fracture data (Raleigh and others, 1972). Fluid pressure along the active section of the fault at the time of the earthquakes was found to be quite close to that required to initiate fracture in previously faulted rock, as calculated from the effective stress relation. A fluid pressure of at least 3,700 psi at about 5,875 ft (for a P/D ratio of 0.63 psi/ft) was required to trigger earthquakes under compressive (strike slip) conditions. When the pressure was reduced by about 525 psi (to a P/D ratio of 0.54 psi/ft), seismicity ceased.

In this chapter, we describe the spatially extensive AHP field in the southern San Joaquin Valley and its likely genesis, with emphasis on its relevance to the 1983 Coalinga earthquake sequence. Our data come from several hundred boreholes, which are limited to the upper 23,000 ft of chiefly Cenozoic sedimentary rocks, whereas the earthquakes occurred chiefly below that depth in the Mesozoic Great Valley sequence and Franciscan rocks. However, data on the rate of increase in fluid pressure with depth and other arguments indicate that near-lithostatic pressures probably exist at seismogenic depths, and inferences of anomalously low rock strength in the seismogenic region can be explained by such pressures.

DISTRIBUTION OF ABNORMALLY HIGH FLUID PRESSURES

AHP's are found in sedimentary rocks worldwide; they are known from all continents, the North Sea, and the East Pacific. However, not all examples are from sedimentary rocks. In "the deepest hole in the world" on the Kola Peninsula near Murmansk, U.S.S.R., a P/D ratio of about 1.14 psi/ft (43,500 psi at 37,700 ft) was reported in fractured rocks containing methane, "other hydrocarbons," and strongly mineralized waters (Kerr, 1984). AHP's are known from deposits of Cambrian to Holocene age and from anhydrite, gypsum, salt, dolomite, and limestone; but they are best documented in thick, massive mudstone-siltstone sequences, such as those of the U.S. gulf coast. P/D ratios as high as 1.55 psi/ft are reported from shallow wells in the Himalayan foreland of Pakistan and India (Fertl and others, 1976). Other examples of P/D ratios greater than 1.00 psi/ft are from shallow wells in Franciscan rocks and the Great Valley sequence of central California; Jurassic oil measures of Wayne County, Miss.; the Zechstein salt domes of northern Germany; a deep well on the north slope of the Elburz Mountains of Iran; shallow wells in Australia, New Guinea, and the Papuan Basin south of New Guinea; and a deep well in Borneo. With these exceptions, fluid pressures in the southern San Joaquin Valley are comparable in both magnitude and depth to those determined elsewhere in world. In California, AHP's are also known in the eastern Santa Barbara Channel-Ventura area of the western Transverse Ranges (McCulloh, 1969; Rehm, 1972). They are widespread in the Cretaceous Great Valley sequence of the Sacramento Valley and have been described in chiefly Tertiary strata of the Kettleman Hills trend southeast of Coalinga (Berry, 1973).

SOUTHERN SAN JOAQUIN VALLEY

The San Joaquin Valley, the largest, southern part of the Great or Central Valley of California, is a northwest-trending, asymmetric syncline locally filled with more than 30,000 ft of upper Mesozoic and Cenozoic deposits. The Eocene and older parts of this sequence are marine except for a band of continental deposits along the eastern margin between Bakersfield and Fresno (see chap. 1). During Oligocene time, sedimentation in the north half of the valley became nonmarine and remained so throughout the rest of the Cenozoic except for a narrow seaway that extended along the northwestern margin during late Miocene time (Hackel, 1966). Marine deposition persisted into Pleistocene time over much of the southwestern part of the valley. Local areas of long-established internal drainage, such as the Tulare Lake basin, contain as much as 3,500 ft of Pliocene to Holocene flood-basin, lacustrine, and marsh deposits (Croft, 1972; Davis and Coplen, 1984).

Much of the 5,100 mi^2 of the San Joaquin Valley south of Panoche Creek (lat 36.8° N.), an area about 150 mi long by about 34 mi wide (fig. 13.1), is underlain at shallow depths by sedimentary deposits with P/D ratios near or greater than 0.5 psi/ft. To a depth of about 14,100 ft, the bottom-hole P/D ratios in several hundred wells average about 0.6 psi/ft, those in many wells exceed 0.8 psi/ft, and those in a few wells approach the local lithostatic gradient. All data come from boreholes drilled for oil, commonly on structural highs or along their trends. Because oil fields in the valley are generally old and their wells

shallow, deep data for the fields are sparse. Sampling is thus erratic both geographically and vertically, and as much as 15 percent of the area has not been sampled at all. A few modern deep wells, however, sample the AHP field to depths greater than 20,000 ft.

METHODS

Fluid pressures are estimated from unit weights of drilling fluid (mud) as determined at the surface. Drilling-fluid weights are carefully monitored and controlled, especially in overpressured terrain, because of the expense of drill-rig downtime and measures required to correct accidental imbalances. Correction is required when mud is lost by entry into the formation being drilled (mud too dense or overcompensated for pore-fluid pressure), or when the well "kicks" or "blows out"—the drill string is lifted, sometimes catastrophically, or pore fluid dilutes the mud—(mud density undercompensated). To avoid these and similar problems, the lightest possible mud, sufficient to balance pore-fluid pressure, is used. Mud weight is adjusted continually as drilling proceeds, to compensate for normally increasing bottom-hole pressure. The need for more radical adjustment to compensate for abrupt increases in pore-fluid pressure (the top of the AHP field) is determined by carefully monitoring the drilling rate as penetration from normally pressured to overpressured beds results in an abrupt increase in drilling rate (Chapman, 1983). Comparison of our derived equivalents with measured formation pressures shows that our estimates are commonly within 10 percent of the measured values at a given depth (see fig. 13.3).

To facilitate comparison, we express the pressure at a given point in terms of the P/D ratio at that depth. Generally, assuming a lithostatic gradient of 1.00 psi/ft (avg bulk density, 2.31 g/cm^3), this ratio approximates the Hubbert and Rubey expression, the ratio of fluid pressure to total overburden pressure (or percent lithostatic gradient). This expression, however, requires knowledge of the average bulk density of the rock column (which ranges from about 2.24 g/cm^3 or 0.97 psi/ft for the Cenozoic sequence in the San Joaquin Valley to about 2.57 g/cm^3 or 1.11 psi/ft below the Coalinga anticline; see table 13.2), whereas the P/D ratio is quickly determined directly from well records.

FLUID-PRESSURE RELATIONS

PRESSURE VERSUS DEPTH

We examined data for more than 300 boreholes, selected for depth of penetration and quality of records, to evaluate the relations between measured fluid pressures, mud weight, equivalent pressures, and depth (table 13.1). Our results show a regional average of about 0.6 psi/ft for bottom-hole pressures to a depth of about 14,000 ft, a lower bound near 0.465 psi/ft, and an upper bound near the local lithostatic gradient (fig. 13.2); the regional average is exceeded in about 90 wells (table 13.1). The P/D data to a depth of 22,000 ft (fig. 13.2) are fitted by a quadratic equation (r^2=0.89):

$$P(\pm 979 \text{ psi}) = 2.9 \times 10^{-5}D^2 + 0.144D + 1{,}043 . \quad (2)$$

All wells with abnormal overpressures (P/D ratio, ≥0.60 psi/ft) are located southwest of a line trending about N. 45° W. near the axis of the valley. The Sierran basement surface rises gently northeastward from about 15,000-ft depth near the valley axis (Smith, 1964). East of this axis, the sedimentary sequence thins and becomes nonmarine (see sec. *A–A'*, chap. 1). The AHP field is generally confined to lower Pliocene and older strata. The top of this field locally coincides with the top of a mudstone-siltstone sequence, from 5,000 to more than 10,000 ft thick; elsewhere, it cuts sharply across stratigraphic boundaries (figs. 13.3, 13.4). In an effort to locate the eastward extent of the Franciscan rocks, we include all wells in the valley proper known or inferred to bottom in basement rocks (fig. 13.2; table 13.1), about 30 in all. Most of these wells are located east of the valley axis, in non-AHP terrain, and bottom in plutonic rock. Four basement wells (27, 55, 277, and 285), however, penetrate the AHP field. In each well, the AHP appears to extend unbroken into (non-Franciscan) basement rocks.

Profiles of P/D ratio versus depth for all AHP wells show a relatively abrupt increase in the ratio below a depth of 5,000 to 6,000 ft. Above that depth, the P/D ratio is generally uniform, in the range 0.46–0.6 psi/ft, whereas below that depth it commonly increases to as large as 0.7 psi/ft or more (fig. 5) and locally approaches the lithostatic gradient (fig. 13.2; table 13.2). The record from the modern Joaquin Ridge well (fig. 13.5) shows how carefully mud weight is constantly adjusted to balance pore-fluid pressure; the other wells were drilled 30 to 35 years ago. All four of the wells shown in figure 13.5 had circulation problems, the modern one only at the bottom, the others more frequently at and below the pressure step.

Under conditions of normal compaction in sedimentary rocks, the change in fluid pressure per unit depth ($\Delta P/\Delta D$) cannot exceed the lithostatic gradient, about 1.00 psi/ft (Magara, 1978). The average trend of bottom-hole data below about 14,800 ft indicates that the rate of pressure increase significantly exceeds 1.00 psi/ft in the San Joaquin Valley. Although rates of 1.8 psi/ft are theoretically possible and rates greater than 1.6 psi/ft are indicated by gulf-coast data (Magara, 1978, p. 99), we need many more deep-well data to verify the San Joaquin Valley results.

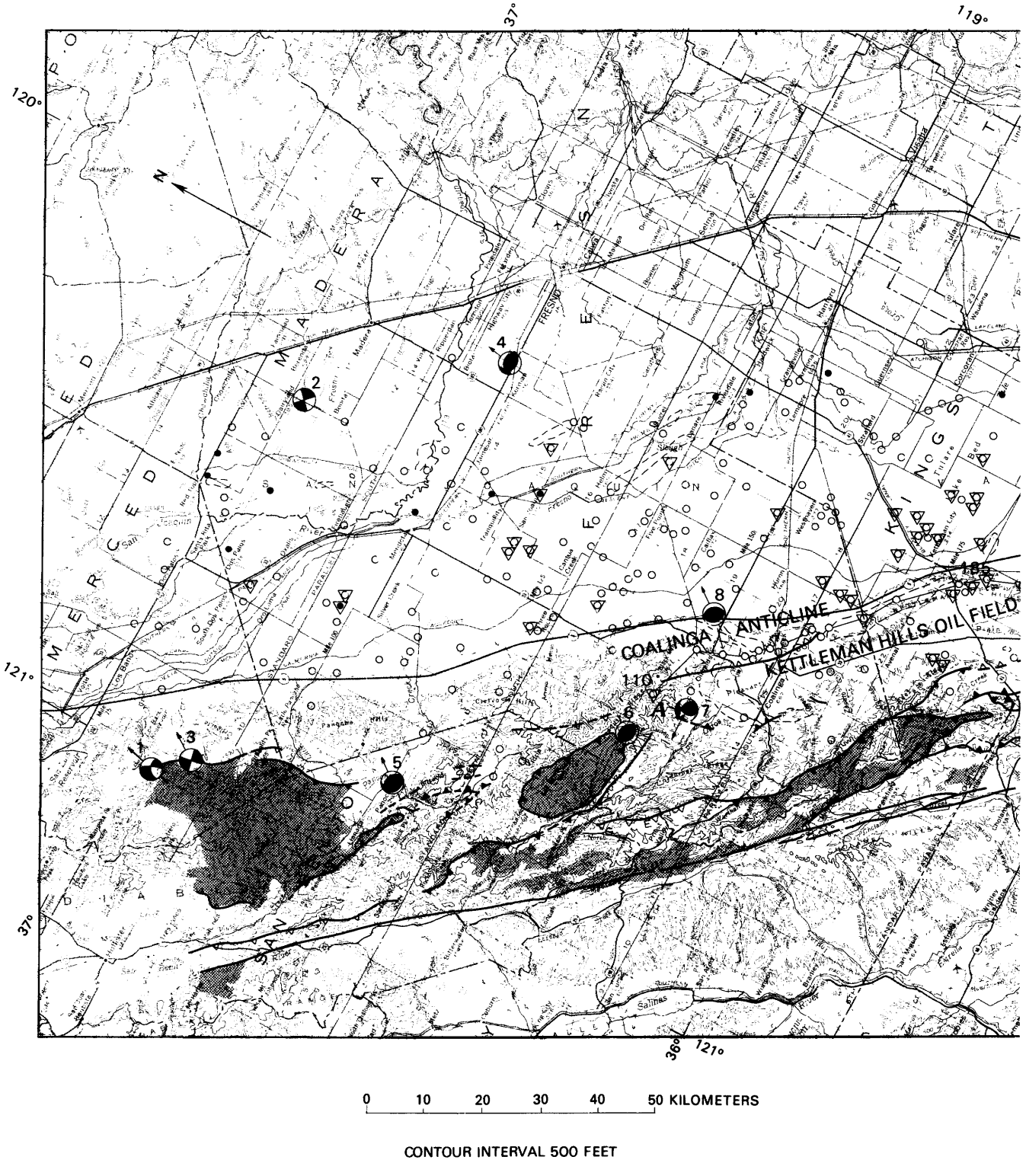

FIGURE 13.1.—Southern San Joaquin Valley, showing exposures of Franciscan assemblage and Sierran basement rocks, selected faults, oil and gas fields, wells that penetrate abnormally high fluid pressures and (or) basement rocks, fault-plane solutions for earthquakes, and lines of structure sections. Numbers refer to wells listed in table 13.1. Data and sources for fault-plane solutions from table 13.3. Base from State of California, U.S. Geological Survey, reduced from 1:500,000.

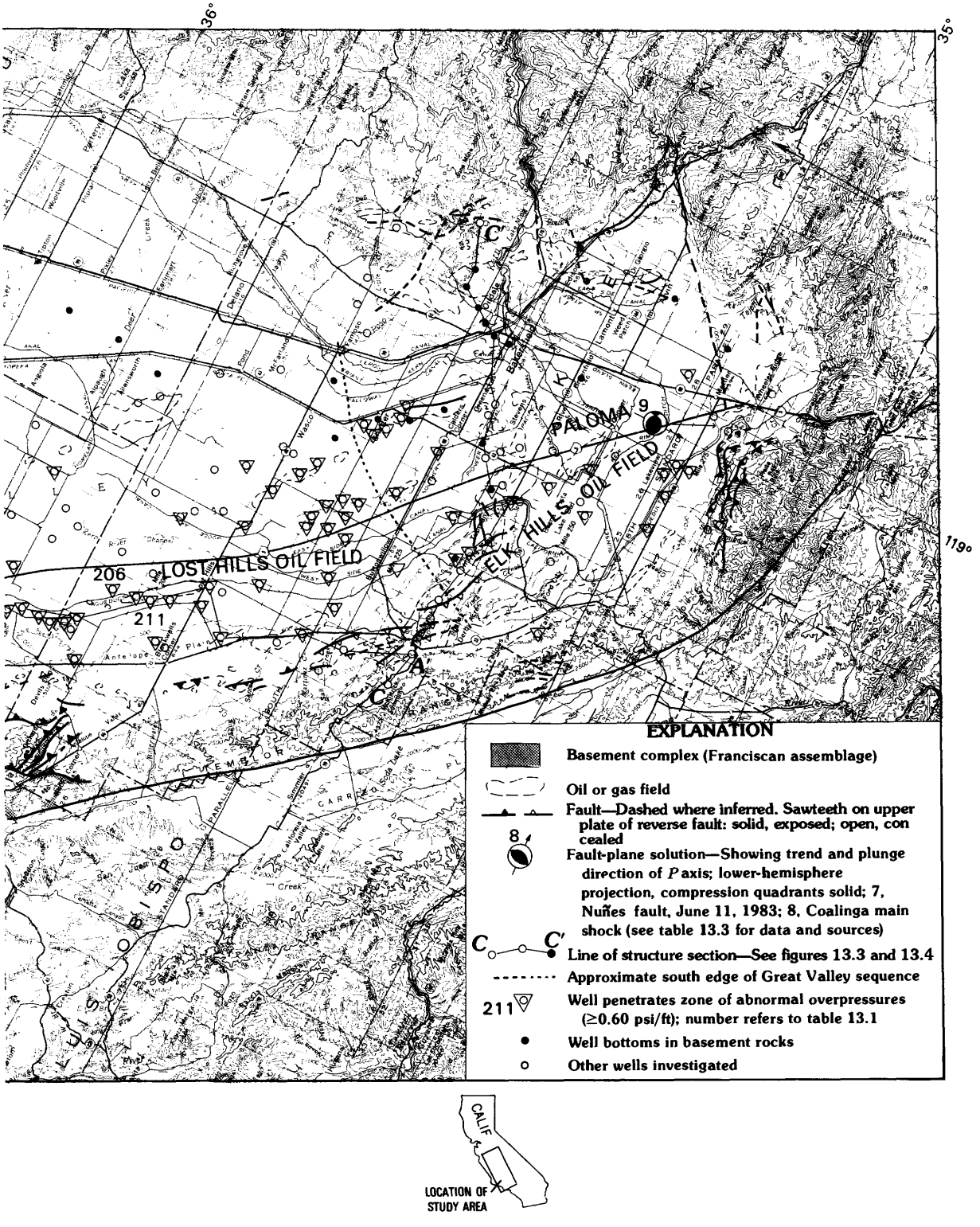

Figure 13.1.—Continued

TABLE 13.1.—*Data from boreholes in the Coalinga, Calif., area*

[AHP, abnormally high pressure; BC, basement complex (Sierran); P/D, pressure/depth; do., ditto]

Well	Location			Year	Operator	Name	Elevation (ft)	Depth to APH zone (ft)	Total depth (ft)	Bottom-hole P/D ratio (psi/ft)	Bottom-hole temperature	Remarks
	Sec.	T. S.	R. E.									
						Mount Diablo base and meridian						
1	7	10	11	1955	Castaic Highlands	Duncan Davis-1	108	---	6,000	0.48	---	---
2	21	10	11	1976	McCulloch Oil Corp	MCO-Makin 1-21	98	---	7,291	.48	---	---
3	2	10	12	1969	Conoco, Inc	Fialho	127	---	10,690	.52	---	---
4	8	10	12	1957	Amerada	Unit-1	117	---	9,004	.51	---	---
5	24	10	13	1954	Shell California Production, Inc.	Strat Test 4	136	---	6,000	.47	---	---
6	27	10	13	1961	Great Basins Petroleum Co.	S.A.R. 66-27	131	---	10,026	.50	181	---
7	3	10	14	1954	Shell California Production, Inc.	Strat Test 11	166	---	7,280	.47	---	BC at 7,260 ft.
8	6	10	14	1954	Getty Oil Co	S. Realty 1-6	132	---	8,083	.51	---	BC at 8,182 ft.
9	6	10	15	1953	Shell California Production, Inc.	Strat Test 3A	190	---	6,235	.45	---	---
10	29	10	15	1954	do	Strat Test 14A-2	173	---	7,582	.47	---	---
11	9	11	10	1961	Sun Exploration and Production Co.	Escobar	227	---	9,080	.60	---	---
12	10	11	11	1962	Great Basins Petroleum Co.	Ambassador Britto-1	104	---	9,920	.52	---	---
13	26	11	12	1972	Phillips Petroleum Co.	Redfern-1	123	<12,278	12,495	.67	218	---
14	28	11	12	1953	Chevron USA, Inc	Redfern-51	131	---	13,005	.57 at 12,690 ft	215	---
15	6	11	13	1961	Shell California Production, Inc.	Antoine 3-6	117	---	12,076	.58	---	BC at 12,073 ft, hornblende andesite.
16	9	11	14	1941	do	Chowchilla Farms-74	145	---	9,062	.51	---	BC at 9,038 ft, schist.
17	31	11	16	1953	do	Strat Test 7	184	---	7,955	.48	---	---
18	22	12	11	1969	Conoco, Inc	Hamburg-1	224	---	6,502	.46	---	---
19	6	12	13	1973	Arco Oil and Gas Co	Triangle-Redfern-1	136	---	11,522	.51	---	---
20	28	12	14	1966	McCulloch Oil Corp	Henry Yip-1	145	---	7,512	.50	---	---
21	27	12	15	1937	Texaco, Inc	General Gill-1	168	---	6,438	.47	---	---
22	13	13	11	1953	Exxon Co., USA	Stone-1	399	---	4,480	.49	---	---
23	28	13	11	1958	Holly Oil Co	E.S. 28-1	639	---	3,510	.48	---	---
24	13	13	12	1945	Union Oil Co	Irvine 65-13	258	---	6,829	.48	---	---
25	31	13	12	1952	Artnell	Etcheverry	455	---	5,501	.41	---	---
26	6	13	13	1962	Great Basins Petroleum Co.	Ambassador Telles-1	207	---	9,997	.55	194	---
27	16	13	13	1955	Shell California Production, Inc.	Shaw 1-16	227	11,975 ---	16,333	.68	290	BC at 627 ft, diabase and greenstone.
28	17	13	13	1963	Occidental Petroleum Corp.	Hammond Ranch-1	231	---	12,491	.61	236	---
29	20	13	14	1954	J.K. Wadley	Mendota	225	---	6,615	.47	---	---
30	12	13	15	1965	Texaco, Inc	Gill 86-12	170	---	6,000	.45	---	---
31	28	13	15	1973	Arco Oil and Gas Co	B.B. Co.-1	180	---	11,567	.50	---	BC at 11,522 ft, granite.
32	19	13	16	1957	Shell California Production, Inc.	Gill 32-19	175	---	4,489	.48	---	---
33	27	13	16	1973	Atlantic Oil Co	Gill	193	---	5,950	.47	---	---
34	30	13	17	1942	Arco Oil and Gas Co	Ponte-1	211	---	8,797	.48	---	---
35	6	13	18	1959	Pyramid Oil Co	Slaven	248	---	5,113	.48	---	---
36	14	14	12	1967	Sun Exploration and Production Co.	Giffen Inc.-1	379	---	4,600	.47	129	---
37	26	14	12	1951	Lockhart	Souza 1-36	431	---	10,636	.55	216	---
38	23	14	13	1957	C.L. Caine	-1	342	---	8,430	.45	185	---
39	31	14	13	1973	E.A. Bender	Silver Creek 54-X	405	---	10,387	.53	190	---
40	33	14	13	1964	Arco Oil and Gas Co	Roberts	384	---	8,772	.50	---	---
41	22	14	14	1954	S. Herndon	Murietta-2	235	---	8,834	.48	171	---
42	16	14	15	1962	Valwood Production Co.	Sterling-Coleman	174	---	13,207	.55		
43	26	14	15	1968	do	Sachs-McNear 1-A	161	---	13,187	.56	208 at 12,701 ft	---
44	6	14	16	1981	Tenneco Oil Co	Sallaberry 1-6	171	---	10,000	.54	182	---
45	22	14	16	1982	Conoco, Inc	Kerhy Prop.-1 62-22	186	---	10,100	.48	---	---
46	33	14	16	1969	Conoco, Inc	Young et al.-1	160	---	11,941	.53	---	BC at 11,912 ft, granodiorite.
47	25	15	11	1958	P. Fiorovich	-1	1,151	---	7,025	.50	---	---
48	36	15	12	1947	Texaco, Inc	Lillis 85-36	823	---	6,059	.50	---	---
49	22	15	13	1942	Union Oil Co	C.L.G.-1	495	---	7,000	.51	---	---
50	24	15	14	1950	Shell California Production, Inc.	Coffin-1	216	---	7,407	.50	---	---
51	22	15	15	1942	do	Henderson 66-22	186	9,992	11,946	.70	---	---
52	23	15	15	1962	do	Eliason 3-23	187	11,430	13,010	.64	---	---
53	30	15	15	1951	do	Friis-Hansen 77-30	203	---	8,402	.49	108	---
54	35	15	15	1982	Union Oil Co	Bravo-1	209	2,625	12,043	.73	218	---
55	23	15	16	1983	Home Petroleum Co	DiBenedotto-1	165	11,320	12,399	.63	209	BC at 12,350 ft, metavolcanic rocks.
56	15	15	17	1974	Occidental Petroleum Corp.	Noble-1	190	7,352	10,784	.63	---	---
57	19	15	18	1969	Norris Oil Co	SA + FL-1	194	---	10,300	.50	185	---
58	30	15	18	1968	Argosy	Noble 22-30	192	---	10,776	.52	182	---
59	20	16	13	1937	Superior Oil Co	C.U.P.-1	2,143	---	6,001	.47	---	---
60	22	16	13	1952	Burmah	Glenn-1	1,610	---	7,345	.49	161	---
61	22	16	14	1974	Orland Oil Co	1-22	429	<10,358	10,358	.68	205	---
62	27	16	14	1969	Rapp Oil Co	Morris Pucheu 67-27	496	---	10,917	.60	---	---
63	36	16	14	1959	Hondo Oil Co	Haber-1	472	---	10,000	.54	190	---
64	18	16	15	1981	Home Petroleum Co	Kimberlin	295	---	8,500	.54	---	---
65	20	16	15	1981	do	Giffen 20-1	327	---	8,657	.53	178	---
66	18	16	16	1945	Chevron USA, Inc	Giffen-74	220	---	10,100	.48	188	---
67	26	16	16	1981	Energy Production and Sales Co.	McDonald-1	237	---	9,250	.59	166	---
68	32	16	16	1943	Arco Oil and Gas Co	McDonald Est.-1	258	---	9,315	.51	164	---

TABLE 13.1.—*Data from boreholes in the Coalinga, Calif., area*—Continued

Well	Location			Year	Operator	Name	Elevation (ft)	Depth to APH zone (ft)	Total depth (ft)	Bottom-hole P/D ratio (psi/ft)	Bottom-hole temperature	Remarks
	Sec.	T. S.	R. E.									
						Mount Diablo base and meridian--Continued						
69	19	16	17	1968	F. & B	Bravo-1	188	---	8,539	.44	165	---
70	29	16	17	1970	Chevron USA, Inc	Bravo-41	186	---	9,233	.51	177	---
71	11	17	11	1980	Tannehill Oil Co	Niccolini	1,717	---	9,887	.56	---	---
72	5	17	12	1957	B.C.B	88-X	1,869	---	5,504	.51	---	---
73	20	17	12	1957	Norris Oil Co	Gonzales	2,057	---	5,602	.51	---	---
74	14	17	15	1969	Chevron USA, Inc	Giffen-67	349	2,707	14,471	.72	---	---
75	15	17	15	1944	Getty Oil Co	SP-82	368	<10,240	13,019	.78	---	---
76	24	17	15	1940	Texaco, Inc	Everding	345	---	10,307	.51	---	---
77	25	17	15	1949	Conoco, Inc	SP-1	358	---	10,342	.51	---	---
78	32	17	15	1953	Helm and Sumpf	Indart-34	487	---	10,500	.52	192	---
79	5	17	16	1955	Burmah	Aminoil USA 77-5	274	---	10,031	.50	---	---
80	13	17	16	1946	Superior Oil Co	K.C.D.-1	241	---	10,511	.54	190	---
81	30	17	16	1939	Shell California Production, Inc.	Port Costa 48-30	330	---	10,711	.51	---	---
82	32	17	16	1981	Hilliard Oil and Gas Co., Inc.	Farelli-1	286	---	10,280	.57	209	---
83	20	17	17	1963	Western Conoco, Inc	Everts 72-20	226	---	10,500	.51	181	---
84	21	17	17	1948	Arco Oil and Gas Co	E.M. Buck-1	234	---	9,750	.54	---	---
85	32	17	17	1968	Shell California Production, Inc.	Saunders 1-32	238	---	10,930	.57	---	---
86	2	17	18	1941	Mobil Oil Corp	Burrel-1	210	---	9,400	.50	195	---
87	16	17	18	1973	Amerada	Brix	198	---	12,341	.62	194	---
88	31	17	18	1968	Mohawk Petroleum Corp., Inc.	Shell-Bravo	237	---	9,525	.49	165	---
89	26	17	19	1946	Amerada	Lawton 58-26	212	---	11,998	.51	---	Bottomed in BC.
90	1	18	14	1966	Santa Fe Energy Corp	S.P.R.R. 68-1	672	---	5,404	.50	---	---
91	4	18	15	1959	Shell California Production, Inc.	Lillis-Christie 78X4-	485	---	10,320	.49	183	---
92	23	18	15	1951	Exxon Co., USA	S.P.C.-1	527	---	10,400	.50	---	---
93	4	18	16	1957	do	C.R. Puck Haber et al.-1.	295	---	11,111	.51	---	---
94	25	18	16	1940	do	S.P.R.R.-1	328	---	11,415	.50	---	---
95	32	18	16	1976	Natomas	Baird Errea 1-32	374	---	10,210	.52	192	---
96	2	18	17	1969	Shell California Production, Inc.	1-2 Ferry	479	---	11,806	.54	---	---
97	5	18	17	1968	do	1-5 O'Neill	263	---	11,222	.58	188	---
98	9	18	17	1957	Marathon Oil Co	Citizens Bank	252	---	11,118	.54	177	---
99	31	18	17	1937	Union Oil Co	S.P.L.-1	350	---	11,673	.49	---	---
100	11	18	18	1956	Texaco, Inc	S.P.-1	238	---	10,202	.50	175	---
101	17	18	18	1968	Shell California Production, Inc.	South Lake Farms 1-17	239	---	10,774	.54	180	---
102	34	18	18	1968	do	A. King 1-34	254	---	11,733	.56	187	---
103	1	18	19	1956	Malco Asphalt Co	Matti Cobb-1	232	---	8,500	.50	---	---
104	4	18	19	1955	Geochem Survey Co	Graeber-Rowen 47-4	221	---	8,860	.48	---	---
105	15	18	19	1978	Buttes Resources Co	Union-Texaco-Bezera et al.	224	---	10,550	.53	176	---
106	6	18	20	1962	Sun Exploration and Production Co.	Borba-1	222	---	11,724	.48	186	BC at 11,710 ft.
107	27	18	20	1948	Getty Oil Co	Grangeville-1	237	---	9,005	.49	82	---
108	31	18	20	1974	Texaco, Inc	Nunes-1	215	---	10,348	.56	166	---
109	35	18	20	1964	R.S. Rheem	Kreyenhagen 23-36	231	---	9,090	.47	145	---
110	3	19	14	1976	Arco Oil and Gas Co	Joaquin Ridge-1	3,786	9,045	14,409	.78	178 at 6,045 ft	Section A.
111	25	19	14	1954	Holmes and Associates	-1	1,439	---	5,298	.51	---	---
112	15	19	15	1952	Shell California Production, Inc.	363-X	1,265	---	10,414	.52	168	Section A.
113	35	19	15	1946	Chevron USA, Inc	213	930	---	5,775	.46	---	Do.
114	25	19	16	1957	Honolulu-Texas-Socal	S.P.L.-48	416	---	13,394	.58	240	---
115	8	19	17	1955	Getty Oil Co	Indian-Westates-25	346	---	12,330	.54	200	---
116	24	19	17	1956	Texaco, Inc	Rhein-1	340	---	13,437	.53	---	---
117	21	19	18	1973	North Central Oil Co	Boston Ranch-1	278	11,485	12,715	.63	210	---
118	29	19	19	1968	Shell California Production, Inc.	Willet 1-29	241	---	13,199	.53	204	---
119	24	19	20	1981	Terra Resources, Inc	Green-1	216	---	10,600	.48	170	---
120	26	19	20	1982	Terra Resources, Inc	Piexoto	234	---	12,850	.49	---	---
121	7	19	21	1961	Exxon Co., USA	Capital Co. G-1	244	---	12,816	.49	---	BC at 12,695 ft, slate.
122	25	20	14	1962	Chevron USA, Inc	8-5 25D	774	---	1,690	.46		
123	12	20	15	1939	Gulf Oil Exploration and Production Co.	Leavitt-Hintz-1	902	---	8,108	.45	---	Section A.
124	13	20	15	1939	Chevron USA, Inc	62-13 C	829	---	7,472	.55	---	Do.
125	12	20	16	1967	Westates Petroleum Co	PVF 11-X-12	430	---	12,150	.44	---	Do.
126	18	20	16	1940	Union Oil Co	68	749	---	8,051	.53	---	Do.
127	20	20	16	1944	do	Estrem 84-20	540	---	9,613	.58	---	---
128	28	20	16	1944	do	Gatchell-68	691	---	11,586	.56	211	Section A.
129	29	20	16	1943	Chevron USA, Inc	PVF 82-29F	543	---	9,151	.51	190	Do.
130	35	20	17	1973	Great Basins Petroleum Co.	N.E. Kettleman 1-35	360	<10,938	15,010	.72	238	Do.
131	10	20	18	1978	Hilliard Oil and Gas Co., Inc.	Woods Ranch-1	276	---	12,223	.58	215	---
132	11	20	18	1978	Texaco, Inc	Boston Ranch-1	276	---	13,512	.54	214	---
133	12	20	18	1976	Tenneco Oil Co	Ladd-Westhaven 26-12-	275	---	13,308	.60	---	---
134	13	20	18	1978	do	Bass-Westhaven	275	---	13,303	.58	---	---
135	14	20	18	1982	Koch Oil Co	Aqueduct-1-14	301	---	13,286	.50	200	---
136	23	20	18	1959	Chevron USA, Inc	U.S.A. Haven-Boston 813.	275	---	14,322	.51	211	---
137	7	20	19	1951	Mobil Oil Corp	B.L.C.-48-7	269	---	14,911	.52	229	---
138	11	20	20	1975	Anshutz	Frietas	202	---	11,495	.44	175	---
139	22	20	20	1979	Conoco, Inc	Watson-1	225	---	12,476	.51	190	---
140	28	20	20	1959	R.S. Rheem	Weaver-Lovelace 37-X-	188	---	10,720	.51	---	---
141	36	20	30	1956	Geochem Survey Co	Campbell 63X-36	209	---	11,711	.50	175	---
142	16	22	22	1979	Union Oil Co	Salyer-1	245	---	11,789	.51	188	---

TABLE 13.1.—*Data from boreholes in the Coalinga, Calif., area*—Continued

Well	Location			Year	Operator	Name	Elevation (ft)	Depth to APH zone (ft)	Total depth (ft)	Bottom-hole P/D ratio (psi/ft)	Bottom-hole temperature	Remarks
	Sec.	T.	S. R. E.									
						Mount Diablo base and meridian--Continued						
143	1	21	16	1944	Chevron USA, Inc------	Bordieu 1-A----------	583	---	10,868	.49	---	Section A.
144	2	21	16	1944	Sun Exploration and Production Co.	Dessel-41----------	630	10,555	11,442	.69	220	Do.
145	12	21	16	1950	Gulf Oil Exploration and Production Co.	Orr-43----------	563	---	11,449	.54	---	Do.
146	20	21	16	1956	Texaco, Inc----------	Lillis-1 NCT-1-------	845	---	10,481	.50	---	---
147	28	21	16	1950	Marathon Oil Co-------	H.C. Lillis-1--------	809	---	11,046	.56	---	---
148	11	21	17	1982	Flynn Energy Co-------	Eravo 11-1----------	400	13,200	15,200	.71	273 at 14,890 ft	---
149	14	21	17	1973	do----------	Carberry-1----------	423	1,498	14,258	.65	243	---
150	18	21	17	----	Chevron USA, Inc------	4-18-J----------	658	---	11,746	.47	173	Section A.
151	34	21	17	1955	do----------	423----------	981	11,468	15,693	.77	309	Do.
152	36	21	18	1975	Great Basins Petroleum Co.	81-X----------	219	3,500	14,209	.84	250	---
153	16	21	19	1979	Tenneco Oil Co--------	API Schutte-1--------	209	4,010	14,915	.61	240	---
154	35	21	19	1959	Marathon Oil Co-------	Westlake Farm-1------	181	7,168	12,028	.63	217	---
155	4	21	20	1963	Empire State Oil Co---	Lovelace 56X-4-------	184	---	6,000	.48	134	---
156	22	21	20	1978	Gas Producing Co------	Chatom-1----------	176	---	5,110	.52	130	---
157	4	21	21	1951	Mobil Oil Corp--------	Richardson 36-4------	202	---	12,064	.56	186	---
158	10	21	21	1959	Getty Oil Co----------	Boswell-Richardson-72	199	---	12,701	.50	185	---
159	24	21	21	1956	Gulf Oil Exploration and Production Co.	Boswell-1----------	184	---	11,166	.51	170	---
160	9	22	15	1958	General American Oil Co.	Standard 52-9--------	1,046	---	5,258	.51	---	---
161	11	22	16	1959	McCulloch Oil Corp----	Standard-1----------	802	---	12,226	.57	219	---
162	24	22	17	1974	Chevron USA, Inc------	DeSmet USL----------	1,033	---	15,073	.55	244	---
163	7	22	18	1939	do----------	E-27-7----------	1,049	---	9,855	.50	---	Section A.
164	4	22	19	1979	Baumgartner Oil Co----	A.P.I.-Tadco 2-14----	184	---	13,302	.55	217	---
165	4	22	19	1979	do----------	A.P.I.-Tadco 3-4-----	184	<12,268	12,268	.65	233	---
166	4	22	19	1980	do----------	A.P.I.-Tadco 3A-4----	187	<13,358	13,358	.66	250	---
167	9	22	19	1971	American Pacific International Inc.	Davis TransAmerica Corp.-1.	182	13,419	15,555	.83	282	---
168	8	22	20	1982	Husky Oil Co----------	KCDC 54-8----------	180	4,179	15,131	.72	234	---
169	17	22	20	1967	Tulare Basin Association.	Salyer Land Co. 78-17	194	---	14,415	.60	---	---
170	28	22	20	1942	Shell California Production, Inc.	Tulare Lake 21-28----	205	8,727	12,109	.61	---	---
171	29	22	20	1978	Hilliard Oil and Gas Co.. Inc.	Sumpf-Williams-1-----	211	4,605	13,932	.69	---	---
172	15	22	21	1956	Lake Oil Co----------	Boswell-1----------	194	---	5,003	.50	121	---
173	18	22	21	1981	Texaco, Inc----------	Boswell-1----------	200	4,300	15,000	.67	---	---
174	5	22	22	1966	Occidental Petroleum Corp.	Hansen-1----------	205	---	14,681	.55	---	BC at 14,662 ft.
								---			---	---
175	22	22	24	1969	Pan Petroleum Co------	R.E.S. Hesse et al.-1	250	---	10,043	.49	---	Bottomed in BC,
											---	weathered granite.
176	9	23	17	1951	Sun Exploration and Production Co.	Lynch-Mauren 68-9----	1,089	7,265	11,968	.66	230	---
177	16	23	17	1961	Macpet Co----------	Shell Mauren-1-------	1,137	<8,693	8,693	.61	158	---
178	16	23	17	1957	Verde Ent. Co--------	Mauren 81X-16-------	1,100	---	10,144	.53	---	---
179	31	23	17	1958	Exxon Co., USA-------	Avenal Land and Oil-2	1,084	---	4,686	.49	---	---
180	1	23	18	1941	Chevron USA, Inc------	1-1U----------	693	---	12,884	.56	---	Section A.
										.66 at 5,709-7433 ft		
										.61 at 9,610-10,968 ft		
181	2	23	18	1935	Getty Oil Co--------	73-2U----------	695	5,745	8,985	.61	---	---
182	12	23	18	1976	Sumpf-Williams-------	Dougherty USL 1-12---	605	5,485	12,628	.71	248	---
183	12	23	18	1981	do----------	Dougherty USL 2-12---	585	---	10,656	.56	---	---
184	2	23	19	1966	Occidental Petroleum Corp.	Howe-1----------	193	1,040	15,797	.67 at 15,565 ft	250	---
185	19	23	19	1954	Chevron USA, Inc------	38-19V----------	597	5,450	12,819	.67	248	Section A.
186	13	23	20	1982	Terra Resources, Inc--	Harvester 1-13-------	209	---	14,800	.52	---	---
187	31	23	20	1978	American Quasar Oil Co	Bravo 1-31----------	252	6,425	19,686	.97	349	---
188	25	23	21	1982	Terra Resources, Inc--	Harvester 1-25-------	218	5,000	15,240	.68	---	---
189	4	23	22	1946	Kings County Oil Co---	Von Glahn-1----------	192	---	13,213	.46	78	---
190	28	23	24	1980	General American Oil Co.	Lucy-1----------	230	---	11,858	.53	---	BC at 11,800 ft, slate.
191	20	24	18	1955	Reserve Oil and Gas Co	Orchard 48-20--------	683	---	5,235	.60	---	---
192	4	24	19	1970	Chevron USA, Inc------	SF + FL-68----------	437	10,521	10,646	.69	252	Section A.
193	10	24	19	1961	do----------	SF + FL 613-10Z------	354	6,500	11,647	.71	220	Do.
194	27	24	19	1961	Occidental Petroleum Corp.	USL 27-27----------	414	11,670	12,150	.75	262	---
195	34	24	19	1964	do----------	SF + FL 123-34-------	492	11,150	11,540	.74	246	---
196	12	24	20	1948	Shell California Production, Inc.	Hacienda-1----------	200	---	5,015	.49	---	---
197	9	24	21	1964	E.A. Bender----------	Lloyd-51----------	206	---	5,000	.45	---	---
198	20	24	21	1966	Sam Manchel----------	Hacienda Farms 63-20-	210	---	4,950	.46	---	---
199	22	24	23	1940	Nord-Montara Petroleum Co.	Daniel-35----------	213	---	11,728	.52	---	---
200	36	24	23	1952	MaGee Inv. Co--------	Morris-1----------	222	---	13,480	.50	---	---
201	20	25	24	1970	Chevron USA, Inc------	GRI-65----------	232	---	12,224	.55	---	Bottomed in BC.
202	2	25	19	1963	Occidental Petroleum Corp.	Hellman 131X-2-------	419	4,200	11,075	.79 at 11,004 ft	236	---
203	12	25	19	1947	Chevron USA, Inc------	SF + FL 4-2----------	374	5,249	12,954	.72	265?	Section A.
204	13	25	19	1945	Union Oil Co----------	South Dome-41--------	397	2,057	8,540	.66	---	---
205	20	25	19	1945	Santa Fe Energy Co----	Bates-2----------	489	7,544	9,147	.61	---	---
206	22	25	20	1967	Shell California Production, Inc.	Arco 123-22----------	303	11,815	16,619	.92	292	---
207	17	25	21	1957	Carl Long----------	Maria-1----------	270	---	4,040	.44	---	---
208	16	25	22	1940	North Kern Oil and Gas Co.	Semitropic----------	248	---	5,310	.50	---	---
209	23	25	24	1955	Tesoro Petroleum Corp-	Dearinger 46-23------	272	---	10,865	.50	---	---

TABLE 13.1.—*Data from boreholes in the Coalinga, Calif., area*—Continued

Well	Location Sec.	T. S.	R. E.	Year	Operator	Name	Elevation (ft)	Depth to APH zone (ft)	Total depth (ft)	Bottom-hole P/D ratio (psi/ft)	Bottom-hole temperature	Remarks
					Mount Diablo base and meridian--Continued							
210	2	26	20	1935	Chevron USA, Inc------	United-1----------	477	1,656	6,887	.74	---	---
211	11	26	20	1949	Mobil Oil Corp-------	Williamson 33-11-----	481	1,800	11,553	.72	232	Section A.
212	24	26	20	1939	California Lands Co---	Occidental-2---------	430	2,300	8,320	.62	---	---
213	30	26	20	1969	King Resources Co-----	OLC-1----------	600	<12,534	12,568	at 5,595 ft .61 at 12,534 ft	230	---
214	31	26	20	1964	Gulf Oil Exploration and Production Co.	Tenby OLC-1----------	615	---	11,904	.53	---	---
215	6	26	21	1957	Superior Oil Co------	Windmill Shallow-1---	283	---	10,511	.50	---	---
216	5	26	22	1945	Getty Oil Co----------	National Royalties-1-	235	9,435	16,431	.83	286	---
217	9	26	22	1968	Occidental Petroleum Corp.	Houchin-1----------	221	---	10,460	.51	---	---
218	26	26	22	1955	D.D. and Dorothy Dunlap.	45-26----------	268	---	8,500	.49	---	---
219	8	26	23	1970	Ebert & Brandt-------	Brandenburger-1------	225	---	5,188	.51	---	---
220	27	26	23	1965	Occidental Petroleum Corp.	Sharples et al------	242	<11,131	14,014	.68	248	---
221	17	26	25	1938	Getty Oil Co----------	KCL Pond-1----------	333	---	9,079	.50	---	---
222	26	27	20	1941	Shell California Production, Inc.	55----------	658	10,309	10,800	.61	---	Section A.
223	4	27	21	1945	Chevron USA, Inc------	Cahn 58-4----------	400	<4,177	11,080	.67	---	Do.
224	6	27	21	1947	ARCO Oil and Gas Co---	Buck-1----------	450	---	7,720	.58	---	---
225	9	27	21	1963	Union Oil Co----------	Ellis 85D-9----------	375	2,309	5,500	.62	---	---
226	36	27	21	1948	Chevron USA, Inc------	Van Sicklin-45-------	320	5,560	14,557	.67	---	---
227	10	27	22	1972	Great Basins Petroleum Corp.	Tenneco 31X-10-------	234	<12,000	21,640	.92	374	---
228	9	27	23	1955	Exxon Co., USA--------	Arthur E. Conn et al.-1.	262	7,329	8,300	.69	---	---
229	25	27	23	1944	Chevron USA, Inc------	Fullerton-1----------	291	14,746	14,770	.61	---	---
230	6	27	23	1974	Tenneco Oil Co--------	Cities-Tenneco-35X---	284	---	16,540	.53 at 14,224 ft	---	---
231	7	27	24	----	Composite: Conoco, Inc. Chevron USA, Inc. Mushrush-5.	Meyer-1 and	288	---	15,866	.46	---	---
232	30	27	24	1956	Exxon Co., USA--------	KCL F-1----------	282	<7,236	7,913	.66	168	---
233	35	27	24	1968	Mobil Oil Corp--------	KCL 86-35----------	320	---	15,476	.57	261	BC at 15,415 ft, 61 ft of hard greenstone.
234	15	27	25	1967	do----------	Pan KCL 3-15----------	376	---	13,374	.58	224	BC at 13,150 ft, diorite.
235	12	27	26	1941	Santa Fe Energy Co----	Famosa 12-1----------	647	---	6,855	.46	---	---
236	22	27	26	1955	Chevron USA, Inc------	C.W.O.D. 87----------	482	---	5,251	.49	---	---
237	4	27	27	1953	A.M. Dunn----------	D.L.K.-1----------	879	---	5,084	.50	---	---
238	9	27	28	1956	Shell California Production, Inc.	Vedder-55----------	1,211	---	3,023	.47	---	---
239	19	28	21	1975	Chevron USA, Inc------	F-554-X-19----------	599	---	11,853	.60	---	---
240	33	28	21	1946	Shell California Production, Inc.	62W-33----------	603	5,622	14,104	.67	---	Section A.
241	34	28	22	1981	Texaco, Inc----------	Bloemhof-1----------	270	3,700	15,989	.78	309	---
242	5	28	23	1949	Chevron USA, Inc------	KCL 27-6----------	294	<4,598	13,614	.76	240	---
243	6	28	23	1958	Texaco, Inc----------	Texas-Standard Stutsman.	290	11,039	12,910	.69	240	---
244	10	28	23	1974	Mobil Oil Corp--------	Tupman 1----------	265	2,113	20,753	.93	354	---
245	14	28	23	1956	Texaco, Inc----------	Breen-1----------	275	<1,300	13,730	.75	258	---
246	17	28	23	1971	Mobil Oil Corp--------	Bravo-1----------	277	6,000	15,450	.78	270	---
247	22	28	23	1965	Texaco, Inc----------	Superior-Mobil Fee-1-	272	10,140	14,105	.66	259	---
248	25	28	23	1962	Harcourt----------	Jacobsen 1----------	270	<5,428	6,002	.63	147	---
249	29	28	23	1981	Austin Oil Co---------	Big Bend-1----------	283	<15,778	15,778	.61	300	---
250	7	28	25	1944	Getty Oil Co----------	86 A-7----------	328	11,095	12,630	.61	---	---
251	17	28	25	1954	Superior Oil Co-------	Russel-73----------	344	---	15,068	.54	245	Bottomed in BC, metasedimentary rocks.
252	18	28	25	1954	Getty Oil Co----------	54-18----------	320	6,418	12,528	.67	215	---
253	20	28	25	1958	Geochem Survey Co-----	Anderson-31----------	338	8,963	12,351	.65	203	---
254	26	28	25	1959	Union Oil Co----------	Kernco 25X----------	339	6,600	11,608	.65	196	---
255	27	28	25	1954	Superior Oil Co-------	Weber 3-S.O.---------	340	---	11,822	.62	210	---
256	33	28	25	1941	Union Oil Co----------	Pacific States-21-----	330	---	13,642	.47	---	BC at 13,621 ft, gabbro.
257	28	28	28	1942	Shell California Production, Inc.	Fuhrman-1----------	934	---	5,254	.46	---	Bottomed in BC, granite; section C.
258	30	28	28	1952	Tenneco Oil Co--------	Fee C 74----------	853	---	6,100	.48	---	BC at 6,035 ft, granite; section C.
259	17	28	29	1946	U.S. Drilling Co------	Olcese-1----------	1,315	---	2,600	.49		---
260	18	29	21	1950	Union Oil Co----------	Richardson 81-18-----	864	---	7,710	.60	---	---
261	22	29	21	1953	Superior Oil Co-------	Cymric-1----------	690	---	12,022	.50	240	Section A.
262	7	29	22	1971	Chevron USA, Inc------	So. SMUG 528-7x------	481	<10,439	15,500	.72	314	---
263	32	29	23	1963	Getty Oil Co----------	Featherstone---------	369	<10,054	15,006	.61	200	---
264	9	29	24	1966	Occidental Petroleum Corp.	Root-1----------	303	<13,493	15,396	.70	---	---
265	25	29	24	1966	Tenneco Oil Co--------	KCL 122-25----------	294	---	11,948	.60	---	---
266	21	29	25	1965	Occidental Petroleum Corp.	Texaco-Sp 15-21------	306	<10,648	10,648	.62	---	---
267	18	29	26	1944	Chevron USA, Inc------	KCL 11-44----------	341	---	13,404	.50	---	BC at 13,127 ft, serpentine.
268	36	29	26	1941	Marathon Oil Co-------	KCL-G-1----------	373	---	10,595	.52	---	Section C.
269	1	29	27	1951	Chevron USA, Inc------	33-52----------	578	---	7,014	.46	---	Bottomed in BC, granite; section C.
270	11	29	27	1948	Superior Oil Co-------	KCL-15----------	447	---	7,724	.44	---	Bottomed in BC, section C.
271	22	29	27	1948	Gulf Oil Exploration and Production Co.	KCL B-45----------	402	---	10,591	.49	---	Bottomed in BC, granite; section C.
272	34	29	27	1956	Western Gulf----------	KCL 33-34----------	396	---	11,577	.49	---	Bottomed in BC.
273	21	30	21	1954	Superior Oil Co-------	Forbes-1----------	2,010	---	4,761	.53	---	Section C.
274	26	30	22	1951	Chevron USA, Inc------	Van Wert-68----------	1,038	---	6,098	.51	---	Do.
275	29	30	22	1948	Texaco, Inc----------	W.P. 15-29----------	1,425	---	4,881	.60	---	---
276	30	30	22	----	Composite, Belgian anticline----------		1,720	---	10,686	---	---	Sections A and C.
277	25	30	23	1977	Unnamed----------	Proprietary----------	1,181	<7,879	18,761	.83	342	Bottomed in BC(?).
278	30	30	23	1951	Chevron USA, Inc., U.O. NPR 1.	X-55-30R----------	1,341	---	12,856	.55	---	Section C.
279	35	30	23	1955	do----------	352-35R----------	1,334	---	7,457	.55	---	Do.

TABLE 13.1.—*Data from boreholes in the Coalinga, Calif., area*—Continued

Well	Location			Year	Operator	Name	Elevation (ft)	Depth to APH zone (ft)	Total depth (ft)	Bottom-hole P/D ratio (psi/ft)	Bottom-hole temperature	Remarks
	Sec.	T. S.	R. E.									
						Mount Diablo base and meridian--Continued						
280	15	30	24	1965	E.A. Bender	Palm Farms-55	287	---	11,300	.63	---	---
281	31	30	24	1941	Chevron USA, Inc., U.O. NPR 1[1]	362-31S	1,270	6,250	9,943	.62	---	Section C.
282	12	30	25	1955	Shell California Production, Inc.	Posuncula-1	338	---	14,224	.57	---	Bottomed in BC.
								---			---	Section C.
283	14	30	25	1941	do	KCL A-44-14	325	---	13,408	.51	---	Do.
284	24	30	25	1958	do	KCL 15x-24	320	---	15,720	.60	---	---
										at 15,405 ft		
285	29	30	25	1952	Arco Oil and Gas Co	CLA 67-29	311	12,262	17,895	.73	300	BC at 17,873 ft.
286	33	30	25	1945	do	CLA 21-33	311	---	13,912	.60	---	---
287	3	30	26	1938	Superior Oil Co	KCL-12	363	---	13,131	.51	---	Section C.
288	4	30	26	1943	Miller and York, Inc	KCL G-1	358	---	8,134	.55	---	
289	30	30	26	1947	Shell California Production, Inc.	KCL A-53-30	329	---	14,224	.49	---	---
								---		at 14,000 ft		
290	10	30	29	1971	Atlantic Oil Co	Camp.-1		---	5,230	.55	---	Bottomed in BC.
										at 4,552 ft		
291	20	30	29	1957	Shell California Production, Inc.	45-20	456	---	8,107	.50	---	Do.
292	4	31	24	1947	Chevron USA, Inc. U.O. NPR 1[1]	343-4G	1,052	---	10,200	.55	---	Section C.
293	5	31	25	1945	Chevron USA, Inc	KCL 20-13	505	15,655	16,246	.62	---	Do.
294	8	31	25	1941	Arco Oil and Gas Co	Feldman U.S. 61-8	403	---	9,346	.60	---	---
295	26	31	25	1975	Texaco, Inc	Elk Vista -1	285	11,211	16,455	.79	290	---
296	16	31	26	1945	Shell California Production, Inc.	KCL 45	316	---	11,500	.49	---	---
297	10	31	29	1968	Termo Co	Digeorgio-1	500	---	6,419	.50	---	Bottomed in BC.
298	21	32	23	1957	Santa Fe Energy Co	CWOD 58-21	1,654	13,617	14,504	.62	---	---
299	10	32	24	1941	Getty Oil Co	10-25-P	915	---	14,622	.60	---	---
										at 12,825 ft		
300	11	32	25	1959	do	BVA 22-11	281	---	11,365	.60	---	---
301	15	32	25	1974	Texaco, Inc	Texaco-Tenneco-B & N-1	287	11,760	16,500	.64	---	---
302	4	32	26	1951	Marathon Oil Co	KCL A-72-4	309	10,947	21,482	.72	334	---
										at 20,003 ft		
303	14	32	26	1941	Union Oil Co	Morgan 51	306	---	11,456	.49	---	---
304	34	32	28	1974	Tenneco Oil Co	Tenneco-Superior Sandhills 64x.	415	<18,250	22,711	.68	320	---
305	3	32	29	1948	Marathon Oil Co	Mitchell-1	413	---	13,792	.51	---	Bottomed in BC.
						San Bernardino base and meridian						
306	3	11	19	1954	Mobil Oil Corp	Tejon 16-3	592	---	11,963	.57	---	Bottomed in BC.
307	15	11	20	1959	Arco Oil and Gas Co	KCL K22	535	---	16,421	.60	241	---
308	28	11	20	1953	do	KCL D-16-28	1,477	---	11,816	.60	---	---
309	5	11	21	1960	do	KCL Q-841-5	476	<12,001	13,960	.62	199	---
										at 12,497 ft		
310	10	11	21	1961	do	KCL 43-10	536	13,444	14,499	.61	254	---
311	15	11	21	1958	do	KCL 33-15	639	14,042	14,443	.62	---	---
312	8	11	22	1948	Conoco, Inc	Sentiago 1	623	<9,185	9,919	.65	---	---
313	12	11	22	1951	Gulf Oil Exploration and Production Co.	KCL 83-12	319	10,712	12,172	.61	---	---
314	8	10	19	1962	Arco Oil and Gas Co	Tejon A 61-8	1,239	---	10,462	.60	---	---
315	11	10	22	1968	Chevron USA, Inc	KCL 69-68-11	2,207	---	11,069	.60	---	---
316	13	10	22	1968	do	69-29-13	2,026	1,003	10,453	.63	---	---

[1]Unit Operation, Naval Petroleum Reserve.

PRESSURE VERSUS SONIC VELOCITY

Sonic logs for 10 wells were examined for fluid-pressure/velocity relations. In all these wells, the top of the AHP field is marked by a sharp reversal in the velocity gradient. Above the AHP field, the velocity increases with depth at a rate of 0.5 to 1.0 km/sec/km. The velocity reversal below the top of the AHP field extends over a vertical range of a few tens of feet to about 1,500 ft and involves a reduction in velocity by 15 to 25 percent. Recovery of a positive trend below the reversal tends toward, but may not attain, the values extrapolated from above the step. In one well where seismic velocities were independently determined from reflection and refraction profiles (Walter and Mooney, 1983; Wentworth and others, 1983; Walter, 1985), a very good correlation exists between the borehole sonic-log and seismic-profile interval velocities, as well as between the top of the reversal on the sonic log, the pressure step, and the top of a seismic-profile low-velocity zone (fig. 13.6).

FLUID PRESSURES BELOW THE COALINGA ANTICLINE

The relatively shallow wells in the Coalinga anticline area do not penetrate to any AHP field that may be present. However, an AHP field with P/D ratios of 0.78 psi/ft and $\Delta P/\Delta D$ greater than 1.20 psi/ft is present in the

TABLE 13.2.—*Estimate of the average density of strata in the Coalinga, Calif., area*

[Densities adjusted to fit observed gravity, seismic velocity, and lithology]

Section	Thickness (ft)	Density (g/cm^3)	P/D ratio (psi/ft)	Total pressure (psi)
Composite Cenozoic section, southern San Joaquin Valley (wells 117, 244, table 23.1)				
Quaternary and Pliocene------	7,220	2.05	0.90	6,498
Pliocene----------	2,625	2.22	.96	2,520
Miocene, upper----------	3,280	2.32	1.00	3,280
Miocene, middle and lower----	2,625	2.37	1.03	2,704
Oligocene----------	1,475	2.52	1.09	1,608
Eocene and Paleocene---------	1,150	[1]2.41	1.04	1,196
Cretaceous, upper----------	---	---	---	---
Great Valley sequence, undifferentiated.	---	---	---	---
Franciscan assemblage--------	---	---	---	---
Total----------	18,275	---	---	17,806
Coalinga anticline (Wentworth and others, 1984, fig. 3)				
Quaternary and Pliocene------	400	2.07	0.897	359
Pliocene----------	2,600	2.25	.975	2,535
Miocene, upper----------	1,400	2.33	1.01	1,414
Miocene, middle and lower----	800	2.41	1.04	832
Oligocene----------	---	---	---	---
Eocene and Paleocene---------	2,200	2.51	1.09	2,398
Cretaceous, upper----------	700	[1]2.46	1.066	746
Great Valley sequence, undifferentiated.	9,200	2.54	1.10	10,130
Franciscan assemblage--------	15,510	2.70	1.17	18,146
Total----------	32,810	---	---	36,560
Average----------	---	2.24	0.97	---

[1]Low-velocity zone.

Great Valley sequence below about 10,000 ft both northwest and southeast of the epicentral area (fig. 13.6). In addition, a seismic low-velocity zone, elsewhere correlated with AHP, exists in the Great Valley sequence of the Coalinga anticline-Pleasant Valley area between 10,000- and 23,000-ft depth (see chap. 3). Once formed, AHP zones in mudstone sequences are believed to form hydrologic barriers to migration of fluids from below (Hunt, 1979, p. 198). The presence of the thick and extensive low-velocity (AHP) zone suggests that any fluids that form below will not drain readily and thus will maintain total fluid pressure.

SOURCES OF OVERPRESSURE

The AHP field described here is about 150 mi long by 15 to 20 mi wide along the western margin of the San Joaquin Valley, where it extends from about 3,300 to more than 23,000 ft below the surface. The west half of this area is underlain, below at least 24,600-ft depth, by a wedge of Franciscan rocks (see fig. 13.8). All but the south fifth of the area is underlain by at least 10,000 ft of Great Valley sequence, and essentially the entire area is underlain by at least 5,000 or more ft of pre-Pliocene Cenozoic strata (Zieglar and Spotts, 1978). Each of these rock units probably contributes to the fluid overpressures in different ways, some in more than one way.

The best known examples of fluid overpressures are attributed to: (1) undercompaction of thick, low-permeability mudstone sequences under loads caused by rapid sedimentation and restricted drainage (compaction disequilibrium); (2) expansion of pore fluids under enhanced thermal gradients (aquathermal pressuring); (3) tectonic compression; and (4) generation of fluids. We have evidence that each of these processes operates in the southern San Joaquin Valley, but their relative contributions cannot be determined.

COMPACTION

In normally compacted sedimentary sequences, from which fluids drain readily with increasing depositional load, the pore-fluid pressure at all depths will reflect the hydrostatic gradient for the density of the fluid. Theoretically, normal compaction of a unit volume of saturated mudstone from a porosity of 0.3 to 0.125 percent expels about 0.2 volume of water (Chapman, 1983). However, in rapidly accumulating sequences of thick, massive clayey deposits with low permeability, compaction may be retarded, owing to inadequate drainage; additional load must then be carried by the fluid, so that overpressures and porosity are greater than normal for the depth of burial (Hunt, 1979, p. 197). Studies of gulf-coast data show that under conditions of normal compaction in mudstone, transit time per unit thickness (reciprocal of sonic velocity) and porosity decrease linearly with depth, and the gradients of both parameters increase rather abruptly at the top of an AHP field (Magara, 1978; Chapman, 1983). In the Joaquin Valley, correlation of the top of the AHP field, reversal of the sonic-velocity/depth gradient, and the top of a low-velocity zone (fig. 13.6) indicates that compaction disequilibrium operates in the thick mudstone sequences.

In most sequences containing a significant thickness of clayey sediment, several relatively impermeable pressure barriers will be present, each of which contains rises in fluid pressure in the beds just below, even in compacting systems lacking sources of excess fluid from below. Fyfe and others (1978, chap. 11) concluded that in such a system, high fluid pressures—commonly equal in magnitude to the lithostatic load—are a natural consequence of dewatering. These pressures will tend to persist until all the rocks, especially the weakest ones that form the

barriers, are cut by vertical fractures (hydraulic fracturing). Such fractures are expectable, however, only in terrain dominated by normal faulting (see next subsection).

THERMAL EXPANSION

Widespread evidence indicates that fluid pressure increases with temperature in Cenozoic basins and that a

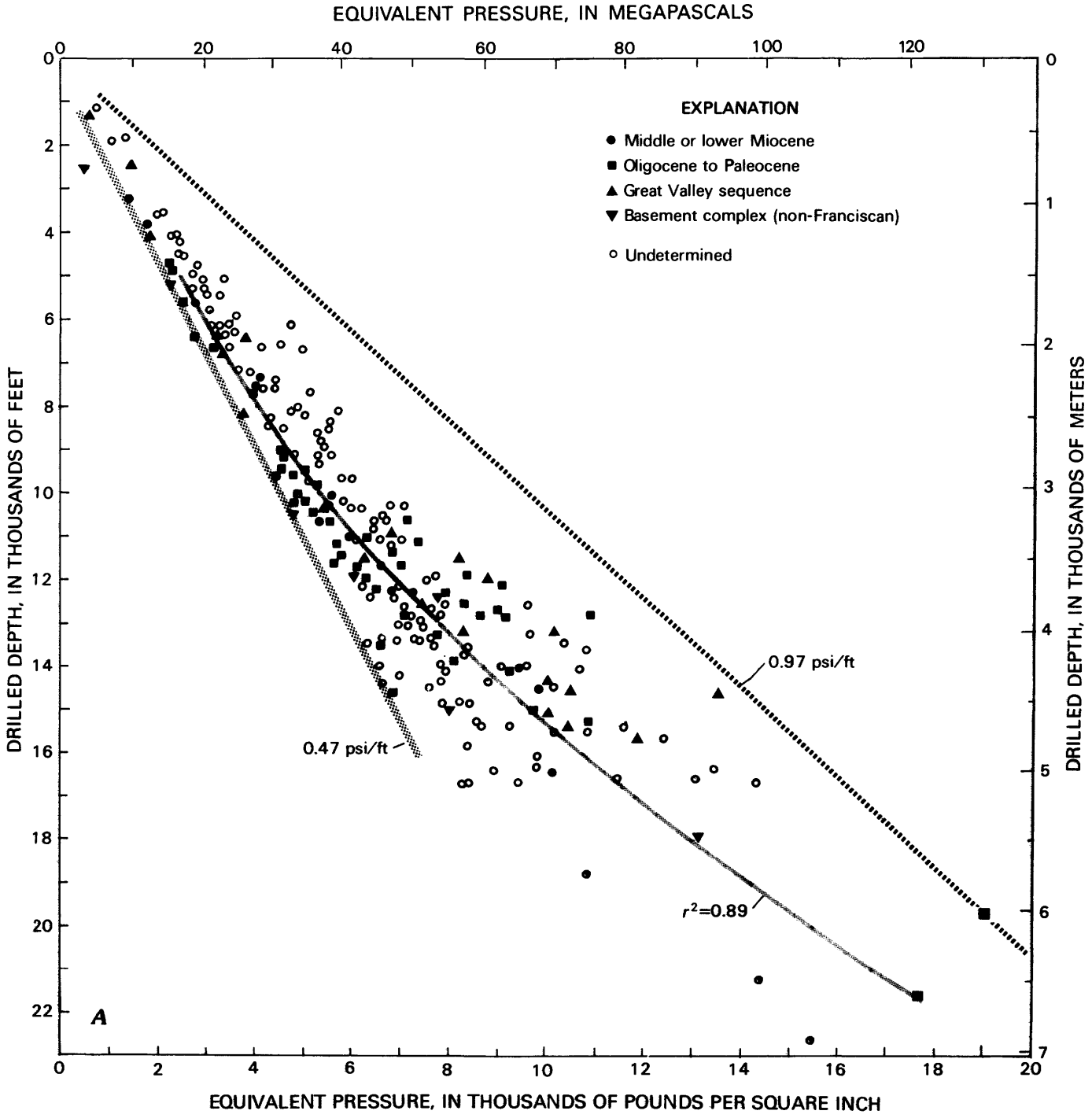

FIGURE 13.2.—Equivalent fluid pressure versus depth by bottom-hole geology, southern San Joaquin Valley. *A*, All wells of record. *B*, Selected wells to show greatest pressures and depths. Statistical fit is a quadratic equation (r^2=0.89): P (±979 psi)=$2.9\times10^{-5}D^2$+ $0.144D$+0.144, Derivative, $dP/dD = 5.8\times10^{-6}D$ + 1,043, indicates that below about 14,800 ft, pressure per unit depth increases at a rate greater than 1.00 psi/ft, or greater than the lithostatic gradient. 0.97-psi/ft bound is estimated lithostatic gradient for Cenozoic sequence in the southern San Joaquin Valley (table 13.2). Well data listed in table 13.1.

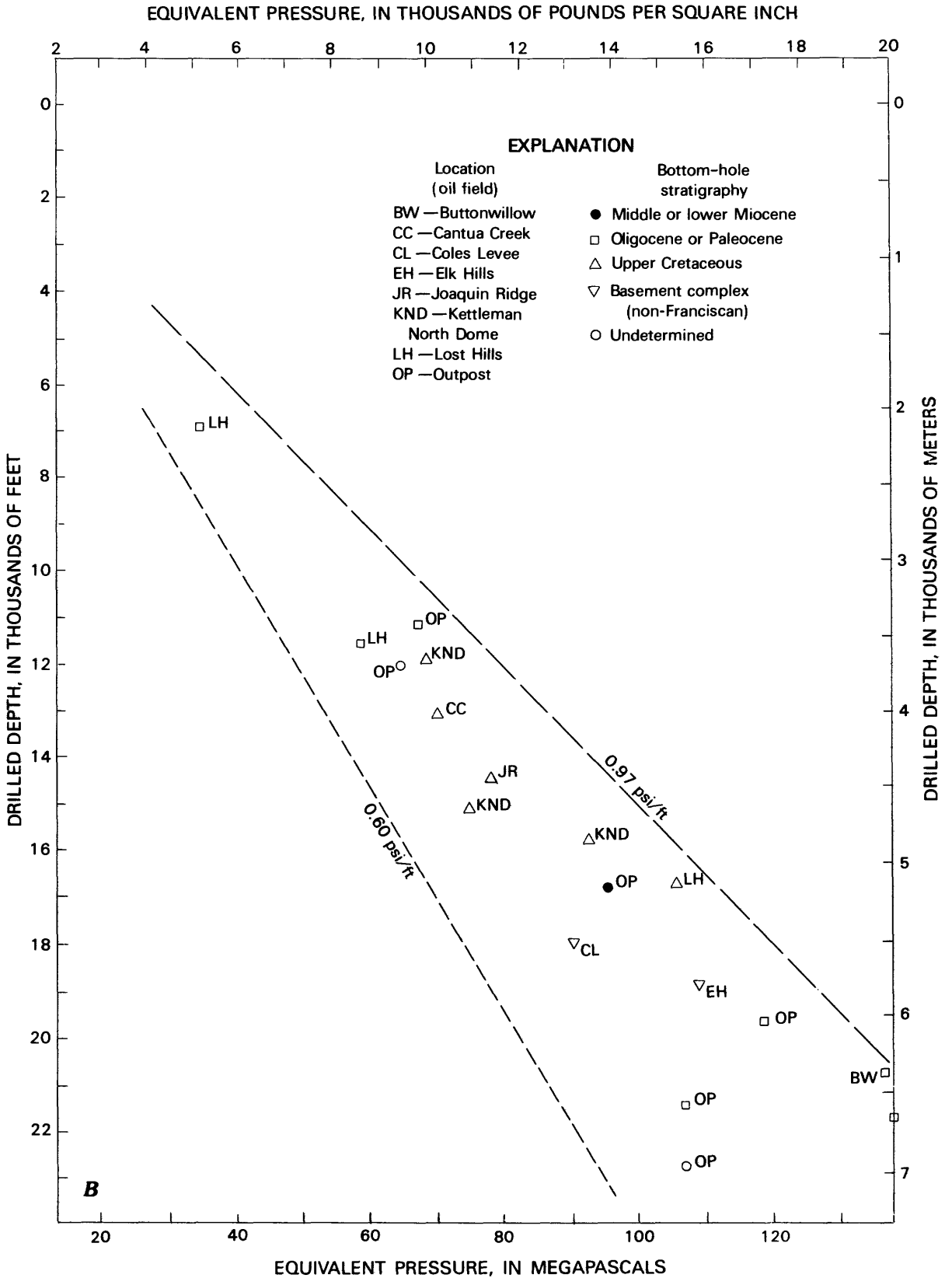

FIGURE 13.2.—Continued

break in the temperature-depth gradient correlates with the top of the AHP zone (Hunt, 1979, p. 244; Wallace and others, 1979). This effect is attributed to the lower conductivity—higher thermal gradient—of pore fluids relative to rock minerals (Hunt, 1979). Temperature data from San Joaquin Valley wells that bottom in AHP rocks define an appreciably higher temperature-depth gradient than than those that bottom in normally pressured rocks (fig. 13.7). In addition, figure 13.3 shows that below about 14,800 ft, the average $\Delta P/\Delta D$ exceeds 1.00 psi/ft, which cannot be caused by compaction disequilibrium. Thermal expansion, however, theoretically may cause $\Delta P/\Delta D$ as high as 1.8 psi/ft, and $\Delta P/\Delta D$'s of 1.4 psi/ft are attributed to thermal expansion in gulf-coast wells (Magara, 1978).

TECTONIC COMPRESSION

Examples of correlation of AHP's with tectonic compression include: the foreland of the Bavarian Alps and the Himalayas (Fertl and others, 1976); buried opposed thrusts in the Ventura Avenue oil field, southern California (Yeats, 1983); and the widespread AHP's in Franciscan rocks of the Coast Ranges (Berry, 1973). However, the Diablo Range-San Joaquin Valley boundary, underlain by eastward-directed tectonic wedges of Franciscan rocks (Wentworth and others, 1984), is the only example of tectonic compression supported by contemporary dynamic evidence—the 1983 Coalinga earthquake sequence—for which the activated structure and its stress field are both known (figs. 13.8, 13.9). This compression is attributable in part to crustal shortening normal to the San Andreas system, possibly induced by westward drift of the Sierra Nevada as the Great Basin extends, and by divergence of the San Andreas fault from the Pacific-North American plate boundary (Minster and Jordan, 1984). Fault-plane solutions for $M \geq 5$ earthquakes throughout central California west of the Sierra Nevada are compatible with this hypothesis because they show *P*-axes oriented in the northeast quadrant (fig. 13.8).

GENERATION OF FLUIDS

Diagenetic-metamorphic generation of fluids is a likely source of the widespread AHP's in the Franciscan assemblage and Great Valley sequence of the Coast Ranges and adjoining parts of the San Joaquin Valley. Such reactions, driven by increasing temperature and (or) chemical disequilibrium between pore fluids and sediment, can progressively add water, carbon dioxide, and methane to the existing fluids and thus increase pore pressure in a sealed reservoir (Yerkes and others, 1985). The gases, carbon dioxide and methane, are unique to Franciscan rocks and the Great Valley sequence and are known to issue from springs along the eastern margin of the Diablo Range (Barnes and others, 1975).

SUMMARY

Available data thus indicate that all generally recognized major sources of AHP's probably operate in the southern San Joaquin Valley and adjoining Diablo Range: compaction disequilibrium, thermal expansion, tectonic compression, and generation of fluids. We believe that the AHP's are a long-established, persistent feature. Recently drilled deep wells penetrate the AHP field, even in structural lows, and show increasing P/D ratios with increasing depth; active springs along the eastern margin of the Diablo Range show that distinctive metamorphic fluids are still forming at depth; and realistic modeling indicates that compaction-induced overpressures may persist for many millions of years (Smith, 1971).

Berry and Kharaka (1981) favored as dominant sources of AHP's in the Coast Ranges and Central Valley: (1) regional compression between the North American and Pacific tectonic plates; (2) local compression of late Cenozoic folds, such as the Kettleman Hills; and (3) aquathermal pressuring (presumably including compaction disequilibrium) of locally thick Tertiary sequences. Berry (1973) favored tectonic compression as the source of AHP's in the Kettleman Hills but found that compression of shale units in the known folds cannot account for the estimated volumes of water produced; he thus favored regional compression of a much larger mass of sediment at depth. We suggest that diagenetic-metamorphic reactions in Franciscan rocks and the Great Valley sequence may account for much of this excess, that an important source of compression is the tectonic wedging identified by Wentworth and others (1984), and that compaction disequilibrium and thermal expansion are important sources in the locally very thick Tertiary sequences.

ABNORMAL OVERPRESSURES AND THE COALINGA EARTHQUAKE SEQUENCE

Although we have no direct evidence of AHP's in the Coalinga anticline, we infer their presence at depths of 10,000 to 20,000 ft on the basis of a mapped low-velocity zone (see chap. 3), suggesting that fluids generated below that depth are contained. In addition, pressure data for deep wells northwest and southeast of the anticline indicate that, below 10,000-ft depth in those areas, $\Delta P/\Delta D$ exceeds 1.20 psi/ft (fig. 13.5).

The 1983 Coalinga earthquake sequence occurred within and near a buried wedge-shaped block of Franciscan rocks, at least 6,500 ft thick and at least 24 mi wide, as

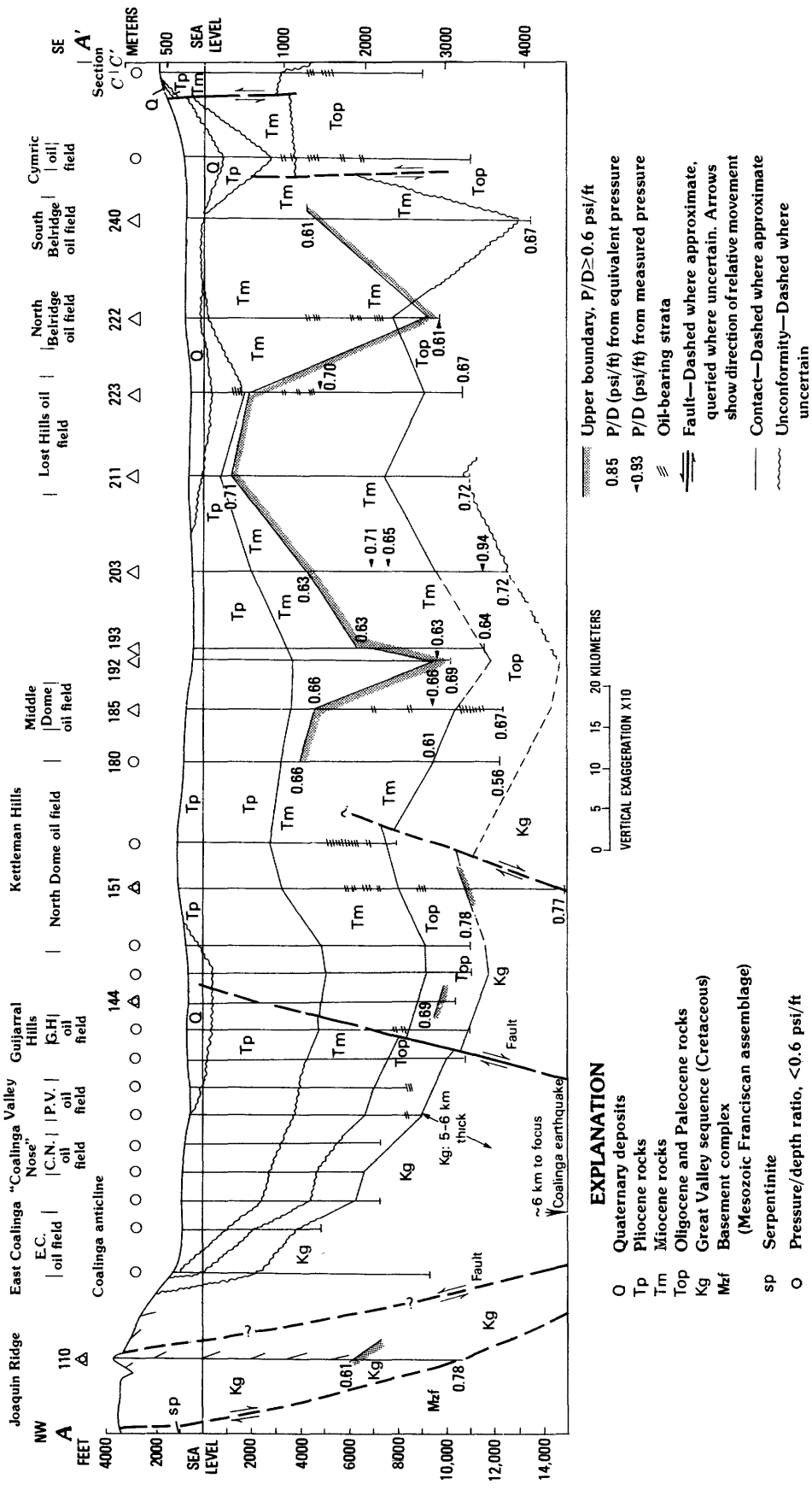

FIGURE 13.3.—Northwest-southeast structure section along line *A–A'* (fig. 13.1) through Joaquin Ridge, Coalinga anticline, Kettleman North and Middle Domes, Lost Hills, Belridge, and Cymric oil fields, showing top of zone of abnormal overpressures, bottom-hole pressure/depth ratios from pressure measurements, and those derived from drilling-fluid densities. Numbers refer to wells listed in table 13.1; slanted lines on drill holes indicate dips. Modified from Church and Krammes (1959).

TABLE 13.3.—*Fault-plane solutions shown on figure 13.1*

Event	Date	Location Lat	Location Long	Depth (Km)	M_L	Source
1	Apr. 6, 1971	36.99	121.09	9.3	2.8	1
2	Nov. 13, 1977-Dec. 1, 1981 (five events).	37	120.25	23-30	1-1.6	2
3	Oct. 24, 1975	36.98	120.08	4.6	3.4	1
4	June 17, 1979	37.75	120.0	19	3.1	2
5	Dec. 12, 1972	36.59	120.88	7.9	2.4	1
6	Oct. 25, 1982	36.32	120.52	---	5.2	3
7	June 11, 1983	36.24	120.46	4.5	5.2	4
8	May 2, 1983	36.22	120.32	10.2	6.7	4
9	July 21, 1952	35.00	119.02	19	7.2	5

measured northeastward from the San Andreas fault. Similar structures are inferred to extend northwestward for several hundred miles along the Coast Ranges-Great Valley boundary (Wentworth and others, 1984). On an east-west cross section through the Coalinga main-shock area, the Franciscan block forms an eastward-tapering wedge with fault-bounded upper and lower surfaces (fig. 13.9). The lower surface may rest on mafic (ophiolitic?) basement rocks or, possibly, on Great Valley sequence, and probably on Great Valley sequence at the leading edge (see chaps. 3, 4). The upper surface may represent a remnant of the Coast Range thrust, commonly consid-

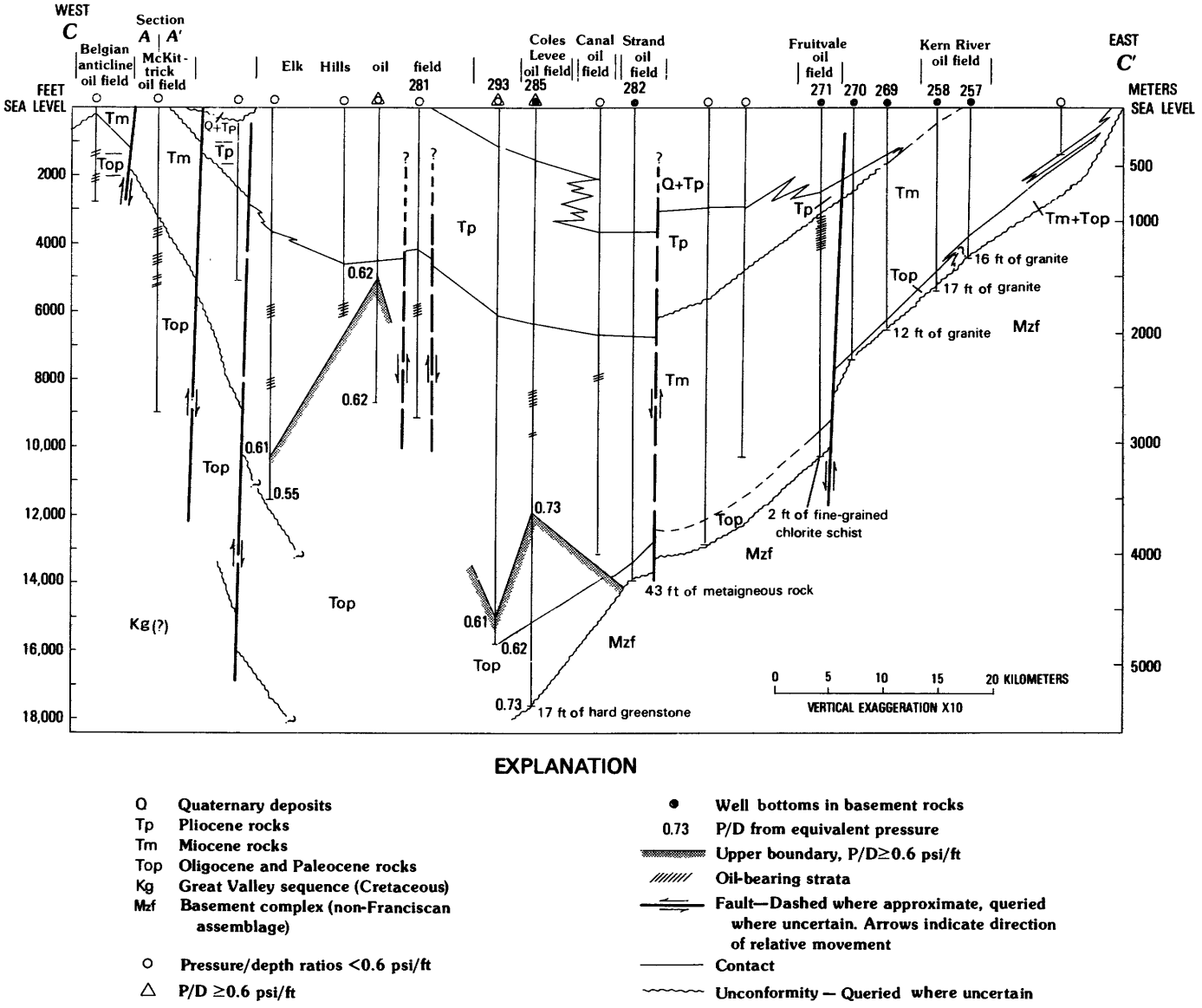

FIGURE 13.4.—West-east structure section along line *C–C'* (fig. 13.1) across the southern San Joaquin Valley, showing top of abnormal overpressures and bottom-hole pressure/depth ratios derived from drilling-fluid densities. Numbers refer to wells listed in table 13.1. Modified from Church and Krammes (1957).

ered to be a remnant of a subduction-zone suture. The Franciscan wedge is overlain by 10,000 to 20,000 ft of Great Valley sequence and more than 10,000 ft of Cenozoic strata, which have been folded over the advancing wedge to form the Coalinga anticline. A steeply east dipping reverse fault cuts the anticlinal axis and offsets the base of the Tertiary section (fig. 13.9). This fault is spatially compatible with the steep nodal plane of the 1983 main-shock fault-plane solution (see chap. 8) and with a linear zone of sheared and overturned lower Tertiary beds exposed along the southwestern limb of the anticline, about 3 mi northwestward and upplunge from its trace on the section.

The 1983 main-shock hypocenter is in or below the Franciscan wedge at about 33,000-ft depth, directly below the axis of the anticline. The inferred seismogenic fault is mapped as a gently southwest dipping thrust that cuts upsection toward the northeast (see Stein, 1983). Other subparallel thrusts are mapped within the wedge above the hypocentral area (see chap. 4). At least one seismic low-velocity zone near the Cretaceous (Great Valley sequence)-Cenozoic boundary is about 3,300 ft thick, 6,500 to 13,000 ft above the wedge, and extends continuously across the wedge and below the anticline (see chap. 3). If this low-velocity zone is caused by AHP, it probably forms a pressure seal and thus retards decay of fluid pressures below.

On August 4, 1985, an M_L=5.5 thrust/reverse-fault earthquake occurred about 11 mi southeast of the 1983 main shock at about 40,000-ft depth (fig. 13.9). After-

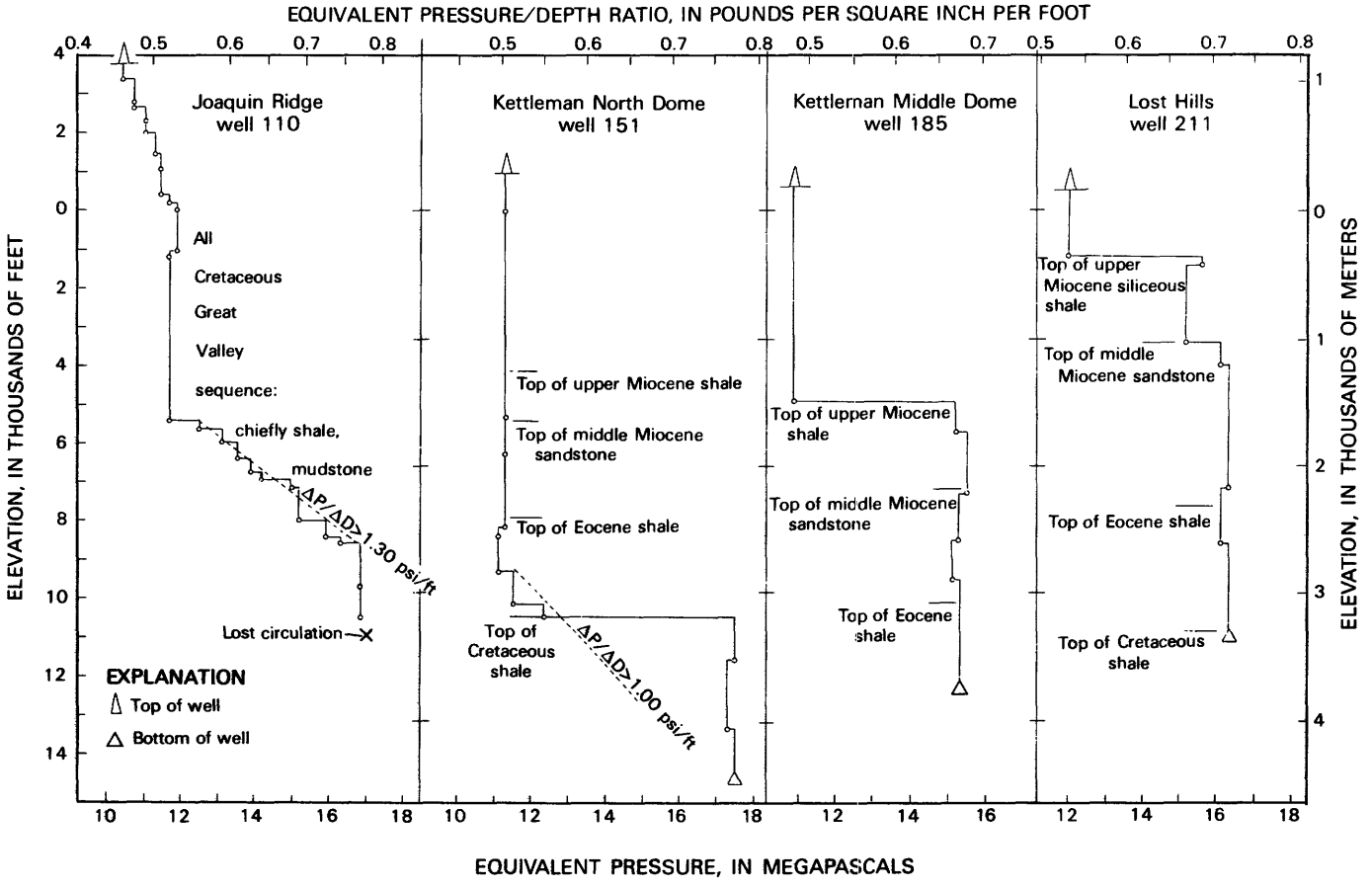

FIGURE 13.5.—Pressure/depth ratio versus depth for selected wells along Joaquin Ridge-Lost Hills trend. The Coalinga anticline is situated between wells 110 and 151. Numbers refer to wells listed in table 13.1.

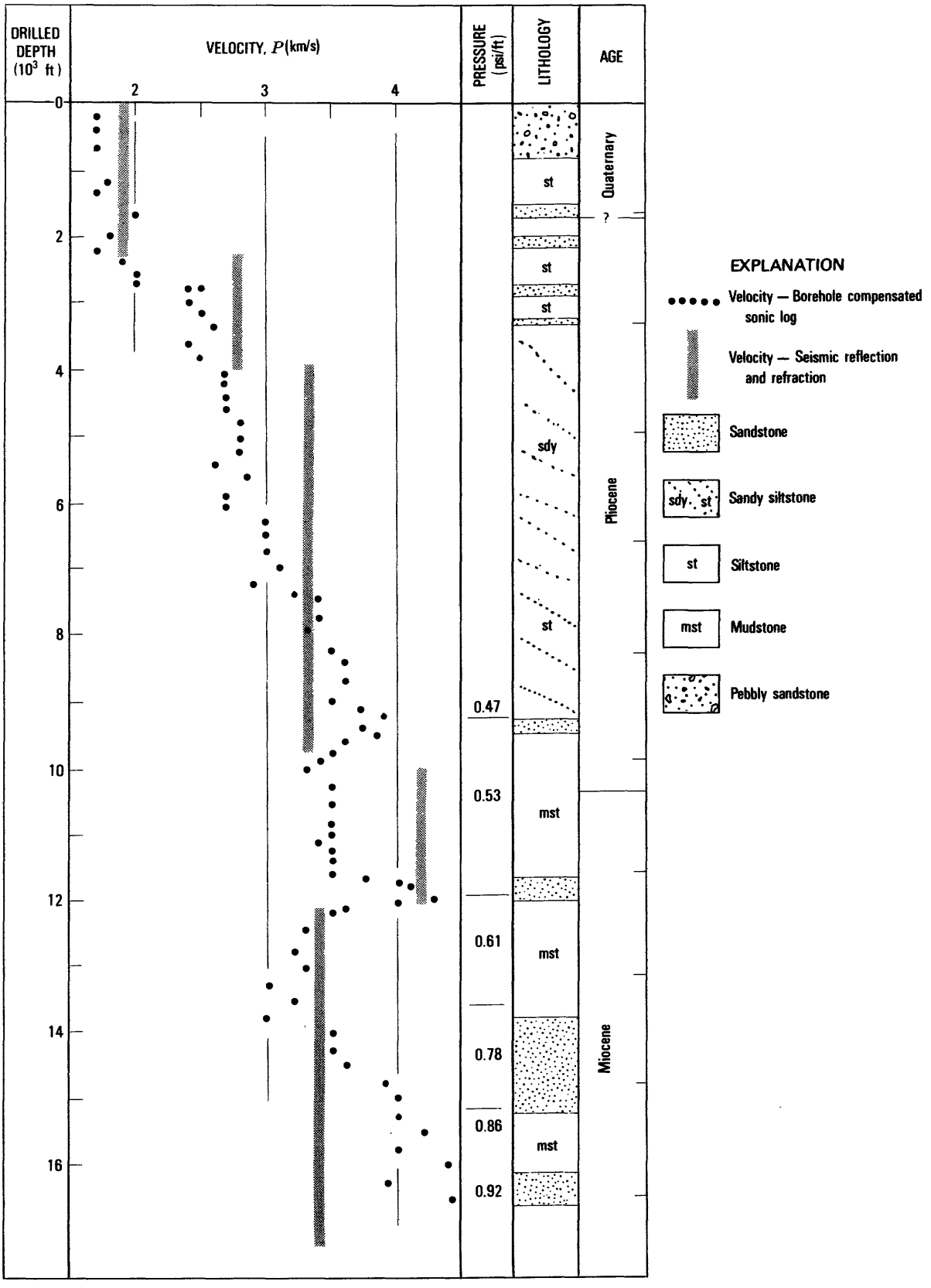

FIGURE 13.6.—Correlation of sonic velocity, interval velocities from seismic reflection and refraction profiles (Walter and Mooney, 1983; Wentworth and others, 1983), pressure/depth ratios, and lithology in well 206 (fig. 13.1). Note reversal of gradients at top of abnormally high pressure zone (P/D ratio, 0.60 psi/ft).

shocks extended southward and southwestward, beneath Kettleman North Dome. In cross section, the 1985 earthquake sequence outlines a gently southwest dipping detachment fault beneath the northern Kettleman Hills (J.P. Eaton, written commun., 1985) and coincides with the independently mapped Franciscan-basement boundary (fig. 13.9).

Seismic data suggest that both the 1983 and 1985 ruptures extended southward and westward (downdip) from the main-shock hypocenter to depths of 42,500 to 46,000 ft (McGarr and others, 1985). In the context of crustal earthquakes, downdip rupture propagation is unusual in that numerical models and many observations indicate that ruptures nearly always propagate upward in the direction of decreasing crustal strength (Sibson, 1982; Das and Scholz, 1983). Most estimates of crustal strength as a function of depth indicate that the base of the seismogenic, or brittle, part of the crust is where peak crustal strength occurs (Sibson, 1974). Thus, we expect large earthquakes to initiate there and propagate laterally and upward; downward propagation would be inhibited by the ductile rheology below the seismogenic layer (Das and Scholz, 1983). The downward propagation associated with the Coalinga main shock suggests that between 33,000 and 46,000 ft, the approximate base of the aftershock pattern (Eaton, 1985), the crust may be brittle; yet the strength appears to decrease with depth instead of increasing, as would be expected (Brace and Kohlstedt, 1980).

The inferred reversal in the crustal-strength/depth gradient below 33,000 ft may be due to near-lithostatic fluid pressure in this depth range below the Coalinga anticline. As indicated by the relation $C=1.5(S_v-P)$, where C is the crustal strength (maximum sustainable shear stress), S_v (density times gravity times depth) is the vertical stress, and P is the fluid pressure, an inverse relation between depth and strength would arise if fluid pressure were to increase with depth at a rate greater than vertical stress (McGarr and others, 1985). Just this relation, $\Delta P/\Delta D>1$, is indicated for depths to about 13,000 ft both northwest and southeast of the Coalinga anticline (fig. 13.5), and for the average of San Joaquin Valley wells below 14,800 ft (fig. 13.3).

The Coalinga thrust/reverse earthquakes occurred within a region of central California that is dominated by north- to north-northeast-directed compressional-stress (P) axes (fig. 13.8), which are approximately equivalent to the maximum principal compressive stress. Maximum fluid pressure is limited by the mechanism of hydraulic fracturing, which commonly occurs in a plane normal to the direction of the least compressive stress (Hubbert and Willis, 1957; Cornet and Valette, 1984). Under the stress conditions at Coalinga, near-horizontal fractures would thus be expected in rocks under high fluid pressures.

Direct detection of AHP's at crustal depths is possible only by very deep drilling. Berry and Mair (1977) seismic activity of the steeply east dipping reverse fault seems well established. Although the steep reverse fault suggested that AHP's may explain seismic low-velocity zones, with velocity reductions as large as 15 percent, at depths of 16,500 to 33,000 ft in crustal rocks of Canada. We have documented the local coincidence of AHP's and a seismic low-velocity zone, with a velocity reduction of as much as 1 km/s, at depths to about 16,500 ft in the San Joaquin Valley; and a continuous low-velocity zone has been mapped over the active tectonic wedge below the Coalinga anticline (see chap. 3). Walder and Nur (1984) evaluated the likelihood that AHP's can cause velocity reductions and concluded that large changes, as much as 1 km/s, can occur (below depths of 16,500–20,000 ft) only where fluid pressure is near the lithostatic gradient.

The fault-plane solution for the 1983 Coalinga main shock yields two possible fault orientations: a steeply northeast dipping reverse fault and a gently southwest dipping thrust (Eaton, 1983). Although the preponderance of geologic and seismic evidence favors the buried, gently southwest dipping thrust as a source of the 1983 main shock (see chaps. 4, 8), the existence and 1983 is inferred not to have ruptured to the surface in 1983 (Stein, 1983), it is aligned with a narrow zone of sheared

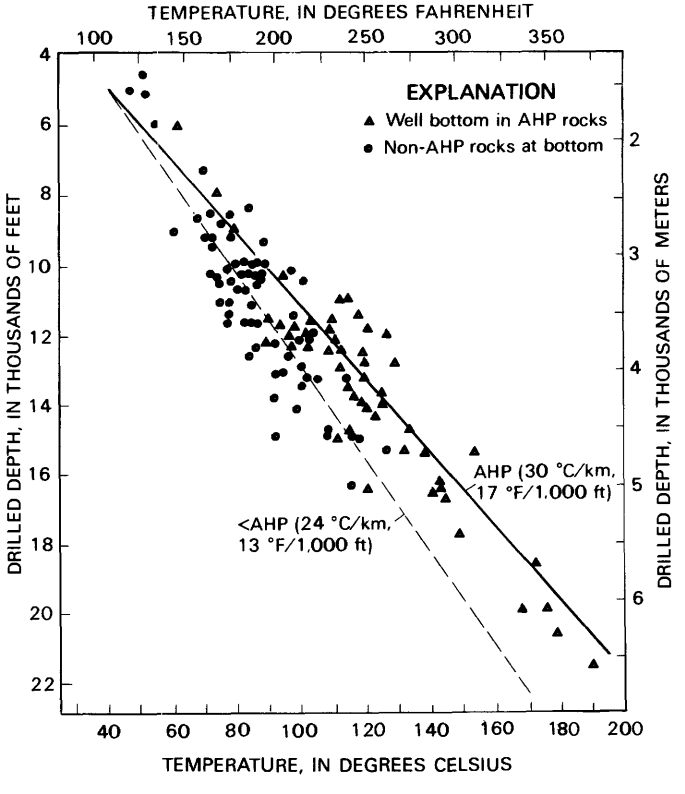

FIGURE 13.7.—Bottom-hole temperatures as logged (not equilibrated) versus depth for 120 wells (table 13.1). Lines show least-squares fit for AHP rocks (solid) and non-AHP rocks (dashed).

and locally overturned Tertiary strata exposed along the southwestern margin of the Coalinga anticline about 4 mi northwest and upplunge from the main-shock area (see fault at upper center of fig. 13.9). We infer such a fault in part to explain the mapped distribution of the top of the AHP field northwest and southeast of the Coalinga anticline, especially its apparent restriction to lower-plate rocks (fig. 13.3). Thus, initial movement on the buried southwest-dipping thrust, presumably aided by near-lithostatic fluid pressures, shortened and loaded

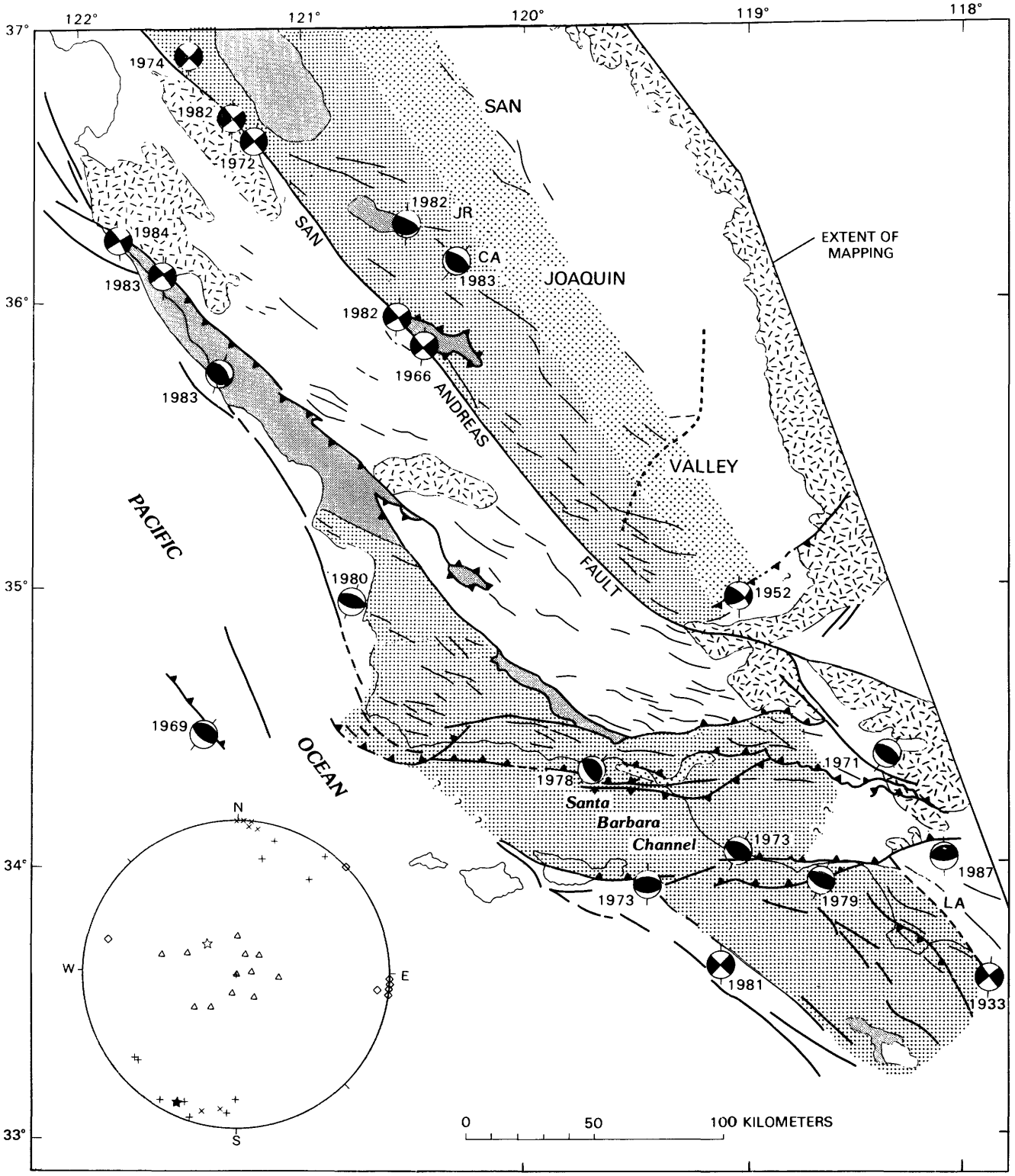

upper-plate rocks and activated steeply dipping reverse faults such as the one described above, as well as the Nuñez fault rupture of June 11, 1983.

ACKNOWLEDGMENTS

We are grateful to R.F. Curtin and the staff of the Coalinga office of the California Division of Oil and Gas for gathering and reviewing the voluminous well data. R.K. Mark facilitated statistical treatment of the data. We greatly appreciate stimulating discussions of the AHP field and its likely sources and effects with Ivan Barnes, M.C. Blake, Jr., T.L. Holzer, Y.K. Kharaka, T.H. McCulloh, A.F. McGarr, Paul Segall, and M.D. Zoback.

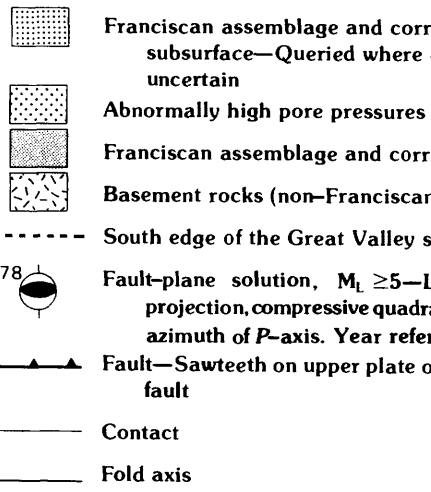

FIGURE 13.8.—Central California and Continental Shelf, showing distribution of the Franciscan assemblage and correlative rocks, fields of abnormally high pore pressure, major faults, fault-plane solutions from special studies of well-located earthquakes since 1933, and orientation of maximum compressional-stress (*P*) axes. East boundary of the Franciscan in the San Joaquin Valley from chapters 3 and 4. CA, Coalinga anticline; JR, Joaquin Ridge; LA, Los Angeles. Inset, *P*- and *T*-axes for fault-plane solutions: plus sign, *P*-axes for thrust/reverse solutions; x, *P*-axes for strike-slip events; triangle, *T*-axes for thrust/reverse events; diamond, *T*-axes for strike-slip events. 108 fault-plane solutions have been derived for earthquakes of the 1983 Coalinga sequence (Eaton, 1985); of these, 97 are thrust/reverse-fault solutions that are compatible with a single set of principal-stress axes derived by the method of Angelier (1984). S_1 (solid star): azimuth, 207°; plunge, 10°; S_3 (open star): azimuth, 322°; plunge, 67°. For the 1971 San Fernando sequence (lower right), Gephart and Forsyth (1982) reported: S_1: azimuth, 197°, plunge 10°; S_3: azimuth, 94°; plunge, 53°. All the thrust/reverse-fault solutions shown here are compatible with these axes. Data and sources from table 2.1.

REFERENCES CITED

Angelier, Jacques, 1984, Tectonic analysis of fault slip data sets: Journal of Geophysical Research, v. 89, no. B7, p. 5835–5848.

Barnes, Ivan, Irwin, W.P., and Gibson, H.A., 1975, Geologic map showing springs rich in carbon dioxide or chloride in California: Menlo Park, Calif., U.S. Geological Survey, Water Resources Investigations Open-File Map, scale 1:1,500,000.

Berry, F.A.F., 1973, High fluid potentials in California Coast Ranges and their tectonic significance: American Association Petroleum Geologists Bulletin, v. 57, no. 7, p. 1219–1249.

Berry, F.A.F., and Kharaka, Y.K., 1981, Origins of abnormally-high-fluid-pressure systems in California [abs.]: Geological Society of America Abstracts with Programs, v. 13, no. 7, p. 409.

Berry, M.J., and Mair, J.A., 1977, The nature of the earth's crust in Canada, *in* Heacock, J.G., ed., The earth's crust: Its nature and physical properties: American Geophysical Union Geophysical Monograph 20, p. 319–348.

Brace, W.F., and Kohlstedt, D.L., 1980, Limits on lithospheric stress imposed by laboratory experiments: Journal of Geophysical Research, v. 85, no. B11, p. 6248–6252.

Chapman, R.E., 1983, Petroleum geology: Amsterdam, Elsevier, 415 p.

Church, H.V., Jr., and Krammes, K.F., compilers, 1957, Cenozoic correlation section across south San Joaquin Valley from San Andreas fault to Sierra Nevada foot hills, California: Los Angeles, American Association of Petroleum Geologists, Pacific Section Correlation Section 8.

—— 1959, Correlation section longitudinally north-south through westside San Joaquin Valley from Coalinga to Midway-Sunset and across San Andreas fault into southeast Cuyama Valley, California: Los Angeles, American Association of Petroleum Geologists, Pacific Section Correlation Section 11.

Cornet, F.H., and Valette, Bernard, 1984, In situ stress determination from hydraulic injection test data: Journal of Geophysical Research, v. 89, no. B13, p. 11527–11537.

Croft, M.G., 1972, Subsurface geology of the Late Tertiary and Quaternary water-bearing deposits of the southern part of the San Joaquin Valley, California: U.S. Geological Survey Water-Supply Paper 1999–H, p. H1–H29.

Das, Shamita, and Scholz, C.H., 1983, Why large earthquakes do not nucleate at shallow depths: Nature, v. 305, no. 5935, p. 621–623.

Davis, G.H., and Coplen, T.B., 1984, Pleistocene paleohydrology of the central and western San Joaquin Valley, California [abs.]: Geological Society of America Abstracts with Programs, v. 16, no. 6, p. 482–483.

Eaton, J.P., 1983, Seismic setting, location and focal mechanism of the May 2, 1983, Coalinga earthquake, *in* Borcherdt, R.D., compiler, The Coalinga earthquake sequence commencing May 2, 1983: U.S. Geological Survey Open-File Report 83-511, p. 20–25.

—— 1985, The May 2, 1983 Coalinga earthquake and its aftershocks: A detailed study of the hypocenter distribution and of the focal mechanisms of the larger aftershocks, *in* Rymer, M.J., and Ellsworth, W.L., eds., Proceedings of Workshop XXVII—Mechanics of the May 2, 1983 Coalinga earthquake: U.S. Geological Survey Open-File Report 85-44, p. 132–201.

Eaton, J.P., Cockerham, R.S., and Lester, F.W., 1983, Study of the May 2, 1983 Coalinga earthquake and its aftershocks, based on the USGS seismic network in northern California, *in* Bennett, J.H.,

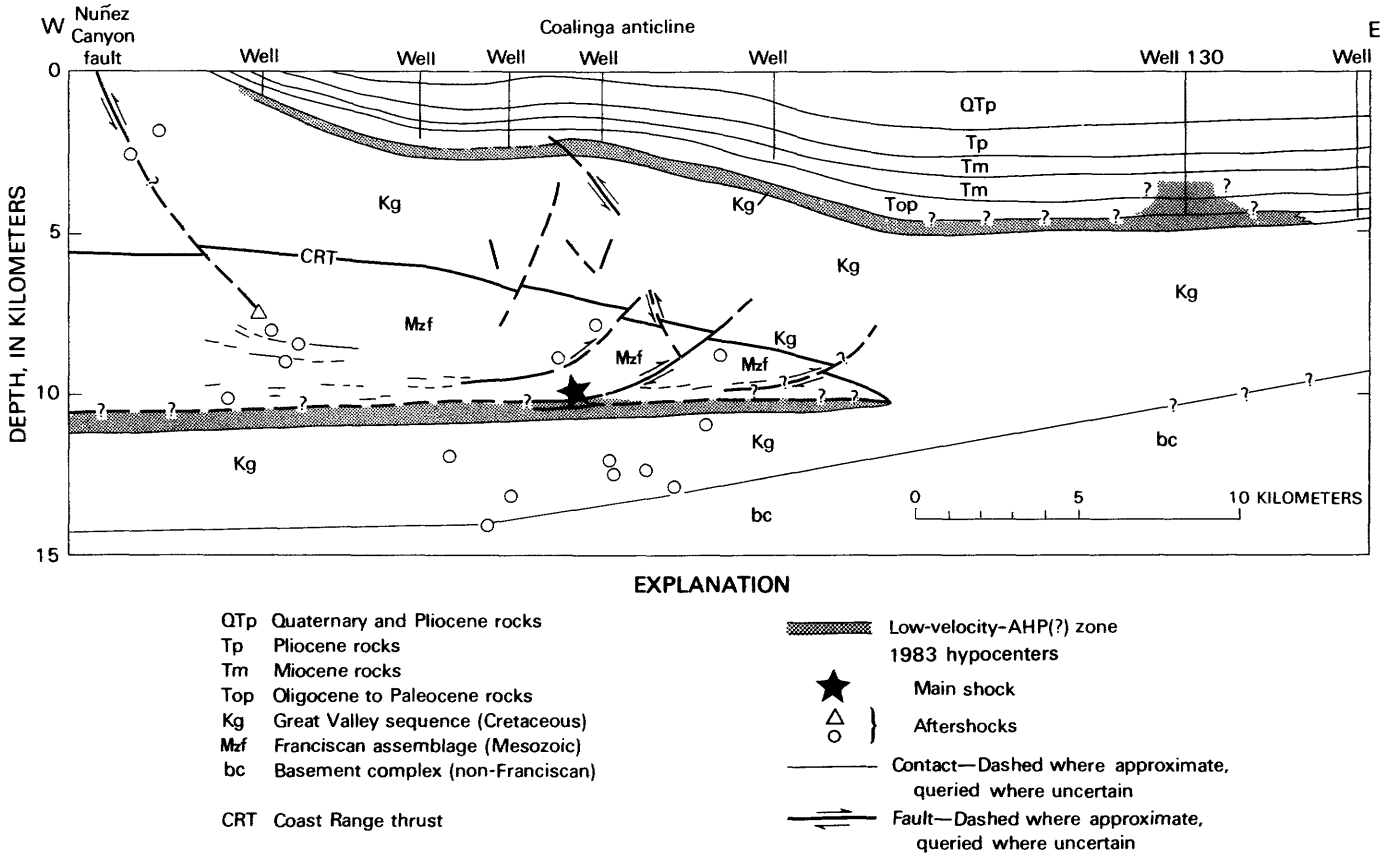

FIGURE 13.9.—West-east crustal section through Coalinga anticline area, showing relation of buried east-thrusting wedge of Franciscan assemblage to selected 1983 and 1985 hypocenters, and low-velocity, abnormally high pressure(?) zone. Modified from chapters 3, 4, and 8. Hypocenters are projected into section parallel to structure.

and Sherburne, R.W., eds., The 1983 Coalinga, California earthquakes: California Division of Mines and Geology Special Publication 66, p. 261–273.

Fertl, W.H., Chilingarian, G.V., and Rieke, H.H., 1976, Abnormal formation pressures: Amsterdam, Elsevier, 382 p.

Fyfe, W.S., Price, N.J., and Thompson, A.B., 1978, Fluids in the Earth's crust: Amsterdam, Elsevier, 383 p.

Gephart, J.W., and Forsyth, D.W., 1982, An improved method for determining the stress tensor from earthquake focal mechanism data: Application to the San Fernando earthquake sequence [abs.]: Eos (American Geophysical Union Transactions), v. 63, no. 18, p. 375.

Hackel, Otto, 1966, Summary of the geology of the Great Valley, *in* Great Valley province, chap. 5 *of* Bailey, E.H., Geology of northern California: California Division of Mines and Geology Bulletin 190, p. 217–238.

Healy, J.H., Rubey, W.W., Griggs, D.T., and Raleigh, C.B., 1968, The Denver earthquakes: Science, v. 161, no. 3848, p. 1301–1310.

Hubbert, M.K., and Rubey, W.W., 1959, Role of fluid pressures in mechanics of overthrust faulting: Geological Society of America Bulletin, v. 70, no. 2, p. 115–166.

Hubbert, M.K., and Willis, D.G., 1957, Mechanics of hydraulic fracturing: Journal of Petroleum Technology, v. 9, no. 6, p. 153–168.

Hunt, J.M., 1979, Petroleum geochemistry and geology: San Francisco, W.H. Freeman and Co., 615 p.

Kerr, R.A., 1984, The deepest hole in the world: Science, v. 224, no. 4656, p. 1420.

LaForge, R., and Lee, W.H.K., 12982, Seismicity and tectonics of the Ortigalita fault and southeast Diablo Range, California, *in* Hart, E.W., Hirschfeld, S.E., and Schulz, S.S., eds., Conference on Earthquake Hazards in the Eastern San Francisco Bay Area, Hayward, Calif., 1982, Proceedings: California Division of Mines and Geology Special Publication 62, p. 93–101.

Magara, Kinji, 1978, Compaction and fluid migration practical petroleum geology: Amsterdam, Elsevier, 319 p.

McCulloh, T.H., 1969, Geologic characteristics of the Dos Cuadras offshore oil field: U.S. Geological Survey Professional Paper 679–C, p. 29–46.

McGarr, Arthur, Mueller, C.S., Fletcher, J.B., and Andrews, M.C., 1985, Ground motion parameters of the 1983 Coalinga, California earthquakes: Implications for crustal strength, *in* Rymer, M.J., and Ellsworth, W.L., eds., Proceedings of Workshop XXVII—Mechanics of the May 2, 1983 Coalinga earthquake: U.S. Geological Survey Open-File Report 85-44, p. 254–275.

Minster, J.B., and Jordan, T.H., 1984, Vector constraints on Quaternary deformation of the western United States east and west of the San Andreas fault, *in* Crouch, J.K., and Bachman, S.B., eds., Tectonics and sedimentation along the California margin (volume 38): Society of Economic Paleontologists and Mineralogists, Pacific Section Annual Convention, San Diego, 1984, Paper, p. 1–16.

Raleigh, C.B., Healy, J.H., and Bredehoeft, J.D., 1972, Faulting and crustal stress at Rangely, Colorado, *in* Heard, H.C., Borg, I.Y., Carter, N.L., and Raleigh, C.B., eds., Flow and fracture of rocks (Griggs volume): American Geophysical Union Geophysical Mono-

graph 16, p. 275–284.

Rehm, Bill, 1972, Worldwide occurrence of abnormal pressures, part II: American Institute of Mining, Metallurgical, and Petroleum Engineers Symposium on Abnormal Subsurface Pore Pressure, 3d, New York, 1972, Preprints, p. 43–47.

Sibson, R.H., 1974, Frictional constraints on thrust, wrench, and normal faults: Nature, v. 249, no. 5457, p. 542–544.

—— 1982, Fault zone models, heat flow and the depth distribution of earthquakes in the continental crust of the United States: Seismological Society of America Bulletin, v. 72, no. 1, p. 151–163.

Smith, J.E., 1971, The dynamics of shale compaction and evolution of pore-fluid pressures: Mathematical Geology, v. 3, no. 3, p. 239–263.

Smith, M.B., 1964, Map showing distribution and configuration of basement rocks in California (south half): U.S. Geological Survey Oil and Gas Investigations Map OM–215, scale 1:500,000, 2 sheets.

Stein, R.S., 1983, Reverse slip on a buried fault during the 2 May 1983 Coalinga earthquake: Evidence from geodetic elevation changes, *in* Bennett, J.H., and Sherburne, R.W., eds., The 1982 Coalinga, California earthquakes: California Division of Mines and Geology Special Publication 66, p. 151–163.

Stein, R.S., and Thatcher, Wayne, 1981, Seismic and aseismic deformation associated with the 1952 Kern County, California earthquake and relationship to the Quaternary history of the White Wolf fault: Journal of Geophysical Research, v. 86, no. B6, p. 4913–4928.

Walder, J.S., and Nur, Amos, 1984, Porosity reduction and crustal pore pressure development: Journal of Geophysical Research, v. 89, no. B13, p. 11539–11548.

Wallace, R.H., Jr., Kraemer, T.F., Taylor, R.E., and Wesselman, J.B., 1979, Assessment of geopressured-geothermal resources in the northern Gulf of Mexico basin, *in* Muffler, L.J.P., ed., Assessment of geothermal resources of the United States—1978: U.S. Geological Survey Circular 790, p. 132–163.

Walter, Allan, 1985, Velocity structure near Coalinga, California, *in* Rymer, M.J., and Ellsworth, W.L., eds., Proceedings of Workshop XXVII—Mechanics of the May 2, 1983 Coalinga earthquake: U.S. Geological Survey Open-File Report 85-44, p. 10–18.

Walter, A.W., and Mooney, W.D., 1983, Preliminary report on the crustal velocity structure near Coalinga, California as determined from seismic refraction surveys in the region, *in* Bennett, J.H., and Sherburne, R.W., eds., The 1983 Coalinga, California earthquakes: California Division Mines and Geology Special Report 66, p. 127–135.

Wentworth, C.M., Walter, A.W., Bartow, J.A., and Zoback, M.D., 1983, Evidence on the tectonic setting of the 1983 Coalinga earthquakes from deep reflection and refraction profiles across the southeastern end of the Kettleman Hills, *in* Bennett, J.H., and Sherburne, R.W., eds., The 1983 Coalinga, California earthquakes: California Division Mines and Geology Special Report 66, p. 113–126.

Wentworth, C.M., Blake, M.C., Jr., Jones, D.L., Walter, A.W., and Zoback, M.D., 1984, Tectonic wedging associated with emplacement of the Franciscan assemblage, California Coast Ranges, *in* Blake, M.C., Jr., ed., Franciscan geology of northern California (book 43): Los Angeles, Society of Economic Paleontologists and Mineralogists, Pacific Section, p. 163–173.

Wong, I.G., and Ely, R.W., 1983, Historical seismicity and tectonics of the Coast Ranges-Sierran block: Implications to the 1983 Coalinga, California earthquakes, *in* Bennett, J.H., and Sherburne, R.W., eds., The 1983 Coalinga, California earthquakes: California Division Mines and Geology Special Report 66, p. 89–104.

Wong, I.G., and Savage, W.U., 1983, Deep intraplate seismicity in western Sierra Nevada, central California: Seismological Society of America Bulletin, v. 73, no. 3, p. 797–812.

Yeats, R.S., 1983, Large-scale Quaternary detachments in Ventura basin, southern California: Journal of Geophysical Research, v. 88, no. B1, p. 569–583.

Yerkes, R.F., Levine, Paia, and Wentworth, C.M., 1985, Abnormally high fluid pressures in the region of the Coalinga earthquakes—a preliminary report, *in* Rymer, M.J., and Ellsworth, W.L., eds., Proceedings of Workshop XXVII—Mechanics of the May 2, 1983 Coalinga earthquake: U.S. Geological Survey Open-File Report 85-44, p. 344–375.

Zieglar, D.L., and Spotts, J.H., 1978, Reservoir and source-bed history of Great Valley, California: American Association of Petroleum Geologists Bulletin, v. 62, no. 5, p. 813–826.

14. STRESS AND FLUID-PRESSURE CHANGES ASSOCIATED WITH OIL-FIELD OPERATIONS: A CRITICAL ASSESSMENT OF EFFECTS IN THE FOCAL REGION OF THE EARTHQUAKE

By PAUL SEGALL and R.F. YERKES,
U.S. GEOLOGICAL SURVEY

CONTENTS

ABSTRACT

The proximity of the May 2 earthquake to the active oil fields on Anticline Ridge has led to speculation that this earthquake might have been triggered by oil-field operations. Elsewhere, earthquakes have been associated with pore-pressure increases resulting from fluid injection and with subsidence resulting from fluid extraction. Simple calculations show that shale units, which underlie the oil-producing strata, hydraulically isolate the oil field from the earthquake focal region. The large volumes of fluid extracted from the oil fields caused a 50-percent decline in reservoir pressures from 1938 to 1983. These observations independently rule out substantial increases in pore pressure at focal depths due to fluid injection. We use a theoretical method, based on Biot's constitutive theory for fluid-infiltrated elastic media, to evaluate the change in stresses acting in the focal region resulting from fluid extraction in the overlying oil fields. As an independent check on this method, the subsidence of the Earth's surface in response to fluid withdrawal is calculated and compared with measured elevation changes on Anticline Ridge. The producing horizons are taken to be horizontal permeable layers, bounded above and below by impermeable horizons. Strains within the producing layers are related to extraction-induced changes in pore-fluid mass. Contraction of the producing layers causes the free surface to subside and strains the elastic surroundings. The calculated subsidence rate of Anticline Ridge between 1933 and 1972 is 3 mm/yr, in good agreement with the measured subsidence rate of 3.3±0.7 mm/yr. Calculated pore-pressure changes in the deepest producing zone also compare well with observed changes in reservoir pressure. Although the sign of the shear stresses induced by extraction favors reverse slip on either the northeast- or southwest-dipping nodal plane, the induced normal stresses are compressive, inhibiting fault slip. The driving stress (shear stress minus frictional resistance) acting across the northeast-dipping plane increased by 10 kPa between 4- and 9-km depth, weakly favoring slip, and decreased by 5 kPa at 9- to 11-km depth, weakly inhibiting slip; the driving stress on the southwest-dipping plane increased by 20 kPa at 10-km depth, slightly favoring slip.

INTRODUCTION

Epicenters of the M=6.7 May 2 earthquake and its early aftershocks were located along Anticline Ridge, 10 km northeast of Coalinga (Eaton and others, 1983; Reasenberg and others, 1983). Anticline Ridge overlies two active oil fields, one of which has been under production for more than 85 years. The proximity of the earthquake to active oil fields has led to speculation that oil-field operations might have accelerated the release of stored elastic strain, thereby triggering the earthquake.

Induced seismicity has been associated with injection of fluids into the shallow crust in several other areas, including the Rocky Mountain Arsenal near Denver (Healy and others, 1968) and the Rangely oil field in western Colorado (Raleigh and others, 1972, 1976). Injection-induced seismicity is generally thought to occur when injection increases pore-fluid pressures, thus decreasing the effective confining stress and allowing fault slip to take place at the existing levels of tectonic shear stress (Raleigh and others, 1972, 1976). The induced earthquakes in the Rangely oil field had focal depths of less than 4 km, within 2 km of the bottoms of the experimental injection wells (Raleigh and others, 1976).

Induced faulting and seismicity have also been attributed to fluid extraction in oil fields (Yerkes and Castle, 1976). The best-documented examples of extraction-induced seismicity occurred in the Goose Creek, Tex., oil field (Pratt and Johnson, 1926) and the Wilmington, Calif., oil field (Kovach, 1974). Most earthquakes previously thought to be associated with fluid extraction had relatively shallow focal depths (Yerkes and Castle, 1976).

We also note that numerous examples of earthquakes induced by filling of reservoirs have been reported, including eight events of $M \geq 5$ (Simpson, 1976). Although the focal depths of these events are generally not well constrained, the data are consistent with depths comparable to that of the May 2 earthquake, that is, 10 km (Gupta and Rastogi, 1976). Reservoir-induced earthquakes are generally considered to have been triggered by increases in pore pressures at depth (Bell and Nur, 1978; Zoback and Hickman, 1982), similar to injection-induced earthquakes.

The main purpose of this chapter is to assess the effects of operations in nearby oil fields on the pore-fluid pressures and stresses acting in the focal region of the May 2 earthquake. Estimates of the magnitude and distribution of pore-pressure changes enable us to evaluate whether this event is reasonably considered as an example of injection-induced seismicity. In a similar fashion, calculations of the fluid-pressure and solid-stress changes associated with fluid extraction enable us to assess the possibility of extraction-induced seismicity.

RELATION OF OIL FIELDS TO THE EARTHQUAKE SEQUENCE

Epicenters of the main shock and aftershocks during May–July 1983 and their relation to the Coalinga oil fields are illustrated in figure 14.1. The aftershocks form an elongate zone striking approximately N. 30° W., parallel to the regional trend of the Coast Ranges and the Coalinga anticlinal axis (Eaton and others, 1983). Figure 14.1 also illustrates *P*-wave fault-plane solutions for $M \geq 5.0$ events. The focal mechanism of the main shock indicates reverse slip on a N. 53° W.-striking fault plane that dips either 67° NE. or 23° SW. (Eaton and others, 1983). Coseismic elevation changes analyzed by Stein (1983) favor a steeply northeast dipping plane, although a shallow plane cannot be ruled out entirely. These elevation changes can be adequately modeled by a single dislocation surface that dips 67° NE. and extends from a depth of 4 ± 1 to 11.2 ± 2 km (Stein, 1983). The Coalinga earthquake sequence is discussed in considerably more detail elsewhere in this volume.

The geology of the Coalinga region is reviewed in chapter 1. Most historical oil production from Anticline Ridge has come from two fields, Coalinga Eastside and the Nose area of the Coalinga East Extension (fig. 14.1). In the Coalinga oil field, the principal producing horizon is the Miocene Temblor Formation. The Temblor, a pebbly sandstone, has an average thickness of 75 m and occurs at depths of 0.2 and 1.4 km (avg depth, 0.6 km). It is capped by shale of the Santa Margarita Formation. The main producing zone in the Coalinga East Extension oil field is the Gatchell sand of local usage in the lower Tertiary Lodo Formation. The Gatchell is found at depths of 2.2 to 2.4 km in the Nose area of the Coalinga anticline. The Gatchell grades into the so-called Turritella silt southwest of Anticline Ridge, creating a strong permeability barrier to flow from the southwest. The maximum thickness of the Gatchell is 190 m.

A cross section of the seismicity through Anticline Ridge (fig. 14.2) demonstrates that the main shock and most aftershocks occurred well below the Tertiary oil-bearing formations. Except for the June 11 aftershock, the main shock and $M \geq 5.0$ aftershocks had focal depths of 9 to 12 km. Little is known about the geology at these depths. The deepest wells on Anticline Ridge penetrate Upper Cretaceous rocks of the Great Valley sequence, a thick section of which crops out to the north and west of Anticline Ridge. The Franciscan assemblage, which lies structurally below the Great Valley sequence, is exposed in the cores of anticlines northwest of Coalinga.

The yearly net liquid production (oil plus water minus returned water) from the oil fields on Anticline Ridge is plotted in figure 14.3. Since the discovery of Coalinga Eastside in 1896, 0.12×10^9 m^3 of liquid has been extracted from it. The average extraction rate from 1905 to 1981 was 1.6×10^6 m^3/yr (10 million bbl/yr). Although oil production from Coalinga East Extension did not begin until 1938, this field has produced 0.15×10^9 m^3 of liquid. The average rate of liquid extraction from 1940 to 1981 was 3.7×10^6 m^3/yr (24 million bbl/yr), as indicated by the dashed line in fig. 14.3*B*.

INDUCED FLUID-PRESSURE CHANGES

Records of average reservoir pressure in the Gatchell sand within the Coalinga East Extension oil field have been maintained by the California Division of Oil and Gas. The average reservoir pressure from the discovery of this field in 1938 until late 1983, after the earthquake, is plotted in figure 14.4. The data from 1953 to the present are average pressures, measured in at least two and as many as seven wells, within the gas zone at a depth of 1,980 m. The measurements from 1938 to 1953 are from the oil zone at a depth of 2,060 m. Although various secondary oil-recovery projects have involved the injection of gas, water, and polymer solutions into the Gatchell, the net effect of oil-field operations between 1938 and 1983 was to reduce the pore pressure by 53 percent, from 23 to 11 MPa. The pressure history is clearly dominated by the large volumes of fluid withdrawn from the reservoir. If the observed decrease in pore pressure was, in fact, transmitted to the focal region of the earthquake, it would have resulted in an increase in effective confining stress and, according to the criteria of Raleigh and others (1972, 1976), a "strengthening" of the fault.

Simple calculations, however, suggest that it is extremely unlikely that any pore-pressure changes within the Gatchell (the deepest producing zone, at a depth of 2.2 km) could have been transmitted to the focal depth of 10 km in the 45 years between 1938 and 1983, primarily because of the low permeability of the argillaceous rocks that are known to underlie the Gatchell sand. Permeabilities of shale, measured in laboratory samples and in place (Brace, 1980), typically range from 10^{-20} to 10^{-18} m^2. For flow of water, these permeabilities correspond to a hydraulic diffusivity c of 10^{-7} to 10^{-5} m^2/s (see below). The penetration depth of a pressure disturbance at time t can be estimated by $\sqrt{ct}$. Taking the larger diffusivity (10^{-5} m^2/s), we find that the pressure disturbance will penetrate 100 m in 45 years ($t \sim 10^9$ s), nearly a hundredfold less than the 8 km between the Gatchell and the

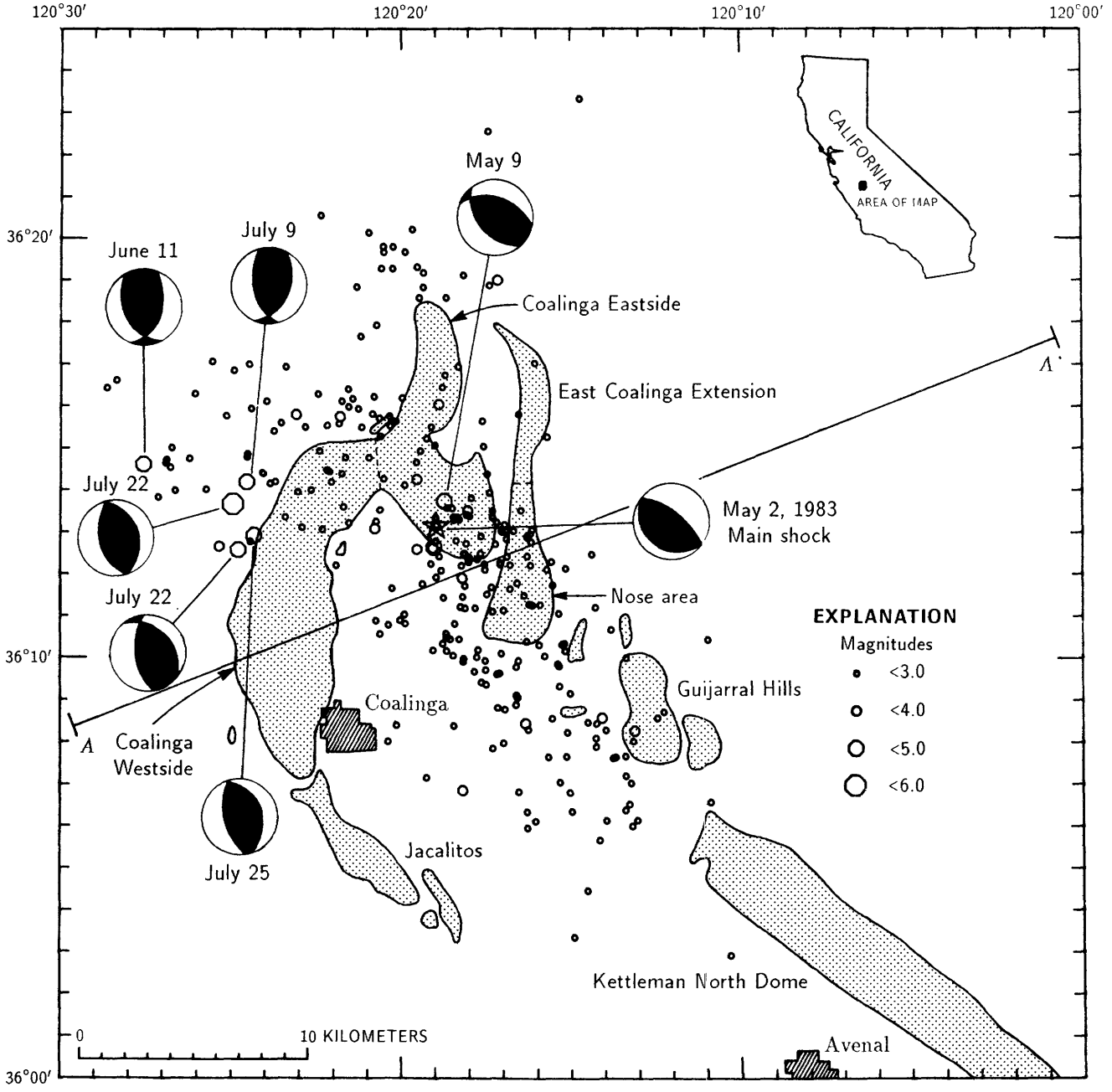

FIGURE 14.1.—Coalinga, Calif., area, showing relation between Coalinga earthquake sequence and oil fields, and locations of main shock (star) and $M>3$ aftershocks for May–July 1983. Focal mechanisms are shown for $M \geq 5$ events. Seismic data replotted from Eaton and others (1983). See figure 14.2 for cross section.

earthquake focus. This calculation illustrates that even a few-hundred-meter-thick section of shale will be effective in hydraulically isolating the focal region from the oil field. Although it could be argued that a highly permeable, fractured zone might link the oil field to the focal region, there is no evidence to support the presence of such a zone. In fact, Cretaceous and lower Tertiary sedimentary rocks at depths of at least 3 km in the Coalinga area contain abnormally high fluid pressures that reach 81 to 93 percent of the lithostatic pressure (see chap. 13). These overpressures attest to the low hydraulic conductivity of the sedimentary rocks below the oil-bearing strata. Finally, we note that even if a highly conductive zone existed, the effect of oil-field activities would be to decrease the pore pressure, as discussed above. In sum, all available evidence argues against the May 2 earthquake having been triggered by injection-induced pore-pressure changes.

STRESS CHANGES INDUCED BY FLUID EXTRACTION

As discussed in the previous section, the principal effects of oil-field operations have been the removal of large volumes of fluid and the consequent decline in reservoir pressures. In this section, we estimate the stress changes in the focal region resulting from fluid extraction. This discussion summarizes the analysis presented by Segall (1985).

THEORY

Stresses induced by fluid extraction arise as the producing rocks contract in response to removal of pore fluid. This process can be understood by considering the simple thought experiment illustrated in figure 14.5. We consider the Earth's crust to be a uniform, isotropic, fluid-infiltrated half-space, which for simplicity will be assumed to be initially unstressed. We imagine that a small element is cut from the half-space (1, fig. 14.5). Because the region is unstressed, this removal induces no strain in the half-space. Subsequently, fluid with a mass per unit solid volume Δm is uniformly extracted from the pores of the element (2, fig. 14.5). This extraction causes the element to undergo a uniform volumetric contraction ϵ^T_{kk}. This "transformation strain" (Eshelby, 1957) occurs without induced stresses in the solid, and so it is referred to as a "stress-free strain." Because the strain resulting from uniform fluid withdrawal is purely volumetric, the strain in the element is simply

$$\epsilon_{ij} = \epsilon^T_{kk}\delta_{ij}/3, \qquad (i, j, k = 1, 2, 3) \qquad (1)$$

where the Kronecker delta, δ_{ij}, is defined by $\delta_{ij}=1$ for $i=j$, and by $\delta_{ij}=0$ for $i\neq j$.

The magnitude of the transformation strain is related to the change in fluid-mass content per unit volume, m, through the constitutive equations for the fluid-infiltrated solid. For a linear, isotropic poroelastic material (Biot, 1941; Rice and Cleary, 1976), the volumetric strain is related to the mean stress σ_{kk} and the change in

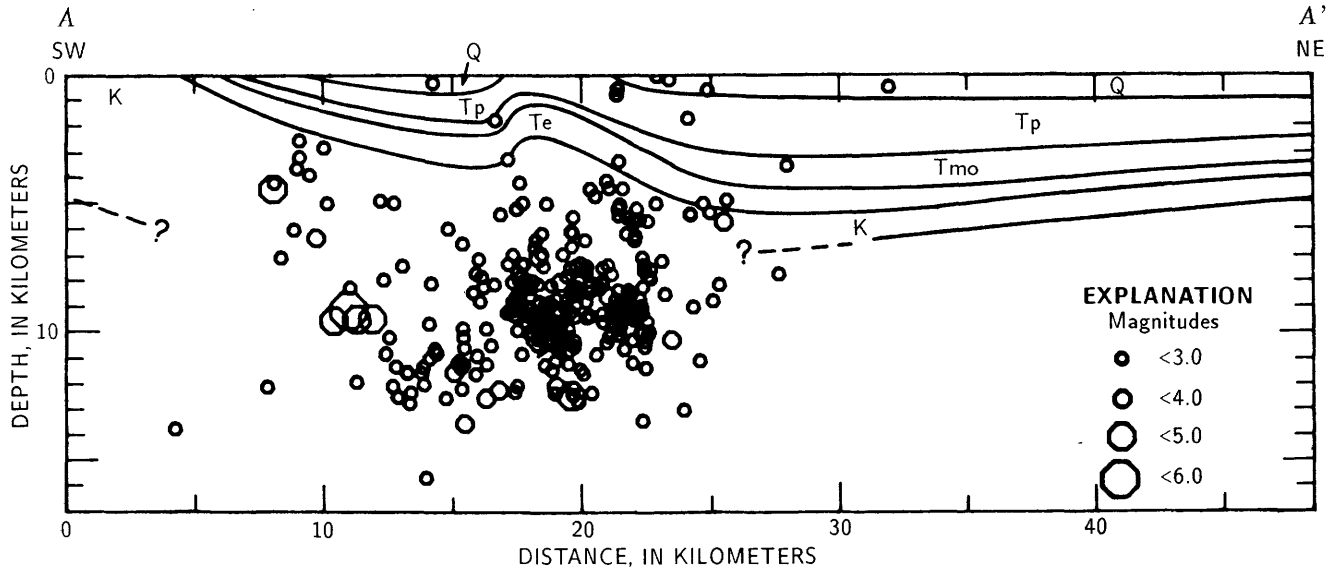

FIGURE 14.2.—Southwest-northeast geologic cross section (see fig. 14.1 for location) through the Coalinga area, showing locations of the main shock and $M>3$ aftershocks for May–July 1983. Main shock and most larger aftershocks have hypocentral depths near 10 km; principal oil-producing horizons have average depths of 0.6 km (Temblor Formation) and 2.2 km (Gatchell sand of local usage). K, Cretaceous rocks; Q, Quaternary deposits; Te, Eocene rocks; Tmo, Miocene and Oligocene rocks. Tp, Pliocene rocks.

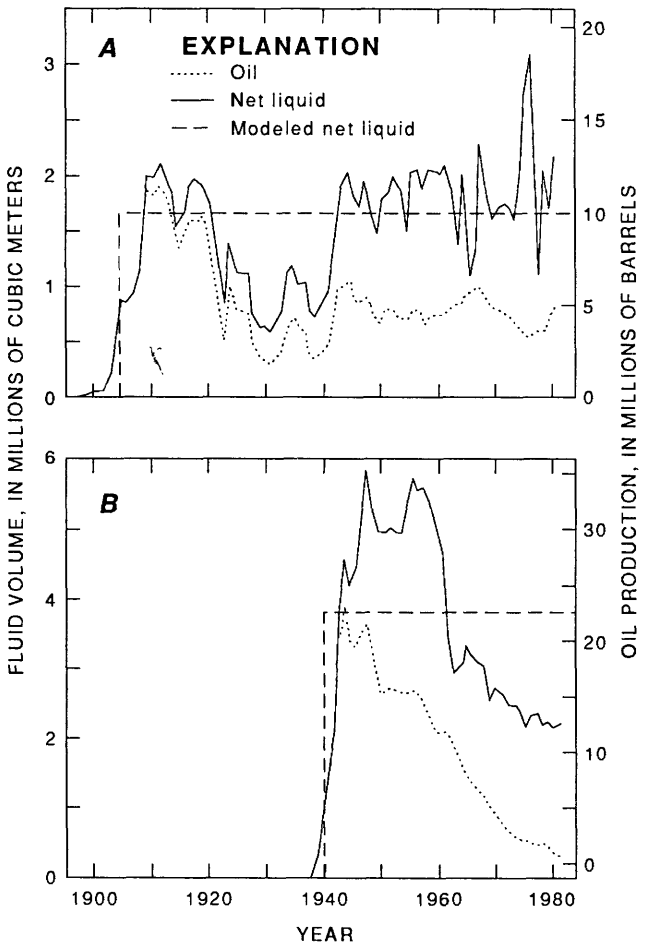

FIGURE 14.3.—Production history of Anticline Ridge oil fields. Net liquid is defined as oil plus water minus returned water. *A*, Coalinga Eastside. *B*, East Coalinga Extension, Nose area. From Conservation Committee of California Oil Producers (1982) and California Division of Oil and Gas (1983).

pore-fluid-mass content through the relation given by Segall (1985):

$$\epsilon_{kk} = \frac{\sigma_{kk}}{3K_u} + \frac{B\Delta m}{\rho_0}, \qquad (2)$$

where K_u is the undrained bulk modulus, that is, the elastic bulk modulus under conditions in which no fluid flow occurs ($\Delta m=0$); B is Skempton's pore-pressure coefficient; and ρ_0 is the fluid density in the undisturbed state.

The solid volumetric strain is seen to be composed of two parts: an undrained elastic strain and a strain resulting from the change in pore-fluid content. For such relatively incompressible fluids as oil and water, the second strain is very nearly $B\Delta v$, where Δv is the change in pore-fluid volume per unit solid volume. Thus, in this case, B is the ratio of the solid-volume change to the change in pore-fluid volume. The range of B is restricted to $0 \leq B \leq 1$; for water-saturated soils, $B \approx 1$, whereas for several diverse rock types ranging from sandstone to granite, B ranges from 0.5 to 0.9 (Rice and Cleary, 1976). Thus, if water is uniformly withdrawn from a rock with $B=0.8$, the volumetric contraction of the rock is 80 percent of the volume of extracted water. For soils, this contraction is nearly 100 percent of the volume of extracted water. Finally, we note that Skempton's coefficient is nearly 0 when the compressibility of the fluid is very large in comparison with that of the solid (Rice and Cleary, 1976), as would be the case for gas and rock.

From figure 14.5, it is now apparent that the stress-free transformation strain resulting from a uniform change in fluid-mass content m is simply

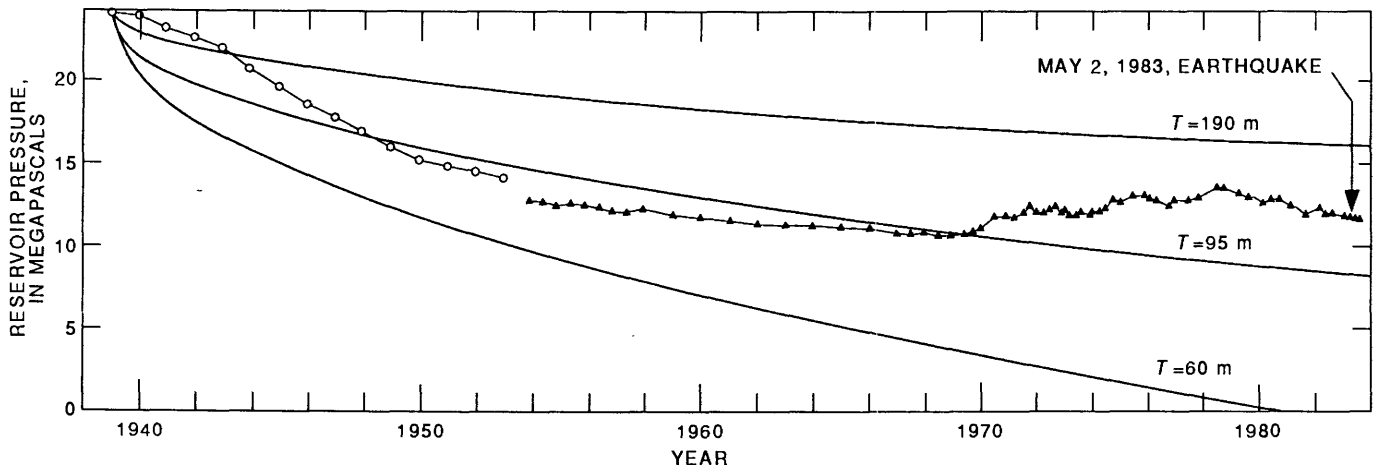

FIGURE 14.4.—Reservoir pressure versus time in the Gatchell sand of local usage, Coalinga Nose area of the Coalinga East Extension oil field. Circles, pressures measured within the oil zone (2,060-m depth); triangles, pressures measured within the gas cap (1,980-m depth); smooth curves, calculated pressure histories, assuming fluid withdrawal at a constant rate. *T*, thickness of producing zone.

$$\epsilon_{kk}^{T} = \frac{B\Delta m}{\rho_0} . \quad (3)$$

To restore the element to its initial shape, it is necessary to elastically strain the element by $-\epsilon_{kk}^{T}$ while maintaining the pore-fluid mass constant (3, fig. 14.5). The elastic straining is achieved by adding tractions T_i to the surface of the element

$$T_i = -K_u \epsilon_{kk}^{T} n_i , \quad (4)$$

where n_i is the unit-surface normal.

The element (inclusion) at this stage has no net strain, and so it fits precisely into the cut in the half-space (matrix). Once the inclusion is reinserted into the matrix, relaxation of the surface tractions will allow the inclusion to contract and strain the matrix. If the dimensions of the element are small in comparison with the depth of burial, the stresses due to contraction can be adequately represented by a point center of contraction or negative center of dilatation. The stresses resulting from the fluid-mass change Δm can be represented by a vertical point force of magnitude Δmg, where g is the acceleration due to gravity.

It can easily be shown that the stress change due to contraction of the solid dominates the gravitational-stress change due to the depletion of fluid mass. In fact, for distances from the producing zones of 10 km or less, the stresses due to contraction are at least 100 times greater than those due to mass depletion (Segall, 1985). Thus, so long as the fluid-depleted zone is elastically coupled to the underlying rocks, the change in gravitational load can be neglected relative to contraction of the fluid-depleted zone.

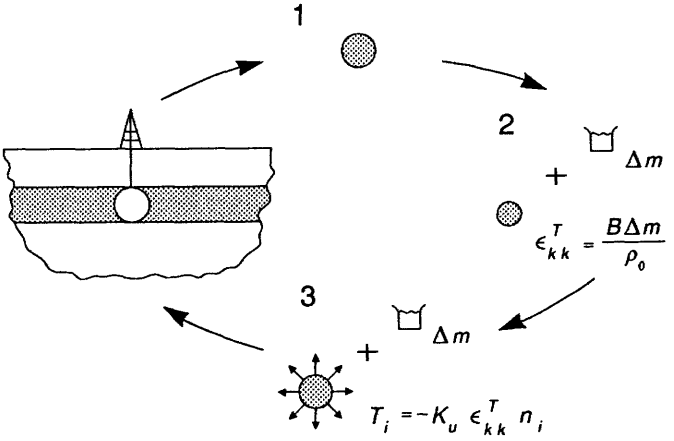

FIGURE 14.5.—Thought experiment demonstrating the effects of fluid extraction: 1, Inclusion is removed from half-space; 2, fluid with mass Δm is extracted from the inclusion, causing the inclusion to contract; 3, applied stresses restore the inclusion to its initial shape, allowing it to be reinserted into the half-space.

The stress and deformation changes resulting from the withdrawal of fluid from a permeable layer embedded in an impermeable half-space (fig. 14.6) can be calculated by solving for the change in fluid-mass content within the layer and then summing the stresses due to fluid depletion at each point within the layer. The thickness of the layer, T, is taken to be much smaller than the layer depth, D. This approximation is reasonable for the oil fields on Anticline Ridge, where the T/D ratio for the principal producing horizons is approximately 0.1. The producing layer has a permeability k, whereas the surrounding rocks are assumed to have negligible permeability. As discussed previously, the oil-bearing horizons are stratigraphically bounded by shale, which is likely to be 100,000 times less permeable than the producing sandstone (Brace, 1980). Over the 80-year period of oil production, the shale is therefore effectively impermeable.

The oil fields are elongate in a northwest-southeast direction along the axis of the Coalinga anticline. This geometry is idealized as a line of wells extending indefinitely in the z-direction (fig. 14.6). The fluid flux out of the layer is taken to be independent of position along the z-direction. As fluid is withdrawn from the line of wells, flow is induced in the layer toward the plane $y=0$. Because the surrounding medium is effectively impermeable, flow occurs only in the y-direction. Finally, we note that the model geometry is such that the induced deformation is one of plane strain; that is, there are no displacements in the z-direction.

The governing equation for the alteration in fluid-mass content is the homogeneous-diffusion equation (Rice and Cleary, 1976), which for one-dimensional flow takes the form

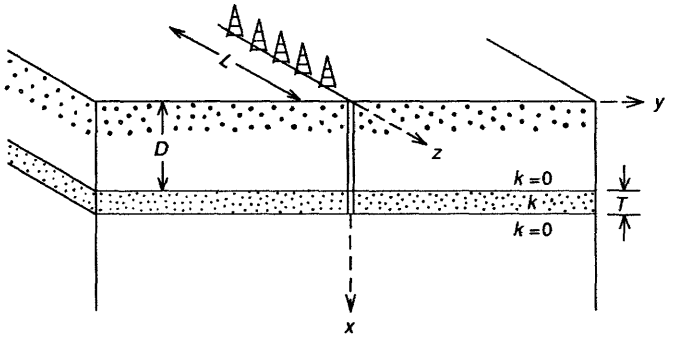

FIGURE 14.6.—Layer of thickness T and permeability k buried at a depth D in a fluid-infiltrated impermeable ($k=0$) half-space.

$$c\frac{\partial^2 \Delta m}{\partial y^2} = \frac{\partial \Delta m}{\partial t}, \tag{5}$$

where c is the hydraulic diffusivity of the medium. The hydraulic diffusivity is given approximately by

$$c \cong k/\eta\phi\beta, \tag{6}$$

where k is the permeability (with units of area), η is the fluid viscosity, ϕ is the porosity, and β is the fluid compressibility (Rice and Cleary, 1976).

The net mass flux out of the producing zone, $-Q$, is taken to be constant for $t>0$ and 0 for $t<0$ (dashed lines, fig. 14.4). If q is the local fluid-mass flux, then the boundary conditions for flow in an infinite layer are

$$q\,(y = 0^+) - q\,(y = 0^-) = -Q \qquad (t>0) \tag{7a}$$

and

$$q\,(y = \pm\infty) = 0\,. \qquad (t>0) \tag{7b}$$

The solution of equation 5 subject to these boundary conditions is (Carslaw and Jaeger, 1959, p. 75)

$$\Delta m\,(y,t) = -Q\sqrt{\frac{t}{c}}\,ierfc\sqrt{\frac{y^2}{4ct}}, \qquad (t>0) \tag{8}$$

where $ierfc(x)$ is the first integral of the complementary error function

$$ierfc(x) = \int_0^x erfc(\xi)d\xi = \frac{e^{-x^2}}{\sqrt{\pi}} - x\,erfc(x). \tag{9}$$

The net mass flux $-Q$ is given by

$$-Q = \frac{-\dot{V}\rho_0}{LT}, \tag{10}$$

where $\dot{V}/L$ is the average rate of fluid extraction per unit length in the z-direction and T is the layer thickness.

The vertical displacement of the free surface $du_x(x=0)$ due to a change in fluid mass Δm at a point along the producing layer $x=D$, $y=\xi$ to $\xi+d\xi$ is that due to a point center of dilatation with strength proportional to the depletion-induced transformation strain at that point:

$$du_x(x = 0,\, y) = \frac{2B(1+\nu_u)T}{3\pi\rho_0}\Delta m(\xi)d\xi\frac{-D}{D^2+(y-\xi)^2} \tag{11}$$

(Segall, 1985), where ν_u is the undrained Poisson's ratio. The net displacement $u_x(0,y,t)$ due to distributed fluid depletion along the entire layer is found by substituting equations 8 and 10 into equation 11 and integrating with respect to ξ from $-\infty$ to ∞:

$$u_x(x = 0,\, y,\, t) = \frac{2B(1+\nu_u)\dot{V}D}{3\pi L}\sqrt{\frac{t}{c}}\int_{-\infty}^{\infty}\frac{ierfc\sqrt{\xi^2/4ct}}{D^2+(y-\xi)^2}\,d\xi\,. \tag{12}$$

The subsidence is found to increase linearly with the rate of fluid extraction. The subsidence also depends strongly on material properties, including Skempton's coefficient and the hydraulic diffusivity. For high diffusivities the fluid depletion is dispersed, the subsidence is spread over a broad area, and the peak subsidence is relatively small, whereas for low diffusivities the subsidence is localized, and the maximum subsidence is relatively large.

The stress change due to fluid extraction can be calculated similarly to the subsidence. The stress change $d\sigma_{mn}$ at a point (x,y) due to an incremental fluid-mass change at $(D,\,\xi)$ is

$$d\sigma_{mm} = \frac{\mu B(1+\nu_u)T}{3\pi\rho_0(1-\nu_u)}G_{mn}(x,y,D,\xi)\Delta m(\xi)d\xi\,. \tag{13}$$

The total stress change due to fluid withdrawal is thus

$$\sigma_{mn}(x,y,t) = \frac{-\mu B(1+\nu_u)\dot{V}}{3\pi(1-\nu_u L)}\sqrt{\frac{t}{c}}\int_{-\infty}^{\infty}G_{mn}(x,y,D,\xi)\,ierfc\sqrt{\frac{\xi^2}{4ct}}\,d\xi \tag{14}$$

(Segall, 1985), where the Green's functions G_{mn} for the different stress components are

$$G_{xx} = \frac{(y-b)^2-(x-a)^2}{r_1^4} + \frac{(5x+a)(x+a)-(y-b)^2}{r_2^4} - \frac{16x(x+a)(y-b)^2}{r_2^6},$$

$$G_{yy} = \frac{(x-a)^2-(y-b)^2}{r_1^4} + \frac{(x+a)\,(3a-x)-3(y-b)^2}{r_2^4} + \frac{16x(x+a)(y-b)^2}{r_2^6}, \tag{15}$$

and

$$G_{xy} = \frac{-2(y-b)(x-a)}{r_1^4} - \frac{2(y-b)(3x+a)}{r_2^4} + \frac{16x\,(x+a)^2(y-b)}{r_2^6}.$$

We emphasize at this point that the stress changes discussed here are generated entirely by contraction of the shallow producing horizon; fluid flow is completely confined to the producing layer. As discussed previously, shale below the producing layer is effectively impermeable, and so there is no fluid transport from depth to the producing zone. In this calculation, the stresses are transmitted to depth elastically, through the solid-rock matrix, without direct fluid transport.

Finally, we calculate the decrease in pore pressure within the producing zone resulting from fluid extraction. In the Biot constitutive theory, the change in pore pressure at a point is simply related to the changes in fluid-mass content and mean stress at that point. For plane-strain conditions, this relation is

$$p(x,y,t) = \frac{(1+\nu_u)B}{3}\left[\frac{2(1+\nu_u)\mu B}{3\rho_0(\nu_u-\nu)}\Delta m(x,y,t) - \sigma_{nn}(x,y,t)\right] \quad (16)$$

(Rice and Cleary, 1976). The change in mean stress at a point within the producing zone is given by

$$\sigma_{nn}(x,y,t) = \frac{-2(1+\nu_u)\mu B}{3\rho_0(1-\nu_u)} \cdot \left\{\frac{-2(1-\nu_u)}{1-2\nu_u}\Delta m(x,y,t) - \frac{2}{\pi}\int_{-\infty}^{\infty}\int_{0}^{\infty}\Delta m(\zeta,\xi,t) \cdot \frac{(x+\zeta)^2 - (y-\xi)^2}{[(x+\zeta)^2+(y-\xi)^2]^2}\,d\zeta\,d\xi\right\} \quad (17)$$

(Segall, 1985). This result can be compared with equation 14, which gives the stresses in the region outside the producing zone $\Delta m(x,y,t)=0$.

Substituting equations 8, 10, and 17 into equation 16 and integrating with respect to (note that m is nonzero only for $D\le\zeta\le D+T$) results in the following expression for pore-pressure change:

$$p(x,y,t) = \frac{-2\mu(1+\nu_u)^2B^2\dot{V}}{9LT}\sqrt{\frac{t}{c}}\left\{\frac{1-2\nu}{(\nu_u-\nu)(1-2\nu_u)}\,ierfc\,\sqrt{\frac{y^2}{4ct}} - \frac{2}{\pi(1-\nu_u)}\int_{-\infty}^{\infty}\left[\frac{x+D}{(x+D)^2+(y-\xi)^2} - \frac{x+D+T}{(x+D+T)^2+(y-\xi)^2}\right] ierfc\,\sqrt{\frac{\xi^2}{4ct}}\,d\xi\right\}, \quad (18)$$

The pressure change depends on several parameters that do not influence the subsidence, namely: shear modulus μ, drained Poisson's ratio ν, and layer thickness T. The pressure change is, in fact, sensitive to the difference between the undrained and drained Poisson's ratio. In the calculations here, ν is taken to be 0.2, and so $\nu_u-\nu=0.13$. In the three sandstone units considered by Rice and Cleary (1976), this difference ranged from 0.13 to 0.19. The pressure change in the Gatchell also depends inversely on layer thickness.

APPLICATION OF METHOD TO THE COALINGA AREA

For the purposes of this study, there are three principal oil-producing zones: Coalinga Westside, Coalinga Eastside, and the Nose region of East Coalinga Extension. The geometry adopted to model the effects of fluid extraction in this area is illustrated in figure 14.7. The Temblor Formation, which extends between the East and West Coalinga fields, is located at a depth of 0.6 km, the average depth of the Temblor in the Coalinga Eastside field (California Division of Oil and Gas, 1973). In the calculation, 1.6×10^6 m^3/yr of liquid was extracted from Coalinga Eastside beginning in 1905 (see fig. 14.3*A*). The rate of extraction from Coalinga Westside was 1.1×10^6 m^3/yr, also beginning in 1905. The Gatchell sand, which grades into the Turritella silt southwest of Anticline Ridge, is modeled as a semi-infinite layer located at a depth of 2.3 km; an average of 3.7×10^6 m^3/yr of liquid was extracted from the Gatchell beginning in 1940 (see fig. 14.3*B*).

The material properties used in the calculation are summarized in table 14.1. Thickness T, porosity ϕ, and permeability k for both the Gatchell and the Temblor were reported by the California Division of Oil and Gas (1983). Measured permeabilities of the Temblor range from 3×10^{-13} to 10^{-11} m^2; however, 2×10^{-12} m^2 is considered to be representative of the entire horizon

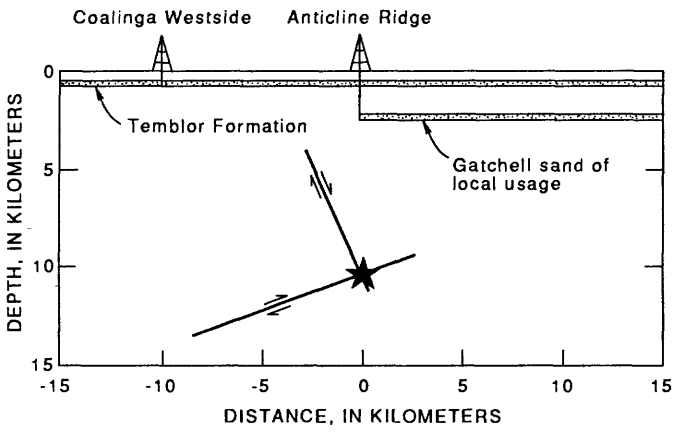

FIGURE 14.7.—Geometry used to model stress change and subsidence in the Coalinga region, showing modal planes and directions of relative movement (arrows). Star, hypocenter of main shock.

TABLE 14.1.—*Average properties of producing horizons in the Coalinga oil fields*

	Temblor Formation	Gatchell sand
Depth ($\underline{D}$) (km)	0.6	2.3
Thickness ($\underline{T}$) (m)	75	0-190
Rate of liquid extraction ($-\dot{\underline{V}}$) (10^6 m^3/yr).	1.6	3.7
Year extraction began	1905	1940
Characteristic length (L) along strike (km).	10	10
Porosity (ϕ)	.3	.2
Permeability ($\underline{k}$) (10^{-9} m^2)	2	.41
Liquid compressibility (β) (10^{-9} Pa^{-1}).	.3	.3
Viscosity (η) (mPa·s)	100	1
Diffusivity ($\underline{c}$) (m^2/s)	.2	7.0
Skempton's coefficient ($\underline{B}$)	.6	.6
Poisson's ratio:		
Undrained (ν_u)	.33	.33
Drained (ν)	.20	.20
Shear modulus (μ) (GPa)	8	8

(Richard Curtain, oral commun., 1983). Oil viscosities also vary. Oil produced from the Gatchell has a viscosity of approximately 10^{-3} Pa·s; however, viscosities of Temblor oils range from 10^{-2} to 2.5 Pa·s (California Division of Oil and Gas, 1983), with an average over the life of the field of 0.15 to 0.2 Pa·s (Richard Curtain, oral commun., 1983). Considering that nearly half of the net liquid withdrawn from the Temblor is water (fig. 14.4*A*), 0.1 Pa·s is taken to be a reasonable value for the average liquid viscosity. Using the above values, hydraulic diffusivities calculated from equation 6 are 0.2 m^2/s for the Temblor and 7.0 m^2/s for the Gatchell (table 14.1). The uncertainties in permeability and viscosity appropriate for the Temblor zone lead to uncertainties in the calculated diffusivity for the Temblor; the actual diffusivity may be as low as 0.02 m^2/s.

Skempton's coefficient and Poisson's ratio under undrained conditions are not routinely measured and are unavailable for either the Gatchell or the Temblor. The values used in the calculations here (table 14.1) are those given by Rice and Cleary (1976) for the Berea Sandstone. The shear moduli of the producing rocks have not been reported but can be inferred from borehole velocity measurements. Compressional-wave velocities in the Gatchell sand average 3.8 km/s. With these data, the shear modulus can be calculated from

$$\mu = \frac{1 - 2\nu_u}{2(1 - \nu_u)}\rho v_p^2 , \qquad (19)$$

where v_p is the *P*-wave velocity and ρ is the density. Equation 19 gives a value of 8×10^3 MPa for v_p=3.8 km/s, assuming ν_u=0.33 and ρ=2,300 kg/m^3.

The change in stress acting on the two nodal planes due to liquid extraction was calculated by using the methods developed in the previous section. The location and dip of the two model fault planes were chosen to be consistent with the main-shock location and focal mechanism. For the northeast-dipping plane, the top of the slipped zone is at a depth of 4.0 km, and the base at 11.2 km (Stein, 1983). For the southwest-dipping plane, the top of the slipped surface is at a depth of 9.5 km, and the base at 13.5 km (fig. 14.7). The stresses were rotated into the possible fault planes to determine the shear and normal stress acting across these surfaces. The stresses reported here represent the changes in the existing stress state due to extraction of liquid from the Temblor and Gatchell zones. The total stress is the sum of the existing tectonic stress and the stress resulting from extraction.

NORTHEAST-DIPPING PLANE

The change in resolved shear stress on the 67°-N.-dipping plane as a function of depth is plotted in figure 14.8*A*. Each curve in figure 14.8*A* represents the stress change at a given time after the onset of extraction; the sign convention employed is such that positive shear stresses favor reverse faulting. Note that the shear stresses favor reverse faulting on a high-angle fault beneath Anticline Ridge. The magnitudes of the stresses, however, are small—less than 40 kPa at depths of 8 km or more.

The corresponding changes in normal stress acting across the northeast-dipping plane are plotted in figure 14.8*B*. The normal stresses are found to be compressive (negative) for all depths and times of interest. In general, the magnitude of the induced compression decreases with depth and increases at a given depth over time after the onset of extraction.

The change in driving stress $\Delta\sigma_d$, which is calculated to assess the net effect of changes in shear and normal stresses on the fault, is defined as

$$\Delta\sigma_d = \Delta\sigma_s + f(\Delta\sigma_n + \Delta p) , \qquad (20)$$

where $\Delta\sigma_s$ and $\Delta\sigma_n$ are the changes in shear and normal stress, f is the coefficient of friction, and Δp is the change in pore pressure. Although the calculations involve no fluid transport to or from the fault, there is an undrained or "instantaneous" pore-pressure change due to changes in the mean stress σ_{nn}. The undrained pressure response is

$$\Delta p = -\frac{(1+\nu_u)B}{3}\Delta\sigma_{nn} . \qquad (n=1, 2) \qquad (21)$$

Substituting equation 21 into equation 20 yields an expression for the driving stress in the form

$$\Delta\sigma_d = \Delta\sigma_s + f\Delta\sigma_n - \frac{1+\nu_u}{3}\Delta\sigma_{nn} . \quad (22)$$

The change in driving stress acting on the northeast-dipping plane is plotted in figure 14.8*C*, assuming a coefficient of friction of 0.6. Near the hypocenter—that is, for depths greater than 9 km—the increasing compression dominates the increasing shear stress. The situation reverses at shallow depths after approximately 50 years of extraction, when the increasing shear stresses dominate and cause an increase in the driving stress. The net effect of fluid extraction is to slightly inhibit slip on the northeast-dipping plane in the vicinity of the hypocenter and to slightly favor slip on the same plane at shallow depths.

SOUTHWEST-DIPPING PLANE

The change in shear stress acting on the southwest-dipping plane as a function of depth is plotted in figure 14.9*A*. The sign convention is such that positive shear stresses favor reverse (or thrust) faulting. As is the case for the northeast-dipping plane, the shear stresses generated by extraction favor reverse faulting on a deep low-angle fault beneath Anticline Ridge. The maximum shear stress here is slightly less than 30 kPa. The induced normal stresses acting across the southwest-dipping plane (fig. 14.9*B*) are compressive, tending to inhibit slip.

The change in driving stress acting across the southwest-dipping plane is plotted in figure 14.9*C*. In contrast to the result for the steeply dipping plane, the change in driving stress has the correct sense to favor reverse motion on the southwest-dipping plane. At the time of the earthquake, the driving stress increased by nearly 20 kPa at a depth of 9.5 km and by 10 kPa and 13.5 km.

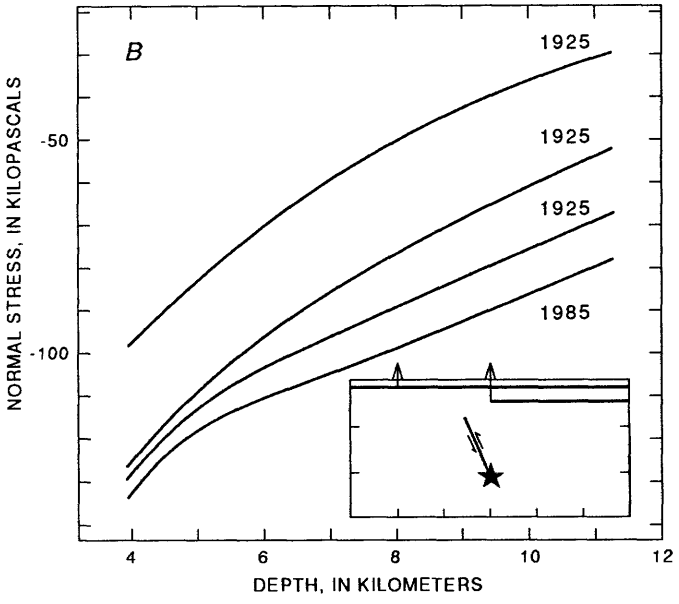

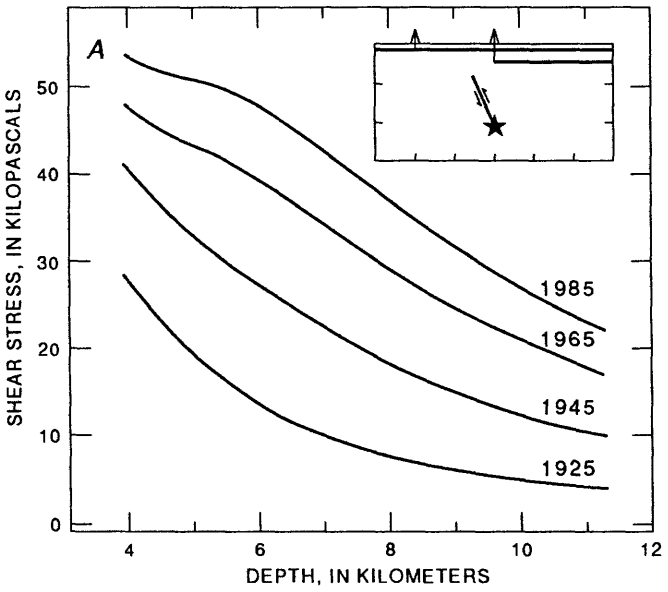

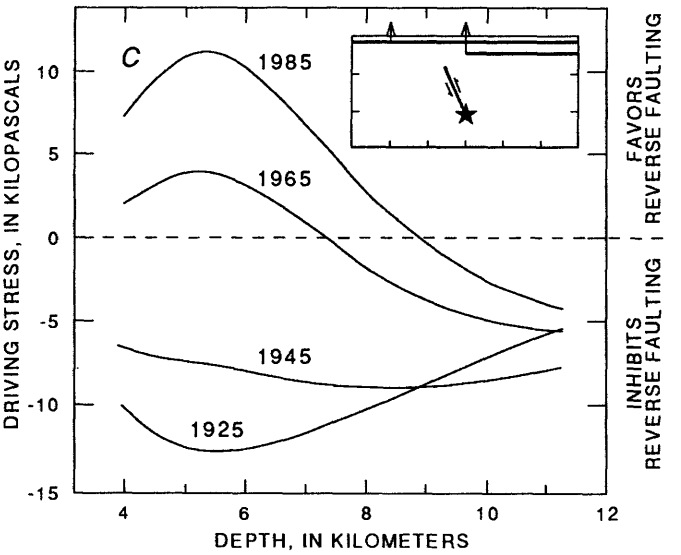

FIGURE 14.8.—Change in stresses due to fluid extraction resolved on northeast-dipping plane, as a function of depth at four different times. Extraction was from the Temblor Formation, which begins in 1905, and from the Gatchell sand of local usage in 1940. See figure 14.7 for explanation of symbols. *A*, Change in resolved shear stress. Positive shear stresses favor reverse slip on fault. *B*, Change in resolved normal stress. Negative normal stresses indicate compression, which inhibits frictional slip. *C*, Change in resolved driving stress $\Delta D\sigma_s + f(\Delta\sigma_n + \Delta p)$. Coefficient of friction f is taken to be 0.6. Pore-pressure change Δp is undrained or instantaneous response to changes in mean stress. Positive values of driving stress favor reverse slip; negative values inhibit slip.

SUBSIDENCE

As an independent check on the analytical methods employed to calculate stress change, the theory can be used to calculate the subsidence of Anticline Ridge resulting from fluid extraction. The calculated subsidence can then be compared with the observed elevation changes of bench marks on Anticline Ridge determined by repeated leveling surveys. The parameters used in this calculation are the same as those employed in the previous stress calculation (table 14.1). Three bench marks on Anticline Ridge (W156, V156, and V237) were chosen for this comparison because they are located on Tertiary rocks and should not be influenced by soil subsidence related to ground-water pumping. All three bench marks were surveyed in 1960, 1966, 1969, and 1972 (Stein, 1983); in addition, bench marks W156 and V156 were surveyed in 1933–35 and 1958–59 (Prokopovich and Magleby, 1968).

Elevation changes of the Anticline Ridge bench marks relative to an assumed stable site on Cretaceous rocks within the Diablo Range west of Coalinga (bench mark F1046, Stein, 1983; bench mark F156, Prokopovich and Magleby, 1968) are plotted in figure 14.10. The 1960–72 leveling has been corrected for refraction error (Stein, 1983), using the method of Holdahl (1981). Although the 1933–35 and 1958–59 levelings have not been corrected for refraction error, the reference station is at nearly the same elevation as Anticline Ridge, and so these errors should be less than 15 mm. In fact, the refraction corrections for bench marks W156 and V156 between 1960 and 1966 are only 5 and 7 mm, respectively. Random errors between the reference station and Anticline Ridge are assumed to be less than 9 mm for first-order leveling (1958–59, 1960, and 1966 surveys) and less than 19 mm for second-order leveling (1933–35, 1969, and 1972 surveys).

The average subsidence rates of bench marks W156 and V156 between 1933 and 1972 were 3.2 ± 0.6 and 4.1 ± 0.4 mm/yr, respectively (fig. 14.10); bench mark V237 subsided at a rate of 2.6 ± 0.1 mm/yr between 1960 and 1972. The mean subsidence rate of Anticline Ridge from these data is 3.3 ± 0.7 mm/yr. The model subsidence calculated by setting $y=0$ in equation 12 is also plotted in figure 14.10. The calculated subsidence agrees well with

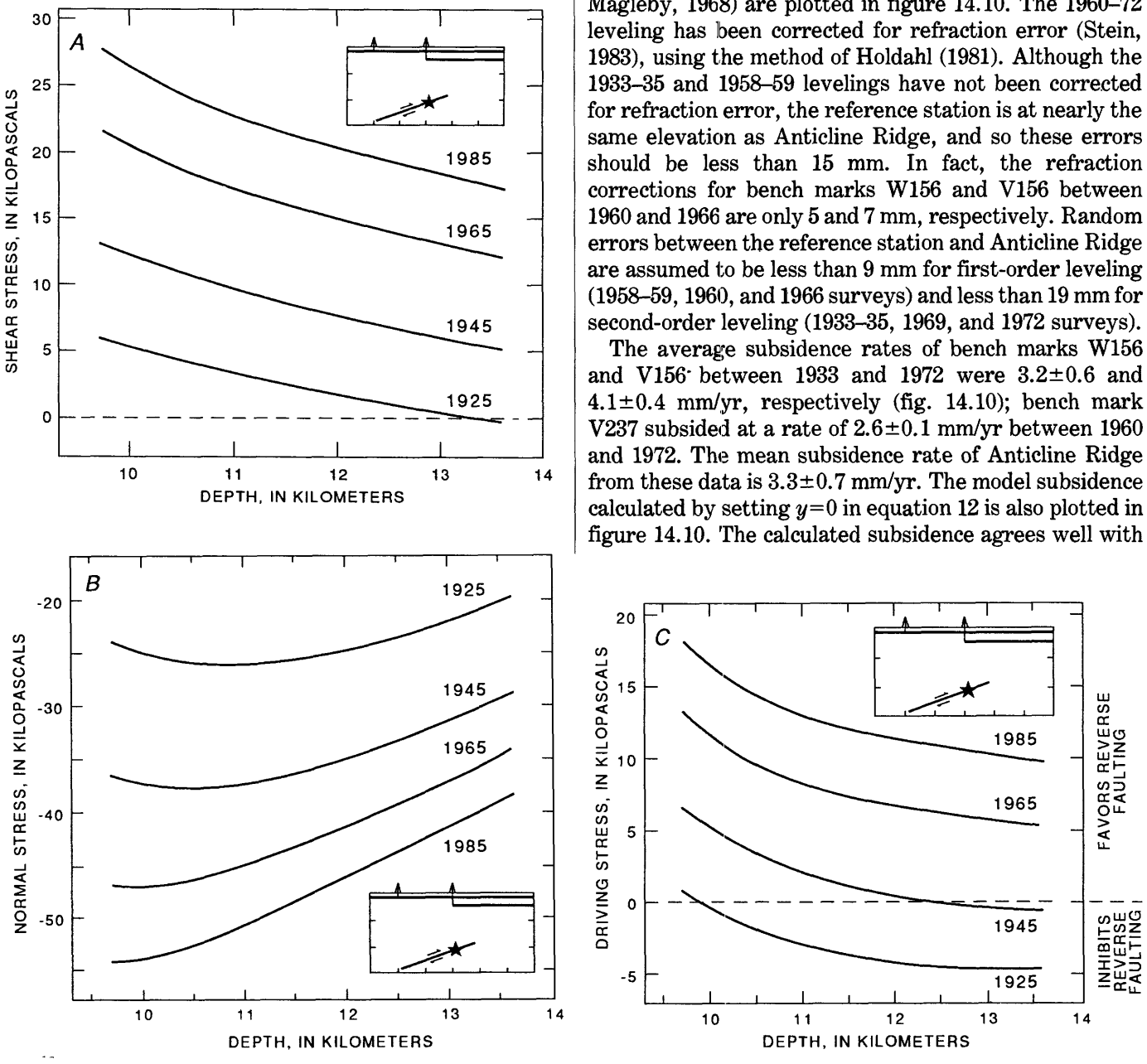

FIGURE 14.9.—Change in stress resolved on southwest-dipping plane. See figure 14.7 for explanation. *A*, Shear stress. *B*, Normal stress. *C*, Driving stress. Sign convention same as in figure 14.8.

the observed elevation changes; in fact, the subsidence rate between 1933 and 1972 predicted by the model is 3.3 mm/yr. We emphasize that the model parameters were all estimated from independent data, and none was adjusted to fit the measured elevation changes. Nevertheless, the material parameters, including hydraulic diffusivity, are imperfectly known. For comparison, the effect of decreasing the diffusivity of the Temblor by one order of magnitude to 0.02 m/s is plotted in figure 14.10. The average subsidence rate for the same time interval in this case is 6.6 mm/yr, about twice the observed rate.

As a further check, the predicted pore-pressure change is compared with the observed pressure decline in the Gatchell sand in figure 14.5. The predicted pore-pressure change is found by evaluating equation 18 at $x=D+T/2$ and $y=0$; the results are shown for thickness of the Gatchell of 190, 95, and 60 m. For a thickness of 190 m, the predicted pressure decline is approximately a factor of 2 less than that observed. This discrepancy could be due to several causes. Considering the varying thickness of the Gatchell and the possibility of varying properties within the zone, the average thickness of the producing section probably is somewhat less than 190 m. Decreasing this thickness by a factor of 2 to 95 m yields a reasonably good fit to the measured pressures (fig. 14.5). The misfit in calculated pressures might also result from inaccurate estimates of material properties; for example, an equally good fit to the data is obtained by increasing the drained Poisson's ratio from 0.20 to 0.28. Given the simplicity of the model, the overall fit to the data is adequate, although detailed features of the pressure history are not reproduced, mostly because the actual fluid-extraction rate is not constant, as is assumed in the calculation (see fig. 14.4*B*).

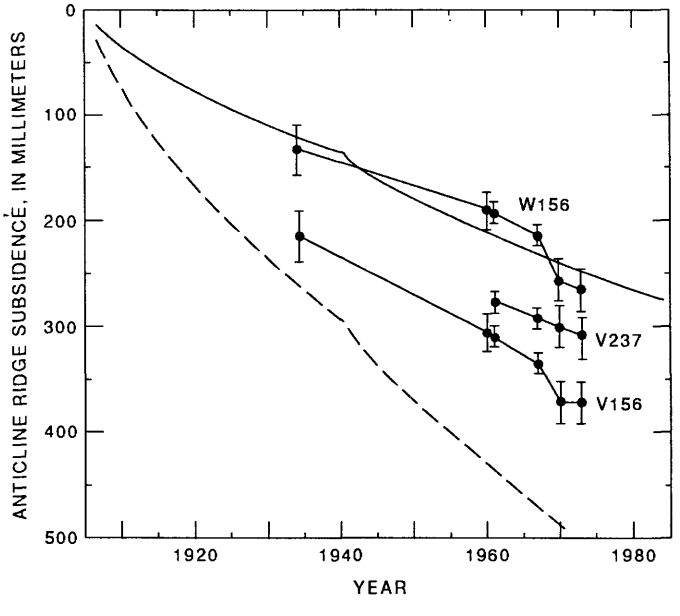

FIGURE 14.10.—Observed elevation changes of three bench marks (W156, V156, and V237) on Anticline Ridge, in comparison with vertical displacements calculated from equation 12. Solid curve illustrates subsidence calculated with hydraulic diffusivity of the Temblor Formation equal to preferred value of 0.2 m^2/s; dashed curve illustrates effect of decreasing this value to 0.02 m^2/s. Diffusivity of the Gatchell sand of local usage is 7.0 m^2/s in both cases.

DISCUSSION

At present, stress changes at seismogenic depths resulting from fluid extraction cannot be measured directly and so must be inferred from near-surface observations. At first glance, it might appear that any stresses inferred in this way would be almost entirely unconstrained. However, the analytical methods used to compute stress can also be used to calculate other quantities, such as surface displacement or reservoir pressure, that can be measured directly. Quantitative agreement between theory and observation would then lend credence to the stresses calculated at depths, which are currently inaccessible to direct measurement.

The excellent agreement between calculated subsidence rate and observed rate of elevation change on Anticline Ridge (fig. 14.10) is particularly significant. The consistency between the calculated decline in reservoir pressure and measured pressures in the Gatchell sand further supports the calculated stresses. This agreement between theory and observation is particularly encouraging because the parameters in the theory either are known from independent observations or can be inferred from measurements on similar rocks.

For several reasons, estimates of hydraulic diffusivity, particularly in the Temblor Formation, are likely to be accurate only to within an order of magnitude. A decrease in the diffusivity of the Temblor by one order of magnitude was found to increase the predicted subsidence rate from 3 to 6 mm/yr, significantly greater than the observed rate of 3.3 ± 0.7 mm/yr. The change in stress acting on the fault also depends nonlinearly on the diffusivity. Stress changes calculated for a range of diffusivities, assuming only that the diffusivities are known to within an order of magnitude, exhibit somewhat varying behavior. In some cases, the changes in driving stress are negative, indicating that extraction inhibits slip. For the northeast-dipping plane, the driving-stress changes are always less than 40 kPa at depths of 8 km or more, and less than 75 kPa anywhere on the fault surface. The change in driving stress acting on the southwest-dipping plane tends to be positive for all plausible combinations of hydraulic diffusivities. The magnitudes of the driving-stress changes are less than or

equal to 30 kPa at hypocentral depths on the southwest-dipping plane.

It is difficult to evaluate the effect of these relatively small stress changes on the stability of a tectonically loaded fault. One possibility is to compare the stress changes resulting from fluid extraction with the stress drop from the May 2 earthquake. Using the ordinary relation for stress drop (Chinnery, 1969) and taking the average slip and fault width to be 1.8 m and 8 km, respectively (Stein, 1983), the stress drop of the main shock is found to be approximately 10 MPa; the precise value depends on assumptions about the geometry of the fault plane. The change in driving stress due to fluid extraction (figs. 14.8, 14.9) at hypocentral depths (10±1 km) is thus less than 0.2 percent of the stress drop. For the range of diffusivities considered plausible here, the change in driving stress at hypocentral depths is no greater than 0.4 percent of the stress drop.

A second, possibly more interesting comparison is to contrast extraction-induced stresses with the stresses resulting from solid-earth tides. Tidal stresses within the crust have amplitudes of approximately 5 kPa (Stacey, 1969). The shear stresses induced by fluid extraction are 30 to 40 kPa, an order of magnitude greater than the tidal stresses. Thus, although extraction-induced stresses are small, they cannot be ruled out as a potential triggering mechanism because of their small magnitude.

If the rate of tectonic-stress accumulation across the Coalinga fault were known, the natural stress rate could be compared with the stresses induced by extraction. To take a purely hypothetical example, if the rate of tectonic-stress accumulation is 10 kPa/yr and the main-shock fault surface is the southwest-dipping plane (fig. 14.9), then the effect of fluid extraction might have been to shorten the interearthquake time by 1 to 2 years. Similarly, if the tectonic-stress rate is 1 kPa/yr, then extraction would be expected to advance the time of the earthquake by 1 to 2 decades. If, however, the steeply northeast dipping plane is the main-shock surface (fig. 14.8), then the most likely effect of extraction would have been to increase the interearthquake time by a comparable amount. These examples clearly demonstrate that to properly assess the significance of the stress changes calculated here, it will be necessary to determine the tectonic rate of stress accumulation (or the recurrence interval) and to identify which of the two possible planes was the main-shock fault plane.

CONCLUSIONS

The presence of thick argillaceous units below the oil-producing horizons in the Coalinga area is almost certain to have prevented flow of pore fluids between the oil fields and the focal region of the May 2 earthquake. In any case, the predominant effect of oil-field operations (namely, extraction of pore fluids) has been to decrease pore pressures in the producing strata. In the unlikely event that fluid transport occurred between the producing zones and the earthquake focus, the result would have been to diminish pore pressures along the fault zone and thus to inhibit frictional slip.

Extraction of large volumes of fluid from the oil fields resulted in a 50-percent decrease in pore pressure within the Gatchell sand between 1938 and 1983 and caused Anticline Ridge to subside at approximately 3 mm/yr. Stress changes at hypocentral depths, calculated from a model based on Biot's constitutive theory for fluid-infiltrated elastic media, are small in comparison with the earthquake-stress drop. The calculated driving stress (shear stress minus frictional resistance) depends on the hydraulic diffusivity of the producing rocks and the orientation of the fault plane. For the steeply northeast dipping plane, the driving stress increased by less than 10 kPa at depths of 4 to 9 km, weakly favoring slip at shallow depths. At depths of 9 to 11 km, a decrease in driving stress by less than 5 kPa due to fluid extraction slightly inhibited slip near the earthquake hypocenter. For the shallowly southwest dipping plane, an increase in the driving stress by less than 20 kPa slightly favored fault slip. Although these calculated stress changes are not easily verified by direct measurement, the ability of the theory to quantitatively explain observed changes in the elevation of Anticline Ridge and reservoir pressures in the Gatchell sand suggests that the method yields reasonable estimates of the stress change at depth.

ACKNOWLEDGMENTS

We thank Richard Curtain of the California Division of Oil and Gas for providing valuable data on the Coalinga oil fields, Ross Stein for his assistance in interpreting the leveling data, and Donna Eberhart-Phillips and Paul Reasenberg for their assistance with the aftershock data.

REFERENCES CITED

Bell, M.L., and Nur, Amos, 1978, Strength changes due to reservoir-induced pore pressure and stresses and application to Lake Oroville: Journal of Geophysical Research, v. 83, no. B9, p. 4469–4483.

Biot, M.A., 1941, General theory of 3-dimensional consolidation: Journal of Applied Physics, v. 12, p. 155–164.

Brace, W.F., 1980, Permeability of crystalline and argillaceous rocks: International Journal of Rock Mechanics and Mining Sciences & Geomechanics Abstracts, v. 17, no. 5, p. 241–251.

California Division of Oil and Gas, 1973, North and east central California, v. 1 *of* California oil and gas fields: Sacramento.

—— 1983, State Oil and Gas Supervisor Annual Report 69: Sacramento.

Conservation Committee of California Oil Producers, 1982, Annual review of California oil and gas production, 1982: Los Angeles.

Carslaw, A.R., and Jaeger, C.J., 1959, Conduction of heat in solids (2d ed.): Oxford, Clarendon Press, 510 p.

Chinnery, M.A., 1969, Theoretical fault models, *in* Kasahara, Keichi, and Stevens, A.E., eds., A symposium on processes in the focal region: Ottawa, Ontario, Canada, Dominion Observatory Publications, v. 37, no. 7, p. 211–223.

Eaton, J.P., Cockerham, R.S., and Lester, F.W., 1983, Study of the May 2, 1983 Coalinga earthquake and its aftershocks, based on the USGS seismic network in northern California, *in* Bennett, J.H., and Sherburne, R.W., eds., The 1983 Coalinga, California earthquakes: California Division of Mines and Geology Special Publication 66, p. 261–273.

Eshelby, J.D., 1957, The determination of the elastic field of an ellipsoidal inclusion, and related problems: Royal Society of London Proceedings, ser. A, v. 241, no. 1226, p. 376–396.

Gupta, H.K., and Rastogi, B.K., 1976, Dams and earthquakes: New York, Elsevier, 229 p.

Healy, J.H., Rubey, W.W., Griggs, D.T., and Raleigh, C.B., 1968, The Denver earthquakes: Science, v. 161, no. 3848, p. 1301–1310.

Holdahl, S.K., 1981, A model of temperature stratification for correction of leveling refraction: Bulletin Géodésique, v. 55, no. 3, p. 231–249.

Kovach, R.L., 1974, Source mechanisms for Wilmington oil field, California, subsidence earthquakes: Seismological Society of America Bulletin, v. 64, no. 3, pt. 1, p. 699–711.

Pratt, W.E., and Johnson, D.W., 1926, Local subsidence of the Goose Creek oil field [Tex.]: Journal of Geology, v. 34, no. 7, pt. 1, p. 577–590.

Prokopovich, N.P., and Magleby, D.C., 1968, Land subsidence in Pleasant Valley area, Fresno County, California: American Water Works Association Journal, v. 60, no. 4, p. 413–424.

Raleigh, C.B., Healy, J.H., and Bredehoeft, J.D., 1972, Faulting and crustal stress at Rangely, Colorado, *in* Heard, H.C., Borg, I.Y., Carter, N.L., and Raleigh, C.B., eds., Flow and fracture of rocks (Griggs volume): American Geophysical Union Geophysical Monograph 16, p. 275–284.

—— 1976, An experiment in earthquake control at Rangely, Colorado: Science, v. 191, no. 4233, p. 1230–1237.

Reasenberg, Paul, Eberhart-Phillips, Donna, and Segall, Paul, 1983, Preliminary views of the aftershock distribution of the May 2, 1983, Coalinga earthquake, *in* Borcherdt, R.D., compiler, The Coalinga earthquake sequence commencing May 2, 1983: U.S. Geological Survey Open-File Report 83-511, p. 27–37.

Rice, J.R., and Cleary, M.P., 1976, Some basic stress diffusion solutions for fluid-saturated elastic porous media with compressible constituents: Reviews of Geophysics and Space Physics, v. 14, no. 2, p. 227–241.

Segall, Paul, 1985, Stress and subsidence resulting from subsurface fluid withdrawal in the epicentral region of the 1983 Coalinga earthquake: Journal of Geophysical Research, v. 90, no. B8, p. 6801–6816.

Simpson, D.W., 1976, Seismicity changes associated with reservoir loading: Engineering Geology, v. 10, no. 2–4, p. 123–150. Stacey, F.D., 1969, Physics of the Earth: New York, John Wiley & Sons, 324 p.

Stein, R.S., 1983, Reverse slip on a buried fault during the 2 May 1983 Coalinga earthquake: Evidence from geodetic elevation changes, *in* Bennett, J.H., and Sherburne, R.W., eds., The 1983 Coalinga, California earthquakes: California Division of Mines and Geology Special Publication 66, p. 151–163.

Yerkes, R.F., and Castle, R.O., 1976, Seismicity and faulting attributable to fluid extraction: Engineering Geology, v. 10, no. 2–4, p. 151–167.

Zoback, M.D., and Hickman, S.M., 1982, In situ study of the physical mechanisms controlling induced seismicity at Monticello Reservoir, South Carolina: Journal of Geophysical Research, v. 87, no. B8, p. 6959–6974.

15. ALLUVIAL PLAINS AND EARTHQUAKE RECURRENCE AT THE COALINGA ANTICLINE

By BRIAN F. ATWATER, DAVID A. TRUMM, JOHN C. TINSLEY III, and ROSS S. STEIN,
U.S. GEOLOGICAL SURVEY;

ALLEN B. TUCKER,
SAN JOSE STATE UNIVERSITY;

DOUGLAS J. DONAHUE and A.J.T. JULL,
UNIVERSITY OF ARIZONA, TUCSON;

and

LOUIS A. PAYEN,
UNIVERSITY OF CALIFORNIA, RIVERSIDE

CONTENTS

ABSTRACT

Late Holocene alluvial plains cross the Coalinga anticline with so little apparent deformation that the fold-building May 2 earthquake seems to have been an extremely rare event. The alluvial plains, exposed in stratigraphic section along Los Gatos Creek, provide structural datums as old as 5,000 ^{14}C yr that can be traced discontinuously from the Pleasant Valley syncline to the axial part of the Coalinga anticline about 10 km downplunge from the epicenter of the May 2 earthquake. The buried plains of 2,000, 2,500, and 5,000 ^{14}C yr B.P. nearly parallel the present alluvial plain, whose age is 200 to 500 ^{14}C yr. If the initial profiles of the 2,000-, 2,500-, and 5,000-^{14}C-yr-B.P. plains approximately paralleled the profile of the present alluvial plain, then at Los Gatos Creek the Coalinga anticline has grown slower than 1 m per 1,000 yr during the late Holocene. Even slower growth—probably less than a few tenths of a meter per 1,000 yr—best explains the present configuration of the 5,000-^{14}C-yr-B.P. plain. These average growth rates imply a minimum average repeat time in the range 200–1,000 yr for major Coalinga-anticline earthquakes during the late Holocene, provided that (1) all such earthquakes entail at least 0.2 m of anticlinal uplift across Los Gatos Creek, as happened in 1983, and (2) the anticline does not shrink between the major earthquakes.

An average late Holocene repeat time of at least 200 to 1,000 yr is compatible with the average Quaternary repeat time of 500 to 1,500 yr that has been previously inferred from the maximum dip of tilted bedding in the Tulare Formation near the 1983 epicenter. Long repeat time during the Holocene is also consistent with four lines of evidence that collectively argue against a high average rate of anticlinal growth during the latest Pleistocene and the Holocene. (1) No conspicuous terrace higher than the present alluvial plain lines the gap through which Los Gatos Creek crosses the Coalinga anticline; if terraces were elevated at this gap during the latest Pleistocene and the Holocene, they may have been uplifted too slowly to escape erosion. (2) Contrary to a previous interpretation, clayey sediment upstream of the anticline is probably alluvial rather than lacustrine and thus does not suggest anticlinal impoundment of Los Gatos Creek. (3) The creek's sinuosity, less through the anticline than in the syncline upstream of it, is inconsistent with rapid anticlinal uplift if the creek adjusts its sinuosity across the anticline so as to maintain a constant channel gradient across a deforming alluvial plain. (4) A hump in the creek's present alluvial plain, centered 2.5 km upstream of the anticlinal axis, is not necessarily a structural bulge because it may be due to changes in the velocity and turbidity of overbank flow.

In addition to providing loose constraints on earthquake recurrence, Holocene alluvium along Los Gatos Creek contains evidence of range

fires, prehistoric human occupation, minimal redeposition of ancient charcoal, and distinctly episodic aggradation and incision. Red layers and lenses, mostly 5 to 10 mm thick, represent tens of prehistoric fires later than about 5,500 ^{14}C yr B.P., some of which may have been started by indigenous people, who left chert flakes in deposits as old as 4,600 ^{14}C yr (approx 5,300 sidereal yr). These flakes are among the oldest well-dated human artifacts in the San Joaquin Valley. Angular charcoal found in and atop the reddish layers and lenses yields ^{14}C ages that, with one exception, suggest less than 800 yr of discordance between deposit age and charcoal age. Rounded, relatively far traveled charcoal from ripple-crosslaminated sand yields ^{14}C ages that show similarly small discordance, as judged from mutually consistent ages on individual pieces of charcoal from the same deposit, and as judged from ages on superposed, laterally equivalent, and near-modern samples. One to several fining-upward sequences, containing coarser sediment than most of the alluvium exposed beneath them, form a tabular unit in the upper part of most large exposures along Los Gatos Creek. Deposition of this unit began about 500 sidereal yr B.P. but ceased by A.D. 1854 or 1933, when Los Gatos Creek had become so deeply incised that its arroyo had a bankfull capacity at least 4 to 18 times larger than the probable discharge of a 50-yr flood.

INTRODUCTION

Having approached 0.5 m during the May 2 earthquake, the uplift of Quaternary deposits on the Coalinga anticline may provide evidence of the average repeat time of similar earthquakes during the recent geologic past. Stein and King (1984) estimated the average late Quaternary repeat time to be 500 to 1,500 yr from the degree of folding in the upper Pliocene and Pleistocene Tulare Formation; in addition, they estimated the average Holocene repeat time to be at least 200 to 600 yr on the basis of an alluvial-plain profile near Los Gatos Creek, whose arroyo extends across the Coalinga anticline from the synclinal Pleasant Valley into the synclinal San Joaquin Valley (fig. 15.1). In this chapter, we estimate an average repeat time from the stratigraphy of Holocene alluvium exposed in the walls of that arroyo. Largely deposited overbank, this alluvium reveals the approximate configuration of former alluvial plains whose present configuration over the anticline should reflect the rate of anticlinal growth. Resulting constraints on the Holocene uplift rate, though made uncertain by possible differences in the initial configuration of the alluvial plains, suggest an average repeat time of at least 200 to 1,000 yr for major (M=6–7) Coalinga-area earthquakes during the late Holocene.

METHODS

We studied Holocene alluvial stratigraphy at 34 measured sections in the banks of Los Gatos Creek. Most of these sections, which range in thickness from 2.3 to 10.5 m (pls. 15.1, 15.2), are located on the outsides of meanders and are separated from one another by hundreds of meters of poor exposure. Although most of the sections extend upward to the present alluvial plain, only a few extend downward to the thalweg; a talus apron or an inset terrace typically conceals strata between the thalweg and the base of the section. One of us (Trumm) used backhoe trenches and hand-auger borings to extend seven sections below the thalweg.

Elevations within the sections were established by field measurement and topographic-map interpolation. We measured each section by means of hand levels and rulers, with the Los Gatos Creek thalweg as temporary datum. Most sections at and west of the anticline were linked to the National Geodetic Vertical Datum by means of unreversed vertical-angle leveling, with a transit-mounted electronic distance-measuring device, between bench marks Coalinga RM4 and T1228 (pl. 15.1; fig. 15.1). The vertical difference between these bench marks was 57.664 m in late 1983, according to U.S. National Geodetic Survey leveling; 1 year later, we determined a difference of 57.502 m. Treating this 0.162–m discrepancy as our error, we distributed it evenly along our line of leveling. Measured sections not reached by this leveling are positioned vertically by means of interpolation between the topographic contours shown in plate 15.1. We have not corrected these contours, constructed from ground surveys and aerial photographs dated 1955–56, for subsequent ground-water-overdraft subsidence, nor have we corrected for the coseismic deformation in 1983 (pl. 15.1). Ground-water-overdraft subsidence since the middle 1950's ranges from near 0 near the anticline to about 2 m at the east end of the cross section shown in plate 15.2 (Ireland and others, 1984, figs. 4, 19).

Isotopic ages of alluvium were determined by radiocarbon dating of 73 charcoal samples from 55 charcoal-bearing beds, representing 27 of the measured sections (pl. 15.2). Of these ages, 54 are on small (chiefly 5–50 mg) samples consisting of one or more pieces of charcoal; these small samples were made into iron-carbide or graphite beads and analyzed by means of tandem accelerator and mass spectrometer (Bennett and others, 1978; Muller and others, 1978). Each of the other 19 samples weighed at least 1,000 mg and comprised many pieces of charcoal; these larger samples were ^{14}C dated by conventional proportional-gas or liquid-scintillation methods. All radiocarbon ages reported here are calculated with an assumed δ^{13}C value of −25 permil; "yr B.P." denotes years before A.D. 1950.

Depths to the Tulare Formation beneath the western part of our cross section were estimated from seismic-refraction surveys (pl. 15.2). P-wave arrivals, from a sledge-hammer acoustic source, were detected with a six-trace signal-enhancement seismograph. Velocities for the Tulare were calibrated in an area we call Turk narrows (fig. 15.1), where the Tulare crops out in the creekbed (pl. 15.1).

PHYSICAL SETTING

The Coalinga anticline has grown largely or entirely during Quaternary time. Its youngest conspicuously folded rocks, the continental Tulare Formation, dip parallel to underlying Pliocene marine rocks of the San Joaquin Formation and the upper part of the Etchegoin Formation (pl. 15.1) and, possibly, to strata or seismic reflectors as old as Cretaceous (Fielding and others, 1984; see chaps. 4, 23). The anticline plunges southeast toward and on echelon with the Kettleman Hills (fig. 15.1), whose anticlinal uplift also appears to have occurred during the Quaternary (Woodring and others, 1940). The most recent episode of growth by the Coalinga anticline entailed as much as 0.5 m of coseismic uplift in May 1983. This uplift, accompanied by 0.1 to 0.2 m of

FIGURE 15.1.—Coalinga anticline and vicinity. Dashed line enclosing subsidence trough is 6.1-m subsidence contour of Ireland and others (1984, p. 18). Epicentral location from Eaton (1985, p. 159). Location of Oudjiu, a 19th-century Tachi townsite, from von Werlhof and Vierhus (1956). View eastward. Photograph by U.S. Air Force, April 1970.

subsidence to the west near Coalinga, decreased downplunge to about 0.2 m in the vicinity of Los Gatos Creek (pl. 15.1; see Stein, 1985).

The arroyo that transects the Coalinga anticline, named "Los Gatos Creek" on current topographic maps (pl. 15.1) but also known as Arroyo Pasajero (Munn and others, 1981) and Arroyo Poso de Chane (von Werlhof and Vierhus, 1956), carries the intermittent discharge of upper Los Gatos Creek and two tributaries, Warthan Creek and Jacalitos Creek, that join Los Gatos Creek in Pleasant Valley (fig. 15.1). Still another intermittent stream, Zapato Chino Creek, joins Los Gatos Creek in the San Joaquin Valley after skirting the Coalinga anticline via the gap between the Guijarral Hills and the Kettleman Hills (fig. 15.1). Upstream from Pleasant Valley, Los Gatos Creek has a drainage-basin area of about 270 km^2 and, since 1931, a maximum recorded discharge of about 130 m^3/s (table 15.1). Periods of no discharge last several months during most years (Water Resources Division, 1959, p. 74–75). Warthan and Jacalitos Creeks also have drainage-basin areas in the range 200–300 km^2 and, though mostly ungaged, probably resemble upper Los Gatos Creek in their discharge.

Within the study area (pl. 15.1), the arroyo through which Los Gatos Creek flows is mostly 100 to 200 m wide and 5 to 10 m deep. These dimensions indicate great incision: Bankfull channel capacity is about 2,000 m^3/s at a constriction (Turk narrows) and about 9,000 m^3/s at a more typical reach near the aboriginal townsite of Oudjiu (table 15.2); by contrast, a 50-yr flood at these sites is probably no more than 500 m^3/s, which is 4 times the peak recorded discharge of upper Los Gatos Creek (table 15.1). Most of this incision has occurred within the past 500 yr (see subsection below entitled "Depositional History") but predates A.D. 1933 (King and Stein, 1983); it also may largely predate A.D. 1853–54, when arroyo widths and one arroyo depth were recorded by township-subdivision surveyors (pl. 15.1). Deep historical incision appears restricted to a reach east of the anticline, near the east end of the cross section, where present thalweg depths are as much as 6.5 m greater than those determined in 1955–56 (dotted line, pl. 15.2). This recent incision is probably due to ground-water-overdraft subsidence centered near Huron (fig. 15.1; Munn and others, 1981), which totals as much 6 m and occurred chiefly between 1949 and 1969 (Ireland and others, 1984, fig. 19).

SURFICIAL EVIDENCE CONCERNING ANTICLINAL UPLIFT

If earthquakes comparable to that of 1983 have recurred frequently (say, at 100-yr intervals), then today's landscape should contain clues that the Coalinga anticline has grown during the latest Pleistocene and the Holocene. Anticlinal growth during that time could have created flights of uplifted terraces in the gap through which Los Gatos Creek crosses the anticline. In addition, according to King and Stein (1983), prehistoric uplift may have impounded the creek, influenced its sinuosity, and warped its alluvial plain. However, conspicuous elevated terraces are absent, purportedly lacustrine deposits upstream of the anticline are probably alluvial, the creek's sinuosity does not necessarily imply anticlinal uplift, and the profile of the present alluvial plain may be a purely depositional feature.

HIGH TERRACES

Terraces higher than the present alluvial plain, whose age is 200–500 ^{14}C yr, are either obscure or absent in the gap through the Coalinga anticline (pl. 15.1; fig. 15.1). By contrast, flights of conspicuously uplifted terraces commonly line major streams elsewhere at the western margin of the San Joaquin Valley (McGill, 1951, pl. 26; Bull, 1964, fig. 66; Lettis, 1982, fig. 26). This contrast may be due to factors other than uplift rate: Former terraces on the north side of the gap through the Coalinga anticline may now be obscure because of the gentle slope of that area, or they may have been destroyed by erosion of thin terrace-forming deposits or weakly consolidated Tulare Formation on sparsely vegetated, south-facing slopes; terraces on the steeper south side of the gap may have been narrow initially, then removed by lateral stream erosion. Nevertheless, all other factors being equal, rapid uplift should help protect terraces from erosion by the stream that formed them. On the basis of elevated terraces it is difficult to infer latest Pleistocene or Holocene uplift of the Coalinga anticline across Los Gatos Creek.

CLAYEY SEDIMENT UPSTREAM OF THE ANTICLINE

Silty-clay soils of the Levis series, named for alluvial-fan soils 55 km northwest of Huron, were mapped by Harradine and others (1952) in gently sloping, poorly drained areas southwest of the Guijarral Hills (pl. 15.1). Harradine and others (1952, p. 36) interpreted the Levis of these areas as consisting of alluvium. We tested this interpretation against the lake-or-marsh hypothesis of King and Stein (1983) by drilling 10-cm-diameter auger holes 2 to 2½ m deep at three localities near the Guijarral Hills (pl. 15.1) and at one other locality in an analogous topographic setting southwest of Avenal Gap (fig. 15.1). In hand specimen, none of the augered deposits resembles the intermittent-lake deposits of nearby Tulare Lake (fig. 15.1), which are noticeably grayer and more abundantly mottled than the typical yellowish-brown (2.5Y 5/4 in Munsell notation) clayey silt of the Los Gatos Creek

TABLE 15.1.—*Drainage-basin area and maximum recorded discharge for principal creeks draining through the Coalinga anticline*

[n.d., not determined owing to incompleteness or absence of gaging data]

Creek	Drainage-basin area (km^2)	Maximum discharge (m^3/s)	Remarks
Los Gatos (upper part)[1]-----	270	128	Recorded during the February flood.
Warthan[2]----------	312	n.d.	---
Jacalitos[2]----------	230	n.d.	---
All streams above Turk Narrows (fig. 15.1).	1,040	500?	Liberally extrapolated from 1938 measurements in upper part of Los Gatos Creek; prorated for the nearly fourfold difference in drainage-basin area but not for the likelihood of relatively low runoff from such low-lying areas as Pleasant Valley and the Guijarral Hills.

[1]Above a point about 12 km northwest of Coalinga.
[2]Above confluence with Los Gatos Creek.

TABLE 15.2.—*Bankfull channel capacity along two reaches of Los Gatos Creek*

[Estimated from a form of the Mannings equation: $Q=\frac{AR^{2/3}S^{1/2}}{n}$; n is set at 0.035, a suitable value for rough, slightly brushy channels (Henderson, 1966)]

Reach	Channel dimensions and slope					Channel capacity (Q)
	Width (m)	Depth (m)	Cross-sectional area (m^2) (A)	Hydraulic radius (m) (R)	Slope (m^3/s) (S)	
Oudjiu[1]-------	180	8	1,440	7.35	0.00319	8,780
Turk Narrows--	60	7	420	5.68	.00328	2,190

[1]Aboriginal townsite described by von Werlhof and Vierhus (1956), located in plate 15.1 and figure 15.1.

alluvial fan (Atwater and others, 1986; see Meade, 1967, p. C7). Instead, the augered deposits consist of interbedded yellowish-brown silt and sand that is almost certainly alluvial except for 1.7 m of well-sorted, probably eolian sand in auger hole AH–5 (pl. 15.1). We also looked for lacustrine deposits in the banks of Los Gatos Creek upstream from the Coalinga anticline. We found no candidates, with the doubtful exception of two layers of yellowish-brown to grayish-brown fine and medium silt 2.0 to 2.5 m below the banktop about 1 km west of the mouth of Jacalitos Creek (locs. 9, 27, pl. 15.2). A smear of the grayer of these layers revealed no diatoms or ostracodes. Thus, if coseismic growth of the Coalinga anticline dammed Los Gatos Creek since deposition of the oldest deposits we have seen in auger sample or in outcrop (as long ago as 7,000 ^{14}C yr B.P.; pl. 15.2), the dam was so low or short lived that it left little or no stratigraphic evidence of the impoundment.

SINUOSITY ACROSS THE ANTICLINE

Los Gatos Creek is more sinuous upstream of the Coalinga anticlinal axis than at most places farther downstream, and it is least sinuous between the anticlinal axis and the mouth of Zapato Chino Creek (fig. 15.1). King and Stein (1983) interpreted the decrease in sinuosity downstream of the anticlinal crest as consistent with a broad uplift extending from the Coalinga anticline into Pleasant Valley. Flume experiments by Ouchi (1985), however, suggest that a stream meandering across actively uplifting alluvium should straighten upstream of the uplift and become more sinuous downstream, so as to maintain a constant channel gradient across a bulged alluvial plain (see Schumm, 1977, p. 137–140). The relatively low sinuosity of Los Gatos Creek in the western part of the anticline may be due to entrenchment into the Tulare Formation at Turk Narrows (pls. 15.1, 15.2). Sinuosity in the vicinity of the anticline may also be influenced by an abrupt increase in discharge and sediment load at the confluences with Jacalitos and Zapato Chino Creeks, by a decrease in discharge due to infiltration, and by variation in the width and depth of the arroyo. These complicating factors, together with the implications of Ouchi's experiments, argue against a strictly tectonic origin for variations in the sinuosity of Los Gatos Creek.

ALLUVIAL-PLAIN HUMP

Projected onto a generally straight-line profile (pls. 15.1, 15.2; fig. 15.1), the alluvial plain into which Los Gatos Creek is incised resembles two concave-upward profiles joined end to end (fig. 15.2). The junction, near the mouth of Jacalitos Creek about 2.5 km upstream of the Coalinga anticlinal axis, forms a hump as much as 10 m above a single concave-upward curve fitted to points farther upstream (near Coalinga) and downstream (near the mouth of Zapato Chino Creek). The thalweg of Los Gatos Creek forms a similar but shorter hump if similarly projected (King and Stein, 1983; Stein and King, 1984). Straight-line profiles for Zapato Chino Creek (King and

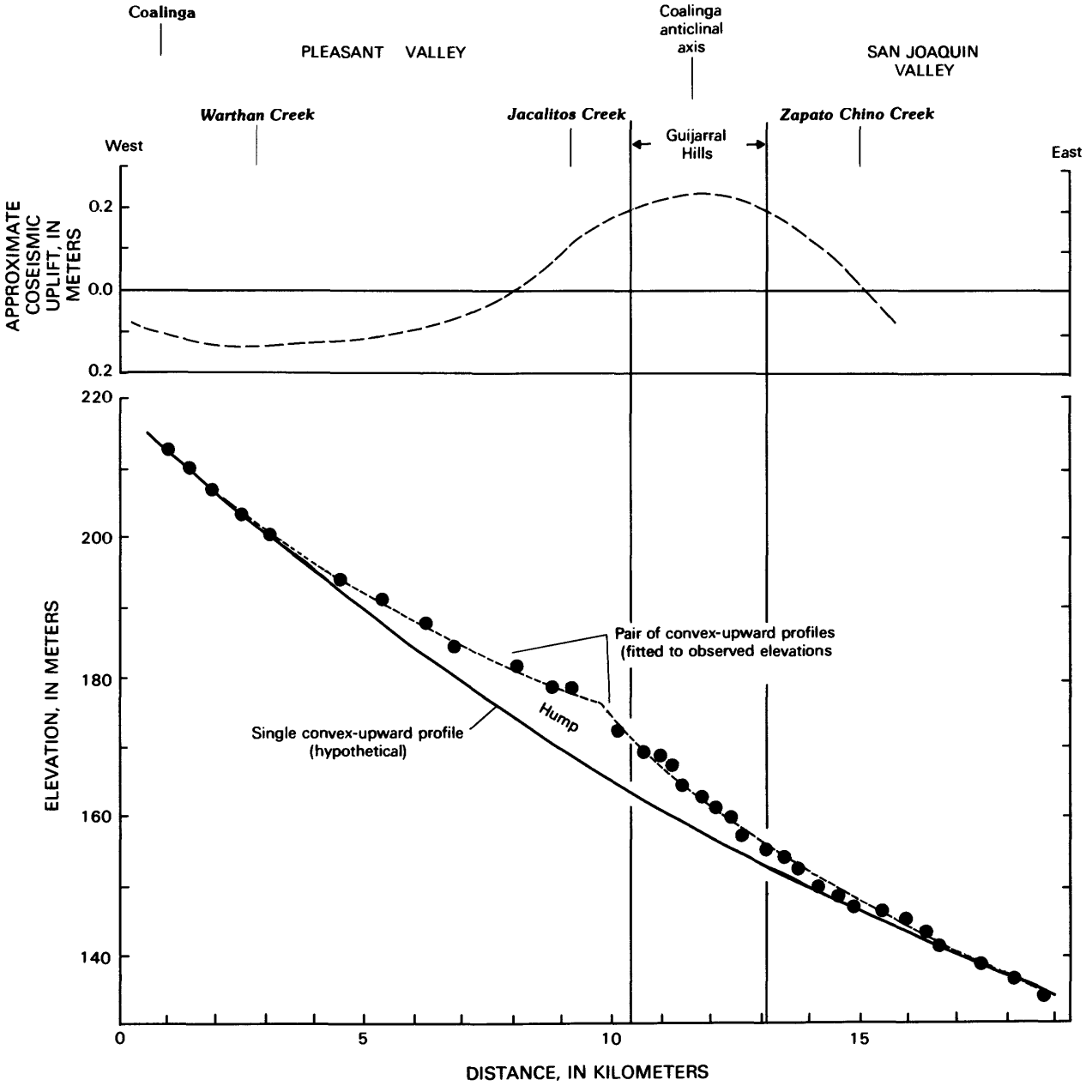

FIGURE 15.2.—Observed and hypothetical alluvial-plain profiles across the Coalinga anticline near Los Gatos Creek, compared with inferred 1983 coseismic change in elevation along that profile. Alluvial-plain profiles, mostly coincident with profile shown in plates 15.1 and 15.2, are redrawn from King and Stein (1983, fig. 2a). Dots show elevations from topographic contours on base maps for plate 15.1. Hypothetical profile was assumed by King and Stein (1983) to be that which the stream would follow in the absence of recent uplift along the Coalinga anticline; this assumption was questioned by Stein and King (1984) and by us. Curve showing inferred coseismic uplift is extrapolated from geodetic data plotted in plate 15.1, discussed in chapter 13.

Stein, 1983) and for the drainage through Avenal Gap likewise show alluvial-plain and thalweg humps cresting slightly upstream of the anticlinal ridges that these creeks skirt or cross.

The hump in the alluvial-plain profile beside Los Gatos Creek is the basis for the Holocene earthquake-recurrence estimate of Stein and King (1984). If this hump is a structural bulge formed chiefly during earthquakes of M=6–7, then the average repeat time for such earthquakes can be estimated from the relation $T=H^{-1}AU$, where T is the repeat time, H is the structural component of the height of the hump, A is the age of the youngest stratum uplifted a distance H within the hump, and U is the amount of coseismic uplift of the hump during a major (M=6–7) earthquake. Stein and King (1984) reckoned T at greater than 200 to 600 yr by setting H=0–10 m, A=2,500–10,000 yr, and U=0.6 m. With U=0.4 m, the maximum 1983 uplift near Los Gatos Creek relative to downdropped areas near Coalinga (pl. 15.1; fig. 15.2; see chap. 13), the minimum repeat time shortens to 100 to 400 yr. Still shorter repeat times, in the range 75–300 yr, seem permitted because at the crest of the alluvial-plain hump, the 1983 U value was only about 0.3 m with respect to Coalinga (fig. 15.2).

All these estimates of repeat time are doubtful because they depend on the assumption that the alluvial-plain hump is chiefly structural. If this hump is at least partly a depositional feature, then the repeat times suggested by it are no more than limiting minimums (Stein and King, 1984). We suspect that the hump is at least partly depositional. Suppose that, with Los Gatos Creek less incised than it is today, the combined floodflows of Los Gatos and Warthan Creeks routinely spread overbank onto the alluvial-plain floor of Pleasant Valley. Slowed by basal friction and diminished by infiltration, these flows readily aggrade the alluvial plain. The water gap through the Coalinga anticline, however, forces the overbank flows to converge with each other and with discharge from Jacalitos Creek. Thereby gaining depth and head as they enter a constriction, the overbank flows deposit relatively little sediment until spreading out again in the San Joaquin Valley. Thus, the stream builds an alluvial plain with two convex-upward reaches that join just west of the water gap; this junction creates the alluvial-plain hump upstream of the anticlinal axis.

We sought to lessen dependence on the assumption that the hump is chiefly depositional or chiefly structural, by comparing the present alluvial-plain profile with its underlying Holocene ancestors (fig. 15.3) rather than with a purely hypothetical profile, such as that shown in figure 15.2. Our stratigraphic approach is not free of paleogeographic assumptions, however, because it cannot work without a substantial parallelism of initial (undeformed) profiles. Moreover, even if the initial profiles are similar, successive smoothly sloping plains uplifted equally may be indistinguishable from a series of superimposed depositional humps that have not been

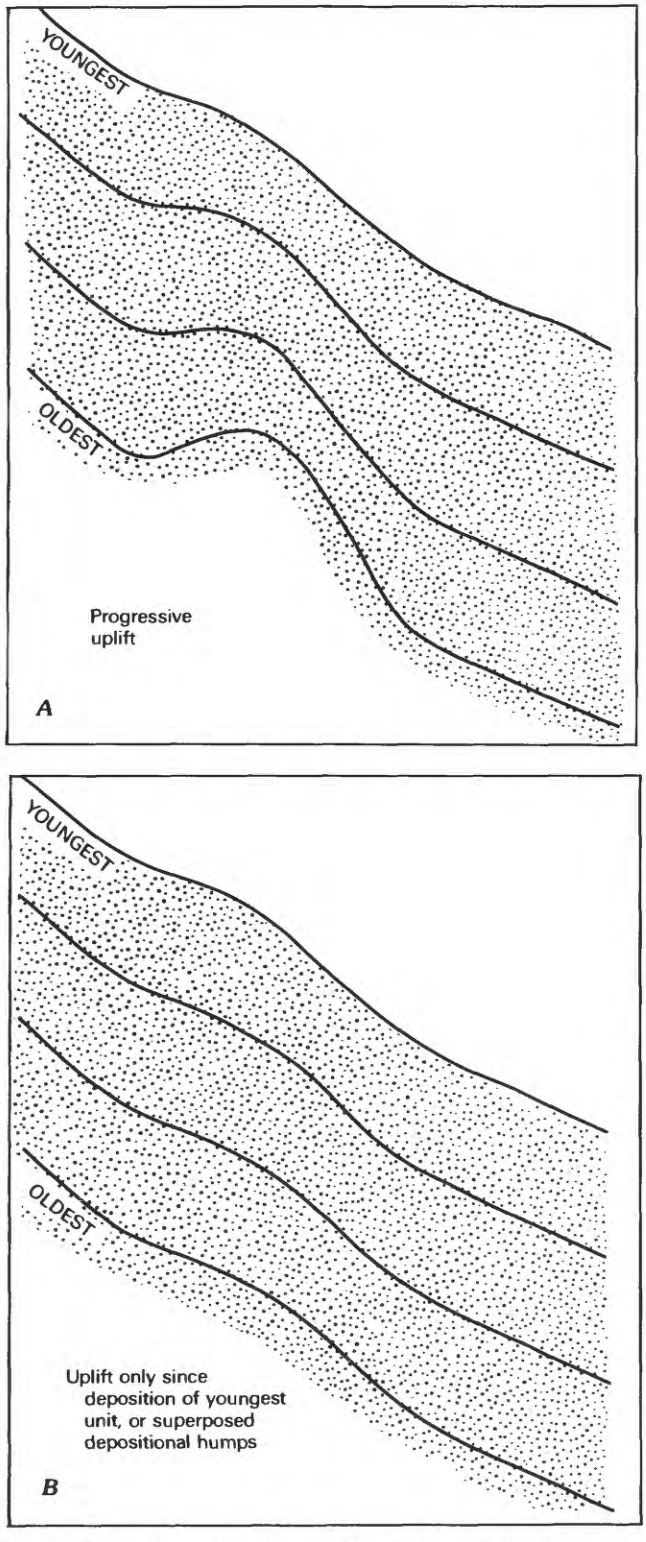

FIGURE 15.3.—Successive alluvial plains of similar initial profile as evidence of anticlinal uplift (*A*) or its absence (*B*). Compare with figure 15.2.

uplifted at all (fig. 15.3). Nevertheless, if cumulative coseismic uplift increases progressively with age in a stratigraphic sequence of alluvial plains across the Coalinga anticline, then such a sequence should provide constraints on the rates of uplift and the repeat times of earthquakes near Coalinga.

STRATIGRAPHIC EVIDENCE CONCERNING ANTICLINAL UPLIFT

Late Quaternary alluvial plains crossing the Coalinga anticline are well exposed only as buried stratigraphic features cropping out in the banks of Los Gatos Creek. The creekbank deposits can be divided into three main units. The oldest, the Tulare Formation, which is distinguished by moderate consolidation and the presence of conglomerate, is exposed only in Turk narrows. Similarly localized is the informally named side-stream alluvium, which is both unconsolidated and gravelly, probably derived from the Tulare Formation at the Guijarral Hills. The only widespread unit consists chiefly of sand and silt and localized gravel deposited by Los Gatos Creek and its major tributaries during the late Holocene. With two locally conspicuous subdivisions (figs. 15.4, 15.5) that extend across the anticline and contain much charcoal, this informally named main-stream alluvium is the only deposit that we found sufficient in extent and datable material to reveal the present configuration of successive late Quaternary alluvial plains across the Coalinga anticline.

MAIN-STREAM ALLUVIUM

STRATIGRAPHY

The main-stream alluvium makes up all the large exposures studied by us along Los Gatos Creek except

FIGURE 15.4.—Planar contact between lower and upper units of the main-stream alluvium, south bank of Los Gatos Creek downstream of the Coalinga anticline. Relatively light colored, sandy upper unit contains a fining-upward sequence that extends downward to contact. Underlying silt and minor sand, forming a low cliff, are assigned to lower unit. View eastward from locality 12 toward the mouth of Zapato Chino Creek (pls. 15.1, 15.2).

between Turk narrows and the mouth of Zapato Chino Creek, where it locally overlies exposed Tulare Formation and part of the side-stream alluvium, and where it may interfinger with another part of the side-stream alluvium (pl. 15.2). The minimum thickness of the main-stream alluvium generally equals the height of the exposure (max 10.5 m); more of the alluvium is evidently concealed by talus, inset-terrace deposits, and modern streambed deposits. The thickest exposed sections are between the mouth of Jacalitos Creek and the anticlinal axis (locs. 1, 7, 9, 24, 101) and in the San Joaquin Valley near the east end of our cross section (locs. 15, 16).

We subdivided the main-stream alluvium into two units on the basis of grain size, buried soils, and radiocarbon ages. The upper unit, chiefly 1 to 4 m thick, commonly contains more and coarser sand than beds of comparable thickness in the underlying lower unit (fig. 15.4). Buried soils in the upper unit lack $CaCO_3$ nodules and noticeable reddening; in contrast, some soils developed in the lower unit contain soft $CaCO_3$ nodules (firm calcareous concretions that can be cut with a knife) and are reddened from light olive brown (2.5Y 5/4), the dominant color of the alluvium, to yellowish brown (10YR). Radiocarbon ages from widely distributed localities in Pleasant Valley (locs. 3, 26), the Coalinga anticline (loc. 101), and the San Joaquin Valley (loc. 15) suggest an age of about 500 ^{14}C yr for the lowermost part of the upper unit (pl. 15.2). This age estimate allows projection of the upper-unit/lower-unit contact through ^{14}C-dated sections in which the upper unit is silty or the uppermost part of the lower unit is sandy and lacks conspicuous buried soils (locs. 1, 2, pl. 15.2).

FIGURE 15.5.—Outcrops (*A*, *B*) and columnar sections (*C-E*) of lower and upper units of the main-stream alluvium in Pleasant Valley and in the Coalinga anticline, exposed in banks of Los Gatos Creek (see pls. 15.1 and 15.2 for locations). Radiocarbon ages, in ^{14}C yr, on charcoal that is detrital (dots) or burned in place (diamonds). *A*, Locality 9, showing lenticular and sloping beds probably deposited as fill of a large channel about 2,500 ^{14}C yr B.P., succeeded by mostly tabular, thin-bedded silt and sand probably deposited overbank. Tallest part of vertical bluff is 9 m high. *B*, Locality 24, showing tabular beds probably deposited chiefly overbank, consisting of sand (light) and silt (dark). *C*, Locality 9 (see fig. 15.5*A*). *D*, Locality 24 (see fig. 15.5*B*). *E*, Locality 101.

Although the base of the upper unit typically is planar and conformable (fig. 15.4), disconformities locally form the contact between the upper and lower units and also appear to be common within the lower unit. The base of the upper unit defines talus-lined channel walls that truncate bedding in the lower unit at two localities near the mouth of Jacalitos Creek (locs. 8, 102, pl. 15.2). The disconformity at locality 8 cuts into the lower unit at least 4 m. Major disconformities within the lower unit are exposed near Jacalitos Creek between localities 9 and 86–12 and between localities 24 and 86–6. Additional major disconformities are suggested by lateral discontinuities in ^{14}C age within the lower unit, such as near Jacalitos Creek between localities 25 and 27 and in the Coalinga anticline between localities 100 and 101.

LITHOLOGY AND SEDIMENTARY STRUCTURES

Both units of the main-stream alluvium consist chiefly of laminated medium to coarse silt and very fine to fine sand (fig. 15.6). Coarser sand is widespread only in the San Joaquin Valley, near the east end of the cross section. Although gravel is abundant in natural outcrop only near Coalinga, at the west end of the cross section, trenching shows that the lower unit contains additional pebble and cobble gravel below the modern thalweg level of Los Gatos Creek in Pleasant Valley at localities 86–2, 86–3, 86–5, and 25 (pls. 15.1, 15.2). Sand grains are mainly quartz, feldspar, and lithic fragments. Ripple-drift cross-lamination and planar lamination of the lower flow regime make up most of the primary sedimentary structures. Secondary structures include mud cracks, raindrop imprints, animal burrows, and root fillings. Seams of gypsum and soft nodules of calcium carbonate are present in some strata whose lamination has been mostly or entirely destroyed by incipient soils. A few of these strata are slightly redder (to hue 10YR) than the typical olive brown, but none is a well-developed buried soil. Notable constituents of the main-stream alluvium include the following.

Flakes of serpentinite are locally abundant in cross-laminated sand. The only known sources of this serpentinite are the New Idria diapir, part of which lies within the drainage basin of the upper part of Los Gatos Creek, and smaller bodies of serpentinite in the drainage basin of Warthan Creek (see Jennings and Strand, 1959). This provenance justifies the genetic term "main stream" in our name for the alluvium.

Red iron oxide defines scores of lenses and layers 5 to 10 mm thick (pl. 15.2; fig. 15.6); most of these lenses and layers are in silt, but a few are in sand. The reddish color (chiefly hue 5YR) typically has an abrupt upper contact

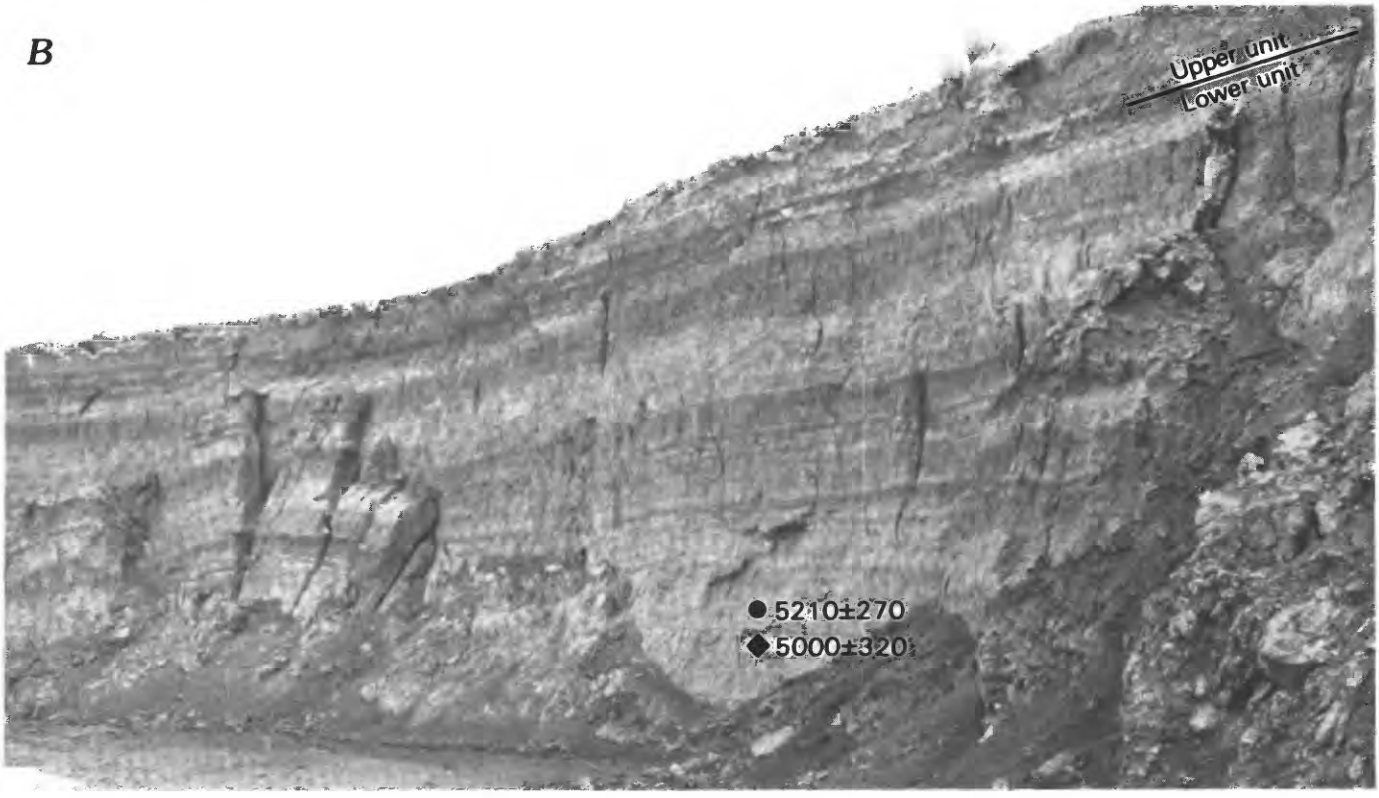

FIGURE 15.5.—Continued

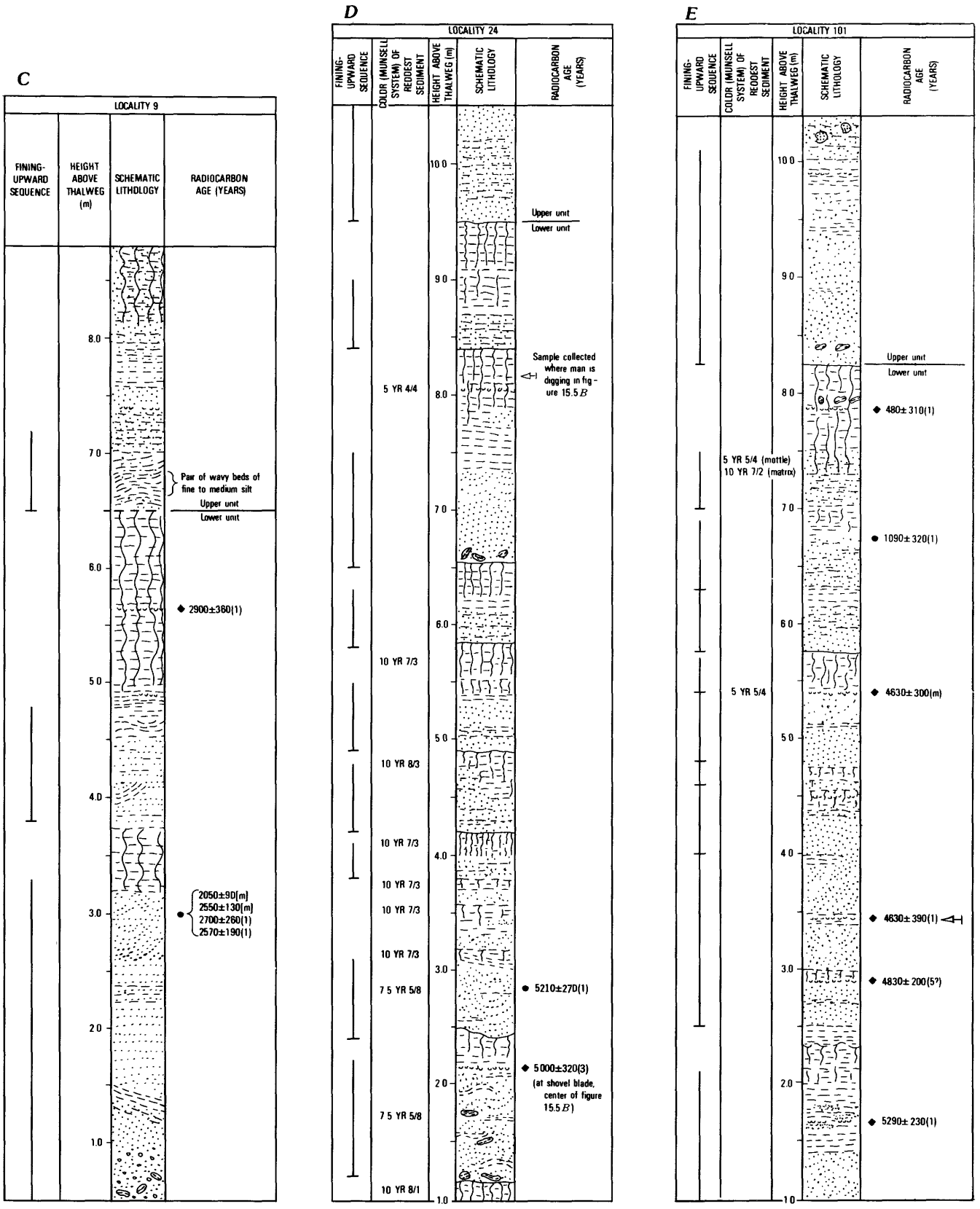

FIGURE 15.5.—Continued

and a gradational lower contact. Many of the upper contacts are veneered with millimeter-size flecks and twigs of charcoal, and the red sediment itself locally contains charred roots and stems in probable growth position. These features suggest fire. If each such noncoeval red layer or lens represents a fire, then alluvial-plain areas near Los Gatos Creek have been swept by probably 18 or more fires since 5,500 ^{14}C yr B.P. (fig. 15.7). Some of these fires may have been started by the native folk who left the artifacts discussed below; such purposeful burning is known to have been practiced widely in aboriginal California (Lewis, 1973).

Charcoal is associated not only with the red lenses and layers but also with crosslaminated, serpentinite-bearing, very fine sand. In this sand the charcoal is mostly rounded, less than 5 mm in diameter, and typically makes up less than 3 percent of the deposit. We interpret the charcoal associated with the red lenses and layers as the little-moved litter and below-ground remains of burned grass and shrubs; in contrast, we regard the charcoal in unreddened crosslaminated sand as relatively far-traveled detritus of charred shrubs and trees. Collectively, such burned-in-place and detrital charcoal provides all of our radiocarbon material except for charcoal from an animal burrow at locality 1 near the anticlinal axis, and except for wood from a log at locality 86–6 (pl. 15.2), near the mouth of Jacalitos Creek.

EXPLANATION

Grain size

Silt

Sand

Very fine and fine

Medium, coarse, and very coarse

Gravel—Rounded. Angular, probably cultural chert shown separately by arrow

Sandy silt and silty sand

Red (probably burned) silt

Gravel-size *rip*-up clast of silt

Sedimentary structures

Horizontal lamination

Crosslamination

Inclined bedding

Wavy bedding and draped lamination

Lamination disrupted by bioturbation, pedogenesis, or both—Line across top denotes sharp upper contact

Sand-filled burrow

Fining-upward sequence—Line across bottom of symbol indicates where base of sequence is exposed

Radiocarbon samples—Number following age denotes number of charcoal pieces dated. m, more than 10; parentheses, dating by accelerator and mass spectrometer; square brackets, dating by conventional (proportional-gas chromatography and liquid scintillation) methods

Charcoal dated

Detrital

Burned in place

FIGURE 15.5.—Continued

Vertebrate fossils are dominated by the remains of rabbits and rats (table 15.3), all of which appear to represent species found in or near the area today (C.A. Repenning, written commun., 1984). Some of the fossil rabbit bones come from the cultural deposit at locality 101 described in the following paragraph.

Human artifacts are preserved in burned layers of silt in main-stream alluvium near Oudjiu (locs. 24, 101, pl. 15.2; table 15.4). At locality 24 a concave-upward lens of burned silt—probably a hearth—yielded a percussion-flaked, apparently heat-altered piece of angular chert (fig. 15.8*A*). Nearby at locality 101, a burned layer yielded eight chert fragments (one of which is shown in fig. 15.8*B*), many broken animal bones, and a marine bivalve shell possibly of the family Arcidae (Louis Marincovich, Jr., written commun., 1988). This burned layer, probably a midden, is securely dated at about 4,600 ^{14}C yr B.P. (approx 5,300 calibrated yr B.P.; Pearson and others, 1986) on the basis of four stratigraphically consistent ^{14}C ages on burned-in-place charcoal. Human artifacts with ^{14}C ages earlier than 4,600 ^{14}C yr have been reported at only one locality in the San Joaquin Valley—near Buena Vista Lake, where mollusk shells associated with cultural remains yield ^{14}C ages ranging from 7,600 to 8,200 ^{14}C yr (Fredrickson and Grossman, 1977).

VERTICAL AND LATERAL SEQUENCE

Most wide outcrops of the main-stream alluvium contain tabular, fining-upward, gravel-free beds that are tens to hundreds of meters long and mainly less than 3 m thick. One to several such beds typically make up the alluvium's upper unit (fig. 15.4); others commonly make up most or all of the exposed lower unit (figs. 15.5*B*, 15.5*D*). Despite this abundance of extensively tabular beds, the main-stream alluvium also contains many beds that are lenticular at outcrop scale, some of which are part of fining-upward sequences that are thicker than 4 m. The best exposed of these sequences crops out continuously in 0.3 km of creekbank that includes localities 9 and 27, about 1.2 km upstream of the mouth of Jacalitos Creek. At locality 9, trough-crossbedded gravel and coarse sand grade upward through lenses of sand and silt into tabular silt that forms the uppermost part of the lower unit (figs. 15.5*A*, 15.5*C*). This overall upward fining is interrupted by a lens of bioturbated silt that is absent farther upstream at locality 27. Radiocarbon ages from localities 9 and 27, though mutually inconsistent by as much as 1,300 yr (tests 3, 4, 7, table 15.5) suggest rapid deposition of the overall sequence was underway by about 2,500 ^{14}C yr B.P. (pl. 15.2). A thick, overall

FIGURE 15.6.—Laminated silt and sand of lower unit of the main-stream alluvium near Oudjiu (loc. 100, pls. 15.1, 15.2), containing four red layers and one red lens (all labeled "R"). Ages, in ^{14}C yr, were obtained from burned-in-place charcoal in the reddened sediment. Faint horizontal marks on shovel handle are 10 cm apart.

fining-upward sequence is also exposed nearby in the upper unit at locality 8. The beds in this sequence lack gravel and trough crossbedding and terminate, in buttress unconformity, against the disconformity that is cut into the lower unit. A radiocarbon age of about 200 ^{14}C yr from one of the lowest of these beds indicates rapid deposition of the sequence.

DEPOSITIONAL ENVIRONMENT

Many of the thin, tabular fining-upward beds in the main-stream alluvium were probably deposited in overbank areas rather than in well-defined, vertically aggrading or laterally migrating channels. Even the sandy parts of some fining-upward beds, such as the lower part of the upper unit shown in figure 15.4, appear to represent overbank deposition, because of their great lateral continuity and absence of basal disconformity. Similarly, there is little sign of channeling in such deposits as those shown in figure 15.5*B*.

Most of the lenticular beds and thick fining-upward sequences in the main-stream alluvium probably formed in vertically aggrading or laterally migrating channels. Some of these channels were active courses of the main stream, as indicated at locality 9 by the lenses of trough-crossbedded coarse sand and gravel. Others apparently had been abandoned and then were filled by slackwater deposits of floods, as implied at locality 8 by the absence of coarse crossbedded fill. The narrowness (11 m, greatly exaggerated in pl. 15.2) of the filled

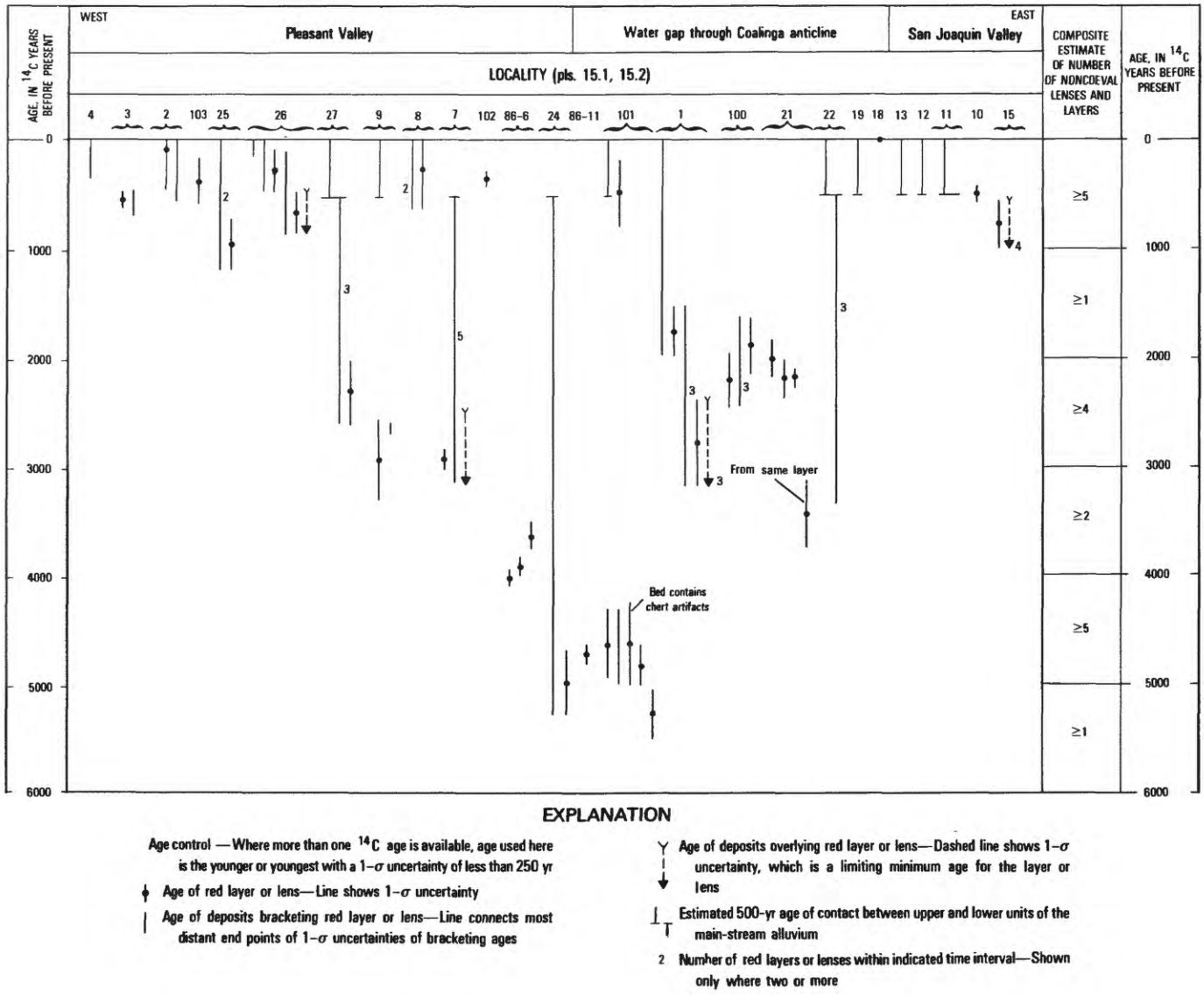

FIGURE 15.7.—Ages and spatial distribution of red layers and lenses (fig. 15.6) in alluvium along Los Gatos Creek. We found 82 red layers and lenses (pl. 15.2), at least 18 of which are probably noncoeval with one another (see composite column).

TABLE 15.3.—*Vertebrate fossils from late Holocene alluvium along Los Gatos Creek*

[Identifications by C.A. Repenning, 1984; localities listed from west to east. Do., ditto]

Locality (pls. 15.1, 15.2)	Height above thalweg (m)	Fossil	Estimated age (^{14}C yr B.P.)	Evidence of age (pl. 15.2)
2	3.97	Dipodomys sp. aff. D. heermani (kangaroo rat), incomplete innominate.	500	Age on detrital charcoal from same deposit.
101	3.35	Rabbit toe (claw) bone, possibly Lepus sp.	4,700	Age on bracketing deposits of burned-in-place charcoal.
101	2.90	Seven fish vertebrae, three fish ribs; mammalian bone fragments, possibly rabbit.	4,800	Age on burned-in-place charcoal from same deposit.
22	4.70	Lepus sp. cf. L. californicus (jackrabbit), mandible.	500-3,300	Age on burned-in-place charcoal 1.8 m below the sample, and estimated age of upper-unit/lower-unit contact, fragments.
14	6.3	Sylvilagus sp. (cottontail), tibia and vertebra.	0-500	Within upper unit.
14	4.45	Dipodomys sp. aff. D. ingens (kangaroo rat), pes.	0-500	Do.

channel at locality 8 further suggests that this channel originated as a gully analogous to those of the modern landscape 0.5 km south of locality 8 and, farther east, at Oudjiu (pl. 15.1).

AGE

Radiocarbon ages on charcoal from the exposed main-stream alluvium range from about 7,000 ^{14}C yr to modern. The youngest ages from the lower unit are 330±200 and 480±310 ^{14}C yr; ages from the upper unit range from 610±170 ^{14}C yr to modern.

We attempted to check the accuracy of individual ages by testing their stratigraphic consistency, because of concern that a charcoal age might substantially exceed the age of the deposit. For example, detrital-charcoal ages obtained from some modern Australian stream deposits are as old as 1,500 ^{14}C yr (Blong and Gillespie, 1978). One of our detrital-charcoal populations shows an age discordance that might approach 1,500 yr (test 4, table 15.5). However, other detrital-charcoal populations suggest much less discordance, and the ages obtained from superposed, laterally equivalent, and near-modern samples suggest that most of our detrital-charcoal ages do not exceed the deposit age by more than about 800 yr (tests 5–8). Similar tests (1–3) likewise indicate that most of the ages obtained from burned-in-place charcoal closely approximate the age of the host deposit. We also applied the chi-square distribution test to check the statistical consistency of individual charcoal populations, using the procedures outlined by Wilson and Ward (1981). This test shows that three out of our seven detrital-charcoal populations have significant statistical difference, whereas only one out of our seven burned-in-place charcoal populations has any significant statistical difference (tests 1, 4).

DEPOSITIONAL HISTORY

The main-stream alluvium appears to record at least three episodes of incision and one episode of exceptionally vigorous aggradation that predate cutting of the present arroyo. The earliest recorded episode of incision occurred before about 3,900 ^{14}C yr B.P., as recorded by a channel fill at locality 86–6. Another episode of incision before about 2,500 ^{14}C yr B.P. would account for the channel filled by the lower part of the section at localities 9 and 27 (figs. 15.5*A*, 15.5*C*), and might partly explain the scarcity of deposits between 4,500 and 1,000 ^{14}C yr B.P. in the middle of the section at locality 101 (pl. 15.2; fig. 15.5*E*). A still later episode of downcutting, during which coarse sediment was confined to incised channels, may have also contributed to that scarcity and, furthermore, would account for the common fineness of grain size in the upper part of the lower unit relative to the lower part of the upper unit. This later downcutting may have formed the paleochannel at locality 8, which was cut before 220±400 yr ^{14}C B.P. into deposits dated nearby at about 2,500 ^{14}C yr B.P. (locs. 7, 9, pl. 15.2.). The exceptional aggradation marked by the upper unit began about 500 ^{14}C yr B.P. (approx 500 calibrated yr B.P.; Stuiver and Pearson, 1986) and ceased before A.D. 1854 or 1933 (see section above entitled "Physical Setting"). This aggradation shows no sign of long-term (1,000–10,000 yr) upstream migration of the locus of deposition, such as that detected at Cajon Creek, southern California, by R.J. Weldon (written commun., 1984).

Many tens of meters of latest Pleistocene aggradation and incision in the eastern San Joaquin Valley are known to have resulted from glacially induced change in sediment yield from the Sierra Nevada (Arkley, 1962; Janda and Croft, 1967; Marchand and Allwardt, 1981). By analogy, climatic change in the nonglaciated southern Coast Ranges probably contributed to the episodic

TABLE 15.4.—*Human artifacts from late Holocene alluvium along Los Gatos Creek*

Specimen (fig. 15.8) / Property	24J (loc. 24, 8.2 m above thalweg)	101Q (loc. 101, 3.45 m above thalweg)
Context (pl. 15.2; figs. 15.5B, 15.5D, 15.5E)	2.2 m below top of creekbank in otherwise gravel-free deposits (at point of knife held by person in fig. 15.5B); estimated age, 500 to 2,000 yr B.P.	In burned layer of silt dated at 4,630±390 ^{14}C yr B.P. located 7 m below top of creekbank.
Category	Unmodified flake struck from a larger piece of stone.	Unmodified flake struck from a larger larger piece of stone.
Material	Reddish-brown and yellowish-brown chert referable to the Franciscan assemblage. Vitreous luster and feathered distal margin (see below) suggest heat treatment, which causes structural changes that make microcrystalline materials easier to flake (Crabtree and Butler, 1964).	Reddish-brown chert referable to the Franciscan assemblage. Dull surface luster and step fracture (see below) suggest that the material probably was heat treated. Unflaked surface of striking platform suggests that raw material was a stream cobble.
Dimensions (mm):		
Length	33	61
Width	22	44
Thickness	3	16
Platform thickness	Unknown	15
Striking platform (surface receiving the force that detached the flake).	Collapsed; probably crushed during removal.	Natural surface of waterworn cobble.
Flake angle (with respect to platform).	Probably low	Detached at 72°. Two previous flake removals on dorsal surface were detached at 88° and 69°.
Dorsal surface	Three negative flake scars indicating previous removals from proximal margin.	Three negative flake scars indicate that previous flakes were removed from core. one scar exhibits a step fracture where the flake terminated abruptly at a right-angle break.
Ventral surface	Pronounced ripple marks and large bulbar scar that indicate flake was removed by a strong force.	Bulb of percussion makes up much of surface. Flake scar lacks ripple marks and has split longitudinally along a natural check (flaw) in the stone. Some retouching or damage is present on one lateral margin.
Flake termination	Feathered (sharp) distal margin	Stepped termination with irregular distal margin.
Interpretation	Percussion-thinning flake probably produced during manufacture of a bifacial artifact from heal-altered Franciscan chert.	Percussion-struck flake removed from core produced from stream cobble of Franciscan chert that had not been heat treated.
Context (pl. 15.2; fig. 15.5E)	In burned layer of silt dated at 4,630±390 ^{14}C yr B.P. located 7 m below top of creekbank.	In burned layer of silt dated at 4,630±390 ^{14}C yr B.P. located 7 m below top of creekbank.
Category	Unmodified flake struck from a larger piece of stone.	Unmodified flake struck from a larger piece of stone.
Material	Reddish-brown chert referable to the Franciscan assemblage.	White chert referable to the Franciscan assemblage. Feathered distal margin suggests heat treatment.
Dimensions (mm):		
Length	13	15
Width	9	9
Thickness	5	4
Platform thickness	Unknown	Unknown
Striking platform	Prepared by previous flake removal	Prepared by previous flake removal.
Flake angle (with respect to platform).	Detached from core at 77°	Detached from core at 78°.
Dorsal surface	One negative flake scar indicating previous removal.	One negative flake scar indicating previous removal.
Ventral surface	Bulb of percussion and bulbar scar present. The flake has split longitudinally.	Bulb of percussion present. The flake has split longitudinally.
Flake termination	Snapped	Feathered (sharp) distal margin.
Interpretation	Percussion-struck flake removed from a prepared core produced from Franciscan chert.	Percussion-struck flake produced during manufacture of a stone artifact from probably heat-altered Franciscan chert.

Holocene incision and aggradation that we infer for Los Gatos Creek. The types of climatic change are not easily specified, however, because of uncertainties in our dating of aggradation and incision, and because of the scarcity of paleoclimatic data directly applicable to the late Holocene of the southwestern San Joaquin Valley. Our best dated and most noteworthy event, the aggradation that formed the upper unit, coincides at least in part with a relatively cool and wet period in southwestern California. This period, dated at 550 to 300 sidereal yr B.P., succeeded a relatively warm and dry period in southeastern California, according to the bristlecone-pine records of LaMarche (1974, fig. 6). If these records are applicable to the catchments of Los Gatos Creek and its tributaries, then the upper unit of the main-stream alluvium may reflect a relative climatic shift from warm and dry to cool

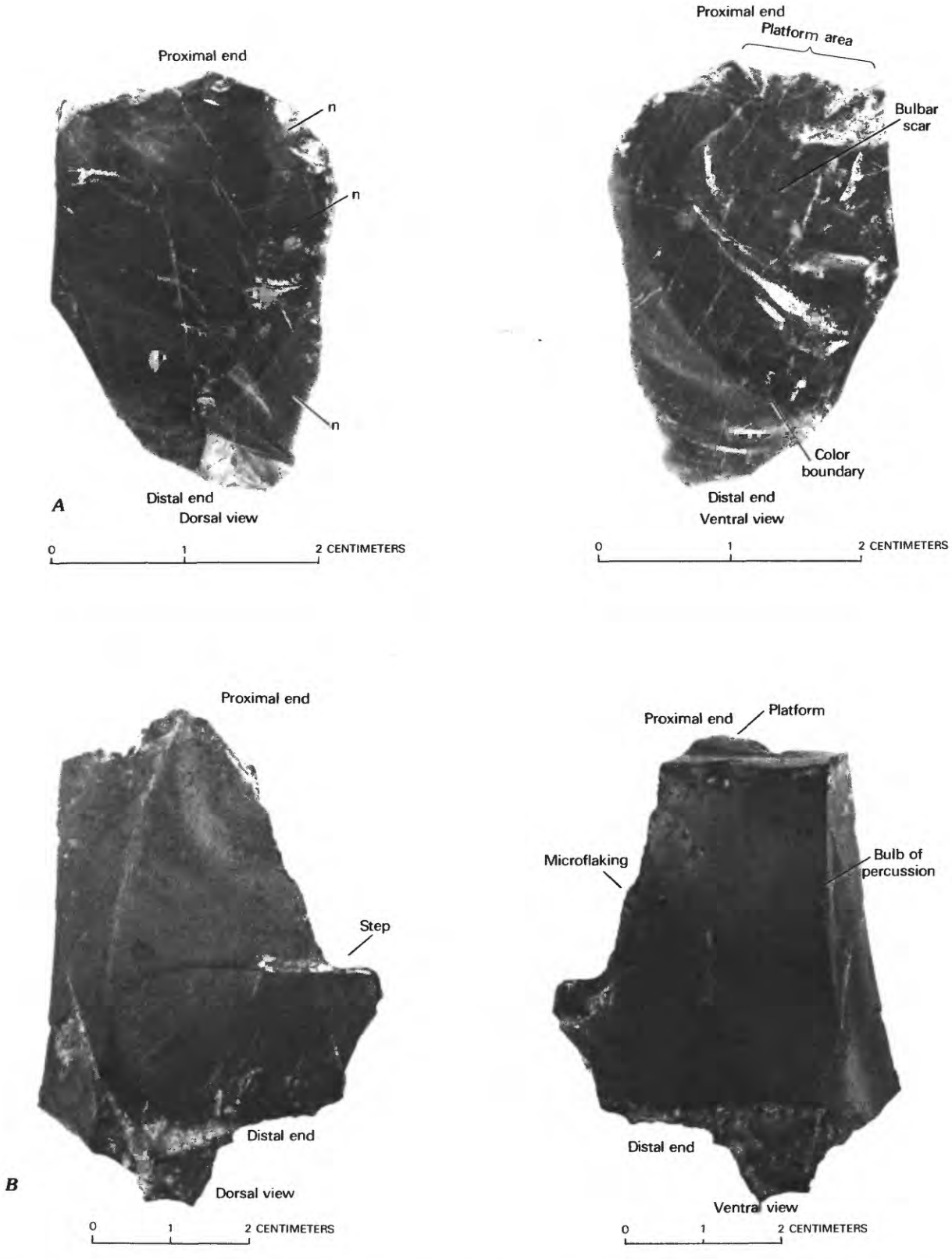

FIGURE 15.8.—Human artifacts from late Holocene alluvium along Los Gatos Creek (table 15.4). *A*, Chert flake from locality 24; n, negative flake scar. *B*, Chert flake from locality 101.

TABLE 15.5.—*Tests of the stratigraphic consistency of ^{14}C ages on charcoal from Holocene alluvium along Los Gatos Creek*

[Horizontal lines denote stratigraphic superposition of samples and ages being compared: Samples and ages below line are those used to infer limiting-maximum age of the deposit whose charcoal samples and ages are shown above line. Slant (test 7) denotes probable lateral equivalence of sample 27A with samples 9Q, 9X, 9X1, and 9X3. Numbers after ages denote number of pieces of charcoal dated: m, more than 10; parentheses, accelerator/mass-spectrometer age; brackets, conventional (proportional gas or liquid scintillation) age. Inconsistencies are at the 1-σ-uncertainty level reported by the radiocarbon laboratories (see pl. 15.2); in tests 2, 3, 5, and 6, maximum inconsistency equals overlap between oldest apparent age above line and youngest apparent age below line. *Do., ditto*]

Test	Sample (pl. 15.2)	Age (^{14}C yr B.P.)	Type	Inconsistency (^{14}C yr)	Test statistic (T)	Implication
1. Concordance of ages on different pieces of burned-in-place charcoal from the same deposit.	3D3 3D4	685±95(1) 520±55(10)	Discordance within deposit.	15-315	[1]2.26	Discordance is probably less than 500 yr within most deposits of burned-in-place charcoal; exception is age range 880-1,660 ^{14}C yr B.P. in sample 21A.
	26C1 26C2 26C3	740±210(1) 640±190(1) 510±430(1)	do	0-870	[1]2.74	
	1F2 1F3	1,830±240(1) 1,720±240(3)	do	0-390	[1].11	
	21C1 21C2	1,990±170(2) 2,040±300(1)	do	0-520	[1].02	
	21A 21A1	2,150±80[m] 3,420±310(1)	do	880-1,660	15.74	
2. Consistency of age on burned-in-place charcoal with limiting maximum deposit age implied by age on underlying burned-in-place charcoal.	26D1 26C1, 26C2, 26C3	260±200(1) 740±210(1), 640±190(1), 510±430(1)	Charcoal age exceeds limiting-maximum deposit age.	0-380	---	Age on burned-in-place charcoal typically accords with stratigraphic order and probably does not exceed deposit age by more than 400 yr in most samples but possibly exceeds deposit age by 800 yr or even more.
	101X	480±310(1)	do	0	---	
	101F	4,630±300(m)	do	0-690	---	
	101E	4,630±390(m)	do	0-390	---	
	101C	4,830±200(5?)	do	0	---	
	101Z	5,290±230(1)				
	100C 100A	2,190±250(2) 1,860±250(m)	do	0-830	---	
	1F2, 1F3 1A	1,830±240(1), 1,720±240(1) 2,760±400	do	0	---	
3. Consistency of age on burned-in-place charcoal with limiting maximum deposit implied by age on underlying detrital charcoal.	3D3, 3D4 3B	685±95(1), 520±55(1) 570±50[m]	do	0-250	---	Do.
	2C 2A	50±390(m) 750±45[m]	do	0	---	
	9A2 9Q, 9X, 9X1, 9X3	2,900±360(1) 2,050±90[m], 2,550±130[m], 2,700±260(1), 2,570±190(1)	do	0-1,310	---	
	101X 101G	480±310(1) 1,090±320(1)	do	0-70	---	
4. Concordance of ages on different pieces of detrital charcoal from the same deposit.	3E1 3E2	100±70(1) 170±80(1)	Discordance within deposit.	0-200	[1].43	Discordance varies within deposits of detrital charcoal; range is less than a few hundred years in some deposits, as much as 1,500 in others.
	3A 3A1 3A3 3A4	665±40[m] 670±80(1) 860±210(1) 700±80(1)	do	0-480	[1].94	
	2B 2B1 2B2	510±50[m] 1,210±190(1) 520±90(1)	do do	460-490 (2B vs. 2B1) 0-150 (2B vs. 2B2)	12.81	
	26E1 26E2	25±100(1) 450±220(1)	do	0-670	[1]3.09	
	9Q 9X 9X1 9X3	2,050±90[m] 2,550±130[m] 2,700±260(1) 2,570±190(1)	do	0-1,000	15.77	
	7Y1 7Y2	2,790±340(1) 3,530±360(2)	do	40-1,440	[1]2.23	
	102C1 102C2	-270±185(1) 610±170(2)	do	440-780	5.90	

5. Consistency of detrital-charcoal age with limiting maximum deposit age implied by age on underlying burned-in-place charcoal.	3E1, 3E2 / 3D3, 3D4	100±70(1), 170±80(1) / 685±95(1), 520±55(10)	Charcoal age exceeds limiting-maximum deposit age.	0	---	Detrital-charcoal age may exceed deposit age by 800 yr or more, or by 50 yr or less.
	26E1, 26E2 / 26D1	25±100(1), 450±220(1) / 260±200(1)	do	0-5 (26E1) 0-610 (26E2)	---	
	102C1, 102C2 / 102B	-270±185(1), 610±170(2) / 320±70(1)	do	0 (102C1) 50-530 (102C2)	---	
	24C / 24A2	5,210±270(1) / 5,000±320(3)	do	0-800	---	
	101G / 101F	1,090±320(1) / 4,630±300(m)	do	0	---	
6. Consistency of detrital-charcoal age with limiting maximum deposit age implied by age on underlying detrital charcoal.	3E1, 3E2 / 3B / 3A, 3A1, 3A3, 3A4	100±70(1), 170±80(1) / 570±50[m] / 665±40[m], 670±80(1), 860±210(1), 700±80(1)	do	0-30	---	Do.
	2A / 2B, 2B1, 2B2	750±45[m] / 510±50[m], 1,210±190(1), 520±90(1)	do	0-365	---	
7. Consistency of detrital-charcoal age with deposit age suggested by age on buried-in-place charcoal from probable lateral equivalent of detrital-charcoal-bearing deposit.	9Q/ 9X/ 9X1/ 27A (burned in place)/ 9X3 (detrital)	2,050±90[m]/ 2,550±130[m]/ 2,700±260(1)/ 2,280±205(1)/ 2,570±190(1)	Discordance between ages on detrital and burned-in-place charcoal.	0-895	---	Detrital-charcoal age may exceed deposit age by as much as 900 yr, but typical discordance is probably less than 600 yr, possibly negligible.
8. Youthfulness of detrital-charcoal near present alluvial-plain surface.	3E1 3E2	100±70(1) 170±80(1)	Charcoal age exceeds bypothetical zero age of deposit.	30-250	---	Detrital-charcoal age may exceed deposit age by as much as 800 yr; actual discordance is less than the maximum if, as is likely, at least two of these deposits predate the 20th century.
	26E1 26E2	25±100(1) 450±220(1)	do	0-670	---	
	102C1 102C2	-270±185(1) 610±170(2)	do	0-780	---	

[1]No significant difference among samples at $p<0.05$.

and wet. This shift may have been sufficient to boost sediment-transport capacity (runoff) without greatly increasing the effectiveness of vegetation in preventing drainage-basin erosion (see Schumm, 1977, p. 29, 44–46).

The approximately 10 m of mostly overbank-facies alluvium younger than 5,300 ^{14}C yr (approx 6,000 calibrated yr B.P.; Pearson and others, 1986) at the upstream edge of the Coalinga anticline (locs. 24, 101) implies that Los Gatos Creek has aggraded at that part of the anticline at an average rate of nearly 2 m per 1,000 years during the late Holocene. This rate is some 2 to 3 times faster than post-Wisconsin aggradation of the toe of the Los Gatos Creek fan beside Tulare Lake, where the uppermost 10 m of Los Gatos Creek alluvium spans the past 10,000 to 15,000 ^{14}C yr (Atwater and others, 1986, fig. 6A). Therefore, although the wet-year level of Tulare Lake has been higher during the Holocene than during most of the Wisconsin (Atwater and others, 1986), a high Holocene base level at Tulare Lake does not seem responsible for the relatively rapid late Holocene aggradation by Los Gatos Creek at the Coalinga anticline.

CONFIGURATION OF BURIED ALLUVIAL PLAINS

Among the alluvial plains that pass through the lower unit of the main-stream alluvium, those we have reconstructed most widely date from about 1,000, 2,000, 2,500, and 5,000 ^{14}C yr B.P. (approx 1,000, 1,900–2,000, 2,400–2,700, and 5,600–5,900 calibrated yr B.P.; Stuiver and Pearson, 1986; Pearson and Stuiver, 1986; Pearson and others, 1986). We represent each of these plains by a profile line in plate 15.2—a line that probably samples a family of plains from an interval of several hundred years. We used two rules of thumb in drawing the lines: (1) The profile for a plain of a given age should be drawn through the highest overbank deposits of that age and can be projected across areas from which those deposits may have been eroded; and (2) insofar as is possible, the profile for a plain of a given age should not be drawn through the lower part of a fining-upward sequence of that age. This second rule presupposes that most fining-upward sequences in the main-stream alluvium formed in a geologic instant (representing much less time than the stratigraphic intervals dominated by burrowed or bioturbated silt) within channels incised at least partly below alluvial-plain level (except possibly for tabular, extensive fining-upward sequences like that shown in fig. 15.4).

The 1,000-^{14}C-yr-B.P. plain lies a little below the base of the upper unit where that basal contact is conformable. Additional constraints are ^{14}C ages of about 1,000 ^{14}C yr on detrital charcoal near Oudjiu (loc. 101), 1,700 to 2,000 ^{14}C yr on burned-in-place charcoal near the anticlinal axis (locs. 1, 21), and 1,600 ^{14}C yr on detrital charcoal at the east end of the cross section (loc. 16).

The 2,000-^{14}C-yr-B.P. plain probably lies at or slightly above presumable overbank deposits of the uppermost part of the lower unit near the mouth of Jacalitos Creek, at localities 9 (fig. 15.5) and 27 (pl. 15.2). Farther downstream, near the anticlinal axis, this plain also appears to lie in the uppermost part of the lower unit, as shown by concordant pairs of ^{14}C ages near 2,000 ^{14}C yr on burned-in-place charcoal from localities 1 and 21. In between, near Oudjiu at locality 101, evidence of the 2,000-^{14}C-yr-B.P. plain may have been eroded from the interval between deposits dated at 4,630±300 and 1,090±320 ^{14}C yr (pl. 15.2). Both the 1,000- and 2,000-^{14}C-yr-B.P. plains appear to be truncated, probably by a concealed disconformity, upstream of locality 27.

The earliest alluvial plain that we have traced from Pleasant Valley to the axis of the Coalinga anticline dates from about 2,500^{14}C yr B.P. This plain nearly parallels the present alluvial plain (whose age is 200–500 ^{14}C yr) from eastern Pleasant Valley (locs. 7, 9) through the west flank of the anticline (loc. 101), to the axial part of the anticline (locs. 1, 21). The 2,500-^{14}C-yr-B.P. plain is probably near the top of the lower unit in Pleasant Valley because, though ranging from 2,100 to 2,900 ^{14}C yr, the six ages on the channel fill at localities 9 and 27 average about 2,500 ^{14}C yr and include one age of 2,900±360 ^{14}C yr on burned-in-place charcoal high in the fill.

The alluvial plain of about 5,000 ^{14}C yr B.P. is the oldest one that we have traced from Pleasant Valley onto the Coalinga anticline. This plain nearly parallels the present alluvial plain from western Pleasant Valley nearly to the axis of the Coalinga anticline. Constraining ^{14}C ages come from detrital charcoal at two localities in Pleasant Valley (86–3, 86–12) and from burned-in-place charcoal at two localities on the west flank of the anticline (24, 101). Because detrital charcoal elsewhere in the main-stream alluvium is typically less than about 800 yr older than its host deposit (table 15.5, tests 5, 6, 7), we plot the 5,000-^{14}C-yr-B.P. plain above the detrital-charcoal sample dated 6,920±170 ^{14}C yr at locality 86–3 and at the top of the fining-upward sequence with a detrital-charcoal age of 5,780±140 ^{14}C yr at locality 86–12. The 5,000-^{14}C-yr-B.P. plain would remain above the 6,920-^{14}C-yr-old detrital charcoal at locality 86–3 even if that charcoal predated its host deposit by 1,500 yr, which is the maximum discordance permitted by ages on detrital charcoal elsewhere in the main-stream alluvium (table 15.5, test 4).

STRUCTURAL SIGNIFICANCE OF BURIED ALLUVIAL PLAINS

The buried alluvial plains of 2,000-, 2,500-, and 5,000 ^{14}C yr B.P. are those best suited for gaging anticlinal uplift because they are the oldest that can be traced from

synclinal Pleasant Valley onto the Coalinga anticline. The other widely traced alluvial plains shown in plate 15.2 (the plain of 1,000 ^{14}C yr B.P. and the plain of approximately 500 ^{14}C yr B.P. that is defined by conformable parts of the base of the upper unit) are so young that their depositional features may have greater amplitude than any bulge created by anticlinal growth. These depositional features could include broad alluvial-plain humps (figs. 15.2, 15.3), as well as natural levees, surficial examples of which are subtle or absent along most of Los Gatos Creek but are as high as 1.5 m near the mouth of Zapato Chino Creek (pl. 15.1). Although also subject to undulation from levees and humps, the 2,000-, 2,500-, and 5,000-^{14}C-yr-B.P. plains provide evidence that late Holocene anticlinal uplift has averaged less—probably much less—than 1 m per 1,000 sidereal yr.

The anticlinal uplift that can be inferred most reasonably from the 2,000-^{14}C-yr-B.P. alluvial plain is implied by 1.5 m of apparent convergence of the 2,000-^{14}C-yr-B.P. plain toward the present alluvial plain between Pleasant Valley (loc. 9) and the axial part of the Coalinga anticline (loc. 21). If this convergence is a primary depositional feature of the 2,000-^{14}C-yr-B.P. plain (say, a high natural levee at loc. 21) or of the present alluvial plain (say, a high hump at loc. 9), then no anticlinal uplift is indicated (figs. 15.9*A*, 15.9*B*); but if the initial profiles of the 2,000-^{14}C-yr-B.P. plain and the present alluvial plain were parallel, then the 1.5 m of convergence toward locality 21 signifies 1.5 m of uplift at locality 21 (fig. 15.9*C*). Greater uplift is indicated if the initial profiles converged toward Pleasant Valley, as could be the case if the depositional hump at locality 9 was higher 2,000 ^{14}C yr B.P. than it is today (fig. 15.9*D*). In all these examples, the period of record is 1,500 to 1,900 yr long because the present alluvial plain is no older than the lowermost part of the upper unit (approx 500 calibrated yr) and probably no younger than incision of the present arroyo in Pleasant Valley and in the Coalinga anticline (A.D. 1933, 1854, or earlier; see section above entitled "Physical Setting"). Therefore, the alluvial plain of 2,000 ^{14}C yr B.P. (1,900–2,000 calibrated yr B.P.; Stuiver and Pearson, 1986) indicates that uplift of the Coalinga anticline between 2,000 and 500–100 sidereal yr B.P. probably was in the range 0 to 1 m per 1,000 yr, provided that the initial alluvial-plain profiles of those ages were parallel or eastward convergent between localities 9 and 21.

The approximate present parallelism of the 2,500-^{14}C-yr-B.P. plain and the present alluvial plain (pl. 15.2) also suggests that the Coalinga anticline has grown across Los Gatos Creek no faster than 1 m per 1,000 yr. This parallelism implies little or no uplift, unless it resulted from fortuitous superposition of a natural levee or depositional hump younger than 2,500 ^{14}C yr atop a structural hump in the 2,500-^{14}C-yr-B.P. plain. Such superposition cannot be ruled out because it is consistent with the 2-m vertical separation of the 2,000- and 2,500-^{14}C-yr-B.P. plains near the anticlinal axis at localities 1 and 21. But if a 2-m-high structural bulge in the 2,500-^{14}C-yr-B.P. plain was covered by a parallel depositional hump by 2,000-^{14}C yr B.P., then the Coalinga anticline grew by 2 m within about 500 to 800 sidereal yr. Such rapid growth would have to have been anomalous because, had the anticline grown 2.5 to 4 m per 1,000 yr throughout the late Holocene, the 2,000-^{14}C-yr-B.P. plain would have been uplifted on the anticline by 5–8 m, the 2,500-^{14}C-yr-B.P. plain by 6–11 m, and the 5,000-^{14}C-yr-B.P. plain by 17–23 m—amounts that surely would be conspicuous in profile (pl. 15.2).

Much less than than 1 m of net anticlinal uplift per 1,000 yr best explains the present configuration of the 5,000-^{14}C-yr-B.P. plain. This plain apparently diverges from the present alluvial plain between Pleasant Valley and the axis of the Coalinga anticline (pl. 15.2). Such divergence would imply that the western flank of the Coalinga anticline has undergone net *subsidence* with respect to synclinal Pleasant Valley during the approximately 5,000-sidereal-yr interval between 5,000 and 500–100 ^{14}C yr B.P. (figs. 15.10*A*, 15.10*B*). Net late Holocene uplift of the Coalinga anticline remains possible (1) if the 5,000-^{14}C-yr-B.P. plain in Pleasant Valley lies many meters lower than we infer from ages on detrital charcoal at localities 86–3 and 86–12 (in which case this charcoal must predate its host deposit by more than any other detrital charcoal we have dated in the main-stream alluvium; see section above entitled "Configuration of Buried Alluvial Plains"), or (2) if in its initial profile the 5,000-^{14}C-yr-B.P. plain descended much more steeply toward the Coalinga anticline than does the present alluvial plain (as conceivably could result from depositional humps; fig. 15.10*C*). Only under extreme versions of these conditions, however, would the present configuration of the 5,000-^{14}C-yr-B.P. plain imply more than 1 or 2 m of two of net uplift on the west flank of the Coalinga anticline. Therefore, we infer that, on average, net late Holocene uplift of the Coalinga anticline at Los Gatos Creek might not have exceeded several tenths of a meter per 1,000 yr.

Little anticlinal uplift in the late Holocene is consistent with the absence of compelling geomorphic evidence of late Holocene growth of the Coalinga anticline. As noted above, flights of uplifted terraces are notably absent where Los Gatos Creek crosses the anticline, and nontectonic processes may explain other surficial features (clayey sediment upstream of the anticline, variation in the sinuousity of Los Gatos Creek across the anticline, and the hump in the present alluvial plain) that were previously interpreted as neotectonic.

IMPLICATIONS FOR EARTHQUAKE RECURRENCE

Anticlinal uplift slower than 1 m per 1,000 sidereal yr (our preferred interpretation of the apparently minimal deformation of the 2,000-, 2,500-, and 5,000-^{14}C-yr-B.P. alluvial plains) suggests an average repeat time of at least 200 years for major earthquakes during the past 6,000 sidereal yr. Still longer repeat times—possibly of 1,000 yr—are implied by the present configuration of the 5,000-^{14}C-yr-B.P. plain, whose net anticlinal uplift does not appear to have exceeded a few tenths of a meter per

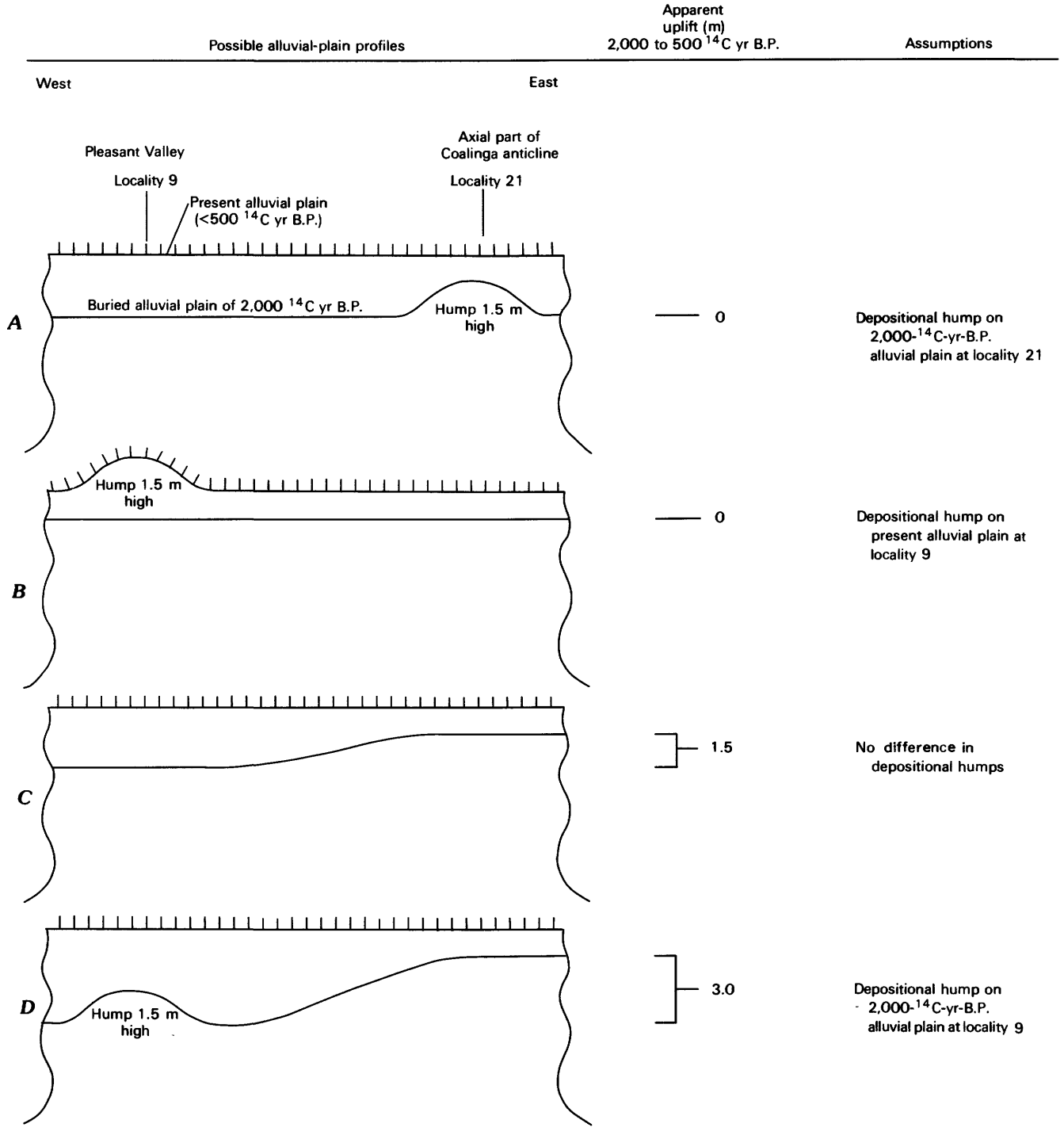

FIGURE 15.9.—Four interpretations of apparent convergence of the 2,000-^{14}C-yr-B.P. and present alluvial plains between Pleasant Valley and the Coalinga anticline (pl. 15.2). *A*, *B*, No anticlinal uplift required; convergence explained by depositional hump or natural levee. *C*, *D*, Anticlinal uplift.

1,000 yr. Repeat times shorter than these estimates seem unlikely unless (1) at Los Gatos Creek each major earthquake is usually accompanied by much less than the 0.2 m of uplift observed for 1983 (pl. 15.1) or (2) the anticline shrinks between earthquakes.

Late Holocene alluvial plains crossing the Coalinga anticline thus give little or no hint that the May 2 earthquake should have occurred. Apparently negligible late Holocene growth of a Quaternary anticline does not necessarily mean a negligible seismic potential.

ACKNOWLEDGMENTS

We thank Stacy Moore, Sandra L. Wert, Eduardo A. Rodriguez, Robert T. Versical, and James C. Yount for

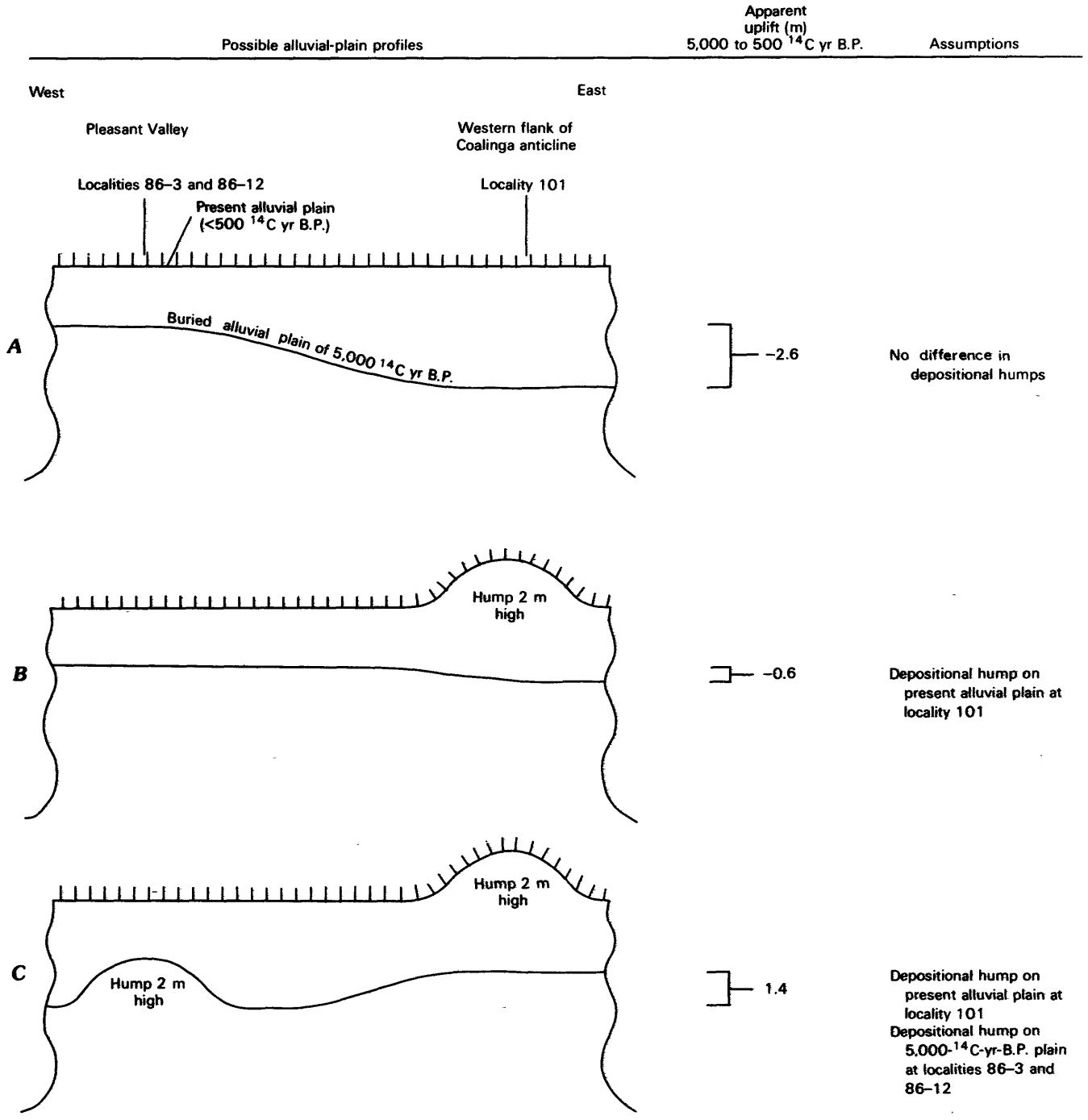

FIGURE 15.10.—Three interpretations of approximate parallelism of the 5,000-^{14}C-yr-B.P. and present alluvial plains between western Pleasant Valley and west flank of the Coalinga anticline. *A*, *B*, Subsidence of the anticline's west flank relative to western Pleasant Valley. *C*, Relative uplift at the anticline.

help in the field; Stephen W. Robinson and Deborah A. Trimble for proportional-gas radiocarbon ages; Charles A. Repenning for fossil identifications; Meade B. Norman III for X-ray identification of serpentine; and G. James West and Valmore C. LaMarche, Jr., for discussions of paleoclimate. The fieldwork was done by Atwater, Trumm, Tinsley, and Stein; radiocarbon dating by Tucker, Donahue, Jull, and Trumm; and artifact studies by Payen.

REFERENCES CITED

Arkley, R.J., 1962, The geology, geomorphology, and soils of the San Joaquin Valley in the vicinity of the Merced River, California, *in* Geologic guide to the Merced Canyon and Yosemite Valley, California: California Division of Mines and Geology Bulletin 182, p. 25–31.

Atwater, B.F., Adam, D.P., Bradbury, J.P., Forester, R.M., Mark, R.K., Lettis, W.R., Fisher, G.R., Gobalet, K.W., and Robinson, S.W., 1986, A fan dam for Tulare Lake, California, and implications for the Wisconsin glacial history of the Sierra Nevada: Geological Society of America Bulletin, v. 97, no. 1, p. 97–109.

Bennett, C.L., Beukens, R.P., Clover, M.R., Elmore, D., Gove, H.E., Kilius, L.R., Litherland, A.E., and Purser, K.H., 1978, Radiocarbon dating with electrostatic accelerators: Dating of milligram samples: Science, v. 201, no. 4353, p. 345–347.

Blong, R.J., and Gillespie, Richard, 1978, Fluvially transported charcoal gives erroneous ^{14}C ages for recent deposits: Nature, v. 271, no. 5647, p. 739–741.

Bull, W.B., 1964, Geomorphology of segmented alluvial fans in western Fresno County, California: U.S. Geological Survey Professional Paper 352–E, p. 89–129.

Crabtree, D.E., and Butler, B.R., 1964, Notes on experiments in flint-knapping: I. Heat treatment of silica minerals: Tebiwa, v. 7, p. 1–6.

Dibblee, T.W., Jr., 1971, Geologic maps of the Coalinga, Joaquin Rocks, New Idria, and Priest Valley 15-minute quadrangles, California: U.S. Geological Survey open-file maps, scale 1:62,500.

Eaton, J.P., 1985, The May 2, 1983 Coalinga earthquake and its aftershocks: A detailed study of the hypocenter distribution and of the focal mechanisms of the larger aftershocks, *in* Rymer, M.J., and Ellsworth, W.L., eds., Mechanics of the May 2, 1983 Coalinga earthquake: U.S. Geological Survey Open-File Report 85–44, p. 44–60.

Fielding, Eric, Barazangi, Muawia, Brown, Larry, Oliver, Jack, and Kaufman, Sidney, 1984, COCORP seismic profiles near Coalinga, California: Subsurface structure of the western Great Valley: Geology, v. 12, no. 5, p. 268–273.

Fredrickson, D.A., and Grossman, Joel, 1977, A San Diguito component at Buena Vista Lake, California: Journal of California Anthropology, v. 4, p. 173–190.

Harradine, F.F., Smith, Alfred, Smith, L.H., Hannesson, H.A., Huntington, G.L., Horton, C.R., Whiteside, E.P., Stevenson, E.W., and Veale, P.T., 1952, Soil survey of the Coalinga area: U.S. Department of Agriculture, Bureau of Plant Industry, Soils, and Agricultural Engineering Series 1944, no. 1, 91 p.

Henderson, F.M., 1966, Open-channel flow: New York, Macmillan, 522 p.

Ireland, R.L., Poland, J.F., and Riley, F.S., 1984, Land subsidence in the San Joaquin Valley, California, as of 1980: U.S. Geological Survey Professional Paper 437–I, p. I1–I93.

Janda, R.J., and Croft, M.G., 1967, The stratigraphic significance of a sequence of noncalcic brown soils formed on the Quaternary alluvium of the northeastern San Joaquin Valley, California, *in* Morrison, R.B., and Wright, H.E., eds., Quaternary soils: International Union for Quaternary Research Congress, 7th, Reno, Nev., Proceedings, v. 9, p. 158–190.

Jennings, C.W., and Strand, R.G., compilers, 1959, Santa Cruz sheet *of* Geologic map of California: California Division of Mines and Geology, scale 1:250,000.

King, G.C.P., and Stein, R.S., 1983, Surface folding, river terrace deformation rate and earthquake repeat time in a reverse faulting environment, *in* Bennett, J.H., and Sherburne, R.W., eds., The 1983 Coalinga, California earthquakes: California Division of Mines and Geology Special Publication 66, p. 165–176.

LaMarche, V.C., Jr., 1974, Paleoclimatic inferences from long tree-ring records: Science, v. 183, no. 4129, p. 1043–1048.

Lettis, W.R., 1982, Late Cenozoic stratigraphy and structure of the western margin of the central San Joaquin Valley, California: U.S. Geological Survey Open-File Report 82–526, 202 p.

Lewis, H.T., 1973, Patterns of Indian burning in California: Ecology and ethnohistory: Romona, Calif., Ballena Press Anthropological Papers, no. 1, 101 p.

Marchand, D.E., and Allwardt, Alan, 1981, Late Cenozoic stratigraphic units, northeastern San Joaquin Valley, California: U.S. Geological Survey Bulletin 1470, 70 p.

McGill, J.T., 1951, Quaternary geology of the north-central San Emigdio Mountains, California: Los Angeles, University of California, Ph.D. thesis, 103 p.

Meade, R.H., 1967, Petrology of sediments underlying areas of land subsidence in central California: U.S. Geological Survey Professional Paper 497–C, p. C1–C83.

Muller, R.A., Stephensen, E.J., and Mast, T.S., 1978, Radioisotope dating with an accelerator: A blind measurement: Science, v. 201, no. 4353, p. 347–348.

Munn, T.R., Busacca, A.T., and Trott, K.E., 1981, California aqueduct sedimentation study for the Arroyo Pasajero and tributary watersheds: Sacramento, California Department of Conservation special report, 72 p.

Ouchi, Shunji, 1985, Response of alluvial rivers to slow active tectonic movement: Geological Society of America Bulletin, v. 96, no. 4, p. 504–515.

Pearson, G.W., Stuiver, and Minze, 1986, High-precision calibration of the radiocarbon time scale, 500–2500 BC: Radiocarbon, v. 28, no. 2B, p. 839–862.

Pearson, G.W., Dilcher, J.R., Baillie, M.G.L., Corbett, D.M., and Qua, F., 1986, High-precision ^{14}C measurement of Irish oaks to show the natural ^{14}C variations from AD 1840 to 5210 BC: Radiocarbon, v. 28, no. 2B, p. 911–934.

Schumm, S.A., 1977, The fluvial system: New York, John Wiley & Sons, 338 p.

Stein, R.S., 1985, Evidence for surface folding and subsurface fault slip from geodetic elevation changes associated with the 1983 Coalinga, California, earthquake, *in* Rymer, M.J., and Ellsworth, W.L., eds., Mechanics of the May 2, 1983 Coalinga earthquake: U.S. Geological Survey Open-File Report 85–44, p. 225–253.

Stein, R.S., and King, G.C.P., 1984, Seismic potential revealed by surface folding: 1983 Coalinga, California, earthquake: Science, v. 224, no. 4651, p. 869–872.

Stuiver, Minze, and Pearson, G.W., 1986, High-precision calibration of the radiocarbon time scale, AD 1950–500 BC: Radiocarbon, v. 28, no. 2B, p. 805–838.

von Werlhof, Jay, and Vierhus, Judith, 1956, Survey report on the Tachi tribe: Berkeley, University of California Archeological Research Facility, manuscript 235B, pt. 1, 70 p.

Water Resources Division, 1959, Compilation of records of surface waters of the United States through September 1950. Part 11–B. Pacific slope basins in California, Central Valley: U.S. Geological

Survey Water-Supply Paper 1315–A, 459 p.
Wilson, S.R., and Ward, G.K., 1981, Evaluation and clustering of radiocarbon age determinations: Procedures and paradigms: Archaeometry, v. 23, no. 1, p. 19–39.
Woodring, W.P., Stewart, Ralph, and Richards, R.W., 1940, Geology of the Kettleman Hills oil field, California: Stratigraphy, paleontology, and structure: U.S. Geological Survey Professional Paper 195, 170 p.

16. THE NUÑEZ FAULT AND ITS SURFACE RUPTURE DURING THE COALINGA EARTHQUAKE SEQUENCE

By MICHAEL J. RYMER, KATHERINE J. KENDRICK, JAMES J. LIENKAEMPER, and MALCOLM M. CLARK,
U.S. GEOLOGICAL SURVEY

CONTENTS

ABSTRACT

A 3.3-km-long, right-reverse surface rupture developed along the Nuñez fault at the time of the shallow M_L=5.2 earthquake on June 11, 1983, 40 days after the Coalinga main shock. The north-south-trending surface rupture contained two echelon segments separated by a 0.4-km gap with a 0.3-km projected right stepover. The north and south segments, 1.3 and 1.6 km long, respectively, dip about 65° E. along most of their length. Displacement along the north segment in 1983 consisted predominantly of east-side-up reverse slip, with a minor right-lateral component. Maximum reverse and right-lateral components of slip in the north segment were 64 and 20 cm, respectively. Along the north one-fourth of the south segment, the relative proportion of slip components was similar to that in the north segment. Farther south along the south segment, however, the reverse component generally diminished, and the right-lateral component dominated. Maximum reverse and right-lateral components of slip in the south three-fourths of the south segment were 8 and 11 cm, respectively. Maximum net slip for the north and south segments were 65 and 13 cm, respectively.

The surface expression of the Nuñez fault, 4.2 km in total length, extends about 0.15 km northward and 0.75 km southward of the 1983 surface rupture. Thus, about 80 percent of the known fault length ruptured in 1983.

Total displacement on the Nuñez fault is poorly constrained because of repetitious lithologies and poor exposure, but, from general lithologic contrasts, we estimate a total displacement of a few hundred meters. Although the timing of fault movement also is poorly constrained, the movement postdates the development of the White Creek syncline, which contains Pliocene strata. An offset Quaternary terrace conglomerate is thought to be a few tens of thousands to few hundreds of thousands of years old, or late Pleistocene in age. Movements on the Nuñez fault both predate and postdate deposition of the conglomerate that truncates some of the clastic sandstone dikes that intrude it. Stratigraphic relations and ^{14}C ages of fluvial deposits exposed in a trench near Los Gatos Creek indicate no movement during the past 1,700 to 1,900 years.

INTRODUCTION

This chapter describes the surface rupture and displacements that formed along the Nuñez fault in association with the M_L=5.2 earthquake of June 11, 1983. It also discusses the probable total displacement, fault history, configuration of the fault at depth, and relations of these characteristics to faulting processes associated with the 1983 Coalinga earthquake sequence.

The Nuñez fault is situated about 12 km northwest of Coalinga and 14 km west of the May 2 main shock (fig. 16.1), which was on a separate, distinct fault. The Nuñez fault is a 4.2-km-long, north-south-trending, right-reverse, oblique-slip fault that parallels local faults of similar size and sense of displacement (see chap. 2). We found surface rupture along a 3.3-km-long stretch of the Nuñez fault (fig. 16.2), which before 1983 was unnamed and not known to be recently active. The fault is named for Nuñez Canyon, about ½ km to the west. Dibblee (1971), Mansfield (1972), and Kusnick (1981) mapped short sections of the Nuñez fault, but its overall short length, subtle surface expression, and the age of strata (Cretaceous) that it displaces are probable reasons why its recency of activity had been overlooked.

Ground and aerial searches immediately after the May 2, 1983, M_L=6.7 main shock revealed cracks and fissures within about 10 km of the instrumental epicenter, none of which appeared to represent movement on deeply rooted fault structures (Clark and others, 1983). A possible exception to the apparent reported absence of surface faulting accompanying the May 2 earthquake was reported by Hart and McJunkin (1983). The style of tectonism

associated with the main shock is northeast-directed thrust faulting on a buried fault, as suggested by seismologic and seismic-reflection studies (see chaps. 4, 8).

SURFACE FAULTING

On the basis of others' observations, we believe that the Nuñez fault ruptured at the time of the June 11 earthquake. A local resident first observed ground breakage (fig. 16.3) about 20 minutes after the June 11 M_L=5.2 earthquake, when he drove over the faulted surface of Los Gatos Road. Local residents who drove over the same road did not report ground breakage for the period shortly before the June 11 earthquake, and we observed no ground breakage at the Nuñez fault after the May 2 main shock. E.J. Fowkes (oral commun., 1983), professor of geology at West Hills College, visited the site about an hour after the earthquake and, the next morning, mapped the rupture in the south segment north of Los Gatos Road and for about 20 m northwest of Los Gatos Creek. V. Birdwell (oral commun., 1983), a nearby resident, was the first to notice the rupture along the north segment on June 12, when she drove over a faulted road near the north end of the segment. J.P. Hughes (written commun., 1983), a geologist with Chevron U.S.A., Inc., first noticed rupture south of Los Gatos Creek on June 24, when he observed it along the full length of the fault that we later mapped.

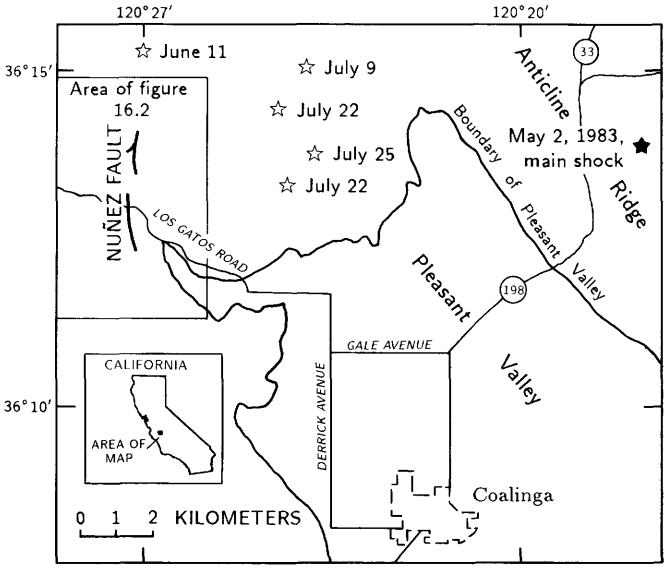

FIGURE 16.1.—Coalinga, Calif., area, showing location of the Nuñez fault, which ruptured at the surface in association with the M_L=5.2 earthquake of June 11, 1983. Open stars, epicenters of earthquakes of $M_L \geq 5.0$ on the Nuñez fault; solid star, epicenter of May 2, 1983, Coalinga main shock.

We investigated the Nuñez fault starting on the morning of June 14, 1983, 3 days after the rupture-associated earthquake. During the following 3 days, we mapped and measured the surface rupture north of Los Gatos Road. We also searched for ground breakage in the area of the south segment on June 14–15 but did not notice rupture south of the creek. Our failure to find the rupture either was an oversight or implies that the rupture formed later, as a result of postseismic slip. We found only two short (approx 10 m long) segments of surface rupture south of the road: in Los Gatos Creek and about 20 m northwest of the creek. Recorded slip values for surface displacement are listed in table 16.1. The timing and distribution of post-June 11 slip along the Nuñez fault are discussed in chapter 17.

A detailed map of surface faulting along the Nuñez fault is shown in figures 16.2 and 16.4. A 3.3-km-long segment of the fault broke at the ground surface during the June 11, 1983, earthquake. Surface faulting contains two north-south-trending echelon segments; the north and south segments are approximately 1.3 and 1.6 km long, respectively, separated by a 0.4-km gap and a 0.3-km projected right stepover (fig. 16.4). The 1983 displacement along the north segment was dominantly east side up, reverse slip, with a minor right-lateral component. North of Los Gatos Road, the 1983 displacement along the south segment was similar to that along the north segment. South of Los Gatos Road, however, the vertical component generally diminished or vanished, and the right-lateral component was commonly dominant.

DESCRIPTION OF SURFACE RUPTURE

Characteristics of surface rupture along the trace of the Nuñez fault range from straight, compressional uplifted soil blocks to left-stepping extensional cracks with little or no vertical displacement. Along the north break, and along the south break north of Los Gatos Road, where the vertical component of slip dominates, the ground fracture is a generally straight compressive rupture trace or "mole track" (fig. 16.5).

Local topography in the rolling hills (fig. 16.6) influenced rupture characteristics along the fault. The fault scarp is nearly everywhere along ridge crests, hilltops, and east- and west-facing slopes, as steep as 26°. On west-facing slopes, the rupture trace steps left, with a zone of extensional cracks on the east (upthrown) side that ranges from 5 to 8 m in width. On east-facing slopes, especially in the 200 m south of hill 1534 (fig. 16.4), near the north end of the north break, the fault scarp is a single rupture with a 0.5- to 1.0-m-wide zone of extensional cracks on the upthrown, downhill side of the fault. Here, the east-side-up displacement of 1983 faulting is

clear because the downhill side of the fault is elevated (figs. 16.6, 16.7*A*, 16.7*B*). Where the fault crosses spurs normal to the fault trend, the east-side-up compressive rupture shows left-stepping echelon extensional cracks on the upthrown side (fig. 16.8), indicative of the right-lateral component of slip. At the south end of the 1983 rupture, the trace consists of echelon cracks nearly parallel to the rupture trace (fig. 16.9). Here, relative uplift of the east side of the fault occurred with almost no component of compression (fig. 16.10).

The one exception to steep topography is between Los Gatos Road and Los Gatos Creek. Surface faulting on the stream terrace there is expressed dominantly by extensional left-stepping echelon cracks with no apparent vertical slip. Individual cracks range in length from 0.5 to 3 m in a zone as much as 10 m wide. For approximately 100 m north of Los Gatos Creek, the rupture is a poorly defined mole track or minor monoclinal flexure. (Local topography suggests a minor flexure, and so post-June 11

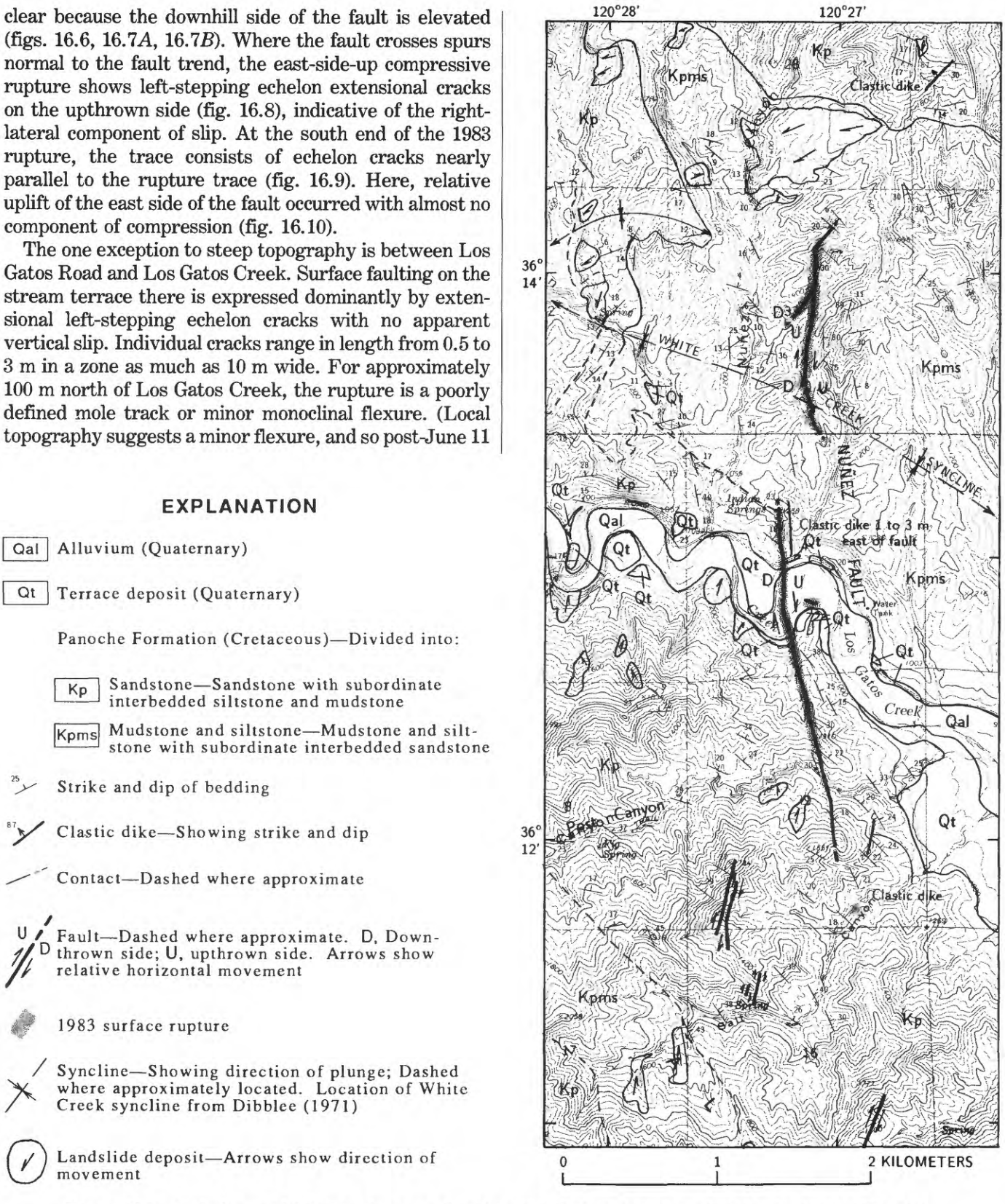

FIGURE 16.2.—Geologic map of the Nuñez fault area. Base from U.S. Geological Survey, 1:24,000 scale, Alcalde Hills, 1969.

slip may have been distributed over a zone at least 23 m wide; see fig. 17.14.)

Subsidiary splays, branches, and detached secondary breaks occurred primarily in two areas along the Nuñez fault; minor irregularities are present all along the fault. The largest subsidiary feature is a 400-m-long branch fault that extends southwestward from the main trace in the north segment (locs. 50–61, fig. 16.4). This branch fault is a compressional feature for nearly its entire length (fig. 16.11); extensional echelon cracks are present near the southwest end of the break. The sense of vertical displacement varies along this branch fault; in some places the southeast side is relatively up, and elsewhere the northwest side is up. The second subsidiary feature is an isolated, east-west-trending secondary break, situated about 150 m east of the Nuñez fault and about 300 m south of Los Gatos Road (locs. 75–77, fig. 16.4).

In the north segment a second, nontectonic, parallel rupture trace was common along west-facing slopes that showed less displacement and was 1 to 2 m downslope from the main trace. Hand-dug trenches across the fault revealed that the less developed, downslope traces were caused by movement on the main trace compressing the top 10 to 20 cm of the rigid soil. Therefore, these are unrooted fractures not directly related to faulting.

DISPLACEMENT

Slip along the Nuñez fault was of two kinds: fractures and, locally, distributed deformation in the form of drag. Distributed deformation was more pronounced in poorly lithified rocks or sediment, even in the Cretaceous Panoche Formation. In well-cemented sandstone no drag was noticeable (see Rymer and others, chap. 17).

Slip components were determined by several techniques. Except for Los Gatos Road, rigid manmade features (for example, roads, curbs, walls) that best record displacement do not cross the Nuñez fault. Thus, we measured slip directly across scarps and fissures in the ground surface. We measured scarp heights to obtain

FIGURE 16.3.—Fault rupture on Los Gatos Road (loc. 32, fig. 16.4), first observed about 20 minutes after the June 11, 1983, earthquake. View eastward; photograph by E.J. Fowkes, taken about 0800 P.d.t. June 11, 1983.

TABLE 16.1.—*Vertical and right-lateral-slip components along the Nuñez fault*

[Slip components were measured in the field with scale or tape; leveling data (see chap. 17) are omitted here. Reverse component of slip (*) was calculated by multiplying vertical component by the inverse of the sine of the dip on the fault, where known. Reverse component at locality 8 is based on leveling over a 10-m-wide zone across the fault. A vertical slip of 58 cm determined at this locality, along with an accurate dip measurement of 65°, results in the maximum reverse slip measured along the Nuñez fault. Note that there are no localities 46–49 and 62–74]

Locality (fig. 16.4)	Distance along reference line (km) (see fig. 16.15)	Distance SW. of juncture with main fault (km)	Slip component (cm)		Sense of movement	Days after June 11
			Vertical	Lateral		
North segment						
1	0.10	---	20	12	Right-reverse.	3
2	.18	---	15	---	do--------	5
			18-20	---		33
3	.25	---	25	---	do--------	6
			25-30	---		33
4	.29	---	15	---	do--------	6
			15	---		33
5	.30	---	32	---	do--------	6
			48	---		33
6	.32	---	30-40	---	do--------	6
7	.34	---	37	---	do--------	5
8	.35	---	42-50	11	do--------	5
			~47	---		35
			64*	---		35
9	.46	---	12	---	do--------	35
10	.48	---	40	---	do--------	5
11	.68	---	---	18	do--------	5
			5	18		35
12	.69	---	5	4	do--------	5
13	.71	---	15	---	do--------	5
			18-20	---		35
14	.72	---	40	15	do--------	5
15	.73	---	12-13	---	do--------	6
			13	---		35
16	.78	---	40	<1	do--------	5
			45-50	---		34
17	.81	---	35	---	do--------	5
18	.89	---	50	---	do--------	5
19	.95	---	10-15	---	do--------	6
			16-17	---		34
20	.95	---	---	20	do--------	79
21	.97	---	9	17	do--------	6
			9	---		34
22	.99	---	35	---	do--------	5
23	1.02	---	30	---	do--------	6
			45	---		34
24	1.03	---	42-47	---	do--------	6
			30-40	---		34
25	1.06	---	8-9	<1	do--------	6
			~5	---		34
26	1.16	---	5	---	do--------	17
			9-10	---		34
27	1.24	---	10	---	do--------	17
South segment						
28	1.81	---	10	---	Right-reverse.	3
			11	3.5		31
29	1.86	---	15	---	do--------	5
			15-16	---		31
30	2.03	---	10	---	do--------	5
			10-11	---		31
31	2.07	---	12	---	do--------	5
			13	---		31
32	2.08	---	10	---	do--------	5
33	2.26	---	<1	1.2	do--------	47
34	2.35	---	<1	1.3	do--------	47
35	2.42	---	<.5	2.2	do--------	48
36	2.82	---	---	6	do--------	48
37	2.85	---	7	8	do--------	48
38	2.90	---	5-6	8	do--------	48
39	2.94	---	<3	9	do--------	48
40	2.98	---	7	6	do--------	48
41	3.07	---	5	8-11	do--------	47
42	3.10	---	4	1.5	do--------	47
43	3.14	---	4	1	do--------	47
44	3.16	---	2	2	do--------	47
45	3.26	---	1	1	do--------	48
Branch fault (north segment)						
50	---	0.05	17	---	E side up	39
51	---	.09	10	---	W side up	39
52	---	.12	7	---	do--------	39
53	---	.14	<1	---	E side up	39
54	---	.15	4	---	do--------	39
55	---	.21	---	---	3 cm extension.	39
56	---	.22	11	---	E side up	39
57	---	.24	6	---	do--------	39
58	---	.28	2	---	W side up	39
59	---	.31	4	---	E side up	39
60	---	.36	<1	---	do--------	39
61	---	.40	<1	---	W side up	39
Secondary break (south segment)						
75	---	---	0.5	0.5	W side up	48
76	---	---	2	---	W side up, reverse.	48
77	---	---	.5	---	W side up, 3 cm extension.	48

vertical-slip components across simple slip surfaces (figs. 16.10, 16.12). Across compressional, piled-up soil blocks (figs. 16.5, 16.13) we visually projected the height of the uplifted (east) side or carefully removed soil blocks and made direct measurements. All of these techniques tend to underestimate total vertical displacement, primarily because they measure only the displacement closest to the rupture and do not include possible drag and deformation distributed over a wider zone.

Right-lateral slip was more difficult to detect and measure than vertical components, especially north of Los Gatos Road where compression dominated (figs. 16.5, 16.13), and so we have fewer measurements of lateral displacement. We measured the lateral-slip component by determining the displacement between matching irregularities in soil blocks along the local trend of the fault (fig. 16.14). Where echelon cracks were present, the right-lateral-slip measurement was the total of the displacements parallel to the fault that spanned the set of cracks.

The right-lateral and vertical components of slip versus distance along the Nuñez fault are plotted in figure 16.15; slip measurements are listed in table 16.1. From these measurements, assuming a fault-plane dip of 65°, the net slip (resultant of dip-slip and strike-slip components) can be calculated. Maximum net slip is 65 cm for the north segment (loc. 8, fig. 16.4), 13 cm for the south segment north of Los Gatos Road (loc. 28, fig. 16.4), and 12 cm for

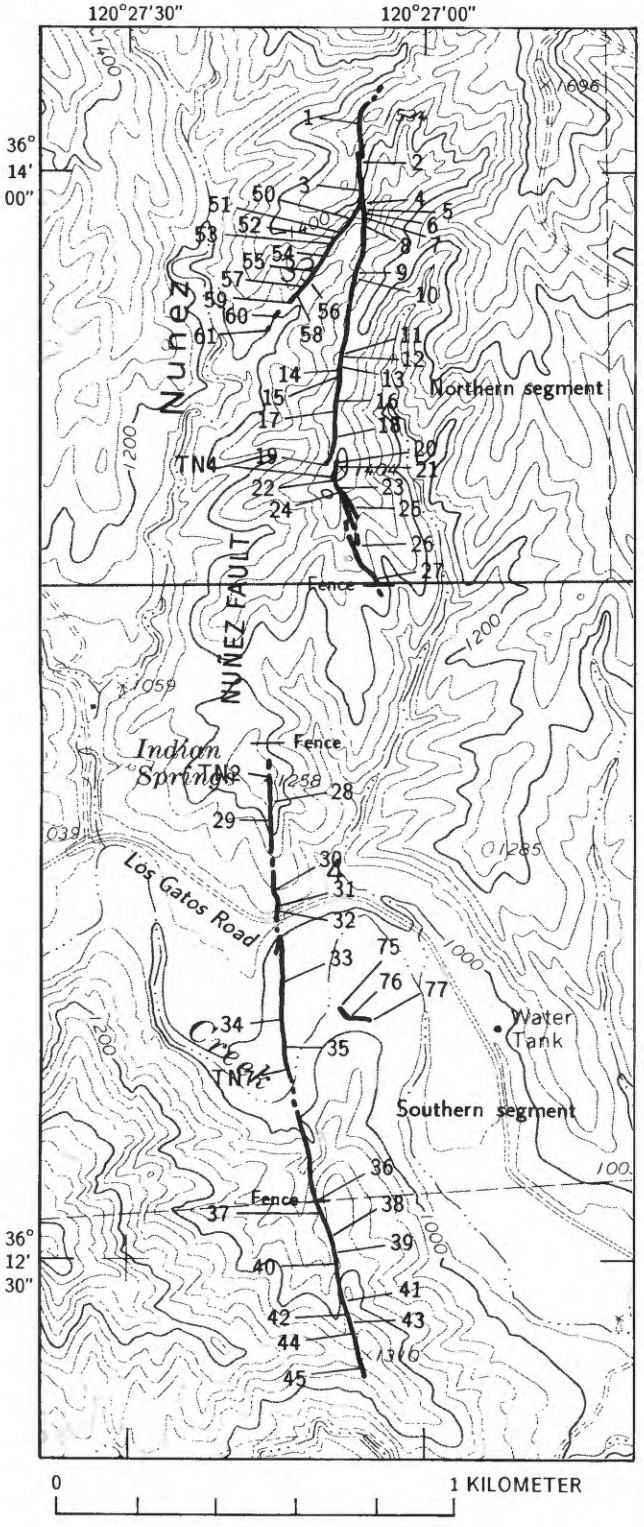

FIGURE 16.4.—Nuñez fault area, showing locations of surface faulting (heavy line) associated with June 11 M_L=5.2 earthquake, backhoe trenches TN2, TN4, and TN7, and section fences where right-lateral component of offset was measured. Numbers denote localities of displacement measurements plotted in figure 16.15 and listed in table 16.1. Base from U.S. Geological Survey, 1:24,000 scale, Alcalde Hills, 1969.

the south segment south of Los Gatos Road (loc. 41, fig. 16.4), where the right-lateral slip is greater than the vertical slip.

Three fencelines, located between secs. 4 and 33 (near loc. 27, fig. 16.4), secs. 4 and 9 (loc. 36, fig. 16.4), and about 25 m north of the south segment (fig. 16.4), recorded the amount of right-lateral slip. These fences were built in 1945, 1956, and 1945, respectively (J. Nuñez and Eath Gaasch, oral communs., 1983). Maps of the two section-boundary fencelines show as much as 3 cm of scatter of post locations (fig. 16.16), probably caused by initial misalignment of the posts. Both fences, however, indicate a right-lateral displacement greater than the background scatter of post locations; the fenceline at the secs. 4/33 boundary has about 36 cm of right-lateral displacement, and that at the secs. 4/9 boundary about 9

FIGURE 16.5.—Rupture (or "mole track") along the Nuñez fault at locality 29 (fig. 16.4). Piled-up soil blocks are compressional mounds that formed when east (left) side of fault moved up and west. Pocket knife for scale. View southward; photograph taken January 30, 1984.

cm (fig. 16.16). The fenceline about 25 m north of the south segment has an apparent right-lateral offset visually estimated at 20 cm.

These three examples are of discrete right-lateral displacement exactly where the fences cross the surface rupture or a projection of the surface rupture. The offsets on the fences are larger than the displacements we measured along the surface ruptures near the fences. The larger offsets of the fences could partly represent sampling of a wider zone than our scarp measurements, earlier unreported slip events, or, possibly, creep along the Nuñez fault since fence construction. Displacement on the Nuñez fault was generally greater to the north (fig. 16.15), toward the epicenter of the June 11 earthquake. Skewed displacement curves have been reported for seismically generated surface ruptures elsewhere. Examples of larger displacement near an initial point of rupture are the 1968 Borrego Mountain, Calif., break (Clark, 1972), the 1979 Imperial Valley, Calif., break (Sharp and others, 1982), the triggered breaks on the Superstition Hills fault in 1968 and 1979 (Allen and others, 1972; Fuis, 1982), and the 1983 Borah Peak, Idaho, break (Crone and Machette, 1984). Fuis (1982) discussed skewed surface rupture in more detail.

FIGURE 16.6.—Surface rupture of north segment of the Nuñez fault, showing grass-covered rolling-hill topography typical of area of surface rupture. East (left) side of fault moved relatively up. View southward; photograph taken January 30, 1984.

EXTENT OF THE NUÑEZ FAULT

Our mapping shows that the total known length of the Nuñez fault is about 4.2 km (fig. 16.2). The trace of the Nuñez fault beyond the 1983 rupture can be recognized by lithologic contrasts and divergent bedding attitudes across the fault (fig. 16.2). The fault extends at least 150 m northeastward of the north end of 1983 rupture. In the conspicuous gully north of the 1983 rupture, bedding attitudes are similar on both sides of the fault, but blocky, well-cemented sandstone is locally present west of the fault, and thin-bedded to massive siltstone and mudstone with no similar sandstone beds are present to the east. We could not identify the fault beyond the end point mapped in figure 16.2. South of the 1983 surface rupture, the fault extends at least 750 m on a south-southeastward trend, similar to the trend of the 1983 rupture south of Los Gatos Creek (fig. 16.2). In this area, the fault juxtaposes contrasting lithologies with slightly divergent attitudes. Displaced strata are evident in the streambanks of Post Canyon (fig. 16.17) and in the north-south-trending gully 200 m east of hill 1551, at the southeast end of the fault (fig. 16.2). Thus, about 80 percent of the fault length ruptured in 1983.

Clastic sandstone dikes, locally common and parallel to the fault in the hanging wall, are another possible indicator of the extent of the Nuñez fault. These dikes are generally within a few meters of the main trace but locally are as much as a few hundred meters away. The dikes are well exposed in the south segment north of Los Gatos Road (north of loc. 30), in the roadcut along Los Gatos Road (loc. 32), and in the north streambank of Post Canyon (figs. 16.2, 16.17, 16.18).

Sandstone dikes along the Nuñez fault are vertical to steeply inclined to the east, paralleling the plane of the fault (fig. 16.17). These dikes, 4 to 150 cm wide and as much as 200 m long, have sharp contacts that transect the bedding structure of the host rocks. North of Los Gatos Road between locality 30 and the north end of the south segment, clastic dikes, 1 to 3 m east of the fault, form a hogback ridge because of their greater resistance to weathering.

The source of the clastic dikes is sandstone beds in the Panoche Formation that are at least 30 m stratigraphi-

FIGURE 16.7.—Nuñez fault near north end of north segment. Upthrown side of fault is on downhill side of slope. Movement on fault formed a sidehill bench. *A*, Fault scarp in left foreground is obscured by tall grasses; hill 1534 is at right. View northwestward; photograph taken July 22, 1983. *B*, Same locality along fault in figure 16.7*A*. Note people (short arrows) for scale and right step in fault trace (long arrows). View westward; photograph taken June 15, 1983.

cally lower than the tops of the exposed dikes (fig. 16.17). Provenance of the source materials from stratigraphically lower horizons is evident because a dike in the roadcut of Los Gatos Road shows an upward termination within a Quaternary terrace conglomerate (fig. 16.18), and the Panoche Formation (Great Valley sequence) is the only unit below the ground surface for at least 4 km (see Walter, chap. 3; Mansfield, 1972). Furthermore, the clastic sandstone dikes have similar mineralogies, which are also similar to that of Panoche sandstone beds but not to the overlying Quaternary terrace conglomerate.

The relation of clastic dikes to the Nuñez fault was also evident in two trenches excavated across the fault at sites TN2 and TN4 (fig. 16.4; see figs. 16.19, 16.20). In both trenches, a clastic dike is situated within a meter of the 1983 main rupture trace, even though at site TN4 the dike is not exposed at the surface. Both dikes are blocky to massive, well-cemented sandstone that intrudes the Cretaceous host rock from below.

The logs of both trenches show contrasting lithologies and bedding-attitude changes across the fault. The steepness and complexity of the 1983 main trace in trench TN4 and of the zone of earlier faulting in both trenches are noteworthy (figs. 16.19, 16.20). In trench TN2, a fault trace lies about 2 m west of the 1983 break. The differences in lithology and dip of bedding across this fault (fig. 16.20) imply a total offset greater than the 3.2-m trench depth. The timing of movement on the fault can be constrained only as post-Cretaceous but before formation of the soil that truncates the upper part of the fault. Because the soil thickness is constant across the fault, we infer that this trace has been inactive since formation of the soil.

FIGURE 16.8.—Dirt road across the Nuñez fault near north end of north segment (loc. 1, fig. 16.4). Note small (approx 12 cm) component of right-lateral offset along edges of road and extensional cracks on upthrown side of fault. View northeastward; photograph taken June 14, 1983.

FIGURE 16.9.—Nuñez fault near south end of south segment (loc. 38, fig. 16.4). Echelon fissures nearly parallel fault trace and show dominantly right-lateral offset. Pocket knife for scale. View north-northwestward; photograph taken September 29, 1983.

HISTORY OF MOVEMENT

AMOUNT OF TOTAL DISPLACEMENT

Truncation of strata and divergent dips across the fault (fig. 16.2) allow an estimation of the minimum total vertical component of slip on the Nuñez fault. In the intermittent-stream gully at locality 8 (fig. 16.21), two well-cemented, resistant sandstone beds west of the fault are absent on the east. At least 24 m of vertical movement on the fault is required to raise the beds on the east side to where they could be erosionally removed. This observation establishes an estimate for the minimum displacement on the fault.

The lithologic contrasts mapped in figure 16.2, however, suggest that the total displacement on the Nuñez fault is probably much greater than this estimate. Although the scarcity of exposures and the repetitious lithologies in the Panoche Formation do not allow direct correlations across the fault, they do allow an approximate estimate of displacement. The general absence of resistant sandstone beds east of the fault and north of Los Gatos Road, in contrast to their presence on the west side, suggests a few hundred meters of reverse slip.

TIMING OF FAULT MOVEMENT

SLOPE PROFILES

Slope profiles across a sidehill bench near locality 2 (figs. 16.4, 16.7) suggest young, possibly Holocene, pre-1983 movement on the Nuñez fault (fig. 16.22). The heights of 1983 fault scarps at two sites about 70 m apart are 9 and 24 cm, whereas the projected slope reconstructions infer total reverse displacements of 92 and 56 cm, respectively, implying that the bench existed before the 1983 rupture. Differential resistance to erosion of contrasting rock types across the fault could create this persistent bench, even if the previous movement was ancient, but the less resistant rock types are on the downhill (upthrown) side of the bench. Also, there is no evidence in the near-surface of resistant clastic dikes that would make the hanging wall locally more resistant to erosion. Thus, the inferred presence of the bench before 1983 implies a geologically recent earlier movement.

FIGURE 16.10.—Nuñez fault near south end of south segment (loc. 40, fig. 16.4), showing faulted cow trail with 7 cm of vertical slip and 6 cm of right-lateral slip. Note absence of mole track here, typical of surface rupture in south segment of fault south of Los Gatos Road. Pocket knife for scale. Photograph taken July 29, 1983.

FIGURE 16.11.—Surface expression of north-segment branch fault (loc. 50, fig. 16.4). Fault plane exposed in shallow hand-dug trench at this locality revealed fault plane dipping 28° SE. (to left). View southwestward; photograph taken January 27, 1984.

QUATERNARY TERRACE CONGLOMERATE AND CLASTIC DIKES

Rocks exposed along Los Gatos Road (loc. 32, fig. 16.4) provide another qualitative estimate of the time of movement on the fault. Here, the Quaternary terrace conglomerate shown in figure 16.23 is offset at the 1983 fault trace by at least 3½ m, approximately the height of the exposure. The conglomerate overlies Panoche strata east of the fault and abuts Quaternary colluvium to the west. Although the exact age of the conglomerate is unknown, it is sufficiently old that Los Gatos Creek has incised 20 m below the conglomerate to its present level. We estimate that the conglomerate is from several tens of thousands to several hundreds of thousands of years old (late Pleistocene).

The age of this deposit is critical to our understanding of the timing and rates of movement on the Nuñez fault, not only because the conglomerate is offset by the fault but also because clastic dikes both predate and postdate its deposition. Truncation of clastic dikes approximately 20 m east of the fault by the conglomerate indicates their emplacement before deposition of the conglomerate. However, a poorly consolidated sand dike about 3 m east of the fault extends into the conglomerate, where the sand forms a sill (fig. 16.18). The dikes presumably resulted from injection of liquefied sand into the conglomerate during strong seismic shaking; similar features have been used to identify prehistoric earthquakes elsewhere (Russ, 1979; Sieh, 1984; Obermeier and others, 1985; Talwani and Cox, 1985). These features have also been observed during historical earthquakes (Muir and Scott, 1982; Youd and Wieczorek, 1982).

FIGURE 16.12.—Nuñez fault near north end of north segment (loc. 3, fig. 16.4). Recently crushed grasses below soil block in center of photograph and soil-block shapes allowed measurement of 5 cm of compression. Pocket knife for scale. View eastward; photograph taken June 16, 1983.

FIGURE 16.13.—Disrupted soil blocks along main trace of the Nuñez fault in central part of north segment (loc. 17, fig. 16.4) made measurement of vertical and, especially, right-lateral components of slip difficult. Pocket knife for scale. View northward, photograph taken July 15, 1983.

TRENCH EXPOSURES

Some additional evidence of the timing of movement on the Nuñez fault comes from a trench in Quaternary fluvial

FIGURE 16.14.—Plan view of surface rupture of the Nuñez fault at locality 20 (fig. 16.4). Right-lateral slip here, the largest measured along the fault (20 cm), was determined by matching soil-block irregularities (points A, B). Pocket knife parallels local fault trend. Photograph taken August 20, 1983.

deposits near Los Gatos Creek (site TN7, fig. 16.4). This trench was excavated normal to the fault at a location where no 1983 rupture occurred at the surface; instead, a 10-cm-high warp developed over a distance of about ½ m. We divide sedimentary deposits exposed in the trench walls into four groups (A–D, fig. 16.24). Unit A is composed of five thin, laterally persistent silt and sand beds that are individually 3 to 15 cm thick. These beds are moderately well sorted and show well-developed lamination and normal grading; they have sharp basal contacts. Below, unit B is a 125- to 160-cm-thick, massive, very poorly sorted pebbly-silty sand that contains local disseminated detrital charcoal and pebbles and cobbles; the cobbles are as much as 11 cm long. The lower contact with unit C is an erosional contact. Unit C is a moderately well sorted silty sand containing local clay and silt laminae, as well as disseminated detrital charcoal; it has a sharp lower contact. Underlying unit C is a pebble to cobble gravel, unit D, that locally contains irregular sand lenses. To the east, unit D grades into a cobble to boulder conglomerate containing clasts as large as 1 m. Radiocarbon ages on detrital charcoal from units B and C provide minimum estimates of the times of previous fault movement. The ages of samples from trench TN7 are listed in table 16.2, and their stratigraphic locations are shown in figure 16.24. In general, unit B was deposited within the past few hundred years (the limits of dating techniques), and unit C about 1,700 to 1,900 years ago, possibly more recently because the ages are on detrital charcoal and the age of the charcoal before deposition is unknown. Thus, a period of nondeposition and (or) erosion intervened between the deposition of units B and C.

Trench TN7 revealed little structural information. The ground surface, the modern soil, and unit A are all monoclinally warped about 10 cm vertically. Lower units are not similarly warped, with the possible exception of

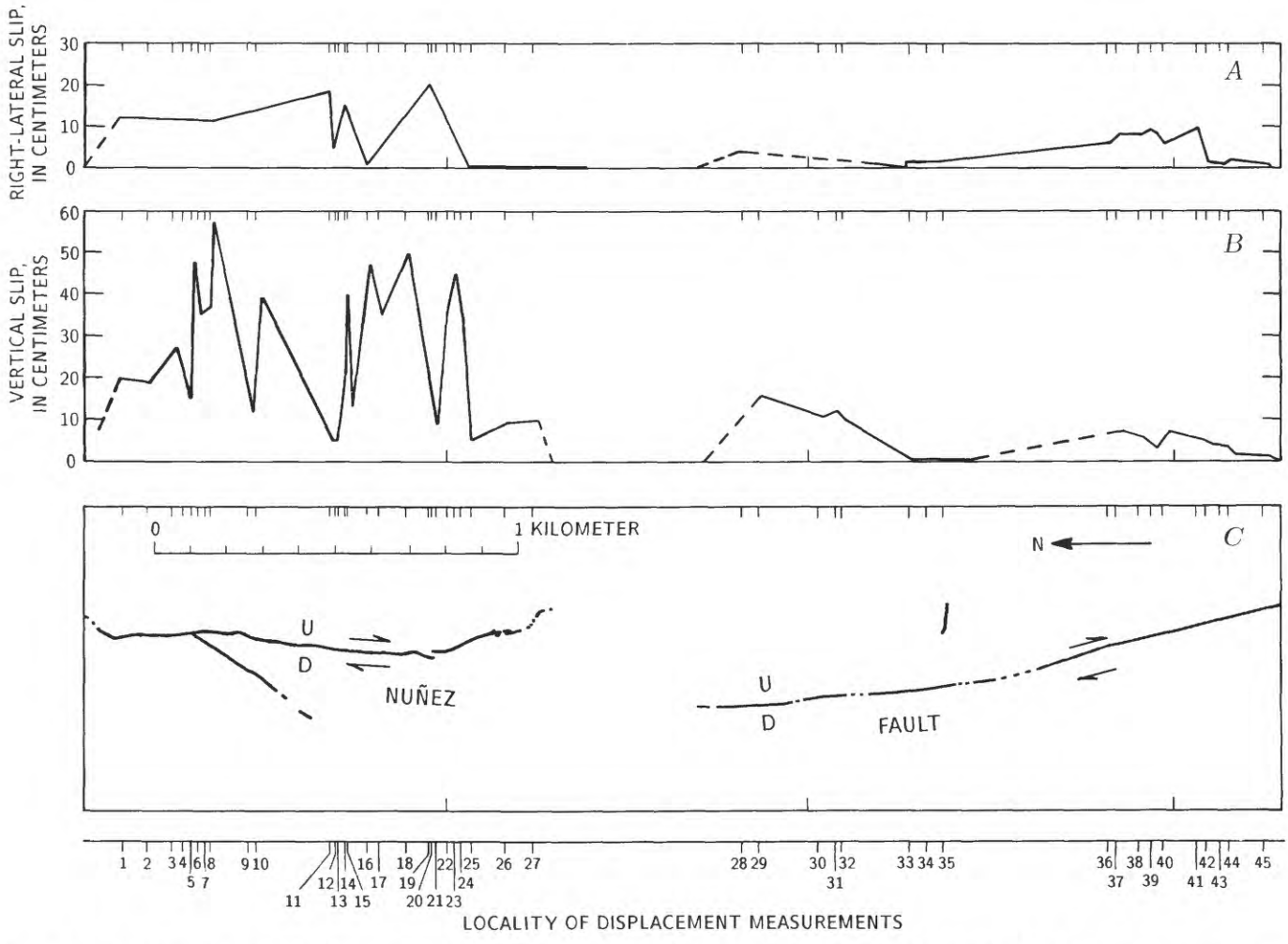

FIGURE 16.15.—Right-lateral (*A*) and vertical (*B*) components of slip as a function of distance along the Nuñez fault (*C*) for the 1983 break. Slip plots dashed where projected. Plots do not include displacement on branch and secondary faults, measured fence offset, or postseismic slip measured along leveling lines (see chap. 17). D, down; U, up. Arrows, direction of relative movement.

the base of unit C. Also, there was no well-defined fault plane, even below the surface trace of the low scarp. Apparently, the coarse grain size and small displacement of these deposits inhibited development of a well-developed, easily noticeable fault plane. The age of unit C and the absence of vertical separation greater than the 10 cm measured in 1983 imply that no earthquakes with attendant vertical separation have occurred in the past few hundred years, probably for as long as 1,700 to 1,900 years. Although the erosional contact between units B and C may have removed evidence of earlier vertical separation of unit C, the contact between units C and D would still record evidence of greater deformation, if present.

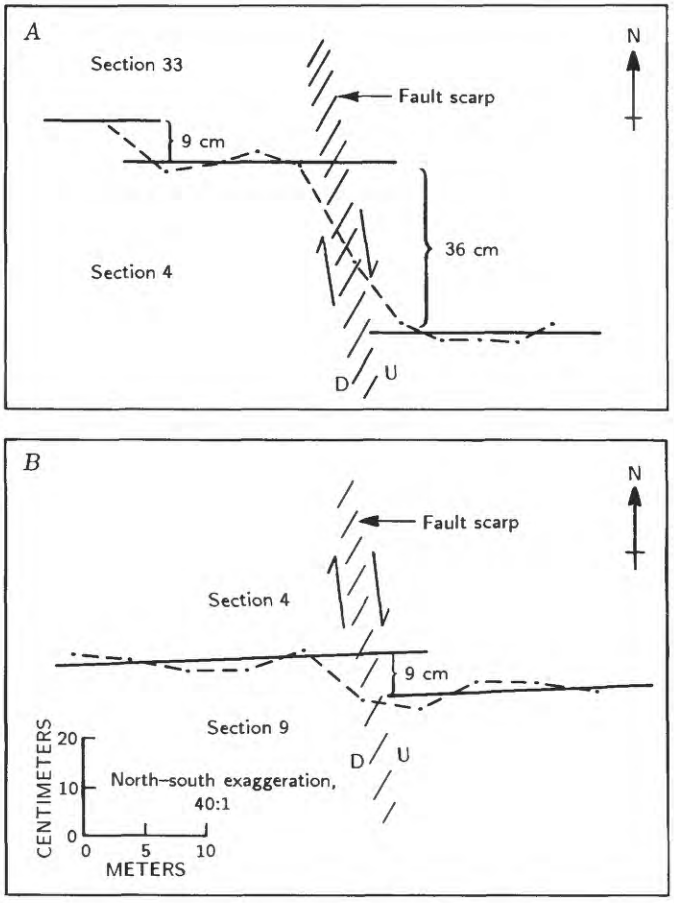

FIGURE 16.16.—Plan view of right-laterally offset fencelines across the Nuñez fault. Lateral offset of fencelines was measured by using a tightened cable strung parallel to, but at an arbitrary distance from, the fencelines. Parallelism of fence and cable was measured by compass. A plumb bob, suspended from the cable, and tape were used to measure distance to base of each fencepost. Dots, fenceposts; dashed line, fence wire. Solid line is estimated fit of fenceposts on either side of fault to line parallel to fence. Arrows show direction of relative movement; D, downthrown side of fault, U, upthrown side. *A*, Fence between sections 4 and 33 (approx 10 m S. of loc. 27, fig. 16.4); fenceline shown is 33 m long. *B*, Fence between sections 4 and 9 (loc. 36, fig. 16.4); fenceline shown is 42 m long.

DIP OF THE FAULT

The location of rupture and the general sense of displacement along the Nuñez fault coincide with those of earlier surface faulting, as shown by relations in natural exposures, the roadcut, and trenches. The Nuñez fault dips steeply east along most of its length. It dips 65°–66° E. near locality 8 (fig. 16.4), in the roadcut along Los Gatos Road, and in Post Canyon, 0.2 km south of 1983 rupture (figs. 16.2, 16.4). In 1.5- to 4-m-deep trenches, dip angles ranged from 45° to 80° E. for the fault in the north and south breaks north of Los Gatos Road (figs. 16.19, 16.20). The relatively straight trend of the fault across topographic irregularities also indicates a generally steep dip. An exception to the steep dips occurs near the north end, where the fault dips about 45° E. in a trench approximately 10 m south of locality 1 (fig. 16.4). The northeastward trend of the fault trace across a topographic low north of this site is consistent with a local decrease in dip of the fault plane. Hypocenters of earthquakes ($M_L \geq 2.2$) projected onto a plane perpendicular to the Nuñez fault show a 61° E. dip for the fault (fig. 16.25). The fault plane in figure 16.25 is drawn to connect the surface rupture and the hypocenter locations of four deep $M_L \geq 5.0$ earthquakes on the fault. Different orientations of the fault plane are possible, given the data plotted in figure 16.25. For example, the hypocenters at less than 5-km depth can be connected with the deeper earthquakes to form a curving fault plane, still dipping steeply east, or they can form echelon faults. Slight steepening of the fault is indicated from surface measurements presented above, which indicate a dip of 65°. However, the locations of the shallow events are not well constrained. In fact, the apparent westward shift of the less-than-5-km-deep events might be an artifact of the velocity model used in the plotting program (J.P. Eaton, oral commun., 1985); or it might be caused by an actual velocity change at that depth, where a boundary is inferred between relatively lower velocity rocks of the Great Valley sequence above and higher velocity Franciscan rocks below (see chap. 3).

SEISMIC MOMENT

Seismic moments determined from instrumental data and from surface displacements of the June 11 earthquake relate to the timing of slip on the Nuñez fault and its relation to the May 2 main shock. The calculated moment of the June 11 event from teleseismic long-period (greater than 20 s) compressional waves (U.S. National Earthquake Information Service, 1983, p. 4) is 1.7×10^{24} dyne-cm. Uhrhammer and others (1983) calculated a moment of 1.1×10^{24} dyne-cm from broadband displacement seismograms. Our calculations use a net right-

reverse surface displacement of 36 cm determined from the area under the high peaks in the curves in figure 16.15 and assume a 65° dip for the fault plane. The area of the fault is estimated from a fault length of 3.3 km and a fault width of 4.5 km (the distance from the hypocenter location determined in chap. 8 to the surface rupture); the resulting area is 14.9 km^2. Our calculated moment, using the formula $M_0=\gamma dA$, is 1.6×10^{24} dyne-cm, where γ (shear modulus)$=0.3\times10^{12}$ dyne-cm^2, which agrees closely with the seismologically determined values. The agreement of instrumentally determined values, which span a period of seconds, with our determination from surface displacements, which were measured 3 to 48 days after the earthquake, implies that most slip was released seismically during the earthquake. This conclusion is also supported by the timing of field observations, as discussed above, and by postseismic-slip studies (see chap. 17, fig. 17.3).

DISCUSSION

Results for rupture location and amount of displacement for 1983 faulting and the faulting history of the Nuñez fault show that it is a right-reverse oblique-slip fault which had not undergone surface rupture before 1983 for at least 1,700 to 1,900 years. What is missing in the above presentation is the significance of this fault in the 1983 Coalinga earthquake sequence and the likelihood of similar faults in the regional tectonic setting.

The seismologic and geologic significance of the Nuñez fault for the 1983 Coalinga earthquake sequence is quite apparent: Five of the nine largest earthquakes were on this fault, including the second largest shock (July 22, 1983, $M_L=6.0$). Also, the July 22 shock on the Nuñez fault that occurred 81 days after the main shock renewed seismic activity on other faults that were activated earlier in the Coalinga earthquake sequence (see chap. 8).

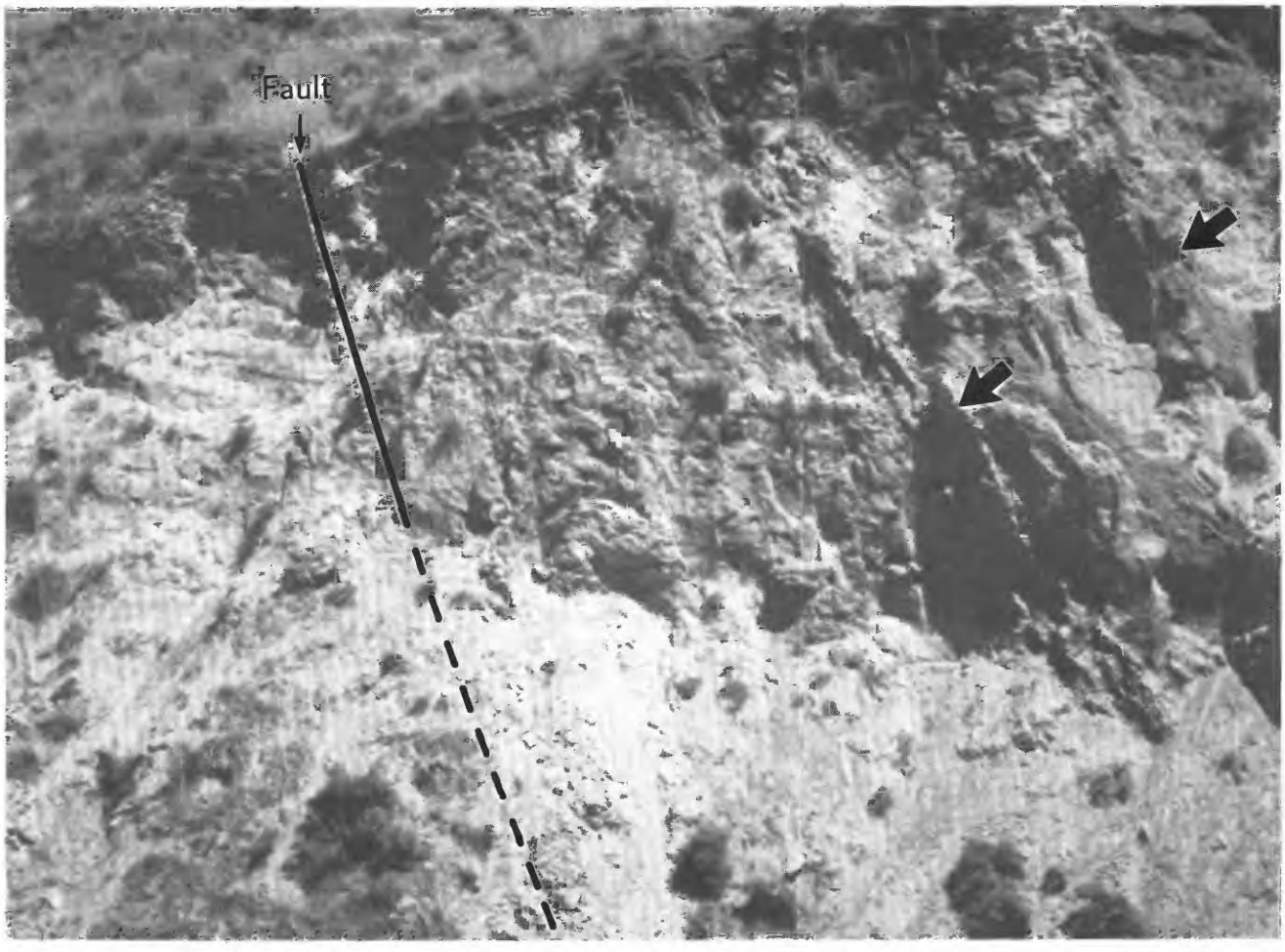

FIGURE 16.17.—Streambank exposure of the Nuñez fault in Post Canyon, approximately 200 m south of 1983 surface rupture. Lithology of the Panoche Formation is similar on both sides of fault here, but discordant bedding attitudes identify the fault (see fig. 16.2). Note clastic dikes (short arrows) cutting across bedding on upthrown (right) side of fault. Exposed fault approximately 20 m of cliff face. View northward; photograph taken July 29, 1983.

TABLE 16.2.—*Radiocarbon age of detrital-charcoal samples from trench TN7 across the Nuñez fault*

Sample No.		Stratigraphic horizon (see fig. 16.24)	Laboratory age (yr)	CAL-B.P. (yr)
Field	Laboratory			
TN7-7	AA-947	B	255±220	349±220
TN7-14	AA-1175	B	350±100	488±121
TN7-15	AA-950	B	140±230	223±201
TN7-2	AA-1173	C	1,800±200	1,784±223
TN7-3	AA-946	C	1,795±124	1,782±140
TN7-4	AA-1174	C	1,880±140	1,888±159

Furthermore, the fact that the Nuñez was the only fault involved in the Coalinga earthquake sequence which exhibited deeply rooted surface rupture allows a detailed study of its faulting history.

Hart and McJunkin (1983) reported surface rupture that was possibly related to the May 2 main shock, but the short length (less than 10 m) of this compressional feature across an unpaved road northwest of Coalinga suggests that it was probably due to sympathetic movement on a minor fault or along a weakened bedding plane and thus is not due to deeply rooted faulting. Further investigations of this site on September 29, 1983, showed that the road broken by the structure had been regraded, and no evidence of fault movement survived. Also, seismologic and seismic-reflection investigations (see chaps. 4, 8) suggest a northeast-directed thrust fault for the May 2 main shock; therefore, the surface breakage seen by Hart and McJunkin (1983) would have been on a secondary feature, at best.

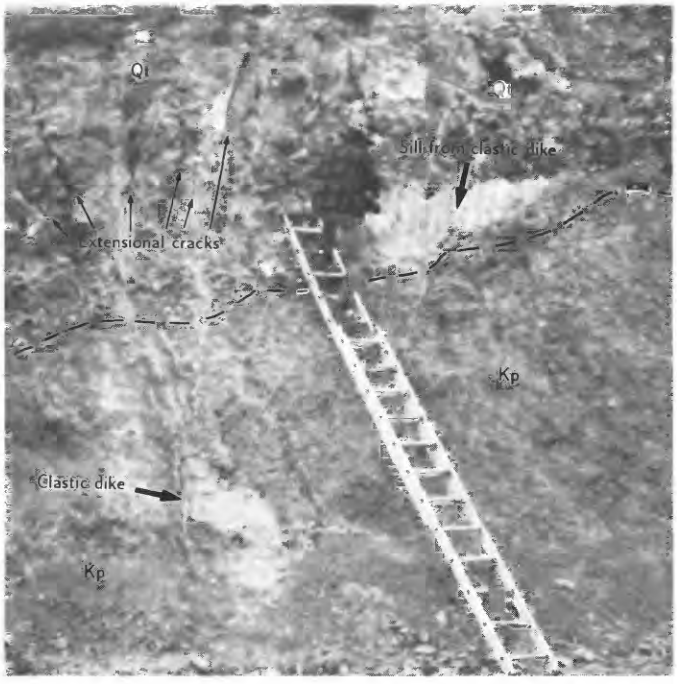

FIGURE 16.18.—Clastic dikes (arrows) in hanging wall of the Nuñez fault in roadcut along Los Gatos Road (loc. 32, fig. 16.4). Clastic dike at upper right forms sill in Quaternary terrace conglomerate (Qt) that overlies the Cretaceous Panoche Formation (Kp). Note extensional cracks formed above clastic dike on left.

In view of the association of seismic activity and surface rupture on the Nuñez fault with seismic activity below the Coalinga anticline in 1983, is there a mechanism that causes movement on this fault each time large slips occur below the anticline? A major limitation to understanding a possible mechanistic or temporal connection is our limited knowledge of faulting processes below Anticline Ridge and on the Nuñez fault. Also, the faulting style for these two areas differs: westward-directed right-reverse movement on the Nuñez fault and deeply buried, northeast-directed thrust movement below the Coalinga anticline. Nevertheless, we know enough to address this question. Repeat times for earthquakes with characteristic 1983-type surface warping on the Coalinga anticline (Stein, 1985) are estimated to be at least 200 to 1,000 years during the past 2,000 to 2,500 years (see chap. 15). In contrast, investigations at trench TN7 on the Nuñez fault showed that surface ruptures similar to that in 1983 have not occurred for at least 1,700 to 1,900 years. Thus, at least for about the past 2,000 years, the Nuñez fault has ruptured less often than the fault below the Coalinga anticline.

The long-term geologic record also argues against coeval ruptures on these two faults. Folding on the Coalinga anticline is surficial evidence of faulting below the anticline. Because Pliocene strata are folded approximately as much as Cretaceous strata, the time of folding is inferred to be post-late Pliocene (see chap. 4). In contrast, the existing topography and structural relations near the Nuñez fault suggest only a few hundred meters of displacement, significantly less than the 2 km of warpage for the Coalinga anticline.

The importance of the Nuñez and similar faults inboard of the Coast Ranges-Great Valley structural boundary is that they record tectonic movement, even though they may not show as frequent or as much displacement as faults at this structural boundary. Thus, farther north of the Coalinga anticline, where there is no surficial expression of buried faults at the structural boundary, the inboard, smaller-displacement, less seismically active faults are essential for understanding the compressional tectonics of the region. In this light, understanding of the Nuñez fault and its tectonic setting and processes may help the study of tectonic processes elsewhere along the Coast Ranges-Great Valley structural boundary.

ACKNOWLEDGMENTS

F.W. Lester and J.P. Eaton generously provided seismicity data. We also thank the people of Coalinga,

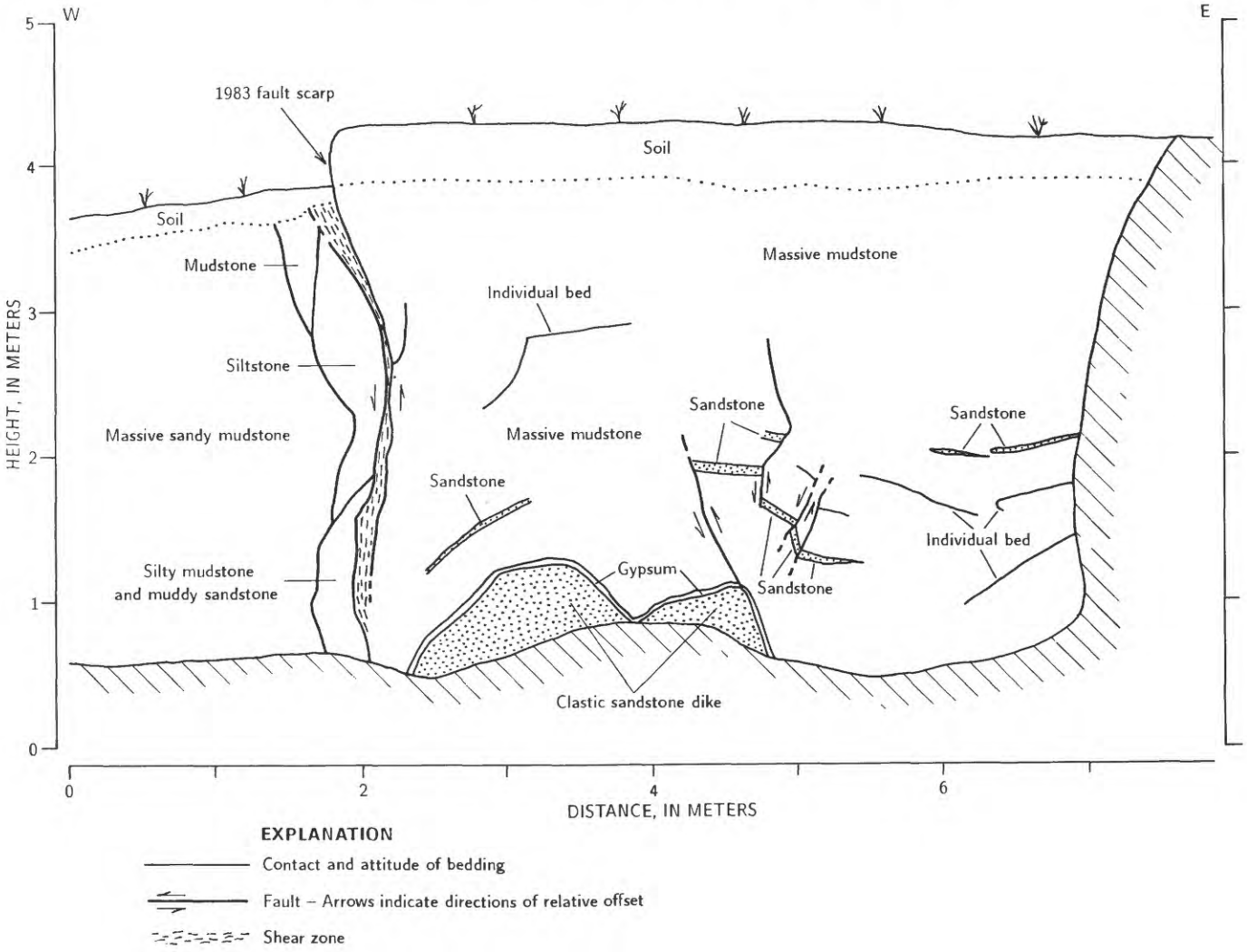

FIGURE 16.19.—Log of trench TN4 in the Cretaceous Panoche Formation near locality 22 (fig. 16.4) in the north segment. View northward.

especially those living near the Nuñez fault, for their generous cooperation, interest, and friendship; without their help this study would not have been possible.

REFERENCES CITED

Allen, C.R., Wyss, Max, Brune, J.N., Grantz, Arthur, and Wallace, R.E., 1972, Displacements on the Imperial, Superstition Hills, and San Andreas faults triggered by the Borrego Mountain earthquake, *in* The Borrego Mountain earthquake of April 9, 1968: U.S. Geological Survey Professional Paper 787, p. 87–104.

Clark, M.M., 1972, Surface rupture along the Coyote Creek fault, *in* The Borrego Mountain earthquake of April 9, 1968: U.S. Geological Survey Professional Paper 787, p. 55–86.

Clark, M.M., Harms, K.K., Lienkaemper, J.J., Perkins, J.A., Rymer, M.J., and Sharp, R.V., 1983, The May 2, 1983 earthquake at Coalinga, California: The search for faulting, *in* Borcherdt, R.D., compiler, The Coalinga earthquake sequence commencing May 2, 1983: U.S. Geological Survey Open-File Report 83-511, p. 8–11.

Crone, A.J., and Machette, M.N., 1984, Surface faulting accompanying the Borah Peak earthquake, central Idaho: Geology, v. 12, no. 11, p. 664–667.

Dibblee, T.W., Jr., 1971, Geologic map of the Coalinga quadrangle: U.S. Geological Survey open-file report, scale 1:62,500.

Fuis, G.S., 1982, Displacement on the Superstition Hills fault triggered by the earthquake, *in* The Imperial Valley, California, earthquake of October 15, 1979: U.S. Geological Survey Professional Paper 1254, p. 145–154.

Hart, E.W., and McJunkin, R.D., 1983, Surface faulting northwest of Coalinga, California, June and July 1983, *in* Bennett, J.H., and Sherburne, R.W., eds., The 1983 Coalinga, California earthquakes: California Division of Mines and Geology Special Publication 66, p. 201–219.

Kusnick, J.E., 1981, Biostratigraphy of Upper Campanian and Maestrichtian ammonites of the Great Valley sequence, California: Davis, University of California, M.S. thesis.

Mansfield, C.F., 1972, Petrofacies units and sedimentary facies of the Late Mesozoic strata west of Coalinga, California, *in* Cretaceous of the Coalinga area: Society of Economic Paleontologists and Mineralogists, Pacific Section Field Trip Guidebook, p. 19–26.

Muir, S.G., and Scott, R.F., 1982, Earthquake-generated sandblows

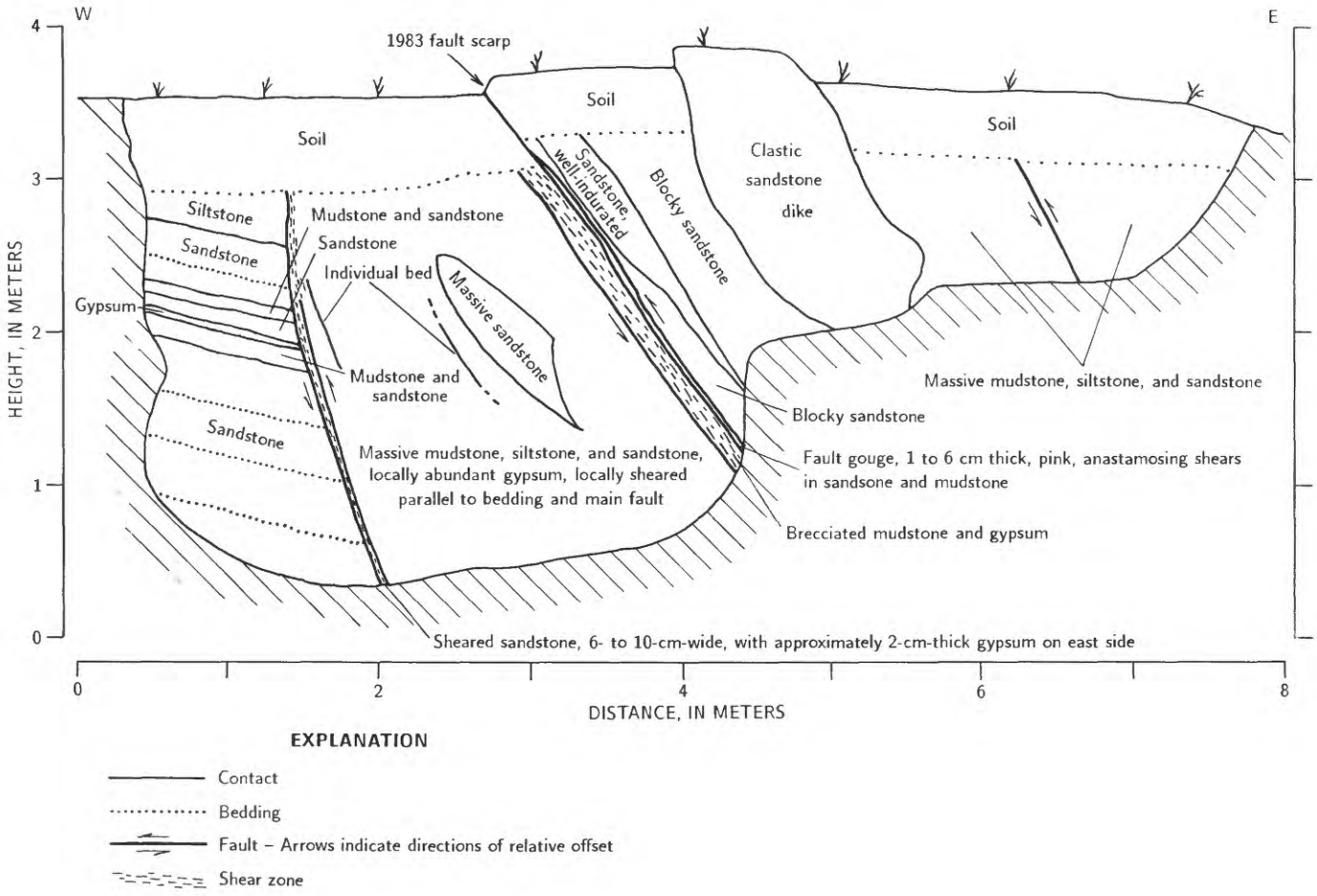

FIGURE 16.20.—Log of trench TN2 in the Cretaceous Panoche Formation near north end of south segment. View northward.

formed during the main shock, *in* The Imperial Valley, California, earthquake of October 15, 1979: U.S. Geological Survey Professional Paper 1254, p. 247–250.

Obermeier, S.F., Gohn, G.S., Weems, R.E., Gelinas, R.L., and Rubin, Meyer, 1985, Geologic evidence for recurrent moderate to large earthquakes near Charleston, South Carolina: Science, v. 227, no. 4685, p. 408–411.

Russ, D.P., 1979, Late Holocene faulting and earthquake recurrence in the Reelfoot Lake area, northwestern Tennessee: Geological Society of America Bulletin, v. 90, pt. 1, no. 11, p. 1013–1018.

Sieh, K.E., 1984, Lateral offsets and revised dates of large prehistoric earthquakes at Pallett Creek, southern California: Journal of Geophysical Research, v. 89, no. B9, p. 7641–7670.

Sharp, R.V., Lienkaemper, J.J., Bonilla, M.G., Burke, D.B., Cox, B.F., Herd, D.G., Miller, D.M., Morton, D.M., Ponti, D.J., Rymer, M.J., Tinsley, J.C., Yount, J., Kahle, J.E., Hart, E.W., and Sieh, K.E., 1982, Surface faulting in the central Imperial Valley, *in* The Imperial Valley, California, earthquake of October 15, 1979: U.S. Geological Survey Professional Paper 1254, p. 119–143.

Stein, R.S., 1985, Evidence for surface folding and subsurface fault slip from geodetic elevation changes associated with the 1983 Coalinga, California earthquake, *in* Rymer, M.J., and Ellsworth, W.L., eds., Mechanics of the May 2, 1983 Coalinga earthquake: U.S. Geological Survey Open-File Report 85-44, p. 225–253.

Talwani, Pradeep, and Cox, John, 1985, Paleoseismic evidence for recurrence of earthquakes near Charleston, South Carolina: Science, v. 229, no. 4711, p. 379–381.

Uhrhammer, R.A., Darragh, R.B., and Bolt, B.A., 1983, The 1983 Coalinga earthquake sequence: May 2 through August 1, *in* Bennett, J.H., and Sherburne, R.W., eds., The 1983 Coalinga, California earthquakes: California Division of Mines and Geology Special Publication 66, p. 221–231.

U.S. National Earthquake Information Service, 1983, Preliminary determination of epicenters, June 1983: Washington, U.S. Government Printing Office.

Youd, T.L., and Wieczorek, G.F., 1982, Liquefaction and secondary ground failure, *in* The Imperial Valley, California, earthquake of October 15, 1979: U.S. Geological Survey Professional Paper 1254, p. 223–246.

FIGURE 16.21.—Well-cemented, blocky sandstone beds west of the Nuñez fault (large arrows) are absent east of fault. Branch fault (short arrows) is near top of lower sandstone bed. Distance between sandstone beds is approximately 24 m. View northward; photograph taken July 22, 1983.

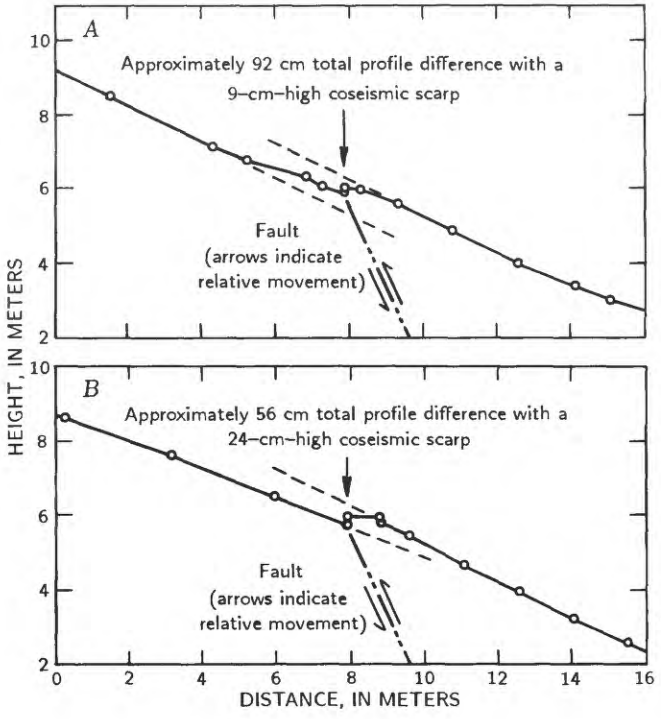

FIGURE 16.22.—Hillslope profiles (dashed where projected) normal to the Nuñez fault at locality 2 (fig. 16.4), showing shape of hillside bench. Profile *B* is 70 m north of profile *A*. Open circles, locality data points.

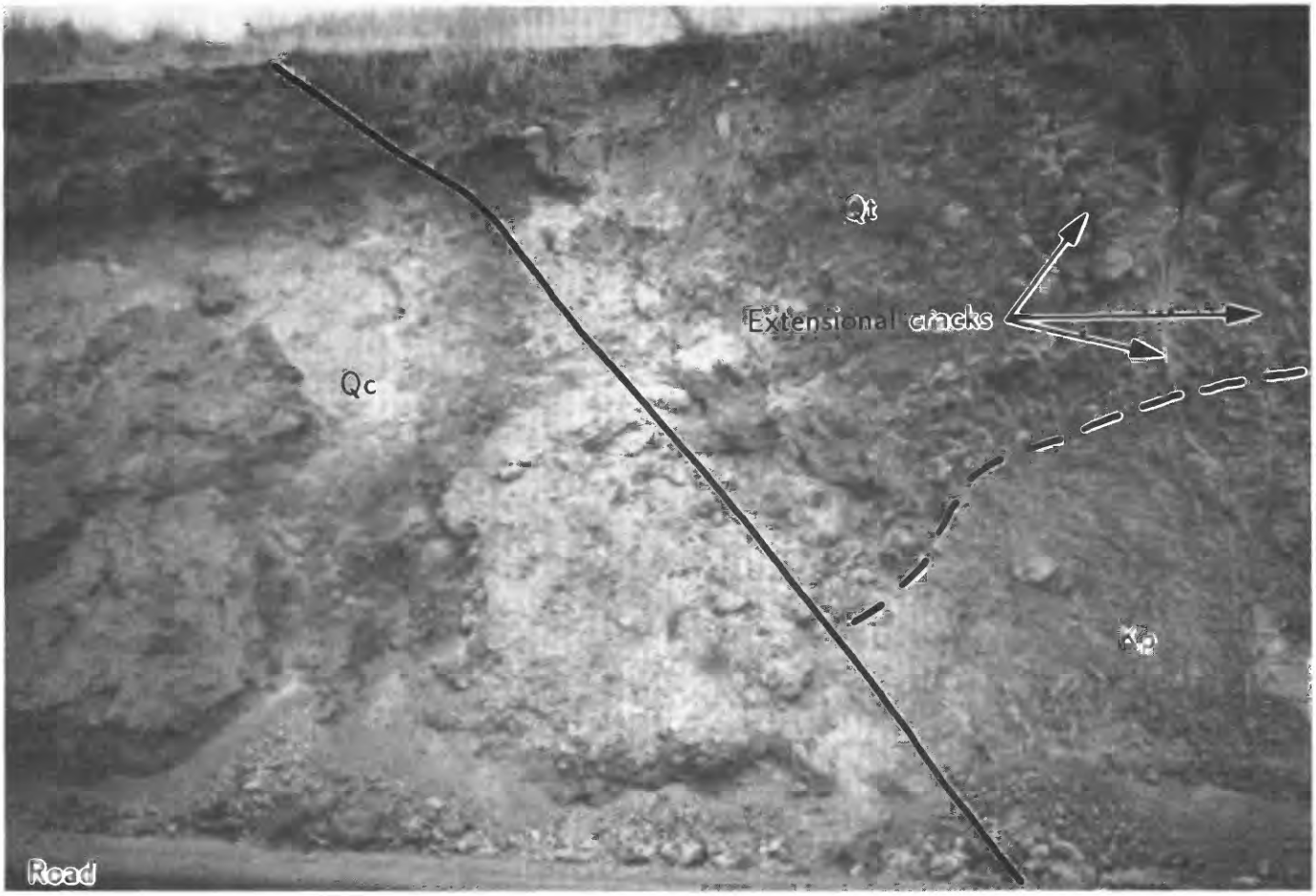

FIGURE 16.23.—Fault in roadcut along Los Gatos Road (loc. 32, fig. 16.4). Colluvium (Qc) on west is faulted against mudstone, siltstone, and sandstone of the Cretaceous Panoche Formation (Kp), capped by Quaternary terrace conglomerate (Qt) on east. Exposure is about 3 m high. Note extensional cracks in hanging wall (right); extensional cracks are same as on left side of figure 16.18. Photograph taken August 20, 1983.

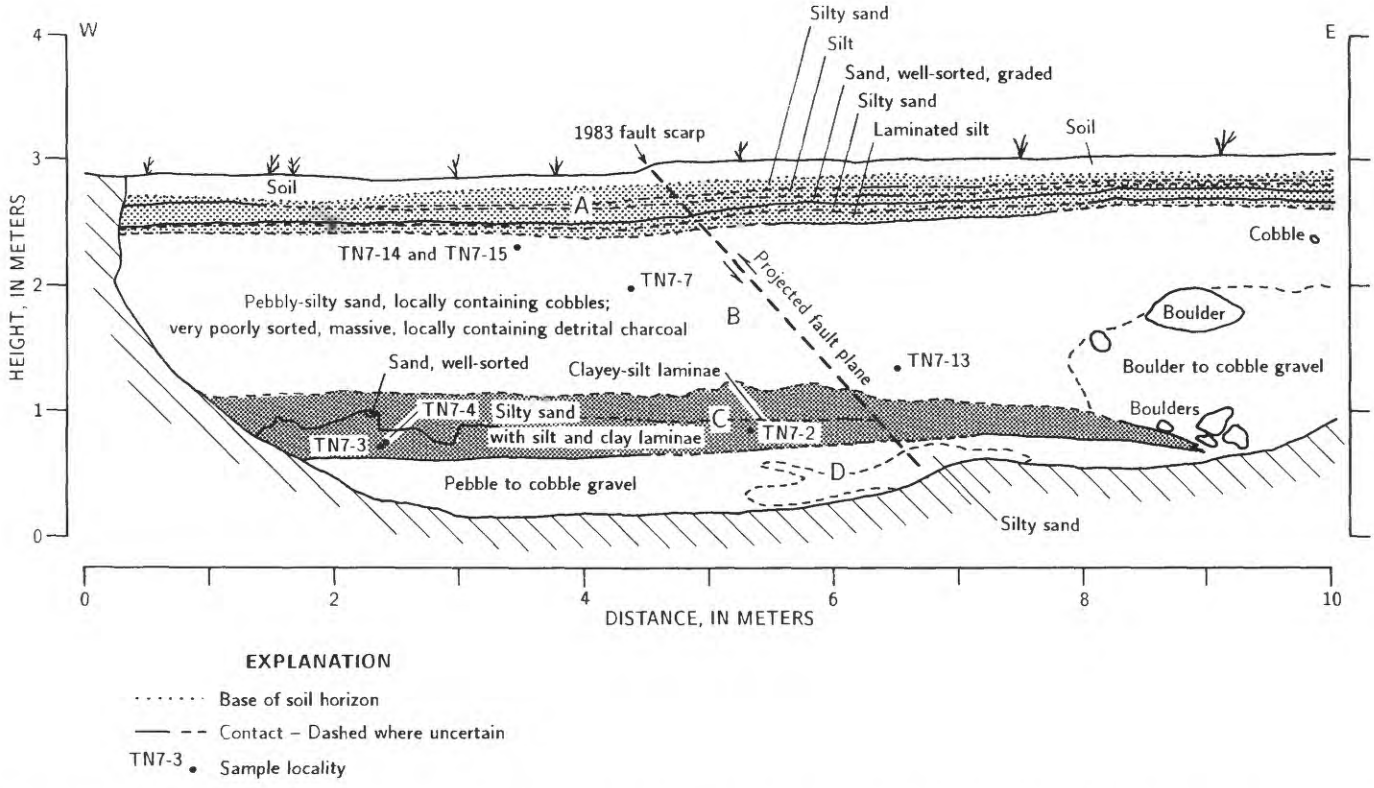

FIGURE 16.24.—Log of trench TN7 in Quaternary fluvial deposits north of Los Gatos Creek (see fig. 16.4 for location). A, five thin, laterally persistent silt and sand beds; B, massive, very poorly sorted pebbly-silty sand with local pebbles and cobbles; C, moderately well sorted silty sand with local clay and silt laminae; D, pebble to cobble gravel.

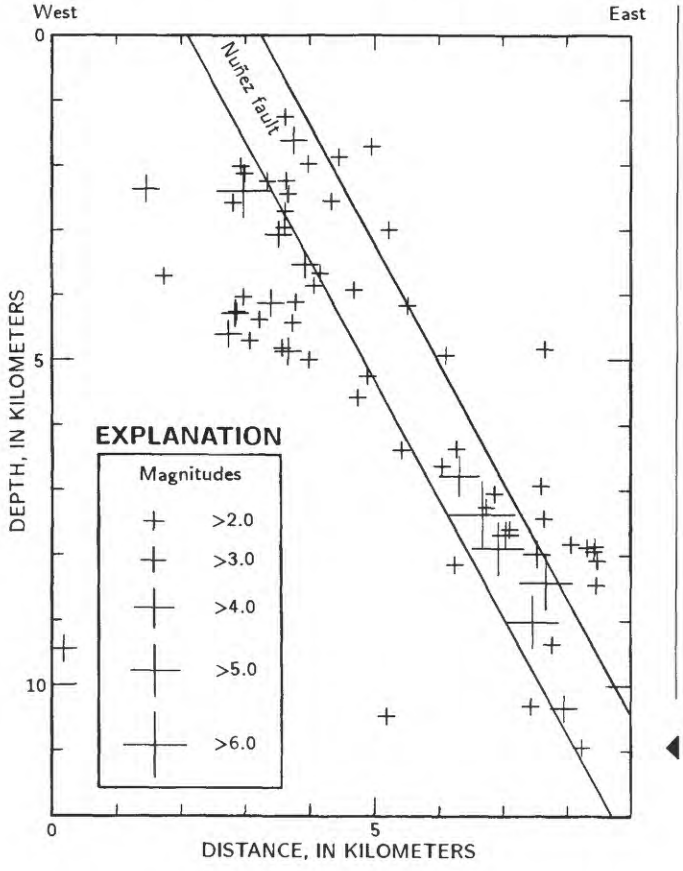

FIGURE 16.25.—Cross section of hypocenters projected onto a plane normal to the Nuñez fault, with interpretation of dip of fault based on locations of $M_L \geq 2.0$ earthquakes. Dip of the Nuñez fault is shown as 61° E. between surface trace and larger, $M_L \geq 5.0$ earthquakes. View along azimuth 010°. Data from Eaton (see chap. 8).

17. DISTRIBUTION AND TIMING OF SLIP ALONG THE NUÑEZ FAULT AFTER JUNE 11, 1983

By MICHAEL J. RYMER, JAMES J. LIENKAEMPER, and BETH D. BROWN,
U.S. GEOLOGICAL SURVEY

CONTENTS

ABSTRACT

Nine leveling lines were installed across the Nuñez fault near Coalinga, Calif., after the second of five moderate earthquakes occurred on the fault. Surface rupture on two north-south-trending fault segments was associated with the first of these earthquakes on June 11, 1983. The lines were installed to record postseismic-slip and possible later coseismic-slip events. Leveling began July 15, 1983, and was repeated five times, ending August 29, 1984. Horizontal-angle surveys measured the lateral component of postseismic slip along one of these leveling lines from August 10, 1983, to February 12, 1985.

Direct measurements of scarp heights and leveling data indicate a complex history for slip on the Nuñez fault during the 1983 Coalinga earthquake sequence. Possible minor postseismic slip on the fault followed the June 11 initial surface rupture. On July 22, 41 days after the initial rupture, the largest earthquake on the Nuñez fault coincided with a second episode of coseismic surface displacement of more than 3 cm. The July 22 earthquake and its aftershocks either initiated or accelerated postseismic slip along the fault. The July 22 coseismic and postseismic slips were greater at the north ends of both fault segments. The largest surveyed value of July 22 coseismic and postseismic slip was more than 6 cm. The right-lateral component of postseismic slip at one site, starting 60 days after the initial surface rupture, amounted to 9 mm. The proportion of right-lateral to vertical components measured for post-July 22 postseismic slip is similar to that for the June 11 coseismic-slip observations.

INTRODUCTION

Nine leveling lines were installed across the Nuñez fault after the June 11 and July 9, 1983, earthquakes, to monitor postseismic slip and to document any coseismic displacements that might accompany further shocks. Monuments for one of these leveling lines were also used for angle measurements to document the horizontal component of postseismic slip.

Right-reverse surface rupture occurred on the Nuñez fault in association with an M_L=5.2 earthquake on June 11, 1983 (see chap. 16). This surface rupture consisted of breaks along two approximately north-south-trending segments (fig. 17.1). Maximum net displacements on the northern and southern segments in association with the initial surface rupture were 65 and 13 cm, respectively (see chap. 16). Four other earthquakes of $M_L \geq 5.0$ occurred on the Nuñez fault on July 9, 22 (two events), and 25 (fig. 17.1; see chap. 8).

The locations of leveling lines across the surface breaks provide a comprehensive coverage of the 1983 rupture; distances between lines or ends of rupture segments are less than 0.7 km. The leveling lines are short, 16 to 60 m long. These short lengths were dictated by steep local topography where the fault is located along ridge crests and hilltops. All but three of the leveling lines are in Cretaceous sedimentary rocks of the Great Valley sequence: Line N7 is installed on Holocene flood deposits (alluvium) of nearby Los Gatos Creek; line N9 is in asphalt pavement, which overlies both Great Valley strata and roadfill; and line N1 is installed on both Quaternary colluvium and Great Valley strata.

Time of installation of the lines varied; lines N1 to N6 were installed on July 13–14, line N9 on July 23, and lines N7 and N8 on July 27. Leveling surveys were made on all available lines on the following dates: July 15, 22–23, and

27–28, 1983; and January 30–31, May 22, and August 29, 1984. Angle surveys were done along line N7 on August 10 and November 14, 1983; on April 28, June 18, and November 23, 1984; and on February 12, 1985. Throughout this chapter, we use only Greenwich mean time for the times of surveys and earthquakes.

The terms "coseismic" and "postseismic" as used for surface slip in this chapter refer only to the time of movement and not to tectonic processes. In the section below entitled "Discussion," we present possible tectonic, fault-rupture processes and our preferred views of faulting on the Nuñez fault.

SURVEYING PROCEDURES

The leveling surveys, except along line N9, were measured from brass bench marks attached to 1.5-m-long copper-coated steel rods pounded into the ground. All nine lines are perpendicular to the fault strike. Lines N1 to N8 each consist of six bench marks, with three marks on each side of the fault. Line N9 consists of 13 nails driven into the pavement near the south edge of Los Gatos Road; the nails are spaced 5 m apart with one at the fault trace and six on each side of it. We minimized variation in surveying results by using the same procedure, instrument, observer, setup sites, and monument type at each site, and, to the extent possible, we scheduled surveys during similar climatic conditions.

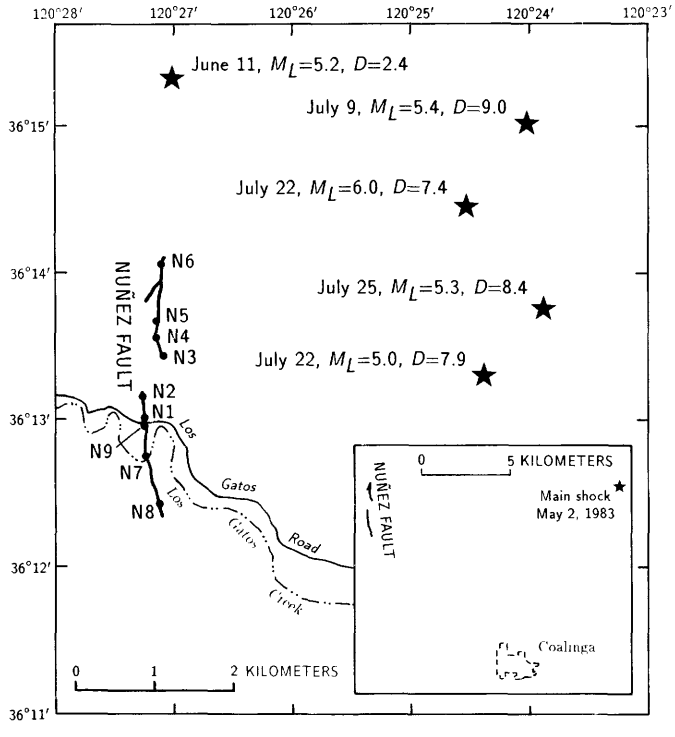

FIGURE 17.1.—Coalinga, Calif., area, showing locations of leveling lines across 1983 surface breakage of the Nuñez fault, which ruptured at the surface in association with an M_L=5.2 earthquake on June 11, 1983. Stars denote locations of earthquakes of $M_L \geq 5.0$ on the Nuñez fault. Locations and depths (D) from Eaton (see chap. 8).

Leveling was done using a Wild NAK–2 automatic level and a Fiberglas rod. A new rod was used for the last three surveys, but both rods were calibrated. Sighting distances did not exceed 25 m. Maximum errors in the relative elevation determined for each mark are estimated to be ±2.0 mm. Local erratic changes in relevelings are probably due to nontectonic processes affecting the ground, rather than to surveying errors or blunders.

Angle measurements were made on line N7, which is the most nearly level of all the Nuñez lines. Angle sightings were made with a Wild T–3 theodolite with Wild T–2 traverse targets. The traversing method used was modified from that of Burford and Harsh (1980) and Galehouse and others (1982). The standard deviation of angles surveyed in this method was no more than ±1.05 s, equivalent to ±0.5 mm per 100 m of array length.

RESULTS OF MEASUREMENTS

The observations reported below are limited by various factors, the most important of which are noted below. Leveling lines on the Nuñez fault range in length from 16 to 60 m, and so the sampling width of the faulted blocks varies. Likewise, sampling density (that is, monument spacing) varies; for example, line N2 has a monument spacing of 2 to 4 m, and N1 of 9 to 10 m. Another factor is variation in the timing of surveys, because some lines were added later, during the course of monitoring; for example, lines N7, N8, and N9 were not installed until the times of first or second relevelings on the other lines. Another limitation to the discussion below is the degree of measurement accuracy. However, despite these limitations, we believe that the Nuñez fault-slip data contribute to a better understanding of fault movement and postseismic slip.

Results of repeated relevelings along the leveling lines are shown in figure 17.2*A*. The leveling data are presented in two sets. The first set is temporally associated with the July 22 M_L=6.0 earthquake (releveling from July 15 to 22), and the second with post-July 22 movement (releveling from July 22, 1983, to August 29, 1984). For both periods of movement, surface slip was greater at the north ends of the respective fault segments. For the July 22 coseismic-slip phase, the maximum vertical component of slip was 3.1 cm, at line N6; for the post-July 22 postseismic-slip phase, it was 4.0 cm, at line N2. Detailed descriptions of line-by-line relevelings are presented below in the section entitled "Supplementary Data."

Results from line N2, located near the north end of the southern segment, are the most interesting and informative of all the Nuñez lines. Plotted on a logarithmic time

scale (fig. 17.3), data on the vertical component of displacement of monument 6 relative to monument 1 reveal an exponential decrease in vertical slip after the July 22 earthquake. Also plotted in figure 17.3 are scaled measurements of the freshly ruptured fault scarp near line N2, made on June 14 and July 12, 1983, before installation of the leveling lines. Scarp height may have increased 1 cm during this time, but because the uncertainty is about ±0.5 cm, postseismic slip during this period is indefinite. The initial leveling data of July 15 are plotted on the slope drawn between the two scarp-height measurements. Thus plotted, the five points based on leveling suggest an increase in slip rate above the rate indicated by the two points based on scarp heights. Thus, we conclude that the postseismic slip at line N2 at least did accelerate after the July 22 earthquake and that postseismic slip may have initiated with that event.

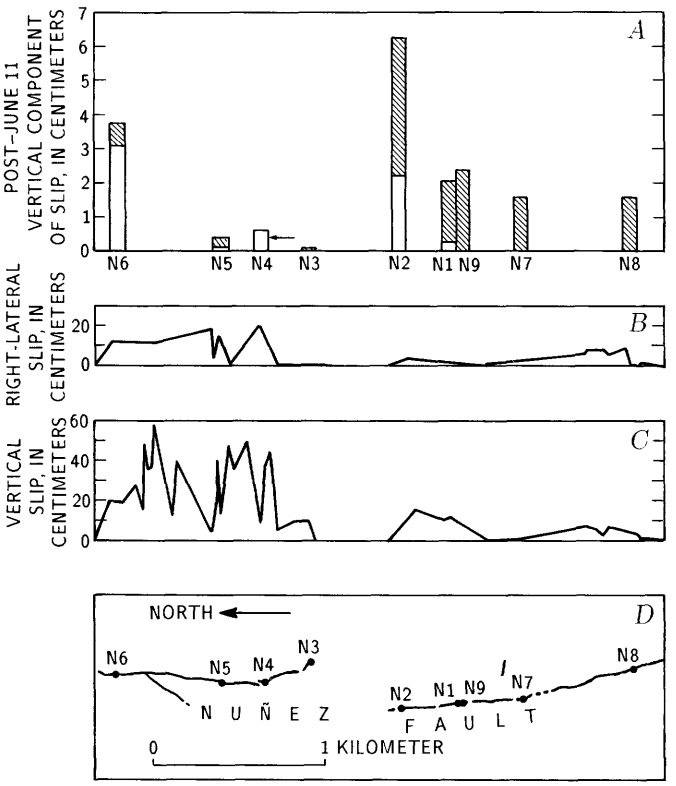

FIGURE 17.2.—Slip along the Nuñez fault in association with the Coalinga earthquake sequence. *A*, Histogram of vertical component of slip measured along leveling lines. Solid bar, coseismic slip for July 22 M_L=6.0 earthquake; hachured bar, postseismic slip for July 22 earthquake. Arrow at line N4 shows cumulative slip until August 1984. *B*, Right-lateral component of slip for June 11 earthquake. *C*, Vertical component of slip for June 11 earthquake. *D*, Sketch map of the Nuñez fault, showing locations of leveling lines. All the displacement data in figures 17.2*A* through 17.2*C* are plotted normal to the measurement locations shown here. Compare figure 16.5.

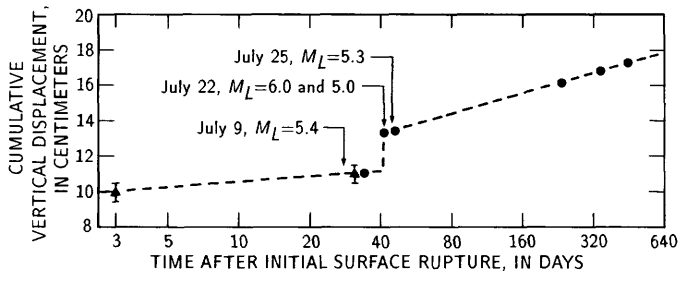

FIGURE 17.3.—Cumulative vertical displacement at leveling line N2 as a function of time after initial surface rupture on June 11, 1983. Triangles, direct measurements of height of freshly formed fault scarp near line N2; circles, vertical elevation changes between monuments 1 and 6. Arrows denote times of major earthquakes on the Nuñez fault.

Figure 17.4 shows the relative elevation changes at line N2 versus time, along with the cumulative seismic moment. In combination, it is apparent that even though the initial surface rupture was associated with the June 11 earthquake, most energy released on the fault was associated with the July 22 earthquake. Therefore, it was not unlikely that the July 22 shock would also be associated with coseismic slip. The inset in figure 17.4 shows the cumulative number of earthquakes ($M_L \geq 1.5$) on the fault for the same period as the main plot. We note that the July 22 shock also coincides with the start of most earthquakes on the Nuñez fault.

The apparent horizontal component of July 22 postseismic slip, measured only at line N7, totaled 9 mm over a 552-day period starting with the first observations made 60 days after the June 11 surface rupture. Right-lateral and vertical components of postseismic slip measured in the same period at line N7 have a ratio of 9:13. This ratio is greater than that indicated by the plunge of slickensides measured in a trench exposure near line N2 but is consistent with a greater proportion of right-lateral component of June 11 coseismic slip in the southern part of the southern segment of the fault (fig. 17.2; see chap. 16).

DISCUSSION

MECHANICS OF NUÑEZ FAULT SLIP

By understanding the timing of slip on the Nuñez fault and the location and source parameters of Nuñez earthquakes, we can describe a tentative mechanical model of post-June 11 coseismic and postseismic slip. Except for the coseismic surface rupture on June 11, 1983, the timing of slip events at site N2 is plotted in figure 17.3. The scarp-height measurements were made directly on the ground rupture near line N2, and the surveyed measurements represent relative block uplift of the hanging wall, on the basis of elevation changes between the westernmost and easternmost monuments (1, 6). Although these two methods measure different widths

across the surface rupture, the simplicity of block movements here (see fig. 17.11) suggests that the effect of combining the two data sets is not misleading. The leveling data, which begin 34 days after the initial surface rupture, are placed on the line projected between the first and second scarp-height measurements, at 3 and 31 days after the initial surface rupture, respectively. Because only six earthquakes, of M_L=1.2 to 2.0, occurred on the Nuñez fault in the period between 31 and 34 days after June 11 (J.P. Eaton, written commun., 1984), it is unlikely that any larger slip could have occurred during this brief hiatus in our data.

The line drawn between the two scarp-height measurements plotted in figure 17.3 suggests a slight vertical component of postseismic slip of about 1 cm for this period. However, given the estimated ±5-mm limitations of these measurements, owing to the effects of local folding, soil-block rotation, disturbance by animals, and the difficulty in precisely reoccupying the same position along the fault trace, the significance of the indicated change in scarp height is unclear. Nevertheless, the slope determined by the two scarp-height measurements yields the relation D=9.5+0.99 log (1+1.3t), which at the origin predicts a coseismic slip of 9.5 cm for June 11. Here, total post-June 11 slip (June 11 postseismic slip, July 22 coseismic slip, and July 22 postseismic slip) as of the last surveyed measurement would be about 7.8 cm, a value that amounts to more than 70 percent of the projected June 11 coseismic slip at site N2. Another possibility, that the July 9 earthquake caused a 1-cm jump in surface displacement, is unlikely, given its 9-km hypocentral depth and small rupture radius (see chap. 12).

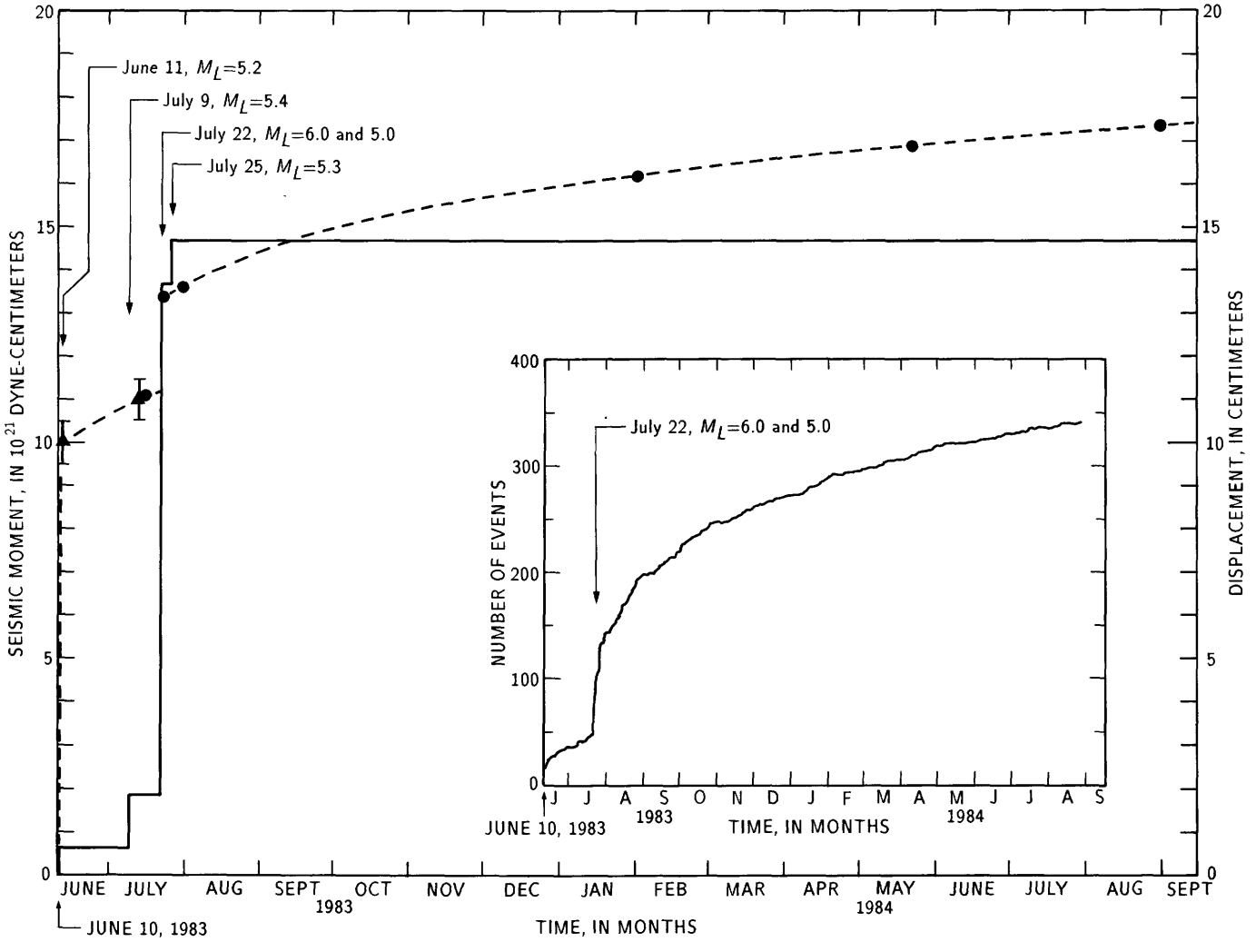

FIGURE 17.4.—Cumulative vertical displacement (dashed line) and cumulative seismic moment of earthquakes on the Nuñez fault as a function of time. Cumulative number of earthquakes (M_L≥1.5) for the same period are plotted in inset. Triangles, direct measurements of height of freshly formed fault scarp near line N2; circles, vertical-elevation changes between monuments 1 and 6. Arrows denote times of major earthquakes on the Nuñez fault. Seismicity data from F.W. Lester and J.P. Eaton (written commun., 1985).

Comparison of the first (July 15) and second (July 22) surveying measurements at line N2 indicates a significant jump in fault displacement of 2.3 cm. The two July 22 earthquakes of M_L=6.0 and 5.0 occurred within this period. The increase in surface displacement coincident with the larger of these two events is plotted in figure 17.3.

A linear exponential decay of surface displacement over time is suggested for the period after the larger July 22 shock. Data for the second to sixth leveling surveys for line N2 fit a straight line (fig. 17.3), despite the occurrence, from 41 to 445 days after initial surface rupture, of the July 25 M_L=5.3 earthquake and other events as large as M_L=4.1. We note also that the slope of the slip data after the July 22 earthquakes indicates a higher rate of postseismic slip after that event relative to the period before July 22 (the period of June 11 postseismic slip).

The hypocenter locations of the five Nuñez earthquakes of $M_L \geq 5.0$ and of aftershocks during 5 days after the larger July 22 event are plotted in figure 17.5 on a vertical, north-south-trending plane. Comparison of the data plotted in figures 17.3 through 17.5 allows speculation on a model for coseismic and postseismic rupture processes on the Nuñez fault. Initial surface rupture was associated with the shallow, approximately 2.4-km-hypocentral depth June 11 event. The abrupt displacement inferred from leveling data near the time of the larger July 22 event is thought to be shallow coseismic slip accompanying the largest shock, even though the primary rupture area calculated in chapter 12 is too small to reach the ground surface (fig. 17.5). Thus, if this calculated rupture area is correct, secondary rupture in the shallow environment may be required.

Depending on the uncertainties of scarp-height measurements and possible postseismic slip in the 34 days following the June 11 earthquake, postseismic slip either began or accelerated at the time of the larger July 22 earthquake. Apparently, primary slip that began during the July 22 earthquakes would have slowly propagated upward some 6 km from the top of the coseismic-rupture area through the area broken by the June 11 event. Therefore, the dominant (possibly the only) postseismic slip on the Nuñez fault was associated with the larger July 22 event and its aftershocks, which were deeper than the initial rupture.

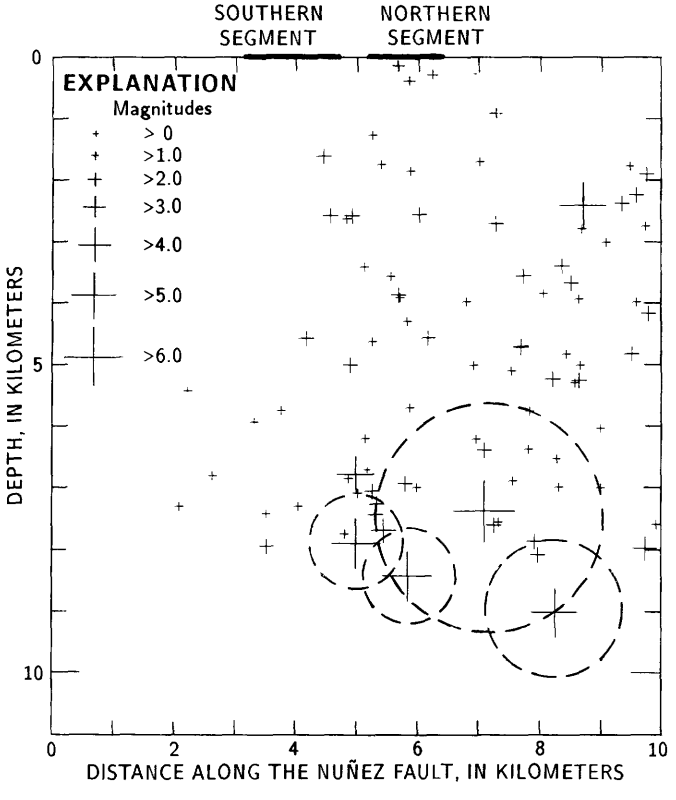

FIGURE 17.5.—Cross-sectional plot of hypocenter locations and calculated rupture areas of deep $M_L \geq 5.0$ earthquakes on the Nuñez fault, showing first 5 days of aftershocks from July 22 M_L=6.0 earthquake. View westward. Hypocenter locations from Eaton (see chap. 8); calculated rupture areas (dashed circles) from McGarr and others (see chap. 12).

VARIATIONS IN AMOUNT AND STYLE OF POST-JUNE 11 SURFACE SLIP

The distribution of leveling lines along the Nuñez fault enables us to point out both spatial and temporal variations in the amount of movement and style of faulting. One readily apparent spatial variation in these data is the large coseismic slip at lines N6 and N2 associated with the July 22 M_L=6.0 earthquake, situated at the north ends of each of the fault segments. Also, continuing postseismic slip after the July 22 earthquake at the north ends of both segments was greater than in other places (fig. 17.2*A*). This asymmetric skewing of coseismic and postseismic slip matches that of the vertical component of June 11 coseismic vertical slip in the southern segment but not in the northern segment, where the distribution along strike of the vertical component of coseismic slip can be described as approximately bell shaped (fig. 17.2*C*). Caution must be applied in comparing coseismic and postseismic slip from the June 11 and July 22 earthquakes because the later event was located 4 to 6 km deeper and 1 to 2 km farther south (compare June 11 and July 22 events, figs. 17.1 and 17.5).

Another spatial variation in the leveling data is that leveling lines with larger amounts of July 22 coseismic and postseismic slip (lines N1, N2, N7–N9) are in areas with moderate to low amounts of June 11 coseismic slip, and, conversely, lines with little to no July 22 coseismic and postseismic slip (lines N3–N5) are in areas with the greatest June 11 coseismic slip. Although an inverse correlation between coseismic slip and large postseismic

slip has been noted for other earthquakes (Burford, 1972; Sylvester and Pollard, 1975; Bucknam and others, 1978), the Nuñez fault differs because most of the postseismic slip was probably associated with a different earthquake than was the initial coseismic slip.

A third point of spatial comparison is that lines in the southern segment (except line N2) showed similar rates of July 22 postseismic slip (fig. 17.6), even though the vertical components of June 11 coseismic displacement at all these lines ranged from 4 to 10 cm.[1] The similar rates of July 22 postseismic slip for lines in the southern segment suggest a more regional effect of propagating postseismic slip, which compensates for lithologic variations in the near-surface and for the small June 11 coseismic displacement in the entire fault segment.

The leveling data indicate local variations in the style of July 22 coseismic and postseismic slip, even though the 1983 Nuñez fault rupture was everywhere a steeply dipping, right-reverse oblique fault. The variations in faulting style associated with the June 11 coseismic rupture are described in detail in chapter 16. The accumulated slip plotted in profile for each line (see section below entitled "Supplementary Data" and fig. 17.11) is clearly related to near-surface rock type. Leveling lines on colluvium, roadfill, and alluvium (such as lines N1, N9, and N7) show broad ramplike or steplike displacement patterns throughout a wide zone. In contrast, leveling lines on well-cemented sandstone (lines N2, N8) show simpler, blocklike movements across the fault (see figs. 17.11*G*, 17.16*E*). Near-surface, well-cemented sandstone is indicated at lines N2 and N8 by the presence of nearby outcrops and by the degree of difficulty during pounding in of the steel rods used for leveling monuments. Similar variations from distinct scarps in bedrock (blocklike signals) and monoclinal warping (ramplike signals) in alluvium were recorded for the slip associated with the 1971 San Fernando, Calif., earthquake (U.S. Geological Survey staff, 1971, p. 67–71).

POSTSEISMIC SLIP ON OTHER REVERSE FAULTS

To compare postseismic slip behavior of the Nuñez rupture to other cases of historical reverse and oblique-reverse faulting, we reviewed the literature for 17 events. In addition, we reviewed 16 events selected from Lewis and others (1981) and Bonilla and others (1984, table 3). Except for the 1971 San Fernando rupture in southern California, no reverse-faulting event has been so thoroughly monitored for postseismic slip as the Nuñez fault rupture.

For the reviewed events, no significant postseismic slip was measured across the causative fault. However, the sparsity of observations of postseismic slip in reverse-faulting events is hardly conclusive that postseismic slip did not occur. The remoteness of many ruptures, harsh weather, and limited resources for investigations severely limited collection of data. In fact, mention of repeated measurements by a single investigator is rare. Ambraseys (1965) reported that the 1962 Iran rupture grew from a small displacement at one locality a month after the earthquake, to become an obvious scarp 17

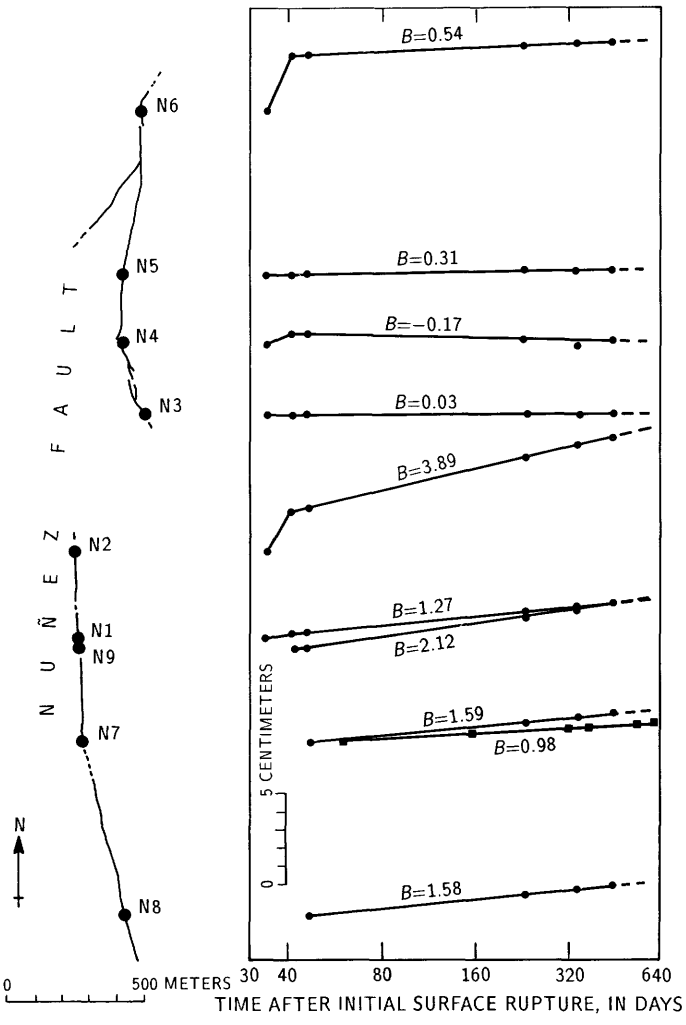

FIGURE 17.6.—Variation in vertical component of July 22 coseismic and postseismic slip as a function of time at leveling lines across the Nuñez fault. Initial measurement of each line is plotted adjacent to location of line on adjoining map of fault trace. Slopes (*B* values) are based on least-squares regression of observed displacement on the logarithm of time only for data after July 22 M_L=6.0 earthquake. Circles, leveling data; squares, right-lateral alignment data.

[1]Table 16.1 indicates less than 1 cm of June 11 coseismic (vertical component) displacement at line N7 from measurements of the offset ground surface at the scarp, but not from displacement spread across the length of the leveling line, as for July 22 postseismic slip (fig. 17.6). A June 11 coseismic vertical component of warpage of both surface and near-surface strata of approximately 10 cm, spread across a 0.5-m-wide zone, was mapped in nearby trench TN7 (see fig. 16.24).

months later. A pavement repair after the 1952 Kern County, Calif., rupture was broken again at a branch of the White Wolf fault (Buwalda and St. Amand, 1955), indicating possible postseismic slip. Probable postearthquake tensional faulting in the hanging-wall block away from the primary rupture was observed in both the 1968 and 1970 Australian earthquakes (Gordon and Lewis, 1980). The 1929 New Zealand rupture area was resurveyed along a railroad leveling line crossing the fault. These survey comparisons showed possible continued movement on secondary faults, but not on the main trace. Various methods used to measure postseismic slip near the fault after the 1971 San Fernando earthquake all indicated no significant postseismic slip near the fault, that is, no slip exceeding a centimeter within a few tens of meters from the surface of the fault (Burford and others, 1971; Lahr and others, 1971; Nason, 1971; Sylvester and Pollard, 1975). One reported apparent exception (Savage and others, 1975) of greater postseismic slip (42 cm) is attributable to a mistake in field reduction of the data, and, in fact, no such large postseismic slip did occur (Lienkaemper and Burford, 1985).

Thus, the more than 6 cm of July 22 coseismic and postseismic slip measured across the Nuñez fault at line N2 (probable 7.8 cm of total vertical component of slip), in comparison with a projected value of 9.5 cm for the June 11 coseismic displacement, exceeds any postseismic slip previously measured on a reverse fault. In fact, the absence of measured large postseismic slip on reverse faults before the Nuñez event led Sylvester and Pollard (1975) to conclude that significant postseismic slip cannot occur because of the compressional regime and probable large stress drops associated with reverse faulting. Large stress drops in the fault plane would require rapid release of much of the built-up stress and thus leave little potential for postseismic slip. This model, however, does not fit the observations for the Nuñez fault, not only because large postseismic slip did occur but also because the July 22 M_L=6.0 and July 25 M_L=5.3 events had even larger stress drops (see table 12.1) than did the June 11 earthquake associated with the initial surface rupture.

CONCLUSIONS

The dense spacing of leveling lines across the Nuñez fault and the timing of measurements allow us to evaluate the geographic distribution, sense of motion, and rate of postseismic slip more completely than in previous studies. Together, measurements of scarp height and surveyed measurements of relative monument heights indicate that the vertical component of slip on the Nuñez fault exhibited various systematic behaviors. Possible minor postseismic slip occurred on the fault after the June 11, 1983, M_L=5.2 event and initial surface rupture. On July 22, 41 days after the initial rupture, the largest of five $M_L \geq 5.0$ earthquakes on the Nuñez fault was accompanied by another coseismic surface displacement, amounting to as much as 3.1 cm. Coseismic surface slip on July 22 was distributed asymmetrically along the length of the fault, skewed to the north ends of both fault segments (at lines N6 and N2), but was also detected at lines N4 and N1. The July 22 earthquake initiated or accelerated the postseismic slip. As with coseismic slip, postseismic slip was also skewed to the north ends of both fault segments, and the largest values were measured on the southern segment.

The maximum vertical component of displacement measured on our lines was about 6 cm at line N2 at the north end of the southern segment. This surveyed amount, in combination with a scaled scarp-height difference of 1 cm (11 cm on July 12 less 10 cm on June 14), amounts to more than 70 percent of the June 11 coseismic vertical component of slip at that site. Measured slip across lines elsewhere in the southern segment amounts to only 41 to 59 percent of that at line N2 during comparable survey periods. However, all four of the more southerly lines in the southern segment have approximately similar rates of July 22 postseismic slip (fig. 17.6).

The post-June 11 slip behavior of the northern segment was similar to that of the southern segment, in that the largest values of July 22 coseismic and postseismic slip occurred at the north end of each segment. In contrast to the southern segment, however, which showed more nearly uniform July 22 postseismic slip, the southern part of the northern segment showed little or no postseismic slip.

Despite the short length of leveling lines (16–60 m), we were able to detect variations in expression or style of faulting as viewed in profile. The various faulting styles are related to the rigidity of the near-surface materials. Leveling lines emplaced in well-cemented sandstone (lines N2, N8) showed blocklike displacement signatures, whereas lines emplaced in unconsolidated materials (alluvium, colluvium, and roadfill) showed ramplike or steplike signatures that dispersed movement of the relatively upthrown eastern block over tens of meters.

ACKNOWLEDGMENTS

We thank Jack Boatwright, R.O. Burford, A.F. McGarr, S.S. Schulz, and R.V. Sharp for insightful discussions concerning measurement of postseismic slip and the mechanics of postseismic slip. J.P. Eaton and F.W. Lester kindly shared seismicity data that helped in the construction of figure 17.5. We especially thank the landowners, the Birdwell, Nuñez, and Zwang families, who allowed access to their property and helped immeas-

urably with their cooperation and generosity. Special thanks are also due to K.J. Kendrick, who energetically helped install the leveling-line monuments and assisted in the surveying procedures. The extensive, well-organized archive of literature on historical surface ruptures assembled by M.G. Bonilla made possible a rapid and thorough review of literature on reverse-faulting rupture events.

REFERENCES CITED

Ambraseys, N.N., 1965, An earthquake engineering study of the Buyin-Zahra earthquake of September 1, 1962, in Iran: World Conference on Earthquake Engineering, 3d, Auckland and Wellington, New Zealand, 1965, Proceedings, v. 3, p. V7–V26.

Bonilla, M.G., Mark, R.K., and Lienkaemper, J.J., 1984, Statistical relations among earthquake magnitude, surface rupture length, and surface fault displacement: Seismological Society of America Bulletin, v. 74, no. 6, p. 2379–2411.

Bucknam, R.C., Plafker, George, and Sharp, R.V., 1978, Fault movement (afterslip) following the Guatemala earthquake of February 4, 1976: Geology, v. 6, no. 3, p. 170–173.

Burford, R.O., 1972, Continued slip on the Coyote Creek fault after the Borrego Mountain earthquake, *in* The Borrego Mountain earthquake of April 9, 1968: U.S. Geological Survey Professional Paper 787, p. 105–111.

Burford, R.O., Castle, R.O., Church, J.P., Kinoshita, W.T., Kirby, S.H., Ruthven, R.T., and Savage, J.C., 1971, Preliminary measurements of tectonic movement, *in* The San Fernando, California, earthquake of February 9, 1971: U.S. Geological Survey Professional Paper 733, p. 80–85.

Burford, R.O., and Harsh, P.W., 1980, Slip on the San Andreas fault in central California from alinement array surveys: Seismological Society of America Bulletin, v. 70, no. 4, p. 1233–1261.

Buwalda, J. P., and St. Amand, Pierre, 1955, Geological effects of the Arvin-Tehachapi earthquake, *in* Oakeshott, G.B., ed., Earthquakes in Kern County, California during 1952: California Division of Mines and Geology Bulletin 171, p. 41–56.

Galehouse, J.S., Brown, B.D., Pierce, Brian, and Thordsen, J.J., 1982, Changes in movement rates on certain East Bay faults, *in* Hart, E.W., Hirschfeld, S.E., and Schulz, S.S., eds., Conference on Earthquake Hazards in the Eastern San Francisco Bay Area, Hayward, Calif., 1982, Proceedings: California Division of Mines and Geology Special Publication 62, p. 239–250.

Gordon, F.R., and Lewis, J.D., 1980, The Meckering and Calingiri [Australia] earthquakes, October 1968 and March 1970: Geological Survey of Western Australia Bulletin 126, 229 p.

Lahr, J.C., Wyss, Max, and Hileman, J.A., 1971, Repeated surveys of small scale figures established across surface fault ruptures following the earthquake, *in* The San Fernando, California, earthquake of February 9, 1971: U.S. Geological Survey Professional Paper 733, p. 86–88.

Lewis, J.D., Daetwyler, N.A., Bunting, J.A., and Moncrieff, J.S., 1981, The Cadoux [Australia] earthquake, 2 June 1979: Geological Survey of Western Australia Report 11, 99 p.

Lienkaemper, J.J., and Burford, R.O., 1985, No large afterslip in Little Tujunga Canyon following the 1971 San Fernando [California] earthquake: Seismological Society of America Bulletin, v. 75, no. 2, p. 627.

Nason, R.D., 1971, Instrumental monitoring of post-earthquake fault movements (afterslip), *in* The San Fernando, California, earthquake of February 9, 1971: U.S. Geological Survey Professional Paper 733, p. 89–90.

Savage, J.C., Burford, R.O., and Kinoshita, W.T., 1975, Earth movements from geodetic measurements, *in* Oakeshott, G.B., ed., The San Fernando earthquake of February 1971: California Division of Mines and Geology Bulletin 196, p. 175–186.

Sylvester, A.G., and Pollard, D.D., 1975, Afterslip on the Sylmar fault segment, *in* Oakeshott, G.B., ed., The San Fernando earthquake of February 1971: California Division of Mines and Geology Bulletin 196, p. 227–233.

U.S. Geological Survey staff, 1971, Surface faulting, *in* The San Fernando, California, earthquake of February 9, 1971: U.S. Geological Survey Professional Paper 733, p. 55–76.

SUPPLEMENTARY DATA

Elevation profiles and profiles of elevation changes are shown in figures 17.7 through 17.14 and 17.16, progressing from north to south, in order of presentation of the leveling lines; data for the apparent right-lateral component of offset are shown in figure 17.15. The vertical components of offset (leveling data) are plotted at the same scale for all figures. For all the leveling lines, the westernmost monument is arbitrarily held fixed. The westernmost monument of every line is designated "monument 1," and the easternmost "monument 6," except for line N9, where the nails are designated by their distance (in meters) and direction from the fault—for example, "nail 10E." Leveling lines N3 through N6 are in the northern segment, and the other lines are in the southern segment (fig. 17.1).

LINE N6

Releveling of line N6, 24 hours after the July 22 M_L=6.0 earthquake, showed a maximum vertical component of displacement of about 3.1 cm (fig. 17.7*B*), the largest displacement of all lines for any two consecutive surveys. In the same period, monument 3, immediately west of the fault scarp, also moved up relative to monument 1. Movement of monument 3 on leveling line N6 is anomalous relative to the other leveling lines founded in Great Valley strata. The relative movement of monument 3 was probably caused by uplift of soil blocks pushed by the hanging wall, similar to that we exposed in a shallow trench only 2 m south of line N6. In the trench, however, the secondary break is only 0.7 m west of the main scarp, whereas monument 3 is 3.5 m west of the main break, and no other surface breaks were seen west of it.

FIGURE 17.7—Relative elevation and amount of vertical component of slip on the Nuñez fault at leveling line N6. *A*, Profile of relative elevations along leveling array. *B*, Vertical component of slip across fault trace from July 15 to 22, 1983. *C*, Vertical component of slip from July 22 to 27, 1983. *D*, Vertical component of slip from July 27, 1983, to January 30, 1984. *E*, Vertical component of slip from January 30 to May 22, 1984. *F*, Vertical component of slip from May 22 to August 29, 1984. *G*, Cumulative vertical component of slip from July 15, 1983, to August 29, 1984.

The second releveling of line N6 was 3 days later. Between the first and second relevelings, an M_L=5.3 earthquake occurred on the Nuñez fault on July 25. The monuments moved less than 1 mm during this period (fig. 17.7*C*), less than our limits of accurate detection, which are ±2 mm.

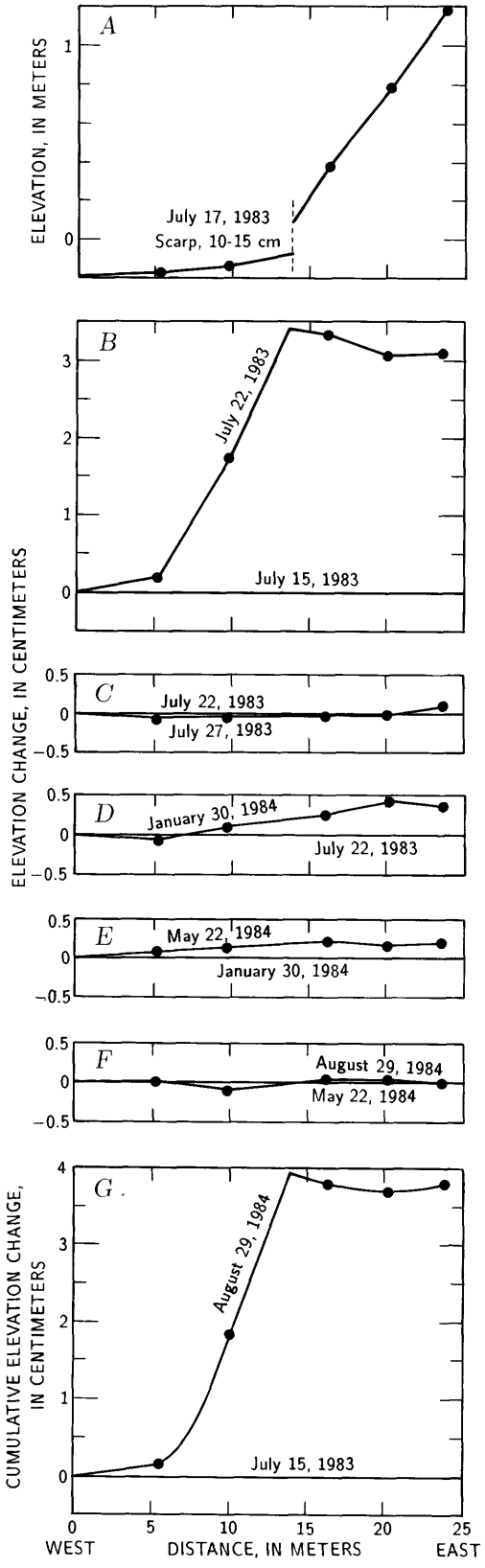

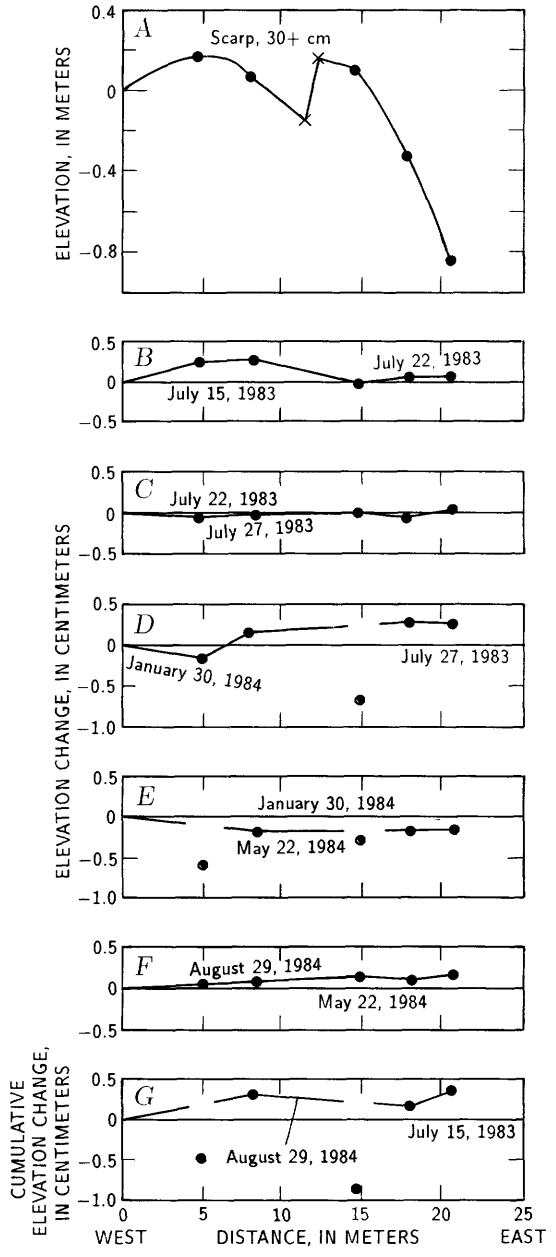

FIGURE 17.8.—Relative elevation and amount of vertical component of slip on the Nuñez fault at leveling line N5. *A*, Profile of relative elevations along leveling array. *B*, Vertical component of slip across fault trace from July 15 to 22, 1983. *C*, Vertical component of slip from July 22 to 27, 1983. *D*, Vertical component of slip from July 27, 1983, to January 30, 1984. *E*, Vertical component of slip from January 30 to May 22, 1984. *F*, Vertical component of slip from May 22 to August 29, 1984. *G*, Cumulative vertical component of slip from July 15, 1983, to August 29, 1984.

The third releveling of line N6 was 188 days later; it showed elevation changes similar to the first releveling but with about 10 times less slip (fig. 17.7*D*); relative uplift across the array was 4 mm. During this period, the largest earthquake along the Nuñez fault was only M_L=4.5, on September 11, 1983. The last two relevelings of line N6 were made after 113- and 99-day intervals, on May 22 and August 29, 1984, respectively. These relevelings showed continuing decay of the rate of postseismic slip until it returned to zero (figs. 17.7*E*, 17.7*F*).

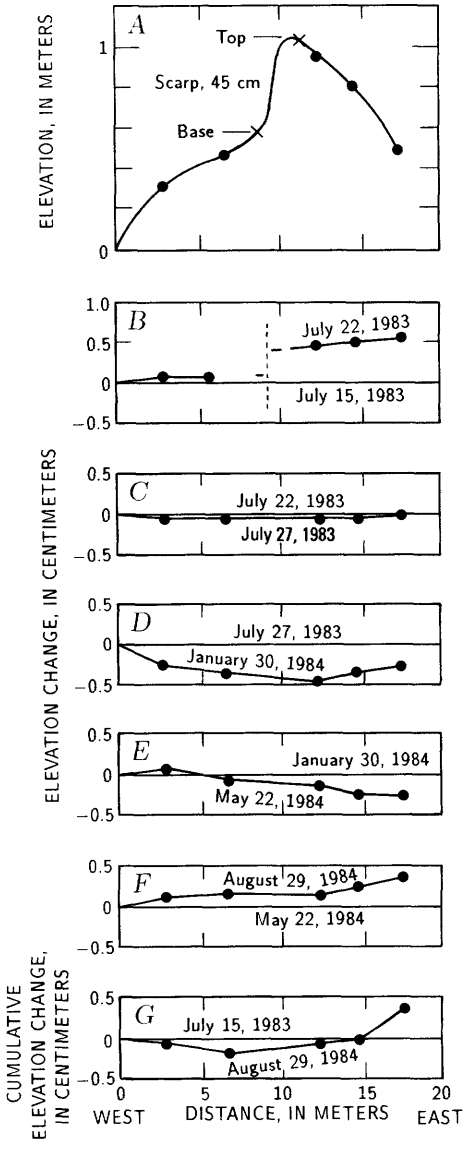

FIGURE 17.9.—Relative elevation and amount of vertical component of slip on the Nuñez fault at leveling line N4. *A*, Profile of relative elevations along leveling array. *B*, Vertical component of slip across fault trace from July 15 to 22, 1983. *C*, Vertical component of slip from July 22 to 27, 1983. *D*, Vertical component of slip from July 27, 1983, to January 30, 1984. *E*, Vertical component of slip from January 30 to May 22, 1984. *F*, Vertical component of slip from May 22 to August 29, 1984. *G*, Cumulative vertical component of slip from July 15, 1983, to August 29, 1984.

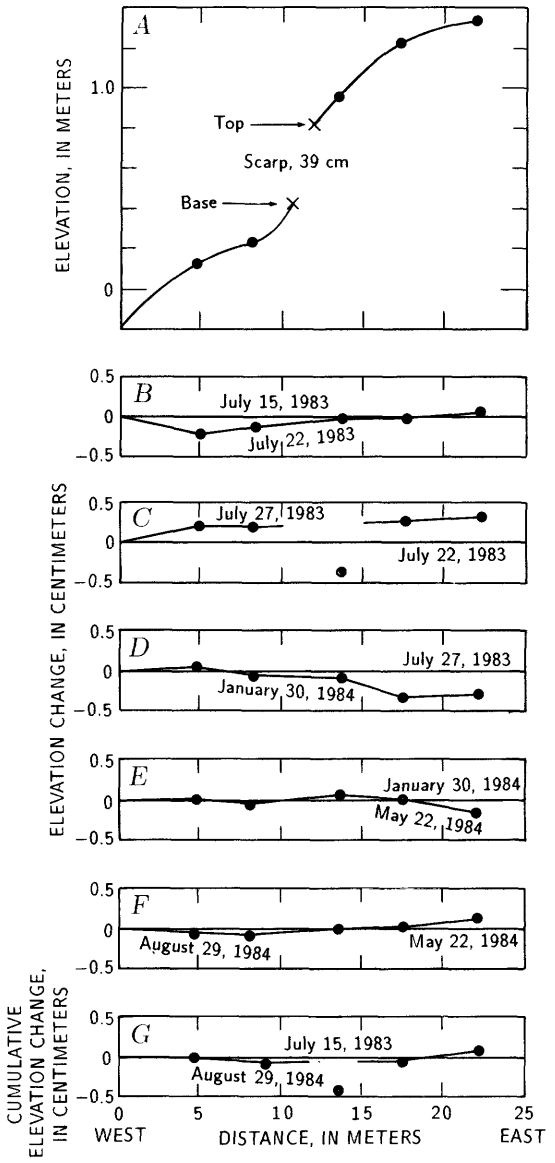

FIGURE 17.10.—Relative elevation and amount of vertical component of slip on the Nuñez fault at leveling line N3. *A*, Profile of relative elevations along leveling array. *B*, Vertical component of slip across fault trace from July 15 to 22, 1983. *C*, Vertical component of slip from July 22 to 27, 1983. *D*, Vertical component of slip from July 27, 1983, to January 30, 1984. *E*, Vertical component of slip from January 30 to May 22, 1984. *F*, Vertical component of slip from May 22 to August 29, 1984. *G*, Cumulative vertical component of slip from July 15, 1983, to August 29, 1984.

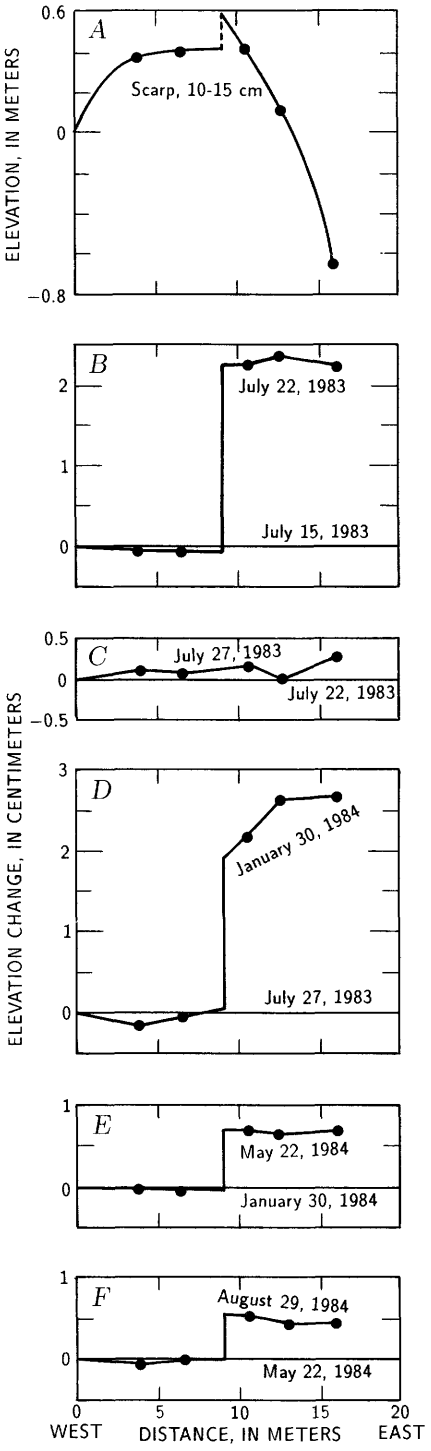

FIGURE 17.11.—Relative elevation and amount of vertical component of slip on the Nuñez fault at leveling line N2. *A*, Profile of relative elevations along leveling array. *B*, Vertical component of slip across fault trace from July 15 to 22, 1983. *C*, Vertical component of slip from July 22 to 27, 1983. *D*, Vertical component of slip from July 27, 1983, to January 30, 1984. *E*, Vertical component of slip from January 30 to May 22, 1984. *F*, Vertical component of slip from May 22 to August 29, 1984. *G*, Cumulative vertical component of slip from July 15, 1983, to August 29, 1984.

Cumulative elevation change along leveling line N6 (fig. 17.7*G*) shows 3.7 cm of movement since installation of the line: 3.1 cm of July 22 coseismic slip and 0.6 cm of post-July 22 postseismic slip. The three monuments east of the fault, on the hanging wall, rose relative to monuments on the west side as a block.

LINE N5

Leveling surveys were made along line N5 on the same days as on line N6. Surveys of line N5 showed no postseismic slip within the limits of detection (figs. 17.8*B*–17.8*F*). In fact, the largest indicated changes along the line were recorded on January 30 and May 22, 1984, but we attribute these movements to instability of monuments 2 and 4. The cumulative measurement of monuments during the entire 411-day period of the study shows no more than 4 mm of vertical movement across line N5 (fig. 17.8*G*), indicating only minor, if any, postseismic slip on line N5.

LINE N4

The first releveling of line N4 showed a minor but smooth profile of elevation change of 5 mm (fig. 17.9*B*). Succeeding leveling surveys showed this line to fluctuate in apparent slip by only minor amounts, always less than 5 mm (figs. 17.9*C*–17.9*F*). The cumulative slip along line

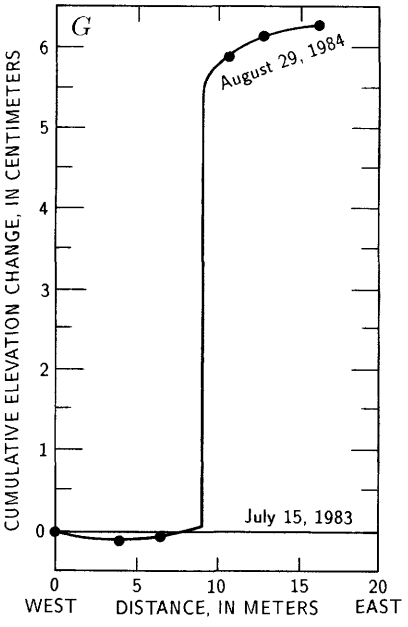

N4 showed negligible net movement for all monuments; monument 6 has a net elevation change relative to monument 1 of 4 mm, and the other monuments all changed less than 2 mm. Similar to line N5, we interpret no demonstrable postseismic slip on line N4.

LINE N3

Line N3, at the south end of the northern segment, showed little, if any, vertical slip. In fact, the profile changes plotted in figures 17.6*B* through 17.6*F* indicate

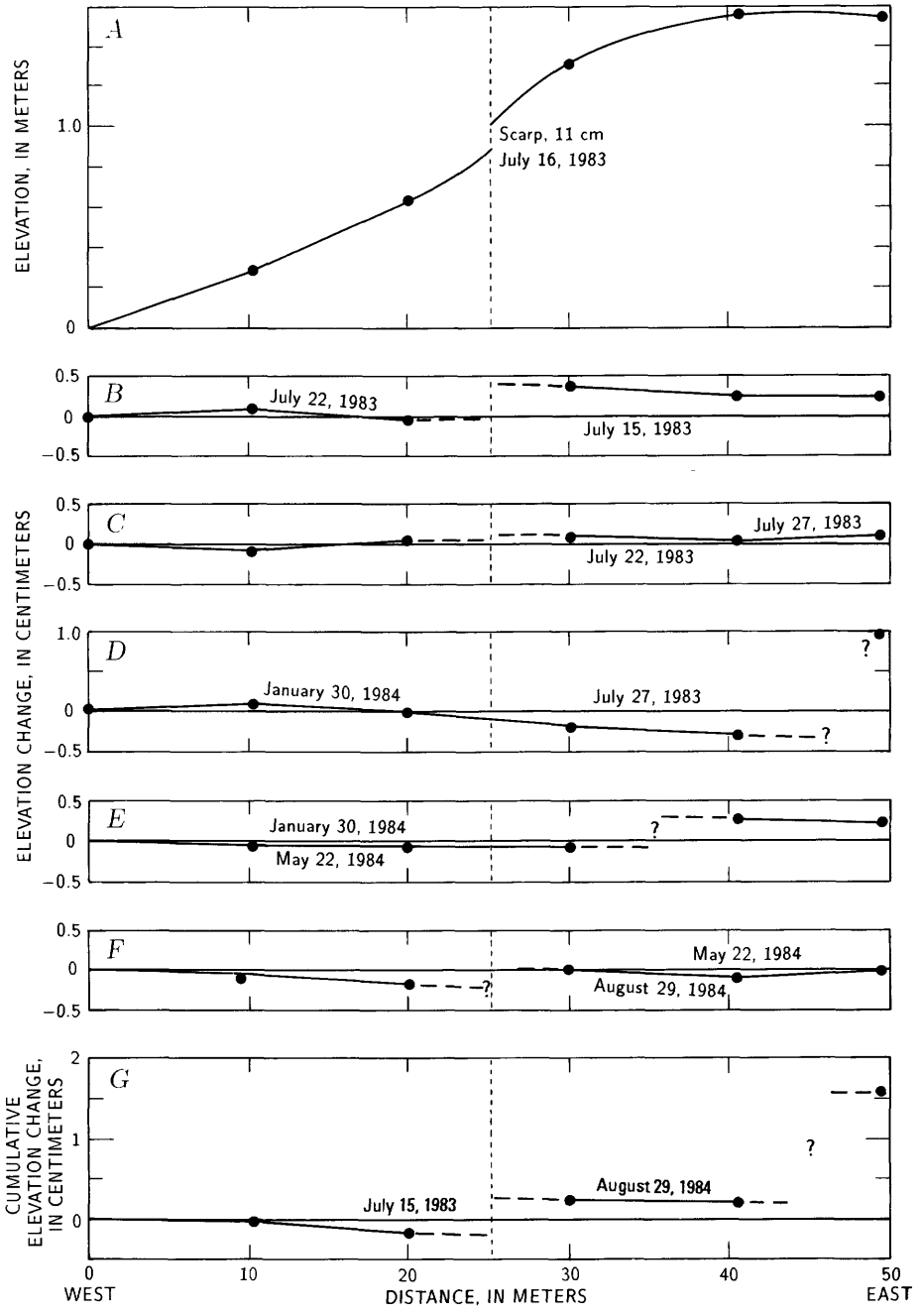

FIGURE 17.12.—Relative elevation and amount of vertical component of slip on the Nuñez fault at leveling line N1. *A*, Profile of relative elevations along leveling array. *B*, Vertical component of slip across fault trace from July 15 to 22, 1983. *C*, Vertical component of slip from July 22 to 27, 1983. *D*, Vertical component of slip from July 27, 1983, to January 30, 1984. *E*, Vertical component of slip from January 30 to May 22, 1984. *F*, Vertical component of slip from May 22 to August 29, 1984. *G*, Cumulative vertical component of slip from July 15, 1983, to August 29, 1984.

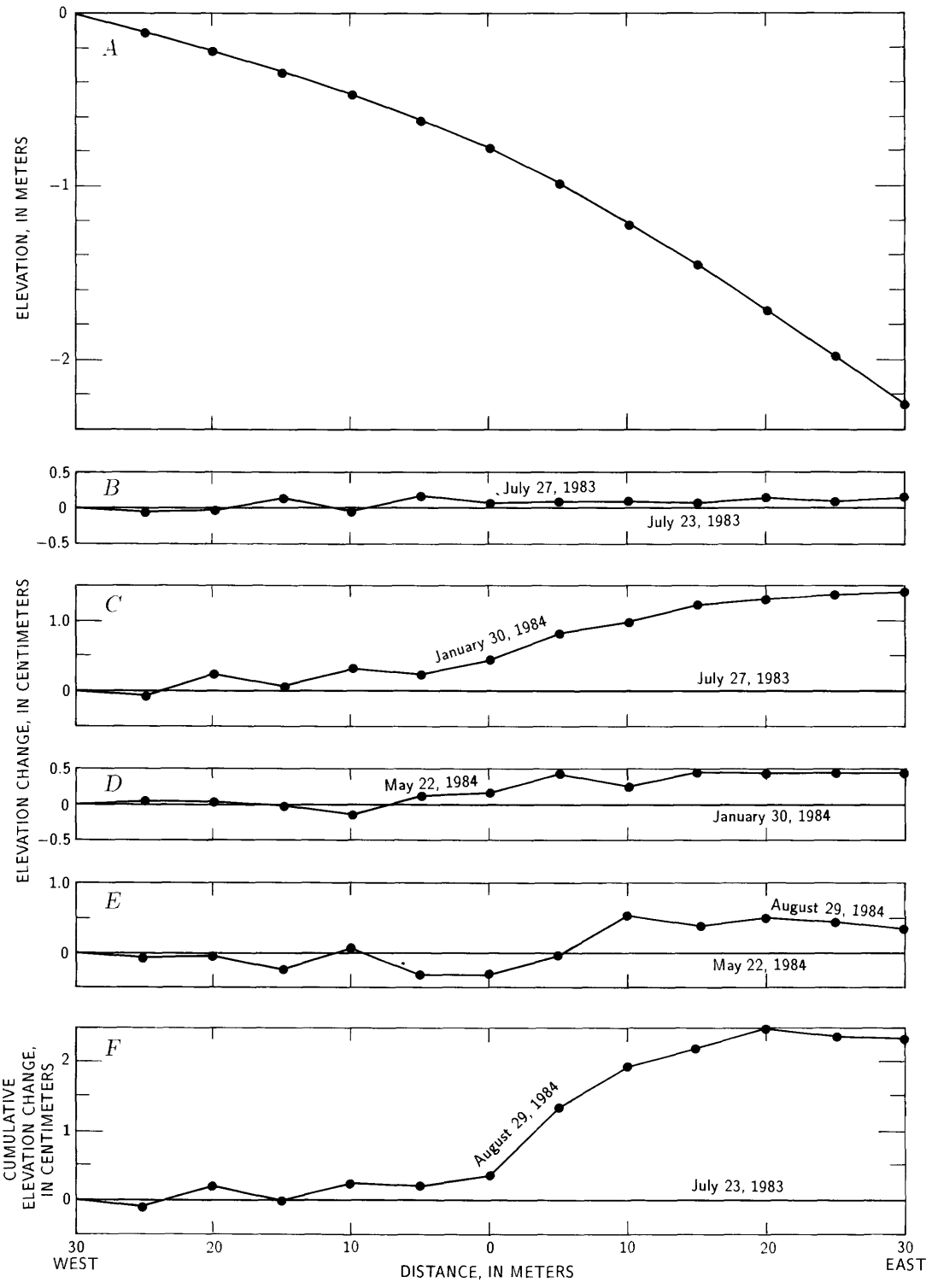

FIGURE 17.13.—Relative elevation and amount of vertical component of slip on the Nuñez fault at leveling line N9. *A*, Profile of relative elevations along leveling array. *B*, Vertical component of slip across fault trace from July 23 to 27, 1983. *C*, Vertical component of slip across fault trace from July 27, 1983, to January 30, 1984. *D*, Vertical component of slip from January 30 to May 22, 1984. *E*, Vertical component of slip from May 22 to August 29, 1984. *F*, Cumulative vertical component of slip from July 23, 1983, to August 29, 1984.

≤3 mm of maximum variation in relative elevation. The cumulative plot of the vertical component of slip on line N3 (fig. 17.10*G*), except for one unstable monument, shows that this is the stablest of all the lines.

LINE N2

Releveling of line N2 20 hours after the July 22 M_L=6.0 earthquake showed a distinct blocklike movement of 2.3 cm (fig. 17.11*B*). The second releveling, 3 days later and after the July 25 M_L=5.3 earthquake, showed minimal movement (fig. 17.11*C*). The third through fifth relevelings, however, showed detectable slip (figs. 17.11*D*–17.11*F*). Similar to the first releveling, these sets of measurements showed simple blocklike behavior of both east and west sides of the fault. The plot of the cumulative vertical component of post-June 11 slip along line N2 shows the largest surveyed slip of all the Nuñez lines, 6 cm (fig. 17.11*G*).

LINE N1

The first releveling of line N1 showed a minor blocklike vertical component of movement (fig. 17.12*B*). The second releveling showed minimal slip, consistent with continued reverse-fault movement for this 5-day interval. The third releveling indicated that monument 6 had moved relatively upward 10 mm (fig. 17.12*D*). A seventh monument, located 9 m north of monument 6 at the same distance east of the fault scarp, also showed upward relative movement (14 mm) during this period, suggesting a branch or subsidiary break between monuments 5 and 6 that slipped vertically during this interval. Numerous extensional cracks parallel to the fault scarp were noted after the initial surface rupture in a 13-m-wide zone east of the fault scarp at line N1. No fresh cracking or offset was seen between bench marks 5 and 6 on January 31, 1984. The result of the change in slip location is a steplike pattern of relative uplift (fig. 17.12*G*). Similar

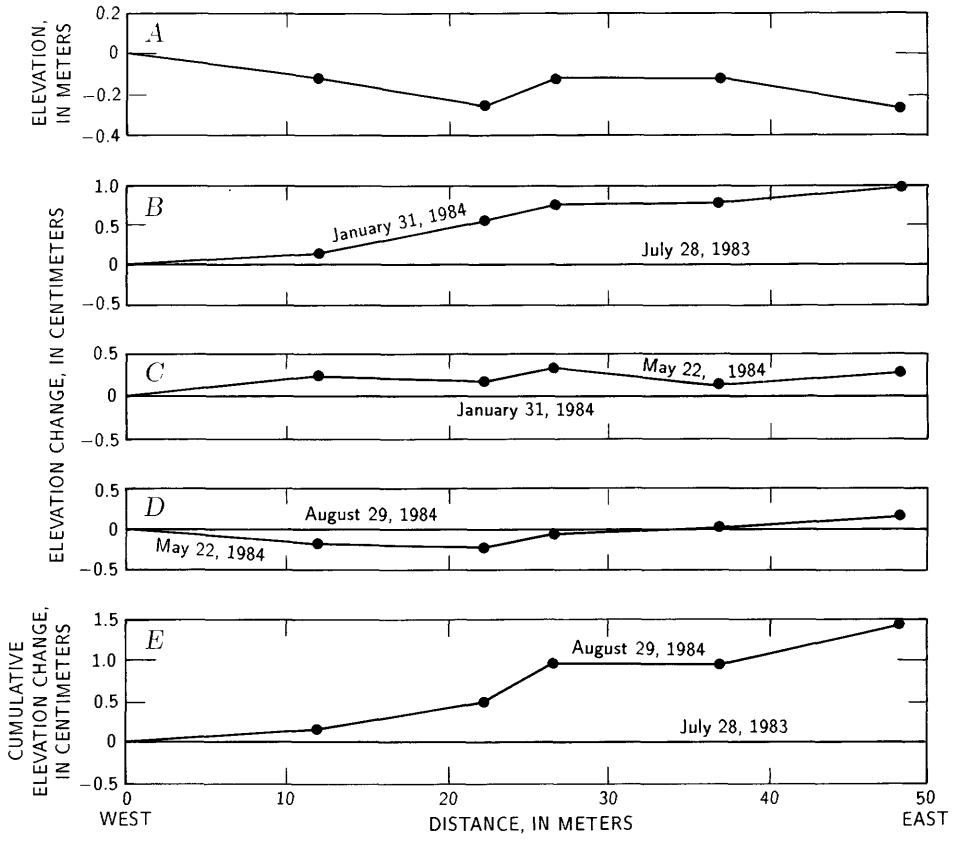

FIGURE 17.14.—Relative elevation and amount of vertical component of slip on the Nuñez fault at leveling line N7. *A*, Profile of relative elevations along leveling array. *B*, Vertical component of slip across fault trace from July 28, 1983, to January 31, 1984. *C*, Vertical component of slip from January 31 to May 22, 1984. *D*, Vertical component of slip from May 22 to August 29, 1984. *E*, Cumulative vertical component of slip from July 28, 1983, to August 29, 1984.

steplike features were not seen along other leveling lines, possibly because most lines are much shorter. Line N9, however, which is the longest and located only 20 m south of line N1, showed different but not inconsistent elevation-change profiles (fig. 17.13).

LINE N9

During the first survey period, from July 23 to 28, no vertical component of movement of the east side of the fault was demonstrable. The second releveling, however, on January 30, 1984, showed 14 mm of relative uplift of the east end of the array (fig. 17.13*C*). The profile is ramplike, inferring distributed slip or folding of the eastern, relatively upthrown block. The third and fourth relevelings of line N9 showed a continuation of this trend (figs. 17.13*D*, 17.13*E*). The plot of cumulative elevation change again shows the ramplike form, where the slip is expressed as evenly distributed movement in a 20-m-wide zone east of the scarp (fig. 17.13*F*). Installation of line N9 in an asphalt pavement built partly on fill brings to mind two possible exceptions for measurement comparisons: (1) The blacktop itself may deform differently from the rock and soil underlying the other lines, and (2), vertical deformation may be distributed differently in roadfill that supports the pavement.

LINE N7

Line N7 had the smallest free-face scarp height after the June 11 earthquake relative to the other Nuñez lines (see chap. 16). Lines N7 and N8 were first leveled on July 28, 1983. The first releveling of line N7 showed 10 mm of relative uplift of the east side of the fault in a ramplike form similar to those at lines N6 and N9 (figs. 17.7*B*, 17.13*C*, 17.14*B*). Relevelings of line N7 on May 22 and August 29, 1984, showed minor continued relative uplift of the east end of the line (figs. 17.14*C*, 17.14*D*). The plot

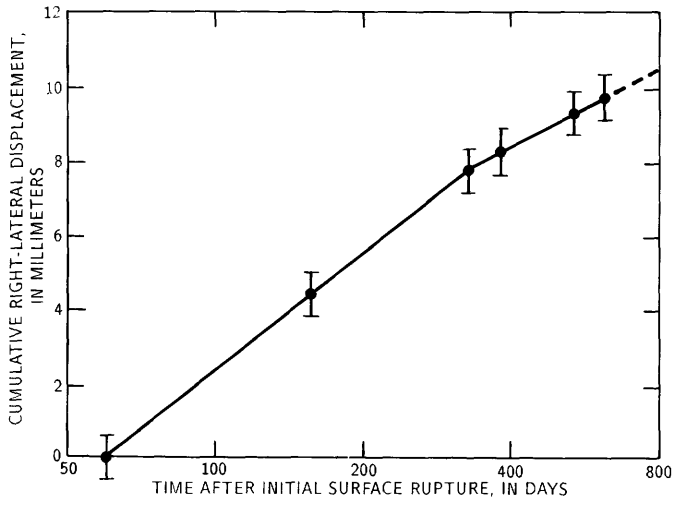

FIGURE 17.15.—Apparent right-lateral component of slip measured at line N7 as a function of time.

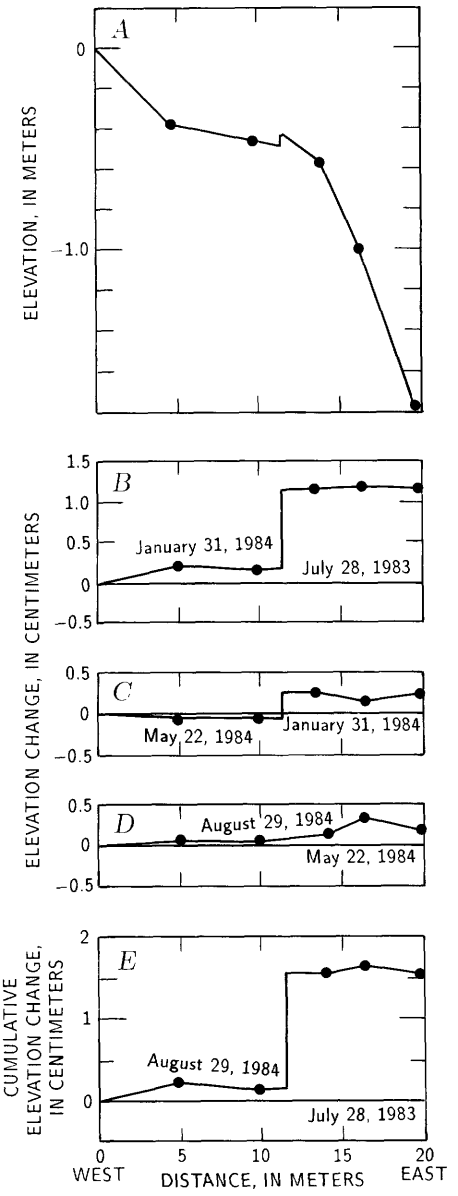

FIGURE 17.16.—Relative elevation and amount of vertical component of slip on the Nuñez fault at leveling line N8. *A*, Profile of relative elevations along leveling array. *B*, Vertical component of slip across fault trace from July 28, 1983, to January 31, 1984. *C*, Vertical component of slip from January 31 to May 22, 1984. *D*, Vertical component of slip from May 22 to August 29, 1984. *E*, Cumulative vertical component of slip from July 28, 1983, to August 29, 1984.

of cumulative profile changes along line N7 (fig. 17.14*E*) shows relative movement of the east side of the fault that is broadly ramplike, similar to the profile of line N9.

Measurements of apparent right-lateral displacement along line N7 also show continuing slip. What appears to be the cumulative right-lateral component of displacement at line N7 is plotted in figure 17.15. Apparent right-lateral components of displacement based on angle changes for the first through fifth resurveys were 4.4±0.6, 3.4±0.6, 0.6±1.0, 0.9±0.5, and 0.5±0.3 mm, respectively, totaling 9.8±0.6 mm.

LINE N8

Line N8 is the third shortest of all the Nuñez leveling lines but, like line N2, shows clear tectonic signals for each measurement period. The first releveling shows a distinct blocklike movement of 1 cm (fig. 17.16*B*). The second and third relevelings show continuing but smaller displacements. Different amounts of relative uplift are related to the variations in sample intervals and the decay of slip rate over time. The plot of cumulative profile changes for line N8 shows the simple blocklike behavior of movement at this site (fig. 17.16*E*).

18. LANDSLIDES TRIGGERED BY THE EARTHQUAKE

By EDWIN L. HARP and DAVID K. KEEFER,
U.S. GEOLOGICAL SURVEY

CONTENTS

ABSTRACT

The May 2 earthquake triggered landslides numbering in the thousands. Most numerous were rockfalls and rockslides that occurred mainly on slopes steeper than 60° within sandstone, siltstone, and shale units of Upper Cretaceous and Tertiary strata. Soil falls from cutbank slopes along streams were also numerous. Seven slumps in natural slopes were triggered, and minor liquefaction-induced lateral-spread failures occurred along Los Gatos Creek.

Rockfalls and rockslides occurred as far as 34 km northwest, 15 km south, and 26 km southwest of the epicenter. There were few slope failures to the east of the epicenter, owing to the absence of steep slopes in that direction. Throughout the area affected, rockfalls and rockslides were concentrated on southwest-facing slopes; the failures on slopes facing in the southwest quadrant accounted for as much as 93 percent of all failures in some areas. Rockfalls and rockslides from ridge crests were predominantly from sandstone units. Along steeply incised canyons, however, failures in shale and siltstone units were also common.

Small rockslides and soil slides occurred from cut slopes above oil-well pump pads in the oil fields; slumps were common in the outer parts of steep fill slopes of the pump pads. The distribution of seismically induced landslides throughout the entire earthquake-affected area was mapped from true-color airphotos taken on May 3, 1985.

INTRODUCTION

Landslides from the May 2 earthquake numbered in the thousands. The most abundant landslides were rockfalls and rockslides; soil falls from cutbank slopes along streams were also numerous. Seven deep-seated slumps in natural slopes were triggered, and minor liquefaction-induced lateral-spread failures occurred along Los Gatos Creek.

Rockfalls and rockslides occurred mainly within sandstone, siltstone, and shale units of the Big Blue Formation, Domengine Formation, Etchegoin Formation, and Panoche Formation. The largest rockfalls occurred in the Big Blue Formation. The most susceptible slopes were those steeper than 60°, especially near vertical or overhanging cliffs of the Big Blue Formation.

Rockfalls and rockslides were triggered as far as 34.0 km northwest, 15.0 km south, and 26.0 km southwest of the epicenter (pl. 18.1). Near the epicenter and to the east, only a few small rockfalls and soil falls occurred (mainly from roadcuts and other artificial slopes), owing to the absence of steep slopes. Slope failures caused minor damage to cut-and-fill pads for pumps in the oil fields near Coalinga. Small rockslides and soil slides occurred from cut slopes above the pads, and slumps were common in the outer parts of steep fill slopes.

The landslides caused by the earthquake were mapped (pl. 18.1) at 1:24,000 scale from true-color airphotos at 1:40,000 and 1:20,000 scales taken by the U.S. National Aeronautics and Space Administration (NASA) on May 3, 1983. Field-reconnaissance trips were made to inspect many slope-failure sites, so as to check the reliability of the airphoto interpretation. Observations from the first reconnaissance trip of May 3–5, 1983, were described by Keefer and others (1983, 1984).

This chapter documents the landslide distribution, assesses the factors affecting the distribution, compares the landslides and their distribution with those in other historical earthquakes, and compares the susceptibility of different geologic materials. The distribution of landslides triggered by the May 2 earthquake is mapped in plate 18.1. Many of the smallest falls and slides, such as those that occurred near pump pads in the oil fields, were too small to distinguish on the airphotos and so are not mapped. Place names and the locations of the photographs used here are shown on plate 18.1.

TABLE 18.1.—*Tertiary and Cretaceous stratigraphic units of the Coalinga area involved in rockfalls and rockslides*

[Data from Bartow, chapter 1]

Unit	Age	Thickness (m)	Lithology	Falls and slides within formation (percent)
Etchegoin Formation.	Pliocene and late Miocene.	200-1,600	Silty sandstone, siltstone, mudstone, and conglomerate.	15
Santa Margarita Formation.	Late Miocene----	0-250	Silty arkosic sandstone, conglomerate, siltstone, and mudstone, locally calcareous.	1
Big Blue Formation.	Miocene---------	0-50	Breccia, conglomerate, sandstone, conglomeratic mudstone, and mudstone, all composed of serpentinite debris.	20
Temblor Formation.	Oligocene to middle Miocene.	0-1,200	Calcareous sandstone, sandy siltstone, silty shale, conglomerate, and shale.	7
Kreyenhagen Shale.	Eocene----------	60-900	Porcelaneous or diatomaceous shale, porcelaneous mudstone, and shale	3
Domengine Sandstone.	Middle Eocene---	0-125	Arkosic sandstone and conglomerate, locally glauconitic.	7
Lodo Formation.	Late Paleocene and early Eocene.	50-300	Silty shale or mudstone, claystone, and sandstone.	8
Panoche Formation.	Late Cretaceous.	1,000-6,000	Arkosic sandstone, siltstone, shale, and conglomerate.	40

TOPOGRAPHY AND GEOLOGY

The landforms in the hills surrounding Coalinga have been influenced largely by the northwest-southeast-trending regional structure of faulting and folding. This structure results in alternating ridges and valleys whose predominant trend is also northwest-southeastward. The surface expression of the regional structure is evident in exposures of the Cretaceous and Tertiary sedimentary rocks. The formations most severely affected by landslides are from the Cretaceous and Tertiary section and from some of the overlying Quaternary alluvium and colluvium. Besides the landslides triggered by the earthquake, many landslides are present (slumps, debris flows, earthflows) that were initiated by past rainstorms and seasonal high levels in the water table. A generalized listing of the main Cretaceous and Tertiary stratigraphic units of the Coalinga area involved in rockfalls and rockslides from the May 2 earthquake is given in table 18.1.

Because of the arid conditions in the Coalinga region, the structure and stratigraphy are well exposed, especially next to streamcourses. Rapid downcutting by ephemeral streams has created steep slopes in even the least resistant units along stream margins. In general, sandstone units stand out as steep ridges, and mudstone and shale units form intervening valleys. On Anticline Ridge, the sandstone units form steep to vertical cliffs facing the anticlinal axis and more gently dipping slopes away from the axis.

In general, the lithologies of the fine-grained units (Panoche Formation, Kreyenhagen Shale, and Lodo Formation) are alike: They are nonresistant, fissile, highly fractured shale, siltstone, and mudstone that do not form cliffs or ridges except where they have been eroded along a streamcourse. An exception to this generalization is the Big Blue Formation, which consists of thin- to thick-bedded, weakly cemented siltstone, mudstone, and shale containing varying amounts of detrital serpentine. The Big Blue Formation forms steep, commonly overhanging cliffs along the northeastern limb of the Coalinga anticline. Here, prominent cliffs, as much as 60 m high, are highly susceptible to the formation of seismically induced rockfalls. In this respect, this fine-grained unit mimics the sandstone units.

Although the sandstone units are generally more tightly cemented than sedimentary rocks of the Big Blue Formation, they are not well indurated. For example, sandstone of the Panoche Formation ranges from weakly to moderately well cemented. In some places, the sandstone can be broken apart easily by hand; in others, it requires a moderate hammerblow. The sandstone units in all the formations also contain extensive throughgoing fractures and form cliff faces only slightly less susceptible to seismically induced rockfalls than those of the Big Blue Formation.

FALLS AND SLIDES

DISTRIBUTION AMONG GEOLOGIC UNITS

Of the several thousand landslides triggered by the May 2 earthquake, several hundred were soil falls, seven were slumps, three were liquefaction-induced lateral

spreads; the rest were rockfalls and rockslides. The landslide classification used herein is that of Varnes (1978). The largest rockfalls were situated approximately 8 km north of the epicenter on the eastern and northeastern flanks of the Coalinga anticline (fig. 18.1). There, southwest-facing, near-vertical to overhanging cliffs in the Big Blue Formation formed rockfalls of 10,000- to 50,000-m^3 volume (fig. 18.1) at four different sites where cliffs are especially prominent. The Big Blue Formation at these sites is composed of relatively soft, well-jointed or fractured green, red, yellow, and brown serpentinous siltstone, mudstone, and shale, containing varying minor amounts of sand in all these rock types. Elsewhere in this formation, rockfalls and rockslides, though typically small (less than 100 m^3-volume), are numerous as far as 14 km from the epicenter. The Big Blue Formation essentially defines the northeast limit of rockfalls and rockslides along the northeastern flank of the Coalinga anticline.

Small rockfalls and soil falls occurred on cut slopes throughout the oil field on Anticline Ridge (fig. 18.2). Typically, failures occurred from steep cut slopes above pump pads and from roadcuts. Most of these falls were less than 3 m^3 in volume. Soil falls were also common along riverbanks in weakly cemented alluvium that consisted mostly of gravel and cobbles (fig. 18.3). These failures were fairly small (max 10 m^3 volume) but not systematically located except that they were common along Los Gatos Creek between 12 and 29 km northwest of Coalinga.

Toward the central part of the Coalinga anticlinal axis, rockfalls and rockslides originated from cliffs in sandstone and shale units within the Panoche Formation. Failures from this formation are also scattered widely in the Joaquin Ridge and Alcalde Hills areas. Although these failures are not so large or so concentrated as in the Big Blue Formation, approximately 40 percent of the total number of landslides associated with the earthquake were within the Panoche Formation, partly owing to its widespread exposure.

Along Los Gatos Creek Road, several tens of rockfalls occurred within massive cliff-forming sandstone of the Panoche Formation (fig. 18.4). This sandstone is weakly cemented, and many boulders that were shaken loose readily disintegrated on impact to individual sand grains. The largest rockfalls in this unit partly blocked the road along Los Gatos Creek about 13 km northwest of Coalinga (fig. 18.4).

An estimated 10 to 15 percent of the rockfalls and rockslides occurred within the Etchegoin Formation in the Kreyenhagen Hills and Jacalitos Hills south of Coalinga. The rest of the rockfalls and rockslides from natural slopes were approximately evenly divided between other Tertiary sandstone and shale units: Temblor Sandstone, Domengine Sandstone, Kreyenhagen Shale,

FIGURE 18.1.—Rockfalls from cliffs in the Big Blue Formation (*A*). Cliff is approximately 60 m high. (*B*) Rockfall viewed from top of scarp, showing overhang of cliff. Largest blocks in rockfall deposit are 3 m in diameter.

and Lodo Formation. The lithologic units involved in rockfalls and rockslides, their thickness, and their approximate relative abundance (determined from visual estimates) with respect to lithology are briefly described in table 18.1.

DISTRIBUTION WITH RESPECT TO SLOPE ASPECT

Rockfalls are noticeably concentrated on southwest-facing slopes along the northeastern limb of the anticline forming Anticline Ridge. The northeast-facing dip slopes are less involved in seismically induced failure because the regional dip of beds on this side of the anticlinal axis is typically 15°–30°, whereas the southwest-facing slopes are formed by joint surfaces typically dipping 45°–90°. The relative steepness of southwest-facing slopes is accentuated by the resistant sandstone units, whereas the less resistant shale units generally have low slopes in all directions.

The preponderance of rockfalls and rockslides on slopes facing toward the southwest quadrant within individual 1-mi^2 area quadrangle sections in the Anticline Ridge and Big Blue Hills areas ranges from 26 to 93 percent and averages 66 percent. Although steep southwest-facing slopes are not so apparent to the south and west of Anticline Ridge, the rockfall concentration from southwest-facing slopes in this area still ranges from 40 to 83 percent and averages 63 percent.

DISTRIBUTION ALONG STREAMCOURSES

Along the steep lower slopes of stream valleys throughout most of the Coalinga area, the distribution of rockfalls and rockslides was influenced only slightly by lithology; geologic contacts between shale and sandstone commonly seem to have little or no effect on the rockfall and rockslide concentration. For example, along Nuñez Canyon, the failure concentration is essentially the same across contacts between sandstone and shale units in the Panoche Formation. Similarly, the Lodo Formation exhibits equal concentrations of rockfalls and rockslides along Arroyo Hondo on either side of sandstone-shale contacts. Far more important in these localities is slope steepness. Near the canyon bottoms, both shale and sandstone units commonly form slopes of 70° to vertical and overhanging of approximately equal heights. The rapid downcutting of these ephemeral streams and the aridity of the local climate have created extremely steep slopes in most rock types and diminished any differences in susceptibility to seismically induced failures.

DISTRIBUTION ON RIDGE CRESTS

Only resistant units, such as the sandstones of the Panoche Formation, the Domengine Sandstone, the Temblor Formation, and the Lodo Formation, form cliffs at ridge crests (fig. 18.5). These sandstone units, because of their greater resistance to erosion, account for most of

FIGURE 18.2.—Rockfall and soil fall from cut slope above oil-field pump pad in Anticline Ridge oil field.

FIGURE 18.3.—Soil fall in alluvial deposits along Los Gatos Creek.

the rockfalls emanating from ridge crests. Thus, the rockfall and rockslide distribution from the earthquake fits into two major categories of slope: (1) failures along steep slopes and cliffs immediately above streams, and (2) failures from cliffs at ridge crests.

FAILURE MECHANISM OF ROCKFALLS AND ROCKSLIDES

All the lithologic units producing rockfalls and rockslides from the May 2 earthquake are mostly weakly cemented. Even the most indurated and massive of the sandstone units are not sufficiently strong for dislodged fragments to remain intact when collisions occur as they fall. Only minor parts of the sandstones are hard enough to ring when struck with a hammer. Nonetheless, these sandstones and even the weaker shale units failed primarily along preexisting fractures (joints) and bedding planes, not by fracture through unbroken rock. Inspections of numerous rockfall and rockslide scarps and the rock debris reveal that most initial failures took place along preexisting fractures or joints. These observations are consistent with others from past earthquake investigations which suggest that all rocks except for the least indurated of pyroclastic deposits preferentially fail along preexisting fractures or joints (Harp and others, 1981, 1984; Keefer, 1984). Exposed joint and bedding-plane surfaces in scarps illustrate this behavior (fig. 18.6).

Many fractures widened by the earthquake extend 5 to 10 m behind the cliff faces where rockfalls occurred. Such fractures are present along ridgetops in the Big Blue Formation and overlying the basal part of the Santa Margarita Formation, where earthquake-induced fractures have followed joint patterns. Figure 18.7 shows how such fractures extend along first one joint orientation and then another.

SLUMPS

All the slumps in natural slopes triggered by the May 2 earthquake occurred on slopes immediately adjacent to streams. This relation, as well as the concentration of rockfalls and rockslides near streams, reflects the effect

FIGURE 18.4.—Rockfalls from sandstone cliffs of the Panoche Formation. Rockfalls partly blocked road 13 km northwest of Coalinga.

of rapid incision by streams in this area on the stability of slopes. Such slumps as that shown in figure 18.8 along Los Gatos Creek formed in slopes being undercut by the outer edges of stream meanders. This slump occurred in dry, weakly cemented sandstone of the Panoche Formation; its volume is approximately 200,000 m^3.

Two large slumps on Domengine Creek near Ragged Valley (fig. 18.9) that predate the earthquake sustained no apparent displacement in response to the shaking. The slump to the southeast (right, fig. 18.9) had been active earlier in the spring and had partly dammed Domengine Creek (Keith Pierce, oral commun., 1984). Additional movement may have occurred on this slide during the earthquake, but evidence was inconclusive. Much of the terrain throughout the earthquake-affected area is covered by slump/earthflow deposits; however, few of these deposits showed any renewed movement due to earthquake shaking.

Slumps in artificial fill were common. Many of these slumps occurred within the Anticline Ridge oil field at the outer edges of oil-pump pads, where the fill is least compacted (fig. 18.10). Vibrational compaction also created small scarps and cracks around concrete pump aprons (fig. 18.11). Slumps within fill occurred in roadways. Several such failures in the Los Gatos Creek roadbed had cracks and displacement coincident with the fill margins (fig. 18.12).

FIGURE 18.5.—Rockfall from cliff in sandstone of the Panoche Formation. Only such resistant rock types as this sandstone form cliffs at ridge crests. Except for mudstone, siltstone, and shale of the Big Blue Formation, fine-grained deposits form cliffs only adjacent to actively incising streams. Cliff is approximately 50 m high.

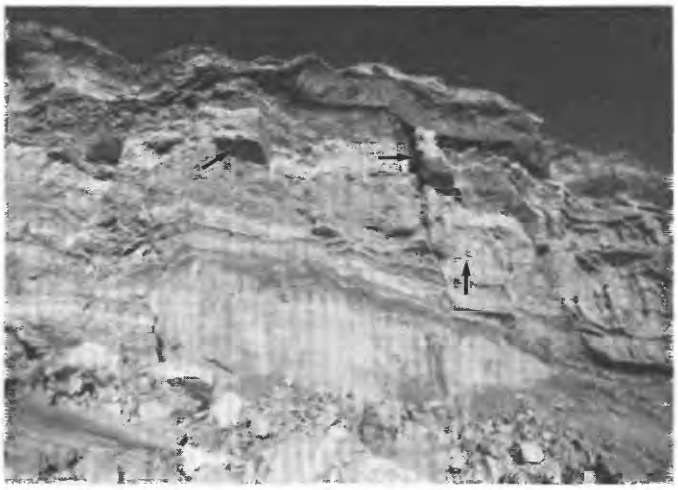

FIGURE 18.6.—Rockfall scarp in cliff of the Big Blue Formation, showing joint and bedding-plane surfaces (arrows) along which failure occurred. Vertical fracture or joint at right center of photograph opened in response to shaking. Cliff is approximately 30 m high from top of talus to horizon.

FIGURE 18.7.—Incipient failures in surface above rockfall scarp. Note that failure surface follows preexisting fracture planes. Horizontal surface, with cliff face at top of photograph. Fracture is 3 cm.

LIQUEFACTION EFFECTS

Liquefaction effects were observed from the main shock along the channel of Los Gatos Creek at three sites between 13 and 15 km northwest of Coalinga. These effects were confined to cracking, lateral spreading, and extrusion of sediment and water from thin alluvial deposits of silt and fine sand that overlie the gravel and cobble deposits which compose the channel bed. The silt and sand deposits are concentrated in braided lenses on river bars. The silt and sand deposits range in thickness from a few centimeters to 0.6 m. The deformation of these finer grained deposits typically consisted of cracks of as much as 10 cm extension and a few small sand boils (fig. 18.13).

At the southeasternmost site, approximately 300 m west of the mouth of Nuñez Canyon, a sandbar about 100 m long sustained extensive cracking and minor lateral spreading (fig. 18.14). Individual cracks were open as much as 10 cm. None of the cracks at any of the sites of liquefaction extended into the underlying gravel. M.J. Rymer (oral commun., 1983) reported that the July 22 M_L=6.0 event caused additional liquefaction along Los Gatos Creek near Nuñez Canyon; he documented sand boils and cracks that extended into the gravel and cobble deposits of the creekbed (fig. 18.15). The epicenter of this aftershock was on the Nuñez fault, 5 km from these observed effects. Because of its proximity to the source of this event and, possibly, to the relatively shallow focal depth, shaking was probably greater at this site during the July 22 event than during the May 2 earthquake; this shaking apparently caused liquefaction in the sand deposits underlying the gravel and cobbles of the creekbed.

CRACKS ON RIDGES

The above-mentioned cracks on ridge crests, such as those associated with rockfalls in the Big Blue Forma-

FIGURE 18.8.—Rotational slump of about 200,000-m^3 volume along Los Gatos Creek, approximately 14 km northwest of Coalinga. Scarp is approximately 6 m high.

tion, are related to bedrock fractures. However, cracks not associated with rockfalls were reported on a ridge crest near Nuñez Canyon (M.J. Rymer, oral commun., 1983). Rymer reported the formation of extensive ridge cracking that gives the appearance of "ploughed ground" on a north-south-trending ridge in the NE. cor. sec. 33, northeast of the Nuñez Ranch (fig. 18.16; see pl. 18.1). Cracks here formed in both the June 11 M_L=5.2 and July 22 M_L=6.0 events. Presumably, these features are extension fractures in the soil and were concentrated at the ridge crest because of topographic focusing of seismic waves from nearby source zones along the Nuñez fault. Rymer also noted the presence of displaced stones, as much as 2.0 m^3 in volume, along ridge crests in the Nuñez fault area. Similar features and concentration of slope failures near ridge crests have been reported from other earthquakes: the 1971 San Fernando, Calif. (Nason, 1971), 1968 Borrego Mountain, Calif. (Castle and Youd, 1972), 1957 Daly City, Calif. (Bonilla, 1959), and 1976 Guatemala (Harp and others, 1981) earthquakes.

COMPARISON WITH OTHER EARTHQUAKES

The types, geologic environments, and distribution of landslides in the May 2 earthquake are generally consistent with findings from other historical earthquakes worldwide. The most abundant landslides caused by the Coalinga event were rockfalls and rockslides, respectively the first and third most common landslides triggered by earthquakes worldwide (Keefer, 1984). The rockfalls and rockslides in the Coalinga event involved weakly cemented sedimentary rocks and occurred on steep slopes (most steeper than 60°)—characteristics that are also consistent with previous observations.

The next most abundant landslides in the Coalinga event were soil falls and soil slumps, which are moder-

FIGURE 18.9.—Two adjacent large preearthquake slumps on north side of Domengine Creek near Ragged Valley. Slumps showed little, if any, reactivation during May 2 earthquake, even though slump to right had dammed Domengine Creek earlier that spring. Slump at left is approximately 300 m long from scarp to toe.

ately common to abundant in historical earthquakes worldwide (Keefer, 1984). The soil falls occurred in poorly consolidated sandy and gravelly alluvium along steep streambanks, a particularly common environment for earthquake-triggered landslides of this type. Most soil slumps were in manmade fill, which has proved to be the material most susceptible to slumps in previous earthquakes. In the Coalinga event, most slumps in fill involved graded pads for oil-field pumps; the high susceptibility of these fills is probably due to the steep frontal slopes of the pads and to the low density of the fill material. Several slumps in highway fills also were probably due to steep side slopes and low-density material.

FIGURE 18.10.—Slump in fill at edge of oil-well pump pad, Anticline Ridge oil field.

FIGURE 18.11.—Settlement at margin of concrete oil-pump apron. Scale is marked in centimeters.

Although many large slump and earthflow deposits that predate the earthquake are present in the epicentral area, our observations show that few, if any, of these deposits were reactivated by the earthquake shaking. This nonreactivation is also consistent with previous experience (Keefer, 1984) and suggests that (1) these large landslides originally moved in response to nonseismic causes, such as the elevation of pore-water pressures by prolonged or intense precipitation; and (2) these landslides are relatively insensitive to seismic shaking, except when they are only marginally stable, owing to nonseismic causes.

Few liquefaction-induced lateral spreads were observed in this earthquake, partly due to incomplete reporting, because such features generally are not discernible on aerial photographs. During our ground-based

FIGURE 18.12.—Slump in highway fill, Los Gatos Creek Road. Largest cracks are 4 cm wide.

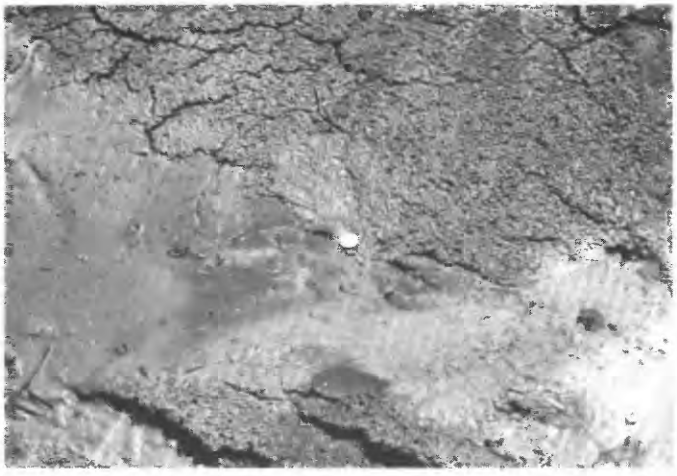

FIGURE 18.13.—Lateral-spreading cracks and small sand boils in alluvium of Los Gatos Creek.

reconnaissance, however, we examined many areas along streambanks and canal banks in the Great Valley east of Coalinga, and many areas along streams west of Coalinga; we found lateral spreads at only three localities, as shown on plate 18.1. This small number of lateral spreads is consistent with observations in previous earthquakes of M_L=6.5 (Keefer, 1984).

The area affected by landslides in the May 2 earthquake was about 650 km^2, small relative to that in other historical earthquakes of approximately the same magnitude (fig. 18.17). This difference is partly due to the general absence of steep slopes east of the epicenter. However, even if the affected area were arbitrarily doubled to account for this absence of steep slopes, the area would remain below average for earthquakes in the same magnitude range.

The maximum distances of various types of landslides from the epicenter are also small relative to those in most other historical earthquakes of similar magnitude (fig. 18.18). For rockfalls and rockslides (fig. 18.18*A*), steep slopes in susceptible, weakly cemented materials extend far to the west, beyond the limit of landsliding. Thus, the relatively short maximum distance for rockfalls and rockslides suggests that the shaking which causes such landslides was either weaker or more attenuated than the average for the other worldwide events studied. The relatively short maximum distances for soil slumps (fig. 18.18*B*) and lateral spreads (fig. 18.18*C*) may be partly due to incomplete reporting or to restricted distribution of susceptible materials. However, the absence of these features in the Great Valley east of Coalinga, where numerous susceptible streambanks, canal banks, and manmade fills are present, also suggests that the small number of slumps and lateral spreads was due to attenuated ground shaking.

FIGURE 18.14.—Lateral-spreading cracks in sandbar of Los Gatos Creek, 13 km northwest of Coalinga. Large crack in lower left corner is about 5 cm wide.

SUMMARY

The May 2 earthquake caused several thousand landslides, mostly rockfalls and rockslides. Soil falls from alluvial gravel and cobble deposits were numerous along cutbank slopes adjacent to Los Gatos Creek northwest of Coalinga. Small rockfalls and soil falls and slides were common from cut slopes above oil-well pump pads in the Anticline Ridge oil field. Seven deep-seated slumps occurred in natural slopes adjacent to streams. Slumps in artificial fill occurred in roadbeds and in material forming the outer edges of oil-well pump pads in the Anticline Ridge area. Minor liquefaction-induced lateral spreading and sand boils were observed along Los Gatos Creek.

The largest and most spectacular rockfalls occurred in the Anticline Ridge area within the Big Blue Formation. Most rockfalls and rockslides occurred within the Panoche Formation, partly owing to its widespread exposure, as well as to the susceptibility of its rock types. Throughout the landslide-affected area, failures were concentrat-

FIGURE 18.15.—Sand boils in Los Gatos Creek alluvial deposits from July 22 M_L=6.0 event. Photograph by M.J. Rymer.

FIGURE 18.16.—Cracks (arrows) in north-south-trending ridge near the Nuñez Ranch from June 11 and July 22 events. Cracks may be from focusing of seismic energy at ridge top. Note collapse of barbed-wire fence into extension cracks on left side of road. Photograph by M.J. Rymer.

ed on southwest-facing slopes—a result of the regional structure, in which relatively gently dipping slopes face northeast and steep slopes formed by joints and fractures face southwest.

Near actively incising streams, rockfalls and rockslides were common, with little influence from lithology. Shale and sandstone units showed little difference in concentration of failures where these units were exposed in steep cliffs next to streams. Except for shale and mudstone of the Big Blue Formation, only sandstone units form cliffs at ridge crests, and so they accounted for most of the rockfalls at these localities.

Although many slumps and earthflow deposits are apparent throughout the earthquake-affected area, few,

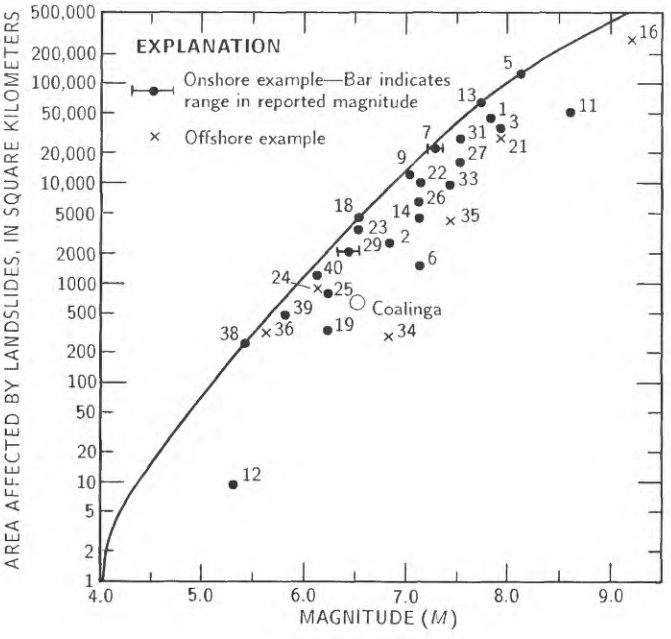

FIGURE 18.17.—Area affected by landslides versus magnitude for worldwide historical earthquakes (after Keefer, 1984). Curve indicates upper bound. Numbers refer to data points of Keefer (1984).

if any, of these deposits were reactivated. This nonreactivation is consistent with observations from other earthquakes and suggests that these slumps and earthflows are controlled mainly by climatic factors and that they are relatively insensitive to seismic shaking, except where they are marginally stable at the time of an earthquake.

Few liquefaction effects were observed from the May 2 earthquake. Three localities of liquefaction-induced lateral spreading with small sand boils were noted along Los Gatos Creek. Along Los Gatos Creek, the July 22 M_L=6.0 event produced sand boils that apparently originated from alluvial deposits deeper than those affected by the May 2 earthquake.

The area affected by landslides from the May 2 earthquake is small relative to those of other historical earthquakes of similar magnitude. The maximum distances of all types of landslides from the epicenter are also small relative to those in most other earthquakes of nearly equal magnitude. These observations suggest that the shaking which caused the landslides was attenuated in the May 2 event.

REFERENCES CITED

Bate, M.A., 1984, Sedimentary facies and depositional environments of the Big Blue Formation between Anticline Ridge and the Domengine Ranch, *in* Carlson, Christine, ed., Depositional facies of sedimentary serpentinite: Selected examples from the Coast Ranges, California: Society of Economic Paleontologists and Mineralogists Midyear Meeting, San Jose, Calif., 1984, Field Trip Guidebook 3, p. 81–85.

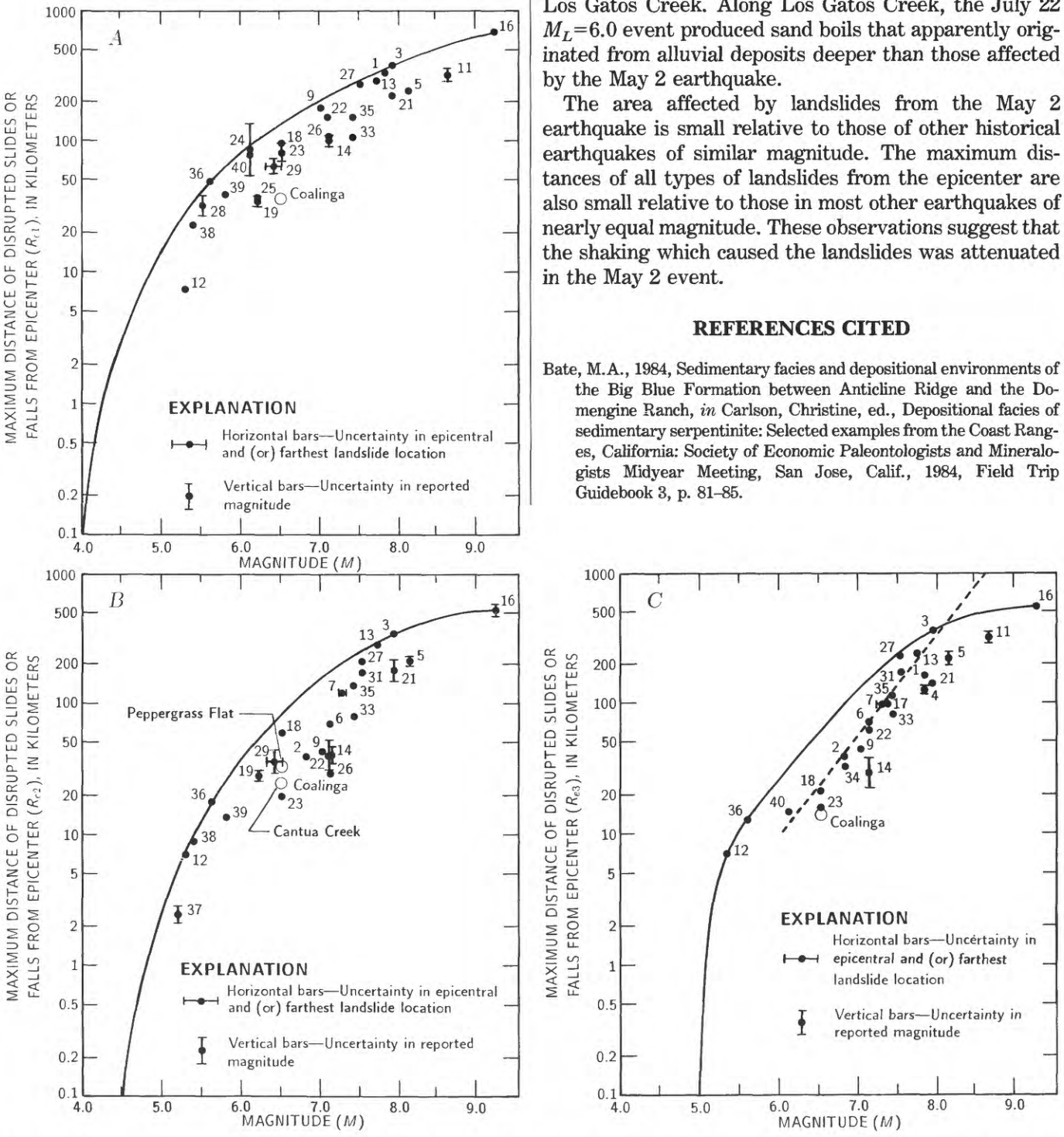

FIGURE 18.18.—Maximum distance of various types of landslides from earthquake epicenter versus magnitude for worldwide historical earthquakes. *A*, Disrupted slides or falls. *B*, Coherent slides. *C*, Lateral spreads or flows. Curves indicate upper bounds. Dashed line from Youd and Perkins (1978; after Keefer, 1984). Numbers refer to data points of Keefer (1984).

Bonilla, M.G., 1959, Geological observations in the epicentral area of the San Francisco earthquake of March 22, 1957, *in* Oakeshott, G.B., ed., San Francisco earthquakes of March 22, 1957: California Division of Mines Special Report 57, p. 25–37.

Castle, R.O., and Youd, T.L., 1972, Engineering geology, *in* The Borrego Mountain earthquake of April 9, 1968: U.S. Geological Survey Professional Paper 787, p. 158–174.

Dibblee, T.W., Jr., 1971, Geologic maps of the Coalinga, Joaquin Rocks, New Idria, and Reef Ridge 15-minute quadrangles, California: U.S. Geological Survey open-file maps, scale 1:62,500.

Harp, E.L., Tanaka, Kohei, Sarmiento, J.S., and Keefer, D.K., 1984, Landslides from the May 25–27, 1980, Mammoth Lakes, California, earthquake sequence: U.S. Geological Survey Miscellaneous Investigations Series Map I–1612, scale 1:62,500.

Harp, E.L., Wilson, R.C., and Wieczorek, G.F., 1981, Landslides from the February 4, 1976, Guatemala earthquake: U.S. Geological Survey Professional Paper 1204–A, 35 p.

Keefer, D.K., 1984, Landslides caused by earthquakes: Geological Society of America Bulletin, v. 95, no. 4, p. 406–421.

Keefer, D.K., Harp, E.L., and Wilson, R.C., 1984, Landslides and related ground failures, *in* Scholl, R.E. and Stratta, J.L., eds., Coalinga, California, earthquake of May 2, 1983: Reconnaissance report: Berkeley, Calif., Earthquake Engineering Research Institute Report 84-03, p. 99–105.

—— 1983, Landslides and related ground failures, *in* Borcherdt, R.D., ed., The Coalinga earthquake sequence commencing May 2, 1983: U.S. Geological Survey Open-File Report 83-511, p. 12–19.

Nason, R.D., 1971, Shattered earth at Wallaby Street, Sylmar, *in* The San Fernando, California, earthquake of February 9, 1971: U.S. Geological Survey Professional Paper 733, p. 97–98.

Varnes, D.J., 1978, Slope movement types and processes, chap. 2 *of* Schuster, R.L., and Krizek, R.J., eds., Landslides: Analysis and control: U.S. National Academy of Sciences, Transportation Research Board Special Report 176, p. 11–33.

Youd, T. L., and Perkins, D. M., 1978, Mapping liquefaction-induced ground failure potential: American Society of Civil Engineers Proceedings, Geotechnical Engineering Division Journal, v. 104, no. GT4, p. 433–446.

19. INTENSITY STUDIES

By LYNN M. HIGHLAND, CARL W. STOVER, MARGARET G. HOPPER,
PAUL C. THENHAUS, and S.T. ALGERMISSEN,
U.S. GEOLOGICAL SURVEY

CONTENTS

ABSTRACT

The May 2 earthquake was felt over an area of 205,000 km^2 and generated a maximum modified Mercalli intensity (MMI) of VIII in the city of Coalinga (approx 12 km southwest of the epicenter) and at Pacific Gas and Electric Substation 2 (1 km southwest of the epicenter). The main shock also generated an MMI of VII at Avenal (30 km southeast of the epicenter). Field investigation of the damage showed that 75 percent of the old (pre-1945) unreinforced-brick structures in the central business district of Coalinga were severely damaged, whereas newer masonry buildings in the same area sustained no damage or only nonstructural damage. About 15 percent of the single-family dwellings in Coalinga were thrown off their foundations, and more than half of the chimneys were damaged. An MMI of VIII was assigned to the main shock because of the toppling of many chimneys, the partial collapse of old, unreinforced-masonry buildings, and the absence of serious damage to substantial masonry structures. Coalinga underwent many strong aftershocks through August 1983. A strong aftershock on July 25 caused extensive damage, primarily to structures that had been weakened by effects of the main shock.

DISTRIBUTION OF INTENSITIES

The May 2 earthquake was felt over an area of at least 205,000 km^2 in California and Nevada. The areal distribution of intensities is mapped in figure 19.1. The area of maximum intensity was concentrated in and near the city of Coalinga; a modified Mercalli intensity (MMI) of VIII was rated for Pacific Gas and Electric Substation 2 near the abandoned town of Oilfield, located northeast of Coalinga. The substation, a concrete-block building, was virtually destroyed when sections of both the front and back walls failed.

The most significant earthquake damage outside the vicinity of Coalinga occurred at Avenal (MMI VII), located 31 km southeast of the epicenter. A nursery building was moved 0.6 m off its foundation, breaking sewer connections and causing considerable damage to the floor. Chimneys were reported fallen in some areas of Avenal. Plate-glass windows were shattered on Kings Street.

Most of the damage in the MMI VI localities consisted of cracked plaster or brick walls; a few cracked chimneys, sidewalks, or foundations; cracked or broken windows; and broken dishes or glassware. To more completely canvass the effects of earthquakes, the U.S. National Earthquake Information Service (NEIS) sends questionnaires to area post offices after an earthquake occurs. Most of the MMI VI-rated questionnaires received by NEIS for the May 2 earthquake reported damage in about 5 percent of the buildings.

DAMAGE IN COALINGA

A damage survey of the city of Coalinga was undertaken by the U.S. Geological Survey to systematically document earthquake damage or absence of damage to buildings. This survey was begun on May 3, 1983, the day after the main shock. Detailed damage information was obtained in a 12-block area of the downtown business district before May 5, when this area was restricted to all but public-works personnel, who were involved in the demolition of heavily damaged buildings. A reconnaissance damage assessment was conducted for the rest of the city.

CENTRAL BUSINESS DISTRICT

The most severe earthquake damage to buildings in Coalinga was primarily concentrated in the older downtown section. Half of the buildings in the 12-block commercial section of Coalinga were one- and two-story unreinforced-brick structures. About 75 percent of the

buildings in this 12-block district were total losses. All the buildings destroyed were unreinforced-masonry structures more than 40 years old.

Buildings inventoried for damage in the area outlined in figure 19.2 were grouped according to the building-classification system developed by Steinbrugge (Algermissen and others, 1977). A detailed description of each building class is given in the section below entitled "Supplementary Data." The percentage of damage was estimated for each building on the basis of structural or

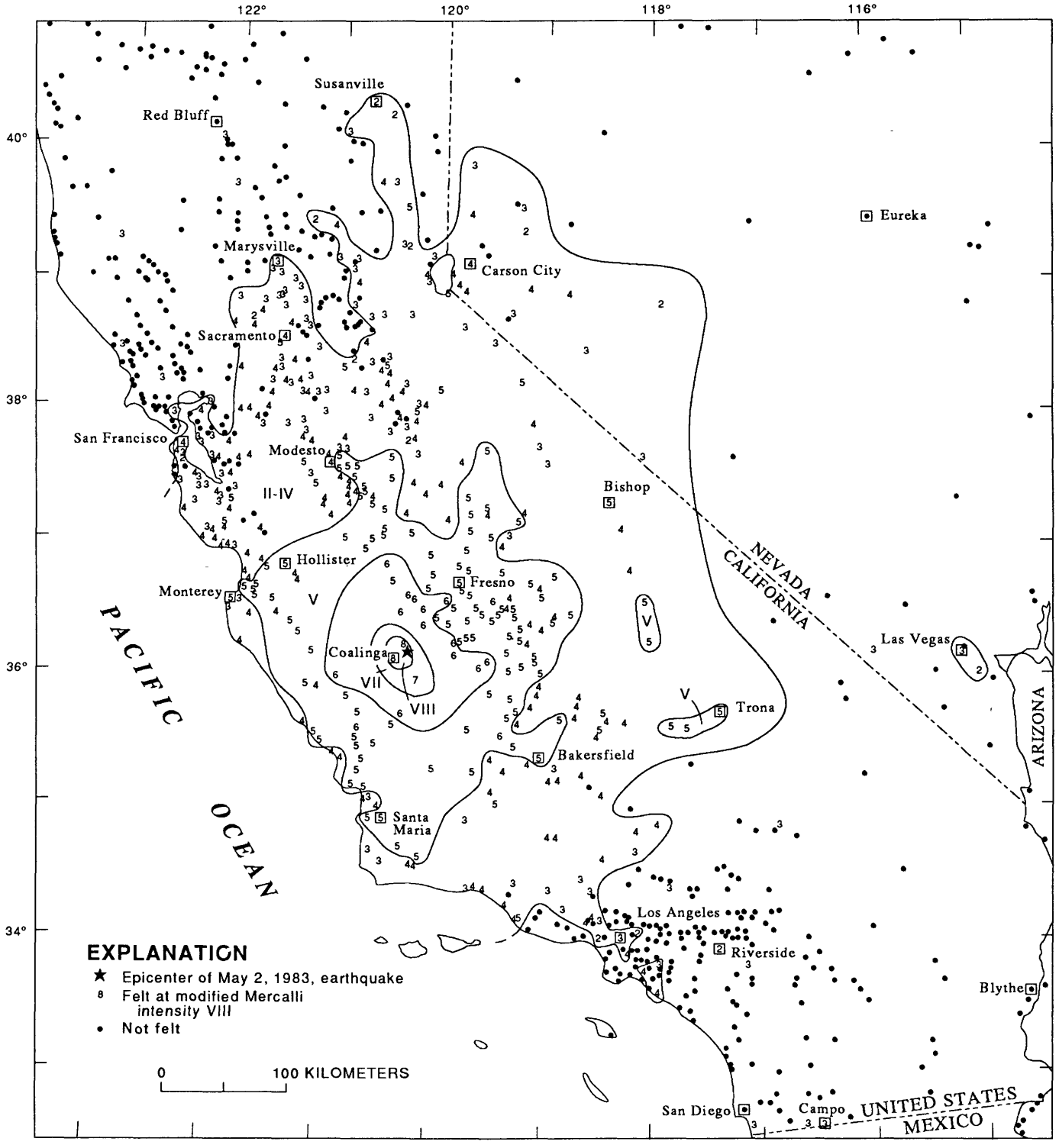

FIGURE 19.1—Isoseismal map for the May 2 earthquake (from Stover, 1983).

nonstructural (exterior/interior) damage; these data are summarized in table 19.1. A graphic representation of the damage to one particular building class is shown in figure 19.3. Buildings in class VE are characterized by solid-unit masonry of unreinforced brick, unreinforced-concrete brick, unreinforced stone, or unreinforced concrete, where loads are carried in whole or in part by the walls and partitions (see section below entitled "Supplementary Data"). The largest number of buildings in Coalinga fell into class VE; they sustained the greatest percentage of damage in terms of both structural and nonstructural designations. At least 58 percent of the 78 buildings inventoried in the area shown in figure 19.2 were estimated to be more than 40 years old. These buildings were characteristically constructed of unreinforced-masonry walls with timber roof trusses. Very few buildings (8 percent) were less than 5 years old; they were constructed of reinforced brick, block masonry, or reinforced concrete. These buildings performed very well, with only minor nonstructural damage. Damage to structures in the downtown area is illustrated in figures 19.4 through 19.6. As shown, exterior walls and brick facades were extensively damaged in older, wood-frame and concrete-block structures.

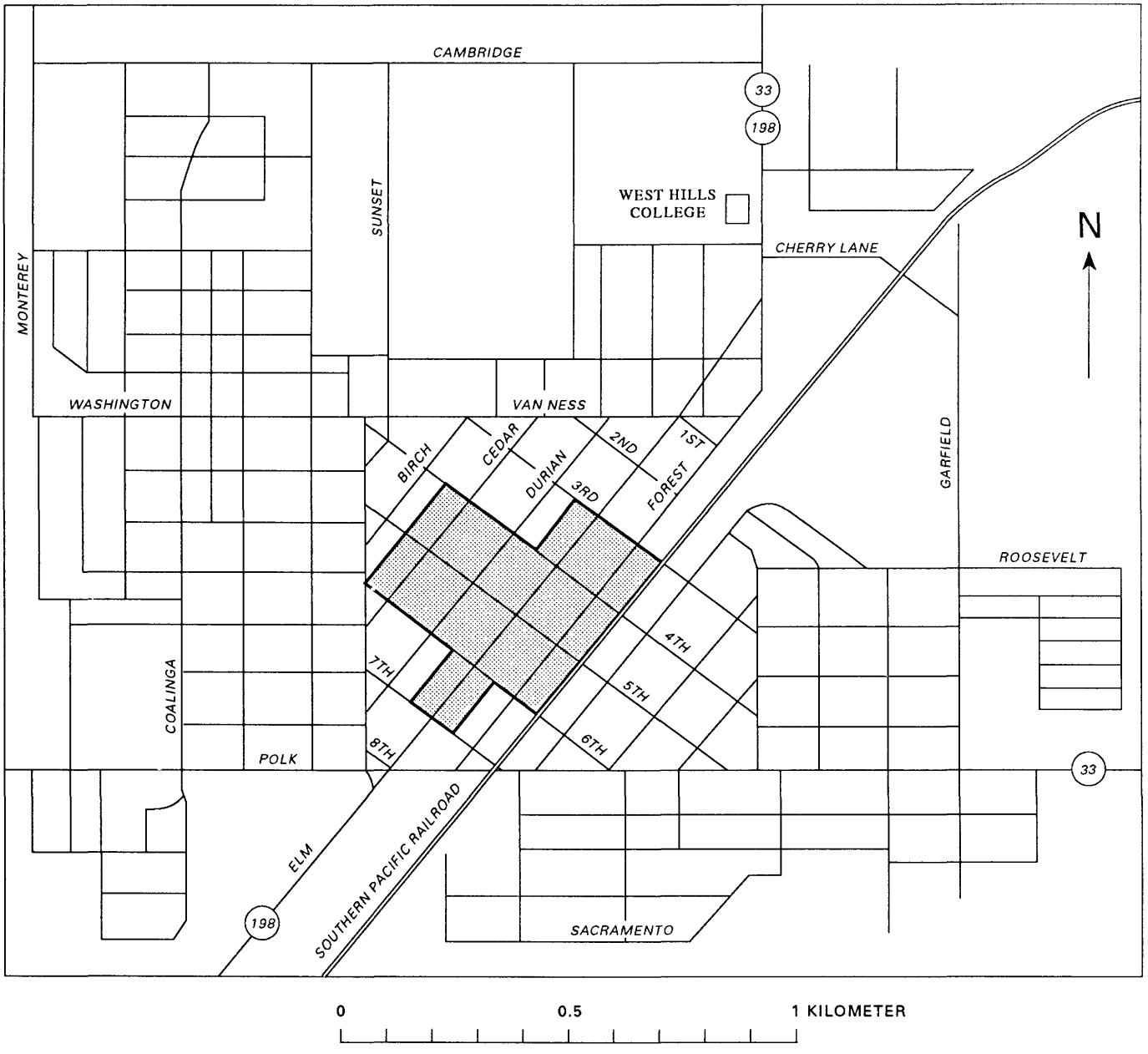

FIGURE 19.2—Downtown Coalinga, showing locations of buildings inventoried and evaluated according to building class (stippling).

TABLE 19.1.—*Percentage of damage to buildings in the Coalinga area, California*

Building class	Total no. buildings damaged	Percentage of buildings	Exterior (non-structural)	Interior (non-structural)	Structural
VE	37	0	0	0	0
		1-10	0	1	1
		11-25	0	0	0
		26-50	1	1	3
		76-100	22	22	23
VE-1	11	0	0	0	8
		1-10	5	5	1
		11-25	2	6	2
		26-50	4	0	0
		51-75	0	0	0
		76-100	0	0	0
II-A	10	0	3	6	10
		1-10	7	4	0
		11-25	0	0	0
		26-50	0	0	0
		51-75	0	0	0
		76-100	0	0	0
I-A-2	7	0	3	2	6
		1-10	3	4	0
		11-25	0	0	0
		26-50	0	0	0
		51-75	0	0	0
		76-100	1	1	1
IV-A	4	0	2	4	4
		1-10	2	0	0
		11-25	0	0	0
		26-50	0	0	0
		51-75	0	0	0
		76-100	0	0	0
VA-2	2	0	0	2	2
		1-10	2	0	0
		11-25	0	0	0
		26-50	0	0	0
		51-75	0	0	0
		76-100	0	0	0
II-B	1	0	1	1	1
		1-10	0	0	0
		11-25	0	0	0
		26-50	0	0	0
		51-75	0	0	0
		76-100	0	0	0
III-D	1	0	0	0	1
		1-10	0	0	0
		11-25	0	0	0
		26-50	0	0	0
		51-75	0	0	0
		76-100	1	1	0
I-A-I	4	0	2	0	3
		1-10	2	4	0
		11-25	0	0	0
		26-50	0	0	0
		51-75	0	0	1
		76-100	0	0	0
I-A-3	7	0	2	3	5
		1-10	4	3	1
		11-25	0	0	0
		26-50	0	0	0
		51-75	0	0	0
		76-100	1	1	1

Newer, more substantial structures adjacent to the damaged buildings did not exhibit major structural damage, although these buildings sustained broken window glass, interior cracking, and some slight external brick failure.

No structural damage was noted to the 12 percent of the buildings in the central business district that were wood frame or steel frame with sheet-metal siding. Nonstructural damage to this class of buildings consisted of broken glass and fallen brick veneer from front facades.

RESIDENTIAL AREAS

Earthquake damage in residential areas was fairly widespread. Types of damage included shifting of houses off foundations, failure of exterior walls of buildings, damage to residential chimneys, falling of cornices and coping, caving in of roofs, interior cracking (mainly of gypsum board), and falling of plaster. Nearly every block sustained some kind of damage.

A total of 287 houses (15 percent of the 1,938 houses in Coalinga) were shifted off their foundations. As many as 100 of these dwellings had been moved to Coalinga from the nearby oil fields between the years 1930 and 1955. As many as 90 percent of the dwellings moved before 1940 or

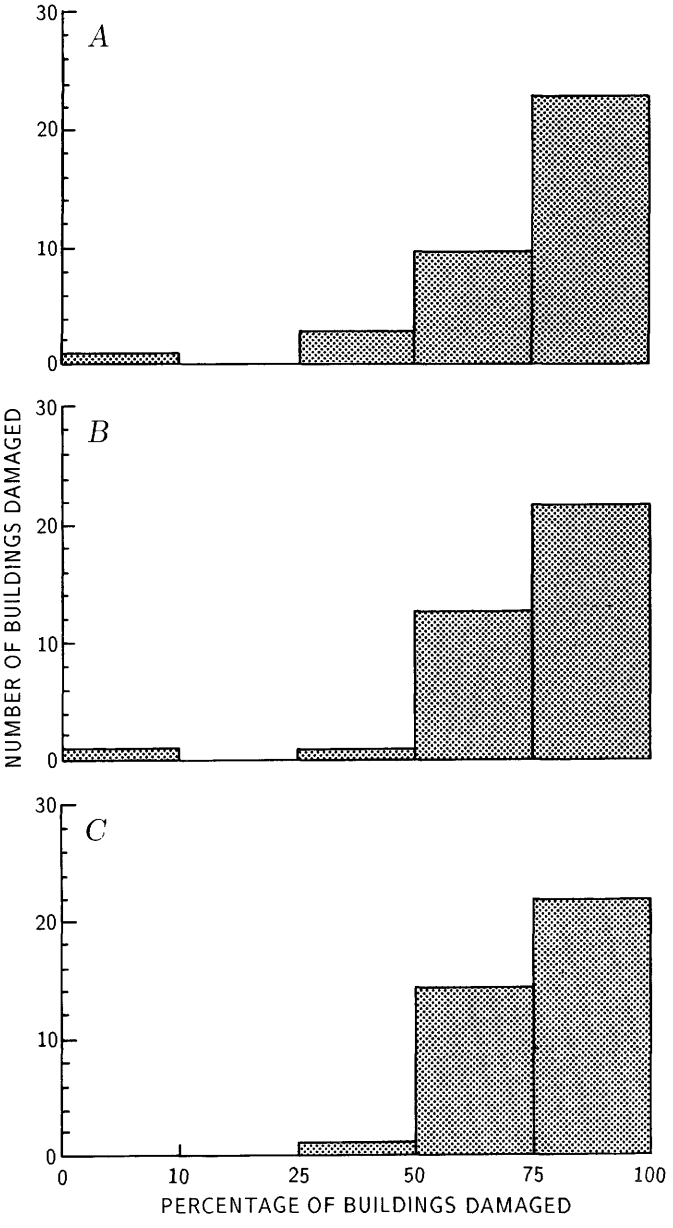

FIGURE 19.3—Damage that occurred to class VE buildings (total, 37). *A*, structural. *B*, Interior (nonstructural). *C*, Exterior (nonstructural). Data from table 19.1.

FIGURE 19.4—Failed brick exterior of automotive store in downtown Coalinga.

FIGURE 19.5—Damage to downtown store by fallen wall of adjacent theater.

FIGURE 19.6—Failed second-floor exterior wall of downtown-area building.

1945 were placed on wooden mud sills, which are directly on the earth. These houses, placed directly on grade (with concrete first floors), performed well, for one reason because they had no foundation to slide off (see chap. 20). The cripple-wall type of house construction fared the worst (figs. 19.7–19.9). This construction type consists of an 18- to 24-in.-high stud wall interposed between floor joists of the first story and a concrete foundation. If not sufficiently braced, this type of construction is highly vulnerable to collapse when subjected to horizontal ground motion, because of poor lateral resistance. Exterior plank siding proved insufficient bracing to withstand the lateral loads in many of the collapsed houses. Some houses, though placed directly on their foundations rather than on cripple walls, slid off their foundations because they were not bolted down. Many of these houses had been moved from the oil fields after 1950 (figs. 19.7–19.9; see chap. 20). Houses characteristically moved off foundations in an easterly or southeasterly direction.

One extensively damaged house (fig. 19.10) sustained a collapsed concrete-block wall and subsequent collapse of the wood-frame ceiling. This house had to be completely demolished a few days after the earthquake. Interestingly, houses on the same block, commonly of the same age and construction type, sustained widely differing degrees of damage.

The distribution of chimney failures in Coalinga is mapped in figure 19.11. Chimney damage was extensive in residential areas where many older, wood-frame structures were located (fig. 19.12), but chimney damage also occurred in some new houses as well (fig. 19.13). Many chimneys on older houses were fairly uniform in construction and did not appear to contain significant reinforcement. Of a total of 388 chimneys counted in

FIGURE 19.7—House built on a cripple wall that is leaning but has not collapsed. Note that leaning cripple studs (below three windows on right) are all approximately 1 ft high.

residential Coalinga, 206 (53 percent) had fallen, and 18 (15 percent) sustained extensive cracking. Most mobile homes were damaged to some degree, and many fell from their supports—again, there was no effective bracing against ground movement for these structures (see chap. 20).

Damage to the public schools in Coalinga consisted of cracked concrete-block walls, plaster cracks, broken windows, and damaged ceiling tiles. School buildings constructed in the early 1930's were not designed to be earthquake resistant; a few newer school additions, conforming to the provisions of California's Field Act (enacted in 1933), sustained minimal damage. As of this writing, evaluation and retrofitting of school buildings, which are provisions of the Field Act, are still taking place (Meehan, 1984).

At West Hills College, located just north of downtown Coalinga (fig. 19.11), damage was not structural, but the school's underground water main and electrical system sustained extensive damage. The college theater also was extensively damaged in the form of cracking and fallen plaster, cracked ceilings, and fallen light grills. Most classrooms at the college lost acoustic ceiling tile and light fixtures.

BUILDING DAMAGE

Surveys of newer "engineered" buildings (constructed using earthquake-resistant design) were conducted by several private firms 2 days after the earthquake (Messinger and others, 1984). The buildings observed during these surveys included those with commercial, religious, public, or industrial use. Overall, these buildings were found to have sustained no structural damage, and what little damage occurred was mostly to the building interiors—cracked ceiling tiles, broken glass, and cracked masonry veneer (Messinger and others, 1984). Newer wood-frame dwellings constructed in the past 10 to 20 years have earthquake-resistant features, such as continuous concrete foundations anchored to exterior sills of the walls, and provide effective lateral bracing. Unreinforced-masonry buildings performed poorly.

Two stores and two residences were the only structures damaged by fire. Only one of these fires occurred immediately after the earthquake. Although only one downtown building burned, this fire required the resources of the entire municipal fire department and lasted 4 hours. Minor grass fires occurred outside of Coalinga, caused by downed or arcing powerlines. These grass fires were not reported to have caused extensive damage and did not spread to the town of Coalinga (Scawthorn and Donelan, 1984).

AFTERSHOCK DAMAGE

The Coalinga region underwent numerous strong aftershocks through August 1, 1983. The two largest aftershocks occurred 3 minutes and 27 seconds after the May 2 main shock and on July 25, 84 days after the main shock. These two aftershocks were assigned magnitudes (M_L) 5.6 and 6.0, respectively (U.S. National Earthquake Information Service, 1983).

As a result of the July 20 aftershock, at least eight houses along College Street that had sustained initial damage during the main shock were further, irreparably damaged in their foundations and walls. Many sewer pipes in Coalinga were ruptured as a result of this aftershock; those that ruptured were already extensively decayed. Additional chimney damage occurred in the newer residential area in the southern part of Coalinga, where houses are less than 5 years old (J. Markison, oral commun., 1985). No damage was reported from the other, weaker aftershocks occurring during the 3 months after the main shock.

FIGURE 19.8—House, located within area of heavily damaged downtown Coalinga, that was shifted off its foundation (*A*). Doors and windows were below level of porch and offset from steps (*B*).

FIGURE 19.9—One-story wood-frame house that was shifted off its foundation.

FIGURE 19.10—Failed exterior wall of residence. Wall was constructed of unreinforced-concrete blocks.

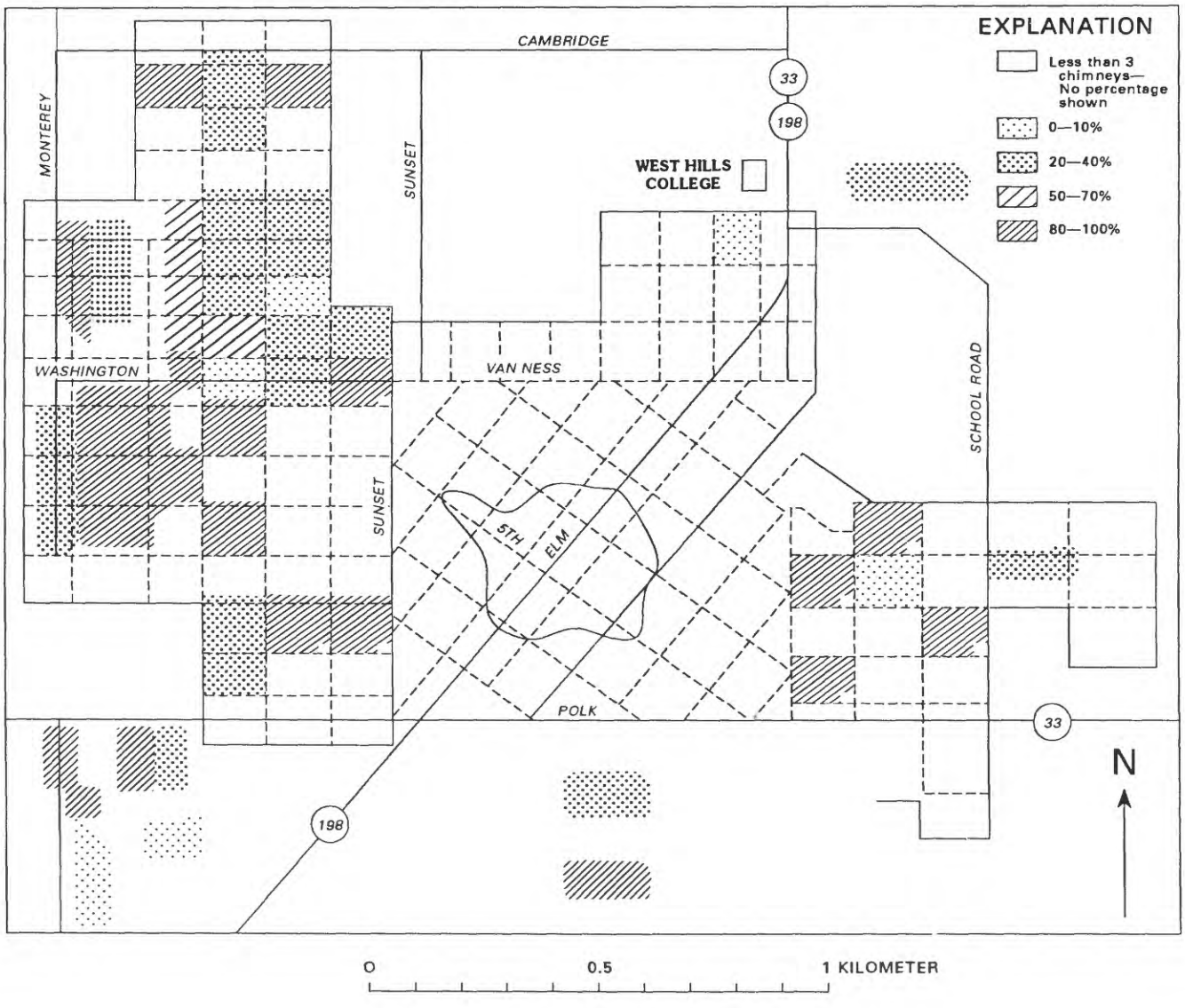

FIGURE 19.11—City of Coalinga, showing distribution of chimney damage. Oval indicates heavily damaged central business district (Shah and others, 1984). Areas with no stippling had only one or two chimneys per block. Percentages of damaged chimneys are given for all blocks having at least three chimneys.

MAXIMUM INTENSITY

A maximum MMI of VIII was assigned to Coalinga on the basis of (1) partial collapse of old, unreinforced-masonry buildings in the downtown business district; (2) nonstructural damage to somewhat newer masonry buildings; (3) absence of serious damage to modern masonry buildings; (4) fall of many houses off foundations (shifting of houses off foundations generally indicates MMI IX; however, because houses on cripple walls are inherently unstable during strong horizontal shaking, shifting is assumed to indicate only MMI VIII in this case); and (5) fall of more than half the chimneys. Chimneys were thrown or damaged in every neighborhood in Coalinga, on every type of house from the oldest to the newest. Many chimneys broke off at the roof line and fell in one piece, indicating an MMI of VIII.

FIGURE 19.12—Failure of chimney in older residential section of Coalinga.

FIGURE 19.13—Chimney damage to house located in newer residential subdivision in Coalinga.

In addition to the MMI of VIII at Coalinga, both Hopper and others (1983) and Stover (1983) assigned an MMI of VIII to Pacific Gas and Electric Substation 2, located 1 km southwest of the main shock. Thus, VIII was the maximum MMI observed at any location for the May 2 earthquake. Comparison of the intensity attenuation of this earthquake with that of other southern California earthquakes suggests an MMI of VIII for the Coalinga shock.

CONCLUSIONS

Earthquake damage in Coalinga clearly demonstrated the marked difference in response of the various types of structures prevalent in central California to strong horizontal earthquake shaking. Those that fared worst were the oldest unreinforced-masonry structures in the central business district. Other types of structures that were seriously damaged were adobe buildings and wood-frame houses on cripple walls. In contrast, many buildings in Coalinga built during the past 50 years performed very well; these buildings included substantial public structures, such as public schools and college buildings. Certain types of privately owned buildings, such as reinforced-masonry structures, wood-frame houses not on cripple walls, and metal buildings with wood or steel frames also performed well; many of these structures sustained only minor or no damage. Chimney damage, however, was not restricted to older houses, and even some new, well-constructed chimneys were damaged. Total monetary loss for all buildings, regardless of construction type, was estimated by the American Red Cross to be $10 million.

A maximum MMI of VIII was assigned to this earthquake because of the characteristics of the damage, including partial collapse of old, unreinforced-masonry buildings, absence of serious damage to some modern masonry buildings, fall of more than half the chimneys, and shifting of houses off foundations.

REFERENCES CITED

Algermissen, S.T., Steinbrugge, K.V., and Lagorio, H.J., 1977, Estimation of earthquake losses to buildings (except single family dwellings): U.S. Geological Survey Open-File Report 78-441, 161 p.

Hopper, M.G., Thenhaus, P.C., Barnhard, L.M., and Algermissen, S.T., 1983, Damage survey in Coalinga, California for the earthquake of May 2, 1983, *in* Bennett, J.H., and Sherburne, R.W., eds., The 1983 Coalinga, California earthquakes: California Division of Mines and Geology Special Publication 66, p. 5–8.

Meehan, J.G., 1984, Performance of public school buildings in the 1983 Coalinga earthquake, *in* Scholl, R.E., and Stratta, J.L., eds., Coalinga, California, earthquake of May 2, 1983: Reconnaissance report: Berkeley, Calif., Earthquake Engineering Research Institute Report 84-03, p. 189–202.

Messinger, D.L., Kellam, H.S., Graham, L.W., Martin, H.W., and Ellfifritt, D.S., 1984, Survey of "engineered buildings" after the

Coalinga earthquake, *in* Scholl, R.E., and Stratta, J.L., eds., Coalinga, California, earthquake of May 2, 1983: Reconnaissance report: Berkeley, Calif., Earthquake Engineering Research Institute Report 84-03, p. 157–181.

Scawthorn, Charles, and Donelan, John, 1984, Fire-related aspects of the Coalinga earthquake, *in* Scholl, R.E., and Stratta, J.L., eds., Coalinga, California, earthquake of May 2, 1983: Reconnaissance report: Berkeley, Calif., Earthquake Engineering Research Institute Report 840-3, p. 273–276.

Shah, H.C., Gere, J.M., Krawindler, Helmut, Rojahn, Chris, and Zsutty, T.C., 1984, An overview of damage to the Coalinga commercial district, *in* Scholl, R.E., and Stratta, J.L., eds., Coalinga, California, earthquake of May 2, 1983: Reconnaissance report: Berkeley, Calif., Earthquake Engineering Research Institute Report 84-03, p. 107–112.

Stover, C.W., 1983, Intensity distribution and isoseismal map, *in* Scholl, R.E., and Stratta, J.L., eds., Coalinga, California, earthquake of May 2, 1983: Reconnaissance report: Berkeley, Calif., Earthquake Engineering Research Institute Report 84-03, p. 182–188.

SUPPLEMENTARY DATA: BUILDING CLASSIFICATIONS

CLASS I: WOOD FRAME

Excluded are structure that are classed for fire as wood frame but have concrete supported floors and (or) some walls of masonry or concrete.

CLASS I–C

Habitational: Wood frame and frame stucco habitational buildings no higher than two stories, regardless of area.

Nonhabitational: Wood-frame and frame stucco buildings no higher than three stories and no larger than 3,000 ft^2 in ground-floor area.

CLASS I–D

Wood-frame and frame stucco buildings not falling into class I–C.

CLASS II: ALL METAL

CLASS II–A

All-metal buildings one story high and no larger than 20,000 ft^2 in ground-floor area. Wood or cement-asbestos is an acceptable alternative to metal roofing and (or) siding.

CLASS II–B

Buildings that would fall into class II–A except for exceeding area or height limitations.

CLASS III: STEEL FRAME

CLASS III–B

Buildings having a complete steel frame, with all loads carried by the steel frame. Floors and roofs shall be of poured-in-place reinforced concrete or metal, or any combination thereof, except that roofs on buildings higher than three stories may be of any material. Exterior and interior walls may be of any non-load-carrying material.

CLASS III–C

Buildings having some of the favorable characteristics of class III–A but otherwise falling into class III–B.

CLASS III–D

Buildings having a complete steel frame, with floors and roofs of any material and with walls of any non-load-bearing material.

CLASS IV: REINFORCED CONCRETE, COMBINED REINFORCED CONCRETE AND STRUCTURAL-STEEL FRAME

Note: Buildings falling into classes IV–A through IV–C shall have all vertical loads carried by a structural system consisting of one or a combination of the following: (a) poured-in-place reinforced-concrete frame, (b) poured-in-place reinforced-concrete bearing walls, (c) partial structural-steel frame with (a) and (or) (b). Floors and roof shall be of poured-in-place reinforced concrete, except that materials other than reinforced concrete may be used for the roofs on buildings higher than three stories.

CLASS IV–A

Buildings having a structural system as defined by the note above, with poured-in-place reinforced-concrete exterior walls or reinforced-unit-masonry exterior walls placed within the frame. Buildings shall have at least a width-to-height-above-ground (or above any setback) ratio not exceeding 1 to 3. Not qualifying are buildings with column-free areas larger than 2,500 ft^2 (such as auditoriums, theaters, public halls, and so on).

CLASS IV–B

Buildings having a structural system as defined by the note above, with exterior and interior nonbearing walls of any material.

CLASS IV–C

Buildings having some of the favorable characteristics of class IV–A but otherwise falling into class IV–B.

CLASS IV–D

Buildings having (a) a partial or complete load-carrying system of precast concrete, and (or) (b) reinforced-concrete lift-slab floors and (or) roofs, and (c) otherwise falling into class IV–A, IV–B, or IV–C.

CLASS IV–E

Buildings having a complete reinforced-concrete frame or a complete frame of combined reinforced concrete and structural steel. Floors and roofs may be of any material, and walls of any non-load-bearing material.

CLASS V: MIXED CONSTRUCTION

CLASS V–A

1. Dwellings, not higher than two stories, constructed of poured-in-place reinforced concrete, with roofs and second floors of wood frame.
2. Dwellings, not higher than two stories, constructed of adequately reinforced brick or hollow-concrete-block masonry, with roofs and floors of wood.

CLASS V–B

One-story buildings having superior earthquake-damage-control features, including exterior walls of (a) poured-in-place reinforced concrete, and (or) (b) precast reinforced concrete, and (or) (c) reinforced-brick masonry or reinforced-concrete-brick masonry, and (or) (d) reinforced-hollow-concrete-block masonry. Roofs and supported floors shall be of wood or metal diaphragm assemblies. Interior bearing walls shall be of wood frame or any one or a combination of the aforementioned wall materials.

CLASS V–C

One-story buildings having construction materials listed for class V–B but with ordinary earthquake-damage-control features.

CLASS V–D

1. Buildings having reinforced-concrete load-bearing walls, with floors and roofs of wood and not falling into class IV–E.
2. Buildings of any height having class V–B construction materials, including wall reinforcement; also included are buildings with roofs and supported floors of reinforced concrete (precast or otherwise) and not falling into class IV.

CLASS V–E

Buildings having unreinforced solid-unit masonry of unreinforced brick, unreinforced concrete brick, unreinforced stone, or unreinforced concrete, where the loads are carried in whole or in part by the walls and partitions. Interior partitions may be wood frame or any of the aforementioned materials. Roofs and floors may be of any material. Not falling into this class are buildings with nonreinforced load-carrying walls of hollow tile or other hollow-unit masonry, adobe, or cavity construction.

CLASS V–F

1. Buildings having load-carrying walls of hollow tile or other hollow-unit masonry construction, adobe, and cavity-wall construction.
2. Any building not falling into any other class.

CLASSES VI–A THROUGH VI–E: EARTHQUAKE-RESISTANT CONSTRUCTION

A building or structure with any combination of materials and with earthquake-damage-control features equivalent to those in class I through V buildings. Alternatively, a qualifying building or structure may fall into any of classes I through V (instead of VI–A through VI–E) if its construction resembles that described for one of these classes and if the qualifying building or structure has an equivalent damageability.

20. DWELLING MONETARY LOSSES

By KARL V. STEINBRUGGE,
STRUCTURAL ENGINEER, EL CERRITO, CALIF.;

E.J. FOWKES,
WEST HILLS COLLEGE, COALINGA, CALIF.;

HENRY J. LAGORIO,
UNIVERSITY OF CALIFORNIA, BERKELEY;

and

S.T. ALGERMISSEN,
U.S. GEOLOGICAL SURVEY

CONTENTS

ABSTRACT

All one- to four-family dwellings in Coalinga (population, 6,769) were examined after the May 2 earthquake to determine the degree of damage to their exterior and interior finishes, masonry veneers, and other constructional components. At least three sides of these structures were inspected, as well as the interiors of almost 60 percent of them. This information provided the basis for monetary-loss calculations.

Field-inspection methods and computational algorithms were based on those developed in 1969 for the U.S. Department of Housing and Urban Development. These methods were first applied on a simplified basis after the 1971 San Fernando, Calif., earthquake, and again slightly modified to suit 1983 Coalinga conditions.

Monetary losses to all wood-frame one- to four-family habitational units, excluding mobile homes, were $15,290,000. Completely independent data from financial sources provided similar results. The American Red Cross estimate, which was prepared very shortly after the event, amounted to almost $10,000,000 for all dwellings, regardless of construction type.

As expected, newer wood-frame dwellings performed better than older ones. Dwellings with concrete first floors on grade performed much better than those with supported wood floors, in contrast to the 1971 San Fernando experience, where performances of these two construction types were about equal.

The May 2 earthquake provided an opportunity to verify and improve monetary-loss-estimation methodologies used for governmental earthquake-vulnerability studies, as well as to evaluate wood-frame-dwelling probable maximum losses (PML's) used by the California Department of Insurance and by the insurance industry in their reports to the State.

INTRODUCTION

This chapter examines various aspects of dwelling monetary losses as a result of the May 2 earthquake, for uses in vulnerability analyses.

The Coalinga Chamber of Commerce placed the town population before the earthquake at 6,769 within the city limits, whereas the 1980 U.S. Census placed this figure at 6,593. The town is compact; the farthest distance across it is about 2 mi (fig. 20.1). Almost 95 percent of the dwellings were single-family wood-frame structures, and the rest principally unit masonry (brick, hollow tile, hollow concrete block, and adobe) or two-story wood frame.

In the past, Federal and State disaster-response organizations have conducted earthquake-vulnerability studies of the larger metropolitan areas in the Western United States, and they currently are also doing so in the Eastern United States. A highly important aspect of these studies is the damage to dwellings. For example, we might cite the planning needs for postearthquake Federal financial assistance, as well as emergency housing. Quantification of such actual experience as at Coalinga improves the quality of future vulnerability estimates. The private sector, such as insurance companies, banks, and savings and loan associations, needs to know the aggregate of potential losses so as to remain solvent and serve the public after a great earthquake.

Achieving improved loss-estimation data requires a critical examination of "what happened" and "what did it cost." The methods used herein are based on those

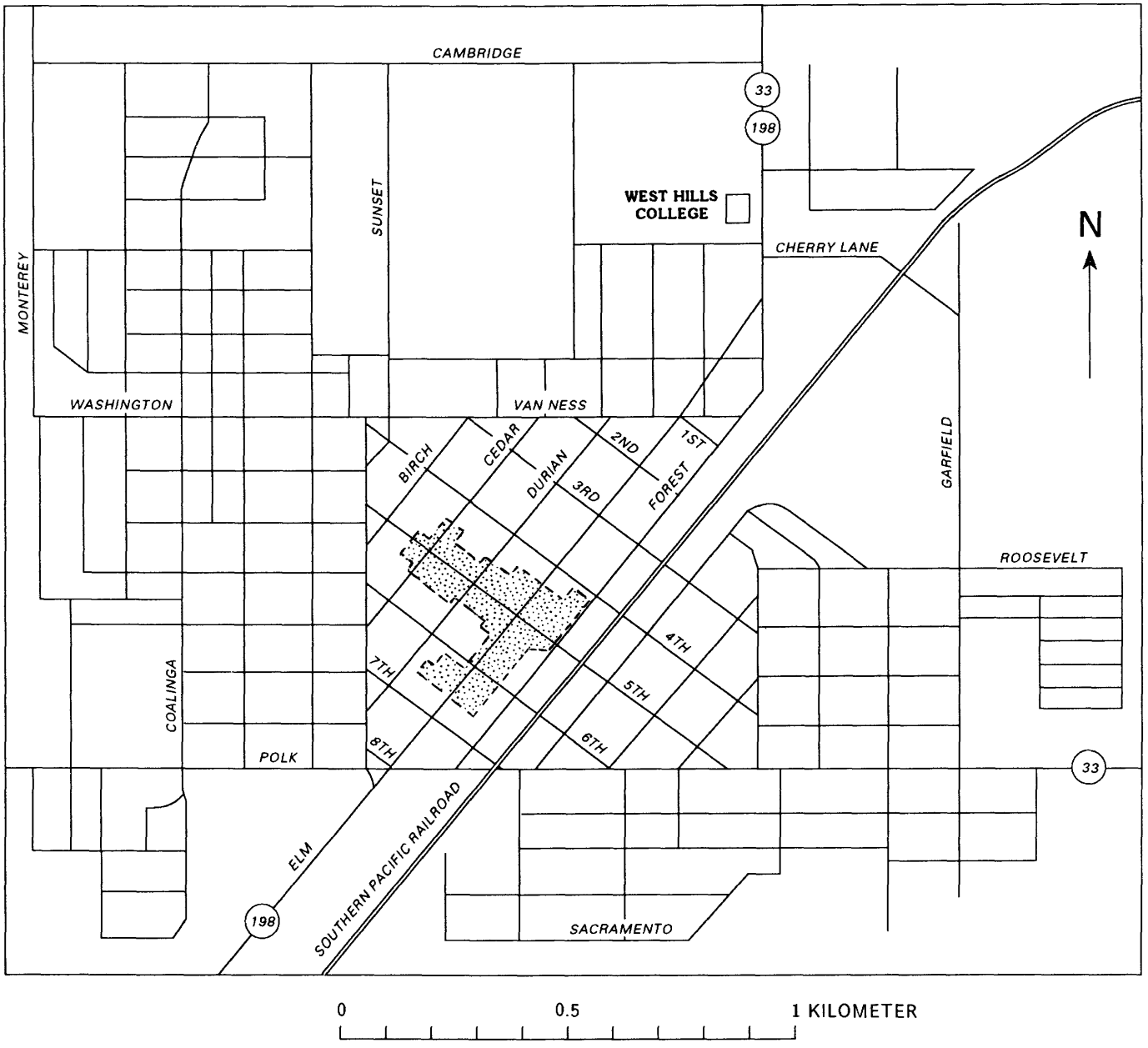

FIGURE 20.1.—Coalinga, Calif., showing location of downtown demolished area.

successfully applied after the 1971 San Fernando, Calif., earthquake. Data must be gathered and results presented in terms that can be readily applied to other cities or regions. A detailed field inspection resulting in detailed loss data generally cannot be cost effectively applied when extrapolating these data to a large, complex metropolitan area.

"What happened" to dwellings in Coalinga was examined visually by quickly trained supervised personnel. The variations from building-code requirements found in Coalinga are probably characteristic of other towns in the San Joaquin Valley wherever building ages and construction materials are similar.

Damage to dwellings is a function of numerous factors, including age, construction materials, and design characteristics. City neighborhoods and housing tracts are developed over different timespans, as well as under different building codes, and construction practices change over time. Thus, damage patterns can and commonly do vary throughout a heavily shaken community, even though ground motions and soil conditions may have been reasonably uniform. Coalinga is one such instance.

TABLE 20.1.—*Information acquired during field inspections of dwellings*

[Each item also allowed a response of "unknown," "undetermined," or "not applicable." See section below entitled "Supplementary Information" for definitions of degrees of damage.]

1. Address and block number (data compiled only by block number).
2. Estimated date of construction: pre-1940, 1940-49, post-1949.
3. Number of stories: one story, two story, one and two story, split level.
4. First-floor construction: Wood joist, concrete slab on grade.
5. Demolished (or permit issued): No, yes, permit issued to demolish.
6. Moved off foundations? (and amount of displacement):
   - No.
   - Amount undetermined. Normally, significant cracking.
   - Yes, 6 in. or less.
   - Yes, greater than 6 in. but less than 12 in.
   - Yes, about 12 in.
   - Yes, greater than 12 in.
7. Structural damage:
   - Foundation damage: none, slight, moderate, severe.
   - Building damage: none, slight, moderate, severe.
8. Interior-finish damage:
   - If plaster on wood lath: none, slight, moderate, severe.
   - If gypsumboard: none, slight, moderate, severe.
   - If wood paneling, plywood, and so on: none, slight, moderate, severe.
   - If other finish, state type _____: none, slight, moderate, severe.
9. Exterior-finish damage:
   - If stucco: none, slight, moderate, severe.
   - If wood finish (rustic, and so on): none, slight, moderate, severe.
   - If aluminum: none, slight, moderate, severe.
   - If other finish, state type _____: none, slight, moderate, severe.
10. Masonry veneer (3 in. or thicker):
    - Percent veneered: 0, 1-10, 11-25, 26-50, more than 50 percent.
    - Veneer damage: none, slight, moderate, severe.
11. Unit-masonry chimney damage:
    Number of chimneys:
    - One chimney: none, slight, moderate, severe, total.
    - Two chimneys: none, slight, moderate, severe, total.

    If damaged, reinforcing steel seen? Yes, no.
12. Were geologic hazards a factor? Yes, no, (not relevant in Coalinga).
13. Describe exceptional damage, such as chimney from neighboring house falling on inspected house.
14. Occupant: renter, owner.

FIELD INSPECTIONS

We conducted reconnaissance surveys in Coalinga immediately after the earthquake. Upon determining the extent of the damage and the feasibility of a dwelling-damage survey, field inspectors were hired and trained. These field inspectors were students at West Hills College (in Coalinga), and the inspections were conducted under the supervision of E.J. Fowkes. The inspections began 16 days after the earthquake. Except for verification problems, field inspections were completed by the end of the month. Inspection procedure included a daily morning briefing with all inspectors to determine survey problems and improve uniformity of inspection methods. Comparison of surveys conducted by different inspectors revealed only slight irregularities. Occasional differences of one degree (for example, severe in place of moderate, and so on) were found in some damage estimates; these irregularities tended to average out because several inspectors were used.

Every dwelling in Coalinga was inspected. Three sides of the exteriors of all one- to four-family dwellings (totaling 2,041 units) were inspected, as well as the interiors of almost 60 percent of all dwellings. The damage was recorded on a form patterned after those used in other earthquakes, to preserve data compatibility. Mobile homes, numbering 105, were also inspected for damage, bringing the final number of inspected habitational units to 2,146.

Data acquisition was confined to direct damage to each dwelling, and the survey did not include such consequential effects as the need for alternative housing. Fire after the earthquake was not a significant problem in dwellings; however, where present, this information was noted on the inspection form by the field inspectors and was available when separating earthquake damage from fire damage. These inspection forms were based on those used for dwellings after the 1971 San Fernando, Calif., earthquake (Steinbrugge and others, 1971; Steinbrugge and Schader, 1973). The acquired information for Coalinga is listed in table 20.1.

The quality of the data obtained by the field inspectors was somewhat influenced by their being local residents who, along with their families, had experienced the earthquake. The data quality can be partly verified by a comparison with independently received information. The field inspectors were asked to determine each dwelling's age by estimate or inquiry, and to record this information in one of three age groups: pre-1940, 1940–49, and post-1949. Each inspector also carried a map stating the year when the various subdivisions were annexed to the town. From one independent financial source, the year built was also known for 17.7 percent (or 353) of the 1,995 dwellings for which ages had been determined by the field inspectors. Internal evidence suggests that a few copying errors may be contained in

the data obtained from financial sources. For an example of another view on errors, an inspector's year-built estimate of 1940 versus financial-source information of 1939 would be computer recorded as a 1- to 10-year mismatch because the inspector placed it within the 1940–49 age group. The average mismatch is about 5 years in these cases. Using a 1-decade maximum mismatch (5-year average mismatch) as an acceptable error limit and restricting the analysis to comparable data, 92.8 percent of the age data between these two sources agree.

Construction information and degrees of damage were visually established by the field inspectors from guidelines that in most cases probably allowed less room for judgmental error than did those for age estimates. Thus, it is reasonable to expect improved quality for most other field data. This study relies heavily on its own field data wherever there are conflicts with those obtained from other sources, including town records, which were gathered during a period of generally high stress.

The potential for discrepancies arose whenever major remodeling or additions were observed. The field inspector's judgment on the predominate construction characteristics and age determination would allow some margin of error.

FIGURE 20.2.—Typical dwelling that fell off its foundation, resulting in severe damage.

FIGURE 20.3.—House that shifted on its foundation, as shown by slant in porch columns.

DWELLING CHARACTERISTICS IN COALINGA

The observed patterns of damage to dwellings generally were the same as those found after all recent California earthquakes. Newer wood-frame dwellings, such as those built within the past 10 to 20 years, had earthquake-resistant features, such as anchorage of the foundation sills of the exterior walls to continuous concrete foundations. Aside from nonstructural cracking of gypsumboard walls, damage to these earthquake-resistant wood-frame dwellings was generally limited to the breaking or collapse of the brick or other-type unit-masonry chimney, commonly at the roofline where it was weakened by metal flashing. Many (but not all) of these damaged chimneys on newer dwellings were reinforced, although the type and amount of reinforcement may not everywhere have conformed to current metropolitan San Francisco or Los Angeles standards. Minimal glass breakage occurred to windows and sliding doors, and this was not a significant problem.

Older houses, such as those built 50 or more years ago, performed badly in a comparative sense. Many were unanchored to their foundations and slid off them. Dwelling construction commonly had deteriorated between the first floor and the foundation, owing to wood decay or termite damage, and effective lateral-force bracing was absent where failures occurred. Those wood-frame dwellings on cripple wood studs without significant lateral-force bracing fell.[1] Examples of severe damage resulting from failure at the foundation level are shown in figures 20.2 and 20.3.

An unusual variant was the dwellings that had been moved into the town of Coalinga from the nearby oil fields. These houses were not moved into any one particular area and were set on any vacant lot available. Requested information was not searched for by town authorities, owing to the press of postearthquake activities, and this information may not exist. However, from conversations with the local Baker Museum staff and from the recollections of older residents, about 200 dwellings may have been moved to Coalinga between

[1]Cripple studs extend from the top of the foundation to the bottom of the platform of the first floor. In an engineering sense, cripple studs have no moment continuity to the studs above and to the foundation below. The deteriorated siding on the cripple-stud walls was normally an inadequate equivalent of a shear wall.

about 1930 and the late 1950's. About 90 percent of those houses imported before 1940 or 1945 were estimated to have been placed on wooden mud sills (directly on the earth). Those subsequently removed to Coalinga, particularly after 1950, probably were placed on concrete foundations but apparently not bolted thereto. In these houses, the top surface of the concrete foundation was smooth where failure was observed, possibly troweled in many cases, and the wooden foundation sills were placed directly on these foundations. There was no anchorage to their foundations. Many of these houses slid off their foundations, as might be expected because the coefficient of friction between the sills and the smooth concrete is small. (Inventories of dwellings that did not show sill anchor bolts could be misleading because it is unknown what percentage of the older houses had wood sills that were set into freshly poured concrete; these houses have considerable resistance to sliding but are susceptible to vertical motions. If nails were driven into the underside of the sill and the sill then embedded in fresh concrete, a significant amount of sliding resistance would also exist, even if no anchorage were visible.)

A significant life hazard was the common failure of the front-porch roof on older houses, as shown in figure 20.4.

Virtually all mobile homes were somewhat damaged, and many fell from their supports—performance consistent with experience in all other recent California earthquakes. Characteristic damage is shown in figure 20.5. Mobile-home damage is not included in this study.

Dwelling damage in such nearby cities as Avenal was very small and did not warrant a damage survey.

CONTEXT WITH NONDWELLING CONSTRUCTION

A few adobe, tile, *unreinforced*-hollow-concrete-block, and *unreinforced*-brick dwellings existed in Coalinga. An example of a failed adobe dwelling is shown in figure 20.6.

FIGURE 20.4.—Typical front-porch roof that collapsed because of inadequate anchorage to main part of dwelling.

The overall performance of these types of masonry was very poor, as might be expected, consistent with damage counterpart to non-earthquake-resistant unit-masonry structures in the central business district. Nonetheless, those few that were designed to be earthquake resistant performed very well.

Wood-frame dwellings performed excellently in comparison with the older, non-earthquake-resistant masonry buildings in the central business district. The older central-core mercantile section consisted almost entirely of buildings with unreinforced-brick bearing walls cemented by sand-lime mortar; roofs and supported floors were of wood. This class of construction was severely damaged, and these buildings were demolished soon after the earthquake. Building losses were essentially 100 percent for this class of construction. Partly surrounding

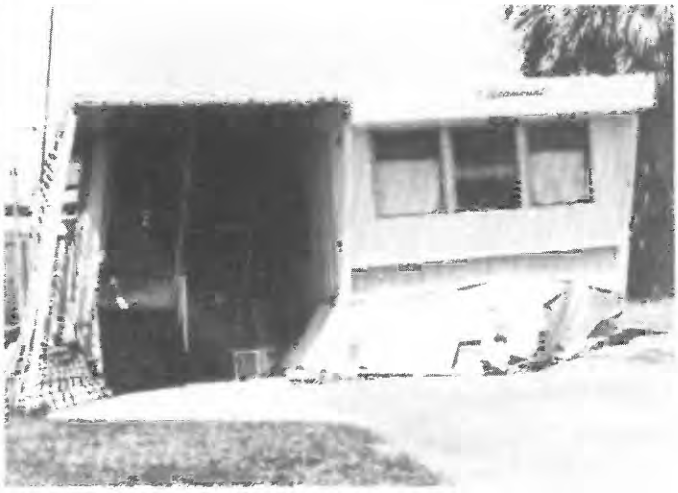

FIGURE 20.5.—Characteristic damage to most mobile homes in Coalinga, as well as in other California earthquakes.

FIGURE 20.6.—Collapsed wall of an adobe dwelling.

this destroyed portion of the central business district were numerous undamaged earthquake-resistant buildings that were commonly constructed of reinforced concrete or reinforced hollow concrete block. Elsewhere, public grammar schools, a high school complex, and a community college complex sustained little or no damage because they, too, were designed to be earthquake resistant in conformity with California's Field Act; construction materials at these schools were of all types, including reinforced-concrete and reinforced-unit masonry, such as hollow concrete block. A major newer earthquake-resistant shopping center near the town limits performed excellently, as did other newer mercantile structures also located outside the central business district.

AGE

As previously mentioned, the field inspectors were asked to estimate the age of each inspected dwelling or to obtain it from the occupants, and to list this age in one of three categories: pre-1940, 1940–49, and post-1949. This method is consistent with those used after the 1971 San Fernando, Calif., earthquake. The reasoning in 1971 for these groupings was that most wood-frame dwellings constructed after 1950 probably had undergone little deterioration due to dry rot and termites over the intervening 21-year period, whereas this was not so true for most pre-1940 construction. Another reason in 1971 was that in most of California, dwelling-construction practices had improved within the decade after the 1933 Long Beach, Calif., earthquake. Also, substantial numbers of new dwellings had been built after the Great Depression and World War II, and much of this construction was easily identifiable by examining the exterior architecture.

On the basis of our reconnaissance surveys, we decided that age groupings should follow those used after the 1971 San Fernando earthquake, for similar reasons: The age groupings could easily be identified by their architectural style; the groupings could be correlated with improvements in earthquake resistance; the groupings could be associated with structural deterioration from natural causes (although this reasoning is weaker for Coalinga than San Fernando, owing to the 30-year time period since 1950); and, finally, the groupings allowed data consistency with previous studies.

The 2,041 Coalinga dwellings are categorized by age and type of construction materials in table 20.2. Wood frame accounts for about 95 percent of the total. A crude indicator of the change (growth) in housing may be obtained from census figures for Coalinga (table 20.3). The population and housing decreases from 1910 to 1920 are attributable to changes in nearby oil-field operations.

TABLE 20.2.—*Coalinga dwelling count by age, height, and construction materials, as obtained by field inspection*

Dwelling type	One Story	Two Story	One and Two Story	Height not Identified	All Heights
Wood frame:					
Pre-1940 construction----	776	26	13	5	820
1940-49 construction-----	309	6	3	6	324
Post-1949 construction---	728	17	6	3	754
Age not identified-------	16	3	1	10	30
Brick, tile, adobe:					
Pre-1940 construction----	19	1	0	0	20
1940-49 construction-----	25	0	1	0	26
Post-1949 construction---	11	0	0	1	12
Age not identified-------	0	0	0	1	1
Unknown (commonly demolished)----------					54
Total number of dwellings----------					2,041

TABLE 20.3.—*Coalinga population and housing units*

[Definitions of dwellings have changed over time, as have the methods in presenting the data; thus, these numbers are not fully compatible. For example, for the 1980 U.S. Census, column 3 refers to "the number of housing units at an address"; see each census for variations. Mobile homes and trailers have been included, whereas our dwelling count of 2,041 excluded these. n.l., not listed. Data from U.S. Bureau of the Census.]

Year	Population	Single-family dwellings	Single-family plus multifamily habitational
[1]1900	n.l.	n.l.	n.l.
1910	4,199	915	n.l.
1920	2,934	747	n.l.
1930	2,851	---	---
1940	5,026	---	1,565
1950	5,539	1,489	1,835
1960	5,880	1,944	2,122
1970	6,161	2,009	2,418
1980	6,593	2,057	2,449

[1]In 1900, there were approximately 20 wood-frame buildings on Forest Street. The population was small when the town incorporated in 1906 (127 votes cast). Tents were common for housing during the early oil-boom years. From Lula Grigsby collection, Coalinga Library.

From the information in table 20.3, applying Coalinga information and conclusions elsewhere is appropriate to 1920 and subsequent construction. Thus, it should be used with great care if applied, for example, to the Victorian houses in San Francisco. Dwelling practices vary with community, as well as over time, and extrapolations of data based on identical age groupings must be tempered with local construction practices. The requirement in some communities for anchoring of dwellings to continuous reinforced-concrete foundations did not necessarily apply in the neighboring communities. However, it has been noted that construction tradesmen tend to transfer their practices from one community to another, though possibly with reduced quality where local governmental inspection is weak.

CONSTRUCTION MATERIALS AND STORY HEIGHT

Story height and (or) exterior-wall construction were not identified for 80 dwellings (3.9 percent) of the total of 2,041 in the city. These omissions were due to demolition of a few dwellings immediately after the earthquake but before the inspections, to mixed construction, or to error when recording on the inspection form. Data on a total of 1,961 adequately identified structures are listed in table 20.4. No split-level dwellings existed.

It is evident from table 20.4 that at the time of the May 2 earthquake, Coalinga was a one-story wood-frame town because 93.3 percent of the housing fell into this category. Two-story wood frame and one-story masonry compose less than 3 percent each of the total. Although a few statistics are presented here on these structures, these data are too few to be useful in vulnerability studies.

TABLE 20.4.—*Story height of dwellings as a function of construction materials*

[Data limited to dwellings where construction was identified]

Story height	Wood frame		Masonry	
	Number of dwellings	Percentage of total	Number of dwellings	Percentage of total
One story----------	1,829	93.3	55	2.8
Two story----------	52	2.7	1	0
One and two story---	23	1.2	1	0
Total----------	1,904	97.2	57	2.8

DAMAGE FACTOR

"Damage factor" is defined as the ratio of the number of houses with a specified degree of damage to a construction component for a given degree of shaking. This degree of shaking may be expressed in engineering terms in the form of spectra, in units of modified Mercalli intensity (or another intensity scale), or as a percentage of the monetary loss. Construction components selected for Coalinga dwellings (table 20.1) include: foundations, structure, interior finish, exterior finish, masonry veneer (when applicable), and masonry chimneys (when applicable).

INTERIOR/EXTERIOR FINISHES TO ONE-STORY WOOD FRAME

The field inspectors cataloged interior- and exterior-finish damage for all dwellings, regardless of story height or materials of construction (for example, wood frame or masonry). Degrees of damage are defined in the section below entitled "Supplementary Information."

Exterior- and interior-finish types are listed in table 20.5 by age group and floor type. (Floor type is of special interest; see section below entitled "Dwelling Displacement from Foundation.") Masonry veneer and masonry chimneys are discussed separately because significant numbers of dwellings did not have this kind of masonry.

Past studies have suggested different damage patterns for plaster on wood lath from that found when gypsumboard is used. It is often difficult to quickly distinguish between them, and their identification is commonly associated with dwelling age and known trade practices for that age. When painting is long overdue, interiors may show slight discoloration indicating the strips of wood lath. Wall or ceiling penetration may also show the type of finish, but determinations made on this basis can be time consuming. These difficulties were also present in the Coalinga inspections, and so a few errors probably occurred.

TABLE 20.5.—*Exterior and interior finishes of one-story wood-frame dwellings*

[Number of dwellings by predominant floor type, excluding masonry veneer]

Finish type	Pre-1940		1940-49		Post-1949	
	Wood floor	Concrete floor	Wood floor	Concrete floor	Wood floor	Concrete floor
Interior finish:						
Plaster----------	89	4	29	1	7	2
Gypsumboard-----	249	9	127	19	228	234
Wood----------	29	0	3	0	4	10
Total------	367	13	159	20	239	246
Exterior finish:						
Stucco/plaster--	95	11	90	12	262	246
Wood----------	607	6	162	21	73	127
Aluminum--------	36	1	20	0	9	5
Total------	738	18	272	33	344	378

The word descriptions of damage (damage factors) for one-story wood-frame dwellings falling into one of the three age groups are summarized in tables 20.6 through 20.8. We note that dwellings which were displaced (moved) on their foundations were excluded from these tabulations. When houses move on their foundations or fall off them, the finishes normally have accentuated damage, as do the utilities located beneath the floor.

Interior plaster and interior gypsumboard were combined in figure 20.7 for ease in presentation. We note that wood exterior finishes performed better than stucco or plaster exterior finishes. Also, exterior finishes on more recently built dwellings performed better than did those on older ones; this observation was only partly true for interior finishes. Aluminum siding was noted on a few houses, and it performed well. Aluminum siding has commonly been placed over existing wood siding for insulation purposes and (or) to reduce painting maintenance costs. Aluminum siding, however, does not contribute any significant structural strength. It may be desirable to combine the effects of older houses falling/sliding off their foundations with the damage to interior and exterior finishes. Coalinga damage-factor experience in this regard is listed in table 20.9. We note that these

TABLE 20.6.—*Damage factors for dwelling finishes in one-story wood-frame construction before 1940*

[No dwelling movement (displacement) with respect to foundation]

Degree of damage---	None		Slight		Moderate		Severe		Total
Finish type	No. of dwellings	Pct of total	No. of dwellings	Pct of total	No. of dwellings	Pct of total	No. of dwellings	Pct of total	No. of dwellings
Interior finish:									
Plaster---------	0	0	20	50.0	19	47.5	1	2.5	40
Gypsumboard-----	20	16.0	87	69.6	15	12.0	3	2.4	125
Wood------------	3	50.0	3	50.0	0	0	0	0	6
Exterior finish:									
Stucco/plaster--	2	2.7	47	64.4	22	30.1	2	2.7	73
Wood------------	135	64.6	66	31.6	8	3.8	0	0	209
Aluminum--------	13	72.2	5	27.8	0	0	0	0	18

TABLE 20.7.—*Damage factors for dwelling finishes in one-story wood-frame construction between 1940 and 1949*

[No dwelling movement (displacement) with respect to foundation]

Degree of damage---	None		Slight		Moderate		Severe		Total
Finish type	No. of dwellings	Pct of total	No. of dwellings	Pct of total	No. of dwellings	Pct of total	No. of dwellings	Pct of total	No. of dwellings
Interior finish:									
Plaster---------	2	7.1	18	64.3	8	28.6	0	0	28
Gypsumboard-----	10	7.6	96	73.3	22	16.8	3	2.3	131
Wood------------	1	50.0	1	50.0	0	0	0	0	2
Exterior finish:									
Stucco/plaster--	6	6.5	59	63.4	27	29.0	1	1.1	93
Wood------------	113	73.4	5	22.7	5	3.2	1	.6	154
Aluminum--------	17	89.5	2	10.5	0	0	0	0	19

TABLE 20.8.—*Damage factors for dwelling finishes in one-story wood-frame construction after 1949*

[No dwelling movement (displacement) with respect to foundation]

Degree of damage---	None		Slight		Moderate		Severe		Total
Finish type	No. of dwellings	Pct of total	No. of dwellings	Pct of total	No. of dwellings	Pct of total	No. of dwellings	Pct of total	No. of dwellings
Interior finish:									
Plaster---------	2	22.2	4	44.4	3	33.3	0	0	9
Gypsumboard-----	106	24.5	294	68.1	30	6.9	2	.5	432
Wood------------	8	61.5	2	15.4	3	23.1	0	0	13
Exterior finish:									
Stucco/plaster--	27	5.6	390	84.1	60	12.5	2	.4	479
Wood------------	152	80.4	35	18.5	2	1.1	0	0	189
Aluminum--------	8	72.7	3	27.3	0	0	0	0	11

data are for one-story wood-frame dwellings that had wood-supported floors and were constructed before 1940. The wood-floor and older-age criteria determine the greatest likelihood for houses falling/sliding off their foundations. The effect of this dwelling movement is apparent when comparing the percentages under the heading "Severe Damage" in tables 20.6 and 20.9. Sample size is small, and extrapolations must bear this in mind.

MASONRY VENEER

Masonry veneer is defined as brick, stone, or other nonstructural masonry that is at least 3 in. thick and supported by a backing wall. For wood-frame dwellings, the structural support in the backing wall is the wood studding. Veneer anchorage to its backing wall can be of various types, many of which are ineffective during

TABLE 20.9.—*Damage factors for dwelling finishes in one-story wood-frame construction before 1940*

[All dwellings moved (permanently displaced) with respect to foundation; all have wood-supported floors]

Degree of damage---	None		Slight		Moderate		Severe		Total
Finish type	No. of dwellings	Pct of total	No. of dwellings	Pct of total	No. of dwellings	Pct of total	No. of dwellings	Pct of total	No. of dwellings
Interior finish:									
Plaster---------	0	0	40	44.9	37	41.6	12	13.5	89
Gypsumboard-----	21	8.4	146	58.6	57	22.9	25	10.0	249
Wood------------	8	27.6	11	37.9	7	24.1	3	10.3	29
Exterior finish:									
Stucco/plaster--	1	1.1	48	50.5	33	34.7	13	13.7	95
Wood------------	182	30.0	247	40.7	130	21.4	48	7.9	607
Aluminum--------	20	55.6	15	41.7	1	2.8	0	0	36

earthquakes, particularly when sand-lime mortar is used. An airspace between the masonry veneer and its backing wall is commonly found in colder climates where additional insulation is desired.

For the reasons previously discussed, the damage survey did not include the degree of code compliance or the kind of anchorage for veneers. The veneer-construction practices in Coalinga probably can be extrapolated to other smaller San Joaquin Valley communities for use in vulnerability studies.

The degrees of damage to masonry veneer (damage factors) on one-story wood-frame dwellings in Coalinga are listed in table 20.10. Dwelling veneer in Coalinga existed primarily for architectural reasons and was found principally on newer homes. The percentages for wood-frame dwellings with 1 percent or more of their exterior

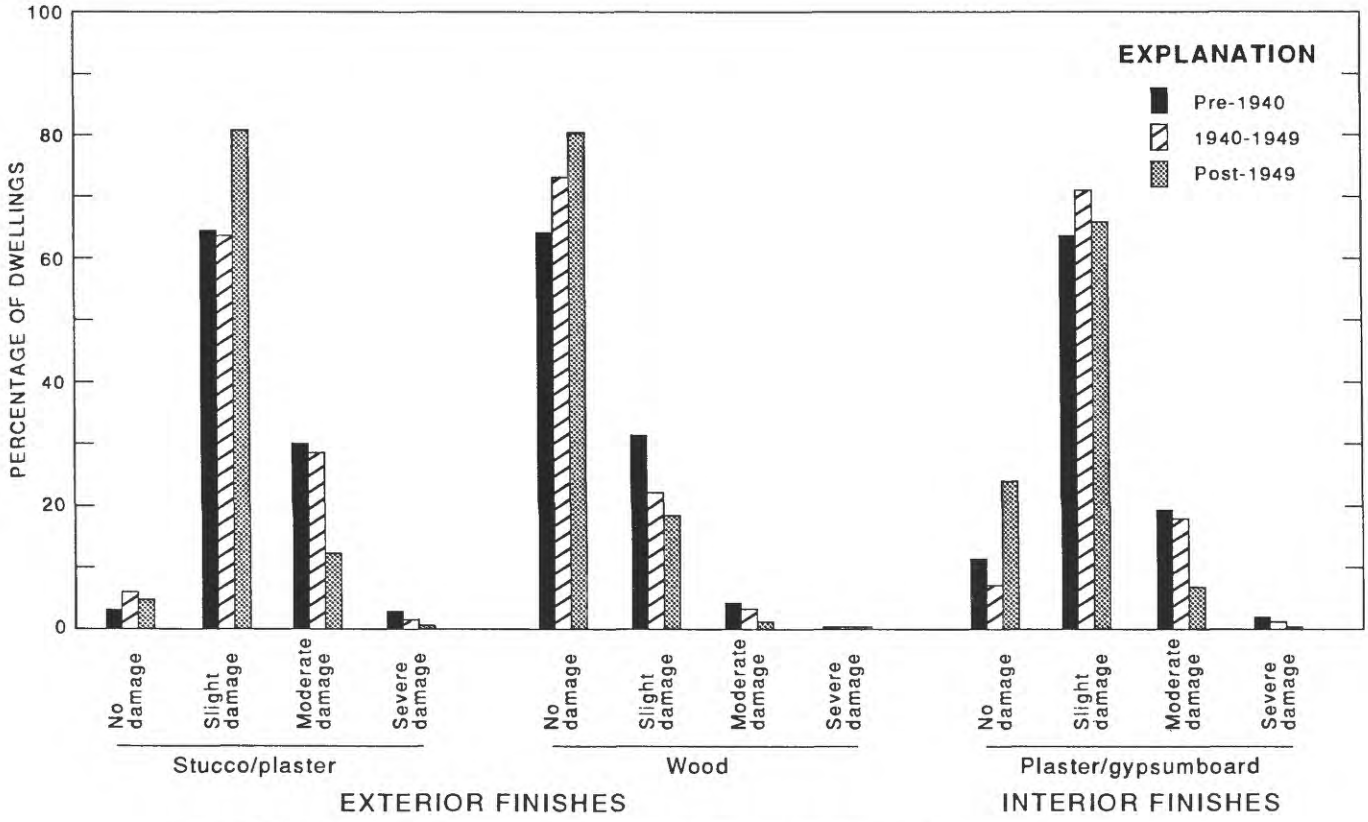

FIGURE 20.7.—Distribution of degrees of damage to exterior and interior finishes as a function of age group.

TABLE 20.10.—*Damage factors for masonry veneer in one-story wood-frame dwellings*

Degree of damage-----		None		Slight		Moderate		Severe		
Age group	Percentage of walls veneered	No. of dwellings	Pct of total	No. of dwellings	Pct of total	No. of dwellings	Pct of total	No. of dwellings	Pct of total	Total number of dwellings
Pre-40	1-10	14	40.0	11	31.4	2	5.7	8	22.9	35
	11-25	1	7.1	5	35.7	4	28.6	4	28.6	14
	26-50	0	0	0	0	2	66.7	1	33.3	3
	More than 50	0	0	1	100.0	0	0	0	0	1
1940-49	1-10	7	36.8	7	36.8	4	21.1	1	5.3	19
	11-25	0	0	13	65.0	2	10.0	5	25.0	20
	26-50	1	11.1	2	22.2	2	22.2	4	44.4	9
	More than 50	0	0	1	20.0	0	0	4	80.0	5
Post-49	1-10	46	26.3	87	49.7	26	14.9	16	9.1	175
	11-25	13	11.5	64	56.6	18	15.9	18	15.9	113
	26-50	2	7.1	20	71.4	5	17.9	1	3.6	28
	More than 50	0	0	4	80.0	0	0	1	20.0	5
All ages	1-10	67	29.3	105	45.9	32	14.0	25	10.9	229
	11-25	14	9.5	82	55.8	24	16.3	27	18.4	147
	26-50	3	7.5	22	55.0	9	22.5	6	15.0	40
	More than 50	0	0	6	54.5	0	0	5	45.5	11

surfaces covered with veneer are as follows (see tables 20.2, 20.10):

Construction period	*Percentage of dwellings covered with veneer*
Pre-1940	6.8
1940–49	17.2
Post-1949	44.1

Small amounts of veneer (1–10 percent of wall area) predominated. Of the dwellings with small amounts of veneer, 75.1 percent had slight or no damage to the veneer—in other words, it performed reasonably well in most structures. As the percentages of veneer increased on the exterior walls, so did the degree of damage; this correlation was probably influenced by the increase in veneer height. The veneer on houses with low veneer percentages, such as 1 to 10 percent, is rarely more than wainscot in height, and failure is not a significant life hazard. Veneer is readily repairable without the use of scaffolding. Economic losses and life hazards increase significantly when the veneer exceeds 50 percent of the wall area; very few such dwellings were found in Coalinga.

MASONRY CHIMNEYS

Masonry chimneys, generally of brick but some of hollow concrete block, were located along the exterior of houses as a part of a fireplace. A very few chimneys were located in the interior of a dwelling as a part of its central heating. A survey of the damage to interior brick chimneys was not undertaken because, to be fully effective, inspections would have had to include brickwork examinations in attics and under building floors. Almost invariably, the damage to the exterior fireplace dominated in cost and in degree of damage. With these caveats, all masonry-chimney damage was cataloged, including that for multiple chimneys on some dwellings. The damage-factor results for one-story wood-frame dwellings are listed in table 20.11; examples of damage are shown in figures 20.8 and 20.9.

It is useful to determine the effectiveness of reinforcing steel in chimneys. The field inspectors noted the presence or absence of reinforcing steel where they could. This determination could not be made if the chimneys were undamaged or only slightly damaged, or if the damaged chimney had been removed before the field inspector's arrival. When for whatever reason the

FIGURE 20.8.—Failure of an unreinforced-hollow-concrete-block chimney on a modern dwelling. Note that failure occurred at roof flashing.

TABLE 20.11.—*Damage factors for chimneys in one-story wood-frame dwellings*

Degree of damage-----		None		Slight		Moderate		Severe		Total		
Age group	Reinforced steel present	No. of chimneys	Pct of total	No. of chimneys	Pct of total	No. of chimneys	Pct of total	No. of chimneys	Pct of total	No. of chimneys	Pct of total	Total number of chimneys
Pre-40	Unknown	2	10.0	2	10.0	6	30.0	6	30.0	4	20.0	20
	Yes	0	0	0	0	3	33.3	4	44.4	2	22.2	9
	No	1	2.5	2	5.0	10	25.0	6	15.0	21	52.5	40
1940-49	Unknown	2	16.7	5	41.7	4	33.3	1	8.3	0	0	12
	Yes	0	0	0	0	2	15.4	5	38.5	6	46.2	13
	No	3	4.7	11	17.2	15	23.4	9	14.1	26	40.6	64
Post-49	Unknown	16	15.8	34	33.7	28	27.7	11	10.9	12	11.9	101
	Yes	0	0	4	6.7	35	58.3	17	28.3	4	6.7	60
	No	9	4.1	21	9.5	116	52.5	43	19.5	32	14.5	221
All ages	Unknown	20	15.0	41	30.8	38	28.6	18	13.5	16	12.0	133
	Yes	0	0	4	4.9	40	48.8	26	31.7	12	14.6	82
	No	13	4.0	34	10.5	141	43.4	58	17.8	79	24.3	325

FIGURE 20.9.—Failure of an unreinforced-brick chimney. Some reinforced-brick chimneys also failed.

inspector could not personally determine the presence of steel, he or she accepted the owner's statements if they appeared to be credible.

A much larger than expected number of reinforced-brick chimneys sustained moderate damage to total failure, and their performance with respect to nonreinforced chimneys is not so reassuring as it might be (see post-1949 age group, table 20.11).

DWELLING DISPLACEMENT FROM FOUNDATION

Significant building damage may occur whenever a dwelling shifts on its foundation. Movements of 6 in. and more can result in major damage to water lines, sewer lines, natural-gas lines, brick chimneys (if their bases go to the ground), and the dwelling's frame. The amount of permanent movement necessary to cause significant damage varies with the individual structure.

Earthquake bracing for wood-frame dwellings includes anchorage of the structure to its foundations, with the foundations normally of concrete. The 1955 Uniform Building Code was apparently adopted by the town of Coalinga on May 20, 1957 (ordinance 311). According to the International Conference of Building Officials: "Requirements for bolting houses to foundations first appeared in the 1935 edition of the Uniform Building Code. The provision adopted at that time is identical to the requirement today, that is, ½-inch anchor bolts 6 feet on center with 7-inch embedment." The permanent displacements listed in table 20.12 are maximums. For example, the rear of a dwelling could have slid 6 in. laterally with respect to its front, resulting in a 6-in. reported displacement, even though the front had minimal displacement. Whenever the dwelling movement was reported on both axes, then the vector resultant is listed in table 20.12. Thus, a reported displacement due to sliding of, say, 6 in.

TABLE 20.12.—*Dwelling displacement with respect to foundation in one-story wood-frame dwellings*

[See also table 20.13.]

Age group	Permanent displacement (in.)	Wood floor		Concrete floor	
		No. of dwellings	Pct of total	No. of dwellings	Pct of total
Pre-1940	None	289	37.7	20	76.9
	Cracking	288	37.5	5	19.2
	Less than 6 in	78	10.2	1	3.8
	6 to 12 in	10	1.3	0	0
	About 12 in	60	7.8	0	0
	Greater than 12 in	42	5.5	0	0
	Total	767	100	26	100
1940-49	None	244	85.3	43	89.6
	Cracking	27	9.4	4	8.3
	Less than 6 in	13	4.5	1	2.1
	6 to 12 in	0	0	0	0
	About 12 in	1	.3	0	0
	Greater than 12 in	1	.3	0	0
	Total	286	100	48	100
Post-1949	None	311	87.9	383	98.7
	Cracking	37	10.5	5	1.3
	Less than 6 in	5	1.4	0	0
	6 to 12 in	1	.3	0	0
	About 12 in	0	0	0	0
	Greater than 12 in	0	0	0	0
	Total	354	100	388	100
All ages	None	844	60.0	446	96.5
	Cracking	352	25.0	14	3.0
	Less than 6 in	96	6.8	2	.4
	6 to 12 in	11	.8	0	0
	About 12 in	61	4.3	0	0
	Greater than 12 in	43	3.1	0	0
	Total	1,407	100	462	100

would not necessarily move all of a house off its foundation.

Dwelling displacement resulted from either of two general conditions. If the house was not anchored to its continuous concrete foundation, then it could have slid off (figs. 20.10, 20.11). Alternatively, the house could have rested on cripple studs and fallen laterally the length of the studs (fig. 20.12).

A concrete first floor resting on grade cannot fall off its foundations, and so performance of these kinds of houses should be better than of those with supported wood floors. This observation was true for Coalinga, but not in the 1971 San Fernando earthquake.

For each of the three age groups in table 20.12, dwellings with concrete slabs performed much better than those with supported wood floors. Also, newer construction evidently fared better than older. Pre-1940 single-family wood-frame dwellings with supported wood floors performed very poorly by any comparison.

Table 20.13 restates the information listed in table 20.12 in a condensed manner and more clearly points out the relative performance by age and by floor type. These two tables are intended to point out expected performances in other cities where similar construction exists; these findings are not a recommendation for concrete-floor slabs on grade over supported wood floors. Improved design and construction practices can make them equal (see Steinbrugge and others, 1971; Steinbrugge and Schader, 1973).

The direction of principal damaging Earth motion has been of major interest for many years in many countries. With the advent of strong-motion seismic equipment, it has become apparent that no simple use of this kind of field information has practical application in design practices. In this study, direction of displacement was incidentally recorded by the field inspectors as a part of their damage survey but did not enter into the loss analyses. Direction of displacement was noted for 345 dwellings, commonly as two components parallel to the principal

FIGURE 20.10.—Unanchored wood-frame house that slid off its concrete foundation. See figure 20.11 for closeup of smooth top of concrete foundation.

axes of each dwelling; the results are summarized in table 20.14. From this table, 71.9 percent of the dwellings moved in an easterly direction, apparently somewhat more southeasterly than easterly. If the dwelling count is restricted to those structures with displacements exceeding 6 in., then 81 percent moved in an easterly direction.

From figure 20.1, the streets around central Coalinga run east-west and north-south, whereas those in the central business district are at 45° to this system. No significant differences were noted in the direction of displacements in the central business district from those in the surrounding town. This observation may indicate that dwelling orientation has little significance in this respect. Details on the direction of Coalinga dwelling displacements were reported by Mustart and others (1983).

TABLE 20.13.—*Dwelling displacement with respect to foundation in one-story wood-frame dwellings*

[Movement was by a measurable amount, including "less than 6 in." through "greater than 12 in." (table 12)]

Age group	Pre-1940	1940-49	Post-1949
Wood floor:			
Number of dwellings	767	286	354
Number moved	190	15	6
Percent moved	24.8	5.2	1.7
Concrete floor:			
Number of dwellings	26	48	388
Number moved	1	1	0
Percent moved	3.8	2.1	0

DATA FROM OTHER SOURCES

Numerous surveys were conducted shortly after the earthquake by the town of Coalinga and by other governmental agencies, as well as by private relief organizations and research groups. Very few of these surveys, however, provided data of use in this study.

FIGURE 20.11.—Top of concrete foundation shown in figure 20.10. Markings in top of concrete were apparently made when the concrete was freshly poured.

FIGURE 20.12.—First floor of dwelling in figure 20.10 (now at ground level) was originally at same level as porch floor. Gap between porch and house indicates height of failed house supports, normally studs.

TABLE 20.14.—*Direction of wood-frame-dwelling displacement*

Direction of displacement	Percentage of dwellings: Identifiable displacement	Percentage of dwellings: Greater than 6 in. displacement
North---------	10.1	5.4
Northeast-----	4.9	5.0
East----------	54.8	62.4
Southeast-----	12.2	13.6
South---------	8.1	7.7
Southwest-----	2.0	1.8
West----------	7.2	3.2
Northwest-----	.6	.9

A list of town demolition permits was compared with our damage surveys. Correlation was poor in many places; some discrepancies could be attributed to clerical errors under high-stress conditions, but others could not. Nonetheless, whenever a field inspector noted a town demolition permit on the dwelling or other information to the effect that the house was condemned or to be torn down for whatever reason, then this information was recorded and used in the damage analysis.

Lists of "house damage ratings" determined by county health inspectors working with the town of Coalinga were also examined. The emphasis of this survey was on suitability for habitational use. A house rated at 3 was deemed to be uninhabitable and would probably have to be demolished, in their opinion, but some such ratings were later changed to habitable. A nonfunctioning house (such as one with destroyed plumbing) may be considered uninhabitable, but it may not necessarily be unsafe or irreparable. Therefore, these data were used for background information.

MONETARY LOSSES: DEFINITIONS AND INTERPRETATIONS

Certain terms used in the computational methodology have different meanings among various persons; our definitions and interpretations are as follows.

VALUE

Definitions of "value" are found in many sources, and some publications treat solely this subject. For example, see "Actual Cash Value Guidelines—Buildings" by the National Committee on Property Insurance (1982) for some of the difficulties when using actual cash value. The value of a building may be defined as its replacement cost in kind or equivalent, actual cash value, market value, or one of several other kinds of values. If the definition is clearly understood, coefficients (or transfer functions) can be developed that will convert values determined by one definition to those of another. This coefficient is of little importance when relatively new dwellings are involved, but not so for older buildings. For example, an older wood-frame "Victorian" dwelling might have a very low resale value in a blighted area, but an identical one would have a much better resale value in a well-maintained neighborhood. The value based on cost to replace each Victorian in kind might be equal, but replacement cost might differ from the resale value of either.

In this chapter, we used dwelling resale values just before the earthquake, less land values. To calculate these values, two local realtors working independently determined average preearthquake market values on a block-by-block basis, or groups of blocks in some instances.

PERSONAL VERSUS IMPERSONAL LOSSES

The viewpoint expressed in this chapter is that of "impersonal losses," which are not influenced by the costs of combining solutions of social problems with property damage. It also presumes that postearthquake material and labor costs will remain reasonably stable; Coalinga did not pose either of these problems. However, for vulnerability studies of a great earthquake, such as a repeat of the 1906 San Francisco shock, repair-cost estimates should anticipate the possibility of unstable labor and material costs.

A brief discussion of impersonal losses may be of interest to those who have not undertaken postdisaster loss surveys. Assume, for example, that damage is confined to minor cracking of the interior finishes, and patching and repainting are the only repair requirements. The owner may consider the damage as not unduly unsightly, and repair by the owner might await the next normal repainting of the interior. "Negligible loss" is correct on the basis of the owner's out-of-pocket expenses; these kinds of losses are defined as "personal." Should, however, the cost of dwelling repair be part of a governmental grants program that has no minimum loss limit, or be covered by an insurance contract, then experience indicates that these damages would be paid. Payment might—or, more likely, might not—be based on the depreciated value of the interior finishes. This viewpoint on loss is defined as "impersonal loss."

Although Government, insurance, and private relief organizations (such as the American Red Cross) are all involved in the payment of impersonal losses, their viewpoints may differ. Local, State, and Federal Governments may be influenced by social goals in their damage surveys and building condemnations; for example, preearthquake planned redevelopment of the damaged areas, as well as of vice and high-crime districts. Grants and loan programs also can be influenced by postearthquake social goals. It has been observed that

TABLE 20.15.—*Comparisons of monetary-loss estimates*

Age group	Financial source 1 Comparison of 331 dwellings			Financial source 2 Comparison of 28 dwellings			Financial sources 1 and 2 Comparison of 359 dwellings		
	Authors estimate (column A)	Financial source 1 (column B)	Ratio of column A to B	Authors estimate (column C)	Financial source 2 (column D)	Ratio of column C to D	Authors estimate (column E)	Financial sources (column F)	Ratio of column E to F
Pre-1940	$1,268,000	$1,431,000	0.89	$146,700	$381,100	0.38	$1,414,700	$1,812,100	0.78
1940-49	379,800	317,300	1.20	22,300	31,600	.71	402,100	348,900	1.15
Post-1949	876,000	553,200	1.58	65,800	77,400	.85	941,800	630,600	1.49
All ages	2,559,000	2,375,000	1.08	244,000	490,400	.50	2,803,000	2,865,400	.98

the degree of earthquake damage leading to condemnation may vary as a function of the number of persons killed. These aspects were not present in the Coalinga earthquake, to the best of our knowledge. However, extrapolation of the Coalinga data to other vulnerability studies should consider these possibilities.

LOSS (DAMAGE) RATIO

"Loss ratio," or "damage ratio," is defined as the ratio of the full cost of repair to the value of the dwelling. As previously discussed, values were determined by realtors, using preearthquake market values, less land.

The cost of repair (in percent) as a function of the degree of damage to construction components was developed during a study by the U.S. Coast and Geodetic Survey (1969). This study was intended for loss-simulation purposes and did not use actual loss figures developed after an earthquake because this information was unavailable in the desired form. The 1971 San Fernando earthquake provided this opportunity and resulted in loss ratios developed from experience data (Steinbrugge and others, 1971; Steinbrugge and Schader, 1973).

Loss ratios should be sufficiently generalized to include construction components that are not specifically inspected. These noninspected components included electrical, plumbing, water, gas, and air conditioning in Coalinga. The loss ratios differ slightly for low-, medium-, and high-value dwellings, and these differences were applied in San Fernando. However, placing loss ratios into three value categories was judged inappropriate for Coalinga, and so the values were averaged.

The 1971 loss ratios were examined and slightly modified after the May 2 earthquake. A total of 16 contractors provided varying degrees of information on the costs of repair by construction component. All postearthquake building permits were also examined, and pertinent information was extracted therefrom. Although these data were quite diverse and not all useful, they did provide guidelines for minor changes to the 1971 loss ratios to suit Coalinga conditions.

MONETARY LOSSES: RESULTS OF CALCULATIONS

Computation of monetary losses is a simple process: Loss ratios for each construction component of each dwelling were added together, and this sum was multiplied by the market value (less land) for each dwellings. The aggregate losses were obtained by summation. The computed loss for all wood-frame houses in Coalinga is $15,290,000.

Opportunity arose to partly confirm this estimate by using completely independent information obtained from two similar financial organizations. Detailed loss information on 331 wood-frame dwellings (or 17.2 percent of the total) was obtained from one organization designated as source 1. An identical kind of data was received from a second similar type organization (source 2) on 28 additional dwellings. All these data are listed in table 20.15. The data from source 2 were received so late during this study that they are included only here and not elsewhere.

It is desirable to examine each data source for biases among them and the resulting scatter of combined data. Comparisons and results among the data sources are listed in table 20.15. We note that loss estimates from source 1 are less than those determined by us except for the pre-1940 age group. For source 2, however, the reverse is true except for the pre-1940 group. Upon eliminating from the data base the five dwellings for which the highest unpaid reserves existed (and which had much lower "authors estimates"), the "Ratio of column C to D" in table 20.15 changed from 0.50 to 0.81. Standing alone, the data from source 1 clearly are too small to have numerical credibility.

When the data from sources 1 and 2 are combined (last three columns, table 20.15), correlations are reasonably good and indicate that credible results can be obtained for vulnerability studies. When the sample of 359 dwellings is divided into three age groups, the credibility of the comparisons decreases.

Another source of Coalinga dwelling-loss information was the survey conducted by the American Red Cross

immediately after the earthquake; their damage estimate was $9,823,000, or 64.2 percent of ours. This estimate apparently included the very few unit-masonry dwellings that were not included in our estimate.

In general, whenever estimated losses begin to exceed 50 or 75 percent of a dwelling's value, then total losses are commonly agreed upon between the owner and the payee for any of several political, legal, economic, and (or) humanitarian reasons. For example, governmental condemnation may combine safety requirements with functional requirements, such as damaged and (or) inadequate plumbing. Legal/economic aspects of a potential contested insurance adjustment may also have an influence.

Some of the dwelling-loss relations that we determined are summarized in figure 20.13.

LOSSES BY AGE GROUP AND FLOOR TYPE

The highest losses for wood-frame dwellings were in the pre-1940 group with wood-supported floors, whereas the lowest losses were in modern construction with concrete floors on grade (table 20.16; see tables 20.6, 20.11). The improvement in performance with age was to be expected.

The difference in performance between concrete floors on grade and wood-supported floors within the same age group contrasts sharply with 1971 San Fernando experience, where these performances were essentially the same. This difference can be attributed to variations in construction practices, as well as to local viewpoints on the Uniform Building Code. Unanchored dwellings brought in from the nearby oil fields between 1930 and 1955 could also have contributed to this difference.

The information plotted in figure 20.13 and listed in table 20.16 has been recast in table 20.17. We note that if these data were plotted as frequency curves or histograms, they would peak rather sharply between 6- and 20-percent loss. The lines with asterisked values in column 1 of table 20.17 contain anomalous data for 0 and 100 percent and should be viewed separately from the

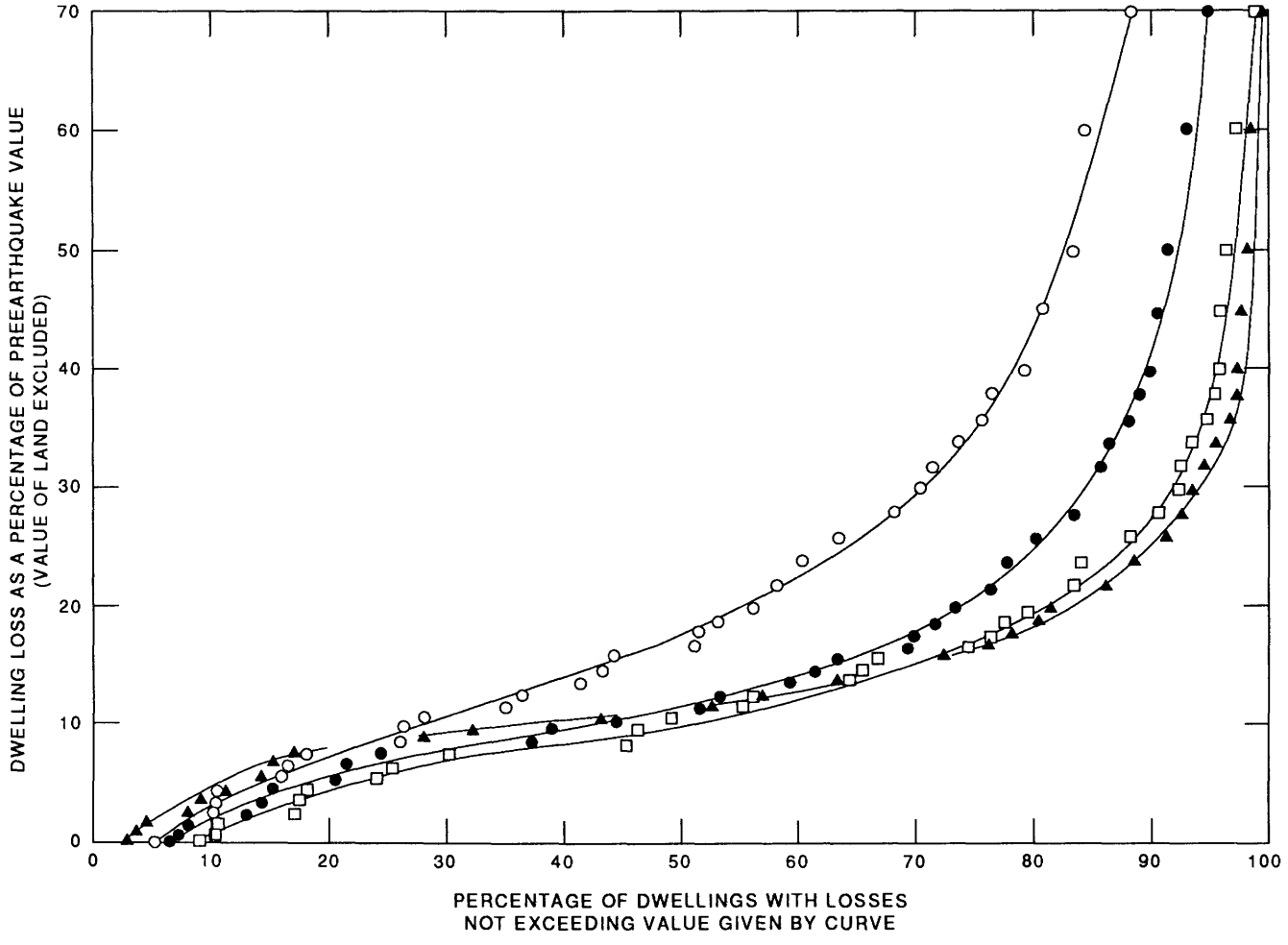

FIGURE 20.13.—Wood-frame-dwelling loss relations. Data for dwellings with wood floors: circles, pre-1940 age group; squares, 1940–49 age group; triangles, post-1949 age group. Dots, data for dwellings in all age groups, with both wood and concrete floors.

TABLE 20.16.—*Wood-frame-dwelling losses in Coalinga, as functions of age group and floor type*

Age group	Number of dwellings	Average loss (percent)
Pre-1940:		
Wood-supported floor------	780	28.7
Concrete floor on grade---	29	17.9
Both of the above---------	799	28.4
1940-49:		
Wood-supported floor------	287	14.2
Concrete floor on grade---	34	11.5
Both of the above---------	321	13.9
Post-1949:		
Wood-supported floor------	352	14.3
Concrete floor on grade---	395	9.5
Both of the above---------	747	11.8
All age groups:		
Wood-supported floor------	1,442	21.2
Concrete floor on grade---	453	9.9
Both of the above---------	1,895	18.1

other data lines. The line for 100 percent monetary loss has high values, for reasons previously discussed regarding condemnation, owner-authorized demolition, or loss payments by financial organizations. The line for 0 percent monetary loss was influenced by owners who had negligible loss and stated "none" to the field inspectors, and by the inspectors making value judgments from partial interior examinations. The slight rise in losses in the 56- to 60-percent-loss group is attributable to loss ratios that change by steps as losses increase; this effect is greater at larger losses. The average values listed in table 20.16 differ from the peak values, which may be estimated from table 20.17.

DAMAGE FACTORS

We may appropriately ask whether dwelling-damage factors are consistent among earthquakes and among field workers, using the same damage definitions. Table 20.18 summarizes a comparison of damage factors determined after the 1971 San Fernando and 1983 Coalinga earthquakes, using the same damage definitions (see section below entitled "Supplementary Information") but different field personnel and field supervisors. We note that the damage factors for Coalinga follow a reasonably consistent pattern with those of San Fernando for similar percentage of losses, although the values are not identical.

Some damage-factor comparisons for specific construction components or combinations thereof show significant variations (for example, wood versus concrete floors). A fuller discussion of these regional variations is beyond the scope of this study.

EFFECT OF DEDUCTIBLES

Dollar or percentage deductibles, or their equivalents, are of interest to insurance carriers, as well as when determining governmental postdisaster loan/grant policies. For example, the aggregate financial effect of thousands of low-interest loans with a "forgiveness" feature for the first few thousand dollars of each loan involves the concepts of deductibles.

The average percentage of loss over the deductible is plotted as a function of the percentage deductible in figure 20.14 for a range from 0 to 50 percent for the town of Coalinga. The same information is plotted as a function of a dollar deductible in figure 20.15 in the range of $0 to $12,000. The exact fit of the curve with the points computed from the damage survey data is to be expected because the only variable (deductible) is mathematically related to the values of the ordinate and abscissa. Percentage deductible relations (fig. 20.14) are more readily transferable to other communities than are dollar-deductible relations (fig. 20.15); losses over deductibles for identical houses located elsewhere, but valued higher, would change the ordinates of the curve.

As previously noted, buildings with concrete floors performed better than those with wood floors. The degree of difference is indicated by the spread between their respective curves in figures 20.14 and 20.15. The wood/concrete curve includes all dwellings with either wood or concrete floors. To the extent that Coalinga construction is typical of other Central Valley towns, the wood/concrete curve may be the most useful of those shown.

Other magnitude earthquakes, other focal depths, other construction characteristics, and other distances to the zone of seismic-energy release are expected to develop similar curves, or families of curves (Steinbrugge and others, 1984).

Deductibles from 0 to 5 percent (and their dollar counterparts) are of special interest. Upon examining isoseismal maps of great earthquakes, we noted that large areas were shaken sufficiently to cause many losses in this deductible range. Considering the possible number of dwellings in these areas, it follows that dollar loss can be greatly modified by the deductible. The curve between 9 and 5 percent in figure 20.14 is sufficiently linear to be used in that manner, and the assumption of linearity to 10 percent (fig. 20.16) can be safely assumed for many purposes.

Damage to unanchored dwellings from the oil fields undoubtedly increased the losses, and to that extent the values shown in figures 20.14 through 20.16 are on the high side. The locations of these moved dwellings (and even whether they still existed at the time of the earthquake) are as yet unknown. However, removal from

TABLE 20.17.—*Frequency of loss in wood-frame dwellings, as functions of age group and floor type*

[--, sample size too small to be significant]

Monetary loss (pct)	Percentage of dwellings with wood-supported floors				Percentage of dwellings with concrete floors on ground surface				Percentage of dwellings with wood or concrete floors			
	Pre-1940	1940-49	Post-1949	All ages	Pre-1940	1940-49	Post-1949	All ages	Pre-1940	1940-49	Post-1949	All ages
0	5.5	9.1	2.0	5.3	--	--	9.9	9.5	5.6	8.7	6.2	6.3
1-5	5.5	9.1	9.1	7.1	--	--	16.7	16.3	5.5	10.0	13.1	9.3
6-10	15.4	28.2	21.3	19.5	--	--	37.5	36.9	15.9	28.7	29.9	23.6
11-15	17.1	19.2	36.1	22.0	--	--	24.8	24.5	17.0	19.9	30.1	22.6
16-20	12.7	14.3	12.8	13.1	--	--	7.1	7.5	12.5	13.7	9.8	11.8
21-25	7.3	8.4	9.1	8.0	--	--	2.0	2.4	7.5	7.5	5.4	6.6
26-30	6.7	4.2	3.1	5.5	--	--	1.3	1.5	6.5	4.4	2.1	4.5
31-35	5.4	2.1	2.8	4.0	--	--	.3	.2	5.3	1.9	1.5	3.1
36-40	3.7	1.0	1.1	2.6	--	--	0	.2	3.8	.9	.5	2.1
41-45	1.2	.3	.3	.8	--	--	0	0	1.1	.3	.1	.6
46-50	2.7	.7	.6	1.7	--	--	.3	.2	2.6	.6	.4	1.4
51-55	.5	.7	0	.4	--	--	0	0	.5	.6	0	.3
56-60	.8	.3	.3	.6	--	--	0	.2	.8	.6	.1	.5
61-65	.3	.3	0	.3	--	--	0	0	.3	.3	0	.2
66-70	3.6	1.0	1.1	2.4	--	--	0	0	3.5	.9	.5	1.8
71-75	.3	0	.3	.2	--	--	0	0	.3	0	.1	.2
76-80	0	0	0	0	--	--	0	0	0	0	0	0
81-85	0	0	0	0	--	--	0	0	0	0	0	0
86-90	0	0	0	0	--	--	0	0	0	0	0	0
91-95	0	0	0	0	--	--	0	0	0	0	0	0
96-99	0	0	0	0	--	--	0	0	0	0	0	0
100	11.5	1.0	0	6.5	--	--	.3	.4	11.4	.9	.1	5.1

TABLE 20.18.—*Examples of comparative damage factors for stucco/plaster exterior finishes from the 1971 San Fernando and 1983 Coalinga earthquakes*

[Data for age groups 1940-49 plus post-1949. To maintain compatibility, data for dwellings that moved on their foundations have been excluded. For San Fernando data, see Steinbrugge and Schader (1973, p. 697, fig.4)]

Earthquake	Dwellings with percent loss in the range of	Nearest MMI	Percentage of dwellings with loss			
			None	Slight	Moderate	Severe
San Fernando, 1971.	2-5	VII[1]	26.3	72.6	1.0	0.1
	6-10	VIII[1]	6.7	87.3	5.1	0.9
	>11	IX[1]	2.9	81.4	10.3	5.4
Coalinga, 1983.	12.3	VIII[2]	5.8	78.5	15.2	0.5

[1]K.V. Steinbrugge (unpub. data, 1983).
[2]U.S. Geological Survey Bulletin 1698, "United States Earthquakes, 1983."

the data base of all dwellings that showed displacement from their foundations or were demolished significantly lowered the percentage loss over the deductible (table 20.19). Indeed, table 20.19 also shows that the age grouping under this theoretical condition loses much of its significance, as does floor type. Clearly, adequate foundation anchorage was a critical damage-control feature.

GENERAL FINDINGS AND CONCLUSIONS

The aggregate monetary loss as a result of direct damage to all wood-frame one- to four-family dwellings in Coalinga was $15,290,000. Wood-frame habitational units constituted about 95 percent of this total, and the rest were of brick, adobe, or hollow clay tile. The following discussion applies to one-story wood-frame dwellings unless otherwise stated.

The average loss per dwelling was 18 percent of its preearthquake market value, less land value (fig. 20.16). This percentage is considerably higher than that which had been used for estimation purposes for modern coastal California cities; it is also higher than that found in the most heavily shaken areas of San Fernando after the 1971 earthquake. A 5-percent deductible would have resulted in a 13.6-percent loss over deductible, whereas a 10-percent deductible would have resulted in a 9.8-percent loss over deductible.

Construction period was a major monetary-loss discriminant for wood-frame dwellings in Coalinga:

Construction period	*Average loss (percent)*
Pre-1940	28.4
1940–49	13.9
Post-1949	11.8

The type of first-floor construction was also a major monetary-loss discriminant for wood-frame dwellings:

Type of first-floor construction	*Average loss (percent)*
Wood supported	21.2
Concrete on grade	9.9

The high percentage of loss for a central California city relative to those commonly used for coastal cities may have been influenced by the attitude and attention given to building codes in agricultural communities, where earthquakes are not believed to be a great threat. Coalinga, however, is reasonably representative of many other communities, including in construction characteristics, except for the houses moved to Coalinga from the nearby oil fields.

Additional study should probably be given to interpretation of the high average loss, including geophysical factors. In passing, we note the reported effects of the 1906 San Francisco earthquake in Coalinga: "The tops of a few of the walls of brick buildings were slightly damaged * * *. A few dishes and bottles were thrown from the shelves * * *." (Lawson, 1908, v. 1, pt. 2, p. 318). The earthquake provided an opportunity to test, verify, and further develop monetary-loss-estimation methods useful for earthquake-vulnerability studies conducted by governmental disaster-response planners, as well as for earthquake-insurance purposes. To fulfill this opportunity, quickly trained local personnel used previously estab-

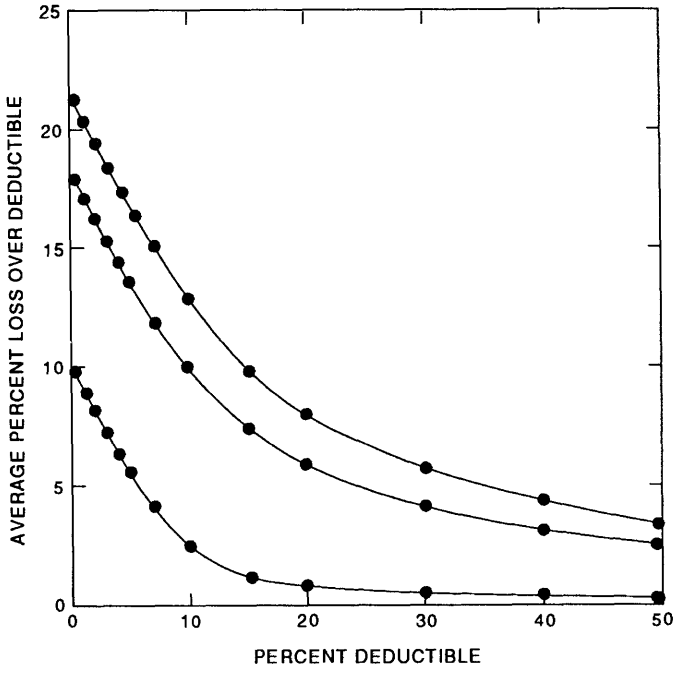

FIGURE 20.14.—Average percent loss over deductible versus percent deductible for wood-frame dwellings in all age groups. Dots, computed values.

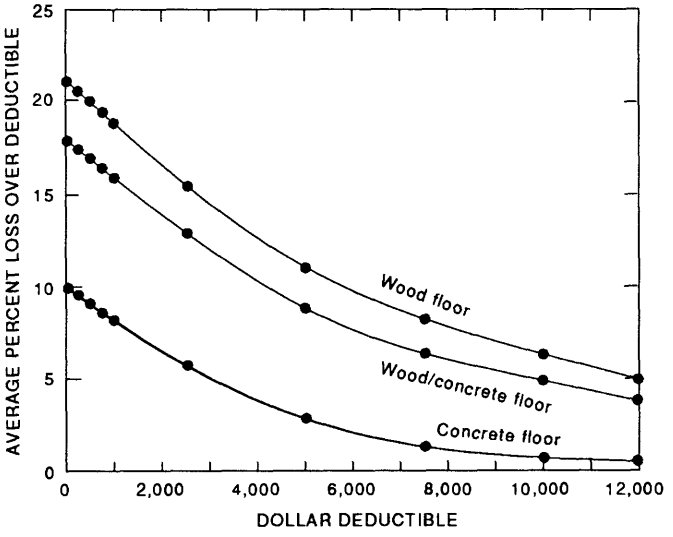

FIGURE 20.15.—Average percent loss over deductible versus dollar deductible for wood-frame dwellings in all age groups. Dots, computed values.

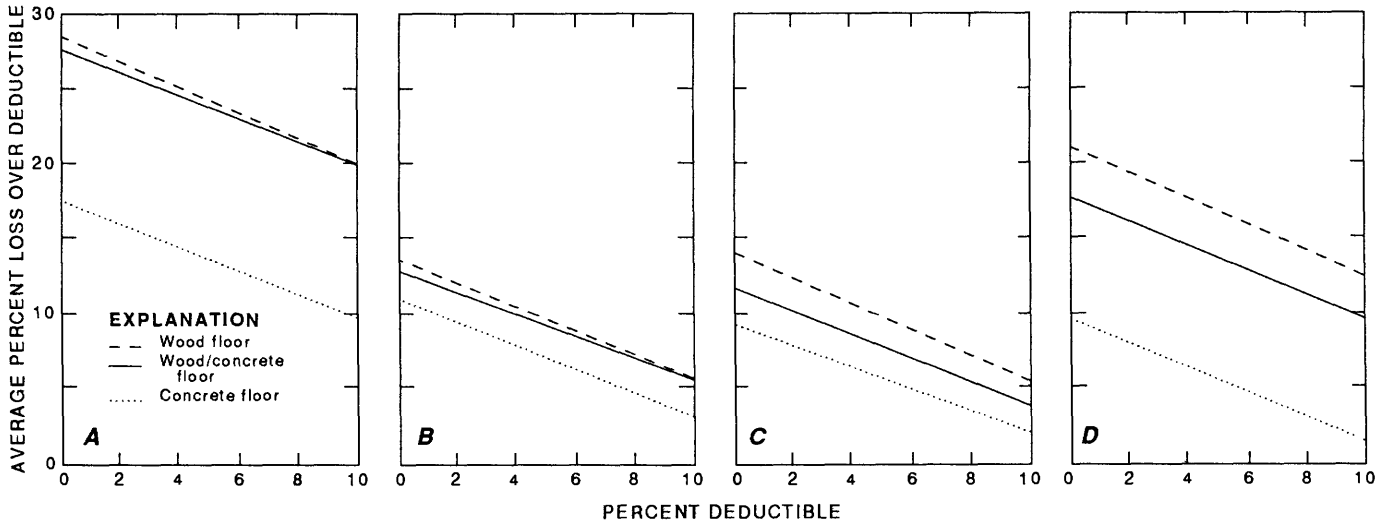

FIGURE 20.16.—Average percent loss over deductible (in 0–5-percent deductible range) versus percent deductible for pre-1940 age group (*A*), 1940–49 age group (*B*), post-1949 age group (*C*), and all age groups (*D*).

TABLE 20.19.—*Wood-frame-dwelling losses in Coalinga for houses with no observable foundation displacement, as functions of age group and floor type*

[Average percent loss for dwellings with no foundation displacement includes those demolished and (or) posted for demolition. --, sample to small to be significant]

	Average percent loss over deductible			
	All dwellings		Dwellings with No foundation displacement	
Percent deductible---------	0	5	0	5
Age group				
Pre-1940:				
Wood-supported floor-----28.7	24.1		11.0	6.8
Concrete floor on grade--17.9	13.5		--	--
Both of the above--------28.4	23.8		--	--
1940-49:				
Wood-supported floor-----14.2	9.8		12.4	8.0
Concrete floor on grade--11.5	7.0		10.7	6.3
Both of the above--------13.9	9.5		12.2	7.8
Post-1949:				
Wood-supported floor-----14.3	9.6		12.4	7.7
Concrete floor on grade-- 9.5	5.2		9.4	5.1
Both of the above--------11.8	7.3		10.7	6.3
All age groups:				
Wood-supported floor-----21.2	16.6		12.0	7.5
Concrete floor on grade-- 9.9	5.6		9.6	5.3
Both of the above--------18.1	13.6		11.1	6.7

lished field-inspection forms and previously defined degrees of damage. Wherever compared, a good correlation existed between damage factors determined after the 1983 Coalinga and 1971 San Fernando earthquakes. This correlation indicated that degrees of damage to construction components could be similarly gathered and similarly interpreted into dollar losses by using different personnel and different magnitude earthquakes, provided that the inventory of structures was similar in materials and earthquake resistance. As data are further gathered, it will become practical to eliminate the intermediate step in which degree of damage is related to intensity scales.

REFERENCES CITED

Lawson, A.C., chairman, 1908, The California earthquake of April 18, 1906: Report of the State Earthquake Investigation Commission: Carnegie Institution of Washington Publication 87, 2 v.

Mustart, D.A., Sullivan, Raymond, and Pestrong, Raymond, 1983, Directional pattern of building displacement in the Coalinga earthquake, May 2, 1983, *in* Bennett, J.H., and Sherburne, R.W., eds. The 1983 Coalinga, California earthquakes: California Division of Mines and Geology Special Publication 66, p. 9–17.

National Committee on Property Insurance, 1982, Actual cash value guidelines—buildings: Boston, 34 p.

Rinehart, W.A., Algermissen, S.T., and Gibbons, Mary, 1976, Estimation of earthquake losses to single family dwellings: Denver, Colo., U.S. Geological Survey report to U.S. Department of Housing and Urban Development, 57 p. [available as U.S. National Technical Information Service Report PB–251 677].

Steinbrugge, K.V., Algermissen, S.T., and Lagorio, H.J., 1984, Determining monetary losses and casualties for use in earthquake mitigation and disaster response planning: World Conference on Earthquake Engineering, 8th, San Francisco, 1984, Proceedings, v. 7, p. 615–622.

Steinbrugge, K.V., and Schader, E.E., 1973, Earthquake damage and related statistics, *in* Benter, N.A., and Coffman, J.L., eds., San Fernando, California, earthquake of February 9, 1971: Washington, U.S. Department of Commerce, National Oceanic and Atmospheric Administration, v. 1, pt. B, p. 691–724.

Steinbrugge, K.V., Schader, E.E., Bigglestone, H.C., and Weers, C.A., 1971, San Fernando earthquake, February 9, 1971: San Francisco, Pacific Fire Rating Bureau, 93 p.

Steinbrugge, K.V., McClure, F.E., and Shaw, A.J., Studies in seismicity and earthquake damage statistics, 1969, app. A *of* U.S. Coast and Geodetic Survey, Studies in seismicity and earthquake damage statistics, 1969: Summary and recommendations: U.S. Department of Commerce, National Technical Information Service Report COM–71–00053, 142 p.

U.S. Coast and Geodetic Survey, 1969, Studies in seismicity and earthquake damage statistics, 1969: Summary and recommendations: U.S. Department of Commerce, National Technical Information Service Report COM–71–00052, 23 p.

SUPPLEMENTARY INFORMATION: DEFINITIONS OF DEGREES OF DAMAGE

Definitions of the degrees of damage used during the field inspections are essentially those given by Steinbrugge and others (1969) and the U.S. Coast and Geodetic Survey (1969). Use of these same definitions for the 1971 San Fernando earthquake dwelling-damage studies (Steinbrugge and others, 1971; Steinbrugge and Schader, 1973), ensures consistency with the results and conclusions of the U.S. Coast and Geodetic Survey.

INSPECTOR-TRAINING PROGRAM USING THESE DEFINITIONS

After an earthquake, there is a great need to train field inspectors quickly on the use of inspection forms and the meanings of the subjective terms describing damage. For Coalinga, training sessions included field inspections around typical city blocks to show the inspectors different types of houses and damage types. Instructions were also given on how to show authorization and talk to occupants. Each day, all the personnel met to turn in completed survey forms and to discuss the problems or difficulties that they had encountered.

Field inspectors were to examine all, or at least three, sides of a house for damage. If the occupant was at home, then the inspector was to ask (1) whether the house was owned or rented and (2) whether he or she could inspect one room (not the whole house) for cracks. If entry was not permitted, the inspector was to ask about the type of wallboard, whether there were few or many cracks, and whether they were large or small (see table 20.1).

DEGREES OF STRUCTURAL DAMAGE

"Slight structural damage" is normally associated with localized finish damage, and so this damage is included in the repair cost assigned to interior-finish damage. Slight structural damage would not require raising of the house on jacks, although one local area might require jacking. Some cracking of plaster might be classed as indicative of

slight structural damage. The term "slight structural damage" should rarely be used by a field inspector.

"Moderate structural damage" is defined as that which occurs when a dwelling has moved slightly off its foundation. A typical example would be where the short studs under the first-floor construction (called cripple studs) moved to the extent that the upper part of the dwelling was displaced relative to the foundations. Moderate structural damage commonly requires that the house be underpinned and returned to its original position. New cripple-stud walls might have to be constructed, and plumbing and other utility lines would commonly be fractured. Reconstruction of the brick chimney (if any) and extensive repair of the interior and exterior finishes should be anticipated. Old and new cracks might open up in basement and foundation walls.

"Severe structural damage" is defined as that which occurs when structural elements, such as the walls, roof, and floors, partly collapse. Some reconstruction of the dwelling from the foundations to the roof would be necessary. New cracking of the foundations and basement walls, and severe to total chimney damage, can be anticipated. (Chimney damage is treated as a separate cost item; see subsection below entitled "Masonry-Chimney Damage.")

DEGREES OF INTERIOR-FINISH DAMAGE

"Slight damage" is defined as old cracks in walls enlarging and minor new cracks forming around doors and window openings in plaster and gypsumboard. This damage could be repaired by filling in the cracks without cutting out the crackings and repairing them; the ceilings are not anticipated to require any repair. In calculating the repair cost for slight damage, all the walls must be repainted in any room that sustained this damage. For wood finishes, slight damage will be difficult to detect because of the ability of wood to accept minor displacements with normal nail slip or movement without buckling or other distress to the wooden element.

"Moderate damage" to plaster on walls is defined as cracking that is sufficient to require cutting out of the new and old cracks, and patching of these cracks before repainting. "Moderate damage" to gypsumboard walls is defined as the enlarging of old cracks and new cracking along the edges of the gypsumboard panels; this damage would require retaping before repainting or repapering. Ceilings would not be damaged to this degree but would be "slightly" damaged, as previously defined for walls, and would require repainting. For wood finishes, "moderate damage" is defined as minor working of the wood elements (such as plywood panels, or boards), causing nails to work free and, in turn, requiring resetting of the nails, with attendant refinishing work.

"Severe damage" to plaster on walls is defined as badly cracked plaster, some of which has come loose. This damage would require replacement of loose plaster and repair of the rest of the plaster, in accord with moderate damage. "Severe damage" to gypsumboard wall panels is defined as that which would require replacement of some panels and reattachment of other panels, with retaping and repainting of all panels. Ceilings would be moderately to severely damaged, as described for walls, and would require appropriate repairs. For wood finishes, "severe damage" is defined as bulging or buckling of wood members, requiring their replacement, which may become difficult when, for example, attempting to match finishes on expensive prefinished plywood.

Some general comments on interior-finish-damage classifications are in order. When not otherwise classified, it was assumed that the interior-wall-finish materials were usually plaster for dwellings built before and including 1940, and usually gypsumboard for dwellings built since 1940. Dwellings might have different wall finishes in different rooms; modern bathrooms usually have plaster or a special waterproof gypsumboard, or tile, or some combination thereof. Walls, particularly in more expensive dwellings, may be finished with wallpaper that can represent a high cost of repair, because complete replacement of the wallpaper would be necessary if the backing materials were damaged even only slightly. Repair costs used in this study compensated for the foregoing and included the damage to such items as cabinet work, electric, and plumbing as related to the finishes.

DEGREES OF EXTERIOR-FINISH DAMAGE (EXCLUDING MASONRY VENEER)

"Slight damage" to exterior (plaster) is defined as old cracks enlarging and minor new cracks forming around door and window openings, requiring minor patching and repainting. For wood finishes, metal siding, cement-asbestos shingles, and the like, slight damage will be difficult to detect because of the ability of nails to accept minor displacements without buckling or other noticeable distress to the finishes.

"Moderate damage" is defined as plaster cracking in amounts sufficient to require cutting out of the cracks and more complete patching of the plaster before repainting. For nonplaster finishes, "moderate damage" is defined as minor working of the surface elements, causing the nails or fasteners to work free and, in turn, requiring resetting of the nails or fasteners, with other attendant refinishing work.

"Severe damage" is defined as portions of the plaster coming loose or being so extensively cracked that it

would all have to be removed and replaced. For nonplaster finishes, "severe damage" is defined as bulging or buckling of these finishes, requiring in most cases their replacement.

DEGREES OF EXTERIOR-MASONRY-VENEER DAMAGE

"Slight damage" is defined as damage sufficient to require repair of new hairline cracks in the masonry joints; preearthquake hairline cracks probably would be classified as "new." We may assume that, on average, about 25 percent of the veneer area would require repair to the extent of repointing of the joints.

"Moderate damage" is defined as damage sufficient to require repointing of all masonry joints and replacement, on average, of 10 percent of the masonry units.

"Severe damage" is defined as damage sufficient to require repointing of all masonry joints and replacement, on average, of 60 to 80 percent of the masonry units.

DEGREES OF MASONRY-CHIMNEY DAMAGE

"Slight damage" is defined as damage sufficient to cause cracking of the chimney at or above the roof, requiring cutting out and patching of the cracks. Bricks at the chimney top may be displaced, and a few may fall.

"Moderate damage" is defined as damage sufficient to cause fracture or breaking off and (or) falling of the chimney above the roofline.

"Severe damage" is defined as loss of the chimney above the roofline and loss of part of the chimney below the roofline. Extensive cracking will occur in the standing portion.

"Total damage" is defined as damage so extensive that the whole chimney, from foundation to top, would have to be rebuilt. The degree of chimney damage will vary greatly, depending on the amount of earthquake bracing; such factors are generally reflected in the age of the house and its location.

Note added in proof.—Continuing studies of additional data from other California earthquakes (K.V. Steinbrugge and S.T. Algermissen, unpub. data, 1990) have improved the damage factors and effect of deductibles as reported in this chapter and made them more applicable for general use in California.

---

21. EFFECTS OF THE EARTHQUAKE ON INDUSTRIAL FACILITIES: A PRELIMINARY SUMMARY

By TOM K. CHAN, JOSHUA D. LICHTERMAN, SAM W. SWAN, and PETER I. YANEV,
EQE ENGINEERING

CONTENTS

BACKGROUND

The May 2 earthquake occurred at about 4:43 p.m. P.d.t. and had a Richter magnitude (*M*) of 6.7. It was centered near the town of Coalinga, which is midway between San Francisco and Los Angeles near U.S. Interstate Highway 5. Coalinga is located in a large oil field that includes numerous petrochemical and other industrial and power installations. About 2 hours after the earthquake, we organized an investigative team of 7 engineers; this team arrived in Coalinga just after sunrise on May 3. We wanted to arrive at the scene as soon as possible before repairs could be initiated, so that we could collect important unaltered information on the performance of equipment and other systems in the many industrial facilities.

Subsequently, we have spent about 2 engineering months in the Coalinga area and have collected extensive data. This chapter gives a brief overview of the data, intended for both technical and nontechnical readers.

The May 2 earthquake provided excellent examples of typical seismic damage to structures and equipment in industrial facilities. Available ground-motion records in the Coalinga vicinity indicate that peak ground accelerations were quite high; depending on the location, they ranged from 0.20 to more than 0.60 *g*. Most of the facilities that we evaluated were located in the areas of highest ground motion.

Power, water, natural-gas, petrochemical, and agricultural facilities were surveyed in detail. The following sections summarize the performance of these facilities.

The locations of Coalinga and the various facilities discussed below, as well as the approximate location of the epicenter, are shown in figure 21.1. The observed damage at these facilities is summarized in table 21.1.

It is important to make two remarks before proceeding with descriptions of the effects of the earthquake. 1. Because of the devastating damage to unreinforced-brick and other masonry buildings and many older homes, the press conveyed the idea that the May 2 earthquake was a disaster; the public was left with a strong impression that every building in Coalinga was destroyed. Actually, most newer buildings performed rather well. Typically, well designed and engineered, earthquake-resistant buildings and equipment systems performed very well; damage was commonly minimal. The damage and the resulting business interruptions were well correlated with the degree of seismic resistance of the facilities. 2. The May 2 earthquake was followed by numerous aftershocks that continued for several months. The aftershock of July 22, 1983, had a magnitude of 6.0; that, in itself, was a strong earthquake of moderate magnitude. As of August 1983, at least five aftershocks with magnitudes exceeding 5.0 have occurred; the effects of these events are not discussed in this chapter.

TOWN OF COALINGA

The town was severely affected by the earthquake (figs. 21.2–21.8). Old unreinforced-masonry buildings and old wood-frame houses sustained the most damage. The central area of the town consisted primarily of old unreinforced-brick and concrete-block one- and two-story buildings. Most masonry structures partly or completely collapsed or were irreparable; these structures have since been demolished. It was extremely fortunate that no one was killed; however, numerous injuries occurred.

Older one-story and a few two-story wood-frame houses sustained heavy damage; about a third of these buildings were severely damaged. Most damage was caused by (1) inadequate bracing of the crawlspace walls (the part of the house between the concrete foundation and the first floor) and (2) absence of anchorage of the wood sill plates to the concrete foundations. Most of this damage could have been avoided with minor bracing and anchoring.

The newer houses performed well. Damage was generally limited to collapse of masonry chimneys and masonry veneers; otherwise, serious damage was rare. There were few structurally complex houses, such as split-level or two-story buildings with garages on the first floor; these types of houses have performed poorly in past earthquakes.

Many well-designed commercial and school buildings were located in Coalinga, mostly one- and two-story wood, concrete, concrete-block, and steel-frame structures (there were no complex large structures). These buildings performed remarkably well, especially given the extensive damage to unreinforced buildings. A detailed discussion of these structures is beyond the scope of this chapter.

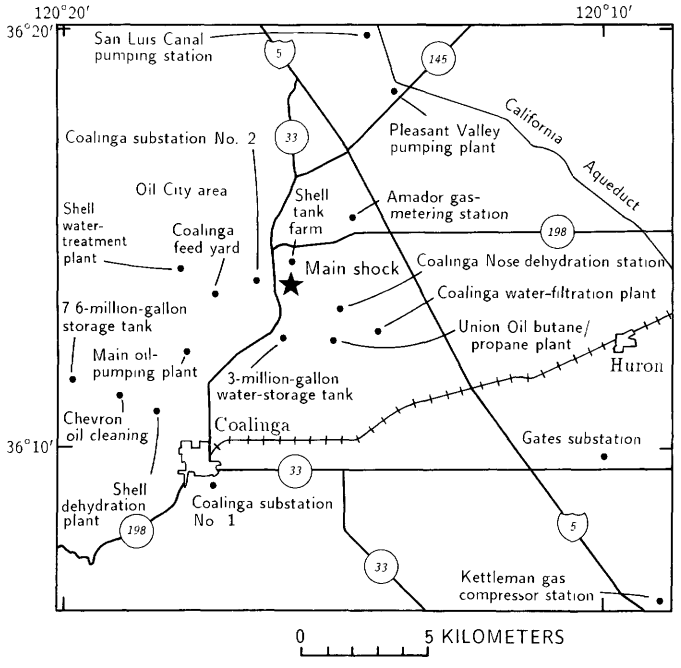

FIGURE 21.1.—Coalinga, California, area showing locations of visited facilities and epicenter of May 2 earthquake.

ELECTRIC-POWER FACILITIES

All the surveyed electric-power facilities in the affected area are owned and operated by the Pacific Gas & Electric Co. (PG&E). Those facilities surveyed include the Gates Substation, Coalinga Substation 1, and Coalinga Substation 2. Damage to the equipment at these facilities was minor. All these facilities were on line at the time of our initial surveys on May 3, 1983.

GATES SUBSTATION (SITE 2, FIG. 21.1)

The Gates Substation, the largest distribution facility in the Coalinga area, is located about 1 mi east of U.S. Interstate Highway 5, on Jayne Road. This site is about 12 mi southeast of the epicenter. The substation contains two large switchyards, a 250-kV station (constructed in the 1950's), and a larger, 500-kV station (constructed in the 1960's). The facility also has two control buildings and several other adjacent shops and storage buildings. All these buildings are one-story structures of reinforced concrete-block or precast-concrete construction; all the structures were designed to be earthquake resistant. Most equipment at this substation was well anchored; all the electrical cabinetry (including various relay and control panels) in the control buildings was anchored.

Damage to the Gates Substation was minor (fig. 21.9). At the 500-kV station, several larger oil-filled transformers in the switchyard spilled oil through the seals of their bushings. Only one ceramic bushing on a transformer broke. The transformers were welded to embedded base plates in their concrete pads; these transformers did not slide during the earthquake and remained operational. The electrical cabinetry was not damaged and did not slide. The two control buildings were undamaged except for minor interior details. Several suspended ceiling panels buckled or fell.

COALINGA SUBSTATION 1 (SITE 4, FIG. 21.1)

Coalinga Substation 1 is located in the southeast corner of Coalinga on Jayne Road. This site is about 8 mi south of the epicenter. The substation includes a small office-control building, a small steel shed that houses relay panels, and a switchyard containing several types of oil-filled transformers, circuit breakers, and associated transmission lines. All the equipment at this substation appeared to be well anchored. Damage at the substation was relatively minor. One ceramic bushing was broken on

TABLE 21.1.—*Summary of observed damage from the May 2 earthquake to industrial facilities*

Site (fig. 20.1)	Facility	Estimated distance from epicenter (mi)	Primary damage observed
1	Kettleman Gas-Compressor Station (PG&E).	16	Cracking in walls of adjacent wood-frame houses. Indications of minor movement of piping. Facility operated through the earthquake.
2	Gates Substation (PG&E)--------	12	Minor spilling of oil from large transformers. One broken ceramic bushing on a transformer. Fallen ceiling tiles in control building. No apparent structural damage.
3	San Luis Canal pumping stations.	8-12	Stretching of surge-tank anchorbolts. Ground settlement at two stations, resulting in piping failures.
4	Coalinga Substation 1 (PG&E)---	8	Broken ceramic bushing on transformer. Broken bolts on transformer mounted on steel racks. Sloshed oil from transformers. No apparent structural damage.
5	7.6-million-gal water-storage tank.	8	Evidence of rocking of tank on concrete pad; spalling of concrete-pad grout. No loss of water from tank or piping.
6	Shell Oil Co. Dehydration Plant.	7	Sliding of large heat exchangers and breakage of attached piping. Malfunctioning valve resulting in a large oil-spill. Buckled leg of tall liquid-nitrogen tank.
7	Chevron Oil-Cleaning Plant----	7	Sliding of heat exchangers and rupture of attached piping. Failure of about 20 percent of oil-storage tanks, with subsequent loss of oil.
8	Pleasant Valley Pumping Plant.	7	Surge tank and transformer stretched their bolts and moved. Light fixtures fell. Canal gate malfunctioned. Damage to several bolts in bridge-crane rail. No structural damage.
9	Town of Coalinga----------	6	Extensive collapse of masonry structures; extensive damage to older wood-frame houses; other damage.
10	Getty Coalinga Oil Facility---	4	Sliding of heat exchangers and rupture of attached piping. Rupture of one large oil-storage tank out of four. Overturning of cabinetry in control room. Loss of onsite power due to sliding of transformer. Sliding of motor-control centers and switch-gear. Cracking of concrete-block structures. Ground failures. Operators unable to stand during earthquake.
11	Shell Oil Co. Water-Treatment Plant.	4	Extensive sliding of unanchored tanks with rupture of attached piping. Yielding of supports of anchored tanks. Cracking in foundations of heat exchangers. No apparent structural damage. Ground failures, landsliding.
12	Coalinga Feed Yard----------	3	Extensive damage to equipment and structures. Tanks overturned. Piping attachments ruptured. Equipment slid extensively. Retaining wall failures. Major cracks in block buildings. Other structural damage to tiltup and steel buildings. Ground failures.
13	Coalinga Water-Filtration Plant.	3	Sliding of switchgear and switchyard transformer. Sliding of motor-control center pumphouse. Broken baffle board in a sedimentation basin. Overturning of storage shelving. Minor structural damage.
14	Union Oil Co. butane/propane Plant.	3	Tilting of vertical towers. Several tanks rocked and slid. Rupture of attached piping. Small-bore-piping failures. Ceiling panels fell. Control equipment and building undamaged. Structural damage to two buildings. Settlement of fills resulted in damage to tank and piping supports.
15	Coalinga Nose Gas-Dehydration Station.	3	Sliding of odorant tank, resulting in leakage of odorant. Sliding of small, unanchored tanks, and reboiler. Cracks in small pipe-support bracket.
16	Amador Gas-Metering Station----	3	Minor leak at valve.
17	3-million-gal water-storage tank.	2	Evidence of rocking of tank on concrete pad and spalling of concrete pad. No loss of water from tank or piping.
18	Coalinga Substation 2 (PG&E)---	1	Partial collapse of unreinforced-block structure. Failure of anchorbolts around transformers and subsequent sliding. Yielding of supports of rack-mounted transformers.
19	Shell Oil Co. Tank Farm--------	1	Failure of four out of six oil tanks.

an oil-filled transformer mounted off the ground on a steel stand. An identical transformer broke one of its U-bolt anchors; this second transformer slid several inches and was on the verge of falling off its stand. Oil spilled from several transformers.

COALINGA SUBSTATION 2 (SITE 18, FIG. 21.1)

Coalinga Substation 2 is located on California Highway 33 north of Coalinga, in the area of highest seismic motion, about 1 mi west of the epicenter. This small substation includes two buildings (one of concrete block and one of reinforced concrete) and a switchyard. Both buildings were constructed in the 1920's. The walls of the block building were constructed of reinforced-hollow-concrete blocks; this building was totally destroyed (fig. 21.10*A*). The short walls failed along diagonal lines in a typical shear failure pattern; parts of the walls fell into the structure. The other building was of reinforced concrete; it had cracks at the corners of large openings, and its small clerestory roof collapsed onto the main roof. The heavily damaged block-wall building contained well-anchored relay panels and other equipment of an early vintage (fig. 21.10*B*); this equipment was reported to be operable after the earthquake.

In the switchyard, several large oil-filled transformers slid on their foundation pads. This sliding occurred in spite of the (small) anchor bolts or steel bumpers that were provided at the corners of the transformer base. The anchor bolts were sheared off or pulled out on most of the transformers. Oil spilled from most transformers. A horizontal tank shifted and rotated several inches on its concrete saddles.

WATER FACILITIES

Several different water-utility facilities were surveyed, including the Coalinga Water Filtration Plant,

FIGURE 21.2.—Typical collapsed unreinforced-masonry buildings in downtown Coalinga. Almost the entire central business district was lost. Note that the interior walls, which are lath and plaster on wood framing, kept the building shown in figure 21.2*A* from collapsing, whereas the buildings shown in figure 21.2*B* had few, if any, such walls and collapsed completely.

two large water-storage tanks, the Pleasant Valley Pumping Plant, and several pumping stations along the San Luis Canal. In general, these facilities are well designed to be earthquake resistant and sustained only minor damage.

The earthquake apparently caused no surface faulting in the surveyed area. Most underground pipes were undamaged. A few isolated breaks in the water-distribution network were reported. These breaks, however, were primarily at house connections where collapsed buildings damaged piping attachments.

COALINGA WATER FILTRATION PLANT (SITE 13, FIG. 21.1)

The Coalinga Water Filtration Plant, operated by the town, is located on Palmer Road east of Coalinga, about 3 mi southeast of the epicenter. This is a modern, 12-million-gal/d facility consisting of the typical sedimentation basins, chemical-storage tanks (small), backwash tank (large), filter gallery, pumphouse and associated pumps, piping, other equipment, and control systems. At the time of our survey (May 4), all systems except one sedimentation basin were in operation. The facility lost all electrical power for about 30 minutes after the earthquake. The plant has no emergency power, but the storage tanks had enough capacity to handle the demand for water.

Damage to the buildings of this facility was minimal (fig. 21.11*A*). The concrete-block pumphouse had hairline cracks in the walls that may have been caused by the earthquake. The main building houses the offices, laboratory, and control center. A steel diagonal brace tore loose from its anchorage in the rear of the building, and some minor cracking at the corners of the concrete-block walls was observed. Much of the unanchored equipment and supplies on shelves and tabletops slid or overturned. Many chemical containers on the testing-laboratory shelves and benches toppled and spilled their contents.

There was no major damage to the equipment at this facility. Wooden baffle boards in one sedimentation basin

FIGURE 21.2.—Continued

broke (this basin was shut down at the time of our survey). We observed evidence of severe rocking of the aerator support platforms located in the basins. Stretching of the anchor bolts on the large ground-mounted backwash tank (fig. 21.11*B*) caused minor leakage in an outlet pipe flange, owing to rocking of the tank. The transformer and adjacent switchgear in the facility substation slid in spite of anchor clips holding it to the concrete pad. An unanchored motor-control center and attached switchgear in the pumphouse slid several inches; it was prevented from overturning by overhead conduits. Storage shelving in the warehouse and machine shop overturned. In the chlorine-tank room, all the liquid-chlorine tanks, which were on standard saddle roller supports, slid, some as far as 10 in. Sufficient slack in the attached tubing prevented rupture of the lines and a subsequent chlorine-gas leak.

WATER-STORAGE TANKS (SITE 5, FIG. 21.1)

We also investigated water-storage tanks. One tank, a 7.6-million-gal reservoir that supplies the town, is located west of Coalinga, about 8 mi southwest of the epicenter. A second tank is located on California Highway 33 north of Coalinga, on Palmer Road, about 4 mi south of the epicenter. This tank, which has a capacity of 3 million gal, serves as a feeder tank for the main reservoir. At the time of our survey (May 3), both tanks were nearly full. According to the operators of the Coalinga Filtration Plant, the two tanks were about half-full during the earthquake.

Damage to both tanks was minimal. The concrete-foundation pads showed evidence of rocking of the tanks (spalling of grout around the tank bases); this rocking created a gap about an inch wide between the incoming

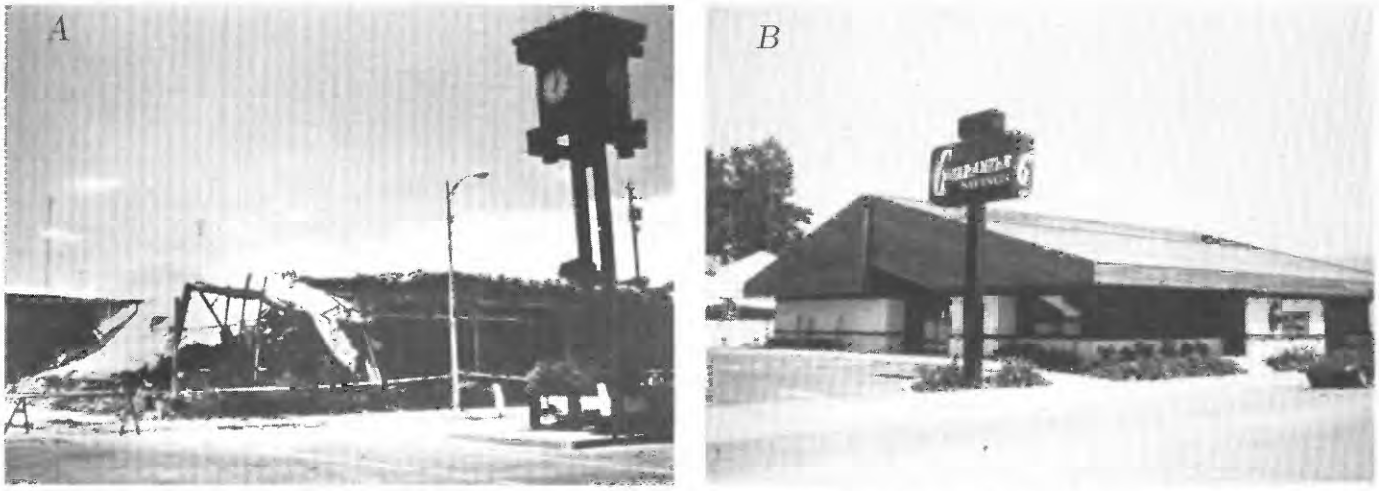

FIGURE 21.3.—Two commercial buildings across the street from each other in central Coalinga. *A*, Single-story unreinforced-brick building. *B*, Wood-frame building with shear walls that sustained only broken glass and minor cracking of stucco walls.

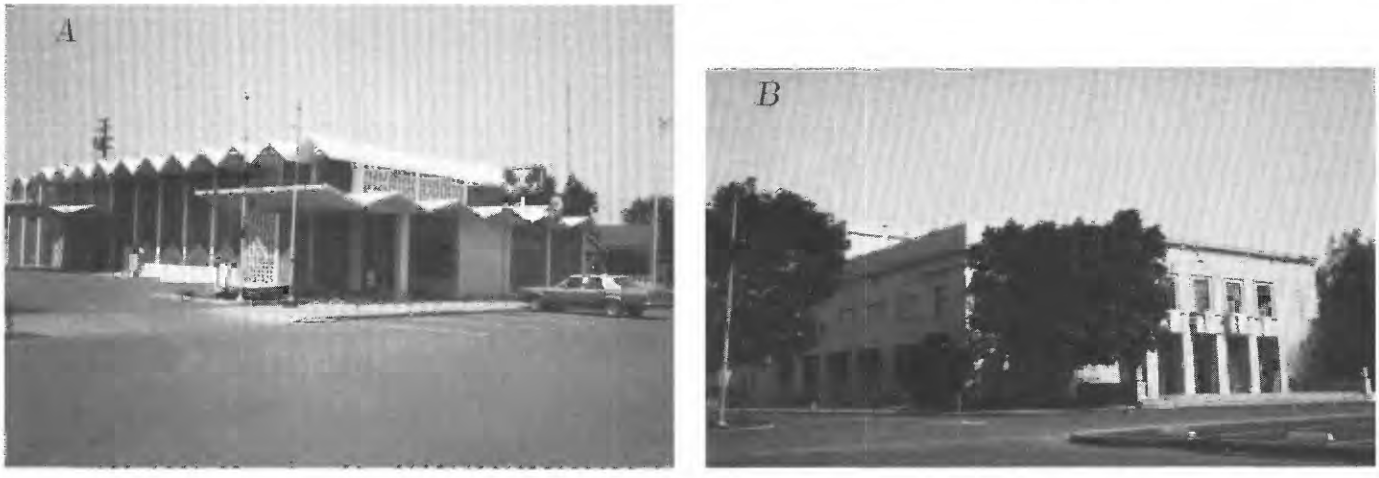

FIGURE 21.4.—Modern reinforced-masonry and concrete-shear-wall buildings in central Coalinga. *A*, Bank of America. *B*, Coalinga High School. Damage to these building was light, in spite of the strong ground motion.

24-in.-diameter line and the ground. Damage to the underground piping was unknown at the time of our survey. In conversations with the water-filtration plant director, we learned of some damage to underground waterlines. Two breaks were reported in the two 24-in.-diameter transmission lines to the town reservoir (the 7.6-million-gal tank). Two additional breaks were reported along a 10-in.-diameter booster line to water-storage tanks in the oil fields; all of these breaks were at pipe joints. The failure modes were varied; some were pushed together (compression failure), and others were pulled apart (tension failure).

PLEASANT VALLEY PUMPING PLANT (SITE 8, FIG 21.1)

The Pleasant Valley Pumping Plant, located east of U.S. Interstate Highway 5, is about 7 mi northeast of the epicenter. This was the nearest facility to the epicenter to have accelerometers that recorded ground motions of the May 2 earthquake. One accelerometer in the yard of the station triggered and recorded a peak ground acceleration of 0.54 *g*; after corrections by the U.S. Geological Survey, the other horizontal component was reported to have recorded a peak acceleration of 0.60 *g*. Another accelerometer, located in the basement of the pumphouse, indicated a peak floor acceleration of 0.33 *g*. Two other instruments, located on the operating floor (first floor) and on the roof, failed to operate. All four instruments, however, recorded several aftershocks. These data are summarized in table 21.2.

The pumping plant, in its overall dimensions and operations, is similar to the intake structure of a typical large nuclear powerplant. Because of the numerous records taken at different levels of motion during the main shock and the aftershocks, many valuable data exist that can be used for soil-structure-interaction and structural-behavior studies.

The building is located in an excavated channel, some 60 ft below the original grade (fig. 21.12). It is a deeply embedded, massive concrete structure with a rigid steel-frame superstructure of a single high bay. The framing is enclosed with reinforced-brick panels that are segmented with flexible joints. Damage to the pumping-station building and equipment was minor, in spite of the very high seismic motion recorded at the site. No cracking of the brickwork was observed. An expansion joint located about midway along the building indicated a permanent displacement after the earthquake between the two halves of the building. This displacement was about 1 in. at roof level and about in. at the operating-floor level.

The pumping station contains nine large vertical centrifugal pumps that lift water from the San Luis Canal into the branch channel of the Coalinga Canal. The drive motors of these pumps are located on the main operating floor at grade level, along with their associated control panels. The pump impellers are located in the basement below the canal waterline and are connected to the motors by vertical drive shafts. In addition to the main pumps, the plant contains an array of associated piping, valving, switchgear, tanks, air compressors, and a large bridge crane above the operating floor.

Some minor damage to equipment within the building was caused by the fall of several light fixtures from the ceiling of the main operating bay; these light fixtures struck the control panel and caused superficial damage to a few face-mounted devices. Controls and instrumentation within the plant sustained no loss of functionality except for one pump-bearing monitor that gave faulty readings after the earthquake. The main operating floor is served by a bridge crane supported on rails near the

FIGURE 21.5.—Lightly damaged steel-frame buildings in Coalinga. *A*, Building with metal siding. *B*, Building with brittle Transite siding that was heavily damaged.

roof (fig. 21.13). Several bolts anchoring this crane rail failed adjacent to the location of the crane and at the building expansion joint; the failure was due to poor anchorage detailing and construction.

Transformers located adjacent to the plant structure failed at their anchor bolts and slid several inches; these transformers were undamaged. The large surge tank located about half a mile from the plant rocked severely and stretched its anchor bolts, causing leakage at piping connections. This surge tank was later sealed off from the water-supply system because of indications that it had been structurally weakened to an unsafe condition by the earthquake and subsequent aftershocks.

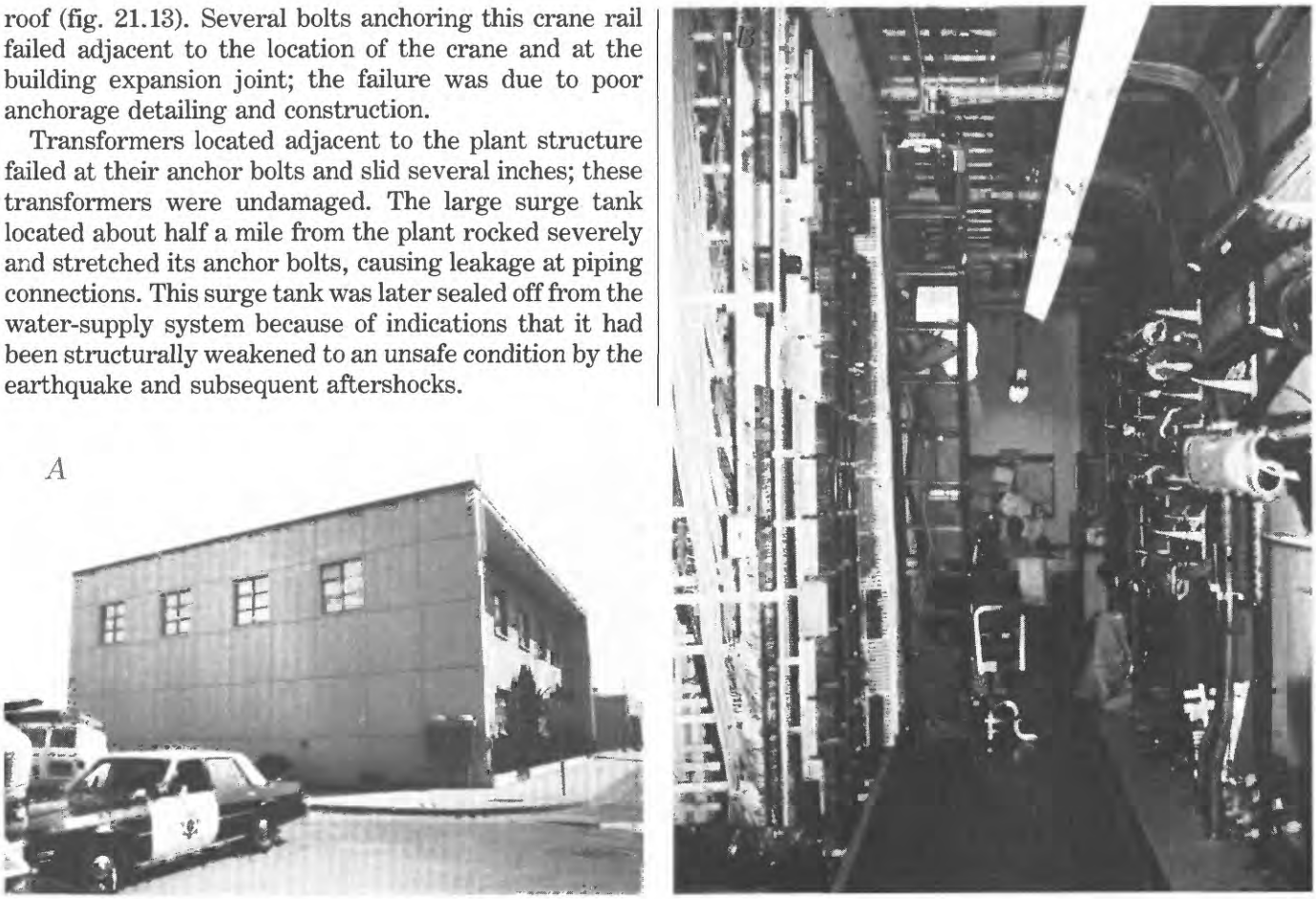

FIGURE 21.6.—Telephone building in central Coalinga, an engineered shear-wall structure (*A*) that was not damaged significantly. Anchored switching equipment inside (*B*) was undamaged and remained functional after the earthquake.

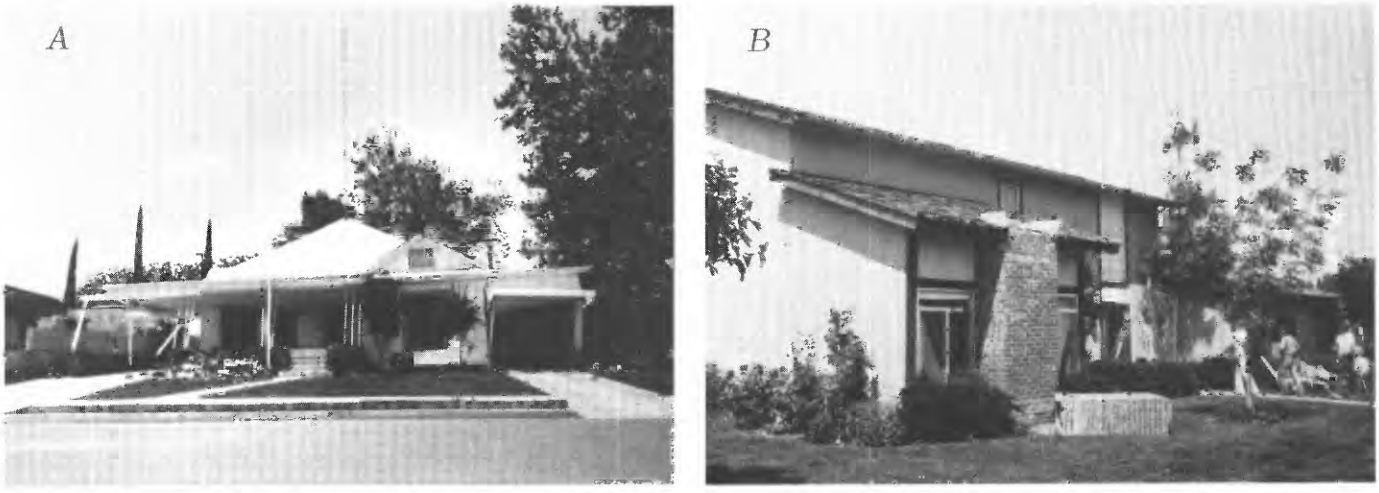

FIGURE 21.7.—Contrasting behavior of older and newer houses in Coalinga. *A*, Older house that slid off its foundation, owing to absence of anchorage. *B*, Newer house that sustained only minor damage except for the brick chimney. In general, about a third of the homes in Coalinga were damaged beyond repair. Damage to newer homes was primarily limited to such details as chimneys and brick or other masonry veneers.

PLEASANT VALLEY PUMPING PLANT DISCHARGE CANAL GATE

The Pleasant Valley Pumping Plant Discharge Canal Gate is located at the crossing of California Highway 145 and U.S. Interstate Highway 5, about 6 mi northeast of the epicenter. The gate and the supporting concrete structure is on a levee about 15 ft above the natural grade.

Significant cracking and slumping of the fill around the concrete structure occurred; the fill was probably compacted from the earthquake vibrations. Although the surrounding ground settled as much as 6 in., the gate and concrete support structures sustained no apparent damage. A quick survey of the concrete-lined canal in the immediate vicinity of the gate also revealed no damage. A broken conduit supplying power to the gate drive motor prevented operation of the gate immediately after the earthquake. This conduit break was attributed to differential displacement due to the soil settlement described below.

PUMPING STATIONS ALONG THE SAN LUIS CANAL (SITE 3, FIG. 21.1)

Pumping stations along the San Luis Canal are located at intervals of about half a mile on both sides of the canal. These pumping stations draw water from the canal through buried irrigation piping and pass it to the surrounding farms. The pumping stations typically include a set of four or five large vertical turbine pumps, with associated piping and automatic control valves. Each station has a tall vertical surge tank. Power is supplied to each station through a transformer and a set of switchgear mounted in metal outdoor enclosures.

Approximately 20 of the pumping stations along the San Luis Canal were sufficiently close to the epicenter to undergo strong ground motion. In nearly all these stations, damage was confined to stretched or broken anchor bolts caused by rocking of the station surge tank. Two adjacent pumping stations, located about 5 mi north of the junction of California Highway 145 and U.S. Interstate Highway 5, about 10 mi north-northeast of the epicenter, were somewhat damaged. At one of these pumping stations, a switchyard transformer slid about 8 in. and disconnected the overhead electrical leads. The other station underwent local ground settlement that caused differential displacement between the pumps and their discharge piping, resulting in rupture of a flanged connection on a 36-in.-diameter discharge header. The rocking of the surge tank at this station was so severe that connections with the tank discharge lines were ruptured. A pipe break was also reported in the buried section of the discharge line near the station, at the junction of the concrete and cast-iron sections of the line.

Cracking of the concrete canal liner and local settlement of the levee enclosing the canal was observed in the vicinity of these pumping stations. The pumping stations and surrounding area may have been damaged because of much stronger ground motion caused by focusing of the seismic waves. The canal and the other pumping stations were significantly less damaged even at locations closer to the epicenter.

OIL FACILITIES

The Coalinga-Tulare Lake area is one of the larger onshore drilling-development areas in California. Several major oil companies have oil drilling and processing facilities in this area. The economies of most towns in the area depend on this industry. Oil-production operations were interrupted by the earthquake. At most facilities, production was resumed within a few days.

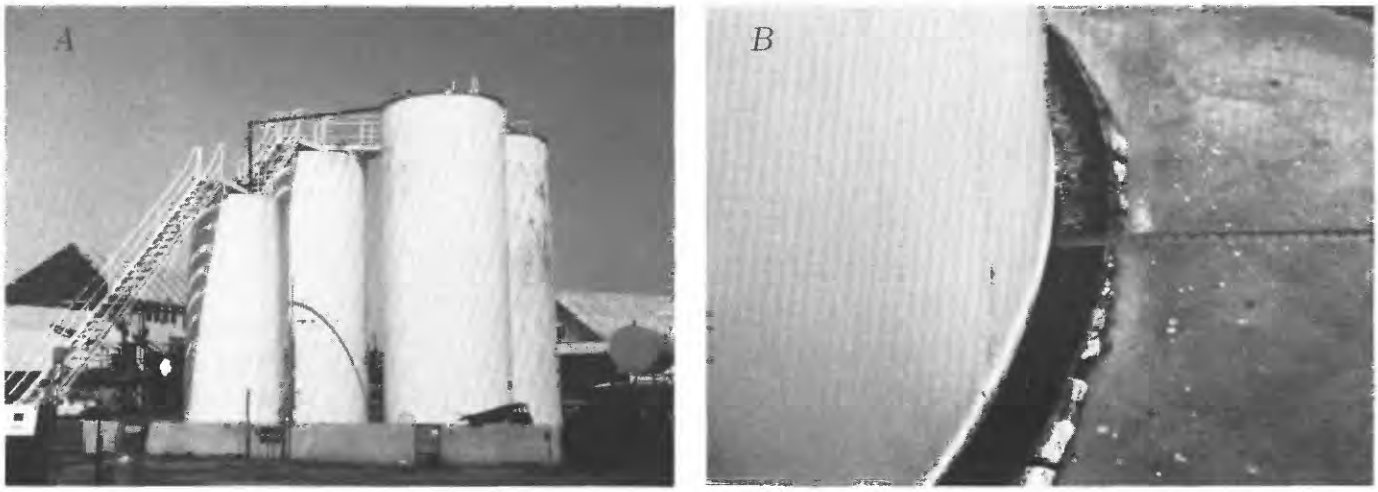

FIGURE 21.8.—Four gasoline-storage tanks located in south end of Coalinga (*A*) did not leak, in spite of sliding about 4 in. (*B*). Sliding was common for unanchored equipment and structures throughout the area.

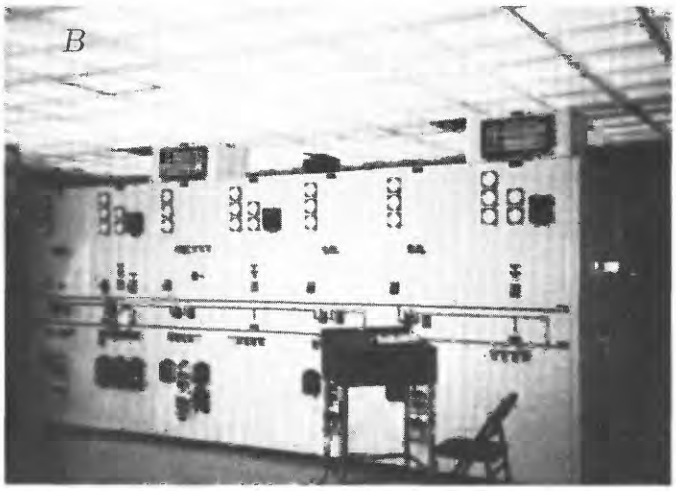

The oil facilities had numerous spills as a result of piping-attachment failures, mostly caused by differential motions between the structures supporting the pipes and the tanks. Most common was failure of a pipe that emerges from the ground at the tank connection; rocking or sliding of the tank would break the attached piping if the flexibility of the pipe was insufficient to accommodate the displacement. Most tanks spilled at least minor amounts of oil by sloshing of their contents through ventilation holes in the tank roofs. Numerous tank failures were found, as described below.

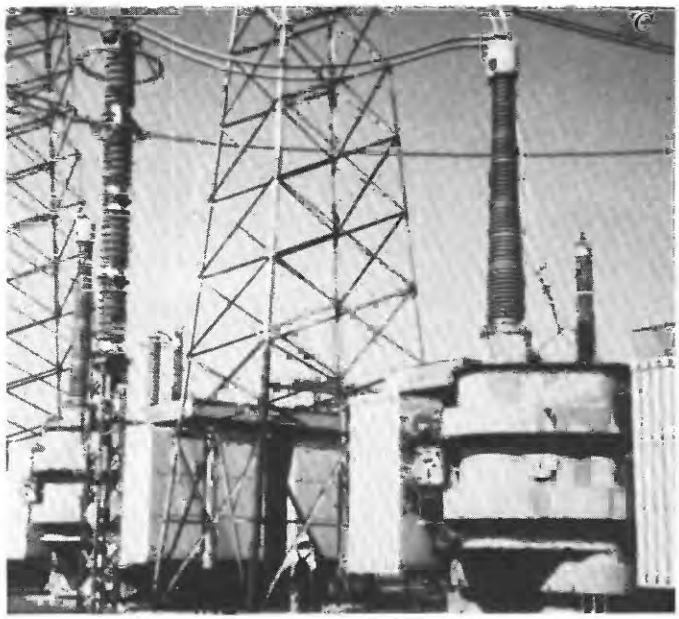

FIGURE 21.9.—Precast-concrete control building (*A*) at the PG&E Gates Substation was undamaged. Electrical equipment inside (*B*) was well anchored and also undamaged; damage within the building was limited to a few buckled or fallen ceiling panels. In the switchyard, large transformers lost oil through leakage or seals at ceramic bushings; one broken bushing is visible on ground adjacent to transformer (*C*).

FIGURE 21.10.—Unreinforced-concrete-block building (foreground, *A*) at PG&E Coalinga Substation 2 was severely damaged and had to be demolished; it was constructed in the 1920's. Adjacent reinforced-concrete shear-wall building (background, *A*) was only lightly damaged. Relay panels inside the damaged structure (*B*) were well anchored; they were undamaged and remained functional after the earthquake.

The facilities surveyed include the Chevron Oil Co. Cleaning Plant, the Shell Dehydration Plant, the Getty Coalinga Oil Facility, the Union Oil Co. Butane/Propane Plant, the Shell Water-Treatment Plant, and the Shell Tank Farm. Many other oil facilities are located in the Coalinga-Tulare Lake area.

CHEVRON OIL-CLEANING PLANT (SITE 7, FIG. 21.1)

The Chevron Oil-Cleaning Plant is located just west of Coalinga, about 7 mi southwest of the epicenter. The facility consists of several large ground-mounted tanks, heat exchangers, and their associated piping, valves, and pumps. Several tanks were not full at the time of the earthquake and sustained no damage; however, all the full tanks sustained some loss of oil due to sloshing of their contents through vents, rupture of the tank, or breakage of the connected piping. No damage was observed to heat exchangers, piping (except at tank attachments), pumps, or other peripheral equipment such as air compressors and electrical switchboxes. The plant was being repaired at the time of our survey (May 3).

SHELL OIL CO. DEHYDRATION PLANT (SITE 6, FIG. 21.1)

The Shell Oil Co. Dehydration Plant is located near the Chevron Oil Cleaning Plant, about 7 mi southwest of the epicenter. The equipment contained at the facility consists of tanks, heat exchangers, piping, and pumps.

Some large heat exchangers slid, breaking the attached piping. Several oil tanks showed minor losses of oil (due either to small leaks or to sloshing from the top of the tank). The opening of valves on a 1-in.-diameter pipe attached to an oil-clarifying tank resulted in a major oilspill at the site. These valves, which were reported to have shaken open during the earthquake, were apparently undamaged. The facility also includes a tall liquid-nitrogen tank mounted on steel legs anchored to a concrete pad. The legs of the tank buckled, but the tank did not overturn. Piping damage other than at equipment attachments was not observed. At the time of our survey (May 4), the facility was closed down for inspection and repair.

GETTY COALINGA OIL FACILITY (SITE 10, FIG. 21.1)

The Getty Coalinga Oil Facility is located on Shell Road north of Coalinga, about 4 mi southwest of the epicenter. The facility includes several large ground-supported oil and water tanks and their associated pumps, piping, valves, and heat exchangers, as well as a one-story reinforced concrete-block control building that contains extensive electrical and control equipment. The control-room operator reported that he was unable to stand

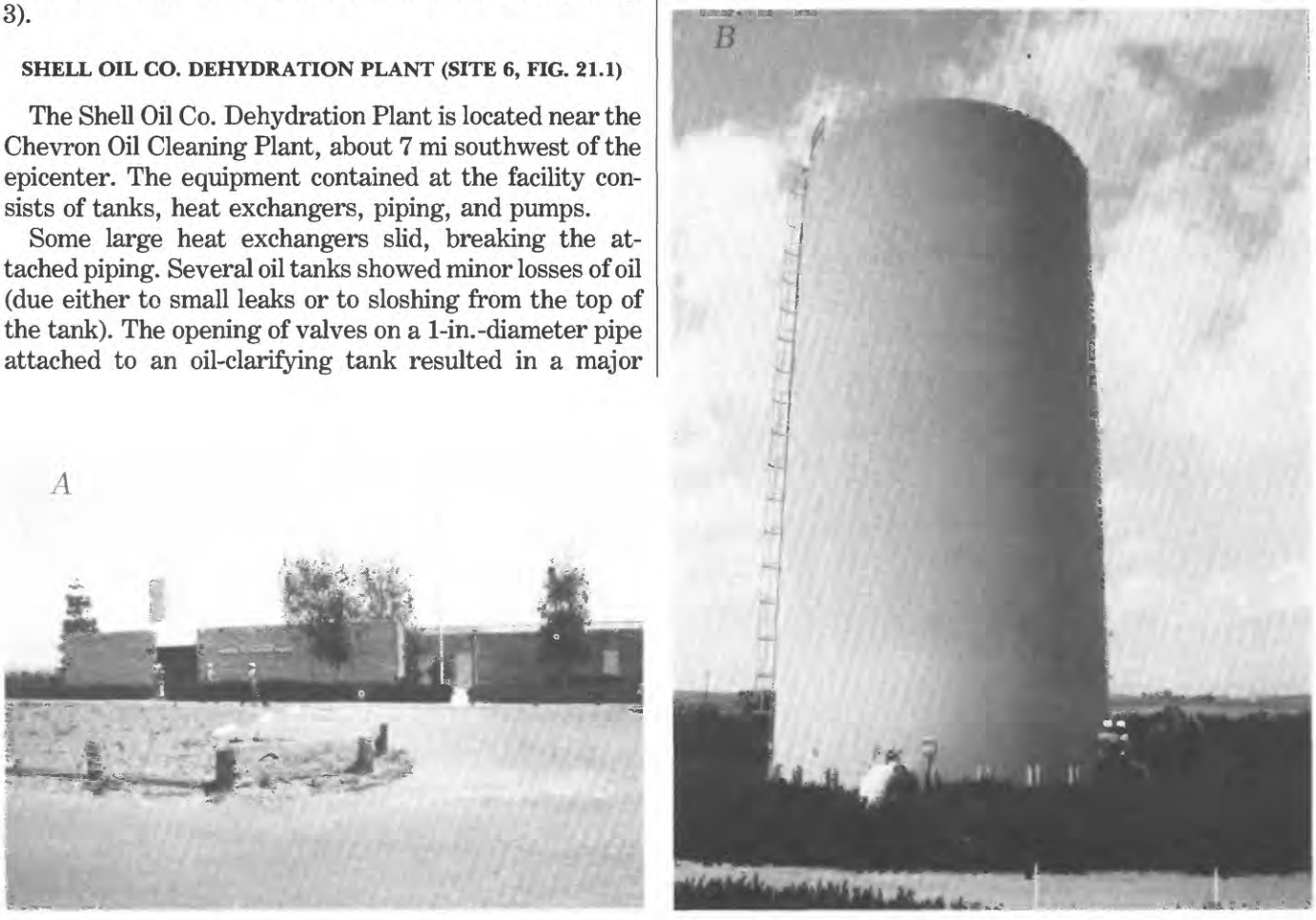

FIGURE 21.11.—Coalinga Water-Filtration Plant sustained only minor damage. Main building (*A*), a steel-braced concrete-block shear-wall structure, sustained minor wall cracking and failure of a steel-brace anchorage; damage within the building consisted mostly of items sliding off shelves. Well-anchored backwash tank (*B*) stretched its anchorbolts and sustained minor leaks at attached piping. This type of damage to tall tanks was common throughout the Coalinga area.

TABLE 21.2.—*Recorded peak accelerations at the Pleasant Valley Pumping Station*

Event	M_L	Record (horizontal-135°, vertical, horizontal-045°)											
		Switchyard			Basement			First floor			Roof		
May 2	6.7	0.54	0.37	0.60	0.28	0.22	0.33	---	---	---	---	---	---
May 4	4.8	.07	.08	.26	.05	.05	.17	.04	.04	.16	.08	.07	.44
May 9	5.1	.22	.11	.10	.14	.04	.05	.13	.05	.06	.23	.06	.24
May 24	4.6	.07	.09	.11	.05	.04	.06	.04	.04	.07	.08	.04	.22
July 22	6.0	.38	.29	.58	.13	.08	.43	.12	.08	.47	.25	.20	1.10

during the earthquake. From the operator's description and damage observations, we conclude that the ground motion at this site was very strong. Extensive ground and paving cracking and breakage in soil and pavement occurred on the facility grounds. Operators also reported that they saw cars "uplifted" in the parking lot.

Of the four large ground-mounted oil tanks, one tank ruptured at its buried discharge line and lost much of its contents (fig. 21.14*A*). Large oil heaters (heat exchangers) failed their small anchor clips and slid several inches (fig. 21.14*B*). The sliding of the heat exchangers resulted in some ruptures of attached piping. No damage was observed to pumps, piping (other than direct attachments to heat exchangers), or the numerous motor- and air-operated valves.

Data-processing cabinetry overturned in the facility control building (fig. 21.14*C*), and switchgear and motor control centers pulled their anchor bolts and slid. One switchgear cabinet was dented, owing to impact with adjacent equipment; at the time of our survey (May 4), repairmen were straightening the cabinet walls. The facility substation transformer also pulled its anchor bolts and slid, breaking overhead electrical connections. The reinforced concrete-block control building sustained only minor cracks. Much of the control-room suspended ceiling collapsed.

FIGURE 21.12.—Pleasant Valley Pumping Plant sustained only minor damage. Main building (*A*) is an embedded massive concrete structure with a steel-frame superstructure and panelized reinforced-brick siding, built in 1970. No damage to the building was observed other than a permanent displacement at the seismic gap near building midpoint. Building consists of a main operating floor at grade level (*B*) and a basement; the station contains nine large vertical centrifugal pumps that lift the water about 150 ft from the San Luis Canal into the Coalinga Canal. Pump motors and control panels are located on operating floor; centrifugal pumps are located in basement below waterline and are connected to motors by a vertical drive shaft.

UNION OIL CO. BUTANE/PROPANE PLANT (SITE 14, FIG. 21.1)

The Union Oil Co. Butane/Propane Plant is located east of Coalinga on Calaveras Road, about 3 mi southeast of the epicenter. This large facility (fig. 21.15*A*) contains much typical oil-refinery equipment, such as vertical towers, heat exchangers, pressure vessels, pumps, valves, electrical equipment, tanks, and extensive runs of piping. Local ground settlement at several fill sites occurred throughout the facility. Operators reported that they were unable to stand during the earthquake. Minor tilting was observed in several 110-ft-high vertical towers after the earthquake; it is uncertain whether this tilting was caused by the earthquake. The facility includes several liquid-butane storage tanks with capacities of 15,000 to 25,000 gal. Settlement of fills, coupled with rocking of these tanks, resulted in stretched anchor bolts, spalled concrete, and, in one case, a failed concrete pedestal. Rocking or sliding of some other tanks caused breaks in rigid interconnecting small lines (fig. 21.16*B*). Otherwise, piping failures were not found, in spite of the extensive runs of piping built without specific seismic bracing (fig. 21.16*A*).

The reinforced concrete-block control building was undamaged. The control equipment inside was also undamaged, although most ceiling panels fell down. Strip-chart recorders in the main control board slid out from the front face of the board and had to be pushed back into place. Other structural damage included severe cracking of the walls of an older unreinforced-brick storage building that had an independent steel frame. Another one-story concrete block building was extensively damaged. A one-story wood-frame office building and several large old steel-framed compressor buildings were not damaged significantly (fig. 21.15*B*). The facility was shut down for repairs for about 2 weeks.

FIGURE 21.13.—Close-up of traveling service-bridge crane near roof of Pleasant Valley Pumping Plant. Estimated peak acceleration here was about 1.0 *g*. Several rail anchorbolts failed because of inadequate welding of the bolts to the supporting girder; the crane itself was undamaged.

SHELL OIL CO. WATER-TREATMENT PLANT (SITE 11, FIG. 21.1)

The Shell Oil Co. Water-Treatment Plant is located on a branch of Shell Road north of Coalinga, about 4 mi west of the epicenter. This new plant is built into a hillside in the foothills north of Coalinga (fig. 21.17*A*). Minor landsliding occurred in the rain-saturated slopes above and below the plant; the landslides occurred within the plant yard but did not cause any direct damage. The facility includes about a dozen ground-mounted oil tanks, several smaller tanks supported on legs, and extensive runs of piping and associated pumps and control valves. One ground-mounted tank sustained an "elephant's foot" failure of its wall, with subsequent loss of contents (fig. 21.17*B*). The other ground-mounted steel tanks were undamaged except for sloshing of oil through roof vents. Two tall steel-bottomed fiberglass tanks failed at the interface between the steel and fiberglass and lost their contents; these tanks are typical of vessels used for the storage of caustic material.

In general, the smaller tanks, pressure vessels, and filters were not anchored to their concrete pads (fig. 21.17*C*). Sliding was observed in all these tanks, with subsequent rupture of much of the attached short piping connections (fig. 21.17*D*). The facility includes several tall vertical tanks that were anchored to their concrete pads. Rocking of these tanks caused stretching of anchor bolts and yielding of steel supports, but the tanks did not overturn. One tall diatomaceous-earth silo was severely damaged internally and had to be replaced.

Different sections of the plant are connected by extensive runs of piping. No piping failures were observed other than rupture of short tank attachments due to excessive tank sliding. The facility includes a concrete-block control building that houses motor-control centers and switchgear. The electrical equipment was well anchored and sustained no damage; the concrete-block building was also undamaged. Because of the extensive tank and attached piping damage and subsequent spills, the facility was partly inoperable for several months after the earthquake.

SHELL OIL CO. TANK FARM 29 (SITE 1, FIG. 21.1)

The Shell Oil Co. Tank Farm is located along California Highway 33 north of Coalinga, about 1 mi north of the epicenter. The tank farm includes a total of six old ground-mounted oil tanks, four of which contained oil at the time of the earthquake. These tanks buckled at their

walls and lost some of their contents; one tank burst its walls (fig. 21.18), and two empty tanks were undamaged. The tank farm also includes a few pumps, air compressors, and control valves; that equipment was undamaged.

NATURAL-GAS FACILITIES

The surveyed natural-gas facilities in the Coalinga area are all owned and operated by PG&E; these facilities include the Kettleman Compressor Station, the Coalinga Nose Gas-Dehydration Station, and the Amador Gas-Metering Station. All these facilities performed very well and were on line at the time of our survey (May 3). There were no reports of damage to major underground gaslines.

KETTLEMAN GAS COMPRESSOR STATION (SITE 1, FIG. 21.1)

The Kettleman Gas Compressor Station is located near U.S. Interstate Highway 5, about 20 mi southeast of the epicenter. The facility is the primary compressor station on the natural-gas pipelines that convey gas from El Paso, Tex., through the San Joaquin Valley, to the San Francisco Bay Area. It contains several buildings and extensive equipment installations that include large gas compressors, diesel generators, pressure vessels, tanks, piping and valving, electrical switchgear, and instrumentation and controls (fig. 21.19).

The compressor station operated through the earthquake. The only significant problem was failure of the telephone system, which also caused loss of the station's telemetering system. Other observed effects included

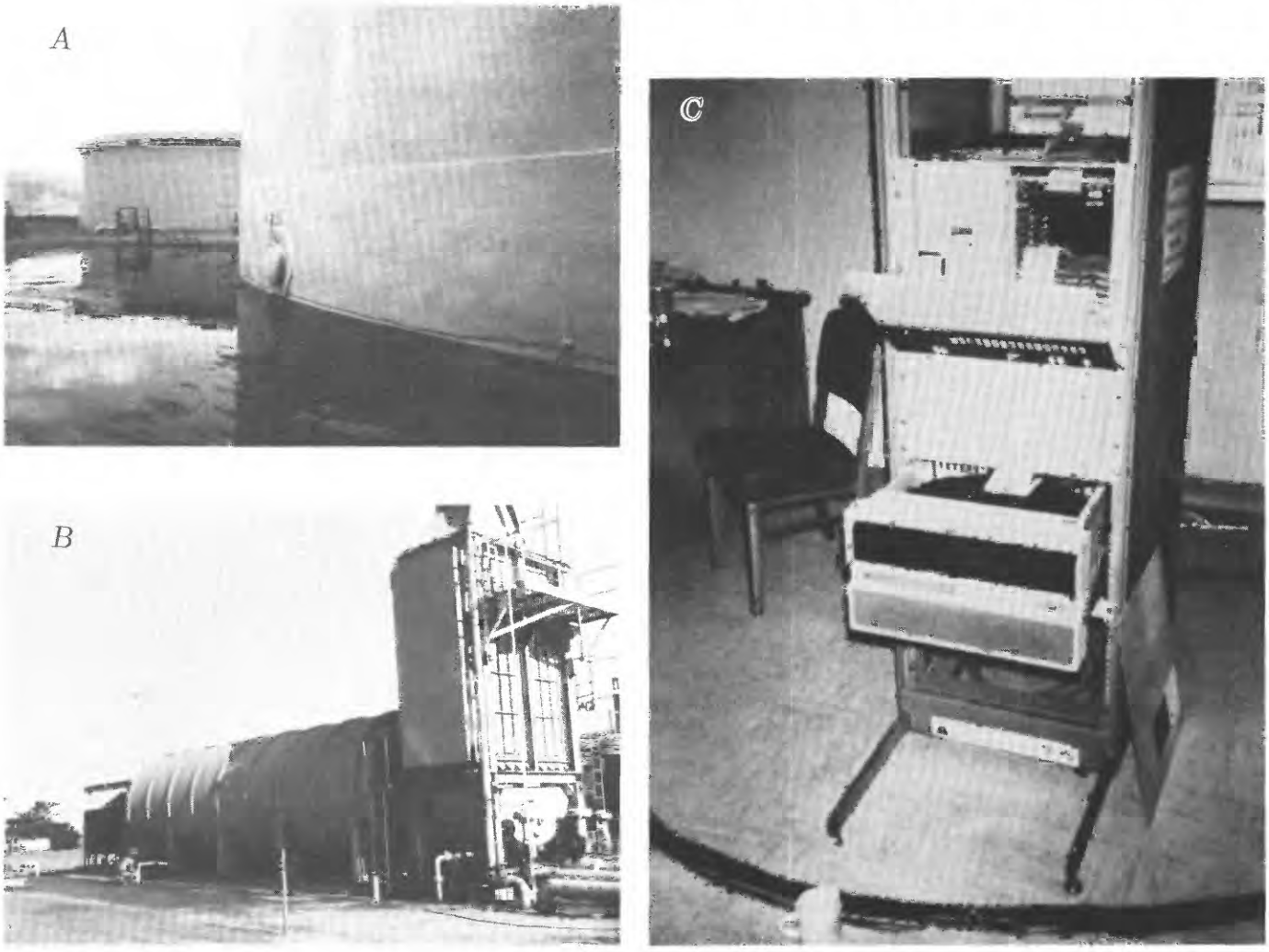

FIGURE 21.14.—One of four large oil-storage tanks at the Getty Coalinga Oil Facility ruptured at its buried discharge line, with subsequent oilspill (*A*). Very minor leakage was observed over a period of weeks after the earthquake in a second tank. Much of the equipment located in the plant yard slid several inches because small anchorages failed; large oil heaters (*B*) slid about 6 in. after slipping from steel clips that anchored them to their basepad. Inside the one-story control building, most electrical cabinetry either slid or overturned. The computer (*C*) overturned and required offsite repairs; meanwhile, the facility had to be operated manually.

some minor sliding of piping relative to its supports, falling of unanchored tabletop equipment and ceiling panels, and cracking of the walls of nearby employee residences (single-story houses).

COALINGA NOSE GAS-DEHYDRATION STATION (SITE 15, FIG. 21.1)

The Coalinga Nose Gas Dehydration Station is located on Palmer Road west of Coalinga, about 3 mi southeast of the epicenter. This relatively small facility includes several tanks (mounted both vertically and horizontally) and a large reboiler (heat exchanger).

Several tanks slid on their pads. A tall odorant tank slid and, at the time of the survey on May 3, was still leaking odorant; this leak was probably due to a cracked piping attachment. A few small unanchored tanks also slid on their saddles. One piping-support bracket cracked at its bolt holes. The skid-mounted reboiler was unanchored and slid several inches. The station operated through the earthquake and was on line at the time of our survey (May 3).

FIGURE 21.15.—Union Oil Co. Butane/Propane Plant sustained minor light damage, in spite of its location (less than 3 mi from epicenter). *A*, Partial view of the facility; towers at center of plant were found to be only slightly misaligned after the earthquake. *B*, Large gas compressors that are housed in several large light-steel-frame buildings were undamaged.

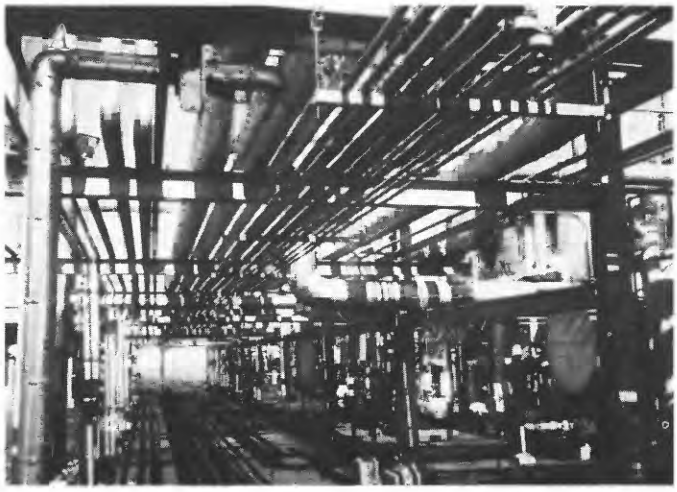

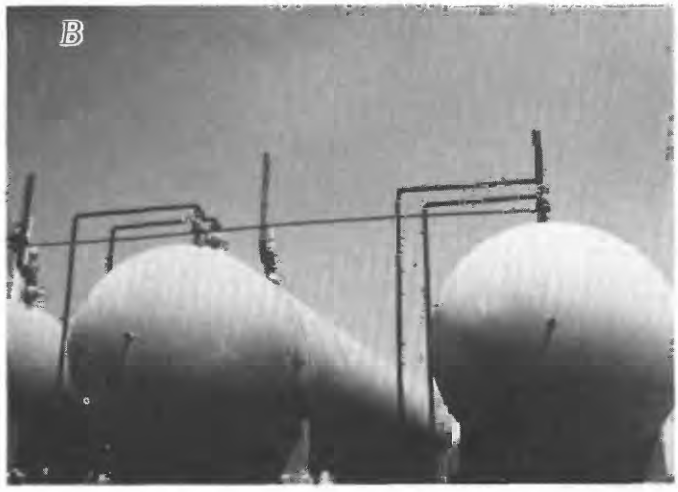

FIGURE 21.16.—Union Oil Co. Butane/Propane Plant contains a large array of piping (*A*), most of which rests without positive anchorage on overhead crossbeams. No piping ruptures occurred except at short, inflexible connections with tanks. For example, small piping connecting large butane-storage tanks across top (*B*) ruptured owing to insufficient flexibility to accommodate differential displacement between tanks that, in some cases, was caused by local ground failure at several places in the plant. No major gas leaks and no fires occurred at the plant.

FIGURE 21.17.—Shell Oil Co. Water-Treatment Plant was one of the most heavily damaged facilities inspected. Large ground-mounted tanks (*A*) generally performed well. One tank out of 10 sustained an "elephant's foot" buckling failure in the wall (*B*), with a resulting loss of contents. Two steel-bottom fiberglass tanks failed. Most damage to equipment was caused by sliding of unanchored tanks and pressure vessels (*C*) that ruptured short spans of connecting piping (*D*); long spans of primary piping at the plant were undamaged. As at the Union Oil Co. Butane/Propane Plant, piping was primarily supported without seismic bracing or anchorage on steel frames.

AMADOR GAS-METERING STATION (SITE 16, FIG. 21.1)

The Amador Gas-Metering Station is located on California Highway 198 near U.S. Interstate Highway 5, about 2 mi east of the epicenter. This small facility includes one vertical tank, attached piping, and a small steel shed for instrumentation. A minor leak at a valve in an underground vault was the only damage observed at the station; this leak could have been due to natural wear rather than the earthquake. The station was on line at the time of our survey (May 3).

AGRICULTURAL FACILITIES

COALINGA FEED YARD (SITE 12, FIG. 21.1)

The Coalinga Feed Yard, about 3 mi west of the epicenter, is a large animal-feed-processing facility (fig.

21.20*A*). Nothing at the facility appeared to have been designed to be earthquake resistant. From observations of the damage, it appears that practically the entire equipment installation in the feed mill slid several inches. The facility includes various silos, tanks, hoppers, boilers, piping, and electrical control equipment. Most equipment is unanchored.

Damage to the facility was very extensive. Several unanchored vertical tanks storing molasses tilted, and one tank overturned (fig. 21.20*B*); some damage was caused by the failure of retaining walls. A large unanchored grain silo slid 10 to 12 in. (fig. 21.21). An unanchored boiler slid off its concrete support. The boiler-shed firewall (unreinforced brick) also collapsed. A large high-voltage electrical transformer slid 8 in. The walls of a small precast-concrete tiltup building, housing electrical equipment, pulled away from the roof. The reinforced concrete-block two-story main office building sustained wall damage, some of which may have been caused by ground cracking.

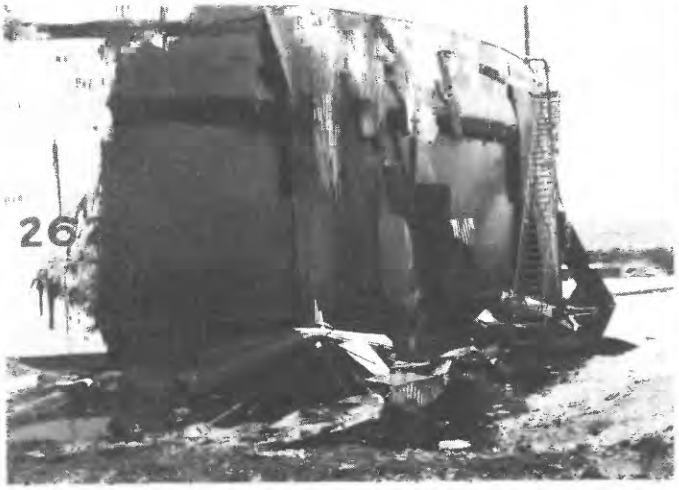

FIGURE 21.18.—Shell Oil Co. Tank Farm 29 was located within 1 mi of the epicenter. Of the six large oil tanks at the facility, four ruptured and lost contents; the two that escaped damage were empty. Most serious tank failure is shown here. Pumps, air compressors, buried piping, and control valves at the plant were undamaged.

SUMMARY

We visited several industrial facilities immediately after the earthquake to review their performance during the earthquake. The facilities surveyed (except the Kettleman Gas-Compressor Station, the Gates Substation, and several pumping stations), which are all located within 10 mi of the epicenter, were all subjected to high ground accelerations.

Considering the high levels of ground acceleration generated by the earthquake (which, at most of the facilities, was near 0.60 *g*), most anchored equipment performed very well. Most anchored equipment and flexible piping runs were undamaged. Where damage occurred, it was generally attributable to the absence of or inadequate anchorage. Equipment and most structures with even a minimal amount of seismic provision in their design generally performed well.

The earthquake damaged many structures in the various facilities surveyed. The damaged buildings, however, were generally old, unreinforced, or poorly designed concrete-block structures that would not meet today's building-code requirements. Newer structures that did fail were poorly designed or constructed. Well designed and constructed structures and most steel-frame buildings were generally undamaged.

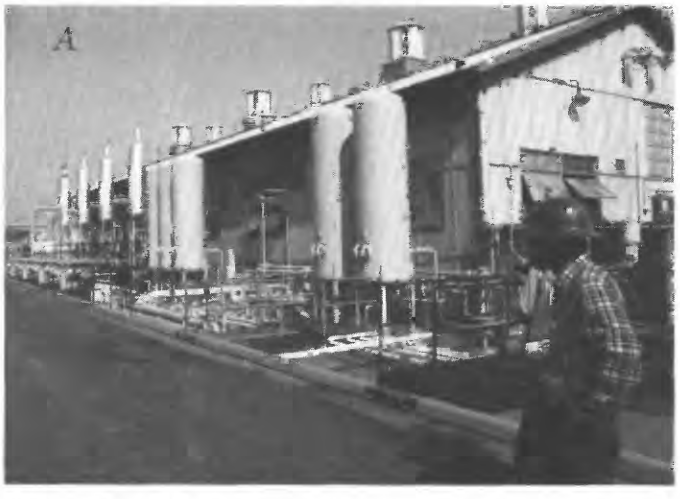

FIGURE 21.19.—Kettleman Gas-Compressor Station consists of a concrete-block control house and several large steel buildings (*A*). The plant, which is located about 16 mi from the epicenter, underwent only moderate shaking, was essentially undamaged, and operated through the earthquake. Primary equipment in the plant includes gas-powered compressors and diesel generators (*B*), as well as extensive arrays of piping and numerous tanks.

ACKNOWLEDGMENTS

We thank the following people who cooperated with and assisted in collection of the information contained in this chapter: Richard V. Bettinger, J.M. Pickell, and David D. Craig of the Pacific Gas and Electric Co.; Eldon W. Williams of the Westlands Water District; Carl N. Bidinger and Ray Walker of the Union Oil Co.; Gary Hohnstein of the Getty Oil Co.; Tito Balling of the town of Coalinga; Bob Bonilla of the Shell Oil Co.; Doug Morris of the Coalinga Feed Yard; the staff of KMC Inc., Washington, D.C.; and the Seismic Qualification Utility Group, Washington, D.C., who funded the investigation.

FIGURE 21.20.—Damage to mill facility at the Coalinga Feed Yard (*A*) was extensive. Large vertical tanks tilted, and one overturned (*B*); note damage to steel legs of tank on right. Entire steel structure was badly deformed and out of alignment. The facility was not designed for seismic loads.

FIGURE 21.21.—Grain silo (tank) at the Coalinga Feed Yard (*A*) moved 10 to 12 in. (*B*). It was partly filled with grain at the time of the earthquake and appeared to have no bottom.

22. EARTHQUAKE DAMAGE TO THE COALINGA OIL FIELDS

By J.P. HUGHES, W. WON, and R.C. ERICKSON,[1]
CHEVRON U.S.A., INC.

CONTENTS

ABSTRACT

The May 2 earthquake caused local damage to oil-field installations and shut down all production for 1 day. By the end of July 1984, the oil fields had returned to their former 30,000 bbl/d of production. Most oil-field damage occurred at surface facilities, and very little in subsurface facilities. No surface or subsurface damage patterns could be associated with active-fault movements. Also, no preearthquake production changes were noted that could have been interpreted as precursors of the earthquake.

INTRODUCTION

The town of Coalinga is almost completely surrounded by oil fields (fig. 22.1). The history of oil in the Coalinga area dates from the late 1800's, and the first production began in 1890. All of this early production came from Cretaceous rocks in the Oil City area (fig. 22.2). When statistical recording of oil production began in 1896, yearly production was only 14,119 bbl (or just over 38½ bbl/d). Shortly thereafter, drilling spread to the main Coalinga oil field (fig. 22.2), where production was found in the Temblor (Oligocene and Miocene) Formation. Notwithstanding the low price of oil, which dropped down to $0.15/bbl in 1905, drilling increased more or less steadily until 1920, when annual production reached about 16 million bbl. The next year, an oil workers' strike started a slump in production that lasted until about World War II, when an increasing demand again caused drilling to pick up. By that time, drilling had spread to the East Coalinga Extension (fig. 22.3) and Pleasant Valley fields (fig. 22.1). In 1948, commercial hydrocarbons were discovered at the Guijarral Hills (fig. 22.1). Commencing in 1953, a secondary-recovery project, in the form of a pilot water flood, was started in the Coalinga field. This project proved successful and was expanded to cover a considerable surrounding area. Other smaller water floods have also been started since the early 1960's. The latest secondary-recovery projects, which are proving to be quite successful, involve either cyclic or continuous steam injection into the shallow Temblor oil sands. To date, some 1,256 million bbl of oil has been produced from all these Coalinga-area fields; 700 million bbl has been produced from the Coalinga field, 75 percent by 1960. A total of 500 million bbl has been produced from East Coalinga Extension, 70 percent before 1960. The Pleasant Valley and Guijarral Hills fields have produced 14 million and 50 million bbl, respectively. Currently, there are more than 2,100 actively producing wells in the Coalinga fields.

On May 2, 1983, the Coalinga main shock caused a shutdown of production over the entire area. Damage to wells and equipment in the oil fields, though minimal, was quite extensive. To assess the amount and type of damage to oil fields in the Coalinga area, field superintendents of the major producers were interviewed during the weeks following the main shock. Operators of small holdings or those lacking local offices were canvassed by mail.

In this chapter, the results have been grouped under two fairly broad categories: damage to subsurface equipment and damage to surface equipment and facilities. These summaries are followed by a discussion of damage patterns. Some brief notes on both preearthquake and postearthquake changes in oil production, and so on, are included at the end of this chapter.

[1]Deceased.

SUBSURFACE DAMAGE

Very little downhole wellbore damage was reported as a result of the Coalinga earthquake sequence. The wells reported to be earthquake damaged through March 22, 1984, are listed in table 22.1. The Shell Oil Co. wells listed in table 22.1 were the only 26 out of their 935 active wells reported to have sustained earthquake-related damage. Chevron U.S.A., Inc., has 785 wells in the Coalinga area. The "kinks" or "doglegs" found in the damaged wells were discovered by running full-bore scrapers in the wells. If the casing is straight, the scraper can generally reach the bottom of the well (fig. 22.4*A*); however, if the casing is deformed, then the scraper may be unable to get through the tight spot (fig.22.4*B*). We note that except for something striking, like parted casing, subtle wellbore or even reservoir damage might be rather hard to recognize and pinpoint.

In the Coalinga oil fields, all production is lifted to the surface by either a surface pumping unit or a gas-lift assembly. After the May 2 earthquake, all production facilities were shut down because of a massive electric-power failure. Serious subsurface damage to the wells was not apparent until an attempt was made to place each well back in production. Any minor deformation in a casing string or minor sanding caused by the earthquake may go undetected if it does not affect the mechanical functioning of the production system.

A postearthquake casing-failure pattern is not apparent in the few damaged wells reported to date. The reported failure pattern is so randomly scattered throughout the field that it appears to be related to casing corrosion (corroded sections of casing are weak points that are susceptible to damage). Although numerous shallow faults are present in the sedimentary section that makes up the productive zones, none of this damage appears to be associated with the mapped faults. Also, no evidence exists of any major reverse faulting within the productive limits of the Coalinga oil field, on the basis of abundant oil-well control.

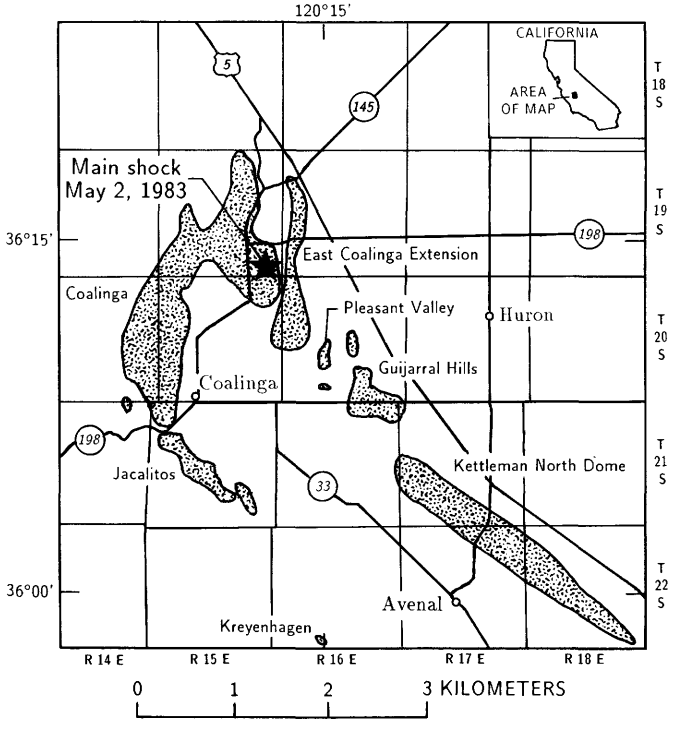

FIGURE 22.1.—Coalinga, Calif., area, showing locations of oil fields (shaded areas) and epicenter of May 2 earthquake (star). From California Division of Oil and Gas (1982).

SURFACE DAMAGE

ELECTRIC-POWER FACILITIES

The May 2 main shock cut most electric power to the oil fields. In some places, especially in the epicentral area, several days were needed to repair downed lines and damaged transformers. In other places, power was restored quickly, but the equipment was not restarted until after a damage and safety inspection was made. Several small fires were started by downed powerlines, but these fires were extinguished quickly before any equipment was damaged.

PUMPING UNITS

Although no pumping units were heavily damaged, many units were jostled out of alignment, anywhere from 2 to 10 cm. For example, the Shell Oil Co. reported that some 60 percent of their units in secs. 10, 14, 15, and 29, T. 19 S., R. 15 E., had to be realigned. Chevron U.S.A., Inc., reported that 105 of their units moved around; most movement was located in secs. 28 and 35, T. 19 S., R. 15 E. Texaco U.S.A. likewise reported about 130 pumping units that needed to be realigned. Most other operators experienced similar problems.

OIL-STORAGE TANKS

Oil-storage tanks in the Coalinga area sustained various types of damage as a result of the earthquake ground shaking. The damage, though widespread, was somewhat selective. In places where two or more tanks were in close proximity, it was not uncommon to find that one tank would be damaged, whereas the others were relatively untouched; no patterns have yet been found to account for this phenomenon.

Damage to tanks fell into five main categories: (1) "elephant's foot" bulges at or near the base, (2) bulges near the top, (3) settling of the tank into the gravel pad on which it sits, (4) leaks caused by shearing or buckling

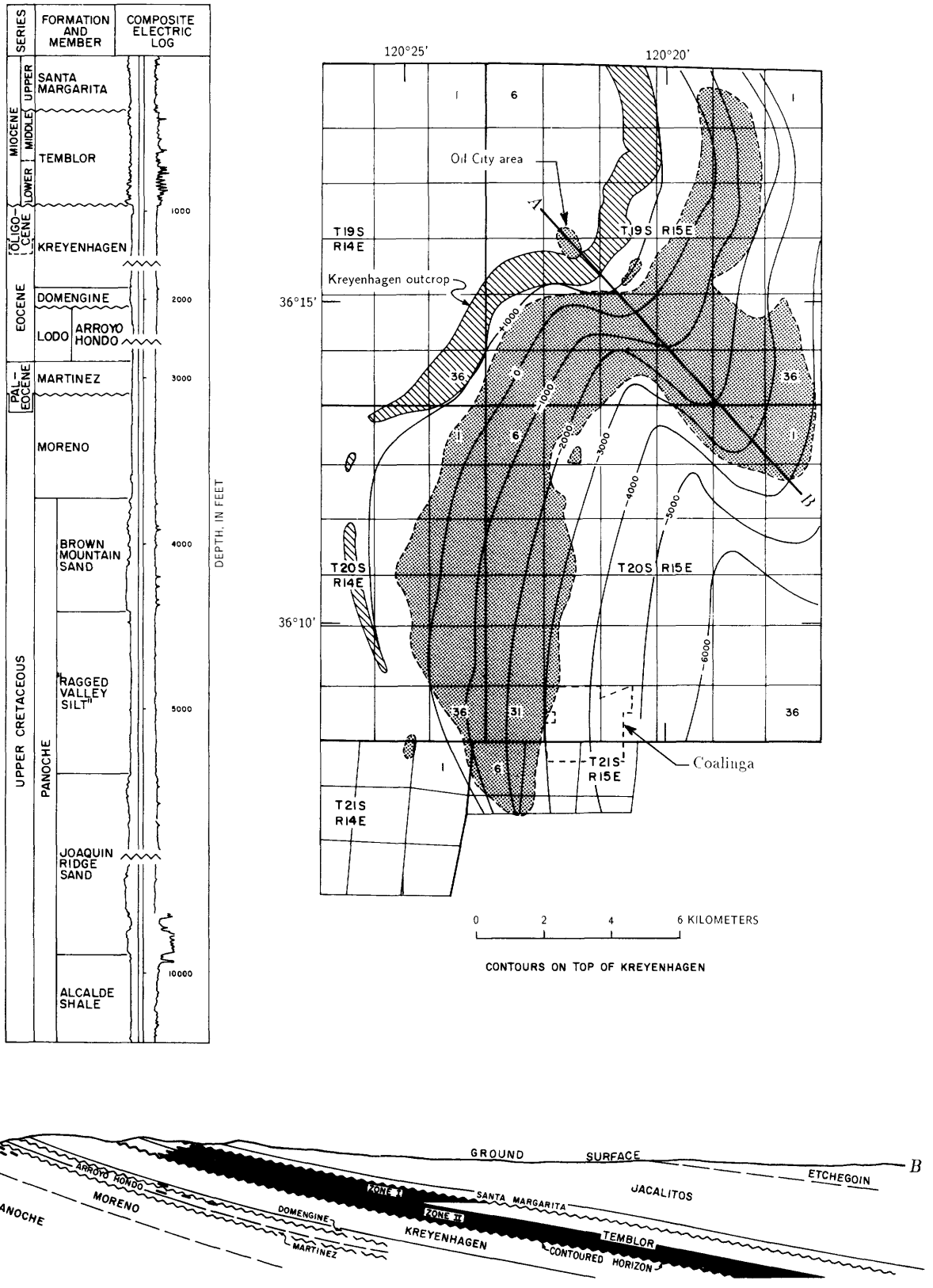

FIGURE 22.2.—Geologic information on the Westside and Anticline Ridge oil fields. From California Division of Oil and Gas (1982).

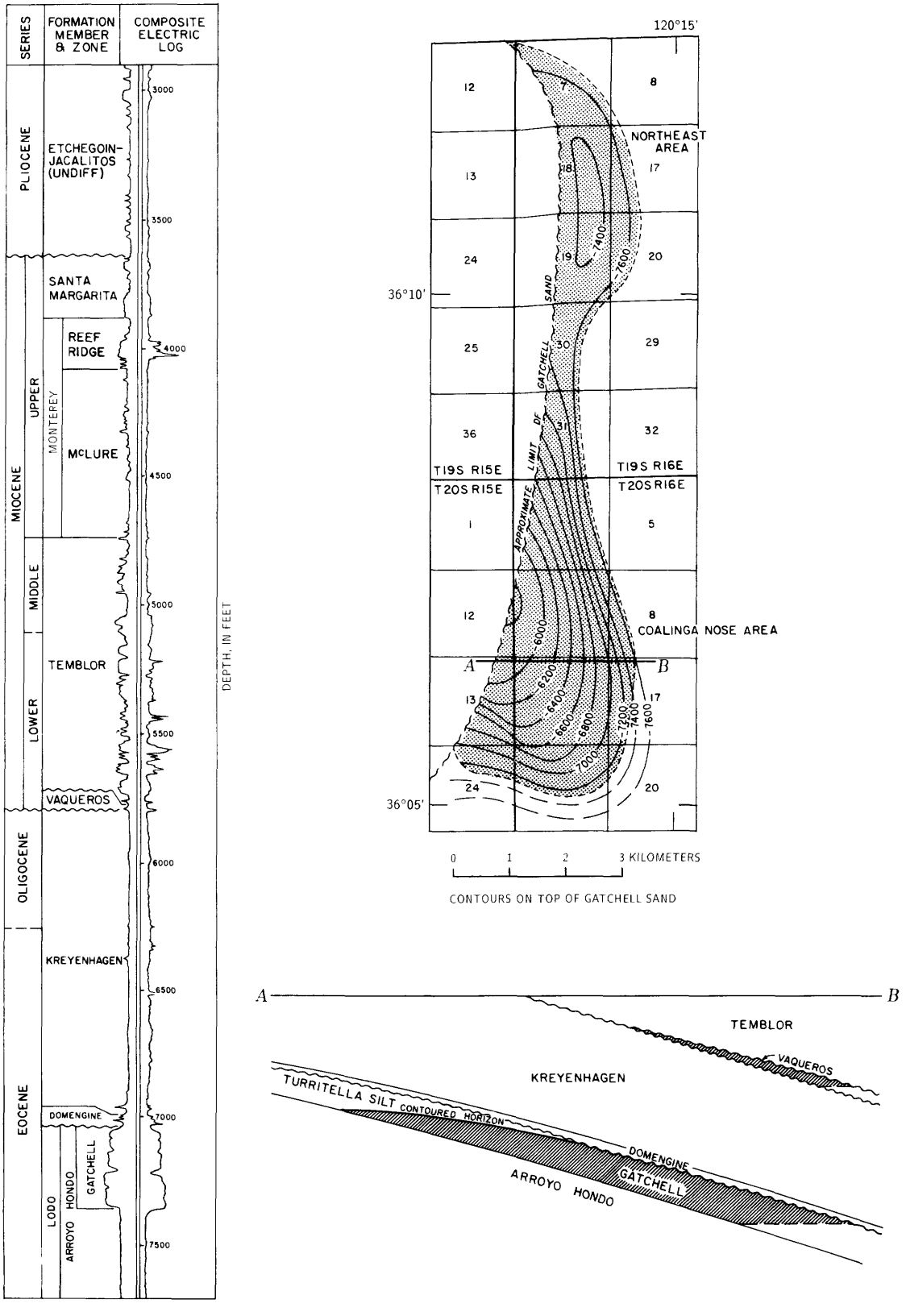

FIGURE 22.3.—Geologic information on the Northeast and Coalinga Nose oil fields. From California Division of Oil and Gas (1982).

of internal baffles, and (5) leaks caused by shearing or buckling at connections with external pipes, valves, or ladders.

"Elephant's foot" bulges were fairly common in unanchored fluid-storage tanks. The mechanism, which probably involved high hydrodynamic pressures imposed onto one side of the tank, is illustrated in figures 22.5 and 22.6*A*. In other cases, liquid slosh and the resulting hydrodynamic pressures were strong enough to cause bulging and occasional rupturing of one of the upper rings in partly full storage tanks. As might be expected, the damage occurred on the two opposite sides of the tanks as the contents sloshed back and forth (figs. 22.6*B*, 22.7).

Ground shaking during the Coalinga earthquake sequence caused several tanks to settle into their gravel pads some 1 to 10 cm. In a few tanks, this settling sheared off one or more of the lower pipe connections, causing leaks. Some tanks had internal baffles; a few leaks appeared where bolts supporting these baffles were sheared off during the twisting motions imparted by the earthquake (fig. 22.8). The most common type of tank leak occurred at the point where external fittings (pipes, valves, ladders, and so on) were attached to the tanks. The problem was basically that these fittings were rigidly attached to both the tank and the ground. When differential movement took place between the tank and the ground during ground shaking, the fittings either sheared off or were pushed into the tank at the point of connection (fig. 22.9*A*). In one case, a catwalk ladder attached rigidly between two adjacent tanks caused the sides of both tanks to be shoved in. Although several oilspills occurred as a result of this kind of leak, most spills were contained in surrounding moats designed for that purpose.

PIPELINES

Pipelines fared rather well during the Coalinga earthquake sequence. Although numerous leaks occurred, most were small and easily repaired. Apparently, all leaks were confined to coupling joints and connections; there were no reports of lines breaking other than at a connection.

MISCELLANEOUS

Like the pumping units discussed previously, many pieces of heavy machinery slid around during the ground shaking and had to be realigned. Examples included heater-treaters, steam generators, stack scrubbers, tanks on skids, and water softeners. Most pieces moved from 1 to 20 cm.

Several support buildings and offices were also damaged. As with the buildings in Coalinga, the severity of the damage seemed to depend on the type of construction.

GROUND FAILURE

A fair amount of minor damage (buckling, cracking) was sustained by lease roads. Although most of this type of damage was found on roads in the epicentral area, some roads as far away as 10 km were also affected. A more widespread form of ground-failure-related damage involved slumping or sloughing on cut-and-fill slopes, dikes, and berms. In most places, this damage either was limited to cracking with little or no movement, or involved a downslope movement of only 5 to 7 cm. There were isolated examples, however, where movement amounted to 30 cm or more. Once again, the slumping and sloughing was more serious in the epicentral area. A more detailed report of ground failures in the Coalinga area was presented by Keefer and others (1983) and is included in chapter 18.

SURFACE DISPLACEMENT PATTERNS

There appears to have been a persistent pattern in terms of the dominant direction of movement of surface objects during the earthquake shaking. As a general rule, most movement appears to have been in either an east-westward or northeast-southwestward direction, as illustrated by the following examples:

1. Many of the large pieces of heavy equipment and pumping units that slid did so to the northeast or southwest.
2. Pipelines running approximately north-south were generally undamaged, whereas most ruptures and, thus, leaks occurred on east-west-trending lines.
3. Equipment supported on stilts or short legs was generally found to be leaning either northeastward or southwestward.
4. Many of the bulges and "elephant's feet" found near the bases of damaged tanks occurred on the northeast and (or) southwest sides.
5. A pillar supporting an awning over a motorpool gas pump broke at an old weld, and the upper part of the pole moved east-northeastward.
6. During one major aftershock, several people reported that objects (books, hanging pictures, and so on) on the west walls of their homes and offices were thrown down during the initial motion. Similar items on their east walls, however, stayed in place, an observation indicating a possible initial ground movement from east to west (fig. 22.10).
7. A large free-standing desk in the downtown Coalinga office of the California Division of Oil and Gas (CDOG) slid along a newly polished floor, scratching out a trace of its path. Figure 22.11 shows a copy of this trace, which is probably a record of the building's motion as it slid around under the desk. We note that the net movement of the desk was east-northeasterly,

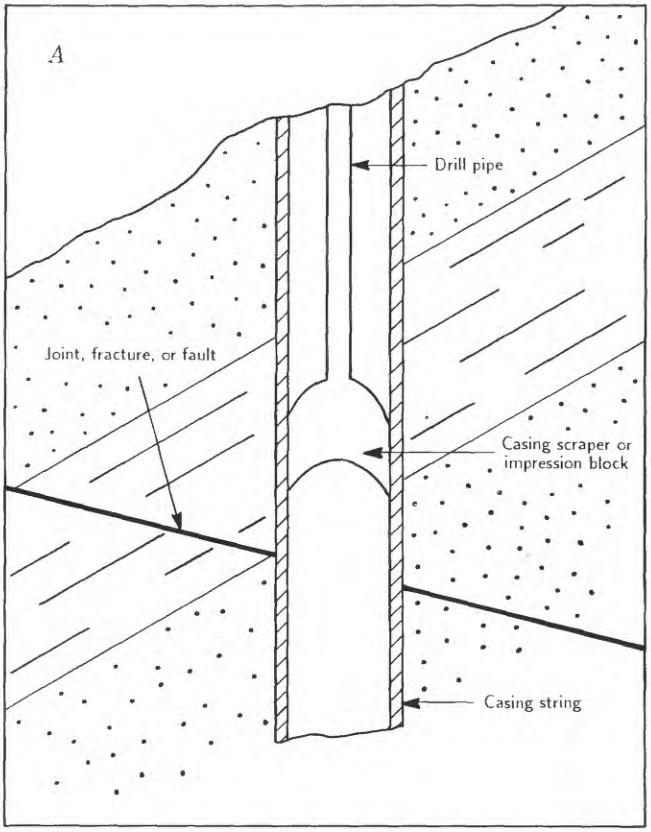

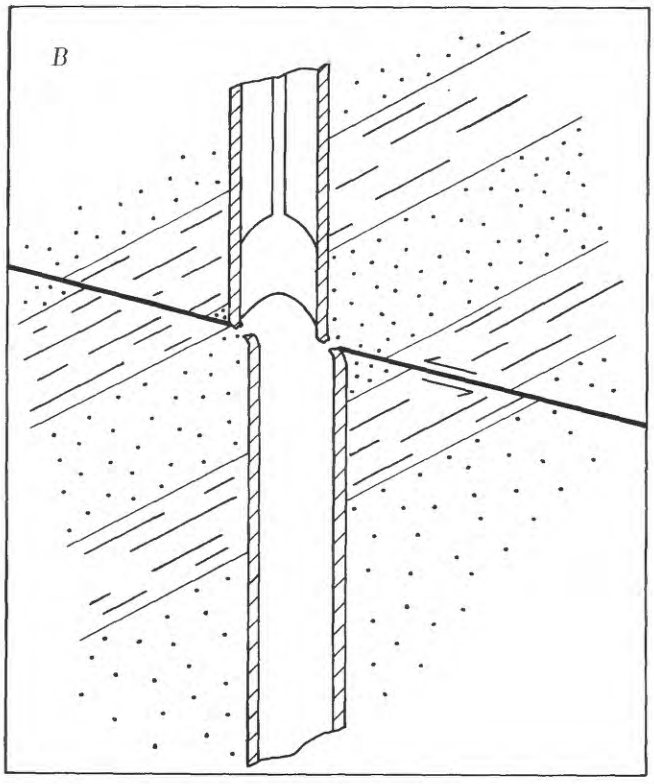

FIGURE 22.4.—Profile through a casing string, showing detection of deformation caused by movement on a fault. *A*, Before the earthquake. *B*, After the earthquake. Arrows, direction of relative movement.

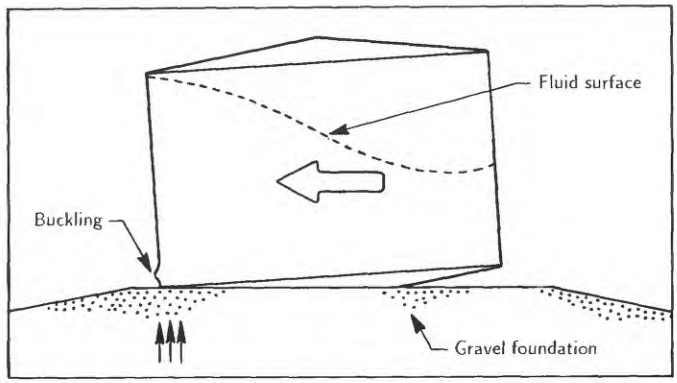

FIGURE 22.5.—Mechanism for "elephant's foot"-type damage in cylindrical storage tanks. Arrows indicate vertical component of ground motion.

FIGURE 22.6.—Storage-tank damage. *A*, "Elephant's foot" bulge at base of storage tank in sec. 13, T. 20 S., R. 14 E. *B*, Bulge and rupture in Shell Oil Co. storage tanks in sec. 26, T. 19 S., R. 16 E., probably caused by mechanism illustrated in figure 22.7.

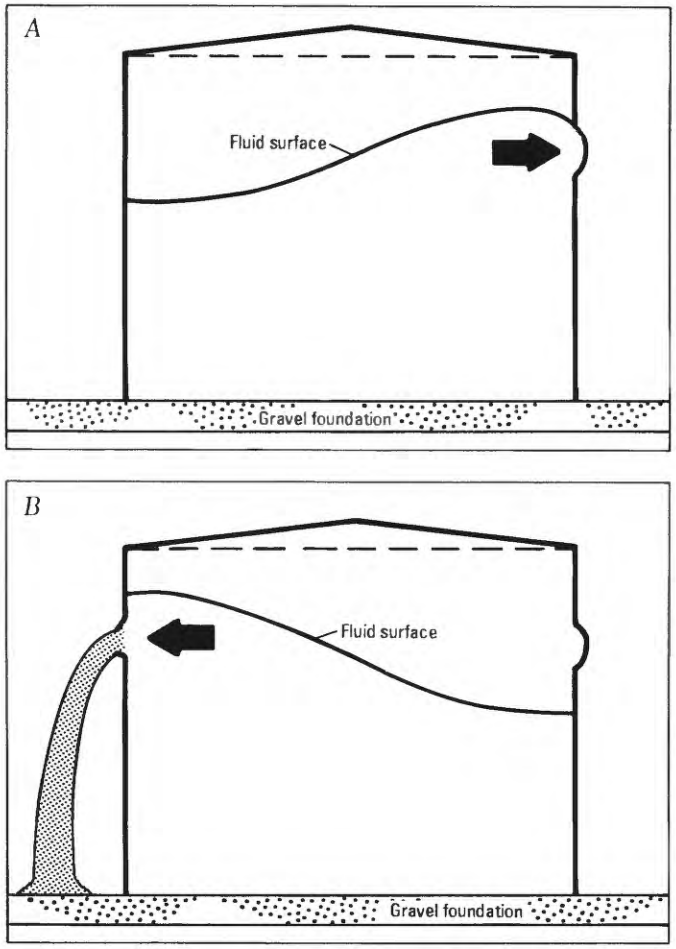

FIGURE 22.7.—Probable mechanism (liquid slosh) for damage sustained in upper rings of cylindrical storage tanks during successive sloshes (*A*, *B*).

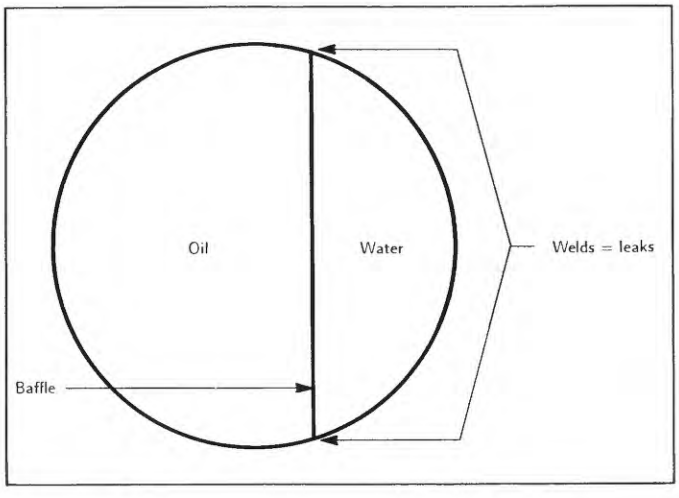

FIGURE 22.8.—Top view showing location of damage in storage tanks with internal baffles.

indicating that the building's net movement was probably west-southwestward.

PREEARTHQUAKE PRODUCTION PATTERNS

We made a quick review of the preearthquake production records reported to CDOG to detect significant variations that might have been precursors of the earthquake. Neither these records nor a more detailed search of Chevron U.S.A., Inc.'s production records revealed any significant changes before the May 2 earthquake.

Some inherent problems exist in the use of oil-field production records for the identification of possible tectonic-pressure changes within the Earth's subsurface. A major problem centers on the frequency with which individual wells are gaged. According to the records of the Conservation Committee of California Oil Producers (1982), the average Coalinga oil-field well produces only

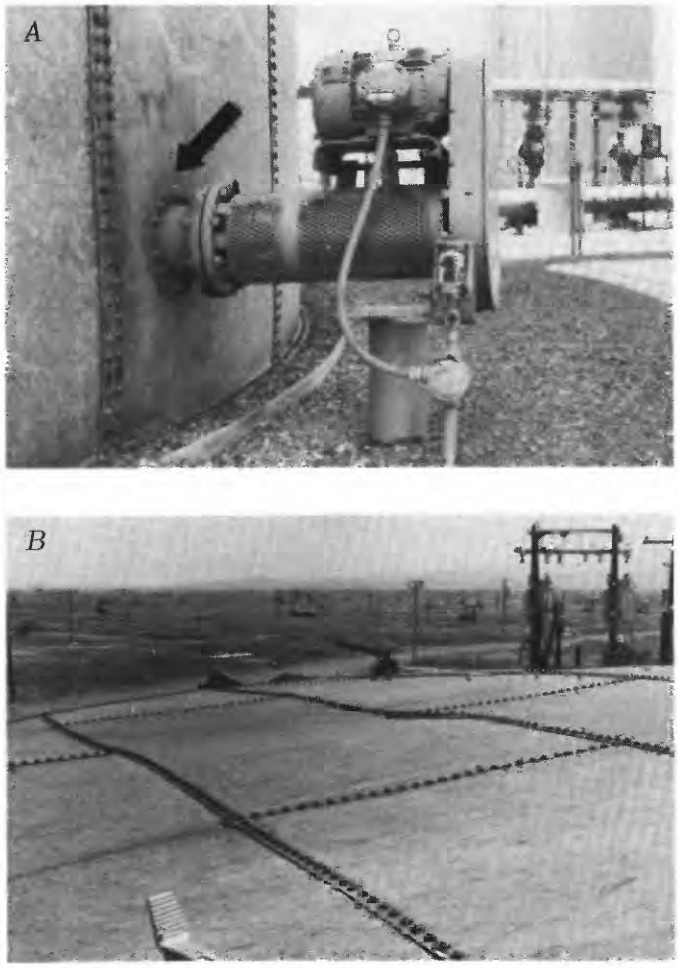

FIGURE 22.9.—Storage-tank damage. *A*, Indentation (arrow) caused by relative movement of storage tank and mixer support column anchored to grade. *B*, Ripples in top of a storage tank in sec. 13, T. 20 S., R. 14 E.

about 12 bbl/d. Because of these low daily rates, it generally is standard practice for most operators to gage individual wells on a set, but periodic, schedule. For example, a well producing no more than 3 bbl/d may be gaged only once every 5 days; thus, a significant short-term change in production might go unnoticed. Total lease-production records, however, are accurately maintained for payment of royalties. It appears that other than for a few individual well-production changes, no overall significant production changes occurred before the earthquake.

The next problem involves reservoir-pressure recordings. Unless the production is coming from a significant project, this type of record is generally unobtainable. A significant project ordinarily involves a secondary-recovery operation. In the case of water floods, the injection pressures and injection intervals are periodically checked by CDOG to ensure that they are not exceeding the limits set by their initial approval of the project. These projects, as well as the cyclic-steam-injection projects, create a dynamic situation within the reservoir that will most likely mask any pressure changes due to outside tectonic forces. This masking is particularly evident in cyclic-steam-injection projects, where production changes quite rapidly over a short period (fig. 22.12).

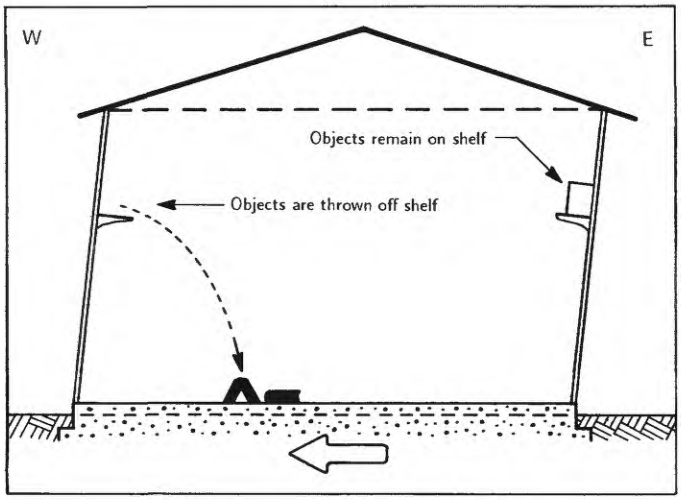

FIGURE 22.10.—Response of objects on shelves in oil-field-operation offices to initial ground motion in one of the numerous aftershocks.

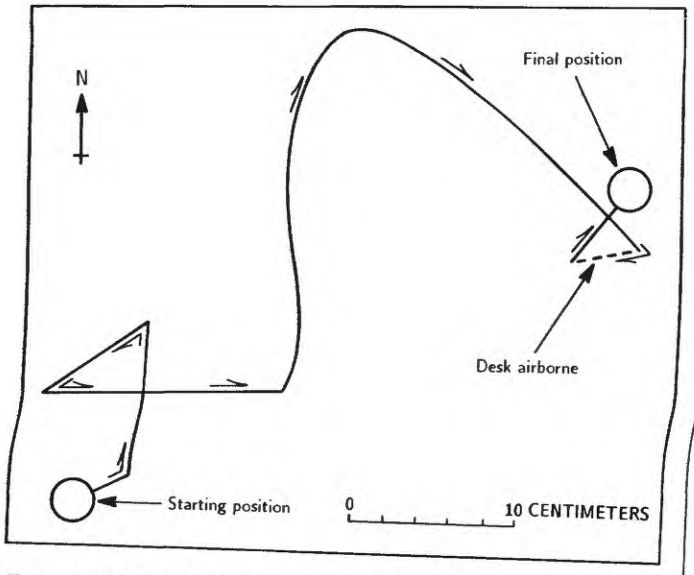

FIGURE 22.11.—Relative movement of a large, freestanding desk in Coalinga during the May 2 earthquake.

POSTEARTHQUAKE PRODUCTION PATTERNS

Most active wells showed little or no change in production other than a short break due to the main shock and

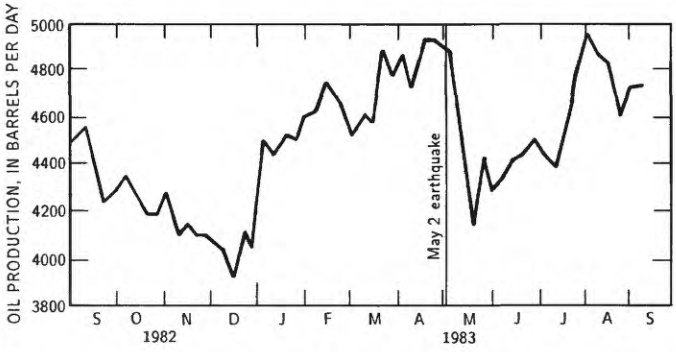

FIGURE 22.12.—Oil-production history for all Chevron U.S.A., Inc.'s wells in sec. 13D, T. 20 S., R. 14 E. A steam flood was in operation at the time of the earthquake.

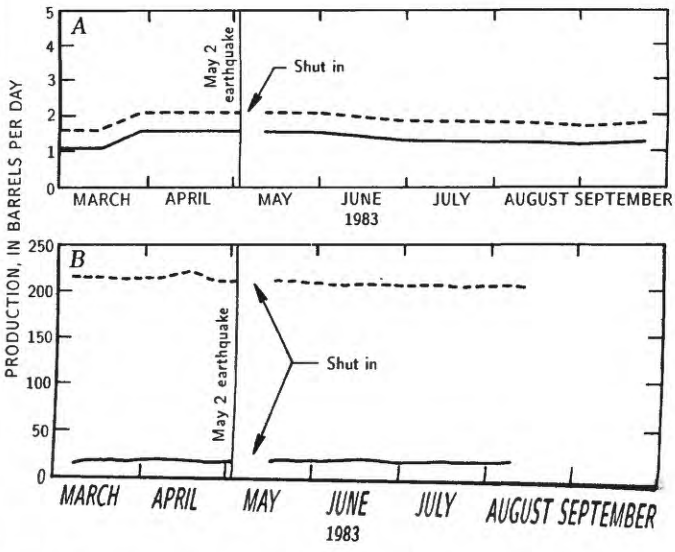

FIGURE 22.13.—Production history of wells relatively unaffected by the earthquake. Solid curve, oil; dashed curve, total fluids. "Shut in" refers to the period of time during which the production pump was turned off after the May 2 main shock. *A*, A low-water-cut well, Chevron No. 13, in sec. 11A, T. 19 S., R. 15 E. *B*, A high-water-cut well, Chevron No. 6–10, in sec. 13D, T. 20 S., R. 14 E.

subsequent power failure (fig. 22.13). A few wells either could not be returned to production by their operators or sputtered and died shortly after the main shock (fig. 22.14). The primary problem in these cases appears to have been heavy "sanding" of the wells; that is, the wells began to produce mostly sand and thus were uneconomical to continue to operate. Another small percentage of active wells did show a change in production rates. Some of the wells in this group eventually returned to "normal" production levels within a few months (figs. 22.15, 22.16), whereas others remained at slightly abnormally high fluid levels (fig. 22.17). No pattern, however, is evident in these various responses.

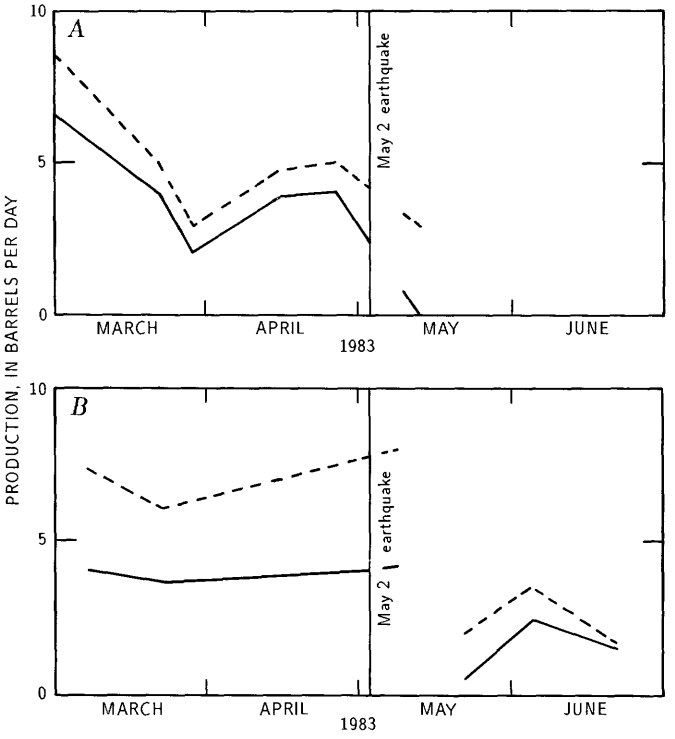

FIGURE 22.14.—Production history of wells that sanded up as a result of ground shaking due to the earthquake. Solid curve, oil; dashed curve, total fluids. *A*, A low-water-cut well, Chevron No. 2–4, in sec. 5E, T. 21 S., R. 15 E. *B*, A moderate-water-cut well, Cal-Calg-Lakeport No. 24.

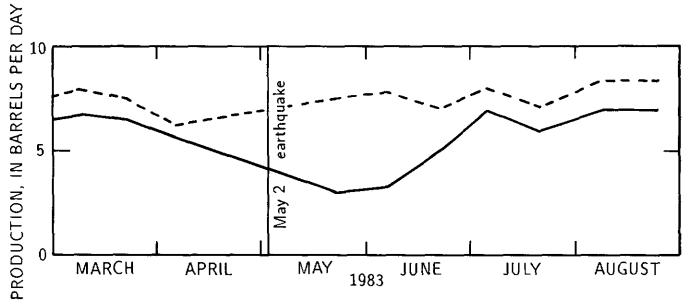

FIGURE 22.15.—Production history of Chevron U.S.A., Inc.'s well No. 59, in sec. 28., T. 19 S., R. 15 E., showing a production change immediately after the earthquake. Solid curve, oil; dashed curve, total fluids. Total production stayed near normal, while water cut increased for a short period.

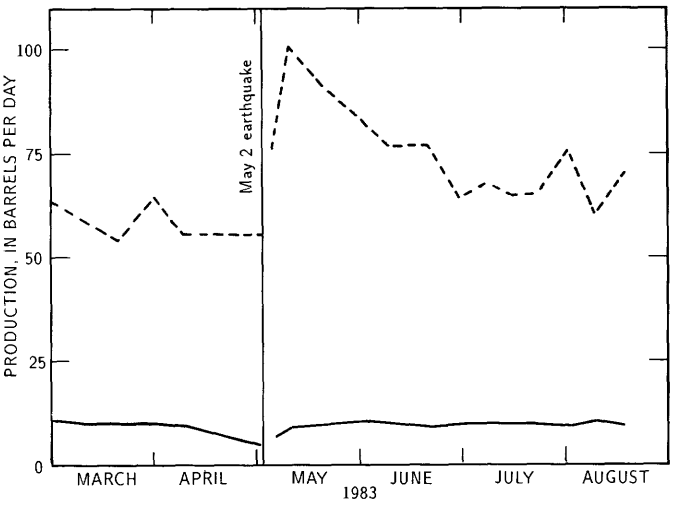

FIGURE 22.16.—Production history of Chevron U.S.A., Inc.'s well No. 10–5 in sec. 7C, T. 20 S., R. 15 E., showing an increase in water production after the earthquake and a later return to normal production. Solid curve, oil; dashed curve, total fluids.

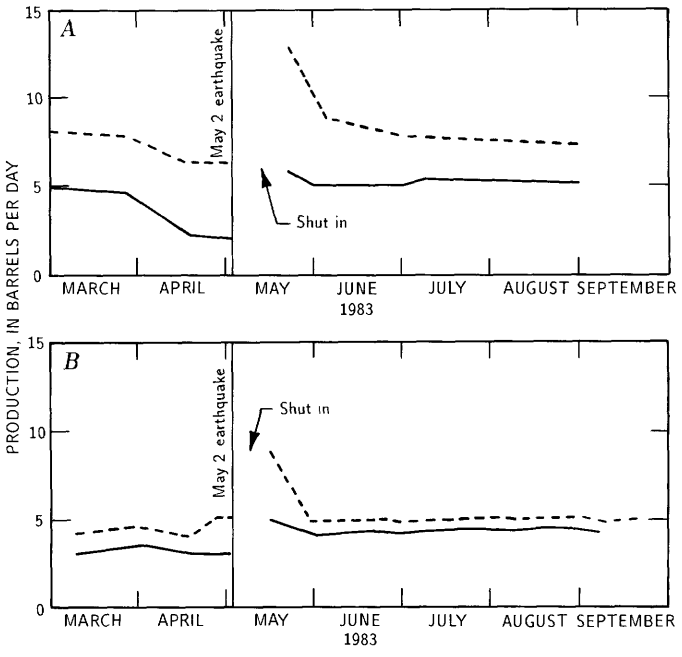

FIGURE 22.17.—Production history of two Chevron U.S.A., Inc., wells, showing temporarily high water production after the earthquake. Solid curve, oil; dashed curve, total fluids. "Shut in" refers to the period of time during which the production pump was turned off after the May 2 main shock. *A*, Well No. 6–6, in sec. 31A, T. 19 S., R. 15 E. *B*, Well No. 28, in sec. 22E, T. 21 S., R. 15 E.

ACKNOWLEDGMENTS

We thank Chevron U.S.A., Inc., for permission to publish these data. The following individuals generously provided information on oil-company facilities damaged by the earthquake: Carl Bidinger (Union Oil Co. of California), Cal Bottum (Santa Fe Energy Co.), Dick Lewis (Shell Oil Co. of California), Jim McDaniel and Myles Monroe (Chevron U.S.A., Inc.), and John Young (Texaco U.S.A.). E.J. Fowkes, a geologist at West Hills College in Coalinga, Vic Van Matre of the California Division of Oil and Gas, Coalinga office, and Tom Wright of Chevron U.S.A., Inc., also provided useful information.

REFERENCES CITED

Arnold, Ralph, and Anderson, Robert, 1910, Geology and oil resources of the Coalinga district, California: U.S. Geological Survey Bulletin 398, 354 p.

California Division of Oil and Gas, 1982, California oil and gas fields, central California, (4th ed.): Sacramento.

Conservation Committee of California Oil Producers, 1982, Field and pool production, [sec.] K *of* Production record, pt. 2 *of* Annual review of California oil and gas production, 1982: Los Angeles, p. K–1 to K–160.

Kaplow, E.J., 1945, Coalinga oil field: California Division of Oil and Gas Summary of Operations—California Oil Fields, v. 31, no. 2 (California State Oil and Gas Supervisor Annual Report 31), p. 5–22.

23. RESPONSE OF CREEPMETERS ON THE SAN ANDREAS FAULT NEAR PARKFIELD TO THE EARTHQUAKE

By SANDRA S. SCHULZ, GERALD M. MAVKO,[1] and BETH D. BROWN,
U.S. GEOLOGICAL SURVEY

CONTENTS

ABSTRACT

A total of 14 U.S. Geological Survey creepmeters on the San Andreas fault in central California recorded coseismic steps coincident with the M=6.7 May 2 earthquake. Creepmeters near Parkfield recorded the largest effects. Postearthquake creep rates slowed significantly, and creep at one station reversed to left lateral. About 4 months after the earthquake, decreased rates caused cumulative creep at four Parkfield stations to fall below long-term linear trends observed before May 2. At several stations, creep continued to be either left lateral or slower than normal for the rest of 1983. By January 31, 1984, all but two stations recorded resumption of right-lateral creep at reduced rates. As late as April 1, 1984, however, one station north of Parkfield continued to record left-lateral drift, and another station at the south end of the creeping section south of Parkfield recorded little or no movement. One interpretation of the creep slowdown after May 2 is that the Coalinga main shock released accumulated stress in the upper kilometer or so of the San Andreas fault near Parkfield, and several months elapsed before stress built up sufficiently to allow creep to resume. A multiple-linear-regression analysis of coseismic-step size as a function of distance from the creepmeter to an earthquake focus and (or) earthquake magnitude showed a linear correlation between step size and magnitude for the data from two stations. No correlation was found between step size and distance to focus for the data from any of the stations. Reduction in step sizes after May 2, despite numerous large aftershocks, suggests that stored local stress is the dominant factor in coseismic-step size.

INTRODUCTION

Mavko and others (1984) reported that U.S. Geological Survey (USGS) creepmeters along 190 km of the San Andreas fault in central California recorded coseismic steps coincident with the M=6.7 May 2 earthquake and several of its larger aftershocks (fig. 23.1; table 23.1). Two stations at the south terminus of the normally creeping zone near Cholame recorded left-lateral steps (creepmeter contraction), and 12 stations northward toward San Juan Bautista station recorded right-lateral steps (creepmeter extension). The San Juan Bautista station showed no response. Mavko and others concluded that these steps represented slip induced in the upper kilometer or so of the San Andreas fault.

Creepmeters near Parkfield recorded the largest steps on May 2, followed by a marked change in creep rates at several stations, and a reversal of creep direction at one station (figs. 23.1, 23.2). In this chapter, we discuss the changes induced in Parkfield long-term creep trends and the significance of the size of coseismic creep steps.

OBSERVATIONS

In addition to the coseismic-creep steps observed along the San Andreas fault, plots of cumulative creep for the 10 months following the Coalinga main shock show a marked disruption of long-term trends at eight stations near Parkfield (fig. 23.2). Long-term rates determined for USGS creepmeters in central California before the Coalinga earthquake sequence were presented by Schulz and others (1982); they are summarized along with newer calculated rates in table 23.2.

STATION RESPONSE TO THE MAY 2 EARTHQUAKE

The USGS creepmeter is an Invar wire, 10 to 30 m long, installed across a fault trace at 30°–45° to the fault strike. An onsite recorder samples the wire's position relative to a sensor every 2 s and produces a continuous data trace on a strip chart. At 10-minute intervals, a telemetry system transmits the most recent data point to a USGS computer in Menlo Park, Calif. Descriptions of

[1]Current affiliation: Department of Geophysics, Stanford University, Stanford, CA 94305.

the creepmeter and telemetry instrumentation have appeared elsewhere (Roger and others, 1977; Schulz and others, 1982).

Station XSC1 (Slack Canyon) commonly records 23 mm/yr of event-free creep, on the basis of 1983 totals (fig. 23.2; table 23.1). The coseismic step and subsequent slowdown at station XSC1 and at two other stations are listed in table 23.3 for two earthquakes, the Coalinga main shock and an $M=5.5$ earthquake 23 km northwest of Coalinga on October 25, 1982. The 5-month slowdown in 1983 is the most extensive rate change seen in 14 years of recording at this site. Station XSC1 also recorded right-lateral steps during several $3.4 \leq M_L \leq 4.3$ Coalinga aftershocks about 35 km distant. However, no aftershocks of $M<5.0$ were recorded after May, even though aftershocks in this range continued through December 1983. Station XSC1 recorded slight accelerations during rainfall in 1980 and 1983. Rain began falling in September 1983, about the same time that creep resumed slower than the previous long-term rate.

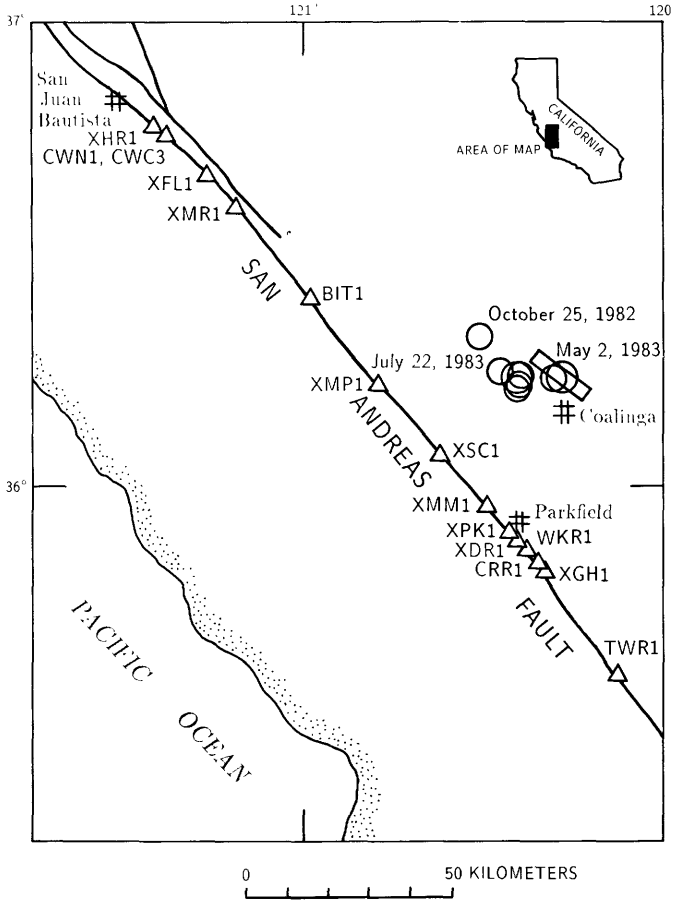

FIGURE 23.1.—Sketch map of the Coalinga, Calif., area, showing locations of U.S. Geological Survey creepmeter stations (triangles) that recorded coseismic steps on May 2, 1983, and during several aftershocks. Rectangle, epicentral area of main shock; circles, larger aftershocks.

Station XMM1 (Middle Mountain) recorded 18 mm/yr of right-lateral creep during the 3½ years between installation in 1979 and early 1983. Immediately after the May 2 earthquake, the creep direction reversed to left lateral, at approximately one-third the previous rate. This trend gradually decayed and appeared to be ending in early December 1983. However, after a right-lateral event during rain in January 1984, left-lateral movement resumed and continued to the present (April 1984).

Within the timing accuracy of the telemetry record from station XMM1 (±9 minutes), left-lateral steps occurred during 19 Coalinga aftershocks of $M_L \geq 3.4$ and distances of about 35 km. The strainmeter at station CLS1, 1 km west of station XMM1, recorded 13 of the same aftershocks as north-south extensional steps ranging from 8×10^{-9} to 8.2×10^{-8} strain (Alan Jones, oral commun., 1983). Station XMM1 continued to record local response to these distant aftershocks until December 1983. On December 21, both stations recorded a step coincident with an $M=3.6$ Coalinga aftershock; but for this event, station XMM1 recorded right-lateral movement, and station CLS1 recorded contraction. The magnitude of aftershocks decreased after December, and no other coseismic steps have been seen on the records from station XMM1.

Station XPK1 (Parkfield) recorded creep at 7.5 mm/yr from its installation in 1979 to 1983. On May 2, the second largest coseismic step on the fault was recorded at station XPK1 (6.6 mm), and two aftershocks about 35 km distant with magnitudes of 4.0 and 4.7 were recorded shortly afterward. Station XPK1 recorded right-lateral accelerations in the unusually wet winters of 1979–80 and 1982–83. This acceleration, added to the May 2 step, caused cumulative creep to exceed by 10.5 mm the linear trend through 1980. After a 9-month creep slowdown, cumulative creep at station XPK1 remained above the trend through 1983 (fig. 23.2).

Station XDR1 (Durham Ranch) recorded 8 mm/yr of right-lateral creep from 1969 to 1983 through the noise of large extensions in winter and contractions in spring, and a rebound from a spring dip was underway when the May 2 earthquake occurred. This station recorded a 1.81-mm step, in contrast to 6.6 mm recorded at station XPK1 north of it and 8.2 mm recorded at station WKR1 south of it. Since then, the creep rate at station XDR1 appears to have stabilized to near normal. Close to station XDR1, fractures were photographed 11 days before the June 27, 1966, Parkfield, Calif., earthquake (Wallace and Roth, 1967).

Station WKR1 (Work Ranch) had a long-term creep rate of 11 mm/yr until an unexplained slowdown in late 1981. A large right-lateral acceleration was underway

TABLE 23.1.—*Observed coseismic steps*

[Station location is distance southward along fault from San Juan Bautista. All values in millimeters; accuracy, ±0.05 mm except where noted. Negative numbers indicate left-lateral movement. Dashes, no data; NA, no apparent step]

Stations, north to south	Location (km)	10/25/82 $M_L = 5.4$	5/2/83 $M_L = 6.7$	5/9/83 $M_L = 5.3$	6/11/83 $M_L = 5.2$	7/9/83 $M_L = 5.4$	7/22/33 $M_L = 6.0$	7/22/83 $M_L = 5.0$	7/25/83 $M_L = 5.3$	Range of typical event amplitudes
1. XHR1	17.7	NA	0.27	NA	NA	NA	NA	NA	NA	0.13–3.24
2. CWN1	21.3	.13	.24	NA	NA	.06	.09	NA	NA	.20–5.08
3. CWC3	21.3	.07	.16	NA	NA	.01	.09	NA	NA	.20–5.08
4. XFL1	35.1	NA	.16	NA	NA	NA	NA	NA	NA	.21–2.16
5. XMR1	47.1	.14	[1]	NA	.08	NA	.26	NA	NA	.05–2.70
6. BITI	75.3	.48	--	--	--	.17	[2].01	NA	[(2)].15	.10–6.70
7. XMP1	101.8	.09	[2]1.08	NA	NA	--	--	--	--	−.80 to 0.36
8. XSC1	123.4	.23	3.3	NA	NA	NA	.08	NA	.06	.11–0.61
9. XMM1	139.7	.13	2.7	−.07	−.12	−.10	−.12	NA	−.09	.06–1.04
10. XPK1	148.6	.36	6.6	NA	.07	NA	−.13	NA	−.29	.10–1.09
11. XDR1	150.0	.05	1.81	.04	NA	.05	.03	NA	NA	−.44 to 2.30
12. WKR1	154.2	.10	8.22	.02	.06	.05	−.07	−.03	−.01	.03–0.21
13. CRR1	157.0	−.04	[2].50	NA[3]	NA[3]	--	NA[3]	NA[3]	NA[3]	1.67–2.25
14. XGH1	158.8	NA	−.19	NA	NA	−.01	.05	−.01	.05	.12–1.61
15. TWR1	193.7	NA	−.75	--	−.74	−.03	−.02	.02	NA	−1.17 to 0.49

[1] Shaking only, no coseismic step. A 1.54-mm creep event began within 5 minutes after the earthquake.
[2] Irregularities in data change accuracy to within ±0.08 to ± 0.90.
[3] Possible electronic problems.

when the May 2 earthquake occurred. This station recorded the largest coseismic step on the fault (8.2 mm) on May 2, and then creep returned to the 1981 slow rate. Right-lateral creep resumed in January 1984. Between stations WKR1 and CRR1, an irrigation pipeline across the fault ruptured and separated about 9 hours before the 1966 main shock (Wallace and Roth, 1967).

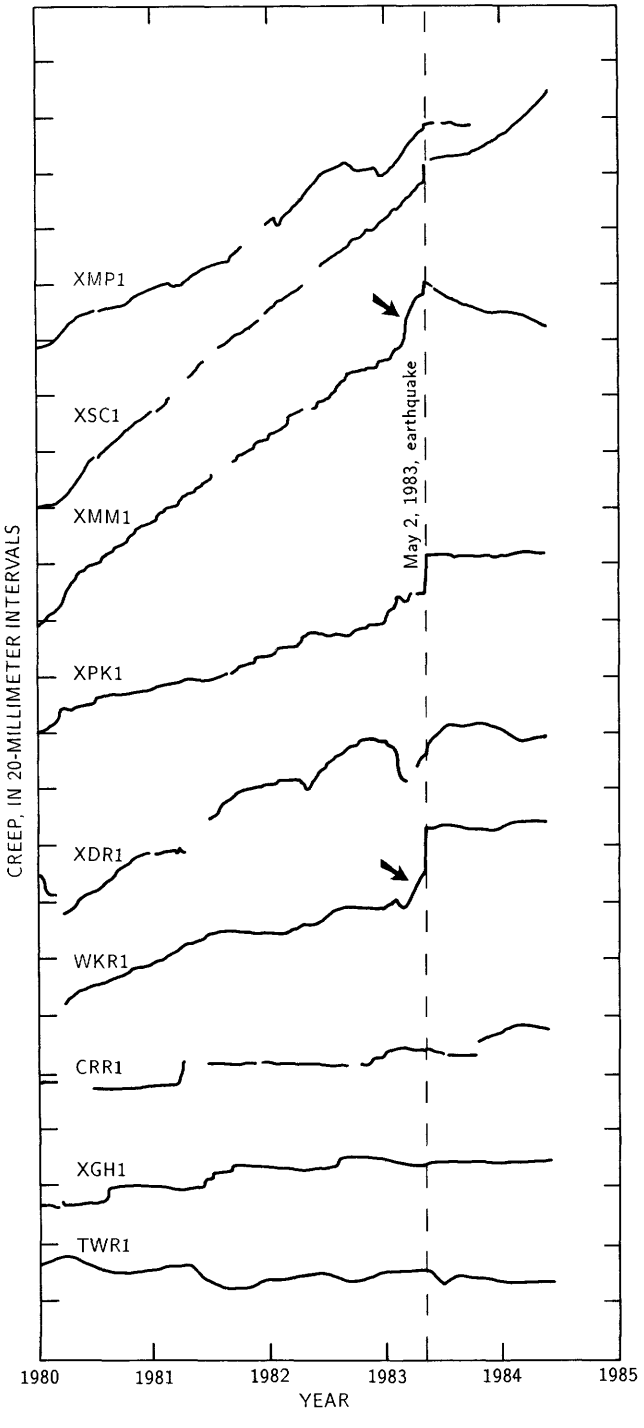

FIGURE 23.2.—Long-term creep patterns at stations near Parkfield, reflecting disruption of creep rates after May 2, 1983. Arrows indicate surges that may represent reactions to excessive rainfall.

TABLE 23.2.—*Annual creep rate, calculated using least-squares-fit method*

Station	Rate from	To Nov. 1980	To Oct. 1981	To Jan. 1983
XSC1–Slack Canyon - - -	6/1969	23.36	23.12	22.82
XMM1–Middle Mountain -	10/1979	22.43	19.68	18.03
XPK1–Parkfield - - - -	10/1979	12.56	7.39	7.52
XDR1–Durham Ranch - -	7/1969	8.44	8.47	8.63
WKR1–Work Ranch - - -	5/1976	11.02	10.40	9.53
CRR1–Carr Ranch - - -	5/1966	6.92	6.17	5.18
XGH1–Gold Hill - - - -	7/1969	3.49	3.69	3.79
TWR1–Twisselman Ranch -	11/1976	.94	[1]−3.13	[1]−1.89

[1]Negative value indicates that left-lateral creep is predominant.

TABLE 23.3.—*Slowdown at three Parkfield, Calif., stations after two Coalinga earthquakes*

Station	10/25/82, $M = 5.4$ Coseismic step size (mm)	10/25/82, $M = 5.4$ Postearthquake slowdown (days)	5/2/83, $M = 6.7$ Coseismic step size (mm)	5/2/83, $M = 6.7$ Postearthquake slowdown (mo)
XSC1	0.23	21	3.3	5
XMM1	.13	36	2.7	?
XPK1	.36	28	6.6	9

Station CRR1 (Carr Ranch) recorded 10 mm/yr of creep from 1966 to 1978 (Scholz and others, 1969; Goulty and Gilman, 1978). Creep abruptly halted in 1978 and began again in 1981 at a reduced rate (6 mm/yr). Results of future alignment surveys at this station should help explain the change, if it results from a new site of creep within the fault zone. We note here only that station CRR1 recorded a small right-lateral step on May 2, followed by a creep lag. Although a lag is not unusual here, an apparent right-lateral acceleration in October 1983 is of interest if it signals a return to the pre-1978 rate.

Station XGH1 (Gold Hill) recorded 3.8 mm of creep from 1969 to 1983, with right-lateral movement in late summer and left-lateral movement during winters. Left-lateral movement during winter also occurs at other sites and may result from moisture expansion of fault-gouge clay around the instrument piers (Schulz and others, 1983). This station recorded a small left-lateral step on May 2, followed by a small right-lateral creep event several days later. Creep at station XGH1 currently remains below its pre-1981 3.5-mm/yr rate.

Station TWR1 (Twisselman Ranch) monitors a section of the fault north of the Carrizo Plain thought to be locked. On May 2, this section recorded a small left-lateral (contraction) step, and subsequent creep has been left-lateral. A similar trend appeared in 1982, and may not be unusual for this station.

DISCUSSION

LONG-TERM TRENDS

The creep history of each instrument shows variations over time that make determination of a single long-term rate difficult (fig. 23.2). A station can record steady movement with only occasional events (for example, sta. XSC1), or movement that occurs primarily in events, with little steady-state creep (for example, sta. CRR1). Other patterns also occur, including left-lateral slip in winter (for example, sta. XGH1).

We infer that the tectonic-rate slowdown from 25 mm/yr (sta. XSC1) to 3 mm/yr (sta. XGH1) throughout the Parkfield area affects creep patterns, because movement appears to be concentrated in a few large events as the rate slows (fig. 22.2). We also infer that nontectonic site responses affect creep patterns. For example, the cyclical spring contraction recorded at station XDR1 (fig. 23.2) has occurred each spring for 14 years, except for the drought years of 1976 and 1977 (Schulz and others, 1982). The large accelerations recorded at stations XMM1 and WKR1 in early 1983 (arrows, fig. 23.2) may be due to excessive rainfall, and, conversely, creepmeters have recorded decreases in creep rates during drought periods (Schulz and others, 1983). All these factors complicate the calculation of long-term rates.

In the past, we have used both a least-squares-fit method and a simple line drawn between data end points to establish a creep rate. Results of these two methods differ by only about 1 mm/yr at the stations that record fairly regular movement. However, for stations that record long (1+ years) slowdowns, the results of these two methods differ by as much as 3 mm/yr (table 23.2; Schulz and others, 1982). Because of a slowdown recorded at the Parkfield stations that began in 1981, and the long pause recorded at several of these stations after the May 2 earthquake, we chose to work with the simple line method of rate determination.

Best-fit-by-eye lines were drawn through the past 3 1/2 years of data from each station to establish a point where creep might be expected to resume, if the previous trend were to continue (fig. 23.3). Our lines proved to be distorted by a slowdown that had begun in 1981 at some stations, and only station XSC1 showed resumption of movement as the trend intersected our experimental line. The other stations recorded little or no creep, or left-lateral movement (sta. XMM1).

Stations XPK1 and WKR1 both recorded resumption of some right-lateral movement in January 1984, and lines drawn from end to end of each station's data show a fairly uniform distribution of data on either side (fig. 23.3). At these two stations, similar in creep rate and site characteristics, there appear to be similar long-term creep rates that persist through periodic swings in cumulative creep total.

Station XGH1 has not yet recorded a resumption of movement (April 1984). In 1979, an anomalous period of accelerated creep began at station XGH1 that nearly coincided with a period of decreased creep at station XSC1 and with gradual slowdown at the other Parkfield stations. The May 2 earthquake probably had no effect at station XGH1 beyond the slight left-lateral coseismic step. The fault at this site apparently did not release all accumulated stress during the earthquake, because a small (0.5 mm) creep event began 6 days after the earthquake and lasted 3 days. Thus, we suggest that the changes in creep rate at station XGH1 between 1979–84, including the current slowdown, are probably related more to Parkfield earthquake cycles than to perturbations from the May 2 event.

A creep-rate decrease began at station XSC1 in 1979, shortly after creep at station XGH1 accelerated. As at

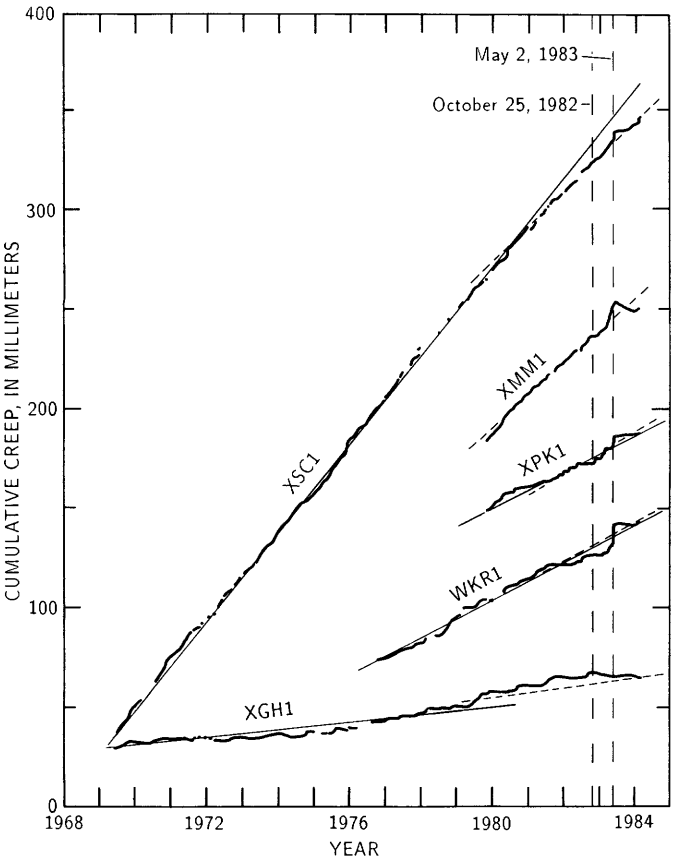

FIGURE 23.3.—Creep rates at five Parkfield stations from date of installation to January 1984. Dashed lines were drawn to project rate line, with expectation that creep would resume when data trends intersected the lines. Solid lines through data from stations XSC1 and XGH1 show change in trend in late 1979 at both stations. Solid lines through data from stations XPK1 and WKR1 show a tendency to fit a single long-term rate over a 5-year period.

station XGH1, we suggest that this long-duration change is probably related to strain changes along the San Andreas fault near Parkfield, and not to any lasting influence of the Coalinga main shock.

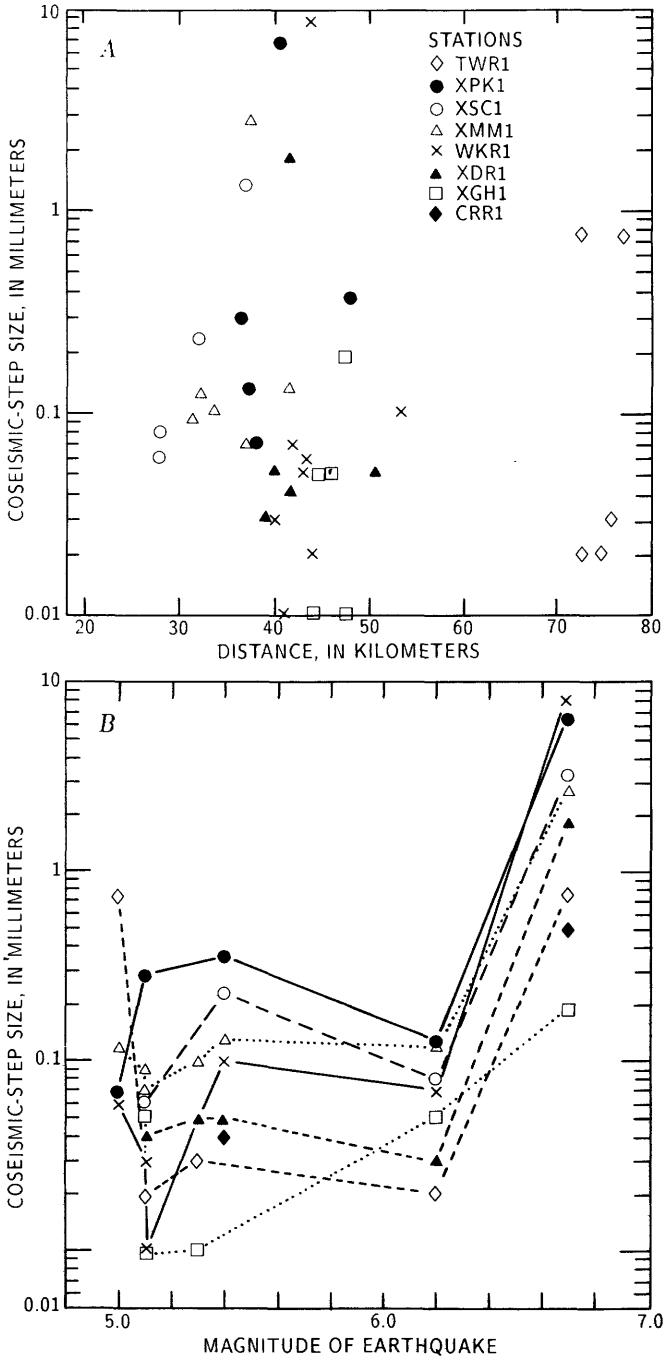

FIGURE 23.4.—Variations in coseismic-step size with distance, magnitude, and time. *A*, Coseismic-step size at seven Parkfield stations versus distance to foci for eight Coalinga earthquakes. Not all stations recorded a step for each earthquake. Data from station CRR1 are not shown because electronic problems make them suspect. *B*, Coseismic-step size at seven Parkfield stations versus magnitude for eight Coalinga earthquakes. Not all stations recorded a step for each earthquake. *C*, Coseismic-step size versus time for the three northernmost Parkfield creepmeters. Small response to M=6.0 aftershock of July 22, 1983, probably reflects absence of stored slip after large slip releases on May 2, and suggests that slip stored at a site at any given time strongly influences coseismic-step size.

No line is necessary to show that the creep at XMM1 has completely changed (fig. 23.3). Creep activity may have shifted to an adjacent trace, and the instrument may be monitoring ground-water changes instead of fault movement. The fault beneath the station may also be moving left laterally. If so, it is a local phenomenon because data from station XPK1, 8 km to the south, and station XSC1, 15 km to the north, show a resumption of right-lateral movement. Owing to station XMM1's key position near the epicenter of the 1966 Parkfield earthquake, we were relying heavily on it to record accelerated creep before the next Parkfield earthquake; thus, the abrupt change at station XMM1 after the Coalinga earthquake may make it difficult to distinguish any precursory signal from simple resumption of creep.

SIGNIFICANCE OF COSEISMIC-STEP SIZE

At stations recording large coseismic steps for the October 25, 1982, and May 2, 1983, earthquakes, Mavko and others (1984) found a weak correlation between step size and distance from the earthquake. We used those two earthquakes, as well as six M>5.0 aftershocks during May–June 1983, to try to determine the significance of the step size.

No clear linear correlations appeared in plots of step size versus distance to each earthquake's focus (fig. 23.4*A*), or to earthquake magnitude (fig. 23.4*B*). We used

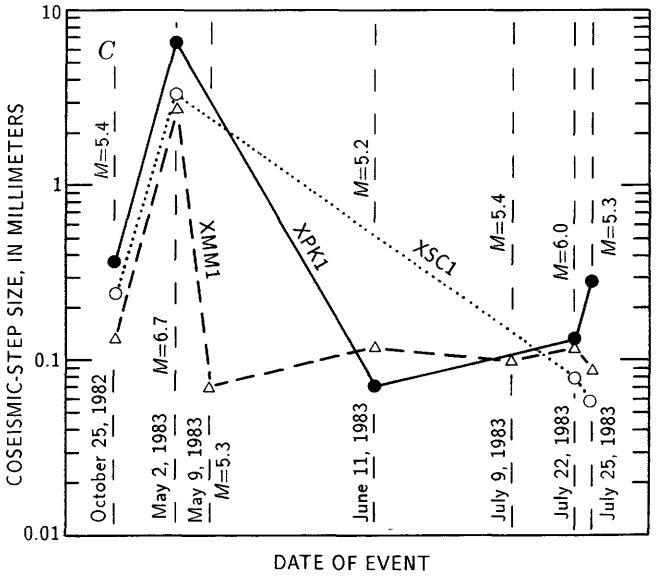

data from each station that recorded steps during five or more earthquakes, to perform a multiple-linear-regression analysis of step size as a function of earthquake magnitude and (or) distance to the earthquake focus; common logarithms of step size and distances were used. For two stations (XMM1 and WKR1), we found a linear correlation between step size and magnitude that was significant at the 95-percent-confidence level. From figure 23.4*B*, the correlation for data from station XMM1 is more understandable than that for data from station WKR1 (fig. 23.4*B*). Although data from the other four stations did not show a significant linear correlation for these two variables, positive regression coefficients for data from three of those stations indicate a weak trend. An apparent visual linearity in figure 23.4*B* appeared for the station XGH1 data, but the calculated regression coefficient was negative and the linear correlation lowest of all six stations. No data from any station showed more than a chance linear correlation between step size and distance to earthquake focus.

It may be significant that the data from stations XMM1 and WKR1, the two stations that showed statistical correlations, had the most samples (seven and eight, respectively), whereas data from the other stations had only five samples each. Thus, better statistical correlations may appear with more samples per station.

A decrease in step size did appear after the May 2 main shock, possibly indicating that the large strain release at that time used up the local stored slip "budget" (fig. 23.4*C*). For example, an M=6.2 aftershock on July 22 produced steps comparable to or only slightly larger than those during an M=5.0 earthquake 40 days earlier. Figure 23.4*C* suggests that the amount of slip stored near a station at the time of an earthquake will strongly influence coseismic-step size.

CONCLUSIONS

The May 2 earthquake disrupted creep patterns at several Parkfield stations. Large coseismic steps were followed by creep stoppage of 5 months at station XSC1 and of 9 months at stations XPK1 and WKR1 (April 1984). The earthquake had a minimal effect at station XGH1, near the south end of the creeping station, but appears to have completely altered the creep pattern at station XMM1, close to the epicenter of the 1934 and 1966 Parkfield earthquakes.

We found no clear correlation in plots of coseismic-step size to earthquake magnitude or to distance from each earthquake focus. However, data from two of six stations in a multiple-linear-regression analysis showed a linear correlation between coseismic-step size and earthquake magnitude, significant at the 95-percent-confidence level. None of the data showed a linear correlation between step size and distance to earthquake focus. We conclude that we need more M>5.0 earthquakes to perform definitive statistical tests.

Step sizes generally leveled off after the May 2 main shock. We conclude that the large steps on May 2 released slip stored on the fault, and repeated aftershocks evoked comparatively little response because of the absence of local stress. If so, then local stored stress is probably the dominant factor in coseismic-step size.

We do not know whether the disruption caused by the May 1983 Coalinga seismicity may have advanced or delayed onset of the next Parkfield earthquake. On the basis of observations in 1966, we hope to observe premonitory creep at least several hours before such a shock. Owing to the variety of local slip patterns, premonitory creep must exceed routine event sizes, or occur simultaneously at several stations, to be recognized. Given the diverse instrumental responses to the Coalinga disturbance, and the subsequent disruption of local creep rates, any premonitory creep signals that do occur at Parkfield may be highly ambiguous.

AUTHOR'S NOTE, AUGUST 1987

Since this chapter was submitted in 1984, several noteworthy changes have occurred. One Parkfield creepmeter data set (XPK1) shows a return to the pre-1983 creep rate, with no apparent overall slip deficit. Resumption of right-lateral creep at XPK1 on August 9, 1985, coincided with an M=3.55 aftershock of the Kettleman Hills earthquake (M=3.5; Aug. 4, 1985).

The most striking effect recorded after the Coalinga earthquake in 1983 was reversal of creep from right- to left-lateral at station XMM1. Resumption of right-lateral movement was recorded at the station in summer 1984, coincident with a swarm of M<2.0 earthquakes at depths greater than 6.5 km under the station (Poley and others, 1987).

Five stations (XSC1, XMM1, XDR1, WKR1, CRR1) continue to record rates decreased from pre-1983 values; data from two stations at the south end of the valley (XGH1, TWR1) currently indicate higher rates. Data from one station (TWR1) show a cumulative slip surplus of 2 mm. Six data sets show cumulative slip deficits ranging from 10 to 35 mm.

The 1984–87 data are summarized in table 23.4 and illustrated in fig. 23.5. Our conclusions of April 1984 remain unchanged.

REFERENCES CITED

Goulty, N.R., and Gilman, R., 1978, Repeated creep events on the San Andreas fault near Parkfield, California, recorded by a strainmeter array: Journal of Geophysical Research, v. 83, no. B11, p. 5415–5419.

TABLE 23.4.—*Creep rates recorded at eight Parkfield, Calif., creepmeters, 1983–87*

[Rates determined by best-fit lines drawn through data. Negative values indicate left-lateral movement]

Station	Pre–1983 rate (mm/yr)	Unusual rates		Cumulative slip deficit or surplus (mm)	Comments
		(yr)	(mm)		
XSCI	23	1980-83	19	-19	--------
		1983–87	20		
XMM1	17-19	1983-84	-6	-30	RL creep resumed in 1984, coincident with swarm of M<2.0 earthquakes at depths greater than 6.5 km under station.
		1984–85	12		
		1985–87	15-17		
XPK1	7.5	1983–85	0	0	RL creep resumed coincident with 8/9/85 $M = 3.55$ aftershock of Kettleman Hills earthquake ($M = 3.5$, 8/4/85).
		1985–86	13		
		1986–87	7.5		
XDR1	8-9.5	1983–87	7.5	-11.5	--------
WKR1	11	1983–86	2	-14	$M = 4.0$ earthquake in 1986 in Parkfield, followed shortly by $M = 3.0$ earthquake near Gold Hill, apparently triggered an increase.
		1986–87	10		
CRR1	6	1983–87	3.5	-35	Cultivation, planting, and seasonal irrigation that began in 1984 add noise to signal.
XGH1	3.5	1983–86	.5	-12.5	Large surge in 1986 precedes an $M = 4.0$ earthquake in Parkfield and an $M = 3.0$ earthquake near Gold Hill.
		1986–87	4.5		
TWR1	-1	1983–87	-1.6	+2	--------

Mavko, G.M., Schulz, S.S., and Brown, B.D., 1984, Effects of the 1983 Coalinga, California, earthquake on creep along the San Andreas fault: Seismological Society of America Bulletin, v. 75, no. 2, p. 475–489.

Poley, C.M., Lindh, A.G., Bakun, W.H., and Schulz, S.S., 1987, Temporal changes in microseismicity and creep near Parkfield, Calif.: Nature, v. 327, no. 6118, p. 134–137.

Roger, J., Johnston, M.J.S., Mortensen, C.E., and Myren, G.D., 1977, A multi-channel digital telemetry system for low frequency geophysical data: U.S. Geological Survey Open-File Report 77-490, 111 p.

Scholz, C.H., Wyss, Max, and Smith, S.W., 1969, Seismic and aseismic slip on the San Andreas fault: Journal of Geophysical Research, v. 74, no. 8, p. 2049–2069.

Schulz, S.S., Mavko, G.M., Burford, R.O., and Stuart, W.D., 1982, Long-term creep observations in central California: Journal of Geophysical Research, v. 87, no. B8, p. 6977–6982.

Schulz, S.S., Burford, R.O., and Mavko, Barbara, 1983, Influence of seismicity and rainfall on episodic creep on the San Andreas fault system in central California: Journal of Geophysical Research, v. 88, p. 7475–7484.

Wallace, R.E., and Roth, E.F., 1967, Rates and patterns of progressive deformation, *in* Brown, R.D., Jr., Vedder, J.G., Wallace, R.E., Roth, E.F., Yerkes, R.F., Castle, R.O., Waananen, A.O., Page, R.W., and Eaton, J.P., The Parkfield-Cholame, California, earthquakes of June–August 1966—surface geologic effects, water-resources aspects, and preliminary seismic data: U.S. Geological Survey Professional Paper 579, p. 23–40.

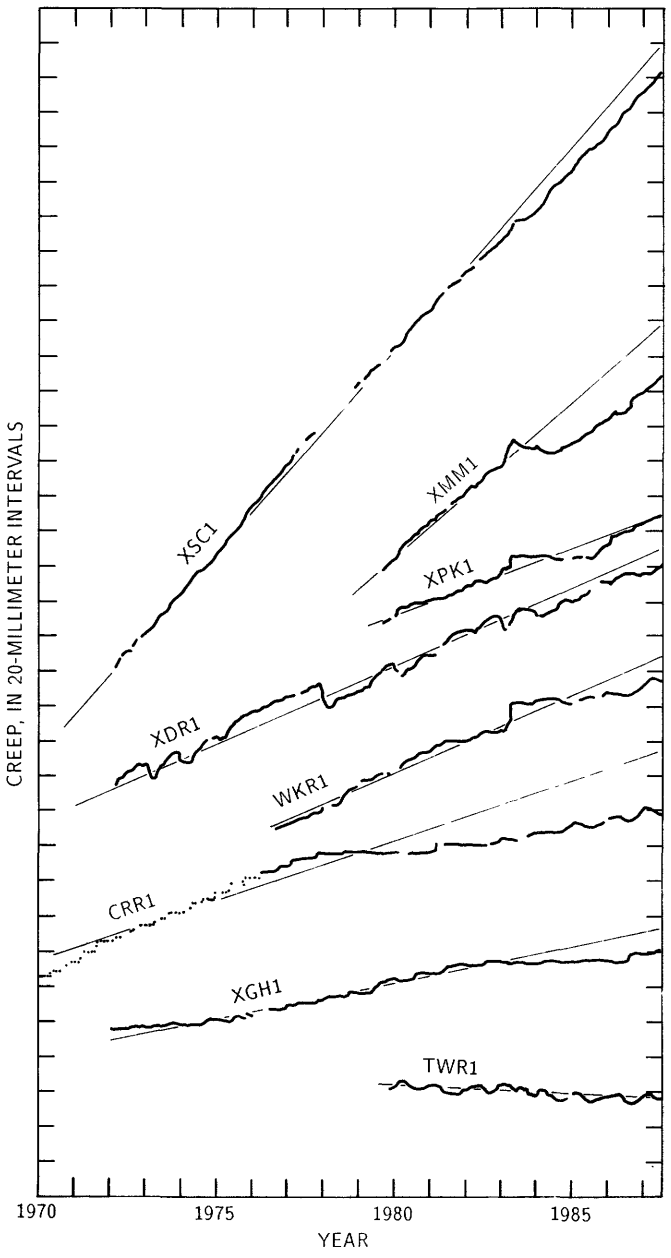

FIGURE 23.5.—Long-term creep patterns at stations near Parkfield, updated through July 1987 (see section in text entitled "Author's Note, August 1987").